Die Küste, 63 Global Storm Surges (2001), 1-623

# GLOBAL STORM SURGES

## Theory, Observations and Applications

by
Gabriele Gönnert, Shishir K. Dube,
Tad Murty and Winfried Siefert

Edited by:
German Coastal Engineering
Research Council

Die Küste

ARCHIV FÜR FORSCHUNG UND TECHNIK
AN DER NORD- UND OSTSEE

ARCHIVE FOR RESEARCH AND TECHNOLOGY
ON THE NORTH SEA AND BALTIC COAST

Sonderheft

# GLOBAL STORM SURGES

## Theory, Observations and Applications

by
Gabriele Gönnert, Shishir K. Dube,
Tad Murty and Winfried Siefert

Edited by:
German Coastal Engineering
Research Council

Heft 63 · Jahr 2001

Herausgeber: Kuratorium für Forschung im Küsteningenieurwesen

Druck- und Kommissionsverlag:
Westholsteinische Verlagsanstalt Boyens & Co. Heide i. Holstein

ISSN 0452-7739
ISBN 3-8042-1054-6

Anschriften der Verfasser dieses Heftes:

MURTY, TAD, Dr., c/o Baird & Associates, 1145 Hunt Club Rd, Suite 1, Ottawa, Ontario K1V 0Y3, e-mail: tmurty@baird.com; DUBE, SHISHIR K., Prof. Dr., Centre for Atmospheric Sciences (CAS), Hauz Khas, New Delhi 110 016, India, e-mail: skdube@cas.iitd.ernet.in; GÖNNERT, GABRIELE, Dr., Department of Port and River Engineering, Dalmannstr. 1–3, 20457 Hamburg, e-mail: Gabriele.Goennert@ht.hamburg.de

---


Vorsitzender des Kuratoriums: Dr.-Ing. CHR. HEINZELMANN, Robert-Schuman-Platz 1, 53175 Bonn
Geschäftsführer: Dr.-Ing. V. BARTHEL, Am Alten Hafen 2, 27472 Cuxhaven
Schriftleitung „DIE KÜSTE“: Dr.-Ing. V. BARTHEL, Am Alten Hafen 2, 27472 Cuxhaven

Die Küste, 63 Global Storm Surges (2001), 1-623

# Prof. Dr. Winfried Siefert

6th March 1940 to 17th March 1999

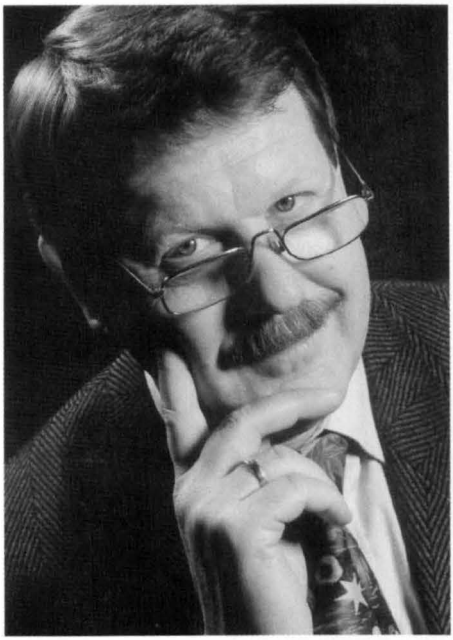

Winfried received his Ph.D. in Hydraulic Engineering in 1968 at the Franzius Institut, University of Hannover, and his thesis topic was storm surge forecasting. Thus began his life long interest in tidal and storm surge research.

Many projects concentrated on the Elbe Estuary but were followed by topics such as environmental impact in the Wadden Sea, morphology and wave climate. The latter was also the topic of his habilitation in Hydraulic Engineering. His interest in storm surges never diminished, and he gave new dimensions to storm surge prediction and established himself as not only a national, but also an international expert in this field of great practical importance. He developed very precise storm surge forecasting methods for Hamburg and contributed to the definition of design water levels for dikes.

During the IUGG conference in 1987 held in Vancouver, Canada, Tad Murty and Winfried Siefert met for the first time, even though they had been well aware of each other's work for a long time. At that first meeting mutual collaboration was discussed and as a consequence, Winfried spent six weeks visiting Tad at the Institute of Ocean Sciences, Department of Fisheries and Oceans, in Victoria, Canada. Subsequent to this visit, both collaborated within the International Hydrology Programme of UNESCO. They organized and participated in three conferences held in Germany in 1991, Netherlands in 1993 and in Thailand in 1995.

Winfried taught coastal engineering as well as carried out research projects at the University of Braunschweig and also at the Technical University of Hamburg. He published more than 100 scientific papers. He was an excellent and very popular teacher and always made difficult and complex appear simple to his students. With his wit and short stories from his research experience, he always made drab and routine topics sound very exciting. His sense of humor facilitated following weary discussions and committee meetings and always led to sensible conclusions.

We, the co-authors, Gabriele Gönnert, Shishir Dube and Tad Murty express our deep appreciation and gratitude not only to an accomplished scientist, but also to a great colleague and friend, without whose vision and dedicated effort, this monograph would not have been possible. Therefore, we dedicate it to him. His friends and colleagues around the world, particularly in the field of storm surge research, will greatly miss him.

# Global Storm Surges: Theory, Observations and Applications

GÖNNERT, G. M. / DUBE, S. K. / MURTY, T. S. / SIEFERT, W.

## Vorwort

Im Mai 1979 bat die World Meteorological Organization (WMO) den Meteorologen Dr. TAD MURTY, Wissenschaftler bei der Bundesregierung von Kanada, den meteorologischen Dienst von Bangladesh (BMD) bei der Entwicklung von Sturmflutvorhersagemodellen für Bangladesh zu unterstützen. Bei der Literaturrecherche stellte er fest, dass es kein umfassendes Lehrbuch über Sturmfluten gab. Mit Unterstützung der Bundesregierung von Kanada schrieb er deshalb das Buch „Storm Surges – Meteorological Ocean Tides", das 1984 als Monographie veröffentlicht wurde. Die dem Buch zugrunde liegenden Literaturrecherchen reichten bis in das Jahr 1982.

Wegen der starken Entwicklung in der Sturmflutforschung in den Jahren 1985 bis 1995 schlugen viele Kollegen TAD MURTY vor, das Buch zu überarbeiten und die neuesten Forschungsergebnisse einzubeziehen. Während einer Diskussion mit dem verstorbenen Prof. Dr.-Ing. WINFRIED SIEFERT, Leiter der Hydrologie in der Wirtschaftsbehörde Strom- und Hafenbau Hamburg und Experte in den Bereichen Sturmfluten und Vorhersage, einigte man sich auf eine gemeinsame Überarbeitung und Neuauflage dieses Buches. In den Kreis der Mitautoren wurden Prof. Dr. SHISHIR K. DUBE aus Indien, der zu den wichtigsten Sturmflutmodellierern der Welt gehört, und Dr. GABRIELE GÖNNERT, wissenschaftliche Mitarbeiterin von Prof. SIEFERT bei der Wirtschaftsbehörde Strom- und Hafenbau Hamburg, einbezogen. Frau GÖNNERT hat zudem die Veröffentlichung des neuen Buches mit dem Titel „Global Storm Surges: Theory, Observations und Applications" geplant und organisiert. Es war die Absicht der Autoren, die wichtigen und grundlegenden Abschnitte der Monographie „Storm Surges – Meteorological Ocean Tides" von Dr. MURTY in einer überarbeiteten Version zu übernehmen.

Zwei Treffen von je einer Woche in Hamburg 1996 und 1998 dienten der Koordination der Buchinhalte, die von den vier Autoren geschrieben wurden. Das Abschlusstreffen über zwei Wochen fand im Centre of Atmospheric Sciences, Indian Institute of Technology, Delhi, Indien, statt. Hier wurde das gesamte Manuskript fertiggestellt.

Das Bundesministerium für Forschung und Technologie (BMBF) stellte Fördermittel für die Arbeit am Buch, die Arbeitstreffen und den Druck zur Verfügung. Darüber hinaus entschied das Kuratorium für Forschung im Küsteningenieurwesen (KFKI), dass das Buch als Sonderheft des *Archivs für Forschung und Technik an Nord- und Ostsee „Die Küste"* erscheinen soll. Für Beantragung von Geldmitteln für den Druck, Organisation und Revision des Buches danken die Autoren Dr.-Ing. V. BARTHEL.

Dr. GÖNNERT möchte den Mitgliedern der Projektgruppe des Forschungsprojektes „Windstauanalysen in Nord- und Ostsee" mit LBD P. PETERSEN, Dr.-Ing. G. FLÜGGE, RD H. SCHMIDT, Dr.-Ing. E. RENGER, Prof. Dr.-Ing. H. KUNZ und Dipl.-Ing. D. SCHALLER für die Diskussionen und Ideen während der Forschungsarbeit zu Sturmfluten und der Neubearbeitung des Buches danken. RD R. ANNUTSCH gilt besonderer Dank für die Unterstützung bei der Diskussion wesentlicher Fragen im Forschungsbereich Sturmfluten. Er investierte viel Zeit in die Gespräche zum Thema Tide und Sturmfluten.

Keine Worte können den tiefen Dank von Dr. GÖNNERT gegenüber Prof. Dr.-Ing. WINFRIED SIEFERT realistisch beschreiben. Er war ihr Lehrer im Küsteningenieurwesen, Doktorvater und ihr Vorgesetzter in der Hydrologie bei Strom- und Hafenbau Hamburg.

Prof. DUBE dankt dem Indian Institute of Technology, Delhi, und hier besonders Direktor Prof. V. S. RAJU dafür, dass er alle Einrichtungen des Instituts zur Verfügung stellte sowie für die moralische Unterstützung bei der Fertigstellung des Buches. Großer Dank geht an Prof. SINHA, Dr. A. D. RAO, Dr. P. CHITTIBABU, Dr. BHASKARAN, Ms. RUCHI KALRA und Mr. DEBASIS MAHAPATRA vom Centre for Athmospheric Sciences, IIT Delhi für ihre Beiträge.

Dr. MURTY dankt der Regierung von Kanada, die das erste Buch ermöglicht hat, und dem Ingenieurbüro Baird and Associates Coastal Engineers, Ottawa, Kanada, für die Möglichkeit, das zweite, hier vorliegende Buch, zu erstellen. Dank und Anerkennung gilt weiterhin den Beiträgen von Prof. GEORGE W. PLATZMAN von der Universität von Chicago und den Kollegen Dr. D. RAO, Dr. R. F. HENRY sowie den verstorbenen Dr. T. J. SIMONS und Dr. M. I. EL SABH bei der Weiterentwicklung des Verständnisses des Sturmflutphänomens. Dr. M. B. DANRD und Dr. JOHN LUICK und dem verstorbenen Dr. N. G. FREEMAN sei ebenfalls für ihre Beiträge gedankt.

## Preface

In May 1979 the World Meteorological Organization (WMO) invited Dr. TAD MURTY, a senior Research Scientist working for the Federal Government of Canada, to help the Bangladesh Meteorological Department (BMD) with the development of storm surge prediction models for the Bay of Bengal. Dr. MURTY looked for lecture material on storm surges for talks in Bangladesh and elsewhere and found that as yet there was no textbook on storm surges. Using the resources of the Canadian Government, he wrote a book titled "Storm Surges – Meteorological Ocean Tides" which was published as a monograph by the Canadian Government. This book was published in October 1984, and the references that were cited were up to date till the end of 1982.

During the years 1985 to 1995, several colleagues of MURTY around the world suggested to him that in view of the tremendous advances made in storm surge research during those years, it will be very useful for the global research community to have an updates version of the book which includes a synthesis of the new material and this should be the goal of an updated version. In 1995 during discussions with the late Dr. WINFRIED SIEFERT, head of hydrology at the Department of Port and River Engineering of Free and Hanseatic City of Hamburg and specialist in storm surges and protection, Drs. MURTY and SIEFERT realised that the book by Dr. MURTY should be updated. Subsequently Prof. SHISHIR K. DUBE, an eminent storm surge modeler from India, who is among the top surge modelers in the world was recruited to be a co-author in this effort. Also Dr. GABI GÖNNERT, scientist for climatology, tides, storm surges and protection at the Department of Port and River Engineering of Free and Hanseatic City of Hamburg was recruited to be a co-author and she took the lead in organizing, planning and publication of the new book, which is titled "Global Storm Surges: Theory, Observations and Applications". It is the intention in this new book to use necessary and basic parts from the monograph of Dr. MURTY "Storm Surges – Meteorological Ocean Tides". Therefore revised repetitions from the book of MURTY (1984) were included in the new book.

Two meetings (each one week long) were held in Hamburg during 1996 and 1998 to coordinate the parts written by the four authors. A final meeting, two weeks long was held at

the Centre for Atmospheric Sciences, Indian Institute of Technology, Delhi, India, to put together the full manuscript.

The Federal Government of Germany (BMBF) provided funding for work on the book, for the necessary meetings and for printing. Moreover, the Coastal Engineering Research Council (KFKI) decided to have the book printed as a special issue of "Die Küste". For providing funding for printing, organization and for reviewing the book the authors express their gratitude to Dr. V. BARTHEL.

Dr. GÖNNERT would like to recognize the contributions of the members of the working group for the research project "Storm Surges in the German Bight" with LBD PETERSEN, Dr. G. FLÜGGE, RD H. SCHMIDT, Dr. E. RENGER, Prof. Dr. H. KUNZ and Dipl.-Ing. D. SCHALLER for discussion and productive ideas enabling her research in storm surges and revising this book. RD RALF ANNUTSCH's help is greatly acknowledged. He assisted in developing her understanding in storm surges and took always time for discussions on tides and storm surges.

No words can describe realistically Dr. GÖNNERT's acknowledgement of and deep gratitude towards the late Prof. Dr. W. SIEFERT. He was her teacher in coastal engineering, supervisor and head at the Department of Port and River engineering.

Professor DUBE is grateful to the Indian Institute of Technology Delhi in general and Professor V. S. RAJU, Director in particular for extending all facilities and providing moral support for the completion of the book. Contributions made by Professor P. C. SINHA, Dr. A. D. RAO, Dr. P. CHITTIBABU, Dr. P. K. BHASKARAN, Ms. RUCHI KALRA and Mr. DEBASIS MAHAPATRA of the Centre for Atmospheric Sciences, IIT Delhi is greatly acknowledged.

Dr. MURTY expresses his gratitude to the Government of Canada to make the first book possible and to Baird and Associates Coastal Engineers of Ottawa, Canada, to make the second book possible. He also would like to recognize the contributions from Prof. GEORGE. W. PLATZMAN of the University of Chicago, and his professional colleagues Dr. D. B. RAO, Dr. R. F. HENRY and the late Drs. T. J. SIMONS and M. I. EL-SABH, in developing his understanding of the storm surge phenomena. Contributions made by Dr. M. B. DANARD and Dr. JOHN LUICK and the late Dr. N. G. FREEMAN are also greatly acknowledged.

## Contents

Die Küste, 63 Global Storm Surges (2001), 1-623



# 1. Introduction and General Considerations

## 1.1 Introduction to Oceanographical Aspects of Storm Surges

**Storm surges** are oscillations of the water level in a coastal or inland water body in the period range of a few minutes to a few days, resulting from forcing from the atmospheric weather systems. By this definition, the so-called wind-generated waves (often referred to as wind waves) and swell, which have periods of the order of a few to several seconds, are excluded. The term "storm surge" is commonly used in European literature, especially in the literature pertaining to the water level oscillations in the North Sea. In North American literature, the terms "wind tides" and "storm tides" are also used to refer to the same phenomenon.

Unfortunately, the term "wind tides" has occasionally been used as a synonym for low storm tides and – in aeronomy – to refer to atmospheric tides (which have the same astronomical origin as oceanic tides). Hence, the term will not be used here. The term "storm tide" is used in North American literature in a confusing manner: at times it is used in the same sense as storm surge, and at other times it is used to denote the sum of the storm surge and the astronomical tide. Here, the term will be used only in the latter sense and describes the whole event. Sometimes the term "storm tide" is meant to be the highest peak due to interaction of tide and storm surge. This parameter will be denoted here as "high water level" (HWL). As an alternative to the term "storm surges", the term "meteorological ocean tides" will be used. In some sense, storm surges are similar to astronomical tides: although storm surges are not periodic in the sense that tides are, they do exhibit certain periodicities, and since the forcing functions are due to meteorological causes, it is not inappropriate to call them meteorological ocean tides. Here, the word "ocean" is used to denote a water body of any scale, and not necessarily the oceans. In Russian literature (e.g. see LAPPO and ROZHDESTVENSKIY, 1979), the term "meteorological ocean tide" is commonly used.

The spectrum of ocean waves is shown schematically in Fig. 1.1, and it can be seen that storm surges are centered at about $10^{-4}$ cycles per second (cps or Hz), which gives a period of about 3 h. However, depending mainly on the topography of the water body and secondarily on other parameters, such as the direction of movement of the storm, strength of the storm, stratification of the water body, presence or absence of ice cover, nature of tidal motion in the water body, etc., the periods in the water level oscillations may vary consider-

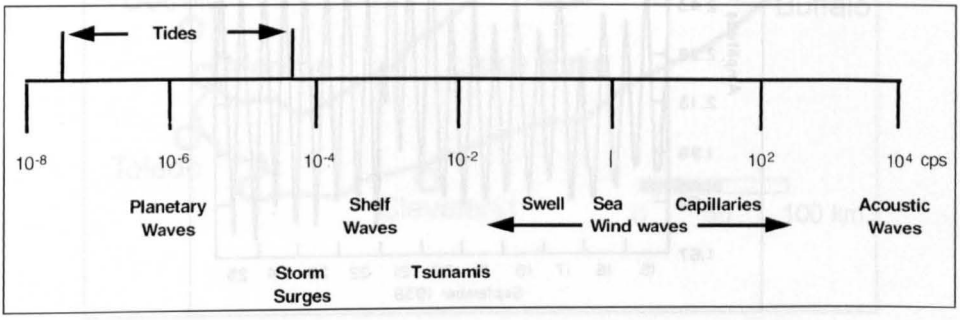


Fig. 1.1: Frequencies of oceanic wave motion in cycles per second (cps) (PLATZMAN, 1971)

ably. Even the same water body, storm surge records at different locations can exhibit different periods.

Although storm surges belong to the same class known as long waves, as do astronomical tides and tsunamis, there are at least two important differences. First, whereas tides and tsunamis occur on the oceanic scale, storm surges are simply a coastal phenomenon. Second, significant tsunamis and tides cannot occur in a completely closed small coastal or inland water body, but storm surges can occur even in completely enclosed lakes, or in canals and rivers.

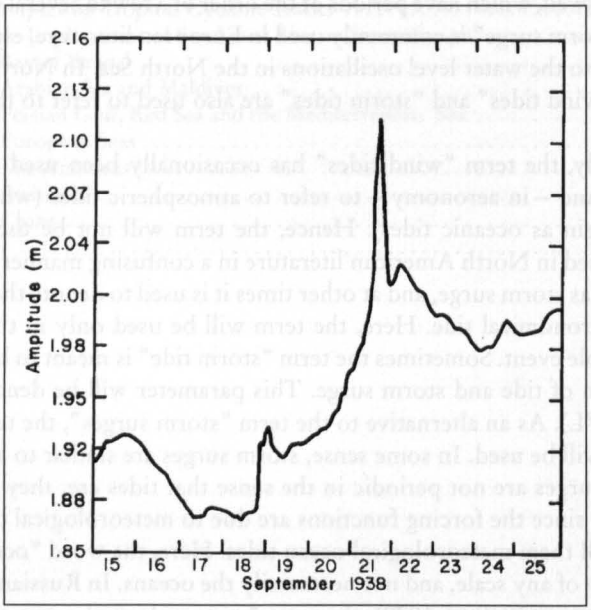


Fig. 1.2: Storm Surge at Forest Hills, New York (PAULSEN et al., 1940)

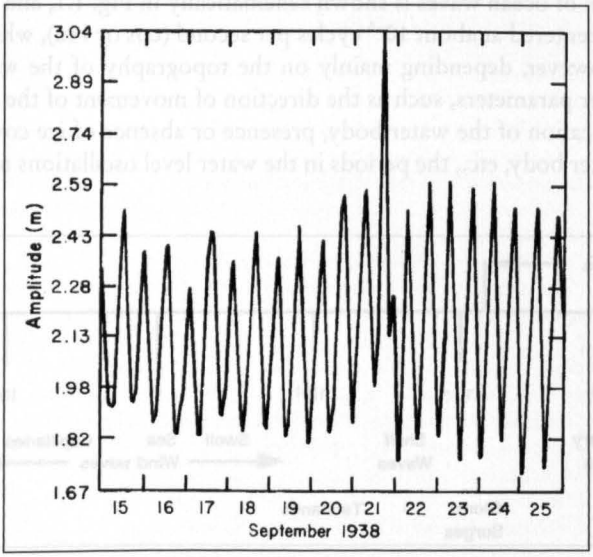


Fig. 1.3: Storm Surge at Rockaway Park, New York (PAULSEN et al., 1940)

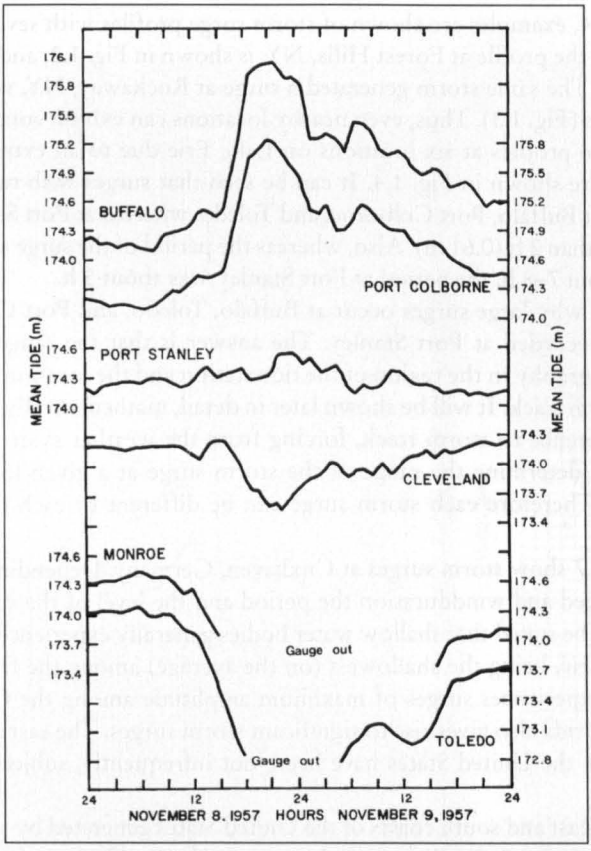


Fig. 1.4: Observed storm surges at six locations on Lake Erie. Mean tides are shown on the left ordinate for Buffalo, Port Stanley, and Monroe and on the right ordinate for Port Colborne, Cleveland, and Toledo. Mean tides are metres above the Great Lakes Datum with reference to the mean tide at New York (HUNT, 1959)

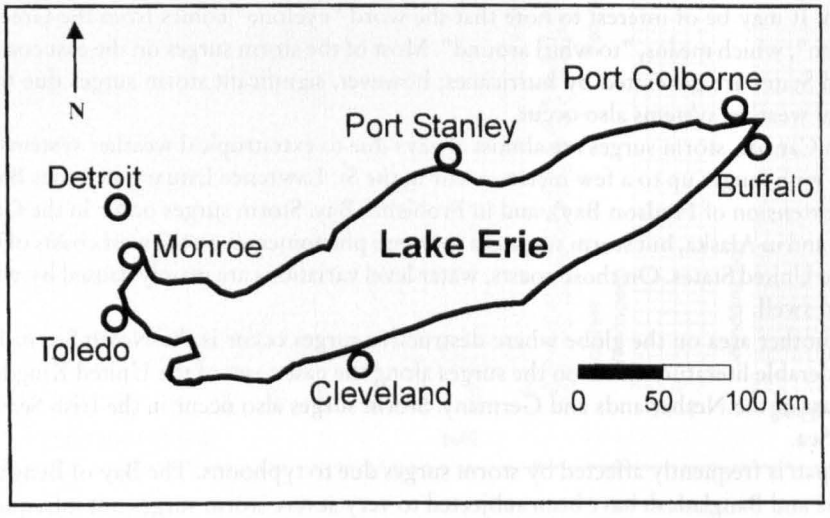


Fig. 1.5: Map of Lake Erie

In Fig. 1.2–1.4, examples are shown of storm surge profiles with several different periods. For example, the profile at Forest Hills, NY, is shown in Fig. 1.2, and a period of about 2.5 d can be seen. The same storm generated a surge at Rockaway, NY, with periods of the order of 1 d or less (Fig. 1.3). Thus, even nearby locations can exhibit considerably differing periods. The surge profiles at six locations on Lake Erie due to an extratropical storm in November 1957 are shown in Fig. 1.4. It can be seen that surges with ranges of up to 8 ft (2.4 m) occurred at Buffalo, Port Colborne, and Toledo, whereas at Port Stanley the range of the surge was less than 2 ft (0.61 m). Also, whereas the period of the surge at Buffalo and Port Colborne was about 7–8 h, the period at Port Stanley was about 3 h.

One may ask why large surges occur at Buffalo, Toledo, and Port Colborne and only small surges are recorded at Port Stanley. The answer is that the range of the surge depends on the topography in the region of the tide station and the location of the tide station relative to the storm track. It will be shown later in detail, mathematically, how topography, position with reference to storm track, forcing from the weather systems, plus a host of secondary factors determine the range of the storm surge at a given location in a specified water body. Therefore each storm surge can be different to each other at one location.

Fig. 1.6 and 1.7 show storm surges at Cuxhaven, Germany. Depending upon the winddirection, windspeed and windduration the period and the level of the surge differs considerably. But it can be stated that shallow water bodies generally experience surges with greater ranges. Lake Erie, being the shallowest (on the average) among the five Great Lakes of North America, experiences surges of maximum amplitude among the Great Lakes. Lake Okeechobee in Florida also gives rise to significant storm surges. The east coast and the Gulf of Mexico coast of the United States have been, not infrequently, subjected to destructive storm surges.

Surges on the east and south coasts of the United States generated by tropical storms are referred to as "hurricanes". Similar tropical storms in the Pacific are referred to as "typhoons". (The Japanese refer to them also as "Reppus".) In Australia, they are called "willy-willies", in the Philippines "Baguios", and in Arabia "Asifat". Tropical cyclones in the Indian Ocean, Bay of Bengal, and the Arabian Sea are popularly referred to as "depressions", although there is a strict classification based on maximum wind speed attained in the weather system. It may be of interest to note that the word "cyclone" comes from the Greek word „kyklon", which means, "to whirl around". Most of the storm surges on the east coast of the United States are generated by hurricanes; however, significant storm surges due to extratropical weather systems also occur.

In Canada, storm surges are almost always due to extratropical weather systems. Storm surges with ranges up to a few metres occur in the St. Lawrence Estuary, in James Bay (southern extension of Hudson Bay), and in Frobisher Bay. Storm surges occur in the Canadian Arctic and in Alaska, but storm surge is a very rare phenomenon on the west coasts of Canada and the United States. On those coasts, water level variations are mainly caused by wind waves and swell.

Another area on the globe where destructive surges occur is the North Sea in Europe. Considerable literature exists on the surges along the east coast of the United Kingdom and the coast of the Netherlands and Germany. Storm surges also occur in the Irish Sea and the Baltic Sea.

Japan is frequently affected by storm surges due to typhoons. The Bay of Bengal coasts of India and Bangladesh have been subjected to very severe storm surges not infrequently. It will be seen later that the peculiar topography (i.e. triangular or V-shaped basin), shallowness

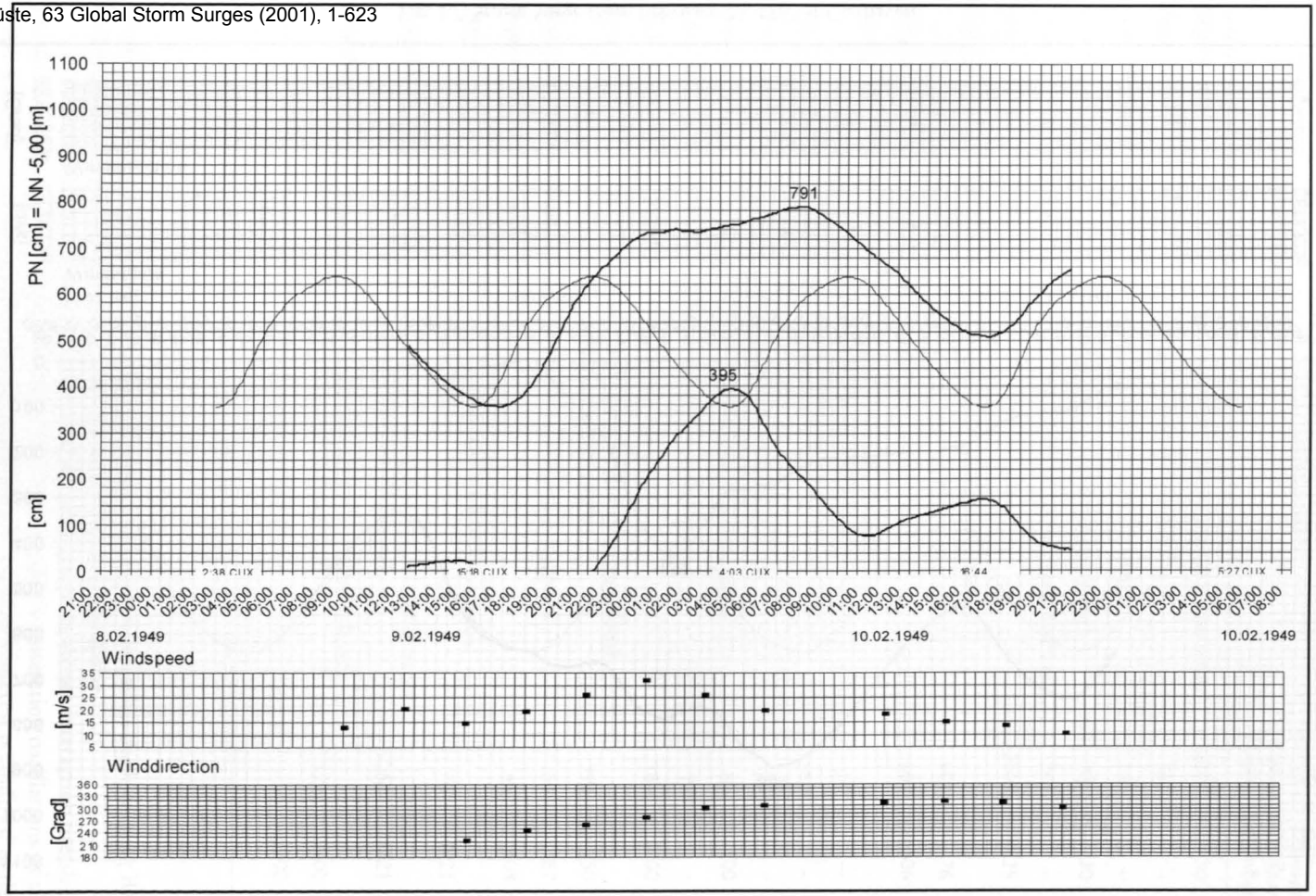


Fig. 1.6: Storm Surge from February 10, 1949 at Cuxhaven

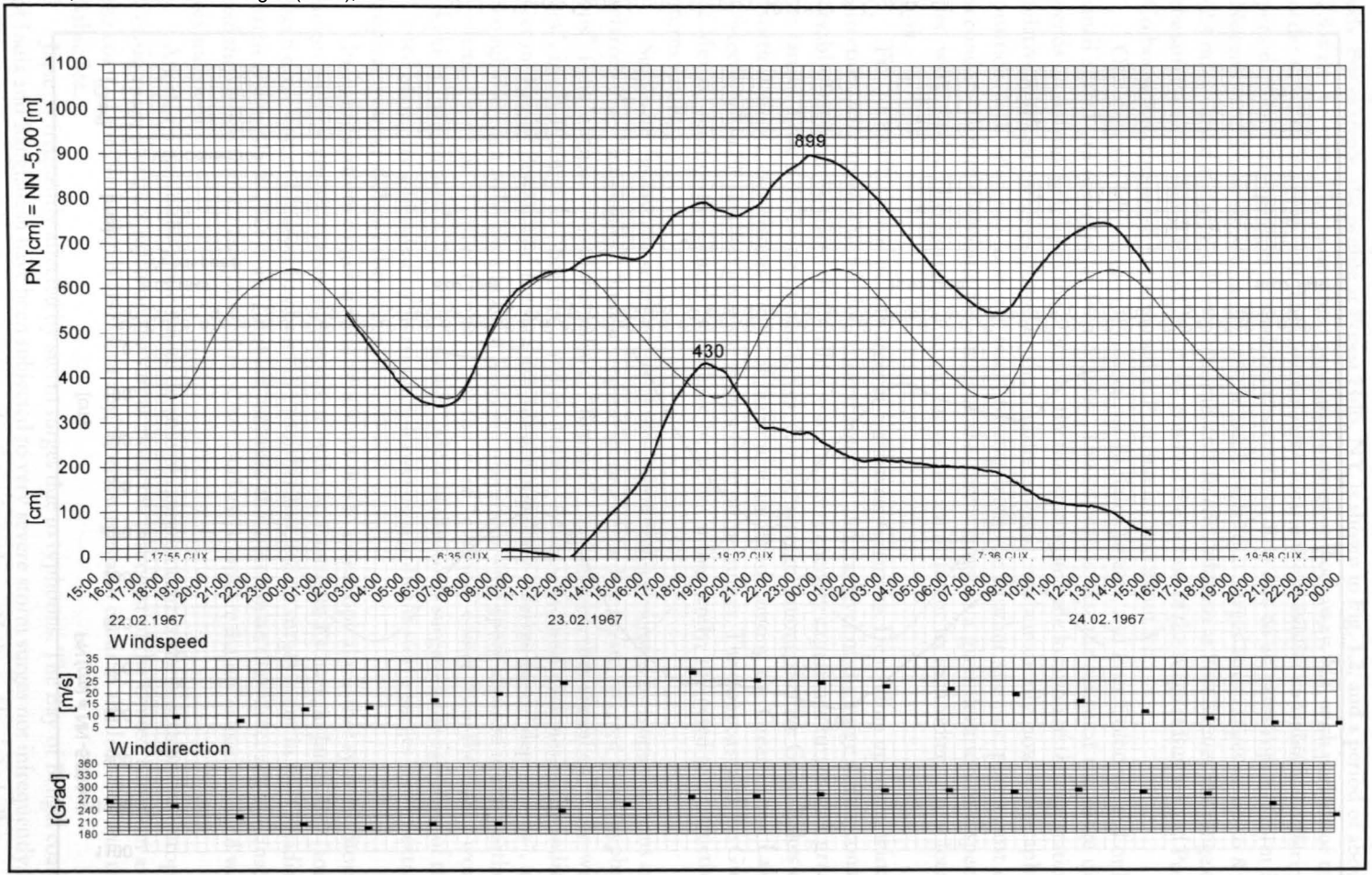


Fig. 1.7: Storm Surge from February 23, 1967 at Cuxhaven

Table 1.1: Some of the most disastrous hurricanes affecting the United States (1900–1979)

| Date | Name of hurricane | Area affected | No. of people killed | Damage in millions of dollars |
|---|---|---|---|---|
| Sept. 8, 1900 | – | Storm surge at Galveston greater than 6.5 m | 6000 | 30 |
| Sept. 20, 1909 | – | Louisiana coast (Grand Isle) | 353 | – |
| Sept. 29, 1915 | – | Mississippi Delta (New Orleans) | 284 | – |
| Sept. 14, 1919 | – | Florida Keys, Corpus Christi (Texas) | 600–900 | 20 |
| Sept. 20, 1926 | – | Miami and Pensacola to Southern Alabama | 243 | – |
| Sept. 16, 1928 | – | Palm Beach, Okeechobee | 2000 | 25 |
| Sept. 1, 1935 | Labor Day storm | Florida Keys (winds greater than 332 km · $h^{-1}$) | 408 | 76 |
| Sept. 21, 1938 | – | New England and Long Island | 600 | 306 |
| Aug. 7–11, 1940 | – | South-eastern United States (Georgia to Tennessee) | 50 | – |
| Sept. 14–15, 1944 | – | Atlantic coast | 390 | – |
| Sept. 19, 1947 | – | Florida, Louisiana, Mississippi | 51 | – |
| Aug. 31, 1954 | Carol | North Carolina to New England | 60 | 500 |
| Oct. 13–17, 1954 | Hazel | South Carolina to New York | 95 | – |
| Aug. 16–20, 1955 | Diane | Northeast United States | 184 | 1000 |
| June 27, 1957 | Audrey | Texas to Alabama (4-m surge inundated Louisiana 40 km inland) | 390 | 150 |
| Sept. 9–11, 1960 | Donna | Florida, New York, New England | 50 | 387 |
| Sept. 7–12, 1961 | Carla | Texas | 46 | 408 |
| Sept. 8, 1965 | Betsy | Florida, Louisiana, mid-Atlantic States, New England | 75 | 1421 |
| Aug. 15–16, 1969 | Camille | Louisiana, Mississippi, Virginia (7.4-m surge on Pass Christian, Mississippi) | >250 | 1421 |
| Mid-June, 1972 | Agnes | Florida, Virginia, Maryland, Pennsylvania, North Carolina to New York | 122 | 2100 |
| Late Aug.–early Sept. 1979 | David and Frederic | Alabama, Mississippi, Florida | 5 | 2300 |

of the water body, together with a large tidal range make storm surges on the low-lying Bay of Bengal coast more dangerous than in any other region of the globe.

It is recognised by now that the storm surge problem is an air-sea interaction problem; i.e. the atmosphere forces the water body, which responds by generating oscillations of the water level with various frequencies and amplitudes. Our present interest is confined to that part of the oscillation between a few minutes and a few days. Study of the storm surge problem will begin with a consideration of the global weather systems.

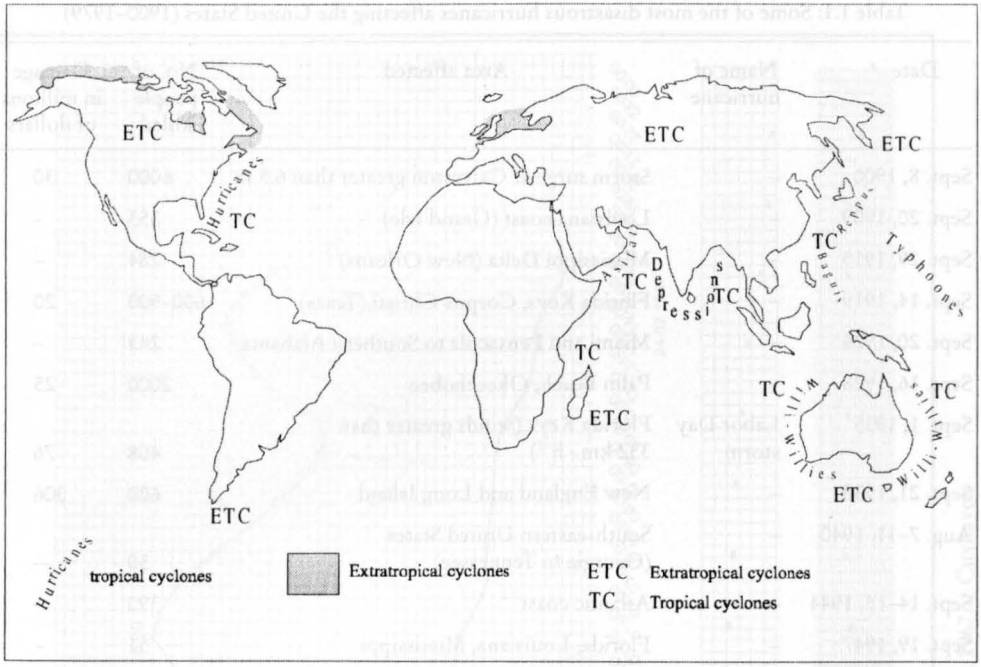


Fig. 1.8: Global Storm Surges due to Tropical Cyclones (TC) and Extratropical Cyclones (ETC)

## 1.2 Global Weather Systems

In order to understand global weather systems, it is convenient to begin with the so-called "general circulation of the atmosphere," which refers to the motion of the atmosphere around the globe in an average sense, both in space and time. Before discussing the general circulation, it is appropriate to introduce certain nomenclature. There are two important characteristics of the atmosphere, which can be seen in Fig. 1.9:

- the pressure decrease with height above the earth surface
- the change of temperature with height above the earth surface.

The pressure decreases with height in a monotonic fashion, as can be seen from the ordinate on the right side of Fig. 1.9. The units of pressure are millibars (another internationally used unit is the kilopascal, 1 kPa = 10 mb). On average, the atmospheric pressure at sea level is 1013.2 mb. The height scale (kilometres) is shown on the left hand side of the graph. For general interest, the maximum heights of three mountain peaks, namely, Mount Everest, Mount Blanc, and Ben Nevis, are included. The heights of different cloud types are also indicated.

The second important characteristic is the change of temperature with height, indicated by the curve in Fig. 1.9. Temperature inversions occur several times with increasing height, and this gives rise to three warm and two cold regions. The warm regions are near the earth's surface, at a height between 40 and 60 km, and above 150 km (i.e. more or less the top of the atmosphere). The first cold region extends from about 10 to 35 km and the second cold region from about 80 to 90 km. The exact distribution of temperature with height depends on latitude and, to a certain extent, on the season.

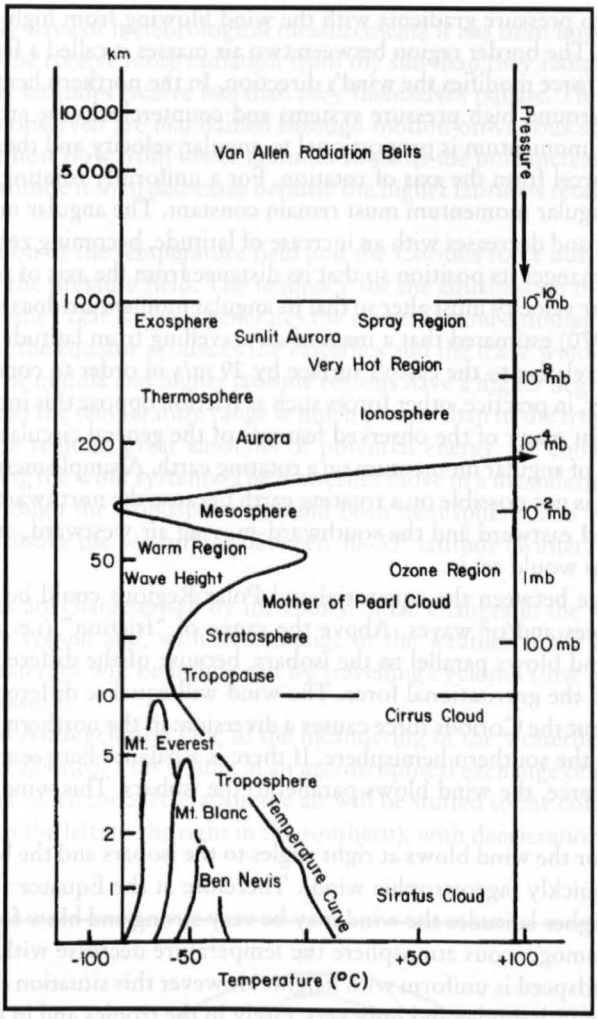


Fig. 1.9: Vertical structure of the atmosphere (DOBSON, 1963)

It can be seen that the temperature decreases from the earth's surface as far as the tropopause. The atmosphere below the tropopause is called the troposphere, and the region immediately above the troposphere is referred to as the stratosphere. The electrical conductivity of air above the 80-km level is much greater than that at lower levels, especially during sunlight hours. This region of the atmosphere, called the ionosphere, allows radio waves to propagate great distances.

The knowledge obtained from the observations of troposphere and stratosphere led to a more definitive theory concerning the general circulation of the atmosphere. The foundation among the general circulation is the interdependence of the three-dimensional fields of temperature, pressure and wind (FLOHN, 1971). There are three possible movements of an air mass: 1) vertical, 2) horizontal and 3) partly vertical and partly horizontal. The vertical movements means that wind blows at the height from warm to cold regions and near the ground from cold to warm areas, which is thermally induced. The horizontal movement of an air

mass occurs due to pressure gradients with the wind blowing from high pressure area to a low pressure area. The border region between two air masses is called a frontal zone.

The Coriolis force modifies the wind's direction. In the northern hemisphere, the wind blows clockwise around high pressure systems and counterclockwise around areas of low pressure. Angular momentum is proportional to angular velocity and the square of the distance of the air parcel from the axis of rotation. For a uniformly rotating earth and atmosphere, the total angular momentum must remain constant. The angular momentum is greatest at the equator and decreases with an increase of latitude, becoming zero at the poles. If a large mass of air changes its position so that its distance from the axis of rotation also changes, then its angular velocity must alter so that its angular momentum does not change. BARRY and CHORLEY (1970) estimated that a mass of air travelling from latitude 42° to 46° would increase its speed relative to the earth's surface by 29 m/s in order to conserve angular momentum. However, in practice, other forces such as friction oppose this increase, but it is important to note that many of the observed features of the general circulation are due to the poleward transfer of angular momentum on a rotating earth. A simple meridional (i.e. north-south) circulation is not possible on a rotating earth because the northward-moving air mass would be deflected eastward and the southward-moving air westward, and thus zonal (i.e. east-west) motions would set in.

Heat exchange between the equatorial and Polar Regions could be achieved through a system of vortices and/or waves. Above the range of "friction" (i.e. above a height of >1–2 km), the wind blows parallel to the isobars, because of the different direction of the Coriolis force and the gravitational force. The wind will equalise differences in pressure at the frontal zone, but the Coriolis force causes a diversion: in the northern hemisphere to the left, to he right in the southern hemisphere. If there is a balance between the gradient force and the Coriolis force, the wind blows parallel to the isobars. This wind is called the geostrophic wind.

At the Equator the wind blows at right angles to the isobars and the balance of pressure is regained very quickly (ageostrophic wind). Therefore at the Equator the winds are very light whereas at higher latitudes the wind may be very strong and blow for a long duration.

In an ideal homogeneous atmosphere the temperature decrease with high is about 10° C/km and the windspeed is uniform with height. However this situation of an ideal air mass never happens in mid-latitudes and only very rarely in the tropics and in the Polar Regions. The horizontal exchange of air is carried out (geostrophically) by travelling weather systems such as cyclones and anticyclones; the ageostrophic wind of the vertical circulation is proportionally much smaller, but cannot be ignored. Furthermore the horizontal component of the movement can either be stable or not unstable. If the horizontal gradient of the wind exceeds a threshold value – which may occur in the frontal zone – the situation of the wind and pressure fields will be changed on a large scale. That will result in the development of new cyclones (low pressure) and anticyclones (high pressure).

In a frontal zone the windspeed is much greater in the upper layers. These strong winds at a high of about 8 to 12 km above sea level are referred to as the Jet stream. There are at least two types of Jet streams, one in the polar front and the other in the subtropics.

For weather and climate purposes, as well as for the atmospheric forcing of storm surges, interest here is primarily in the troposphere and, to a lesser extent, in the lower part of the stratosphere. Earlier, the term "general circulation of the atmosphere" was introduced. In practice, this term is used to describe the more or less permanent wind and pressure systems of the troposphere and the lower stratosphere. To explain the dynamics of the climate system, initially we will omit orographical effects (FLOHN, 1971, BARRY and CHORLEY, 1992)

Since the early days of meteorological measurements it has been known that the tropical areas of the globe receive more radiation from the sun than they radiate back into space, whereas the higher latitudes receive less than they themselves radiate. The average temperature distributions observed are maintained through motion on various scales in the atmosphere. The rate of heat flow from lower latitudes towards the pole increases from the equator to about 35° latitude it then decreases because the higher latitudes retain some of this imported heat.

The distribution of the temperature field and the Coriolis force due to earth's rotation largely determine the pressure field. The tendency for the equalisation of pressure between the subtropics and the Polar Regions generates the westerlies and a similar tendency between the subtropics and the equator produces the easterlies and the trade winds.

**Westerlies:** The middle and higher latitude regions have a higher degree of baroclinicity than the tropics, and the temperature range is much greater than in the tropics. In the middle and higher latitude regions, great amounts of potential energy are converted into kinetic energy, thus creating the wind systems. The westerlies move in a meandering path (Fig. 1.10). They meander through the troposphere around both hemispheres and reach their highest speed at 9–11 km above the sea surface between 30–35° latitude (winter) and in summer at 40–45° latitude.

The westerlies are characterised by instability. Small changes in the Jet stream result in disturbance to the system and, with this, change of the weather at the earth's surface. At the surface the westerlies will be influenced by travelling cyclones (low pressure) and anticyclones (high pressure).

**Cyclones and Anticyclones:** Due to the meandering of the westerlies the wind is both accelerated and decelerated. This results in an ageostrophical exchange of air mass perpendicular to the isobars. With the acceleration the air will be shifted to the cold side (in the northern hemisphere to the left; to the right in the southern), with deceleration on the warm side

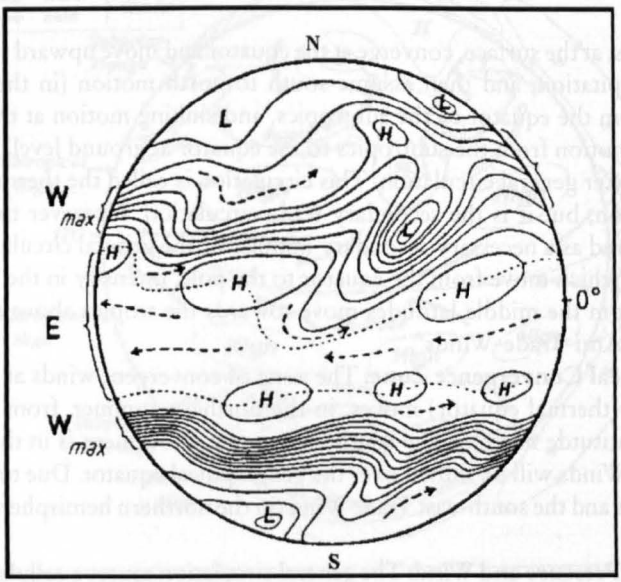


Fig. 1.10: Schematic repesentation of general circulation (4–10 km; line = isobars; winds = broken line; trade = dotted line) (FLOHN, 1971)

(in the northern to the right; to the left in the southern). This results in cells of low and high pressure: cyclones and anticyclones.

Due to the Coriolis force, the cyclones move with their winds rotating around them in an anticlockwise sense in the Northern Hemisphere.

**Secondary Trade Circulation:** The subtropical high pressure cells at 30° latitude north and south indicate a drop in pressure from the subtropics to the equator, which is due to the ageostrophical east wind, the Trade Winds (Fig. 1.11). This Trade Wind may reach a level of 10 km above the sea surface and also have an effect at ground level. Frictional effects mean that the wind at the surface moves to the southeast in the northern hemisphere/northeast in the southern hemisphere.

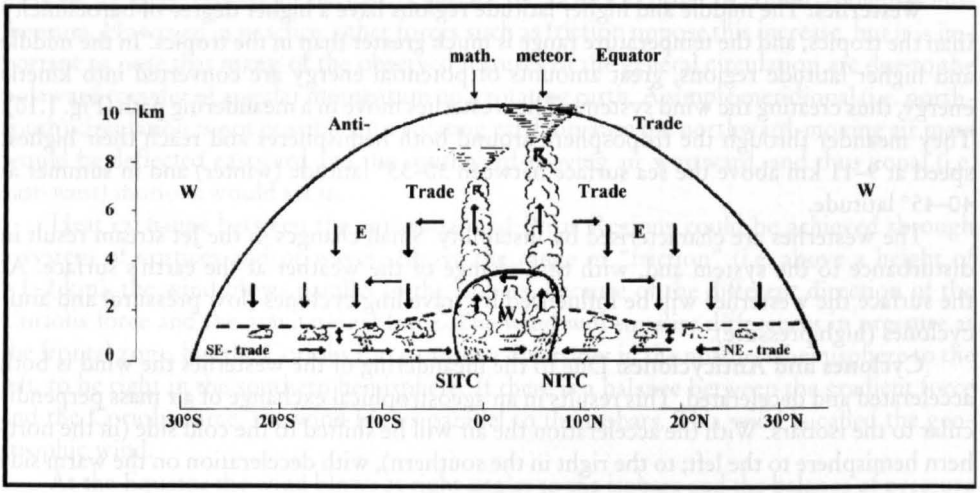


Fig. 1.11: Trade winds with ITCZ and equatorial westerlies (FLOHN, 1971)

These winds, at the surface, converge at the equator and move upward to the tropopause, producing precipitation, and then assume south to north motion (in the northern hemisphere) aloft from the equator to the subtropics, and sinking motion at the subtropics and south to north motion from the subtropics to the equator at ground level, referred to as the thermal motor after general circulation. This circulation is called the thermical motor of the general circulation, but it is the secondary trade circulation. However the thermic motor must be considered as a necessary secondary impulse of the general circulation.

The winds, which move from the equator to the pole, intensify in the westerlies. When the westerlies from the middle latitudes move towards the tropics above the Trade Winds, they are called "Anti-Trade-Winds".

**Inter-Tropical Convergence Zone:** The zone of convergent winds at ground level and lowest pressure (thermal equator) moves, in the northern summer, from the geographical equator to 20° latitutde north, in the southern summer, movement is in the opposite direction. The Trade Winds will be shifted over the geographical equator. Due to this the pressure situation changes and the south-east Trade Wind (in the northern hemisphere) becomes equatorial westerlies.

**Patterns of Pressure and Wind:** The general circulation causes a cellular pattern of pressure and wind at the surface (level of 0–2 km). This structure changes with the season, because of the inclination of the earth and, with this, the changing solar radiation.

It must be considered that the "only true zonal distribution of pressure exists in the region of the subpolar low in the southern hemisphere where the ocean is continuous. To a lesser extent, the equatorial low is zonal. At other latitudes, particularly in the northern Hemisphere, where the bulk of the land exists, large seasonal temperature differences disrupt the idealised zonal patterns." (LUTGENS and TARBUCK, 1986).

The sea level pressure distribution for the month of July (representative of summer in the northern hemisphere) and January (representative of winter) is shown in Fig. 12. It can be seen that the observed pressure regimes are cellular. The high pressure centres are over the eastern side of the Atlantic and Pacific oceans (this affects the west coast climates of adjacent continents), north and south of the equator, South Indian Ocean, Arctic Ocean, and Antarctica. Occasionally, names are given to these centres. For example the one over the eastern Pacific is called the "Hawaiian High" and the one over the eastern Atlantic is called the "Azores High". The low pressure centres are the "Iceland Low" (over the North Atlantic), the "Aleutian Low" (over the North Pacific), and one each over the South Atlantic, South Pacific and Indian oceans in a shifting zone along the equator, and one in the Southern Ocean near Antarctica. The two semipermanent cells, the Iceland Low and the Aleutian Low "represent the great number of cyclonic storms that migrate eastward across the globe and converge in these areas." (LUTGENS and TARBUCK, 1986).

With reference to Fig. 1.13, the following remarks may be made. Pressure is higher and the gradients are steeper in the winter hemisphere (i.e. the hemisphere that has winter at that time), and the pressure centres shift northward in July and southward in January (TREWARTHA, 1968). The pressure belts in the subtropics are more or less continuous in the winter hemisphere, whereas in the summer hemisphere, the heated continents break the continuity. Between the subtropical high and the subpolar lows lies the main zone of travelling

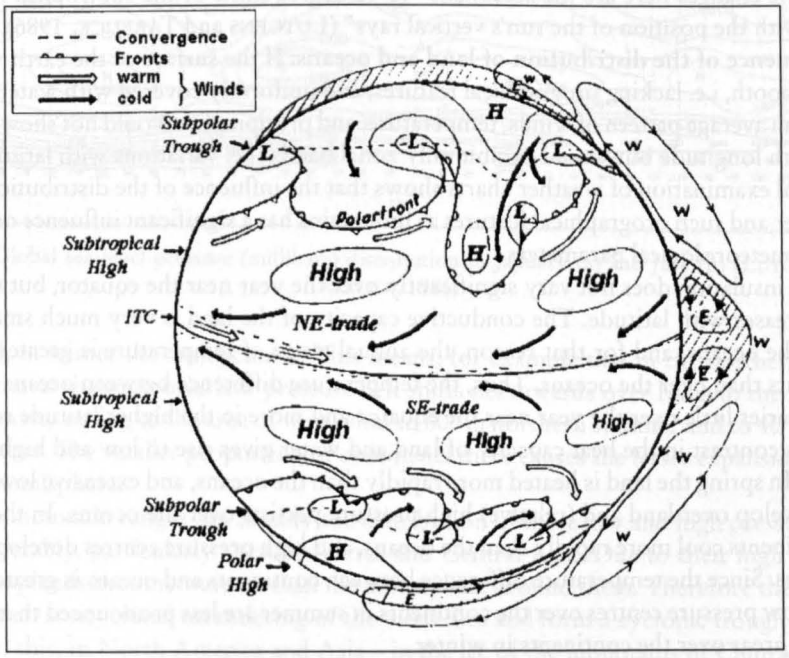


Fig. 1.12: Schematic representation of atmospheric circulation between 0–2 km eight and vertical circulation to 15 km height (FLOHN, 1971)

Table 1.2: Planetary Pressure and vertical Wind Belts

| Pressure belt | latitude | Wind belt (0–3 km) | Wind belt (> 3 km) | |
|---|---|---|---|---|
| Polar High | 80–90° | Polar Easterlies (0–3 km) | westerlies 18–30 km; during winter more than 50 km | Sinking air dominates, with evaporation of clouds and dryness. |
| Subpolar Trough | 55–65° | extratropical (mid-latitude) westerlies | | Cyclonic disturbance with clouds and precipitation moving from west to east. |
| Subtropical High Pressure Area | 25–30° | Tropical Easterlies (Trade; 0–10 km) | | Sinking air dominates, with evaporation of clouds and dryness. |
| Equatorial Trough | 0–10° | Tropical Easterlies and equatorial westerlies | | Cyclonic disturbance with clouds and precipitation moving from west to east. |

cyclones and anticyclones (westerlies). The high and low pressure areas are called centres of action, because their strength over a given period (e.g. week, month or season) as compared with long term averages, is an indication of the departure of the weather from its average.

"Relatively little pressure variation occurs from midsummer to midwinter in the southern hemisphere, a fact we attribute to the dominance of water in that hemisphere. The most noticeable changes here are the seasonal 5- to 10 degree shifts of the subtropical highs that moves with the position of the sun's vertical rays" (LUTGENS and TARBUCK, 1986).

**Influence of the distribution of land and oceans:** If the surface of the earth were perfectly smooth, i.e. lacking orographical features, and uniformly covered with water, then the long-term average pattern of winds, temperature, and precipitation would not show any variation with longitude but would exhibit only zonal bands (i.e. variations with latitude only). A general examination of weather charts shows that the influence of the distribution of land and water and such orographical features as mountains has a significant influence on the patterns of meteorological parameters.

The insulation does not vary significantly over the year near the equator, but the variation increases with latitude. The conductive capacity of the land is very much smaller than that of the oceans, and for that reason, the annual range of temperature is greater over the continents than over the oceans. Thus, the temperature difference between oceans and continents varies little over the year near the equator and more in the higher latitude regions.

This contrast in the heat capacity of land and water gives rise to low and high pressure centres. In spring the land is heated more rapidly than the oceans, and extensive low pressure areas develop over land and (relative) high pressure persists over the oceans. In the autumn the continents cool more rapidly than the oceans, and high pressure centres develop over the land areas. Since the temperature difference between continents and oceans is greater in winter, the low pressure centres over the continents in summer are less pronounced than the high pressure areas over the continents in winter.

The different heat capacity of land and water results in the following significant consequences: in summer the planetary low pressure belts will be taken over the continents and

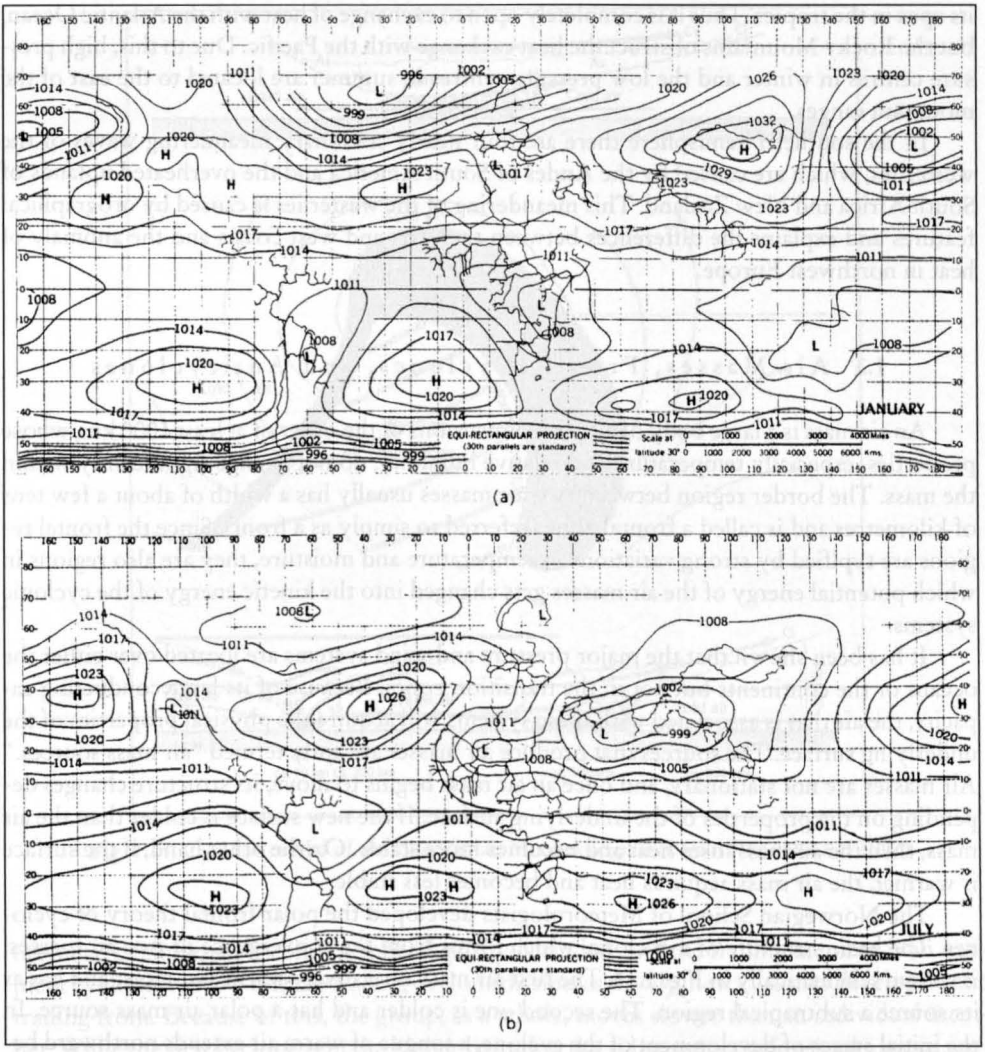


Fig. 1.13: Global sea-level pressure (millibars) distribution in January (a) and July (b) (LUTGENS and TARBUCK, 1986)

reinforced, in winter the anticyclones. This means, for example that in the northern hemisphere summer the equatorial low pressure belt shifts northwards over India to the 30° latitude and an expanding of the area of west wind to 60° in northern summer and to 40° in southern summer. The smaller proportion of continents there causes the lesser expansion in the southern hemisphere.

Large mountain ranges can modify the distribution of these low and high pressure centres considerably, particularly the Cordilleras and Central Asia. Due to their high heating area these uplands become warmer than the atmosphere around them. Therefore the mountains cause an anticyclonal meandering of the westerlies and form a cyclonic trough in their lee. Due to this, in North America and Asia – in the lee of the mountains of Central Asia – there is a high trough with cold air on the eastern side and warm air on the western side (FLOHN, 1971). North America may be considered as a triangle with its base in the Arctic and

its apex in the tropics. Thus it is completely open to exchange of heat with the Atlantic Ocean, but the Rocky Mountains obstruct the heat exchange with the Pacific. Due to this, high pressure centres in winter and the low pressure centres in summer are located to the east of the mountain ranges.

In the southern hemisphere there are four nearly stationary meandering waves of the westerlies, which are caused by the Andes of South America and the overheated uplands of South Africa and New Zealand. This meandering of the westerlies is caused by orographical features and explains the differences between the east- and west coasts and the anomaly of heat in northwest Europe.

## 1.3 Air Masses, Fronts, Cyclones, and Anticyclones

An air mass is a large body of air with dimensions of the order of at least 1000 km, whose properties, especially temperature and relative humidity, do not change significantly within the mass. The border region between two air masses usually has a width of about a few tens of kilometres and is called a frontal zone (referred to simply as a front). Since the frontal regions are typified by strong variations in temperature and moisture, they are also regions in which potential energy of the air masses gets changed into the kinetic energy of the cyclonic systems.

It has been shown that the major pressure and wind systems are located over either the oceans or the continents but not in the transition zones. Because of its large conducting capacity, the air that is associated with these systems will acquire the physical properties of the underlying surface. The sources that produce air masses are aptly termed "air mass sources." Air masses are not stationary, and once an air mass begins to move, its structure changes depending on the properties of the underlying surface. If the new surface is colder than the air mass, then the air mass loses heat and becomes more stable. On the other hand, if the surface is warmer, the air mass acquires heat and becomes less stable.

The Norwegian School of Meteorologists developed the polar frontal theory of cyclones. The basic structure of a cyclone, which forms from the convergence of two air masses, is shown schematically in Fig. 1.14. The first air mass is relatively warm and moist and has as its source a subtropical region. The second one is colder and has a polar air mass source. In the initial stages of development of the cyclone, a tongue of warm air extends northward between these two air masses. The narrow region separating the air masses its the front and is referred to as the polar front, since it represents the southern edge of the polar air mass.

A warm front is one along which cold air is displaced by warm air, and a cold front is one in which the reverse is true; a stationary front is one that does not move.

In the frontal theory of cyclones, the initial stage is characterised by a quasi-stationary front separating a warm and a cold air mass. The next stage involves the development of wave motion on the front, with the subsequent development of a low pressure center. At this stage of cyclogenesis, the cyclone is referred to as nascent. In the next stage, the cold front overtakes the warm front, and this process is called occlusion. With the progress of the occlusion process, the warm air is lifted to higher levels and becomes replaced at the lower levels by colder and heavier air. Because of this, the center of gravity of the air mass is lowered, and large amounts of potential energy are released. This potential energy is converted into kinetic energy of the wind systems that surround the cyclone center.

PETTERSSEN (1969) stated that an extratropical cyclone is usually accompanied by three or four similar cyclones to form a series, or a family. The first member of this family is an

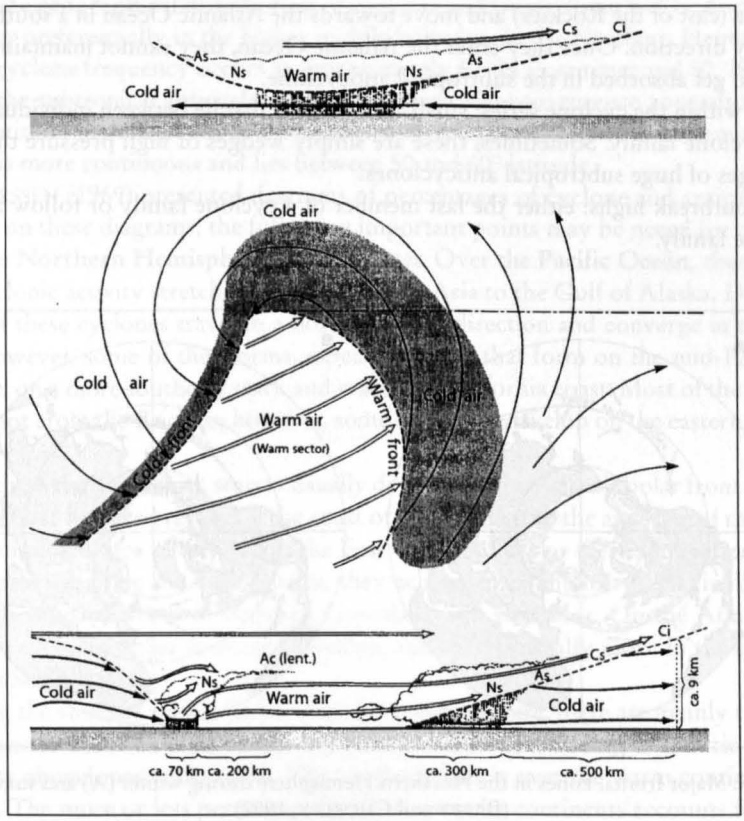


Fig. 1.14: Cyclone model of the Norwegian Meteorological School (WARNECKE, 1997)

occluded cyclone, the second member is partly occluded, and the trailing member is an incipient cyclone wave. While the leading cyclone dissipates slowly, new cyclones develop on the trailing front. Because of this, the group, as a whole, moves slower than an individual member. While the first cyclone is in the higher latitudes, the subsequent cyclones take more southerly paths, and in the rear of the frontal member, cold air moves southward into the subtropics. This phenomenon is called a polar outbreak and will lead to the development of an arctic cyclone. At times, on the surface weather charts, it is difficult to recognise a coherent cyclone family. This is especially true in North America because of the influence of the Rockies. Coherent cyclone families, with three to six members, travel eastward over the northern oceans with a period of 3–8 d.

**Anticyclones**, as the name implies, are opposite to cyclones, i.e. they are centers of high pressure. Their intensities are lower than those of cyclones, they exhibit a more irregular behaviour than cyclones, an as a rule, they move slower. PETTERSSEN (1969) gave the following classification for anticyclones.

(1) Subtropical highs: vast, elongated, and deep (in height) anticyclones located in the subtropics. These are highly persistent, are either stationary or slowly moving, and can be seen on practically any weather chart.

(2) Polar continental highs: anticyclones that develop predominantly over northern continents during winter. In North America, they develop mainly in Alaska and western

Canada (east of the Rockies) and move towards the Atlantic Ocean in a southeasterly to easterly direction. Once they enter the Atlantic Ocean, they cannot maintain their identity and get absorbed in the subtropical anticyclone.

(3) Highs within the cyclone series: small anticyclones that lie between individual members of a cyclone family. Sometimes, these are simply wedges of high pressure that travel at the edges of huge subtropical anticyclones.

(4) Polar-outbreak highs: either the last member of a cyclone family or follow any intense cyclone family.

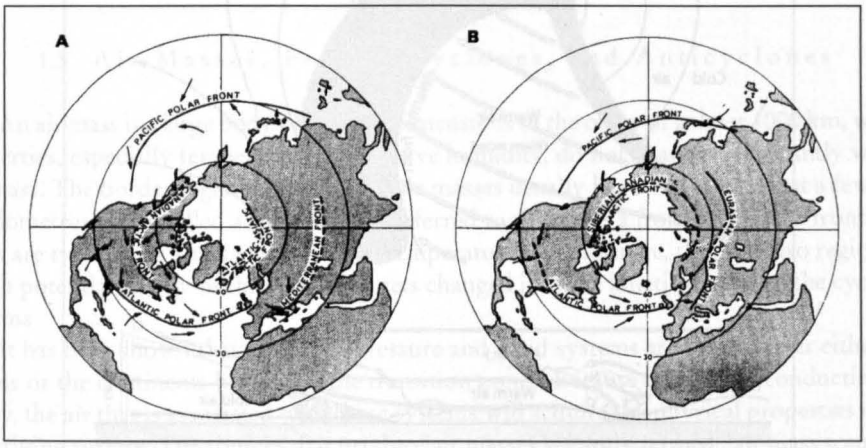


Fig. 1.15: Major frontal zones in the Northern Hemisphere during winter (A) and summer (B) (BARRY and CHORLEY, 1992)

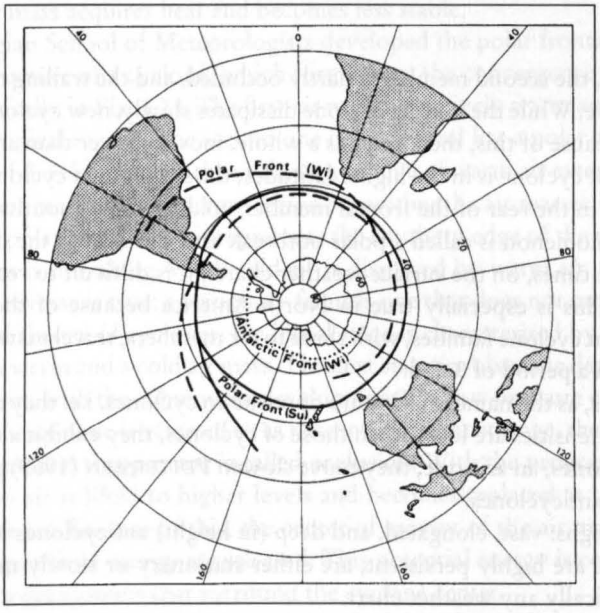


Fig. 1.16: Major frontal zones in the Southern Hemisphere during summer (Su) and winter (Wi) (BARRY and CHORLEY, 1992)

Next, the **geographical distribution** of cyclones and anticyclones will be discussed. Cyclones occur preferentially in the higher middle latitudes. In the Northern Hemisphere, the maximum cyclone frequency occurs at approximately 60 °N in summer and 50 °N in winter. Note that the subtropical anticyclones and the equatorial convergence zone also have a similar 10° latitude seasonal shift. In the Southern Hemisphere, the belt of maximum cyclone frequency is more continuous and lies between 50 and 60° latitude.

PETTERSSEN (1969) presented diagrams of percentages of cyclone and anticyclone centers. Based on these diagrams, the following important points may be noted for cyclone activity in the **Northern Hemisphere** during winter. Over the **Pacific Ocean**, there is a wide zone of cyclonic activity stretching from Southeast Asia to the Gulf of Alaska. During winter, most of these cyclones travel in a northeastward direction and converge in the Gulf of Alaska. However, some of the storms, especially those that form on the mid-Pacific polar front, travel on a more southerly track and reach the California coast. Most of the Pacific cyclones cannot cross the Rockies; however, some of them redevelop on the eastern side of the Rockies.

Over the **Atlantic Ocean**, storms usually develop on the Atlantic polar front (Fig. 1.15). One of the most favoured regions is the coast of Virginia and to the area east of the southern Appalachians. These are referred to as the East Coast Storms or the Cape Hatteras Storms, and while moving along the Gulf Stream, they achieve great intensity, and finally they become stagnant near Iceland or between Greenland and Labrador. On the Atlantic-Arctic front, many cyclones either form or redevelop, and they generally move in the direction of the Barents Sea.

During the summer period for the Northern Hemisphere, there are mainly two belts of high frequencies of storm occurrence. The northern belt surrounding the Arctic is irregular and consists of cyclones with fronts. The southerly belt is over the warm continents of the subtropics. The more or less permanent heat low over the continents accounts for the high frequencies found over southern California, Nevada, Arizona, and northern Mexico. At the higher levels, there is an anticyclone with strong subsidence, and because of this, clouds and weather systems are absent in the second belt.

The principal tracks of the depressions in the Northern Hemisphere for the winter period are shown in Fig. 1.17. Note that these tracks basically reflect the influence of the major frontal zones.

Next, the geographical distribution of the anticyclones in the Northern Hemisphere will be briefly discussed. There is a belt over the oceans with a maximum occurrence frequency off the subtropical west coast. In the eastern North Pacific, strong frequencies occur. Regarding the distribution of the anticyclonic centres in the Northern Hemisphere during summer, note that the belt of subtropical anticyclones is now farther north than in winter. The occurrence frequency is again significant in the eastern Pacific but is low in the western Pacific because of the summer monsoon.

Earlier, a front was defined as a sloping zone of transition between two air masses of different density. Although a front is several kilometres wide, it is narrow compared with the horizontal dimensions of the air masses. On weather charts, fronts appear as lines of discontinuity in wind and temperature. At the front, there is a kink in the isobars (i.e. lines of equal pressure) directed from low to high pressures.

Next, the **principal frontal zones on the globe** will be identified. Although fronts are not usually stationary, certain regions nevertheless consistently show high frequency of fronts, these regions being the areas of confluence between the main air mass sources discussed earlier. Fig. 1.17 shows the major frontal zones in the Northern Hemisphere during

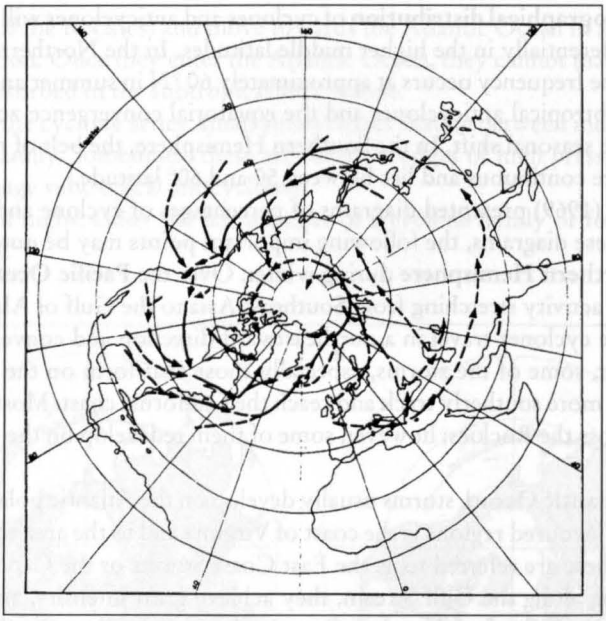

Fig. 1.17: Principal Northern Hemisphere depression tracks in January. Tracks represented by broken lines are less certain than those represented by solid lines (KLEIN, 1957)

winter. In the Atlantic Ocean region, one has the Atlantic polar front, which is the confluence region between the polar continental and the tropical maritime air mass sources, and the opposing currents indicated maintain the front. Quite often, the Atlantic polar front extends eastward over Europe. Its position varies quite drastically in the meridional direction; i.e. it can be anywhere from the West Indies to Portugal in the south to the Great Lakes and Iceland in the north (PETTERSSEN, 1969). This frontal zone is responsible for the cyclones that bring precipitation over a wide belt from the eastern part of the North American continent to northwest Europe.

In the southern hemisphere the Polar Front has more cyclonic activity in summer than the northern hemisphere in its summer. The Polar Front is located in January about 45° S with branches spiralling poleward towards eastern South America and from 30° S in the South Pacific (150° W) (Fig. 1.16). In winter of the southern hemisphere there are two Frontal zones spiralling towards Antarctica from about 20° (BARRY and CHORLEY, 1992).

A second important frontal zone is formed by the Atlantic-Arctic fronts, which are in the confluence region between the arctic source region and the polar maritime air. The storms that form on this frontal zone usually travel from Iceland along the northern part of Norway to the Barents Sea. A third important frontal zone is the Mediterranean front, which forms at the confluence of the cold air from Europe and the mild air from North Africa and Mediterranean Sea area. The cyclones that develop here usually travel in northeasterly direction to southern parts of central Asia. However, some travel eastward to northwest India.

Over the North Pacific Ocean, there are usually two polar fronts, the one nearest the Arctic coast being the more pronounced. Most of the North Pacific storms form along this frontal zone and travel towards the Gulf of Alaska, but some of them take a southerly route to California and northern Mexico. The Pacific-Arctic front usually extends towards the Great Lakes, and many of the storms between the Great Lakes and the Rockies develop on

this front. Cold air from the Arctic may reach as far south as Texas, or even northern Mexico, in the rear of these storms.

A second weak polar front is found in winter in the southern hemisphere at 65°–70 °S. Zones of airstream confluence in the southern hemisphere are less numerous and more persistent, pariculary in coastal regions, than in the northern hemisphere.

The frontal zone distribution during the summer period for the Northern Hemisphere is shown in Fig. 1.15. Since, in summer, the differences in the properties of the various air masses are not as pronounced as in winter, one can find permanent frontal zones only in the Arctic region. The polar fronts over the western Atlantic and Pacific are usually 10° farther north in summer as compared with their winter positions. There is now a frontal zone over Eurasia and over the middle part of North America. These new zones reflect the prevailing meridional temperature gradient and the large scale orographical influences. The Arctic front, in summer, is formed along the Arctic coasts of Siberia and North America and is associated with the snow (and ice) boundaries of the higher latitudes.

## 1.4 Regional Weather System

In this section, the regional weather systems of North America, South America, Europe, Africa, Asia, Australia, and the ocean region will be briefly considered. The detailed meteorological problems associated with storm surges will be considered in Chapter 5.

### 1.4.1 Weather Systems of North America

The climate of North America is determined by its location in the Northern Hemisphere and its great range from 9° N (Isthmus of Panama) to 71° N (Point Barrow) and to 84° N if the Arctic Archipelago is included. Furthermore it is influenced by its great Landmass with its greatest breadth (4250 km along 40° N) in the temperate zone, the long meridional barrier of the Western Cordilleras, the cold Hudson Bay in the North and the warm Gulf of Mexico from the south, the surrounding oceans and their currents with the warm Gulf Stream, cold Labrador Current, the warm Alaska Current and the cool California Current. The region, where the currents meet – for example the region of Newfoundland where the Gulf stream meets the Labrador Current – its one of cyclogenesis and fog formation.

The atmospheric circulation develops from the interaction of the stationary Hawaiian, Azores, Arctic and Greenland Highs and of the Aleutian and Icelandic Lows, which are semipermanent, are seasonable and variable in intensity (MARTYN, 1992).

During both winter and summer, the mean pressure field at the midtropospheric level shows a prominent trough over the eastern part of North America. The origin of this can be traced to the influence of the Rockies on the upper westerlies, but in winter, the strongly baroclinic zone along the east coast of North America is also responsible. Over the midwestern states, cyclones generally move in a southeast direction, bringing continental polar air southward, whereas along the Atlantic coast the cyclones travel northeastward. If the upper air trough is far to the west of is average position, then depressions form ahead of it over the South Central States (PETTERSSEN, 1969) and move in a north-easterly direction towards the lower St. Lawrence.

Considering January as a typical month for the winter period, the surface pressure chart shows an extension of the subtropical high over the southwest part of the United States (this

high being referred to as the "Great Basin High") and a polar anticyclone over the Mackenzie River area. On both the Atlantic and Pacific coasts, the pressure is low because of the Icelandic and Aleutian lows. Because of heating over the land, the Icelandic low is split and a secondary low appears over the northeastern part of Canada. The cyclone frequency is maximum on the Pacific coast and in the Great Lakes area during winter, whereas in the Great Plains, the maximum frequency is in spring and early summer. On the average, in the month of December, the Gulf of Alaska has the maximum frequency of lows and the Great Basin region has the maximum frequency of highs, as compared with any other region in the Northern Hemisphere.

In winter, there are three main depression tracks across North America

(1) Depressions from the west move eastward between 45 and 50° N.
(2) Some depressions first travel southeastward as far as the Central States and then travel northeastward towards New England and the Gulf of St. Lawrence. Depressions developing over the Pacific cross the western mountains as upper troughs and redevelop in the lee of the mountains in Alberta and Colorado.
(3) Depressions form on the polar front off the east coast of the United States and move northeastward towards Newfoundland.

In the summer period, the frequency of depressions originating in the east coast is less, and the tracks of depressions from the west are somewhat northward as compared with their winter positions. The tracks pass over Hudson Bay, Ungava Bay, Labrador, or the Gulf of St. Lawrence. The maritime frontal zone that gives rise to these depressions is not pronounced.

In early April, the Aleutian low (which is located approximately at 55° N, 165° W during September to March) splits into two; one centre is over the Gulf of Alaska and the other is over northern Manchuria. Cyclogenesis increases in Alberta and Colorado. By the end of June, the subtropical high pressure cells in the Northern Hemisphere are displaced northward, and because of this, the depression tracks also move northward.

The essential features of the sea level circulation in the eastern and central parts of the United States and Canada can be determined from sea level pressure maps. However, due to the presence of mountains and rugged orographical features in the west, sea level pressure gradients do not accurately reflect the wind distribution. Because of the presence of high coastal mountains, the Aleutian low pressure system does not extend far inland. HAURWITZ AUSTIN (1944) stated that because the inland pressures are reduced to sea level, they appear quite high compared with those over the surrounding ocean, and this sea level correction gives rise to steep fictitious pressure gradients in northern British Columbia and southern Alaska. Due to the presence of several fjords and the banking effect produced by the coastal mountains, the average surface winds do not agree with the mean isobaric pattern.

### 1.4.2 Weather Systems of Mexico and Central America

Central America includes the continental strip joining North to South America (between 18 and 8° N) and the West Indies, a string of islands from Florida (25° N) to Venezuela (10° N) separating the Caribbean Sea from the Atlantic (MARTYN, 1992).

The main mountain range in Central America is the Sierra Madre in Mexico. This region generally lies between the subtropical belt of high pressure and the equatorial belt of low pressure, whose boundary changes with the ITCZ. The Hawaiian High and the Azores in-

fluence it. The prevailing winds are trade wind (easterly) and the migratory low pressure centers generally move from east to west. Thus, these secondary circulations are significantly different from those of middle and high latitudes.

Central America is exposed to tropical cyclones, which spring up from June to November over the Gulf of Mexico, the Caribbean Sea and in the vicinity of the Bahamas and over the tropical part of eastern Pacific. These affect the coast of Central America, and all the way to Newfoundland (MARTYN, 1992). The number varies from 1 (1890) to 21 (1933) a year (DUNN AND MILLER, 1960).

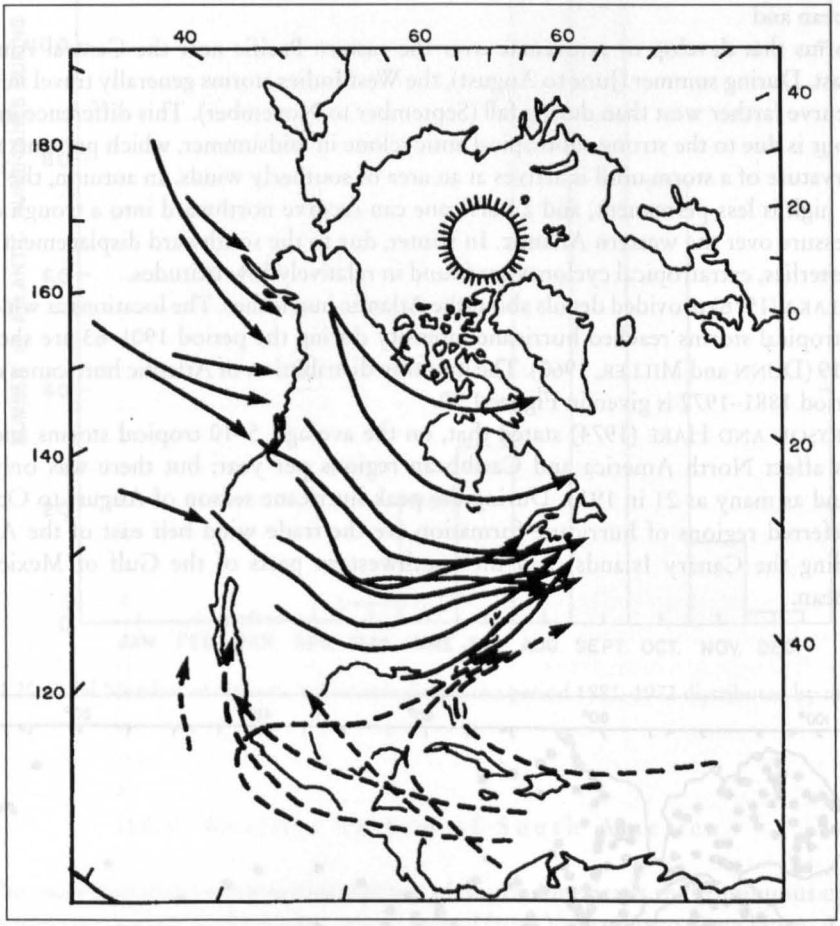


Fig. 1.18: Cyclone tracks of North and Central America. Solid lines represent extratropical cyclones and broken lines represent tropical cyclones. (HAURWITZ and AUSTIN, 1944)

The tracks of the hurricanes are shown in Fig. 1.18. The following is a summary of the average conditions associated with these tracks in Mexico and Central America:

(a) The Antillean hurricanes recurve in the eastern part of the Gulf of Mexico, and the hurricane season is August to October. During August, the recurvature occurs farther north than during October.

(b) A frequently observed track is over the Caribbean Sea, the Yucatan Peninsula, and then over the northeast coast of Mexico or along the coast of Texas.
(c) Occasionally, the hurricanes, after crossing the Yucatan Peninsula, travel over Central Mexico and arrive at the Pacific coast and then travel northwestward.
(d) Similar to across Central America, and then the track is towards the north-west, parallel to the Pacific coast and passing over the Gulf of California.
(e) These storms develop over the southeast Pacific and travel towards the Gulf of Mexico. Some tropical cyclones also form south of the Revillagigedo Islands.

Thus, two main classes of cyclones can be noted:

(1) hurricanes that develop over the warm waters of the Caribbean Sea and the Atlantic Ocean and
(2) storms that develop or rejuvenate over the eastern Pacific near the Central American coast. During summer (June to August), the West Indies storms generally travel inland or recurve farther west than during fall (September to November). This difference in behaviour is due to the strong subtropical anticyclone in midsummer, which prevents the recurvature of a storm until is arrives at an area of southerly winds. In autumn, the Atlantic high is less permanent, and a hurricane can recurve northward into a trough of low pressure over the western Atlantic. In winter, due to the southward displacement of the westerlies, extratropical cyclones are found in relatively low latitudes.

ALAKA (1976) provided details about the Atlantic hurricanes. The locations at which Atlantic tropical storms reached hurricane intensity during the period 1901–63 are shown in Fig. 1.19 (DUNN and MILLER, 1960). The monthly distribution of Atlantic hurricanes during the period 1881–1972 is given in Figure 1.20.

BRYSON AND HARE (1974) stated that, on the average, 5–10 tropical storms and hurricanes affect North America and Caribbean regions per year; but there was only 1 in 1914 and as many as 21 in 1933. During the peak hurricane season of August to October, the preferred regions of hurricane formation are the trade wind belt east of the Antilles (including the Canary Islands) and the southwestern parts of the Gulf of Mexico and Caribbean.

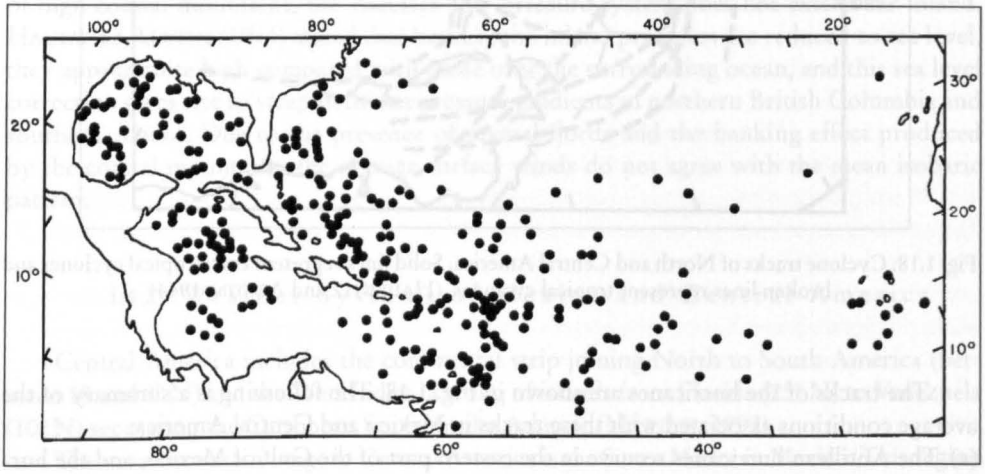


Fig. 1.19: Locations at which Atlantic tropical storms reached hurricane intensity during the period 1901–63. (DUNN and MILLER, 1960)

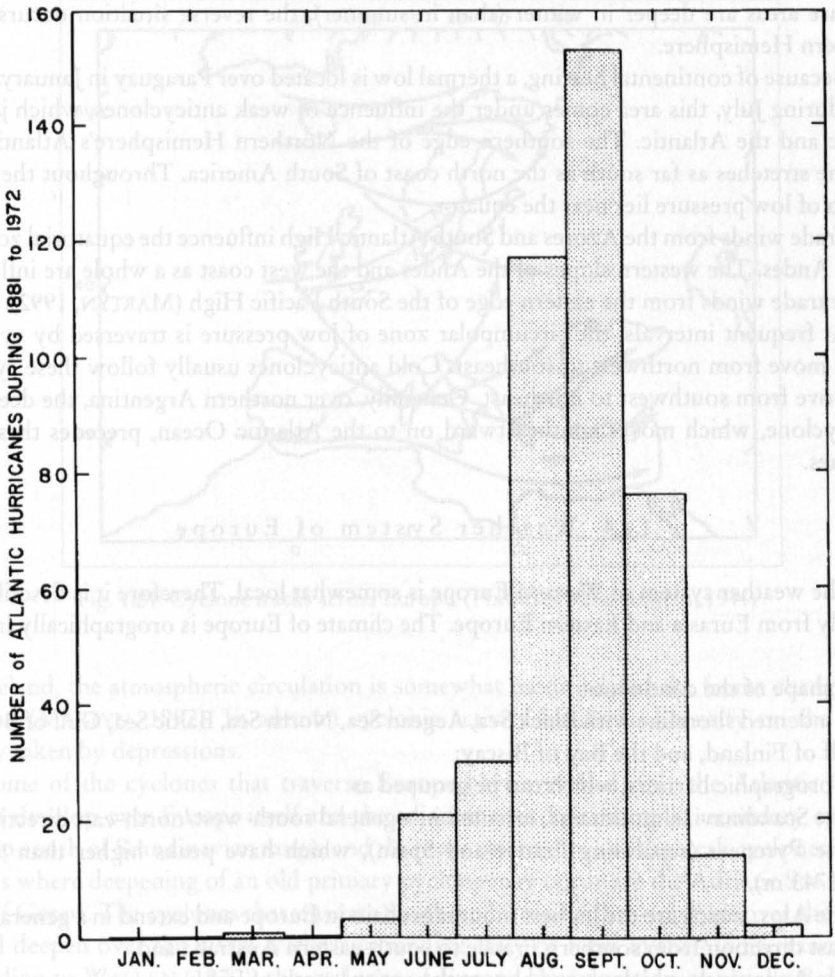


Fig. 1.20: Total Number of Atlantic hurricanes during the period 1881–1972 distributed by month

### 1.4.3 Weather System of South America

The most important orographical feature of South America is the continuous chain of high mountains, known as the Andes, which extend from Venezuela to Cape Horn. Another topographical feature is that South America does not have prominent coastal indentations (such as Hudson Bay, Gulf of St. Lawrence, and Gulf of Mexico in North America) or large inland lakes.

A more or less persistent feature is the presence of two semipermanent anticyclones, one over the Atlantic and the other over the Pacific, near the east and west coasts, respectively. The southern end of South America is affected by the zone of polar front depressions, which in July reach as far north as 35–45° S (MARTYN, 1992). South of Cape Horn, there are deep semipermanent cyclones of the Weddel and Belgique seas. One main difference between the Northern and Southern hemispheres is that, whereas in the Northern Hemisphere the low

pressure areas are deeper in winter (than in summer), the reverse situation occurs in the Southern Hemisphere.

Because of continental heating, a thermal low is located over Paraguay in January. However, during July, this area comes under the influence of weak anticyclones, which join the Pacific and the Atlantic. The southern edge of the Northern Hemisphere's Atlantic anticyclone stretches as far south as the north coast of South America. Throughout the year, a trough of low pressure lies near the equator.

Trade winds from the Azores and South Atlantic High influence the equatorial zone east of the Andes. The western slopes of the Andes and the west coast as a whole are influenced by the trade winds from the eastern edge of the South Pacific High (MARTYN, 1992).

At frequent intervals, the circumpolar zone of low pressure is traversed by cyclones, which move from northwest to southeast. Cold anticyclones usually follow these cyclones and move from southwest to northeast. Generally, over northern Argentina, the deepening of a cyclone, which moves southeastward on to the Atlantic Ocean, precedes these anticyclones.

### 1.4.4 Weather System of Europe

The weather system of Western Europe is somewhat local. Therefore it is described separately from Eurasia and Eastern Europe. The climate of Europe is orographically influenced by

1. the shape of the continent;
2. the indented shoreline with Black Sea, Aegean Sea, North Sea, Baltic Sea, Gulf of Bothnia, Gulf of Finland, and the Bay of Biscay;
3. the orographic barriers, which can be grouped as
   - the Scandinavian mountains, oriented in a general south-west/north-east direction
   - the Pyrenees (separating France and Spain), which have peaks higher than 9000 ft (2743 m),
   - the Alps, which are the highest mountain chain in Europe and extend in a general west-east direction from southern France to south-eastern Australia and
   - the Apennines, which extend almost the entire length of Italy;
4. the huge continental mass to the east and
5. the extensive ocean to the west.

MARTYN (1992) summarised that the climate of Europe is influenced by the permanent Icelandic Low stationed over the North Atlantic and the Azores High. While the Icelandic Low is deeper in winter, the Azores High reinforces in summer. The seasonal Asian High influences Europe in winter. Summer is characterised by the presence of the Arctic High in the Spitzbergen region and the South Asian Low. This pressure system gives rise to prevailing south-westerlies over northern, western and central Europe, and north-westerlies and westerlies in southern Europe (MARTYN, 1992). The westerly airstream changes in easterly or northeasterly, when high pressure develops over eastern or northeastern Europe.

In winter, the cyclones that travel across North America, or those that develop on the Atlantic Front, travel south of Iceland in a general northeasterly direction towards Norway. The latitudinal variation of cyclones that approach the west coast of Europe for the different seasons of the year is listed in Table 1.3. The cyclone tracks across Europe are shown in Fig. 1.21. This difference in frequency is more pronounced in summer than in winter.

„In summer, when the Azores High becomes stronger and extend in a ridge across western Europe, the Iceland Low weakens and the Arctic High lies across eastern Greenland

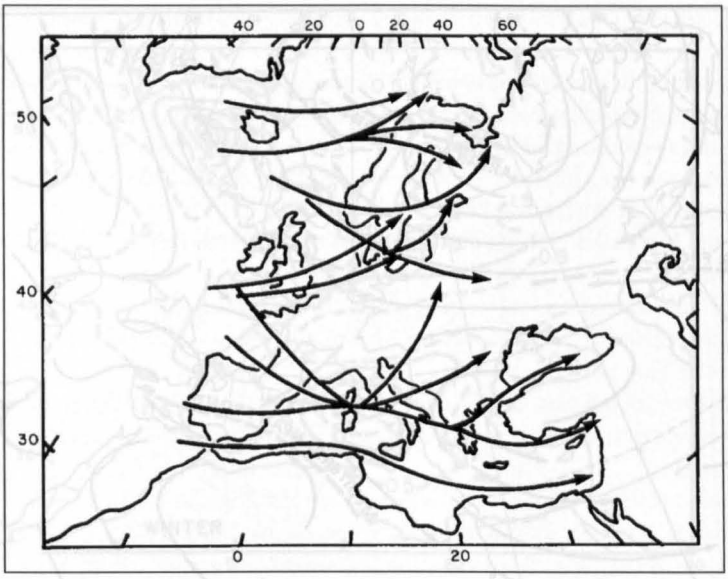


Fig. 1.21: Cyclone tracks across Europe. (HAURWITZ and AUSTIN, 1944)

and Iceland, the atmospheric circulation is somewhat modified and the fronts change their position (MARTYN, 1992). In autumn cyclonic activity begins to intensify on the tracks usually taken by depressions.

Some of the cyclones that traverse Europe have travelled over the Atlantic Ocean. Others develop over Europe itself and the adjacent seas. For example, secondary cyclones develop south of Scandinavian range, and these are referred to as Skagerrak cyclones. Other regions where deepening of an old primary cyclone may occur are the Adriatic Sea and the Gulf of Genoa. The cyclones that traverse Southern Europe either originate over the Atlantic and deepen over the warm water surrounding Italy or form in the Mediterranean Sea. According to WALLEN (1970), the cyclones of Europe have duration of usually 8 d but at times up to 17 d. Fig. 1.23 shows the frequency of cyclones in winter and summer for Europe.

Table1.3: Cyclone frequency (% of the total annual occurrence) at 15° W longitude (Atlantic Ocean). (HAURWITZ and AUSTIN, 1944).

| Latitude | Winter | Spring | Summer | Autumn | Year |
|---|---|---|---|---|---|
| 30–35 ° N | 1.7 | 2.0 | 0.4 | 2.0 | 6.1 |
| 35–40 ° N | 3.0 | 3.9 | 1.1 | 3.8 | 11.8 |
| 40–45 ° N | 3.3 | 4.2 | 2.3 | 3.1 | 12.9 |
| 45–50 ° N | 2.1 | 3.0 | 3.7 | 2.7 | 11.5 |
| 50–55 ° N | 2.3 | 3.7 | 4.5 | 2.4 | 12.9 |
| 55–60 ° N | 3.0 | 4.5 | 6.0 | 4.1 | 17.6 |
| 60–65 ° N | 3.2 | 5.1 | 5.0 | 5.4 | 18.7 |
| 65–70 ° N | 1.9 | 2.1 | 2.2 | 2.3 | 8.5 |
| 30–70 ° N | 20.5 | 28.5 | 25.2 | 25.8 | 100.0 |

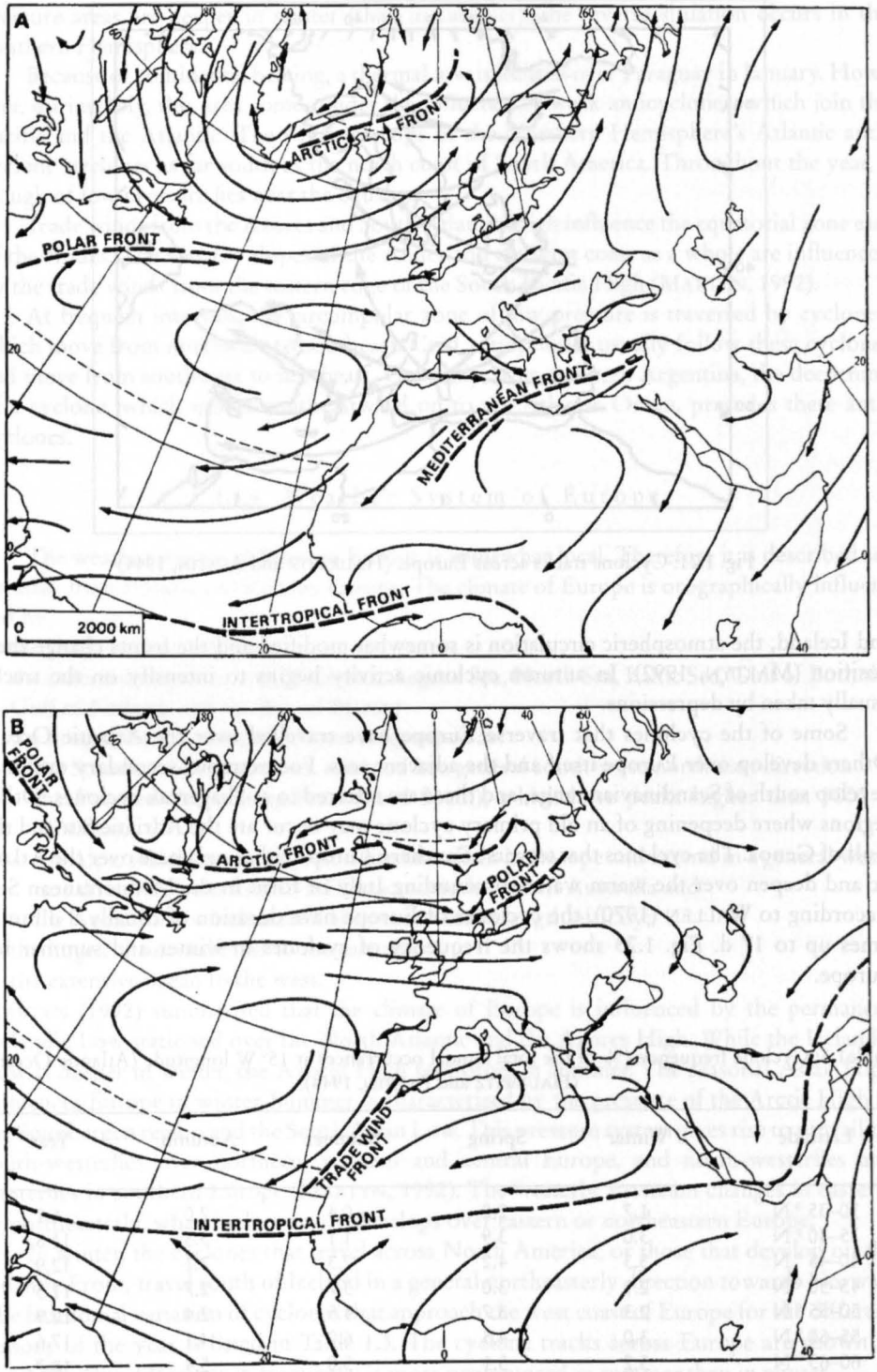


Fig. 1.22: Prevailing wind directions and atmospheric fronts over Europe and the North Atlantic. January (A) July (B) (MARTYN, 1992)

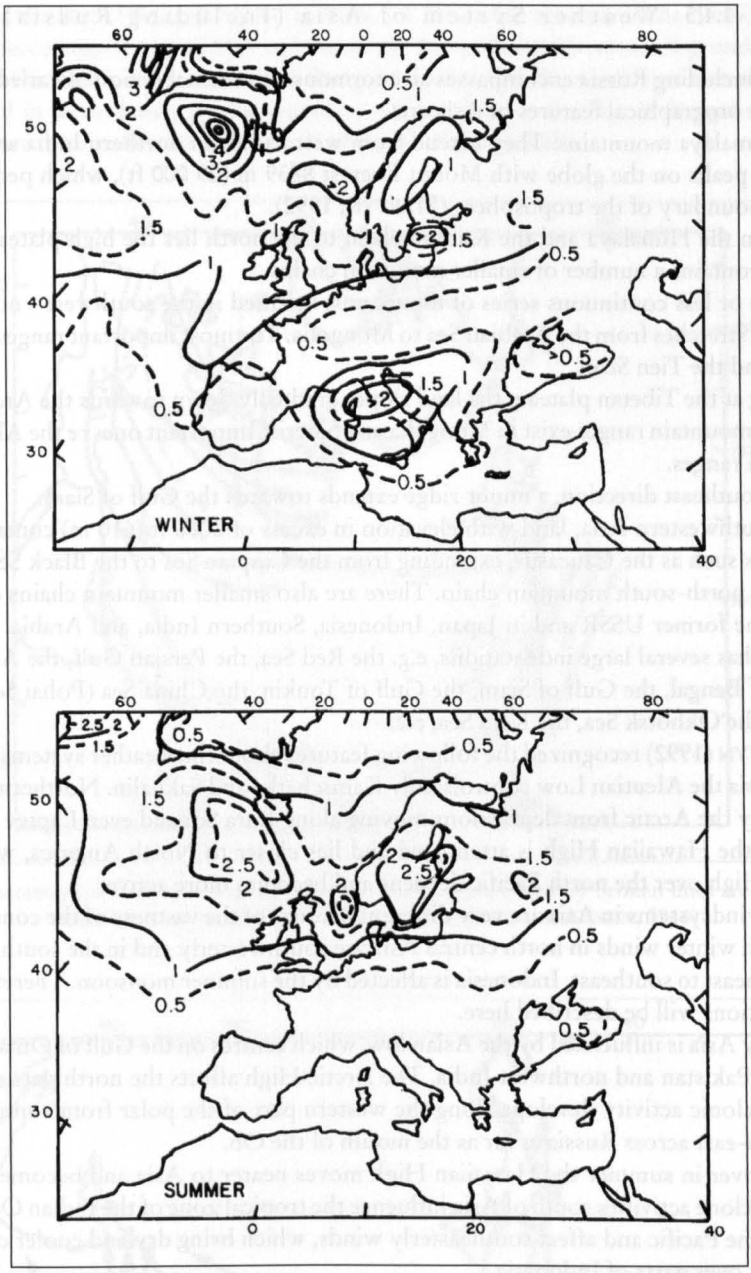


Fig. 1.23: Average Frequency of cyclones with central pressure less than 1000 MB during a winter season (top) and a summer season (bottom) (HAURWITZ and AUSTIN, 1944)

### 1.4.5 Weather System of Asia (Including Russia)

Asia including Russia encompasses an enormous continental region of varied relief. The important orographical features of Asia are:

1. The Himalaya mountains: They extend from west to east in northern India and have the highest peaks on the globe with Mount Everest 8839 m (29 000 ft), which penetrates the upper boundary of the troposphere (MARTYN, 1992).
2. Between the Himalaya and the Kunlun chain to the north lies the high plateau of Tibet, which contains a number of smaller mountain chains.
3. A more or less continuous series of mountains, oriented in the southwest - northeast direction, stretches from the Arabian Sea to Mongolia. The most important ranges are Hindu Kush and the Tien Shan.
4. Starting at the Tibetan plateau, the land slopes gradually down towards the Arctic Ocean. Several mountain ranges exist in Mongolia and Siberia. Important ones re the Altai and Yablonova ranges.
5. In the southeast direction, a minor ridge extends towards the Gulf of Siam.

In southwestern Asia, land with elevation in excess of 2000 ft (610 m) contains mountain ranges such as the Caucasus, extending from the Caspian Sea to the Black Sea. The Urals form a north-south mountain chain. There are also smaller mountain chains on the east coast of the former USSR and in Japan, Indonesia, Southern India, and Arabia. The Asian continent has several large indentations, e.g. the Red Sea, the Persian Gulf, the Arabian Sea, the Bay of Bengal, the Gulf of Siam, the Gulf of Tonkin, the China Sea (Pohai Sea), the Sea of Japan, the Okhotsk Sea, the Kara Sea, etc.

MARTYN (1992) recognized the following features about the weather systems in Asia. In Eastern Asia the Aleutian Low controls only Kamschatka and Sakhalin. Northern Asia is influenced by the Arctic front depressions moving along Kara Sea and even Laptev Sea coasts. In winter the Hawaiian High is attenuated and lies closer to North America, whereas the Aleutian High over the north Pacific deepens and becomes more active.

The windsystems in Asia are very different because of the vastness of the continent. For example, in winter winds in north central Asia are southwesterly and in the south they blow from northeast to southeast. Indonesia is affected by the summer monsoon. Therefore not all winddirections will be described here.

In July Asia is influenced by the Asian low, which centres on the Gulf of Oman, the Persian Gulf, Pakistan and northwest India. The Arctic High affects the north part of the continent. Cyclonic activity develops along the western part of the polar front running southwest-north-east across Russia as far as the mouth of the Ob.

Moreover in summer the Hawaiian High moves nearer to Asia and becomes stronger. The anticyclone activities south of Asia influence the tropical zone of the Indian Ocean, Australia and the Pacific and affect southeasterly winds, which bring dry and cooler continental tropical air over parts of Indonesia.

South-east and east Asia, the coasts of the Seas of Okhotsk and Japan, the Amur, Sakhalin and Kamchatka regions, the Philippines and Indonesia are dominated by a monsoon circulation. In winter the wind blows opposite its direction in summer. Then cyclonic activities increase rapidly over very warm seas and oceans and, though the affected area is limited, it is extremely violent and can be disastrous owing to the exceptional heights of waves, and the torrential rain (tropical cyclones known as typhoons).

The tracks of extratropical and tropical cyclones across Asia are shown in Fig. 1.24 and 1.25, respectively. The approximate percentage distribution of tropical cyclones in the Ara-

bian Sea and the Bay of Bengal is given in Table 1.4. Note that whereas in the Arabian Sea the maximum percentage is during May to June, in the Bay of Bengal it is from September to October. Later the Arabian Sea and Bay of Bengal cyclones and the resulting storm surges will be discussed in more detail. Special attention will be given to the Bay of Bengal surges because they are responsible for almost half of the lives lost globally.

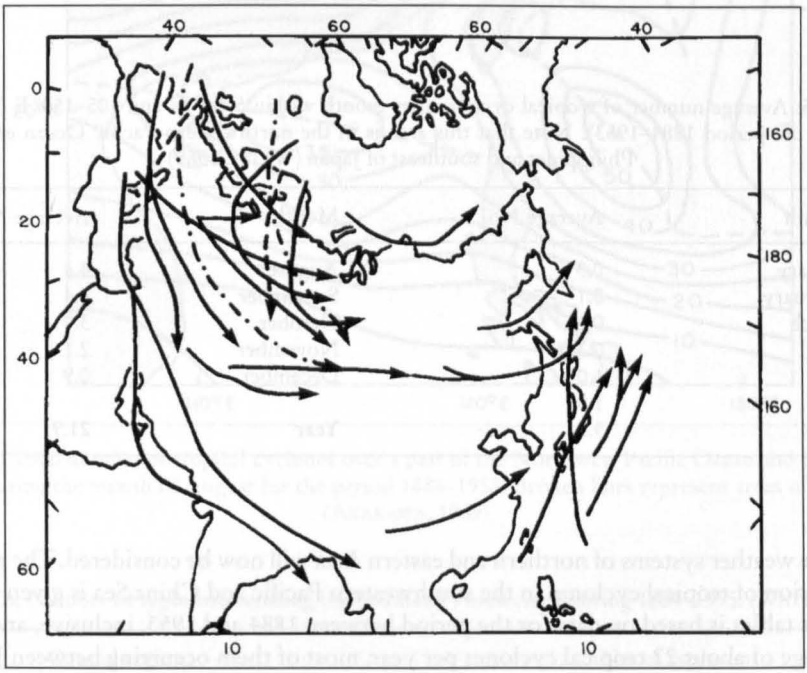


Fig. 1.24: Extratropical cyclone tracks across Asia. Tracks represented by broken lines are less certain than those represented by solid lines. (HAURWITZ and AUSTIN, 1944)

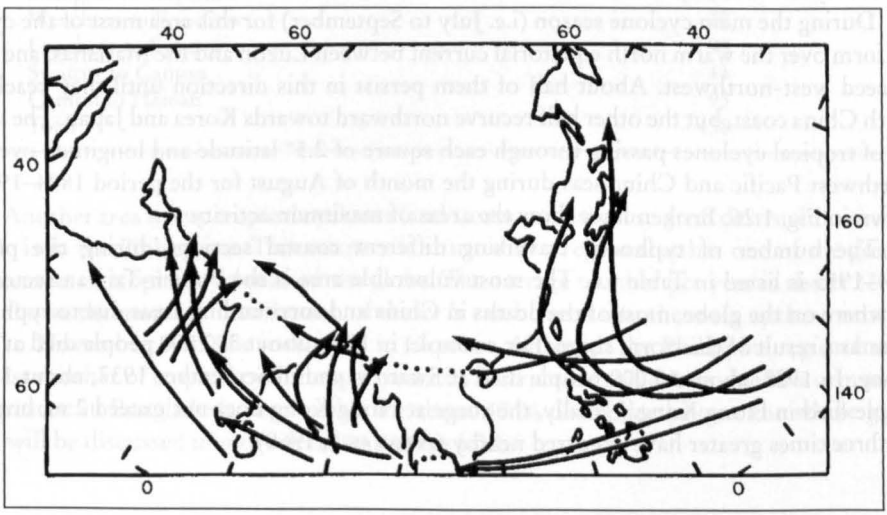


Fig. 1.25: Tropical cyclone tracks across Asia. (HAURWITZ and AUSTIN, 1944)

Table 1.4: Bimonthly distribution (approximate %) of tropical cyclones in the Arabian Sea and the Bay of Bengal (HAURWITZ and AUSTIN, 1944)

| Water body | Jan.–Feb. | Mar.–Apr. | May–June | July–Aug. | Sept.–Oct. | Nov.–Dec. |
|---|---|---|---|---|---|---|
| Arabian Sea | 1 | 11 | 50 | 1 | 11 | 26 |
| Bay of Bengal | 1 | 2 | 17 | 29 | 34 | 17 |

Table 1.5: Average number of tropical cyclones per month within 5–30° N and 105–150° E (based on data for the period 1884–1953). Note that this area is in the northwestern Pacific Ocean east of the Philippines and southeast of Japan (WATTS, 1969)

| Month | Average No. | Month | Average No. |
|---|---|---|---|
| January | 0.3 | August | 4.4 |
| February | 0.1 | September | 4.4 |
| March | 0.1 | October | 3.0 |
| April | 0.3 | November | 2.1 |
| May | 1.0 | December | 0.9 |
| June | 1.5 | | |
| July | 3.8 | **Year** | **21.9** |

The weather systems of northern and eastern Asia will now be considered. The monthly distribution of tropical cyclones in the southwestern Pacific and China Sea is given in Table 1.5. This tables is based on data for the period between 1884 and 1953, inclusive, and shows an average of about 22 tropical cyclones per year, most of them occurring between July and October (ARAKAWA, 1969). During July to September, tropical cyclones frequently travel over the coasts of China and Korea; however, the southern parts of China experience them sometimes as early as May and as late as mid-November. Between mid-November and April, tropical cyclones rarely traverse the mainland of China.

During the main cyclone season (i.e. July to September) for this area most of the cyclones form over the warm north equatorial current between Luzon and the Marianas, and they proceed west-northwest. About half of them persist in this direction until they reach the South China coast, but the other half recurve northward towards Korea and Japan. The number of tropical cyclones passing through each square of 2.5° latitude and longitude over the Northwest Pacific and China seas during the month of August for the period 1884–1953 is shown in Fig. 1.26. Broken lines show the areas of maximum activity.

The number of typhoons traversing different coastal sections during the period 1884–1955 is listed in Table 1.6. The most vulnerable area is the Fukien-Taiwan sector. As elsewhere on the globe, most of the deaths in China and surrounding areas due to typhoons occur as a result of the storm surge. For example, in 1881, about 300 000 people died at Haiphong. In 1922, about 60 000 people died at Swatow, and in September 1937, about 11 000 people died in Hong Kong. Usually, the surge at Hong Kong does not exceed 2 m, but surges three times greater have occurred nearby (ARAKAWA, 1969).

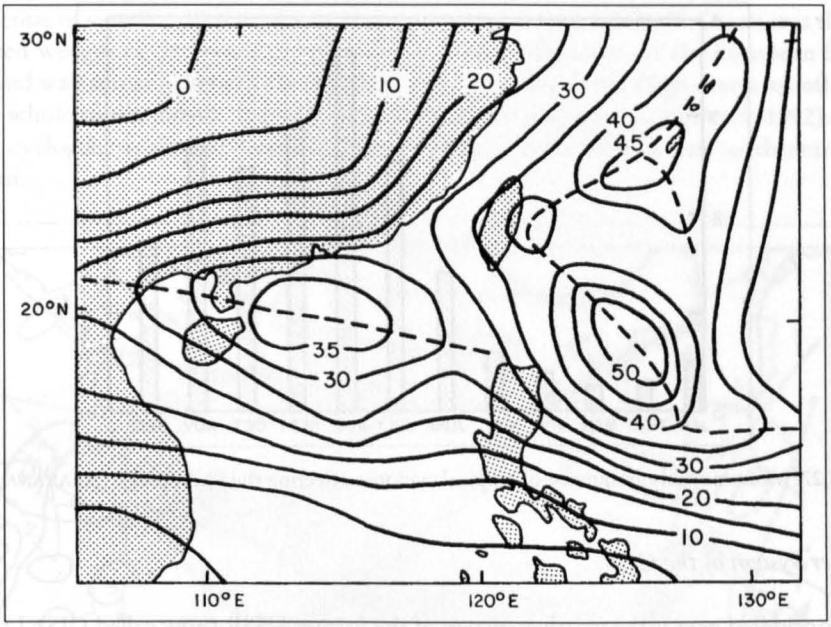


Fig. 1.26: Total number of tropical cyclones over a part of the Northwest Pacific Ocean and the Sea of China during the month of August for the period 1884–1953. Broken lines represent areas of maxima. (ARAKAWA, 1969)

Table 1.6: Number of typhoons crossing the Southeast Asian coast during 1884–1955. (WATTS, 1969)

| Coastal region | No. of typhoons |
|---|---|
| Korea and further east | 87 |
| Liaoning to Shantung Peninsula | 39 |
| Shantung Peninsula to Shanghai | 22 |
| Shanghai to Wenchow | 34 |
| Wenchow to Foochow | 30 |
| Foochow to Swatow | 90 |
| Swatow to Canton | 43 |
| Canton to Hainan | 93 |
| Total | 438 |

Another area where tropical cyclones (and storm surges) cause great destruction and loss of life is in the Philippines. This country is situated in a region that has one of the greatest frequencies of tropical cyclones on the globe. The average number per year is about 22. Fig. 1.27 shows the monthly distribution of these. It can be seen that the main cyclone season is July to November, with the maximum in October. Although the Philippine region has the highest number of tropical cyclones per year, the destruction and deaths due to storm surges are greatest in Bangladesh, responsible for about 40 % of the deaths over the whole globe. This will be discussed in more detail in section 6.3.1.

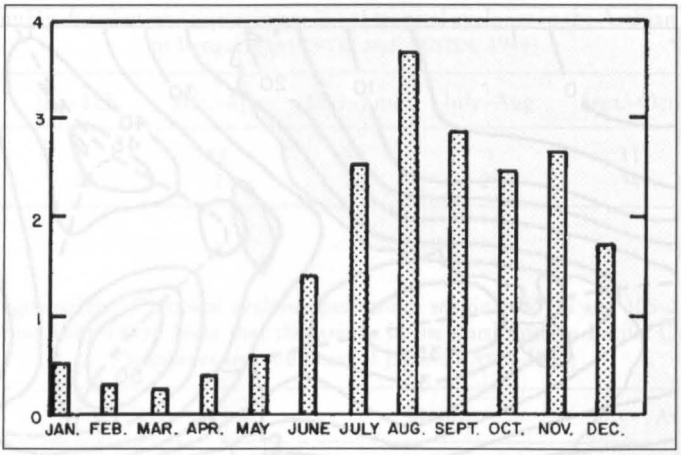


Fig. 1.27: Mean monthly frequency of tropical cyclones affecting the Philippines. (ARAKAWA, 1969)

*Weather System of the CIS*

Considered next is the weather system of the former USSR (now called CIS). LYDOLPH (1977) mentioned that during winter, the strong dominance of a high pressure cell over Eurasia causes the majority of fronts and cyclone tracks to be located along the edges of the land mass. In winter, the polar front generally lies south of the former CIS. This front has two branches: the western branch lies in the Mediterranean – Asia Minor – Middle East area, and an eastern segment lies off the coast of China and across Japan, stretching into the Aleutians. Many cyclones that affect the weather over the CIS develop on the western segment. The cyclones forming in the eastern Mediterranean usually move northeastward across the Black Sea, the Caucasus, Ukraine, the lower Volga, and western Siberia. Cyclones developing in the Middle East travel into Soviet Central Asia. Cyclones forming along the eastern branch of the polar front in winter travel north of the CIS.

Thus, many of the cyclones affecting the CIS in winter either originate in the Icelandic low area or in the Mediterranean Sea. The Barents Sea also acts as a region of cyclogenesis and redevelopment. The Black Sea and the Caspian Sea also act as areas of cyclogenesis during winter. Other areas of cyclogenesis are western Siberia, the Baltic Sea, and southern Finland. In the Far East, cyclogenesis occurs over the northern part of the Okhotsk Sea (sea level pressures as low as 970 mb occur). However, in the Far East, most of the cyclogenesis occurs over Japan and the Sea of Japan. These cyclones affect southern portions of the Kamchatka Peninsula, Sakhalin Island, and Kuril Islands.

In winter, one of the stormiest areas in the CIS is the Ob Estuary region where cyclones travelling from the west along the Arctic coast meet those from the southwest travelling along the Black and Caspian seas. During spring, the center of maximum cyclone frequency shifts eastward from the Barents Sea to the Ob Gulf. In summer, the location of maximum cyclone frequency shifts southeastward into central Siberia south of the Taymyr Peninsula. In summer, the frequency of cyclones over the Black and Caspian seas diminishes considerably. In the Far East, the Aleutian low becomes weak, and the Amur Valley becomes a region of strong cyclogenesis.

Generally speaking, cyclones are more evenly distributed across the CIS landmass in summer. In winter, most of the cyclones affecting the former CIS originate outside the coun-

try, whereas in summer, most of the cyclogenesis occurs in the CIS itself. Summer is the season when wedges of the Azores High can stretch over the centre of the European former USSR and way across as far as Lake Baykal. In the north the Arctic High exerts its influence, but the whole south, mostly Turestan, is covered by the Asian Low (MARTYN, 1992). Areas of high cyclogenesis are the Amur Valley, the Urals, western Siberia, and northcentral Kazakhstan.

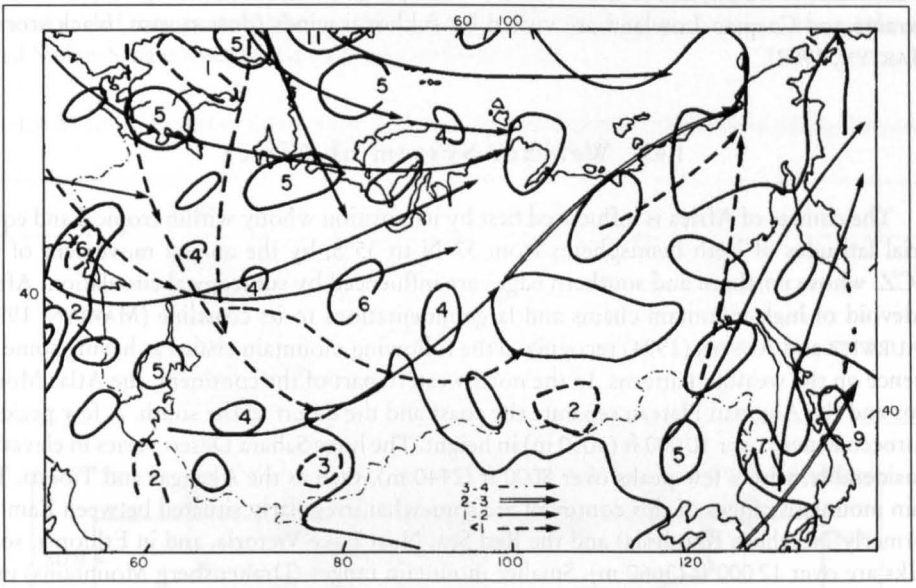


Fig. 1.28: Total number of cyclones during a 20-yr-period over the Soviet Union during the month of January. The principal tracks of cyclones are also shown. (LYDOLPH, 1977)

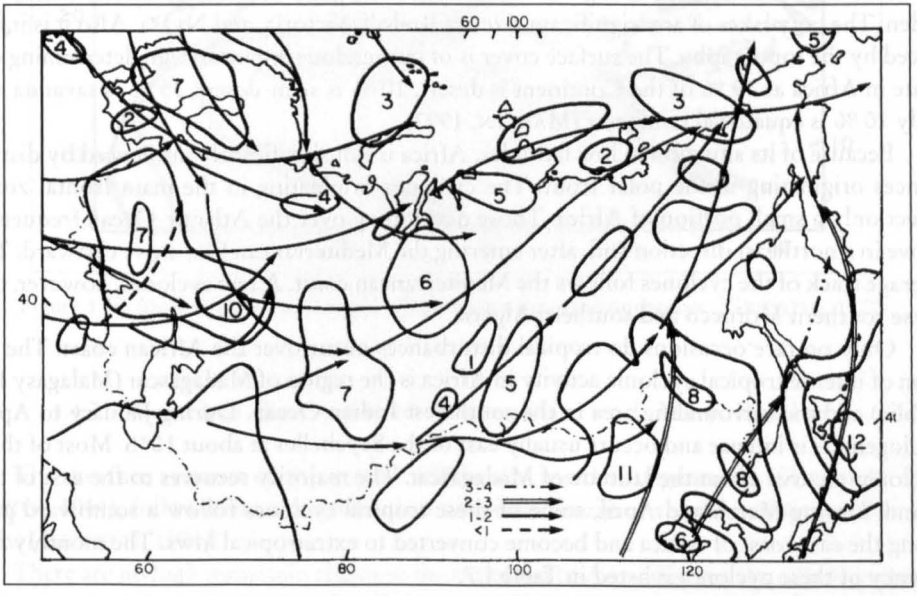


Fig. 1.29: Total number of cyclones during a 20-yr-period over the Soviet Union during the month of July. The principal tracks of cyclones are also shown. (LYDOLPH, 1977)

Generally, the movement of cyclones and fronts over the former CIS is slower than over the eastern part of North America. Also, there is frequent stagnation for a day or more. On the average, about 32 cyclones per year affect central Asia. The frequencies of cyclogenesis and the main routes of cyclones in January and July are shown in Fig. 1.28 and 1.29, respectively.

In winter, strong winds causing blizzards in the steppes and deserts of central Asia go by the name of buran, and in the north are called purga. In the summer months the eastern Ukraine and Caspian Lowland are visited by sukhovei winds (dust storms, black storms) (MARTYN, 1992).

### 1.4.6 Weather System of Africa

The climate of Africa is influenced first by its position wholly within tropical and equatorial latitudes of both hemispheres from 37°N to 35°S, by the annual movement of the ITCZ, whose northern and southern edges are influenced by subtropical circulation. Africa is devoid of high mountain chains and large indentations to its coastline (MARTYN, 1992). HAURWITZ and AUSTIN (1994) recognized the following mountain chains as having some influence on the weather patterns. In the northwestern part of the continent, the Atlas Mountains and the Algerian Plateau separate the coast and the desert to the south. A few peaks in Morocco extend over 10 000 ft (3050 m) in height. The huge Sahara Desert varies in elevation considerably, with a few peaks over 8000 ft (2440 m), such as the Ahaggar and Tibesti. The main mountain ranges of this continent are somewhat irregularly situated between Zamibia (formerly Northern Rhodesia) and the Red Sea. Near Lake Victoria, and in Ethiopia, some peaks are over 12 000 ft (3660 m). Smaller mountain ranges (Drakensberg Mountains) exist in the southeast; the Auaz Mountains in the southwest, the Cameroon Mountains in Cameroon, and the Ankaratra Mountains in Madagascar (Malagasy Republic) are other examples.

The only indentations along the coastline are the gulfs of Guinea, Gabès, Sidra, and Aden. The only lakes of any significant size are Rudolf, Victoria, and Nyasa. Also it is influenced by the topography. The surface cover is of tremendous importance in determining climate in Africa as 39 % of the Continent is desert, 10 % is semi-desert, 35 % is savanna and only 10 % is equatorial rainforest (MARTYN, 1992).

Because of its situation in low latitudes, Africa is not significantly influenced by disturbances originating in the polar front. The cyclones originating in the main frontal zones affect only a small portion of Africa. Those developing over the Atlantic Ocean frequently move in a northeast direction and, after entering the Mediterranean Sea, move eastward. The average track of the cyclones follows the Mediterranean coast. A few cyclones, however, traverse southern Morocco and southern Algeria.

Only on rare occasions do tropical disturbances occur over the African coast. The region of intense tropical cyclonic activity in Africa is the region of Madagascar (Malagasy Republic) and the surrounding area in the southwest Indian Ocean. During January to April, cyclogenesis is intense and occurs usually east of the Seychelles at about 10° S. Most of these cyclones recurve about the latitude of Madagascar. The majority recurves to the east of this island. During March and April, some of these tropical cyclones follow a southward path along the east coast of Africa and become converted to extratropical lows. The monthly frequency of these cyclones is listed in Table 1.7.

GRIFFITHS (1972) provides the following information about the weather systems of Africa, with particular reference to those of Egypt. During winter, the Mediterranean Sea is

a center of cyclogenesis. These Mediterranean depressions mainly affect northern parts of Egypt. During spring (March to May), the tracks of the Mediterranean depressions shift southward, and during this season, these are referred to as the „desert" or „Khamsin" depressions. The frequency of these varies from two to six per month. Also, these depressions, in spring, are smaller in size than the winter depressions.

During summer, the depressions do not traverse Egypt. In fall (October to November), Khamsin-type depressions move across Egypt. Compared with the spring depressions, these are weaker and move more slowly towards the east. The most frequent trajectories of the so-called Sudan-Sahara disturbances are shown in Fig. 1.30.

Table1.7: Monthly distribution (totals) of cyclones in the Mozambique Channel area during the period 1848–1966. (GRIFFITHS, 1972)

| Month | No. |
|---|---|
| January | 28 |
| February | 30 |
| March | 18 |
| April | 6 |
| May–November | 3 |
| December | 15 |

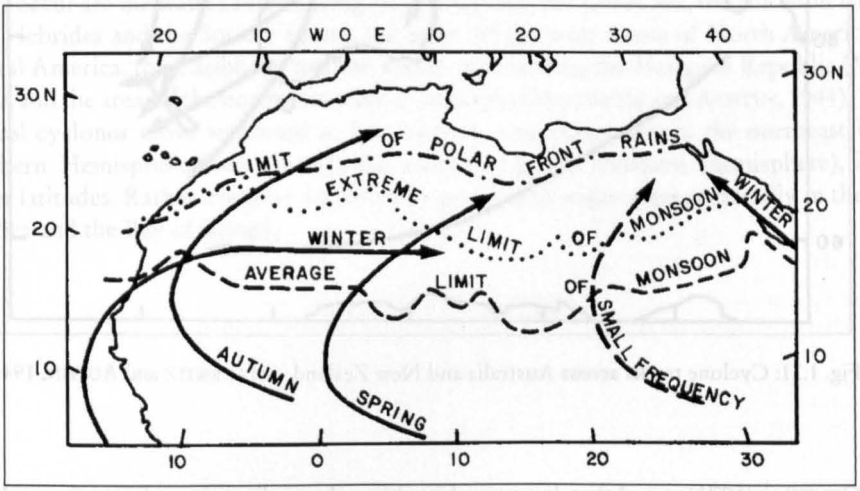


Figure 1.30: Most frequent trajectories of the Sudan-Sahara disturbances. (GRIFFITHS, 1972)

### 1.4.7 Weather Systems of Australia and New Zealand

The weather systems of this region will be discussed first generally (HAURWITZ and AUSTIN, 1944), followed by a consideration of certain details of the Australian weather systems (GENTILLI, 1971).

There are no high mountain chains in the mainland of Australia, and the only significant indentations to the coastline are the Great Australian Bight and the Gulf of Carpentaria. However, Tasmania is mountainous. New Zealand is also relatively mountainous. The con-

tinent is small and no other continents are in its vicinity. Therefore the two neighbouring oceans, the Indian and the Pacific, have a very great influence. In January low pressure centre forms over northern Australia. The ITCZ is lying at around 20° S, north of it there are northwesterly winds, south are south-east trade winds. In July an anticyclonic centre comes into existence over central Australia and joins up along an axis over 30° S with permanent tropical highs over the adjacent oceans.

The tracks of cyclones across Australia and New Zealand are shown in Fig. 1.31 Cyclones developing along the polar front off South Africa usually move south-eastward to the south of New Zealand. Also, stationary cold fronts over Queensland lead to cyclones that move in a general south-easterly direction, either to the north of New Zealand or across North Island of New Zealand. Cyclones developing over New South Wales travel across South Island of New Zealand. Sometimes, cyclones develop along the south coast of Australia.

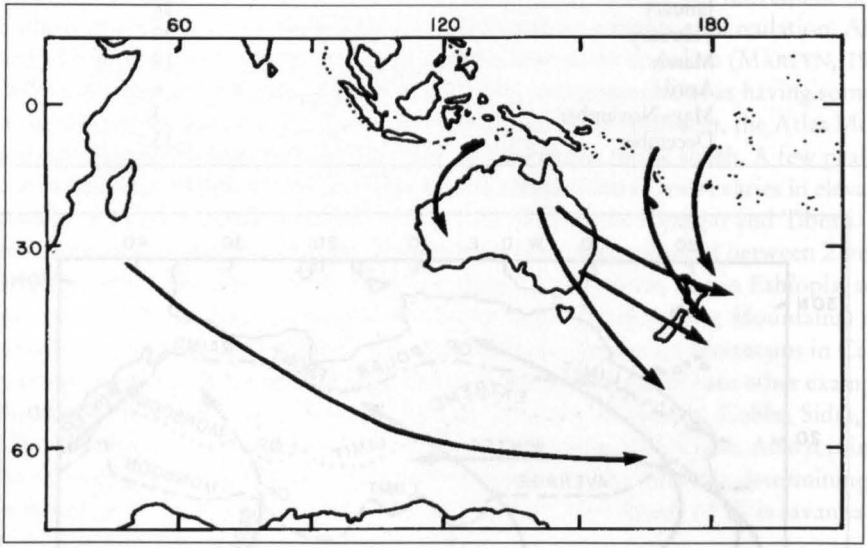


Fig. 1.31: Cyclone tracks across Australia and New Zealand. ( HAURWITZ and AUSTIN, 1944)

GENTILLI (1971) stated that, because of its shape, Australia is the only continent that has roughly the same frequency of tropical cyclones on both the east and west coasts. Data for the period 1870–1955 show that, on the average, Northern Territories and Queensland together experience about 3.3 tropical cyclones per year, whereas the west coast average is 2.1. As far as the monthly distribution is concerned, western Australia experiences the highest frequency during December to April.

Generally, in the Australian region, tropical cyclones originate in the belt of 4–20° latitude (north and south). One significant feature of tropical cyclones in the region of Australia are their relatively short tracks. Those originating in the Timor Sea travel in a southwest direction with a speed ranging from 8 to 24 km $s^{-1}$.

### 1.4.8 Weather Systems of the Oceanic Regions

Since tropical and extratropical cyclogenesis depends on the positions of the various frontal zones, the positions of these will be briefly summarized. The intertropical front lies in the low pressure belt between the large anticyclones of both hemispheres, whereas the polar fronts are mainly located off the east coasts of the continents, and the Arctic and Antarctic fronts lie in the troughs that extend from the high latitude deep cyclones (HAURWITZ and AUSTIN, 1944).

The cyclones of the middle and high latitudes generally develop as wave disturbances on the polar front. Since the position of the front varies considerably, the positions of cyclogenesis also vary with the season. In the Northern Hemisphere, most of these cyclones move in a north-easterly direction towards the Aleutian and Icelandic lows, whereas in the Southern Hemisphere, they move southeastward toward the circumpolar low. The seasonal variation is more pronounced in the Northern Hemisphere. In summer, cyclogenesis usually occurs farther north; the cyclones move slower and they are shallower than the winter cyclones.

Tropical cyclones develop in the intertropical front beyond 5° latitude in the summer hemisphere. Tropical cyclones are a rare phenomenon in the South Atlantic and eastern part of the South Pacific. Their frequency in the North Indian Ocean is quite different from elsewhere. In the Arabian Sea and the Bay of Bengal, they occur mainly in the periods between the southwest and the northeast monsoon seasons. Other water bodies where tropical cyclones occur are the waters surrounding the Philippines, the China Sea, the Solomon Islands, New Hebrides and the Society Island, the areas off the west coasts of North America and Central America, the Caribbean Sea, the waters surrounding the Malagasy Republic (Madagascar, and the area off the northwest coast of Australia (HAURWITZ and AUSTIN, 1944). These tropical cyclones move westward in low latitudes and then towards the northeast in the Northern Hemisphere (and towards the southeast in the Southern Hemisphere), in the higher latitudes. Rather irregular trajectories can occur in many areas, especially in the Arabian Sea and the Bay of Bengal.

# 2. Basic Storm Surge Equations and Standard Methods of Solutions

## 2.1 Formulation of the Storm Surge Equations

In numerical models for storm surges, the equations most frequently used are linearized versions of the Navier-Stokes equations in vertically integrated form. MURTY (1984) has given the detailed derivation of these equations. He used a right-handed rectangular Cartesian coordinate system with the origin located at the undisturbed level of the free surface. The coordinate system is such that the x-axis points towards east, the y-axis points towards north, and the z-axis points upwards.

*Linear Storm Surge Equations and Boundary Conditions*

We will first consider the linear storm surge equation most commonly used, following WELANDER (1961). Assume that the water is homogeneous and incompressible, and that friction due to vertical shear is much more important than horizontal friction. Then, the equations of motion in a right-handed Cartesian coordinate can be written as

$$\frac{\partial u}{\partial t} + u\frac{\partial u}{\partial x} + v\frac{\partial u}{\partial y} + w\frac{\partial u}{\partial z} - fv = -\frac{1}{\rho_0}\frac{\partial P}{\partial x} + \frac{1}{\rho_0}\frac{\partial \tau_x}{\partial z} \tag{2.1}$$

$$\frac{\partial v}{\partial t} + u\frac{\partial v}{\partial x} + v\frac{\partial v}{\partial y} + w\frac{\partial v}{\partial z} + fu = -\frac{1}{\rho_0}\frac{\partial P}{\partial y} + \frac{1}{\rho_0}\frac{\partial \tau_{yx}}{\partial z} \tag{2.2}$$

$$\frac{\partial w}{\partial t} + u\frac{\partial w}{\partial x} + v\frac{\partial w}{\partial y} + w\frac{\partial w}{\partial z} = -\frac{1}{\rho_0}\frac{\partial P}{\partial z} - g \tag{2.3}$$

The continuity equation is

$$\frac{\partial u}{\partial x} + \frac{\partial v}{\partial y} + \frac{\partial w}{\partial z} = 0 \tag{2.4}$$

where u, v, w are velocity fields in the x, y, and z directions, f is the Coriolis parameter, g is gravity, $\rho_0$ is the uniform density of water, P is the pressure and $\tau_x$ and $\tau_y$ are the x and y components of the frictional stress.

With reference to the origin of the coordinate system located at the undisturbed level of the free surface (z = 0), the free surface can be denoted by z = h (x, y, t) and the bottom by z = –D (x, y). Let $\tau_{sx}$ and $\tau_{sy}$ denote the tangential wind stress components and let $P_a$ be the atmospheric pressure on the water surface. Then, the following boundary conditions must be satisfied. At the free surface z = h:

$$\tau_x = \tau_{s_x}, \tau_y = \tau_{s_y} \tag{2.5}$$

$$P = P_a \tag{2.6}$$

Since the free surface has to follow the fluid, we have an additional condition given by

$$\frac{\partial h}{\partial t} + u\frac{\partial h}{\partial x} + v\frac{\partial h}{\partial y} = w \qquad \text{at} \quad z = h \tag{2.7}$$

At the bottom, all the velocity components have to vanish. Thus

$$u = v = w = 0 \text{ at } z = -D \tag{2.8}$$

The traditional storm surge equations are derived by performing two operations of vertical integration and linearization. To perform the vertical integration, we define the x and y components of horizontal transport as follows:

$$M \equiv \int_{z=-D}^{h} u\,dz \quad \text{and} \quad N \equiv \int_{z=-D}^{h} v\,dz \tag{2.9}$$

Integrating the horizontal equations of motion (2.1) and (2.2) and the continuity equation (2.4) with respect to z from z = –D to h and using the boundary conditions defined by equations (2.5)–(2.8) gives

$$\frac{\partial M}{\partial t} + \frac{\partial}{\partial x}\widetilde{u^2} + \frac{\partial}{\partial y}\widetilde{uv} - fN = -\frac{1}{\rho_0}\int_{z=-D}^{h}\frac{\partial P}{\partial x}dz + \frac{1}{\rho_0}(\tau_{s_x} - \tau_{s_x}) \tag{2.10}$$

$$\frac{\partial N}{\partial t} + \frac{\partial}{\partial y}\widetilde{v^2} + \frac{\partial}{\partial x}\widetilde{uv} + fM = -\frac{1}{\rho_0}\int_{z=-D}^{h}\frac{\partial P}{\partial y}dz + \frac{1}{\rho_0}(\tau_{s_y} - \tau_{s_y}) \tag{2.11}$$

$$\frac{\partial h}{\partial t} + \frac{\partial M}{\partial x} + \frac{\partial N}{\partial y} = 0 \tag{2.12}$$

where, $\tau_{Bx}$ and $\tau_{By}$ are the x and y components of the bottom stress $\tau_B$. In equations (2.10) and (2.11), the following notation was used:

$$\frac{\partial}{\partial x}\widetilde{u^2} = \frac{\partial}{\partial x}\int_{-D}^{h} u^2\,dz$$

$$\frac{\partial}{\partial y}\widetilde{uv} = \frac{\partial}{\partial y}\int_{-D}^{h} uv\,dz \tag{2.13}$$

Next, the hydrostatic approximation will be made ignoring the nonlinear acceleration terms. To justify this, two assumptions are made: (a) the amplitude of surge is small with the water depth and (b) horizontal scale of the surge is large compared with the water depth. Following CHARNOCK and CREASE (1957), the following scale analysis can be performed to ascertain the relative importance of the various terms. Let L and H represent the characteristic horizontal scale and depth, respectively. The vertical velocity varies from zero at the bottom to about Z/T at the surface, where Z is characteristic amplitude of the surge and T is a characteristic period. The horizontal velocity is of the order of L/H. Z/T.

From equations (2.1) and (2.3), the pressure field is eliminated to obtain the following equation:

$$\frac{\partial^2 u}{\partial t \partial z} + \frac{\partial^2}{\partial x \partial z} u^2 + \frac{\partial^2}{\partial y \partial z} uv + \frac{\partial^2}{\partial z^2} uw - f\frac{\partial v}{\partial z} = \frac{\partial^2 w}{\partial t \partial z} + \frac{\partial^2}{\partial x^2} uw + \frac{\partial^2}{\partial x \partial y} vw + \frac{\partial^2}{\partial x \partial z} w^2 \tag{2.14}$$

$$1 \quad \frac{Z}{H} \quad \frac{Z}{H} \quad \frac{Z}{H} \quad fT \quad \left(\frac{H}{L}\right)^2 \quad \frac{Z}{H}\left(\frac{H}{L}\right)^2 \quad \frac{Z}{H}\left(\frac{H}{L}\right)^2 \quad \frac{Z}{H}\left(\frac{H}{L}\right)^2$$

In equation (2.14), the order of magnitude of each term relative to the first term is indicated under the term. If $(H/L)^2$ is small, all the term on right hand side of equation (2.14) can be neglected. This means that the amplitude of the surge is at most equal to water depth. Ignoring these terms amounts to the hydrostatic approximation. If Z/H is small, one can ignore the three nonlinear terms on the left side of equation (2.14).
The pressure terms can be evaluated follows:

$$\frac{\partial P}{\partial x} = g\rho_0 \frac{\partial h}{\partial x} + \frac{\partial P_a}{\partial x} = 0 \tag{2.15}$$

On vertical integration

$$\int_{-D}^{h} \frac{\partial P}{\partial x} dz \sim g\rho_0 D\frac{\partial h}{\partial x} + D\frac{\partial P_a}{\partial x} \tag{2.16}$$

Note that, here, h relative to D is ignored, which is consistent with the above approximation. Under the above simplifications, equations (2.14) and (2.12) finally reduce to so called linear storm surge prediction equations:

$$\frac{\partial M}{\partial t} - fN = -gD\frac{\partial h}{\partial x} - \frac{D}{\rho_0}\frac{\partial P_a}{\partial x} + \frac{1}{\rho_0}(\tau_{s_x} - \tau_{B_x}) \tag{2.17}$$

$$\frac{\partial N}{\partial t} + fM = -gD\frac{\partial h}{\partial y} - \frac{D}{\rho_0}\frac{\partial P_a}{\partial y} + \frac{1}{\rho_0}(\tau_{s_y} - \tau_{B_y}) \tag{2.18}$$

$$\frac{\partial h}{\partial t} + \frac{\partial M}{\partial x} + \frac{\partial N}{\partial y} = 0 \tag{2.19}$$

For convenience, hereafter, the subscript on the density field will be omitted.

In this linear storm surge prediction equations, the dependent variables are the transport components M and N and the water level h. The forcing functions are the atmospheric pressure gradients given by $\partial P_a/\partial x$ and $\partial P_a/\partial y$ and the wind stress components $\tau_{sx}$, and $\tau_{sy}$. The retarding force is the bottom stress. At this stage, there are more unknowns than the available equations. To get a closed system of equations, the bottom stress must be expressed in terms of the known parameters, such as the volume transports.

Die Küste, 63 Global Storm Surges (2001), 1-623



*Bottom Stress*

Here, parameterization of bottom stress, based on SIMONS (1973), will be discussed. Let $\mathbf{V}_B$ denote the velocity vector near the bottom. Then, the bottom stress $\tau_B$ can be expressed as

$$\tau_B = \rho_k \mid \mathbf{V}_B \mid \mathbf{V}_B \tag{2.20}$$

where, k is a non dimensional coefficient referred to as skin friction; the value of k is about $2.6 \times 10^{-3}$. If one assumes a uniform velocity distribution in the vertical and nothing that the horizontal transport vector **M** is given by

$$\mathbf{M} = (M, N) = \int_{-D}^{h} \mathbf{V_B} dz = \int_{-D}^{h} (u, v) dz \tag{2.21}$$

one obtains

$$\frac{\tau_B}{\rho} = B\mathbf{M} \quad \text{where} \quad B = \frac{k \mid \mathbf{M} \mid}{(D+h)^2} \tag{2.22}$$

In most storm surge studies, either for obtaining analytical solutions or for economizing on computer time in numerical models, the bottom stress relation (2.20) is linearized by assuming typical values either for the average velocities or the transport components. For a model of Lake Ontario, SIMONS (1973) assumed average velocities of the order of 10 $cms^{-1}$ in the shallow waters and about 1 $cms^{-1}$ in the deep waters of the lake. Thus, *B* varies from 0.0025/D to 0.025/D in C.G.S. units. RAO and MURTY (1970) used value of 0.01/D for *B* in their model for Lake Ontario.

Instead of the average velocity field, one can examine the mass transport, which varies more smoothly, for Lake Ontario, SIMONS (1973) gave a value of $2 \times 10^4$ to $4 \times 10^4$ $cm^2s^{-1}$ in the shallow as well as deep water, and this leads to $B = 50/D^2$ to $100/D^2$ in C.G.S. units. Another approach to prescribing the bottom stress is to specify the vertical turbulent diffusion of momentum by a constant eddy viscosity $\nu$. PLATZMAN (1963) deduced bottom friction coefficients as a function of the Ekman number, $D\sqrt{f/2\nu}$, in such a way that $B \to 0$ for grate depth and gives $B = 2.5\nu/D^2$ for shallow water. For lake Erie, PLATZMAN (1958a) took $\nu = 40$ $cm^2s^{-1}$, which gives $B = 100/D^2$ in C.G.S. units.
Thus the alternative for the bottom friction can be summarized

linear form $B = a/D$, $a \sim 0.01$ $cms^{-1}$
quasilinear form $B = b/D^2$, $b \sim 100$ $cm^2s^{-1}$ (2.23)
non linear form $B = k|\mathbf{V}|/D^2$, $k \sim 0.0025$

In most early storm surge studies the linear form has been used. FISCHER (1959) used the quasi-linear form, where as HANSEN (1956), UENO (1964), and JOHNS et. al (1981) used the nonlinear forms.

*Forcing Terms and Lateral Boundary Conditions*

In eq. (2.17) and (2.18), the forcing terms are gradients of the atmospheric pressure, $\delta P_a/\delta x$ and $\delta P_a/\delta y$, and the components of the wind stress, $\tau_{Sx}$ and $\tau_{Sy}$. In chapter 5, the meteorological problems will be considered in detail; here the forcing term will be discussed briefly. In principle, the atmospheric pressure gradients can be prescribed either from observations or from the prognosis of numerical weather prediction models. However, the wind stress is not routinely measured and must be deduced from wind observations or predicted winds. The wind stress is usually expressed as

$$\tau_S = \rho_a k \mid \mathbf{V_a} \mid \mathbf{V_a} \tag{2.24}$$

where, $\rho_a$ is the density of air ($1.2 \times 10^{-3}$ gm. cm$^{-3}$) and $\mathbf{V_a}$ is the wind velocity at the anemometer level. The parameter K is the drag coefficient (non dimensional) and is usually given a value of about $3 \times 10^{-3}$ (PLATZMAN, 1958a; UENO, 1964). However, SIMONS (1973) suggested that for the Great Lakes, a more appropriate value for k is about $1.2 \times 10^{-3}$.

Next follows a brief consideration of the lateral boundary conditions to be specified so that the system of equations described by equation (2.17) and (2.19) is complete (details of the lateral boundary conditions will be discussed later). The main lateral boundary condition is that the transport normal to the coastline is zero, i.e.

$$M \cos\phi + N \sin\phi = 0 \tag{2.25}$$

where, $\phi$ is the angle between the x-axis and the normal to the coastline. If it is assumed that the depth of the water is zero at the shoreline, then the tangential component of the volume transport vector must also be zero. The boundary condition in the open part of the water body is more difficult to prescribe. Since the contribution to the storm surges comes mainly from the shallow water region, a generally followed procedure is to locate the outer boundary in the deep water and assume that the water level perturbation there is zero. However, this may not be satisfactory in certain situations, as will be shown later.

## 2.2 Numerical Finite Difference Solutions

Beginning in the late 1940s, several finite-difference techniques were developed by people working in the field of meteorology with the aim of predicting the weather through numerical solutions of the governing partial differential equations.

MURTY (1984) has discussed in detail the numerical finite-difference solutions for two-dimensional models for storm surges and tides. Finite differencing of the time derivative and the computational stability of the finite difference schemes has also been described in detail by MURTY (1984). Readers are advised to refer to the book of MURTY (1984) for detailed mathematical description.

## 2.3 Staggered and Nonstaggered Grid Schemes

MURTY (1984) described in detail the numerical integration using conjugate Richardson lattice. The Richardson lattice is a "staggered grid" because the variables are staggered in

Die Küste, 63 Global Storm Surges (2001), 1-623



space on the grid. The leapfrog scheme for integration in time is also a staggered scheme (in time). Nonstaggered grids and time integration were used in storm surge calculations until the early 1960s.

Away from the boundaries, central differencing is the most convenient manner of space discretization. However, near (and at) the boundaries, special attention is required; one can place fictitious points outside the boundary or use one-sided difference schemes.

MURTY (1984) has discussed various kind of grid schemes used in discritization of storm surge model equations. He has also described the advantages and the limitations of these grids.

## 2.4 Treatment of Open Boundaries

At times, storm surge calculations might have to be performed in a limited region of a large water body. This problem could be tackled in at least two different ways. In one approach, one can perform the calculations in the large water body of which the smaller water body is a part and then use the results for the area of interest. However, this approach is not economical and may not even be possible for certain water bodies. Also, there may be a problem with the resolution, since one has to model a larger water body. In the second approach, artificial open boundaries can be introduced around the area of interest and the calculations can be performed in the limited region of interest. However, along these artificial open boundaries, certain conditions have to be introduced, and without proper considerations, these conditions might make the results in the interior region inaccurate.

The commonly used practice of putting zero surface elevation at the sea boundary is not at all satisfactory, because this amounts to perfect reflection at the sea boundary. A better approximation (HEAPS, 1974; HENRY and HEAPS, 1976) is to assume that all outward travelling waves are normal to the boundary and to calculate the volume transports M (or N) from the water level h at the nearest interior grid point; i.e. $M = [g (D + h)]h^{1/2}$ . This is the so-called radiation condition.

REID (1975) corrected a misconception commonly held (e.g. FORRISTALL, 1974) in applying open boundary conditions. FORRISTALL (1974, p. 2722) stated at shallow water (lateral) boundary points, derivative of velocity perpendicular to the boundary is set equal to zero so that the transport across the boundary may be calculated from the adjacent flow. This condition is designed to let long waves pass unimpeded through the artificial boundary.

Reid showed that, although such a condition will permit flow of fluid to or from the system, it would produce total reflection of long waves and not zero reflection as FORRISTALL stated.

HERPER and SOBEY (1983) considered the specification of realistic open-boundary conditions for the numerical simulations of hurricane storm surge in the context of the very considerable spatial extend of the meteorological forcing. They reviewed existing practice and proposed an alternative approach, a Bathystrophic Storm tide approximation to open boundary water level. This boundary condition is closely related to the Hydrodynamics, responds realistically to storm forcing and also gives realistic water level contour and flow pattern close to the open boundaries.

BODE and HARDY (1997) while giving a detailed review of open boundary conditions conclude that in spite of the effort expanded on the development of artificial open boundary conditions, model studies show that the ideal way to minimise the problem is to use as large a domain as possible.

## 2.5 Numerical Treatment of the Nonlinear Advective Terms

The linearized versions of the storm surge equations have widely been used in storm surge modelling. However, in shallow-water areas and in the computation of the horizontal motion, at time the nonlinear advective terms might have to be included. CHARNOCK and CREASE (1957) showed through dimensional analysis that the nonlinear advective terms become important when the free surface height is of the same order of magnitude as the water depth.

FLATHER and HEAPS (1975) developed a model for Morecambe Bay allowing for the inclusion of the nonlinear advective terms.

The scheme for the nonlinear advective terms used by FLATHER and HEAPS (1975) is based on the angled derivative approach suggested by ROBERTS and WEISS (1966).

FALCONER (1980) introduced a conditionally stable three time level implicit scheme including the nonlinear advective terms. This scheme is especially suitable for narrow entrance harbors and estuaries where the nonlinear instability problems associated with rapidly changing velocity fields might be very important.

JOHNS et al. (1981) and DUBE et al. (1985a) used conditionally stable semi-explicit finite difference scheme to model storm surge in the Bay of Bengal and Arabian Sea. Vertically integrated predictive equations written in the flux form for their models are:

$$\frac{\partial \zeta}{\partial t} + \frac{\partial \tilde{u}}{\partial x} + \frac{\partial \tilde{v}}{\partial y} = 0 \tag{2.26}$$

$$\frac{\partial \tilde{u}}{\partial t} + \frac{\partial}{\partial x}(u\tilde{u}) + \frac{\partial}{\partial y}(v\tilde{u}) = f\tilde{v} = -g(\zeta + h)\frac{\partial \zeta}{\partial x} + \frac{Fs}{\rho} - \frac{c_f + \tilde{u}}{(\zeta + h)}(u^2 + v^2)^{1/2} \tag{2.27}$$

$$\frac{\partial \tilde{v}}{\partial t} + \frac{\partial}{\partial x}(u\tilde{v}) + \frac{\partial}{\partial y}(v\tilde{v}) = f\tilde{u} = -g(\zeta + h)\frac{\partial \zeta}{\partial x} + \frac{Gs}{\rho} - \frac{c_f + \tilde{v}}{(\zeta + h)}(u^2 + v^2)^{1/2} \tag{2.28}$$

where, $\tilde{u} = (\zeta + h)u$ and $\tilde{v} = (\zeta + h)v$; and depth integrated currents are defined as

$$(u, v) = \frac{1}{(\zeta + h)} \int_{-h}^{\zeta} (u, v)\, dz$$

$(F_s, G_s)$ are the x and y components of wind stress and $(\zeta + h)$ represents the total water depth. The grid scheme used by the authors is a staggered grid in which there are three distinct computational points. The arrangement of grid points is indicated in Fig. 2.1.

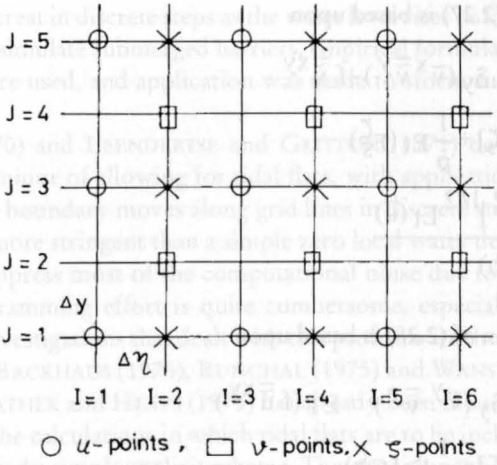


Fig. 2.1: Grid point arrangement.

Any variable X, at a grid point (i, j) may be represented by

$$X(x_i, y_j, t_p) = X_{ij}^{p}$$

In order to describe the finite – difference equations, they defined difference operators by

$$\Delta_t x = (X_{ij}^{p+1} - x_{ij}^{p})/\Delta t$$
$$\delta_x x = (X^{p}_{i+1,j} - X^{p}_{i-1,j})/(2\Delta x)$$
$$\delta_y x = (X_{i,j+1}^{p} - X_{i,j-1}^{p})/(2\Delta y)$$

Averaging operations are defined by

$$\overline{X}^{x} = \frac{1}{2}(X^{p}_{i+1,j} + X^{p}_{i-1,j})$$
$$\overline{X}^{y} = \frac{1}{2}(X^{p}_{j,j+1} + X^{p}_{i,j-1}) \qquad (2.29)$$
$$\overline{X}^{xy} = \overline{\overline{X}^{x}}^{y}$$

and a shift operator is defined by

$$E_t X = X_{i,j}^{p+1} \qquad (2.30)$$

The continuity equation is discretized as

$$\Delta t(\xi) + \delta x(\tilde{u}) + \delta y(\tilde{v}) = 0 \qquad (2.31)$$

Equation (2.31) yields an updating procedure to compute the elevation at all the interior ζ-points and is consistent with the mass conservation in the system.

The discretization of (2.27) is based upon

$$\Delta t(\bar{u}) + \delta_x(\bar{u}^x \bar{\bar{u}}^x)\ \delta_y(\bar{v}^x \bar{\bar{v}}^y) - f\,\bar{\bar{v}}^{xy}$$
$$= -g\,Et[(\bar{\zeta}^x + h)\,\delta_x \zeta] + \frac{1}{\rho} Et(F_\zeta) \qquad (2.32)$$
$$- \frac{C_f + [(u^2 + (\bar{v}^{xy})^2]^{1/2}\, Et(\bar{u})}{Et(\bar{\zeta}^x + h)}$$

A similar discretization of (2.28) is based upon

$$\Delta t(\bar{v}) + \delta_x(\bar{u}^y \bar{\bar{v}}^x)\,\delta_y(\bar{v}^y \bar{\bar{v}}^y) + ET(f\,\bar{\bar{u}}^{xy})$$
$$= -g\,Et[(\bar{\zeta}^y + h)\,\delta_x \zeta] + \frac{1}{\rho} Et(G_\zeta) \qquad (2.33)$$
$$- \frac{C_f + [(\bar{u}^{xy})^2 + v^2]^{1/2}\, Et(\bar{v})}{Et(\bar{\zeta}^y + h)}$$

The following general points are made about the discretizations. In equations (2.32) and (2.33), the pressure gradient terms are evaluated at the advanced time-level. This is possible explicitly using values of $\zeta$ previously updated by application of (2.31) and, following SIELECKI (1968), ensures computational stability subject only to the time-step being limited by the space increment and gravity wave speed. In (2.32), the Coriolis team is evaluated explicitly at the old time level whereas in (2.33) it is evaluated at the advanced time level using the previously updated value of u. Finally in both (2.32) and (2.33), the friction term is evaluated partly implicitly, the resulting difference equations being solved algebraically before their incorporation into the updating scheme. This ensures unconditional computational stability with reference to the treatment of the dissipative terms.

DAVIS (1976) included nonlinear advective terms in the equations of motion and continuity written in the spherical polar coordinate system.

BOOK et al. (1975) developed "flux-correlated" transport schemes for the proper inclusion of the nonlinear advective terms. In this scheme, any artificial diffusion added to the advection term in the first step is subtracted in the subsequent step. LAM (1977) compared various schemes of this type and showed that a central-difference scheme produces oscillations of great amplitude, whereas a one-sided upstream-differencing scheme shows a large false diffusion. However, the one-sided upstream-differencing scheme combined with a flux-corrected transport scheme gave reliable results.

## 2.6 Moving Boundary Models and Inclusion of Tidal Flats

Moving boundary models have been developed to allow for the climbing of the surge on the coastline as well as to include tidal flats, which become submerged during flood and dry during ebb.

Omitting the non-linear advective and Coriolis terms, REID and BODINE (1968) developed a technique for the inclusion of tidal flats. The coastal boundary that follows the grid

lines can advance or retreat in discrete steps as the water level rises or falls. To allow for flooding of dry land and to simulate submerged barriers, empirical formulae based on the concept of flow over weirs were used, and application was made to storm surges in Galveston Bay, *TX*.

LEENDERTSE (1970) and LEENDERTSE and GRITTON (1971) developed an alternating direction implicit technique of allowing for tidal flats, with application to Jamaica Bay, NY. In this model also, the boundary moves along grid lines in discrete steps. However, the condition for dry area is more stringent than a simple zero local water depth (the stringent condition was used to suppress most of the computational noise due to the movements of the boundary). The programming effort is quite cumbersome, especially due to the implicit scheme used. Other investigations that dealt with this problem are those of RAMMING (1972), ABBOTT et al. (1973), BACKHAUS (1976), RUNCHAL (1975) and WANSTRATH (1977a, 1977b).

The model of FLATHER and HEAPS (1975) has already been introduced in the section on nonlinear terms. For the calculations in which tidal flats are to be included, they omitted the advective terms and used a simple explicit scheme. The conditions they used depended on an examination of the local water depth and the slope of the water level. Use of the condition on the water level slope specially suppresses the unrealistic movements of the boundary. As in the models of REID and BODINE (1968) and LEENDERTSE and GRITTON (1971), the water-land boundary follows grid lines in discrete time steps.

Before the calculation of current $u$ and $v$ in the $x$ and $y$ directions at each time step, each grid point was tested to see if it was wet (i.e. positive water depth) or dry (zero water depth). If the point was dry, then the current was prescribed as zero. For wet points, u and v were computed from the relevant equations.

YEH and YEH (1976) developed a moving boundary model; i.e. the boundary between dry land and the water can move with time using an ADI technique. Since the technique was found to be numerically inefficient, YEH and CHOU (1979) developed an explicit technique. They showed that the moving boundary (MB) model gives storm surge amplitudes that could be 30 % smaller than those given by a fixed boundary (FB) model, FB models that assume a fixed vertical wall at the water-land boundary could overestimate the surge by about 30 %. YEH and CHOU (1979) used a model to compute surges in the Gulf of Mexico.

TETRA TECH INC. (1978) developed coastal flooding storm surge models, which included the nonlinear advective terms. Coriolis terms, wind stress, atmospheric pressure gradients, and bottom stress. Here, discussion will be confined to the treatment of the land-water boundary. Usually, the landslope onshore is much greater than the slope of the ocean floor. In such situations, the coastal surge is assumed to propagate overland to its corresponding contour level (when the distance to that contour line is much less than one grid interval). However, there are certain regions, such as western Florida, where the onshore slope is very small and the limiting contour interval may be several kilometers inland. For such cases, a one-dimensional run up model is used at various traverses.

SIELECKI and WURTELE (1970) developed a moving boundary scheme in which the lateral boundary of the fluid is determined as a part of the solution. They tested the validity of their scheme by comparing the results of some simple numerical experiments with the results from analytical solutions. Actually, their scheme consists of three different methods: (a) Lax-Wendroff scheme (LAX and WENDROFF, 1960) as modified by RICHTMEYER (1963); (b) using the principle of energy conservation as formulated by ARAKAWA (1966); (c) using the quasi implicit character of the difference equations.

REID and WHITAKER (1976) and REID et al. (1977b) allowed for vast stretches of vegetation and marsh grass (such as in Lake Okeechobee in Florida) in storm surge models. They

showed that when the marsh grass extends above the water surface, a single canopy flow regime results, whereas when the vegetation does not extend above the water surface, a two-layer regime exists. Flooded marsh areas are treated as an ensemble of subgrid scale obstacles.

For submerged vegetation the model is similar to a two-layer system. The interfacial stress is formulated in terms of a coupling coefficient and the flow differential. The friction due to individual canopies is parameterized through a drag coefficient and the dimensions of the elements. When the canopy elements are not submerged, a sheltering factor is introduced.

JOHNS et al. (1982) and subsequently DUBE et al. (1986a) describe a finite difference method, which models a continuously moving lateral boundary. JOHNS et al. (1982) applied it to the numerical simulation of the surge generated by 1977 Andhra cyclone which struck the east coast of India while DUBE et al. (1986) applied it to 1970 Bangladesh cyclone. In both the studies author employ a curvelinear representation of the lateral boundaries, which allow the continuous deforming of the coastline to be model in a fairly realistic way.

For the formulation of model they considered the coastal boundary as time variant situated at $x = b_1 (y, t)$ and an off shore open sea boundary situated at $x = b_2 (y)$. They also introduced a coordinate transformation to facilitate the numerical treatment of an irregular boundary configuration. The transformation is of the type

$$\xi = \frac{x - b_1(y,t)}{b(y,t)} \tag{2.34}$$

where, $b_1 (y, t) = b_2 (y)-b_1 (y, t)$

The equation of continuity and momentum are written in flux form with $\xi$ , y, t as new independent variables

$$\frac{\partial}{\partial t}(Hb)+\frac{\partial}{\partial \xi}(HbU)+\frac{\partial}{\partial y}(\tilde{v}) = 0 \tag{2.35}$$

$$\frac{\partial \tilde{u}}{\partial t}+\frac{\partial}{\partial \xi}(U\tilde{u})+\frac{\partial}{\partial y}(v\tilde{u})-f\tilde{u} = -gH\frac{\partial \zeta}{\partial \xi}+\frac{bF_s}{\rho}-\frac{c_f \tilde{u}}{H}(u^2+v^2)^{1/2} \tag{2.36}$$

$$\frac{\partial \tilde{v}}{\partial t}+\frac{\partial}{\partial \xi}(U\tilde{v})+\frac{\partial}{\partial y}(v\tilde{u})+f\tilde{u} = -gH[\frac{\partial \zeta}{\partial y}-\{\frac{\partial b_1}{\partial y}+\xi\frac{\partial b}{\partial y}\}\frac{\partial \zeta}{\partial \xi}] \tag{2.37}$$

$$+\frac{bG_s}{\rho}-\frac{c_f \tilde{u}}{H}(u^2+v^2)^{1/2}$$

Where

$$bU = u-[\frac{\partial b_1}{\partial t}+\xi\frac{\partial b}{\partial t}]-v[\frac{\partial b_1}{\partial y}+\xi\frac{\partial b}{\partial y}],$$

$\tilde{u} = Hbu$ $\tilde{v} = Hbv$ and H is total depth ($\zeta$ + h)

The changing position of the coastline is determined by the condition that the depth of the water be zero at the coastline. This leads to

$H = 0$ at $x=b_1 (y, t)$ (2.38)

or equivalently,

$$\zeta\,(\xi = 0, y, t) + h\,\{x = b_1\,(y, t), y\} = 0 \tag{2.39}$$

Depending on whether $b_1\,(y, t) \gtrless b_1\,(y, 0)$ the authors either interpolate or use new inland orographical data to fix the value of $h\,[b_1\,(y, t), y]$. This is done by differentiating (2.39) with respect to t. This leads to

$$\zeta(\xi = 0, y, t) + \frac{\partial b_1}{\partial t} s = 0 \tag{2.40}$$

where,

$$S = [\frac{\partial h}{\partial x}]_{x=b_1(y,t)} \tag{2.41}$$

If S is prescribed, (2.40) yields a prognostic equation for $b_1$. The most simple case corresponds to constant value of s when (2.41) immediately integrates to

$$b_1(y, t) = b_1(y,0) - \frac{1}{S}\zeta(\xi = 0, y, t) \tag{2.42}$$

Then if $\zeta\,(\xi = 0, y, t) < 0$ the sea surface at the shoreline depressed and the shoreline has consequently recoded from its initial position. If $\zeta\,(\xi = 0, y, t) > 0$, there is a positive surge; the elevation at the shoreline is raised above its equilibrium level and there is a corresponding inland penetration of water.

## 2.7 Nested Grids and Multiple Grids

In this section, the use of multiple grids, such as combinations of coarse and fine grids, to model storm surges in a water body will be considered. The philosophy behind using multiple grids is to be able to reduce the total computational effort by placing a coarse grid in the deep (and offshore) region and couple this with a finger grid in the shallow coastal area.

In connection with storm surge studies in the Beaufort Sea, HENRY (1975) and HENRY and HEAPS (1976) used a combination of coarse and fine grids but the grids were not coupled dynamically. Examples of studies in which the grids are dynamically coupled are those of ABBOTT et al. (1973), RAMMING (1976), SIMONS (1978), and JOHNS and ALI (1980) and JOHNS et al. (1983a).

GREENBERG (1975, 1976, 1977, 1979) used a combination of grids in his numerical model tides in the Bay of Fundy.

# 3. Finite-Element Models

## 3.1 Introduction

This chapter will be concerned with the finite-element approach to storm surges and tides. Compared with the finite-difference methods, the finite-element methods are more recent (they began to appear in the literature in the middle 1960s) but they are better suited for representing the topography realistically than are regular-grid finite-difference techniques.

Following WANG and CONNOR (1975a), the literature on finite-element methods will be briefly reviewed. Unlike in the finite-difference method, in the finite element method the variables satisfying the governing equations and boundary conditions are approximated be piecewise polynomials. The main advantage of the finite-element method is the highly flexible grid so that real water bodies can be modeled more realistically.

WANG and CONNOR (1975a) distinguished between the finite-element method and the discrete-element method as follows. The discrete-element method makes use of both the finite difference and finite-element methods. The discrete-element method, rather than using differential equations for the infinitesimal element, one can perform all the balances on the computational discrete element which can have an arbitrary shape. However, one generally uses square, rectangular, or triangular elements. In an element the variation of any given parameter is represented by discrete nodal values. Usually, these nodes are located at the center of the sides of the elements. To satisfy conservation, the discrete equation must approximate the differential equations as the control volume is reduced to zero. This may be difficult to prove for odd-shaped elements. SIMON-TOV (1974) and ERASLAN (1974) gave some examples of the discrete-element method. WANG and CONNOR (1975a) pointed out that one drawback of the discrete-element method is that if one wants to refine the grid at one point, e.g. $(x_0, y_0)$, then one must have the same value of $\Delta x$ for all the elements along the line $y = x_0$ and the same value of $\Delta y$ for all elements along the line $x = y_0$. However, this is not a serious shortcoming, because either an interpolation technique or trapezoidally shaped elements can be developed to get around this problem.

According to WANG and CONNOR (1975a) the finite-element method was first used in 1956 in aeronautics. Until the late 1960s its use was mainly confined to solid and structural mechanics (ZIENKEWICZ, 1971). In the early stages the success of the finite-element method dependent on the existence of a variational statement of the problem. However, FINLAYSON and SCRIVEN (1965) showed that Galerkin's method can be derived from the method of weighted residuals and there is no need for a variational statement.
Consider the differential equation

$$Lu = f_0 \tag{3.1}$$

where, L is a differential operator, u is an exact solution, and $f_0$ is the inhomogeneous term. Define the residual R as

$$R = L\hat{u} - f_0 \tag{3.2}$$

Application of a weighting function w to the residual and summation over the complete domain $\Omega$ gives

$$WR = \int_{\Omega} Rwd\omega = \int_{\Omega} (L\hat{u} - f_o)wd\omega \tag{3.3}$$

where, WR is the weighted residual. The finite-element solution is based on the condition that the weighted residual should vanish.

For some application of the finite-element method to circulation in shallow water bodies, see GALLAGHER and CHAN (1973), who calculated the steady wind driven circulation in shallow lakes under the rigid lid approximation. TAYLOR and DAVIS (1972) used a fourth-order predictor-corrector method for the time integration. They compared the trapezoidal rule and the finite elements in time. GROTKOP (1973) studied the same problem using linear finite elements in time. According to WANG and CONNOR (1975a) this method is less accurate than the trapezoidal rule. Consider the equation

$$\underset{\sim}{M}\,\dot{\underset{\sim}{x}} = \underset{\sim}{F} \tag{3.4}$$

where the tilde denotes a matrix quantity. Applying the linear finite elements in time to this equation gives the following recurrence relation:

$$\underset{\sim}{M}\,\underset{\sim}{x}_{n+1} = \underset{\sim}{M}\,\underset{\sim}{x}_{n} + \Delta t\left(\frac{1}{3}F_n + \frac{2}{3}F_{n+1}\right) \tag{3.5}$$

On the other hand, the trapezoidal rule can be written as

$$\underset{\sim}{M}\,\underset{\sim}{x}_{n+1} = \underset{\sim}{M}\,\underset{\sim}{x}_{n} + \frac{\Delta t}{2}\left(F_n + F_{n+1}\right) \tag{3.6}$$

Note that the trapezoidal form is centered around time $n + {}^1\!/_2$ and is better than the skewed form (eq. 3.5). TAYLOR and DAVIS (1972) made use of a cubic expansion in time based on trial runs. It should be noted that the predictor-corrector method and the cubic finite-element method give more accurate results than the trapezoidal rule; however, they require much more computational effort. Because of asymmetric matrices, even the trapezoidal rule is not very efficient.

NORTEN et al. (1973) used the Newton-Ralphson method including the nonlinear terms. WANG and CONNER (1975a, 1975b) gave some new concepts, which helped to solve troublesome details encountered in an earlier studies. The boundary condition of nonzero slip in the tangential velocity field is conceptually difficult to apply when curved land boundaries are approximated by triangular elements. At the break points of the model boundary, the nonzero tangential velocity component gives rise to flow across the adjoining segments. Then, to satisfy the continuity equation at the break points, one is forced to equate both velocity components to zero. NORTON et al. (1973) suggested that one should keep as few break points as possible and these points both the velocity component must be prescribed equal to zero. Once one is forced to do this, the flexibility of the finite-element grid is sacrificed; also, near the break points one must use a fine grid. This will necessitate the use of the long and narrow triangles (distorted elements) WANG and CONNOR (1975a) resolved this problem by a proper definition of a normal direction at the break points, and this permits a nonzero tangential component of the velocity without reducing the number of break points.

For a detailed derivation of the equations involved in the finite-element method see WANG and CONNOR (1975a). They solved several simple problems to enable comparison with analytical solutions. Finally, they applied the technique to a study of tides in the Massachusetts Bay. WANG and CONNOR (1975a) also formulated a two-layer model (for other details see CONNOR and WANG [1973] and WANG and CONNOR [1975b]).

WEARE (1976) compared the computational expenses for the shallow-water problems using finite-difference and finite-element methods and concluded that, at present, finite-element methods are less economical due to the use of band algorithms. However, the situation is changing now. GRAY and PINDER (1976) made a comprehensive comparison of finite-difference and finite-element methods and showed that the finite-element representation of the differential equations is essentially a spatial average of standard finite-difference equations written for each mode of the grid.

KLEINSTREUER and HOLDEMAN (1980) developed an interactive triangular finite-element mesh generator for water bodies of the arbitrary geometry. NIEMEYER (1979a) applied a finite-element technique to study tidal flow in certain water bodies in Hawaii. ORLOB (1972) used triangular grids for studying circulation in the San Francisco Bay area, but he wrote the equation in finite-difference form. FIX (1975) used a finite-element model to study the circulation in a limited area of the mid-ocean.

GROTKOP (1973) used a finite-element technique for studying waves in the North Sea. CHENG (1972, 1974), CHENG et al. (1976), CHENG and TUNG (1970), GALLAGHER et al. (1973), GALLAGHER and CHAN (1973) and HUEBNER (1974) applied finite-element techniques to study wind-driven circulation in lakes. Other relevant works are those of CHENG (1978), WALTERS and CHENG (1980a, 1980b), JAMART and WINTER (1979), MEI and CHEN (1975), REICHARD and CELIKOL (1978), HAUGUEL (1978), LE PROVOST (1978), LEIMKUHLER et al. (1975), and TAYLOR and HOOD (1973).

JAMART and WINTER (1978) used the finite-element approach to study tidal propagation. One of their important assumptions is periodic motion. Because of this assumption, this model cannot be used to study storm surges (which are not periodic). KAWAHARA et al. (1977) used a mixed approach of the finite element method and perturbation method, again with the assumption of periodic motion. THACKER (1977) studied the normal modes in a circular basin using an irregular-grid finite difference model (this will be considered in detail below). WANG (1977) criticized Thacker's work and pointed that Thacker's model is unstable and inaccurate.

MEI and CHEN (1975) introduced a hybrid-element method for water problems in infinite fluid domain. They introduced artificial boundaries and thus divided the fluid into a finite-element region, in the neighborhood of infinity or of singular points. In the finite element region polynomial interpolating functions are used to approximately represent the unknown functions. In the super-element region, infinite series solutions are used. Numerical computations involve only integrals in a finite domain and the inversion of a banded symmetric matrix. Examples of shallow-water waves in a harbor are included.

HOUSTON (1978) used a finite-element numerical model to study the interaction of tsunamis with the Hawaiian Islands. This model solves the generalized Helmholtz equation:

$$\nabla[D(x,y)\nabla\phi(x,y)]+\frac{\omega^2}{g}\phi(x,y)=0$$

where, $\phi(x, y)$ is the velocity potential, $\omega$ is the angular frequency, and $D(x, y)$ is the water depth. This equation is not relevant for storm surge studies, at least in its present simple form.

Die Küste, 63 Global Storm Surges (2001), 1-623



## 3.2 Finite-Element Models for Tides and Storm Surges

BREBBIA and PARTRIDGE (1976) studied the tides and storm surges in the North Sea using two finite-element models. In both models they used six-noded triangular elements. One model made use of an implicit integration scheme with curved sides, and the other utilized an explicit integration scheme. The models are vertically integrated and include tides, wind stress, atmosphere pressure gradients, bottom friction, Coriolis force, and advection terms.

Following BREBBIA and PARTRIDGE (1976), a Cartesian coordinate system, with the origin at the equilibrium water level and the z-axis pointing upwards, is used. Let D (x, y) be the deviation of the free surface from its equilibrium position. The horizontal momentum equations can be written in the following form:

$$\frac{\partial u}{\partial t} + u\frac{\partial u}{\partial x} + v\frac{\partial u}{\partial y} = B$$
$$\frac{\partial v}{\partial t} + u\frac{\partial v}{\partial x} + v\frac{\partial v}{\partial y} = B \qquad (3.7)$$

$$B_x = fv - g\frac{\partial h}{\partial x} - \frac{\partial}{\partial x}\left(\frac{P_a}{\rho}\right) + \frac{1}{\rho}\tau_{S_x} - \frac{1}{\rho}\tau_{B_x}$$
$$B_y = fu - g\frac{\partial h}{\partial y} - \frac{\partial}{\partial y}\left(\frac{P_a}{\rho}\right) + \frac{1}{\rho}\tau_{S_y} - \frac{1}{\rho}\tau_{B_y} \qquad (3.8)$$

where, u and v the x and y components of the velocity field averaged in the vertical direction. The following expressions can be written for the surface stress, $\tau_s$, and the bottom stress, $\tau_B$.

$$\tau_{S_i} = \frac{\gamma}{\rho}\frac{W_i}{H^2}(W_x^2 + W_y^2)^{1/2}, \qquad i = x \text{ or } y$$
$$\tau_{B_i} = \frac{-g}{C^2}\rho\frac{V_i}{H}(u^2 + v^2)^{1/2}, \qquad i = 1, 2 \qquad (3.9)$$

If i = 1, $V_i$ = u; if i = 2, $V_i$ = v. Here, C is a Chezy coefficient, $W_x$ and $W_y$ are the x and y components of the wind, and $\gamma$ is a parameter related to the atmospheric density, $\rho_a$ ($\gamma = \rho_a$, constant). Finally, H = D + h.

The vertically integrated from of the continuity equation is

$$\frac{\partial H}{\partial t} + \frac{\partial}{\partial x}(Hu) + \frac{\partial}{\partial y}(Hv) = 0 \qquad (3.10)$$

At closed boundaries, the velocity component perpendicular to the boundary is set to zero, while the tangential component is nonzero. At open boundaries, either the normal component of the velocity or the water level is prescribed.

To develop the finite-element model, two momentum equations and the continuity equation (3.10) together with the influx type boundary condition must be written in the following weighted residual manner:

$$\iint\left(\frac{\partial u}{\partial t}+u\frac{\partial u}{\partial x}-B_x\right)\delta u\,dA=0$$
$$\iint\left(\frac{\partial v}{\partial t}+u\frac{\partial v}{\partial x}+v\frac{\partial v}{\partial y}-B_y\right)\delta v\,dA=0 \qquad (3.11)$$
$$\iint\left[\frac{\partial H}{\partial t}+\frac{\partial}{\partial x}(Hu)+\frac{\partial v}{\partial y}(Hv)\right]\delta H\,dA=\int(HV_n-H\overline{V}_n)\delta H\,dS=\int H\overline{V}_n\delta H\,dS$$

Where n denotes the normal and $V_n$ denotes the component of the velocity. It will be assumed that over an element, the same interpolation for the unknown u, v, and H. Thus

$$u=\phi u^n$$
$$v=\phi v^n \qquad (3.12)$$
$$H=\phi H^n$$

where, $\phi$ is the interpolation function and $u^n$, $v^n$, and $H^n$ are the nodal of u, v, and H. A six-nodal triangular finite-element grid was used. These elements were referred to as "isoparametric" by BREBBIA and PARTRIDGE (1976). The advantage of using curved elements is the suppression of the spurious forces generated on the boundaries by straight-line segments joining at an angle (CONNOR and BREBBIA 1976).
From eq. (3.11) and (3.12)

$$M\frac{\partial u^n}{\partial t}+Ku^n-fMv^n+G_xH^n+F_x=0$$
$$M\frac{\partial v^n}{\partial t}+Kv^n-fMu^n+G_yH^n+F_y=0 \qquad (3.13)$$
$$M\frac{\partial H^n}{\partial t}+C_xu^n-C_yy^n+F_H=0$$

with the following definitions (superscript T denotes the transpose):

$$K=\int\frac{\partial}{\partial x}(\phi^T\phi)u\,dA+\int\frac{\partial}{\partial y}(\phi^T\phi)v\,dA+\frac{g}{C^2}\int\frac{\phi^T(u^2+v^2)^{1/2}}{H}\phi\,dA$$

$$G_x=g\int\frac{\partial}{\partial x}(\phi^T\phi)\,dA$$

$$G_y=g\int\frac{\partial}{\partial y}(\phi^T\phi)v\,dA$$

$$M=\int\phi^T\phi\,dA$$

$$F_x=\int\phi^T\frac{\partial}{\partial x}\left(\frac{P_a}{\rho}\right)dA+\frac{\gamma}{\rho}\int\phi^T\frac{W_x}{H}(W_x^2+W_y^2)^{1/2}\,dA$$

$$F_y=\int\phi^T\frac{\partial}{\partial y}\left(\frac{P_a}{\rho}\right)dA+\frac{\gamma}{\rho}\int\phi^T\frac{W_y}{H}(W_x^2+W_y^2)^{1/2}\,dA$$

$$C_x=\int\frac{\partial}{\partial x}(\phi^T)H\phi\;dA$$

$$C_y=\int\frac{\partial}{\partial y}(\phi^T)H\phi\;dA$$

$$F_H=\int H\overline{V}_n\phi^T)dA$$

$$\begin{bmatrix} M & & \\ & M & \\ & & M \end{bmatrix} \begin{Bmatrix} \frac{\partial u^n}{\partial t} \\ \frac{\partial v^n}{\partial t} \\ \frac{\partial H^n}{\partial t} \end{Bmatrix} + \begin{bmatrix} K & -fM & G_x \\ fM & K & G_x \\ -C_x & -C_y & O \end{bmatrix} \begin{Bmatrix} u^n \\ v^n \\ H^n \end{Bmatrix} + \begin{Bmatrix} F_x \\ F_y \\ F_H \end{Bmatrix} = \begin{Bmatrix} 0 \\ 0 \\ 0 \end{Bmatrix} \tag{3.14}$$

or in the abbreviated form

$$MQ + KQ = F \tag{3.15}$$

Then, all such elements must be assembled and the boundary conditions applied. Two different time integration procedures were used. The first one an implicit scheme involving the tapezoidal rule. Assume

$$\dot{Q} = \frac{Q_T - Q_0}{\Delta t}$$

$$Q = \frac{Q_T + Q_0}{2} \tag{3.16}$$

$$F = \frac{F_0 + F_t}{2}$$

Then eq (3.15) becomes

$$\left( \frac{2}{\Delta t} M + K \right) Q_t = \left( F_0 + F_t \right) + \left( \frac{2M}{\Delta t} - K \right) Q_0 \tag{3.17}$$

This can be written in the abbreviated form as

$$K^* Q_t = F^* \tag{3.18}$$

Then, the recurrence relationship is given by

$$Q = \left( K^* \right)^{-1} F^* \tag{3.19}$$

The $K^*$ matrix which must be inverted will generally be a large asymmetrical banded matrix of size approximately three times the number of nodes by six times the element band width (i.e. the maximum difference between element nodal point numbers plus one). The explicit time integration used here follows the fourth-order Runge-Kutta method.

HAMBLIN (1976) and WILLIAMSON (1999) used finite-element techniques to study seiches, circulation and storm surges in Lake Winnipeg. His paper will be considered in some detail below. With reference to a Cartesian coordinate system (x, y) directed towards east and north, respectively, for a homogeneous fluid, under the hydrostatic approximation, with the neglect of the nonlinear terms and assuming a uniform value for the Coriolis parameter f:

$$\frac{\partial u}{\partial t} - fv + g\frac{\partial h}{\partial x} = 0$$
$$\frac{\partial v}{\partial t} + fu + g\frac{\partial h}{\partial y} = 0 \qquad (3.20)$$
$$\frac{\partial h}{\partial t} + \frac{\partial}{\partial x}(Du) + \frac{\partial}{\partial y}(Dv) = 0$$

where u and v are the vertically averaged horizontal velocity components in the x and y directions, D(x, y) is the water depth, and h(x, y, t) is the deviation of the water level from its equilibrium position.

Since we are concerned with periodic motion, the explicit time dependence can be eliminated by using an exponential time factor in the investigation of seiches. Then, the modified set of equations in (3.20) can be written using an elliptical operator (self-adjoint) for all boundary conditions (except when energy radiates through the openings). A variational formulation of the problem may be made and a numerical solution can be sought. For this, multiply the first equation of (3.20) by $u^*$ ($u^*$ is the complex conjugate of u) and add this to the product of the second equation (3.20) of with $v^*$. Then, use the continuity equation, integrate over the volume of the lake, and use Green's theorem to give the total kinetic and potential energy in the lake:

$$I(h) = \int_A \int \left\{ hh^* + \frac{gD}{f^2+\sigma^2}\left[\frac{f}{i\sigma}\left(\frac{\partial h}{\partial y}\frac{\partial h^*}{\partial x} - \frac{\partial h}{\partial x}\frac{\partial h^*}{\partial y}\right) + \left(\frac{\partial h}{\partial x}\frac{\partial h^*}{\partial x} + \frac{\partial h}{\partial y}\frac{\partial h^*}{\partial y}\right)\right]\right\} dxdy \qquad (3.21)$$

Where $i = \sqrt{-1}$ and $\sigma$ is the frequency of oscillation (i.e. seiche).

In deriving this equation, it is assumed that any of the following three boundary conditions can be used, noting that all of them permit zero energy flux across the boundaries: (a) vanishing depth at the shore line and finite values of h and its gradients, (b) finite depth at shoreline and zero velocity normal to the shoreline, and (c) finite depth and nonzero normal current but zero value of h across the boundary. HAMBLIN (1976) took zero depth at the coastline.

It can be shown that the function that minimizes eq. (3.21) will be the solution of eq. (3.20). The parameters h and $h^*$ are expanded in a series of trial functions $\Psi_i$ and weighting coefficients $q_i$':

$$h = \sum_i q_i' \Psi_1 \quad \text{and} \quad h^* = \sum_i q_i'^* \Psi_i$$

Substituting into eq. (3.21) gives

$$I\left(q'q'^*\right) = q'^{*T}\sigma^3 [L]q' + q'^{*T}\sigma [M]q' + q'^* [N]q' \qquad (3.22)$$

Here, [L], [M], and [N] are Hermitian matrices, q' is the vector of unknown coefficients, and $q'^{*T}$ is the transpose of q'*.

To determine the minimum of the approximating function:

$$\frac{\partial I}{\partial q'^*} = 0$$

which gives form eq. (3.22)

$$\sigma^3 [L]z + \sigma [M]z + [N]z = 0 \qquad (3.23)$$

where, z is the vector of weights minimizing I. The calculation of the approximating function proceeds as follows.

Lake Winnipeg is subdivided into triangular elements (Fig. 3.1a) giving a total of 144 elements. In the interior, the sides of the elements are straight lines, whereas at the coast they are curved. In locations where details are not important, a coarser grid has been used. The trial function is chosen such that the weighting coefficients become the free surface displacements, h, at the vertices and the three middle points (left side of Fig. 3.1b). Six points are required to determine the six coefficients of the second order polynomial in x and y. The quadratic surface determined in this manner is continuous across the edges between the triangles, but the gradients may not be continuous.

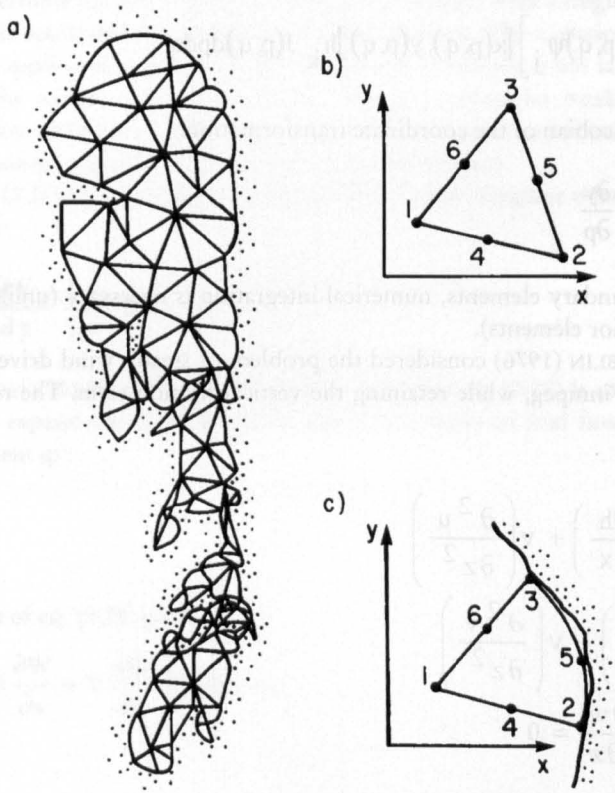


Fig. 3.1: (a) Triangular finite-element grid for Lake Winnipeg (144 elements); (b) a typical triangular element in the interior of the lake (the six nodes defining the element are numbered; (c) element adjacent to a boundary. (HAMBLIN, 1976)

Next, the depth D is expanded using an identical polynomial expression, in which the weighting coefficients become the specified depths at the six nodes of the triangle. If one expresses the Lagrangian interpolation functions in terms of the local triangular coordinates (rather than the global x and y coordinates), all the integrations in eq. (3.21) can be performed analytically for the interior elements. The matrices [L], [M], and [N] are formed by summing the contributions from each element I. Owing to the symmetry of the variational formulation, the computer storage requirements and the number of integrations required are halved.

In general, the side of a triangle along the coastline will not coincide with the boundary (right side of Fig. 3.1b) and one must transform the curved shoreline into a straight line by means of a coordinate transformation. Define a coordinate system such that

$$x = x(p, q)$$

$$y = y(p, q)$$

Then, a boundary integration of the form

$$\iint \Psi_i(x, y)\Psi_j(x, y)h_k \, dxdy$$

becomes

$$\iint \Psi_i\Big[x(p, q), y(p, q)\Psi_j\Big]\Big[x(p, q), y(p, q)\Big]h_k \, J(p, q)dpdq$$

where, J is the Jacobian of the coordinate transformation:

$$J = \frac{\partial x}{\partial p}\frac{\partial y}{\partial q} - \frac{\partial x}{\partial q}\frac{\partial y}{\partial p}$$

For the boundary elements, numerical integration is necessary (unlike analytical integration for interior elements).

Next, HAMBLIN (1976) considered the problem of steady wind driven circulation and setup in Lake Winnipeg, while retaining the vertical friction term. The relevant equations are

$$\begin{aligned} -fv &= -g\left(\frac{\partial h}{\partial x}\right) + \nu\left(\frac{\partial^2 u}{\partial z^2}\right) \\ fu &= -g\left(\frac{\partial h}{\partial y}\right) + \nu\left(\frac{\partial^2 v}{\partial z^2}\right) \\ \frac{\partial u}{\partial x} &+ \frac{\partial v}{\partial y} + \frac{\partial w}{\partial z} = 0 \end{aligned} \qquad (3.24)$$

where, is the vertical eddy viscosity and w is the vertical component of the velocity (here, u and v are not vertically averaged).

The boundary conditions are the following:

$$\nu\left(\frac{\partial u}{\partial z}\right)_{z=0} = \frac{\tau_{s_x}}{\rho} \quad \text{and} \quad \nu\left(\frac{\partial v}{\partial z}\right)_{z=0} = \frac{\tau_{s_y}}{\rho} \tag{3.25}$$

where, $\tau_{s_x}$ and $\tau_{s_y}$ are the wind stress components at the surface and

$$u\xi_{z=-D} = 0 \text{ and } v\xi_{z=-D} = -D = 0 \tag{3.26}$$

In the vertically integrated form the continuity equation is

$$\frac{\partial U}{\partial x} + \frac{\partial V}{\partial y} = 0 \tag{3.27}$$

where

$$(U, V) = \int_{-D}^{0} (u, v) dz$$

is the horizontal transport vector. At the lateral boundaries the normal transport is taken as zero.

Making use of the Galerkin method, HAMBLIN (1976) developed a technique, which enables one to determine the free surface and transport variables with a single solution of the equations, which is applicable for multiple-connected regions. The variational formulation used earlier is not applicable because the self-adjointness condition is not satisfied owing to the presence of the surface wind stress terms. Hence, a somewhat weaker formulation, namely the Galerkin method, is used. In this method, a stationary point (rather than a minimum) of an expression related to the function will be determined.

Multiply eq. (3.27) by a weighting function W(x, t) and integrate over the area of the whole lake to give

$$\int W \left( \frac{\partial U}{\partial x} + \frac{\partial V}{\partial y} \right) dx\, dy = 0 \tag{3.28}$$

Using Galerkin's method, W must be chosen such that eq. (3.27) is satisfied at all the nodes. As above, expand the variables U, V, and h in a series of trial functions i and the weighting coefficient qi':

$$h = \sum_i q_i \Psi_i$$

Partial integration of eq. (3.28) gives

$$\oint W(\bar{V} d\bar{n}) - \iint \left( U \frac{\partial W}{\partial x} + V \frac{\partial W}{\partial y} \right) dxdy = 0$$

Note that the line integral is zero in the case where there is no river input or outflow. Using eq. (3.26) one can eliminate U and V and write

$$\iint gD\left(E\frac{\partial h}{\partial x}-F\frac{\partial h}{\partial y}\right)\frac{\partial W}{\partial x}dxdy+\iint gD\left(F\frac{\partial h}{\partial x}+E\frac{\partial h}{\partial y}\right)\frac{\partial W}{\partial y}dxdy$$
$$=-\iint\left[C\tau_{s_x}-D\tau_{s_y}\right]\frac{\partial W}{\rho\partial x}dxdy-\iint\left[A\tau_{s_x}+C\tau_{s_y}\right]\frac{\partial W}{\rho\partial x}dxdy \qquad (3.29)$$

(For details on the parameters C, A, E and F, see WELANDER (1957). In this section, Welander's parameter D has been replaced by A.)

For evaluating eq. (3.29) the parameters D, C, A, E, F, $\tau_{s_x}$ and $\tau_{s_y}$ are expanded in a series of the same trial functions, i.e.:

$$\tau_{s_x}=\sum_{i}^{6}\tau_{s_{x_i}}\psi_i$$

Then, eq. (3.29) gives a system of six equations for each element:

$$\sum_{j=1}^{6}\iint gD\left(E\frac{\partial\psi_j}{\partial x}-F\frac{\partial\psi_j}{\partial y}\right)\frac{\partial\psi_i}{\partial x}dxdy+\iint gD\left(F\frac{\partial\psi_j}{\partial x}+E\frac{\partial\psi_j}{\partial y}\right)\frac{\partial\psi_i}{\partial y}dxdy$$
$$=-\iint\left(C\tau_{s_x}-A\tau_{s_y}\right)\frac{\partial\psi_i}{\rho\partial x}dxdy- \qquad (3.30)$$
$$\iint\left(A\tau_{s_x}-C\tau_{s_y}\right)\frac{\partial\psi_i}{\rho\partial x}h_j dxdy \quad \text{for } i=1 \text{ to } 6$$

For the whole water body, the equations are obtained by successive integrations of each element and by adding all these, which assumes continuity of $h_i$ at each node. The matrix

$$[M]h=B$$

is solved by Gaussian elimination.

Finally, HAMBLIN (1976) considered storm surges in Lake Winnipeg by beginning with the following time-dependent equations:

$$\frac{\partial u}{\partial t}-fv+g\frac{\partial h}{\partial x}=\frac{\tau_{S_x}}{D\rho}+\frac{\tau_{B_x}}{D\rho}$$
$$\frac{\partial v}{\partial t}-fu+g\frac{\partial h}{\partial y}=\frac{\tau_{S_y}}{D\rho}+\frac{\tau_{B_y}}{D\rho} \qquad (3.31)$$
$$\frac{\partial h}{\partial t}+\frac{\partial}{\partial x}(Du)+\frac{\partial}{\partial y}(Dv)=0$$

where, $\tau_B$ is the bottom stress.

HAMBLIN used a semianalytic technique (spectral method) in which the time variable is treated analytically and the space variables are treated numerically. Equations (3.31) can be written as in the finite element method as

$$\frac{dQ}{dt} = [M]Q + T(t) \tag{3.32}$$

where, the vector Q consists of the individual components of the current and h, the vector T consists of the wind stress components at each node, and the matrix [M] consists of coefficients which include f, g, D and the bottom friction.
For the initial condition, Q(0), the general solution of eq. (3.32) can be written as

$$Q(t) = [X(t)]Q(0) + \int_0^t [X(t-t')]T(t')dt' \tag{3.33}$$

where,

$$[X(t)] = [C]\begin{bmatrix} e^{\sigma_1 t} & & \\ & \ddots & \\ & & e^{\sigma_n t} \end{bmatrix}[C]^{-1}$$

Here, σ are the eigenvalues and [C] is the matrix of eigenvectors of

$$\{[M] - \sigma[I]\}\{C_i\} = 0$$

If the water body is initially at rest, Q(0) = 0 and a suddenly imposed wind stress can be written as T(t) = K. Integrating of eq. (3.33) gives

$$[Q(t)] = -[C]\begin{bmatrix} \frac{1}{\sigma_1} & & \\ & \ddots & \\ & & \frac{1}{\sigma_n} \end{bmatrix}[C]^{-1}K + [C]\begin{bmatrix} \frac{e^{\sigma_1 t}}{\sigma_1} & & \\ & \ddots & \\ & & \frac{e^{\sigma_n t}}{\sigma_n} \end{bmatrix}[C]^{-1}K \tag{3.34}$$

The first term in this equation can be shown to be $[M]^{-1}K$, which is the solution to the steady-state problem

$$[M]Q = K$$

The second term is a weighted sum of the free modes of oscillation of the discrete problem of order *n:*

$$\sum_i^n W_i \{C_i\} e^{\sigma_i t}$$

The transient response of the lake interpreted in this manner shows the connection between the general time-dependent problem and the steady-state seiche problems considered earlier.

Let the vector of the free surface displacements be denoted by S and let the eigenvectors, $C_i$, consist only of h; then, eq. (3.34) can be approximated:

$$h(t) \sim S + \sum_{i}^{n'} W_i \{C_i\} e^{\sigma t}$$

Where the limit n' is a subset of the total n eigenvectors of [M]. Since the water body is at rest initially, h(0) = 0. Then

$$[C]\, W = S$$

noting that the imaginary part of S is zero. Since initially, $u$ and $v$ are zero, then

$$\left.\frac{\partial h}{\partial t}\right|_{t=0} = 0 \quad \text{and} \quad \left.\frac{\partial^2 h}{\partial t^2}\right|_{t=0} = 0$$

Hence,

$$[C]\, \sigma\, W = 0 \text{ and } [C]\, \sigma^2\, W = 0$$

From these equations the weighting coefficients may be determined by minimizing the square of the free surface deviation, h, at each node in the water body.

After obtaining the step function response, h may be calculated for a general time history of wind forcing using the convolution integral. The unit impulse response can be obtained by differentiation of the step function response. The free surface displacement, h, can be calculated by convoluting the wind input, T(t), with $h_{imp}$

$$h(t) = \int_0^t h_{imp}\,(t - t')T(t')dt'$$

In the discrete form, this can be written as

$$h_K = \Delta t \sum_{i=0}^{j} h^i_{imp}\, T_{K-i}$$

### 3.3 Development in the late 1970s and early 1980s

PLATZMAN (1979) paid particular attention to proper treatment of the multiconnected regions in finite-element models and applied these concepts to a study of the normal modes of the world ocean. PLATZMAN (1981) discussed the response characteristics of finite-element tidal models.

LYNCH and GRAY (1980b) developed a variable size triangular-grid finite-element model in which the boundary is permitted to deform. This technique is especially suitable for simulating the penetration of storm surges over land. Certain details of their earlier works lea-

ding to this model are contained in GRAY and LYNCH (1977, 1979), LYNCH (1980) and LYNCH and GRAY (1978, 1979, 1980a). Here, mainly the moving boundary model will be considered.

LYNCH and GRAY (1980b) used the Galerkin finite-element approach (for fixed boundaries) with certain modifications to the moving boundary problem. First, consider the fixed boundary problem. In their notation, the problem may be stated as

$$Lu = f \tag{3.35}$$

where, L is a differential operator with derivatives in space and time, u(X, t) is the unknown function, f(X, t) is the known forcing function, X is the set of independent space variables, and t is time. One can use an approximate solution (x, t) as

$$u \sim \hat{u} = \sum_{j=1}^{N} u_j(t)\phi_j(X) \tag{3.36}$$

where, $\phi_j(X)$ are known basic functions.
Substituting eq. (3.36) into eq. (3.35) produces a nonzero residual r(X, t):

$$L \cdot - f \equiv r(X, t) \tag{3.37}$$

The basic requirement in the Galerkin procedure is that the residual must be orthogonal to each of the basis functions $\phi_j$, i.e.:

$$\left\langle r(X, t), \phi_i \right\rangle = 0 \quad i = 1, \ldots, N \tag{3.38}$$

where, angle brackets denote the inner product. It can be seen that eq. (3.38) forms a set of ordinary differential equations for the function $u_i(t)$.

For the moving boundary problem, the following modifications must be made to this procedure. The basis function $\phi_j$ now becomes an implicit function of time because its value at any point depends on the location of the nodes (of a grid which is deforming):

$$\phi_j = \phi_j[X, Xb(t)] = \phi_j(X, t) \tag{3.39}$$

where, the node coordinates are denoted by $X_b(t)$. In eq. 3.38, the integration domain of the inner product changes in time. Thus, the equations becomes nonstationary and nonlinear, as can be seen, for example, from the fact that the mass matrix, $\langle\phi_j, \phi_i\rangle$, which multiples the time derivative terms, duj/dt, changes with time.
Next, an additional relation must be added for the node motion:

$$\frac{d}{dt} X_b(t) = V_b(t) \tag{3.40}$$

where, $V_b$ is the velocity of node b. Generally, for the interior nodes $V_b = 0$ and for the boundary nodes $V_b = v_b$ where $V_b$ is the velocity of the node and $v_b$ is the fluid velocity at node b. Finally, eq. (3.36) must be replaced with

$$\hat{u}(X, t) = \sum_{j=1}^{N} u_j(t)\phi_j(X, t) \tag{3.41}$$

where, $u_j(t)$ is the value of · at node j (i.e. at the moving joint, $X_j(t)$).

The time derivatives of *(X, t)* will have, as expected, additional terms (underlined) not contained in a fixed boundary model:

$$\frac{\partial \hat{u}}{\partial t} = \sum_{j=1}^{N} \frac{du_j}{dt}\phi_j + \sum_{j=1}^{N} u_j \frac{d\phi_j}{dt} \tag{3.42}$$

and

$$\frac{\partial^2 \hat{u}}{\partial t^2} = \sum_{j=1}^{N} \frac{d^2 u_j}{dt^2}\phi_j + 2\sum_{j=1}^{N} \frac{du_j}{dt}\frac{\partial \phi_j}{\partial t} + \sum_{j=1}^{N} u_j \frac{\partial^2 \phi_j}{\partial t^2} \tag{3.43}$$

Since the spatial domain is changing with time, the terms $\partial\phi_j/\partial t$ and $\partial^2\phi_j/\partial t^2$ must be defined throughout the domain. Since these terms depend exclusively on the node locations $X_j(t)$ and their derivatives, in principle one can write expressions for $\partial\phi_j/\partial t$ and $\partial^2\phi_j/\partial t^2$. However, since this is a tedious procedure, LYNCH and GRAY (1980b) developed an alternate procedure, which is applicable to any isoparametric element. For any two-dimensional isoparametric element, let $x$ and $y$ represent the global coordinates and $\xi$ and $\eta$ represent the local coordinates. It is convenient to transform this element from the global domain (in which it may have an irregular shape) to the local domain in which it will always have the shape of a square (in the $\xi$, $\eta$) domain the basis functions depend only on $\xi$ and $\eta$). Since the ($\xi$, $\eta$) space does not deform, a basis function $\phi(\xi, \eta)$ at a location ($\xi_0$, $\eta_0$) will not change with time. The corresponding location to ($\xi_0$, $\eta_0$) in the (x, y) domain, however, may change with time and it depends on the isoparametric transformation:

$$X(t) = \sum_{i=1}^{N} X_i(t)\phi_i(\xi, \eta)$$

From this at a given point ($\xi$, $\eta$):

$$\frac{dX}{dt} = \sum_{i=1}^{M} \frac{dX_i}{dt}\phi_i(\xi, \eta) = \sum_{i=1}^{M} V_i(t)\phi_i(\xi, \eta) = V^e \tag{3.44}$$

Where $V^e$ is the elemental velocity (i.e. the velocity with which the element is moving). In a reference frame, which is moving with the elemental velocity, there is no change in $\phi_i$, and one can write

$$\frac{d\phi_i}{dt} = \frac{\partial \phi_i}{\partial t} + V^e \nabla\phi_i = 0 \tag{3.45}$$

Similarly, one can write

$$\frac{\partial^2 \phi_i}{\partial t^2} = -\left[\sum_{i=1}^{M} \frac{dV_i}{dt}\phi_j\right]\nabla\phi_i + 2V^e(\nabla V^e)\nabla\phi_i + V^e(\nabla\nabla\phi_i)V^e \tag{3.46}$$

LYNCH and GRAY (1979) showed that, for the shallow-water problem, rather than using the continuity equation in its ordinary form, a computationally superior way is to use the following wave equation, which can be derived form the momentum and continuity equations:

$$\frac{\partial^2 H}{\partial t^2} + \tau\frac{\partial H}{\partial t} = \nabla(gH\nabla\zeta) + HV(\nabla\tau) + \nabla[\nabla(HVV) + fXHV - W] \tag{3.47}$$

This has to be integrated in time together with the horizontal momentum equation

$$\frac{\partial V}{\partial t} = - V\nabla V - fXV - g\nabla\zeta - \tau V + \frac{W}{H} \tag{3.48}$$

where, H(X, t) is the total depth, ζX, t) is the free surface perturbation, h(X) is the equilibrium water depth, V(X, t) is the horizontal velocity vector (vertically averaged), f is the Coriolis parameter, g is gravity, and W(X, t) is the wind stress. The bottom stress is written as

$$\tau V(X,t) = \frac{g|V|V}{C^2 H} \tag{3.49}$$

where, C(X, t) is the Chezy coefficient.
The boundary condition is

$$H = 0 \text{ on } X = X_0 + \int_0^t V\,dt \tag{3.50}$$

Where X(t) is the location of the boundary at time t, $X_0$ is the initial time position of the boundary, V is the velocity of the boundary, and v is the velocity of the fluid.
Solutions of eq. (3.47) and (3.48) can be written in the finite-element form as follows:

$$\begin{aligned} H(X,t) &\sim \sum_{j=1}^{N} H_j(t)\phi_j(X,t) \\ V(X,t) &\sim \sum_{j=1}^{N} V_j(t)\phi_j(X,t) \\ \tau(X,t) &\sim \sum_{j=1}^{N} \tau_j(t)\phi_j(X,t) \end{aligned} \tag{3.51}$$

Substituting eq. (3.51) into eq. (3.47) and (3.48) and equating the weighted residuals to zero gives the following set of ordinary differential equations:

$$\sum_{j=1}^{N} \left( \frac{d^2 H_j}{dt^2}\left\langle \phi, \phi_i \right\rangle + 2\frac{dH_j}{dt}\left\langle \frac{\partial\phi}{\partial t}, \phi_i \right\rangle + H_i\left\langle \frac{\partial^2 \phi_j}{\partial t^2}, \phi_i \right\rangle \right.$$
$$\left. + \frac{dH_j}{dt}\left\langle \tau\phi_j, \phi_i \right\rangle + H_j\left\langle \pi\frac{\partial \phi}{\partial t}, \phi_i \right\rangle = \left\langle R_W, \phi_i \right\rangle \right. \tag{3.52}$$

and

$$\sum_{j=1}^{N} \left( \frac{dV_j}{dt}\left\langle \phi_j, \phi_i \right\rangle + V_j\left\langle \frac{\partial\phi}{\partial t}, \phi_i \right\rangle \right) = \left\langle R_M, \phi_i \right\rangle, i = 1,.....N \tag{3.53}$$

Here $R_w$( X,t) and $R_M$(x,t) are the right sides of eq. (3.47) and (3.48), respectively.

For the time derivative terms, a standard three-level finite-difference scheme has been used. For a stationary grid and one-dimensional case the C-F-L stability criterion reduces to

$$gH\left(\frac{\Delta t}{\Delta x}\right)^2 \leq \frac{1}{3} \tag{3.54}$$

The boundary condition v = v (i. e. fluid velocity equals the velocity of boundary movement) may lead to significant shearing of the boundary elements. To avoid this, LYNCH and GRAY (1980b) satisfied the mass conservation by requiring that

$$H = 0 \quad \text{or} \quad X = X_0 + \int_0^t V\,dt \qquad (V - v)n = 0 \tag{3.55}$$

Where n is a unit vector normal to the boundary. Rather than attempting to satisfy this relation at every boundary grid point, one can satisfy it in an average sense by requiring that

$$\int_S (V - v)n\,dS = 0 \tag{3.56}$$

Using the finite-element solution forms for V and v:

$$V \sim \sum_i V_i \phi_i$$
$$v \sim \sum_i v_i \phi_i \tag{3.57}$$

Substituting eq. 3.57 into 3.56 gives

$$\sum_i \int_S (V_i - v_i)n\phi_i\,dS = 0 \tag{3.58}$$

To obtain an expression for the local normal direction that each term of eq. (3.58) be zero, i.e.:

$$(V_i - v_i)\int_S n\phi_i\,dS = 0 \tag{3.59}$$

From this one can define the modal normal direction, $n_i$, as follows:

$$n_i \equiv \int_S n\phi_i\,dS \Big/ \left|\iint_S n\phi_i\,dS\right| \tag{3.60}$$

where, node i represent the junction of two moving segments of the boundary. Using the divergence theorem:

$$\int_S n\phi_i\,dS = \iint_A \nabla\phi_i\,dA \tag{3.61}$$

where, A is the total domain. The moving boundary condition becomes, finally,

$$H_i = 0 \quad \text{on} \quad X_i = X_{i,0} + \int_0^{t1} V_i dt, \qquad (V_i - v_i)n_i = 0 \tag{3.62}$$

$$V_i \lambda_i = 0$$

where, i represent all moving boundary nodes. Here, is the tangential direction at node $\lambda_i$. The second relation in eq. (3.62) is invoked to reduce element shearing.

A typical time step proceeds as follows.

1) Using eq. (3.60) and based on the existing grid, the nodal normal directions are determined.
2) The nodal velocities at the boundary are determined eq. (3.62). The locations of the nodes are calculated from the following finite-difference from of the first relation in eq. (3.62).

$$X_{i,t+\Delta t} \sim X_{i,t-\Delta t} + 2\Delta t V_{i,t} \tag{3.63}$$

3) The term dVi/dt (which is required to evaluate $\partial^2\phi_j / \partial t^2$ is calculated from

$$\frac{dV_i}{dt} = \frac{d^2X_i}{dt^2} \sim \frac{X_{i,t+\Delta t} - 2X_{i,t} + X_{i,t-\Delta t}}{(\Delta t)^2} \tag{3.64}$$

4) From eq. (3.52) and (3.53) $H_i$ and $V_i$ are calculated at $t + \Delta t$. Then steps are repeated by begining with the determination of the nodal normals.

## 3.4 The Corps of Engineers Models

In a series of reports and papers (BLAIN, 1997; CIALONE, 1991; LUETTICH et al., 1991, 1992; MARK and SCHEFFNER, 1993; SCHEFFNER et al., 1994; WESTERINK et al., 1992, 1993a, 1993b) the so-called "ADCIRC" model of the U.S. Army Corps of Engineers has been described. The following material is based on (WESTERINK et al., 1993b). "ADCIRC" stands for "An advanced three-dimensional circulation model for shelves, coasts and estuaries". The ADCIRC – 2DDI is a depth-integrated option of a system of two and three-dimensional hydrodynamic codes of "ADCIRC".

ADCIRC – 2DDI uses the depth-integrated equations of mass and momentum conservation, subject to the incompressibility, Boussinesq, and hydrostatic pressure approximations. Using the standard quadratic parameterization for bottom stress and neglecting baroclinic terms and lateral diffusion/dispersion effects leads to the following set of conservation statements in primitive non-conservative form expressed in a spherical coordinate system (FLATHER, 1988; KOLAR et al., 1994):

$$\frac{\partial \zeta}{\partial t} + \frac{1}{R\cos\varphi}\left[\frac{\partial UH}{\partial \lambda} + \frac{\partial (VH\cos\varphi)}{\partial \varphi}\right] = 0 \tag{3.65}$$

$$\frac{\partial U}{\partial t} + \frac{1}{R\cos\varphi} U\frac{\partial U}{\partial \lambda} + \frac{1}{R} V\frac{\partial U}{\partial \varphi} - \left(\frac{\tan\varphi}{R} U + f\right)V =$$

$$-\frac{1}{R\cos\varphi}\frac{\partial}{\partial \lambda}\left[\frac{p_s}{\rho_0} + g(\zeta - \eta)\right] + \frac{\tau_{s\lambda}}{\rho_0 H} + -\tau_* U \tag{3.66}$$

$$\frac{\partial V}{\partial t}+\frac{1}{R\cos\varphi}U\frac{\partial V}{\partial \lambda}+\frac{1}{R}V\frac{\partial V}{\partial \varphi}+\left(\frac{\tan\varphi}{R}U+f\right)U=$$
$$-\frac{1}{R}\frac{\partial}{\partial \varphi}\left[\frac{p_s}{\rho_0}+g(\zeta-\eta)\right]+\frac{\tau_{s\varphi}}{\rho_0 H}+-\tau_* V \qquad (3.67)$$

where

$t$ = time
$\lambda,\varphi$ = degrees longitude (east of Greenwich positive) and degrees latitude (north of the equator positive)
$\zeta$ = free surface elevation relative to the geoid
$U$, $V$ = depth-averaged horizontal velocities
$R$ = radius of the earth
$H = \zeta + h$ = total water column
$h$ = bathymetric depth relative to the geoid
$f = 2\,\Omega \sin\varphi$ = Coriolis parameter
$\Omega$ = angular speed of the earth
$p_s$ = atmospheric pressure at the free surface
$g$ = acceleration due to gravity
$\eta$ = effective Newtonian equilibrium tide potential
$\rho_0$ = reference density of water
$\tau_{s\lambda}, \tau_{s\varphi}$ = applied free surface stress

$$\tau_* = Cf\,\frac{\left(U^2+V^2\right)^{1/2}}{H}$$

$C_f$ = bottom friction coefficient

A practical expression for the effective Newtonian equilibrium tide potential as given by Reid (1990) is:

$$\eta(\lambda,\varphi,t)=\sum_{n,j}\alpha_{jn}C_{jn}f_{jn}(t_0)L_j(\varphi)\cos\left[\frac{2\pi(t-t_0)}{T_{jn}+j\lambda+V_{jn}(t_0)}\right] \qquad (3.68)$$

where

$C_{jn}$ = constant characterizing the amplitude of tidal constituent n of species j
$\alpha_{jn}$ = effective earth elasticity factor for tidal constituent n of species j
$f_{jn}$ = time-dependent nodal factor
$V_{jn}$ = time-dependent astronomical argument
$j$ = 0,1,2 = tidal species (j = 0, declinational; j =1, diurnal; j = 2, semidiurnal)
$L_0 = 3\sin^2\varphi - 1$
$L_1 = \sin(2\varphi)$
$L_2 = \cos^2(\varphi)$
$\lambda, \varphi$ = degrees longitude and latitude, respectively
$t_0$ = reference time
$T_{jn}$ = period of constituent n of species j

Values for $C_{jn}$ are presented by REID (1990). The value for the effective earth elasticity factor is typically taken as 0.69 for all tidal constituents (SCHWIDERSKI, 1980; HENDERSHOTT, 1981) although its value has been shown to be slightly constituent dependent.

To facilitate an FE solution to equations (3.65)–(3.67), these equations are mapped from spherical form into a rectilinear coordinate system using a Carte Parallelogrammitque (CP) projection (PEARSON, 1990):

$$x' = R(\lambda - \lambda_0)\cos\varphi_0 \tag{3.69}$$

$$y' = R\varphi \tag{3.70}$$

where, $\lambda_0, \varphi_0$ = center point of the projection. Applying the CP projection to equations (3.65)–(3.67) gives the shallow-water equations in primitive non-conservative form expressed in the CP coordinate system:

$$\frac{\partial \zeta}{\partial t} + \frac{\cos\varphi_0}{\cos\varphi}\frac{\partial (UH)}{\partial x'} + \frac{1}{\cos\varphi}\frac{\partial (VH\cos\varphi)}{\partial y'} = 0 \tag{3.71}$$

$$\frac{\partial U}{\partial t} + \frac{\cos\varphi_0}{\cos\varphi}U\frac{\partial U}{\partial x'} + V\frac{\partial U}{\partial y'} - \left(\frac{\tan\varphi}{R}U + f\right)V = -\frac{\cos\varphi_0}{\cos\varphi}\frac{\partial}{\partial x'}\left[\frac{p_s}{\rho_0} + g(\zeta - \eta)\right] + \frac{\tau_{s\lambda}}{\rho_0 H} - \tau_* U \tag{3.72}$$

$$\frac{\partial V}{\partial t} + \frac{\cos\varphi_0}{\cos\varphi}U\frac{\partial V}{\partial x'} + V\frac{\partial U}{\partial y'} - \left(\frac{\tan\varphi}{R}U + f\right)U = -\frac{\partial}{\partial y'}\left[\frac{p_s}{\rho_0} + g(\zeta - \eta)\right] + \frac{\tau_{s\varphi}}{\rho_0 H} - \tau_* V \tag{3.73}$$

Utilizing the FE method to resolve the spatial dependence in the shallow-water equations in their primitive form gives inaccurate solutions with severe artificial near 2. Δ However, reformulating the primitive equations into a GWCE (Generalized Wave Continuity Equation) form gives highly accurate, noise free, FE-based solutions to the shallow-water equations (LYNCH AND GRAY, 1979; KINNMARK, 1984). The GWCE is derived by combining a time-differentiated form of the primitive continuity equation and a spatially differentiated form of the primitive momentum equations recast into conservative form, reformulating the convective terms into non-conservative form and adding the primitive form of the continuity equation multiplied by a constant in time and space, $\tau_0$ (LYNCH and GRAY, 1979; LUETTICH et al., 1992). The GWCE in the CP coordinate system is:

$$\frac{\partial^2 \zeta}{\partial t^2} + \tau_0 \frac{\partial \zeta}{\partial t} + \frac{\cos\varphi_0}{\cos\varphi} \frac{\partial}{\partial x'} \frac{\partial \zeta}{\partial t}$$

$$\left\{ U - \frac{\cos\varphi_0}{\cos\varphi} U H \frac{\partial U}{\partial x'} - V H \frac{\partial U}{\partial y'} + \left( \frac{\tan\varphi}{R} U + f \right) V H - \right.$$

$$\left. H \frac{\cos\varphi_0}{\cos\varphi} \frac{\partial}{\partial x'} \left[ \frac{p_s}{\rho_0} + g(\zeta - \eta) \right] - (\tau_* - \tau_0) U H + \frac{\tau_{s\lambda}}{\rho_0} \right\}$$

$$+ \frac{\partial}{\partial y'} \left\{ V \frac{\partial \zeta}{\partial t} - \frac{\cos\varphi_0}{\cos\varphi} U H \frac{\partial V}{\partial x'} - V H \frac{\partial V}{\partial y'} - \right.$$

$$\left. \left( \frac{\tan\varphi}{R} U + f \right) U H - H \frac{\partial}{\partial y'} \left[ \frac{p_s}{\rho_0} + g(\zeta - \eta) \right] - (\tau_* - \tau_0) V H + \frac{\tau_{s\varphi}}{\rho_0} \right\} \tag{3.74}$$

$$- \frac{\partial}{\partial t} \left( \frac{\tan\varphi}{R} V H \right) + - \tau_0 \left( \frac{\tan\varphi}{R} V H \right) = 0$$

The GWCE (equation 3.74) is solved in conjunction with the primitive momentum equations in non-conservative form (equations 3.72 and 3.73).

The high accuracy of GWCE-based FE solutions is a result of their excellent numerical amplitude and phase propagation characteristics. In fact, Fourier analysis indicates that in constant depth water and using linear interpolation, a linear tidal wave resolved with 25 nodes per wavelength is more than adequately resolved over the range of Courant numbers ($C = \sqrt{gh}\Delta t/\Delta x \leq 1.0$ (LUETTICH et al., 1992)). Furthermore, the monotonic dispersion behavior of GWCE-based FE solutions avoids generating artificial near 2. $\Delta x$ modes, which plague primitive-based FE solutions (PLATZMAN, 1981; FOREMAN, 1983). The monotonic dispersion behavior of GWCE-based FE solutions are very similar to that associated with staggered finite difference solutions to the primitive shallow-water equations (WESTERINK and GRAY, 1991). GWCE-based FE solutions to the shallow-water equations allow for extremely flexible spatial discretizations, which result in a highly effective minimization of the discrete size of any problem, (FOREMAN, 1988).

The details of ADCIRC, the implementation of the GWCE-based solution to the shallow-water equations, are described by LUETTICH et al. (1992). As most GWCE-based FE codes, ADCIRC applies three-noded linear triangles for surface elevation, velocity and depth. Furthermore, the decoupling of the time and space discrete form of the GWCE and momentum equations, time-independent and/or tri-diagonal system matrices, elimination of spatial integration procedures during time-stepping, and full vectorization of all major loops results in a highly efficient code.

SCHEFFNER et al. (1994) used ADCIRC to simulate storm surges from hurricanes on the Gulf of Mexico and east coasts of U. S. A. Fig. 3.2 shows the finite element grid used in these simulations.

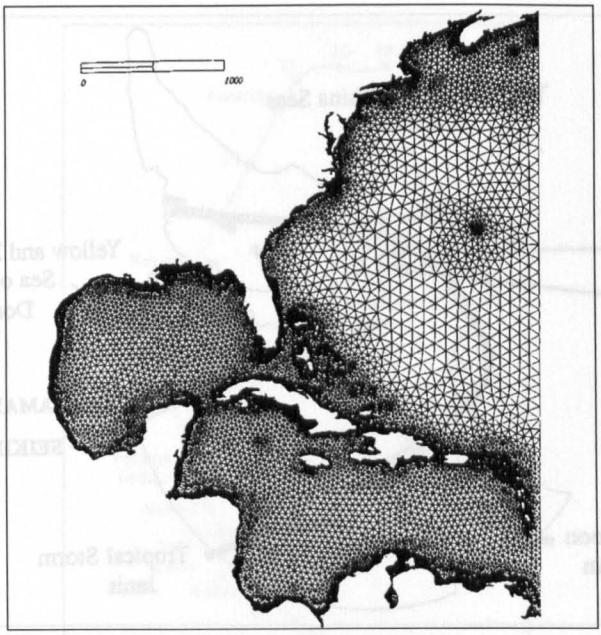


Fig. 3.2: The east coast, Gulf of Mexico, and Caribbean Sea computational domain. (SCHEFFNET et al., 1994).

BLAIN (1997) simulated hurricane generated storm surges on the coast of Florida and also for the coast of Northeast Asia. These model domains are respectively shown in Fig. 3.3 and 3.4.

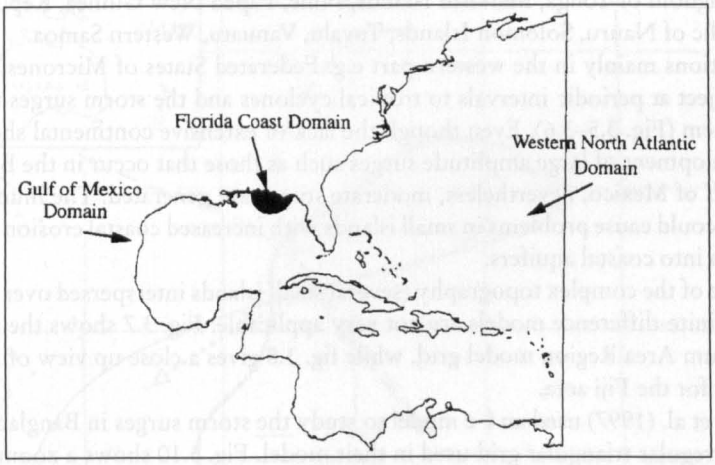


Fig. 3.3: Three domain sizes evaluated in the prediction of storm surge on the US Florida coast from hurricane Kate, 1985. (BLAIN, 1997).

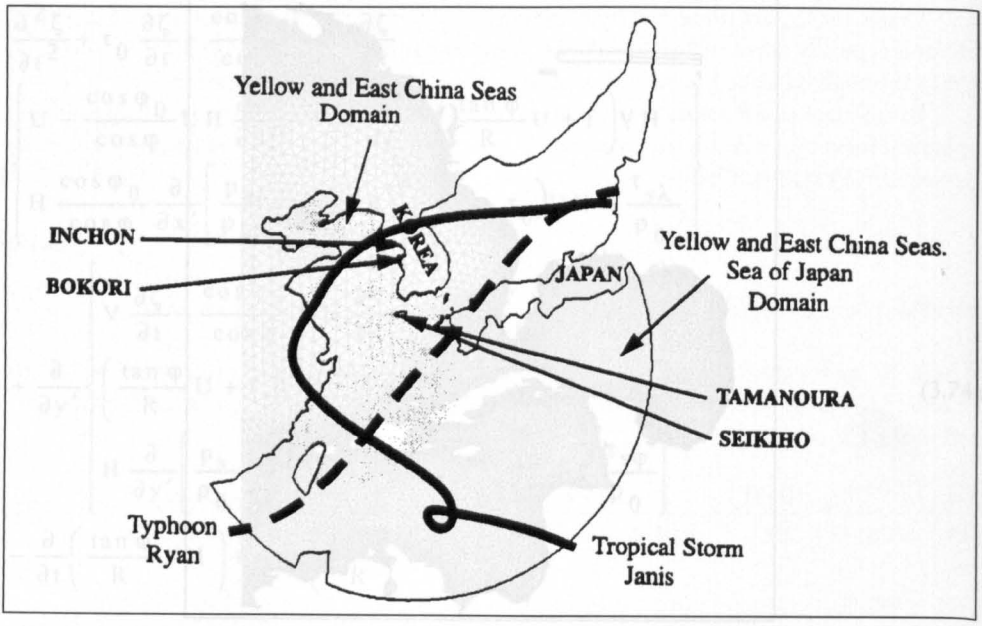


Fig. 3.4: Two domain sizes for the Yellow and East China Seas region, together with the paths of tropical storm Janis (August, 1995) and typhoon Ryan (September, 1995) and four hydrograph station locations. (BLAIN, 1997)

## 3.5 Other f-e Models

LUICK et al. (1997) studied storm surges in the Pacific forum region. The South Pacific region consists of the following island nations: Cook Islands, Federated States of Micronesia, Fiji, Kingdom of Tonga, Marshall Islands, Nine, Papua New Guinea, Republic of Kiribati, Republic of Nauru, Solomon Islands, Tuvalu, Vanuatu, Western Samoa.

The nations mainly in the western part e.g. Federated States of Micronesia (FSM) and Fiji, are subject at periodic intervals to tropical cyclones and the storm surges that are produced by them (Fig. 3.5–3.6). Even though the lack of extensive continental shelves precludes the development of large amplitude surges such as those that occur in the Bay of Bengal and the Gulf of Mexico, nevertheless, moderate surges are generated. The inundation from such surges could cause problems in small islands with increased coastal erosion and salt-water intrusion into coastal aquifers.

Because of the complex topography (several small islands interspersed over a large area), traditional finite-difference models are not very applicable. Fig. 3.7 shows the irregular triangular Forum Area Region model grid, while fig. 3.8 gives a close up view of irregular triangular grid for the Fiji area.

HENRY et al. (1997) used an f-e model to study the storm surges in Bangladesh. Fig. 3.9 shows the irregular triangular grid used in their model. Fig. 3.10 shows a zoom-in-view for the Meghna Estuary region. Fig. 3.11 and 3.12 respectively compare the computed and observed surges at Cox's Bazaar, Khepupara (April 1991 event). The discrepancies between the observed and computed surges could be mostly attributed to deficiencies in the prescribed meteorological input data.

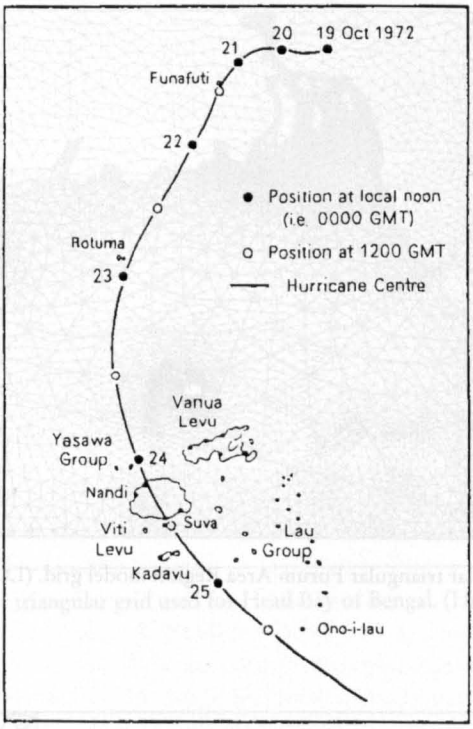


Fig. 3.5: Track of Hurricane Bebe October 1972 (from New Zealand Meteorological Service)

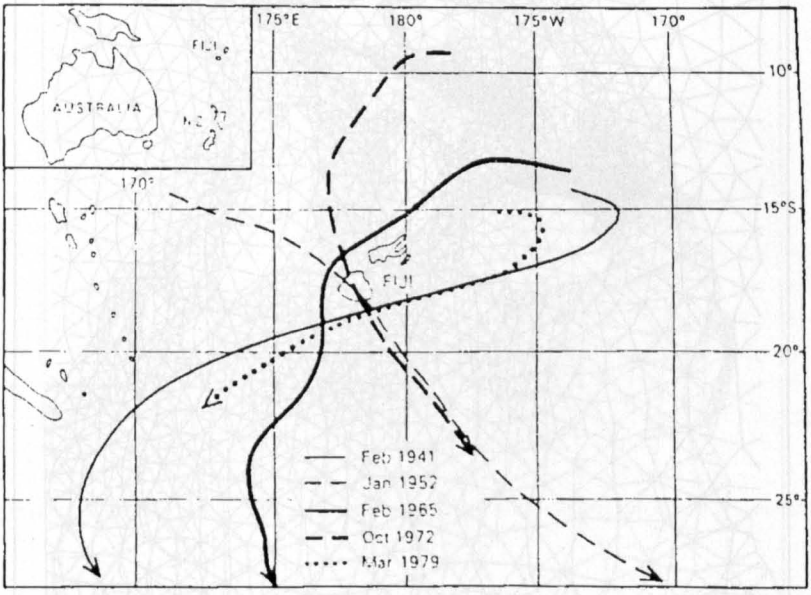


Fig. 3.6: Tracks of severe Hurricanes in Fiji area between 1940 and 1979 (from Fiji Meteorological Service)

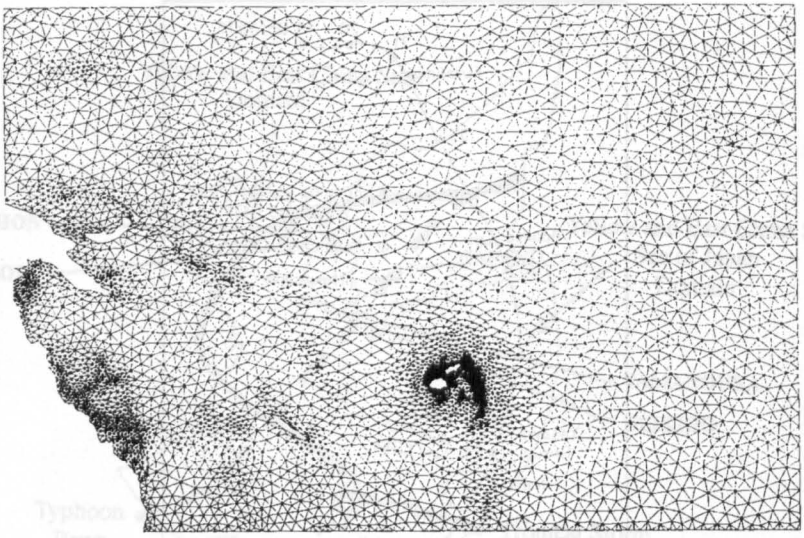

Fig. 3.7: Irregular triangular Forum Area Region model grid. (LUICK et al., 1997)

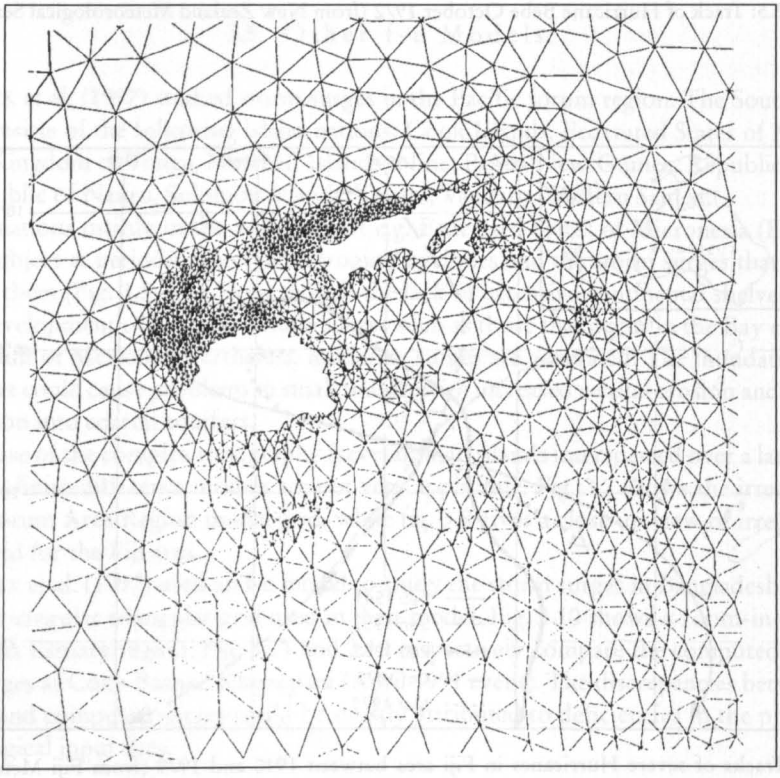

Fig. 3.8: Close up view of irregular triangular grid for the Fiji area. (LUICK et al., 1997)

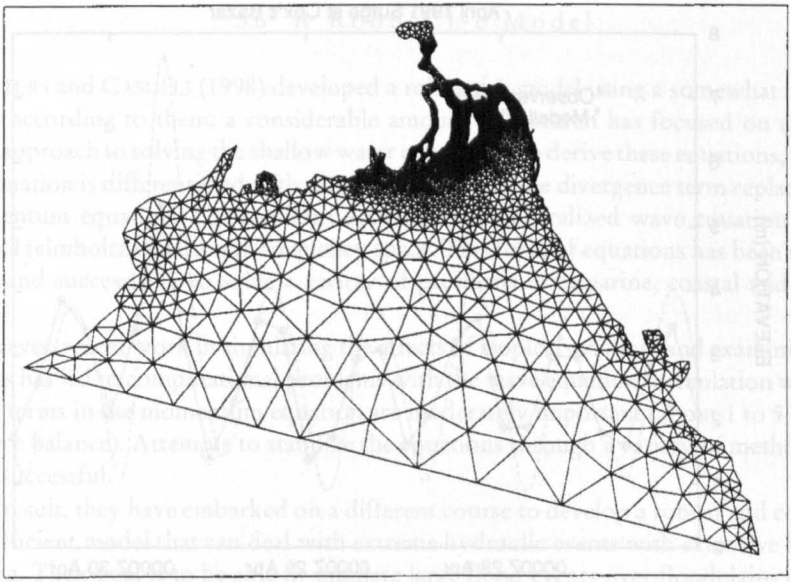

Fig. 3.9: Irregular triangular grid used for Head Bay of Bengal. (HENRY et al., 1997)

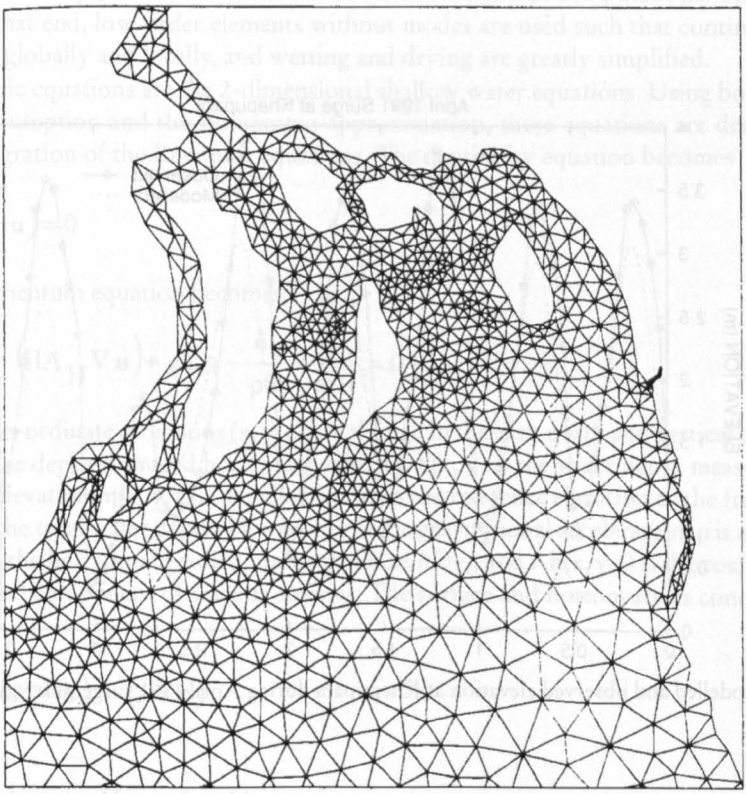

Fig. 3.10: Close up of part of grid covering Meghna Estuary. (HENRY et al., 1997)

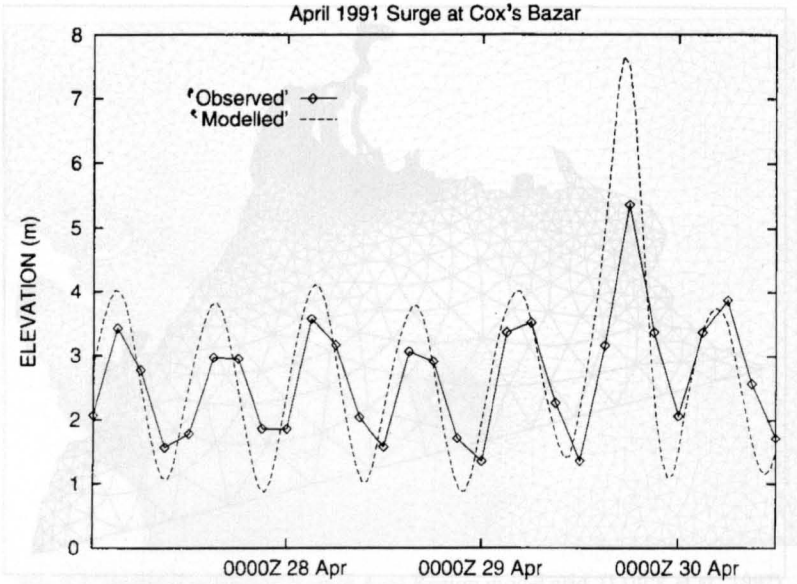


Fig. 3.11: Modelled and observed elevation at Cox's Bazaar during April 1991 surge. (HENRY et al., 1997)

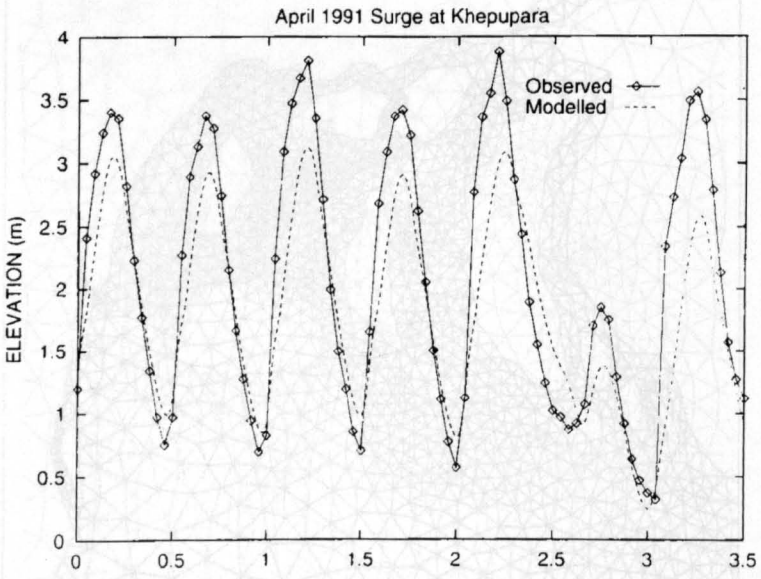


Fig. 3.12: Modelled and observed elevation at Khepupara during April 1991 surge. (HENRY et al., 1997)

### 3.6 A Robust f-e Model

WALTERS and CASULLI (1998) developed a robust f-e model using a somewhat different approach according to them; a considerable amount of research has focused on the wave equation approach to solving the shallow water equations. To derive these equations, the continuity equation is differentiated with respect to time, and the divergence term replaced with the momentum equation. The resultant equations are generalized wave equation in time space or a Helmholtz equation in frequency space. This form of equations has been used extensively and successfully to solve a variety of problems in estuarine, coastal and oceanic flows.

However, recent work in simulating the effects of tropical cyclones and examining river hydraulics has led to computational problems with the wave equation formulation when the advective terms in the momentum equation are moderately important (about 1 to 5 per cent of the force balance). Attempts to stabilize the equations through a variety of methods have not been successful.

As a result, they have embarked on a different course to develop a robust and computationally efficient model that can deal with extreme hydraulic events with extensive flooding and drying. Their goal is to be able to simulate large flood events over floodplains of variable extent.

The method adopted here is to use the primitive shallow water equations and form a wave equation at the discrete level. This procedure carries through the properties of the original discretized equations so that the use of elements without computational modes is essential. To that end, low-order elements without modes are used such that continuity is satisfied both globally and locally, and wetting and drying are greatly simplified.

The basic equations are the 2-dimensional shallow water equations. Using both the hydrostatic assumption and the Boussinesq approximation, these equations are derived by a vertical integration of the Reynolds equations. The continuity equation becomes

$$\frac{\partial \eta}{\partial t} + \nabla \cdot (\mathbf{H}\mathbf{u}) = 0 \tag{3.75}$$

and the momentum equation becomes

$$\frac{d\,\mathbf{u}}{dt} - \frac{1}{H}\nabla \cdot \left(HA_H \nabla \mathbf{u}\right) + g\nabla\eta - \frac{\hat{\mathbf{o}}_s}{\rho H} + \frac{\hat{\mathbf{o}}_b}{\rho H} = 0 \tag{3.76}$$

where, the co-ordinate directions (x, y, z) are aligned in the east, north and vertical directions; $\mathbf{u}(x, y, t)$ is the depth-averaged horizontal velocity; $h(x, y)$ is the water depth measured from a reference elevation; $\eta(x, y, t)$ is the distance from the reference elevation to the free surface; $H(x, y, t)$ is the total water depth, $H = \eta - h$; $g$ is the gravitational acceleration; $\rho$ is a reference density; $\nabla$ is the horizontal gradient operator $(\partial/\partial x, \partial/\partial y)$; and $Ah(x, y, t)$ is the coefficient for the horizontal component of viscous stresses. The surface and bottom stress conditions are given by

$$\frac{\hat{\mathbf{o}}_s}{\rho} = \gamma_T H(\mathbf{u}_a - \mathbf{u}) \quad (z = \eta) \tag{3.77}$$

$$\frac{\hat{\mathbf{o}}_b}{\rho} = C_D |\mathbf{u}| \mathbf{u} = \gamma_B H \mathbf{u} \quad (z = h) \tag{3.78}$$

where, the surface and bottom stress are denoted as $\tau_s$ and $\tau_b$ respectively, $\mathbf{u}_a$ is the wind velocity, and $C_D$ is a bottom drag coefficient. Essential boundary conditions on $\eta$ or volumetric flux are set at open boundaries, and $(\mathbf{u} \cdot \hat{\mathbf{n}}) = 0$ (no normal flow, where $\hat{\mathbf{n}}$ is the unit normal) is set on land boundaries.

This study focuses on the solution for surface elevation in the two-dimensional, discrete wave equation form of the continuity equation and the solution for the horizontal velocity components in the momentum equation. The governing equations are approximated using standard Galerkin techniques. The equations are discretized after defining a set of 2-dimensional triangular elements in the horizontal plane. Mixed methods are used in such a way that the elements use a piecewise constant basis for $\eta$ and a constant normal velocity on each edge.

The continuity equation (3.75) can be expressed in weighted residual form as: find $\eta \in S$ such that

$$\int_\Omega \hat{\eta} \frac{\partial \eta}{\partial t} d\Omega + \int_\Omega \hat{\eta} \nabla \cdot (H \mathbf{u}) d\Omega = 0, \qquad \forall \hat{\eta} \in S \tag{3.79}$$

Here S is the space of square integrable functions and $\Omega$ is the flow domain. Expanding $\eta$, $\hat{\eta}$ in terms of the finite basis $\phi$ and numerically integrating produces an algebraic problem for the nodal unknowns.

The weak form of momentum equation can be given as: find $\mathbf{u} \in U$ such that

$$\int_\Omega \hat{\mathbf{u}} \left[ \frac{d\mathbf{u}}{dt} + \gamma_B \mathbf{u} - \gamma_T (\mathbf{u}_a - \mathbf{u}) - \nabla \cdot (A_h \nabla \mathbf{u}) \right] d\Omega = -\int_\Omega \hat{\mathbf{u}} g \nabla \eta d\Omega, \quad \forall \hat{\mathbf{u}} \in U \tag{3.80}$$

where, the equation is interpreted component-wise and $U$ is the space of vector functions that have a divergence. Note that the term $(\nabla H/H)(A_h \nabla \mathbf{u})$ arising from the expansion of the horizontal viscous stress term has been neglected. Expanding $\mathbf{u}$, $\hat{\mathbf{u}}$ in terms of the finite element basis $\phi$ again produces an algebraic problem for the nodal unknowns. The surface pressure gradient term and the horizontal stress term are integrated by parts to give

$$\int_\Omega \ddot{\mathbf{O}} \left[ \frac{d\mathbf{u}}{dt} + \gamma_B \mathbf{u} - \gamma_T (\mathbf{u}_a - \mathbf{u}) \right] d\Omega + \int_\Omega \nabla \ddot{\mathbf{O}} \cdot (A_h \nabla \mathbf{u}) d\Omega$$
$$= \int_\Omega g \nabla \ddot{\mathbf{O}} \eta d\Omega - \oint_\Gamma [g(\ddot{\mathbf{O}} \eta) - \ddot{\mathbf{O}} A_h \nabla \mathbf{u} \cdot \hat{\mathbf{n}}] d\Gamma \tag{3.81}$$

where, $\Gamma$ is the boundary of the flow domain $\Omega$. The line integral in this equation provides a convenient means to specify the boundary conditions on $\eta$ and horizontal stress.

These equations are discretized in time using a semi-implicit method such that the equations are evaluated in the time interval $(t^m, t^{m+1})$, where the superscript denotes the time level. The distance through the interval is given by the weight $\theta$. The semi-implicit approach is given as

$$\frac{\eta^{m+1} - \eta^m}{\Delta t} + \nabla \cdot \left[ H^m \left( \theta \mathbf{u}^{m+1} + (1-\theta) \mathbf{u}^m \right) \right] = 0 \tag{3.82}$$

$$\frac{\mathbf{u}^{m+1} - \mathbf{u}^*}{\Delta t} + \theta \mathbf{G}^{m+1} + (1-\theta) \mathbf{G}^* = \mathbf{F}^* \tag{3.83}$$

$$\mathbf{G} = \gamma_B \mathbf{u} - \gamma_T (\mathbf{u}_a - \mathbf{u}) + g\nabla\eta \tag{3.84}$$

$$\mathbf{F}^* = \nabla \cdot (A_h \nabla \mathbf{u})^* \tag{3.85}$$

Semi-Lagrangian methods are used in order to take advantage of the simplicity of Eulerian methods and the enhanced stability and accuracy of Lagrangian methods. Here the superscripts m and m+1 denote variables evaluated at the fixed nodes in the Eulerian grid at times time $t^m$ and $t^{m+1}$. The subscript * denotes a variable evaluated at time $t^m$ at the end of the Lagrangian trajectory form a computational node (see Fig. 3.13). At each time step, the velocity is integrated backwards with respect to time to determine where a particle would be at time $t^m$ to arrive at a grid node at time $t^{m+1}$. The material derivative in equation (3.83), the first term, thus has a very simple form.

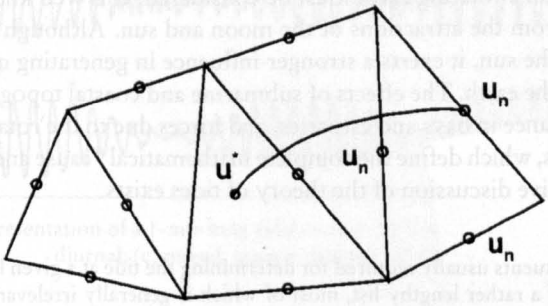


Fig. 3.13: Definition of the elements used and the Lagrangian trajectories. At time $t^m$, a particle starts at the location where velocity is $u^*$, and arrives at a node in the grid at time $t^{m+1}$. (WALTERS AND CASULLI, 1998)

There are three test problems studied (i) a simulation of tides in a polar quadrant region that indicates that there are no computational nodes; (ii) a simulation of tides in a regular channel with sloping bottom that provides an assessment of accuracy and convergence rate; and (iii) a simulation of a flood on the Big Lost River, Idaho, that assesses performance in a highly irregular but realistic geometry. The results look quite satisfactory.

KAWAHARA et al. (1982, 1983) used multi-level f-e models including stratification. Such models will be useful for the computation of currents associated with storm surges.

# 4. Special Hydrodynamic Problems

## 4.1 Tides

Tide is the rise and fall of the sea surface due to gravitational forces. To following material based on LEBLOND and MYSAK (1978) and GODIN (1972, 1980a, 1980b, 1988, 1991, 1996), IHP-OHP (1987, 1991), DEAN (1966), DIETRICH et al. (1975), DEFANT (1961).

An extremely useful qualitative description of some tidal phenomena is obtained by considering the equilibrium shape that a layer of water on a spherical earth would assume under the action of a tide-producing body. This is the "Equilibrium Theory of Tides", presented by Darwin in 1898 and describing the tides as those water fluctuations apparent to an observer traversing along a constant latitude line through the stationary and deformed water layer.

To describe the tides in a more realistic manner, dynamic aspects of the tidal waves in the oceanic basins and on a rotating earth must be considered. It is well known that the oceanic tides arise mainly from the attractions of the moon and sun. Although the moon is a much smaller body than the sun, it exerts a stronger influence in generating oceanic tides because of its proximity to the earth. The effects of submarine and coastal topography in altering the tidal features, resonance in bays and estuaries, and forces due to the rotating earth all contribute to tidal features, which define the complete mathematical "cause and effect" description. Therefore an extensive discussion of the theory of tides exists.

Table 4.1: Tidal constituents usually required for determining the tide at a given location. Note that this is only a small part of a rather lengthy list, most of which is generally irrelevant for storm surge-tide interaction purposes

| Nature of constituent | Symbol for constituent | Frequency (degrees.h$^{-1}$) | Period (h) |
|---|---|---|---|
| Semidiurnal | $M_2$ | 28.98 | 12.42 |
| Semidiurnal | $N_2$ | 28.44 | 12.66 |
| Semidiurnal | $S_2$ | 30.00 | 12.00 |
| Semidiurnal | $K_2$ | 30.08 | 11.97 |
| Diurnal | $O_1$ | 13.94 | 25.82 |
| Diurnal | $K_1$ | 15.04 | 23.94 |
| Diurnal | $P_1$ | 14.96 | 24.06 |

Following GODIN (1980a, 1980b), the vertical component z (t) of the tide is defined as follows:

$$z(t) = zo + \sum_{j=1}^{n} A_j \cos(\sigma_j t - a_j) \qquad (4.1)$$

where, $z_o$ is a constant that denotes the reference level, which is chosen such that the observed water level rarely, if ever, falls below $z_o$, and the other term on the right is a summation of *n* constituents of amplitude Aj, frequency $\sigma_j$, and phase $a_j$ where j varies from 1 to *n*. Note that the frequencies yj of the constituents are the same for any tidal record (for the same constituent); however, the amplitude and phase of the constituent might vary from one tidal station to another. Through a harmonic analysis of the observed tidal record, one can determine the amplitudes and phases of the various tidal constituents. In principle, the total number of

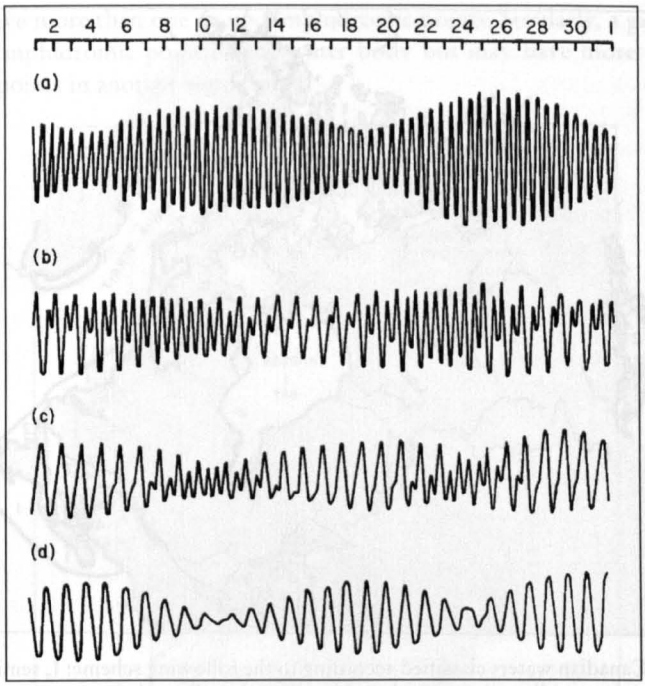


Fig. 4.1: Schematic representation of a 1-mo-long tidal record. (a) Semidiurnal; (b) mixed, mainly semidiurnal; (c) mixed, mainly diurnal; (d) diurnal

constituents could be as high as 500, but rarely must one use more than a dozen or so of the important constituents in representing a tidal record.

As described above, the tide is the rise and fall of the sea's surface. The flowing to and fro is called tidal current. The tide is a wave period of about 12.4 hours, the semi-diurnal tide, or of about 24.8 hours (diurnal tide) or of varying periods (mixed tides). The most important of the semidiurnal and diurnal tidal constituents that are needed in representing an observed tidal record are listed in Table 4.1.

In practical tidal studies, it was found convenient to classify the tides into these four types: semidiurnal, mixed-mainly semidiurnal, mixed-mainly diurnal, and diurnal. A tide is referred to as semidiurnal if there are two high waters and two low waters daily of roughly the same amplitude (Fig. 4.1a). Mixed tides of the mainly semidiurnal type have two high waters and two low waters with the amplitudes being unequal (Fig. 4.1b). Mixed tides of the mainly diurnal type are said to exist if at times there is only one high water and one low water per day and at other times there are two large inequalities (Fig. 4.1c). For diurnal tides, there is one high water and one low water per day (Fig. 4.1d).

Three examples will be shown with this classification. First DOHLERS (1967) has classified the Canadian waters according to this scheme in Fig. 4.2, second EASTON (1970) for Australia (Fig. 4.3) and third PRIDA (1990, personal communication, quotation from IHP-OHP-BERICHTE 1991) (Fig. 4.4).

A cotidal chart is a convenient way of presenting tidal information for each tidal constituent separately. Two sets of lines exist on a cotidal chart. Corange (coamplitude) lines represent contours of the range (amplitude) of the constituent, whereas cophase lines represent the contours of equal phase (usually with reference to Greenwich, expressed in degrees per

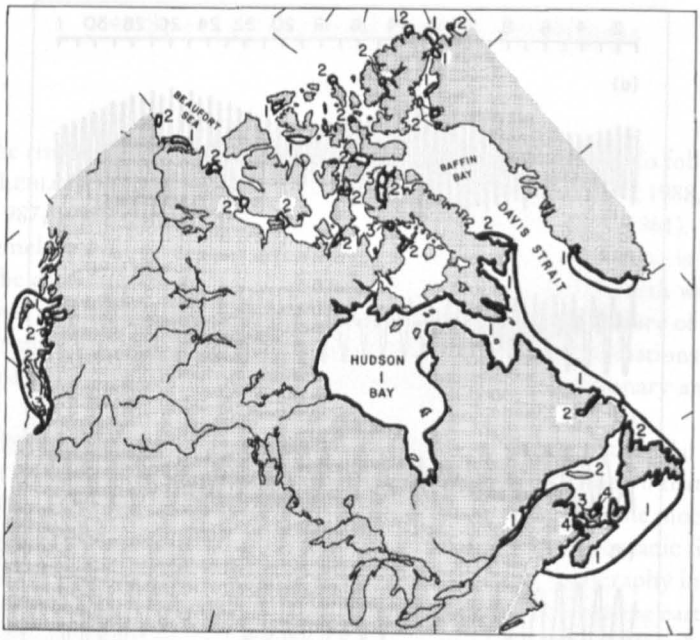


Fig. 4.2: Tides in Canadian waters classified according to the following scheme: 1, semidiurnal; 2, mixed, mainly semidiurnal; 3, mixed, mainly diurnal; 4, diurnal. (DOHLER, 1967)

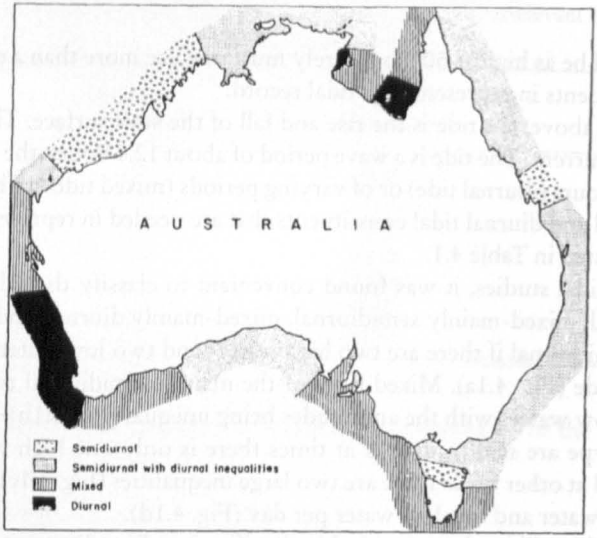


Fig 4.3: Tidal types along the Australian coast (EASTON, 1970)

hour). Amphidromic points, which appear for certain constituents in water bodies, are the locations where the range (amplitude) of the particular constituent is zero. Thus, it is basically a node for the vertical motion, the nodal line becoming just a point either due to the presence of transverse motion or due to the influence of the earth's rotation (GEORGE, 1980). In a water body, one tidal constituent may have an Amphidromic point, whereas another con-

stituent may have more than one or no Amphidromic points. Similarly, a given constituent may have an Amphidromic point in one water body but may have more than one or no Amphidromic points in another water body.

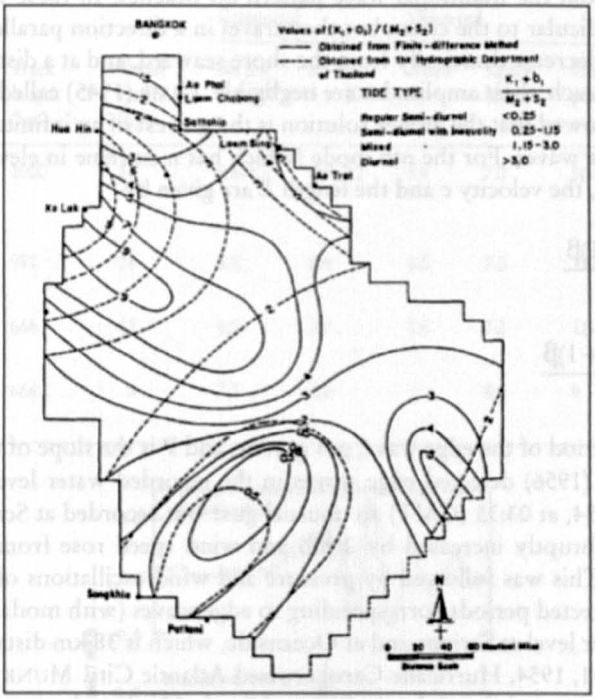


Fig. 4.4: Types of tide in the Gulf of Thailand (Prida, personal comment, quotation from IHP-OHP-BERICHTE, 1991)

## 4.2 Resonance, Edge Waves

The topic of resonance, although relevant to storm surges, is so vast that it cannot be considered in detail here.

Any water body, such as a lake, inlet, bay, gulf, or a continental shelf, has natural modes of oscillation whose periods are determined by the geometry of the water body and the water depth. A knowledge of the natural modes of the water body is quite important in determining whether a given storm surge will be amplified or not and in determining the detailed characteristics of the surge in a particular water body for a given forcing.

For convenience, this section will be divided into three subsections: in the first subsection the theory of seiches will be described in some detail; in the second subsection the Helmholtz mode will be considered; in the final subsection the correct boundary conditions at the open part of the water body will be discussed.

### *Edge Waves and Their Role in Storm Surges*

The literature on the topic of edge waves has grown enormously in recent times, and the reader is referred to LEBLOND and MYSAK (1978) and MURTY (1977) for a review. Here, edge

waves will be considered strictly for the role they play in storm surges; discussion will not deal with the general phenomenon of edge waves.

STOKES (1847) obtained solutions for wave motion over a sloping beach, these solutions being different from the traditional wave pattern on beaches. In these new solutions, the crests are perpendicular to the coast, but they travel in a direction parallel to the coast and their amplitudes decrease drastically from the shore seaward, and at a distance of one wavelength from the beach, their amplitudes are negligible. LAMB (1945) called them edge waves. URSELL (1952) showed that the Stokes solution is the gravest of an infinite number of possible modes of edge waves. For the nth mode (which has n extreme in elevation between the coast and the sea), the velocity c and the length $L$ are given by

$$c = \frac{gT\sin(2n+1)\beta}{2\pi} \tag{4.2}$$

$$L = \frac{gT^2\sin(2n+1)\beta}{2\pi} \tag{4.3}$$

where, T is the period of the edge wave, g is gravity, and P is the slope of the beach.

MUNK et al. (1956) detected edge waves in the recorded water levels at Scripps Pier. On January 6, 1954, at 03:35 (GMT) an unusual gust was recorded at Scripps Pier. Atmospheric pressure abruptly increased by 2 mb and wind speed rose from 3 to 14 mi – h-' (4.8-22 km.h-1). This was followed by pressure and wind oscillations of an 8-min period. These authors detected periods corresponding to edge waves (with modal number n = 1) in the recorded water level at Scripps and at Oceanside, which is 38 km distant.

On August 31, 1954, Hurricane Carol crossed Atlantic City. MUNK et al. (1956) computed the edge wave modes at Atlantic City and Sandy Hook and compared the calculated periods with observed periods. The main result is that the edge wave periods are largely due to the gently sloping bottom. The longest edge wave period is associated with the fastest hurricane.

MUNK et al. (1956) also computed the edge wave modes for Osaka Bay, Japan, over which a storm passed on August 29, 1953. The bottom slope in Osaka Bay is about 15 times greater than that of the New Jersey coast. Hence, the periods of edge waves in Osaka Bay should be about 1/15 those on the New Jersey coast, and this result is supported by observations.

GREENSPAN (1970) did a theoretical study of edge waves in an exponentially stratified fluid. He showed that the first mode is completely insensitive to the density field. Stratification modifies the range of existence of higher modes.

On June 26, 1954, a squall line passed over the southern part of Lake Michigan and caused a surge on the Chicago waterfront. Several people were killed. This was explained by resonant coupling between the squall line and the resulting gravity waves generated in the lake (DONN and EWING, 1956). A resurgence (i.e. reflection of the waves from the eastern shore of the lake) explains its unexpected arrival at Chicago some 2 h after the squall line had passed.

On July 6–7, 1954, another squall line crossed Lake Michigan from north to south with an average speed of 50 mi. h-' (80.5 km. h-'). Long-period waves were recorded at several locations following this squall line. DONN and EWING (1956) invoked edge waves to account for these water level disturbances. The time of arrival of the squall line and the magnitude of the pressure change at several stations are listed in Table 4.3, and the travel time curves of the

Table 4.2: Periods and durations of edge waves generated by four hurricanes. (MUNK et al., 1956)

| Hurricane | Velocity $U$ (km.h$^{-1}$) | Track length (km) | Travel time (h) | Wave period $T$ (h) Computed $\sin\beta = 5 \times 10^{-4}$ | Computed $\sin\beta = 5 \times 10^{-4}$ | Observed Atlantic City | Observed Sandy Hook | Duration (h) Computed | Observed Atlantic City | Observed Sandy Hook |
|---|---|---|---|---|---|---|---|---|---|---|
| Aug. 30–Sept. 1 (Carol) | 59–63 | 1000 | 24 | 5.8–6.1 | 6.9–7.2 | 5.5 | 7.0 | 16–24 | 20 | 26 |
| Sept. 11–12, 1954 (Edna) | 59 | 981 | 24 | 5.8 | 6.9 | 6.0 | 7.0 | 17–24 | 23 | ? |
| Sept. 14–15, 1944 | 61 | 666 | 12 | 6.0 | 7.1 | 5.6 | 7.2 | 11–12 | 23 | 30 |
| Sept. 21–22, 1938 | 74 | 666 | 9 | 7.3 | 8.6 | – | 8.0 | 9 | – | 16 |

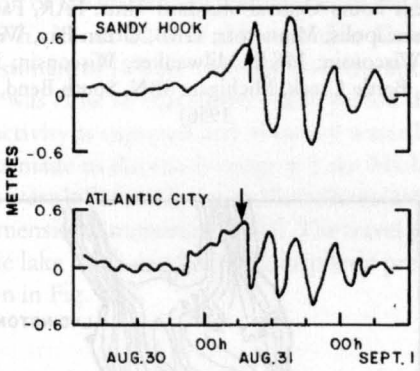


Fig. 4.5: Storm surges at Sandy Hook and Atlantic City, New Jersey, during Hurricane Carol of August 30–September 1, 1954. Arrows indicate the time of passage of the storm centre. (MUNK et al., 1956)

Table 4.3: Time of occurrence and pressure change for the squall line of July 6, 1954, in the United States. (DONN and EWING, 1956)

| Station name | Station code | State | Time (CST) of occurrence of pressure change | Magnitude of Pressure change (mb) |
|---|---|---|---|---|
| Fargo | FAR | North Dakota | 06:50 | 2.03 |
| St. Cloud | STC | Minnesota | 08:39 | 3.05 |
| Minneapolis | MSP | Minnesota | 09:54 | 2.37 |
| Green Bay | GRB | Wisconsin | 11:00 | 1.36 |
| Traverse City | TVC | Michigan | 12:30 | 0.68 |
| Madison | MSN | Wisconsin | 13:02 | 2.71 |
| Milwaukee | MKE | Wisconsin | 13:24 | 2.03 |
| Muskegon | MKG | Michigan | 14:00 | 1.36 |
| Chicago | CHI | Illinois | 15:30 | 3.39 |
| Battle Creek | BTL | Michigan | 15:30 | 1.36 |
| South Bend | SBN | Indiana | 15:55 | 2.03 |

squall line are shown in Fig. 4.6. The abbreviations for the stations shown in this diagram are the same as in Table 4.3. The water level records from Waukegan, Wilson Avenue (Chicago), Calumet Harbour (Chicago), and Ludington (see Fig. 4.7) were used.

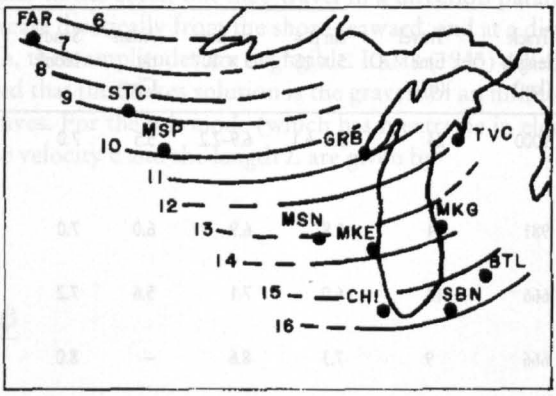


Fig. 4.6: Travel time curves (isochrones) of the squall line on July 6, 1954, over Lake Michigan and surroundings. Numbers represent hours Central Standard Time. FAR, Fargo, North Dakota; STC, St. Cloud, Minnesota; MSP, Minneapolis, Minnesota; GRB, Green Bay, Wisconsin; TVC, Traverse City, Michigan; MSN, Madison, Wisconsin; MKE, Milwaukee, Wisconsin; MKG, Muskegon, Michigan; CHI, Chicago, Illinois; BTL, Battle Creek, Michigan; SBN, South Bend, Indiana. (DONN and EWING, 1956)

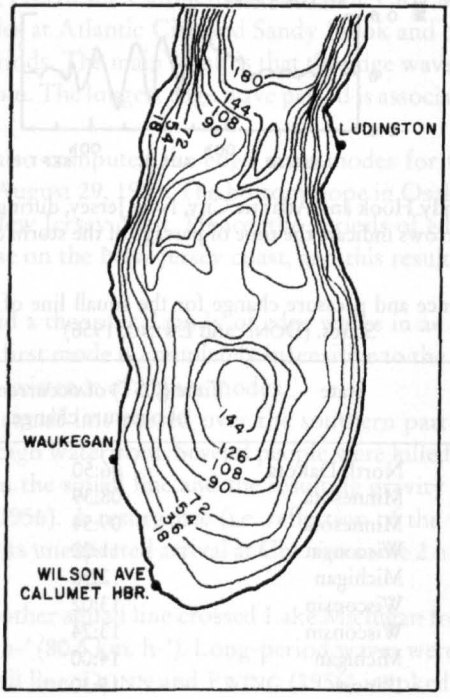


Fig. 4.7: Bottom topography of the southern port of Lake Michigan and the water level stations used in the study. (DONN and EWING, 1956)

The pertinent meteorological and water level data at these four stations are summarised in Table 4.4. It can be seen from Fig. 4.7 that the depth increases more or less uniformly with distance from the shore. The distance (i.e. X/21r) at which the edge wave amplitude should be negligible is about 16 mi (25.6 km). Starting just north of Chicago to up to 50 mi (80.5 km) north of Waukegan, the bottom slope was determined to the 300-ft (91.4 m) contour at six different locations. These values (i.e. of sin P) were 0.0016, 0.0021, 0.0024, 0.0035, 0.0034, and 0.0029. For the phase velocity c of the edge wave a value of 72.5 ft. s-' (22 m. s-') was used. This gives from eq. (4.2) (for n = 1) a period of 103 min. From Table 4.4 the average period is 109 min. Thus, the calculated period of edge waves agrees with the observed period.

Calculations gave values of 50 mi. $h^{-1}$ (80.4 km. $h^{-1}$) and 61 mi. $h^{-1}$ (98 km. $h^{-1}$), respectively, for the edge wave velocity in the northern and southern parts of Lake Michigan. Since the speed of travel of the squall line was 50 mi. $h^{-1}$ (80.4 km. $h^{-1}$), resonance transfer of energy occurred from the squall line to the gravity waves in the water. At Ludington, the bottom topography precludes generation of edge waves. Hence, just after the passage of the squall line (at 1:00 p.m.) the amplitudes of the water waves were small. However, at 8:00 p.m. much larger waves appeared at Ludington. This was explained due to the reflected larger waves from other areas travelling towards Ludington.

The observed duration of the water level disturbance in the Chicago – Waukegan area is estimated to be about 29 h. About 20 h of this record at Calumet Harbour is shown in Fig. 4.8. The theoretical estimate of 18 h for the edge wave duration is somewhat smaller. The period of the edge waves was close to that of the seiche period in the southern part of Lake Michigan; hence, seiche activity is expected and observed water levels confirm this.

Earlier, reference was made to the storm surge in Lake Michigan due to a squall line on June 26, 1954 (six persons were killed in Chicago). PLATZMAN (1958a) studied this surge using a time-dependent two-dimensional numerical model. The travel time curves of this squall line are shown in Fig. 4.9. The lake level, wind, and atmospheric pressure at the Wilson Avenue crib in Chicago are shown in Fig. 4.10.

Table 4.4: Arrival time of pressure jump and first wave of surge and wave periods and duration of the water level disturbance at four stations in Lake Michigan associated with the squall line of July 6, 1954. (DONN and EWING, 1956)

| Station | Pressure jump arrival time (CST) | Time of arrival of first wave of surge (CST) | Period (min)[a] Long-period waves | Period (min)[a] Short-period waves | Duration of wave disturbance (h) |
|---|---|---|---|---|---|
| Waukegan (Illinois) Wilson Ave. (Chicago) | ~15:00 | 15:30 | 110–120 | 20 | 29 |
| Calumet Harbour (Chicago) | 15:30 | 15:30 | 97–100 | 18–20 | 29 |
| Ludington (Michigan) | 15:30 | 15:30 | 115 | 20 | –[b] |
| | ~13:00 | 20:00–22:00 | 84 | – | –[b] |

[a] Not to be confused with wind waves whose periods are of the order of a few seconds.
[b] Record incomplete.

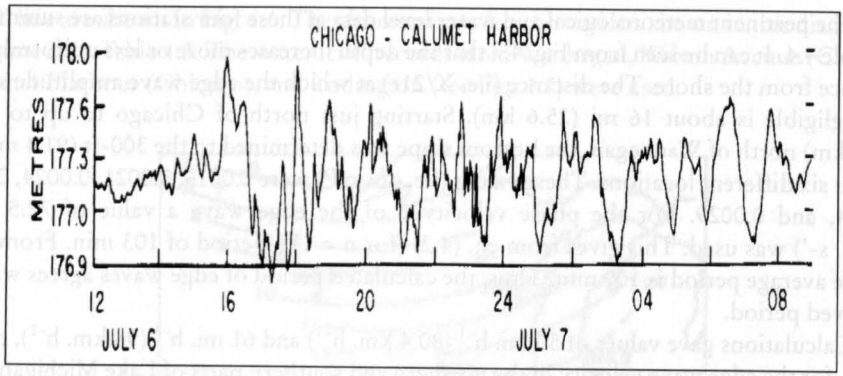


Fig. 4.8: Water level disturbance at Chicago's Calumet Harbour during July 6–7, 1954. (DONN and EWING, 1956)

PLATZMAN made five computations, i.e. using five different speeds of propagation for the squall line. These were 42, 48, 54, 60 and 66 knots (1 knot = 1.85 km – h-'). In each of these five computations he took the direction of propagation of the squall line as north-west to south-east, the width of the squall line as 10 nautical miles (18.5 km) and the magnitude of the pressure rise as 4 mb. The observed and computed results are compared in Table 4.5. In interpreting these results, it should be noted that the computations include atmospheric pressure gradient as a forcing term, but not wind stress. (Also, the Coriolis terms were ignored, although this omission may not be significant.)

PLATZMAN (1958a) summarised the results at the Wilson Avenue crib as follows:

1) The computed amplitude of the main (reflected) surge is approximately one-half the observed amplitude, but the inclusion of wind stress probably will remove this discrepancy.
2) The computed phases between significant events (Table 5.6) are in good agreement with the observations.
3) The structure of the tail of the reflected surge (and probably also the primary surge) is not in agreement with the observed structure, probably because the resolving power of the grid is inadequate for this purpose.

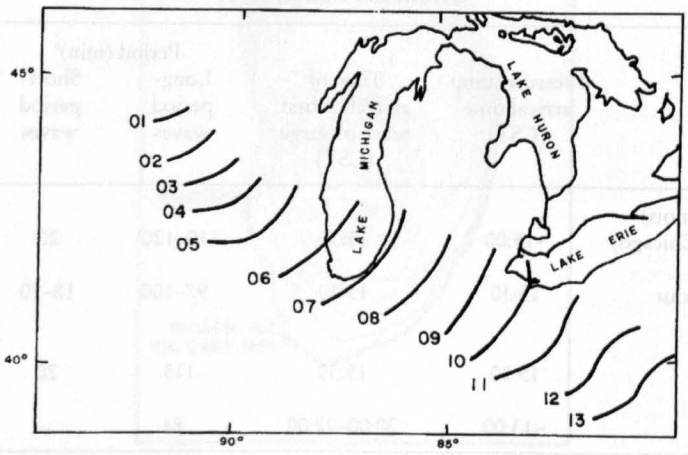


Fig. 4.9: Isochrones of the pressure jumpline of June 26, 1954, over Lake Michigan and surroundings. Numbers represent hours Central Standard Time. (PLATZMAN, 1958a)

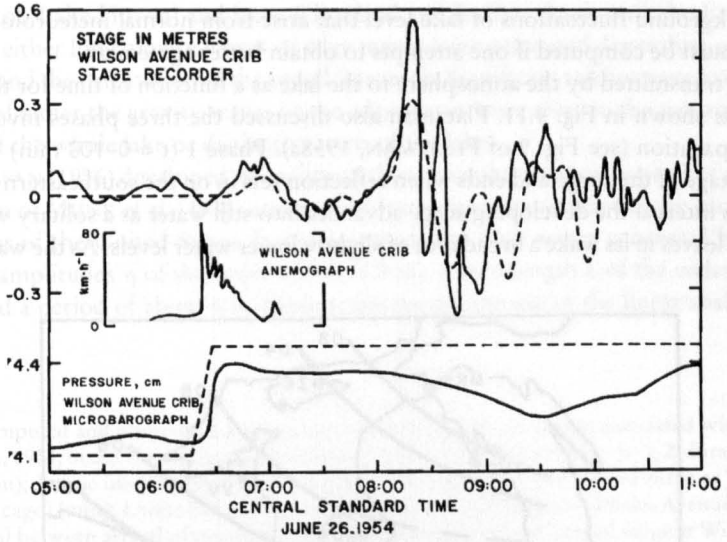


Fig. 4.10: Lake level, wind and atmospheric pressure records at Wilson Avenue crib on June 26, 1954. The broken curve of lake level shows the results of numerical computation for a squall line speed of 100 km. h-'; the broken curve of pressure gives the corresponding pressure increase assumed in the calculation. (PLATZMAN, 1958a)

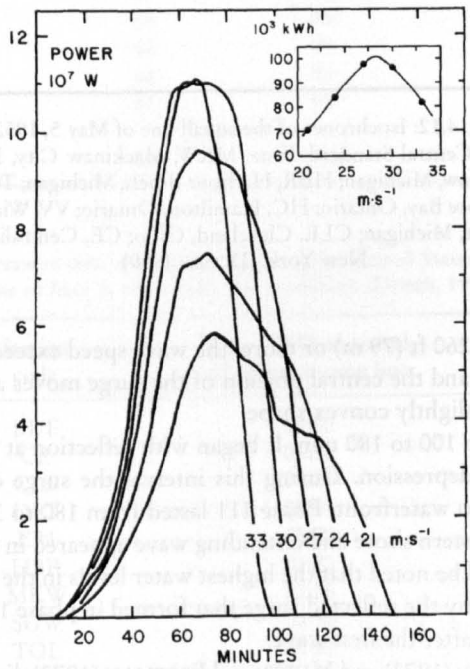


Fig. 4.11: The power transmitted by the atmosphere to the lake as a function of time for each of the five computed cases. Inset shows the total energy absorbed by the lake as a function of a squall line speed. (PLATZMAN, 1958a)

4) The background fluctuations of lake level that arise from normal meteorological disturbances must be computed if one attempts to obtain better agreement.

The power transmitted by the atmosphere to the lake as a function of time for the five cases computed is shown in Fig. 4.11. Platzman also discussed the three phases involved in this surge's propagation (see Fig. 9 of PLATZMAN, 1958a). Phase 1 (t = 0–100 min) includes the formative stage of the surge and ends when reflection sets in on the southeastern shore of the lake. In this interval the developing surge advances into still water as a solitary wave (of elevation) and leaves in its wake a broad area of slightly lower water levels. As the wave advances

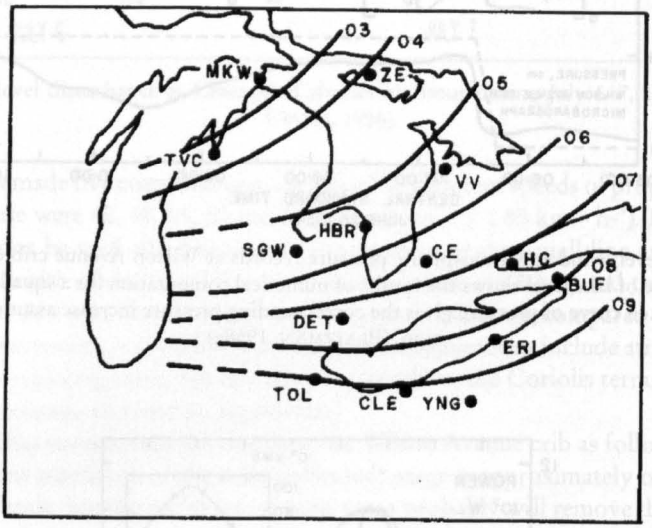


Fig. 4.12: Isochrones of the squall line of May 5, 1952.
Numbers represent hours Central Standard Time. MKW, Mackinaw City, Michigan; TVC, Traverse City, Michigan; SGW, Saginaw, Michigan; HBR, Harbour Beach, Michigan; TOL, Toledo, Ohio; YNG, Youngstown, Ohio; ZE, Gore Bay, Ontario; HC, Hamilton, Ontario; VV, Wiarton, Ontario; ERI, Erie, Pennsylvania; DET, Detroit, Michigan; CLE, Cleveland, Ohio; CE, Centralia, Ontalio; BUF, Buffalo, New York. (DONN, 1959)

into depths greater than 260 ft (79 m) or more, the wave speed exceeds the squall line speed (54 knots [100 km. h-']) and the central portion of the surge moves ahead of the squall line and the surge assumes a slightly convex shape.

Phase 11 lasted from 100 to 180 min. It began with reflection at the southeastern shore followed by a wave of depression. During this interval the surge contracted and moved southwest to the Chicago waterfront. Phase 111 lasted from 180 to 300 min. It began with reflection at the southwestern shore and a standing wave appeared in the southernmost portion of the lake. It should be noted that the highest water levels in the Chicago area were not produced in phase 1 but by the reflected surge that formed in phase 11 and arrived from the north-east about 85 min after the first wave.

FREEMAN and MURTY (1972) and MURTY and FREEMAN (1973) discussed a squall line generated surge on Lake Huron. This will be discussed in section 7. 1. DONN (1959) studied the storm surges in Lakes Huron and Erie due to a squall line on May 5, 1952. The travel time curves of the squall line are shown in Fig. 4.6. The pressure and wind data are summarised in Tables 4.6 and 4.7, respectively. Water level data are used from MacKinaw City and Harbour

Beach (both on Lake Huron) and from Cleveland and Buffalo (both on Lake Erie). DONN showed that either long gravity waves or edge waves were generated depending on the local topography and the orientation of the squall line track. Significant seiches were excited when the periods of either the gravity waves or the edge waves were close to the natural modes of oscillation of the whole lake or distinctive parts of the lake.

GREENSPAN (1956) developed an analytical theory for the transient aspects of the steady-state problem of MUNK et al. (1956) and applied it to edge wave generation by hurricanes on the east coast of the United States. It was assumed that edge waves generated here in this fashion had amplitudes $\eta$ of the order of 3 ft (0.9 m), a wavelength $\lambda$ of the order of 200 mi (322 km), and a period of about 6 h. These scales permit the use of the linear shallow-water theory.

Table 4.5: Computed and observed time intervals between significant events associated with the squall line of June 26, 1954, in the United States. Columns: 1, speed of squall line (km – h-'); 2, duration of pressure jump (min); 3, time interval between first surge at Michigan City and second surge at Wilson Avenue Crib (Chicago) (min); 4, time interval between first and second surges at Wilson Avenue Crib (min); 5, time interval between arrival of pressure jump and occurrence of and second surge at Wilson Avenue Crib (min); 6, time interval between second surge and first one following depression at Wilson Avenue Crib (min). (PLATZMAN, 1958a)

| 1 | 2 | 3 | 4 | 5 | 6 |
|---|---|---|---|---|---|
| | | | Computed | | |
| 78 | 14.3 | 55 | 85 | 109 | 35 |
| 89 | 12.5 | 63 | 85 | 114 | 25 |
| 100 | 11.1 | 66 | 85 | 118 | 20 |
| 111 | 10.0 | 68 | 85 | 121 | 18 |
| 122 | 9.1 | 67 | 85 | 121 | 18 |
| | | | Observed | | |
| | 5 | 68 | 88 | 113 | 6 |

Table 4.6: Atmospheric pressure data at several stations in the United States and Canada for the squall line of May 5, 1952 (NA, not available). (DONN, 1959)

| Location | Station code | Time (EST) of arrival of pressure jump line | Magnitude of pressure jump (mb) |
|---|---|---|---|
| Buffalo, NY | BUF | 08:00 | 4.06 |
| Centralia, Ont. | CE | 06:30 | 5.08 |
| Cleveland, OH | CLE | 09:28 | 2.71 |
| Detroit, MI | DET | 07:38 | 2.37 |
| Erie, PA | ERI | 08:00 | 3.39 |
| Harbour Beach, | HBR | 05:20 | NA |
| Mackinaw City, MI | MKW | 02:36 | NA |
| Saginaw, MI | SGW | 05:40 | 2.03 |
| Toledo, OH | TOL | 09:40 | 0.68 |
| Traverse City, MI | TVC | 03:45 | 0.68 |
| Youngstown, OH | YNG | 09:30 | 3.39 |
| Gore Bay, Ont. | ZE | 04:30 | 3.39 |
| Hamilton, Ont. | HE | 07:30 | NA |
| Wiarton, Ont. | VV | 05:15 | 4.74 |

The equations of motion and continuity are in the usual notation:

$$\frac{\partial u}{\partial t} = -\frac{1}{\rho}\frac{\partial \rho}{\partial x}$$

$$\frac{\partial v}{\partial t} = -\frac{1}{\rho}\frac{\partial \rho}{\partial y} \qquad (4.4)$$

Table 4.7: Wind data at several stations in the United States and Canada for the squall line of May 5, 1952. (DONN, 1959)

| Station | Wind data |
|---|---|
| Buffalo, NY | On arrival of pressure jump, weak winds shifted from east to north |
| Cleveland, OH | On arrival of pressure jump, winds at 32 km. h-' from north-east shifted to 48 km. h-' from south-east |
| Detroit, MI | On arrival of pressure jump, winds at 40 km. h-' from south east shifted to 63 km. h-' from north-east |
| Erie, PA | Winds of 35 km. h-' from the north. On arrival of pressure jump, winds shifted to south-east |
| Mackinaw City, MI | Winds of 58 km. h-' shifted at 02:36 (EST) |
| South Bend, IN | Winds of 29 km. h-' from northwest. On arrival of jump, wind shifted to north-east to north-north-east |
| Toledo, OH | On arrival of jump, wind shifted from south to north (19–24 km.h-1) |
| Tranverse City, MI | On arrival of jump, wind shifted from south-east to east (32–40 km. h-') |
| Youngstown, OH | On arrival of jump, wind shifted from north to southeast. (48–56 km. h-') |
| Centralia, Ont | On arrival of jump, wind shifted from south-south-west to north-north-east |
| Gore Bay, Ont. | Wind shifted from east to north (16–41 km. h-') |
| Hamilton, Ont. | Wind from northeast at 16 km/h-'. |
| Wiarton, Ont | Wind speed increased from 5 to 27 km. h-' and shifted from north-east to north-north-east |

The computed and observed edge wave periods and duration for four hurricanes are compared in Table 4.2.

REDFIELD and MILLER (1957) divided hurricane-produced surges into three parts: the forerunner, the hurricane surge, and resurgence. The forerunner is a slow and gradual change in the water level, commencing several hours before the arrival of the storm. There appears to be good coherence between the records at nearby stations in this stage, and one must consider winds over a more extended region than the hurricane proper. Facing the coast from the ocean, if the hurricane moves to the right along the coast, the forerunner usually is a rise in the water level and if the hurricane moves to the left, the forerunner consists of a decrease in the water level.

The hurricane surge is a sharp rise in the water level that occurs at about the time the hurricane center passes over the station. The duration of this stage usually does not exceed 2.5-5 h. In this stage, the coherence between neighbouring stations is not good. This means that the strong winds in the hurricane proper are responsible for the water level oscillations. In the Northern Hemisphere, the highest water levels occur to the right of the hurricane track.

The resurgence, being unexpected (since the storm has passed), could be dangerous. These were attributed by MUNK et al. (1956) to a wake of waves in the trail of the hurricane, and these have periods of free edge waves. KAJIURA (1959) mentioned that even at stations close by (i.e. separated only by one wavelength) the periods could be considerably different. He attributed the resurgence to a free onshore-offshore standing wave on the shelf.

WEBB (1976) considered resonance problems of long gravity waves on the continental shelf. He began with a simple model of a rectangular continental shelf at the end of a canal. It is assumed that a Kelvin wave propagates along the canal, which is partly absorbed and partly reflected by the continental shelf. The depth of the canal is of the same order as that of the deep oceans and the shelf parameters are taken to represent the Patagonian Shelf off Argentina. The simple analytical model showed that usually most of the incident wave energy is reflected by the edge of the shelf. However, at the dominant shelf resonance frequencies, more than 95% of the energy is absorbed by the shelf.

## 4.3 Interaction between Storm Surges and Tides

The traditional method of subtracting the astronomical tide from the observed water level and treating the residue as storm surge assumes that tide and surge are linearly additive and that there is no non-linear interaction. However, observations show that there are situations in which there is an interaction (i.e. tide influencing the propagation of the surge and vice-versa), especially in shallow areas. The interaction phenomenon, although probably present in other water bodies as well, appears to be quite pronounced in the Thames Estuary of the North Sea. In a series of papers, PROUDMAN (1955a, 1955b, 1957, 1958) studied this problem analytically.

### 4.3.1 Numerical Models of Tide-Surge Interaction in the Bay of Bengal

FLIERL and ROBINSON (1972) have documented many cases where the occurrence of abnormally high sea-surface level in the Bay of the Bengal has led to coastal flooding and inundation. The genesis of these events is to be found in the combined effect of the astronomical tide and a surge generated by a tropical cyclone. The principle component is the surge but, depending on the relative phase of the two processes, the sea-surface elevation may either be increased above, or decreased below its pure surge value. The mutual interaction is, however, nonlinear and the dynamics of both processes must be considered simultaneously.

Many analyses of surge generation by hurricanes, typhoons and tropical cyclones have now been made. Particular mention is made here of the numerical modelling of these phenomena by JELESNIANSKI (1965, 1966, 1967), MIYAZAKI et al. (1961), DAS et al. (1974) and SINHA et al. (1996). More recently, JOHNS et al. (1981, 1982, 1983 a, b) have developed several numerical models for application along the east coast of India. A fully nonlinear model to

analyse tide-surge interaction in the Bay of Bengal has been described and applied to the coastal waters off Bangladesh by JOHNS and ALI (1980), JOHNS et al. (1985), ROY (1995, 1999 a, 1999 b), ALI et al. (1997a, b) and ALI (1980c), DAS (1980), HENRY et. al (1997).

The general procedure followed in the modelling of tide-surge interaction is to begin by generating the co-oscillating tide in a semi-enclosed basin by prescribing the temporal variation of the sea-surface elevation along the open boundary. The value of this is supposed known from observations of the tidal state in the adjacent ocean. The pure tidal solution developed in the basin then provides the initial dynamical conditions for the storm surge simulation with tidal forcing along the open-sea boundary continuing during the integration. This method has been successfully applied in studies of the tide-surge interaction in the North Sea (see, for example, BANKS, 1974) but its practical application in the Bay of Bengal is hampered by the absence of adequate tidal data along the boundary separating the Bay from the northern Indian Ocean.

DAS (1980) used a nonlinear model to study the tide-surge interaction in the Meghna estuary. ALI (1980c) stated that about one third of the area of Bangladesh is penetrated by tide (through estuaries and rivers). Maximum tidal range (up to 6.1 m) and surge are found in the Meghna estuary.

Tide-surge interaction during the November 1970 Chittagong cyclone is shown in Fig. 4.13–4.15. It may be seen that at Patenga, maximum surge occurred at time of high tide whereas at Amatali the peak surge occurred after the occurrence of high tide. However, at Kaikhali the peak water level elevation is smaller than due to the tide alone. ALI (1980c) ascribed this to the effect of the offshore wind component, which drives the water from the rivers located to the west of the cyclonic track. The two small peaks in the total elevation near the time of high tide are probably due to the tide-surge interaction.

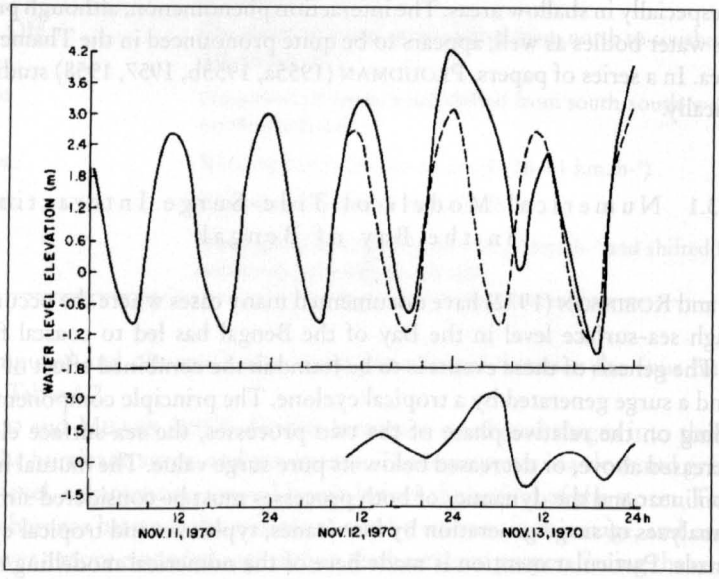


Fig. 4.13: Water level at Patenga, Bangladesh, during November 11–13, 1970. Top: Observed water level (tide + surge) is shown by the solid line and the computed water level by the broken line; bottom: observed storm surge. (ALI, 1980c)

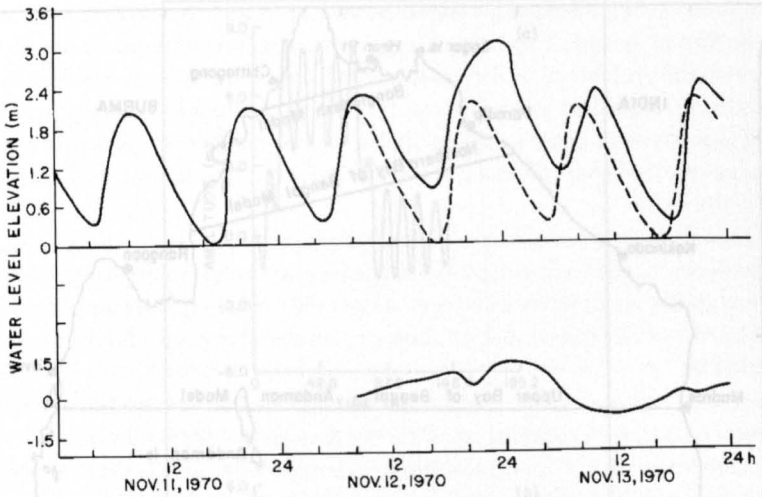


Fig. 4.14: Water level at Amtali, Bangladesh, during November 11–13, 1970. Refer to Fig. 4.13 for explanation. (ALI, 1980c)

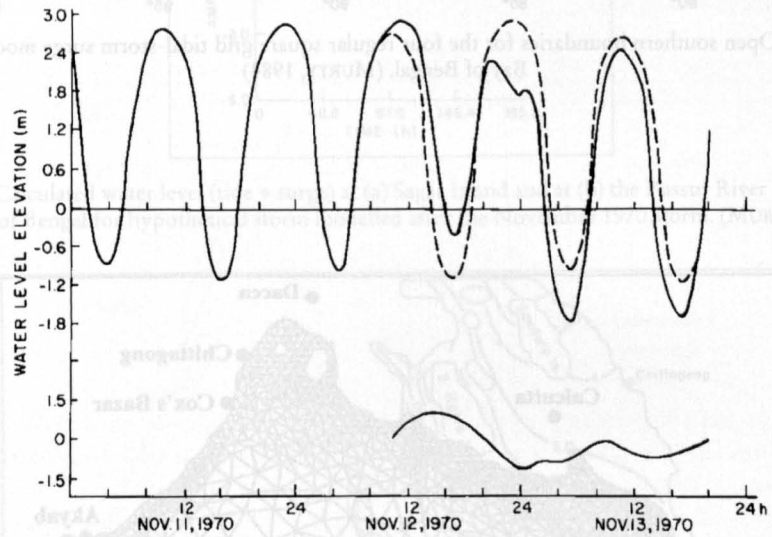


Fig. 4.15: Water level at Kaikhali, Bangladesh during November 11–13, 1970. Refer to Fig. 4.13 for explanation. (ALI, 1980c)

MURTY and HENRY (1983) and HENRY and MURTY (1982) developed a series of numerical models for tides and surges in the Bay of Bengal. The regions covered by the various regular grid models are shown in Fig. 4.16. The irregular triangular grid that has also been used is shown in Fig. 4.17. The computed water level (tide + surge) at Sagar Island and the Pussur River entrance is shown in Fig. 4.18. The contours of the computed surge are shown in Fig. 4.19.

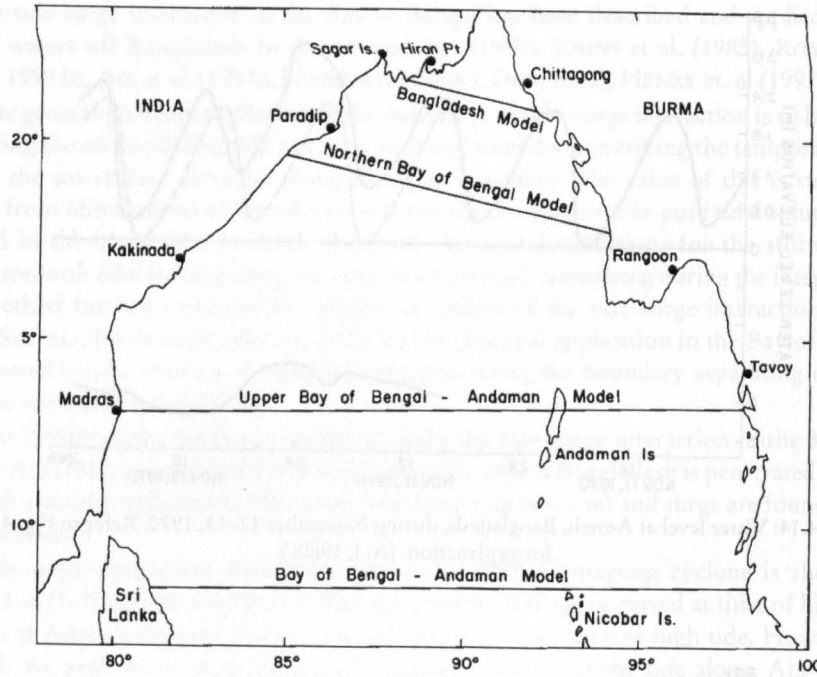


Fig. 4.16: Open southern boundaries for the four regular square grid tidal-storm surge models for the Bay of Bengal. (MURTY, 1984)

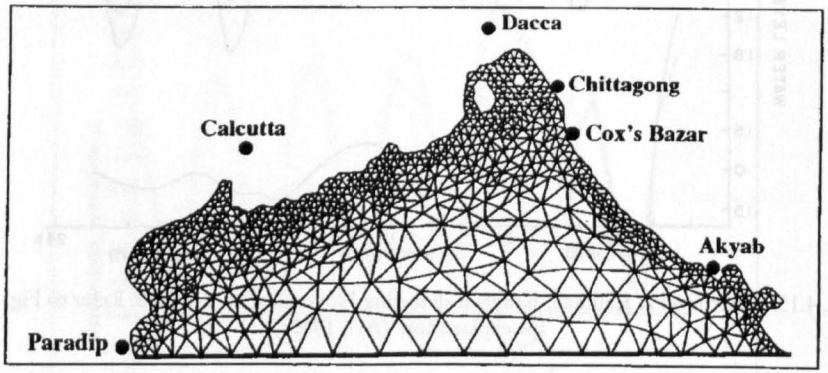


Fig. 4.17: Irregular triangular grid model for tides and storm surges in the northern part of the Bay of Bengal. (MURTY, 1984)

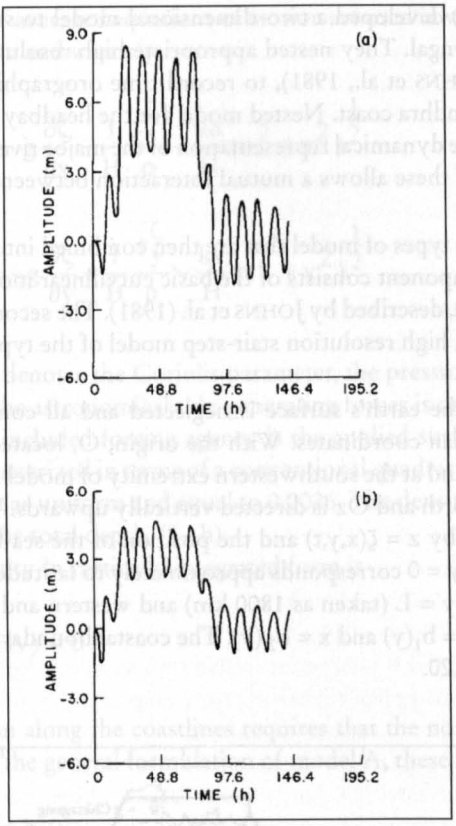


Fig. 4.18: Calculated water level (tide + surge) at (a) Sagar Island and at (b) the Pussur River entrance in the Bay of Bengal for hypothetical storm modelled after the November 1970 storm. (MURTY, 1984)

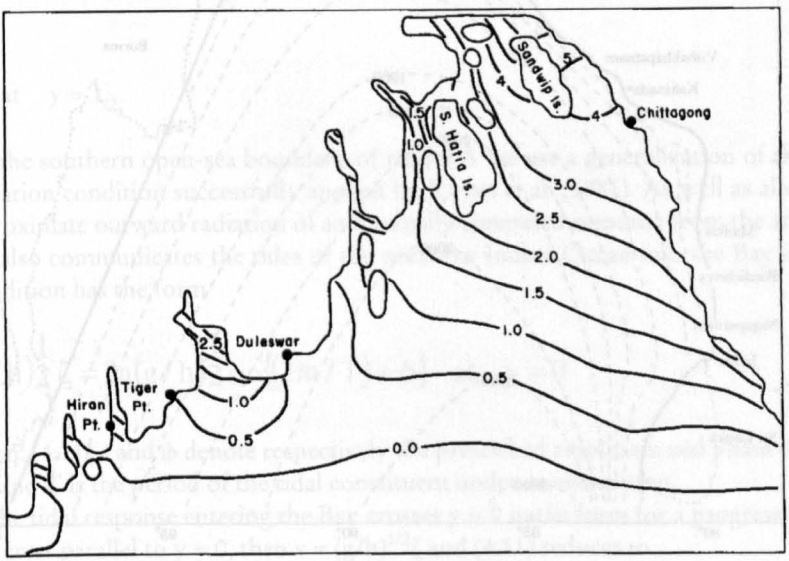


Fig. 4.19: Storm surge heights in the northern part of the Bay of Bengal from the hypothetical storm modelled after the November 1970 storm. (MURTY, 1984)

JOHNS et al. (1985) developed a two-dimensional model to study the tide-surge interaction in the Bay of Bengal. They nested appropriate high resolution models in their basic storm surge model (JOHNS et al., 1981), to record time orographical detail in the headbay region and along the Andhra coast. Nested model for the headbay region is particularly important as it includes the dynamical representation of the major rivers comprising the Ganges Delta. The inclusion of these allows a mutual interaction between the dynamics in the Bay and those in the Delta.

They consider two types of model that are then combined into a unified computational scheme. The major component consists of the basic curvilinear model for the Bay of Bengal (referred to as model A), described by JOHNS et al. (1981). The second component is a nested, and more conventional, high resolution stair-step model of the type described, for example, by HEAPS (1969).

The curvature of the earth's surface is neglected and all conditions are referred to a system of plane Cartesian coordinates. With the origin, O, located within the equilibrium level of the sea-surface and at the southwestern extremity of model A, Ox points towards the east, Oy towards the north and Oz is directed vertically upwards. The displaced position of the sea surface is given by $z = \zeta(x,y,t)$ and the position of the sea floor by $z = -h(x,y)$. An open / sea boundary at $y = 0$ corresponds approximately to latitude 6°N. A northern coastal boundary is situated at $y = L$ (taken as 1800 km) and western and eastern coastlines correspond respectively to $x = b_1(y)$ and $x = b_2(y)$. The coastal boundary configuration in model A is delineated in Fig. 4.20.

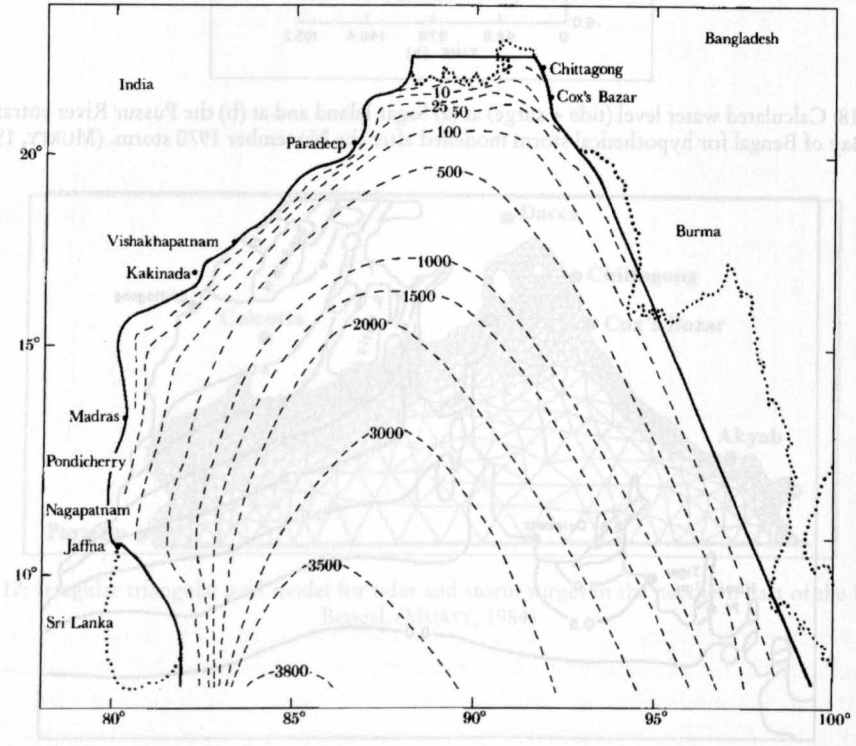


Fig. 4.20: The coastal configuration in model A and the isobaths of the model bathymetry. The numbers refer to depth in meters. (JOHNS et al., 1985)

Conventional depth-averaged equations of motion are used in which the depth-averaged components of velocity, u and v satisfy

$$\frac{\partial u}{\partial t}+u\frac{\partial u}{\partial x}+v\frac{\partial u}{\partial y}-fv=-g\frac{\partial \zeta}{\partial x}-\frac{1}{H}\frac{\tau_x^{\zeta}}{\rho}-\frac{ku}{H}(u^2+v^2)^{\frac{1}{2}} \tag{4.5}$$

$$\frac{\partial v}{\partial t}+u\frac{\partial v}{\partial x}+v\frac{\partial v}{\partial y}-fu=-g\frac{\partial \zeta}{\partial y}+\frac{1}{H}\frac{\tau_y^{\zeta}}{\rho}-\frac{kv}{H}(u^2+v^2)^{\frac{1}{2}} \tag{4.6}$$

In (4.5) and (4.6), f denotes the Coriolis parameter, the pressure is taken as hydrostatic and the direct effect of the astronomical tide-generating forces is omitted.

The sole explicitly included forcing agency is the applied surface wind stress ($\tau^{\zeta}_x$, $\tau^{\zeta}_y$). Bottom friction is parameterized in terms of a conventional quadratic stress law with the friction coefficient, k, taken as uniform and equal to 0.0026. The density of the water, ρ, is assumed uniform and H is the total depth, $(\zeta+h)$.
The equation of continuity in vertically integrated form is

$$\frac{\partial \zeta}{\partial t}+\frac{\partial}{\partial x}(Hu)+\frac{\partial}{\partial y}(Hv)=0 \tag{4.7}$$

Boundary condition along the coastlines requires that the normal component of velocity is zero. In terms of the general formulation of model A, these lead to

$$u-vb_1'(y)=0 \quad \text{at} \quad x=b_1(y), \tag{4.8}$$

$$v-vb_2'(y)=0 \quad \text{at} \quad x=b_2(y), \tag{4.9}$$

and

$$v=0 \quad \text{at} \quad y=L, \tag{4.10}$$

At the southern open-sea boundary of model A we use a generalization of the linearized radiation condition successfully applied by JOHNS et al. (1981). As well as allowing for the approximate outward radiation of an internally generated response from the analysis region, it also communicates the tides of the northern Indian Ocean into the Bay of Bengal. The condition has the form

$$v+(g/h)^{\frac{1}{2}}\zeta=2a(g/h)^{\frac{1}{2}}\sin\{(2\pi t/T)+\phi\} \quad \text{at} \quad y=0 \tag{4.11}$$

In eq. (4.11) a and ϕ denote respectively the prescribed amplitude and phase of the tidal forcing and T is the period of the tidal constituent under consideration.

If the tidal response entering the Bay crosses y = 0 in the form for a progressive wave with its crest parallel to y = 0, then $v=(g/h)^{1/2}\zeta$ and (4.11) reduces to

$$\zeta=a\sin\{(2\pi t/T)+\phi\} \quad \text{at} \quad y=0 \tag{4.12}$$

In this case, a and $\phi$ correspond to the amplitude and phase of the tidal elevation along $y = 0$. A consequence of applying (4.11) rather than (4.12) is that the values of neither $\zeta$ nor v are separately prescribed along the open-sea boundary of model A. Thus, during the solution process, the boundary values of both $\zeta$ and v may correlatively adjust subject only to (4.11). We anticipate that such a solution procedure, which is based on prescribing conditions on an incoming characteristics will be superior to one using (4.12), especially if $y = 0$ should coincide with a nodal line. Further generalization of (4.11) to a discrete spectrum of tidal constituents follows without difficulty.

High resolution stair-step models are nested within model A so as to represent more fully the orographical detail of the headbay region and the Andhra coast of India. For the headbay, the nested model is referred to as model B and the stair-step boundary configuration is delineated Fig. 4.21. In contrast with the parent model A, the northern boundary of model B does not consist of a continuous vertical wall. Instead, one-dimensional dynamical models have been included to represent some of the rivers entering the head of the Bay of Bengal. The southernmost limit of model B consists of an open-sea boundary along latitude 19° 33' N where elevation values are prescribed. These are determined from the response in model A. An important feature of the scheme is that the response in model A is independent of that in model B. On the other hand, the response in model B is dependent on that generated in model A. Indeed, we find that the results from model A become increasingly unrealistic in the region of the Ganges Delta owing to the omission of any representation of the complex river system. Model B is superior in this respect as the representation of the rivers, although crude, avoids a complete refection of the response at $y = L$ and the local development of unrealistically high sea-surface elevations.

In model B, east-west separation distance between points at which the elevation is compute is approximately 17.6 km. The north-south distance between computational points is approximately 19.8 km. The grid-point arrangement is staggered in such a way that $\zeta$ is computed at the centre of a grid cell while u and v are computed at the mid-points of its y-directed and x-directed sides respectively. The vanishing of the normal component of velocity at a coastline is then readily achieved by an appropriate stair-step representation of the boundary.

Conditions in each of the rivers satisfy equations of the form.

$$\frac{\partial v}{\partial t} + v\frac{\partial v}{\partial y} = -g\frac{\partial \zeta}{\partial y} - \frac{kv|v|}{H} \tag{4.13}$$

and

$$b\frac{\partial \zeta}{\partial t} + \frac{\partial}{\partial y}(bHv) = 0 \tag{4.14}$$

Thus, in the dynamical equation (4.13), we omit the effect of wind-stress forcing in the rivers. At the point of entry into model B, the elevation and momentum flux are made continuous. In the continuity equation (4.14), b denotes the local breadth of the river. At the river's point of communication with model B, the mass flux is made continuous. Juncture conditions of a similar kind have been described by JOHNS and ALI (1980). It is noteworthy that the resulting interaction between the rivers and model B is two-way because the dynamical response in either may affect that in the order.

Each of the rivers is taken to have a length of 200 km with no mass flux of water through its head. Each river has a uniform breadth of 18 km except the Meghna (in the extreme east),

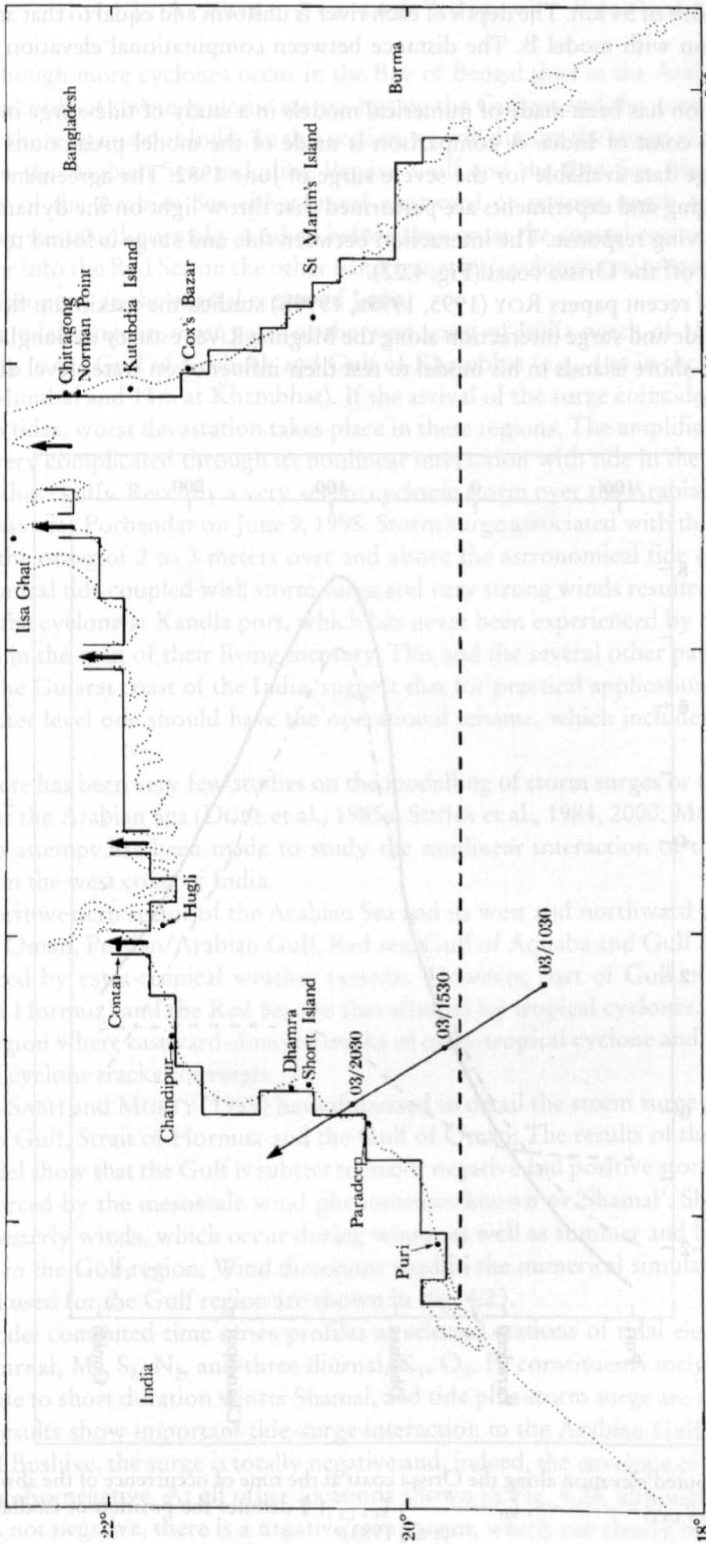


Fig. 4.21: The coastal configuration in model B and the idealized track of the Orissa cyclone. The numbers on the track refer to the times (IST) at which the centre of the cyclone passed through the marked positions on 3 June 1982. (JOHNS et al., 1985)

which has a breadth of 54 km. The depth of each river is uniform and equal to that at its point of communication with model B. The distance between computational elevation points is taken as 20 km.

An application has been made of numerical models in a study of tide-surge interaction along the Orissa coast of India. A comparison is made of the model predictions with the limited tide-gauge data available for the severe surge of June 1982. The agreement between these is encouraging and experiments are performed that throw light on the dynamical character of the evolving response. The interaction between tide and surge is found to lead to a substantial effect off the Orissa coast (Fig. 4.22).

In a series of recent papers ROY (1995, 1999a, 1999b) studied the maximum flood levels associated with tide and surge interaction along the Meghna River estuary in Bangladesh. He also included off-shore islands in his model to test their influence on water level due to tide surge interaction.

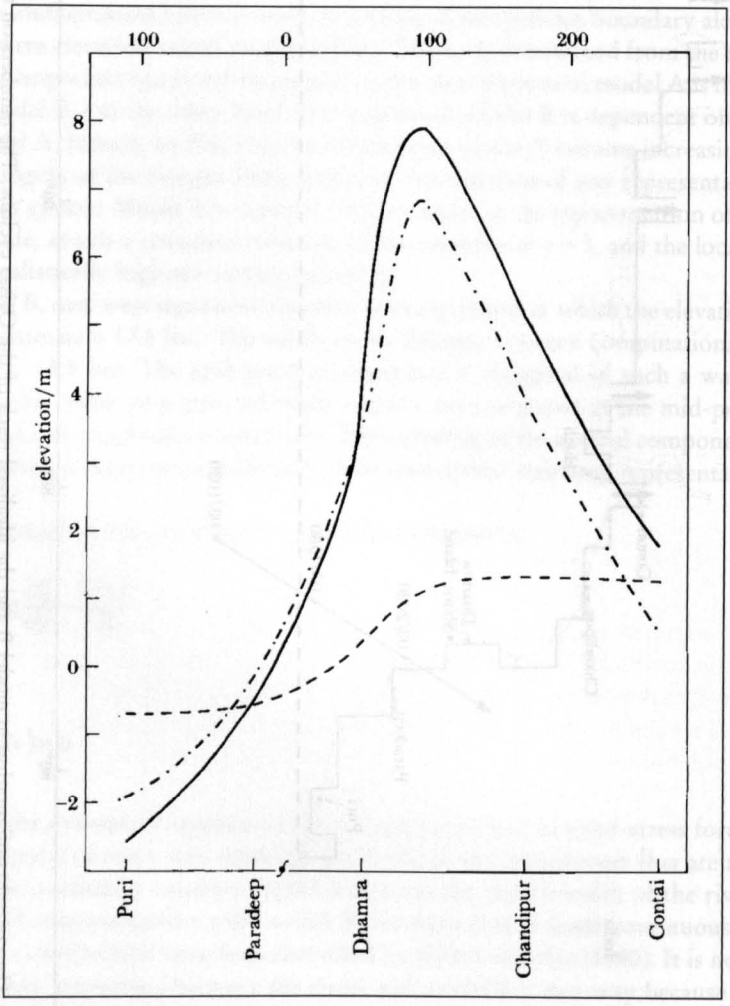


Fig. 4.22: The computed elevation along the Orissa coast at the time of occurrence of the absolute peak elevation; ___, $\zeta_{s+t+I.S.T}$; - - - - - -, $\zeta_t$; ——— . —, $\zeta_{s+I.S.T}$; § denotes the position of landfall. (JOHNS et al., 1985)

### 4.3.2 Arabian Sea and Adjacent Persian Gulf

Although more cyclones occur in the Bay of Bengal than in the Arabian Sea, there are several records of severe cyclonic storms hitting the Gujarat and the north Maharashtra regions of the west coast of India. In this section we will discuss the storm surge and tide interaction in the Arabian Sea, including Persian Gulf and the Red Sea. Most of the tropical cyclones of the Arabian Sea either travel westward or recurve north eastward, cyclones travelling westward normally weaken before they cross the coastal regions of Saudi Arabia and enter into the Red Sea on the other hand recurving cyclones are intense and cause loss of life and property in the coastal region of India.

The tidal range in most parts of the west coast of India north of 18° N is quite large especially in the Gulf of Kachchh and Gulf of Khambhat (e.g., 4 m in the Gulf of Kachchh, 8 m at Mumbai and 11m at Khambhat). If the arrival of the surge coincides with the time of the high tides, worst devastation takes place in these regions. The amplification of surge becomes very complicated through its nonlinear interaction with tide in the shallow water region of these gulfs. Recently a very severe cyclonic storm over the Arabian Sea crossed Gujarat coast near Porbandar on June 9, 1998. Storm surge associated with this tropical cyclone was of the order of 2 to 3 meters over and above the astronomical tide of 6.6 meters. The astronomical tide coupled with storm surge and very strong winds resulted in a phenomenal fury of the cyclone at Kandla port, which has never been experienced by the community of the area in the span of their living memory. This and the several other past cyclones, which struck the Gujarat coast of the India, suggest that for practical application of predicting the total water level one should have the operational scheme, which includes tide-surge interaction.

There has been very few studies on the modelling of storm surges or tides in the eastern sector of the Arabian Sea (DUBE et al., 1985a; SINHA et al., 1984, 2000; MITRA, 1990). However, no attempt has been made to study the nonlinear interaction of the tide and storm surges on the west coast of India.

Northwestern sector of the Arabian Sea and its west and northward extension through Gulf of Oman, Persian/Arabian Gulf, Red sea, Gulf of Aquaba and Gulf of Suez are mainly influenced by extra-tropical weather systems. However, part of Gulf of Oman (South of Strait of Hormuz) and the Red Sea are also affected by tropical cyclones. Strait of Hormuz is the region where eastward-directed tracks of extra-tropical cyclone and westward moving tropical cyclone tracks converge.

EL-SABH and MURTY (1989) have discussed in detail the storm surge phenomena in the Arabian Gulf, Strait of Hormuz and the Gulf of Oman. The results of their two-dimensional model show that the Gulf is subject to major negative and positive storm surges. The model is forced by the mesoscale wind phenomenon known as 'Shamal'. Shamal refers to the northwesterly winds, which occur during winter as well as summer and have significant influence in the Gulf region. Wind directions used in the numerical simulation together with the grid used for the Gulf region are shown in Fig. 4.23.

Model computed time series profiles at selected stations of tidal elevation (with three semi-diurnal, $M_2$, $S_2$, $N_2$, and three diurnal, $K_1$, $O_1$, $P_1$ constituents included), storm surge alone due to short duration winter Shamal, and tide plus storm surge are shown in Fig. 4.24. These results show important tide-surge interaction in the Arabian Gulf. At Shat-Al-Arab Bar and Bushive, the surge is totally negative and, indeed, the envelope of the tide plus surge curve is also negative. At all other locations shown in Fig. 4.24, although the predominant surge is not negative, there is a negative component, which can clearly be seen. These nega-

Die Küste, 63 Global Storm Surges (2001), 1-623

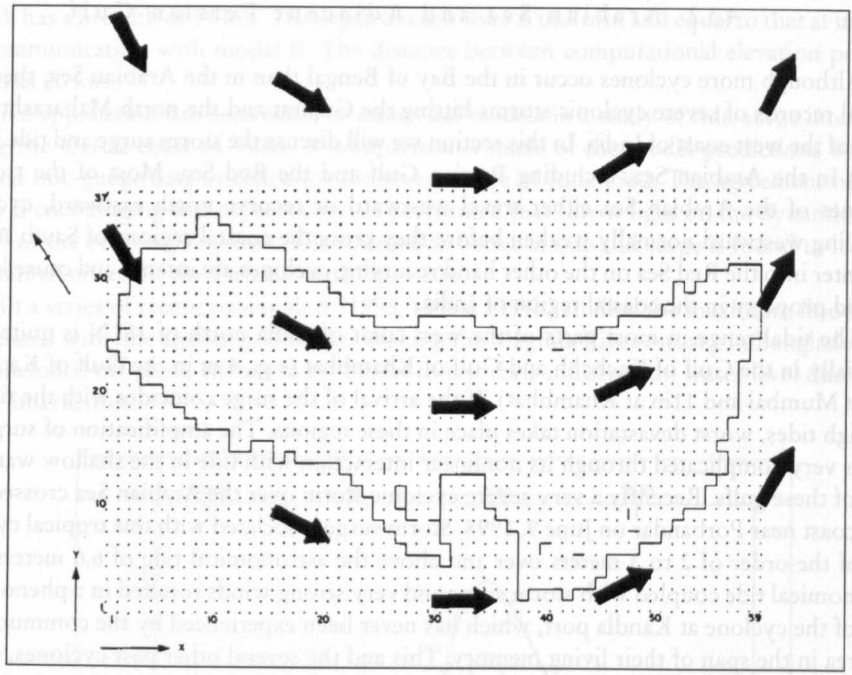


Fig. 4.23: Wind directions used in the numerical simulation. (EL-SABH and MURTY, 1989)

tive surges are due to the orientation of the storm track with reference to the topography. It may, overall, be seen that maximum amplitude of the negative surge reaches to about 3 m while maximum amplitude of positive surges is only 1m. The nature of the tide-surge interaction is different at different locations, due to the change in the tidal and surge regimes at various areas in Gulf.

### 4.3.3 Gulf of Suez-Red Sea System

Gulf of Suez is located in the extreme north of the Red Sea bounded by the Sinai Peninsula to the east and the Eastern Desert of the Egypt to the west (Fig. 4.25). It is connected with the Mediterranean Sea through the Suez Canal and with the Red Sea through the strait of Jubal.

Storm surges are considered to be one of the most important natural hazards that affect the Gulf and its surroundings. The analysis made by MURTY and EL-SABH (1981), based on the water levels at Port Suez for the year 1965–1966, indicated that significant surges could develop in the Gulf of Suez. On the other hand, $M_2$ semidiurnal tidal component dominates the tidal signal. Generally, the tidal range decreases from the entrance of the Gulf towards the bank of Tor where it reaches a very small value, and then increases again to about 1.5 m at Suez. A difference of 6 hours exists between the times of high water at the southern and northern ends of the Gulf (MORCOS, 1970). RADY et al. (1994a) used a vertically integrated two-dimensional and a five-layer three-dimensional numerical model to simulate Gulf is principal tidal component $M_2$. Known to be an area that is vulnerable to significant surges (MURTY and EL-SABH, 1984) and that has the largest tidal range and the shallowest water

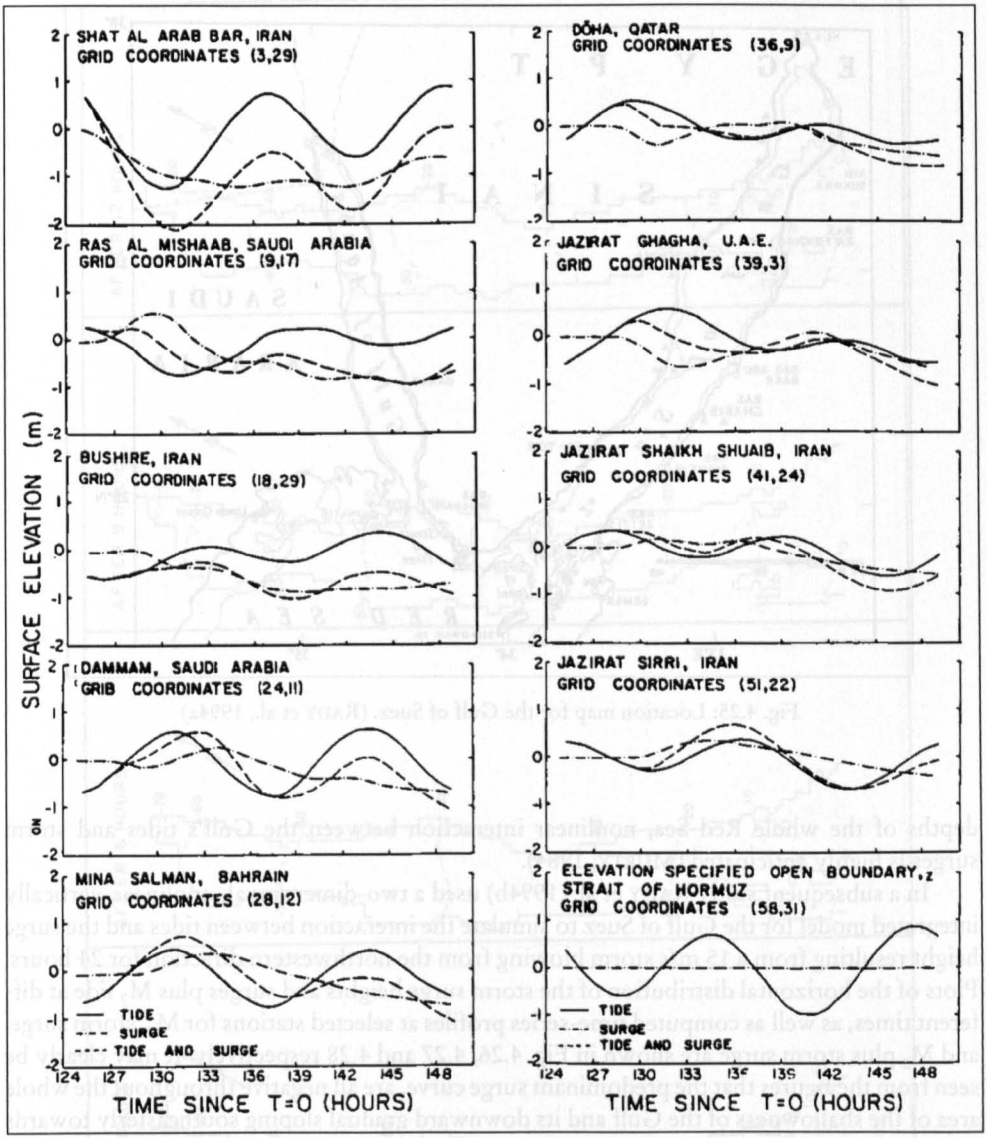


Fig. 4.24: Computed profiles of tides (including six constituents), surge only and surge plus tide at selected locations. (EL-SABH and MURTY, 1989)

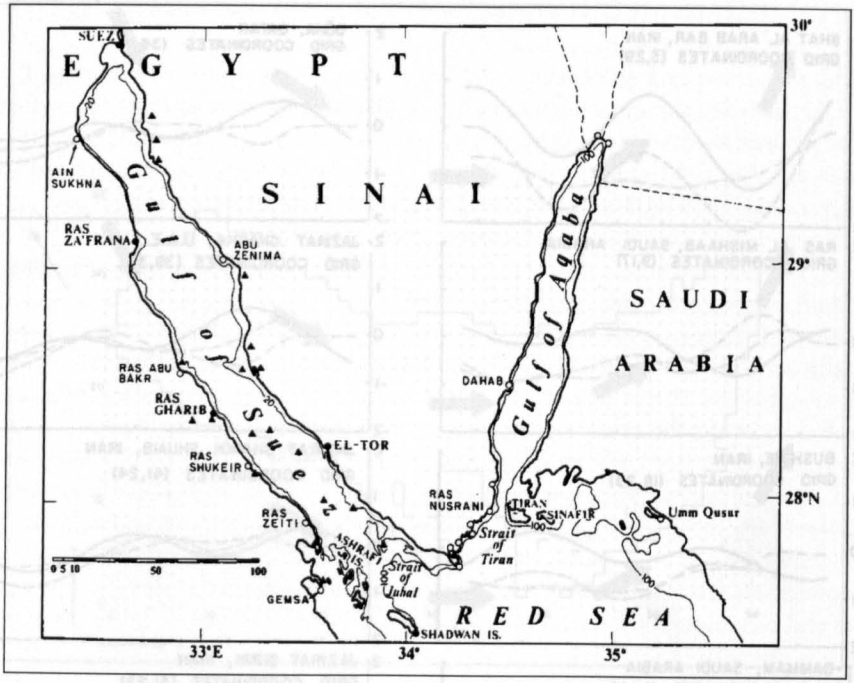


Fig. 4.25: Location map for the Gulf of Suez. (RADY et al., 1994a)

depths of the whole Red Sea, nonlinear interaction between the Gulf's tides and storm surges is highly anticipated (MURTY, 1984).

In a subsequent study RADY et al. (1994b) used a two-dimensional, nonlinear, vertically integrated model for the Gulf of Suez to simulate the interaction between tides and the surge height resulting from a 15 m/s storm blowing from the northwestern direction for 24 hours. Plots of the horizontal distribution of the storm surge heights and surges plus $M_2$ tide at different times, as well as computed time-series profiles at selected stations for $M_2$, storm surge, and $M_2$ plus storm surge are shown in Fig. 4.26, 4.27 and 4.28 respectively. It may clearly be seen from the figures that the predominant surge curve, are all negative throughout the whole area of the shallowness of the Gulf and its downward gradual sloping southeasterly towards the great depths of the Red Sea in the same direction of the blowing storm. Since the Gulf of Suez is part of the Red Sea system, positive surges should be expected to occur in other parts of the Red Sea. This aspect has been discussed in detail by RADY et al. (1994b).

Surge heights increase from a few centimeters at the southern end of the Gulf to over one meter in the extreme north at Suez. These heights become larger when the effect of the tide is included.

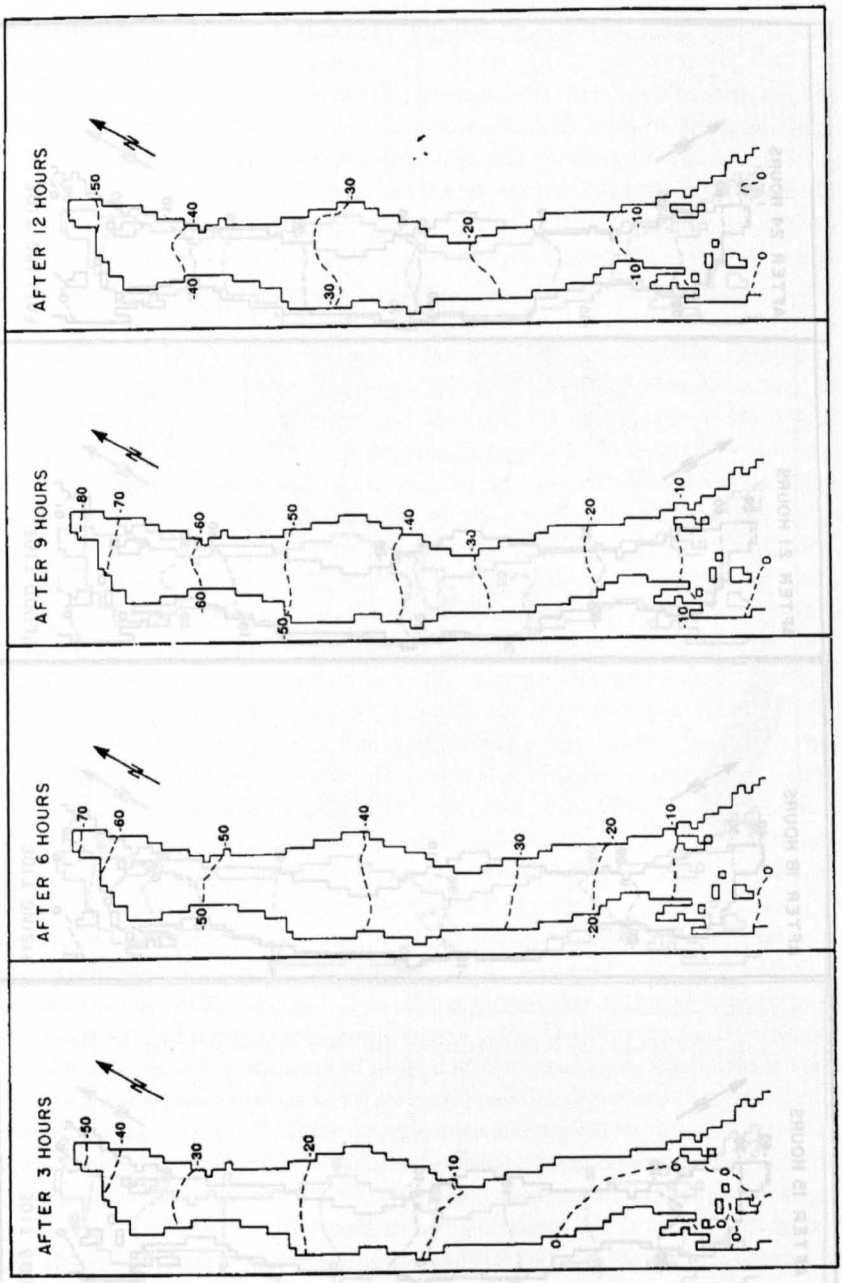


Fig. 4.26: Distribution of storm surge heights at eight different times. Elevations are in centimeters. (RADY et al., 1994 b)

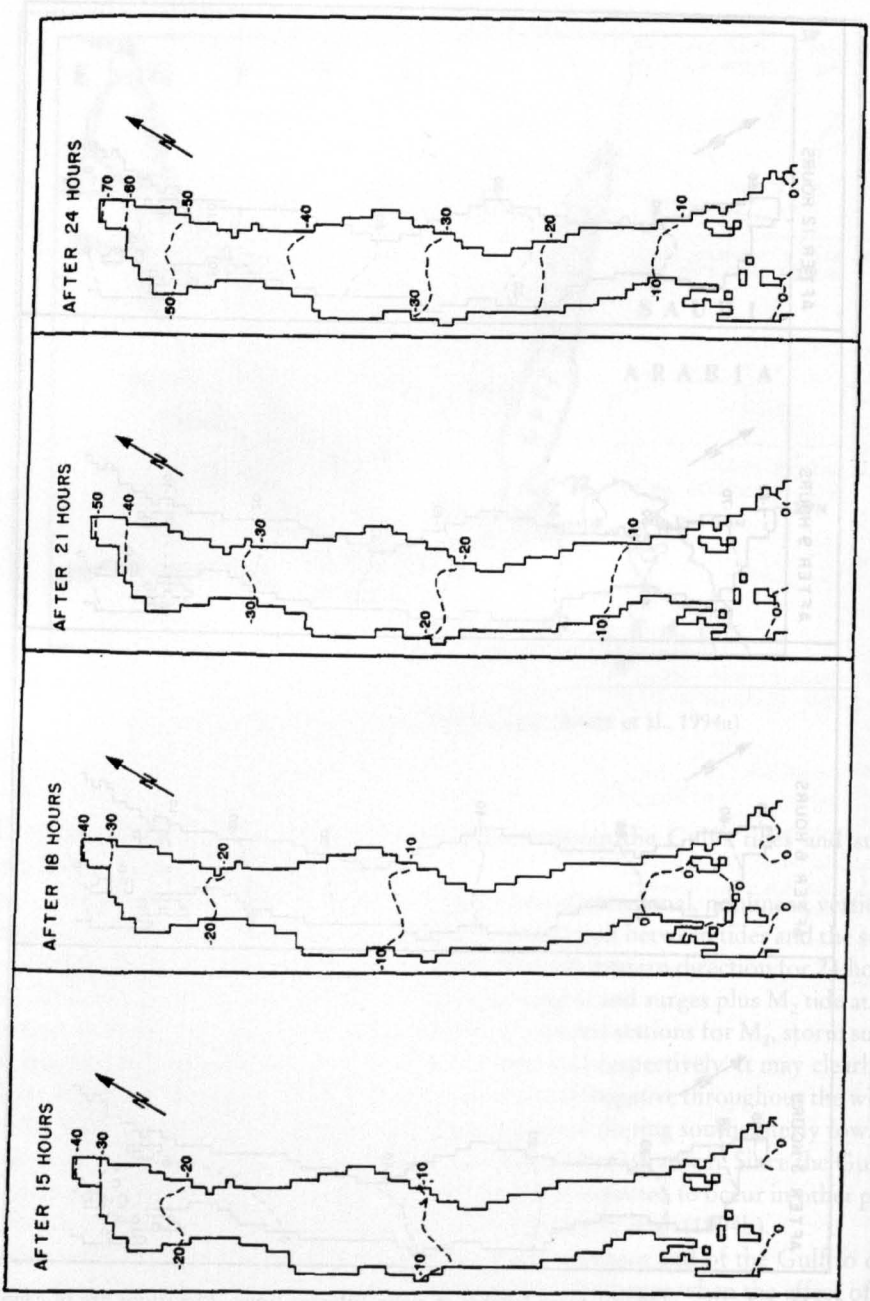


Fig. 4.27: Distribution of storm surge heights at eight different times. Elevations are in centimeters. (RADY et al., 1994 b)

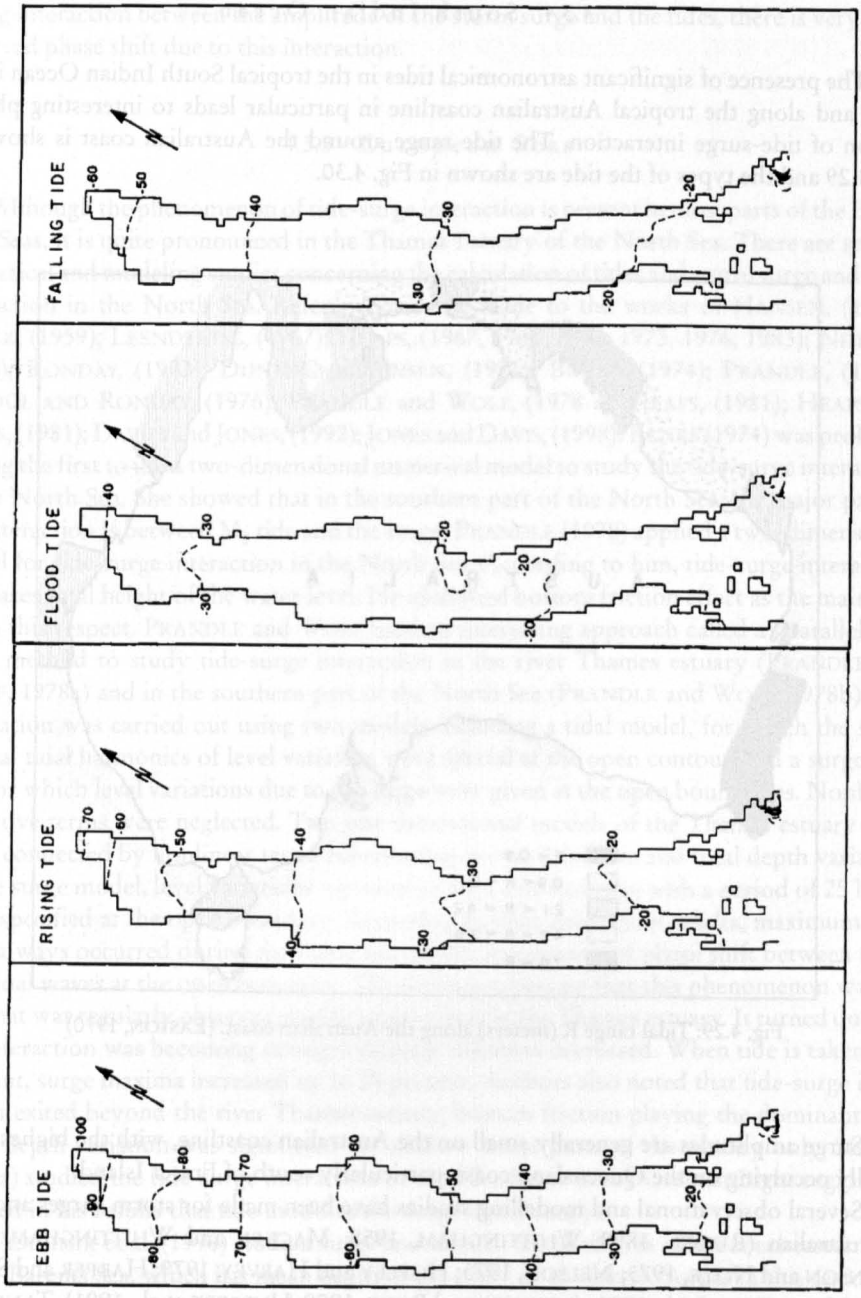


Fig. 4.28: Distribution of storm surge heights plus $M_2$ tide during the different stages of tide. (RADY et al., 1994 b)

### 4.3.4 South Indian Ocean

The presence of significant astronomical tides in the tropical South Indian Ocean in general and along the tropical Australian coastline in particular leads to interesting phenomenon of tide-surge interaction. The tide range around the Australian coast is shown in Fig. 4.29 and the types of the tide are shown in Fig. 4.30.

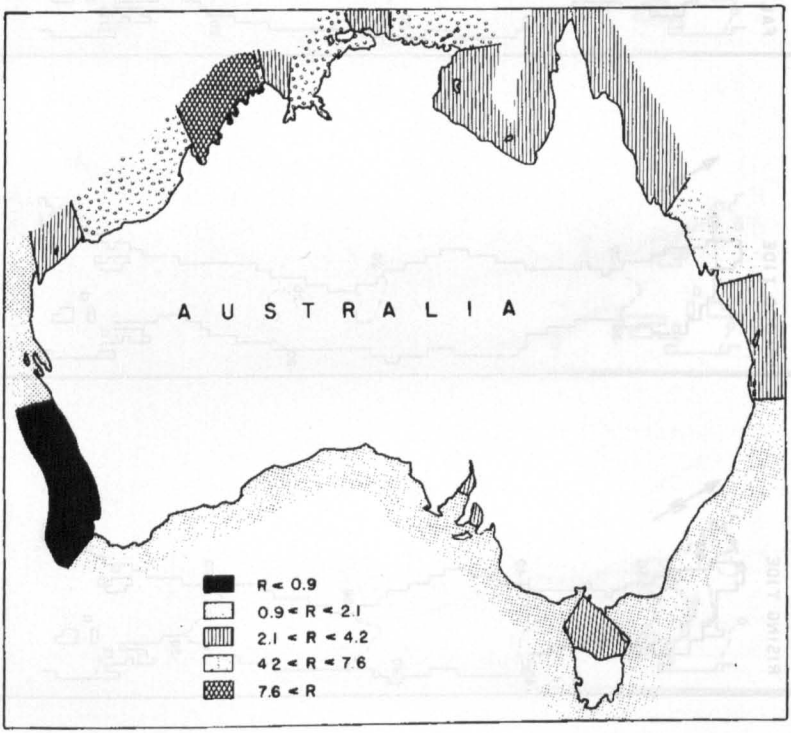


Fig. 4.29: Tidal range R (meters) along the Australian coast. (EASTON, 1970)

Surge amplitudes are generally small on the Australian coastline, with the highest level usually occurring on the Queensland coast, particularly south of Fraser Island.

Several observational and modelling studies have been made for storm surges and tides in Australian (RUSSEL, 1898; WHITTINGHAM, 1958; MACKEY and WHITTINGHAM, 1956; TRONSON and NOYE, 1973; NELSON, 1975; HOPLEY and HARVEY, 1979; HARPER and SOBEY, 1983; MIDDLETON et al., 1984; ANDREWS and BODE, 1988; HUBBERT et al., 1991). TANG et al. (1996) appear to have done the first detailed study of the tide-surge interaction for the Mackay region of the North Queensland coast. They used a two-dimensional model to simulate storm surge and tides. Their results show that with the tides included in the storm surge model the sea level elevation is generally lower than if astronomical tides are simply added to the surges. This effect is attributed by authors to the quadratic bottom friction law rather than the commonly explained reason of nonlinear interaction between the storm surge and the tides. Further, they note that although the quadratic bottom friction does cause a

strong interaction between the amplitude of the storm surge and the tides, there is very little observed phase shift due to this interaction.

### 4.3.5 European Seas

Although the phenomenon of tide-surge interaction is present in most parts of the European Seas, it is quite pronounced in the Thames Estuary of the North Sea. There are several theoretical and modeling studies concerning the calculation of tides and storm surge and their interaction in the North Sea. Reference may be made to the works of HANSEN, (1956); FISHER, (1959); LEENDERTSE, (1967); HEAPS, (1967, 1969, 1972, 1973, 1976, 1983); NIHOUL, (1973); RONDAY, (1973); DUNN-CHRISTENSEN, (1971), BANKS, (1974); PRANDLE, (1975); NIHOUL AND RONDAY, (1976); PRANDLE and WOLF, (1978 a); HEAPS, (1981); HEAPS and JONES, (1981); DAVIES and JONES, (1992); JONES and DAVIS, (1998). BANKS (1974) was probably among the first to use a two-dimensional numerical model to study the tide-surge interaction in the North Sea. She showed that in the southern part of the North Sea, the major part of the interaction is between $M_2$ tide and the surge. PRANDLE (1978) applied a two-dimensional model for tide-surge interaction in the North Sea. According to him, tide-surge interaction decreases total height of the water level. He identified bottom friction effect as the main factor in this respect. PRANDLE and WOLF used an interesting approach called a "parallel models" method to study tide-surge interaction in the river Thames estuary (PRANDLE and WOLF, 1978a) and in the southern part of the North Sea (PRANDLE and WOLF, 1978b). The simulation was carried out using two models including a tidal model, for which the semidiurnal tidal harmonics of level variation were special at the open contour, and a surge model, for which level variations due to the surge were given at the open boundaries. Nonlinear advective terms were neglected. Two one-dimensional models of the Thames estuary were used, connected by nonlinear terms representing power 2 friction and total depth variation. In the surge model, level variations represented by a sine function with a period of 25 hours were specified at the open boundary. According to their simulation results, maximum total level always occurred during the rising tide phase, irrespective of phase shift between surge and tidal waves at the open boundary. The authors supposed that this phenomenon was the one that was regularly observed during surge events in the Thames estuary. It turned out that the interaction was becoming stronger as surge duration decreased. When tide is taken into account, surge maxima increased up to 25 percent. Authors also noted that tide-surge interaction exited beyond the river Thames estuary, bottom friction playing the dominant role. Total depth variation was significant for shallow water parts of the estuary only. SIEFERT (1978a) studied the tide-surge interaction in the Elbe River in the German Bight region. He showed in his results that tide modifies the surge significantly.

VLADIMIR et al. (1996) studied surge and tides in the shelf area of the southeastern part of the Barents Sea, which has mean depth of the order of 45 meters. Surges in this region are of the same order as the tides and may even exceed them. For the model verification and for obtaining information necessary for specification of boundary conditions, results of a special observational programme in the shallow water Pechorskaya Guba were used, which provided data for the analysis of total motion and estimation of tide-surge interaction. Their results show strong nonlinear tide-surge interaction for Shvedskie Stvory where total water level decreases during rising tide period and increase during the opposite phase.

There have also been several attempts to simulate the nonlinear interaction of tides and storm surges in North Sea and Irish Sea using a three-dimensional model. It may not be pos-

sible to describe here the details of these studies. However, one may refer to the works of HEAPS, (1973, 1976, 1981); HEAPS and JONES, (1981); DAVIES and JONES, (1992, 1996); JONES and DAVIES, (1998).

### 4.3.6 Canada and United States

In this section we will discuss the interaction between storm surges and tides in selected water bodies in Canada and North America. The tidal range along the Canadian coast is significant. In the Bay of Funding the tidal range is more than 12 m. Along the Atlantic coast of Canada, the tide is semidiurnal and the tidal range is usually less than 2 m while the tidal range in the Gulf of St. Lawrence is less than 2.5 m. MURTY (1984) has described in detail the tidal regimes in the coastal waters of Canada and North America. In these shallow coastal waters the interaction between storm surge and tides is found to be significant.

In the St. Lawrence estuary in eastern Canada, observations indicate a predominant occurrence of positive storm surges with low tide and negative surges with high tide. MURTY and EL-SABH (1981) studied the interaction between astronomical tides and storm surges in the St. Lawrence estuary by extending simple analytical theory developed by PROUDMAN (1955a, b, 1957) for the Thames estuary. Based on PROUDMAN (1957) it can be shown that an estuary is short (with reference to long wave propagation) provided the following two conditions are satisfied

$$\left.\begin{aligned} \frac{\sigma L}{c} A &<< 1 \\ \frac{K\sigma^2 L^3 A}{hc^2} A &<< 1 \end{aligned}\right\} \qquad (4.15)$$

Where $\sigma$ is the angular frequency of the tide, L is the length of the estuary, and $c = \sqrt{gh}$ The parameter A is defined as

$$A \equiv \frac{B}{2H} \qquad (4.16)$$

where, B is the tidal amplitude at the mouth. Parameter K is a coefficient of bottom friction and is taken as 0.0025. Note that it is not the physical length alone that determines whether or not an estuary is short, in the sense used by PROUDMAN.

Length L, Average depth h, and tidal amplitude B for the two portions of the St. Lawrence Estuary are summarized in Table 4.8. The values of the two PROUDMAN parameters defined by eq. (4.15) are also listed for the two sections. Based on these values, the classification into long or short estuary is made in the final column.

Table 4.8: Dimensions and classifications of the two sections of the St. Lawrence Estuary.

| System | Length (km) | Average depth (cm) | Tide amplitude, B (cm) | Proudman's 1st parameter | Proudman's 2nd parameter | Classification |
|---|---|---|---|---|---|---|
| Sept-Iles to Saguency River | 350 | $25 \times 10^3$ | 107 | 0.002 | 0.007 | Short estuary |
| Saguency River to Quebec City | 193 | 1800 | 215 | 0.12 | 6.7 | Long estuary |

Table 4.9: Number of occasions of positive and negative surges exceeding a given height at Tadoussac during 1965–75. Each hourly reading is treated as one occasion.

| State of tide | Surge height (cm) 10 | 20 | 30 | 40 | 50 | 60 | 70 | 80 | 90 | 100 | 110 | 120 | 130 | 140 | 150 | 300 |
|---|---|---|---|---|---|---|---|---|---|---|---|---|---|---|---|---|
| | | | | | | | (a) Positive surges | | | | | | | | | |
| Low | 3806 | 1763 | 904 | 468 | 260 | 147 | 77 | 48 | 26 | 16 | 10 | 5 | 3 | 2 | 0 | 0 |
| Rising | 4195 | 2090 | 1016 | 515 | 263 | 129 | 81 | 61 | 47 | 29 | 12 | 8 | 4 | 3 | 3 | 3 |
| High | 4063 | 1843 | 849 | 390 | 185 | 96 | 59 | 33 | 23 | 14 | 3 | 2 | 2 | 2 | 2 | 2 |
| Falling | 4210 | 2082 | 1057 | 571 | 315 | 187 | 115 | 60 | 25 | 5 | 3 | 2 | 2 | 0 | 0 | 0 |
| | | | | | | | (b) Negative surges | | | | | | | | | |
| Low | 4466 | 2046 | 894 | 412 | 192 | 94 | 44 | 22 | 8 | 1 | 0 | 0 | 0 | 0 | 0 | 0 |
| Rising | 4533 | 2275 | 1146 | 634 | 324 | 178 | 94 | 56 | 35 | 16 | 5 | 3 | 2 | 1 | 0 | 0 |
| High | 3441 | 1513 | 710 | 363 | 205 | 108 | 52 | 34 | 19 | 15 | 13 | 12 | 9 | 7 | 4 | 2 |
| Falling | 4110 | 1934 | 851 | 385 | 205 | 102 | 53 | 35 | 18 | 12 | 8 | 7 | 5 | 3 | 1 | 0 |

Table 4.10: Comparison between theory and observation of the tide-surge interaction in the St. Lawrence Estuary. H, High tide; L, low tide; R, rising tide; F, falling tide; A, inagreement; D, in disagreement; N, neither agreement nor disagreement.

| Station | State of tide with which the Maximum surge is associated | | |
|---|---|---|---|
| | Theory | Observation | Comparison |
| Ste-Anne-des-Monts | H–F | F | A |
| Baie-Comeau | H–F | H | A |
| Pointe-au-Pere | H–F | R–H | N |
| Tadoussac | H–F | R–H | N |
| Rivviere-du-Loup | L–R | L | A |
| St-Joseph-de-la-Rive | L–R | H–R | N |
| St-Jean-Port-Joli | L–R | H | D |
| St-Francois | L–R | L–R | A |
| Quebec City | L–R | L | A |

Table 4.11: Tidal range and maximum amplitudes of positive and negative surges in the St. Lawrence Estuary

| Station | Spring tidal range (cm) | Amplitude maximum positive surge (cm) | Amplitude of maximum negative surge (cm) | No. of occurrence of positive surges with amplitude ≥ 180 cm during the period 1965–75[a] | No. of occurrences of negative surges with amplitude ≥ 130 cm |
|---|---|---|---|---|---|
| Ste-Anne-des-Monts | 347 | 180 | 140 | 2 (24) | 2 |
| Baie-Comeau | 402 | 290 | 130 | 2 (15) | 8 |
| Pointe-au-Pere | 460 | 300 | 130 | 2 (2) | 5 |
| Tadoussac | 519 | 300 | 160 | 5 (11) | 16 |
| Rivviere-du-Loup | 567 | 300 | 180 | 3 (3) | 21 |
| St-Joseph-de-la-Rive | 695 | 300 | 250 | 5 (29) | 20 |
| St-Jean-Port-Joli | 573 | 190 | 180 | 4 (34) | 33 |
| St-Francois | 686 | 240 | 230 | 17 (100) | 93 |
| Quebec City | 580 | 300 | 210 | 32 (157) | 20 |

[a] Value in parentheses is number of occurrence for ≥ 130 cm.

The results of PROUDMAN (1957) can be summarized as follows: (a) for a long estuary, for a tide of progressive wave type, maximum surges are associated more with low tide; (b) for a long estuary, for a tide of standing wave type, maximum surges are associated more with high tide; (c) for a short estuary, maximum surges are associated more with high tide. PROUDMAN'S results were reinterpreted (with justification) to read low tide (or rising tide) and high tide (or falling tide) wherever "low tide" or "high tide" appears in the above statements.

The nature of the tide in the section between Sept-Iles and Tadoussac is more of a standing wave type than of a progressive wave type, whereas between Tadoussac and Quebec City the tide is more of a progressive wave type. The cumulative frequency of surges of given amplitude associated with a given state of the tide for Tadoussac is listed in Table 4.9. Although the theory does not distinguish between positive and negative surges, they are listed separately. Similar tables were prepared (not shown here) for the other stations. The observed and theoretical results are compared in Table 4.10. Some pertinent data on the surges in the St. Lawrence Estuary are given in Table 4.11.

The astronomical tide is quite significant in the northern parts of the east coast of the United States and it becomes less and less important as we proceed south and also along the Gulf coast. The problem of tide-surge interaction has not received much attention in the United States. MURTY (1984) has summarised the results of few tide-surge interaction studies carried out for the east coast of United States.

The degree of importance of interaction between tides and surges in United States depends on the location. The tide, surge, and the observed water level at Atlantic City on November 25, 1950, are shown in Fig. 4.30. It can be seen that the maximum surge occurred almost at the time of low tide (SWANSON, 1976).

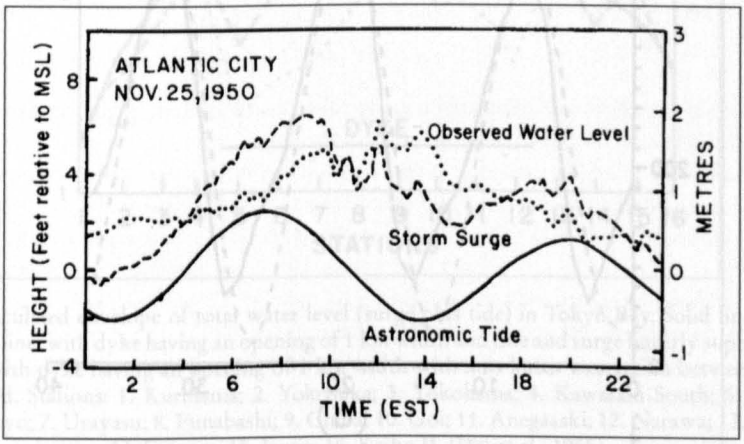


Fig. 4.30: Observed water level, storm surge and astronomical tide at Atlantic City on November 25, 1950. (MURTY, 1984)

### 4.3.7 China and Japan

Storm surges up to 6 m can occur occasionally on the coast of China, with surges up to 2–3 m occurring frequently. Nonlinear coupling of storm surges and tides is quite pronounced in the shallow water regions of Shanghai on the East China Sea. The mechanism of tide-surge interaction in the coastal waters of China has been investigated by many workers using both analytical and numerical models (CHAI and JINGYONG, 1990; QIN et al., 1994; ZHANG and WANG, 1989; CHOI, 1986; FENGSHU and WENLAN, 1990; YANTING and WANG, 1986, 1990; CHUNYAN, 1990; JINQUAN et al., 1990; YANTING et al., 1992).

More recently QIN and DUAN (1996) have made a detailed study of tide-surge interaction in the coastal water of Shanghai. They used a two-dimensional model to simulate the surge generated by eight tropical cyclones of different tracks crossing the East China Sea

coast near Shanghai. They also analysed in detail the contributions of various nonlinear terms in the dynamic equations to the water levels. Their results show that the nonlinear bottom friction term is of prime importance in controlling the water level and nonlinear tide surge interaction.

Other conclusions drawn by the authors may be summarized as:

(i) Nonlinear tide surge interaction is prominent in coastal waters of Shanghai.

(ii) The simulated storm surges comprising the nonlinear tide-surge effect give better results than pure storm surge simulations both in their peak values and the temporal variations (Fig. 4.31)

(iii) The oscillations with the main tidal period occurring in temporal variation of the water level residuals during tropical cyclone passage are attributed to nonlinear tide-surge interaction.

(iv) Generally the peak surges occur on rising tides whereas they become weaker during the falling tides. This is because of the nonlinear tide-surge interaction.

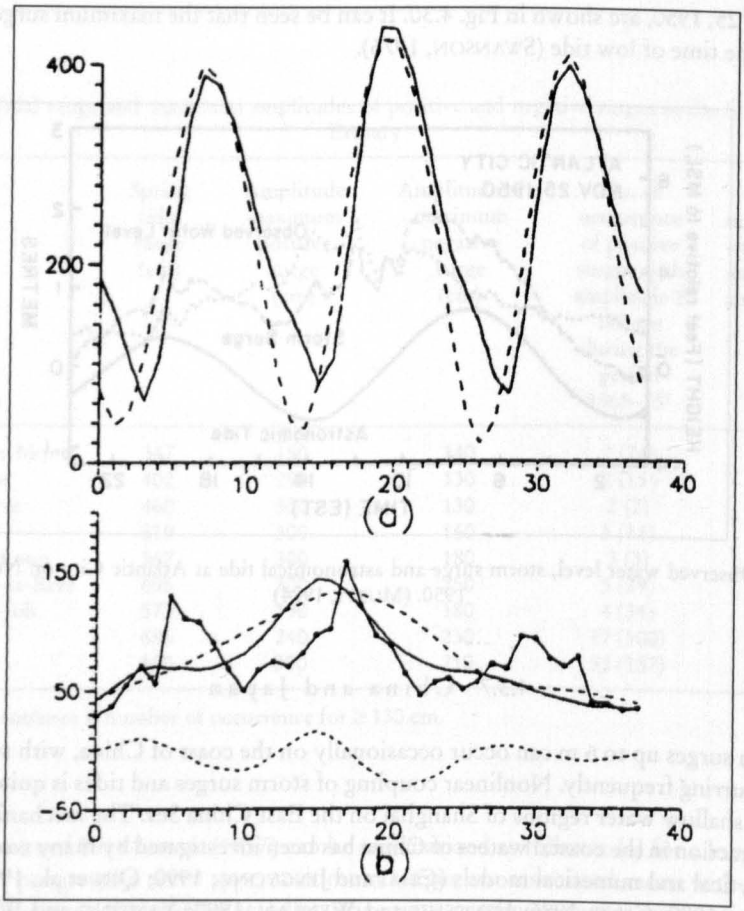


Fig. 4.31: Simulations of tide, storm surge and water level caused by nonlinear T – S coupling during TC Mary (1974). (a) Tide level: solid line – tidal level prediction with 63 constituents (observed), dash line – tidal level prediction with 8 constituents (simulated). (b) Storm surge: solid line with symbols – observed surge, solid line without symbols – simulated surge comprising T – S coupling effects, long dash line: simulated pure surge, short dash line: simulated. (QIN and DUAN, 1996)

Tide-Surge interaction on the coast of Japan is not as important as in China Sea and therefore not many studies have been done in this area. Using two-dimensional numerical model, ITO et al. (1965) studied the problem of tide-surge interaction and the influence of a dyke in Tokyo Bay. Based on the analysis of the results of several runs they conclude that linear superposition of the tide and surge tends to overestimate the total water level (Fig. 4.32).

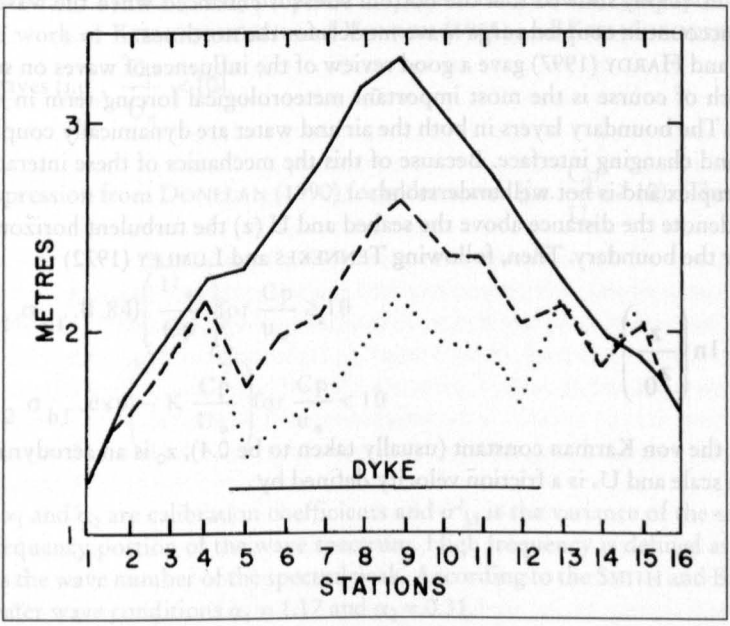


Fig. 4.32: Calculated envelope of total water level (surge plus tide) in Tokyo Bay. Solid line: without dyke; broken line: with dyke having an opening of 1 km width and tide and surge linearly superimposed; dotted line: with dyke having an opening of 1 km width with non-linear interaction between tide and surge included. Stations: 1. Kurihama; 2. Yokosuka; 3. Yokohama; 4. Kawasaki South; 5. Kawasaki North; 6. Tokyo; 7. Urayasu; 8. Funabashi; 9. Chiba; 10. Goi; 11. Anegasaki; 12. Narawa; 13. Kisarazu; 14. Futtusu; 15. Isone; 16. Kaiho II. (ITO et al., 1965)

## 4.4 Surge-Wind wave Interaction

The state of the art in this field is still evolving and there are at present no universally accepted and definitive approaches. Hence we will discuss the methodologies used by a few different authors.

We start with the excellent review of BODE and HARDY (1997). They point out that the specification of wind stress only as a function of the wind speed – underestimates the very important role played by wind waves in the transfer of momentum across the atmosphere-ocean interface, particularly for tropical cyclones.

These interactions occur through at least the following three mechanisms:

1) Radiation Stress 2) Enhanced Surface Wind Stress and 3) Enhanced Bottom Stress

The Radiation Stress concept, originally proposed by LONGUET-HIGGINS and STEWART (1964) has been used in computing wave set up in storm surge models (e.g., HUBERTZ, 1985).

MASTENBROEK et al. (1993) included radiation stress forcing in a coupled storm surge-wind wave model. They subtracted the gradient of the radiation stress from the wind stress terms in the momentum equations. Their results for the North Sea showed that the contribution from the radiation stress is negligible compared to the contribution from the wind stress. The tide, surge and wind wave components of the water level contribute to the bottom current. The bottom stress depends upon the bottom current in a nonlinear fashion. In shallow water, waves could have a significant influence on the bottom current. WU and FLATHER (1992) and WU et el. (1994) showed that the bottom stress is enhanced when the wave effects are taken into account in coupled surge-wave models for the north sea.

BODE and HARDY (1997) gave a good review of the influence of waves on surface wind stress, which of course is the most important meteorological forcing term in storm surge generation. The boundary layers in both the air and water are dynamically coupled through a moving and changing interface. Because of this the mechanics of these interactions is extremely complex and is not well understood.

Let z denote the distance above the seabed and U (z) the turbulent horizontal velocity profile near the boundary. Then, following TENNEKES and LUMLEY (1972)

$$U(z)=\frac{U_*}{k}\ln\left(\frac{z}{z_0}\right) \tag{4.17}$$

where, k is the von Karman constant (usually taken to be 0.4), $z_0$ is an aerodynamic roughness length scale and $U_*$ is a friction velocity defined by

$$U_*^2=\frac{\tau_s}{\rho_w} \tag{4.18}$$

where $\tau_s$ is the surface and $\rho_w$ is the density of air.

CHARNOCK (1955) suggested that

$$z_*=\frac{gz_0}{U_*^2}=\alpha \tag{4.19}$$

where, $\alpha$ is a constant. This means that $z_0$ (which is a measure of the aerodynamic roughness) varies linearly with the surface stress $\tau_s$.

Field observations suggest that $\alpha$ is not constant but is dependent on at least the water depth and wave age. The value of $\alpha$ varies from about 0.011 for older or deep water waves SMITH (1980, 1988) to about 0.018 for younger or shallow water waves (WU, 1980, 1982)

Further analysis of field data showed that $Z_0$ is a function of wave age, usually specified as $Cp/U_*$ where Cp is the wave celerity of the peak frequency and $U_*$ is the friction velocity. Hence

$$z_*=\frac{gz_0}{U_*^2}=f\left(\frac{Cp}{U_*}\right) \tag{4.20}$$

As given by DONELAN (1982), GEERNAERNT et el. (1986) and SMITH et al. (1992). Equation (4.20) was rewritten as

$$z_* = \frac{gz_0}{U_*^2} = \frac{\mu}{Cp/U} \tag{4.21}$$

where, $\mu$ is a constant (MAAT et al., 1991)

JOHNSON and VESTED (1992) proposed a hybrid model for the computation of $Z_0$, following the work of KITAIGORODSKII and VOLKOV (1965) and KITAIGORODSKII (1973) for younger waves (i.e., $\frac{Cp}{U_*} < 10$).

With an expression from DONELAN (1990) for older waves (i.e. $\frac{Cp}{U_*} \geq 10$). This leads to

$$Z_0 = \begin{cases} \alpha_1 . \sigma_{hf} . (1.84) \left( \frac{U_*}{Cp} \right) \text{for } \frac{Cp}{u_*} \geq 10 \\ \alpha_2 . \sigma_{hf} . \exp \left( -K \frac{Cp}{U_*} \right) \text{for } \frac{Cp}{u_*} < 10 \end{cases} \tag{4.22}$$

Here $\alpha_1$ and $\alpha_2$ are calibration coefficients and $\sigma^2_{hf}$ is the variance of the sea surface in the high frequency portion of the wave spectrum. High frequency is defined as $K > 1.5\ K_p$, where $K_p$ is the wave number of the spectral peak. According to the SMITH and BANKE (1975) for deep water wave conditions $\alpha_1 = 1.17$ and $\alpha_2 = 0.31$.

This means that the drag coefficient is a function of wave age, wave height and water depth. MASTENBROEK et al. (1993) examined the effect of waves on the drag coefficient. Instead of parameterizing the dimensionless roughness coefficient, they followed the theory of JANSSEN (1991), which hypothesizes that close to the water surface waves contribute separately to the surface shear stress. Thus

$$\tau_S = \tau_t + \tau_W \tag{4.23}$$

Where $\tau_t$ is the turbulent shearing stress and $\tau_W$ is the wave-induced stress.

This $\tau_w$ changes the boundary layer in the air close to the surface, so that the velocity profile assumes a modified logarithmic form.

They coupled the surge and wave models dynamically, and their results were significantly greater surges than would be obtained by using the drag coefficient of SMITH and BANKE (1975).

However, the disappointing point is that, instead of these more complicated computations, a simple increase of the drag coefficient of SMITH and BANKE (1975) would have given same results.

*Approach by Yamashita and Watson*

During surges there are complex mutual interactions between wind, waves and currents. The wind generates waves, which influence the wind drag coefficient and hence the wind-driven currents and the surge height. In turn, the currents influence the wave field and the waves influence the wind field. In order more accurately to predict surges, waves and flooding, a thorough understanding of these air-sea interaction processes is important.

The relation between mean wind and wind stress and the influence of waves on this relationship is investigated using data from a new observation tower about 2 km offshore in Tanabe Bay. This measures wave elevation, 20-m wind and 10-m depth current in about 30 m of water. Wind stress and drag coefficient estimates are made using the inertial dissipation method. Data taken during a typhoon are found to show enhanced stress compared with values from empirical formulae in the literature.

For storm surge modelling, the most important forcing terms are the atmospheric pressure, the surface wind stress and the bottom friction stress. The former is of course theoretically well defined and depends only on a reasonably accurate knowledge of the relevant time-dependent pressure field. The stress terms however are not so simple and are normally represented using empirical approximations. These are based on what data are available, which are rather limited and scattered. There is much room for improving our physical understanding of these stresses and then the accuracy of the corresponding forcing terms.

One current area of research is the influence of waves, on both wind stress and bottom stress. Waves are a crucial and complex part of the process of momentum transfer between air and sea, involving the two-dimensional wave spectrum wave growth and decay, non-linear interactions and wave breaking. A forcing term in which the surface stress is a simple function of wind speed is a useful first approximation, and produces acceptable results in many circumstances. However, it is certainly oversimplified and there may be important cases where it is inaccurate, especially in situations where the wind is rapidly changing (such as in tropical storms), near the coast where the water is shallow and the waves fetch-limited, or where the wave spectrum has more than one significant component. Such cases could potentially be more accurately represented by a theory, which correctly accounts for momentum transfer between wind and waves, and between waves and the mean current.

Another effect of waves, which may be important in some circumstances, is their influence on the bottom, stress. In shallow water, wave orbital velocities can be quite large and the flow over the rough bottom produces turbulence. This increases the eddy viscosity experienced by the mean flow and thus the force acting between the mean flow and the bottom.

Using a wave model to predict wave conditions during surge generation, and then modifying the surface may estimate the effect of these processes on surge models and bottom drag coefficients, depending on appropriate properties of the local wave spectrum as outlined below.

The mean force acting on the surface of a body of water due to wind stress is usually approximated as

$$\bar{\tau}_s = \rho_a C_{D10} \bar{U}_{10} | \bar{U}_{10} | \qquad (4.24)$$

where, $\bar{\tau}_s$ is the wind stress at the surface (the horizontal force per unit area acting on the surface), $\rho_a$ the air density, $\bar{U}_{10}$ the mean wind at 10 m and $C_{D10}$ the drag coefficient for wind at 10 m.

With a constant drag coefficient, this formula is found to be reasonable for airflow over

solid rough surfaces. However, as wind speed increases over the sea, the waves get bigger and the surface gets rougher. Thus, for eq. (4.24) to be useful, the drag coefficient must be allowed to vary with wind speed: $C_D(U)$.

For fully developed seas in which the waves are approximately in equilibrium with the local wind, observations of wind stress as a function of wind speed have led to several empirical relations for $C_D$ (U). The data are scattered, but the relationships resulting from the various datasets are all quite similar. Four examples of such formulae are listed in Table 4.12. Note that these data mainly apply to wind speeds greater than about 5–10 $ms^{-1}$.

However, these results only apply to well-developed seas in deep water. Higher values of $C_D$ found both in growing waves, such as during the onset of a storm and in shallow water. Both of these conditions are necessary for the development of a storm surge, so the effect is potentially important. However, what field data exist are hard to interpret, because the effect is comparable in size with measurement errors, and therefore cannot be determined very accurately. It has not so far been possible to derive any empirical relationship between wind stress and wave conditions, based on the data.

JANSSEN (1991) considers the extra momentum extracted from the wind by growing waves, and then passing into the mean flow. This enhancement of momentum transfer effectively increases the drag. An important parameter here is the ratio of dominant wave phase speed to wind speed, known as the wave $C_p/U$, which is a measure of whether or not the wind and waves should have reached equilibrium. The effect is not usually incorporated in surge models, and it is uncertain how significant it may be.

The mean retarding force acting on a body of water due to bottom friction is usually approximated as

$$\bar{\tau}_b = \rho_w C_{Db} \bar{u} |\bar{u}| \qquad (4.25)$$

where, $\bar{\tau}_b$ is the bottom stress, $\rho$ the water density, $\bar{u}$ the wave-averaged bottom current and $C_{Db}$ a bottom drag coefficient. For many applications, it is found good enough to use a constant value for $C_{Db}$.

In shallow water, wave-induced flow near the bottom results in an increase in turbulence. Amongst other things, this increases the rate of vertical transfer of horizontal momentum, and hence the mean drag force between the water and the seabed. This is represented theoretically as an increase in eddy viscosity (which parameterizes the effect of small-scale turbulence in increasing the shear stresses) and hence of the drag coefficient in eq. (4.25).

MASTENBROEK (1992) estimated the size of this effect for storm surges in the North Sea using the relationship between drag coefficient and significant wave height, $C_{Db}(H_s)$. He found that in some shallow areas it could significantly affect the predicted surge, more so than the effect of a wave-dependent wind drag coefficient. However, the size of this effect is similar to that of geographical variations in $C_{Db}$ due to variations in bed roughness. This makes practical implementation difficult because of the lack of sufficiently detailed data on bed roughness.

It should also be pointed out that another effect of waves on local water level at the coast is that of wave set-up. Depending on the beach topography and wave conditions, this can sometimes raise sea level within the surf zone by up to about 1 m. It is an effect that should also be taken into account when considering the flood risk during storms and surges.

The Kyoto University Disaster Prevention Research Institute's Tanabe-Nakajima Storm Surge Observation Tower is located in 30 m of water about 2 km from the coast near Tanabe, in southern Honshu Island, Japan (Wakayama Prefecture). The tower stands at the mouth of

Tanabe Bay, on a plateau of about 10 m depth, around 100 m in diameter, in an area where the depth is predominantly 30 m. It is possible that this plateau will have some local influence on the waves, but it is difficult to determine. The site is in the approaches to the densely – populated area around Osaka Bay. Typhoons regularly cause surges in this area and defenses against these form a significant element of coastal engineering works.

The main instruments of interest here are a 3-component ultrasonic anemometer at about 20 m heights, and a downward-looking ultrasonic wave gauge. Data are recorded at 20 Hz during 20 minutes of each hour. There is also an electromagnetic current meter at a depth of 10 m.

Following YELLAND et al. (1994), wind stress was estimated from the anemometer data using the turbulent (or inertial) dissipation method. This is one of the two commonly used methods, the other being the direct, or eddy-correction method. The latter was also attempted but it was found that 20-minute data samples were not long enough to give convergent results.

The turbulent dissipation method is based on the assumption of a cascade of energy from lower to higher frequencies, at a rate, which is governed, by the rate of dissipation of energy by turbulence at the high-frequency end of the spectrum. The turbulence is assumed to be "frozen", i.e. the time scales are slow compared with the time scale of advection past the observation point. These assumptions yield:

$$S(f) = K\varepsilon^{2/3} f^{-5/3} \left( \frac{U}{2\Pi} \right)^{2/3} \qquad (4.26)$$

where, S(f) is the power spectrum of the down-wind component, K is the 1-D Kolmogorov constant, taken as 0.55, and $\varepsilon$ is the high frequency turbulent dissipation rate. If the measured spectrum is found to obey the $f^{-5/3}$ law reasonably well, then an average value of $S(f)f^{-5/3}$ over an appropriate frequency range (0.8–2.0 Hz was used here) may be used in (4.22) to estimate $\varepsilon$. The wind stress $\tau$ is then estimated from

$$\tau = \rho(k_v \varepsilon z)^{2/3} \qquad (4.27)$$

where, $k_v$ is the von Karman constant (here taken as 0.4), z is the measurement height (20 m). The drag coefficients is then obtained from (4.20) after correcting the observed mean wind to an estimated value at 10 m using the relation for a logarithmic boundary layer,

$$\frac{U(z)}{U(10)} = \frac{\ln(z/z_0)}{\ln(10/z_0)} \qquad (4.28)$$

where, $z_0$ is the roughness length $z_0 = e^{-k_v \sqrt{C_D}}$. It should be noted that (4.26) applies to neutral atmospheric stability. A correction is possible for non-neutral conditions, but was found to be small in this case.

The final estimates of wind stress for 29th Sept 1994, excluding the data from 22:00 and 23:00 are plotted against mean wind speed in Fig. 4.33. The four empirical relations from Table 4.12 are plotted for comparison. Particularly at intermediate wind speeds (5–15 $ms^{-1}$), the data lie well above these curves. These data appear to be an example of departure from

the standard formulae and are thus worthy of further investigation. There is no obvious trend with wind speed, and as with other such data, they are rather scattered. If anything, these data suggest that a constant drag coefficient may be appropriate in this instance. The mean value is $2.2 \times 10^{-3}$. However, this is only a small amount of data and it will be necessary to examine a larger amount, including normal wind conditions, in order to draw firm conclusions.

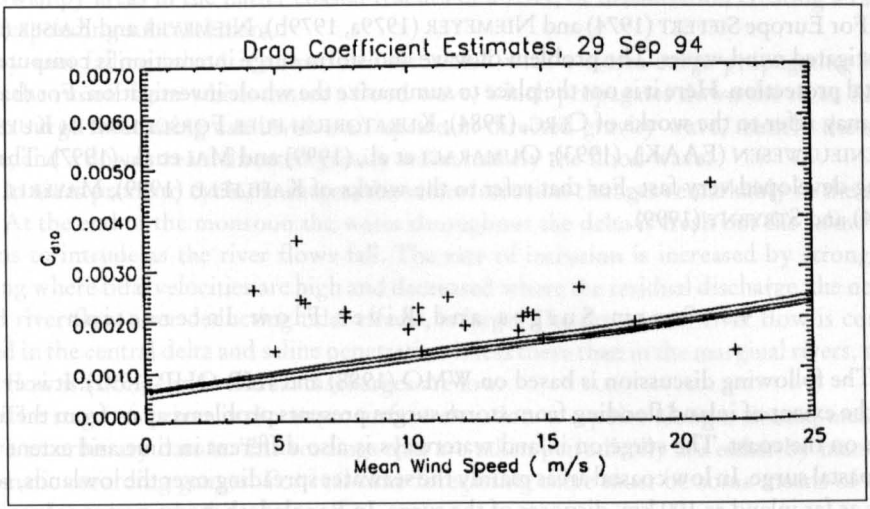


Fig. 4.33: Drag coefficient estimates against wind speed during the typhoon. (YAMASHITA and WATSON, 1997)

The next stage of this work, in addition to further analysis of the wind stress data, will be to incorporate wave effects into a surge model. The first step is to use an ocean wave model to predict the time-dependent wave field during the storm. This has been done for the cyclone, which struck Bangladesh in April 1991, causing a severe disaster in which 150,000 people died. The model is that of YAMAGUCHI et al. (1979) and is a second-generation model, whereas third generation models, which include a more accurate calculation of non-linear interactions, such as WAM, are now available. However, it is uncertain whether this would be any more applicable in the highly nonlinear situation in the extensive shallow region near Bangladesh, and so the more convenient second-generation model was used. Qualitative differences are not expected.

The calculation gives contours of significant wave height during the approach of the cyclone, with a maximum of 15 m being predicted near the cyclone centre. The next step will be to take the results for wave height and use them to modify the surface and bottom drag coefficients in the surge model, as outlined above. In this way the size of wave effects on the surge prediction will be accessed.

ZHANG and LI (1996) have implemented a coupled wave-surge model using JANSSEN's theory for the effect of waves on wind stress, including radiation stress terms, but not considering the effect of waves on bottom stress.

Table 4.12: Empirical Formulae for Wind Drag Coefficient as a function of Wind Speed. (From YAMASHITA and WATSON [1997])

| | | |
|---|---|---|
| YELLAND and TAYLOR (1996) | $C_{D10} = (0.60 + 0.070U_{10}) \times 10^{-3}$ | $U > 6\ ms^{-1}$ |
| SMITH et al. (1992) | $C_{D10} = (0.66 + 0.072U_{10}) \times 10^{-3}$ | (HEXOS data) |
| ANDERSON (1993) | $C_{D10} = (0.49 + 0.071U_{10}) \times 10^{-3}$ | |
| SMITH and BANKE (1975) | $C_{D10} = (0.63 + 0.066U_{10}) \times 10^{-3}$ | |

For Europe SIEFERT (1974) and NIEMEYER (1979a, 1979b), NIEMEYER and KAISER (1997) investigated wind waves. The problem of wave and storm surge interaction is computed for coastal protection. Here it is not the place to summarize the whole investigation. For that readers may refer to the works of CERC, (1984); KURATORIUM FUER FORSCHUNG IM KUESTENINGENIEURWESEN (EAAK), (1993); OUMARACI et al., (1999) and MAI et al., (1997). The modeling developed very fast. For that refer to the works of KAHLFELD (1999), MAYERLE et al. (1994) and STRYBNY (1999).

## 4.5 Storm Surges and River Flow Interaction

The following discussion is based on WMO (1988) and IHP-OHP (1991). It is evident that the extent of inland flooding from storm surges presents problems apart from the actual surge on the coast. The surge on inland waterways is also different in time and extent from the coastal surge. In low coastal areas mainly the seawater spreading over the lowlands, sometimes as far inland as 100 km, disposes of the surge. In Bangladesh storm surges are reported to reach as far as 160 km inland in recent times. The invasion of the surge water into the marshes creates and expands open bodies of water. The waves, generated by the wind over these bodies, help to transport greater amounts of water inland. The return of this water to the sea is a slow complicated process.

The seiches in inland lakes must be taken into consideration along with the surge to determine flooding possibilities.

As more industries and people continue to move into coastal areas subject to flooding, the determination of the extent of inland flooding becomes increasingly important for the protection of life and property. It is also becoming more difficult to determine the extent of the flooding. The continual construction or changing of levees, canals, navigable waterways, drainage, protective barriers, and other factors, contribute to the complexity of the inland inundation problem. Further complications arise by the changes, which occur in the maze of levees. Natural changes, erosion and subsidence take their toll; also pilfering of the fill or actual cutting of the levees weakens the systems.

An important distinction arises between the tropical and extra-tropical situations; although much more intense, the rainfall flooding arising from tropical cyclones are much more limited in extent than the low-pressure systems associated with extra-tropical surges. Thus, only small regions adjacent to landfall will affected, but this response will very probably coincide with the most severe portion of the surge. If coincidence occurs in the larger, longer lag-time basins affected by extra-tropical low-pressure systems, it is probable that the cause of the flood was due to an earlier event.

Thus the following sets of conditions can be listed as criteria for joint fluvial and surge flooding (WMO, 1988):

(a) In small islands subject to hurricanes, such as the Philippines, Japan and the West Indies, where river response times are short;
(b) Where antecedent conditions have predisposed a larger river to flood and this coincides with a sea surge. This can occur in both tropical and extratropical locations. As an example of the former, a stationary front often lies over Japan in September and early October; the saturated conditions and regular rainfall, often intensified by a typhoon, lead to regular coincidences of floods and surges;
(c) Where human activities have shortened the lag time. Examples are reclamation of the swampy areas in the flatter coastal reaches of a river, or urbanisation creating a rapidly responding subcatchment.

Heavy rain falling inland is sometimes associated with a storm surge propagating into a river, the runoff from which causes a flood wave, which propagates down the river. Hence, storm surge forecasting can involve an upstream-directed gravity wave, namely the storm surge, and a downstream directed gravity wave, namely the flood wave.

In areas prone to cyclonic surges, the saline intrusion changes remarkably in the estuaries. At the end of the monsoon the water throughout the delta is fresh but the saline front begins to intrude as the river flows fall. The rate of intrusion is increased by strong tidal mixing where tidal velocities are high and decreased where the residual discharge, the net seaward river flow after deducting tidal effects, is large. The dry season river flow is concentrated in the central delta and saline penetration is less there than in the marginal rivers, where tidal flow is strong- and residual discharges are low.

The stage of a river is the water surface elevation at a point along a stream, measured above an arbitrary datum. The readings that are taken periodically are either by manual or automatic recording gauges. For real-time forecasting there must be some means of transmitting the stage to the forecast centre.

If required, the stage is converted to a discharge by a stage discharge relationship (often termed the rating curve). A regular programme of current measurements of simultaneous flow and stage observations calibrates the relationship. Such a curve is approximately parabolic, or else linear, on double logarithmic paper. Detailed guidelines on observational practices are to be found in many textbooks and manuals including the WMO Guide to Hydrological Practices.

In a tidally affected river the uniqueness of the stage discharge relationship will be lost. However, it is often possible to construct an approximate relationship for a given downstream stage if a sufficient number of current measurements is available and the estuary level is also read simultaneously.

Efforts should also be made to derive a roughness coefficient for the river. This will be required for the models to be described in subsequent chapters. Again, techniques for this are to be found in hydrometric manuals such as the WMO Manual on Stream Gauging (WMO, 1988).

Tropical cyclones produce large amounts of rainfall. Extra-tropical surges also are associated with rain-producing weather systems. While rain does not have a direct influence on the surge magnitude in the sea, its influence on the river and its coincidence with the sea surge can create critical conditions.

Statistical information required for design work is obtained from climatological reports. Information should include depth-duration-frequency data, areal reduction factors and temporal patterns of past major events.

Rivers are small compared with the adjacent ocean region. The tidal energy of the river can therefore be regarded as originating in the estuary and arriving at the river mouth as a

specifiable boundary condition. The theory that has been applied has related mainly to idealised estuaries and has discussed the surge in terms of standing waves, progressive waves or possible resonance effects. As a general statement, frictional damping becomes the dominant influence in long narrow shallow water bodies. This is the factor most difficult to assess accurately hydrodynamic computer models as well as in empirical formulations.

If water levels fail to respond to upstream floods then the location is tidedominated. Conversely, river domination can be assumed for a location with no response to the flows.

### 4.5.1 Elbe Estuary (Germany) as case study

The following is based on IHP-OHP (1987, 1991) using SIEFERT (1978b, 1979, 1991) and SIEFERT and HAVNOE (1989).

The concept for understanding the dynamics of storm surges is very simple: Storm surge behaviour in a river is treated as a problem of combination of boundary values and eigenvalues. To solve these problems mathematically, a lot of differential equations have to be solved. Alternatively a hydraulic model (including all eigenvalues) with variation of the boundary values can be applied. This was done for the Elbe (for 200 long river-km) with special respect to Hamburg (Fig. 4.34) and consequently transferred to other rivers (Fig. 4.35).

It turned out that all other influences than astronomical result in a special, individual surge curve in the estuary. Thus we have to consider only two curves as seaward boundary values: the (more or less regular) tide curve and the (irregular) surge curve. These have to be combined with the eigenvalues of the tide-river dynamics. The latter can be considered constant during individual storm events. They are mainly changed by man (deepening and widening of fair-way, course corrections, new dyke lines, weirs, dams, sluices etc.) and are varying through the decades. The upper boundary value (discharge) can also be treated as constant during a surge.

The identification of the seaward boundary values is done by separation of the astronomical or (in first-order approximation for this area) of the mean tide and the surge (Fig. 4.36).

In a first step of approximation the surge curve was characterised by 5 parameters as shown in Fig. 4.37. After these treatments it was investigated how these curves behave when they proceed in a river, and especially, how they interact.

Correlations between storm tide elevations at different locations along a tidal river show no significant coherence. For interpretation of tidal dynamics it is necessary to take into account the complete curves.

IIARLEMAN and LEE give some methods for the solution of tidal propagation in estuaries. The harmonic solution of the linear function equation for the tidal elevation at any x and t

$$\eta = \frac{\eta_0 H}{2} \cdot e^{-\frac{\delta x}{2}} \cdot \left( e^{\mu x} \cos(\sigma t + kx) + e^{-\mu x} \cos(\sigma t + kx) \right) \qquad (4.29)$$

contains the amplitude attenuation coefficient $\mu$ or the damping parameter $\mu x$.

Using $\mu$ and the variation of the damping parameter $d\mu x / dx$ the simple equation for wave propagation in shallow water could be modified to

$$c = S \sqrt{g \cdot d^*} \qquad (4.30)$$

with g = acceleration of gravity $\quad$ $d^*$ = representative water depth in a river

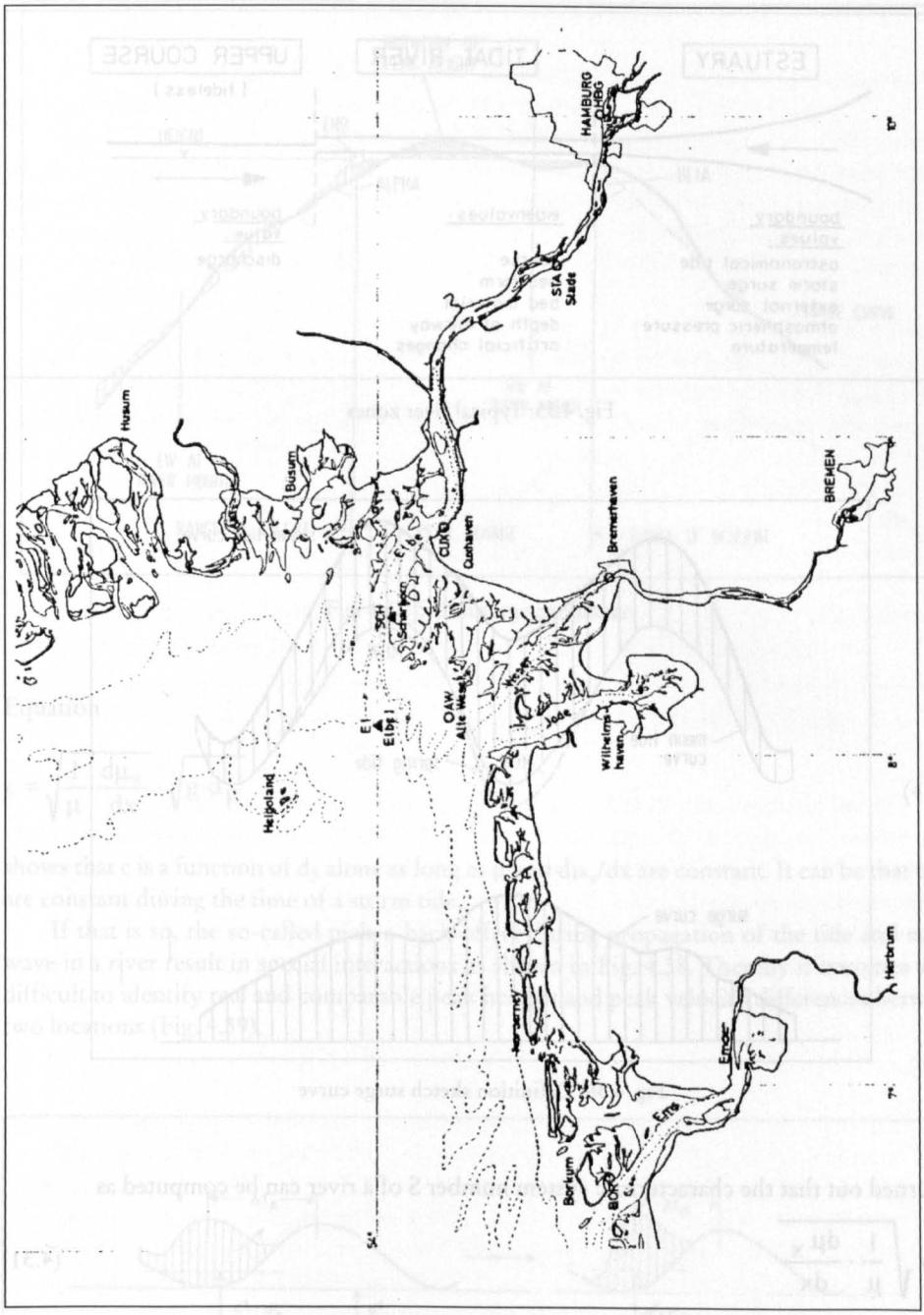


Fig. 4.34: German Bight with Elbe estuary

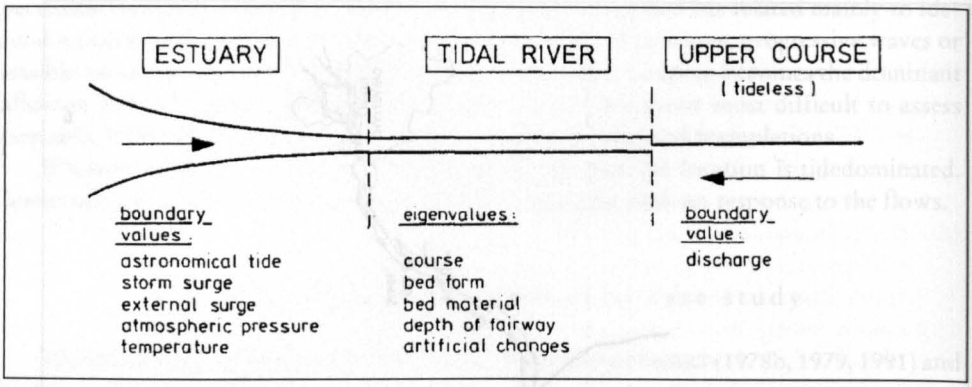


Fig. 4.35: Typical river zones

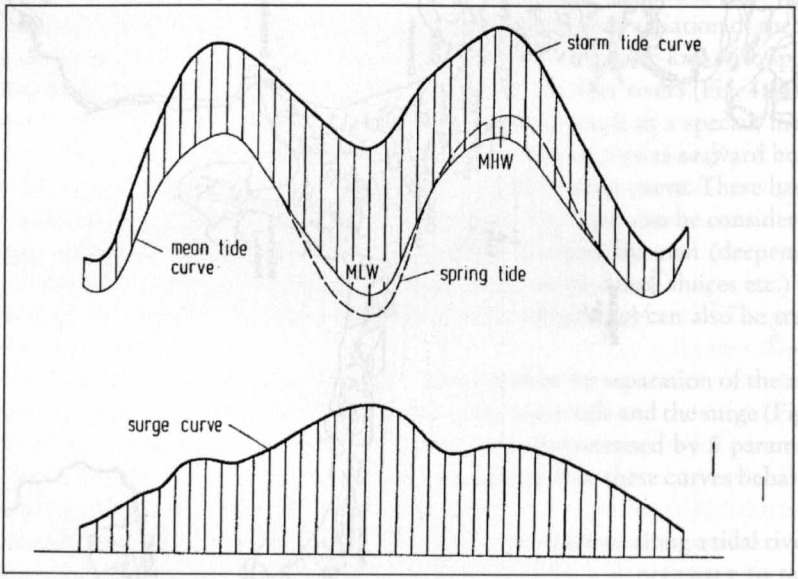


Fig. 4.36: Definition sketch surge curve

It turned out that the characteristic system number S of a river can be computed as

$$S = \sqrt{\frac{1}{\mu} \cdot \frac{d\mu_x}{dx}} \qquad (4.31)$$

The values vary from 0.56 for the Elbe to 1.11 for the Delaware. It changes with time, i. e. with secular changes in the river as was mentioned before.

Computations of a lot of tide and storm surges showed that the "representative water depth" d* in a river is characterised by the depth of the fair-ways $d_F$. This fact is best proved in rivers with a distinct fair-way of a certain length, as tide and storm surge dynamics are the more concentrated at the fair way the deeper it is, relative to the remaining cross-section.

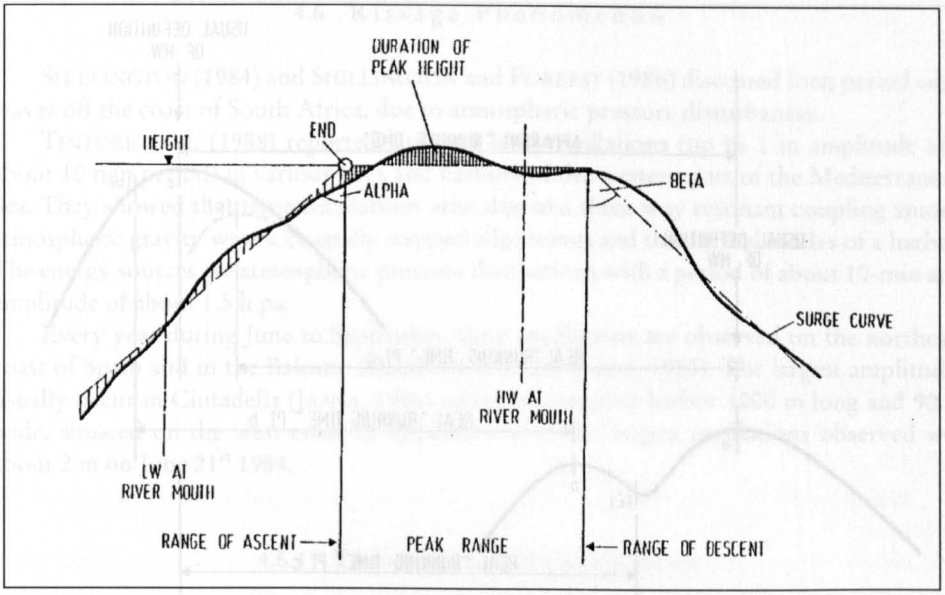


Fig. 4.37: Storm surge parameters

Equation

$$c = \sqrt{\frac{1}{\mu} \cdot \frac{d\mu_x}{dx}} \cdot \sqrt{g \cdot d_F} \qquad (4.32)$$

shows that c is a function of $d_F$ alone as long as $\mu$ and $d\mu_x/dx$ are constant. It can be that they are constant during the time of a storm tide.

If that is so, the so-called pick-a-back-effect during propagation of the tide and surge wave in a river result in special interactions as shown in Fig. 4.38. Thereby it becomes very difficult to identify real and comparable peak heights and peak velocity differences between two locations (Fig. 4.39).

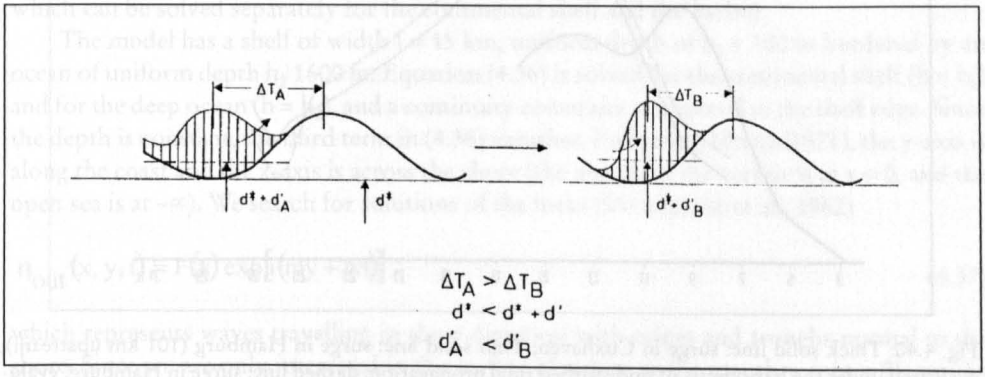


Fig. 4.38: So-called pick-a-back-effect

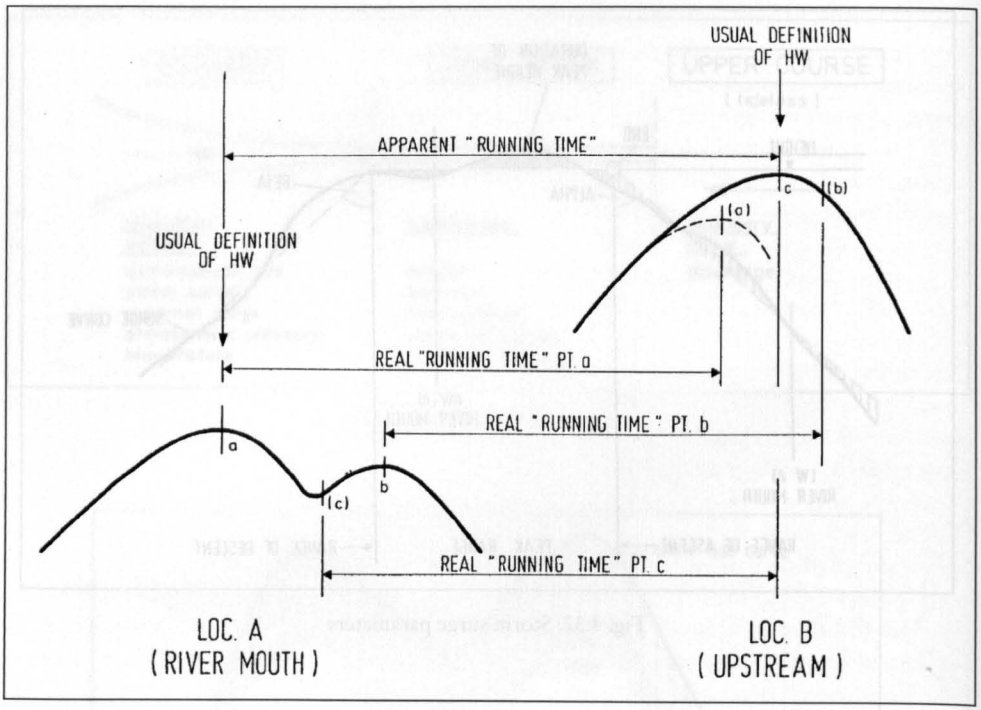


Fig. 4.39: Example of shape variation of the tide curve between two locations

The interactions result in differing propagation velocities not only of the surge, but also of the tide. The shape of the surge curves in Fig. 4.40 may illustrate this. Surges occurred on January 3, 1976, during the highest storm tide ever registered in the Elbe. The comparison of shapes indicates that tidal wave must run a lot faster than usual. As only small alterations of the surge curves are to be expected, best-fit shifts have to be found.

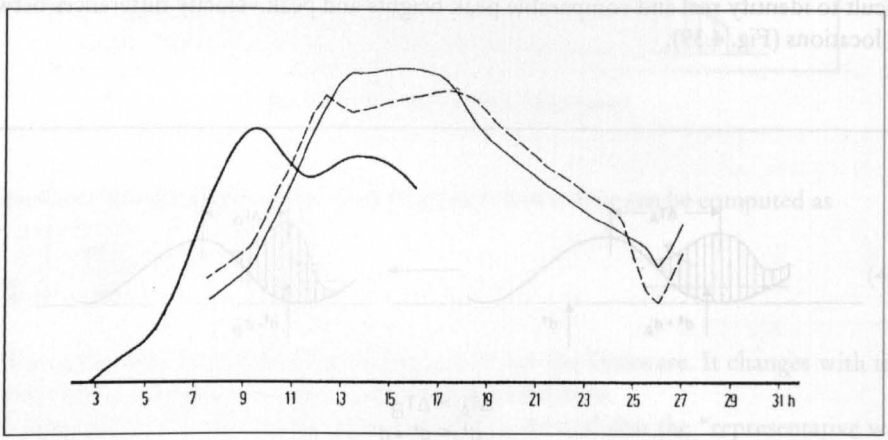


Fig. 4.40: Thick solid line: surge in Cuxhaven; Thin solid line: surge in Hamburg (101 km upstream), evaluated under the hypothesis of undisturbed tidal propagation; dashed line: surge in Hamburg, evaluated under the hypothesis that tidal propagation from C. to H. lasted 3 h instead of the usual 4 h

## 4.6 Rissaga Phenomenon

SHILLINGTON (1984) and SHILLINGTON and FOREEST (1986) discussed long period edge waves off the coast of South Africa, due to atmospheric pressure disturbances.

TINTORE et al. (1988) reported large sea level oscillations (up to 1 m amplitude and about 10 min period) in various bays and harbors of the western part of the Mediterranean Sea. They showed that these oscillations arise due to a three way resonant coupling among atmospheric gravity waves, coastally trapped edge waves and the normal modes of a harbor. The energy sources are atmospheric pressure fluctuations with a period of about 10-min and amplitude of about 1.5 h pa.

Every year during June to September, these oscillations are observed on the northeast coast of Spain and in the Balearic Islands (RAMIS and JANSA, 1983). The largest amplitudes usually occur in Ciutadella (JANSA, 1986) which is elongated harbor 1000 m long and 90 m wide, situated on the west coast of Minorca one of the largest oscillations observed was about 2 m on June 21st 1984.

### 4.6.1 Theoretical Explanation

For the theoretical development, we follow TINTORE et al. (1988) closely. The linearised shallow-water equations for a nonrotating inviscid fluid with variable depth h are

$$\partial u / \partial t + g \partial \eta / \partial x = 0 \tag{4.33}$$

$$\partial v / \partial t + g \partial \eta / \partial y = 0 \tag{4.34}$$

and the continuity equation is

$$\partial \eta / \partial t + \partial (hu) / \partial x + \partial (hv) / \partial y = 0 \tag{4.35}$$

where, u, v are the x, y velocities, $\eta$ is the surface elevation and g is the gravitational acceleration. Eliminating u and v from (4.33)–(4.35), we obtain the wave equation

$$\partial^2 \eta / \partial t^2 - gh(\partial^2 \eta / \partial x^2 + \partial^2 \eta / \partial y^2) - g \partial h / \partial x \partial \eta / \partial x = 0 \tag{4.36}$$

which can be solved separately for the continental shelf and the harbor.

The model has a shelf of width l = 15 km, uniform depth of $h_1$ = 100 m bordered by an ocean of uniform depth $h_2$ 1600 m. Equation (4.36) is solved for the continental shelf ($h = h_1$) and for the deep ocean ($h = h_2$), and a continuity constraint is imposed at the shelf edge. Since the depth is constant, the third term in (4.36) vanishes. Following MILES (1971), the y-axis is along the coast and the x-axis is across the shore (the mouth of the harbor is at x = 0, and the open sea is at $-\infty$). We search for solutions of the form (SNODGRASS et al., 1962)

$$\eta_{out}(x, y, t) = F(x) \exp[i(my + wt)] \tag{4.37}$$

which represents waves travelling in the y direction with ridges and troughs normal to the shore. Since we are only interested in the surface elevation at the mouth $\eta_{out}$ (x = 0), we can replace F (x = 0) by $A_{out.}$

Edge waves are trapped if the phase velocity c is in the range (BUCHWALD and DE SZOEKE, 1973).

$$(gh_1)^{1/2} \le c \le (gh_2)^{1/2} \tag{4.38}$$

For the edge waves trapped in the Balearic Shelf the phase speed must be between 30 $ms^{-1}$ and 125 $ms^{-1}$. Substitution of (4.37) into (4.36) gives the dispersion relation for trapped edge waves

$$(h_1/h_2)\tan\left[(w^2/gh_1 - m^2)^{1/2} l\right] = \left[\frac{(m^2 - w^2/gh_2)}{(w^2/gh_1 - m^2)}\right]^{1/2} \tag{4.39}$$

Equation (4.39) is solved numerically to obtain the wave number m in terms of the frequency w.

Next we consider the normal modes of the harbor. We solve (4.36) analytically for a rectangular harbor with a constant cross-channel depth and an exponential along-channel sloping bottom of the form

$$h(x) = h_0\{1 - \exp[\alpha(x - L)]\} \tag{4.40}$$

The x coordinate is taken along the channel (the mouth being at x = 0, and the head at x=L) and the y coordinate is across the channel (harbor sides at y = ±d). Values for the harbor of Ciutadella are:

Length = L = 1000 m.
Width = 2d = 90 m.
$\alpha = 4.549 \times 10^{-3}\ m^{-1}$
$h_0 = 5.75$ m.

The following boundary conditions are used: no flow at the side walls, v = 0

At y = ±d, and finite values for the surface elevation and the along-channel velocity at the closed end, η (x = L) and u (x = L). At the mouth, η (x = 0) and u (x = 0) remain undetermined since they must match with the outside solution. We look for solutions of the form (MILES, 1971) and the substitution into (4.36) yields a differential equation for each variable.

$$\eta_{in}(x, y, t) = X(x)Y(y)\exp(iwt) \tag{4.41}$$

The equation for Y (y) is easily solved; applying boundary conditions we obtain

$$Y(y) = C_n \cos[n\pi(y - d)/2d], \qquad n = 0, \pm1, \pm2, \ldots \tag{4.42}$$

The equation for X (x) is more complicated; after some algebra, it reduces to a special form of Gauss' hypergeometric equation (ABRAMOVITZ and STEGUN, 1965) with two linearly independent solutions expanded about the regular singular point at x = L; because of the boundary conditions one of these solutions must be rejected, and we obtain (LEMON, 1975)

$$X(x) = B\exp\left[\alpha\left(k^2-\sigma^2\right)^{1/2}(x-L)\right]{}_2F_1\{a,b;1;1-\exp[\alpha(x-L)]\} \tag{4.42a}$$

where,

$${}_2F_1(a,b;1;z) = \sum_{j=0}^{\infty}[\Gamma(a+j)\Gamma(b+j)/\Gamma(a)\Gamma(b)j!\,j!]z^j \tag{4.42b}$$

$$a = \frac{1}{2}\left[1+2\left(k^2-\sigma^2\right)^{1/2} \pm \left(1+4k^2\right)^{1/2}\right] \tag{4.42c}$$

$$b = \frac{1}{2}\left[1+2\left(k^2-\sigma^2\right)^{1/2} m\left(1+4k^2\right)^{1/2}\right] \tag{4.42d}$$

$$k = n\pi/2d\alpha \qquad \sigma^2 = w^2/gh_0\alpha^2 \tag{4.42e}$$

The full expression for the free surface elevation for the $n^{th}$ cross-channel mode is

$$\eta_{in}(x,y,t) = \mathrm{Re}\left\{A\exp\left[\alpha\left(k^2-\sigma^2\right)^{1/2}(x-L)\right]{}_2F_1[a,b;1;1-\exp(\alpha(x-L))]\right\} \cdot\cos[n\pi(y-d)/2d]\exp(iwt) \tag{4.43}$$

Note that for a given frequency, both surface elevation and velocity obtained from (4.43) using (4.33) at any position in the harbor are completely determined for each mode except for a constant $A_n$.

To determine the constant $A_n$ in (4.43), the interior solution has to match the outside coastally trapped wave at the mouth of the harbor. The boundary conditions are continuity of pressure and of mass flux across the mouth.

For a correct matching, the outside edge wave must be expressed in terms of the interior cross-channel modes given by (4.43) (to achieve the matching for the whole hierarchy of modes). However, since the wavelengths of the outside edge waves are much longer than the width of the mouth, we may neglect the excitation of higher cross-channel modes, leaving only the fundamental mode (n=0); the surface elevation will not depend on y. On the other hand, an oscillating free surface in an open basin will radiate energy out into the open ocean. Therefore a complete solution outside the harbor must include the radiated long waves as well as the coastally trapped waves. The matching conditions are

$$\eta_{in}(0) = \eta_{out}(0) + \eta_s(0) \tag{4.44a}$$

$$u_{in}(0) = u_{out}(0) + u_s(0) \tag{4.44b}$$

where, $\eta_s$ and $u_s$ are the free surface elevation and the offshore velocity for scattered waves.

To account for scattered waves, we followed the equivalent circuit analysis originated by MILES (1971) and modified by GARRETT (1975). In that scheme the sea level elevations at the mouth (m) are taken as voltages inducing a current between the harbor and the open sea. Equation (4.44a) becomes

$$\int_m K_m(y,y')F(y')dy' = \eta_{out}(y) - \int_m K_S(y,y')F(y')dy' \tag{4.45}$$

where, $K_{in}(y, y')$ and $K_s(y, y')$ are respectively the responses of the harbor and the open sea, produces by a point source of transport $\delta(y-y') = hu.n$ at the mouth. Equation (4.45) becomes an integral equation for the velocity distribution across the mouth. However, the exact solution is difficult to obtain. We use a normalized trail function

$$F(y) = I\,f(y) \qquad \int_m f(y)dy = 1 \tag{4.46}$$

Where I is the mass flux at the mouth.

Defining the voltages V as the mean surface elevation across the mouth weighted by the velocity distribution f (y), (4.45) becomes

$$Z_{in} I = V_{out} - Z_S I \tag{4.47}$$

where,

$$V_{out} = \int_m \eta_{out}\, f(y)dy \tag{4.48}$$

$$Z_{in} = \int_m K_{in}(y,y')f(y)f(y')dydy' \tag{4.49}$$

$$Z_s = \int_m K_s(y,y')f(y)f(y')dydy' \tag{4.50}$$

($Z_{in}$ and $Z_s$ are the impedances of the equivalent circuit). Resonance occurs for maximum fluxes across the mouth. These fluxes can be directly obtained from (4.47).

$$I = V_{out}/(Z_{in} + Z_S) \tag{4.51}$$

Therefore we need to know the voltage $V_{out}$ and the impedances $Z_{in}$ and $Z_s$.

1. $V_{out}$ is obtained just introducing (4.37) into (4.48). Using the velocity distribution estimated by RAYLEIGH (1945), f (y) = 1/2d.

$$V_{out} = A_{out}\,\sin(md)/m \tag{4.52}$$

where, m (which is a function of frequency) has to be substituted by its value obtained from eq.(4.39).

2. Since the inside solution is known and does not depend on *y*, (4.49) reduces to

$$Z_{in} = V_{in}/I = \eta_{in}(0)/\{2dh_m u_{in}(0)\} \tag{4.53}$$

where, $h_m$ is the water depth at the mouth.

We use (4.33) to obtain $u_{in}$ (L) from (4.43). There is always a phase difference of $\pi/2$ between surface elevation and velocity and therefore (4.53) becomes a pure imaginary number of the form g (w) exp. ($-i\pi/2$) (the sign of g [w] can be positive or negative).

$$Z_{in} = -iw\,\mathrm{Re}[X(0)]/\{2gdh_0(1-\exp[\alpha(x-L)]).\mathrm{Re}[X'(0)]\} \tag{4.54}$$

On a first approximation (without taking $Z_s$ into account), resonance occurs for $Z_{in} = 0$ ($\eta_{in}(0) = 0$). Physically, $Z_{in}$ accounts for the free surface oscillations of a harbor open to an ocean of infinite depth.

3. The problem of scattered waves is solved for an ocean of constant depth $h_{out}$. The solution is obtained by using Hankel functions as Green's function (MILES, 1971; BUCHWALD, 1971). Using velocity distribution the following expression for $Z_s$ is obtained

$$Z_S = (w/2gh_{out})\left\{1+(2i/\pi)\left[3/2-\Gamma-\ln(wd/(gh_{out})^{1/2})\right]\right\} \tag{4.55}$$

where, $\Gamma = 0.5772\ldots$ is the Euler's constant, and $h_{out} = 100$ m is the depth of the open shelf.

In an equivalent circuit, the real part of $Z_s$, would be the resistance linearly depending on w. Physically the main effect of $Z_s$, is to prevent the flux from becoming infinite ($Z_s$ accounts for the energy radiated from the harbor out into the open sea).

However, $Z_s$, also produces a shift of the resonant frequencies from the frequencies of the harbor free oscillations.

A physical interpretation of (4.51) may be deduced from the above observation on impedances, taking into account that (4.51) is also a time dependent relationship. When $Z_{in} = -\mathrm{Im}(Z_s)$, $V_{out}$ and I have the same time dependency; therefore there is phase difference of $\pi/2$ between $\eta_{in}$ and $\eta_{out}$. On the other hand, when $|Z_{in}| >> |Z_s|$, $V_{out}$ and I have a phase difference of $\pi/2$; therefore $\eta_{in}$ at the head and $\eta_{out}$ are in phase if g (w) > 0 and are out of phase if g (w) < 0.

Since we are interested in oscillations with periods of about 10 min, we computed the mass flux through the mouth of the harbor for frequencies lower than $4 \times 10^{-2}$ rad $s^{-1}$ (T = 2.6 min). Due to the narrowness of the mouth, sin (md)/md •1, evaluation of $Z_{in}$ and $Z_s$ shows that $Z_{in}$ has much higher amplitude than $Z_s$ for most frequencies and it also varies much faster. Consequently,

1. Resonance occurs when $Z_{in} = -\mathrm{Im}(Z_s)$. The location of the resonant peaks depends mainly on the geometry of the harbor and is almost independent of the shelf geometry.
2. The height of the peaks $I_{max}$ depends only on the real part of $Z_s$, and since this is proportional to w, then $I_{max} \alpha w^{-1}$. Resonant peaks appear at $w = 1.123 \times 10^{-2}$ rad $s^{-1}$ (T = 9.33 min) and at $w = 3.060 \times 10^{-2}$ rad $s^{-1}$ (T = 3.43 min). Coastally trapped waves with these frequencies have wavelengths of 18 km and 5 km, respectively. Their corresponding phase velocities are 33 $ms^{-1}$ and 31 $ms^{-1}$.

Given the flux at the mouth (I), and dividing it by the cross sectional area, $u_{in}$ (L) can also be obtained from (4.33) and (4.43). Therefore the constant $A_0$ in (4.43) is determined. For the first frequency peak $A_0 = 300A_{out}$ the surface elevation at the head is 300 times the amplitude of the edge wave. At the mouth of the surface elevation is 3 times the amplitude of the edge wave (the two are not equal at the mouth because of the presence of scattered waves). For example, with an outside wave of amplitude 1cm, we obtain surface elevations of 3 m at the head and a current of about 3 $ms^{-1}$ at the mouth. It is also interesting to note that because of the

phase difference of $\pi/2$, the maximum surface elevation inside the harbor occurs at the zero elevation of the edge wave.

### 4.6.2 The Work of Monserrat and Colleagues

MONSERRAT and THORPE (1992) summarized the vertical structure of the atmosphere and the synoptic situation during the Rissaga phenomena as follows:

i) Two distinct air masses in the mid and lower troposphere, one cold and humid below and the other warm and dry above, separated by a shallow and usually strong temperature inversion near the surface.
ii) Very weak winds normally from the east or southeast below the inversion veering toward southwest above it.
iii) Strong wind shear at middle levels with a layer of small Richardson number near 500 Mb.

They point out that above meteorological factors while providing a general synoptic situation, cannot fully describe the necessary conditions for gravity wave generation, since the above are not the most dynamically significant factors.

These authors examined the vertical structure of the atmosphere to determine the potential for wave generation by shearing instability and see whether it fulfills the requirements postulated by LINDZEN and TUNG (1976) for the existence of a wave duet to account for maintaining wave coherence.

MONSERRAT and THORPE (1992) considered various source mechanisms and concluded that the vertical profiles of wind and temperature suggest that wind shear is the most likely mechanism. They go onto say that these gravity waves could be trapped modes in a duct and this could be the reason why in certain cases, the waves maintain their coherence for long distances involving at least one full wave-length. RABINOVICH and MONSERRAT (1996, 1998) expanded this study further and included the Kuril Islands also. Fig. 4.41 shows some typical Rissaga type water level oscillations in Japan and China. Figs. 4.42 and 4.43 respectively show the locations of the instruments used in this study for Balearic and Kuril Islands. Fig. 4.44 shows types A, B, C oscillations.

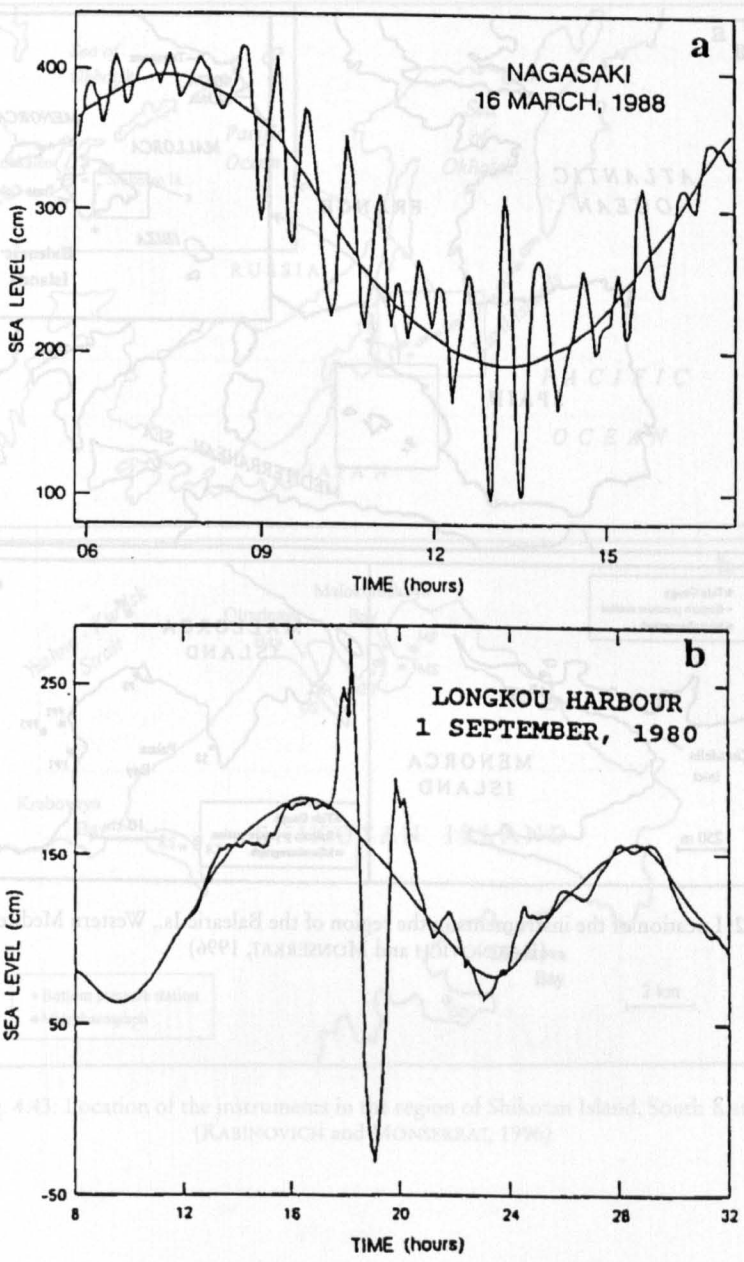


Fig. 4.41: Strong seiche oscillations recorded in Nagasaki Bay, Japan (courtesy of Japan Meteorological Agency) (a) and in Longkou Harbour, China. (WANG et al., 1987) (b)

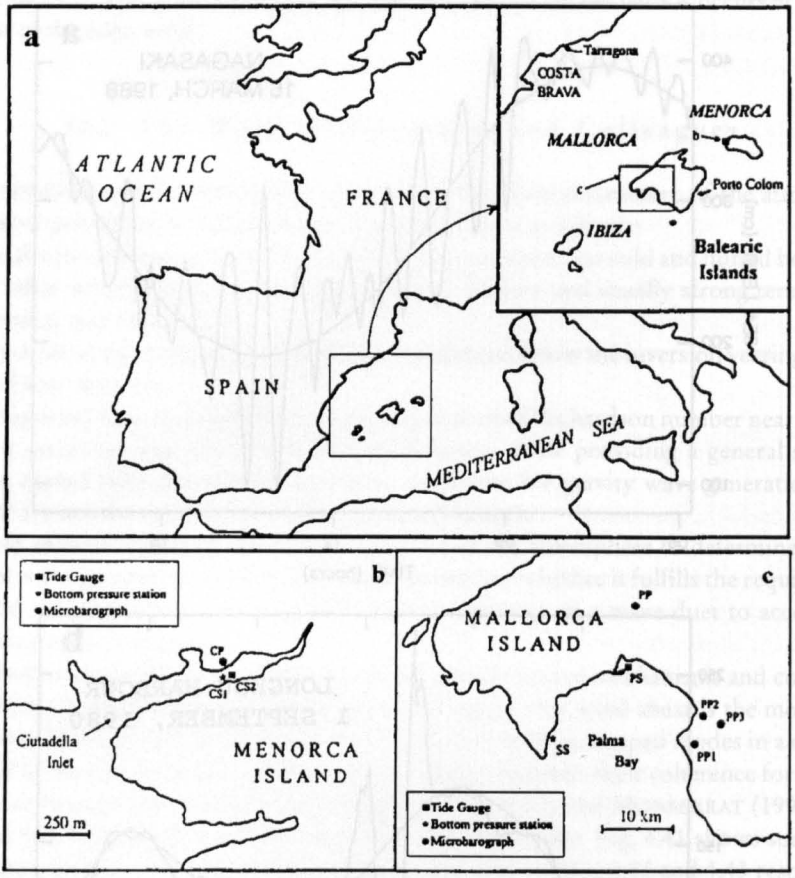


Fig. 4.42: Location of the instruments in the region of the Balearic Is., Western Mediterranean. (RABINOVICH and MONSERRAT, 1996)

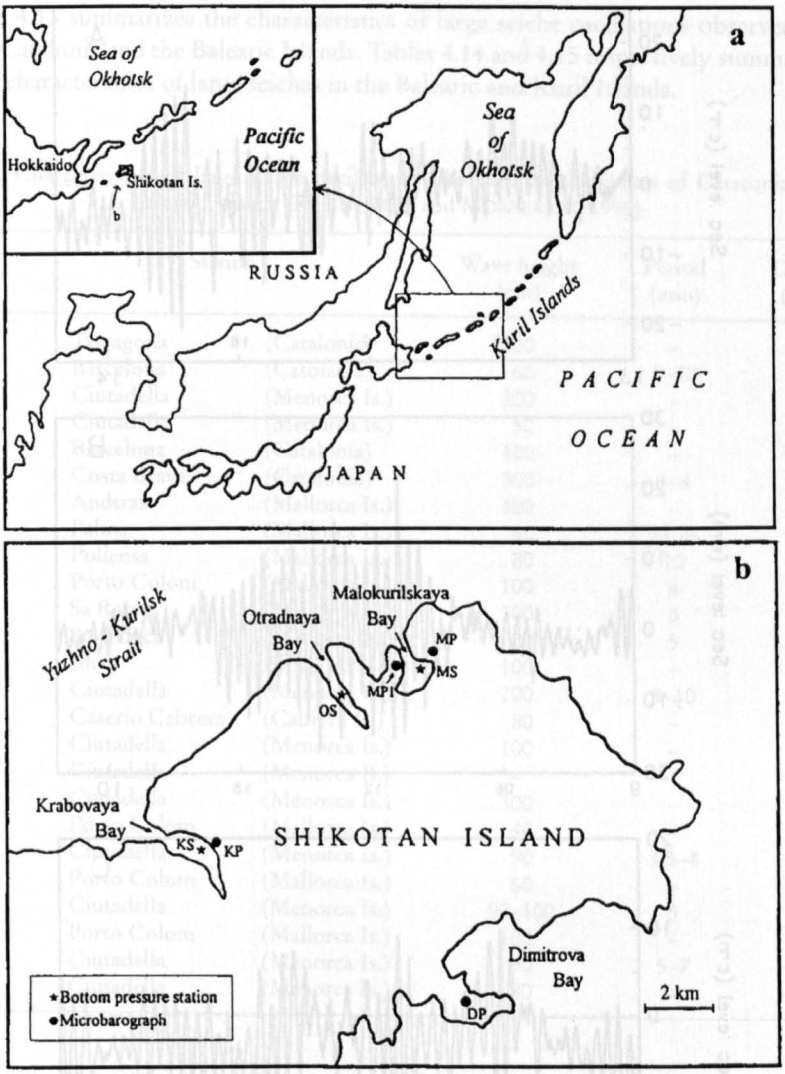


Fig. 4.43: Location of the instruments in the region of Shikotan Island, South Kurils. (RABINOVICH and MONSERRAT, 1996)

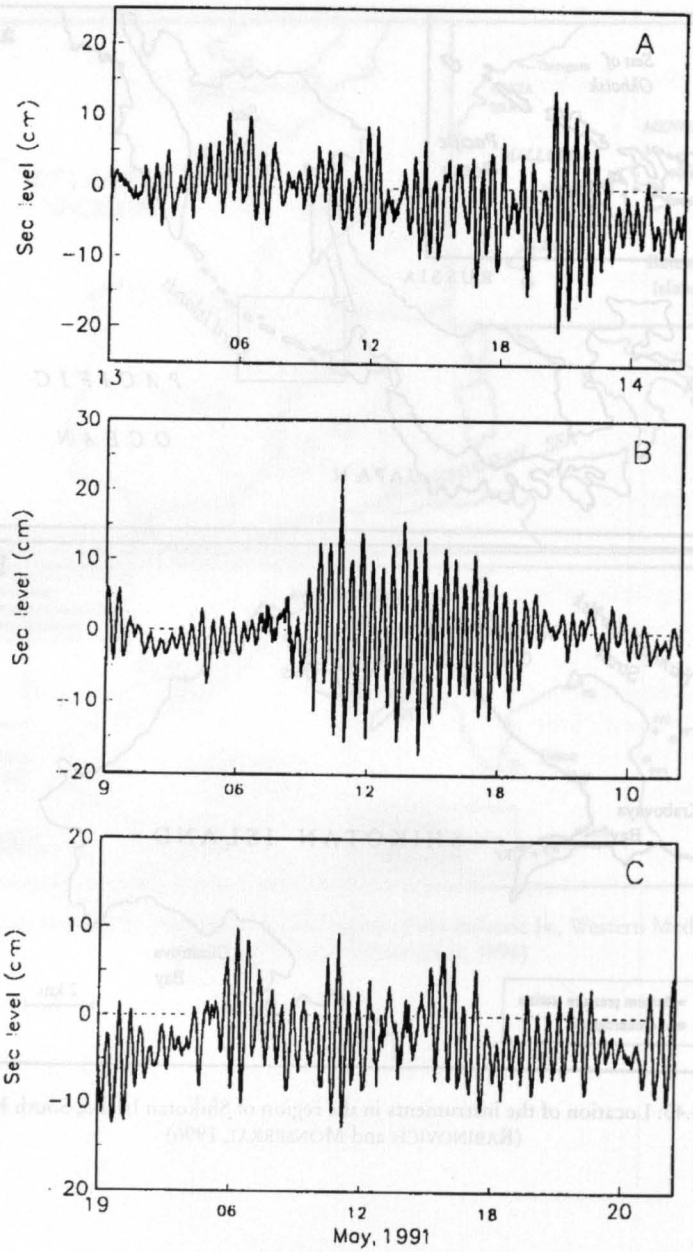


Fig. 4.44: Three recording sections of significant seiches observed in Krabovaya Bay (KS) in May 1991 which may be considered as examples of different types (A, B, and C) of 'seiche events'. (RABINOVICH and MONSERRAT, 1996)

Table 4.13 summarizes the characteristics of large seiche oscillations observed on the coasts of Catalonia and the Balearic Islands. Tables 4.14 and 4.15 respectively summarize the statistical characteristics of large seiches in the Balearic and Kuril Islands.

Table 4.13: Characteristics of large seiche oscillations observed on the coasts of Catatonia and the Balearic Islands (RABINOVICH and MONSERRAT, 1996)

| Date | Station | | Wave height (cm) | Period (min) | Duration (hours) |
|---|---|---|---|---|---|
| 11-Jul-72 | Tarragona | (Catalonia) | 300 | – | – |
| 16-Sep-75 | Barcelona | (Catolania) | 60 | 8–10 | 12 |
| 16-Sep-75 | Ciutadella | (Menorca Is.) | 200 | – | 48 |
| 14-Jul-77 | Ciutadella | (Menorca Is.) | 50 | – | – |
| 2-Jul-81 | Barcelona | (Catalonia) | 100 | – | – |
| 2-Jul-81 | Costa Brava | (Catalonia) | 300 | 3–4 | – |
| 2-Jul-81 | Andtrax | (Mallorca Is.) | 100 | – | – |
| 2-Jul-81 | Palma | (Mallorca Is.) | 40 | 14,28 | – |
| 2-Jul-81 | Pollensa | (Mallorca Is.) | 80 | 10 | – |
| 2-Jul-81 | Porto Colom | (Mallorca Is.) | 100 | 6 | – |
| 2-Jul-81 | Sa Rapita | (Mallorca Is.) | 100 | 5 | – |
| 2-Jul-81 | Sta Ponca | (Mallorca Is.) | 200 | 5 | – |
| 2-Jul-81 | Ibiza | (Ibiza Is.) | 100 | – | – |
| 2-Jul-81 | Ciutadella | (Menorca Is.) | 200 | 8–10 | 15 |
| 2-Jul-81 | Caserio Cabrera | (Cabrera Is.) | 80 | – | – |
| 18-Jul-81 | Ciutadella | (Menorca Is.) | 100 | – | – |
| 29-Jul-82 | Ciutadella | (Menorca Is.) | – | – | 48 |
| 21-Jun-84 | Ciutadella | (Menorca Is.) | 300 | – | – |
| 14-Jun-85 | Porto Colom | (Mallorca Is.) | 40 | – | – |
| 14-Jun-85 | Ciutadella | (Menorca Is.) | 90 | 3.5–4 | 7 |
| 19-Jun-85 | Porto Colom | (Mallorca Is.) | 60 | – | – |
| 19-Jun-85 | Ciutadella | (Menorca Is.) | 90–100 | 5 | 10 |
| 3-Jul-85 | Porto Colom | (Mallorca Is.) | 100 | – | 2 |
| 3-Jul-85 | Ciutadella | (Menorca Is.) | 90 | 5–7 | 8 |
| 31-Jul-85 | Ciutadella | (Menorca Is.) | 80 | – | 4 |

Table 4.14: Statistical characteristics of large seiche oscillations recorded in the Balearic Islands in 1989–90 (RABINOVICH and MONSERRAT, 1996)

| Event | | | | | Stations | | | | | | | | |
|---|---|---|---|---|---|---|---|---|---|---|---|---|---|
| | | | | | Ciutadella | | | Palma | | | Sol de Mallorca | | |
| No. | Beginning Time | | Duration (hours) | Type | Max height (cm) | Mean height (cm) | Mean Period (min) | Max height (cm) | Mean height (cm) | Mean Period (min) | Max height (cm) | Mean height (cm) | Mean Period (min) |
| | 1989 | | | | | | | | | | | | |
| 1 | 04/07 | 21:20 | 63.4 | C/A | 196.7 | 39.1 | 10.7 | 32.3 | 14.3 | 27.5 | – | – | – |
| 2 | 05/08 | 3:35 | 19.2 | B | 126.8 | 34.2 | 10.5 | 23.9 | 9.3 | 25.8 | 10.3 | 3.7 | 10.9 |
| 3 | 10/08 | 20:38 | 10.2 | A | 103.8 | 44.4 | 11.7 | 23.5 | 10.8 | 25.9 | 15.1 | 5.9 | 15.7 |
| 4 | 31/08 | 10:58 | 0.9 | C | 44.3 | 38.5 | 10.8 | – | – | – | – | – | – |
| 5 | 04/09 | 18:09 | 4.6 | C | 64.4 | 26.2 | 11.1 | – | – | – | – | – | – |
| 6 | 05/09 | 5:27 | 30.0 | C | 72.8 | 23.7 | 10.8 | – | – | – | – | – | – |
| 7 | 07/09 | 16:40 | 21.5 | C | 51.5 | 18.6 | 10.3 | – | – | – | – | – | – |
| 8 | 10/09 | 10:42 | 7.7 | B | 95.8 | 42.4 | 11.5 | – | – | – | – | – | – |
| | 1990 | | | | | | | | | | | | |
| 1 | 24/09 | 12:31 | 4.8 | B | 66.4 | 28.5 | 9.6 | – | – | – | – | – | – |
| 2 | 25/09 | 12:45 | 11.5 | C | 92.8 | 36.6 | 10.9 | – | – | – | – | – | – |

Table 4.15: Statistical characteristics of large seiche oscillations recorded in the region of Shikotan Island in May 1991 (RABINOVICH and MONSERRAT, 1996)

| Event | | | | | Stations | | | | | | | | |
|---|---|---|---|---|---|---|---|---|---|---|---|---|---|
| | | | | | Krabovaya | | | Otradnaya | | | Malokurilskaya | | |
| No. | Beginning Time | | Duration (hours) | Type | Max height (cm) | Mean height (cm) | Mean Period (min) | Max height (cm) | Mean height (cm) | Mean Period (min) | Max height (cm) | Mean height (cm) | Mean Period (min) |
| 1 | 09/05 | 7:14 | 9.6 | B | 37.4 | 21.8 | 28.6 | 15.2 | 5.9 | 15.4 | 23.8 | 9.3 | 18.3 |
| 2 | 13/05 | 12:00 | 12.0 | A | 34.0 | 13.8 | 26.7 | 15.3 | 5.7 | 15.8 | 21.7 | 10.8 | 18.1 |
| 3 | 19/05 | 6:00 | >24.0 | C | 21.9 | 8.5 | 26.1 | 12.9 | 3.8 | 15.1 | – | – | – |

A key question related to the problem of generation of the *rissaga* phenomenon is the following:

– Why are such strong sea-level oscillations generated in just some specific places?

The stable recurrence of such disastrous events in the same places proves that they are certainly strongly related to the topography and geometry of the correspondingly bays, inlets, or harbors. Ciutadella inlet, Menorca Island (as well as Nagasaki Bay, Japan and some other basins) is just one of such remarkable places. Simultaneous sea-level measurements in Ciutadella inlet and Palma Bay, presented above, demonstrated that during the same events, seiches in Ciutadella are about 6 times larger. What is the reason?

MILES and MUNK (1961) demonstrated that the relative intensity of seiche oscillations in harbours and bays is determined first of all by the Q-factor of the corresponding basin. Reducing the harbour entrance by wave-protection constructions increases the Q-factor and therefore the harbour oscillations. From this point of view it is quite understandable why the narrow inlet of Ciutadella has much stronger seiches than the open-mouthed inlets and harbours in the Balearic Islands with seiches much weaker than in Ciutadella.

GOMIS et al. (1993) tried to explain this fact by the influence of the inlet geometry. They estimated the amplification factor (1) for three inlets in this region (Ciutadella, Mahon and Porto Colom) and showed that in Ciutadella it is much larger than in the other two inlets. But in the region of the Japanese Islands there are several other bays and inlets with this factor no lesser (or even greater) than in Nagasaki Bay although abnormal seiches are known only in the latter basin.

RABINOVICH (1993) proposed that the extreme seiche oscillations observed in some places are forced by some kind of double resonance effect, e.g., by the coincidence of resonant frequencies of the shelf and inner basin, or eigenfrequencies of the harbour and outer bay. The relatively small probability of such coincidences is the main reason of the rareness of basins where large-amplitude seiches are reported.

# 5. Meteorological Aspects

Storm surges occur because of meteorological problems associated with extratropical and tropical cyclones. This chapter will discuss the dynamics of extratropical cyclones and tropical cyclones and the meteorological problems associated with these cyclones in the Pacific, Atlantic, and Indian oceans, as well as in other smaller water bodies. The problems associated with obtaining wind stress data for synoptic scale and mesoscale weather systems will be examined in detail.

## 5.1 Extratropical Cyclones

### 5.1.1 Development Theory

The treatment in this section follows closely PETTERSSEN (1956) and WARNECKE (1997). FITZ-ROY (1863) appears to be among the first to propose a model of an extratropical cyclone as originating on the boundary between two different air masses (e.g. a warm and moist air mass originating in subtropical latitudes and a colder and drier air mass originating in the polar regions). Some later authors who recognized that discontinuities in temperature, moisture content, and speed of motion were essential for cyclone development were BLASIUS (1875), HELMHOLTZ (1888, 1889), MARGULES (1905) and SHAW (1921).

BJERKNES (1919) proposed the first dynamical model for cyclones and agreed with MARGULES (1905) that the kinetic energy of the cyclones comes from the potential energy due to the juxtaposition of warm and cold air masses and a decrease of the potential energy that follows the development of a cyclone. According to Bjerknes the cold air forms a wedge under the warm air, with a slope of separation of about 1 : 100, and the cyclonic disturbances travel along the frontal surface similar to waves traveling along a discontinuity.

The life cycle of a cyclone has several stages. In the initial stage, a small amplitude wave forms on a more or less straight quasi-stationary front. The currents on either side of the front could be in the same direction or in opposite directions. In the second stage, the warm air rises to higher levels over the warm front and the cold front wedges in under the warm air. In the third stage, the warm air sectors become progressively narrower and the cold front tends to overtake the warm front. At this stage the cyclone has reached the occlusion stage (Fig. 5.1).

It is customary to refer to cyclone families (Fig. 5.2), rather than individual cyclones (FITZ-ROY, 1863). Usually there would be two to four or five cyclones in a series, one following the other and all moving in a general southwest to northeast direction. BJERKNES and SOLBERG (1921, 1922) accounted for cyclone families as wave disturbances on the polar front. In a family of four cyclones, typically the first one would be old and occluded, the second would be somewhat younger, the third would be a young wave cyclone, and the fourth would be a nascent cyclone wave. On the average, a cyclone family takes 5–6 d to pass a given location. The occurrence of cyclone families is a regular phenomenon over the North Atlantic and Western Europe (because of regular major polar outbreaks from the Greenland-Labrador area) and not as regular over North America and Central Eurasia.

Usually, cyclone formation begins near sea level and develops to higher levels in the atmosphere as the occlusion develops. Once a complete occlusion occurs, generally a closed cyclonic circulation can be found in the middle and upper troposphere (located over the cold rear of the occluded sea level cyclone). Sometimes, the depression in the pressure field aloft

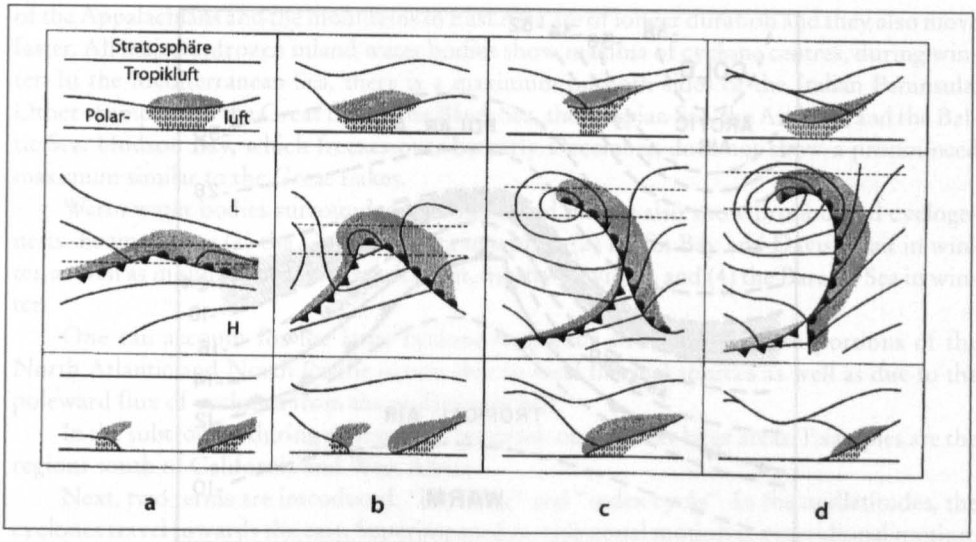


Fig. 5.1: Stages of cyclogenesis (WARNECKE, 1997)

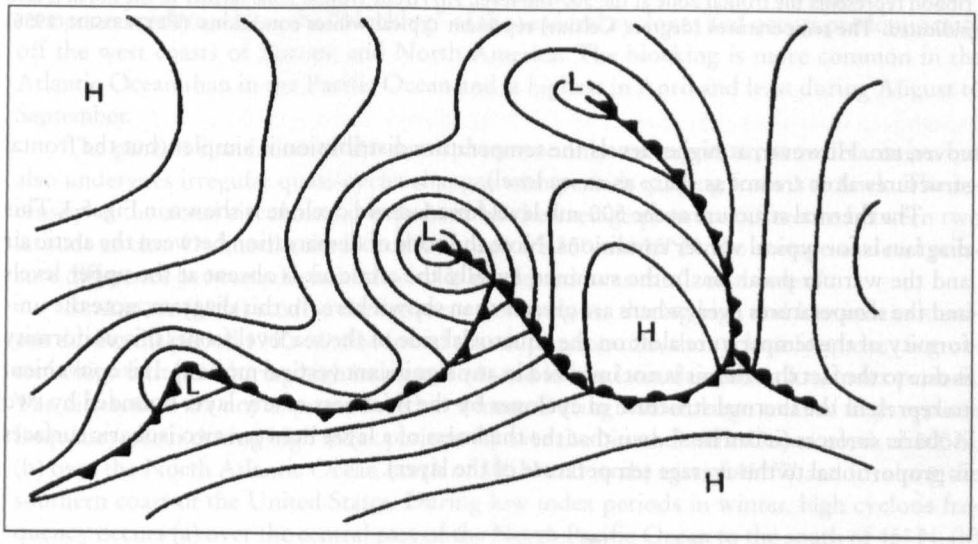


Fig. 5.2: Cyclone families (WARNECKE, 1997)

may merge with the semipermanent low over the polar region. When this happens, a high-level trough can be noticed in the rear of the occluded sea level cyclone. Thus, these upper level troughs represent the vertical extension of the cyclones. However, sometimes (particularly during winter), cyclone development may begin at the higher levels and at other times simultaneously with the lower level development. One refers to these more or less independent developments aloft (middle and upper troposphere) as "cutoff" cyclones.

Next, the thermal structure of cyclones will be briefly examined. At sea level there is no definite thermal pattern and irregularities occur because of the diurnal variations, cloud

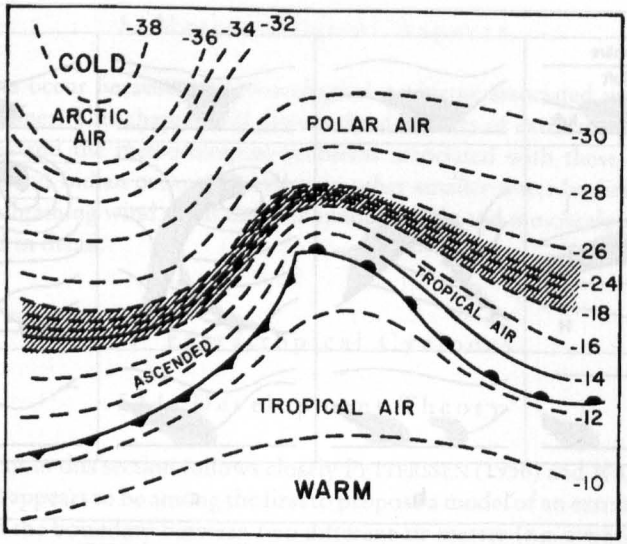


Fig. 5.3: Schematic representation of the isotherms at the 500-mb level associated with a wave cyclone. The front at sea level is represented by conventional symbols (warm front; cold front) and a hatched ribbon represents the frontal zone at the 500-mb level. An Arctic frontal zone farther to the north is also indicated. The temperatures (degrees Celsius) represent typical winter conditions. (PETTERSSEN, 1956)

cover, etc. However, at higher levels the temperature distribution is simpler (but the frontal structures aloft are not as sharp as at sea level).

The thermal structure at the 500-mb level for a 1-d-old cyclone is shown in Fig. 5.3. This diagram is for typical winter conditions. Note the zone of demarcation between the arctic air and the warmer polar air. In the summer, usually the arctic air is absent at the upper levels and the temperatures everywhere are greater than shown here. In this diagram, note the uniformity of the temperature aloft on the equatorial side of the sea level front (this uniformity is due to the fact that the air is not involved in any significant vertical motion). It is convenient to represent the thermal structure of cyclones by the thickness of any layer bounded by two isobaric surfaces (it can be shown that the thickness of a layer between two isobaric surfaces is proportional to the average temperature of the layer).

*Cyclone Patterns*

The patterns of cyclogenesis during winter will be examined first. In the North Pacific Ocean a zonal pattern exists around 30–35°N. Also, over the continents, large maxima of cyclogenesis occur in the lee of great mountain chains. These patterns are not sensitive to seasonal variations. Three pronounced maxima are associated with the Rockies: Sierra Nevada, Colorado, and Alberta regions. Similar maxima can be located to the east of the Appalachian mountains, the Scandinavian mountains, and also in East Asia.

If the frequency of cyclone centres is examined, the influence of mountain ranges can be seen even more. Examples are the leeward side of the Colorado and Alberta ranges. The cyclones that develop here are mostly of short duration, whereas those that develop in the lee

of the Appalachians and the mountains in East Asia are of longer duration and they also move faster. All major unfrozen inland water bodies show maxima of cyclone centres, during winter. In the Mediterranean Sea, there is a maximum on both sides of the Italian Peninsula. Other examples are the Great Lakes, the Black Sea, the Caspian Sea, the Aral Sea, and the Baltic Sea. Hudson Bay, which freezes over by early December, does not show a pronounced maximum similar to the Great Lakes.

Warm water bodies surrounded by colder land masses also show pronounced cyclogenesis. Examples are (1) the Gulf of Alaska in winter, (2) Baffin Bay and Davis Strait in winter, as well as in summer, (3) Denmark Strait, mostly in winter, and (4) the Barents Sea in winter.

One can account for the large cyclone frequency over the northern portions of the North Atlantic and North Pacific oceans due to local thermal sources as well as due to the poleward flux of cyclones from the midlatitude belt.

In the subtropics, during summer, cyclogenesis occurs over large areas. Examples are the regions south of California and West Africa.

Next, two terms are introduced: "blocking" and "index cycle". In the midlatitudes, the cyclones travel towards the east. Superimposed on this zonal motion is a meridional motion. The thermal wind in the middle troposphere to some extent guides the movement of the cyclones. Sometimes, when a warm cutoff high forms in the middle and upper troposphere, cyclones at sea level are steered either to the south or to the north of these highs. This phenomenon is referred to as the "blocking" of the sea level cyclones and occurs predominantly off the west coasts of Europe and North America. The blocking is more common in the Atlantic Ocean than in the Pacific Ocean and is highest in April and least during August to September.

The general circulation of the atmosphere not only undergoes an annual variation but also undergoes irregular quasi-cyclic changes with periods ranging from 3 to 8 wk. The intensity of the zonal circulation is expressed by the average pressure difference between two latitude circles. Ordinarily, the latitudes chosen are 35° and 55° N, the average sea level pressure difference between the latitude circles is referred to as the "zonal index".

BRADBURY (1954) studied the frequency of cyclones during high and low index situations during the period 1900–39. She found that during summer, the cyclone frequency is greater in high latitudes during high index periods and in low latitudes during low index periods. The differences are not as pronounced in winter. During winter, large areas of high cyclone frequency occur during high index periods (a) over the North Pacific Ocean north of 50° N, (b) over the North Atlantic Ocean north of 50° N and to the east of 45° W and (c) along the southern coast of the United States. During low index periods in winter, high cyclone frequency occurs (a) over the central part of the North Pacific Ocean to the south of 45° N, (b) over the western part of the North Atlantic Ocean and (c) over the Mediterranean Sea.

*Instability Theories*

MARGULES (1905) speculated that the potential energy associated with horizontal temperature gradients provides the kinetic energy of cyclones. SOLBERG (1936) showed that frontal cyclones would grow as a result of the inherent instability of the polar front (similar to the growth of a wave at a discontinuity). CHARNEY (1947), EADY (1949), BERSON (1949), and FJORTOFT (1950) have shown that the baroclinicity of the zonal current may lead to instability in which the kinetic energy of the growing perturbations is derived from the potential

and internal energies due to horizontal thermal gradients. KUO (1949) and FJORTOFT (1950) showed that certain categories of horizontal velocity patterns across a zonal current would lead to instability.

It has generally been observed that cyclones develop within a period of 1–3 d. In this short time scale, it is customary to assume that the motion is adiabatic and frictionless. Another assumption is that even during growth, the energy of an unstable zonal current is conserved. Let *K*, *P*, and *E* denote the kinetic, potential, and internal energies, respectively. Hence, according to the above assumptions:

$$K + P + E = \text{constant}$$

The kinetic energy per unit mass can be expressed as

$$\frac{1}{2}V^2 = \frac{1}{2}\overline{V}^2 + \overline{V}.V' + \frac{1}{2}V'^2 \tag{5.1}$$

where, V is the averaged velocity of the undisturbed current and V' is a deviation from this value. The kinetic energy K can be determined by integration over the total mass. During this integration, the second term on the right side of the above equation disappears. Hence

$$K = K_m + K_d \tag{5.2}$$

where, $K_m$ and $K_d$ are the integrated forms of the first and third terms, respectively, and these are referred to as the kinetic energy of the mean current and the kinetic energy of the perturbation. Equation (5.2) may be rewritten as

$$K_m + K_d + P + E = \text{constant} \tag{5.3}$$

Since $K_d$ represents the average intensity of all the disturbances, for the growth of these, $K_d$ must increase with time. This means that $K_d$ can increase only at the expense of one of the three sources $K_m$, P, or E or from combinations of these.

Next, the potential energy of a column of air of unit cross-section is given by

$$P = \int_0^\infty gz\rho \, dz$$

Using the hydrostatic equation $dp = g\rho \, dz$ and integrating by parts:

$$p = \int_0^{\rho_0} z \, d\rho = [zp]_{p=p_0} - [zp]_{p=0} - \int_0^{\rho_0} p \frac{\partial z}{\partial p} dp$$

where, $p_0$ is the pressure at the bottom of the air column. In this equation, on the right side the first term becomes zero at $z = 0$ (bottom of the air column) and the second term vanishes because $pz \to 0$ as $p \to 0$. The third term becomes, after noting $\alpha = 1/\rho$ where $\alpha t$ is the specific volume.

The equation of state is

$$\alpha P = RT$$

Using this, the above equation becomes

$$P = R\int_0^\infty T\rho dz \tag{5.4}$$

The internal energy of the air column may be written as

$$E = C_v\int_0^\infty T\rho dz \tag{5.5}$$

where, $C_v$, is the specific heat of air at constant volume. Hence

$$\frac{P}{E} = \frac{R}{C_v} \sim 0.4 \tag{5.6}$$

Thus, it can be seen that the potential and internal energies of a column of air (from the sea level to the top of the atmosphere) will change proportionately to each other. For this reason, the potential and internal energies in eq. (5.3) should not be treated as two different energy sources; hence, only two energy sources exist for the perturbations to amplify: (1) the kinetic energy $K_m$ of the mean motion and (2) the sum of the potential and internal energies P + E.

The perturbations of the basic zonal current may grow through three different types of instability. The first one is the so-called linear current instability. The energy for the perturbations is derived from the kinetic energy of the basic current. This instability mechanism is similar to the hydrodynamic instability of a linear flow of a homogeneous and incompressible fluid between two parallel walls. The second type of instability is referred to as baroclinic instability. In this case, the potential and internal energies of the basic baroclinic current supply the energy for the growth of the disturbances. The third type of instability is referred to as Solberg-Holland instability. SOLBERG (1936) considered a system that initially consists of two barotropic layers separated by a sloping frontal surface in the east-west direction. Both layers are assumed to move towards the east, with the warmer (southern) layer moving faster. He found that waves with lengths less than a few kilometres and also those with lengths between 1000 and 3000 km will amplify and waves with lengths in the remaining range will dissipate. The growth of the waves with lengths shorter than a few kilometers is similar to the classical Helmholtz instability problem, and these short waves are of no relevance to the cyclone problem. A sharp discontinuity is essential for their generation. The growth of waves with lengths of 1000–3000 km can account for the growth of cyclone disturbances.

It can be shown that each of these barotropic layers can give rise to stable wave motion. The wave motion in each layer can be tuned so that each can grow as a result of a resonance effect. In this type of instability the disturbances derive energy from the kinetic energy of the mean motion whereas the potential and internal energies are sink terms.

*Some Examples of Cyclone Development*

REITAN (1974) summarized the frequencies of cyclones and cyclogenesis for North America. DANARD and ELLENTON (1980) examined the physical influences on the cyclogenesis on the east coast of North America making use of an eight-level primitive equation model. This model includes sensible and latent heat from the ocean surface, parameterized convective and large-scale precipitation and release of latent heat, surface frictional drag and

orography. One of the important results of this study is that input of heat and water vapour from the ocean surface did not contribute significantly during the deepening of the low. However, these fluxes produced an initial vertical distribution of temperature and moisture that helped subsequent development.

BRAND and GUARD (1979) studied the evolution of extratropical storms from tropical cyclones. According to these authors, a tropical cyclone is identified as becoming extratropical when it loses its tropical nature (i.e. northward displacement from the tropics as well as the conversion of the cyclone's primary energy source from latent heat release to baroclinic processes). The movement of recurved tropical cyclones is difficult to predict. According to BURROUGHS and BRAND (1973), errors as high as 30 % could occur. Even when the recurved tropical cyclone becomes somewhat weaker, if it becomes an extratropical cyclone, it could

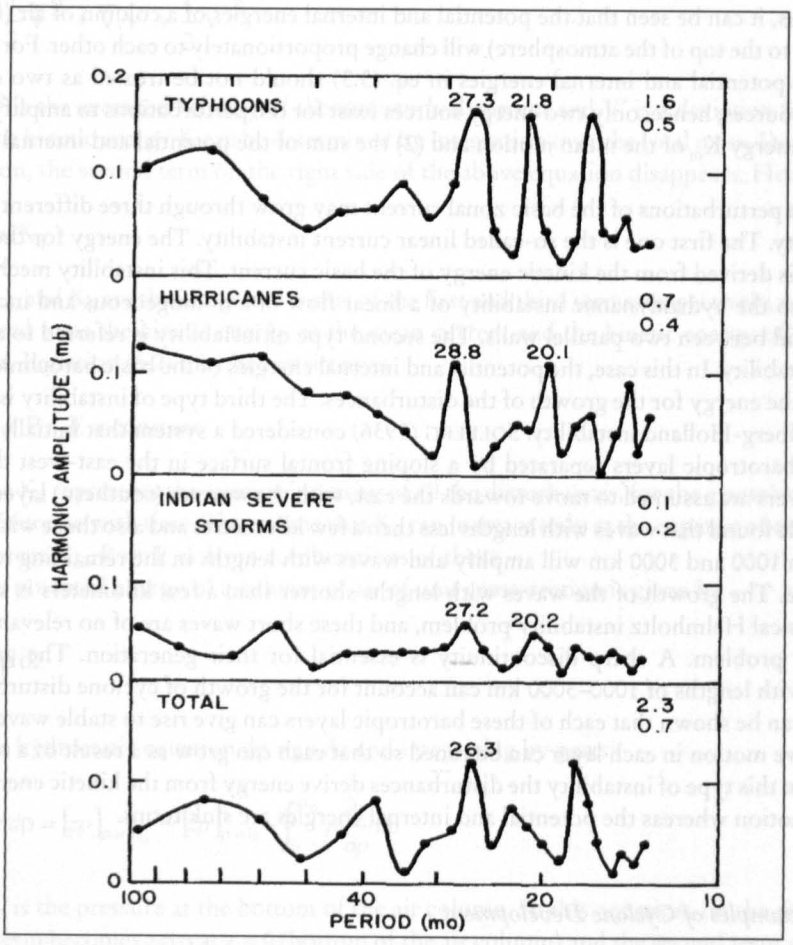


Fig. 5.4: Harmonic amplitude of the mean monthly frequency of North Pacific typhoons, North Atlantic hurricanes, severe storms (winds greater than 25 m $s^{-1}$) in the vicinity of India, and the total of all three. Numbers above the peaks indicate the dominant quasibiennial periods of oscillation (months). The two numbers in the upper right-hand corner represent the harmonic amplitudes of the annual (upper number) and semiannual (lower number) oscillations in surface pressure at the station. (ANGELL et al., 1969)

still be important. For typhoons to the east of China, during the period 1971–75, the average value of the maximum wind when the cyclones extratropical at 34° N and at that time the maximum wind speed was 51 m $s^{-1}$.

According to SEKIOKA (1970, 1972a, 1972b) and MATANO and SEKIOKA (1971a, 1971b), this transformation of tropical cyclones to extratropical cyclones can occur at least in two ways: (1) a tropical cyclone meets an already existing front causing a new extratropical cyclone to form and grow on the front and (2) a pre-existing extratropical cyclone merges with a tropical cyclone and usurps the tropical vortex.

ANGELL et al. (1969) detected a quasi-biennial (period of about 28 mo) variation in the centres of action such as the Icelandic and Aleutian low pressure centers. They related the frequency of hurricanes and typhoons to this quasi-biennial activity. Mean monthly surface pressures at stations with long data records were subjected to harmonic analysis. The following important results emerged.

Quasi-biennial variations in the surface pressure occur near the North Atlantic and North Pacific subtropical highs and subpolar lows, with amplitudes up to 0.4 mb. The quasi-biennial variations in latitude and longitude of the subtropical highs are about 1°.

The Atlantic high moves in a northwest-southeast direction. Hurricanes in the North Atlantic, typhoons in the North Pacific, and severe storms in the vicinity of India show a quasi-biennial variation in frequency (Fig. 5.4).

It is possible that the relatively large annual oscillation may contaminate the harmonic analysis for the quasi-biennial band. For this reason ANGELL et al. (1969) also performed an alternate analysis. In the so-called even-minus-odd-year difference method, the number of hurricanes or typhoons in the odd-numbered years is subtracted, year-by-year, from the number in the even-numbered years, and these first differences are smoothed through determination of a 3-yr running average. The results agree reasonably with observations.

It will not be discussed here in detail, but it must be considered that the work on reason and results of the existence of storm tracks continues. HOSKINS and VALDES (1990) investigate the question, why concentrated regions of eddy activity exist, i.e. storm tracks in the Northern Hemisphere. They have found that "the direct thermal effect of the eddies does indeed act against the storm tracks. Their vorticity fluxes lead to some reduction of this effect. It is argued that the mean diabatic heating in the storm track region is an indirect eddy effect." (HOSKINS and VALDES, 1990).

### 5.1.2 Regions of occurrence

*Extratropical Storm Surges in Canada*

Storm surges are generated in Canada by extratropical storms and occasionally by a hurricane that has transformed into an extratropical storm. In eastern Canada, storm surges occur in the Great Lakes, St. Lawrence Estuary, Gulf of St. Lawrence, Bay of Fundy and along the Atlantic coast. Storm surges also occur in Hudson Bay, James Bay, Lake Winnipeg, Beaufort Sea, Hecate Strait and Queen Charlotte Sound. The main storm surge season is autumn and early winter, and occasionally, storm surges could occur in summer and in late winter. Since all the surge-producing storms are extratropical in origin, the calculation of the meteorological forcing terms from the weather charts is straightforward (it does not necessarily mean the values are accurate). For convenience, Alaska will be discussed in this section along with western Canada. Similarly, the Great Lakes will be treated in this section. How-

ever, meteorological problems associated with mesoscale systems such as squall lines will be deferred to section 5.7.

Principal tracks of intense storms (based on the data for the period 1963–67) are shown in Fig. 5.5 (A) for January to March, in Fig. 5.5 (B) for July and August, and in Fig. 5.5 (C) for October to December. The tracks of storms of tropical origin are shown in Fig. 5.6, and the tracks of storms for the Hudson Bay region for different months are shown in Fig. 5.7A–5.7D. However, occasionally, rather irregular tracks can occur. In Fig. 5.8 are shown the tracks for four storms in 1969 over Hudson Bay. While the track for the November storm is not unusual, the tracks for the other three storms show forward – backward

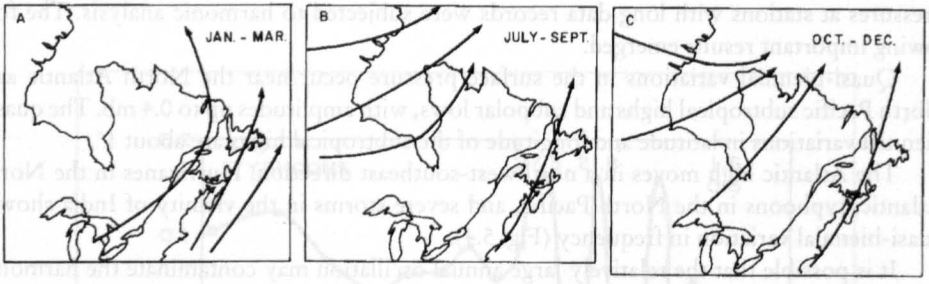


Fig. 5.5: Tracks of intense storms over eastern Canada (A) January–March, (B) July–September, and (C) October–December. (ARCHIBALD, 1945)

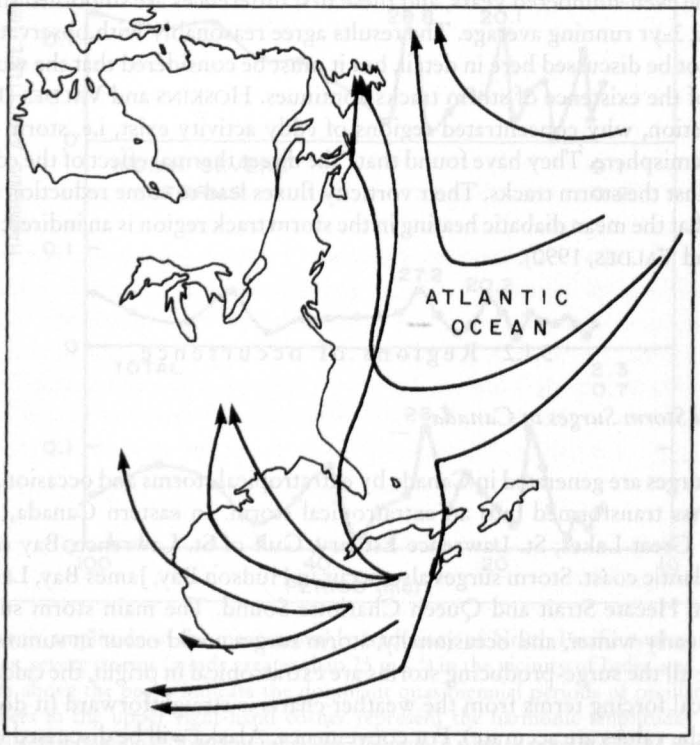


Fig. 5.6: Tracks of storms of tropical origin along the east coast of North America. (ARCHIBALD, 1945)

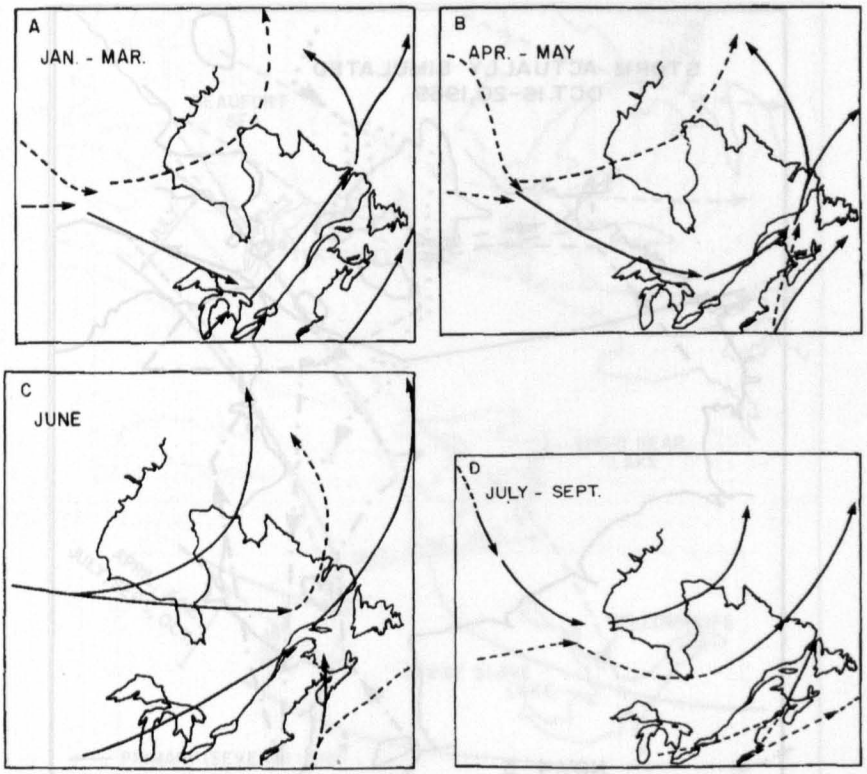


Fig. 5.7: Storm tracks over Hudson Bay and surroundings (A) January–March, (B) April and May, (C) June, and (D) July–September. (Archibald, 1945)

movements of the storm center, which could be the result of improper observations or could be real on certain occasions.

The corridors for the tracks of intense and ordinary storms in the northwestern part of Canada are shown in Fig. 5.9. The surface weather map for the Alaska area during a storm on October 3, 1963, is given in Fig. 5.10A. The distribution of the computed wind stress field is illustrated in Fig. 5.10B and the variation of the computed wind stress with time near Barrow, Alaska, is shown in Fig. 5.10C.

*Great Lakes*

BARRIENTOS (1970) discussed objective methods for predicting winds over Lakes Erie and Ontario. Making use of 1000-mb geostrophic wind and sea level pressure forecasts issued routinely for eight stations surrounding these lakes, as well as marine observations from anemometer-equipped vessels, two sets of regression equations were derived for predicting wind speed.

VENKATESH and DANARD (1976) used a one-level primitive equation model for computing the mesoscale influences of orography, friction, and heating on surface winds. They included the influence of atmospheric stability and land-water temperature contrast. ESTOQUE

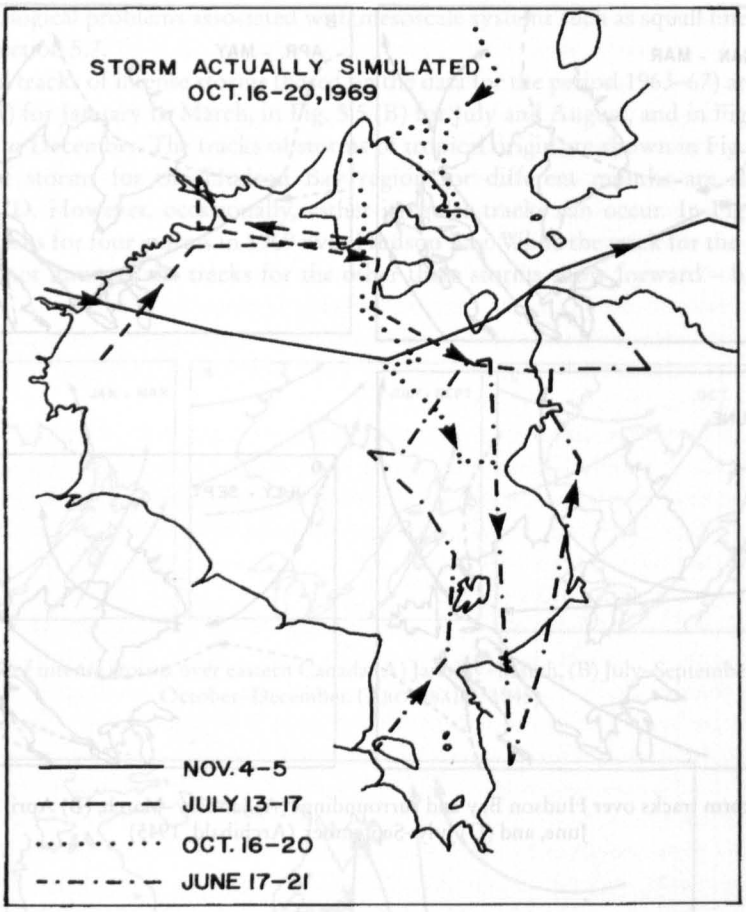


Fig. 5.8: Selected storm tracks over Hudson Bay for the year 1969

and GROSS (1979) discussed diurnal wind variations over Lake Ontario, as deduced from Rawinsonde data at six stations.

RESIO and VINCENT (1977) estimated winds over the Great Lakes knowing winds over adjacent land. FEIT and PORE (1978) discussed objective wind forecasting for all of the Great Lakes using a technique developed by FEIT and BARRIENTOS (1974). The predictors are the various forecast parameters computed by the National Meteorological Center's primitive equation (PE) model. The 12 locations at which wind forecasts are made at 6-h intervals, 36 h in advance, are shown in Fig. 5.11. Mean absolute error in wind speed is 5–8 knots (2.6–4.1 m. $S^{-1}$) and mean absolute error in wind direction is about 20° for short-term forecasts (6–12 h) and about 70° for long-term forecasts (30–36 h).

KEULEGAN (1953) took a somewhat different approach. He derived the wind stress and the roughness parameter for Lake Erie using water level data for a 50-yr period. In other words, he used the observed storm surge data to estimate the wind stress. He defined an effective lake wind velocity as the wind velocity that would be needed to produce the observed storm surge, assuming that the wind blows with this effective velocity along the lake axis. Recently, SCHWAB (1982) used a similar but more sophisticated inverse technique.

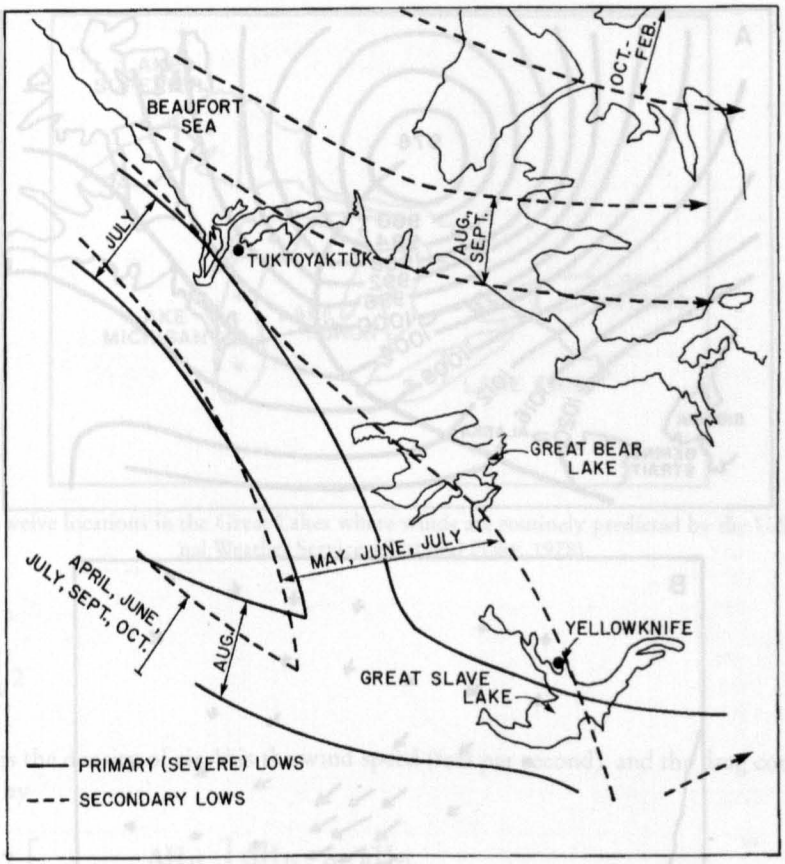


Fig. 5.9: Corridors of primary and secondary lows over the northwest part of Canada. (BURNS, 1973)

KEULEGAN (1953) used the following relationship to deduce the wind stress from the storm surge:

$$\frac{(\tau_S + \tau_0)}{\rho g H_0}\frac{L}{H_0} = 0.867\frac{\Delta H_0}{H_0} - 0.134\left(\frac{\Delta H_0}{H_0}\right)^2 \tag{5.7}$$

where, $\tau_S$ is the wind stress, $\tau_0$ is the bottom stress, $\rho$ is the density of water, g is gravity, $H_0$ is the average water depth, $\Delta H$ is the storm surge (feet), and L is the length of the lake (feet). The bottom stress $\tau_0$ was related to the surface wind stress through

$$\tau_0 = n\tau_S \tag{5.8}$$

Then, eq. (5.7) becomes

$$\tau_S = \frac{1}{(1+n)}\left[0.867\frac{\Delta H_0}{H_0} - 0.134\left(\frac{\Delta H_0}{H_0}\right)^2\right]\frac{H_0}{L} \tag{5.9}$$

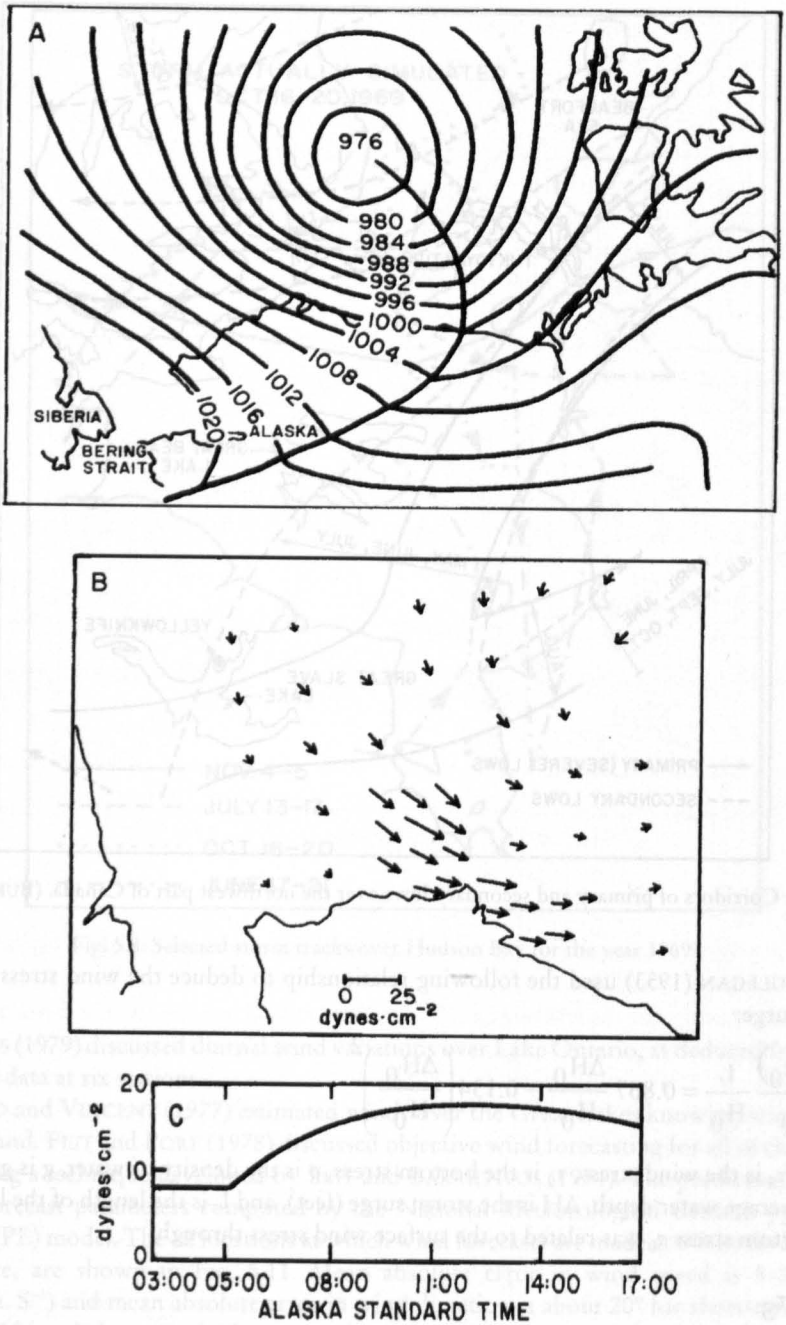


Fig. 5.10: (A) Simplified surface weather chart for October 3, 1963, at 11:00 (Alaska Standard Time); (B) computed wind stress field for 11:00–14:00; (C) variation of wind stress with time at Barrow, Alaska (1 dyne = 10 N). (SCHAFER, 1966)

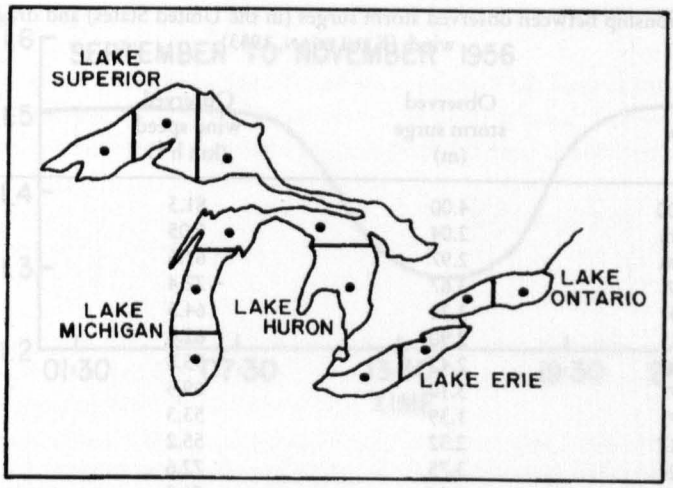


Fig. 5.11: Twelve locations in the Great Lakes where winds are routinely predicted by the U.S. National Weather Service. (FEIT and PORE, 1978)

Write

$$\tau_S = \gamma \rho_a V^2 \tag{5.10}$$

where, $\rho_a$ is the density of air, V is the wind speed (feet per second), and the drag coefficient $\gamma$ is given by

$$\gamma = \frac{0.867}{(1+n)}\left[1 - 0.16\,\frac{\Delta H_0}{H_0}\right]\frac{\Delta H_0}{H_0}\,\frac{\rho}{\rho_a}\,\frac{gH_0}{V^2} \tag{5.11}$$

The 22 storms during the period 1900–47 on Lake Erie, the observed wind speed, the observed storm surge (during westerly winds), and the calculated value of $\gamma$ from eq. (5.11) are listed in Table 5.1.

HUNT (1959) discussed the relationship between the parameter $\alpha$ defined as

$$\alpha \equiv \frac{\tau_S + \tau_B}{\tau_S} \tag{5.12}$$

and D/K where D is the water depth, K is the bottom roughness coefficient, and $\tau_S$ and $\tau_B$ are the wind and bottom stresses. The relationship for Lake Erie is shown in Fig. 5.12. HUNT (1959) also gave diagrams showing the variation with time in fall and spring of the ratio $U_W/U_L$ at Cleveland on Lake Erie (Fig. 5.13). Here, $U_W$ and $U_L$ are the overwater and overland wind speeds. The reason for examining this ratio is to account for atmospheric stability. The ratio $U_W/U_L$ at four stations on Lake Erie for stable, adiabatic, and unstable atmospheric conditions is given in Table 5.2. The overwater wind speeds on Lake Erie at 21:00 on November 8, 1957, are shown in Fig. 5.14.

IRISH and PLATZMAN (1961) discussed the meteorological conditions associated with extreme storm surges on Lake Erie. The monthly frequency distributions of severe storms

Table 5.1: Relationship between observed storm surges (in the United States) and drag coefficients of wind. (KEULEGAN, 1953)

| Date of storm surge | Observed storm surge (m) | Observed wind speed (km $h^{-1}$) | Drag coefficient $\gamma \cdot 10^3$ |
|---|---|---|---|
| Nov. 21, 1900 | 4.00 | 81.3 | 2.13 |
| Oct. 20, 1905 | 2.04 | 5.05 | 2.87 |
| Oct. 20, 1906 | 2.97 | 61.6 | 2.78 |
| Jan. 20, 1907 | 3.67 | 77.4 | 2.17 |
| Dec. 7, 1909 | 3.20 | 64.5 | 2.73 |
| Dec. 31, 1911 | 2.90 | 62.6 | 2.63 |
| Jan. 31, 1914 | 2.42 | 55.8 | 2.76 |
| Dec. 9, 1917 | 3.10 | 69.5 | 2.23 |
| Dec. 9, 1917 | 1.39 | 53.3 | 1.78 |
| Dec. 10, 1917 | 2.32 | 55.2 | 2.71 |
| Dec. 18, 1921 | 3.75 | 72.6 | 2.52 |
| Dec. 8, 1927 | 4.04 | 76.3 | 2.44 |
| Dec. 9, 1927 | 1.26 | 43.8 | 2.35 |
| Dec. 9, 1927 | 1.05 | 42.0 | 2.15 |
| Dec. 9, 1927 | 0.53 | 35.6 | 1.53 |
| Apr. 1, 1929 | 4.06 | 82.6 | 2.88 |
| Jan. 22, 1939 | 2.87 | 62.4 | 2.64 |
| Sept. 25, 1941 | 2.76 | 57.5 | 2.96 |
| Jan. 2, 1942 | 3.82 | 65.0 | 3.22 |
| Jan. 3, 1942 | 0.73 | 31.4 | 2.68 |
| Nov. 22, 1946 | 2.55 | 55.0 | 2.99 |
| Mar. 25, 1947 | 2.54 | 57.5 | 2.77 |

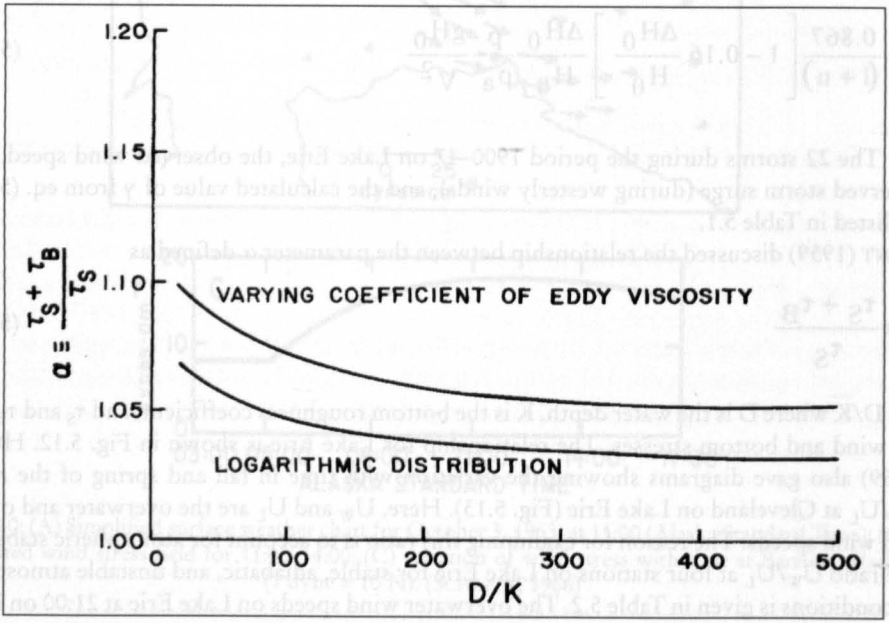


Fig. 5.12: Variation of $a$ versus $D/K$ ($D$ = water depth, $K$ = bottom roughness parameter, $\tau_S$ = wind stress, and $\tau_B$ = bottom stress). The relationship is shown for two different distributions of bottom stress. (HUNT, 1959)

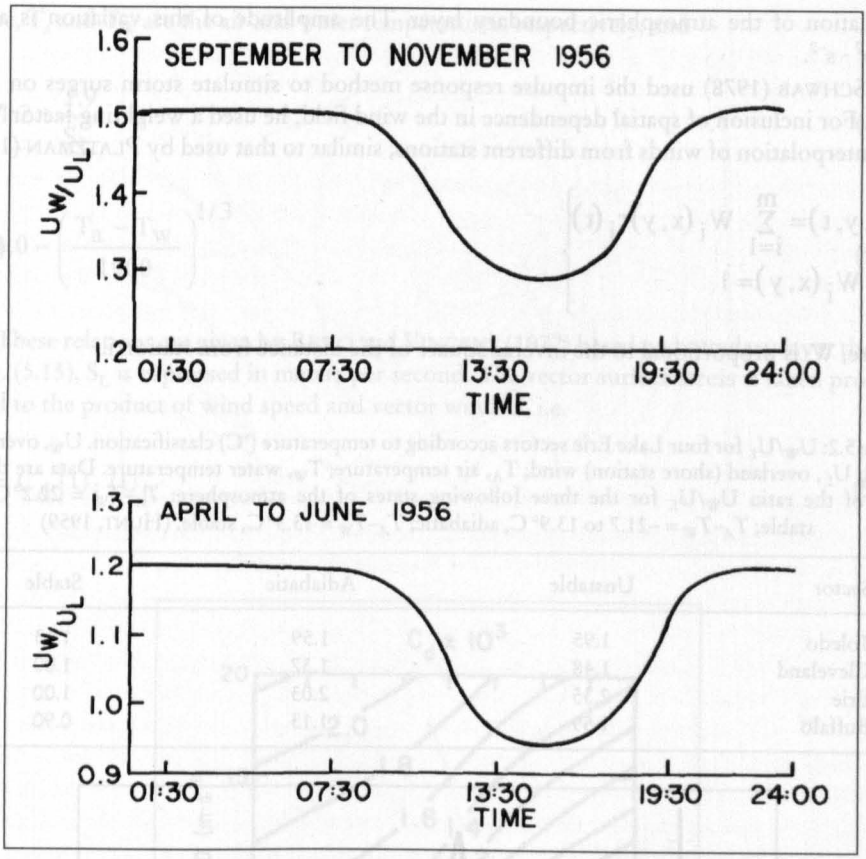


Fig. 5.13: Daily variation in $U_W/U_L$ for southwesterly winds by season at Cleveland, Ohio, during 1956. (HUNT, 1959)

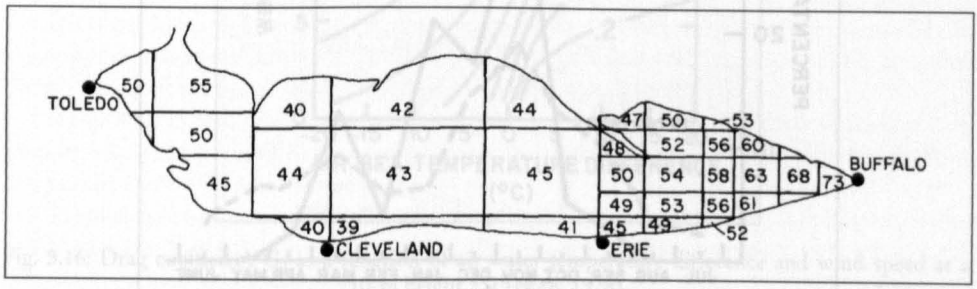


Fig. 5.14: Overwater wind speeds (feet per second) in Lake Erie (1 ft = 0.3048 m). (HUNT, 1959)

on the Great Lakes, as given by these authors for the period 1876–1900, are given in Fig. 5.15. It can be seen that maximum frequency occurs during October to December, November being the month of greatest frequency.

PLATZMAN (1965) showed that over Lake Erie, there is a distinct diurnal constituent of the longitudinal component of the wind square vector, with maximum in the direction Toledo to Buffalo shortly after noontime. This variation is due to the usual convective

oscillation of the atmospheric boundary layer. The amplitude of this variation is about 10 $m^2 \cdot s^{-2}$.

SCHWAB (1978) used the impulse response method to simulate storm surges on Lake Erie. For inclusion of spatial dependence in the wind field, he used a weighting factor $W_i$ in the interpolation of winds from different stations, similar to that used by PLATZMAN (1963):

$$\left.\begin{aligned} \tau(x,y,t) &= \sum_{i=1}^{m} W_i(x,y)\tau_i(t) \\ \sum_{i=1} W_i(x,y) &= 1 \end{aligned}\right\} \qquad (5.13)$$

where, $W_i$ is proportional to the inverse square of the distance from station i.

Table 5.2: $U_W/U_L$ for four Lake Erie sectors according to temperature (°C) classification. $U_W$, overwater wind; $U_L$, overland (shore station) wind; $T_A$, air temperature; $T_W$, water temperature. Data are the values of the ratio $U_W/U_L$ for the three following states of the atmosphere: $T_A - T_W$ = 22.2° C, unstable; $T_A - T_W$ = –21.7 to 13.9° C, adiabatic; $T_A - T_W$ = 13.3° C, stable. (HUNT, 1959)

| Sector | Unstable | Adiabatic | Stable |
|---|---|---|---|
| Toledo | 1.95 | 1.59 | 1.13 |
| Cleveland | 1.48 | 1.37 | 1.00 |
| Erie | 2.35 | 2.03 | 1.00 |
| Buffalo | 1.59 | 1.13 | 0.90 |

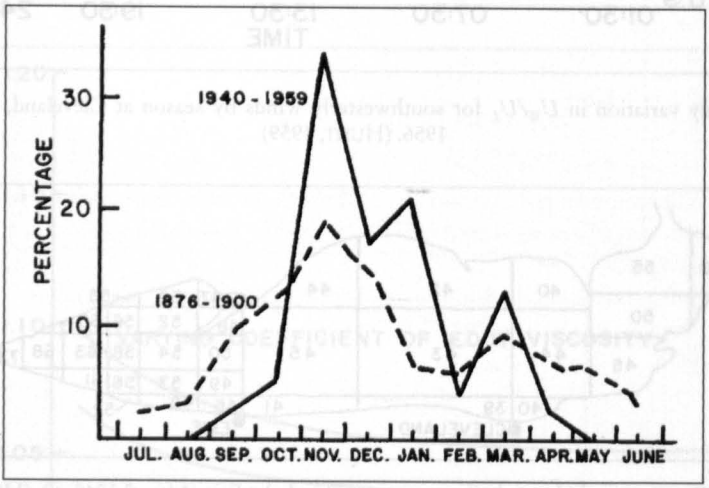


Fig. 5.15: Monthly frequency distribution of severe storms on the Great Lakes for the period 1940–59 (solid line) and for the period 1876–1900 (broken line). (IRISH and PLATZMAN, 1961)

SCHWAB (1978) converted the observed wind speeds $S_L$ at the coastal stations into overlake wind speeds $S_W$ through

$$\frac{S_W}{S_L} = \psi(S_L)\phi(T_a - T_W) \qquad (5.14)$$

where, $T_a$ and $T_W$ are the air and water temperatures, respectively, and

$$\psi = 1.2 + \frac{1.9}{S_L} \tag{5.15}$$

$$\phi = 1.0 - \left( \frac{T_a - T_W}{1900} \right)^{1/3} \tag{5.16}$$

These relations are given by RESIO and VINCENT (1977) based on boundary layer theory. In eq. (5.15), $S_L$ is expressed in meters per second. The vector surface stress is taken proportional to the product of wind speed and vector wind U, i.e.

$$\frac{\tau_i}{\rho_a} = C_d \left| U_i \right| U_i \tag{5.17}$$

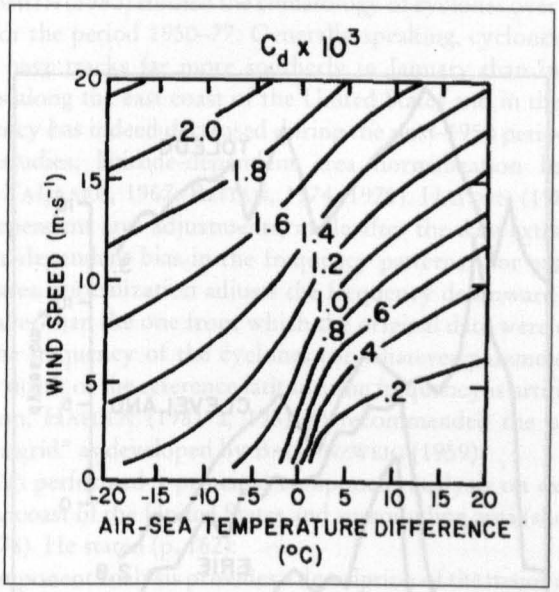


Fig. 5.16: Drag coefficient $C_d$ as a function of air-water temperature difference and wind speed at a 10-m height. (SCHWAB, 1978)

The air density $\rho_a$ is taken as $1.25 \times 10^{-3}$ g · cm$^{-3}$. The drag coefficient $C_d$ as a function of ($T_a$–$T_W$) and wind speed (at a 10-m height) is shown in Fig. 5.16.

HAMBLIN (1979) numerically simulated the storm surge of April 6, 1979, which produced a record set-up of 4.5 m on Lake Erie. The surface isobaric field for this storm is shown in Fig. 5.17 and the time variation of the wind stress at four stations is given in Fig. 5.18. HAMBLIN (1979) mentioned that the computed drag coefficients varied from $0.9 \times 10^{-3}$ to $3.5 \times 10^{-3}$ during the duration of the storm.

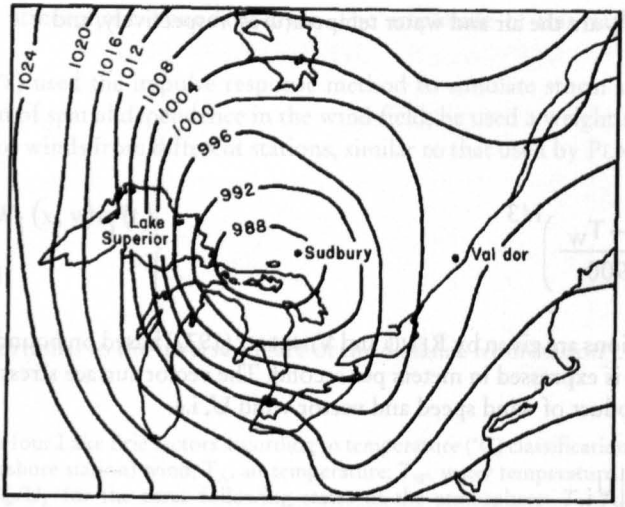


Fig. 5.17: Simplified surface weather chart at 01:00 (Eastern Standard Time) on April 6, 1979. The pressure field is in millibars. (HAMBLIN, 1979)

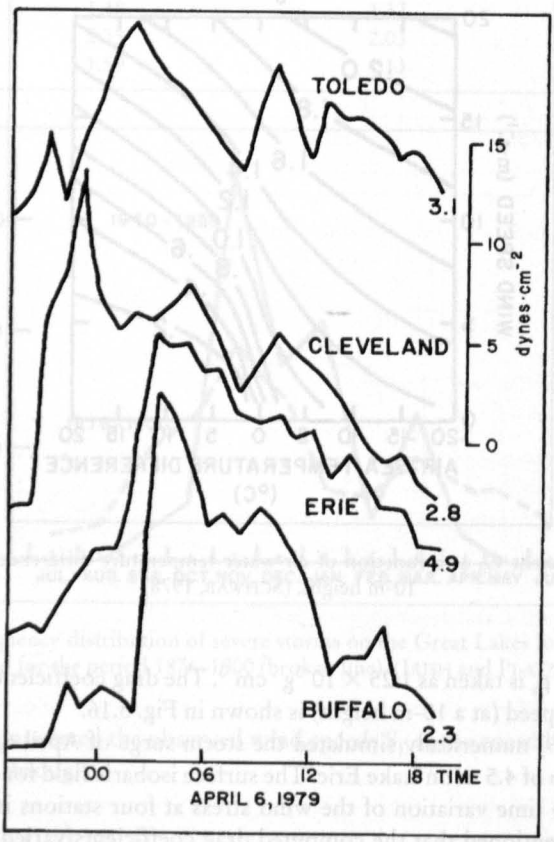


Fig. 5.18: Time history of wind stress at four locations on Lake Erie. (HAMBLIN, 1979)

SIMONS (1975) determined the effective wind stress over Lakes Erie and Ontario from long-term numerical water level simulations. He showed that the effective wind stress over water is greater than indicated by atmospheric boundary layer measurements over Lake Ontario; the theoretically derived drag coefficient appears to be about $1.85 \times 10^{-3}$. Over Lake Erie, the drag coefficient is about the same magnitude in spring and early summer, but increases to about $2.5 \times 10^{-3}$ during the stormy autumn season. These results confirm DONELAN's (1975) study of the interaction between wind waves and the atmospheric boundary layer, whose primary result was that the drag coefficient increases significantly if the wave field is not completely adjusted to the wind field. Usually, boundary layer observations are made during steady winds (when no storms are present) and, hence, such measurements are not representative of drag coefficient during stormy periods.

*Extratropical Storm Surges in the United States*

REITAN (1979) extended his earlier study (REITAN, 1974) to cover the period 1949–76, which is characterized by gradually decreasing temperature in the Northern Hemisphere. This study showed a general trend for a decrease in the number of cyclonic events in recent years. ZISHKA and SMITH (1980) studied the climatology of cyclones over North America and surrounding area for the period 1950–77. Generally speaking, cyclones are more frequent, more intense, and have tracks far more southerly in January than in July. Predominant cyclogenesis occurs along the east coast of the United States and in the lee of the Rockies. The cyclone frequency has indeed decreased during the post-1950 period.

In a lot of studies, latitude-dependent area normalization has been used (e.g. O'CONNOR, 1964; TAIJAARD, 1967; REITAN, 1974, 1979). HAYDEN (1981a, 1981b) pointed out that latitude-dependent area adjustments, made after the data extraction is completed, introduce a latitude-dependent bias in the frequency patterns. For example, south of the reference latitude, area normalization adjusts the frequency downward and forces it to represent an area smaller than the one from which the original data were extracted. This artificially decreases the frequency of the cyclones (or whatever parameter being tabulated). On the other hand, north of the reference latitude, the frequency is artificially increased. To correct this situation, HAYDEN (1981 a, 1981 b) recommended the use of the so-called "practical equal area grid" as developed by BALLENZWEIG (1959).

HAYDEN (1981a) performed a principal component analysis on extratropical cyclone data for the Atlantic coast of the United States and surrounding area (shown in Fig. 5.19 for the period 1885–1978). He stated (p. 162):

... principal component analysis provides a description of the major modes of variability in the data set. Typically, each component is identified with some property of the data field. The analysis also provides an index, which measures the importance of each component within each year. Finally, the analysis provides an estimate of the total percent of variance in the data set, which can be explained on the basis of each component.

The objective of the analysis is to isolate characteristic, recurrent, and independent modes of covariance among variables into a new set of independent variables. Basically, the analysis transforms a set of intercorrelated variables into a new coordinate system in which the axes are linear combinations of the original variables and are mutually orthogonal. To prevent those grid cells with high mean cyclone frequencies (high latitudes) from dominating the total variance and consequently from dominating the eigenvector forms, the correlation matrix was used rather than the covariance matrix.

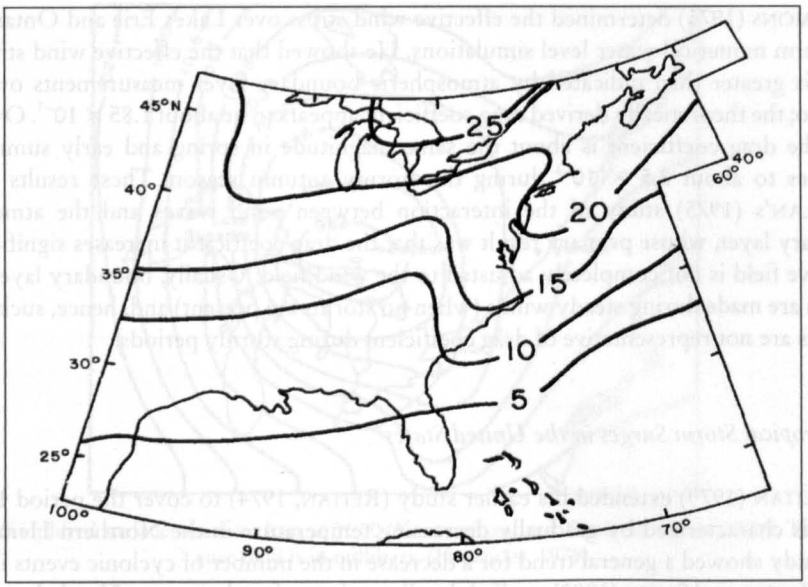


Fig. 5.19: Average annual frequency of extratropical cyclones over the eastern part of the United States. (HAYDEN, 1981a)

The area shown in Fig. 5.19 was divided into 74 rectangles (2.5° latitude by 5° longitude). The first principal component showed that, since the beginning of the twentieth century, the frequency of cyclones over the marine areas has increased whereas the frequency decreased over the continental areas. This trend peaked in the 1960s. The second principal component was identified as a cyclogenesis function for the east coast of the United States. This showed an increased cyclogenesis starting at the beginning of the twentieth century with a maximum in the 1950s. The third and fourth components explain the geographic variations in cyclogenesis in the Gulf coast and Great Lakes regions. The average cyclone frequencies over the eastern United States for the period 1885–1978 are also shown in Fig. 5.19.

Usually, one uses the Norwegian cyclone model to explain extratropical cyclogenesis. REED (1979) pointed out that it is not always necessary for the cyclone to originate as a wave perturbation on a polar front separating tropical and polar air masses. An alternate mechanism is the formation of cyclones in polar air streams behind or poleward of the polar front, as sometimes happens in winter over the oceans.

Cyclones that form in this manner are relatively small in size. One interesting feature is that, in their mature stage, these cyclones exhibit a comma-shaped pattern. A surface low pressure centre may not always be easily identifiable. When it exists, such a low pressure centre is situated beneath the head of the comma. Also, under the trailing edge of the comma tail, there is almost always a surface trough of low pressure. Thus, cyclones of this type somewhat resemble large frontal cyclones.

*Wind Stress and pressure in extratropical cyclones over the United States*

TANCRETO (1958) used the significant wave (wind waves) height as an indication of the intensity of the storm. An extratropical cyclone generated storm surge during March 1962

caused tremendous damage in Atlantic City (New Jersey). The surge was so severe it bisected a steel pier (PORE, 1964). Extratropical cyclone generated storm surges are not rare on this part of the east coast of the United States (e.g. February 1958).

MILLER (1957) showed that maximum surges at Norfolk are associated with east-northeast winds. There is a lag of 12 h between the wind and the surge. PORE (1964) studied 18 storm surges during the period 1956–61. For these 18 storms, there was a total of 1910 hourly observations available. Most of these storms passed over the southeastern United States and then moved offshore over the Atlantic Ocean. Maximum wind speeds varied from 22 to 50 knots (41–93 km $h^{-1}$). Three meteorological forcing terms were considered separately:

a) onshore component of the wind stress (which produces a set-up),
b) alongshore component of the wind stress (which generates alongshore currents, which then are deflected to the right by the Coriolis force, and this creates an upward slope of the water surface toward the right) and
c) atmospheric pressure (inverse barometer effect).

An interesting result of this study is that the storm surge at Atlantic City is strongly dependent on the alongshore component of the wind. There appears to be little difference between the results obtained using linear wind stress and quadratic wind stress.

WANG (1979) examined the response of the water level in Chesapeake Bay to the time scale of atmospheric forcing. For time scales longer than 7 d, the water levels in the bay were driven nonlocally by the coastal water levels. For periods between 4 and 7 d, the water level in the bay was driven both by the coastal sea level as well as the lateral component of the wind. For time scales of 1–3 d, the water level in the bay was driven by the longitudinal component of the wind.

SAUNDERS (1977) computed seasonal averages of wind stress over the eastern continental shelf of North America making use of about 1 million ship observations for the period 1941–72. He assumed a drag coefficient that increases with the wind speed from $1.0 \times 10^{-3}$ at 5 m $s^{-1}$ wind speed to $2.3 \times 10^{-3}$ at 25 m $s^{-1}$. Atmospheric stratification was found to have little effect. The stress is strongest in winter (1–15 dynes $cm^{-2}$) and weakest in fall (0.25–0.5 dynes $cm^{-2}$). In summer the stress is directed towards the northeast whereas in the other three seasons it is directed south and east. The wind stress generally increases with increasing latitude, but local maxima are found over the Gulf of Maine and the Gulf of St. Lawrence. SAUNDERS (1977) attributed the local maxima and minima to cyclonic activity.

### *Storm Surges in Europe*

Cyclones causing storm surges in the waters in and around Europe are mainly of the extratropical type, and the meteorological problems associated with these storms are somewhat simpler than those due to tropical cyclones. Most of the storm surges in Europe occur in the North Sea; other areas where surges occasionally occur are the Baltic Sea, the Irish Sea, Adriatic Sea, Ligurian Sea, the Atlantic coast of Portugal and the coasts of Norway and Sweden.

### *North Sea and Baltic Sea*

A special meteorological situation must occur to induce storm surges in the North Sea. When a depression reaches the North Sea from west or northwest, an air stream develops.

The strength of an air stream depends on the pressure situation in the high, the location of the storm depression to the neighbouring high pressure area, the location of the fronts and speed and direction of the depression. For example, when the centre of the depression travels north of the Southern North Sea Coast wind there coming from west to northwest is generated and can lead to storm surges at this coast.

The depressions take different routes (Fig. 5.20). The meteorological situation leading to high or very high storm surges at the Southern North Sea Coast can be classified into three types (PETERSEN and ROHDE, 1991), here complemented by the fourth, called mixed type:

1. Jutland-Type
   It forms south of 60° N over Newfoundland and travels from west to east from England over the North Sea to Jutland and then either over the south of Sweden in easterly direction or turns off to northeast. These low pressure systems travel mostly very fast and cause strong storms for a short period. The winds change from southwest to northwest or north. As pointed out by GÖNNERT (1999), a fast increase of wind speed causes high storm surge peaks at the coast of the German Bight. Examples of the storm surge of February 23–24, 1967 and January 3, 1976 are shown in Fig. 5.21. The curve of the surge has mostly a steep slope. When high wind speed persists for more than 2–5 hours and water levels only drop slowly this type of cyclonic track can cause dangerous storm surges.
2. Scandinavia-Type:
   These depressions form over Greenland and Iceland and travel towards southeast. They cross Scandinavia between 60° N and 65° N. This type causes storms with long duration from northwest over the North Sea. Therefore more than one tidal peak (sometimes with 3–4 lower peaks following) is caused from this type of cyclone. The storm surge curve shows a slow ascent and a slow drop. Due to the long duration of this type of storm surge with its high water level dikes can become water-saturated, soggy and unstable.
   Examples for this type can be found on February 16–17, 1962 and January 20–22, 1976 (Fig. 5.22).
   Sometimes the tracks of the Jutland-Type and of the Scandinavia-Type are mixed. The Storm surge of November 22–23, 1981 started with a path of the Scandinavia-Type, but changed direction and travelled over Scandinavia to the southern Baltic Sea like the Jutland-Type.
3. Skagerrak-Type
   The tracks of these cyclones lie between both types described before. They cross the 8$^{th}$ degree of Longitude between 57° to 60° N. Mostly they travel from WNW to ESE, but sometimes they travel from W to E and NW to SE. The wind blows from WNW and NW towards the entire coast of the North Sea and causes storm surges. The storm surges of February 12, 1894, March 13, 1906, February 13 and 16, 1916, October 10, 1926, October 18 and 27, 1936 and November 16, 1973 were caused by this cyclonic type.
4. Mixed-Types
   Many surges are not caused by one type of meteorological situation only. The track of the depression is composed of different types. For example, the storm depression of February 1, 1953, which caused a very high storm surge at the coast of the Netherlands and at the east coast of the United Kingdom, took the direction of the Skagerrak-Type and then changed direction between Scotland and south of Norway to the south. Because of the change of direction at the German Coast only a small storm surge occurred. WEMELSFELDER (1954) mentioned that the meteorological conditions associated with the storm of February 1, 1953, were quite different from the traditional storm tracks that emerge over Scotland and disappear over Norway or Denmark. In this 1953 case, the storm track cros-

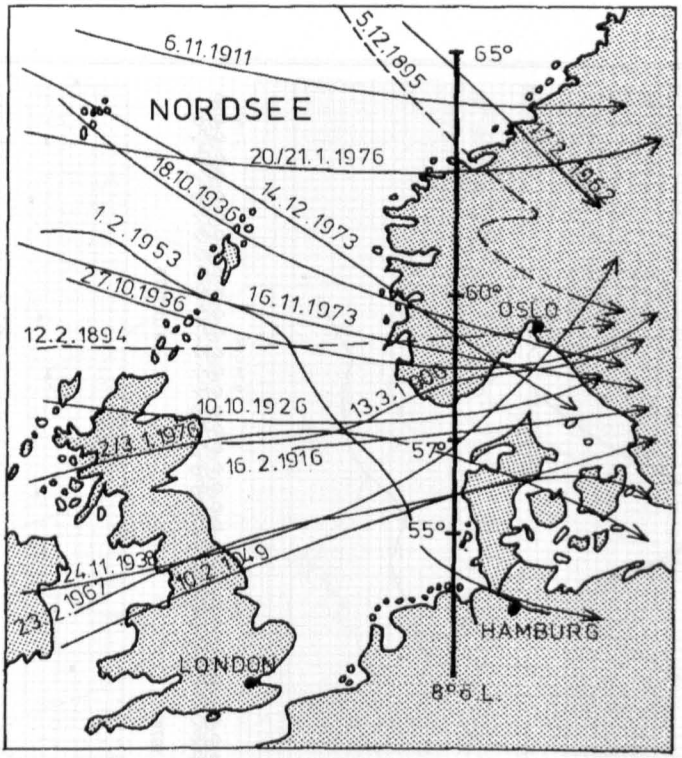


Fig. 5.20: Storm depression, which causes storm surge tracks at the North Sea Coast (PETERSEN and ROHDE, 1991)

sed the North Sea from Scotland to Hamburg. The Netherlands coast is very vulnerable to this type of track. Detailed meteorological data about this storm are presented by SNEYERS (1953).

DOODSON (1929) classified the meteorological situations for the Thames Estuary in the same way as presented here. Most of the major storm surges in the Thames Estuary are associated with type I meteorological situations. One example of type I is the storm of December 30–31, 1921, which reached a speed of 161 km/h (NNW) and caused a very high storm surge. The surface isobaric patterns at two different instants of time are shown in Fig. 5.23. DOODSON (1929) and DINES (1929) listed the storm surges in the Thames Estuary during the period 1912–28 (MURTY, 1984).

The Baltic Sea can be described as a relatively closed basin because the connection between North Sea and Baltic Sea is very small in relation to the surface of the bordering sea. Strong wind from southwest causes storm surges in the North and low water levels in the South. A change of wind direction to NNE causes high water levels in the southern part of the Baltic Sea. At the north-eastern as well as at the south-western part of the longitudinal axis of the Baltic Sea high water levels of more than 3 m over mean water level can be observed.

The special meteorological situation in Europe causes stormy weather and, with this, storm surges only during the period from September to April. The highest frequency occurs in the period from October to February, the highest level was reached in the same period. Fig. 5.24 shows the average annual distribution of storm surges at Cuxhaven for the period

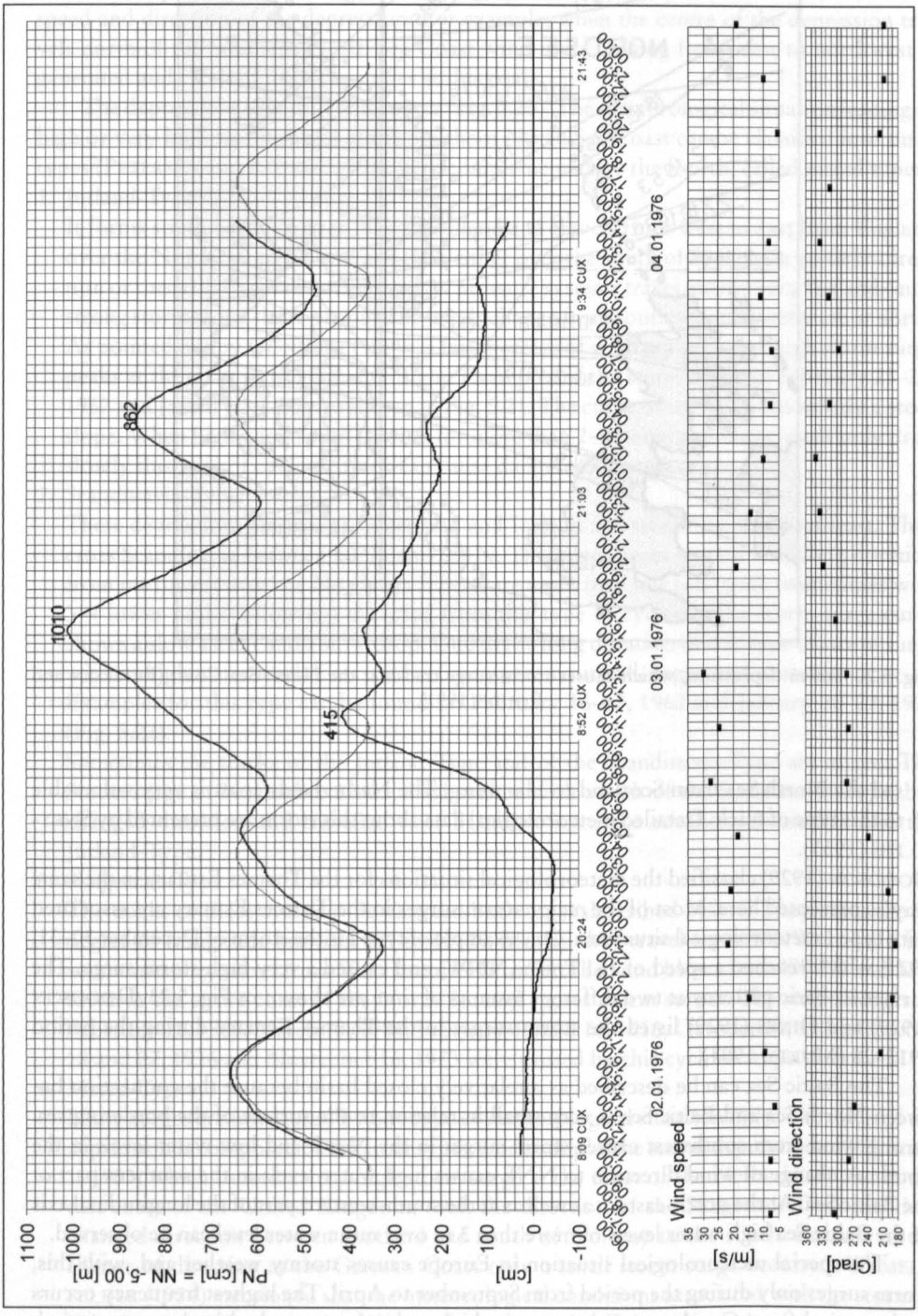


Fig. 5.21: Storm surge at Cuxhaven from January 3, 1976 (GÖNNERT and SIEFERT, 1998)

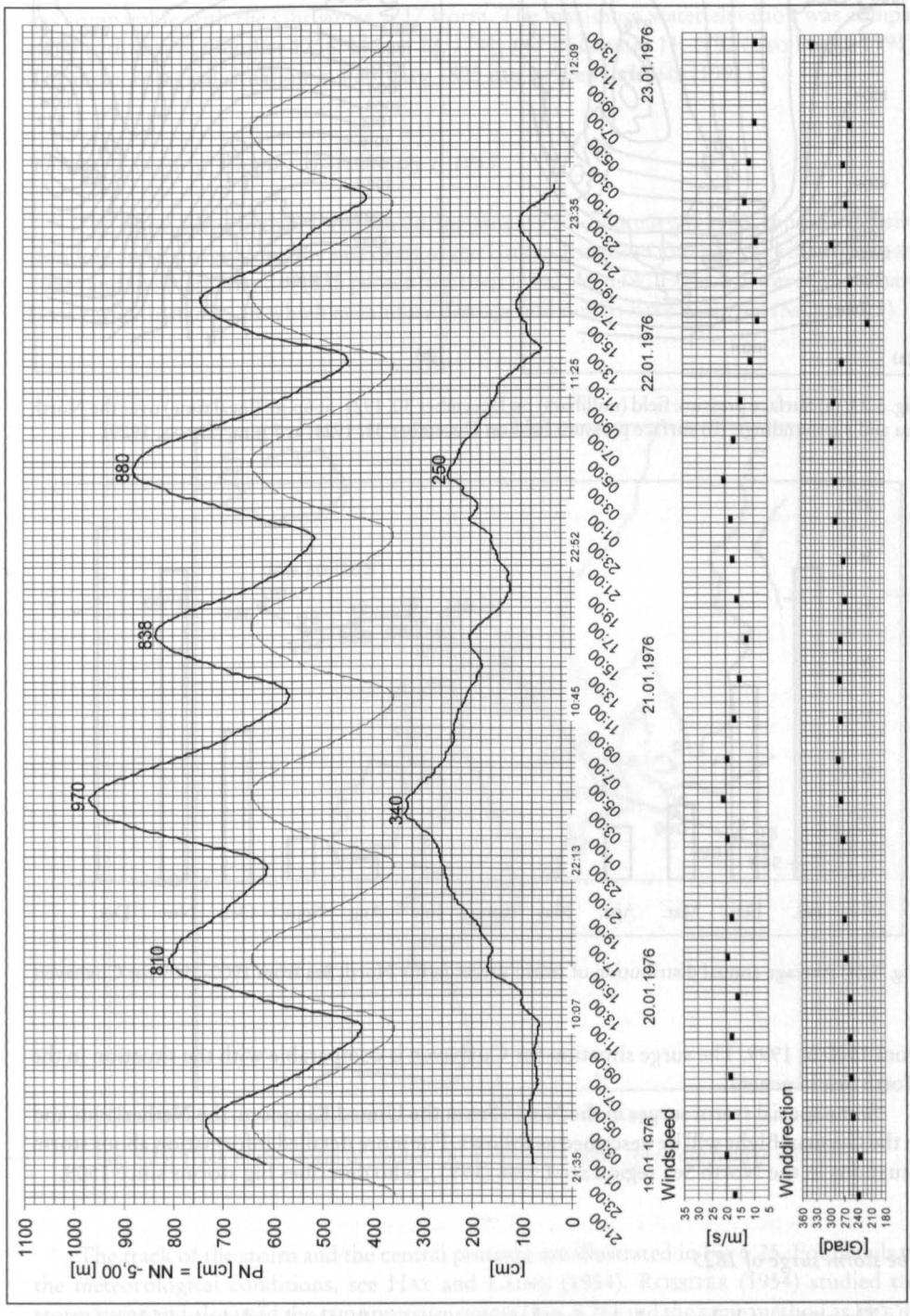


Fig. 5.22: Storm surge at Cuxhaven from January 20–22, 1976 (GÖNNERT and SIEFERT, 1998)

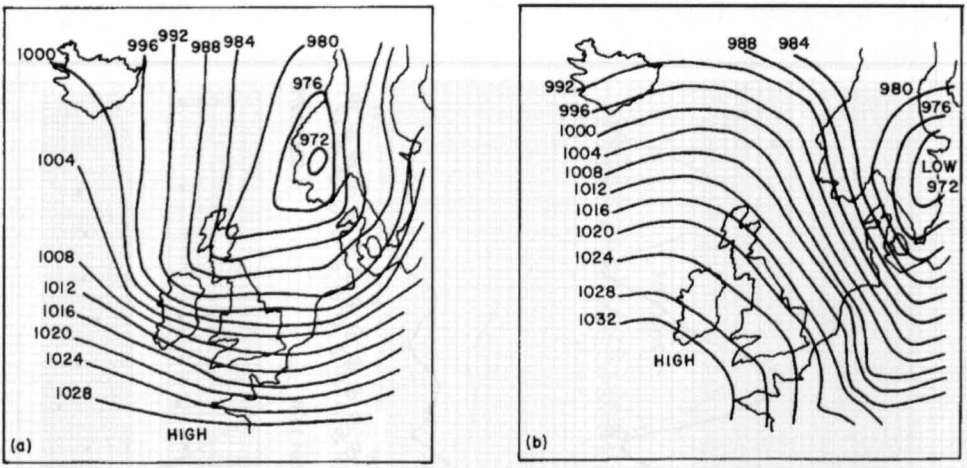


Fig. 5.23: (a) Surface pressure field (millibars) on December 30, 1921, at 6p.m. (local time) over the North Sea and surroundings; (b) surface pressure field on December 31, 1921, at 7 p.m. (DINES, 1929)

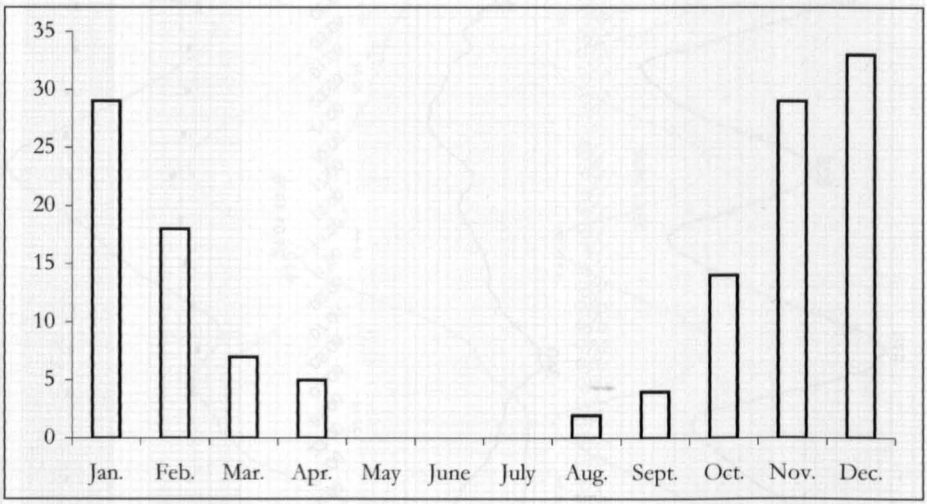


Fig. 5.24: Average annual distribution of storm surges in the North Sea from 1900–1999 for Cuxhaven

from 1900 to 1999. The surge situation for Cuxhaven is comparable with the situation in the North Sea in general.

Some special storm surges in the North Sea at the United Kingdom, the Netherlands and in the German Bight will be described as follows. For more detailed information about storm situations in the North Sea region see LAMB (1991), who describes big storms since 1509.

*The storm surge of 1825*

The storm of February 1–2, caused storm surges in Scotland and the neighbouring sea areas to north and east. The storm of February 2–5 caused a disastrous storm surge from

Holland to Denmark. The storm tide crest reached a level of more than 350 cm over mean high tide level at Cuxhaven (German Bight) and was therefore one of the highest storm surges comparable with the Christmas 1717 storm. The maximum water elevation was comparable with that of October 1756, March 22, 1791, and December 11, 1792 (also LAMB, 1991). The meteorological situation in February 1825 can be seen in LAMB (1991).

*The storm surge of January 31–February 1, 1953*

The storm surge in the North Sea during January 31–February 1, 1953, caused extensive flooding and damage along the east coast of the United Kingdom (307 people killed) (STEERS, 1954) and the Netherlands (1835 people lost their lives) (MALDE, 1996). However, there have been earlier instances in which even more damage and deaths have occurred (Section 7.3).

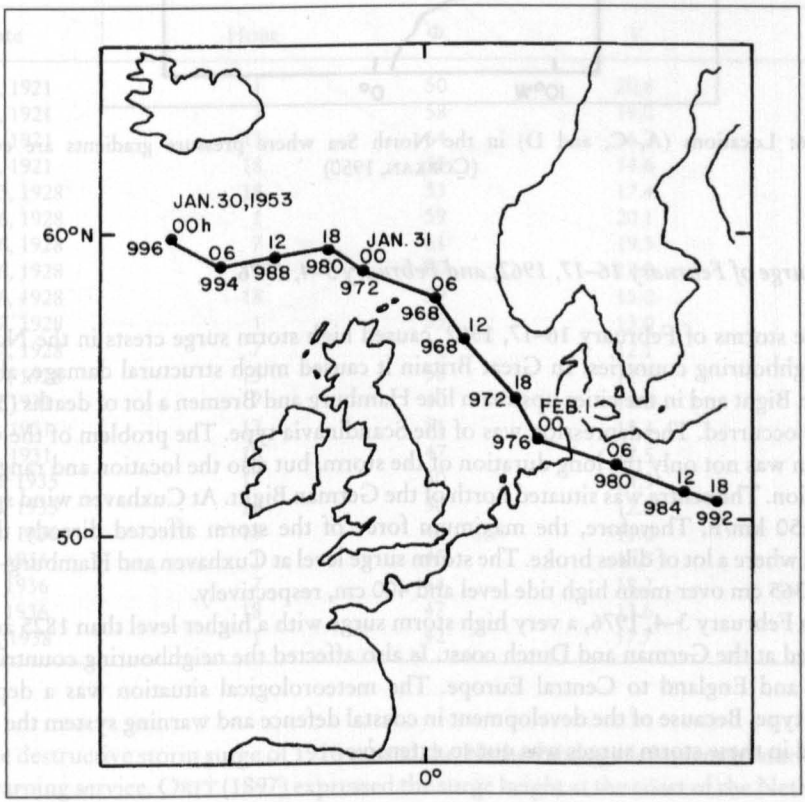


Fig. 5.25: Track of the storm of January 30–February 1, 1953 (pressure field in millibars).

The track of the storm and the central pressure are illustrated in Fig 5.25. For details on the meteorological conditions, see HAY and LAING (1954). ROSSITER (1954) studied this storm surge and also used the same pressure points (Fig. 5.26) and the same method as DOODSON (1924, 1929) and CORKAN (1948, 1950).

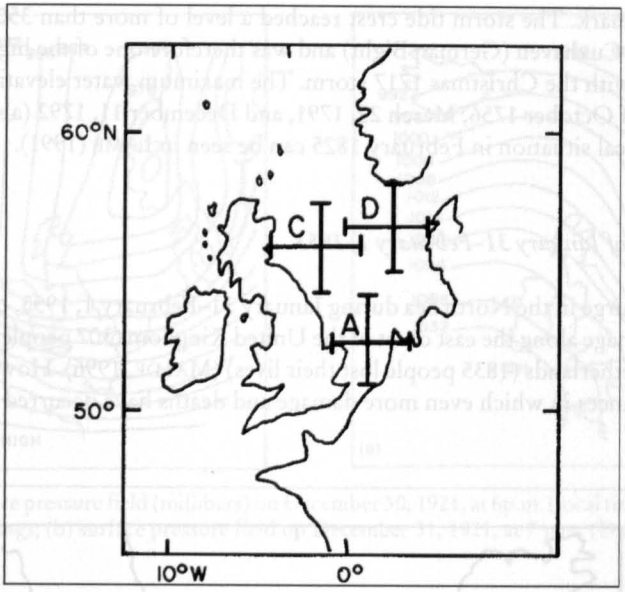


Fig. 5.26: Locations (A, C, and D) in the North Sea where pressure gradients are evaluated. (CORKAN, 1950)

*Storm surge of February 16–17, 1962, and February 3–4, 1976*

The storms of February 16–17, 1962, caused high storm surge crests in the North Sea and neighbouring countries. In Great Britain it caused much structural damage, along the German Bight and in the cities upstream like Hamburg and Bremen a lot of deaths (340) and damage occurred. The depression was of the Scandinavia type. The problem of the weather situation was not only the long duration of the storm, but also the location and range of the depression. The centre was situated north of the German Bight. At Cuxhaven wind speed reached 150 km/h. Therefore, the maximum force of the storm affected directly the Elbe estuary, where a lot of dikes broke. The storm surge level at Cuxhaven and Hamburg-St Pauli rose to 365 cm over mean high tide level and 400 cm, respectively.

On February 3–4, 1976, a very high storm surge with a higher level than 1825 and 1962 happened at the German and Dutch coast. Is also affected the neighbouring countries from Ireland and England to Central Europe. The meteorological situation was a depression Jutland type. Because of the development in coastal defence and warning system the damage incurred in these storm surges was not so extensive.

*Surges in the German Bight and at the coast of the Netherlands*

SCHALKWIJK (1947) gave a comprehensive analysis of storm surges at the coast of the Netherlands until 1940, and the following discussion is based on his paper.

Table 5.3: International and Bleck equivalents of the Beaufort Scale. (SCHALKWIJK, 1947)

| Degrees Beaufort | International equivalent of wind speed ($m \cdot s^{-1}$) | Bleck equivalent of wind speed ($m \cdot s^{-1}$) | Degrees Beaufort | International equivalent of wind speed ($m \cdot s^{-1}$) | Bleck equivalent of wind speed ($m \cdot s^{-1}$) |
|---|---|---|---|---|---|
| 1 | 1.1 | 1.8 | 7 | 13.8 | 17.4 |
| 2 | 2.5 | 4.4 | 8 | 16.7 | 20.0 |
| 3 | 4.3 | 7.0 | 9 | 19.9 | 22.6 |
| 4 | 6.3 | 9.6 | 10 | 23.3 | 25.2 |
| 5 | 8.6 | 12.2 | 11 | 27.1 | 27.8 |
| 6 | 11.1 | 14.8 | 12 | >29.0 | >29.0 |

Table 5.4: Values of deviation angle $\Psi$ (degrees), wind speed V ($m \cdot s^{-1}$), and surge $\eta$ (cm) for the storm surges at the Netherlands coast. (SCHALWIJK, 1947)

| Date | Hour | $\Phi$ | $V$ | $\eta$ |
|---|---|---|---|---|
| Jan. 19, 1921 | 1 | 50 | 20.8 | 155 |
| Jan. 19, 1921 | 7 | 58 | 19.0 | 134 |
| Jan. 19, 1921 | 13 | 64 | 16.7 | 99 |
| Jan. 19, 1921 | 18 | 55 | 14.6 | 70 |
| Nov. 25, 1928 | 18 | 53 | 17.4 | 115 |
| Nov. 26, 1928 | 1 | 59 | 20.1 | 172 |
| Nov. 26, 1928 | 7 | 61 | 19.3 | 142 |
| Nov. 26, 1928 | 13 | 60 | 17.0 | 105 |
| Nov. 26, 1928 | 18 | 59 | 15.0 | 86 |
| Nov. 27, 1928 | 1 | 55 | 13.0 | 74 |
| Nov. 27, 1928 | 7 | 54 | 12.1 | 71 |
| Nov. 27, 1928 | 13 | 58 | 12.3 | 71 |
| Jan. 17, 1931 | 7 | 40 | 18.9 | 133 |
| Jan. 17, 1931 | 13 | 51 | 18.4 | 139 |
| Jan. 18, 1931 | 18 | 47 | 12.5 | 45 |
| Oct. 30, 1935 | 13 | 50 | 14.3 | 71 |
| Oct. 20, 1935 | 18 | 50 | 12.4 | 44 |
| Oct. 20, 1936 | 18 | 46 | 11.0 | 54 |
| Dec. 1, 1936 | 1 | 43 | 18.3 | 141 |
| Dec. 1, 1936 | 7 | 44 | 18.2 | 176 |
| Dec. 2, 1936 | 18 | 47 | 13.6 | 71 |
| Jan. 30, 1938 | 1 | 42 | 17.7 | 119 |

The destructive storm surge of 1916 caused the Netherlands government to start a storm surge warning service. ORTT (1897) expressed the surge height at the coast of the Netherlands through

$$\eta = KR + R_b(76 - p) \tag{5.18}$$

where $\eta$ is the storm surge (centimetres), K is a factor representing the influence of the strength of the wind, R is a factor representing the wind direction, $R_b$ is a factor representing the effect of atmospheric pressure, and p is the atmospheric pressure (centimetres of mercury).

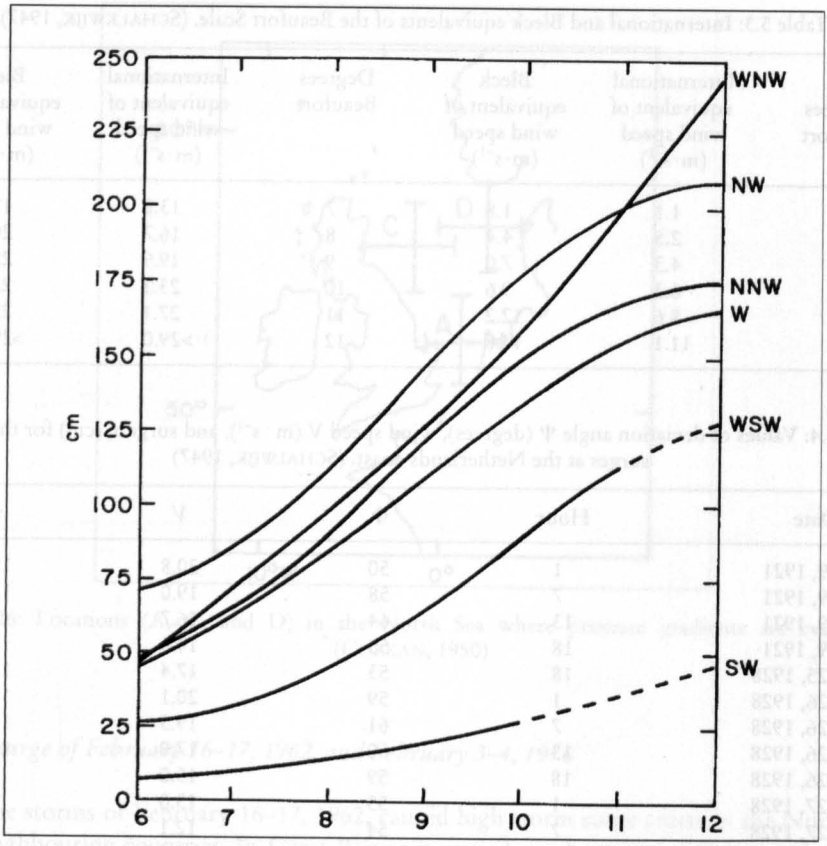


Fig. 5.27: Storm surge versus wind speed at Hook of Holland. Schalkwijk, based on earlier studies by a Netherlands Government committee, summarized these results. (SCHALKWIJK, 1947)

For the Netherlands coast

$$K = 0.14V^2 \tag{5.19}$$

where, V is the wind velocity. SCHALKWIJK (1947) gave tables of R and $R_b$ for various wind directions. ORTT (1897) showed that large surges are produced by W to WNW winds and the smallest surges are produced by E to ESE winds and, in general, there is a lag of about 6 h between the wind and the surge.

The committee (Rotterdamsche Waterweg) established by the Netherlands government in 1920 studied 19 storm surges for the period 1887–1917. They related the surges to the wind but ignored time lag and atmospheric pressure gradients. The results of this study are shown in Fig. 5.27 (the Beaufort Scale is explained in Table 5.3). One interesting result is that the winds over the southern part of the North Sea are more relevant than the local winds in generating these surges.

$$\eta = \frac{aV^2 L \cos\psi}{H} \tag{5.20}$$

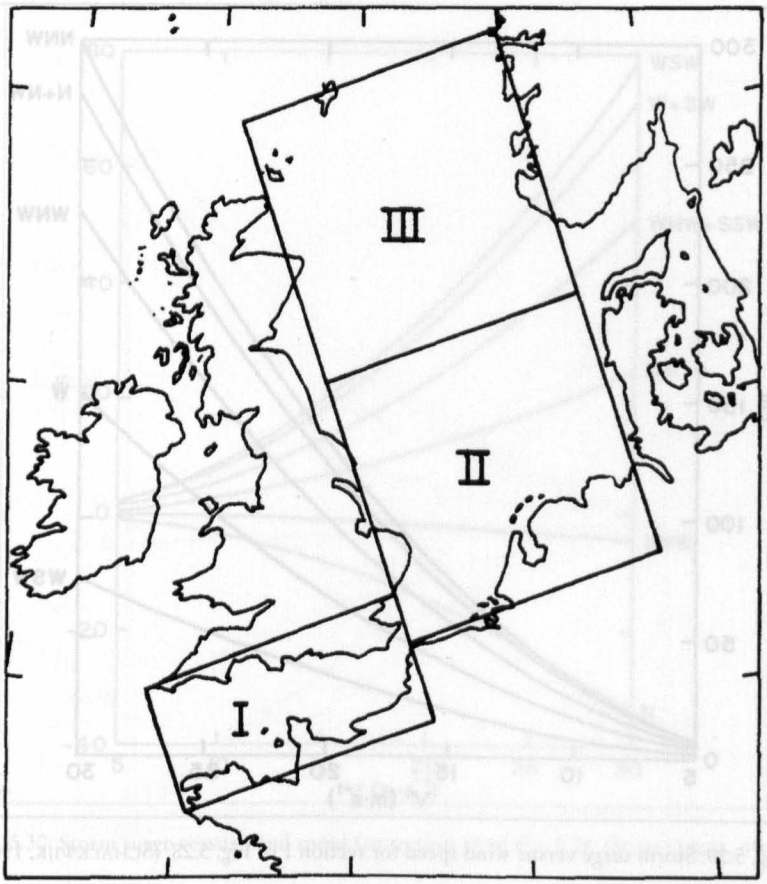


Fig. 5.28: Three sections of the North Sea for which the storm surge study was made. (SCHALKWIJK, 1947)

where, a = 0.0036, V is the wind velocity (metres per second), $\eta$ is the surge (centimetres), H is the water depth (metres), L is the channel length (kilometres), and $\Psi$ is the angle between the wind direction and the channel axis. COLDING (1880, 1881) used a slightly different formula:

$$\eta = \frac{0.048 L V^2 \cos^2 \psi}{H} \tag{5.21}$$

This formula was successfully used to hindcast the storm surges of November 12–14, 1872, on the Danish coast and in the Baltic Sea.

Based on several studies (MAZURE, 1937; PALMEN, 1932) and verified by more recent research (GÖNNERT, 1999), the following results can be deduced for the Southern North Sea coast. The time lag between the wind and surge is 3–6 h. The most effective wind direction in generating surges is NW. The relationship between the surge and atmospheric pressure gradient is related to the structure and movement of the pressure field. The surge in the southern part of the North Sea is closely related to the average wind over the whole North

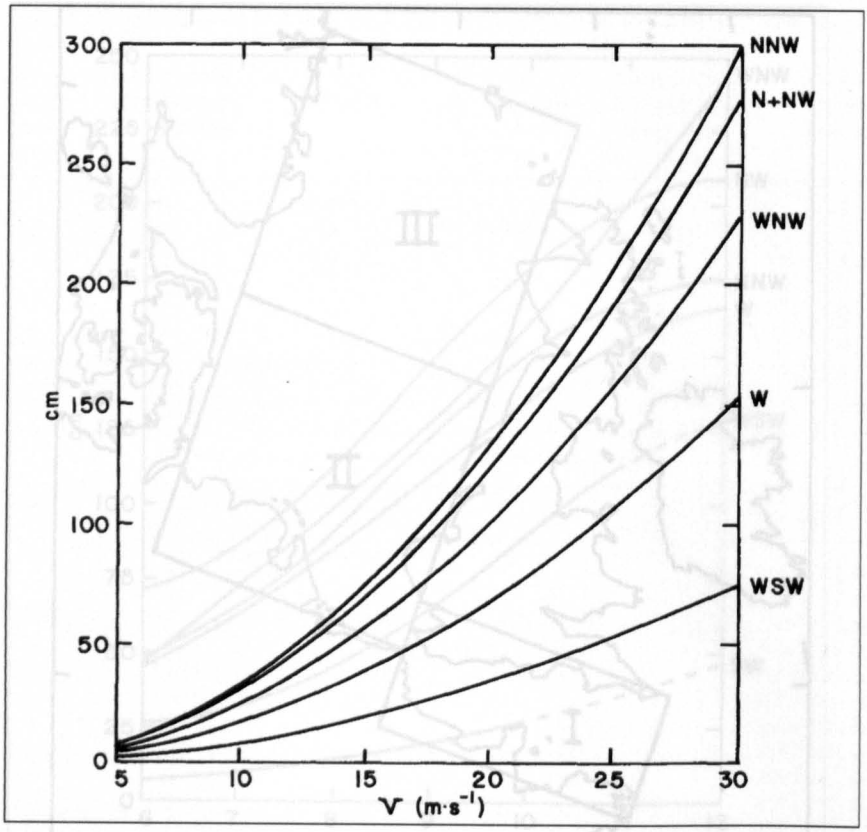


Fig. 5.29: Storm surge versus wind speed for section 1 of Fig. 5.28. (SCHALKWIJK, 1947)

Sea. Along the coast of the Netherlands, the variations in the surge south of Helder are not significant.

SCHALKWIJK (1947) developed an analytical theory applicable to an enclosed sea, a partly open sea, a bay of uniform depth, and a bay of variable depth. He included the influence of the Dover Strait and inhomogenities and time variations in the wind field. He selected 14 surges for the period 1920–40. These cases with factors $\Psi$, V, and $\eta$ (from eq. 5.20) are listed in Table 5.4 (in this table, 22 cases appear because some cases are broken down into separate events).

Schalkwijk's 1947 study showed that the average deviation of the wind from the isobars is 8°, which is somewhat smaller than the values given by other authors, which ranged from 13 to 20°. He also found that on the rising part of the curve the time lag between wind and surge is 2.2 h whereas on the falling part of the curve the lag is 2.8 h.

The three separate regions of the North Sea for which this study is made are shown in Fig. 5.28. The results for sections 1, 11, and 111 are summarized in Fig. 5.29, 5.30, and 5.31, respectively. The results for the whole North Sea are shown in Fig. 5.32. Comparison of Fig. 5.27 and 5.32 shows that differences exist between the results of SCHALKWIJK'S (1947) study and the Netherlands government committee's earlier study.

Schalkwijk also examined the surges in the East Scheldt Estuary. The results for this case are summarized in Fig. 5.33.

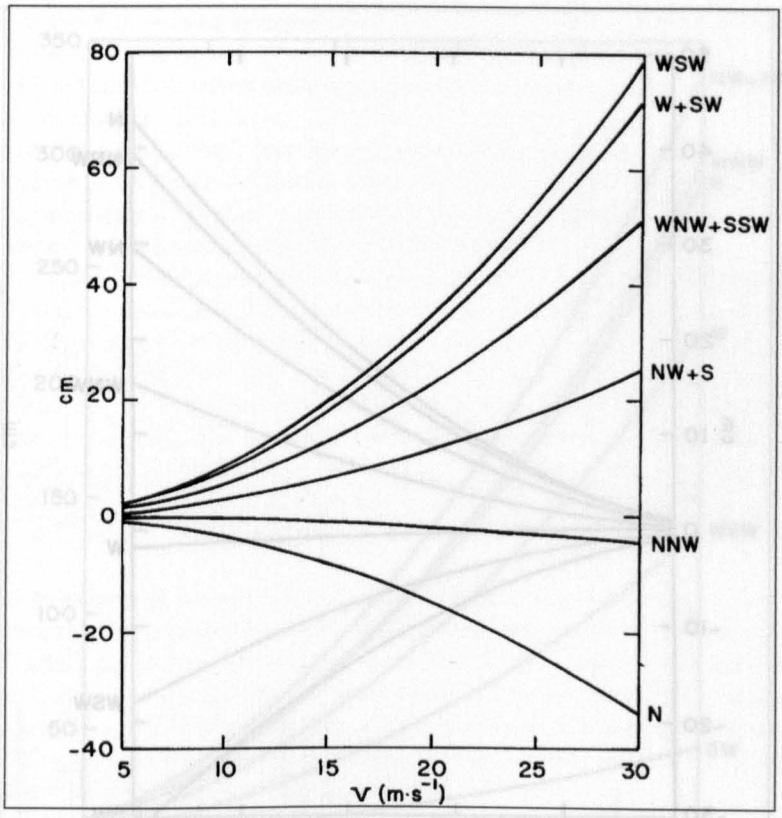


Fig. 5.30: Storm surge versus wind speed for section 11 of Fig. 5.28. (SCHALKWIJK, 1947)

*Special Meteorological Influence on Storm Surges in the North Sea (Atmospheric Pressure Gradient / External Surges)*

TIMMERMAN (1975) showed that storm surges can be generated in the North Sea not only by westerly winds over the continental shelf but also by atmospheric pressure gradients near the area of transition from deep to shallow water. He mentioned that this effect is usually disregarded in storm surge calculations. For the storm surge of February 16, 1962, the atmospheric pressure gradient effect was very significant. KOOPMAN (1963) studied the surge of October 16–17, 1963. In this case, atmospheric pressure gradients were also a significant factor. Other important storm surge dates are December 11–15, 1972, and January 29, 1974, where atmospheric pressure gradients were important (TIMMERMAN, 1975).

Until now the issue of externally generated surges in the German Bight has not been adequately addressed. External surges originated in deep water in the open sea (SCHMITZ 1965). Their genesis in the North Sea depends upon the speed of movement and the pressure deficit of the extratropical cyclone travelling over the Atlantic Ocean. Note that the amplitude of this external surge is completely independent of the local meteorological conditions over the German Bight. These external surges travel from Aberdeen to Immingham, then through the Straits of Dover to arrive at the Dutch and German coasts.

KOOPMANN (1962) investigated external surges for the period of 1956–1960; SCHMITZ et

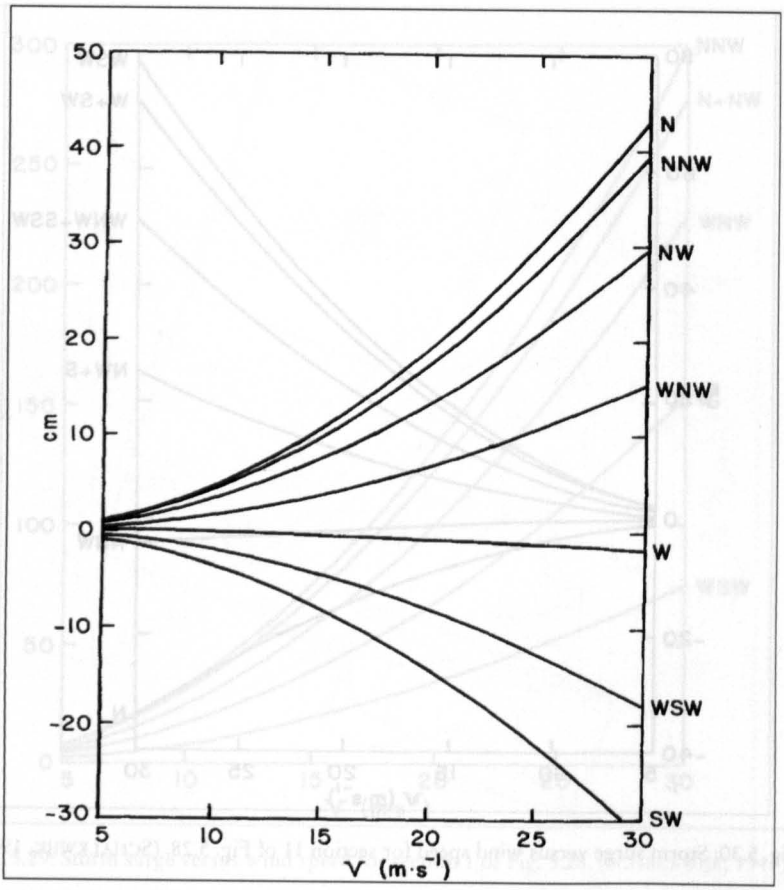


Fig. 5.31: Storm surge versus wind speed for section III of Fig. 5.28. (SCHALKWIJK, 1947)

al. (1988) specified the meteorological situation. GÖNNERT (1999) investigated this phenomenon in the North Sea and its influence on the normal tide level and storm surge level for the period of 1971–1995. The research showed that at Cuxhaven a peak level of 10 cm to 108 cm (Fig. 5.35) can occur. The peak external surge needs not coincide with the high tide at the coast. Normally it is disturbed over the entire tide, mostly 3 h before high tide and 3 h after high tide. External surges occur from October to March, sometimes also in August, September and April (Fig. 5.34). This is the same period as the storm surge period in the German Bight. Furthermore, for every 4$^{th}$ to 5$^{th}$ storm surge case an external surge influences the water level, till now mostly before and after the high water level. Because of the fact that external surges at Cuxhaven have a long duration they influence the storm surge. Till now, the peak external surge never coincided with the local surge peak.

*Storm surges in the Irish Sea*

Storm surge studies for the Irish Sea are fewer than those for the North Sea, although large surges occur in the Irish Sea. Surges in the Irish Sea originate in the Atlantic (AMIN, 1985). LENNON (1963) examined the meteorological situations associated with large surges

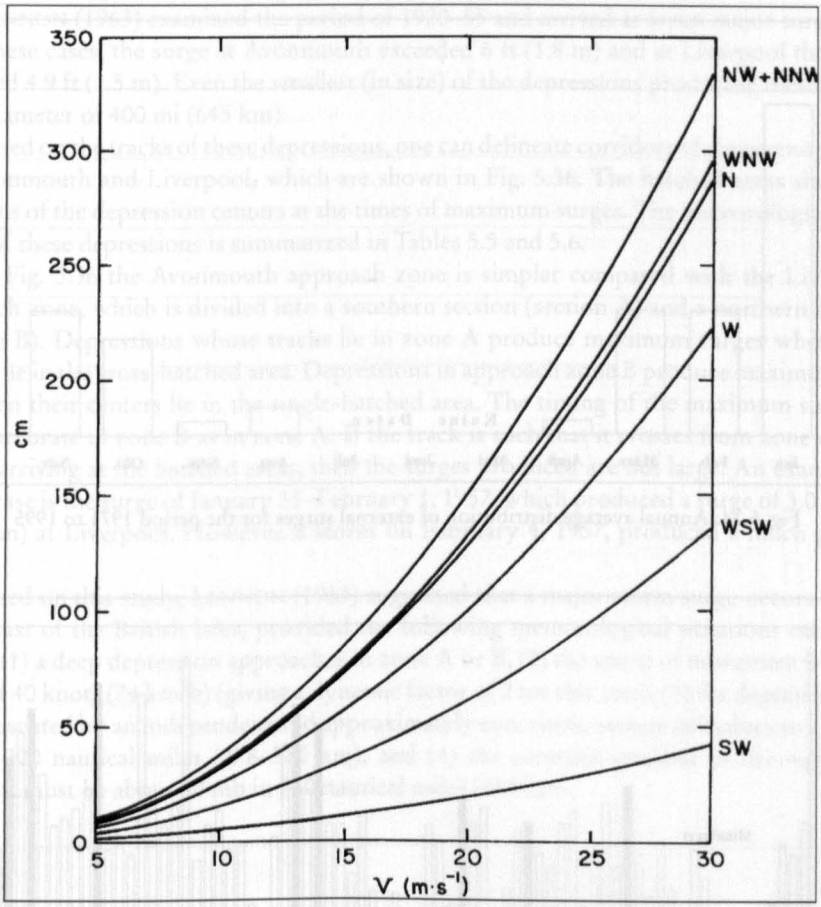


Fig. 5.32: Storm surge versus wind speed for the entire North Sea based on Schalkwijk's results (SCHALKWIJK, 1947)

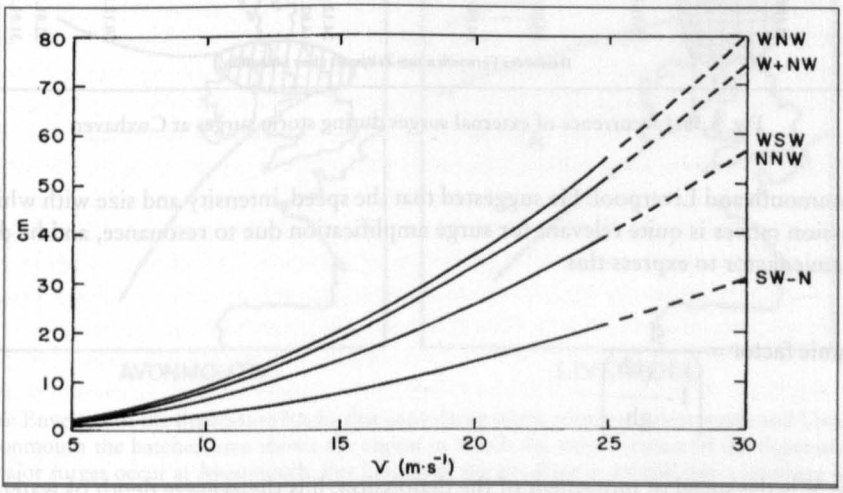


Fig. 5.33: Storm surge versus wind speed for the East Scheldt Estuary. (SCHALKWIJK, 1947)

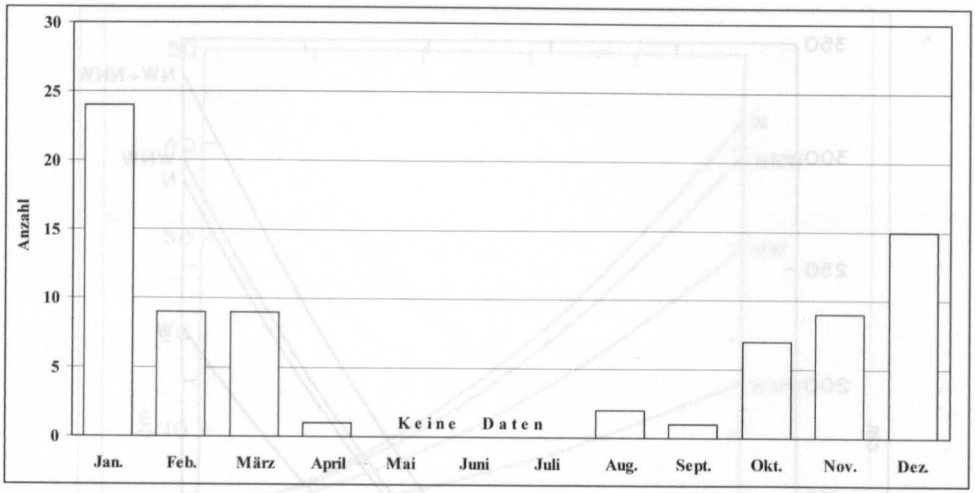


Fig. 5.34: Annual average distribution of external surges for the period 1971 to 1995

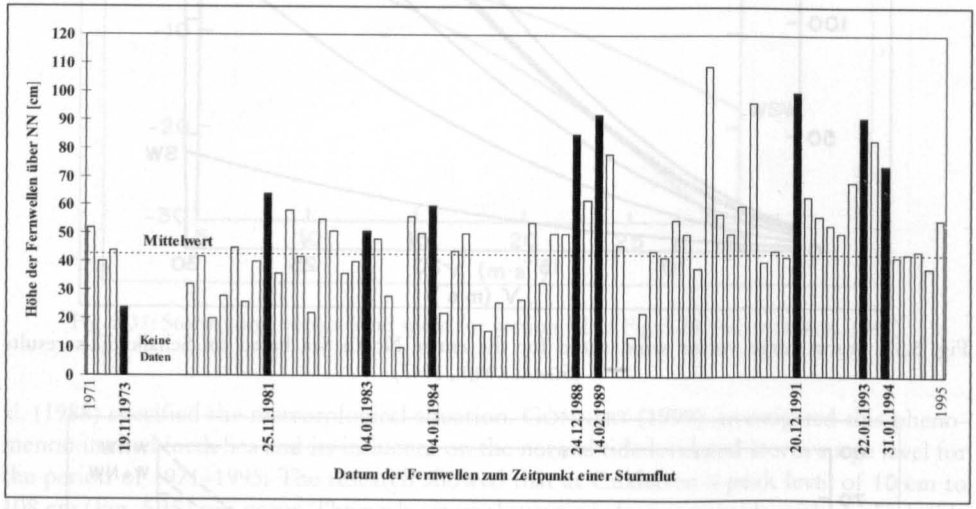


Fig. 5.35: Occurrence of external surges during storm surges at Cuxhaven

at Avonmouth and Liverpool. He suggested that the speed, intensity and size with which the depression moves is quite relevant for surge amplification due to resonance, and he defined a dynamic factor to express this:

$$\text{Dynamic factor} = \frac{1}{\left(1 - \frac{V^2}{gh}\right)} \qquad (5.22)$$

where, V is the speed of movement of the depression, h is the average depth of water, and g is the acceleration of gravity.

LENNON (1963) examined the period of 1920–55 and arrived at seven major surges; i.e. in all these cases, the surge at Avonmouth exceeded 6 ft (1.8 m) and at Liverpool the surge exceeded 4.9 ft (1.5 m). Even the smallest (in size) of the depressions producing these surges has a diameter of 400 mi (645 km).

Based on the tracks of these depressions, one can delineate corridors of dangerous zones for Avonmouth and Liverpool, which are shown in Fig. 5.36. The hatched areas show the positions of the depression centers at the times of maximum surges. The meteorological character of these depressions is summarized in Tables 5.5 and 5.6.

In Fig. 5.36 the Avonmouth approach zone is simpler compared with the Liverpool approach zone, which is divided into a southern section (section A) and a northern section (section B). Depressions whose tracks lie in zone A produce maximum surges when their centers lie in the cross-hatched area. Depressions in approach zone B produce maximum surges when their centers lie in the single-hatched area. The timing of the maximum surges is not as accurate in zone B as in zone A. If the track is such that it crosses from zone A to B before arriving at the hatched areas, then the surges produced are not large. An example of such a case is the surge of January 31–February 1, 1957, which produced a surge of 3.0 ft (less than 1 m) at Liverpool. However, a storm on February 4, 1957, produced a much greater surge.

Based on this study, LENNON (1963) suggested that a major storm surge occurs on the west coast of the British Isles, provided the following meteorological situations occur together: (1) a deep depression approaches in zone A or B, (2) the speed of movement is of the order of 40 knots (74 km/h) (giving a dynamic factor of 2 for this area), (3) the depression can be represented by an independent and approximately concentric system of isobars to a radius of 150–200 nautical miles (278–370 km), and (4) the pressure gradient in the right rear quadrant must be about 30 mb in 250 nautical miles (463 km).

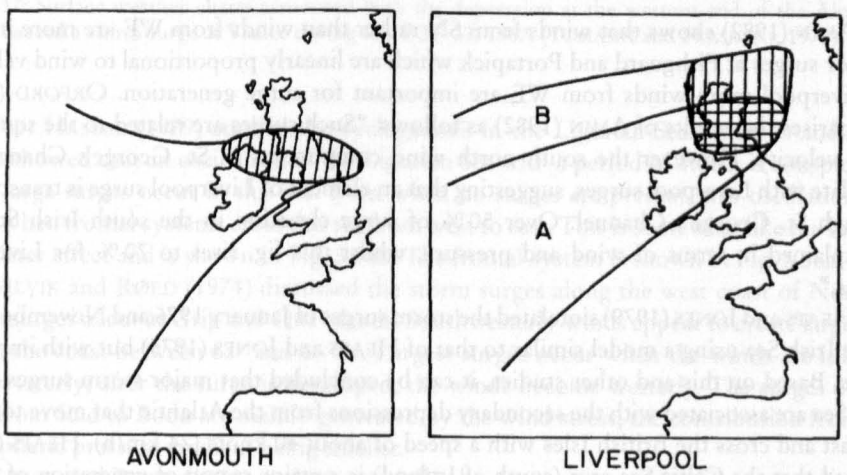


Fig. 5.36: Envelope of the depression tracks that cause large storm surges at Avonmouth and Liverpool. For Avonmouth the hatched area shows the region in which the storm centers of the depressions lie when major surges occur at Avonmouth. For Liverpool the envelope is divided into a southern section (A) and a northern section (B). The cross-hatched and single-hatched areas are, respectively, associated with zones A and B. (LENNON, 1963)

Table 5.5: Some details of the depressions that caused large storm surges at Avonmouth. (LENNON, 1963)

| Date | Speed of movement (km/h) | Location of depression center at time of maximum surge | Radius of depression (km) | Pressure gradient (mb) over 463 km |
|---|---|---|---|---|
| Jan. 12, 1930 | 87 | Irish Sea | 241 | 24 |
| Sept. 17, 1935 | 74 | Irish Sea | 333 | 32 |
| Jan. 9, 1936 | 78 | Ireland | 296 | 34 |
| Nov. 23, 1938 | 65 | South Scotland | 389 | 26 |
| Mar. 16, 1947 | 72 | North England | 333 | 26 |
| Apr. 23, 1947 | 74 | North Ireland | 370 | 28 |
| Nov. 30, 1954 | 59 | East England | 333 | 38 |

Table 5.6: Some details of the depressions that caused large storm surges at Liverpool, U.K. (LENNON, 1963)

| Date | Speed of movement (km/h) | Location of depression center at time of maximum surge | Radius of depression (km) | Pressure gradient (mb) over 463 km |
|---|---|---|---|---|
| Jan. 9, 1936 | 78 | Ireland | 296 | 34 |
| Oct. 27, 1936 | 69 | North of Scotland | 278 | 32 |
| Nov. 23, 1938 | 65 | North England | 389 | 26 |
| Jan. 25, 1944 | 65 | West Scotland | 482 | 23 |
| Dec. 2, 1946 | 70 | Off West Scotland | 333 | 23 |
| Apr. 23, 1947 | 74 | North Ireland | 370 | 28 |
| Nov. 30, 1954 | 59 | East Ireland | 296 | 34 |

AMIN (1982) shows that winds from SN rather than winds from WE are more important for surges at Fishguard and Portapick which are linearly proportional to wind velocity. At Liverpool more winds from WE are important for surge generation. ORFORD (1989) summarises the results of AMIN (1982) as follows: "Such surges are related to the square of wind velocity. However the south north wind components in St. George's Channel do correlate with Liverpool surges, suggesting that an element of Liverpool surge is transported through St. George's Channel. Over 50 % of surge elevation in the south Irish Sea can be explained in terms of wind and pressure, whilst this fig. rises to 70 % for Liverpool surges."

HEAPS and JONES (1979) simulated the storm surges of January 1976 and November 1977 in the Irish Sea using a model similar to that of HEAPS and JONES (1975) but with improvements. Based on this and other studies, it can be concluded that major storm surges in the Irish Sea are associated with the secondary depressions from the Atlantic that move towards the east and cross the British Isles with a speed of about 40 knots (74 km/h). HEAPS (1965) showed that the Celtic Sea area (south of Ireland) is a major region of generation of storm surges.

*Meteorological conditions associated with storm surges in other parts of Europe*

Storm surges occur on the northern part of the Atlantic coast of Portugal. MORAIS and ABECASIS (1975) discussed the storm surge that occurred on Leixoes during January 16–17, 1973.

In the city of Venice at the Adriatic Sea and the Ligurian Sea storm surges occur. The Ligurian Sea is a region of cyclogenesis. Depressions from the Atlantic reaching this sea are intensified here and then travel eastwards. Southeast winds appear to generate the greatest surges in the Venice area. The surface weather charts for two time slots during the surge of April 21–22, 1967, are shown in Fig. 5.37. Note the depression at the western end of the Alps.

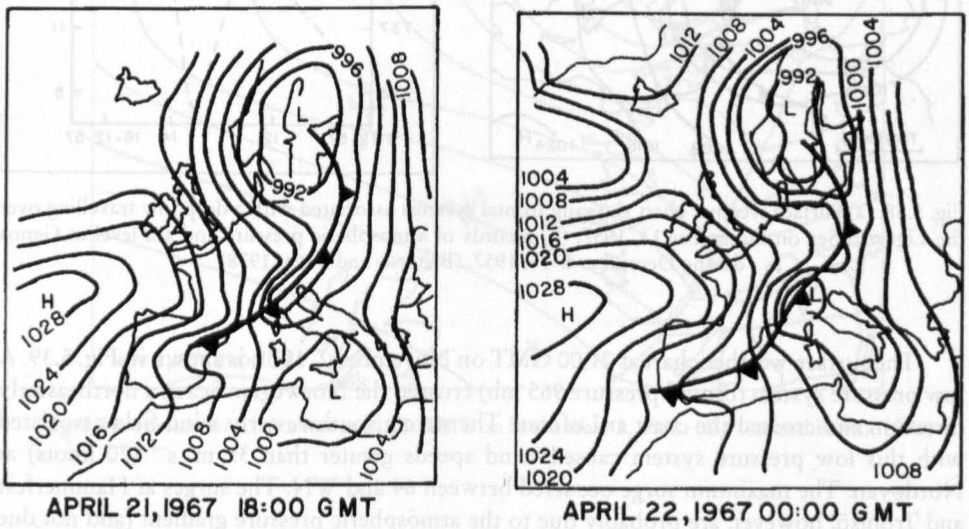


Fig. 5.37: Surface weather charts associated with the depression at the western end of the Alps that caused a storm surge at Venice during April 21–22, 1967. (TOMASIN and FRASETTO, 1979)

VAN HAMME (1979) studied the cyclogenesis in the Ligurian Sea. BASANO and PAPA (1978) showed that an oscillation of the Ligurian Sea with a period of 3.66 h is conspicuous when large surges occur in this sea. Even when no surges are present, this oscillation can occur when frontal systems cross this sea from west to east. This is somewhat like the inverse barometer effect and is shown in Fig. 5.38b. The frontal system is shown in Fig. 5.38a.

GJEVIK and RØED (1974) discussed the storm surges along the west coast of Norway. Severe surges occur at Grip and Ona islands. Southwesterly winds appear to create large surges on the coast between 62° and 66° N. Largest surges occur when the winds are initially southwesterly; after the surge is developed, the winds become westerly. The surges on the coast from Stad to Bodø are mainly generated by the wind stress, the contribution from the atmospheric pressure gradient being smaller.

GJEVIK and RØED (1974) studied especially three storm surges: (1) November 2, 1971, (2) December 30, 1972, and (3) December 31, 1972. The second and third are typical surges that frequently occur along the coast between 62 and 68° N. The first one is exceptional because the peak surge coincided with the peak tide along the coast between Sula and Sandnessjøen.

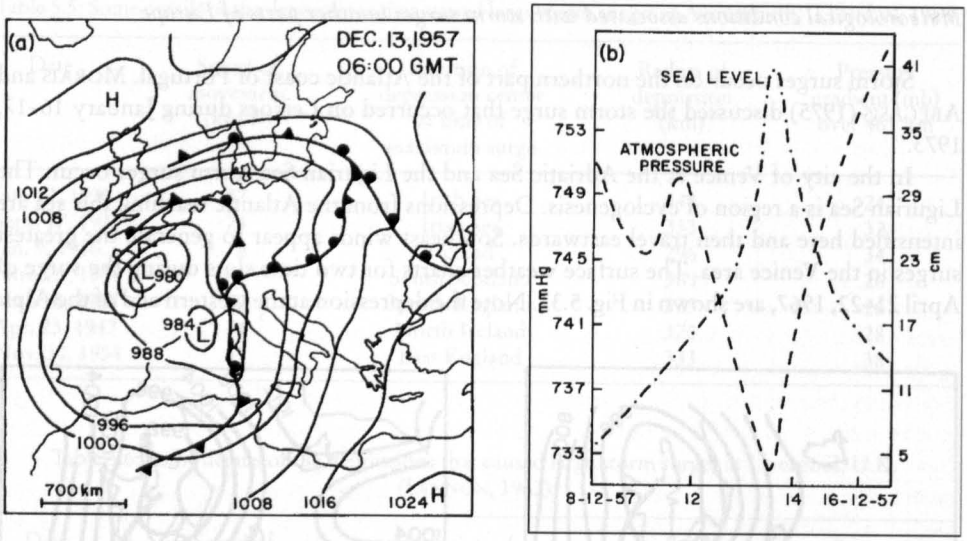


Fig. 5.38: (a) Surface weather chart showing frontal systems associated with a deep low travelling over the Ligurian Sea on December 13, 1957; (b) records of atmospheric pressure and sea level at Genoa during December 8–16, 1957. (BASANO and PAPA, 1978)

The surface weather chart at 21:00 GMT on November 2, 1971, is shown in Fig. 5.39. A low pressure system (central pressure 965 mb) crossed the Norwegian Sea in a northeasterly direction and crossed the coast at Lofoten. The strong southwesterly wind field associated with this low pressure system caused wind speeds greater than 35 m. $s^{-1}$ (70 knots) at Nordøyan. The maximum surge occurred between 64 and WN. The surges at Hammerfest and Tromsö, however, are probably due to the atmospheric pressure gradient (and not due to wind stress) because these two stations are located to the north of the wind field associated with this system.

GJEVIK and RØED (1974) presented detailed surface weather charts for the three surge cases considered here. They showed that the meteorological situation was somewhat similar for cases 1 and 3. The peak of the wind field moved with an average speed of about 25 m $s^{-1}$. These authors used the following values of drag coefficients for different wind speeds:

$$C_D = \begin{cases} 2.5 \times 10^{-3} & \text{for } 25 \text{ m s}^{-1} \\ 3.0 \times 10^{-3} & \text{for } 30 \text{ m s}^{-1} \\ 3.5 \times 10^{-3} & \text{for } 35 \text{ m s}^{-1} \end{cases}$$

In the analytical model for the surges on the Norwegian coast, these authors considered surge development due to a wind field moving along the coast. The following forms are assumed for the wind stress components and the pressure field:

$$\tau_{S_x} = \rho T_{0x} F(x,t) e^{-\alpha y}$$

$$\tau_{S_y} = \rho T_{0y} G(x,t) e^{-\beta y} \qquad (5.23)$$

$$P_0 = \text{cons tan t}$$

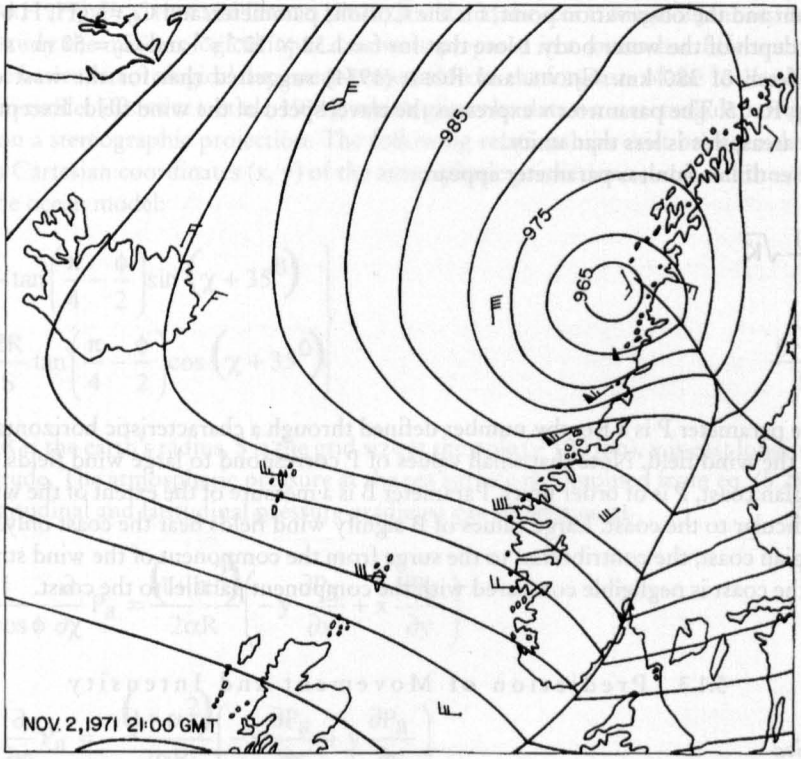


Fig. 5.39: Surface weather chart at 21:00 GMT on November 2, 1971. (GJEVIK and RØED, 1974)

for $t \geq 0$, where $T_{0x}$, $T_{0y}$, á, and â are constants and F and G are functions of x and t only. Here, ñ is the water density and the horizontal coordinate y is directed perpendicular to the coast. The following forms are prescribed for F and G:

$$\left.\begin{aligned} F &= e^{-K\left(x-u_0 t\right)^2} \\ G &= e^{-Kx^2} h(t) \end{aligned}\right\} \tag{5.24}$$

where, h (t) is a function of time and $0 \leq h(t) \leq 1$.

In the non-dimensionalisation of the equations of motion and continuity, the following two parameters appear:

$$R \equiv \frac{f}{C_0} x \tag{5.25}$$

where, R is a dimensionless wind fetch (i.e. distance between the initial position of the wind

$$v \equiv \frac{u_0}{C_0} \tag{5.26}$$

maximum and the observation point, f is the Coriolis parameter, and $C_0 = vgH$, H being the average depth of the water body. Note that for $f = 1.32 \times 10^{-4}\ s^{-1}$ and $C_0 = 50\ m \cdot s^{-1}$, R = 1 gives a fetch of 380 km. GJEVIK and RØED (1974) suggested that for the west coast of Norway, R < 5. The parameter v expresses the travel speed of the wind field. Except in very shallow areas, this is less than unity.
Two other dimensionless parameter appear:

$$P \equiv \frac{C_0}{f}\sqrt{K} \tag{5.27}$$

$$B \equiv \frac{\alpha C_0}{f} \tag{5.28}$$

The parameter P is a Rossby number defined through a characteristic horizontal length scale of the wind field. Note that small values of P correspond to large wind fields. For the Norwegian coast, P is of order unity. Parameter B is a measure of the extent of the wind field perpendicular to the coast. Large values of B signify wind fields near the coast only. For the Norwegian coast, the contribution to the surge from the component of the wind stress normal to the coast is negligible compared with the component parallel to the coast.

### 5.1.3 Prediction of Movement and Intensity

*North Sea*

DAVIES and FLATHER (1977) developed numerical models to study the storm surge of April 1–6, 1973. A coarse grid covered the whole northwestern European continental shelf and a fine grid covered only the North Sea. They determined the wind field from the geopotential height field extracted from 12-h weather charts for a period of 36 h. From the forecast data at 7 and 19 h, the geopotential height H of the 1000-mb level was used. The sea surface pressure p is calculated from

$$p = 1000 + \rho_a g H \tag{5.29}$$

where $\rho_a$. is the air density and g is gravity. From the pressure gradients the geostrophic wind was determined. The surface wind w is determined from the geostrophic wind w using the empirical relationship of HASSE and WAGNER (1971):

$$w = Aw + B \tag{5.30}$$

where, A = 0.56 and B has a range of values depending on atmospheric stability. The above formula is valid when w and w are in meters per second. FLATHER and DAVIES (1975, 1976) used the above formula with $B = 2.4\ m \cdot s^{-1}$. This gave reasonable results for the storm surge of March 26–30, 1972, but gave unsatisfactory results for the surge of April 1–6, 1973.

There was a series of storm surges in the North Sea during the period November 4–December 18, 1973. DAVIES and FLATHER (1978) simulated these numerically, again using a coarse model for the whole shelf and a fine model for the North Sea alone. The meteorological input data were obtained in a manner similar to their earlier study (DAVIES and

FLATHER, 1977). FLATHER and DAVIES (1978) simulated the storm surge of January 2–4, 1976. In this study the meteorological input data were prepared in a somewhat different manner.

The basic meteorological data were extracted from the forecasts of the 10-level Bushby-Timpson model (BENWELL et al., 1971), which gives the data on a rectangular array of grid points on a stereographic projection. The following relationships exist between the dimensionless Cartesian coordinates (x, y) of the atmospheric prediction model and the coordinates of the ocean model:

$$\left.\begin{aligned} x &= \frac{2R}{S}\tan\left(\frac{\pi}{4}-\frac{\phi}{2}\right)\sin\left(\chi+35^0\right) \\ y &= -\frac{2R}{S}\tan\left(\frac{\pi}{4}-\frac{\phi}{2}\right)\cos\left(\chi+35^0\right) \end{aligned}\right\} \tag{5.31}$$

where, R is the earth's radius, S is the grid size at the pole (~ 100 km), $\chi$ is east longitude, and $\phi$ is latitude. The atmospheric pressure at the sea surface is computed from eq. (5.29). Then, the longitudinal and latitudinal pressure gradients can be written as

$$P = \frac{1}{R\cos\phi}\frac{\partial}{\partial\chi}P_a = \frac{\left(1+\alpha^2\right)}{2\alpha R}\left(-y\frac{\partial P_a}{\partial x}+x\frac{\partial P_a}{\partial y}\right) \tag{5.32}$$

$$Q = \frac{1}{R}\frac{\partial}{\partial\phi}P_a = -\frac{\left(1+\alpha^2\right)}{2\alpha R}\left(-x\frac{\partial P_a}{\partial x}+y\frac{\partial P_a}{\partial y}\right)$$

where,

$$\alpha^2 \equiv \frac{S^2\left(x^2+y^2\right)}{4R^2} \tag{5.33}$$

The eastward and northward components of the geostrophic wind are

$$\hat{w}_x = -\left[\frac{\left(1+\alpha^2\right)}{\left(1-\alpha^2\right)}\right]\frac{Q}{2\omega\rho_a} \tag{5.34}$$

$$\hat{w}_\phi = -\left[\frac{\left(1+\alpha^2\right)}{\left(1-\alpha^2\right)}\right]\frac{P}{2\omega\rho_a}$$

where, $\omega$ is the angular velocity of the earth's rotation. A linear relationship was assumed between the geostrophic wind ^wand the surface wind w:

$$\left.\begin{aligned} w_\chi &= \left(\hat{w}_\chi\cos\delta-\hat{w}_\phi\sin\delta\right)\left(A\hat{w}+B\right)/\hat{w} \\ w_\phi &= \left(\hat{w}_\chi\sin\delta-\hat{w}_\phi\cos\delta\right)\left(A\hat{w}+B\right)\hat{w} \end{aligned}\right\} \tag{5.35}$$

where, δ is the angular deviation between the geostrophic and surface winds and a and b are empirical constants, as in the earlier model of DAVIES and FLATHER (1977).

FISCHER (1979) developed a combined atmosphere-ocean model to simulate the storm surge of January 3, 1976, in the North Sea. The atmospheric model has a grid size of 1.4° latitude and 2.8° longitude and has eight levels in the vertical. The ocean model has a 22-km grid. The surface wind calculated from the atmospheric model was used to determine the wind stress $\tau_0$ in the following manner:

$$|\tau_0| = \rho_a C_D \gamma^2 |v_0| v_0 \tag{5.36}$$

where, $v_0$ is the wind at the anemometer level, $C_D$ is the drag coefficient, $\gamma = 1$ (when observed winds were used) and $\gamma = 1.55$ (when predicted winds were used), and $\rho_a$ is the density of air. Wind at the anemometer level is

$$|v_0| = 0.54 - 0.012\Delta\theta |v_{g0}| + 1.68 - 0.015\Delta\theta \tag{5.37}$$

where, the cross-isobar angle is 8° for an unstable atmosphere and 213° for the very stable case and è is the potential temperature. The drag coefficient is

$$C_D = \left(1.18 + 0.016|v_{g0}|\right) \times 10^{-3} \tag{5.38}$$

where, $v_{g0}$ is in meters per second. Here, subscript 0 denotes the water surface.

The storm surge of January 11–12, 1978 (TOWNSEND, 1979), was the worst on record after the January 1953 surge in the North Sea. This surge was simulated successfully by using empirical methods (TOWNSEND 1979).

*Storm surges in the Irish Sea*

The next passage follows closely ORFORD (1989). HEAPS and JONES (1979, 1981) and FLATHER (1981) use running numerical models of Irish Sea conditions in which the dynamics of flow and velocity were addressed using first principle hydrodynamic equations to predict surge elevations. FLATHER (1987) give an example of this type of approach in which observed surge were modelled and predictive results indicate close approximation to observed data.

"He used a numerical model based on non-linear, depth-averaged hydrodynamical equations (FLATHER and PROCTER, 1983) to determine surface elevation, plus north and east components of current velocity, and predicted the water elevation due to combined tide and surge for a number of known parameterized storms over NW Europe (53 days of storm activity). Sea level elevation was obtained for grid points of size 0.5° lat.; 0.33° long. at hourly intervals through the storms. A re-run of the model without meteorological forcing allowed the prediction of tidal elevation per se. The differences between the two runs indicate the surge component. Surge values were calibrated against coastal data from PUGH and VASSIE (1979) for 50 year surge elevation status. The grided data was then interpolated using the nearest reference coastal sites that Pugh and Vassie cite. The resulting prediction of 50 year surge elevation was contoured as increments to the maximum tidal elevation in order to indicate the extreme 50 year height of water level above O.D.

Surge heights are 1–2 m on the west U.K. coast and 1.0–1.5 m on the Irish coast. Highest surge are predicted around the northeast margins of the basin. The joint probability of high

spring and 50 year surge achieves a sea-level elevation commensurate with the 100 year maximum seal-level elevation."

HEAPS and JONES (1975) used a two-and-a-half-dimensional model (they called it a three-dimensional model) of the Irish Sea to simulate storm surges for the period January 10–18, 1965. The first storm surge of this period was associated with a storm of January 13–14. A deep depression moved from the Atlantic with a speed of about 35 knots (65 km. h') on a track (towards the east) lying to the north of Ireland. Fronts from this depression swept across the Irish Sea and winds veered from south to west. The second storm (January 16–18) was associated with a large slow-moving depression to the north of Scotland.

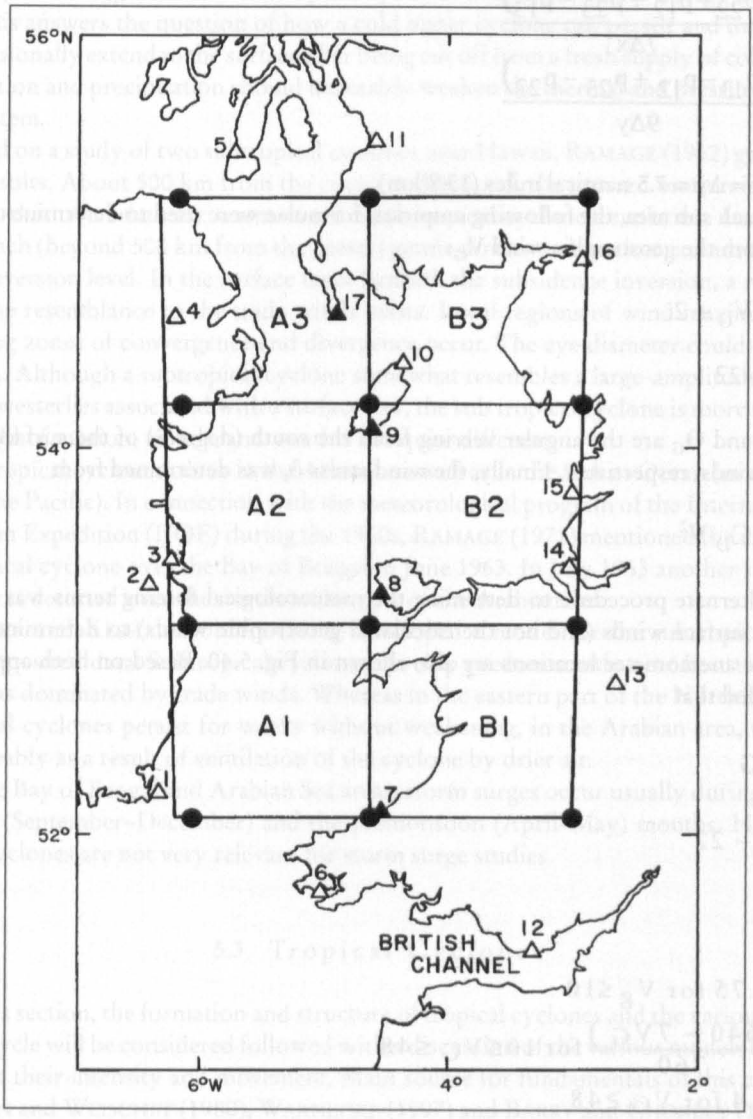


Fig. 5.40: Irish Sea model with six sub areas for determining atmospheric pressure gradients and wind stress. (HEAPS and JONES, 1975)

The following meteorological forcing terms were included in the numerical model: atmospheric pressure gradients over the water surface determined at 3-h intervals from pressure records and wind stress determined at 3-h intervals from geostrophic winds, or alternatively, at 6-h intervals from measured surface winds.

The six rectangular sub areas of the Irish Sea and surroundings (regions AI, A2, A3, B 1, B2, and B3) are shown in Fig. 5.40. From observations of atmospheric pressure, pi,j values were extrapolated for each grid point at each time step. The 16 meteorological stations whose pressure data are used are also shown. Heaps and Jones (1975) wrote the following for sub area A2

$$\frac{\partial p}{\partial x} = \frac{1}{2}\frac{(p_{22} - p_{12} + p_{23} - p_{13})}{7\Delta x} \tag{5.39}$$

$$\frac{\partial p}{\partial y} = \frac{1}{2}\frac{(p_{13} - p_{12} + p_{23} - p_{22})}{9\Delta y} \tag{5.40}$$

where, $\Delta x = \Delta y = 7.5$ nautical miles (13.8 km).

For each sub area, the following empirical formulae were used to determine the surface wind V from the geostrophic wind $V_G$:

$$V = 0.56\, V_G + 2. \tag{5.41}$$

$$\Theta = \Theta_G - 22 \tag{5.42}$$

where, $\Theta$ and $\Theta_G$ are the angular veering from the south (degrees) of the surface and geostrophic winds, respectively. Finally, the wind stress $\hat{o}_s$ was determined from

$$\tau_s = 12.5\, C_D\, V^2 \tag{5.43}$$

An alternate procedure to determine the meteorological forcing terms was to use the measured surface winds (and not the calculated geostrophic winds) to determine the wind stress. The anemometer locations are also shown in Fig. 5.40. Based on both approaches it was deduced that

$$V = \beta V_G$$

$$\theta = \theta_G - 22 \tag{5.44}$$

with

$$\beta = \begin{cases} 0.75 \text{ for } V_g \leq 10 \\ \dfrac{(640 - 7V_G)}{760} \text{ for } 10 \leq V_G \leq 48 \\ 0.4 \text{ for } V_G \geq 48 \end{cases} \tag{5.45}$$

where, $V_G$ is in meters per second.

## 5.2 Subtropical Cyclones

SIMPSON (1952) referred to the upper level cutoff lows, which frequently develop over the eastern part of the North Pacific Ocean during winter, north of Hawaii (locally referred to as Kona storms and which occasionally cause heavy flooding in Hawaii), as subtropical cyclones. BARRY and CHORLEY (1992) use the same definition for this phenomenon, which is usually relatively weak near the surface, but well developed in the middle troposphere. These appear to be preceded by the injection of cold air aloft through the mechanism of large-amplitude troughs in the polar westerlies (PALMEN, 1949). The eye diameter could be of some 150 km with little cloud and precepatiomn about 300 km wide (BARRY and CHORLEY, 1992). RAMAGE (1962) suggested that subtropical cyclones indeed are direct energy-creating systems. This answers the question of how a cold upper cyclone can persist and intensify and even occasionally extend to the surface after being cut off from a fresh supply of cold air when condensation and precipitation should inevitably weaken the thermal and pressure gradients of the system.

Based on a study of two subtropical cyclones near Hawaii, RAMAGE (1962) gave the following results. About 500 km from the center and beyond, the upward motion is weak and resembles that of a relatively warm-cored weak tropical cyclone circulation. In the downward branch (beyond 500 km from the center) gentle downward motion extends to the subsidence inversion level. In the surface layer beneath the subsidence inversion, a regime that bears some resemblance to the trade winds exists. Local regions of wind maxima and corresponding zones of convergence and divergence occur. The eye diameter could be as large as 200 km. Although a subtropical cyclone somewhat resembles a large-amplitude trough in the polar westerlies associated with a surface low, the sub tropical cyclone is more symmetric and its field of motion, clouds, and weather are quite different.

Subtropical cyclones occur in the Atlantic as well as in the Indian Ocean (in addition to those in the Pacific). In connection with the meteorological program of the International Indian Ocean Expedition (IIOE) during the 1960s, RAMAGE (1971) mentioned the existence of a subtropical cyclone over the Bay of Bengal in June 1963. In July 1963 another subtropical cyclone was detected over the northeastern part of the Arabian Sea.

MILLER and KESHAVAMURTHY (1968) developed a model for the subtropical cyclone using composited data. Subtropical cyclones develop predominantly near heat troughs and in the areas dominated by trade winds. Whereas in the eastern part of the North Pacific, the subtropical cyclones persist for weeks without weakening, in the Arabian area, they dissipate, probably as a result of ventilation of the cyclone by drier air.

In the Bay of Bengal and Arabian Sea areas, storm surges occur usually during the post-monsoon (September–December) and the premonsoon (April–May) months. Hence, subtropical cyclones are not very relevant for storm surge studies.

## 5.3 Tropical Cyclones

In this section, the formation and structure of tropical cyclones and the various stages in their life cycle will be considered followed with a discussion of the various models being used to forecast their intensity and movement. Main source for fundamentals of this chapter are BLÜTHGEN and WEISCHET (1980), WARNECKE (1997) and BARRY and CHORLEY (1992).

### 5.3.1 Development Theory

The main source of material for this subsection is GRAY (1978a, 1978b, 1978c, 1978d, 1989) and BARRY and CHORLEY (1992).

Annually over the globe there are about 80 tropical cyclones with maximum sustained wind speeds of 20–25 $m \cdot s^{-1}$. About one half to two thirds of these cyclones reach hurricane strength (i.e. maximum sustained wind speeds greater than 33 $m \cdot s^{-1}$).

At first the necessary conditions for the development of tropical storms and hurricanes be described with six climatological genesis parameters:

(1) low level relative vorticity, $\zeta_r$
(2) Coriolis parameter, $f$
(3) the inverse of the vertical shear $S_z$ of the horizontal wind between the lower and upper troposphere, $1/S_z$
(4) ocean thermal energy, sea temperature excess above 26° C to a depth of 60 m, E
(5) vertical gradient of $\Theta_e$, between the surface and 500 mb, $\partial\Theta_e/\partial p$, where $\Theta_e$ is the equivalent potential temperature of air and
(6) midtroposphere relative humidity, RH.

The rationale for selecting these parameters is the following. The first parameter is selected because, all things being equal, seasonal cyclone frequency should be related to the magnitude of the seasonal lower tropospheric relative vorticity. The Coriolis parameter is relevant because cyclones do not appear to form within 4–5° of the equator. Cyclogenesis does not occur near the equator because wind accelerations are small due to weak pressure gradients whereas frictional dissipation is as large as at any other latitude. The third parameter is relevant because tropical cyclones form when there is minimum vertical shear of the horizontal wind between the lower and upper troposphere.

The fourth parameter becomes relevant when recognizing that tropical cyclones can have considerable influence on the temperature of the water body over which they travel. The feedback effect of the altered ocean temperature influences the cyclone. It appears that the inner region of the average-sized hurricane (0–240 km) can consume up to 4000 $cal \cdot cm^{-2} \cdot d^{-1}$ from the ocean's sensible and latent heat energy (for details see LEIPPER and JENSEN, 1971; LEIPPER and VOLGENAU, 1972; HEFFERMAN, 1972; PERLROTH, 1967, 1969). On the other hand, MALKUS and RIEHL (1960) put this value at 3100 $cal \cdot cm^{-2} \cdot d^{-1}$. According to FRANK (1977) for Pacific typhoons for the inner 80 km, the consumption rate is around 1470 $cal \cdot cm^{-2} \cdot d^{-1}$. If a typhoon crosses the track of another typhoon, the second one may weaken sometimes because of the lowered sea surface temperature due to the upwelling caused by the first typhoon (BRAND, 1971).

The hurricane or typhoon can influence the ocean temperatures down to a depth of 60 m. LEIPPER and JENSEN (1971) and LEIPPER and VOLGENAU (1972) defined an ocean thermal energy potential (for cyclogenesis) $E$ (calories per square centimeter) as the ocean thermal energy above 26T down to a depth of 60 m, i.e.

$$E = \int \rho_W C_W (T - 26) dz \tag{5.46}$$

where, the integral is from the surface down to a depth of 60 m (or to where T = 26° C). Here, $\rho_w$ is the density of seawater, T is the ocean temperature (degrees Celsius) and $C_w$ is the specific heat of water.

The importance of the fifth parameter is obvious when it is considered that cyclones do not form unless the lower and upper tropospheric flow patterns are well coupled. The pri-

mary mechanism for this coupling is the cumulonimbus convection. Hence, cyclogenesis should depend on the seasonally averaged moist buoyancy potential (i.e. the seasonal magnitude of the difference in the equivalent potential temperature $\Theta_e$ between the boundary layer and the middle troposphere). The importance of the sixth parameter can be seen from the observations that tropical cyclones form in areas where seasonal middle level humidity values are high. In other words, when the humidity is high, deep cumulus convection occurs leading to better coupling in the vertical.

Based on these considerations, GRAY (1978a, 1978b, 1978c, 1978d) defined a "seasonal genesis parameter" (SGP) as follows:

SGP = vorticity parameter × Coriolis parameter × vertical shear parameter × ocean energy parameter × moist stability parameter × humidity parameter (5.47)

Here, vorticity parameter = $\zeta_r + 5$ where $\zeta_r$ is in units of $10^{-6} \cdot s^{-1}$, Coriolis parameter = $f$, vertical shear parameter = $1/(S_z + 3)$ where $S_z = |\partial V/\partial p|$ is in units of meters per second per 750 mb and V is the wind vector, ocean energy parameter = $E$ is defined by eq. 6.33 and is in units of $10^{-5}$ cal $\cdot$ cm$^{-2}$, moist stability parameter = $\partial\Theta_e/\partial p \pm 5$ where $\partial\Theta_e/\partial p$ is in K $\cdot$ 500 mb$^{-1}$, and humidity parameter = (RH –40)/30 where $RH$ is the mean relative humidity between 500 and 700 mb but is zero for $RH \leq 40$ and for $RH \geq 70$. Note that in the above expressions, arbitrary units are added to enable daily values to be used instead of seasonal values.
Another interpretation of SGP is as follows:

SGP = dynamic potential × thermal potential (5.48)

where, dynamic potential = $f(\zeta r + 5)\,[1/(S_z + 3)]$ and thermal potential = $E(\partial\Theta_e/\partial p + 5)(RH)$. The thermal potential might be thought of as potential for cumulonimbus convection. The dynamic potential is in units of $10^{-11}$ s$^{-2}$ (m $\cdot$ s$^{-1}$)/750 mb and the thermal potential is in units of $10^{-5}$ cal $\cdot$ cm$^{-2}$ $\cdot$ K $\cdot$ 500 mb$^{-1}$. The SGP is in units of $1.5 \times 10^{-8}$ cal $\cdot$ K $\cdot$ s$^{-1}$ $\cdot$ cm$^{-3}$. GRAY (1978a, 1978b, 1978c, 1978d) reported that there is very close agreement between the predicted (from SGP) and the observed cyclogenesis frequencies.

*Life Cycle of a Tropical Cyclone*

RIEHL (1979) summarized the life cycle of tropical cyclones. For storms with the strength of hurricanes, the duration from their birth to the time of landfall or recurvature into middle latitudes is usually about 6 d. The life cycle of a tropical cyclone may be considered to be made up of the following four stages: formative stage, immature stage, mature stage and terminal stage.

Tropical cyclones form in the vicinity of pre-existing weather systems. The deepening can occupy several days or may occur explosively in as short a time as 12 h. In the formative stage, winds are usually less than hurricane force (i.e. 1-min sustained winds are less than 74 mi $\cdot$ h$^{-1}$ [119 km $\cdot$ h$^{-1}$]). Strongest winds occur in the quadrant that is to the east of the center and poleward. Surface pressure usually drops to 1000 mb.

Several of these incipient cyclones never deepen enough to become hurricanes. In those cases that do deepen, the lowest pressure rapidly decreases to less than 1000 mb. Winds with speeds of up to 74 mi $\cdot$ h$^{-1}$ occur in a tight band around the centre (and not just in one quadrant). The disorganized squalls of the formative stage change into narrow and organized

bands of clouds spiralling inward. In this immature stage only a small area is involved in the intense inner core (30- to 50-km radius) although there may be a large outer core.

In the mature stage, the surface pressure at the center stops decreasing and the maximum wind speeds do not increase further. However, the area of intense circulation expands (up to 300-km radius in certain cases). The symmetry of the immature stage is destroyed and strong winds and bad weather preferentially occur to the right of the center looking downstream in the direction of movement of the cyclone. Some storms with a central low pressure as low as 950 mb could still be only 100–200 km in radius. RIEHL (1979) estimated that for a storm with an average surface pressure of 1000 mb, the total weight of air and water involved in the circulation is about $3 \times 10^{11}$ to $1 \times 10^{12}$ t ($3.05 \times 10^{14}$ to $1.016 \times 10^{15}$ kg). However, another storm with a radius of 1000 km but with the same average surface pressure of 1000 mb will have a weight of about $5 \times 10^{12}$ to $3 \times 10^{13}$ t ($5.8 \times 10^{15}$ to $3.05 \times 10^{16}$ kg). By comparison, in an ordinary midlatitude cyclone, the weight involved is about $5 \times 10^{12}$ to $1 \times 10^{13}$ t ($5.8 \times 10^{16}$ kg).

When the tropical cyclone hits land, usually its core size decreases and sometimes the storm dissipates within 1–2 d. Storms can dissipate even over the ocean if they travel over cold ocean currents (e.g. Northeast Pacific Ocean). Many cyclones recurve (both over land and ocean) into the westerlies and travel towards northeast or east (in the Northern Hemisphere).

*Some Characteristics of Tropical Cyclones*

RIEHL (1979) offered the following classification of tropical cyclones.

(A) Tropical depression: at most, winds barely acquire gale force in one quadrant.
(B) Tropical storm: winds acquire gale force but less than hurricane force of 64 knots (119 km · $h^{-1}$ or 74 mi · $h^{-1}$).
(C) Minimal hurricane: winds above 64 knots only in one quadrant.
(D) Moderate hurricane: winds of 80–90 knots (148–167 km · $h^{-1}$) around the center, with the maximum wind being around 100 knots (185 km · $h^{-1}$) or more.
(E) Severe hurricane: maximum winds up to 200 knots (370 km · $h^{-1}$).

Tropical cyclone intensity classification is not uniformly used in the various meteorological services for the various regions of the globe. For example, in the western part of the Pacific Ocean, unless the maximum winds are about 150 knots (278 km · $h^{-1}$), a typhoon will not be considered severe.

RIEHL (1979) mentioned that the word "hurricane" means "big wind" in the Taino.

Next, some characteristics of tropical cyclones will be briefly examined with respect to their surface pressure, winds, and thermal structure. Since ordinarily, surface pressure varies only by about 3 mb (0.3 %) in the tropics whereas pressure varies 5–10 % below average sea level pressure during tropical cyclones, a useful tool for analysis is the sea level isobar field. Gradients of 0.5–2 mb $km^{-1}$ can occur.

When the tropical cyclone is over an ocean, the increase of wind with height usually occurs in the first 100 m. Above that it increases slowly to about the 300-m level where the winds probably attain maximum values. For Hurricane Eloise of 1977 the wind speed at the 100-m level was 20 m · $s^{-1}$; from 200 to 500 m it was 22 m · $s^{-1}$. Then it decreased to 14 m · $s^{-1}$ at 1200 m. Usually, the wind at 50 m is about three quarters the geostropic wind speed (RIEHL, 1979).

In hurricanes, in the inner 80-km core, winds up to 45 m · $s^{-1}$ can occur. Winds are grea-

ter on the right side because here the carrying current and the circulation are in the same direction whereas to the left they oppose each other. One of the safest ways to identify tropical cyclones is to look for this asymmetry in the surface wind field. For convenience, one may think of the following four quadrants around the center: right front, right rear, left front, and left rear. Inward spiralling of streamlines is pronounced in the rear quadrants. Here, the radial component of the motion is strongest.

RIEHL (1979) gave the following relationship between pressure and wind fields in a tropical cyclone (this was derived empirically based on 28 yr of Pacific typhoon data):

$$V_m = 3.35(1010 - p_c)^{0.644} \tag{5.49}$$

where, $V_m$ is the maximum wind (metres per second) and $p_c$ is the central pressure (millibars).

The theory of vortex flows shows that in the center of every revolving vortex, there is a singular point. In a tropical cyclone this center is referred to as the eye, near which the circulation is weak. At the edge of the eye, strong precipitation abruptly stops and the sky may clear at least partly. The diameter of the eye in a mature hurricane ranges from 30 to 50 km and probably twice this value in a severe typhoon. The eye need not be circular and sometimes it is diffuse and has a double structure.

RIEHL (1979) mentioned that one of the earliest controversies about tropical cyclones concerned their vertical extent. Estimates varied from 3 to 10 km or greater. According to HAURWITZ (1935) the tropical cyclone extends through the troposphere, and high level observations substantiated this idea. However, a surprising result revealed from Rawinsonde data was that the circulation at higher levels is opposite to that at lower levels. This changeover level is at about 300 mb.

As expected, the air inside a tropical cyclone is less dense than its surroundings. For Hurricane Daisy of 1958 near Florida, in the mature stage, the surface pressure in the eye was 950 mb and the maximum wind was 50 m $s^{-1}$. Hurricane Daisy is considered to be a hurricane of moderate intensity, and even in this case more than half the temperature gradient needed for its existence was internally generated. RIEHL (1979), WARNECKE (1997) maintained that this is the main reason why intense hurricanes occur rarely. In contrast, in extratropical cyclones, the cyclone grows at the expense of the potential energy in a pre-existing temperature field, which becomes pronounced. On the other hand, in a tropical cyclone, the cyclone itself must generate most of the required temperature gradient.

RIEHL (1979) suggested that a hurricane may be regarded as a rankine vortex with a velocity profile defined by $v_\theta/r$ = constant in the inner core of maximum winds and $v_\theta r = constant$ in the outer core. Here, $r$ is the radial coordinate and vo is the azimuthal velocity. The outer core can be defined as

$$v \cdot r^x = \text{constant}, \; 0.4 \cdot x \cdot 0.6 \tag{5.50}$$

In the outer core, with increasing distance from the center, $v_\theta$ tends to zero.

*Momentum And Energy Budgets For Tropical Cyclones*

Following RIEHL (1979), the energy and momentum budgets for hurricanes will be considered. In polar coordinates the equations of horizontal motion with the neglect of lateral friction are

$$\frac{dv_\theta}{dt} + \frac{v_\theta v_r}{r} + fv_r = -\frac{1}{\rho}\frac{\partial p}{r\partial\theta} + \frac{1}{\rho}\frac{\partial \tau_{\theta z}}{\partial z}$$
$$\frac{dv_r}{dt} - \frac{v_\theta^2}{r} - fv_\theta = -\frac{1}{\rho}\frac{\partial p}{r\partial r} + \frac{1}{\rho}\frac{\partial \tau_{rz}}{\partial z} \tag{5.51}$$

Here, $v_r$ and $v_\theta$ are the radial and azimuthal velocities respectively. After certain algebra involving these two equations, it can be shown that

$$\frac{d}{dt}\left(v_\theta r + \frac{fr^2}{2}\right) - \frac{r^2}{2}\frac{df}{dt} = -\frac{1}{\rho}\frac{\partial p}{\partial\theta} + \frac{r}{\rho}\frac{\partial \tau_{\theta z}}{\partial z} \tag{5.52}$$

The component of the earth's angular momentum (per unit mass) about the vertical axis of the tropical cyclone is

$$\Omega = v_\theta r + \frac{fr^2}{2} = \text{cons tan t} \tag{5.53}$$

For symmetrical storms, eq. (5.53) is a good representation in the upper troposphere. If eq. (5.52) is integrated over the entire volume in the storm, by definition the pressure term will disappear, but the frictional term will not because of transfer of momentum from the atmosphere to the ocean. To compute the momentum budget, integrate eq. (5.67) over the volume of the storm to obtain expressions for the transport $F_\Omega$ (radial) at any radius and $F_\Omega$ (vertical) between two radii. These are

$$F_\Omega(\text{radial}) = -\frac{2\pi r^2}{g}\left[\int_{p2}^{p1} \bar{v}_\theta \bar{v}_r dp + \int_{p2}^{p1} \overline{v'_\theta v'_r} dp + \frac{fr}{2}\int_{p2}^{p1} \bar{v}_r dp\right] \tag{5.54}$$

$$F_\Omega(\text{vertical}) = -\frac{2\pi}{g}\left[\int_{r1}^{r2} \tilde{v}_\theta \tilde{\omega} r^2 dr + \int_{r1}^{r2} \tilde{v}^*_\theta \omega^* r^2 dr + \frac{f}{2}\int_{r1}^{r2} \tilde{\omega} r^3 dr\right] \tag{5.55}$$

where, $\omega = dp/dt$.

The surface transport to the ocean is given by

$$E_\Omega(\text{surface}) = 2\pi \int_{r_1}^{r} \tau_{\theta,0} r^2 dr \tag{5.56}$$

where $t_{\theta,0}$ is the stress at the ship's deck level (or anemometer level).

In eq. (5.54) the first term represents the transport by the mean ageostrophic circulation $v_r$, the second term denotes the deviation from symmetry when one goes round the perimeter and the third term is the influence due to the earth's rotation, assuming the Coriolis parameter to be constant.

Table 5.7: Transports through 1° radius (1012 kJ · $s^{-1}$) showing the radial energy balance in two different hurricanes (RIEHL, 1979)

| Parameter | Hurricane Daisy (1960) | Hurricane Helene (1951) |
|---|---|---|
| Net latent heat inflow | +34.1 | +31.9 |
| Flux of latent and sensible heat from the sea | +3.4 | +6.2 |
| Import of kinetic energy | +0.4 | +0.2 |
| Total energy source | 37.9 | 38.3 |
| Less net export of (CpT + gz) | − 36.9 | −37.4 |
| Balance for radiation cooling | 1.0 | 0.9 |

One can regard the atmosphere, and particularly a tropical cyclone, in the present situation as a thermal engine for which the efficiency (of converting heat to mechanical energy) is defined as the ratio of the mechanical energy produced to the heat released. For an average hurricane, the kinetic energy produced was estimated by RIEHL (1979) as $15 \times 10^{18}$ ergs $s^{-1}$ or $0.36 \times 10^{12}$ $kWh^{-1}$ (1 erg = 0.1 μJ, 1 kWh = 3.6 MJ). The latent heat released was $13.3 \times 10^{12}$ kWh · $d^{-1}$. Thus, the efficiency E is 3 %. This is very low but is somewhat higher than for extratropical cyclones and the general circulation of the atmosphere. Hence, weather systems and the atmosphere are very inefficient heat engines. This low value of efficiency for the tropical cyclones indicates that the mechanism for energy release is in the central area with local oceanic heat source and not in the advection of large masses of water vapour into the system from outside.

The balance of radial energy for Hurricanes Helen of 1951 and Daisy of 1960 is shown in Table 5.7. Concerning oceanic input of energy, GRAY (1978a) provided the following analysis. In the tropical cyclone, moist static energy *h* can increase or decrease through latent and sensible heat exchange with the ocean *Es* through radiation *R* and through horizontal transport through the boundaries ∇. Vh. One can write for this energy balance

$$\frac{\partial h}{\partial t} = E_S + R - \nabla.Vh \tag{5.57}$$

where,

$$h = gz + C_pT + Lq \tag{5.58}$$

Note that all these terms have been integrated through the thickness of the troposphere.

For the inner 4° radius of tropical storms, $E_S$ + R is slightly positive for weak disturbances, but for hurricanes it is highly positive because strong input of energy takes place from the ocean. The vertical circulations in a tropical cyclone will act as an energy sink dissipating the system and the main energy source is the ocean. For this reason, many tropical systems weaken or dissipate once they are not traveling over the ocean.

*Frequency and region of occurrence*

The conditions for development of tropical storms form the boundary of areas and period of generation of tropical cyclones. Fig. 5.41 shows over a 20-yr period these areas. Over the globe, the percentage change in the number of tropical cyclones over a recent 20-yr period (1958–77) varied from + 23 to – 13, with an average of 8 (Table 5.8). The ratio of the number of tropical cyclones in the Northern Hemisphere to those in the Southern Hemisphere varied from 1.5 to 4.0.

Month by month occurrences of tropical cyclones for the same 20-yr period for the Northern and Southern Hemispheres are shown separately in Table 5.9 and Table 5.10, respectively. The data for the various ocean basins, which are identified in Fig. 5.41, are shown in Table 5.11.

About 80 % of the tropical cyclones occur in the belt between 20° N and 20° S. The rest occurs poleward of 20° latitude, but mainly in the Northern Hemisphere. Annually, about two thirds of all tropical cyclones occur in the Northern Hemisphere; similarly, about two thirds occur in the Eastern Hemisphere (as opposed to the Western Hemisphere). Most of the tropical cyclones form in the latitudinal belt 5–15°, and rarely do they form within 4–5° from the equator. In the Southern Hemisphere, tropical cyclones do not form poleward of 22°, whereas in the Northern Hemisphere they form at latitudes up to 36°.

Considering longitude, there are three favoured locations for the formation of tropical cyclones: 90° E, 140° E, and 105° W. The western part of the North Pacific Ocean accounts for about one third of all tropical cyclones. Generally, summer is the favoured season for tropical cyclone formation, but they do occur in other seasons, especially in the western part of the North Pacific Ocean.

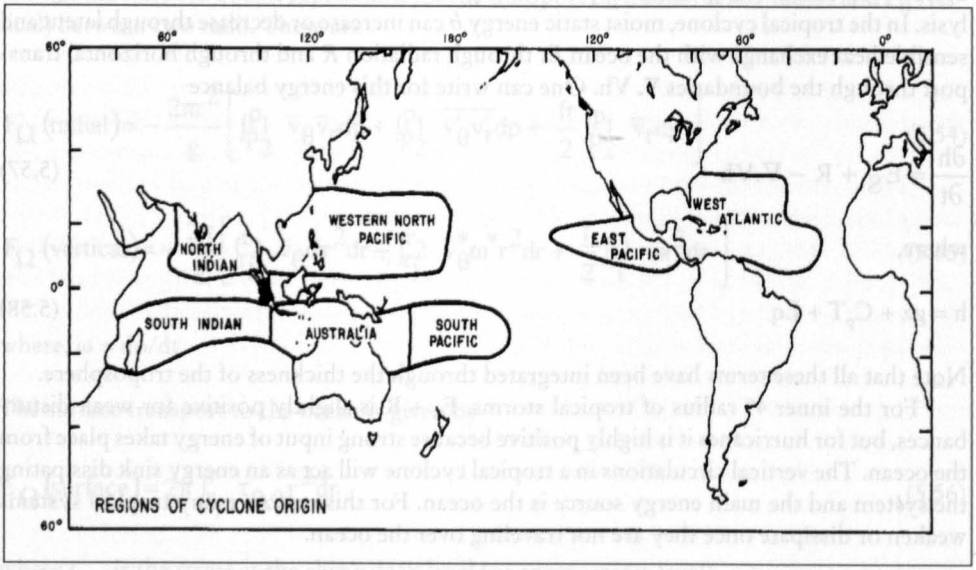


Fig. 5.41: Ocean basins for which tropical cyclone frequency is given in Table 5.10 (GRAY, 1978a)

Table 5.8: Tropical cyclone statistics for the period 1958–77. NH, Northern Hemisphere; SH, Southern Hemisphere (GRAY, 1978a)

| Year | | No. of cyclones | | | % deviation from 20-yr average | Ratio (NH:SH) |
|---|---|---|---|---|---|---|
| NH | SH | NH | SH | Total | | |
| 1958 | 1958–59 | 52 | 25 | 77 | −3 | 2.1 |
| 1959 | 1959–60 | 48 | 21 | 69 | −13 | 2.3 |
| 1960 | 1960–61 | 48 | 22 | 70 | −12 | 2.2 |
| 1961 | 1961–62 | 58 | 23 | 81 | +2 | 2.5 |
| 1962 | 1962–63 | 50 | 30 | 80 | +1 | 1.7 |
| 1963 | 1963–64 | 49 | 23 | 72 | −9 | 2.1 |
| 1964 | 1964–65 | 65 | 19 | 84 | +6 | 3.4 |
| 1965 | 1965–66 | 56 | 22 | 78 | −1 | 2.5 |
| 1966 | 1966–67 | 64 | 16 | 78 | −1 | 4.0 |
| 1967 | 1967–68 | 63 | 28 | 91 | +15 | 2.2 |
| 1968 | 1968–69 | 61 | 23 | 84 | +6 | 2.6 |
| 1969 | 1969–70 | 49 | 23 | 72 | −9 | 2.1 |
| 1970 | 1970–71 | 56 | 26 | 82 | +4 | 2.1 |
| 1971 | 1971–72 | 70 | 27 | 97 | +23 | 2.6 |
| 1972 | 1972–73 | 54 | 35 | 91 | +15 | 1.5 |
| 1973 | 1973–74 | 46 | 28 | 74 | −6 | 1.6 |
| 1974 | 1974–75 | 55 | 19 | 75 | −5 | 2.9 |
| 1975 | 1975–76 | 47 | 29 | 76 | −4 | 1.6 |
| 1976 | 1976–77 | 55 | 30 | 85 | +7 | 1.8 |
| 1977 | 1977–78 | 47 | 20 | 67 | −15 | 2.3 |
| Total | | 1093 | 489 | 1583 | | |
| Average | | 54.6 | 24.5 | 79.1 | ±8 | 2.3 |

Table 5.9: Frequency of Northern Hemisphere tropical cyclone genesis by year and month (GRAY, 1978a)

| Year | Jan. | Feb. | Mar. | Apr. | May | June | July | Aug. | Sept. | Oct. | Nov. | Dec. | Total |
|---|---|---|---|---|---|---|---|---|---|---|---|---|---|
| 1958 | 1 | 0 | 0 | 0 | 2 | 5 | 10 | 9 | 11 | 9 | 4 | 1 | 52 |
| 1959 | 0 | 0 | 0 | 1 | 2 | 6 | 7 | 11 | 9 | 8 | 2 | 2 | 48 |
| 1960 | 0 | 0 | 0 | 1 | 3 | 7 | 6 | 14 | 6 | 8 | 2 | 1 | 48 |
| 1961 | 1 | 1 | 1 | 1 | 4 | 5 | 10 | 5 | 14 | 9 | 6 | 1 | 58 |
| 1962 | 0 | 1 | 0 | 1 | 3 | 2 | 7 | 11 | 11 | 7 | 4 | 3 | 50 |
| 1963 | 0 | 0 | 0 | 1 | 3 | 5 | 6 | 5 | 14 | 11 | 0 | 4 | 49 |
| 1964 | 0 | 0 | 0 | 0 | 3 | 4 | 11 | 15 | 12 | 8 | 10 | 2 | 65 |
| 1965 | 2 | 2 | 1 | 1 | 4 | 8 | 8 | 8 | 12 | 3 | 4 | 3 | 56 |
| 1966 | 0 | 0 | 0 | 2 | 2 | 3 | 9 | 13 | 20 | 5 | 7 | 3 | 64 |
| 1967 | 2 | 1 | 1 | 1 | 2 | 4 | 10 | 12 | 12 | 13 | 3 | 2 | 63 |
| 1968 | 0 | 0 | 0 | 1 | 2 | 5 | 7 | 17 | 11 | 11 | 6 | 1 | 61 |
| 1969 | 1 | 0 | 1 | 1 | 1 | 0 | 7 | 13 | 10 | 9 | 4 | 2 | 49 |
| 1970 | 0 | 1 | 0 | 0 | 4 | 6 | 11 | 10 | 9 | 8 | 7 | 0 | 56 |
| 1971 | 1 | 0 | 1 | 3 | 7 | 3 | 15 | 11 | 15 | 9 | 4 | 1 | 70 |
| 1972 | 1 | 0 | 0 | 1 | 4 | 2 | 9 | 12 | 12 | 6 | 4 | 3 | 54 |
| 1973 | 0 | 0 | 0 | 0 | 0 | 5 | 12 | 8 | 8 | 7 | 5 | 1 | 46 |
| 1974 | 1 | 0 | 0 | 2 | 4 | 6 | 5 | 14 | 13 | 6 | 4 | 0 | 55 |
| 1975 | 2 | 0 | 0 | 0 | 2 | 3 | 6 | 11 | 9 | 8 | 6 | 0 | 47 |
| 1976 | 1 | 1 | 0 | 3 | 2 | 7 | 9 | 15 | 10 | 4 | 0 | 3 | 55 |
| 1977 | 0 | 0 | 1 | 0 | 3 | 4 | 8 | 4 | 13 | 9 | 4 | 1 | 47 |
| Total | 13 | 7 | 6 | 20 | 57 | 90 | 173 | 218 | 231 | 158 | 86 | 34 | 1093 |
| Average | 0.7 | 0.3 | 0.3 | 1.0 | 2.9 | 4.5 | 8.6 | 10.9 | 11.5 | 7.9 | 4.3 | 1.7 | 54.6 |

Table 5.10: Frequency of Southern Hemisphere tropical cyclone genesis by year and month (GRAY, 1978a)

| Year | Oct. | Nov. | Dec. | Jan. | Feb. | Mar. | Apr. | May | Total |
|---|---|---|---|---|---|---|---|---|---|
| 1958–59 | 1 | 1 | 3 | 5 | 7 | 6 | 2 | 0 | 25 |
| 1959–60 | 0 | 1 | 4 | 3 | 2 | 7 | 4 | 0 | 21 |
| 1960–61 | 0 | 1 | 1 | 9 | 7 | 4 | 0 | 0 | 22 |
| 1961–62 | 0 | 1 | 4 | 6 | 8 | 2 | 2 | 0 | 23 |
| 1962–63 | 1 | 0 | 4 | 6 | 9 | 5 | 2 | 3 | 30 |
| 1963–64 | 0 | 1 | 3 | 7 | 3 | 7 | 1 | 1 | 23 |
| 1964–65 | 0 | 2 | 5 | 4 | 5 | 3 | 0 | 0 | 19 |
| 1965–66 | 0 | 0 | 3 | 7 | 6 | 6 | 0 | 0 | 22 |
| 1966–67 | 0 | 1 | 3 | 5 | 1 | 3 | 2 | 1 | 16 |
| 1967–68 | 0 | 2 | 4 | 8 | 7 | 3 | 4 | 0 | 28 |
| 1968–69 | 1 | 1 | 3 | 7 | 8 | 2 | 1 | 0 | 23 |
| 1969–70 | 0 | 1 | 0 | 5 | 6 | 7 | 3 | 1 | 23 |
| 1970–71 | 1 | 3 | 6 | 4 | 7 | 4 | 1 | 0 | 26 |
| 1971–72 | 0 | 1 | 6 | 3 | 10 | 3 | 2 | 2 | 27 |
| 1972–73 | 1 | 3 | 4 | 10 | 6 | 7 | 3 | 1 | 35 |
| 1973–74 | 1 | 3 | 5 | 7 | 4 | 6 | 2 | 0 | 28 |
| 1974–75 | 0 | 0 | 2 | 6 | 2 | 5 | 4 | 0 | 19 |
| 1975–76 | 0 | 4 | 4 | 8 | 5 | 4 | 3 | 1 | 29 |
| 1976–77 | 1 | 0 | 4 | 8 | 9 | 5 | 3 | 0 | 30 |
| 1977–78 | 0 | 3 | 4 | 3 | 4 | 4 | 2 | 0 | 20 |
| Total | 7 | 29 | 72 | 121 | 117 | 93 | 41 | 10 | 489 |
| Average | 0.4 | 1.5 | 3.6 | 6.1 | 5.9 | 4.7 | 2.1 | 0.5 | 24.5 |

Table 5.11: Yearly variation of tropical cyclones by ocean basins. SH, Southern Hemisphere; NW Atl., Northwest Atlantic Ocean; NE Pac., Northeast Pacific Ocean; NW Pac., Northwest Pacific Ocean; S. Pac., South Pacific Ocean; Aust., Australia; N. Ind., North Indian Ocean; S. Ind., South Indian Ocean (GRAY, 1978a)

| Year | SH | NW Atl. | NE Pac. | NW Pac. | N. Ind. | S. Ind. | Aust. | S. Pac. | Total |
|---|---|---|---|---|---|---|---|---|---|
| 1958 | 1958–59 | 12 | 13 | 22 | 5 | 11 | 11 | 7 | 81 |
| 1959 | 1959–60 | 11 | 13 | 18 | 6 | 6 | 13 | 2 | 69 |
| 1960 | 1960–61 | 6 | 10 | 28 | 4 | 6 | 8 | 8 | 70 |
| 1961 | 1961–62 | 11 | 12 | 29 | 6 | 12 | 7 | 4 | 81 |
| 1962 | 1962–63 | 6 | 9 | 30 | 5 | 8 | 17 | 3 | 78 |
| 1963 | 1963–64 | 9 | 9 | 25 | 6 | 9 | 7 | 7 | 72 |
| 1964 | 1964–65 | 13 | 6 | 39 | 7 | 6 | 9 | 4 | 84 |
| 1965 | 1965–66 | 5 | 11 | 34 | 6 | 12 | 7 | 4 | 79 |
| 1966 | 1966–67 | 11 | 13 | 31 | 9 | 5 | 5 | 6 | 80 |
| 1967 | 1967–68 | 8 | 14 | 35 | 6 | 11 | 9 | 8 | 91 |
| 1968 | 1968–69 | 7 | 20 | 27 | 7 | 8 | 7 | 8 | 84 |
| 1969 | 1969–70 | 14 | 10 | 19 | 6 | 10 | 7 | 6 | 72 |
| 1970 | 1970–71 | 8 | 18 | 23 | 7 | 11 | 12 | 3 | 82 |
| 1971 | 1971–72 | 14 | 16 | 34 | 6 | 7 | 14 | 6 | 97 |
| 1972 | 1972–73 | 4 | 14 | 28 | 6 | 13 | 12 | 10 | 88 |
| 1973 | 1973–74 | 7 | 12 | 21 | 6 | 4 | 16 | 8 | 74 |
| 1974 | 1974–75 | 8 | 17 | 23 | 7 | 6 | 10 | 3 | 74 |
| 1975 | 1975–76 | 8 | 16 | 17 | 6 | 8 | 16 | 5 | 76 |
| 1976 | 1976–77 | 8 | 18 | 24 | 5 | 9 | 12 | 9 | 85 |
| 1977 | 1977–78 | 6 | 17 | 19 | 5 | 6 | 7 | 7 | 67 |
| Total | | 176 | 268 | 526 | 121 | 168 | 206 | 118 | 1583 |
| Average | | 8.8 | 13.4 | 26.3 | 6.4 | 8.4 | 10.3 | 5.9 | 79.1 |

In the North Indian Ocean, there are two seasons of cyclone formation in the 5–15° latitude belt: a major period in the autumn associated with the retreat of the southwest monsoon and a minor period in the spring associated with the onset of the monsoon. Note that the Southeast Pacific Ocean and the South Atlantic Ocean are not regions of tropical cyclones. The seasonal location of the intertropical convergence zone (ITCZ) is a favoured region for tropical cyclogenesis.

According to GRAY (1978a, 1978b, 1978c, 1978d), tropical cyclones tend to cluster in time as well as in space. Within a period of 1–2 wk there may be as many as 5–15 tropical cyclones over the globe and then a lull for several weeks. During such active periods there may be as many as two to six times as many cyclones than in the less active periods. GRAY (1978a, 1978b, 1978c, 1978d) attributed this to the influence of the larger scale general circulation of the tropical atmosphere with time scales of 10–20 d.

About 80–85 % of the tropical cyclones originate in or near the poleward side of the ITCZ or the doldrums trough. The remainder occur in the trade winds at some distance from the ITCZ but usually in conjunction with an upper tropospheric trough to their northwest.

There are some anomalous warm core systems belonging to the class of subtropical or semitropical cyclones accounting for about 3–5 % of the tropical cyclones. These originate in the subtropics inside baroclinic regions where stagnant frontal zones exist to the cast of the westerly troughs aloft (e.g. Northwest Atlantic and Northwest Pacific oceans). These mixed type of tropical midlatitude cyclones usually do not generate intense cyclones.

Since tropical cyclones spend most of their lifespan over the warm waters of the tropical oceans, traditional data sources are not dense enough. Aircraft data have contributed significantly. However, for an accurate vertical structure determination, Rawinsonde data are the most pertinent. Since enough synoptic Rawinsonde data are not available, it is necessary to combine the data of different periods for similar weather systems.

*Hurricane Movement Over Ocean and Land*

Earlier, it was seen that hurricanes are born primarily over oceanic areas and they weaken when they travel over the continents. A numerical model simulation by CHANG and MADALA (1980) showed that hurricanes appear to move into areas of higher sea surface temperature (SST) if the SST gradient is perpendicular to the mean ambient flow vector (MAFV). An area of warmer SST located to the right of MAFV is more favorable for hurricane intensification than an area situated to the left.

SCHWERDT (1978) studied the reduction of the wind field when a hurricane moves from the ocean to over land. Once a hurricane crosses the coast from the ocean to the land its central pressure starts increasing and the wind fields start decreasing, and this so-called filling process is most pronounced in the inner portion of the hurricane.

According to PALMÉN and NEWTON (1969), filling occurs because the heat flux from the land is negligible, which causes a reduction of the excess temperature of the hurricane core. Consequently, the kinetic energy decreases. BERGERON (1954) showed that a reduction in the equivalent potential temperature of the ascending air in the core leads to the filling process. MILLER (1963) showed that surface friction plays a minor role in the filling process.

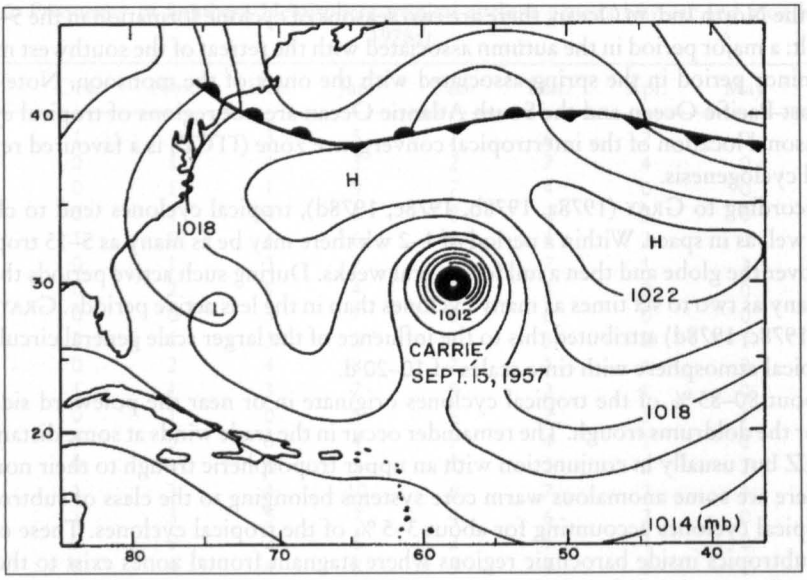


Fig. 5.42: Surface weather chart on September 15, 1957, showing Hurricane Carrie (SIMPSON and RIEHL, 1981)

SIMPSON and RIEHL (1981) defined the habitation layer as the lowest 500 m of the atmosphere. They considered the balance of forces in this layer at a coastal station as a hurricane approaches the station. The centrifugal force $C_e$ and the Coriolis force $C_0$ are directed outwards, whereas the pressure gradient force Pg and the frictional force $F_s$ are directed inward (perpendicular to the streamline). This leads to an acceleration of the tangential wind component as the air spirals inward. (Figs. 5.42, 5.43, 5.44, 5.45, 5.46, 5.67).

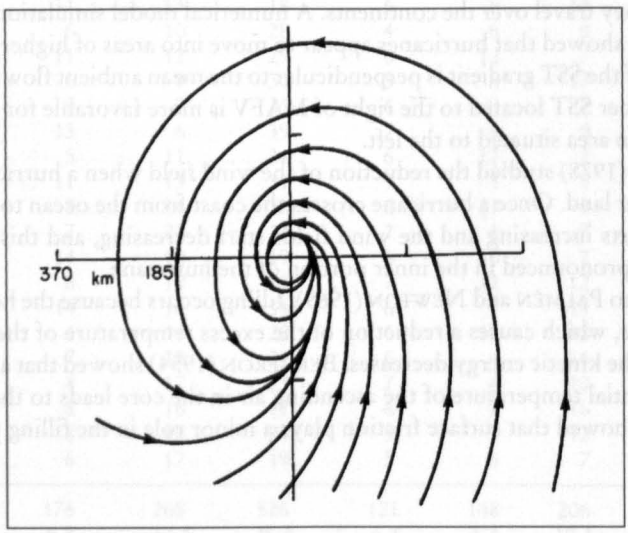


Fig. 5.43: Streamlines showing the circulation in a hurricane (SIMPSON and RIEHL, 1981)

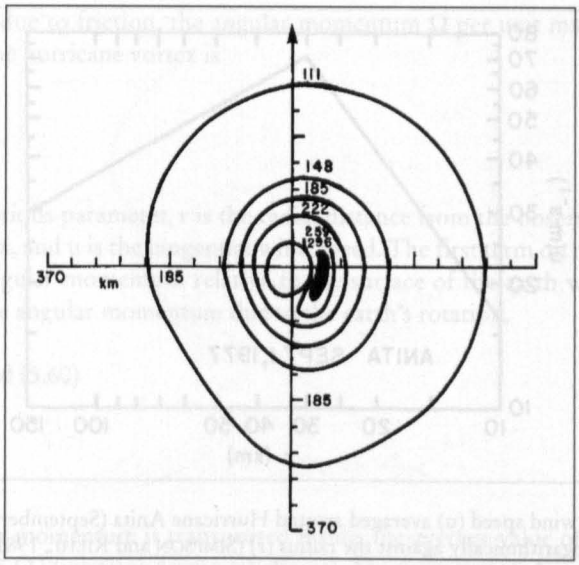


Fig. 5.44: Isotachs of surface wind speed (knots) in an intense hurricane. Black area shows the region of strongest winds (to the right of the eye) (1 knot = 1.852 km · h$^{-1}$) (SIMPSON and RIEHL, 1981)

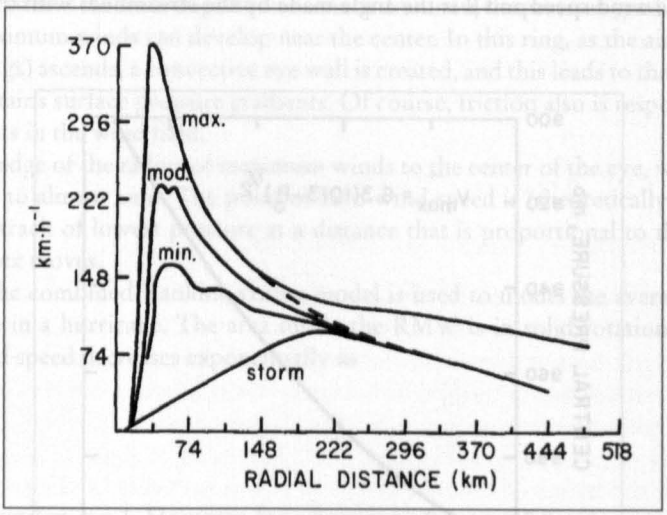


Fig. 5.45: Model of radial profiles of wind speed for three hurricane intensities and for a tropical storm (SIMPSON and RIEHL, 1981)

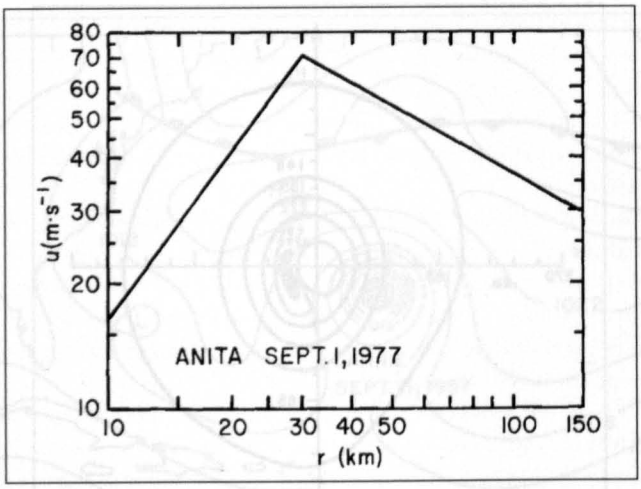


Fig. 5.46: Tangential wind speed (u) averaged around Hurricane Anita (September 1, 1977) and plotted logarithmically against the radius (r) (SIMPSON and RIEHL, 1981)

In a hurricane, mainly the tangential (rotational) component of the wind increases from the periphery of the vortex to the ring of maximum winds (RMW). According to SIMPSON and RIEHL (1981) this ring has a radius of less than 35 km:

$$u = V \cos \beta \tag{5.59}$$

where, V is the wind speed and β is the angle made by the streamlines with the isobars.

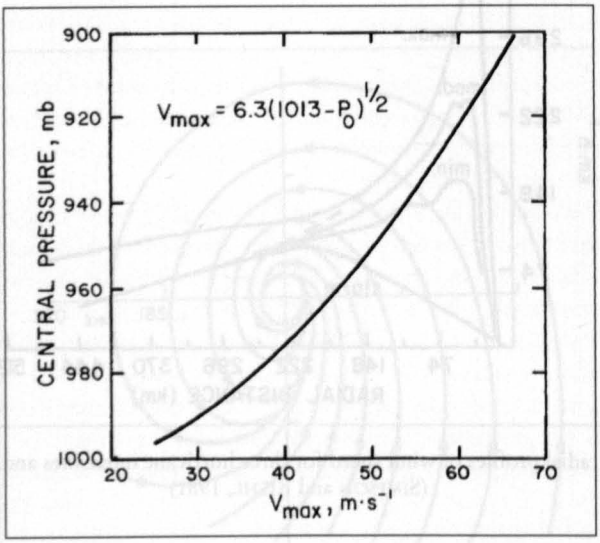


Fig. 5.47: Maximum sustained wind speed versus central pressure for Atlantic hurricanes (SIMPSON and RIEHL, 1981)

Neglecting losses due to friction, the angular momentum Ω per unit mass supplied by the surroundings to the hurricane vortex is

$$\Omega = ur + \frac{fr^2}{2} \tag{5.60}$$

where, $f$ is the Coriolis parameter, r is the radial distance from the observation point to the centre of the vortex, and u is the tangential wind speed. The first term on the right side of eq. (5.60) gives the angular momentum relative to the surface of the earth whereas the second term represents the angular momentum due to the earth's rotation.

From eq. (5.59) and (5.60)

$$u = \frac{\Omega}{r} - \frac{fr}{2} \tag{5.61}$$

As the angular momentum is transported inside, the average value of u increases as can be seen from eq. (5.61) (ignoring frictional effects). The maximum value of u occurs for cyclostrophic balance (i.e. when the pressure gradient force balances the centrifugal plus Coriolis forces) and when β of eq. (5.59) tends to zero.

In principle, the increase of u with decreasing r would create centrifugal forces that would far exceed the pressure gradient forces, and the air should spiral outward towards higher pressure. However, surface friction reduces the value of Ω steadily and this outward spiralling tendency is offset. Hence, surface friction plays a dual role. First of all, it permits a crossing angle between the streamlines and isobars so that air from the surroundings is drawn towards the vortex center by pressure gradient forces. Second, it reduces the imported angular momentum so that the centrifugal forces cannot dominate the pressure gradient forces and a radius of maximum winds can develop near the center. In this ring, as the air (drawn from the surroundings) ascends, a convective eye wall is created, and this leads to the central warm core that maintains surface pressure gradients. Of course, friction also is responsible for the creation of gusts in the wind field.

From the edge of the radius of maximum winds to the center of the eye, wind decreases monotonically to almost zero. The point of zero wind speed is (theoretically) displaced to the left of the track of lowest pressure at a distance that is proportional to the speed with which the vortex moves.

Usually, the combined Rankine vortex model is used to model the average horizontal wind structure in a hurricane. The area inside the RMW is in solid rotation. Outside the RMW the wind speed decreases exponentially as

$$u = \frac{\text{cons tan t}}{r^x} \tag{5.62}$$

For a Rankine vortex, x = 1. However, for a hurricane, $0.4 < x < 0.8$.

Above the first few hundred meters, the strongest winds of a hurricane do not vary much up to 4–5 km of height. The wind speed variation with height in tropical cyclones is shown in Fig. 5.48.

The international standard for sustained winds is the average speed for a 10-min period. In the United States the sustained wind is a 1-min average. For extreme winds in the United

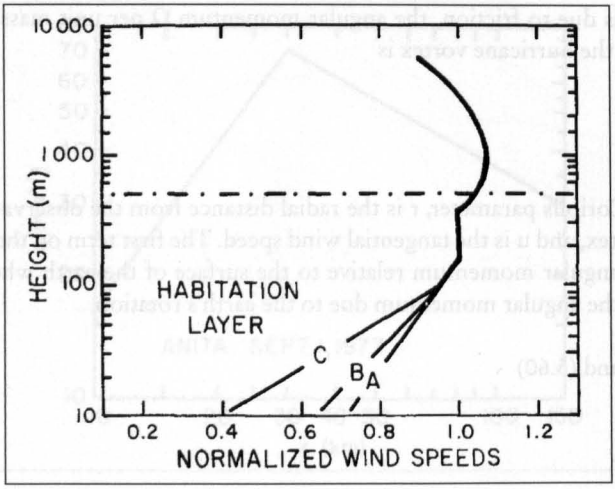


Fig. 5.48: Model of wind speed variation with height in tropical cyclones. Speeds are normalized with reference to wind speeds measured by aircraft in the 150- to 300-m layer. A, over water; B, over land; C, profile for 1/7-power law (BATES, 1977)

States the unit of measurement is the fastest mile (the highest speed at which 1 mi of wind passes the anemometer).

In the U. S. National Weather Service and in the U. S. Army Corps of Engineers, the ideas about Probable Maximum Hurricane (PMH) and Standard Project Hurricane (SPH) originated in the 1950s (e.g. GRAHAM and NUNN, 1959). The PMH is defined as a hypothetical hurricane having that combination of values of meteorological parameters that will make it the most severe that can probably occur at a particular coastal location. The SPH is defined as a hypothetical hurricane with the most severe combination of values of hurricane parameters reasonably characteristic of a specified geographic location, thus excluding extremely rare combinations (SCHWERDT, 1976; MOGOLESKO, 1976).

### 5.3.2 Prediction of Movement and Intensity

*Modelling Of Hurricane Formation and Intensification*

According to GRAY (1978a, 1978b) little effort has gone into numerically modelling tropical cyclogenesis. OOYAMA (1964), CHARNEY and ELIASSEN (1964), OGURA (1964), KUO (1965) and several later authors modelled the intensification of hurricanes. The low level winds for different classes of tropical disturbances were deduced from Rawinsonde composite studies. These winds are much smaller than the initial cyclone strength assumed by numerical modellers, as summarized in Table 5.13. According to GRAY (1978a, 1978b, 1978c, 1978d) the transformation of a disturbance to a cyclone has yet to be realistically modelled.

GRAY (1978a, 1978b, 1978c, 1978d) classified the disturbance stages and gave estimates of central pressure and maximum sustained surface winds. These are shown in Table 5.13. Even in a stage 6 cyclone (i.e. typhoon) approximately 50 % of the mass inflow at 4° radius takes place above the 900-mb layer. Hence, there is significantly more mass inflow than can be accounted for by boundary layer processes. In fact, mass convergence could occur in a layer as high as 400 mb.

Table 5.12: Some numerical modeling papers on tropical cyclone intensification and their assumed initial lower tropospheric cyclone strength (GRAY, 1978a)

| Modellers | Assumed initial maximum wind velocity ($m\ s^{-1}$) and radius (km) of maximum wind | | Vortex vorticity inside the radius of maximum winds ($10^{-6} \cdot s^{-1}$) | Type of vortex |
|---|---|---|---|---|
| KUO (1965) | 10 | 141 | 142 | Symmetrical |
| YAMASAKI (1968) | 4.7 | 100 | 94 | Symmetrical |
| OOYAMA (1969) | 10 | 50 | 400 | Symmetrical |
| MILLER (1969) | 10 | 200 | 100 | Real vortex |
| ROSENTHAL (1970) | 7 | 250 | 56 | Symmetrical |
| SUNDQVIST (1970a, 1970b) | 15 | 200 | 150 | Symmetrical |
| CARRIER (1971) | 21 | 50 | 840 | Symmetrical |
| ANTHES et al. (1971a, 1971b) | 18 | 240 | 150 | Asymmetrical |
| ANTHES (1972) | 18 | 240 | 150 | Asymmetrical |
| MATHUR (1972) | 15 | 200 | 150 | Asymmetrical |
| HARRISON (1973) | ~10 | ~120[a] | ~170 | Asymmetrical |
| KURIHARA and TULEYA (1974) | 12 | 200 | 120 | Symmetrical |
| CESELSKI (1974) | 17 | ~100–150 | ~200 | Real vortex |
| KURIHARA and TULEYA (1974) | 12 | 200 | 120 | Symmetrical |
| ANTHES (1977) | 18 | 240 | 150 | Symmetrical |
| ROSENTHAL (1978) | 7.2 | 220 | 65 | Symmetrical |

NOTE: Typical precyclone cloud cluster vorticity is $10 \times 10^{-6}$ to $15 \times 10^{-6} \cdot s^{-1}$.
[a] Estimated from initial height field.

Table 5.13: Tropical disturbance classification stages and surface pressure and wind estimates at these various stages; two classes of nonintensifying disturbance and six stages of disturbance-to-cyclone intensification are shown. (GRAY, 1978a)

| Disturbance classification | Stage | Estimated minimum sea level pressure (mb) | Estimate of maximum sustained surface winds ($m \cdot s^{-1}$) |
|---|---|---|---|
| General class of nondeveloping disturbances | 0 | 1008 | 8 |
| Nondeveloping disturbances of summer in cyclone genesis region | 00 | 1008 | 8 |
| Initial cluster | 1 | 1007 | 8 |
| Pre-typhoon cluster | 2 | 1005 | 10 |
| Genesis | 3 | 1003 | 12 |
| Intensifying | 4 | 1000 | 18 |
| Tropical storm (980–1000 mb) | 5 | 990 | 25 |
| Typhoon (950–980 mb) | 6 | 965 | 40 |

*Movement of Tropical Cyclones: Prediction and Modelling*

Several different techniques are being used for predicting the tracks of tropical cyclones: empirical, statistical, and dynamical. Empirical techniques will be considered first. According to HEBERT (1979), these may be further classified into three categories:

(a) persistence and climatology,
(b) synoptic and
(c) satellite.

These techniques can be used for prediction of the hurricane track for 12–24 h in advance. Any extrapolation beyond 24 h will result in large errors, except possibly in the deep easterlies of the tropics.

In the persistence technique, one simply extrapolates linearly the last track, assuming uniform speed and no change of direction. One can use a higher order persistence forecast by allowing for variation of speed of movement and direction of the hurricane in the past 12–24 h. The simplicity of this technique is its chief advantage. It is obvious that errors could occur if the persistence assumption does not hold.

In a climatological forecast one makes use of the knowledge of the temporal and spatial frequency of past hurricanes in given grid areas (e.g. 2.5° latitude-longitude squares and time scales up to 5 d). This method works well when the frequency of occurrence is great. It fails with increasing latitude (due to recurvature) as well as for untypical situations. Other time it fails is when a bimodal structure is present.

In the persistence plus climatology forecasts (BELL, 1962; AOKI, 1979) one uses the formula np + mC where p and C represent the persistence and climatology, respectively, and $n$ and m are weighting factors. Usually, $n$ = m = 0.5 is used. AMADORE (1972) gave different weightings to get latitude and longitude components separately for the tropical cyclones east of the Philippines. However, according to HEBERT (1979), similar attempts for the South China Sea region did not significantly improve the results.

In the synoptic technique, the main assumption is that the air mass in which the tropical cyclone is embedded is homogeneous. In the surface geostrophic steering method, the zonal (east-west) and the meridional (north-south) components of the hurricane movement are determined by estimating (from the synoptic charts) the pressure gradient (millibars per degree of latitude) across the storm. Since the surrounding air mass is not uniform, one must apply a correction to the pressure gradient to account for the nonhomogeneity. The main advantage of this technique lies in the fact that almost all forecast centres have surface pressure analysis charts.

In the control point method (CHIN, 1970), which has been in use for several years at the Hong Kong Observatory, one makes use of the observed high correlation between the wind direction at certain locations in the midtroposphere and the direction of movement of the tropical cyclone. The disadvantage is that in areas of sparse data, midtropospheric analyses might be difficult to make.

In predicting the movement of cyclones, one should also consider the so-called Fujiwhara effect (FUJIWHARA, 1921) in which two vortices close to each other will rotate about a common point located on the line joining their centres.

Next, satellite techniques, which are playing an ever-increasing role in the prediction of the tracks of cyclones, will be considered. The basic principle is to relate past changes in cloud features to future changes in the direction of motion.

FETT and BRAND (1975) used six identifiable cloud patterns and extrapolated the rotation of one or more of these patterns during the previous 24 h to calculate the change in the motion direction for the next 24 h. In making this extrapolation, an analogy of the relationship of the turning of a tropical cyclone to its hyperbolic point was used.

The method that is occasionally used in the Australian Bureau of Meteorology was developed by LAJOIE and NICHOLLS (1974). From available satellite pictures, they identify certain cloud features and based on these, extrapolation is made for the next 12 h regarding

Die Küste, 63 Global Storm Surges (2001), 1-623



the change of direction of motion of the cyclone. The two main principles involved are as follows: tropical cyclones frequently move in the direction of the line connecting their centers to the most developed cumulonimbus cluster at or near the downstream end (i.e. in a cyclonic direction of the inflow current) of the outer cloud band and tropical cyclones usually do not move towards a cumulonimbus-free sector.

The advantage of the satellite techniques is that they can be used in regions where conventional data are sparse. The disadvantages are difficulty in obtaining good satellite pictures and the subjectivity involved in interpreting them. Nevertheless, certain simple concepts are useful in the prediction of the tracks. For example, RAMAGE (1973) noted the extent of cloudiness along the track of a tropical cyclone. In Japan, substantial observations exist to show that the successive positions of the spiral cloud band correlate well with the movement of recurving typhoons.

Cyclones moving towards the west sometimes recurve towards northeast after interaction with upper air troughs in the westerlies. CHAN (1978), based on a study of recurring typhoons in the western part of the North Pacific Ocean, suggested that the following two parameters, which can be determined from satellite imagery, can be used to estimate the recurvature: $D/d$, where $D$ is the diameter of the central dense overcast of the tropical cyclone and $d$ is the average width of the cloud band associated with the interacting trough, and $\theta$, which is the angle between the axis of the cloud band and the latitude of the tropical cyclone center. If $30° \leq \Theta \leq 40°$ and $D/d < 1.5$, then it is highly probable that a tropical cyclone will recurve.

*Statistical Techniques of Track Prediction*

Following NEUMANN (1979), statistical models will be discussed. These are broadly divided into two categories: models based on analogs and models based on regression equations. Regression equation models can be further classified into (i) models using predictors based on climatology and persistence, (ii) models that include, but are not limited to, predictors derived from observed synoptic data, and (iii) models that include, but are not limited to, predictors derived from numerically forecasted data. Models of type (i) are referred to as simulated analog, models of type (ii) are referred to as classical models (or statistico-synoptic), and models of type (iii) are called statistical-dynamical models.

The basic principle involved in these models is the recognition of the fact that temporal and spatial analyses of tracks reveal repetitiveness and close association with identifiable synoptic patterns.

The advantage of the analog method is that it is usually the first available forecast for the tracks. Its disadvantage is that it works well only for typical situations. Next, the regression methods will be considered. RIEHL (1956) gave the first objective technique for predicting the movement of tropical cyclones. In this method, known as the Riehl-Haggard technique, one makes use of the steering principle, namely that the tropical cyclone's movement speed is proportional to the speed of the vertically integrated flow surrounding the vortex. The 500-mb level was used for approximating this flow. This technique was originally used for the Atlantic hurricanes.

*Dynamical Methods for Predicting Hurricane Movement*

Following PELISSIER (1979), the numerical models that were developed for predicting hurricane motion will be considered. The numerical modelling effort has been slow until the 1970s principally because tropical storms mainly occur over the data-sparse areas of the tropical oceans, and it is difficult to provide the initial state of the atmosphere. From a grid resolution point, the scale of the intense part of the tropical cyclone is small compared with the synoptic weather disturbances. Generally, prediction of the tracks of tropical cyclones is more successful than prediction of the intensification because the movement of the storm is mainly related to the steering current in which the storm is embedded.

SANDERS and BURPEE (1968) originally developed a barotropic model, referred to as SANBAR, which was modified by PIKE (1972). In this model the tropical cyclone track is predicted based on the track of minimum stream function and maximum vorticity centers. On a Mercator projection using a grid size of 1.5° and extending from the equator to 55° N and from 36.5° W to 123.5° W and using a time step of 30 min, forecasts are made up to 72 h in advance. The initial observations are averaged over the 1000- to 100-mb layer.

After specifying the initial winds, the nondivergent part of the wind field is calculated through a relaxation of the stream function $\psi$ in the interior of the grid using the relation

$$\nabla^2\psi = \frac{\partial v}{\partial x} - \frac{\partial u}{\partial y} + \frac{u \tan(\text{latitude})}{R_E} \tag{5.63}$$

where, u and v are the eastward and northward components, respectively, of the hurricane motion and $R_E$ is the radius of the earth. One must specify the component of the wind parallel to the boundaries. Then, using the barotropic vorticity equation

$$\left(\nabla^2 - M\right)\frac{\partial\psi}{\partial t} = J\left(f + \nabla^2\psi, \psi\right) \tag{5.64}$$

one can determine $\psi$ where J is the Jacobian, $\nabla^2$ is the horizontal Laplacian, and $M$ is the Helmholtz coefficient.

One can identify the storm center with a local minimum in x~ or a maximum in (or as an average between these two positions). Usually, the storm is replaced by an idealized circularly symmetric vortex defined by

$$v_\theta = 0.72 v_{max}\left\{\sin\left[\pi\left(\frac{r}{r_m}\right)\right]\right\}^{\left(\frac{\ln 0.5}{\ln r_c / r_m}\right)}{}^{1.5} \tag{5.65}$$

where, $v_\theta$ is the symmetric tangential wind field.

The Japan Meteorological Agency developed a balanced barotropic model for typhoon track prediction northward of 20 % using a 51 x 15 grid with a mesh length of 381 km at 60° N. At least three types of systematic errors appear: forecast positions for low latitude storms are occasionally poor due to a westward bias in the predicted tracks, the predicted speed of movement is usually smaller than observed values, and the predicted recurvature is usually less than the observed recurvature.

Table 5.14: Frequency distribution of direction using the balanced barotropic model. The angular intervals listed are the ranges of absolute differences between predicted and observed directions of displacement. Data listed under 24 and 48-h forecast periods are the number of typhoons that exhibited these directional deviations (PELISSIER, 1979)

| Angular interval (degrees) | 24-h forecast period | 48-h forecast period |
|---|---|---|
| 0–5 | 10 | 8 |
| 6–10 | 12 | 7 |
| 11–20 | 13 | 9 |
| 21–30 | 5 | 10 |
| 31–45 | 7 | 3 |
| 45 | 7 | 7 |

Table 5.15: Same as Table 5.14, except this is for eastward moving typhoons (PELISSIER, 1979)

| Angular interval (degrees) | 24-h forecast period | 48-h forecast period |
|---|---|---|
| 0–5 | 11 | 15 |
| 6–10 | 14 | 8 |
| 11–20 | 16 | 10 |
| 21–30 | 10 | 14 |
| 31–45 | 5 | 8 |
| 45 | 3 | 5 |

Table 5.16: Errors in predicted speed of movement relative to recurvature point. Overrun No. indicates number of typhoons that moved slower than the forecast. $R$, actual typhoon displacement; $F$, prediction by the balanced barotropic model (PELISSIER, 1979)

| Typhoon position | 24-h forecast period | | | 48-h forecast period | | |
|---|---|---|---|---|---|---|
| | Total No. | Overrun No. | $\frac{\lvert R-F\rvert}{R}$ | Total No. | Overrun No. | $\frac{\lvert R-F\rvert}{R}$ |
| Before recurvature | 42 | 16 | 0.406 | 38 | 14 | 0.341 |
| Near recurvature | 45 | 13 | 0.334 | 34 | 12 | 0.498 |
| After recurvature | 20 | 0 | 0.340 | 9 | 0 | 0.379 |
| Total (mean) | 107 | 29 | (0.381) | 81 | 26 | (0.401) |

In this model the initial stream function $\psi$ is determined from the geopotential by solving the balance equation

$$\nabla\cdot(f\nabla\psi)+2\left(\frac{\partial^2\psi}{\partial x^2}\frac{\partial^2\psi}{\partial y^2}-\frac{\partial^2\psi}{\partial x\partial y}\right)=\nabla^2\psi \qquad (5.66)$$

where, ($\Phi$ is the geopotential and $f$ is the Coriolis parameter. Using ARAKAWA's (1966) finite-difference schemes, the equation is integrated in time. Based on the data at 00:00 and 12:00 GMT, forecasts are issued for 48 h in advance, twice daily.

The frequency distribution of direction errors for westward moving typhoons is shown in Table 5.14. In this table, the first row contains the ranges of absolute differences between observed and predicted directions of displacements. One can see that there is no directional bias in the forecast. The frequency distribution of the direction errors for eastward moving typhoons is shown in Table 5.15. The errors in the forecast speed of the hurricane are classified in Table 5.16 according to the location relative to the point of recurvature. The term "overrun" means the number of typhoons that moved slower than predicted. Usually, this happens before recurvature but never afterwards.

A primitive equation model is considered next. The Fleet Numerical Weather Center (FNWC) at Monterey, C-A, and the Joint Typhoon Warning Center (JTWC) at Guam use a primitive equation model referred to as the coarse mesh grid model (CMG), which is a simplified version of a more elaborate triple-nested grid model (HINSMAN, 1977). The primitive equations are expressed in the pressure coordinates as follows:

$$\frac{\partial u}{\partial t} = -L(u) + fv - M\frac{\partial \phi}{\partial x} + \frac{\partial \tau_{xx}}{\partial x} + \frac{\partial \tau_{yx}}{\partial y} \tag{5.67}$$

$$\frac{\partial v}{\partial t} = -L(v) - fu - M\frac{\partial \phi}{\partial y} + \frac{\partial \tau_{xy}}{\partial x} + \frac{\partial \tau_{yy}}{\partial y} \tag{5.68}$$

$$\frac{\partial \theta}{\partial t} = -L(\theta) \tag{5.69}$$

$$\frac{\partial \phi_{1000}}{\partial t} = -L(\phi_{1000}) \tag{5.70}$$

$$\frac{\partial w}{\partial p} = -M^2\left[\frac{\partial}{\partial x}\left(\frac{u}{M}\right) + \frac{\partial}{\partial y}\left(\frac{v}{M}\right)\right] \tag{5.71}$$

$$\frac{\partial \phi}{\partial p} = \phi C_p \frac{\partial}{\partial p}\left(\frac{p}{1000}\right)^{R/C_p} \tag{5.72}$$

where,

$$L(S) = M^2\left[\frac{\partial}{\partial x}\left(\frac{u_S}{M}\right) + \frac{\partial}{\partial y}\left(\frac{v_S}{M}\right)\right] + \frac{\partial}{\partial p}(w_S) \tag{5.73}$$

The region of computation is like a channel with cyclic boundary conditions in the east and west and free-slip conditions on the north and south walls. In the vertical there are three layers. A movable grid is placed over the tropical cyclone so that initially the storm is in the lower central portion of the grid, which covers a span of 56° of longitude and 48° of latitude, with a mesh interval of 2°. An objective analysis of the flow fields at the 850-, 700-, and 200-mb levels, as well as the temperature at the 850-mb level, serve as input. Using a time step of 10 min, the model is integrated in time. The errors in the predicted track for the western and eastern Pacific are shown separately and together in Table 5.17. The errors are in kilometres and the numbers in parentheses are the cases studied.

At the National Meteorological Center, a multilevel nested grid model was developed (HOVERMALE and LIVEZEY, 1978). This is referred to as the moving fine mesh (MFM) model.

This model appears to be unique in the sense that a nested high-resolution grid cantered over the tropical cyclone moves during the numerical integration through a coarse outer grid. The error analysis for the forecasts based on this model is given in Table 5.18 and comparison is made with the errors from other models. For a review of the forecast errors using barotropic models (SANDERS et al., 1978). HOPE and NEUMANN (1978) provided a survey of tropical cyclone models available worldwide. ELSBERRY (1979) summarized the three-dimensional models that are available for hurricane track prediction. In his survey he omitted the barotropic models. Since it is almost certain that all future forecasts will be made with baroclinic models, these three-dimensional models will be briefly reviewed. The features of some of the baroclinic models presently available are listed in Table 5.19. These models (except the FNWC-TCM) are capable of resolving the inner structure of the tropical cyclone. Although a 60-km grid such as that used by the NMC and NRL-NEPRF models can resolve the primary interaction between the vortex and the steering current, to predict intensification the inner core of the typhoon must be resolved. Since it is impractical to cover the whole region of the typhoon with a fine grid, one can use a nested grid, the fine grid having a resolution of 10 km. Also, this inner grid must be moved with the storm. At present, the JMA model has these capabilities, although the inner grid size is 36 km.

Table 5.17: Average forecast errors (km) for 1976 for the U. S. Navy primitive equation tropical cyclone prediction model (CMG). Number of cases in parentheses (PELISSIER, 1979)

| Area | 24-h forecast period | 48-h forecast period | 72-h forecast period |
|---|---|---|---|
| Western Pacific | 287 (65) | 480 (57) | 693 (43) |
| Eastern Pacific | 263 (18) | 387 (15) | 724 (15) |
| Both together | 283 (81) | 461 (72) | 702 (58) |

Table 5.18: Mean vector errors (km) of the MFM, official forecasts, and other operational objective techniques based on statistical, climatological, and persistence methods (homogeneous sample) for Hurricane Belle of August 7–8, 1976. MFM, movable fine mesh; NHC, National Hurricane Center; NHC-67, National Hurricane Center's 1967 model. For a description of SANBAR and CLIPER, see text (HOVERMALE and LIVEZEY, 1978)

| Forecast period (h) | MFM | Official | NHC-67 | NHC-72 | NHC-73 | SANBAR | CLIPER |
|---|---|---|---|---|---|---|---|
| 12 | 124 | 87 | 67 | 72 | 67 | 86 | 76 |
| 24 | 213 | 185 | 200 | 226 | 152 | 228 | 204 |
| 36 | 215 | – | 241 | 365 | 270 | 426 | 454 |
| 48 | 280 | 404 | 311 | 507 | 369 | 644 | 748 |

Two types of boundary conditions are presently used in these models. In the one-way (OW) type, no feedback is allowed from the tropical cyclone to the hemispherical model. Note that the JMA nested grid model has a two-way (TW) interaction boundary condition for the inner grids. The statistics at 24 and 48 h for selected 1977 typhoons for official (JTWC), NMC-MFM, and FNWC-TCM models are shown in Table 5.20.

Table 5.19: Characteristics of several baroclinic models being applied for prediction of tropical cyclone motion based on operational data. NMC, National Meteorological Center (U.S.A.); MFM, movable fine mesh; FNWC, Fleet Numerical Weather Center (Monterey, CA); TCM, tropical cyclone model; NRL, Naval Research Laboratory; NEPRF, Naval Environmental Prediction Research Facility; PSU, Pennsylvania State University; NPS, Naval Post Graduate School (Monterey, CA); JMA, Japan Meteorological Agency; MNG, multiple-nested grid (ELSBERRY, 1979)

| Agency-model | Vertical coordinate | No.of layers | Grid size (km) | No. of points | Relocatable grid | Lateral boundary conditions[a] |
|---|---|---|---|---|---|---|
| NMC-MFM | σ | 10 | 60 | 50 x 50 | Yes | OW |
| FNWC-TCM | ρ | 3 | 205 | 32 x 24 | No | OW |
| NRL-NEPRF | σ | 5 | 60 | 51 x 51 | No | OW |
| PSU-NPS | σ | 5 | 120 | 40 x 40 | No | OW |
| JMA-MNG | σ | 3 | 291 | 31 x 31 | No | OW |
| | | | 145 | 31 x 31 | Yes | TW |
| | | | 73 | 31 x 31 | Yes | TW |
| | | | 36 | 31 x 31 | Yes | TW |

[a] OW, one-way interaction; TW, two-way interaction

Table 5.20: Track error (km) statistics at 24 and 48 h for selected 1977 typhoons for official (JTWC), NMC-MFM, and FNWC-TCM. JTWC, Joint Typhoon Warning Center, Guam (ELSBERRY, 1979)

| Typhoon | Official | | NW-MFM | | FNWC-TCM | |
|---|---|---|---|---|---|---|
| | 24 h | 48 h | 24 h | 48 h | 24 h | 48 h |
| Vera-1 | 178 | 107 | 294 | 289 | 106 | 111 |
| Ivy | 226 | 472 | 109 | 248 | – | – |
| Dinah-1 | 181 | 778 | 356 | 559 | 152 | 285 |
| Thelma | 159 | 707 | 96 | 148 | 146 | 574 |
| Jean | 126 | 578 | 339 | 441 | – | – |
| Dinah-2 | 206 | 437 | 56 | 385 | 250 | 270 |
| Babe | 583 | – | 282 | 885 | 437 | – |
| Dinah-3 | 204 | 693 | 115 | 324 | 52 | 350 |
| Vera-2 | 300 | 444 | 254 | 181 | 143 | 52 |
| Gilda | 243 | 407 | 183 | 580 | 100 | 376 |
| Babe | 191 | 782 | 217 | 198 | 196 | 726 |
| Homogeneous | 250 | 544 | 206 | 333 | 176 | 343 |
| Sample (N) | | 9 | 8 | | | |

One important data source should be mentioned. The National Climatic Center's (Asheville, NC) magnetic tape deck 993 contains 12-h tropical storm movements for all ocean basins (CRUTCHER et al., 1978) for the period 1886–1975, and this file is continually being updated. CRUTCHER (1971a, 1971b) and CRUTCHER and QUINLAN (1971) used the bivariate normal elliptical distribution as a model for the statistics of the distributions of hurricane movements. CRUTCHER et al. (1978) deduced tropical storm accelerations based on the data contained in this vast file.

*Forcasting Tropical Cyclone Recurvature*

Most of the forecast errors associated with storm track prediction occur when the cyclones turn (or recurve). CHAN et al. (1980) studied tropical cyclones in the West Indies area for the period 1961–77 using compositing. These studies indicated that through an observation of certain parameters around a tropical cyclone (e.g. wind rotation, vertical wind shear between 200 and 900 mb, or a gradient of tropospheric mean temperature), better forecasts for 24–36 h ahead could be made. The basis for this statement is the fact that significant differences exist in the large-scale wind fields at 200-, 500-, and 900-mb levels for left-turning, straight-moving, and right-turning cyclones.

This study was limited to those cyclones west of 55° W and with maximum sustained winds of at least 18 m · $s^{-1}$. Three categories are defined as follows (Fig. 5.49):

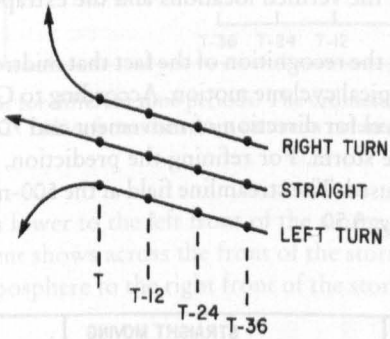


Fig. 5.49: Idealized picture of the three turn classes of tropical cyclones and of the time periods (hours) prior to the turn (CHAN et al., 1980)

Table 5.21: Average 24-h official tropical cyclone track forecast errors (km) issued by the National Hurricane Center, Miami. T, time when the storm begins to turn (CHAN et al., 1980)

| Turn classification | T – 24 | T | T + 24 |
|---|---|---|---|
| Left turn (10 cases) | 235 | 289 | 206 |
| Straight (23 cases) | 148 | 169 | 196 |
| Right turn (22 cases) | 178 | 324 | 239 |
| Special right turn (16 cases) | 148 | 417 | 245 |

Table 5.22: Directional deviation (degrees) of the mean 24-h forecast position made at turn time from the mean verifying position and the mean extrapolated track. A positive number means the forecast position is to the right of the verifying position of the extrapolated track (CHAN ET AL., 1980)

| Turn classification | From mean extrapolated track | From mean verifying position |
|---|---|---|
| Left turn | 21 | 50 |
| Straight | 9 | 11 |
| Right turn | 2 | –38 |

Left-turning: $D(T + 12) - D(T) < -20$

Straight-moving: $-10° < D(T + 12) - D(T - 12)$ (5.74)

Right-turning: $D(T + 12) - D(T) > 20°$

where, D is the direction of movement of the storm at a standard time T (00:00 or 12:00 GMT). A total of 16 left-turning, 33 straight-moving, and 28 right-turning storms were selected for this study.

The 24-h forecasts given by the National Hurricane Center were analysed for each case at three time periods: (a) 24 h before turn time, i.e. T – 24, (b) at turn time T, and (c) 24 h after turn time, i.e. T + 24. The forecast errors are listed in Tab 5.21. The special right-turn class is for those cases with an error greater than 350 km. The average directional deviation of the forecast locations from the verified locations and the extrapolated tracks are given in Table 5.22.

The basis for this study is the recognition of the fact that midtropospheric wind patterns have a strong influence on tropical cyclone motion. According to GEORGE and GRAY (1977), 500 mb is the best steering level for direction of movement and 700 mb is the best level for the speed of movement of the storm. For refining the prediction, flow fields at 900-, 700-, 500-, and 200-mb levels were used. The streamline field at the 500-mb level for the three classes of cyclones is shown in Fig. 5.50.

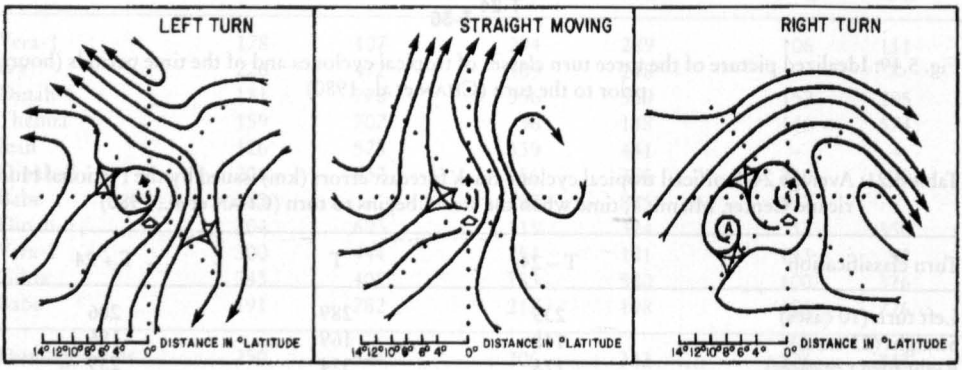


Fig. 5.50: Streamlines (500 mb) for the three turn cases shown in Fig. 5.49, at turn time. Open arrows indicate the instantaneous direction of storm motion. Solid arrows indicate the movement of the storm during the next 12 h (CHAN et al., 1980)

The vertical wind shear for these three classes is shown in Fig. 5.51. Here, $V_p$ represents the wind component parallel to the track and $V_N$ is the wind component perpendicular to the track. It can be seen from this diagram that usually the shear (i.e. $V_p$ at 200 mb minus $V_p$ at 900 mb) is greater than 5 m · s$^{-1}$ for left-turning tropical cyclones, is in the range of – 5 to 5 m · s$^{-1}$ for straight-moving storms, and is less than - 5 m · s$^{-1}$ for right-turning cyclones.

Sometimes it may not be possible to derive satellite winds at the 900- and 200-mb levels because of extensive cloud cover. In these situations, the satellite sounder (which can measure tropospheric difference) could be used. Generally, for left-turning storms the mean tro-

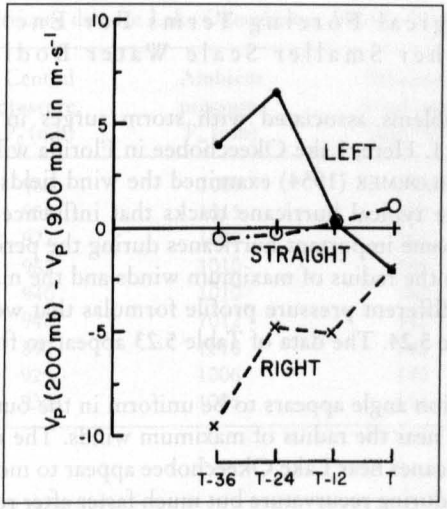


Fig. 5.51: Vertical wind shear for different time periods. The ordinate is the value of the average vertical wind shear within 7–11° radius from the storm centre in octants 1 and 5 (CHAN et al., 1980)

pospheric temperature is lower to the left front of the storm. For straight-moving storms a weak temperature gradient shows across the front of the storm. Right-moving storms indicate a relatively cold troposphere to the right front of the storm.

*Project Stormfury*

Project Storm fury is a scientific program aimed at studying the structure and dynamics of tropical cyclones and the possibility of modifying them, e.g. through cloud-seeding experiments (SHEETS and LASEUR, 1978). The project formally began in 1962, although some initial seeding experiments were done in 1961. These experiments are designed to effect a reduction in the maximum wind speeds in cyclones through changing the location of the energy released near the cyclone's centre. It is well known that the source of energy for a tropical cyclone is the latent heat released during convective overturning of the atmosphere. The active convective area in which updrafts of 10–20 m · s$^{-1}$ occur is less than 1 % of the area of the hurricane. Hence, one must modify only a small area of the hurricane to change its characteristics. The dynamics of the modification through seeding is explained by SHEETS and LASEUR (1978, p. 281) as follows:

Injection of silver iodide particles into the upper portion of these clouds causes the droplets to freeze, releasing the latent heat of fusion. This additional heat causes that portion of the cloud to be warmer and thereafter lighter than the surrounding air and thus triggers an increase in the ascending flow. As the air rises, it expands and cools, and water vapour condenses or sublimates, releasing considerably more latent heat. The result is that the seeded cloud grows to the outflow level, providing a new convective conduit that intercepts the inflowing low level air. The result is that a new eye wall is formed at a greater distance from the storm centre than the initial eye wall.

The tests on Hurricane Debbie of 1969 showed that winds could be reduced by 15–30 %. For experiments on typhoon modification, see World Meteorological Organization (1975) report No. 408.

### 5.3.3 Meteorological Forcing Terms For Enclosed Lakes and other Smaller Scale Water Bodies

Meteorological problems associated with storm surges in the Great Lakes were considered in section 7. 1. Here, Lake Okeechobee in Florida will be used as an example of an enclosed lake. SCHLOEMER (1954) examined the wind fields over Lake Okeechobee due to hurricanes. Some typical hurricane tracks that influence this lake are shown in Fig. 5.52. The dates of some important hurricanes during the period 1925–50 are listed in Table 5.23 together with the radius of maximum winds and the maximum wind speed and the pressure field. Ten different pressure profile formulas that were used by SCHLOEMER (1954) are listed in Table 5.24. The data of Table 5.23 appear to fit the second equation of Table 5.24.

The average deflection angle appears to be uniform in the outer portion of the storm, and it decreased rapidly near the radius of maximum winds. The most common deflection angle was 35°. The hurricanes near Lake Okeechobee appear to move with a speed of about 16 km · $h^{-1}$ prior to and during recurvature but much faster after recurvature. However, the maximum winds appear to occur before recurvature. Hurricane winds over lake Okeechobee for a synthesized storm at 0, 1 and 2 h are shown in Fig. 5.53. Notice the changes in pattern that could occur even in a 1-h time interval.

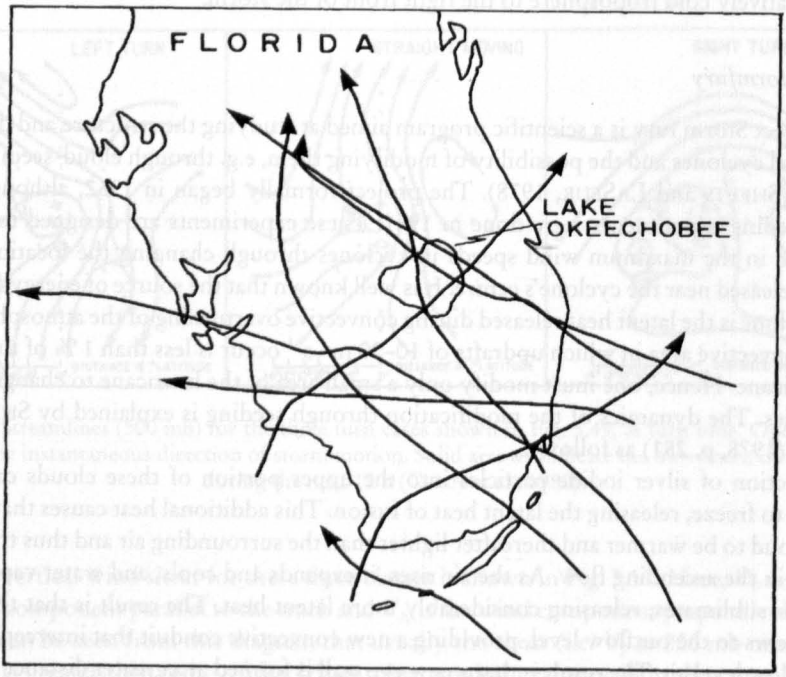


Fig. 5.52: Typical hurricane tracks over and near Lake Okeechobee, Florida (SCHLOEMER, 1954)

Table 5.23: Hurricane data for Lake Okeechobee, Florida (SCHLOEMER, 1954)

| Date of hurricane | Central pressure, $P_0$ (mb) | Ambient pressure, $P_\infty$ (mb) | Maximum wind speed ($km \cdot h^{-1}$) | Radius of maximum winds (km) |
|---|---|---|---|---|
| Sept. 18, 1926 | 960 | 1009 | 199 | 28 |
| Sept. 16–17, 1928 | 955 | 1015 | 185 | 43 |
| Sept. 2–3, 1935 | 977 | 1008 | 163 | 27 |
| Sept. 15–16, 1945 | 962 | 1010 | 185 | 24 |
| Sept. 17, 1947 | 940 | 1010 | 180 | 37 |
| Sept. 21–22, 1948 | 946 | 1012 | 140 | 30 |
| Oct. 5, 1948 | 892 | 1010 | 142 | 51 |
| Aug. 26–27, 1949 | 929 | 1006 | 140 | 37 |
| Oct. 17–18, 1950 | 935 | 1005 | 117 | 21 |

Table 5.24: Ten different forms used to approximate $(P - P_0)/(P_\infty - P_0)$ in a hurricane. Here, P is the pressure at a distance $r$ from the centre, $P_0$ is the central pressure, and $P_\infty$ is the ambient pressure. Parameters $n$, i, and j must be determined empirically (SCHLOEMER, 1954)

| | | | |
|---|---|---|---|
| (1) | $1 - e^{-nri}$ | (6) | $\frac{2}{\pi} \arctan \frac{1}{nr^i}$ |
| (2) | $e^{-n/ri}$ | (7) | $\frac{2}{\pi} \operatorname{arc\,cot} \frac{1}{nr^i}$ |
| (3) | $\frac{1}{1 + 1/nr^i}$ | (8) | $\frac{2}{\pi} \operatorname{arc\,sec} (1 + nr')$ |
| (4) | $\frac{1}{(1 + 1\,nr)^j}$ | (9) | $\frac{2}{\pi} \operatorname{arc\,cosec} (1 + 1/nr')$ |
| (5) | $\frac{1}{(1 + 1\,nr^i)^j}$ | (10) | $\tanh nr$ ' |

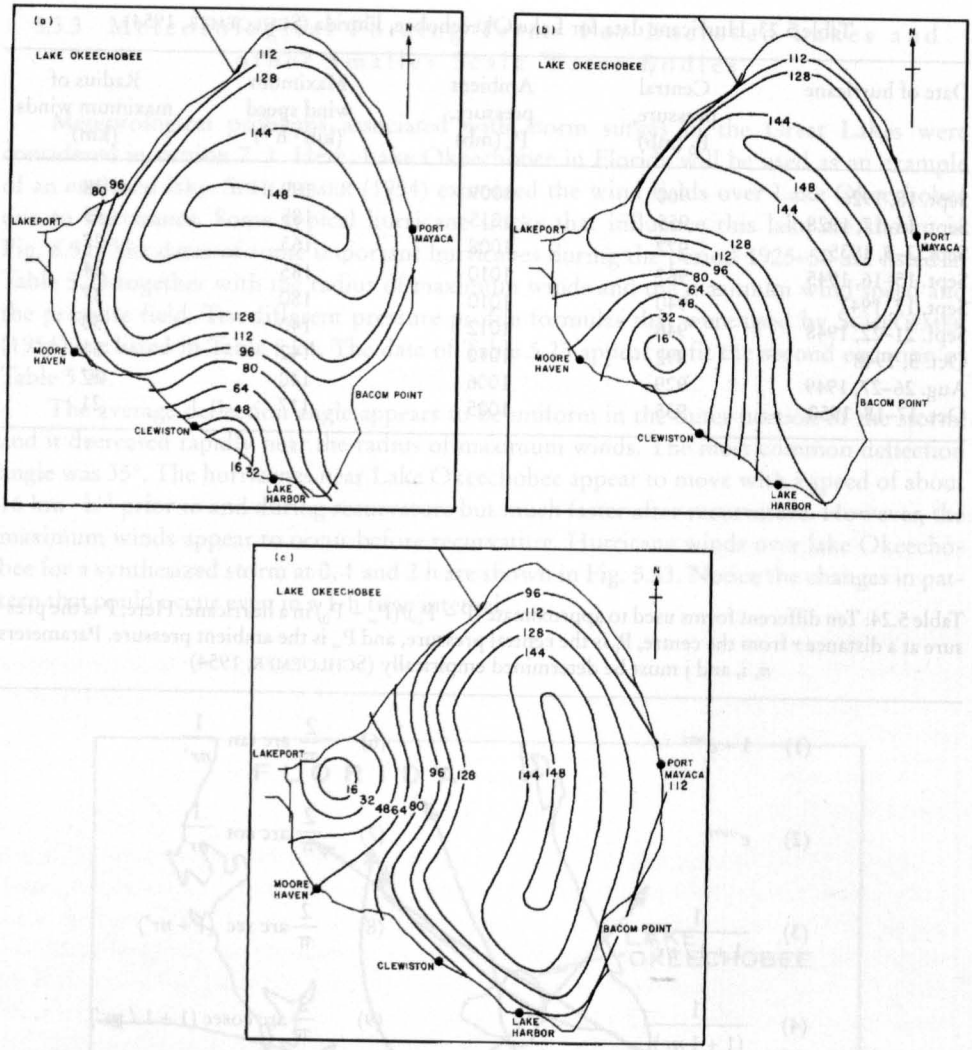


Fig. 5.53: Wind field (kilometers per hour) for a synthesized hurricane over Lake Okeechobee at (a) 0 h, (b) 1 h, and (c) 2 h after a specified zero time (SCHLOEMER, 1954)

## 5.4 Cyclones of the Pacific Ocean

Most of the damage from storm surges on the coast of the Pacific Ocean results from tropical storms. Hence, these will be emphasized in this section. Note that a storm surge is a rare event on the Pacific coasts of Canada and the United States (with the exception of Alaska); along these coasts, wind waves and swell are of primary importance.

Table 5.25: Record number of storms by basin based on data from 1968–1989 (1968/69 to 1989/90) for the Southern Hemisphere (NEUMANN, 1993)

| | Tropical Strom or stronger (greater than 17 m/s sustained winds) | | | Hurricane / Typhoon / Severe Tropical Cyclone (greater than 33 m/s sustained winds) | | |
|---|---|---|---|---|---|---|
| Basin | Most | Least | Average | Most | Least | Average |
| Atlantik * | 18 | 4 | 9.7 | 12 | 2 | 5.4 |
| NE Pacific | 23 | 8 | 16.5 | 14 | 4 | 8.9 |
| NW Pacific | 35 | 19 | 25.7 | 24 | 11 | 16.0 |
| N Indian | 10 | 1 | 5.4 | 6 | 0 | 2.5 |
| SW Indian | 15 | 6 | 10.4 | 10 | 0 | 4.4 |
| Aus SE Indian | 11 | 1 | 6.9 | 7 | 0 | 3.4 |
| Aus SW Pacific | 16 | 2 | 9.0 | 11 | 2 | 4.3 |
| Globally | 103 | 7.5 | 83.7 | 65 | 34 | 44.9 |

* Note that the data include subtropical storms in the Atlantic basin numbers.

Table 5.26: Monthly average number of storms per year for each major ocean basin. T, tropical storms only; H, hurricanes only. For the North Indian Ocean, replace the term hurricane with cyclone (winds >– 89 kin -h-'). –, zero (CRUTCHER and QUAYLE, 1974)

| | North Atlantic | | Eastern North Pacific | | Western North Pacific | | Southwest Pacific and Australian area | | Southwest Indian Ocean | | North Indian Ocean | |
|---|---|---|---|---|---|---|---|---|---|---|---|---|
| Month | T | H | T | H | T | H | T | H | T | H | T | H |
| Jan. | – | – | – | 0.2 | 0.3 | 2.7 | 0.7 | 2.0 | 1.3 | 0.1 | – | |
| Feb. | – | – | – | 0.3 | 0.2 | 2.8 | 1.1 | 2.2 | 1.1 | – | – | |
| Mar. | – | – | – | 0.3 | 0.2 | 2.4 | 1.3 | 1.7 | 0.8 | – | – | |
| Apr. | – | – | – | 0.2 | 0.7 | 1.3 | 0.3 | 0.6 | 0.4 | 0.1 | 0.1 | |
| May | 0.1 | – | 0.3 | 0.4 | 0.9 | 0.3 | – | 0.2 | – | 0.3 | 0.5 | |
| June | 0.4 | 0.3 | 1.5 | 0.6 | 0.5 | 1.2 | 0.2 | – | – | – | 0.5 | 0.2 |
| July | 0.3 | 0.4 | 2.8 | 0.9 | 1.2 | 2.7 | – | 0.1 | – | – | 0.5 | 0.1 |
| Aug. | 1.0 | 1.5 | 2.3 | 2.0 | 1.8 | 4.0 | – | 0.1 | – | – | 0.4 | – |
| Sept. | 1.5 | 2.7 | 2.3 | 1.8 | 1.5 | 4.1 | – | – | – | – | 0.4 | 0.1 |
| Oct. | 1.2 | 1.3 | 1.2 | 1.0 | 1.0 | 3.3 | 0.1 | – | 0.3 | – | 0.6 | 0.4 |
| Nov. | 0.4 | 0.3 | 0.3 | – | 0.8 | 2.1 | 0.4 | 0.3 | 0.3 | – | 0.5 | 0.6 |
| Dec. | – | – | – | 0.6 | 0.7 | 1.5 | 0.5 | 0.8 | 0.5 | 0.3 | 0.2 | |

Earlier it was mentioned that tropical cyclones form over all the tropical oceans except in the South Atlantic and in the South Pacific east of 140° W. The highest frequency of tropical cyclones occurs in the western Pacific, although maximum damage has occurred on the coasts surrounding the Bay of Bengal. Indeed one may say that tropical cyclones and their

associated storm surges together are probably the most devastating natural phenomena, even more so than earthquakes.

The number of tropical storms and hurricanes is listed by most, least and average for the period 1969–1989 and by month for various ocean basins in Table 5.25 and Table 5.26. It can be seen that the maximum frequency of tropical storms and Hurricans occurs in the western part of the North Pacific Ocean during the months of August and September. The preferred tropical cyclone tracks over the globe are shown in Fig. 5.54. Again, it can be seen that the tracks in the Pacific Ocean and Indian Ocean have more fine structure than those in the Atlantic Ocean. Contours of the speed of movement of tropical storms for various ocean basins are shown in Fig. 5.55. Maximum values of 35 knots (65 km · $h^{-1}$) occur in the western North Pacific, with maximum values of 30 knots (56 km · $h^{-1}$) in the Atlantic, and with maximum values of 27.5 (51 km · $h^{-1}$) in the eastern edge of the South Indian Ocean. In the following subsections, certain characteristics of tropical cyclones in the eastern North Pacific, central North Pacific, and western North Pacific will be detailed. There are shown for every region special examples and not the whole research.

### 5.4.1 Characteristics of Tropical Cyclones in the Eastern North Pacific

This discussion will be based on the tropical cyclone seasons of 1976, 1977 and 1978 (GUNTHER, 1977, 1978, 1979). For the 1976 season, tropical cyclone activity began on June 1 and ended on October 29. The season was average in the sense that there were eight hurricanes, six tropical storms, and four tropical depressions. The 1977 season began on May 25 and ended on October 23. Thus, the length of the 1977 season was 152 d whereas in 1976 it was 150 d. The total number of tropical storms in 1977 was 17 compared with 18 in 1976. However, in 1977 only 47 % of the storms reached hurricane intensity. Note that the number of tropical cyclones reaching storm or hurricane intensity in 1977 was 47 % less than the average for the period 1966–76. For the 1976 season, the highest sustained wind speed was 125 knots (231 km · $h^{-1}$) whereas for the 1977 season it was 90 knots (167 km · $h^{-1}$).

1978, the season began on May 30 and ended on October 20, with duration of 144 d. Although the 1978 season was 8 d shorter than the 1977 season, there was an increase of 24 % in cyclone activity. The number of cyclones reaching storm or hurricane intensity was 86 % in 1978 compared with 47 % in 1977. The highest sustained wind speed in the 1978 season was 120 knots (222 km · $h^{-1}$).

The first tropical cyclone to hit southern California since 1939 was Hurricane Kathleen in 1976. In the 1977 season, Hurricane Doreen struck again and in the 1978 season Hurricane Norman reached the coast. Though none of these three hurricanes caused any storm surge activity on the California coast, the heavy rains associated with these caused extensive damage.

During the hurricane season bulletins are issued four times per day from the Eastern Pacific Hurricane Center in San Francisco. The number of eastern North Pacific tropical storms reaching hurricane intensity is given in Table 5.27. The tracks of Hurricanes Kathleen of September 1976 and Doreen of August 1977 are shown in Fig. 5.56. All the tropical cyclones during 1977 did not reach land, as they were dissipated over the ocean. Hence, the damage in the 1977 season was less than in the 1976 season (during this season, several hurricanes moved onshore). In the 1978 season, only three cyclones moved onshore. Hurricane statistics prior to 1966 were not used in this study because satellite coverage was not adequate prior to 1966 and some hurricanes might have been missed.

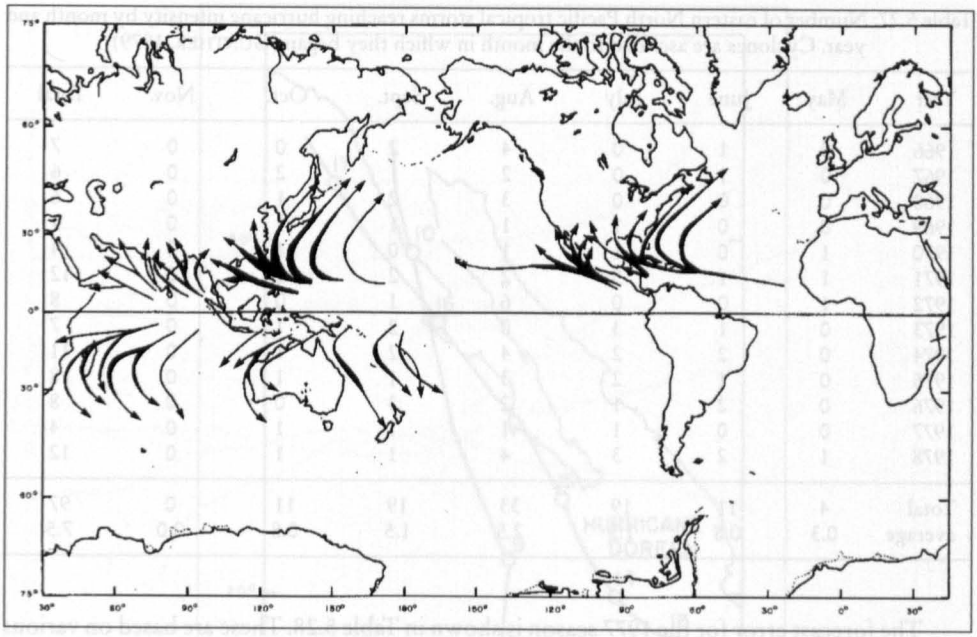

Fig. 5.54: Preferred annual tropical cyclone paths. Arrow widths are proportional to storm frequencies along indicated paths (CRUTCHER and QUAYLE, 1974)

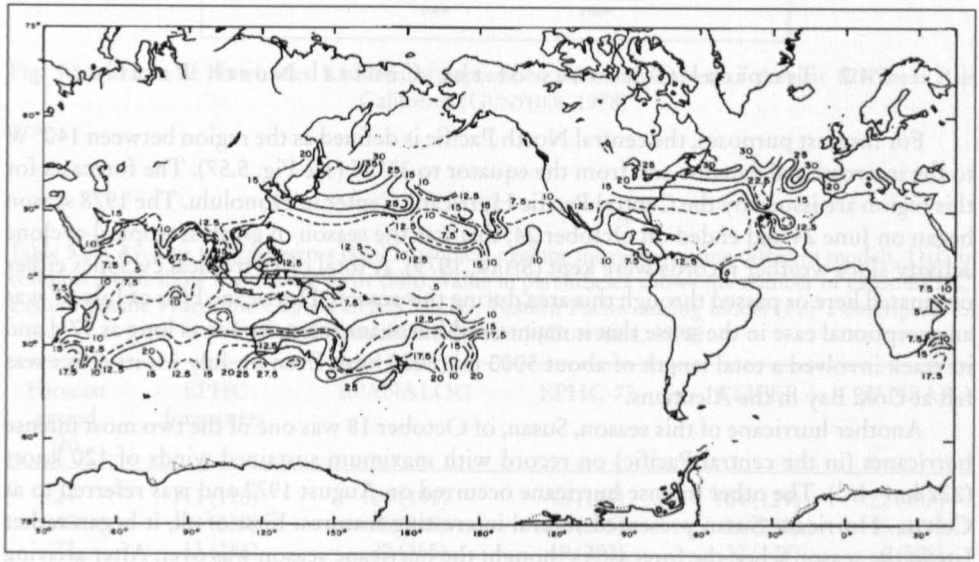

Fig. 5.55: Average (for annual data) speeds (knots) of storm movement (1 knot = 1852 km · $h^{-1}$) (CRUTCHER and QUAYLE, 1974)

Table 5.27: Number of eastern North Pacific tropical storms reaching hurricane intensity by month and year. Cyclones are ascribed to the month in which they began (GUNTHER, 1979)

| Year | May | June | July | Aug. | Sept. | Oct. | Nov. | Total |
|---|---|---|---|---|---|---|---|---|
| 1966 | 0 | 1 | 0 | 4 | 2 | 0 | 0 | 7 |
| 1967 | 0 | 1 | 0 | 2 | 1 | 2 | 0 | 6 |
| 1968 | 0 | 0 | 0 | 3 | 2 | 1 | 0 | 6 |
| 1969 | 0 | 0 | 1 | 1 | 1 | 1 | 0 | 4 |
| 1970 | 1 | 0 | 1 | 1 | 0 | 1 | 0 | 4 |
| 1971 | 1 | 1 | 5 | 2 | 2 | 1 | 0 | 12 |
| 1972 | 1 | 0 | 0 | 6 | 1 | 0 | 0 | 8 |
| 1973 | 0 | 1 | 3 | 0 | 2 | 1 | 0 | 7 |
| 1974 | 0 | 2 | 2 | 4 | 2 | 1 | 0 | 11 |
| 1975 | 0 | 1 | 2 | 3 | 1 | 1 | 0 | 8 |
| 1976 | 0 | 2 | 1 | 2 | 3 | 0 | 0 | 8 |
| 1977 | 0 | 0 | 1 | 1 | 1 | 1 | 0 | 4 |
| 1978 | 1 | 2 | 3 | 4 | 1 | 1 | 0 | 12 |
| Total | 4 | 11 | 19 | 33 | 19 | 11 | 0 | 97 |
| average | 0.3 | 0.8 | 1.5 | 2.5 | 1.5 | 0.8 | 0.0 | 7.5 |

The forecast error for the 1977 season is shown in Table 5.28. These are based on various computer models available at the National Hurricane Center in Miami. In this table, EPI-IC stands for the Eastern Pacific Hurricane Center, CLIPER is a simulated analog model, EPHC77 is a statistical synoptic model, EPRANALOG is an analog model, and SANBAR is a barotropic model. Of these four computer models, EPHC77 gave the best results, and these were subjectively improved by the EPI-IC forecasters.

### 5.4.2 Tropical Cyclones of the Central North Pacific

For forecast purposes, the central North Pacific is defined as the region between 140° W to the international dateline and from the equator to 35° N (see Fig. 5.57). The forecasts for this region are issued by the Central Pacific Hurricane Center in Honolulu. The 1978 season began on June 24 and ended on October 24; this was the season of greatest tropical cyclone activity since weather records were kept (SHAW, 1979). A total of 13 tropical cyclones either originated here or passed through this area during this season. Hurricane Fico of July 17 was an exceptional case in the sense that it maintained hurricane intensity for as long as 17 d and its track involved a total length of about 5000 mi (8000 km). Even on July 31, its effect was felt at Cold Bay in the Aleutians.

Another hurricane of this season, Susan, of October 18 was one of the two most intense hurricanes (in the central Pacific) on record with maximum sustained winds of 120 knots (222 km · $h^{-1}$). The other intense hurricane occurred on August 1972 and was referred to as Celeste. Hurricane Susan presented several interesting features. First of all, it began rather late in the season when the forecasters thought the hurricane season was over. After arriving 220 mi (354 km) southeast of the big island of Hawaii, it abruptly turned southwestward and dissipated rapidly. The central pressure rose more than 50 mb in 24 h.

Hurricane Gilma of July 22 was also somewhat unusual in the sense that it covered an area as large as $3 \times 10^5$ $mi^2$ ($7.8 \times 10^5$ $km^2$). Hurricanes for the 1978 season in the central Pacific are summarized in Tab 5.29.

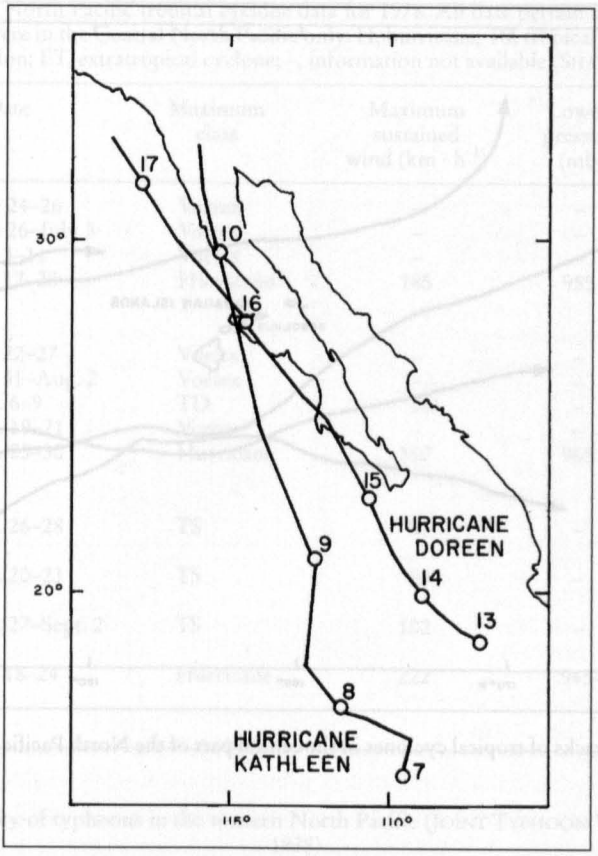


Fig. 5.56: Tracks of Hurricanes Kathleen of September 1976 and Doreen of August 1977 near Baja California (GUNTHER, 1978)

Table 5.28: Average forecast errors (km) in tropical cyclone movement using different models. Data in columns 2 to 6 show the average error (lun). Value in parentheses shows the number of cases. EPI4C, Eastern Pacific Hurricane Center; EPANALOG, Eastern Pacific analog model (For a description of these models, see the text.) (GUNTHER, 1978)

| Forecast period (h) | EPHC forecasters | EPANALOG | EPHC-77 | CLIPER | SANBAR |
|---|---|---|---|---|---|
| 24 | 113 (126) | 104 (141) | 96 (129) | 104 (129) | 22 (137) |
| 48 | 44 (239) | 56 (265) | 50 (255) | 56 (255) | 15 (271) |
| 72 | 13 (284) | 22 (365) | 19 (292) | 22 (378) | 6 (508) |

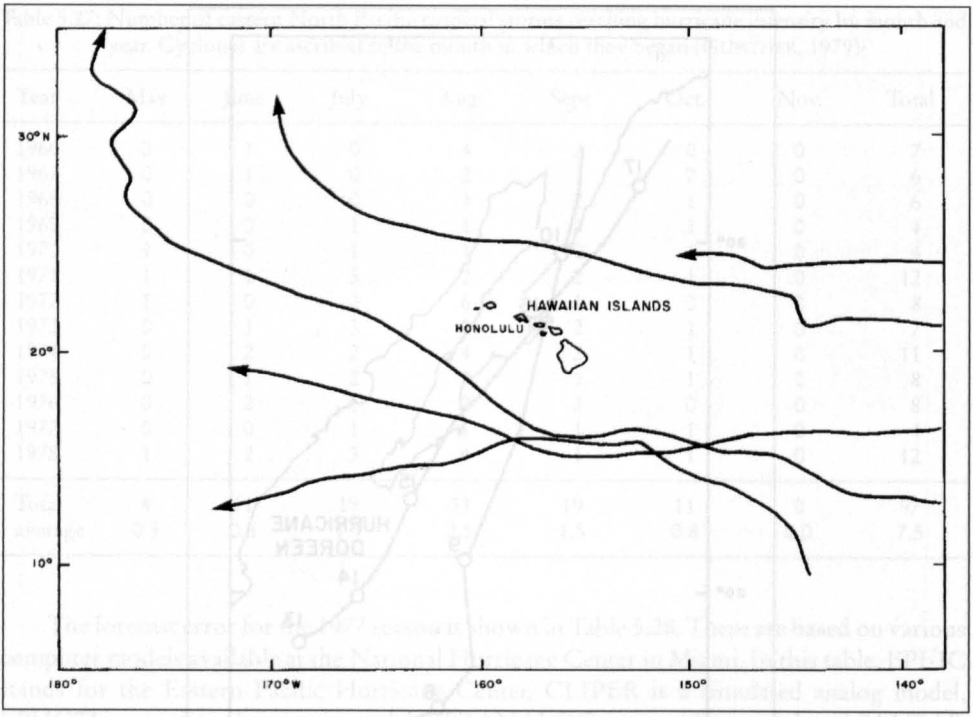


Fig. 5.57: Typical tracks of tropical cyclones in the central part of the North Pacific Ocean (SHAW, 1979)

### 5.4.3 Typhoons of the Western North Pacific

The Joint Typhoon Warning Center for the western North Pacific was set up at Guarn in 1959. The frequency of typhoons by month and year is listed in Table 5.30 and the western North Pacific tropical cyclones for the season of 1977 are listed in Table 5.31. The 1977 season began on March 13 and ended in January 1978. The 1978 season officially began on January 8 and ended on November 30. It can be seen that in the western North Pacific, typhoons can and do occur at any time of the year. In this respect this ocean basin is different from the central North Pacific, eastern North Pacific, and North Atlantic Ocean basins where the tropical cyclone season does not span the full year.

The seasons of 1977 and 1978 (JOINT TYPHOON WARNING CENTER, 1978, 1979) will be compared. The season of 1977 had the lowest number of tropical cyclones since 1959. Of a total of 21, 2 dissipated as depressions, 8 peaked out as tropical storms, and the remaining 11 matured into hurricanes. The monsoon systems of the Indian subcontinent and Southeast Asia appear to have some influence on tropical cyclones in the western North Pacific. During the 1977 season there were only 12 multiple storm days (a multiple storm day is one during which there is more than one tropical cyclone in the region). In 1970 and 1975, at certain times there were three or more tropical cyclones simultaneously. Storms with long durations could occur. Typhoon Kim of November 6, 1977, spanned 12 d. In this season, Typhoon Babe was classified as a super typhoon.

Table 5.29: Central North Pacific tropical cyclone data for 1978. All data pertain to the period during which the storms were in the Central North Pacific only. H, hurricane; TS, tropical storm; TD, tropical depression; ET, extratropical cyclone; –, information not available (SHAW, 1979)

| Name of storm | Date | Maximum class | Maximum sustained wind (km · h$^{-1}$) | Lowest pressure (mb) | Total hours observed |
|---|---|---|---|---|---|
| Bud | June 24–26 | Vortex | – | – | 48 |
| Carlotta | June 26–July 3 | Vortex | – | – | 168 |
| Daniel | July 3–11 | Vortex | – | – | 192 |
| Fico | July 17–28 | Hurricane | 185 | 955 | 225 (H)<br>15 (TS)<br>36 (ET) |
| Gilma | July 22–27 | Vortex | – | – | 144 |
| Hector | July 31–Aug. 2 | Vortex | – | – | 60 |
| TD-10 | Aug. 6–9 | TD | 56 | – | 84 |
| Iva. | Aug. 19–21 | Vortex | – | – | 54 |
| John | Aug. 23–30 | Hurricane | 167 | 965 | 48 (H)<br>72 (TS)<br>48 (TD) |
| Kristy | Aug. 26–28 | TS | 93 | – | 18 (TS)<br>45 (TD) |
| Lane | Aug. 20–23 | TS | 93 | – | 66 (TS)<br>27 (TD) |
| Miriam | Aug. 27–Sept. 2 | TS | 102 | – | 72 (TS)<br>6 (TD) |
| Susan | Oct. 18–24 | Hurricane | 222 | 945–954 | 81 (H)<br>30 (TS)<br>24 (TD) |

Table 5.30: Frequency of typhoons in the western North Pacific (JOINT TYPHOON WARNING CENTER, 1978)

| Year | Jan | Feb | Mar | Apr | May | Jun | Jul | Aug | Sep | Oct | Nov | Dec | Total |
|---|---|---|---|---|---|---|---|---|---|---|---|---|---|
| 1954–58 (average) | 0.4 | 0.1 | 0.3 | 0.4 | 0.7 | 1.1 | 2.0 | 2.9 | 3.2 | 2.4 | 2.0 | 0.9 | 16.3 |
| 1959 | 0 | 0 | 0 | 1 | 0 | 0 | 1 | 5 | 3 | 3 | 2 | 1 | 20 |
| 1960 | 0 | 0 | 0 | 1 | 0 | 2 | 2 | 8 | 0 | 4 | 1 | 1 | 19 |
| 1961 | 0 | 0 | 1 | 0 | 2 | 1 | 3 | 3 | 5 | 3 | 1 | 1 | 20 |
| 1962 | 0 | 0 | 0 | 1 | 2 | 0 | 5 | 7 | 2 | 4 | 3 | 0 | 24 |
| 1963 | 0 | 0 | 0 | 1 | 1 | 2 | 3 | 3 | 3 | 4 | 0 | 2 | 19 |
| 1964 | 0 | 0 | 0 | 0 | 2 | 2 | 6 | 3 | 5 | 3 | 4 | 1 | 26 |
| 1965 | 1 | 0 | 0 | 1 | 2 | 2 | 4 | 3 | 5 | 2 | 1 | 0 | 21 |
| 1966 | 0 | 0 | 0 | 1 | 2 | 1 | 3 | 6 | 4 | 2 | 0 | 1 | 20 |
| 1967 | 0 | 0 | 1 | 1 | 0 | 1 | 3 | 4 | 4 | 3 | 3 | 0 | 20 |
| 1968 | 0 | 0 | 0 | 1 | 1 | 1 | 1 | 4 | 3 | 5 | 4 | 0 | 20 |
| 1969 | 1 | 0 | 0 | 1 | 0 | 0 | 2 | 3 | 2 | 3 | 1 | 0 | 13 |
| 1970 | 0 | 1 | 0 | 0 | 0 | 1 | 0 | 4 | 2 | 3 | 1 | 0 | 12 |
| 1971 | 0 | 0 | 0 | 3 | 1 | 2 | 6 | 3 | 5 | 3 | 1 | 0 | 24 |
| 1972 | 1 | 0 | 0 | 0 | 1 | 1 | 4 | 4 | 3 | 4 | 2 | 2 | 22 |
| 1973 | 0 | 0 | 0 | 0 | 0 | 0 | 4 | 2 | 2 | 4 | 0 | 0 | 12 |
| 1974 | 0 | 0 | 0 | 0 | 1 | 2 | 1 | 2 | 3 | 4 | 2 | 0 | 15 |
| 1975 | 1 | 0 | 0 | 0 | 0 | 0 | 1 | 3 | 4 | 3 | 2 | 0 | 14 |
| 1976 | 1 | 0 | 0 | 1 | 2 | 2 | 3 | 0 | 4 | 1 | 0 | 0 | 14 |
| 1977 | 0 | 0 | 0 | 0 | 0 | 0 | 3 | 0 | 2 | 3 | 2 | 1 | 11 |
| 1959–77 (average) | 0.3 | 0.1 | 0.1 | 0.7 | 0.9 | 1.1 | 2.8 | 3.6 | 3.2 | 3.2 | 1.6 | 0.5 | 18.3 |

Table 5.31: Tropical cyclones in the western North Pacific for the season of 1977. TV, typhoon; TS, tropical storm; STY, supertyphoon (JOINT TYPHOON WARMING CENTER, 1978)

| Name of typhoon | Period of warning | Intensity | Maximum surface wind ($km \cdot h^{-1}$) | Minimum observed sea level pressure (mb) |
|---|---|---|---|---|
| Patsy | Mar. 23–31 | TS | 93 | 981 |
| Ruth | June 14–17 | TS | 111 | 980 |
| Sarah | July 16–21 | TY | 139 | 970 |
| Thelma | July 21–26 | TY | 157 | 957 |
| Vera | July 28–Aug. 1 | TY | 204 | 926 |
| Wanda | July 31–Aug. 4 | TS | 83 | 986 |
| Amy | Aug. 20–23 | TS | 74 | 990 |
| Babe | Sept. 2–10 | STY | 241 | 906 |
| Carla | Sept. 3–5 | TS | 65 | 994 |
| Dinah | Sept. 14–23 | TY | 139 | 964 |
| Emma | Sept. 15–20 | TS | 111 | 966 |
| Freda | Sept. 23–25 | TS | 102 | 997 |
| Gilda | Oct. 3–10 | TY | 130 | 968 |
| Harriet | Oct. 16–20 | TS | 102 | 984 |
| Ivy | Oct. 21–27 | TY | 167 | 945 |
| Jean | Oct. 28–31, Nov. 2–3 | TY | 120 | 972 |
| Kim | Nov. 6–17 | TY | 232 | 916 |
| Lucy | Nov. 28–Dec. 7 | TY | 213 | 919 |
| Maiy | Dec. 20–Jan. 3 | TY | 185 | 947 |

One important feature of the typhoons in the western North Pacific is that they could have rather erratic tracks and loops (usually the loops occur when the steering currents are weak). The 1978 season had about an average number of tropical cyclones. However, there were several surprises. Ten storms and typhoons had erratic tracks. Typhoon Carmen was almost stationary for 3 d. Typhoon Faye's track had a large anticyclonic loop and then it deepened explosively (surface central pressure decreased by 18 mb in just 6 h). Typhoon Trix was the most ill-behaved of all. Storms Hester and Phyllis attained speeds of movement of 40 and 50 knots (74 and 93 $km \cdot h^{-1}$), respectively, after recurvature in their extratropical transition. Typhoons Virginia and Mamie were so compact in size (but not in intensity) that they were called midget typhoons. Typhoon Virginia traveled farthest north (to 42° N) still behaving like a tropical cyclone. Super typhoon Rita covered an amazing distance of 4142 mi (6669 km) and is second only to Typhoon Sarah of 1976, which traveled 4499 mi (8000 km). Some typical tracks of typhoons in the western North Pacific are shown in Fig. 5.58.

*Northwest Pacific Ocean*

LAPPO and ROZHDESTVENSKIY (1977, 1979) studied the energy transferred to the ocean from a typhoon via the storm surge. They referred to the storm surge as meteorological ocean tides. In their calculations they ignored the influence of the wind but included the effect of the atmospheric pressure. When the cyclone is stationary, the energy transferred to the ocean is equal to the potential energy associated with the change in the sea level. For a moving cyclone, however, there is an additional transfer of kinetic energy.

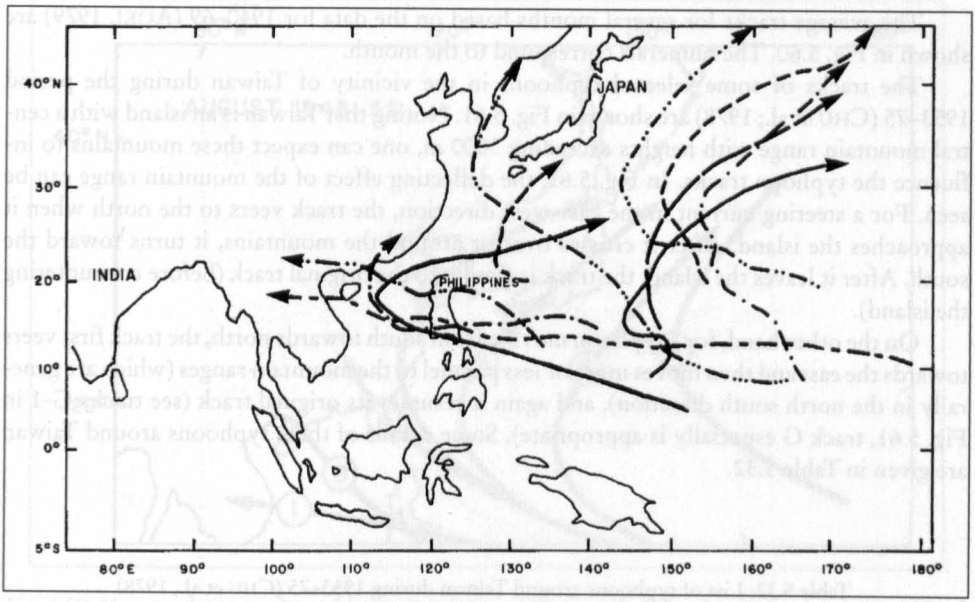


Fig. 5.58: Typical tracks of tropical cyclones in the western North Pacific (JOINT TYPHOON WARNING CENTER, 1977, 1978)

LAPPO and ROZHDESTVENSKIY (1977) formulated this problem along the lines of the classical quasi-stationary Proudman problem (PROUDMAN, 1929). For a plane pressure disturbance, with a pressure deficit of 40 mb, a cross-sectional diameter of the cyclone of $10^3$ km, and the distance traveled as $5 \times 10^3$ km, these authors gave the following values for an average cyclone (Joules):

Total energy of cyclone $= E_1 = 5 \times 10^{17}$ to $8 \times 10^{17}$

Kinetic energy $= E_2 = 5 \times 10^{16}$ to $8 \times 10^{16}$

Mechanical energy imparted to the ocean (ignoring wind stress ) $= E_l = 5 \times 10^{15}$

Potential energy of the storm surge created $= E_0 = 10^{15}$

*Tropical Cyclone Tracks Near Japan, Taiwan And The Philippines*

JAMISON (1956) described the average tracks of typhoons in this region for the month of August based on 11 yr of data (1945–55). These tracks are illustrated in Fig. 5.59.

During this period there was a total of 43 typhoons, of which 15 had rather erratic tracks (not known here). The number along each track is the number of typhoons that occurred during this 11-yr. period. Note that the lowest frequency is for the track that crosses Vietnam and the highest is for the Philippines area and continuing towards the Gulf of Tonkin. The number of tropical cyclones that traveled over Korea and Japan during this period was five.

The average tracks for several months based on the data for 1940–69 (AOKI, 1979) are shown in Fig. 5.60. The numerals correspond to the month.

The tracks of some selected typhoons in the vicinity of Taiwan during the period 1953–75 (CHU et al.; 1978) are shown in Fig. 5.61. Noting that Taiwan is an island with a central mountain range with heights exceeding 3000 m, one can expect these mountains to influence the typhoon tracks. In Fig. 5.61, the deflecting effect of the mountain range can be seen. For a steering current in the east-west direction, the track veers to the north when it approaches the island. After it crosses over or around the mountains, it turns toward the south. After it leaves the island, the track is similar to the original track (before encountering the island).

On the other hand, for a typhoon moving from south towards north, the track first veers towards the east and then moves more or less parallel to the mountain ranges (which are generally in the north south direction), and again it resumes its original track (see tracks G-1 in Fig. 5.61, track G especially is appropriate). Some details of these typhoons around Taiwan are given in Table 5.32.

Table 5.32: List of typhoons around Taiwan during 1953–75 (CHU et al., 1978)

| Name of typhoon | Date | Maximum wind speed ($km \cdot h^{-1}$) | Name of typhoon | Date | Maximum wind speed ($km \cdot h^{-1}$) |
|---|---|---|---|---|---|
| Judy | June 1953 | 74–111 | Gilda | Nov. 1967 | 148–185 |
| Kit | July 1953 | 204 | Elsie | Sept. 1969 | 194 |
| Thelma | Apr. 1956 | 157 | Betty | Aug. 1972 | 157–222 |
| Trix | Aug. 1960 | 204–222 | Joan | Aug. 1973 | 56–83 |
| Agnes | Aug. 1960 | 74–102 | Nora | Oct. 1973 | 111–176 |
| Pamela | Sept. 1961 | 222–278 | Jean | July 1974 | 93 |
| Sally | Sept. 1961 | 130 | Wendy | Sept. 1974 | 93 |
| Wendy | July 1963 | 185–250 | Nina | Aug. 1975 | 250 |
| Dinah | June 1965 | 74–241 | Betty | Sept. 1975 | 157–167 |
| Nora | Aug. 1967 | 111–120 | Elsie | Oct. 1975 | 222–259 |

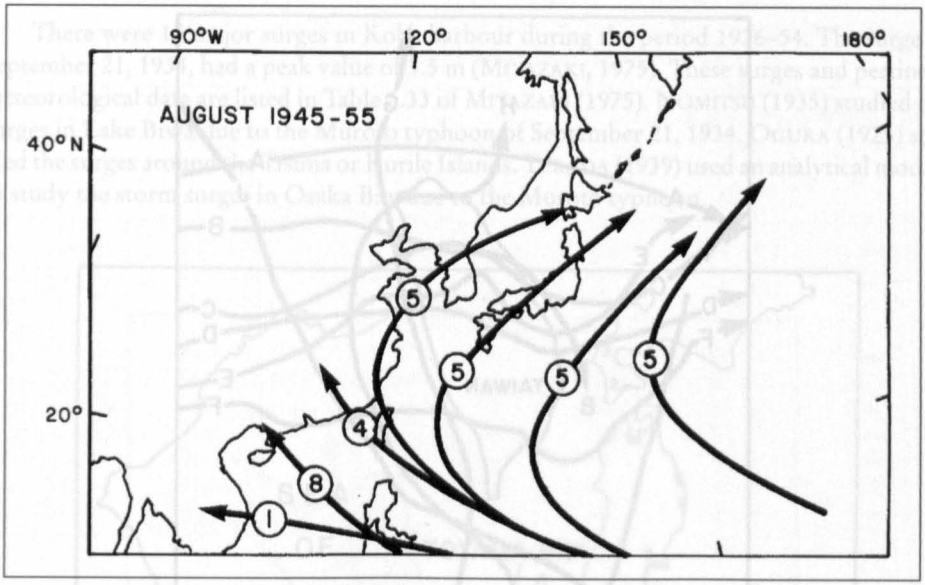


Fig. 5.59: Mean typhoon tracks and frequency (over an 11-yr period) for August in the western North Pacific (JAMISON, 1956)

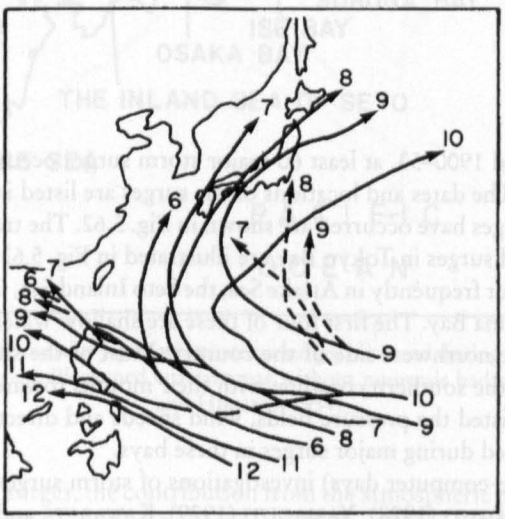


Fig. 5.60: Monthly mean tracks of tropical cyclones in the western North Pacific. Numbers refer to the months (AOKI, 1979)

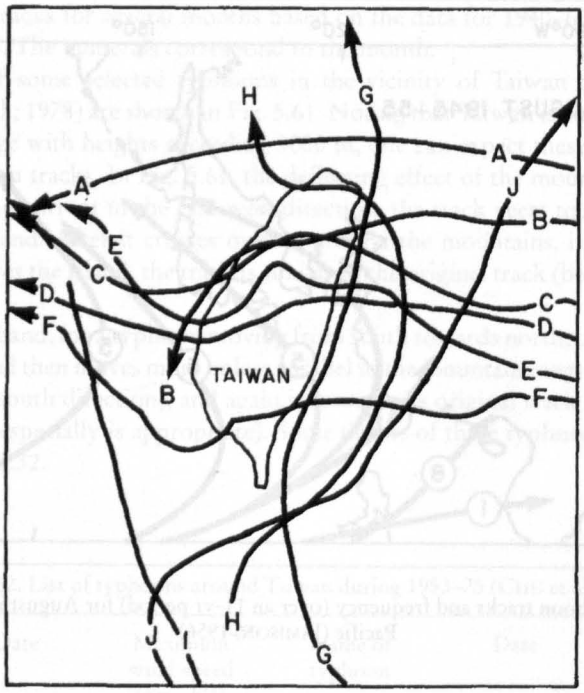


Fig. 5.61: Typical tracks of typhoons around Taiwan. A, Trix, 1960; B, Agnes, 1960; C, Pamela, 1961; D, Nora, 1967; E, Nina, 1975; F, Betty, 1975; G, Dinah, 1965; H, Wendy, 1974; I, Nora, 1973; J, Judy, 1953 (CHU et al., 1978)

*Japan*

During the period 1900–53, at least 60 major storm surges occurred in Japan (WADATI and HIRONO, 1954). The dates and locations of the surges are listed in Table 5.33. The locations where major surges have occurred are shown in Fig. 5.62. The tracks of some of the typhoons that generated surges in Tokyo Bay are illustrated in Fig. 5.63.

Storm surges occur frequently in Ariake Sea, the Seto Inland Sea, Osaka Bay, Tokyo Bay, Suruga Bay, and Toyama Bay. The first four of these are shallow water bodies; only Toyama Bay is situated on the northwest side of the country. Most of the shallow water bodies in Japan are situated on the southern coastline with their mouths towards southwest. WADATI and HIRONO (1954) listed the pressure fields, wind speeds and directions, damage, and the number of people killed during major surges in these bays.

For early (i.e. pre-computer days) investigations of storm surges in and around Japan, see TERADA and YAMAGUTI (1928), YAMAGUTI (1929), KAWABATA and FUJITO (1951), HONSYÛ (1932), and UNOKI (1959). TERADA (1912) and NAKANO (1949) investigated the secondary undulations associated with storm surges in Japan. RABE and BRAND (1980) studied the extreme sea states associated with typhoons.

MIYAZAKI (1975) studied the characteristics of storm surges along the coast of Japan. Some of the major surges (that exceeded 2 m) during the period 1900-73 are listed in Table 5.33. The damage associated with some selected surges is listed in Table 5.34.

There were 15 major surges in Kobe harbour during the period 1926–54. The surge of September 21, 1934, had a peak value of 3.5 m (MIYAZAKI, 1975). These surges and pertinent meteorological data are listed in Table 5.33 of MIYAZAKI (1975). NOMITSU (1935) studied the surges in Lake Biwa due to the Muroto typhoon of September 21, 1934. OGURA (1925) studied the surges around the Tisima or Kurile Islands. TERADA (1939) used an analytical model to study the storm surges in Osaka Bay due to the Muroto typhoon.

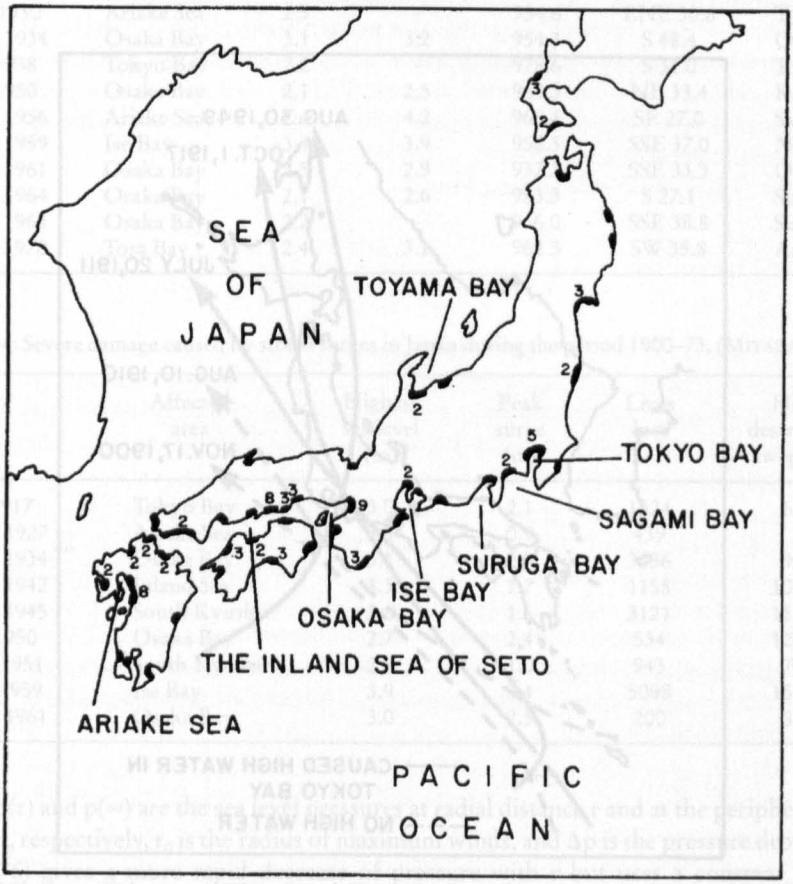


Fig. 5.62: Locations on the coast of Japan where storm surges occurred during 1900–53 (numerals indicate number of occurrences). Blackened coastal areas without numerals had one occurrence (WADATI and HIRONO, 1954)

In Japanese storm surges, the contribution from the atmospheric pressure gradients was at most 15 %. In the numerical model of ISOZAKI (1970a, 1970b, 1970c) the following pressure field distributions were specified:

$$p(r) = p(\infty) - \frac{\Delta p}{\left[1 + \left(\frac{r}{r0}\right)^2\right]^{1/2}} \qquad (5.75)$$

or

$$p(r) = 1010 - \frac{\Delta p}{\left(1 + \frac{r}{r_0}\right)^2} \tag{5.76}$$

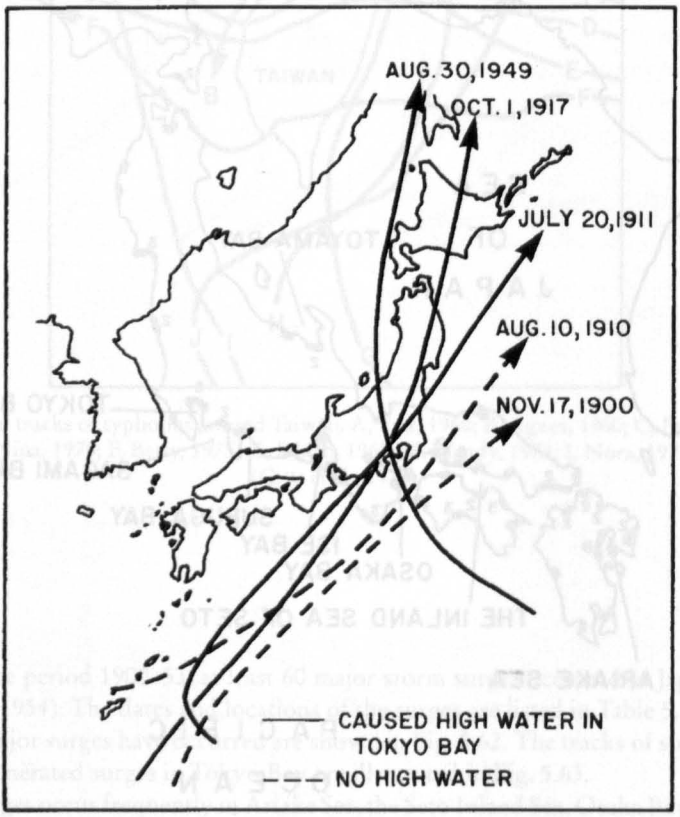


Fig. 5.63: Tracks of typhoons that passed near Tokyo Bay (WADATI and HIRONO, 1954)

Table 5.33: Storm surges in Japan during the period 1900–73 with maximum amplitudes ir, excess of 2 m; highest level includes surge and tide (MIYAZAKI, 1975)

| Date | Affected area | Peak surge (m) | Highest level (m) | Meteorological extreme values: Central pressure (mb) | Wind ($m \cdot s^{-1}$) | Location |
|---|---|---|---|---|---|---|
| Oct. 1, 1917 | Tokyo Bay | 2.3 | 3.1 | 950.4 | SSE 40.0 | Tokyo |
| July 18, 1930 | Ariake Sea | 2.5 | - | 954.6 | ENE 30.6 | Tomie |
| Sept. 21, 1934 | Osaka Bay | 3.1 | 3.2 | 954.3 | S 48.4 | Osaka |
| Sept. 1, 1938 | Tokyo Bay | 2.2 | - | 978.6 | S 31.0 | Tokyo |
| Sept. 3, 1950 | Osaka Bay | 2.1 | 2.5 | 964.3 | NE 33.4 | Kobe |
| Aug. 17, 1956 | Ariake Sea | 2.4 | 4.2 | 968.4 | SE 27.0 | Saga |
| Sept. 26, 1959 | Ise Bay | 3.4 | 3.9 | 958.5 | SSE 37.0 | Nagoya |
| Sept. 16, 1961 | Osaka Bay | 2.5 | 2.9 | 937.3 | SSE 33.3 | Osaka |
| Sept. 25, 1964 | Osaka Bay | 2.1 | 2.6 | 983.5 | S 27.1 | Sumoto |
| Sept. 10, 1965 | Osaka Bay | 2.2 | - | 966.0 | SSE 38.8 | Sumoto |
| Aug. 21, 1970 | Tosa Bay | 2.4 | 3.1 | 962.3 | SW 35.8 | Ashizuri |

Table 5.34: Severe damage caused by storm surges in Japan during the period 1900–73. (MIYAZAKI , 1975)

| Date | Affected area | Highest sea level (m) | Peak surge (m) | Lives lost | Houses destroyed or swept away |
|---|---|---|---|---|---|
| Oct. 1, 1917 | Tokyo Bay | 3.0 | 2.1 | 1324 | 60 175 |
| Sept. 13, 1927 | Ariake Sea | 3.8 | 0.9 | 439 | 2 211 |
| Sept. 21, 1934 | Osaka Bay | 3.1 | 2.9 | 3036 | 92 323 |
| Aug. 27, 1942 | Inland Sea | 3.3 | 1.7 | 1158 | 102 374 |
| Sept. 17, 1945 | South Kyushu | 2.6 | 1.6 | 3121 | 115 984 |
| Sept. 3, 1950 | Osaka Bay | 2.7 | 2.4 | 534 | 120 923 |
| Oct. 14, 1951 | South Kyushu | 2.8 | 1.0 | 943 | 72 648 |
| Sept. 27,1959 | Ise Bay | 3.9 | 3.4 | 5098 | 156 676 |
| Sept. 16, 1961 | Osaka Bay | 3.0 | 2.5 | 200 | 54 782 |

where, p(r) and p(∞) are the sea level pressures at radial distance r and at the periphery of the typhoon, respectively, $r_0$ is the radius of maximum winds, and $\Delta p$ is the pressure drop. Equation (5.76) gives a more rapid decrease of pressure with r but uses a constant value of 1010 mb at the typhoon periphery. The cyclostrophic wind corresponding to eq. (5.76) is

$$V^2 = 4V_m^2\left[\frac{\mu^2}{\left(1+\mu^2\right)^2}\right] \tag{5.77}$$

where, $\mu = r/r_0$ and $V_m$ is the maximum wind at $r_0$. The maximum wind and the pressure drop are related through

$$V_m = C(V_v)^{1/2} \tag{5.78}$$

where, C is a constant.

In other studies, the JELESNIANSKI (1972) model is used:

$$v(r) = V(r_0)\frac{2r_0}{r_0^2 + r^2} \tag{5.79}$$

where, again, $r_0$ is the radius of maximum winds. MYERS and MALKIN (1961) determined the angle of inflow for a stationary storm using the equations of motion. The angle varies from 0 at the center of the storm to about 30° at a radial distance of about $3r_0$ (where $r_0$ is the radius of maximum winds) and is roughly constant after that. Usually, within the region up to $r_0$, the wind field computed from the pressure field (i.e. cyclostrophic or gradient winds) is reasonably correct. Outside $r_0$, the angle of inflow (i.e. the angle of the wind vector across circular isobars) must be considered.
TAKAHASHI (1939) used the following form:

$$p(r) = p(\infty) - \frac{\Delta p}{\left(1 + \frac{r}{r_0}\right)} \tag{5.80}$$

This formula underestimates the pressure field at the center. KAWAHARA et al. (1980) used a finite-element model for storm surge propagation in Suragawa Bay. They used eq. (5.75) to specify the pressure field.

*China*

In China, storm surges mainly occur on the southeastern coast. In the 1970s, the biggest storm surge in China occurred at Shantou on August 2, 1979. The peak surge was over 2 m. In the dynamic models for surge prediction used in China (JIN-CHUAN and GUANG, 1979), MYERS (1954) formula is used:

$$\Delta p = \Delta p_0 (1 - e^{-R/r}) \tag{5.81}$$

where,

$$\Delta p_0 = p_\infty - p_c \text{ and } \Delta p = p_\infty - p \tag{5.82}$$

where, $p_c$ is the central pressure, $p_\infty$ is the peripheral pressure, p is the pressure at any point at distance r from the centre, and R is the radius of maximum winds.

The tangential component of the wind field is expressed as

$$V_\theta = \begin{cases} V_{max}\,\frac{r}{R}\cos\alpha & \text{for} \quad r \le R \\ V_{max}\,\frac{R}{r}\cos\alpha & \text{for} \quad r > R \end{cases} \tag{5.83}$$

The radial component of the wind field is written as

$$V_r = \begin{cases} -V_{max}\dfrac{r}{R}\sin\alpha & \text{for} \quad r \leq R \\ -V_{max}\dfrac{R}{r}\sin\alpha & \text{for} \quad r > R \end{cases} \tag{5.84}$$

where, $\alpha$ is the angle measured inward between the wind direction and the isobars. In the surge computations for the Chinese coast, $\alpha$ was taken as 30°.
The tangential and radial components of the wind stress are computed from:

$$\tau_\theta = K\rho_a \,|V|\, V_\theta$$
$$\tau_r = K\rho_a \,|V|\, V_r \tag{5.85}$$

where, $K = 2.5 \times 10^{-3}$ and $\rho_a = 1.2 \times 10^{-3}\ g \cdot cm^{-3}$.

Storm surges are quite frequent in Hong Kong. About three to four occur per year in Hong Kong Harbour (WORLD METEOROLOGICAL ORGANIZATION, 1978). A total of 35 surges with amplitudes varying from 0.2 to 1.8 m occurred in Hong Kong during 1954–64 (CHENG, 1967). Typhoon Wanda caused one of the important surges in September 1962. The surge was 1.8 m at Hong Kong and 3.2 m at Taipo (farther inland in a narrow channel).

CHAN and WALKER (1979) mentioned that two of the most disastrous surges in Hong Kong occurred on September 2, 1937, and September 1, 1962, in the Tolo Harbour region. WATTS (1959) concluded that pronounced surges occur in Hong Kong when the center of a westward moving storm passes over Hong Kong within several tens of kilometres to the south.

If the storm track lies to the west of Hong Kong, the wind field at Hong Kong will be strong (east-northeast to east-southeast) and a major surge could be generated. On the other hand, if the track is to the east of Hong Kong, the winds will be weak (west–northwest to west–southwest) and surges, if generated, will be small. Most of the storms that affect Hong Kong originate in the Philippine Sea. A few, however, develop in the South China Sea, and in this case, the above criterion (track to the east or west of Hong Kong) does not apply. Also, those storms that make a landfall at Hong Kong usually are associated with weak local winds and would not generate significant surges. The major surges at Hong Kong are associated with storms that make a landfall within 60 nautical miles (111 km) either to the north or south of Hong Kong.

Based on storm surge data at North Point, the storm surges are classified into three categories by CHAN and WALKER (1979): type 0 refers to storms whose centers lie within a 60 nautical mile radius of Hong Kong, type W for storms whose centers are outside the 60 nautical mile radius and which travel to the west of Hong Kong over the land, and type E for storms with centers outside the radius and traveling over the land to the east of Hong Kong. For these three categories, the average values of the peak surges are 2.49 ± 0.25, 1.71 ± 0.13, and 1.31 ± 0.18 ft (1 ft = 0.3048 m).

For type 0 storms, the following empirical relation was deduced:

$$s = 0.102\,(1009.1 - p) \tag{5.86}$$

where, s is the peak surge (feet) and p is the local minimum hourly sea level pressure (millibars). Note that in this relation, the local minimum hourly mean sea level pressure is used to represent the central pressure of the storm when it landfalls near Hong Kong. For type 0 storms, the coefficient of correlation between the central pressure and the peak surge was –0.89. For type W and E storms the correlation was poor.

Again, for type 0 storms, the correlation coefficient between the peak surge s and the maximum hourly mean wind speed $W_{60}$ was 0.84 and the following regression equation was derived:

$$s = 0.088\ W_{60} - 0.75 \tag{5.87}$$

The local wind field appears to have more influence on the type W and E storm surges than type 0. For type W, maximum surges are associated with winds from east-northeast, east, or east-southeast. The following relation has been empirically deduced for type W storm surges:

$$s_w = 0.00217\ W^2_{60} + 0.43 \tag{5.88}$$

The correlation coefficient between $s_w$ and $W^2_{60}$ was 0.88. No correlation could be found for type E storm surges.

LAU (1980a, 1980b) adapted the SPLASH (JELESNIANSKI, 1972, 1974) model to predict storm surges in Hong Kong. Using 57 hypothetical storms, peak surge heights at various locations along the South China coast near Hong Kong were determined. In these calculations, a standard storm is chosen with the following six parameters: (a) a central pressure of 973 mb at nearest approach, (b) a movement on bearing 300° at nearest approach, (c) a speed of 10 knots at nearest approach, (d) a radius of maximum winds of 26 nautical miles at nearest approach, (e) a nearest approach of 26 nautical miles, and (f) landfalling to the west of Hong Kong. This standard storm will generate on an open coast a surge (using the SPLASH program) of 1.92 m at North Point.

### 5.4.4 Explosively developing tropical Cyclones and Superthypoons in the Pacific

CLARK (1978a, 1978b), using satellite imagery, studied rapidly developing tropical cyclones in the northeastern Pacific Ocean during the period 1973–76. In his analysis, he made use of the so-called T number (DVORAK 1975a, 1975b)[1]. During this 4-yr period, of a total of 62 cyclones, 12 underwent a rapid development. The tracks of these rapidly developing tropical cyclones fall within a small area near Mexico (Fig. 5.64). CLARK (1978a, 1978b) cited persistent atmospheric conditions as contributing to the existence of a relatively small area of rapid development.

HOLLIDAY and THOMPSON (1979) made a study of rapidly deepening typhoons in the western part of the North Pacific Ocean using data from the period 1956–76. Their defini-

[1] The T number is based on the maximum wind speed. For example, TI corresponds to 25 knots, T2 to 30 knots, T3 to 45 knots, T4 to 65 knots, etc., with T8 corresponding to 170 knots (1 knot = 1.852 km · $h^{-1}$).

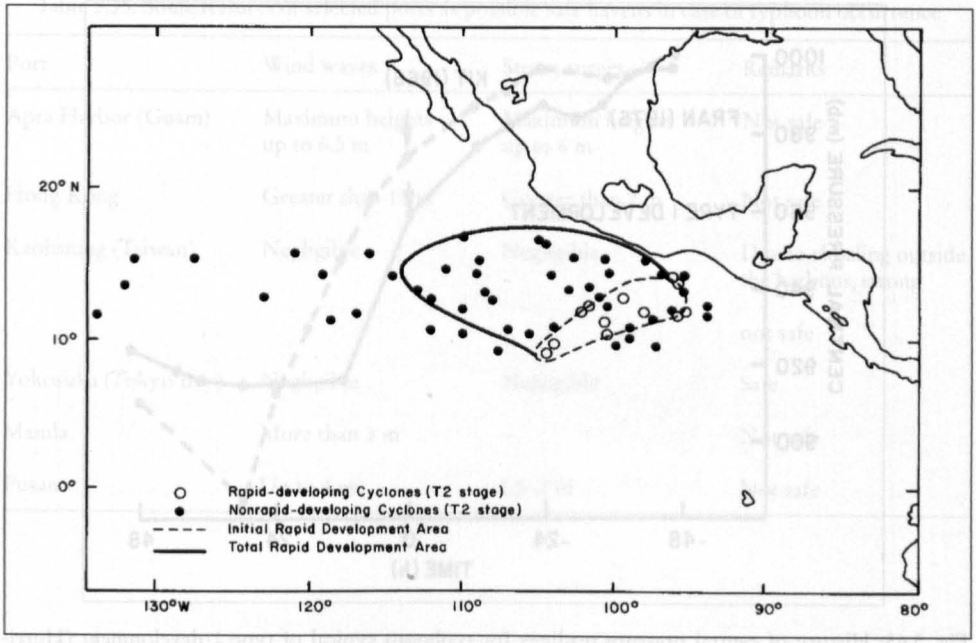


Fig. 5.64: Area of development of eastern North Pacific tropical cyclones, 1973–76 (CLARK, 1978b)

tion of rapid deepening is a fall in the central surface pressure by at least 42 mb in 24 h. In a total of 79 cases, rapid deepening (i.e. over an interval of 18 h with the steepest fall in the first 6 h) produced surface central pressures of 920 mb or less. For a tropical cyclone to mature into a typhoon, the underlying ocean temperature (up to a depth of 30 m) must be at least 28° C. This is a necessary condition for rapid deepening but not a sufficient condition.

Two basic types of deepening were noticed. In type 1 (Fig. 5.65) the central pressure falls at a moderate rate ($\geq 0.8$ mb $\cdot$ h$^{-1}$) at least over a period of 12–24 h. This is accompanied by accelerated development ($\geq 1.75$ mb h$^{-1}$). This behaviour for Typhoons Kit of 1966 and Fran of 1976 is shown in Fig. 5.65. In type 2 behaviour, initially there is slower development ($< 0.8$ mb $\cdot$ h$^{-1}$) suddenly followed by explosive ($\geq 1.75$ mb $\cdot$ h$^{-1}$). This is shown for Typhoons Virginia of 1957 and Anita of 1970 in Fig. 5.66. In the 79 case studies, 36 % exhibited type 1 behaviour and the remainder showed type 2 behaviour.

About 36 % of the rapid deepening occurred during daytime and 64 % occurred during nighttime. SHEETS (1969) suggested that this might be related to the differences in the atmospheric stability during day and night. However, SHEETS' (1969) study of hurricanes and FRANK's (1978) study of typhoons on diurnal variations showed little evidence for diurnal changes except in the temperature field and other Crameters in the upper troposphere and stratosphere.

The time interval between the weak circulation stages to the commencement of rapid deepening varied from 72 to 172 h. The time interval between the tropical storm stages to the onset of rapid deepening varied from 12 to 108 h. The interval between the time of reaching typhoon stage and initiation of rapid deepening varied from 0 to 72 h.

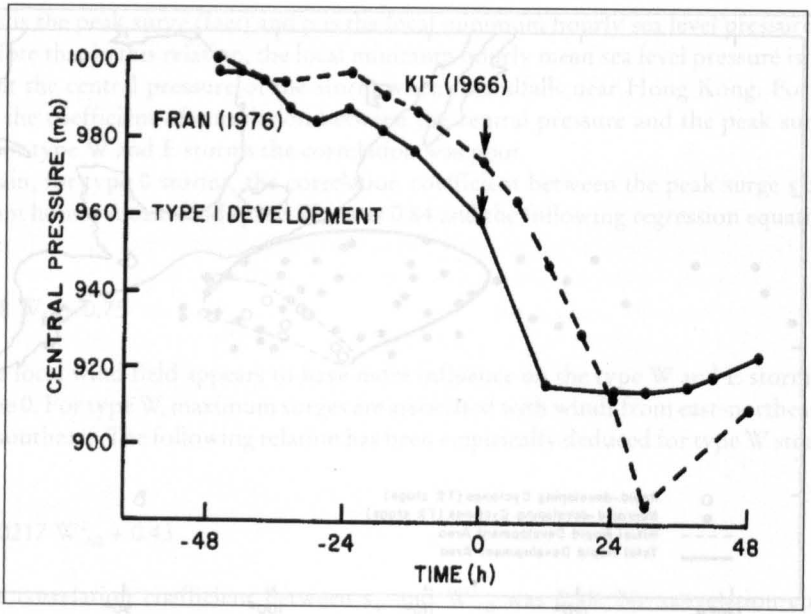


Fig. 5.65: History of central pressure readings for typhoons typical of type 1 development (Hurricanes Kit of June 1966 and Fran of September 1976). Arrow indicates onset of rapid deepening ($\geq 1.75$ mb $\cdot$ h$^{-1}$) (HOLLIDAY and THOMPSON, 1979)

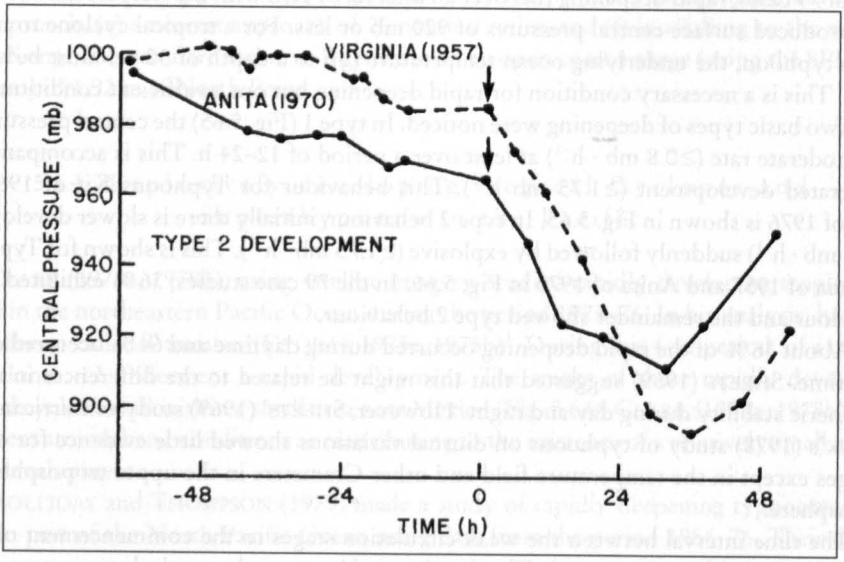


Fig. 5.66: History of central pressure readings for typhoons of type 2 development (Hurricanes Virginia of June 1957 and Anita of August 1970). Arrow indicates onset of rapid deepening ($\geq 1.75$ mb $\cdot$ h$^{-1}$) (HOLLIDAY and THOMPSON, 1979)

Table 5.35: Some features of selected ports as possible safe havens in case of typhoon occurrence

| Port | Wind waves | Storm surges | Remarks |
|---|---|---|---|
| Apra Harbor (Guam) | Maximum heights up to 6.5 m | Maximum heights up to 6 m | Not safe |
| Hong Kong | Greater than 10 m | Greater than 2 m | Not safe |
| Kaohsiung (Taiwan) | Negligible | Negligible | Due to shoaling outside the harbour, strong<br>not safe |
| Yokosuka (Tokyo Bay) | Negligible | Negligible | Safe |
| Manila | More than 3 m | – | Not safe |
| Pusan | Up to 4 m | 1.5–2 m | Not safe |

At the time of initiation of rapid deepening the eye diameters ranged from 29 to 37 km (average 33 km). Twelve hours after initiation of rapid deepening, the mean diameter of the eye decreased to 30 km, and 24 h after rapid deepening commencement, the average diameter was 26 km. Most of the rapid deepening occurred during the period July–November, with maximum activity in August and September. The area where rapid development began is shown in Fig. 5.67. The numerals show the number of cases during 1956–76.

Next, two interesting typhoons will be considered: Agnes of July 1978 and Tip of October 1979. The track of Typhoon Agnes is shown in Fig. 5.68. Because of the loop in the track, according to BELL (1979) it is the only tropical storm on record that caused gale signals to be hoisted twice at Hong Kong. Another unusual feature was that the so-called Fujiwara effect occurred between Typhoons Agnes and Wendy, although they were separated by 1000 mi (1600 km) apart. Another interesting feature from a public information point of view was that the American spacecraft *Apollo* ran into this with 60-knot (111 km · $h^{-1}$) winds and 25-ft (8 m) waves when it splashed down into the Pacific Ocean.

Super typhoon Tip developed in the western part of the North Pacific Ocean in early October 1979. This had at least two unique features: it holds the world record for the lowest minimum sea level pressure (870 mb) ever measured in a tropical cyclone (see Fig. 5.69) and it possessed the largest surface circulation pattern ever observed for a tropical cyclone (about 2200 km in diameter). Finally, this was transformed into an extratropical cyclone around October 18, 1979. Although it caused great destruction in Japan, the destruction was minimal for its size because the maximum intensity was reached while the system was still far away from inhabited areas.

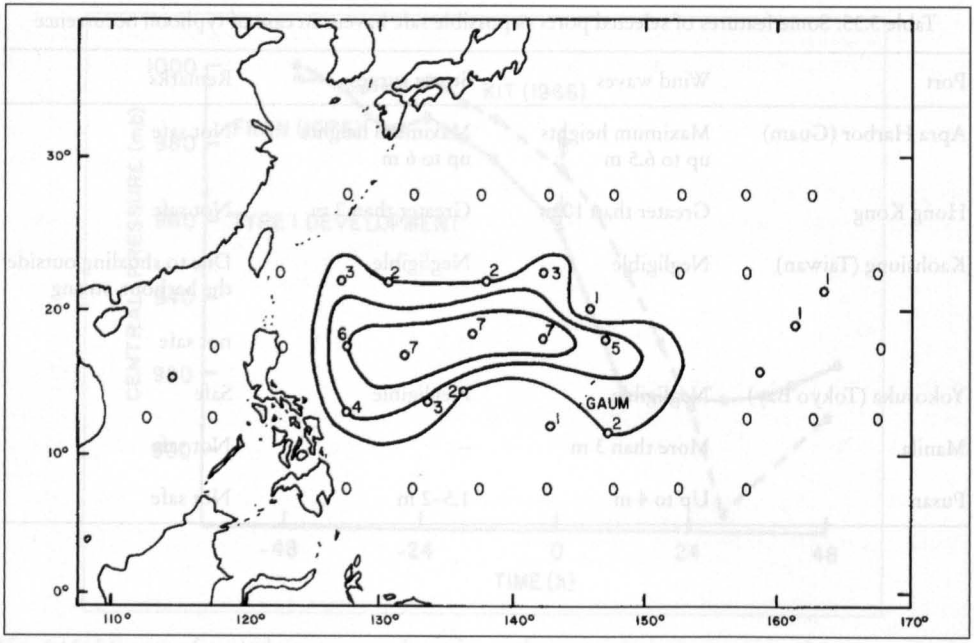


Fig. 5.67: Areas where typhoons intensified rapidly during summer and early fall (June 20–October 16). Numbers represent occurrences during 1956–76 (HOLLIDAY and THOMPSON, 1979)

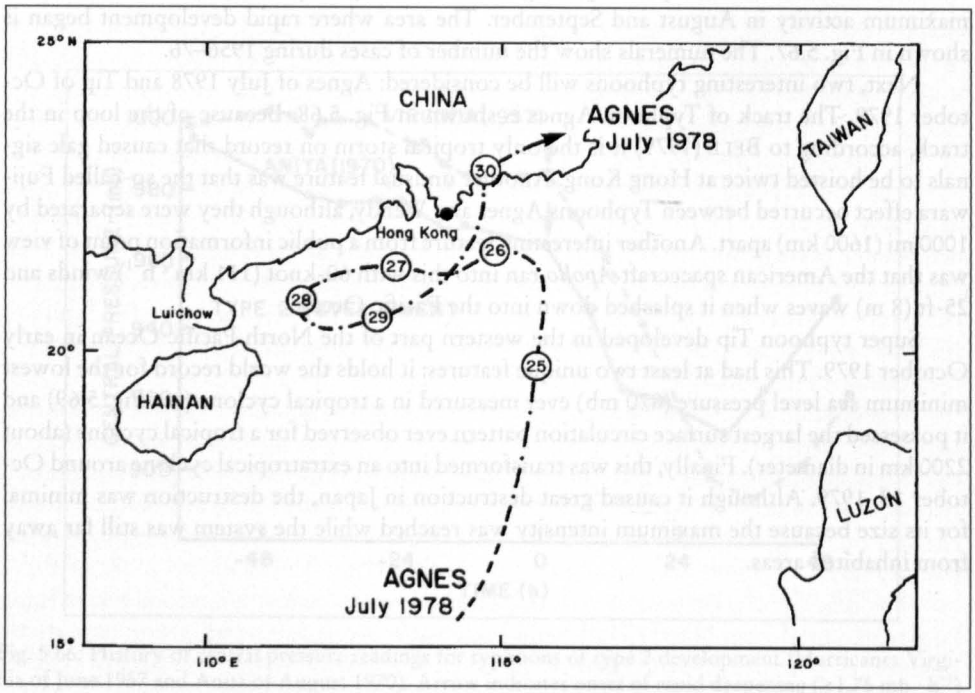


Fig. 5.68: Track of severe tropical storm Agnes from its formation on July 24, 1978, to its passage across the coast on July 30, 1978 (BELL, 1979)

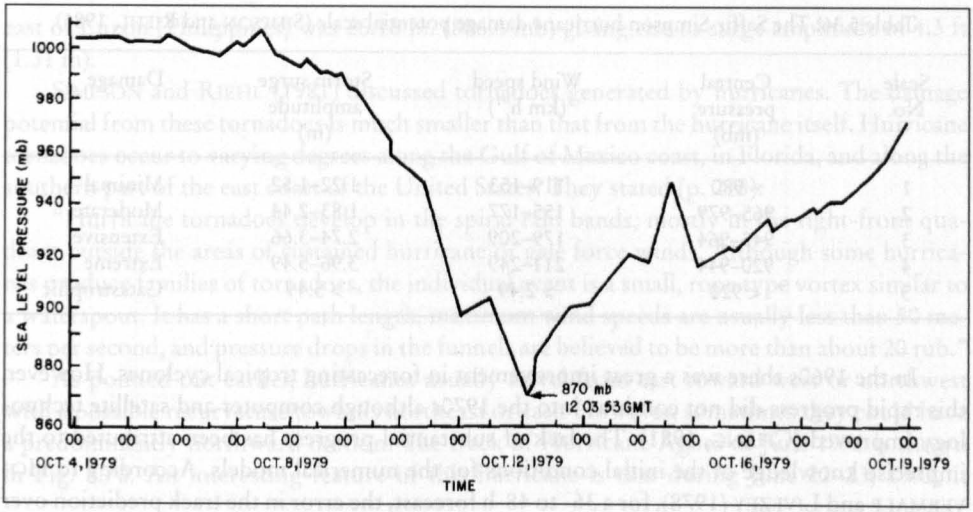


Fig. 5.69: Central pressure trace for Super typhoon Tip of October 1979 (DUNNAVAN and DIERCKS, 1980)

## 5.5 Tropical Cyclones of the Atlantic Ocean

Extratropical cyclones that affect North America are born in the western parts of the continent or in the Pacific Ocean and travel generally towards east (also east-northeast and north-east). Extratropical cyclones originating in the Atlantic generally do not affect North America but will travel towards Europe. Therefore this will be considered in chapter 5.1.3.

Here, basically, tropical cyclones originating in the Atlantic that affect mainly the North American continent will be considered.

### 5.5.1 Hurricanes Affecting the United States

The term "hurricane" comes from the Spanish word "huracon", which probably originated from Maya and Carib Indian usage meaning evil spirit, storm god, or devil. A hurricane is an intense tropical storm with wind speeds in excess of 74 mi · $h^{-1}$ (64 knots or 33 m · $s^{-1}$). Hurricanes originating in the Atlantic Ocean, Caribbean Sea, and the Gulf of Mexico caused about thousands of deaths. About 90 % of the deaths were due to drowning in the storm surge. In the twentieth century, damage in the United States resulting from hurricanes exceeded more than $ 12 billion.

There appears to be no definite periodic cycle for hurricanes. For example during the 1940's Florida took the brunt, during the 1950s the east coast of the United States was mostly affected, and during the 1960s and 1970s most damage occurred along the coast of the Gulf of Mexico. There is some indication in the early 1980s that the same trend as in the 1940s and 1950s may occur (OWEN, 1980).

In the North Atlantic Ocean, from June through November, some 100 disturbances develop every year. Of these, about five to six intensify into hurricanes. About 70 % of these storms originate near the west coast of Africa and are referred to as Cape Verde storms. Locations were shown earlier (Fig. 1.19) at which Atlantic tropical storms reached hurricane intensity during the period 1901–63.

Table 5.36: The Saffir-Simpson hurricane damage potential scale (SIMPSON and RIEHL, 1981)

| Scale No. | Central pressure (mb) | Wind speed (km $h^{-1}$) | Storm surge amplitude (m) | Damage |
|---|---|---|---|---|
| 1 | ~ 980 | 119–153 | 1.22–1.52 | Minimal |
| 2 | 965–979 | 155–177 | 1.83–2.44 | Moderate |
| 3 | 945–964 | 179–209 | 2.74–3.66 | Extensive |
| 4 | 920–944 | 211–249 | 3.96–5.49 | Extreme |
| 5 | < 920 | > 2.49 | > 5.49 | Catastrophic |

In the 1960s there was a great improvement in forecasting tropical cyclones. However, this rapid progress did not continue into the 1970s although computer and satellite technology improved (CHANG, 1981). The lack of substantial progress has been attributed to the imprecise knowledge of the initial conditions for the numerical models. According to HOVERMALE and LIVEZEY (1978), for a 36- to 48-h forecast, the error in the track prediction over the oceans (where data is scarce) is three times the error at coastal stations. Not everybody agrees with this evaluation. The EOS Bulletin (Vol. 61, No. 28, July 15, 1980, p. 538) mentioned that a NOAA satellite that is 22 300 mi (35 680 km) out in space is locating Atlantic Ocean hurricanes with an average accuracy of about 17 nautical miles and is pinpointing their intensity within an average of 10 knots. For a recent summary of the status of operational prediction of tropical cyclone motion over the North Atlantic Ocean, see NEUMANN and PELISSIER (1981). These authors concluded that none of the seven models (five statistical and two dynamical) that are in use at the National Hurricane Center in Miami could be singled out as superior to the others in every respect. One disappointing aspect is that one cannot combine the good points from all these models into a single model.

Hurricanes are classified according to the Saffir-Simpson scale (named after Herbert Saffir, a consulting engineer, and Dr. R. H. Simpson, former director of the National Hurricane Center in Miami), which is an intensity scale based on the central pressure, wind speed, amplitude of the storm surge, and the resulting damage. This scale is illustrated in abbreviated form in Table 5.36. More details about this scale can be found in SIMPSON and RIEHL (1981). Note that in the twentieth century, only three storms affecting the United States are given the highest rank (5) on this scale. These are the Labour Day storm of 1935, Hurricane Camille of 1969, and Hurricane Allen of 1980.

*Hurricane Statistics For The United States*

Some of the most disastrous hurricanes of the twentieth century in the United States and the damage are listed in Table 1. 1. BRUUN et al. (1962) gave a list of major hurricanes affecting Florida during the period 1900–60. In this table there are 40 entries. The inverted barometer effect could be quite significant in the generation of storm surges here. For each inch (of mercury) of reduction of the central pressure of the hurricane (1 in. = 2.54 cm) the corresponding hydrostatic water head is 14 in. (BRETSCHNEIDER, 1967). For the storm of September 2, 1935, at Lower Matecumbe Key in Florida, the lowest central pressure was 26.35 in. Hg (892.3 mb). Taking the normal sea level pressure as 29.92 in. Hg (10 13.2 mb) gives a 4.1-ft (1.3 m) rise in water level. Similar inverted barometer effects could be noticed in typhoons, also. For the typhoon of August 18, 1927, the central pressure some 460 mi (740 km)

east of Luzon (Philippines) was 26.18 in. (886.6 mb) giving rise to surge amplitude of 4.3 ft (1.31 m).

SIMPSON and RIEHL (1981) discussed tornadoes generated by hurricanes. The damage potential from these tornadoes is much smaller than that from the hurricane itself. Hurricane tornadoes occur to varying degrees along the Gulf of Mexico coast, in Florida, and along the southern part of the east coast of the United States. They stated (p. 218):

"Hurricane tornadoes develop in the spiral rain bands, mostly in the right-front quadrant outside the areas of sustained hurricane or gale force winds. Although some hurricanes produce families of tornadoes, the individual event is a small, rope type vortex similar to a waterspout. It has a short path length, maximum wind speeds are usually less than 50 meters per second, and pressure drops in the funnels are believed to be more than about 20 rub."

As pointed out earlier, hurricanes usually travel from east toward west or northwest with a possible recurvature towards northeast or cast. However, sometimes they could have a predominantly northward motion. The track of Hurricane Agnes of June 1972 is shown in Fig. 5.70. An interesting feature of this hurricane is that during June 22–23, 1972, it

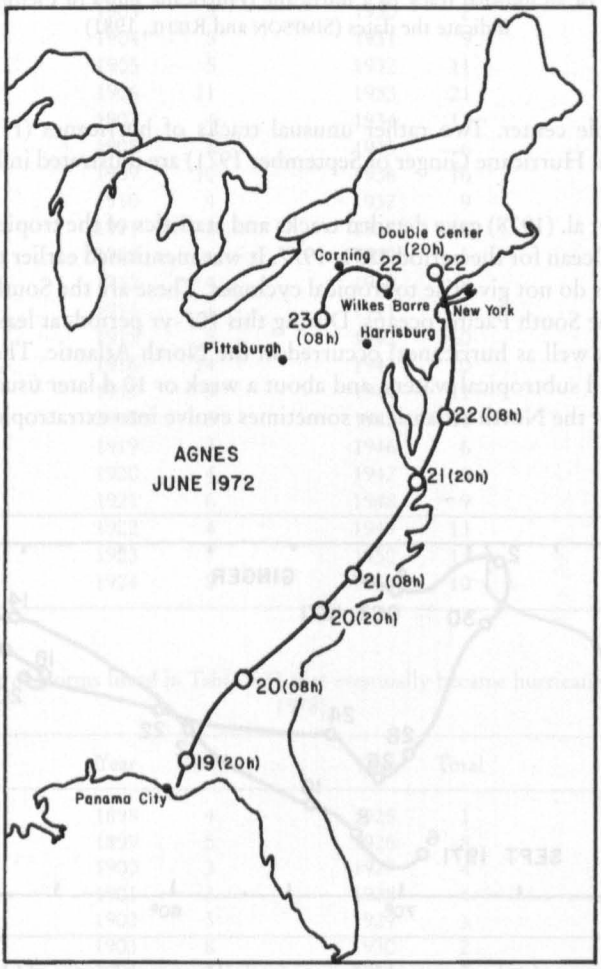


Fig. 5.70: Track of Hurricane Agnes of June 1972

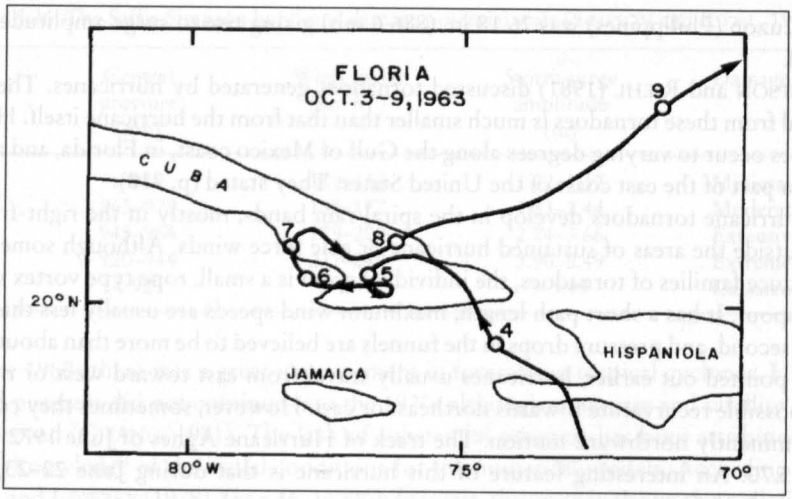


Fig. 5.71: Example of an unusual track of a hurricane (Hurricane Flora of October 1963). Numbers indicate the dates (SIMPSON and RIEHL, 1981)

exhibited a double center. Two rather unusual tracks of hurricanes (Hurricane Flora of October 1963 and Hurricane Ginger of September 1971) are illustrated in Fig. 5.71 and 5.72, respectively.

NEUMANN et al. (1978) gave detailed tracks and statistics of the tropical cyclones of the North Atlantic Ocean for the period 1871–1977. It was mentioned earlier that two large tropical ocean basins do not give rise to tropical cyclones. These are the South Atlantic and the eastern part of the South Pacific oceans. During this 107-yr period, at least 850 tropical cyclones (storms as well as hurricanes) occurred in the North Atlantic. These form over the warm tropical and subtropical waters, and about a week or 10 d later usually dissipate over the cold waters of the North Atlantic or sometimes evolve into extratropical cyclones.

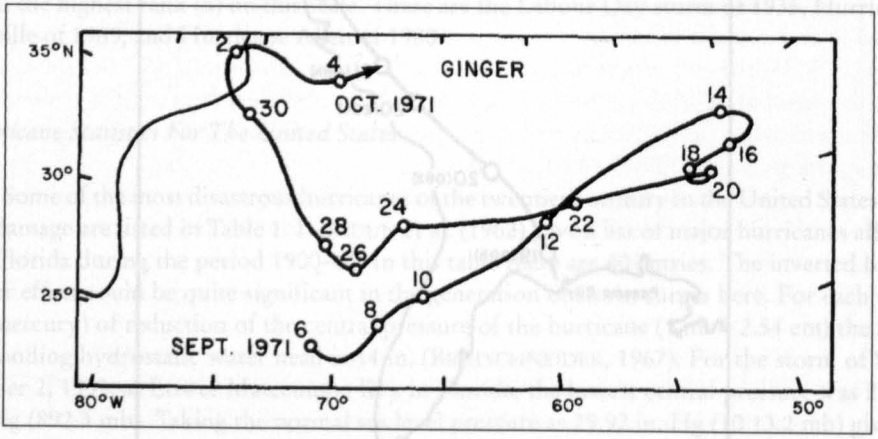


Fig. 5.72: Another example of an unusual hurricane track (Hurricane Ginger of October 1971). Numbers indicate the dates (SIMPSON and RIEHL, 1981)

These storms are listed in Table 5.37 for each of these years. Moreover the list of NEUMANN et al. (1978) encloses storms by month. It can be seen the dominance of storm events from August to October, which increase in number from May to August and decrease from October to December. Those that eventually became hurricanes are listed in Table 5.37. The distribution of the observed duration of hurricanes is given in Fig. 5.73.

Table 5.37: Number of recorded Atlantic tropical cyclones (excluding depressions and after 1967, including subtropical cyclones) that reached at least tropical storm intensity, 1871–1977 (NEUMANN et al., 1978)

| Year | Total | Year | Total | Year | Total | Year | Total |
|---|---|---|---|---|---|---|---|
| 1871 | 6 | 1898 | 9 | 1925 | 2 | 1952 | 7 |
| 1872 | 5 | 1899 | 6 | 1926 | 11 | 1953 | 14 |
| 1873 | 5 | 1900 | 7 | 1927 | 7 | 1954 | 11 |
| 1874 | 7 | 1901 | 10 | 1928 | 6 | 1955 | 12 |
| 1875 | 4 | 1902 | 5 | 1929 | 3 | 1956 | 8 |
| 1876 | 3 | 1903 | 9 | 1930 | 2 | 1957 | 8 |
| 1877 | 8 | 1904 | 5 | 1931 | 9 | 1958 | 10 |
| 1878 | 10 | 1905 | 5 | 1932 | 11 | 1959 | 11 |
| 1879 | 8 | 1906 | 11 | 1933 | 21 | 1960 | 7 |
| 1880 | 9 | 1907 | 4 | 1934 | 11 | 1961 | 11 |
| 1881 | 6 | 1908 | 8 | 1935 | 6 | 1962 | 5 |
| 1882 | 3 | 1909 | 10 | 1936 | 16 | 1963 | 9 |
| 1883 | 4 | 1910 | 4 | 1937 | 9 | 1964 | 12 |
| 1884 | 3 | 1911 | 4 | 1938 | 8 | 1965 | 6 |
| 1885 | 8 | 1912 | 6 | 1939 | 5 | 1966 | 11 |
| 1886 | 10 | 1913 | 4 | 1940 | 8 | 1967 | 8 |
| 1887 | 17 | 1914 | 1 | 1941 | 6 | 1968 | 8 |
| 1888 | 9 | 1915 | 5 | 1942 | 10 | 1969 | 18 |
| 1889 | 9 | 1916 | 14 | 1943 | 10 | 1970 | 10 |
| 1890 | 1 | 1917 | 3 | 1944 | 11 | 1971 | 13 |
| 1891 | 11 | 1918 | 5 | 1945 | 11 | 1972 | 7 |
| 1892 | 9 | 1919 | 3 | 1946 | 6 | 1973 | 8 |
| 1893 | 12 | 1920 | 4 | 1947 | 9 | 1974 | 11 |
| 1894 | 6 | 1921 | 6 | 1948 | 9 | 1975 | 9 |
| 1895 | 6 | 1922 | 4 | 1949 | 13 | 1976 | 10 |
| 1896 | 6 | 1923 | 7 | 1950 | 13 | 1977 | 6 |
| 1897 | 5 | 1924 | 8 | 1951 | 10 | | |

Table 5.38: Number of storms listed in Table 5.37 that eventually became hurricanes (NEUMANN et al., 1978)

| Year | Total | Year | Total | Year | Total | Year | Total |
|---|---|---|---|---|---|---|---|
| 1871 | | 1898 | 4 | 1925 | 1 | 1952 | 6 |
| 1872 | | 1899 | 5 | 1926 | 8 | 1953 | 6 |
| 1873 | | 1900 | 3 | 1927 | 4 | 1954 | 8 |
| 1874 | | 1901 | 3 | 1928 | 4 | 1955 | 9 |
| 1875 | | 1902 | 3 | 1929 | 3 | 1956 | 4 |
| 1876 | | 1903 | 8 | 1930 | 2 | 1957 | 3 |
| 1877 | | 1904 | 2 | 1931 | 2 | 1958 | 7 |
| 1878 | | 1905 | 1 | 1932 | 6 | 1959 | 7 |

Table 5.38: (Continued)

| Year | Total | Year | Total | Year | Total | Year | Total |
|---|---|---|---|---|---|---|---|
| 1879 | | 1906 | 6 | 1933 | 9 | 1960 | 4 |
| 1880 | | 1907 | 0 | 1934 | 6 | 1961 | 8 |
| 1881 | | 1908 | 5 | 1935 | 5 | 1962 | 3 |
| 1882 | | 1909 | 4 | 1936 | 7 | 1963 | 7 |
| 1883 | | 1910 | 3 | 1937 | 3 | 1964 | 6 |
| 1884 | | 1911 | 3 | 1938 | 3 | 1965 | 4 |
| 1885 | | 1912 | 4 | 1939 | 3 | 1966 | 7 |
| 1886 | 8 | 1913 | 3 | 1940 | 4 | 1967 | 6 |
| 1887 | 10 | 1914 | 0 | 1941 | 4 | 1968 | 5 |
| 1888 | 5 | 1915 | 4 | 1942 | 4 | 1969 | 12 |
| 1889 | 5 | 1916 | 11 | 1943 | 5 | 1970 | 5 |
| 1890 | 1 | 1917 | 2 | 1944 | 7 | 1971 | 6 |
| 1891 | 8 | 1918 | 3 | 1945 | 5 | 1972 | 3 |
| 1892 | 4 | 1919 | 1 | 1946 | 3 | 1973 | 4 |
| 1893 | 10 | 1920 | 4 | 1947 | 5 | 1974 | 4 |
| 1894 | 5 | 1921 | 4 | 1948 | 6 | 1975 | 6 |
| 1895 | 2 | 1922 | 2 | 1949 | 7 | 1976 | 6 |
| 1896 | 6 | 1923 | 3 | 1950 | 11 | 1977 | 5 |
| 1897 | 2 | 1924 | 5 | 1951 | 8 | | |

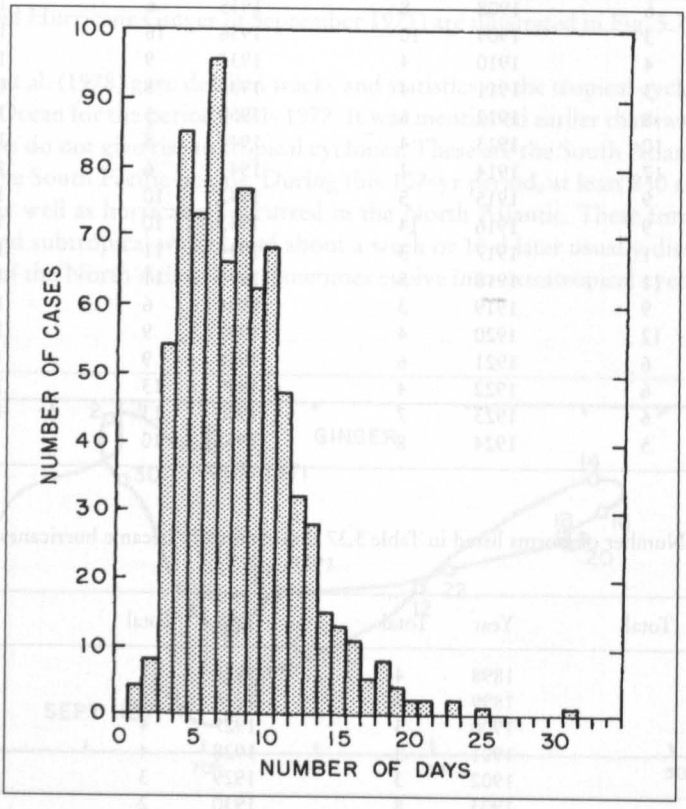


Fig. 5.73: Distribution of observed duration of Atlantic tropical cyclones, 1886–1977 (NEUMANN et al., 1979)

Die Küste, 63 Global Storm Surges (2001), 1-623



FRANK (1978) studied the geographical distribution of the generation areas and other characteristics of these Atlantic storms for the period 1968–77. During this 10-yr period, a total of 1044 systems appeared. Of these, 58 % originated near Dakar (Africa). Of the approximately 100 tropical weather systems developing in each hurricane season (June 1–November 30) about 25 % become depressions and about 10 % become storms.

NEUMANN and HILL (1976) described the computerized tropical cyclone climatological data at the National Hurricane Center in Miami. The tracks of the 680 recorded Atlantic tropical cyclones for the period 1886–1969 were plotted. Later, this number increased to 743 tracks up to the end of the 1975 hurricane season. Most of these data are based on ship reports, and in later years these data were supplemented by aircraft reconnaissance and satellite data. The storm track data are maintained at the National Climatic Center in Asheville, NC. Based on these computerized data. NEUMANN and CRY (1978) discussed the revised Atlantic tropical cyclone climatology.

*Some Comparisons of the Tropical Cyclone Activity in the Atlantic and Pacific Oceans*

NUNEZ and GRAY (1978) and GRAY (1978c) compared some meteorological parameters associated with Atlantic hurricanes and Pacific typhoons, and their findings are summarized in Table 5.39.

Table 5.39: Comparison of Atlantic hurricanes and Pacific typhoons

| Parameter | Atlantic hurricanes (West Indies) | Pacific typhoons |
|---|---|---|
| Temperature anomaly. This is determined as follows. A mean temperature is calculated by averaging the temperature values at 9 and 15° to the east and west of the position of the cyclone. Deviation from this mean temperature is the anomaly | Warm core throughout most of the troposphere. Warmest temperature at about 300 mb. The anomaly is +4°C for the hurricane (at 300 mb)<br><br>Cold core in the upper troposphere and lower stratosphere. This region occurs at a lower level than for typhoons and its radial extent is greater | Warm core throughout most of the troposphere. Warmest temperature at about 250 mb. The anomaly is +7° C for the typhoon (at 250 mb). Cold core in the upper troposphere and lower stratosphere |
| Relative humidity | About 10 % less than for typhoons at equivalent radii and heights<br>Boundary layer relative humidity is about 15 % lower than for the West Pacific | Moister inner core with relative humidities greater than 90 % up to 400 mb whereas in the hurricane, such a high relative humidity cannot be found higher than at 575 mb |
| Radial winds | Maximum inflow at 950 mb with a wind of 8 ms-'. At 150 mb there are two outflow jets: northeast and southwest. The northeast jet is about four times stronger | Maximum inflow at 950 mb with a wind of 6 ms-'. At 150 mb there are two outflow jets: northeast and southwest. The southwest jet is somewhat greater |

Table 5.39: (Continued)

| Parameter | Atlantic hurricanes (West Indies) | Pacific typhoons |
|---|---|---|
| Tangential wind | Maximum cyclonic flow is at the top of the frictional boundary layer at 850 mb | Maximum cyclonic flow is at the top of the frictional boundary layer at 850 mb |
| | The tangential wind is smaller than in typhoons | |
| | The anticyclonic maximum occurs at 150 mb | The anticyclonic maximum occurs at 150 mb. The anticyclonic circulation is relevant also in determining the weather associated with the typhoon |
| | Generally the hurricane size is smaller than a typhoon's | |
| | Vertical shear between 950 and 150 mb is 10–15 ms-' | Vertical shear between 950 and 150 mb is 15–20 ms-' |
| Inflow angle | The boundary layer inflow angle decreases from quadrant to quadrant in the following order: right, front, back, left | The boundary layer inflow angle decreases in the following order: front, right, left, back |
| Steering current concept for predicting tracks | Applies | Applies |
| | | West Pacific typhoons move more to the left of the mean current than do West Atlantic hurricanes |

## 5.6 Tropical Cyclones of the Indian Ocean

There are no extratropical cyclones in the North Indian Ocean. The extratropical cyclones of the South Indian Ocean are not very relevant for storm surge studies and, in any case, these will be briefly considered. In this section will be considered mainly the tropical cyclones of the South and North Indian oceans with emphasis on the Bay of Bengal and to a lesser extent on the Arabian Sea. However, while discussing tropical cyclones, another type of cyclone (which is neither tropical nor extratropical) referred to as a subtropical cyclone will be considered.

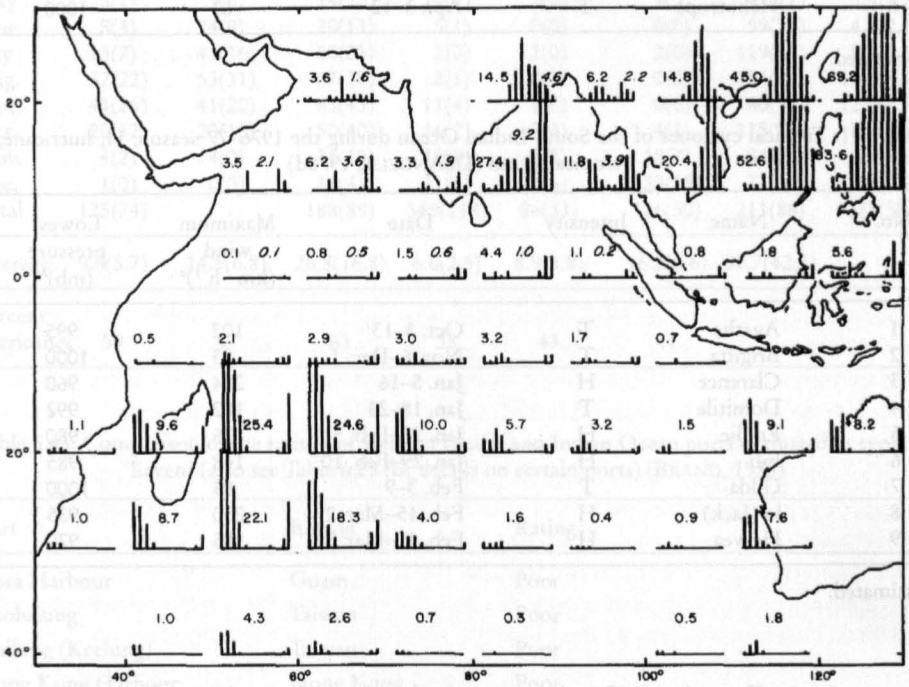


Fig. 5.74: Frequency of tropical cyclones in the Indian Ocean (average numbers of occurrences per 10 yr. for each 10° square by months). Roman-type numbers indicate average 10-yr totals over the northern Indian Ocean. The unblackened segments of the histograms and the italicized numbers given corresponding information for severe tropical storms (RAMAGE, 1971)

Tropical cyclones develop in all parts of the Indian Ocean. This is in contrast with the Atlantic and Pacific Oceans. There are no tropical cyclones in the South Atlantic and eastern part of the South Pacific. The average number of tropical cyclones during a 10-yr period for each 10° square by months is shown in Fig. 5.74. It can be seen that the highest frequencies occur north of Indonesia (not counting the Philippines area). In the Bay of Bengal and to the region east of the Malagasy Republic (Madagascar) high frequencies also occur. However, one difference is that whereas in the Bay of Bengal the highest frequencies are during September–December, in the region east of the Malagasy Republic (i.e. the western part of the South Indian Ocean) and in the region west of the west coast of Australia (i.e. the eastern part of the South Indian Ocean) the high frequencies occur during January–March.

Table 5.40: Tropical cyclones of the South Indian Ocean for the 1975–76 season. H, hurricane; T, tropical storm (DEANGELIS, 1977)

| No. | Name | Intensity | Date | Maximum wind ($km \cdot h^{-1}$)[a] | Lowest pressure (mb)[a] |
|---|---|---|---|---|---|
| 1 | Audrey | T | Nov. 17–29 | 96 | 995 |
| 2 | Barbara | H | Dec. 3–19 | 157 | 980 |
| 3 | Clotilde | H | Jan. 7–20 | 250 | 980 |
| 4 | Danae | H | Jan. 12–29 | 250 | 955 |
| 5 | Gladys | T | Mar. 27–Apr. 10 | 111 | 998 |
| 6 | Heliotrope | T | Apr. 3–12 | 83 | 1000 |

[a]Estimated.

Table 5.41: Tropical cyclones of the South Indian Ocean during the 1976–77 season; H, hurricane; T, tropical storm (DEANGELIS, 1978d)

| No. | Name | Intensity | Date | Maximum wind ($km \cdot h^{-1}$)[a] | Lowest pressure (mb)[a] |
|---|---|---|---|---|---|
| 1 | Agathe | T | Oct. 3–13 | 102 | 995 |
| 2 | Brigitta | T | Nov. 6–Dec. 1 | 83 | 1000 |
| 3 | Clarence | H | Jan. 5–16 | 204 | 960 |
| 4 | Domitile | T | Jan. 18–23 | 102 | 992 |
| 5 | Emilie | H | Jan. 26–Feb. 5 | 176 | 980 |
| 6 | Fifi | H | Jan. 29–Feb. 10 | 148 | 985 |
| 7 | Gilda | T | Feb. 3–9 | 83 | 1000 |
| 8 | Io (Jack) | H | Feb. 15–Mar. 2 | 250 | 935 |
| 9 | Hervea | H | Feb. 17–Mar. 3 | 185 | 970 |

[a] Estimated.

### 5.6.1 Tropical Cyclones of the South Indian Ocean

Certain features of the tropical cyclones of the South Indian Ocean for the seasons 1975–76 and 1976–77 are summarised in Table 5.40 and 5.41, respectively. In the 1975–76 season there was a total of six tropical cyclones of which three reached hurricane strength. In the 1976–77 season, of a total of nine cyclones, five became hurricanes. The tropical cyclones for the period 1965–77 are summarised by month for various ocean basins in Table 5.42. Note that in terms of frequency, the North Indian Ocean has the lowest and the South Indian Ocean has the second lowest. However, this may be misleading when one considers the damage due to tropical cyclones (and storm surges generated by them). More than 60 % of the deaths and almost 40 % of the damage due to tropical cyclones occur on lands bordering the Bay of Bengal, which is only a small part of the North Indian Ocean.

Considered earlier were typhoon waves among harbours located around the Pacific Ocean. Some Indian Ocean harbours as well as some Pacific Ocean harbours (for comparison) are listed in Table 5.43. Among the Indian Ocean harbours, only Colombo is listed as "good" and Karachi as "marginal" (BRAND, 1978).

Table 5.42: Tropical cyclones in various ocean basins during the period 1965–77. Numbers in parentheses indicate tropical cyclones that reached hurricane intensity (i.e. winds ≥ 119 km · h$^{-1}$) (DE-ANGELIS, 1979a)

| Month | North Atlantic | Eastern North Pacific | Western North Pacific | North Indian | South Indian | Australia-South Pacific | Total | Average |
|---|---|---|---|---|---|---|---|---|
| Jan. | 0(0) | 0(0) | 9(5) | 2(1) | 29(17) | 52(20) | 92(43) | 7.1(3.3) |
| Feb. | 0(0) | 0(0) | 4(1) | 0(0) | 30(16) | 41(16) | 75(33) | 5.8(2.5) |
| Mar. | 0(0) | 0(0) | 6(1) | 0(0) | 15(5) | 39(18) | 60(24) | 4.6(1.8) |
| Apr. | 0(0) | 0(0) | 11(9) | 4(2) | 6(1) | 18(6) | 39(18) | 3.0(1.4) |
| May | 3(1) | 5(3) | 14(10) | 14(5) | 3(0) | 4(3) | 42(22) | 3.3(1.7) |
| June | 8(4) | 24(9) | 20(13) | 5(1) | 0(0) | 0(0) | 59(27) | 4.4(2.1) |
| July | 13(7) | 41(16) | 60(35) | 2(0) | 1(0) | 2(0) | 119(58) | 9.2(4.5) |
| Aug. | 32(22) | 53(31) | 67(38) | 2(1) | 0(0) | 0(0) | 154(92) | 11.8(7.1) |
| Sept. | 44(26) | 41(20) | 63(43) | 11(4) | 1(0) | 0(0) | 160(93) | 12.3(7.2) |
| Oct. | 20(12) | 20(10) | 50(40) | 16(7) | 5(3) | 4(1) | 115(73) | 8.8(5.6) |
| Nov. | 4(2) | 4(0) | 34(19) | 19(8) | 5(2) | 18(7) | 84(38) | 6.5(2.9) |
| Dec. | 1(0) | 0(0) | 11(4) | 11(4) | 21(6) | 33(15) | 77(29) | 5.9(2.2) |
| Total | 125(74) | | 188(89) | 349(218) | 86(33) | 116(50) | 211(86) | 1075(550) |
| Average | 9.6(5.7) | 14.5(6.8) | 26.8(16.8) | 6.6(2.5) | 8.9(3.8) | 16.2(6.6) | 82.7(42.3) | |
| Percent hurricanes | 59 | 47 | 63 | 38 | 43 | 41 | | |

Table 5.43: Comparison of the ratings of western Pacific and Indian Ocean ports evaluated as typhoon havens (also see Table 6.29 for details on certain ports) (BRAND, 1978)

| Port | Region | Rating |
|---|---|---|
| Apra Harbour | Guam | Poor |
| Kaohsiung | Taiwan | Poor |
| Chilung (Keelung) | Taiwan | Poor |
| Hong Kong Harbour | Hong Kong | Poor |
| Yokosuka | Japan | Good |
| Nunazu operating area | Japan | Poor |
| Lwakuni | Japan | Marginal (but has easily accessible anchorages close by that are good) |
| Kure | Japan | Good |
| Saskebo | Japan | Good (except for carriers) |
| Kagoshima | Japan | Poor |
| Buckner Bay (Okinawa) | Japan | Poor |
| Naha (Okinawa) | Japan | Poor |
| Subic Bay | Philippines | Marginal to poor |
| Manila | Philippines | Poor |
| Cebu | Philippines | Poor |
| Inchon | Korea | Poor (unless shelter is available in the tidal basin, then it would be considered a good haven) |

Table 5.43: (Continued)

| Port | Region | Rating |
|---|---|---|
| Pusan | Korea | Poor |
| Chinhae | Korea | Marginal (but has easily accessible anchorage's nearby that are considered good) |
| Colombo | Sri Lanka | Good |
| Karachi | Pakistan | Marginal |
| Auckland | New Zealand | Good to marginal |
| Freemantle | Australia | Marginal (unless shelter is available in Cockburn Sound or the inner harbour, then it would he considered good) |
| Diego Garcia Harbour | Diego Garcia | Poor |

*Australia and New Zealand*

Although storm surges are not a serious problem in Australia and New Zealand, they do occur and cause damage. In Australia, the areas particularly susceptible to storm surges are the central north coast of eastern Queensland and parts of the Gulf of Carpentaria. HOPLEY and HARVEY (1979) studied the storm surges all along the coast of Australia. The cyclones in this study are listed in Table 5.44. Cyclones affect the northern parts of the east and west coasts of Australia, as well as its north coast. The frequency of cyclones (capable of generating storm surges) varies from 0.4 to 2.8 per year. Lowest central pressures occur on the east and west coasts between 20 and 25° S. The central pressures on the west coast are usually 3–4 mb lower than those on the coast of Queensland. Central pressures drop gradually towards the north but more drastically towards the south.

Intense cyclones with central pressures less than 960 mb occur on the central part of the west coast (Northwest Cape to Port Hedland), the region between Princess Charlotte Bay and Mackay on the Queensland coast. However, in the Gulf of Carpentaria, central pressures less than 960 mb rarely occur.

Cyclones in the Australian region usually travel with speeds between 6 and 11 knots although sometimes with a speed as high as 35 knots (particularly on the Queensland coast between 25 and 30° S). They travel with low speeds over the Gulf of Carpentaria and off Arnhemland (COLEMAN, 1972). The variability in the meteorological parameters associated with cyclones in the Australian region, based on data for 1960–72, is shown in Table 5.44 of HOPLEY and HARVEY (1979). This variability was determined for the following three parameters: (a) variability in the direction of movement by measuring the difference between the point on the coast for which the cyclone was heading 24 h prior to landfall and the observed landfall location, (b) variability in pressure by comparing changes in the pressure field during the 24 h prior to landfall, and (c) variability in the speed of movement by comparing the average speed in the 24 h prior to landfall with the mean speed in the previous 24 h.

NELSON (1975) listed 30 severe tropical cyclones in the Australian region during the period 1880–1970 that generated storm surges with amplitudes of at least 0.5 m along the north coast of Australia. One of the lowest central pressures ever recorded, a storm on

March 5, 1899, that travelled over Bathurst Bay and struck Barrow Point on the Queensland coast, was 914 mb. The storm and the storm surge together killed 300 people and the surge penetrated 5 km inland (WHITTINGHAM, 1958).

Table 5.44: Cyclones in and around Australia (HOPLEY and HARVEY, 1979)

| Name | Date of landfall or nearest point to coast | Tidal station closest to cyclone | Lowest central pressure (mb) | Highest record of surge at any station (m) | Remarks |
|---|---|---|---|---|---|
| Adeline | Jan. 28, 1973 | Centre Island | 990 | 0.52 | |
| Agnes | Mar. 6, 1956 | Townsville | 961 | 1.4 | |
| Althea | Dec. 24, 1971 | Townsville | 952 | 2.85 | 3.6 m at Toolakea |
| Bridget | Jan. 27, 1969 | Lucinda | 1002 | 0.34 | |
| Emily | Apr. 2, 1972 | Gladstone | 920 | 1.78 | Filled rapidly before crossing |
| Eva | Dec. 4, 1970 | Broome | 970 | 0.16 | 1.2- to 13-m surge reported at Broome (Met. Bur. 1973) |
| Gertie | Feb. 16, 1971 | Lucinda | 983 | 0.52 | |
| Glynis | Feb. 6, 1970 | Perth | 970 | 1.01 | Surge incorrectly reported as 4.1 m above normal at Carnarvon (Met. Bureau, 1973). Record tides elsewhere |
| Ida | Feb. 16, 1971 | Mourilyan | 980 | 0.37 | |
| Ingrid | Feb. 16, 1970 | Carnarvon | 970 | 1.32 | Surge incorrectly reported as 2.3 m above normal at Carnarvon (Met. Bur. 1973) |
| Joan | Dec. 7, 1975 | Port Hedland | -992 | 1.52 | Port Hedland recorder malfunction during rising surge |
| Leah | Feb. 28, 1973 | Milner Bay | 990 | 0.45 | |
| Madge | Mar. 4, 1973 | Milner Bay | 990 | 0.42 | Affected east coast and Gulf |
| Pam | Feb. 6, 1974 | Kirra | 930 | 0.4 | Came within 450 km of Queensland but very large cyclone |
| Sheila-Sophie | Feb. 3, 1971 | Port Hedland | 970 | 1.8 | |
| Tracy | Dec. 24, 1974 | Darwin | 940 | 1.6 | 2.0-m surge reported to north of city |
| Una | Dec. 19, 1973 | Townsville | 988 | 0.72 | |
| Wanda | Jan. 25, 1974 | Noosa | 990 | 0.6 | Associated with Brisbane floods |
| Zoe | Mar. 13, 1974 | Broadwater | 975 | 0.56 | |

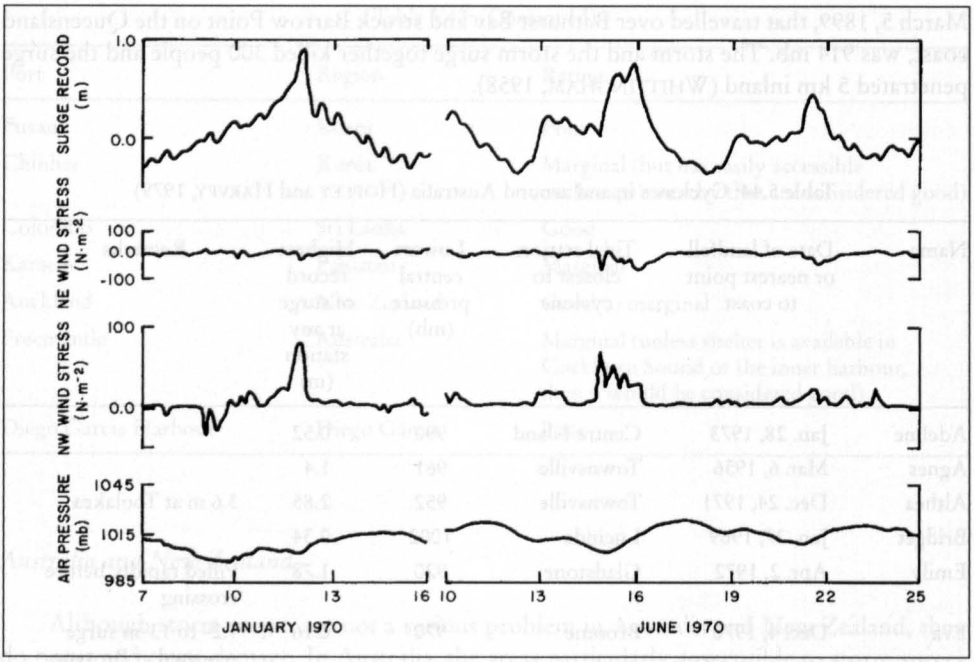


Fig. 5.75: Storm surges, atmospheric pressure, and wind stress at Adelaide, Australia (TRONSON and NOYE, 1973)

In the 1970s two storm surges did considerable damage in Australia. Cyclone Althea of December 24, 1971, made a landfall to the north of Townsville on the Queensland coast. Winds up to 196 km · $h^{-1}$ and lowest central pressure of 971.5 mb generated a maximum surge of about 2.7 m at Townsville. Cyclone Tracy of December 25, 1974, hit Darwin; a central pressure of 955 mb and winds up to 200 km · $h^{-1}$ generated a maximum surge of about 1.6 m.

TRONSON and NOYE (1973) developed statistical models to predict storm surges on the coast near Adelaide in South Australia. The storm surges in this region are particularly sensitive to the wind direction. On April 12, 1948, steady winds from the southwest with a speed of 90 km · $h^{-1}$ caused a surge of about 1.2 m. On June 28, 1972, a surge with the same amplitude was generated by winds from the northwest, with a speed of about 45 km. h'. Surges with amplitudes of up to 4 m can occur at Adelaide, e.g. on May 12, 1960, and June 28, 1972. The atmospheric pressure field, the wind stress, and the surges at Adelaide for two cases (January 7–16 and June 10–25, 1970) are shown in Fig. 5.75.

HEATH (1979) discussed the storm surges on the coasts of New Zealand. Storm surge amplitudes on the coasts of New Zealand are rather small and are usually less than 1 m (AGNEW, 1966; GILMOUR, 1963; PICKRILL, 1972). Even though the amplitudes may be small, they could cause severe erosion, especially on the west coast of the North Island, in the Bay of Plenty, and on the east coast of the North Island, north of Auckland.

HEATH (1979) studied the following three surges: April 9–11, 1968, on the east coast of the North Island, July 30–August 1, 1975, on the east coast of the South Island, and September 11–14, 1976, on the west coast of the North Island. The surface weather chart for the third case is given in Fig. 5.76.

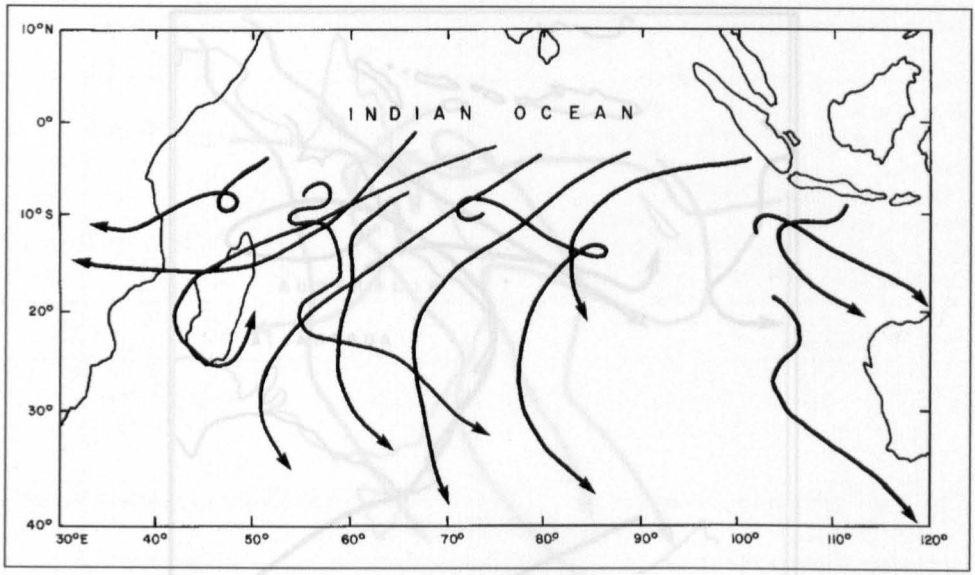


Fig. 5.76: Typical tropical cyclone tracks in the South Indian Ocean between the Malagasy Republic and the west coast of Australia

Australia is the only continent that is affected by tropical cyclones on both the east and west coasts. Certain features of the tropical cyclones of Australia are described in Tables 5.45–5.47. The average tropical cyclone frequencies for the west and east coasts of Australia for the months of December and January are given in Fig. 5.81 and 5.82, respectively. The frequency of cyclone days in Australia is given in Fig. 5.83 and the cyclone frequency change (i.e. trend) during the period 1905–55 is shown in Fig. 5.84.

Some typical tropical cyclone tracks in the region between the Malagasy Republic and the west coast of Australia are illustrated in Fig. 5.77 and typical tracks near the west coast of Australia in Fig. 5.78. For comparison, tropical cyclone tracks near the east coast of Australia and those affecting New Zealand are shown in Fig. 5.79 and 5.80, respectively.

Australia is the only continent that is affected by tropical cyclones on both the east and west coasts. Certain features of the tropical cyclones of Australia are described in Tables 5.45–5.47 The average tropical cyclone frequencies for the west and east coasts of Australia for the months of December and January are given in Fig. 5.77 and Fig. 5.78, respectively. The frequency of cyclone days in Australia is given in Fig. 5.79 and the cyclone frequency change (i.e. trend) during the period 1905–55 is shown in Fig. 5.80.


Fig. 5.77: Typical tropical cyclone tracks near the west coast of Australia

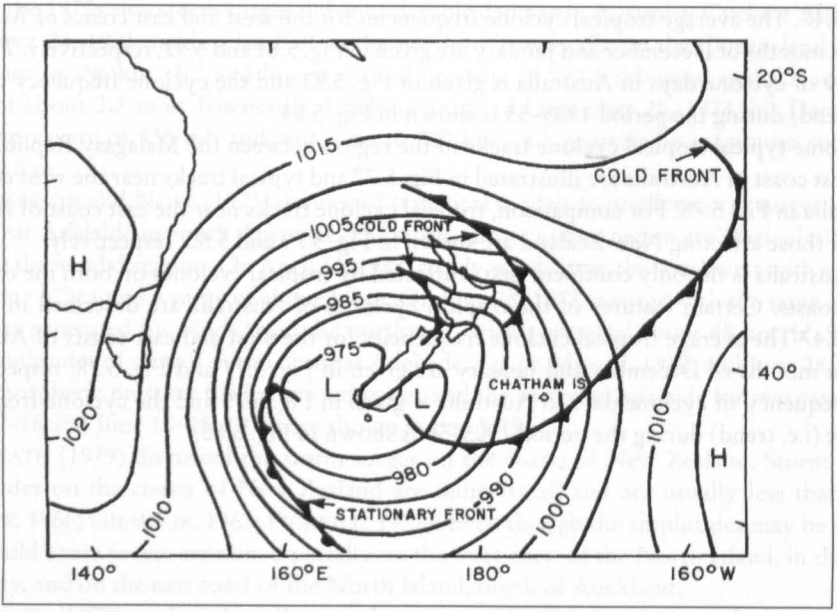


Fig. 5.78. Simplified surface weather chart at 0 h (New Zealand Standard Time) on September 13, 1976 (HEATH, 1979)

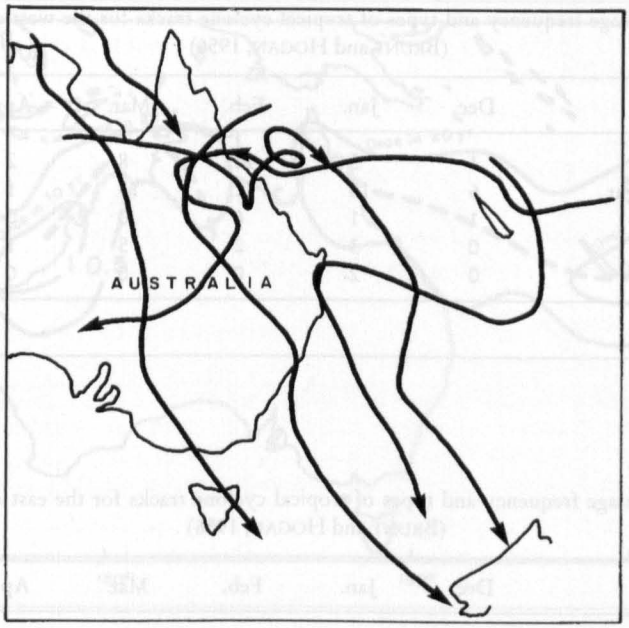


Fig. 5.79: Typical tropical cyclone tracks near the east coast of Australia

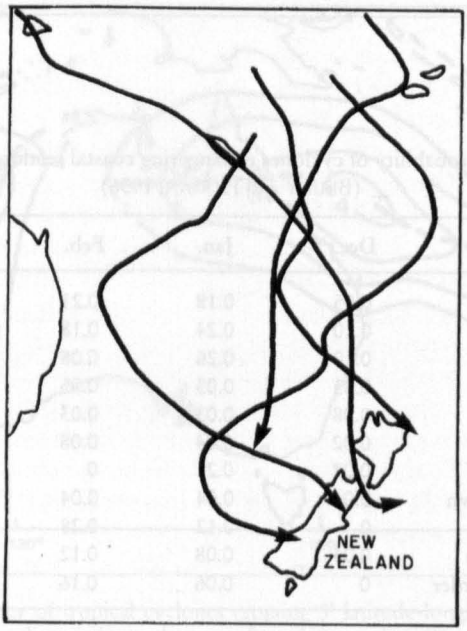


Fig. 5.80: Typical tropical cyclone tracks near New Zealand

Table 5.45: Percentage frequency and types of tropical cyclone tracks for the west coast of Australia (BRUNT and HOGAN, 1956)

| Type of path | Dec. | Jan. | Feb. | Mar. | Apr. | Season |
|---|---|---|---|---|---|---|
| Parabolic | 4 | 5 | 12 | 8 | 2 | 31 |
| More or less straight | 6 | 16 | 12 | 13 | 1 | 48 |
| Reverse curvature | 1 | 1 | 6 | 0 | 0 | 8 |
| Cusp | 0 | 3 | 2 | 5 | 1 | 11 |
| Doubling of track | 0 | 2 | 0 | 0 | 0 | 2 |
| Total | | | | | | 100 |

Table 5.46: Percentage frequency and types of tropical cyclone tracks for the east coast of Australia (BRUNT and HOGAN, 1956)

| Type of path | Dec. | Jan. | Feb. | Mar. | Apr. | Season |
|---|---|---|---|---|---|---|
| Parabolic | 2 | 6 | 14 | 15 | 2 | 39 |
| More or less straight | 2 | 11 | 8 | 11 | 5 | 37 |
| Reverse curvature | 1 | 8 | 0 | 1 | 2 | 12 |
| Cusp | 0 | 2 | 7 | 1 | 0 | 10 |
| Doubling of track | 1 | 0 | 0 | 0 | 1 | 2 |
| Total | | | | | | 100 |

Table 5.47: Probability of cyclones endangering coastal sections in Australia (BRUNT and HOGAN, 1956)

| Section of coast | Dec. | Jan. | Feb. | Mar. | Apr. |
|---|---|---|---|---|---|
| Hamlin Pool-Roebourne | 0.05 | 0.18 | 0.21 | 0.18 | 0 |
| Roebourne-Broome | 0.10 | 0.24 | 0.18 | 0.13 | 0.03 |
| Broome-Wyndham | 0.10 | 0.26 | 0.08 | 0.13 | 0.03 |
| Wyndham-Darwin | 0.03 | 0.03 | 0.05 | 0.03 | 0 |
| Darwin-Melville Bay | 0.08 | 0.03 | 0.03 | 0.03 | 0.03 |
| N.T. Gulf coast | 0.02 | 0.14 | 0.08 | 0.08 | 0 |
| Queensland Gulf coast | 0.02 | 0.21 | 0 | 0 | 0 |
| Thursday Island-Cooktown | 0.04 | 0.04 | 0.04 | 0.08 | 0.04 |
| Cooktown-Townsville | 0 | 0.12 | 0.28 | 0.12 | 0.04 |
| Townsville-Rockhampton | 0.04 | 0.08 | 0.12 | 0.16 | 0.06 |
| Rockhampton-N.S.W. border | 0 | 0.06 | 0.16 | 0.16 | 0.06 |

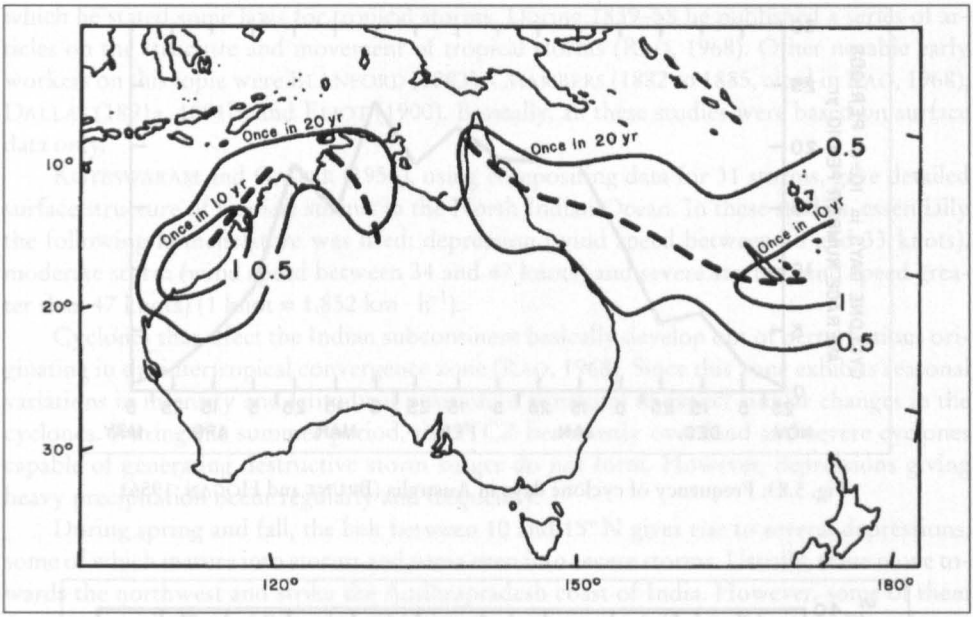


Fig. 5.81: Average frequency of tropical cyclones crossing 5' latitude-longitude squares per 10 yr. in December; heavier broken lines indicate the axes of maximum values (BRUNT and HOGAN, 1956)

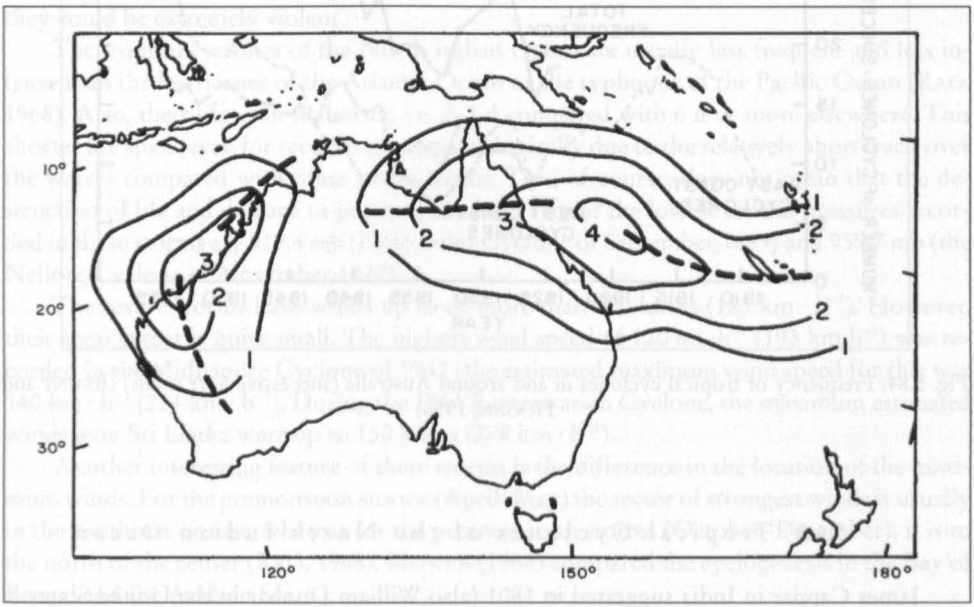


Fig. 5.82: Average frequency of tropical cyclones crossing 5' latitude-longitude squares per 10 yr. in January. Heavier broken lines indicate the axes of maximum values (BRUNT and HOGAN, 1956)

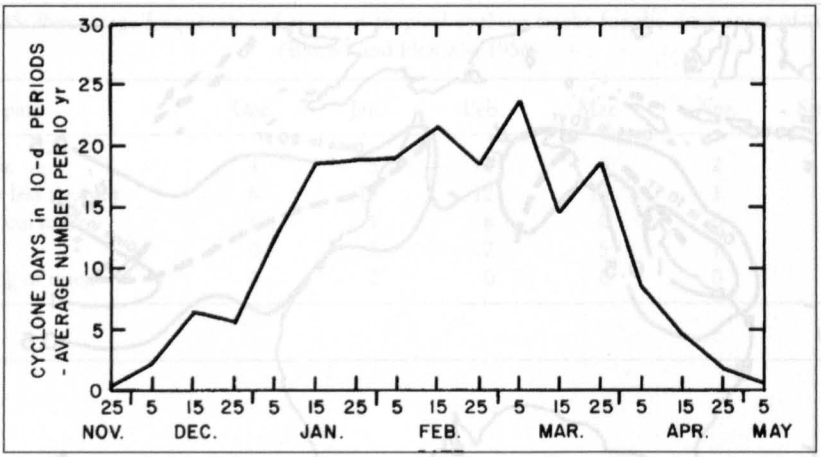


Fig. 5.83: Frequency of cyclone days in Australia (BRUNT and HOGAN, 1956)

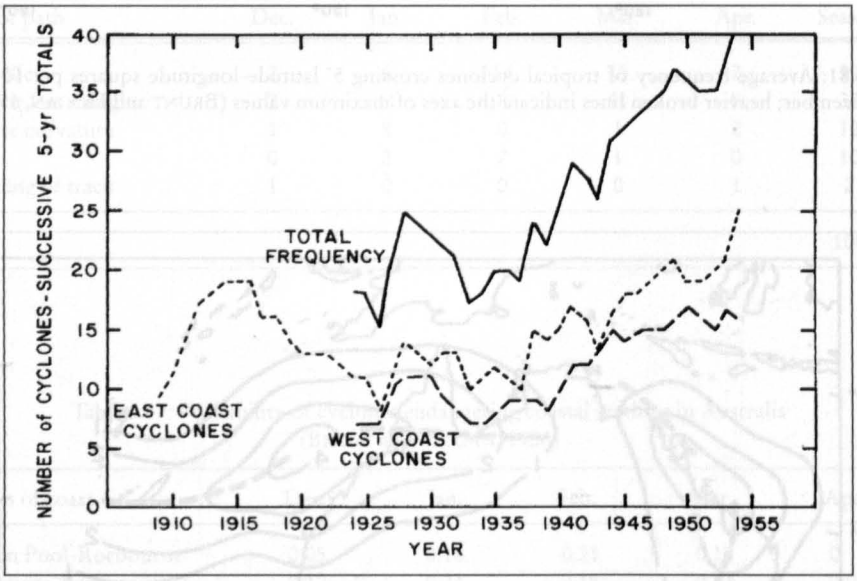


Fig. 5.84: Frequency of tropical cyclones in and around Australia (successive 5-yr totals) (BRUNT and HOGAN, 1956)

### 5.6.2 Tropical Cyclones of the North Indian Ocean

James Cappar in India suggested in 1801 (also William Dunbar in the United States in the same year) that there is a vortex in the center of a tropical cyclone (LUDLAM, 1963). However, it was Henry Piddington who, in 1851, coined the word "cyclone" from the Greek word „kyklon" meaning coil of snake to describe the rotary motion. Piddington was the president of the Marine Courts at Calcutta, India, and in 1851 he published a sailor's handbook in

which he stated some laws for tropical storms. During 1839–58 he published a series of articles on the structure and movement of tropical storms (RAO, 1968). Other notable early workers on this topic were BLANFORD (1883), CHAMBERS (1882 to 1885, cited in RAO, 1968), DALLAS (1891a, 1891b) and ELIOT (1900). Basically, all these studies were based on surface data only.

KOTESWARAM and GASPER (1956), using compositing data for 31 storms, gave detailed surface structure of tropical storms in the North Indian Ocean. In these studies, essentially the following nomenclature was used: depression (wind speed between 18 and 33 knots), moderate storm (wind speed between 34 and 47 knots) and severe storm (wind speed greater than 47 knots) (1 knot = 1.852 km · $h^{-1}$).

Cyclones that affect the Indian subcontinent basically develop out of perturbations originating in the intertropical convergence zone (RAO, 1968). Since this zone exhibits seasonal variations in intensity and latitudinal position, it is natural to expect similar changes in the cyclones. During the summer period, the ITCZ lies mostly over land and severe cyclones capable of generating destructive storm surges do not form. However, depressions giving heavy precipitation occur regularly and frequently.

During spring and fall, the belt between 10 and 15° N gives rise to several depressions, some of which mature into storms and some even into severe storms. Usually, these move towards the northwest and strike the Andhrapradesh coast of India. However, some of them recurve over the Bay of Bengal and hit the northern coast of the bay (the west Bengal state of India and the coast of Bangladesh). During autumn, the storms take a more southerly course and strike the peninsular part of India. Some of these storms recurve and strike the north coast of the bay (the Sunderban coast). Some cross the peninsula and redevelop over the Arabian Sea and travel west-north-west and strike the Arabian Sea coast of the subcontinent. Usually, there are no storms during winter. On the rare occasion when they occur, they could be extremely violent.

The tropical cyclones of the North Indian Ocean are usually less frequent and less intense than the hurricanes of the Atlantic Ocean or the typhoons of the Pacific Ocean (RAO, 1968). Also, their life span is shorter, i.e. 2–3 d compared with 6 d or more elsewhere. This shorter life span (even for recurving storms) is basically due to the relatively short track over the waters compared with other ocean basins. This, of course, does not mean that the destruction of life and damage to property are less. Two of the lowest central pressures recorded in these storms are 919.4 mb (False Point Cyclone of September 1885) and 959.7 mb (the Nellore Cyclone of November 1927).

The severe storms have winds up to or more than 100 knots (185 km · $h^{-1}$). However, their areal extent is quite small. The highest wind speed of 120 mi · $h^{-1}$ (193 km $h^{-1}$) was recorded in the Midnapore Cyclone of 1942 (the estimated maximum wind speed for this was 140 km · $h^{-1}$ (224 km · $h^{-1}$). During the 1964 Rameswaram Cyclone, the maximum estimated winds over Sri Lanka were up to 150 knots (278 km · $h^{-1}$).

Another interesting feature of these storms is the difference in the location of the maximum winds. For the premonsoon storms (April–May) the sector of strongest winds is usually in the southeast or east, whereas for the postmonsoon storms (October–December), it is to the north of the center (RAO, 1968). MOWLA (1968) compared the cyclogenesis in the Bay of Bengal and the Arabian Sea.

Table. 5.48: Number of cyclonic disturbances that originated over the Bay of Bengal and the Arabian Sea in different months for the period 1891–1960. Note that "storms" includes "severe storms" also, whereas „cyclonic disturbances" include storms and severe storms in addition to cyclonic disturbances (RAO, 1968)

| | Cyclonic disturbances | Storms | Severe storms |
|---|---|---|---|
| Jan. | 13 | 4 | 1 |
| Feb. | 3 | 1 | 1 |
| Mar. | 5 | 4 | 2 |
| Apr. | 26 | 18 | 7 |
| May | 56 | 28 | 18 |
| June | 93 | 34 | 4 |
| July | 132 | 38 | 7 |
| Aug. | 145 | 25 | 1 |
| Sept. | 151 | 27 | 8 |
| Oct. | 132 | 53 | 19 |
| Nov. | 102 | 56 | 23 |
| Dec. | 52 | 26 | 9 |
| Year | 910 | 314 | 100 |

After the Second World War, using radiosonde data, the upper structure of these storms was studied, and several articles appeared in the *Indian Journal of Meteorology and Geophysics* (now called *Mausam),* especially on the tracks of cyclonic disturbances in various months with emphasis on the recurvature. These studies revealed that the areas of generation and the tracks in every month are closely related to the anticyclonic cell in the upper troposphere at a 10- to 12-km height. However, variations in the tracks could occur due to changes in the general circulation produced by troughs in the midlatitude westerlies.

*Frequencies of Cyclonic Storms in the Bay of Bengal*

The number of cyclonic disturbances over the Bay of Bengal for each month during the period 1891–1960 is given in Table 5.48. RAGHAVENDRA (1973) performed a statistical analysis of the number of tropical storms and depressions in the Bay of Bengal for the period 1890–1969. The average annual number of storms and depressions is 13. The monsoon season accounts for 56 % of these and the postmonsoon season accounts for 31 %. The highest number (20 storms) occurred in 1927. The frequency distribution of storms and depressions of monsoon and postmonsoon seasons is normal and that of the annual season is almost normal with slight kurtosis. The decade of 1920–29 had the highest mean and the decade of 1950–59 the lowest mean for the annual and monsoon seasons, thus indicating a cycle of 60 yr.

SADLER and GIDLEY (1973) gave tracks of the storms in the North Indian Ocean. CHAKRAVORTHY (1956) discussed the dimensions of the eye of the Bay of Bengal storms. He found that the eye diameter varied from 7 to 20 mi (11.5–32 km).

MOOLEY (1980a, 1980b) studied the severe cyclonic storms of the Bay of Bengal for the period 1877–1977. He found that during the period 1965–77, a higher percentage (than the average) of storms intensified into severe storms and a higher percentage of storms made landfall. Generally, the formation and landfall of these severe storms are random events and are consistent with the Poisson stochastic process.

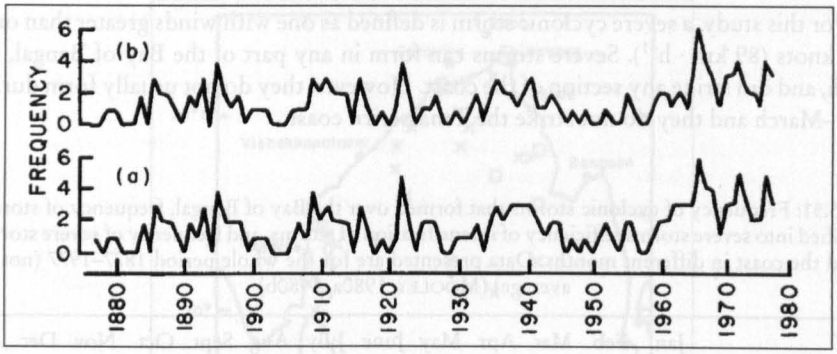


Fig. 5.85: Annual frequency of severe cyclonic storms that over the period 1877–1977 (a) formed over the Bay of Bengal and (b) struck the coast (MOOLEY, 1980a, 1980b)

Table 5.49: Mean and variance of the number of severe storms forming over the Bay of Bengal, and the number of severe storms striking the coast in a year (MOOLEY, 1980)

| | Severe storms forming over the Bay of Bengal | | Severe storms striking the coast | |
|---|---|---|---|---|
| Period | Mean | Variance | Mean | Variance |
| 1891–1964 | 1.50 | 1.420 | 1.22 | 1.087 |
| 1877–1964 | 1.42 | 1.374 | 1.16 | 1.091 |
| 1877–1977 | 1.67 | 1.910 | 1.40 | 1.530 |
| 1965–1977 | 3.38 | 1.923 | 3.00 | 1.833 |

Table 5.50: Number of cyclonic storms that formed over the Bay of Bengal, number that intensified into severe storms over the bay, and number that struck the coast as severe storms in different 13-yr periods (MOOLEY, 1980a, 1980b)

| Period | Number of storms that formed | Number of storms that intensified into severe storms | Number of severe storms that struck the coast | Intensification of storms into severe storms over the bay | Efficiency of Ratio of severe storms that struck the coast to storms that struck the coast |
|---|---|---|---|---|---|
| 1877–99 | 49 | 13 | 12 | 0.26 | 0.31 |
| 1890–1902 | 56 | 19 | 18 | 0.34 | 0.36 |
| 1903–15 | 64 | 19 | 17 | 0.30 | 0.30 |
| 1916–28 | 61 | 19 | 16 | 0.31 | 0.36 |
| 1929–41 | 70 | 24 | 19 | 0.34 | 0.39 |
| 1942–54 | 46 | 13 | 8 | 0.28 | 0.28 |
| 1952–64 | 45 | 21 | 13 | 0.47 | 0.43 |
| 1965–77 | 70 | 44 | 39 | 0.63 | 0.66 |
| 1886–98 | 74 | 24 | 23 | 0.32 | 0.35 |
| 1924–36 | 74 | 16 | 13 | 0.22 | 0.25 |
| 1932–44 | 71 | 27 | 22 | 0.38 | 0.47 |

For this study, a severe cyclonic storm is defined as one with winds greater than or equal to 48 knots (89 km · $h^{-1}$). Severe storms can form in any part of the Bay of Bengal, in any month, and can strike any section of the coast. However, they do not usually form during January–March and they do not strike the Tenasserirn coast.

Table 5.51: Frequency of cyclonic storms that formed over the Bay of Bengal, frequency of storms that intensified into severe storms, efficiency of intensification of storms, and frequency of severe storms that crossed the coast in different months. Data presented are for the whole period 1877–1977 (not annual average) (MOOLEY, 1980a, 1980b)

| | Jan. | Feb. | Mar. | Apr. | May | June | July | Aug. | Sept. | Oct. | Nov. | Dec. | Annual |
|---|---|---|---|---|---|---|---|---|---|---|---|---|---|
| Frequency of storms | 5 | 0 | 5 | 21 | 48 | 43 | 48 | 30 | 42 | 77 | 91 | 43 | 453 |
| Frequency of storms that intensified into severe storms | 2 | 0 | 3 | 9 | 32 | 6 | 8 | 3 | 14 | 30 | 44 | 18 | 169 |
| Efficiency of intensification | | | | 0.43 | 0.67 | 0.14 | 0.17 | 0.10 | 0.33 | 0.39 | 0.49 | 0.42 | 0.37 |
| Frequency of severe storms that crossed the coast | 1 | 0 | 2 | 6 | 29 | 6 | 8 | 3 | 12 | 28 | 35 | 11 | 141 |

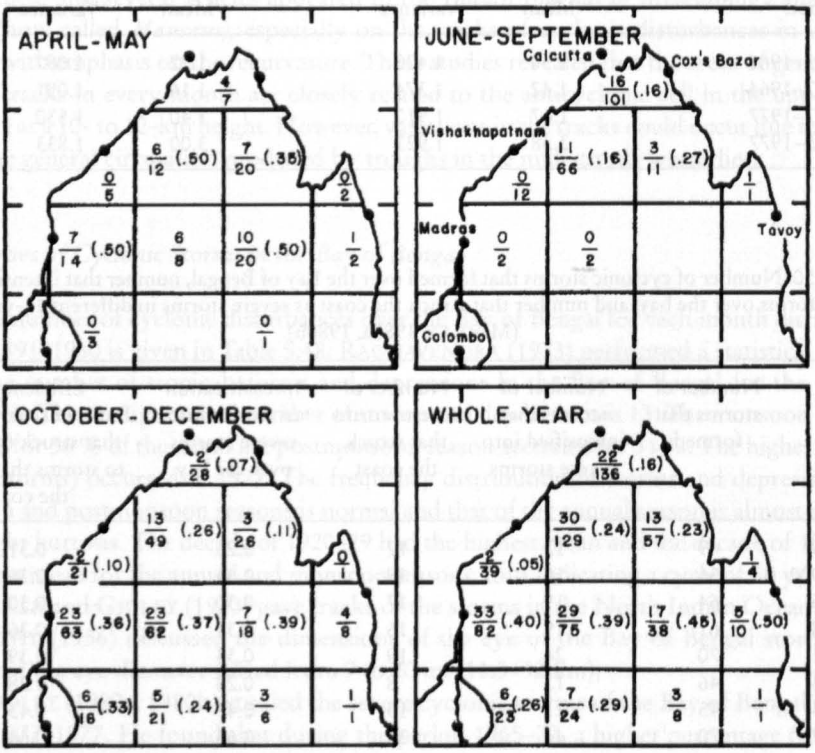


Fig. 5.86: Number of storms located (denominator), number of storms intensified into severe storms (numerator), and the efficiency of intensification (in parentheses) in the different sectors of the Bay of Bengal for the period 1877–1977 (MOOLEY, 1980a, 1980b)

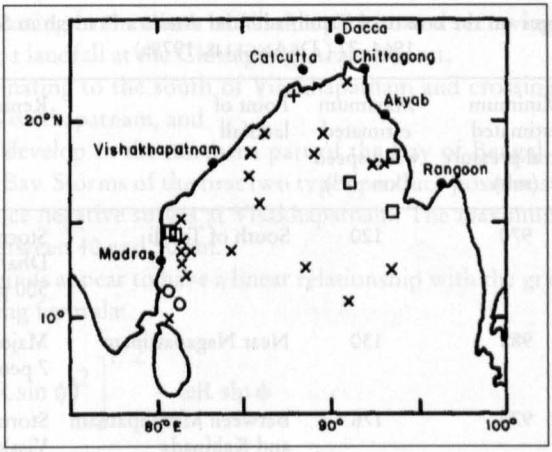


Fig. 5.87: Locations of severe storms just prior to their weakening into storms and depressions over the Bay of Bengal during the period 1877–1977. ○, January–March; □, April and May; June–September; ×, October–December (MOOLEY, 1980a, 1980b)

The annual frequency of severe cyclones that formed over the Bay of Bengal and those that struck the coast is shown in Fig. 5.85. The mean and variance of the number of severe storms forming over the Bay and those striking the coast are listed in Table 5.49. Further details are provided in Table 5.50 and 5.51. The efficiency of intensification (i.e. a cyclonic storm maturing into a severe storm) for different areas in the Bay of Bengal, for the periods April–May, June–September, October–December, and the whole year, is shown in Fig. 5.86. The locations of severe storms just prior to their weakening into storms or depressions are illustrated in Fig. 5.87.

In principle, the entire coast of the Bay of Bengal from Sri Lanka to Thailand is vulnerable to storm surges, although in practice, storm surges occur only on certain stretches. Storm surges are not frequent in Sri Lanka; however, in 1978 a major surge occurred that caused great devastation. Most of the storms developing in the Andaman Sea travel towards northwest and strike the coast of Tamilnadu or Andhrapradesh (south-east part of India), rather than travel towards the west and strike the coast of Sri Lanka. Certain storms have a more northerly component in their motion and these can landfall on the coast of Orissa. Those that recurve can hit the coasts of West Bengal, Bangladesh, and Burma.

On the coasts of Tamilnadu and Andhrapradesh, at least six storm surges occurred during the period 1964–77. These are listed in Table 5.52 along with the minimum central pressure and maximum wind speed. There appears to be some controversy regarding the intensity of the November 1977 cyclone (last entry in Table 5.52). PANT et al. (1980) suggested that the minimum central pressure was 943 mb and the maximum wind speed was 125 knots (231 km · $h^{-1}$). This cyclone intensified from T6 to T7 between November 17 and 19 (see Table 5.53 for the classification of T numbers in terms of pressure drop and wind speed). GHOSH (1980) suggested that the lowest pressure was 919 mb and not 943 mb. In intensity, this cyclone was comparable with that of the 1927 cyclone. However, the 1927 cyclone generated a surge smaller than the 1977 cyclone (in the storm surge of 1927, 300 people died compared with at least 10 000 in the 1977 surge). The 1927 cyclone made a landfall near Nellore where the topography was much steeper and hence the surge was smaller. Another cyclone that had a pressure drop in excess of 90 mb occurred in 1885 (ELIOT, 1890).

Table 5.52: Storm surges on the coasts of Tamilnadu and Andhra Pradesh in Southeast India during 1964–77 ( DEANGELIS, 1978a)

| Date | Minimum estimated central pressure (mb) | Maximum estimated wind speed ($km \cdot h^{-1}$) | Point of landfall | Remarks |
|---|---|---|---|---|
| Dec. 17–24, 1964 | 970 | 120 | South of Tondi | Storm surge amplitude at Dhanushkodi about 5 m, 500 people died |
| Dec. 4–8, 1967 | 988 | 130 | Near Nagapattinam | Major storm surge, 7 people died |
| Nov. 4–9, 1969 | 970 | 176 | Between Masulipatnam and Kakinada | Storm surges at Visakhapatnam, 200 people died |
| Sept. 7–14, 1972 | 957 | 204 | Near Baruva | Storm surges of 1–3 m between Baruva and Chandbali |
| Nov. 15–23, 1972 | 983 | 148 | South of Nellore | Minor storm surge |
| Nov. 14–20, 1977 | 919 | 250 | Chirala | Surges up to 6 m near Divi. At least 10 000 people died. Surges occurred on a coastal stretch 80 km long and penetrated 8–15 km inland |

Table 5.53: Relationship between T number, maximum wind speed, and pressure drop in a cyclone (DVORAK, 1975a; MISHRA and GUPTA, 1976)

| T | Maximum wind speed ($km \cdot h^{-1}$) | Pressure drop (mb) | T | Maximum wind speed ($km \cdot h^{-1}$) | Pressure drop (mb) |
|---|---|---|---|---|---|
| 1 | 46 | - | 5 | 167 | 40 |
| 1.5 | 46 | - | 5.5 | 189 | 52 |
| 2 | 56 | - | 6 | 213 | 66 |
| 2.5 | 65 | 6 | 6.5 | 235 | 80 |
| 3 | 83 | 10 | 7 | 259 | 97 |
| 3.5 | 102 | 15 | 7.5 | 287 | 119 |
| 4 | 120 | 21 | 8 | 315 | 143 |
| 4.5 | 143 | 29 | | | |

At Visakhapatnam, on the east coast of India, the maximum (positive or negative) surge appears to occur usually about a day after the winds attain their maximum intensity. The amplitude of the surge depends more on the wind direction than on the wind speed (RAMANADHAM and VARADARAJULU, 1965). The storm surges at Visakhapatnam are usually associated with three types of storm tracks:

(a) storms originating to the south of Visakhapatnam and recurving near the east coast of India and making a landfall at the Chittagong-Arakan coast,

(b) storms originating to the south of Visakhapatnam and crossing the coast between Masulipatnam and Visakhapatnam, and

(c) storms that develop in the northern part of the Bay of Bengal and cross the coast near the head of the Bay. Storms of the first two types produce positive surges and storms of the third type produce negative surges at Visakhapatnam. The maximum amplitudes of the surges are usually between 40 and 50 cm.

The observed winds appear to have a linear relationship with the gradient wind calculated from the following formula:

$$V_g = \left[ \frac{R}{\rho} \frac{\partial p}{\partial r} + (\omega R \sin \phi)^2 \right]^{1/2} - \omega R \sin \phi \qquad (5.89)$$

where, $V_g$ is the gradient wind, $\omega$ is the angular velocity of the earth's rotation, $\phi$ is the latitude, R is the radius of curvature of the isobars, and p is the density of air. It was found that

$$\frac{V}{V_g} = 0.6$$

where, V is the wind as measured from ships offshore.

Although storm surges may be of small amplitude at Visakhapatnam, south of it, storm surges could have very large amplitudes. The cyclone of October 28, 1949, made a landfall north of Masulipatnam (Fig. 5.88). Winds up to 90 knots (167 km · $h^{-1}$) produced storm surges with amplitudes of 3–4 m along a stretch of the coast shown in Fig. 5.88. The storm crossed the coast at the time of high tide (RAO, 1968).

Another severe storm struck the Coromandel Coast on November 30, 1952 (RAO, 1968). Again, winds up to 90 knots produced surges with amplitudes up to 2.5 m along a stretch of the coast shown in Fig. 5.89. Another severe cyclonic storm travelled towards the west over the northern boundary of the Palk Strait (between India and Sri Lanka) on November 30–December 1, 1955. Two different storm surges occurred (RAO, 1968). The first one was along the coast between Point Calimere and Vettaikaran lruppu and had amplitudes up to 2 m. The second surge occurred between Thambkottai and Kattumavedi with amplitudes over 1 m.

One of the most destructive storm surges in southern India occurred on December 23, 1964 (Fig. 5.92). Winds up to 120 knots (322 km · $h^{-1}$) created storm surges over the islands of Mannar (Sir Lanka) and Rameswaram (India) and the maximum amplitudes of the surges were 5–6 m. This storm exhibited some interesting features: (a) the major surges occurred to the left of the storm track (at Pamban-Dhanushkodi Islands), (h) the surges preceded the arrival of the storm by approximately 3–4 h, (c) although winds up to 80 knots (148 km · $h^{-1}$) were recorded to the west of the Pamban Bridge, no surges occurred along this part of the coastline

It was mentioned that the amplitude of storm surges at Visakhapatnam, is not significant. Generally, north of Visakhapatnam, the storm surge activity is not severe, except on some stretches of the Orissa coast, until one arrives at the coast of Bangladesh. Saugor Island (India) is situated near the head of the Bay of Bengal where the Hoogly Estuary empties into the Bay. On this island, the surge heights usually range from 1/3 to 1 m (JANARDHAN, 1967).

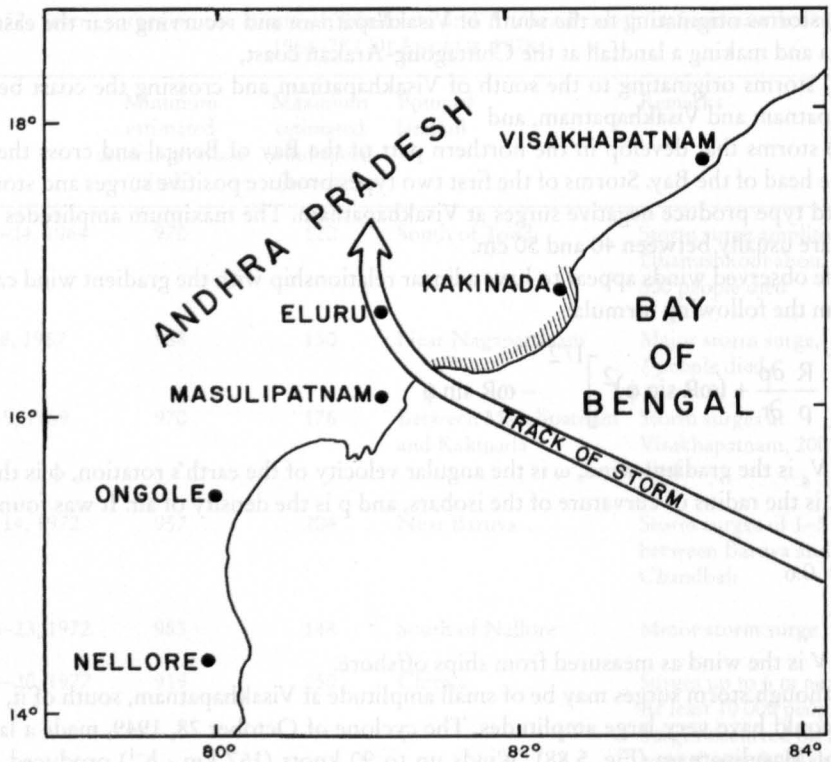


Fig. 5.88: Track of the storm of October 1949 on the southeast coast of India. Hatched area shows the coastline affected by the storm surge (RAO, 1968)

JOHNS and ALI (1980) used the following pressure distribution in their simulation of the November 1970 storm surge that caused great devastation in Bangladesh.

$$p = p_a - \Delta p \exp\left(-\frac{r}{R}\right) \tag{5.90}$$

where, p is the pressure field at radius r, $p_a$ is the ambient pressure, $\Delta p$ is the difference between the ambient and central pressures, and $R$ is the e-folding radius of the pressure distribution.

A value of 350 km was given to HOLLAND (1980) pointed out that $R$ should be the radius of maximum winds and that a typical value of $R$ should be about 35 km.

The argument that $R$ should be the radius of maximum winds was developed by HOLLAND (1981) as follows. For tropical cyclones, a typical Rossby number will be about 100, in the strongest wind region. One may assume a cyclostrophic balance and write

$$V_c = \left(\frac{r}{\rho}\frac{\partial p}{\partial r}\right)^{1/2} \tag{5.91}$$

where, $V_c$ is the cyclostrophic tangential wind and p is the air density. Substituting eq. (5.90) into (5.91)

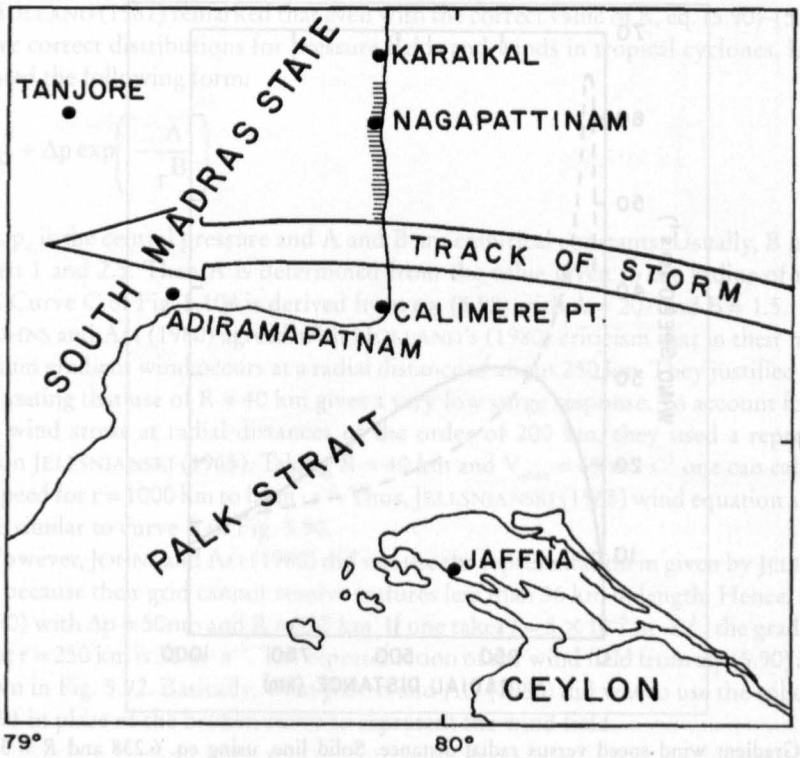


Fig. 5.89: Track of the storm of November 1952 on the southeast coast of India. Hatched area shows the coastline affected by the storm surge (RAO, 1968)

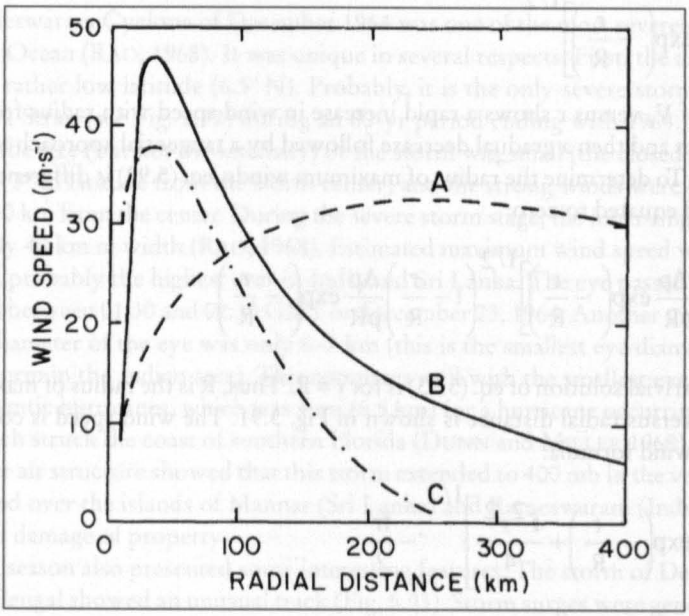


Fig. 5.90: Gradient wind speed versus radial distance. Curve A, $R$ = 350 km; curve B, $R$ 35 km; curve C, from eq. 6.243 (HOLLAND, 1981)

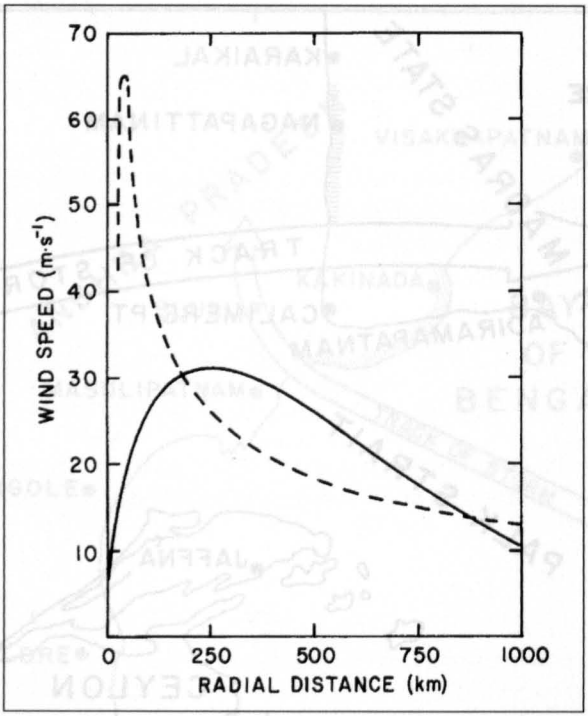


Fig. 5.91: Gradient wind speed versus radial distance. Solid line, using eq. 6.238 and $R$ = 350 km; broken line, using eq. 6.143, $R$ = *40* km, and V, = 65 m. s-' (JOHNS and ALI, 1981)

$$V_c = \left[\frac{r\Delta p}{\rho R}\exp\left(-\frac{r}{R}\right)\right]^{1/2} \tag{5.92}$$

A plot of $V_c$ versus r shows a rapid increase in wind speed with radius from the center to a maximum and then a gradual decrease followed by a tangential approach to zero at infinite distance. To determine the radius of maximum winds, eq. (5.92) is differentiated with respect to r and equated to zero:

$$\frac{\partial V_C}{\partial r} = \frac{1}{2}\left[\frac{r\Delta p}{\rho R}\exp\left(-\frac{r}{R}\right)\right]^{1/2}\left(1-\frac{r}{R}\right)\frac{\Delta p}{\rho R}\exp\left(-\frac{r}{R}\right) \tag{5.93}$$

The nontrivial solution of eq. (5.93) is for r = R. Thus, R is the radius of maximum winds. Wind speed versus radial distance is shown in Fig. 5.91. The wind speed is computed from the gradient wind formula:

$$V_g = \left[\frac{r\Delta p}{\rho R}\exp\left(-\frac{r}{R}\right)+\frac{f^2r^2}{4}\right]^{1/2} - \frac{fr}{2} \tag{5.94}$$

where, $V_g$ is the gradient wind and $f$ is the Coriolis parameter. The following values were used: $\Delta p$ = 50 mb, p = 1.2 km · m$^{-3}$, $f = 5 \times 10^{-5} \cdot s^{-1}$.

HOLLAND (1981) remarked that even with the correct value of R, eq. (5.90)–(5.94) might not give correct distributions for pressure fields and winds in tropical cyclones. Instead, he suggested the following form:

$$p = p_c + \Delta p \exp\left(-\frac{A}{r^B}\right) \tag{5.95}$$

where, $p_c$ is the central pressure and A and B are empirical constants. Usually, B has a value between 1 and 2.5. Then A is determined from the value given to the radius of maximum winds. Curve C of Fig. 5.104 is derived from eq. (5.95) with A = 207 and B = 1.5.

JOHNS and ALI (1980) agreed with HOLLAND'S (1980) criticism that in their model, the maximum gradient wind occurs at a radial distance of about 250 km. They justified their model by stating that use of R = 40 km gives a very low surge response. To account for the role of the wind stress at radial distances of the order of 200 km, they used a representation based on JELESNIANSKI (1965). Taking R = 40 km and $V_{max} = 65\ m \cdot s^{-1}$ one can calculate the wind speed for r = 1000 km to be $m \cdot s^{-1}$. Thus, JELESNIANSKI (1965) wind equation also shows a curve similar to curve B of Fig. 5.90.

However, JOHNS and ALI (1980) did not use the representation in given by JELESNIANSKI (1965) because their grid cannot resolve features less than 36 km in length. Hence, they used eq. (5.90) with Δp = 50mb and R = 350 km. If one takes $f = 5 \times 10^{-5}\ m \cdot s^{-1}$, the gradient wind speed at r = 250 km is $30\ m \cdot s^{-1}$. The representation of the wind field from eq. (5.90) and (5.95) is shown in Fig. 5.92. Basically, what JOHNS and ALI (1980) did was to use the solid curve of Fig. 5.91 in place of the broken curve to represent the wind field.

*Case Studies of Cyclonic Storms in the Bay of Bengal During the Period 1964–99*

The Rameswaram Cyclone of December 1964 was one of the most severe storms of the North Indian Ocean (RAO, 1968). It was unique in several respects. First, the intensification occurred at a rather low latitude (6.5° N). Probably, it is the only severe storm that moved across the Palk Strait (see Fig. 5.92) during an 80-yr period ending with 1964. Another feature was that the size (but not the intensity) of the storm was small (the closed isobaric field extended only 3° in latitude from the storm center) and the strong winds were confined to a region 100–150 km from the center. During the severe storm stage, the inner ring of hurricane winds was only 40 km in width (RAO, 1968). Estimated maximum wind speed was 175 knots ($324\ km \cdot h^{-1}$), probably the highest ever in India and Sri Lanka. The eye passed over Rameswaram (India) between 01:30 and 02:30 GMT on December 23, 1964. Another unusual feature was that the diameter of the eye was only 6–7 km (this is the smallest eye diameter reported for a severe storm in the Indian area). This compares well with the smallest eye diameter reported for Atlantic hurricanes, which was 4 mi (6.5 km) for a hurricane occurring on July 27, 1936, and which struck the coast of southern Florida (DUNN and MILLER 1960).

The upper air structure showed that this storm extended to 400 mb in the vertical. Storm surges occurred over the islands of Mannar (Sri Lanka) and Rameswaram (India) with great loss of life and damage of property.

The 1965 season also presented some interesting features. The storm of December 1965 in the Bay of Bengal showed an unusual track (Fig. 5.93). Storm surges were generated on the coast of Bangladesh and heavy casualties followed. Not only was the track unusual, but also the duration of the storm was 9 d compared with the usual 1–3 d. During a 70-yr period,

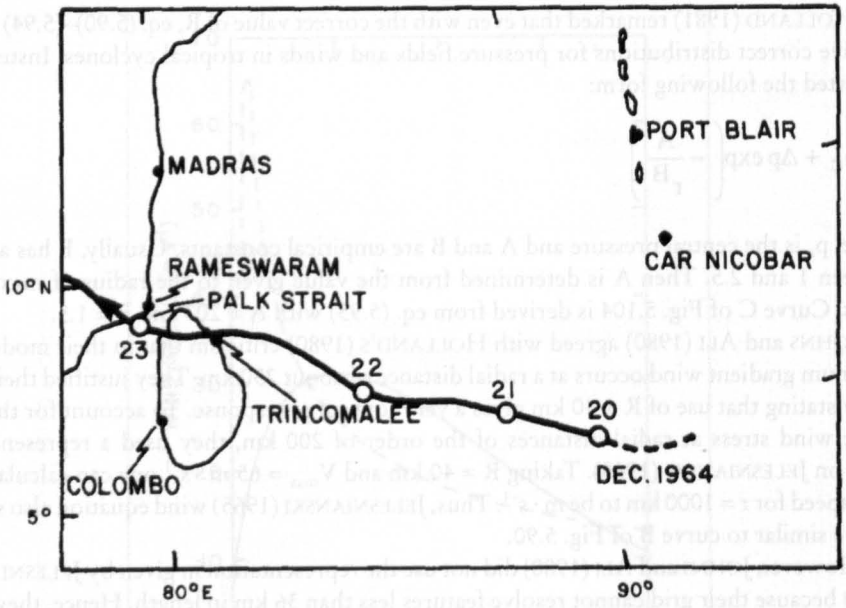


Fig. 5.92: Track of the severe storm of December 1964 over Sri Lanka (RAO, 1968)

about 77 % of the storms in the Bay of Bengal lasted only 1–4 d, 17 % lasted for 5–6 d, and only 7 % (i.e. three storms) lasted for 7 d. The average duration for the Bay of Bengal storms is 3.5 d (compared with the average life span of global tropical cyclones, which is 6.5 d according to RIEHL, 1954). Another unusual feature was that this storm hit Bangladesh and Burma in December. Note that in the 70-yr period only 13 storms did this. A final unusual feature was the simultaneous presence of another storm in the Arabian Sea (see Fig. 5.93). Only five times before has a similar situation existed (i.e. storms in the Bay of Bengal and the Arabian Sea at the same time). These cases are listed in Table 5.54 and their tracks are illustrated in Fig. 5.93.

The 1966 season produced a maximum number of storms in the postmonsoon season (RAMAN et al., 1967). The following deductions were made by RAMAN et al. (1967).

The thermodynamical conditions necessary for the development of cyclone storms, as discussed by PALMÉN (1955), are found in all the postmonsoon months. However, additional conditions must be satisfied. One of the reasons for the high cyclone activity in the 1966 season was the continued northward position of the equatorial trough. Even though the low latitude wind fields in 1959 and 1966 were similar, the absence of northward horizontal shear in the wind field of 1959 inhibited the development.

The required minimum energy for development is available at the air-sea interface during all postmonsoon months. However, for maturity into severe storms, the zones of maximum evaporation should also take place in preferred areas. During the 1966 season, the atmosphere gained the maximum heat over the southwest and west central parts of the Bay of Bengal. Generally, only in this region do all disturbances mature into cyclonic storms. On the other hand, in November 1954, maximum evaporation took place over the southwest part of the bay, south of 10° N. Finally, the origin, intensification and movement of cyclonic storms coincide with the zones of convergence of the total energy that is available in the atmosphere.

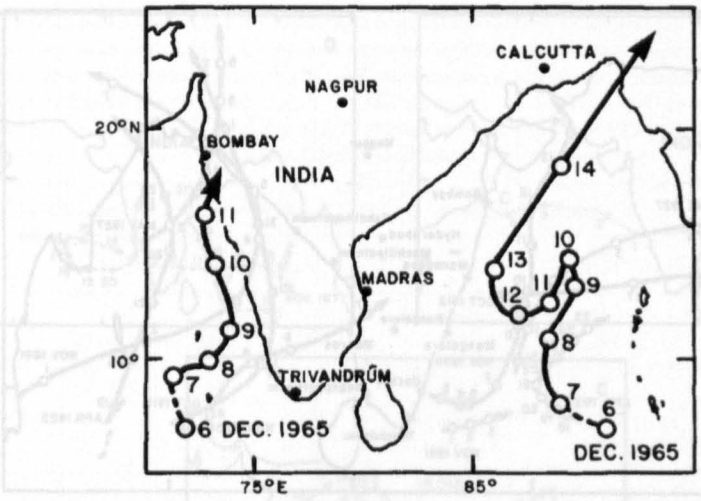


Fig. 5.93: Tracks of a storm pair in the Bay of Bengal (December 7–15, 1965) and Arabian Sea (December 7–12, 1965) (SWAMINATHAN, 1966)

Table 5.54: Details of storm pairs in the Bay of Bengal and the Arabian Sea during the period 1891–1960. Date indicated refers to the original date of the storm. In each pair, the top row is for the Bay of Bengal and the bottom row for the Arabian Sea (SWAMINATHAN, 1966)

| | Origin | |
|---|---|---|
| Date | Latitude (°N) | Longitude (°E) |
| Nov. 1, 1981 | 8.0 | 74.5 |
| Nov. 1, 1891 | 9.5 | 98.5 |
| Oct. 25, 1912 | 15.0 | 72.5 |
| Oct. 28, 1912 | 8.5 | 89.0 |
| Apr. 18, 1922 | 9.0 | 68.5 |
| Apr. 19, 1922 | 9.5 | 93.0 |
| May 31, 1927 | 11.5 | 71.0 |
| May 31, 1927 | 17.5 | 91.5 |
| Nov. 3, 1936 | 9.5 | 75.0 |
| Nov. 4, 1936 | 9.0 | 88.0 |

However, the 1977 season was an especially bad one. On November 19, a cyclone hit the coast of Andhra Pradesh (India) and produced storm surges greater than 5 m in amplitude. The path of this storm is shown in Fig. 5.95 a (track A). Between November 21 and 22, another Bay of Bengal originated storm struck the west coast of India (Fig. 5.95 a, track B). This storm also caused great damage. On October 28, a storm originating in the Bay of Bengal struck the coast of Arabia between November 4 and 5 (Fig. 5.95 b, track C).

WINCHESTER (1979) provided the following details about the Andhra coast storm of November 19. The storm made a landfall near the mouth of the Krishna River with a speed of 12 mi · $h^{-1}$ (19.5 km · $h^{-1}$) with wind speeds of 75 mi · $h^{-1}$ (121 km · $h^{-1}$) and gusting to 120 mi · $h^{-1}$ (193 km · $h^{-1}$). The storm surge was 5 m in amplitude and penetrated at least 10 mi

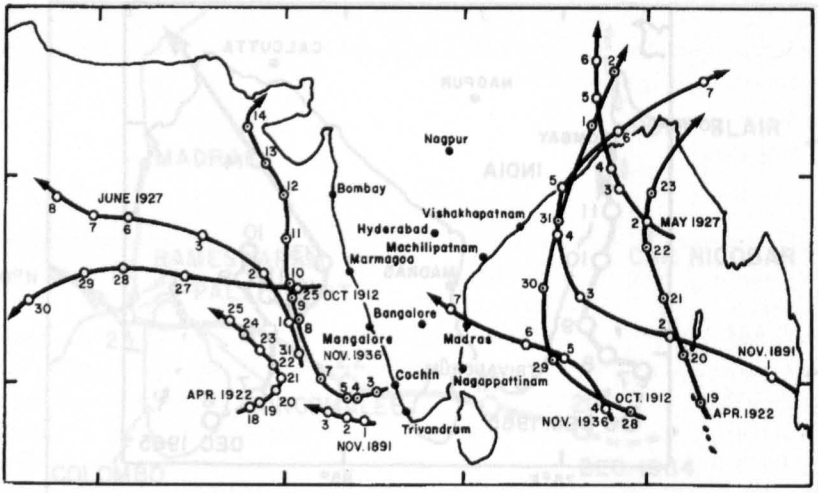


Fig. 5.94: Tracks of storm pairs in the Bay of Bengal and the Arabian Sea during 1891–1960 (SWAMINATHAN, 1966)

(16 km) inland with a speed of about 10 mi · $h^{-1}$ (16 km · $h^{-1}$) over a coastal stretch of 35 mi (56 km). The high water due to the surge remained for about 10 h. The cyclone and the storm surge together totally damaged an area of about 7500 $mi^2$ (195 000 $km^2$). At least 20 000 people died and 2 million people were left homeless (DEANGELIS, 1978a, 1978b, 1978c, 1978d).

There was no significant storm surge activity in India during 1978. However, Sri Lanka experienced a very devastating storm surge during this year (damage of $ 50 million). On November 21, 1978, a tropical storm generated near the Nicobar Islands matured to hurricane strength and on November 23 it struck the east coast of Sri Lanka (Fig. 5.95 c, track D). The resulting storm surge together with the cyclone and the resulting landslides that occurred killed 373 people and destroyed 80 000 houses. Wind gusts up to 204 km · $h^{-1}$ occurred. The storm surge inundated rice fields up to 8 km inland. The storm then moved to India over the Gulf of Mannar where it killed 10 people (DEANGELIS, 1979a, 1979b, 1979c).

One humorous sidelight of this cyclone was that 160 convicts escaped when the roof blew off the jail in Batticaba (Sri Lanka). The fact that not everybody is inconvenienced by a natural disaster such as a storm surge can be seen from the fact that, invariably, after the disaster looters descend upon the scene and helped themselves. These are also good times for black marketeers and food hoarders, especially in the developing countries.

When one of the author of this book (T. S. Murty) visited his native village in Andhrapradesh, India, in 1978 (1 yr after the disastrous storm surge of November 1977), tales of how village officers confiscated the emergency relief funds (provided by the federal government of India as well as by several international agencies) for their own use were mentioned to him. Although this author is not an expert on sociological aspects, his early background in developing countries convinced him that there is much truth to these tales. He was given to understand by the villagers that corruption is minimal to nonexistent with federal (central) government officers (due to the higher calibre of the federal civil service and also due to various built-in checks against corruption), and that corruption increases by an order of magnitude with the provincial (state) government officers, then by another order of magnitude with the district (county) level of government, and to absolute and total corruption at the municipal

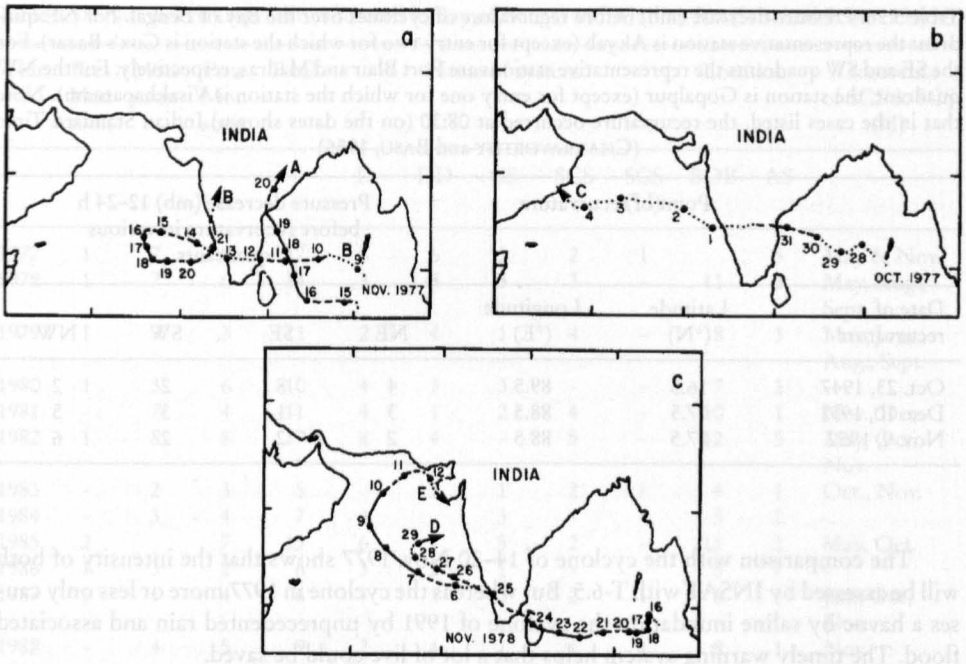


Fig. 5.95: (a) Track A: storm of November 1977 that caused great damage to the Andhra Pradesh Coast of India; track B: storm of November 1977 that did moderate damage to the west coast of India. (b) Track C: storm originating in the Bay of Bengal on October 28, 1977, that struck the coast of Arabia. (c) Track D: storm of November 1978 that did great damage on the cast coast of Srilankas; track E: storm of November 1978 originating in the Arabian Sea and striking the Gujarat coast of India (DE ANGELIS, 1978a,1978b, 1978c, 1978d)

(city, town, village) level. We would like to recommend to the international agencies that provide emergency relief funds to any developing country that only the federal government officials be involved in the handling of the relief operations.

SOM and SOM (1995) describe the Machilipatnam cyclone on 9th May 1990, which hit the Andrha coast (eastern coast of India) with an estimated force reaching 200 to 250 kph. Over the coastal area heavy rainfall has been happened. 967 people died and 650,000 people were evacuated from 546 coastal villages. They pointed out that the storm affected a population of about 7.78 million in 5160 villages in Andhra Pradesh. It was one of the severest cyclones in the Bay of Bengal whereas in Andhra coast another earlier cyclone struck the coast with an equal intense.

Table 5.55: Storms and depressions in the Bay of Bengal, 1945–54. A, total number; B, number that recurved. Storms and depressions that recurved on land or while in the Arabian Sea have been excluded (CHAKRAVORTHY and BASU, 1956)

| Type | Jan. | Feb. | Mar. | Apr. | May | June | July | Aug. | Sept. | Oct. | Nov. | Dec. |
|---|---|---|---|---|---|---|---|---|---|---|---|---|
| A | 5 | 1 | 1 | 5 | 6 | 11 | 18 | 19 | 19 | 18 | 12 | 11 |
| B | 2 | 0 | 0 | 1 | 1 | 0 | 0 | 0 | 0 | 5 | 1 | 4 |

Table 5.56: Pressure decrease (mb) before recurvature of cyclones over the Bay of Bengal. For NE quadrant the representative station is Akyab (except for entry two for which the station is Cox's Bazar). For the SE and SW quadrants the representative stations are Port Blair and Madras, respectively. For the NW quadrant, the station is Gopalpur (except for entry one for which the station is Visakhapatnam). Note that in the cases listed, the recurvature occurred at 08:30 (on the dates shown) Indian Standard Time (CHAKRAVORTHY and BASU, 1956)

| | Point of recurvature | | Pressure decrease (mb) 12–24 h before recurvature in various quadrants | | | |
|---|---|---|---|---|---|---|
| Date of recurvature | Latitude (°N) | Longitude (°E) | NE | SE | SW | NW |
| Oct. 23, 1947 | 16.5 | 89.5 | 4 | 8 | 2 | 2 |
| Dec. 10, 1951 | 17.5 | 88.5 | 3 | 1 | 3 | 5 |
| Nov. 9, 1952 | 17.5 | 88.5 | 2 | 2 | 2 | 6 |

The comparison with the cyclone of 14–20 Nov. 1977 shows that the intensity of both will be assessed by INSAT with T-6.5. But whereas the cyclone in 1977 more or less only causes a havoc by saline inundation the cyclone of 1991 by unprecedented rain and associated flood. The timely warning system helps that a lot of live could be saved.

SOM and SOM (1995) although describe the cyclone on 29 April, 1991 which has been happened about 12 hours long and occurred a 5 meter high storm surge. 10 Million people were affected and the country had suffered incalculable economic damage. SOM and SOM (1995) described the situation as follows:

"Whether it was an island (like Sandwip or Kutubdia) or a place on the main land, one moment there were communities of ten thousands or more, three hours later there was absolutely nothing. Just enormous street of salt water dwarfing everything save the tall palm trees. It swept heavily populated areas several kilometres inland along a 240 km coastal stretch of Bangladesh and all the offshore islands. The seawater took merely 10 minutes to reach neck deep water levels at highest points of Sandwip islands. The official tally of the casualties was approximately 132,000. But exact number of deaths would never be known as no one knew how many people had been washed away in the Bay of Bengal. However, unofficial estimate of casualties was half a million."

*Arabian Sea*

Compared with the Bay of Bengal, the storms of the Arabian Sea are less frequent, generally less intense, and the accompanying storm surges are usually less destructive (Table 5.57). The statistics by month for the period 1891–1960 are given in Table 5.58.

PEDGLEY (1969) mentioned that cyclones develop preferentially over the southeastern quadrant of the Arabian Sea and move in a west to northwest direction towards Arabia. However, sometimes they recurve to the north or northeast towards northwestern India and Pakistan (Fig. 5.96). About one storm in three passes over the western part of the Arabian Sea and strikes the coast of the Arabian peninsula.

Table 5.57: Number of Depressions formed in Bay of Bengal and Arabian Sea (SOM and SOM, 1995)

| Year | Pre-Monsoon | Monsoon | Post Monsoon | Total | Name of system | | | | | Location | | Occurence of SCS & SCS (H) |
|---|---|---|---|---|---|---|---|---|---|---|---|---|
| | | | | | D | DD | CS | SCS | SCS (H) | BOB | AS | |
| 1977 | 1 | 7 | 9 | 17 | 5 | 6 | 3 | 2 | 1 | | 5 | May & Nov. |
| 1978 | 1 | 7 | 6 | 14 | 3 | 5 | 3 | 3 | - | 11 | 3 | May, Aug., Sept. |
| 1979 | 1 | 7 | 3 | 11 | 2 | 4 | 1 | 4 | - | 8 | 3 | May, June, Aug., Sept. |
| 1980 | 1 | 3 | 6 | 10 | 4 | 3 | 3 | - | - | 7 | 3 | - |
| 1981 | - | 7 | 4 | 11 | 4 | 1 | 2 | 4 | - | 10 | 1 | Nov., Dec. |
| 1982 | 1 | 8 | 8 | 17 | 8 | 4 | - | 5 | - | 12 | 5 | May, Oct. Nov. |
| 1983 | - | 2 | 3 | 5 | - | 2 | 1 | 2 | - | 4 | 1 | Oct., Nov. |
| 1984 | - | 3 | 4 | 7 | 4 | - | 3 | - | - | 5 | 2 | - |
| 1985 | 2 | | 7 | 13 | 6 | - | 5 | 2 | - | 11 | 2 | May, Oct. |
| 1986 | 1 | 3 | 2 | 6 | 3 | 2 | 1 | - | - | 5 | 1 | - |
| 1987 | 1 | 1 | 4 | 6 | - | 1 | 2 | 2 | 1 | 6 | - | Jan., Oct, Nov. |
| 1988 | - | 4 | 5 | 9 | 2 | 4 | 1 | 1 | 1 | 8 | 1 | Nov. |
| 1989 | 1 | 5 | 4 | 10 | 3 | 4 | 1 | - | 2 | 9 | 1 | May & Nov. |
| 1990 | 1 | 3 | 5 | 9 | 4 | 3 | - | 1 | 1 | 8 | 1 | May & Dec. |
| 1991 | 2 | 3 | 3 | 8 | 4 | 1 | 2 | - | 1 | 8 | - | April |
| 1992 | 1 | 3 | 8 | 12 | 1 | 4 | 5 | 1 | 1 | 8 | 4 | Nov. |

D – Depression, DD – Deep Depression, CS – Cyclonic Storms, SCS – Severe Cyclonic Storms, SCS (II) – Severe Cyclonic Storms with Hurricane Wind, BOB – Bay of Bengal, AS – Arabian Sea.

Table 5.58: Data on the cyclonic storms of the Arabian Sea during the period 1891–1960 (RAO, 1968)

| Type of storm | Jan. | Feb. | Mar. | Apr. | May | June | July | Aug. | Sept. | Oct. | Nov. | Dec. | Year |
|---|---|---|---|---|---|---|---|---|---|---|---|---|---|
| Total number of cyclonic disturbances | 6 | 0 | 1 | 7 | 20 | 30 | 11 | 21 | 0 | 36 | 36 | 8 | 165 |
| Total number that intensified into storms | 2 | 0 | 0 | 5 | 13 | 13 | 3 | 1 | 4 | 17 | 21 | 3 | 82 |
| Total number that intensified into severe storms | 0 | - | - | 4 | 11 | 8 | 0 | 0 | 1 | 7 | 16 | 1 | 48 |

The frequency of cyclonic storms for the period 1891–1967 is given in Table 5.59. About one cyclonic storm in 3 yr strikes the coast and about half of these that strike have cyclone strength. Usually the cyclones make landfall near Salalah and they show a tendency to turn to the left at a distance of a few hundred kilometres from the coast. The 10 cyclones that hit the Arabian coast during 1943–67 are listed in Table 5.60.

Table 5.59: Number of occurrences of cyclones (Beaufort ≥ 12) and cyclonic storms (BF ≥ 8) over the whole Arabian Sea during the period 1890–1950 and number of occurrences along the Arabian coast during the period 1891–1967. For the Beaufort wind scale, see Tables 5-6-18 (PEDGLEY, 1969)

| Type of storm | Jan. | Feb. | Mar. | Apr. | May | June | July | Aug. | Sept. | Oct. | Nov. | Dec. | Year |
|---|---|---|---|---|---|---|---|---|---|---|---|---|---|
| Cyclones and Cyclonic storms over the whole Arabian Sea | 1 | 0 | 0 | 4 | 10 | 11 | 2 | 1 | 4 | 15 | 12 | 3 | 63 |
| Cyclones and Cyclonic storms along the coast of Arabia | 0 | 0 | 0 | 0 | 8 | 5 | 1 | 0 | 0 | 7 | 6 | 1 | 28 |
| Cyclones along the coast of Arabia | 0 | 0 | 0 | 0 | 6 | 2 | 0 | 0 | 0 | 2 | 2 | 1 | 13 |

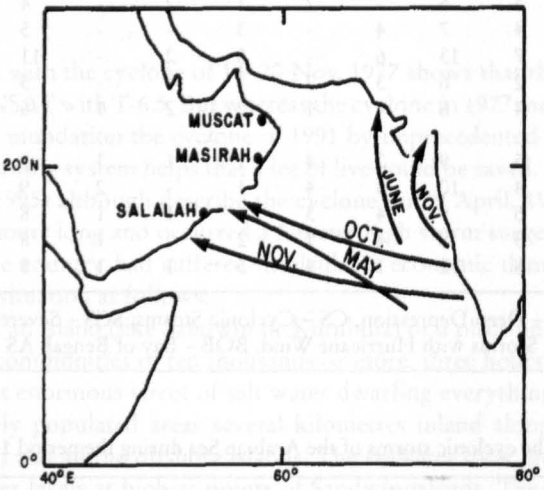


Fig. 5.96: Common tracks of Arabian Sea cyclones (PEDGLEY, 1969)

Table 5.60: Cyclones near the coast of the Arabian peninsula during 1943–1967 (PEDGLEY, 1969)

| Date of approach or crossing the coast | Nature of the cyclone |
|---|---|
| June 6, 1946 | Decaying before approaching Masirah from east-southeast |
| October 1, 1948 | Decaying before approaching coast between Masirah and Ra's al Hadd from east |
| October 25, 1948 | Cyclonic storm crossed Salalah, approaching from southeast |
| May 24, 1959 | Severe cyclone crossed Salalah, approaching from east-southeast |
| October 18, 1959 | Severe cyclone crossed near Ras Madraka, approaching from east |
| May 18, 1960 | Severe cyclone crossed coast at Ras Fartak |
| November 23, 1960 | Cyclonic storm approached entrance to Gulf of Aden from east |
| May 30, 1962 | Decaying before crossing coast at Ras Madraka |
| May 26, 1963 | Severe cyclone, passed just south of Salalah, approaching from east-southeast and then turning towards west-southwest |
| November 13, 1966 | Severe cyclone with a track similar to that of May 1963 |

The following pressure distribution

$$p = 1008 - 1.64(v_r r) \tag{5.96}$$

appears to fit the central pressure of the Arabian Sea cyclones. Here, p is the central pressure (millibars) and $v_r$ is the radial wind speed in knots at a distance from the center of r degrees latitude (KRUEGER, 1959). The maximum wind speed $v_m$ can be estimated from MYERS (1957):

$$v_m = K\sqrt{p' - p} \tag{5.97}$$

where p' is the surrounding pressure and $K$ is a constant (equal to 11). For example, taking p = 960 mb and p' = 1010 mb gives $v_m$ = 80 knots (148 km · $h^{-1}$).

Although most of the Arabian Sea cyclones originate locally, some (6 of the 28 mentioned in Table 5.59) originated in the Bay of Bengal. Usually, cyclones with this distant origin occur towards the end of the cyclone season (i.e. towards November). Occasionally, the Arabian Sea cyclones cross the Gulf of Aden and even rarely the Gulf of Oman.

One difference between the cyclones of the Arabian Sea and the Bay of Bengal is that, whereas in the Bay of Bengal more cyclones occur in the postmonsoon season (September to December) than in the premonsoon season (April to May), in the Arabian Sea they are about equally distributed between the two cyclone seasons (i.e. May to June and October to November). Most of these originate over the southeastern Arabian Sea and move towards west-northwest. However, a few originate in the Bay of Bengal and cross southern Indian peninsula before emerging over the Arabian Sea.

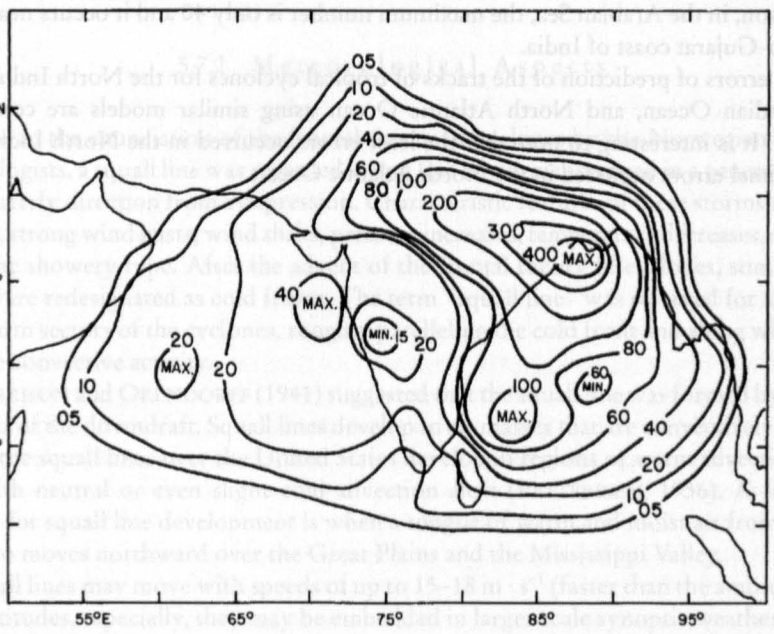


Fig. 5.97: Contours of a number of tropical cyclones (including depressions) passing through 2.5° latitude-longitude squares for the period 1877–1974 (NEUMANN and MANDAL, 1978)

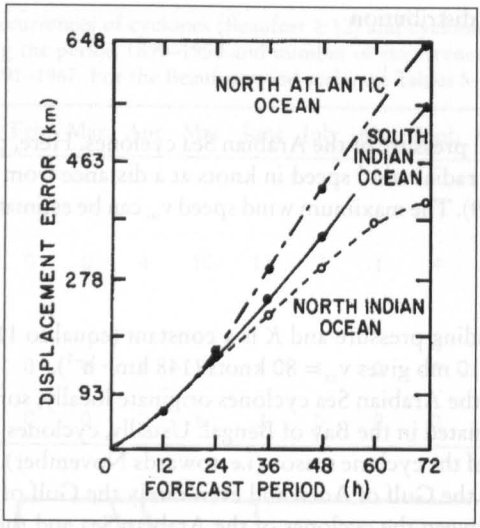


Fig. 5.98: Forecast errors in the tracks of tropical cyclones for three different ocean basins (NEUMANN and MANDAL, 1978)

NEUMANN and MANDAL (1978) used statistical techniques to predict the storm movement over the Arabian Sea and the Bay of Bengal. The number of tropical cyclones (including depressions) passing through 2.5° latitude-longitude squares for the period 1877–1974 is given in Fig. 5.97. It can be seen that maximum values of up to 400 cyclones and depressions occurred near the coasts of West Bengal (India) and Bangladesh in the Bay of Bengal. By comparison, in the Arabian Sea, the maximum number is only 40 and it occurs near the Maharashtra-Gujarat coast of India.

The errors of prediction of the tracks of tropical cyclones for the North Indian Ocean, South Indian Ocean, and North Atlantic Ocean using similar models are compared in Fig. 5.98. It is interesting to note that the least errors occurred in the North Indian Ocean and maximal errors occurred in the North Atlantic Ocean.

## 5.7 Mesoscale Weather Systems

HOBBS (1981) defined a mesoscale weather system as one with horizontal scales in the range of a few to 1000 km and time scales ranging from several hours to 1 d. Squall lines, thunderstorms, and tornadoes fall into the classification of mesoscale weather systems. Here, squall lines are specifically examined, since, as will be seen later, they can give rise to storm surges.

Squall lines are nonfrontal lines of active thunderstorms, several to some tens of kilometers wide and hundreds of kilometers long, which exist for a considerably longer period than the lifetime of the component cumulonimbus clouds (RAMAGE, 1971).

Stationary as well as traveling mesoscale weather systems such as those that occur over the Great Plains of the United States are classified further into the following: regional scale (200–2000 km), or meso-alpha; squall line scale (20–200 km), or meso-beta; cloud scale (2–20 km), or meso-gamma (ANONYMOUS, 1978).

### 5.7.1 Regions Where Squall Lines Occur

Squall lines occur in midlatitudes as well in the tropics. They occur mainly over the United States, Central, West, and South Africa, Venezuela, northern India, and northern Australia. In the United States they occur predominantly during spring and summer.

According to HAMILTON and ARCHBOLD (1945) and TSCHIRHART (1958), sub-Saharan Africa is a fertile ground for squall lines and, in fact, these account for most of the rainfall. Another area where squall lines occur is the Caribbean Sea. On rare occasions, squall lines can also be observed over the southern part of the North Sea.

### 5.7.2 Meteorological Aspects

Prior to the enunciation of the frontal theory of cyclones by the Norwegian School of Meteorologists, a squall line was regarded as any line of storms arranged in a general southerly and easterly direction from a depression. Characteristic features of these storms are strong intensity, strong wind gusts, wind shifts, pressure increases, temperature decreases, and heavy rain of the showery type. After the advent of the frontal theory of cyclones, some of these storms were redesignated as cold fronts. The term "squall line" was reserved for the storms in the warm sectors of the cyclones, roughly paralleling the cold front and along which there is intense convective activity.

HARRISON and ORENDORFF (1941) suggested that the squall line was formed by the rain-cooled air of the downdraft. Squall lines develop in air masses that are convectively unstable. Most of the squall lines over the United States develop in regions of warm advection at low levels with neutral or even slight cold advection aloft (PETTERSSEN, 1956). A favourable situation for squall line development is when a tongue of warm and moist air from the Gulf of Mexico moves northward over the Great Plains and the Mississippi Valley.

Squall lines may move with speeds of up to 15–18 $m \cdot s^{-1}$ (faster than the ambient wind). In midlatitudes, especially, they may be embedded in larger scale synoptic weather systems. In such situations, the intense part of the weather might be concentrated only in about 10 % of the area of the synoptic system. The life span of a squall line is much shorter

than that of the synoptic scale system in which it is embedded (e.g. a few hours versus a few days).

Squall lines have low-level indraft along their forward edge due to rapid motion (RIEHL, 1979). Individual cumulonimbus clouds in a squall line have life times of at most a few hours. Hence, for a squall line to survive, new convective elements continually replace dissipating elements (RAMAGE, 1971). Squall lines usually become most intense during late afternoons when the convective activity is the highest.

NEWTON and NEWTON (1959) and NEWTON (1967) showed that the continuous exchange of mass between the storm and the surroundings leads to a nonhydrostatic pressure that aids the convection process. On the downshear side the convective elements continually develop whereas on the upshear side they dissipate. Hence, the storm moves in the direction of developing elements and away from dissipating elements.

Over the Central United States the squall lines move 25° to the right of and about 4 $m \cdot s^{-1}$ slower than the mean wind at the 700-mb level. Squall lines over the midwestern and northeastern parts of the United States deviate 50 and 70°, respectively, to the right of the wind direction at the 700-mb level.

Squall lines usually develop near topographic discontinuities (mountains and valleys). Generally, squall lines tend to dissipate when they cross a coast because cool and relatively stable surface air suppresses ascent due to buoyancy (RAMAGE, 1971).

In northern India, squall lines occur in spring and fall (DE, 1963). In northern Australia, squall lines occur mainly in spring. The West African squall lines resemble those over the United States in the following respects: they tend to develop and are most intense in the afternoon and are most frequent in spring. However, there are certain differences also. The West African squall lines are usually embedded in an environment possessing easterly vertical shear and they travel westward with velocities of up to 10 $m \cdot s^{-1}$. Although the life span of most squall lines is less than 24 h, some persist for several days and travel more than 3000 km. Although most squall lines weaken after crossing a coastline, some do not (e.g. over the warm Guinea current).

Probably the first systematic study of squall lines emerged from the U.S. thunderstorm project during 1946–48. WILLIAMS (1948) used the data from the automatic recording stations in Ohio operated by the U.S. Weather Service's cloud physics project to deduce the microstructure of squall lines.

TEPPER (1950a, 1950b) described the meteorological features associated with the arrival of an intense squall line at the ground. Initially there is an abrupt rise in the surface pressure, which he referred to as a "pressure jump". FUJITA (1955) called it the "pressure surge". Within 1 min after the pressure jump there is a sudden change in the wind direction, which was referred to as „wind shift." Then, the temperature begins to drop rapidly within 2 min after the wind shift. This drop of temperature was referred to as the „temperature break. The peak wind gust, the onset of rain, and the pressure maximum follow the temperature break.

On the other hand, FUJITA (1955) described the situation somewhat differently. Following the pressure surge, the thunderstorm high occurs and then the pressure decreases. The low pressure areas following the wake drop in pressure are called wake depressions.

BEDARD et al. (1977) and BEDARD and MEADE (1977) described an inexpensive instrument system that was deployed at the Dulles Airport in Washington, DC, to measure the gust fronts associated with squall lines. NOAA (ANONYMOUS, 1978) described the various modeling activities on squall lines that are being done at the National Severe Storms Laboratory (United States). A model being developed by Fritsch (ANONYMOUS, 1978) incorporates the effects of deep convection and shows how a series of thunderstorms can become organized

into groups and how they can influence the winds and pressures in the surroundings. Warm moist air accumulates in front of the squall line, and this leads to a low pressure system at the surface; colder air from the thunderstorm downdraft forms a high pressure area behind the squall line. Presently used weather forecast models cannot resolve the squall lines adequately because the grids used are of the order of 200 km in size.

The official U.S. Weather Service definition of pressure jump (associated with a squall line) is an increase of pressure of more than 0.17 mb $min^{-1}$ with at least a total increase of 0.7 mb. TEPPER (1950) suggested that the detection of the pressure jump could be used as an indication of the movement of the squall line.

Time series data on pressure jumps were published by TEPPER (1950b), FUJITA (1959), and CHARBA (1974). These data show increases of several millibars in surface pressure during a period of a few minutes. TEPPER's (1950a,b) data showed pressure increases of 2.3 mb in 5 min. WILLIAMS' (1948) data showed a 2- to 5-mb rise in 5 min. GOFF (1975) found an average increase of 2.5 mb in 100 s. BLECKER and ANDRE (1950) found significant pressure increases in 10 min.

As for the speed of travel, WILLIAMS (1948) gave a value of 13.4 m $s^{-1}$, TEPPER (1950) found 20.4 m $s^{-1}$, and GOFF (1975) found 10 m $s^{-1}$. On the other hand, DE (1963), based on a study of 44 squall lines in northern India, found a value of 33 km · $h^{-1}$. He quoted values from other authors ranging from 35 to 40 km · $h^{-1}$. DE (1963) also found that the direction of movement of the squall lines is generally within 90° to the right (looking downwind) of the 700-mb wind. They occurred mainly during March–May and their life span varied from 3 to 10 h. Their lengths varied from 40 to 400 km and their speed of travel varied from 20 to 50 km · $h^{-1}$. For comparison, some data on squall lines in Venezuela are listed in Table 5.61.

Table. 5.61: Squall lines over Venezuela (BETTS et al., 1976)

| Major axis of squall line (km) | Minor axis of squall line (km) | Life span (min) | Observed track length (km) | Speed of travel (km · $h^{-1}$) |
|---|---|---|---|---|
| 96 | 32 | 200 | 136 | 51.1 |
| 90 | 46 | 240 | 131 | 38.5 |
| 120 | 27 | 211 | 170 | 55.0 |
| 95 | 20 | 215 | 161 | 59.4 |
| 100 | 30 | 140 | 154 | 52.4 |
| 100 | 31 | 195 | 150 | 52.0 |

The cross-section through a squall line system is shown schematically in Fig. 5.100. Important results on squall lines may be found in LILLY (1979), OGURA and LIOU (1980), BETTS et al. (1976), ZIPSER (1969, 1977), HOUZE (1977), MITCHELL and HOVERMALE (1977), CHARBA (1974), MONCRIEFF and MILLER (1976) and MILLER and BETTS (1977).

### 5.7.3 Squall Line Forcing Terms for Storm Surge Calculation

WILSON (1978) developed simplified pressure and wind profiles for a "historical maximum squall line" for use in estimating water levels near United States nuclear power plants. One very important point to be made is that, whereas with synoptic scale weather systems

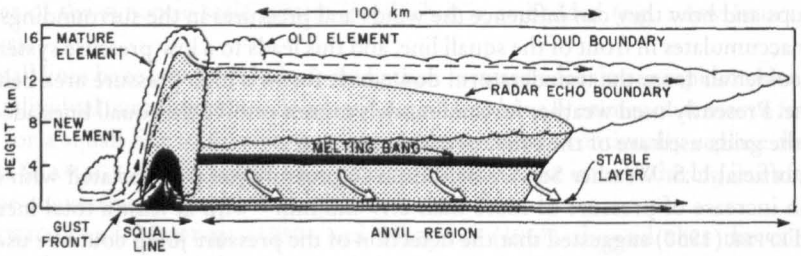


Fig. 5.99: Schematic cross-section through a squall line system. Streamlines show flow relative to the squall line. Broken lines show updraft circulation. Thin solid streamlines show mesoscale downdraft below the base of the anvil cloud. Dark shading shows strong radar echo in the melting band and in the heavy precipitation zone of the mature squall line element. Light shading shows weaker radar echoes. Scalloped line shows visible cloud boundaries (Houze, 1977)

(e.g. tropical and extratropical cyclones) usually the wind stress is much more important than the atmospheric pressure gradients, for squall lines, the pressure gradient terms are at least of equal importance and sometimes much bigger than the wind stress terms.

Following FUJITA (1955), WILSON (1978) developed a simple model for a squall line system, as shown in Fig. 5.100. He also made the following assumptions: (a) the squall line is in a steady state and is in the mature stage, (b) the leading edge of the pressure surge and the gust front move with the same speed (this is in contrast with FUJITA's [1955]) result that the pressure surge moves with a speed some 40 % greater than that of the gust front), and (c) the squall line moves perpendicular to the shoreline.

Making use of these assumptions and the model shown in Fig. 5.100, WILSON (1978) developed the pressure and wind profiles (Fig. 5.101) for a historical maximum squall line. For example, FUJITA et al. (1956) gave a value for the pressure gradient of 9 mb in 50 mi (80 km)

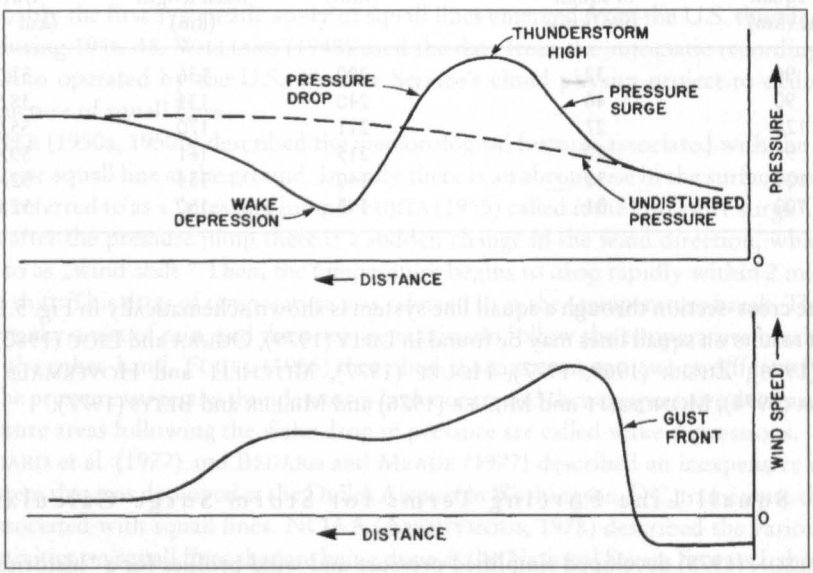


Fig. 5.100: Idealized pressure (top) and wind speed (bottom) field profiles for a squall line system. Negative wind speed denotes inflow into storm system (WILSON, 1978)

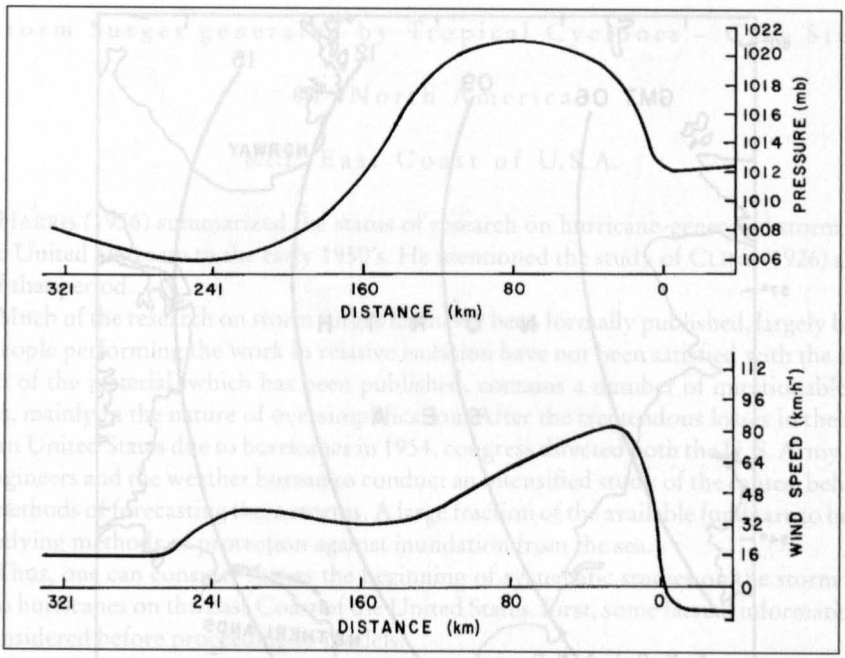


Fig. 5.101: Simplified pressure (top) and wind speed (bottom) profiles for historical maximum squall line system (WILSON, 1978)

for a squall line over Nebraska on June 25, 1953, with a sustained post-gust front wind speed of 45 mi · $h^{-1}$ (73 km · $h^{-1}$). In this model Wilson used a value of 50 mi · $h^{-1}$.

It was mentioned that for squall lines the pressure gradient terms are comparable in magnitude with wind stress terms. This is also borne out by the studies of FREEMAN and MURTY (1972) and MURTY and FREEMAN (1973) for the squall line of August 22, 1971, over Lake Huron. For the squall line, a sharp rise of pressure ($\delta p_a$) of 4.5 mb and wind (W) of 112.6 km · $h^{-1}$ were deduced from the observations. Taking the average depth (D) of the southern part of Lake Huron as 54.7 m, a horizontal scale ($\delta x$) of 8 km, a time interval during which the pressure increased as 5 min, and the speed of travel of the squall line as 96.5 km · $h^{-1}$, the pressure gradient term becomes

$$\frac{1}{\rho} D \frac{\delta p_a}{\delta x} = 34 \text{ cm}^2 \cdot \text{s}^{-2}$$

The wind stress term gives

$$\tau_S = 3 \times 10^{-6} W^2 = 30 \text{ cm}^2 \cdot \text{s}^{-2}$$

For the synoptic scale, the atmosheric pressure gradient as taken from the isobaric plot is a 4-mb change ($\delta$pa) in a 161-km distance ($\delta x$). A wind speed (W) of 32 km · $h^{-1}$ is used as a typical value. The preessure gradient term and the wind stress term become 1.5 and 2.4 cm · $s^{-2}$, respectively.

Earlier, the storm surge calculations in idealized situations using the method of characteristics (e.g. RAO, 1967, 1969; MURTY, 1971) were discussed. The calculations of the storm

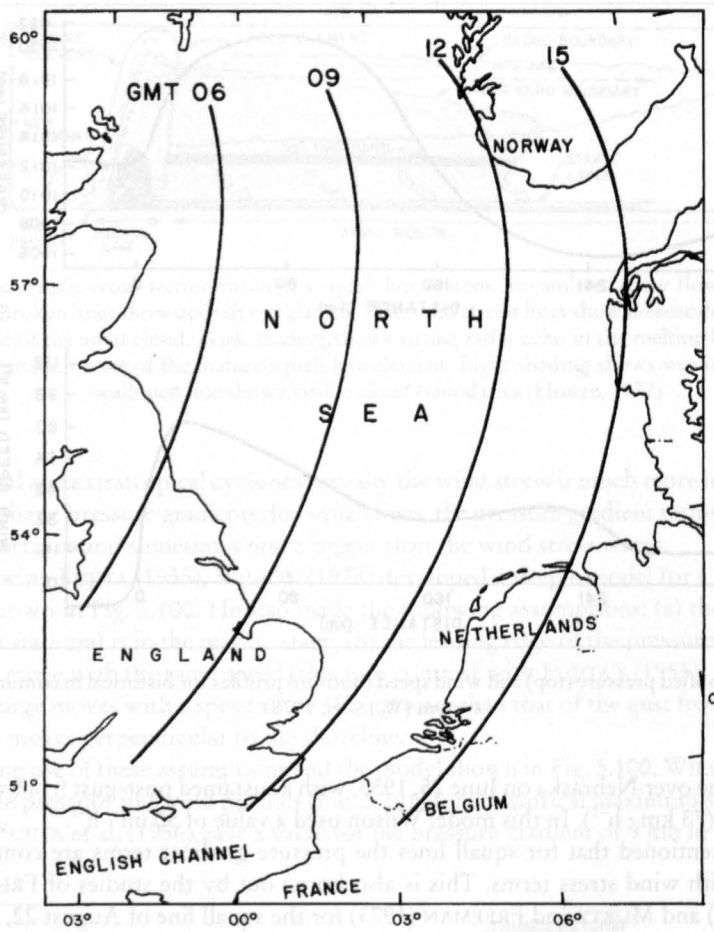


Fig. 5.102: Position of the leading edge of the squall line at four different times (GMT) on December 13, 1956 (TIMMERMANN, 1971)

surge in Lake Michigan due to a squall line on June 26, 1954 (PLATZMAN, 1958a, 1965; IRISH, 1965; HUGHES, 1965) are included elsewhere in the book. DONN and BALACHANDRIAN (1969) discussed the water level oscillations in Long Island Sound (east of New York City) due to a squall line on November 23, 1953. DONN (1959) studied the storm surges in Lake Huron and Erie due to a squall line on May 5, 1952. KRAUSS (1978) studied the response of a stratified sea to a moving squall line.

DOUGLAS (1929) made a simple calculation of the water level oscillations in the English Channel due to a squall line on July 20, 1929. TIMMERMANN (1971) studied the water level oscillations (he referred to therm as "cold fronts") on the Dutch coast of the North Sea. When the speed of the squall line is between 29 and 36 knots, resonance occurs between the squall line and the long gravity waves in the North Sea, and this leads to water level oscillations. During the period December 13, 1956, to January 4, 1968, 20 squall lines with speeds ranging from 25 to 36 knots travelled over the southern part of the North Sea. The positions of tile leading edge of the squall line at four different times on December 13, 1956, are shown in Fig. 5.102.

# 6. Storm Surges generated by Tropical Cyclones – Case Studies

## 6.1 North America

### 6.1.1 East Coast of U.S.A.

HARRIS (1956) summarized the status of research on hurricane-generated storm surges in the United States up to the early 1950's. He mentioned the study of CLINE (1926) as typical of that period.

Much of the research on storm surges has never been formally published, largely because the people performing the work in relative isolation have not been satisfied with the results. Much of the material, which has been published, contains a number of questionable statements, mainly in the nature of oversimplification. After the tremendous losses in the northeastern United States due to hurricanes in 1954, congress directed both the U. S. Army Corps of Engineers and the weather bureau to conduct an intensified study of the causes, behaviour and methods of forecasting these storms. A large fraction of the available funds are to be spent in studying methods of protection against inundation from the sea.

Thus, one can consider this as the beginning of systematic studies on the storm surges due to hurricanes on the East Coast of the United States. First, some factual information will be considered before proceeding to models.

WIEGEL (1964) stated that during the period 1900–55 there was more than 11, 750 deaths caused by hurricanes in the United States. The worst storm surge (from the point of view of loss of life) in United States history occurred in September 1900 when more than 6000 people drowned, most of them at Galveston, Texas (Price 1956). During the 14-year period 1940–53, the loss of life due to hurricane-generated surges over the globe was 3744; 590 of those deaths occurred in the United States (WIEGEL, 1964).

DUNN (1958) mentioned the years and the locations of some of the greatest storm surges on the east coast of United States: Galveston (1900 and 1915), Tampa Bay (1921), Miami (1926), Palm Beach and Lake Okeechobee (1928 and 1949), Florida Keys (1953), and New England, particularly Narragansett Bay (1938 and 1954). The maximum storm surge from these was about 12.5 ft (3.8 m) above mean low water.

HARRIS (1956) and DUNN (1958) mentioned forerunners to storm surges and also resurgence. REDFIELD and MILLER (1957) studied these phenomena in detail and these will be considered now. Also, these authors provided a review of the literature up to 1957; some pertinent information will be extracted.

Between 1635 and 1938 there were at least six major hurricanes on the coast of New England (TANNEHILL, 1950) and between 1938 and 1957 there were at least another six. Since 1874 at least 40 hurricanes passed within 200 nautical miles (370 km) of Rhode Island. NAMIAS (1955) analyzed the tracks of hurricanes and showed that the region most frequently traversed during 1935–55 near the Gulf of Maine was at 40° N, 65° W. One important point made by REDFIELD and MILLER (1957) is that although more than three quarters of the deaths due to hurricanes are caused by the storm surge, until the mid-1950's little attention was paid to the water level problem and all the consideration was given to meteorological problem.

The database for the study by REDFIELD and MILLER (1957) is the following: (1) September 21, 1938, (2) September 14–15, 1944, (3) August 31, 1954 (Carol), (4) September 11, 1954 (Edna), (5) October 15–16, 1954 (Hazel). The tracks of these hurricanes are shown in Fig. 6.1. The three phenomena studied were forerunners, hurricane surge, and resurgence.

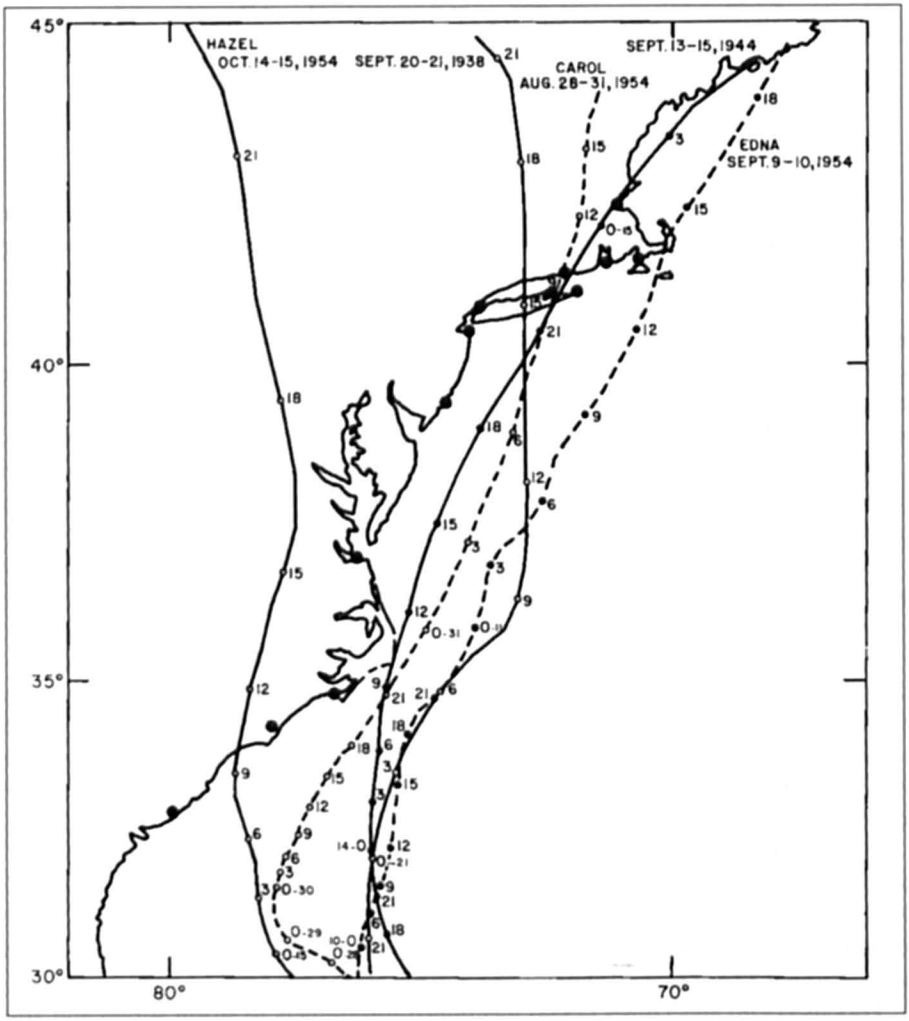


Fig. 6.1: Tracks of some of the hurricanes that affected the New England States. Solid circles show the locations of the tide gauges. Circles on the tracks represent the hours (GMT) and the small numbers denote the dates (REDFIELD and MILLER, 1957)

A forerunner is the gradual rise in sea level along the coast that precedes the arrival of the hurricane, and which may occur while the storm center is at a great distance from the coast regardless of whether or not it reaches the point of observation. The hurricane surge is the sudden and substantial rise in water level that accompanies the violent winds of the storm. Resurgences include a number of phenomena that occur after the passage of a storm center. They may be attributed in general to the free motion of water in returning to the normal level but are augmented in some cases by wind blowing in a changing direction.

CLINE (1920, 1926 and 1933) noticed forerunners in the Gulf of Mexico and called attention to their importance in the prediction of the storm arrival. The sea level began to rise (above the predicted tide) 1 or 2 d before the arrival of the storm. Elevations of several feet were noticed before the rapid rise due to the storm surge itself. Cline explained the forerunners as being due to transport of water by the swell that arrives in advance of the hurricanes.

Table 6.1: Relation of duration of surge to size and speed of storm (REDFIELD and MILLER, 1957)

| Storm | Time (h) half level Preceded maximum Level | Speed at Coast ($km \cdot h^{-1}$) | Diameter of 980-mb Isobar (km) | Time (h) Pressure < 980 mb |
|---|---|---|---|---|
| 1938 | 1.0–1.5 | 96 | 270 | 3.2 |
| 1944 | 2.1–2.2 | 67 | 241 | 4.2 |
| 1954 (Carol) | 1.1–1.3 | 74 | 183 | 2.9 |
| 1954 (Edna) | 2.0–2.3 | 63 | 261 | 4.8 |
| 1954 (Hazel) | 3.0–5.0 | 46 | 261 | 6.5 |

Observations showed that if the tide gauge was within 50 nautical miles (93 km) to the left (in the Northern Hemisphere) of the storm track, or 100 nautical miles (185 km) to its right, the rate of rise of water level increased to more than 1 ft $h^{-1}$ beginning 3 or 4 h before the passage of the center. (This rapid rise is the surge whereas the slow gradual rise before this is the forerunner).

Examples of the forerunners can be found in the storm surge records at Atlantic City and Sandy Hook. At Atlantic City during Hurricane Carol of September 1954, the water level began to increase even before the storm passed Cape Hatteras (260 nautical miles or 481 km to the south). This rise continued for 8–12 h at which time the storm center passed over Atlantic City and the wind shifted. Then the water level dropped abruptly and this was followed by resurgences. The hurricane of September 14–15, 1944, traveled close to the coast and the forerunner was not significant. REDFIELD and MILLER (1957) discounted the fall in barometric pressure as the cause of the forerunners. They cited wind as the main agent responsible. The fact that the water levels decreased abruptly when the wind shifted is another piece of evidence, according to them.

After the storm surge itself, on the outer coast, surges up to 8–9 ft (2.4–2.7 m) occurred. At Long Island, and along the coasts of Rhode Island and Massachusetts, water level deviation up to 18-ft (5.5 m) occurred (but part of this were wind-generated waves). However in Buzzards Bay, Narragansett Bay, Long Island Sound, etc., surges up to 15-ft (4.6 m) have occurred many times. These authors introduced the term „half-level time" to define the time required to develop from one half the maximum to the maximum water level achieved. For hurricanes crossing the coast of New England this time varied from 1.25 to more than 2 h (Table 6.1.). This half-level time that defines the sharpness of the surge varies in proportion with the storm speed at the time the storm crosses the coast, as can be seen from Table 6.1. This Table also lists the size of the storm as typified by the diameter of the 980-mb isobar and the time during which the pressure was less than 980 mb. This time is roughly twice the half-level time.

The storm surge amplitude (meters) along the ordinate versus distance (nautical miles) from the storm center along the abscissa is given in Fig. 6.2. It can be seen that maximum water levels occurred some 50–70 nautical miles (93–130 km) to the right of the storm center. However, REDFIELD and MILLER (1957) pointed out that the highest water levels following Hurricane Hazel of 1954 occurred close to the storm center, and 40 nautical miles (74 km) to

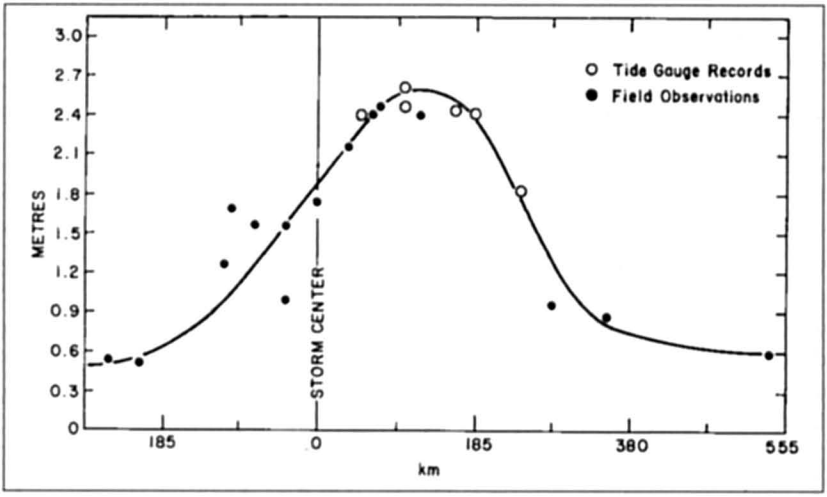


Fig. 6.2: Storm surge amplitude (ordinate) versus distance from storm center (abscissa) (REDFIELD and MILLER, 1957)

the right they were small. HUBERT and CLARK (1955) mentioned that for the coast of the Gulf of Mexico the maximum water levels occurred close to the storm center slightly to its right.

The time of occurrence of the maximum surges with reference to the passage of the storm center differed from one storm to another and from one location to another. If the storm center passed close to a tide gauge, usually, maximum surges occurred within 1 h before or after the storm passage. The differences in the time of occurrence of the maximum surges can be explained by differences in the exposure of the gauges and also by the fact that the wind and pressure centers of a hurricane need not coincide (MYERS, 1954).

The maximum surges on the southern New England Coast and their times of occurrence following the hurricane of September 21, 1938, are shown in Fig. 6.3 and 6.4 respectively. Similar information for Hurricane Carol of August 31, 1954, is given in Fig. 6.5 and 6.6. Large surges on the coast of southern New England might to some extent be accounted for by the presence of a wide and shallow shelf. This topographic effect is most noticeable between Montauk Point (at the eastern tip of Long Island) and Martha's Vineyard. However, greatest surges and most property damage occurred on the Narragansett Bay coast. Extreme surges

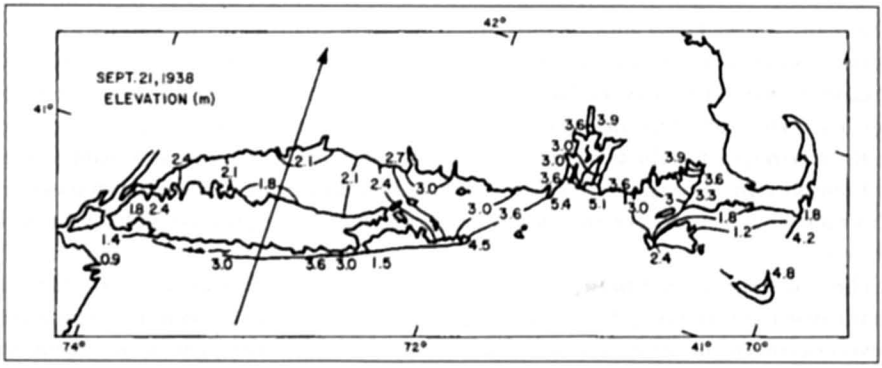


Fig. 6.3: Storm surge heights (meters) on the coast of the southern New England States. The arrow shows the track of the storm of September 21, 1938, that caused this surge (REDFIELD and MILLER, 1957)

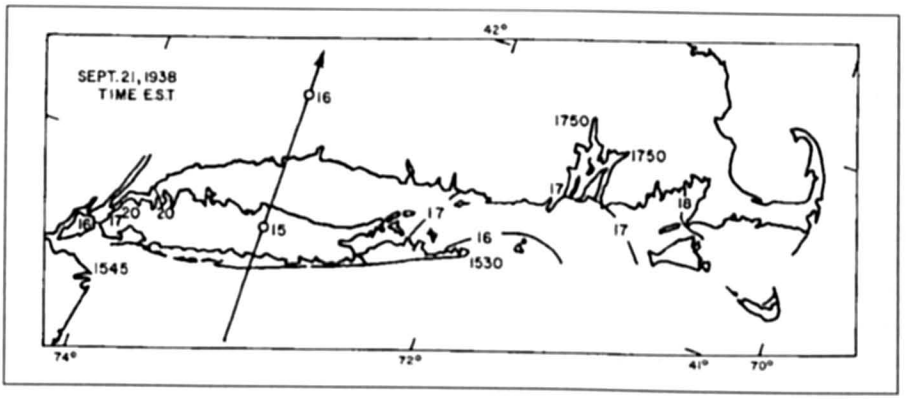


Fig. 6.4: Times of occurrence of maximum surge along the coast of the southern New England States on September 21, 1938 (REDFIELD and MILLER, 1957)

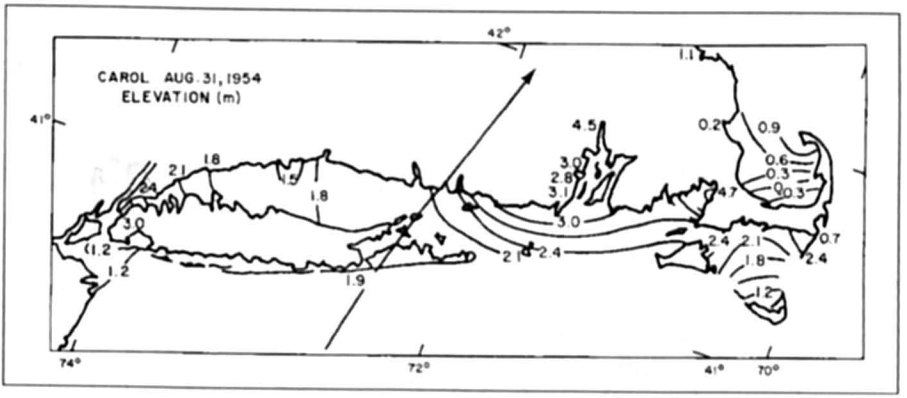


Fig. 6.5: Storm surge heights (meters) along the coast of the southern New England States following Hurricane Carol of August 31, 1954 (REDFIELD and MILLER, 1957)

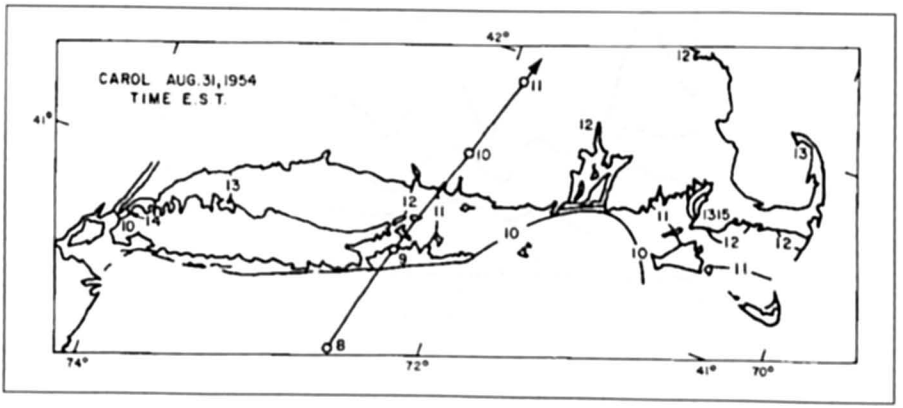


Fig. 6.6: Times of occurrence of maximum surge along the coast of the southern New England States following Hurricane Carol of August 31, 1954. The arrow shows the hurricane track (REDFIELD and MILLER, 1957)

up to 13 ft (4 m) were noted at Providence, Rhode Island, in water of depth less than 20 ft (6.1 m).

According to REDFIELD and MILLER (1957), Providence is among the most frequently flooded (due to surges) in the United States. Surges up to 11 ft (3.4 m) were observed in 1944 (but little damage occurred because the maximum surge coincided with low tide); 15 ft (4.6 m) surges were recorded on August 31, 1954, and there was evidence of 12 to 14 ft (3.7–4.3 m) surges in 1815. In Buzzards Bay, surges of 13 ft (4m) occurred in 1938 and 15 ft (4.6 m) surges were recorded following Hurricane Carol in 1954. A diary entry by Governor Bradford in 1635 (MORRISON, 1952) describes a 20 ft (6.1 m) surge on August 14–15 of that year. There is evidence of negative surges of 1–3 ft (0.3–0.9 m) in Cape Cod Bay and Nantucket Sound. Surges up to 4 ft (1.2 m) were noted at Boston and Portland. North of Cape Cod the amplitudes of surges become small and amount to about 1 ft at Eastport (Miane).

REDFIELD and MILLER (1957) paid particular attention to the resurgences, which are basically free oscillations of the water in trying to return to its normal level. Following Hurricane Carol of August 31, 1954, the damage at the Cape Cod area was a result of the resurgence. In Buzzards Bay, although the main surge had amplitudes of about 12 ft (3.7 m) along the western shore, resurgences with amplitudes up to 15 ft (4.6 m) occurred on the eastern shore. The resurgence following a 1938 hurricane in Buzzards Bay caused great damage and loss of life at Woodshole. In Long Island Sound, resurgences occurred following the hurri-

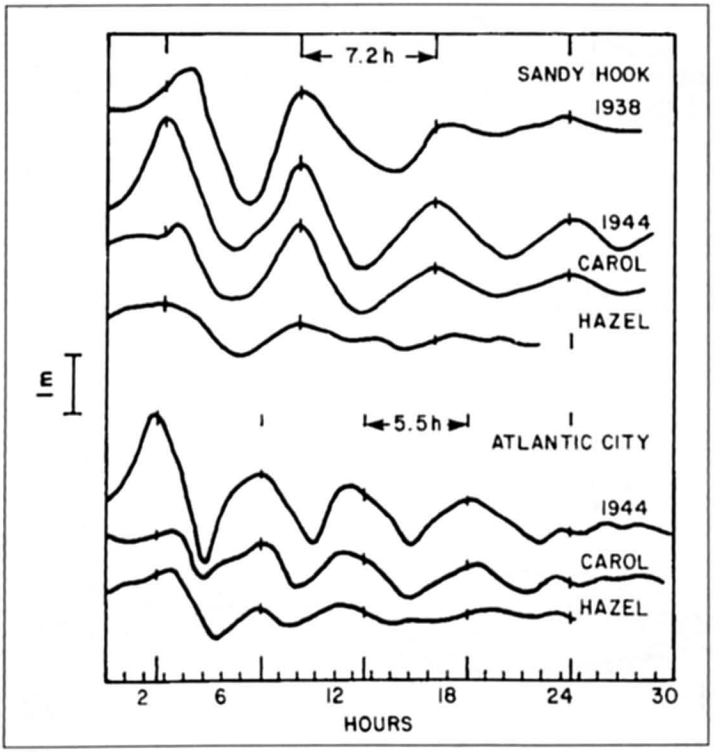


Fig. 6.7: Comparison of resurgences following the passage of several storms at Sandy Hook and Atlantic City. The times were adjusted (for each station) so that the time of occurrence of the first resurgence for the different storms coincide. Vertical ticks denote time separation of 7.2 h for Sandy Hook and 5.5 h for Atlantic City. Ordinate: water level (meters); abscissa: duration of surge (hours) (REDFIELD and MILLER, 1957)

canes of September 21, 1938, and August 31, 1954. Tide gauges at Atlantic City and Sandy Hook showed prominent resurgences (Fig. 6.7.). After the original surge reaches a maximum, the water level drops abruptly to low values and then increases again in a series of undulations with periods of several hours. These resurgences periods are about 5.5 h at Atlantic City and 7.2 h at Sandy Hook. The attenuation rate of the resurgences at Sandy Hook is about 0.07 $h^{-1}$. MUNK et al. (1956) explained these resurgences as due to edge waves.

Storm surges on the east Coast of the United States also occur as a result of extra-tropical cyclones. Some differences between storm surges due to tropical and extra-tropical storms on the east Coast of the United States are listed in Table 6.2.

Some models that were developed with the aim of hindcasting and eventually predicting storm surges will now be considered. The so-called bathystrophic storm surge (FREEMAN et al., 1957) was discussed earlier. PARARAS-CARAYANNIS (1975) used this approach to hind-

Table 6.2: Differences between hurricane-generated and extratropical storm generated surges

| Parameter | Tropical system | Extratropical system |
|---|---|---|
| Size of storm | Small | Large |
| Representation on weather charts | Some times difficult to position on weather charts using ordinary weather reports. The vigorous portion of the storm may lie between two observing stations | Easier |
| Requirement of specialized observations such as satellite, weather, reconnaissance, radar, aircraft | Needed | Usually not required. Standard weather reports usually adequate unless mesoscale systems are embedded |
| Amplitude of surges | Greater The Maximum surge generated in the United States was at Gulfport, MS, following Hurricane Camille in August 1969: 7.5 m | Smaller surges of amplitudes up to 5 m can occur infrequently |
| Duration of surge | Short (Several hours to 1/2 d) | Long (usually 2–5 d). Severe erosion of coastline can occur |
| Inland inundation | Large | Little |
| Length of coastline affected by the surge | Less (usually < 160 km) | Several hundred kilometers |
| Geometry of the storm | Compact and nearly symmetrical | Ill-defined and sprawling geometry |
| Speed of movement of the storm | Variable | Slow motion generally along a regular track |
| Pressure gradients and wind stress associated with the storm | Easy to model the driving forces could be represented analytically | Difficult to model the driving fields |

cast surges on the East Coast and Gulf of Mexico coast of the United States. The observed and computed surges at three locations are compared in Fig. 6.8. PARARAS-CARAYANNIS (1975) simulated surges due to the hurricanes listed in Table 6.3. Pertinent meteorological information is also listed in this table, which is used in the above calculations.

KAJIURA (1959) examined analytically, as well as empirically, hurricane-generated surges on continental shelves. Using dimensional analysis he showed that the surge is determined by the following two dimensionless ratios: V/c and $L_2/L_1$ where V is the speed of movement of the storm, c is the speed of long gravity waves on the shelf, $L_2$ is the scale of the storm and $L_1$ is the width of the shelf, the dynamic response of the water level is significantly influenced by the natural modes of oscillation on the shelf (the dynamic amplification for a one-dimensional case is between 1 and 2). The free oscillations again become important when one considers the transient aspects. Coriolis force becomes relevant if the scale of the disturbance is significant relative to c/f, where f is the Coriolis parameter. When the scale of the shelf is comparable with the scale of storm, the two-dimensional aspects of hurricanes must be considered.

Other important results from KUJIURA'S (1959) study are the following. If the storm moves perpendicular to the coastline from the sea, then the maximum surge always occurs a little later than the time of the nearest approach of the storm center to the water level station. For any other type of track, the maximum surge can occur either before or after the storm center approaches nearest to the observing station. When the storm moves inland from the sea, the maximum surge is found to the right of the track. The dynamic amplification of the surge is maximum when the track is parallel to the coast and the amplification depends on the duration of the storm as well as V/c.

Actual data of hurricane-generated surges along the Atlantic coast showed that significant surges (up to one third of the maximum surge) occur within 70 nautical miles (130 km) to the left and 110 nautical miles (204 km) to the right of storm track. The maximum surge usually occurs about 25 nautical miles (46 km) to the right of the track. Unless the storm center is very close to the station, usually the water levels are greater south of Sandy Hook than on the New England coast.

Table 6.3: Hurricane parameters in the bathystrophic storm surge study (PARARAS-CARAYANNIS, 1975)

| Hurricane | Central pressure (mb) | Peripheral pressure (mb) | Radius of maximum winds (km) | Speed of movement ($km \cdot h^{-1}$) | Maximum gradient wind speed ($km \cdot h^{-1}$) |
|---|---|---|---|---|---|
| Hurricane of Oct. 3–4, 1949 | 963.4 | 1014.2 | 27.8 | 20.4 | 141.6 |
| Carol of Aug. 30–31, 1954 | 971.6 | 1013.2 | 46.3 | 61.7 | 152.9 |
| Audrey of June 26–27, 1957 | 946.5 | 1005.8 | 35.2 | 24.1 | 152.9 |
| Carla of Sept. 7–12, 1961 | 936.0 | 1013.2 | 85.2 | 5.6 | 160.9 |
| Camille of Aug. 15–16, 1969 | 905.2 | 1013.2 | 25.9 | 24.1 | 201.2 |

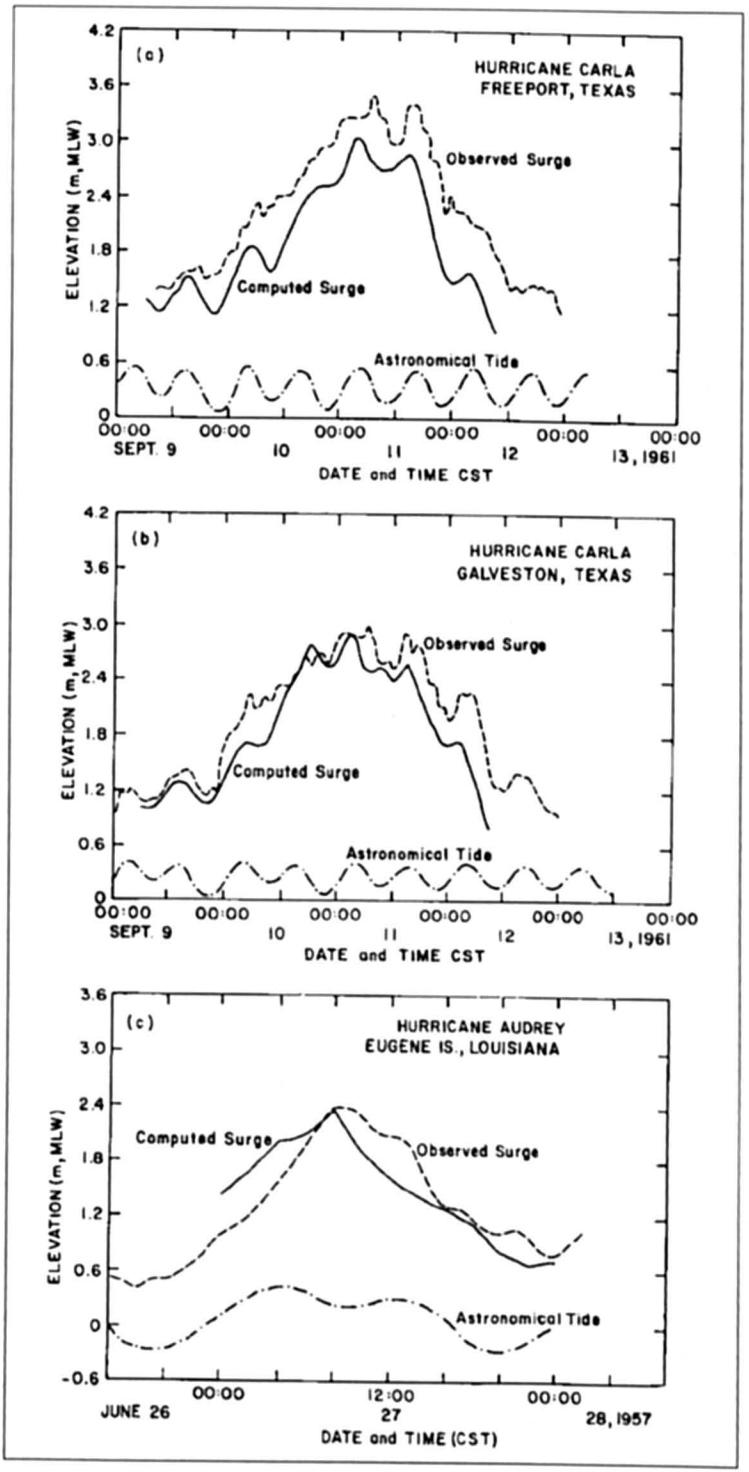


Fig. 6.8: Computed surge (using bathystrophic approach), observed surge, and tide due to (a) Hurricane Carla at Freeport, Texas, (b) Hurricane Carla at Galveston, Texas, and (c) Hurricane Audrey at Eugene Island, Louisiana (PARARAS-CARAYANNIS, 1975)

## SPLASH *Models*

SPLASH is an acronym for "special program to list amplitudes of surges from hurricanes." SPLASH I deals with landfalling hurricanes and SPLASH II takes care of situations in which the hurricanes need not go over land. These models were developed at the Techniques Development Laboratory of the U.S. National Weather Service (JELESNIANSKI 1972, 1974, 1976; JELESNIANSKI and BARRIENTOS 1975; BARRIENTOS and JELESNIANSKI 1976, 1978). This computer program is operationally used at the National Hurricane Center in Miami and is applied to the Atlantic coast and the Gulf of Mexico coast of the United States. The stretch of coast for which these models are used extends about 3000 mi (4827 km) from Brownsville, Texas, to Long Island, New York. Along this coastal stretch, reference stations (for use in hurricane landfall determination) are established with an approximate spacing of 100 mi (161 km).

SPLASH is a numerical storm surge model that involves a linearized version of the transport equations. The geometry of the model is idealized into a rectangle with variable depth. One side of the rectangle is the coast and the other three sides are open boundaries. At the coast the normal transport is zero and at the deepwater open boundary static height is prescribed (this height is zero in the absence of an atmospheric pressure gradient). On the two lateral open boundaries the normal derivative of transport is prescribed to be zero. Depth contours are analysed on overlapping 600 mi × 72 mi (965 km × 116 km) basins. The basins are centerd 50 mi apart.

In SPLASH I, which applies to landfalling hurricanes only, the following meteorological input is required: (1) pressure drop $\Delta p = p_\infty - p_0$ where $p_\infty$ is the ambient pressure outside the storm and $p_0$ is the central pressure of the hurricane, (2) the radius R of maximum winds, (3) the vector storm motion $U_s/\theta$ where $U_s$ is the storm speed and $\theta$ is the storm direction of motion, and (4) point of landfall. This program assumes that the conditions are steady state, i. e., the size, intensity, and speed of movement are constants.

SPLASH II deals with an unsteady storm. The storm track could have any orientation and the storms need no landfall. The input data consist of (among other things) a 24-h track segment, which is defined by latitude and longitude for five points on the track staggered 6 h apart for a 24-h period. These latitude and longitude data not only define the track but also the speed of movement of the storm. Other input data are the radius of maximum winds and pressure drop, which can vary with time.

One very important component in SPLASH is a normalized shoaling correction, which is used to correct the computed surge along the coast if the landfall point is shifted. Shoaling corrections were prepared for the Atlantic and the Gulf coasts by using landfall storms normal to the coast at 16-mi (25.8 km) intervals using a storm speed of 15 mi $\cdot$ h$^{-1}$ (24 km $\cdot$ h$^{-1}$)

The SPLASH models were verified generally against data from 43 hurricanes during five hurricane seasons. These cases, the dates of occurrence, location of the peak surge, and computed and observed peak surges are listed in Table 6.4. The varying location of the peak surge, depending on the nature of the bathymetry, is shown quantitatively in Fig. 6.9.

Whereas SPLASH I can deal with landfalling hurricanes only, SPLASH II can be applied to a general storm track. Especially the following three types of tracks are considered: (1) landfall storm with its track perpendicular to a straight-line coast, (2) an alongshore moving storm (i.e. constant abeam distance of the track from the coast), and (3) a recurving storm (non-landfall). Slow-moving storms are treated as a special case and a hypothetical storm with the following properties is used: (1) the storm traverses the continental shelf with the speed of less than 8 mi $\cdot$ h$^{-1}$ (12.9 km $\cdot$ h$^{-1}$), (2) the storm's closest approach to the coast occurs

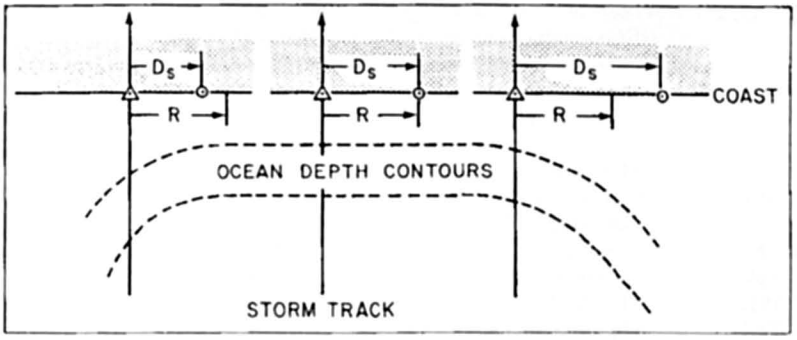


Fig. 6.9: Qualitative illustration showing the varying positions of peak surge on the coast as compared with two-dimensional bathymetry. ⊙, location of peak surge; △, landfall point; R, radius of maximum winds; Ds, distance to peak surge. (JELESNIANSKI, 1972)

near Miami where there is hardly any continental shelf, and (3) the storm's strength and size ($\Delta p$ = 100 mb, R = 15 mi · $h^{-1}$ [24 km · $h^{-1}$]) do not change along the track.

Calculations using SPLASH II gave the following results. The maximum surge is not highly sensitive to storm size for landfall storms. However, for non-landfall storms, the storm size is important because the surge is a function of distance from the coast relative to storm size. When the storm is on the shelf, if the component of the track on the coast is large, the length of the coastline affected by the surge could be very long. For a storm travelling perpendicular to the coast, the component of the track on the coast degenerates to a point, and surges occur only along a small length of the coastline.

One of the main drawbacks of SPLASH II (although it is an improvement over SPLASH I) is that it treats the coast as a straight line and cannot include the curvature of the coastline. To remove this restriction, JELESNIANSKI (1976) developed a sheared coordinate system. In this model, a mildly curving coastline (which does not include bays, estuaries, sounds, deltas, capes, spits, etc.) is sheared into a straight-line. A surface plane, beginning at the ocean shelf and containing the curved coast as one of the boundaries, is fitted with a curve, nonorthogonal grid. The plane with curved boundaries is then transformed via a sheared coordinate system onto an image rectangle. In this transformed system, one deals with a Cartesian, orthogonal, equally spaced grid in which the coast coincides with grid lines. JELESNIANSKI (1976) used such a model incorporating the linearized storm surge equations for a 3000 mi (4827 km) coastline beginning at the United States-Mexico border in the Gulf of Mexico to the eastern tip of Long Island in New York. The storm tracks could be curved and the intensity, the size of the storms, and its speed of movement could be variable.

The somewhat idealized SPLASH models are being replaced with a new generation of models referred to as SLOSH (sea, lake and overland surges from hurricanes). These models are being developed for the east and gulf coasts of the United States. Specifically, the following coastal stretches are being modelled: New Orleans Area, Lake Okeechobee, Tampa Bay, Mobile Bay, Galveston area, Charlotte Harbour (Florida), Florida Bay, Biscayne Bay, Florida Keys, Long Island Sound, Chesapeake Bay, Charleston Harbour (South Carolina), Narragansett Bay, Buzzards Bay, Delaware Bay, Palmico Sound, Massachusetts Bay, Corpus Christi (Texas), Lower Laguna Madre (Texas), Matagorda Bay (Texas), Lake Sabine (Texas), and Pensacola (Florida). Some testing of the SLOSH model during Hurricane Bob in July 1979 showed that the results are quite satisfactory.

Table 6.4: Comparison of observed maximum surges (m) in the United States with those computed from the nomograms using SPLASH (JELESNIANSKI, 1972)

| Date | Location of peak surge | Computed peak surge | Observed peak surge |
|---|---|---|---|
| Oct. 2, 1893 | Mobile, AL | 3.32 | 2.83 |
| Sept.27, 1894 | Charleston, NC | 1.59 | 1.62 |
| Sept. 8, 1900 | Galveston, TX | 4.60 | 4.45 |
| Aug. 14, 1901 | Mobile, AL | 2.07 | 2.26 |
| July 21, 1909 | Galveston, TX | 3.54 | 3.05 |
| Sept. 13, 1912 | Mobile, AL | 0.91 | 1.34 |
| Aug. 16, 1915 | High Island, TX | 3.60 | 4.24 |
| Sept. 29, 1915 | Grand Isle, LA | 3.41 | 2.74 |
| Oct. 18, 1916 | Pensacola, FL | 1.59 | 0.91 |
| Sept. 28, 1917 | Fort Barrancas, FL | 1.77 | 2.16 |
| Sept. 9, 1919 | Key West, FL | 2.23 | 1.98 |
| Oct. 25, 1921 | Punta Rassa, FL | 3.29 | 3.32 |
| Aug. 26, 1926 | Timbalier Island, LA | 3.02 | 2.99 |
| Sept. 18, 1926 | Miami Beach, FL | 3.57 | 3.17 |
| Sept. 20, 1926 | Pensacola, FL | 2.19 | 2.74 |
| Sept. 16, 1928 | West Palm Beach, FL | 2.74 | 2.96 |
| Sept. 28, 1929 | Key Largo, FL | 2.23 | 2.68 |
| Sept. 7, 1933 | Brownsville, TX | 3.02 | 3.96 |
| July 25, 1934 | Galveston, TX | 2.07 | 1.80 |
| Nov. 4, 1935 | Miami Beach, FL | 2.01 | 2.74 |
| July 31, 1936 | Panama City, FL | 1.71 | 1.83 |
| Aug. 7, 1940 | Colcasieu Pass, LA | 1.62 | 1.62 |
| Aug. 11, 1940 | Beaufort, SC | 2.44 | 2.44 |
| Sept. 23, 1941 | Sargent, TX | 2.35 | 2.59 |
| Oct. 7, 1941 | St. Marks, FL | 3.08 | 1.86 |
| Aug. 30, 1942 | Matagorda, TX | 2.90 | 4.27 |
| July 27, 1943 | Galveston, TX | 1.77 | 1.10 |
| Oct. 19, 1944 | Naples, FL | 3.26 | 3.23 |
| Oct. 20, 1944 | Charleston, FL | 1.22 | 1.22 |
| Aug. 27, 1945 | Matagorda, TX | 1.89 | 1.95 |
| Aug. 24, 1947 | Safine Pass, LA | 0.87 | 0.76 |
| Aug. 17, 1947 | Hillsboro Beach, FL | 1.95 | 2.90 |
| Sept. 19, 1947 | Biloxi, MS | 3.41 | 3.32 |
| Oct. 15, 1947 | Quarantine Station, GA | 2.13 | 1.77 |
| Sept. 4, 1948 | Biloxi, MS | 1.59 | 1.55 |
| Aug. 26, 1949 | New Jupiter In., FL | 1.65 | 1.25 |
| Oct. 4, 1949 | Freeport, TX | 3.17 | 2.74 |
| Aug. 30, 1950 | Pensacola, FL | 1.16 | 1.55 |
| Sept. 5, 1950 | St. Petersburg, FL | 2.10 | 1.92 |
| Oct. 15, 1954 | Southport, NC | 3.81 | 3.90 |
| Aug. 17, 1955 | Holden Beach, NC | 1.62 | 1.65 |
| Sept. 24, 1956 | Laguna Beach, FL | 1.43 | 2.16 |
| June 27, 1957 | Calcasieu Pass, LA | 4.82 | 3.81 |

Earlier we referred to the SLOSH models of N.O.A.A., U.S.A. More recent information on these can be found in JELESNIANSKI et al., (1992). One of the strongest Hurricanes to make a landfall on the East Coast of U.S.A. was Hurricane Hugo of September 11–25, 1989 causing a total damage in excess of 7 billion US dollars. The track is shown in Fig. 6.10.

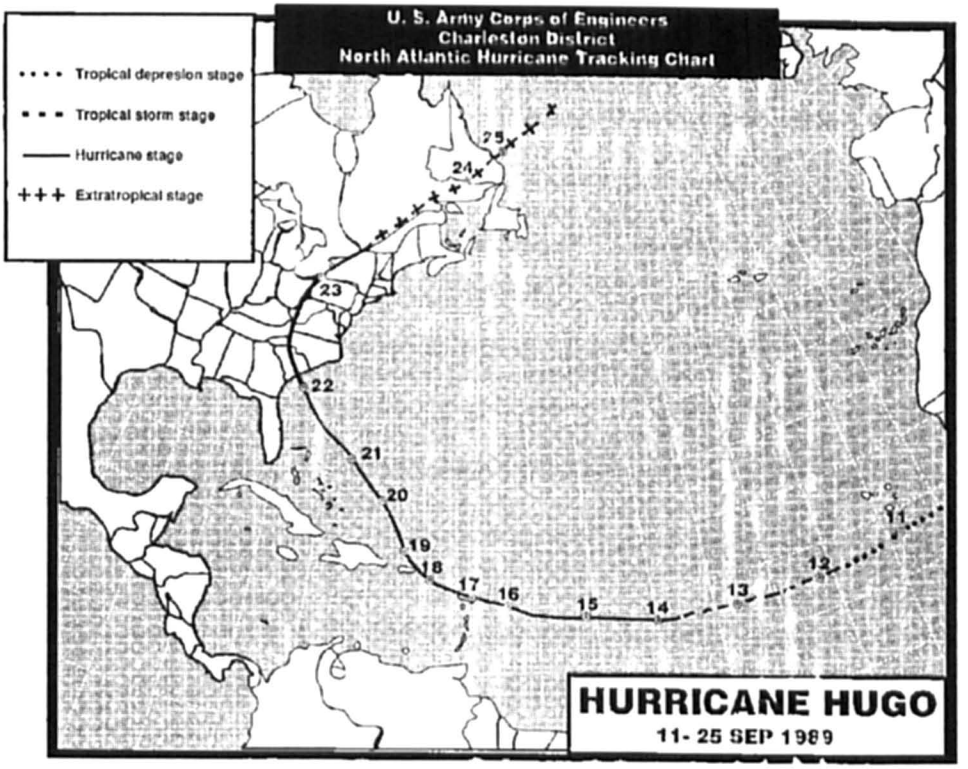
U. S. Army Corps of Engineers
Charleston District
North Atlantic Hurricane Tracking Chart
Tropical depresion stage
Tropical storm stage
Hurricane stage
Extratropical stage
25
24
23
22
21
20
19
18
17
16
15
14
13
12
11
HURRICANE HUGO
11- 25 SEP 1989

Fig. 6.10

### 6.1.2 Gulf of Mexico Coast (Excluding Florida Coast)

Up to this point, storm surges along the Atlantic Coast and the Gulf of Mexico have been studied. The gulf coast will now be considered in some detail. CLINE (1920) discussed the storm surges in the Gulf of Mexico due to hurricanes during the 20-yr period 1900–19. The pertinent information for these hurricanes and the storm surges generated are given in Table 6.5.

Following are some results of the study by CLINE (1920). During 1900–19, about 7225 people were killed and about $ 106 million in property damage occurred as a result of hurricanes in the Gulf of Mexico. The storm surges need not be symmetric about the hurricane track because the wind velocities to the left side of the track are much smaller (and less persistent) than on the right side. Peak surges occur a few kilometers to the right and at about the time of the passage of the center of the hurricane. The high water extends for only a short distance to the left of the point where the center of the storm moves inland. High water, however, occurs to the right of the center for a distance of 100–200 mi (161–322 km).

CONNER et al. (1957) gave a table of hurricanes and associated surges during the period 1893–1950. This table is reproduced here as Table 6.6. Although this table bears some resemblance to an earlier table (Table 6.4), certain entries are different. Also, in Table 6.8 only the observed surge is included (there is no calculated surge). In addition, the lowest pressure in the hurricane is also listed. Two empirical relations best fit these data. One is

$$h_{max} = 0.867(1005 - p_0)^{0.618} \tag{6.1}$$

where, $h_{max}$ is the surge height (feet) and $p_0$ is the lowest central pressure (millibars). The correlation coefficient between $h_{max}$ calculated and $p_0$ is 0.66. Another is

$$h_{max} = 0.154(1019 - p_0) \tag{6.2}$$

In this case the correlation coefficient is 0.68. The difference in the values for the observed surges for the same storms listed in Tables 6.4 and 6.6 are mainly due to different sources.

Hurricane Audrey of 1957 was the first hurricane that caused major storm surges since the organization of the National Hurricane Research Project by the U.S. Weather Bureau. This hurricane crossed the shore near the Texas–Louisiana border on the morning of June 27, 1957. HARRIS (1958a, 1958b) studied the storm surges associated with this hurricane and gave detailed diagrams of the surge height distribution along the coast.

MARINOS and WOODWARD (1968) used the bathystrophic theory to compute storm surges on the Texas-Louisiana coast. They made use of three storms to calibrate their model and checked it against several other storms. Using several synthetic hurricanes, 100-yr surge hydrographs were also constructed.

MIYAZAKI (1965) computed the storm surge in Gulf of Mexico due to Hurricane Carla of September 7–11, 1961, using a time-dependent linearized two-dimensional model. He first used a coarse grid of 48 nautical miles (89 km) for the entire Gulf and then developed a fine-grid model (grid spacing of 9.6 nautical miles or 17.8 km) for the northwestern part where the storm surge was the most significant. In the coarse-mesh model, bottom friction was ignored whereas quadratic bottom friction was used in the fine-mesh model.

Hurricane Carla is an exceptional hurricane in the sense that it moved very slowly (about 7 knots or 13 km · $h^{-1}$). The maximum wind speed was 85–95 knots (137–176 km · $h^{-1}$) and the radius of maximum winds was about 50 nautical miles (93 km). Another remarkable feature of this hurricane is in the generated surge. Along the Texas-Louisiana coast the storm surge occurred for almost a 6-d period (September 7–12, 1961). Maximum surge height of about 10ft. (3.1 m) was estimated on September 10 at Galveston. The calculated surge was compared with the observed surge by MIYAZAKI (1965) at the following stations: Port Isabel (Texas), Port Aransas (Texas), Freeport (Texas), Pier 21 and Pleasure Pier (both in the Galveston area), Fort Point (Texas), Sabine Pass (Texas), Bayou Rigaud (Louisiana), Humble Oil Platform A (Louisiana) and Pensacola (Florida).

Hurricane Betsy struck the southeastern Louisiana coast on September 9, 1965. It was the most destructive (economically) ever to hit the United States coast up to that time (GOUDEAU and CONNER, 1968). Winds reaching up to 125 mi · $h^{-1}$ (201 km · $h^{-1}$) caused a great storm surge resulting in extensive flooding in the Metropolitan area of New Orleans. Goudeau and Conner 1968 also gave detailed diagrams for the storm surge height distribution and flooded areas on the Mississippi River and also in Lake Pontchartrain.

PEARCE (1972) developed a two-dimensional, time-dependent numerical model for studying storm surges in the Gulf of Mexico. He used two different mesh sizes: 16 nautical miles (29.6 km) and 6 nautical miles (11.1 km). These were applied to the surge generated by Hurricane Camille of August 17–22, 1969. There was no significant difference in the results between the smaller grid and larger grid models. Inclusion of the nonlinear advective terms made only a difference of 2 % in the surge heights. The model results were insensitive to bottom friction coefficients between 0.005 and 0.02. PEARCE (1972) also used a one-dimensional model as well as an analytical model. The distribution of surge heights computed for August 17 at 23:40 is shown in Fig. 6.11. Although in this subsection the Gulf of Mexico was considered as a whole, later subsections will consider parts of this system such as Galveston Bay, Mobile Bay, etc. in detail.

Howard Elgison made the following comments in ANNON (1992) on page 60. Hopefully there will never be another storm with the destructive power of Hurricane Andrew. Certainly, there will never be another hurricane named Andrew. Like the great athletes whose numbers have been retired, the great hurricanes, those that were particularly severe or destructive, have their names retired.

Currently, a total of 33 names are enshrined in the Hurricane Hall of Infamy. They are listed below in chronological order:

1954 Carol-Edna – Hazel
1955 Connie – Diane – Ione – Janet
1957 Audrey
1959 Gracie
1960 Donna
1961 Carla
1963 Flora
1964 Cleo – Dora – Hilda
1965 Betsy
1967 Beulah
1969 Camille
1970 Celia
1972 Agnes
1974 Carmen
1975 Eloise
1977 Anita
1979 David - Frederic
1980 Allen
1983 Alicia
1985 Elena – Gloria
1988 Gilbert – Joan
1989 Hugo
1991 Bob

Table 6.5: Hurricanes and storm surges in the Gulf of Mexico during 1900-19.

| Date(s) of hurricane | Hurricane | Storm surge |
|---|---|---|
| Sept. 1–12, 1900 | Hurricane reached Florida Straits on Sept. 5 and moved in a northwesterly direction across the gulf a distance of about 1600 km. Maximum winds observed were 193 km-h$^{-1}$. | Surge of 4.6 m at Galveston on Sept. 8; over 6000 people killed; $ 30 million damage (in 1920 currency) |
| July 5–10, 1901 | Storm of small extent and moderate intensity moved through the Yucatan channel into the Gulf of Mexico on July 7 and reached the Texas coast west of Galveston on July 10. | Surge of 1.4 m at Galveston; no damage |
| Aug. 9–15, 1901 | Hurricane first appeared to the north of Cuba on Aug. 9. It moved across southern Florida and into the Gulf of Mexico on the morning of Aug. 11, continued its course westward to 90° W when, during Aug. 14, it recurved and on the morning of Aug. 15 passed northeastward between New Orleans and Port Eads. Hurricane had small diameter but great intensity and its track was unusual. | Surge of 1.3 m at Port Eads, 1.7 m at New Orleans, and 2.5 m at Mobile; 10 persons killed; $ 1 million damage |
| Sept. 23–27, 1906 | Disturbance passed through the Yucatan channel on the morning of Sept. 24, travelled roughly in a straight line, and moved in on the Mississippi coast on the morning of Sept. 27. Hurricane was of large extent and of unusual intensity. | Surge of 1.2 m at Port Eads, 3.3 m at Pensacola. At Pensacola 32 people killed and near Mobile 31 killed (it is not known whether some of these deaths were due to hurricane and not the surge) |
| July 18–21, 1909 | Hurricane moved from the Caribbean Sea though the Yucatan Channel on July 18 and moved inland on the Texas coast with its centre near Velasco. | Surges (amplitude not known) occurred to the right of the storm center up to Galveston; 4 people killed |
| Sept. 12–21, 1909 | Storm of great extent and unusual intensity. Its effect was felt from east of Pensacola to the west of Galveston. Hurricane passed through the Yucatan channel during Sept. 17 and moved inland on the Louisiana coast on Sept. 20. | 353 people killed; $ 6.4 million damage |
| Oct. 13–18, 1910 | Disturbance moved into the Florida Straits on Oct. 14, moved towards the northwest during Oct. 15, southward during Oct. 16, and then eastward to the Florida Straits by the morning of Oct. 17 after which it moved northward over Florida on Oct. 18. | Negative surge of 2 m at Tampa |
| Aug. 13–17, 1915 | Storm moved across the western end of Cuba into the Gulf of Mexico during the morning of Aug. 14, travelled in a direct line, and passed inland on the Texas coast a short distance to the left of Galveston on the morning of Aug. 17. | $ 21 million damage |

| | | |
|---|---|---|
| Sept. 2–4, 1915 | Disturbance of considerable intensity crossed western Cuba, moved into the east Gulf, and recurving slowly, moved inland near the mouth of the Apalachicola River during early morning of Sept. 4. | Surge of at least 1.5 m at St. Petersburg |
| Sept. 22–30, 1915 | One of the most intense hurricanes in the history of the Gulf coast. Hurricane moved through the Yucatan channel during the night of Sept. 27 and, travelling northwestward, moved inland on the Louisiana coast to the left of and near Grand Isle during Sept. 29. Disturbance recurved slowly after crossing latitude 27° N and moved slowly northward. | 275 persons killed; $ 13 million damage. Surge heights up to 3.7 m on the coast of Lake Pontchartrain and 3–3.4 m on the Louisiana and Mississippi coasts. Inside Lake Pontchartrain, surges up to 4 m |
| July 1–6, 1916 | Disturbances first appeared in the Caribbean Sea on the afternoon of July 1, moved almost in a straight line through the Yucatan channel on July 3, and reached the Mississippi coast late in the afternoon of July 5. Storm covered considerable area and was of great intensity. | Damage at Mobile and along the Albama coast of $ 2.5 million; 12 people killed. Damage at Pensacola of $ 1 million. Maximum surge up to 3.5 m. |
| Aug. 12–19, 1916 | Disturbances passed through the Yucatan channel into the Gulf during the night of Aug. 16, advanced northwesterly in nearly a straight line, and moved inland on the Texas coast midway between Corpus Cristi and Brownsville during the afternoon of Aug. | 15 people killed; $ 1.8 million damage. Surges greater than 2.1m at Mobile. |
| Sept. 21–29, 1917 | Disturbance moved through the Yucatan channel into the Gulf during the night of Sept. 25 and advanced in a direction a little west of north towards the mouth of the Mississippi river. When within about 80 km of Port Eads the storm began recurving to the right and center, passing about 80 km to the right of Port Eads, and moved inland to the right of Pensacola. | Surge of 0.86 m at Pensacola. Surge of 1.77 m at Fort Barancas. Negative surge of 1.52 at Mobile. |
| Aug. 1–6, 1918 | Disturbances moved through the Yucatan channel into the Gulf of Mexico during the night of Aug. 4, travelled in a northwesterly direction, and passed inland over Lake Charles during Aug. 6. Hurricane was small but of marked intensity. | $ 5 million damage and 34 people killed due to the hurricane. Surge of 0.91 m at Morgan City. Surge of 0.86 at Johnson Bayou |
| Sept. 6–14, 1919 | Storm moved through the Yucatan channel into the Gulf towards the mouth of the Mississippi River. Then it moved more or less parallel to the coast. | 284 people killed; more than $ 20 million damage. Surges of up to 3.7 m occurred |

Table 6.6: Lowest central pressures and highest surges of Gulf of Mexico hurricanes (CONNOR et al., 1957)

| Date | Location of highest surge on open coast | Lowest Pressure (mb) | Peak Surge (m) |
|---|---|---|---|
| Oct. 2, 1983 | Mobile, AL | 956 | 2.56 |
| Sept. 8, 1900 | Galveston, TX | 936 | 4.42 |
| Aug. 14, 1901 | Mobile, AL | 973 | 2.26 |
| Sept. 27, 1906 | Fort Barrancas, FL | 965 | 3.29 |
| July, 21, 1909 | Galveston, TX | 959 | 3.05 |
| Sept. 20, 1909 | Mobile, AL | 980 | 2.38 |
| Sept. 13, 1912 | Mobile, AL | 993 | 1.34 |
| Aug. 16, 1915 | High Island, TX | 953 | 4.24 |
| Sept. 29, 1915 | Grand Isle, LA | 944 | 2.74 |
| July 5, 1916 | Fort Morgan, AL | 961 | 1.43 |
| Sept. 28, 1917 | Fort Barrancas, FL | 964 | 2.16 |
| Sept. 14, 1919 | Port Aransas, TX | 948 | 3.38 |
| Oct. 25, 1921 | St. Petersburg, FL | 958 | 2.38 |
| Aug. 25, 1926 | Timbalier Bay, LA | 959 | 3.05 |
| Sept. 20, 1926 | Pensacola, FL | 955 | 2.32 |
| Sept. 5, 1933 | Brownsville, TX | 949 | 3.96 |
| July 25, 1934 | Galveston, TX | 975 | 1.80 |
| July 31, 1936 | Panama City, FL | 964 | 1.83 |
| Aug. 7, 1940 | Calcasieu Pass, LA | 974 | 1.46 |
| Sept. 23, 1941 | Sargent, TX | 959 | 3.02 |
| Oct. 7, 1941 | St. Marks, FL | 981 | 2.44 |
| Aug. 30, 1942 | Matagorda, TX | 951 | 4.51 |
| July 27, 1943 | Galveston, TX | 975 | 1.22 |
| Aug. 27, 1945 | Matagorda, TX | 968 | 2.23 |
| Aug. 24, 1947 | Sabine Pass, LA | 992 | 1.10 |
| Sept. 19, 1947 | Biloxi, MS | 968 | 3.38 |
| Sept. 4, 1948 | Biloxi, MS | 987 | 1.71 |
| Oct. 4, 1949 | Freeport, TX | 978 | 3.17 |
| Aug. 30, 1950 | Pensacola, FL | 979 | 1.68 |
| Sept. 5, 1950 | Cedar Key, FL | 958 | 1.55 |

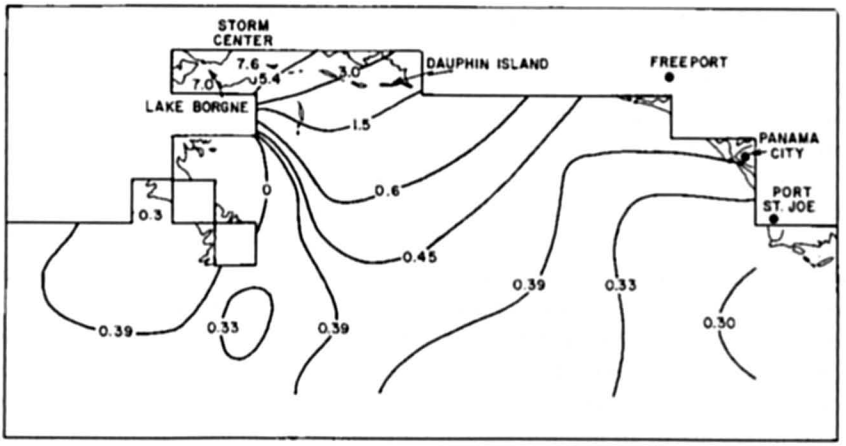


Fig. 6.11: Distribution of the water levels (storm surge with a 0.25 m tide superimposed) along parts of the coasts of Louisiana, Mississippi, and Alabama due to Hurricane Camille of 1969 (PEARCE, 1972)

There are many ways to measure the destructive power of hurricanes. The method chosen by the National Hurricane Center (NHC) is to calculate the total dollar value of property losses in the United States and adjust for inflation. Using this method, the top six hurricanes of all time are listed below. The damage Figs. are given in 1990 dollars. Needless to say, Hurricane Andrew sits atop the list with monetary damages greater than the combined total of the next three most costly storms. Table 6.7 lists the damage from some intense Hurricanes that affected the U.S.A.

Table 6.7: Damage in Billions of U.S. Dollars (at 1990 prices) by the Topio Hurricanes affecting the U.S.A. (ANON, 1993)

| Rank | Hurricane | Year | Damage in Billions of US Dollars at 1990 price levels |
|---|---|---|---|
| 1 | Andrew | 1992 | 30.0 |
| 2 | Hugo | 1989 | 7.0 |
| 3 | Frederic | 1979 | 2.3 |
| 4 | Agnes | 1972 | 2.1 |
| 5 | Alicia | 1983 | 2.0 |
| 6 | Iniki | 1992 | 1.8 |
| 7 | Juan | 1985 | 1.5 |
| 8 | Camille | 1969 | 1.427 |
| 9 | Betsy | 1965 | 1.425 |
| 10 | Elena | 1985 | 1.25 |

Even though only 53 people died in the wake of Hurricane Andrew, it is the single most natural disaster in U.S. history in terms of damage up to that time.

### 6.1.3. Storm Surges along the Coast of Florida

In this subsection, storm surges along the Gulf of Mexico coast and the Atlantic coast of Florida will be considered. Storm surges in Lake Okeechobee will be considered in the next subsection. DAMSGAARD and DINSMORE (1975) used a two-dimensional numerical model to study storm surges in Biscayne Bay, Florida. Their model allows for overtopping of low-lying barrier islands as well as inundation of flood plains. They tested their model against the storm surge generated by Hurricane Betsy of September 8, 1965.

VERMA and DEAN (1969) also used a two-dimensional model to study storm surges in Biscayne Bay. Their model allows for the inclusion of rainfall. ROSS and JERKINS (1977) used two different models to study storm surges in Tampa Bay, Florida. The first model (referred to as USF) was developed at the University of South Florida and is based on the explicit model by REID and BODINE (1968). The second model is based on the Rand model (LEENDERTSE, 1967) and makes use of an implicit-explicit scheme. Based on calculations for Tampa Bay, these authors concluded that the USF model provides a more accurate simulation than the Rand model.

By far the most comprehensive study of storm surges on the Florida coast (which this author could find) is one by BRUUN et al. (1962), in which they studied the storm surges in relation to coastal topography. Forty hurricanes during the period 1900–60 that caused significant storm surges along Florida coast are listed in Table 6.8.

Table 6.8: Major Hurricanes affecting Florida, 1903–65. The last four entries are taken from TETRA TECH INC. (1978) coastal flooding storm surge model, Part I. Methodology prepared by Tetra Tech Inc. for U.S. Dep. Of Insurance Administration, Washington, DC, May 1978 (BRUUN et al., 1962)

| Index No. | Date of occurrence | Coastal area affected |
|---|---|---|
| 1 | Sept. 10–16, 1903 | Fort Lauderdale and Tampa Bay |
| 2 | Oct. 10–23, 1904 | West Palm Beach |
| 3 | Oct. 11–20, 1906 | Florida Keys and Miami |
| 4 | Oct. 6–15, 1909 | Florida Keys and Miami |
| 5 | Oct. 11–13, 1910 | Key West to Tampa Bay and Jacksonville |
| 6 | Sept. 2–14, 1919 | Florida Keys |
| 7 | Sept. 27–Oct. 1, 1920 | Cedar Keys and St. Augustine |
| 8 | Oct. 21–23, 1921 | Tampa Bay and Daytona Beach |
| 9 | July 22–Aug. 2, 1926 | Entire east coast |
| 10 | Sept. 6–22, 1926 | Miami and Everglades to Tampa Bay |
| 11 | Aug. 7–10, 1928 | Fort Pierce and Cedar Key |
| 12 | Sept. 6–20, 1928 | West Palm Beach to Jacksonville |
| 13 | Sept. 22–Oct. 4, 1929 | Florida Keys to Tampa Bay |
| 14 | Aug. 31–Sept. 7, 1933 | West Palm Beach to Cedar Key |
| 15 | Aug. 31–Sept. 8, 1935 | Florida Keys to Cedar Key |
| 16 | Oct. 30–Nov. 8, 1935 | West Palm Beach to Miami and Key West to Fort Myers |
| 17 | July 27–Aug. 1, 1936 | Miami and Everglades to Tampa Bay |
| 18 | Oct. 4–12, 1941 | Miami to Florida Keys and Everglades to Cedar Key |
| 19 | Oct. 13–21, 1944 | Key West to Tampa Bay and Jacksonville |
| 20 | Sept. 12–19, 1945 | Florida Keys to Miami and northeast coast |
| 21 | Oct. 7–9, 1946 | Fort Myers to Cedar Key and Jacksonville |
| 22 | Sept. 11–19, 1947 | Fort Lauderdale and Fort Myers |
| 23 | Oct. 9–15, 1947 | Key West to Miami |
| 24 | Sept. 19–25, 1948 | Key West to Fort Myers and Fort Pierce |
| 25 | Oct. 4–8, 1948 | Florida Keys to Fort Lauderdale |
| 26 | Aug. 24–29, 1949 | West Palm Beach and Cedar Key |
| 27 | Sept. 1–7, 1950 | Key West to Cedar Key |
| 28 | Oct. 15–19, 1950 | Entire east coast |
| 29 | Sept. 30–Oct. 7, 1951 | Fort Myers and Fort Pierce |
| 30 | Oct. 8–10, 1953 | Fort Myers and Fort Pierce |
| | | *Florida Panhandle* |
| 31 | Sept. 10–30, 1906 | Pensacola |
| 32 | Aug. 9–14, 1911 | Key West to Pensacola |
| 33 | Sept. 11–23, 1912 | Tampa Bay to Pensacola |
| 34 | Sept. 4, 1915 | Key West to Apalachicola |
| 35 | July 5, 1916 | Pensacola |
| 36 | Oct. 12–21, 1916 | Pensacola |
| 37 | Sept. 21–29, 1917 | Pensacola |
| 38 | Sept. 13–20, 1924 | Panama City of Apalachicola |
| 39 | Sept. 24–26, 1953 | Pensacola to Panama City |
| 40 | Sept. 9–12, 1960 (Donna) | Florida Keys and South Gulf Coast |
| 41 | Aug. 26–29, 1964 (Cleo) | Southeast Florida |
| 42 | Sept. 7–11, 1964 (Dora) | Northeast Florida |
| 43 | Oct. 8–16, 1964 (Isabell) | Southern Florida |
| 44 | Sept. 6–9, 1965 (Betsy) | Southern tip of Florida |

### 6.1.4 Lake Okeechobee

In an earlier section a storm surge study by REID et al. (1977a, 1977b) was considered, which treated the extensive vegetation areas of Lake Okeechobee as a canopy. MYERS (1954) studied in detail the data from the hurricanes that were pertinent for levee design for this lake. Here, some studies on storm surges in this lake will be considered. KIVISILD (1954) made an extensive study of storm surges in shallow bodies of water and applied this to Lake Okeechobee storm surges.

During the period 1886–1950, the average number of hurricanes reaching Florida was 1.28 per year. The probability that the Okeechobee area would be subjected to winds greater that 75 mi · $h^{-1}$ (121 km · $h^{-1}$) in any given year is 1 in 7. Several tide gauges were located during the Lake Okeechobee project that was organized during the early 1950s. The north-south extent (maximum) of the lake is 30 mi (48 km), the east-west extent (maximum) is 25 mi (40 km), and the total area is 730 $mi^2$ (1891 $km^2$). Extensive marsh and vegetation covers the western portion of the lake. The south shore of the lake from St. Lucie Canal to Fisheating Creek is enclosed by levees constructed to an average crown height of 32.5 ft (9.8 m) above mean sea level. On the north shore a levee of the same height extends from 2 mi (3.2 km) southeast of Taylor Creek to Kissimmee River, and this levee protects the town of Okeechobee. The northwest portion of the lake, bordering low, saw grass marshes, and the northeast shore, bordering comparatively high ground, are unprotected. Ritta, Kreamer, and Torry islands at the southern end of the lake are partially protected by levees but these are insufficient against storm surges such as the hurricane of August 26–27, 1949.

KIVISILD (1954) used simple analytical formulae to calculate the surges in Lake Okeechobee. However, for better resolution of the geometry of the lake, he divided it into triangular elements. The pertinent information of the five hurricanes studied by KIVISILD (1954) and the related surges is summarised in Table 6.9.

LANGHAAR (1951) calculated the storm surges in Lake Okeechobee using simple analytical formulae. These values agreed well with observed surges, which ranged from 3.5 to 10.2 ft (1.1–3. 1 m). In this calculation, Langhaar considered the surge at the leeward end of the lake as a superposition of the surge due to seiches and a statical surge that the wind would maintain if it persisted indefinitely. The surge due to seiche is referred to as the "dynamical surge" and the total surge is the sum of the dynamical and statical surges. FARRER (1958) also used simple analytical formulae to compute storm surges in Lake Okeechobee for the hurricane of August 26, 1949. The water level distribution in the lake at three different times is shown in Fig. 6.12. The shaded area represents the marsh.

DANARD and MURTHY (1994) re-examined the work of REID and WHITAKER (1976) on the effect of vegetation in Lake Okeechobee on the storm surges.

Their assumptions on the equality of various drag coefficients are replaced by more realistic calculations. A new method for calculating wind stress on water is presented for the case when the vegetation extends above the water surface.

For the case of vanishingly small water-depth, it is shown that the horizontal stress is approximately constant in the vertical. This results in a diagnostic relationship for the water current as a function of the wind stress and bottom roughness.

A new expression for the vertically averaged frictional force per unit mass is derived on the assumption that the friction velocity varies linearly with height. The vertical rate of change of friction velocity depends on the mean water current, the wind stress, the bottom roughness, and the water depth.

For coastal defenses against storm surges, traditionally concrete sea walls have been in

Table 6.9. Five hurricanes and storm surges in Lake Okeechobee studied by KIVISILD (1954)

| Date(s) of Hurricane | Meteorological information | Storm surge information |
|---|---|---|
| Sept. 15–16, 1945 | Storm first noted east of the Leeward Islands on Sept. 11; it passed north of Puerto Rico on Sept. 13 and near Turks Island on the night of Sept. 13–14. It began a slow curvature over the great Bahamas Banks during the night of Sept. 14–15 and struck Florida with its center passing over the northern end of Key Largo. Highest measured wind velocity was 222 $km \cdot h^{-1}$ at Carysfort Reef, at the southern tip of Florida. Path of the hurricane-intensity winds was only 32–48 km wide, so that only the southwestern shores of Lake Okeechobee received winds of a velocity greater that 121 $km \cdot h^{-1}$. Storm was, in general, of moderate intensity. | Maximum surge recorded was about 1.8 m in range |
| Sept. 16–18, 1947 | Hurricane center developed on Sept. 5 in the vicinity of Daker (French West Africa). It moved about 27 $km \cdot h^{-1}$ on a west-northwest course to the Bahamas where on Sept. 15 it became almost stationary for about 24 h. Center reached the Florida coast at Fort Lauderdale on Sept. 17. Highest recorded wind velocity in Florida was 250 $km \cdot h^{-1}$ at Hillsboro Light near Pompano. Center moved westward across the state at about 16 $km \cdot h^{-1}$ and entered the Gulf of Mexico just north of Naples. Hurricane force winds were experienced along about 386 km of the Florida east coast, while winds of 160 $km \cdot h^{-1}$ were recorded in a 113-km stretch between Miami and Palm Beach. Hurricane was one of the great storms. Lowest barometric pressure recorded in the Lake Okeechobee area was about 985 mb at Moore Haven. | Maximum positive surge of about 2.13 m and a maximum negative surge of 1.22 m |
| Sept. 21–22, 1948 | Hurricane center developed on Sept. 18 between Jamaica and Grand Cayman Islands and moved slowly in a northerly direction passing over Cuba on Sept. 20 with winds greater than 160 $km \cdot h^{-1}$. When the storm center passed over Florida on Sept. 21–22 there appeared to have been several centers, with lulls reported from 64 to 129 km apart normal to the path of the storm. Speed of movement of the storm was 13-16 $km \cdot h^{-1}$. Strongest wind recorded was in gusts of 196 $km \cdot h^{-1}$ at Boca airport near Key West. By the time the Lake Okeechobee region was reached, wind velocities diminished to gusts of about 145 $km \cdot h^{-1}$. Lowest barometric pressure recorded in the Lake Okeechobee area was 962.8 mb. | Calculated values much bigger because the bottom friction due to the marsh grass was not taken into account |
| Aug. 26–27, 1949 | Storm was noticed on Aug. 23 in its formative stage, 201 km northeast of Leeward Islands. Center was well organized by the time it passed North Nassau on Aug. 26 and it intensified as it approached the Florida coast. Strongest winds occurred some distance to the right of the center near Jupiter, FL, where the anemometer failed after reaching an extreme of 246 $km \cdot h^{-1}$. Center passed the northern part of Lake Okeechobee during the early part of the evening of Aug. 26 with wind velocities ranging from 160 to 203 $km \cdot h^{-1}$. In the Lake Okeechobee section it was the worst hurricane felt since the great disastrous hurricane of September 1928. | Storm surges with ranges up to 4.27 m were recorded |
| Oct. 17–18, 1950 | Storm formed over the northwestern Caribbean Sea on Oct. 15 and moved northeastward and then northward across Cuba as a small hurricane. Center of the hurricane, about 8 km in diameter passed directly over Miami on the midnight of Oct.17–18. Highest recorded wind speed was 201 $km \cdot h^{-1}$. Center crossed northward over Lake Okeechobee during the morning of Oct. 18 with wind gust up to 153 $km \cdot h^{-1}$. In general, the diameter of this storm was smaller than that of most hurricanes, and sustained wind velocities were barely above the minimum hurricane | Surges with a maximum range of 2.74 m were recorded |

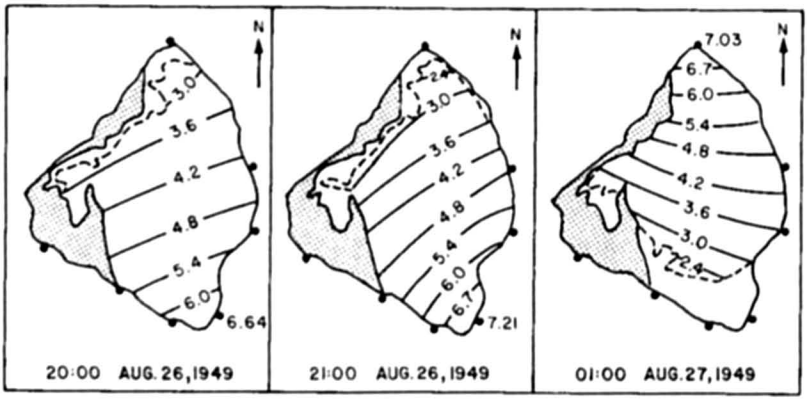


Fig. 6.12: Storm surge height (meters) distribution at three different times in Lake Okeechobee, Florida, due to the hurricane of August 26–27, 1949. (FARRER, 1958)

use. Even such prohibitively expensive structures might not be able to withstand the full force of impact from the incoming surge. Indeed during the 29 April 1991 storm surge in Bangladesh, two-foot thick concrete walls were taken out by the surge.

Earlier it was noticed (REID and WHITAKER, 1976) that surges were of smaller amplitude in those parts of Lake Okeechobee in Florida, wherever there was tall reed grass extending above the water surface. Thus there is observational evidence that a vegetation canopy can reduce storm surges significantly. However, it should be noted that this type of moderation by vegetation would occur more for the locally generated surge by a local wind field, than for that part of the surge that is generated outside and propagates into the region under discussion. This is because for a locally generated surge, the wind speed and therefore wind stress on the water surface are reduced by vegetation protruding above the water. Generally, the locally generated surge accounts for 50 to 80 % of the total surge; hence possible reduction of storm surges by vegetation canopies id of great practical interest.

The case where the water completely covers the canopy is shown in Fig. 6.13. D is the undisturbed total depth of the water and b is the height of the canopy. The velocity of the water above the canopy ($b \leq z \leq D$) is $u_1$, $\tau_a$ is the stress (force per unit area) that the atmosphere exerts on the water surface, $\tau_c$ is the stress the upper layer exerts on the lower, and $\tau_b$ is the stress lower layer exerts on the bottom.

Ignoring atmospheric pressure gradients, the linearized, vertically integrated equation of motion for the lower (canopy) layer is

$$\rho \frac{\partial \mathbf{U}_1}{\partial t} + \rho g b \nabla h = \hat{\mathbf{o}}_c - \hat{\mathbf{o}}_b - \mathbf{F}_c - \rho f \, \mathbf{k} \times \mathbf{U}_1 \qquad (6.3)$$

Where

$$\mathbf{U}_1 = b\mathbf{u}_1$$

h is the perturbation height of the free surface and $\mathbf{F}_c$ is the resistance (force per unit horizontal area) due to the canopy elements. Since the fluid is hydrostatic and homogeneous, the horizontal pressure gradient force is independent of z and is proportional to the gradient of the perturbation height of the free surface even in the lower layer. Let N be the number of

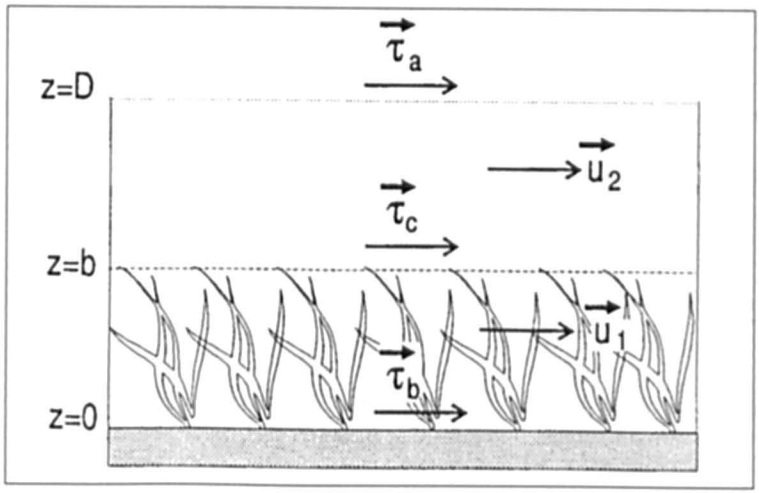


Fig. 6.13: Schematic diagram of stresses and water velocities in case where water completely covers the canopy (DANARD and MURTY, 1994)

canopy elements per unit horizontal area of width w. Then the vertical area obstructing the flow is bw for each canopy element, so the total obstructing area (per unit horizontal area) is Nbw. Thus

$$\mathbf{F}_c = \rho C_d \, Nbw |\mathbf{u}_1| \mathbf{u}_1 \tag{6.4}$$

where, $C_d$ is the drag coefficient for the vertical surface of the canopy elements. For rigid canopy elements presenting a flat surface perpendicular to the water flow, the velocity should be zero or nearly so immediately behind the canopy elements. The dynamic pressure force per unit horizontal area opposing $\mathbf{u}_1$ is

$$F_c = \frac{1}{2} \rho u_1^2 Nbw \tag{6.5}$$

Equating (6.4) and (6.5) gives

$$C_d = 1/2 \tag{6.6}$$

This is of course an upper limit. In general, $C_d$ will be smaller.
Reid and Whitaker write $\tau_c$ as

$$\hat{o}_c = \rho f_1 |\mathbf{U}_2 - \mathbf{u}_1| (\mathbf{u}_2 - \mathbf{u}_1) \tag{6.7}$$

where, $f_1$ is a non-dimensional coefficient. An alternate expression to (6.7) may be derived using reasoning similar to that of CRESSMAN (1960). Let $\epsilon$ ($\perp$ b) be the top part of canopy that $u_2$ senses. The vertical area of the canopy obstructing $\mathbf{u}_2$ is Nw$\epsilon$ per unit horizontal area. Assuming zero velocity immediately behind the canopy elements, the dynamic pressure force opposing $\mathbf{u}_2$ is Nw$\epsilon$ < 1/2 $\rho u_2^2$ Let k (< 1) be an efficiency factor representing the efficiency of the top of the canopy in blocking $\mathbf{u}_2$. Then

$$\hat{\mathbf{o}}_c = kNw\epsilon \cdot \frac{1}{2}\rho|\mathbf{u}_2|\mathbf{u}_2 \tag{6.8}$$

We can write (6.8) as

$$\hat{\mathbf{o}}_c = \rho C|\mathbf{u}_2|\mathbf{u}_2 \tag{6.9}$$

where,

$$C = \frac{kNw\epsilon}{2} \tag{6.10}$$

is the drag coefficient of the top of the canopy. CRESSMAN (1960) estimates k ~1/4 for air flowing over mountain ridges. For k = 0.25, N = 100 $m^{-2}$, w = 0.1 m and $\epsilon$ = 0.1 m, (6.10) gives

$$C = 0.125 \tag{6.11}$$

The equation of motion for the upper layer is

$$\frac{\partial \mathbf{U}_2}{\partial t} + \rho g(D-b)\nabla h = \hat{\mathbf{o}}_a - \hat{\mathbf{o}}_c - \rho f\,\mathbf{k}\times\mathbf{U}_2 \tag{6.12}$$

Where

$\mathbf{U}_2 = (D-b)\mathbf{u}_2$

Write $\tau_a$ as

$$\hat{\mathbf{o}}_a = \rho_a C_w|\mathbf{W}|\mathbf{W} \tag{6.13}$$

where, $\rho_a$ is the air density, $C_w$ is the drag coefficient of the water surface, and $\mathbf{W}$ is the anemometer level wind. A typical value for $C_w$ is (ROLL, 1965)

$$C_w = 2x103, \tag{6.14}$$

although SIMONS (1978) points out that storm surge modellers frequently must use higher values.

Now consider the case where the canopy extends above the water surface as shown in Fig. 6.14. $\tau_w$ is the stress the wind exerts on the top of the canopy, $\mathbf{W}_1$ is the mean wind within canopy, and $\tau_s$ is the stress the wind (i.e., $\mathbf{W}_1$ ) exerts on the water surface. Clearly, $|\mathbf{W}_1| < |\mathbf{W}|$ so $|\tau_s| < |\tau_a|$. Let $\mathbf{R}$ be the stress (force per unit horizontal area) exerted by $\mathbf{W}_1$ on the vertical canopy elements. By analogy to equation (6.4),

$$\mathbf{R} = \rho_a C_d N(b-D)w|\mathbf{W}_1|\mathbf{W}_1 \tag{6.15}$$

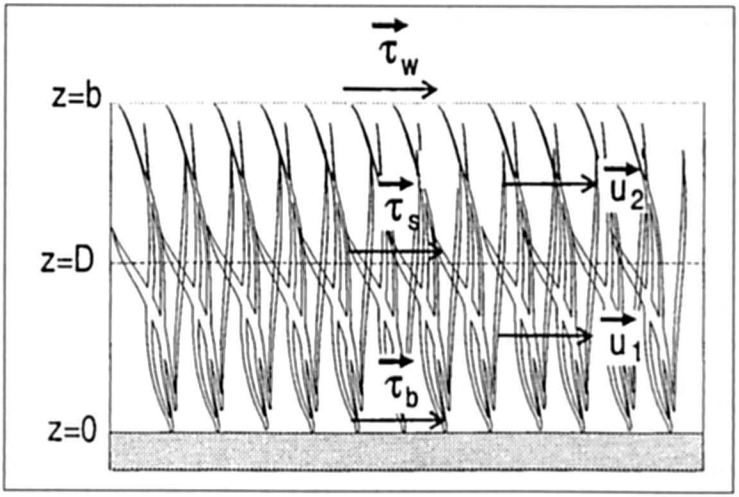


Fig. 6.14: Schematic diagram of stresses in case where canopy extends above the water surface (DANARD and MURTY, 1994)

The same drag coefficient is used in (6.4) and (6.15) since $C_d$ is a function of the roughness of the surface and does not depend on the fluid (water or air) flowing over the surface. By analogy to (6.9),

$$\hat{\mathbf{o}}_w = \rho_a C |\mathbf{W}| \mathbf{W} \tag{6.16}$$

The same drag coefficient applies to (6.9) and (6.16) since they both represent fluid moving over the top of the canopy. By analogy to (6.13)

$$\hat{\mathbf{o}}_s = \rho_a C_w |\mathbf{W}_1| \mathbf{W}_1 \tag{6.17}$$

From the balance of forces in the layer $D \le z \le b$,

$$\hat{\mathbf{o}}_s = \hat{\mathbf{o}}_w \cdot \mathbf{R} \tag{6.18}$$

Each term in (6.18) is in the direction of **W**. Substituting (6.15) – (6.17) in (6.18) gives

$$W_1^2 = \left[\frac{C}{C_w + C_d N(b-D)w}\right] W^2 \tag{6.19}$$

This enables one to calculate $\tau_s$ from (6.17). Reid and Whitaker assume that $C = C_w = C_d$. However, C refers to flow over the top of the canopy whereas $C_w$ refers to flow over a water surface. Clearly, then, $C \neq C_w$. Also, $C_d$ refers to the obstruction to flow of the vertical surface of the canopy elements. Obviously between $C_w \neq C_d$ and $C \neq C_d$. The values given by (6.6), (6.11) and (6.14) show the differences between $C_d$, C and $C_w$.
The equation of motion for the water layer is (6.3)

$$\rho \frac{\partial \mathbf{U}_1}{\partial t} + \rho g D \nabla h = \hat{\mathbf{o}}_s - \hat{\mathbf{o}}_b - \mathbf{R} - \rho f \, \mathbf{k} \times \mathbf{U}_1 \tag{6.20}$$

The magnitude of the wind stress on the water is

$$\hat{o}_S = \rho_a C_w W_1^2 \tag{6.21}$$

where, $W_1^2$ is evaluated from (6.19). Substituting (6.19) in (6.21) yields

$$\hat{o}_S = \left[\frac{\rho_a C_w C}{C_w + C_d N(b-D)w}\right] W^2 \tag{6.22}$$

Using Reid and Whitaker's assumption ($C_w = C = C_d$), $\rho_a = 1.2$ kgm$^{-3}$, $C_w = 2 \times 10^{-3}$, $N = 100$ m$^{-2}$, $b = 2$ m, $D = 1$ m and $w = 0.1$ m, (6.22) gives

$$\hat{o}_S = 2.2 \times 10^{-4} W^2 \tag{6.23}$$

for $\tau_s$ on Pa and W in ms$^{-1}$. On the other hand if we employ (6.6), (6.11) and (6.14) in (6.1.50), we obtain

$$\hat{o}_S = 6.0 \times 10^{-6} W^2 \tag{6.24}$$

There is clearly a significant difference between (6.23) and (6.24), due to the fact that Reid and Whitaker predict a much higher wind speed at the water surface.

Comparison of equations (6.23) derived by Reid and Whitaker and (6.24) derived here shows that for the situation where the vegetation extends above the water surface, the effective wind stress is an order of magnitude smaller. This explains why a vegetation canopy (especially in the situation where the vegetation extends above the water surface) can moderate storm surges quite significantly.

It is well known that most of damage to coastal structures during a storm surge occurs from water currents and wind waves and not from the high water levels themselves. Hence, it is important to compute the water currents and wind waves for building design purposes.

Consider now the case of wind-driven water flow without a canopy. The linearized equation of motion is

$$\frac{\partial \mathbf{u}}{\partial t} + g\nabla h + \frac{1}{\rho}\nabla \rho_a = \frac{1}{\rho}\frac{\partial \hat{o}}{\partial z} - f\,\mathbf{k}\times\mathbf{u} \tag{6.25}$$

where, $\rho_a$ is atmospheric pressure. Tides may be included in (6.25) by imposing boundary conditions on **u** and h at the seaward boundary of the computational domain. The non-linear advective acceleration is omitted from (6.25) although this may be important. Take the vertical average of (6.25) to yield

$$\frac{\partial \bar{\mathbf{u}}}{\partial t} + g\nabla h + \frac{1}{\rho}\nabla \rho_a = \mathbf{F} - f\,\mathbf{k}\times\bar{\mathbf{u}} \tag{6.26}$$

where, ($\bar{\mathbf{u}}$ is the vertically averaged water velocity,

$$\mathbf{F} = \frac{(\hat{o}_a - \hat{o}_b)}{\rho H} \tag{6.27}$$

is the vertically averaged friction force per unit mass and H = D + h is the total water depth. $\tau_a$ is usually calculated from (6.13). $\tau_b$ is frequently computed from a similar expression

$$\hat{o}_b = \rho c |\bar{u}| \bar{u} \tag{6.28}$$

where, c is the drag coefficient of the bottom surface. FLATHER (1979) and GREENBERG (1977) use

$$c = 2.5 \times 10^{-3} \tag{6.29}$$

However, (6.13) and (6.28) are calculated essentially independently, (6.4) therefore has a singularity as the denominator approaches zero. FLATHER and HEAPS (1975) avoid this singularity by specifying a minimum depth $D_0$ = 1m for use in (6.27). While this is preferable to having the model blow up, a better way is needed.

As the water depth becomes smaller, one would expect $\tau_b \rightarrow \tau_a$. Given the dimensionless number $\delta$ ($\leq 0.1$), there exists a depth d ($\delta$) such that

$$\frac{|\hat{o}_a - \hat{o}_b|}{|\hat{o}_a|} \leq \delta \tag{6.30}$$

for $H \leq d$. However, (6.30) simply implies a constant flux layer through which $\tau \approx \tau_a$. For a neutral stratification this means

$$u = \frac{u_{*w}}{k_v} \ln\left(\frac{z}{z_0}\right) \tag{6.31}$$

where $u_{*w}$ is the (constant) water friction velocity, $k_v$ is von Karman's constant, and $z_0$ is the roughness length of the bottom surface. The vertical average of (6.31) is

$$\bar{u} = \frac{1}{(H - z_0)} \int_{z_0}^{H} u dz \tag{6.32}$$

Substituting (6.31) in (6.32) gives

$$\bar{u} = \frac{u_{*w}}{(H - z_0) k_v} \left\{ H \left[ \ln\left(\frac{H}{z_0}\right) - 1 \right] + z_0 \right\} \tag{6.33}$$

For $z_0 \leq H$, (6.33) simplifies to

$$\bar{u} = \frac{u_{*w}}{k_v} \left[ \ln\left(\frac{H}{z_0}\right) - 1 \right] \tag{6.34}$$

Note that (6.33) and (6.34) are diagnostic expressions for the water current. The direction of $\bar{u}$ is the same as $\tau_a$ or W. This will be discussed further in the paragraph following equation (6.41).

To find $u_{*w}$, note that the stress the water surface exerts on the atmosphere is equal in magnitude and opposite in direction to the stress the atmosphere exerts on the water. This is:

$$\varrho u_{*w}^{2} = \tau_a$$

or

$$u_{*w} = \left[\frac{\tau_a}{\varrho}\right]^{1/2} \tag{6.35}$$

An alternate to (6.33) and (6.34) may be obtained by setting $\tau_b = \tau_a$ in (6.28) and solving for $\bar{\mathbf{u}}$ to give

$$\bar{u} = \left(\frac{\tau_a}{c\rho}\right)^{1/2} \tag{6.36}$$

Let's obtain a numerical value for $\bar{\mathbf{u}}$ from (6.36). For $\rho_a = 1.2$ kgm$^{-3}$, $C_w = 2 \times 10^{-3}$ and $W = 10$ ms$^{-1}$, (6.13) gives $\tau_a = 0.24$ Pa. Substitute this value in (6.36) along with $c = 2.5 \times 10^{-3}$ and $\rho = 10^3$ kg m$^{-3}$ to obtain ($\bar{u} = 0.31$ ms$^{-1}$.

An attempt will now be made to estimate the critical depth d following the method of DANARD (1981). Integrate (6.25) from z = 0 to z = d and write as

$$\frac{\left|\hat{\mathbf{o}}_a - \hat{\mathbf{o}}_b\right|}{\hat{\mathbf{o}}_a} = \frac{\varrho d\left|\partial \mathbf{u}/\partial t + g\nabla h + \varrho^{-1}\nabla \varrho_1 + f\,\mathbf{k}\times\bar{\mathbf{u}}\right|}{\left|\hat{\mathbf{o}}_a\right|} \tag{6.37}$$

Equating the right side of (6.37) to ( and solving for *d* gives

$$d = \frac{\delta\left|\hat{\mathbf{o}}_a\right|}{\varrho\left|\partial \mathbf{u}/\partial t + g\nabla l + \varrho^{21}\nabla \varrho_a + f\,\mathbf{k}\times\bar{\mathbf{u}}\right|} \tag{6.38}$$

Suppose the water velocity decreases by 0.1 ms$^{-1}$ in $10^3$ s. Then for $\rho = 10^3$ kg m$^{-3}$, $\rho|\partial \mathbf{u}/\partial t| \sim 0.1$ Pa m$^{-1}$. The terms $g\nabla h$ and $f\mathbf{k} \times \bar{\mathbf{u}}$ frequently offset each other and do so exactly if the current is geostrophically balanced. The sum of these terms should be the same order of magnitude as $\partial \bar{\mathbf{u}}/\partial t$. Now

$$\left|\nabla \varrho_a\right| = \varrho_a f\left|\mathbf{W}_g\right| \tag{6.39}$$

where, $\mathbf{W}_g$ is the geostrophic wind. For $\rho = 1.2$ kg m$^{-3}$, $f = 10^{-4}$ s$^{-1}$ and $|\mathbf{W}_g| = 15$ ms$^{-1}$, (6.39) gives $|\nabla \rho_a| = 1.8 \times 10^{-3}$ Pa m$^{-1}$. This is two orders of magnitude smaller than $\rho|\partial \bar{\mathbf{u}}/\partial t|$ so we will approximate (6.38) by

$$d = \frac{\delta\left|\hat{\mathbf{o}}_a\right|}{\rho\left|\partial \bar{\mathbf{u}}/\partial t\right|} \tag{6.40}$$

In the previous paragraph we calculated $|\tau_a| = 0.24$ Pa. Setting $\delta = 0.1$ in (6.40) yields Larger accelerations attainable in small mesh models would result in smaller values of d.

$$d = 0.24 \text{ m} \tag{6.41}$$

To show that $\bar{\mathbf{u}}$ is in the same direction as $\tau_a$ or $\mathbf{W}$, it has just been demonstrated that if $H \le d$, then $\tau_a$ and $\tau_b$ are approximately parallel. One would expect $\bar{\mathbf{u}}(H)$ to be parallel to $\tau_a$.

For small z, one would expect $\bar{\mathbf{u}}(z)$ to be parallel to $\tau_b$ (6.28). It follows that the direction of $\bar{\mathbf{u}}(z)$ is approximately constant for all z and therefore $\bar{\mathbf{u}}$ is parallel to $\tau_a$.

It is proposed that the prognostic calculation of $\bar{\mathbf{u}}$ using equation (6.26) be replaced by a diagnostic calculation using equation (6.36), when the total water depth falls below a critical value *d*. Here *d* may be estimated from (6.38) or (6.10) using the nearest available data, or replaced by a constant which varies directly with grid size.

One shortcoming of the diagnostic approach is that the water current is always in the direction of the wind. Thus an ebbing tide with an onshore wind of any magnitude would result in onshore water current. Similarly, an incoming tide with zero wind stress would have zero water velocity. However, this is only for points nearest the shore whose depths are less than d.

Next we describe a new method for calculating **F**, which may be used for smaller depths than equation (6.37). Consider 2-dimensional flow (u, w) in the vertical x–z plane. The following derivation in this paragraph [equations (6.42)–(6.49)] is similar to classical boundary layer theory (see e.g., HALTINER and MARTIN, 1957). However, the rest of the derivation is new. The horizontal stress is

$$\tau = -\rho u' w' \tag{6.42}$$

where, the primes denote perturbation velocities (departures from time-average values) and the carat signifies a time average. Assume that

$$u' = \ell\left(\frac{\partial u}{\partial z}\right) \tag{6.43}$$

where, $\ell$ is the mixing length. Assume also that

$$u' = -w'\,\mathrm{sign}\left(\frac{\partial u}{\partial z}\right) \tag{6.44}$$

where, sign($\partial u/\partial z$) has the sign of $\partial u/\partial z$ and a unit magnitude. Substituting (6.43) and (6.44) in (6.42) yields

$$\tau = \rho\left(\ell\frac{\partial u}{\partial z}\right)^2 \mathrm{sign}\left(\frac{\partial u}{\partial z}\right) \tag{6.45}$$

A negative sign ($\partial u/\partial z$) means that $\tau$ is in the -x direction. Now assume that

$$\ell = k_v z \tag{6.46}$$

Substituting (6.46) in (6.45) gives

$$\tau = \rho\left(k_v z\frac{\partial u}{\partial z}\right)^2 \mathrm{sign}\left(\frac{\partial u}{\partial z}\right) \tag{6.47}$$

Define the friction velocity $u_*$ from the equation

$$\tau = \rho u_*^2 \operatorname{sign}(u_*) \tag{6.48}$$

where, sign ($u_*$) = sign($\partial u/\partial z$). Then from (6.47) and (6.48),

$$u_0 = k_v z \frac{\partial u}{\partial z} \tag{6.49}$$

If

$$u_* = u_{*w} = \text{constant}, \tag{6.50}$$

where, $u_{*w}$ is given by (6.35), then (6.31) is obtained. However, to obtain a more general result, instead of (6.50) it will be assumed that the friction velocity varies linearly with height, i.e.,

$$u_* = u_{*w} - a(H - z) \tag{6.51}$$

where, $a$ is a constant, which may be positive or negative. Substituting (6.51) in (6.49) yields

$$u = \frac{(u_{*w} - aH)}{k_v} \ln\left(\frac{z}{z_0}\right) + \frac{b(z - z_0)}{k_v} \tag{6.52}$$

Note that (6.52) is similar to the 'log-linear' profile of stable flows (see, e.g. DEARDROFF, 1972, eq. [13]). The mean velocity is obtained by substituting (6.52) in (6.32), assuming $z_0 \perp H$. and integrating to give

$$\bar{u} = \frac{(u_{*w} - aH)}{k_v}\left[\ln\left(\frac{H}{z_0}\right) - 1\right] + \left(\frac{aH}{2K_v}\right) \tag{6.53}$$

Since $aH$ is unknown, (6.53) is not a diagnostic equation for $\bar{u}$. However, (6.34) and (6.36) are diagnostic equations.
The vertically averaged frictional force per unit mass is

$$F = \frac{u_{*w}^2 \operatorname{sign}(u_{*w}) - u_{*0}^2 \operatorname{sign}(u_{*0})}{H} \tag{6.54}$$

where, from (6.51),

$$u_{*0} = u_{*w} - aH \tag{6.55}$$

The quantity $aH$ is obtained diagnostically from the mean water velocity using (6.53):

$$aH = \frac{u_{*w}\left[\ln\left(\frac{H}{z_0}\right)-1\right]-k_v\bar{u}}{\left[\ln\left(\frac{H}{z_0}\right)-\frac{3}{2}\right]} \tag{6.56}$$

This expression has a singularity for

$$\ln\left(\frac{H}{z_0}\right)=\frac{3}{2}$$

or

$$\frac{H}{z_0}=4.5 \tag{6.57}$$

In deriving (6.56) it was assumed that $H/z_0 \pi 1$, although if this assumption were not made, all that would result would be the appearance of additional terms. If use of (6.56) is limited to cases where $H > d$ (see eq. [6.38]) or $H > 10z_0$, whichever is larger, then the singularity (6.57) will pose no problem. This limitation on H will also help avoid the singularity in (6.54) for $H = 0$. The numerator of the right side of (6.56) won't necessarily become small for small H, nor will the numerator of (6.54).

Equations (6.54)–(6.56) provide a diagnostic procedure for evaluating F given $u_{*w}$, H, $z_0$ and $\bar{u}$. If tides are included, they will affect $\bar{u}$.

It was shown above that a vegetation canopy, especially one that projects above the water surface can significantly dissipate storm surges. This has practical importance because instead of erecting prohibitively expensive sea walls, one can use reed grass whose expense will be orders of magnitude less. A method has been proposed to compute the horizontal currents, which account for most of the damage. A prior knowledge of the possible maximum value of such currents for each surge prone location can help in the design of coastal engineering structures.

### 6.1.5 Galveston Bay

REID and BODINE (1968) developed a two-dimensional numerical model for computing storm surges in Galveston Bay. They also allowed for rainfall by including it in the continuity equation. The observed and computed surges at different locations for two different hurricanes are compared in Fig. 6.15 and 6.16. BUTLER (1979) also developed a two-dimensional numerical model for storm surge computations in Galveston bay. The time dependence is treated implicitly in this model. Spatially varying and time-dependent wind fields and rainfall are included. Flooding of low-lying areas is simulated by treating the location of land-water boundary as a function of the time-varying local water depth. Subgrid barrier effects are also included. Exposed, submerged, and overtopping barriers can be represented in the mesh system; thus, one can allow for the surge waters breaching narrow barriers such as elevated highway, control structures, etc.

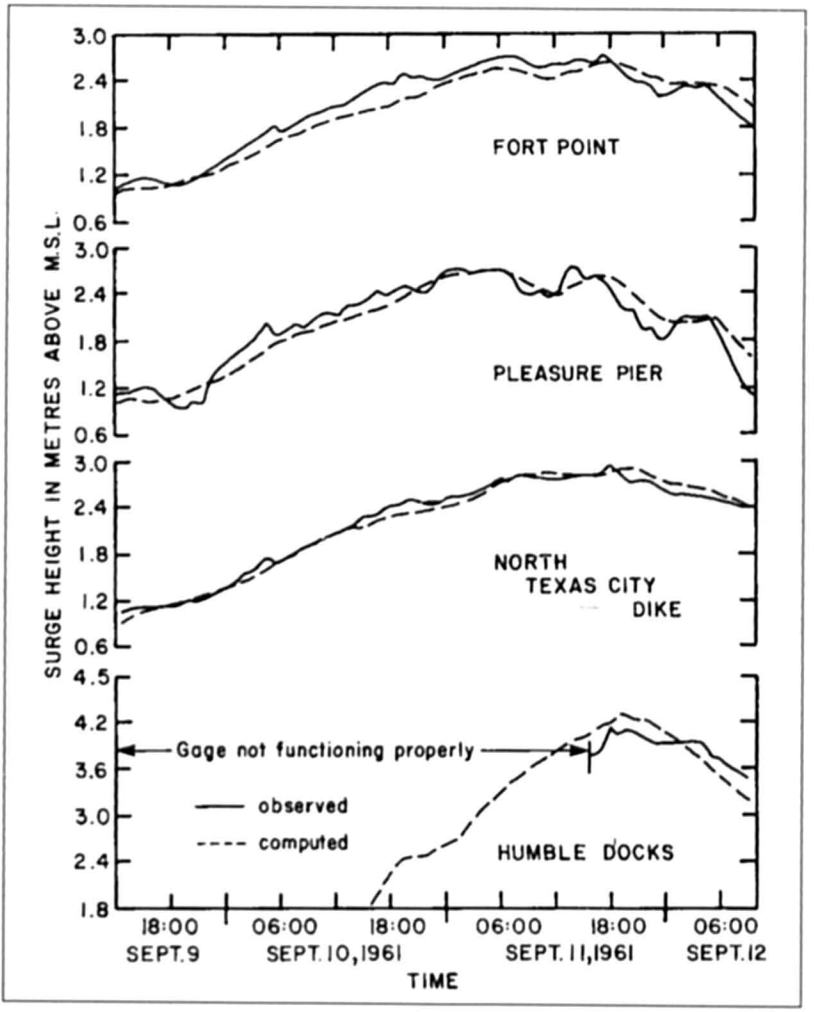


Fig. 6.15: Comparison of observed and computed surges at four locations in Galveston Bay due to Hurricane Carla of September 9–12, 1961 (REID and BODINE, 1968)

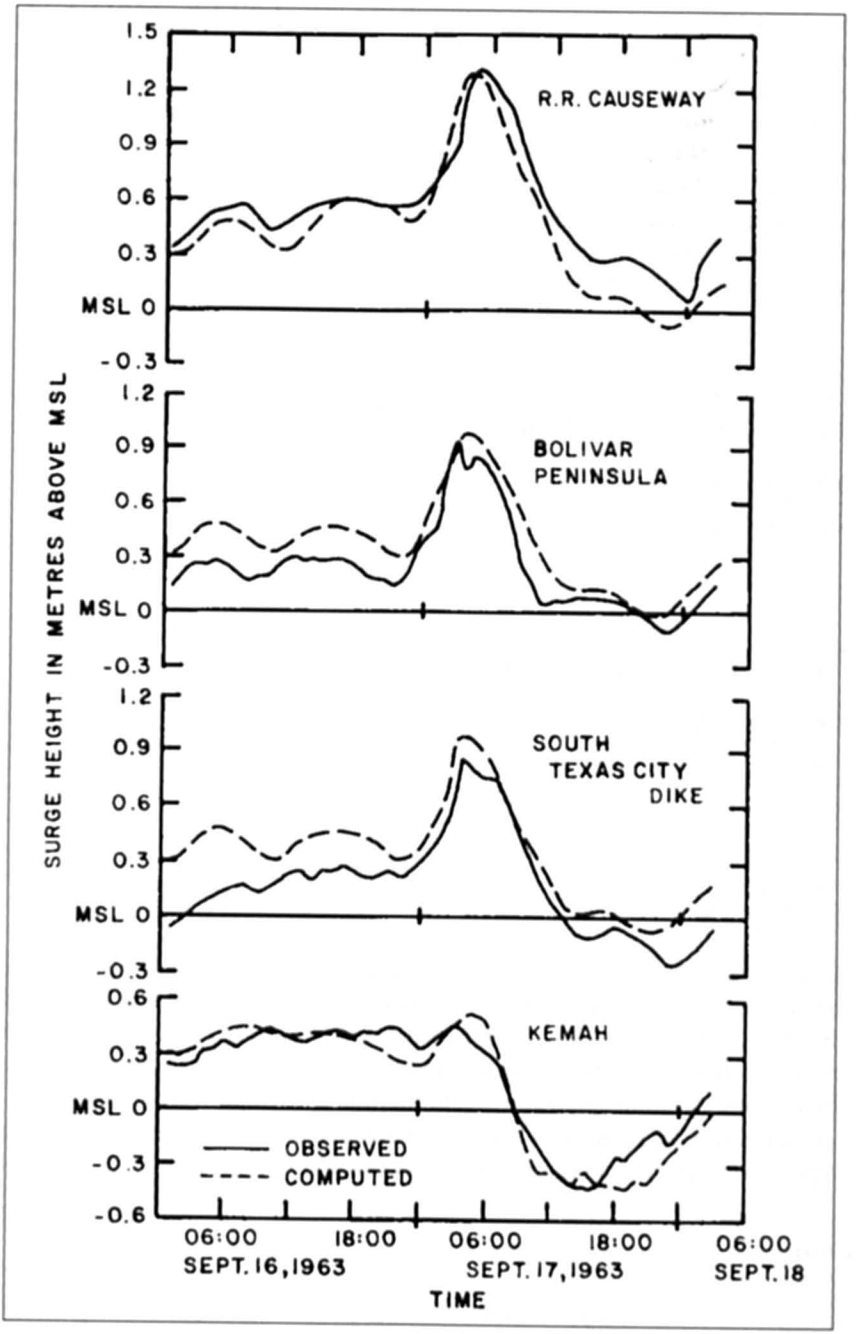


Fig. 6.16: Comparison of computed and observed surges at four locations in Galveston Bay due to Hurricane Cindy of September 16–18, 1963 (REID and BODINE, 1968)

One special feature of this model is the employment of a coordinate transformation in the form of a piecewise exponential stretch. This transformation maps prototype space, discretized with a smoothly varying grid, into computational space with a regularly spaced grid, and in the computational space all the derivatives are cantered. Through this transformation one can simulate a complex domain by locally increasing grid resolution and also by aligning coordinates along physical boundaries. A smoothly varying grid with continuous first derivatives eliminates the problem usually associated with variable grids. Indeed, BUTLER (1979) used expansions of grid length in prototype space by a factor of 10. BUTLER (1979) wrote the vertically integrated two-dimensional equations of motion and continuity as follows:

$$\frac{\partial U}{\partial t}+\frac{\partial}{\partial x}\left(\frac{U^2}{d}\right)+\frac{\partial}{\partial y}\left(\frac{UV}{d}\right)-fV+gd\frac{\partial}{\partial x}(\eta-\eta_a)+F_x+\frac{gU}{c^2d^2}\left(U^2+V^2\right)^{1/2}$$
$$-de\left(\frac{\partial^2 U}{\partial x^2}+\frac{\partial^2 U}{\partial y^2}\right)=0 \qquad (6.58)$$

$$\frac{\partial V}{\partial t}+\frac{\partial}{\partial x}\left(\frac{UV}{d}\right)+\frac{\partial}{\partial y}\left(\frac{V^2}{d}\right)+fU+gd\frac{\partial}{\partial y}(\eta-\eta_a)+F_y+\frac{gV}{c^2d^2}\left(U^2+V^2\right)^{1/2}$$
$$-de\left(\frac{\partial^2 V}{\partial x^2}+\frac{\partial^2 V}{\partial y^2}\right)=0 \qquad (6.59)$$

$$\frac{\partial \eta}{\partial t}+\frac{\partial U}{\partial x}+\frac{\partial V}{\partial v}=0 \qquad (6.60)$$

Here, h is the still-water elevation, $d = h + \eta$ is the total water depth, c is the Chezy friction coefficient, e is a generalized eddy viscosity coefficient, R is the rate at which additional water is introduced into or taken out of the water body (rainfall, evaporation), $F_x$ and $F_y$ represent external forcing functions such as wind stress, $\eta$ is the water surface elevation, and $\eta_a$ is the hydrostatic elevation corresponding to the atmospheric pressure anomaly.

For each direction a piecewise reversible transformation is independently used to map prototype into computational space. The transformation is of the form

$$x = a + b\alpha^c \qquad (6.61)$$

where, a, b, and c are arbitrary constants. The equations of motion in the $\alpha$-space are

$$\frac{\partial U}{\partial t}+\frac{1}{\mu_1}\frac{\partial}{\partial \alpha_1}\left(\frac{U^2}{d}\right)+\frac{1}{\mu_2}\frac{\partial}{\partial \alpha_2}\left(\frac{UV}{d}\right)-fV+\frac{gd}{\mu_1}\frac{\partial}{\partial \alpha_1}(\eta-\eta_a)+F_{\alpha_1}$$
$$+\frac{gU}{C^2d^2}\left(U^2+V^2\right)^{1/2}-T_1=0 \qquad (6.62)$$

$$\frac{\partial V}{\partial t}+\frac{1}{\mu_1}\frac{\partial}{\partial \alpha_1}\left(\frac{UV}{d}\right)+\frac{1}{\mu_2}\left(\frac{V^2}{d}\right)+fU+\frac{gd}{\mu_2}\frac{\partial}{\partial \alpha_2}(\eta-\eta_a)+F_{\alpha_2}$$

$$+\frac{gV}{C^2d^2}\left(U^2+V^2\right)^{1/2}-T_2=0 \qquad (6.63)$$

$$\frac{\partial \eta}{\partial t}+\frac{1}{\mu_1}\frac{\partial U}{\partial \alpha_1}+\frac{1}{\mu_2}\frac{\partial V}{\partial \alpha_2}=R \qquad (6.64)$$

where,

$$\mu_1=\frac{\partial x}{\partial \alpha_1}=b_1c_1\alpha^{c_1-1} \qquad (6.65)$$

$$\mu_2=\frac{\partial y}{\partial \alpha_2}=b_2c_2\alpha^{c_2-1} \qquad (6.66)$$

Table 6.10: Comparison of computed and observed surges (m) at several locations in Galveston Bay due to Hurricane Carla of 1961 (mean absolute error = 0.18 m). (BUTLER, 1979)

| Gauge Location | Observed | Computed | Difference |
|---|---|---|---|
| Oyster Creek | 3.11 | 3.29 | +0.18 |
| San Luis Pass | 3.29 | 3.05 | −0.24 |
| Sea Isle Beach | 3.69 | 3.05 | −0.64 |
| Bermuda Beach | 3.20 | 2.99 | −0.21 |
| Scholes Field | 2.59 | 2.93 | +0.33 |
| Bolivar Beach | 2.83 | 2.83 | +0.00 |
| Crystal Beach | 2.68 | 2.87 | +0.18 |
| Rollover Beach | 2.93 | 2.83 | −0.09 |
| Halls Bayou | 4.36 | 4.30 | −0.06 |
| Highway Six | 3.84 | 3.87 | +0.03 |
| Sievers Cove | 3.23 | 2.83 | −0.39 |
| Dickinson Bayou | 3.47 | 3.60 | +0.12 |
| Carbide Docks | 3.35 | 3.17 | −0.18 |
| Kemah | 4.33 | 3.90 | −0.43 |
| Smith Point | 2.99 | 3.17 | +0.18 |
| Oyster Bayou | 3.20 | 3.35 | +0.15 |
| Scott Bay | 4.33 | 4.30 | −0.03 |
| Humble Docks | 4.18 | 3.84 | −0.34 |
| Ananuac | 3.78 | 3.87 | +0.09 |
| Wallisville | 4.27 | 4.26 | +0.00 |
| Pleasure Pier | 2.83 | 2.87 | +0.03 |
| Fort Point | 2.74 | 2.90 | +0.15 |
| Pier 21 | 2.68 | 2.90 | +0.21 |
| Pelican Bridge | 2.74 | 2.87 | +0.12 |
| Texas City Dyke (south) | 2.90 | 3.05 | +0.15 |
| Texas City Dyke (north) | 2.96 | 3.05 | +0.09 |

The parameters $\mu_1$ and $\mu_2$ define stretching of the regular grid into $\alpha$-space to approximate the study area of real space. The terms $T_1$ and $T_2$ represent the transformed flux terms (which are not included in the application to Galveston Bay).

The above model is applied to storm surge computation in Galveston Bay (which is a large shallow bay of area greater than 1000 km$^2$) due to Hurricane Carla of 1961. The model was calibrated by reproducing the tides. The observed and computed surges at 26 different locations are compared in Table 6.10.

### 6.1.6 Pamlico Sound and Cape Fear Estuary

Two important water bodies along the coast of North Carolina are Palmico Sound in the north and Cape Fear Estuary in the south In Palmico sound the astronomical tides are small (5-cm range) but storm surges could be significant. ROELOFS and BUMPUS (1953) calculated the surges in this water body using the following simple relation of KEULEGAN (1951):

$$\frac{S}{L} = 3.3\times10^{-6}\left[1+63\left(\frac{H}{L}\right)^{1/2}\right]\frac{V^2}{gH} \qquad (6.67)$$

where, S is the setup (i.e. $h_2 - h_1$, where $h_2$ and $h_1$ are the windward and leeward displacements of water level), L is the length of the water body, V is the wind velocity, and H is the mean depth of the water body. From this formula it was calculated that a southwest wind of about 13 knots (24 km $\cdot$ h$^{-1}$) is needed to generate a setup of about 1 feet (0.3 m) and a 40-knot (74 km $\cdot$ h$^{-1}$) wind could produce a surge of 9.8 ft (3 m). This result does not include the funnelling effect due to the geometry of the sound. Northeasterly winds will cause a similar rise along the southwest shore.

MYERS (1975) used a one-dimensional numerical model to calculate the storm surges in Cape Fear Estuary. Some recent dredging operations increased the tidal range at Wilmington, North Carolina. Hence, they used two different depth profiles: the first corresponding to the early 1950's and the second corresponding to the present depths. They generated time histories of the open coast surge from the SPLASH II model for an ensemble of hurricanes, each storm being related to a frequency of occurrence. These time histories are linearly combined with appropriate phases of the astronomical tide at the entrance to Cape Fear River. Three hurricanes were selected: Hazel of 1954, Diane of 1955, and Helene of 1958. The pertinent information for these hurricanes is listed in Table 6.11.

Table 6.11: Meteorological data for Hurricanes Hazel of 1954, Diane of 1955, and Helene of 1958 (MYERS, 1975)

| Hurricane | Central pressure depression (mb) | Radius of maximum winds (km) | Speed of movement (km·h$^{-1}$) | Maximum wind speed (km·h$^{-1}$) |
|---|---|---|---|---|
| Hazel | 66 | 38.9 | 53.2 | 166.7 |
| Diane | 30 | 31.5 | 22.8 | 110.4 |
| Helene | 65 | 38.9 | 24.1 | 165.9 |

Table 6.12: Pertinent information about selected hurricanes affecting Chesapeake Bay. (BRETSCHNEIDER, 1959)

| Parameter | Hurricane of Aug. 22–24, 1933 | Connie of Aug. 11–13, 1955 | Diane of Aug. 15–18, 1955 | Hazel of Oct. 14–17, 1957 |
|---|---|---|---|---|
| Track | Just west of Chesapeake Bay's west coast | Just west of Chesapeake Bay's east coast | About 160 km west of Chesapeake Bay's west coast | About 160 km west of Chesapeake Bay's west coast |
| Radius of maximum winds ($km \cdot h^{-1}$) | 86.9 | 72.4 | 72.4 | 57.9 |
| Central pressure anomaly (mb) | 28.8 | 46.4 | 24.0 | 56.2 |
| Speed of movement over ocean ($km \cdot h^{-1}$) | 46.2 | 22.2 | 38.9 | 101.9 |
| Speed of movement over Chesapeake Bay ($km \cdot h^{-1}$) | 24.1 | 18.5 | 22.2 | 66.6 |
| Maximum wind speed over ocean ($km \cdot h^{-1}$) | 98.2 | 115.9 | 86.9 | 148.1 |
| Maximum wind speed over Chesapeake Bay ($km \cdot h^{-1}$) | 80.5 | 72.4 | 56.3 | 112.7 |
| Peak surge (m) at Hampton Roads, VA | 2.01 | 1.34 | 0.18 | 0.55 |
| Peak surge (m) at Gloucester Point, VA | – | 1.37 | 0.70 | 0.88 |
| Peak surge (m) at Solomon's Island, MD | – | 1.28 | 0.67 | 0.85 |
| Peak surge (m) at Annapolis, MD | 1.77 | 1.49 | 0.98 | 1.28 |
| Peak surge (m) at Baltimore, MD | 2.20 | 1.59 | 1.13 | 1.46 |

### 6.1.7 Chesapeake Bay

Hurricane-generated storm surges in this water body were studied by BRETSCHNEIDER (1959). Of all the hurricanes that generated surges in Chesapeake Bay up to 1959, only four are sufficiently well documented: August 22–24, 1933, August 11–13, 1955 (Connie), August 15–18, 1955 (Diane), and October 14–17, 1954 (Hazel).

The pertinent information for the meteorological aspects of these hurricanes as well as the storm surges recorded is given in Table 6.12. Some typical surge profiles in Chesapeake Bay are illustrated in Fig. 6.17 and 6.18.

For computing the surges outside Chesapeake Bay on the open coast, two model hurricanes were selected. The first (referred to as A) is the September 14, 1944, hurricane transposed to the Chesapeake Bay area but not adjusted for filling. For this hurricane, the radius $R$ of maximum winds is 33.5 nautical miles (62 km); the atmospheric pressure anomaly at the center is 2.2 in. Hg (74.5 mb), and the maximum sustained wind speed at $R$ is 105 $mi \cdot h^{-1}$ (169 $km \cdot h^{-1}$). The path of movement over the open ocean was assumed to be perpendicular to the coast and the speed of travel was 15–25 $mi \cdot h^{-1}$ (24–40 $km \cdot h^{-1}$). After crossing the coast, the path of movement curves and proceeds northward along the west side of Chesapeake Bay, and the speed of movement reduces to 12–15 $mi \cdot h^{-1}$ (19–24 $km \cdot h^{-1}$). The second storm (referred to as B) is exactly the same as A, except that all wind speeds are 5 $mi \cdot h^{-1}$ (8 $km \cdot h^{-1}$) larger. The results for the surges due to hurricanes A and B are summarized in Table 6.13. The prediction curves for hurricane surges at Washington, DC, are given in Fig. 6.19.

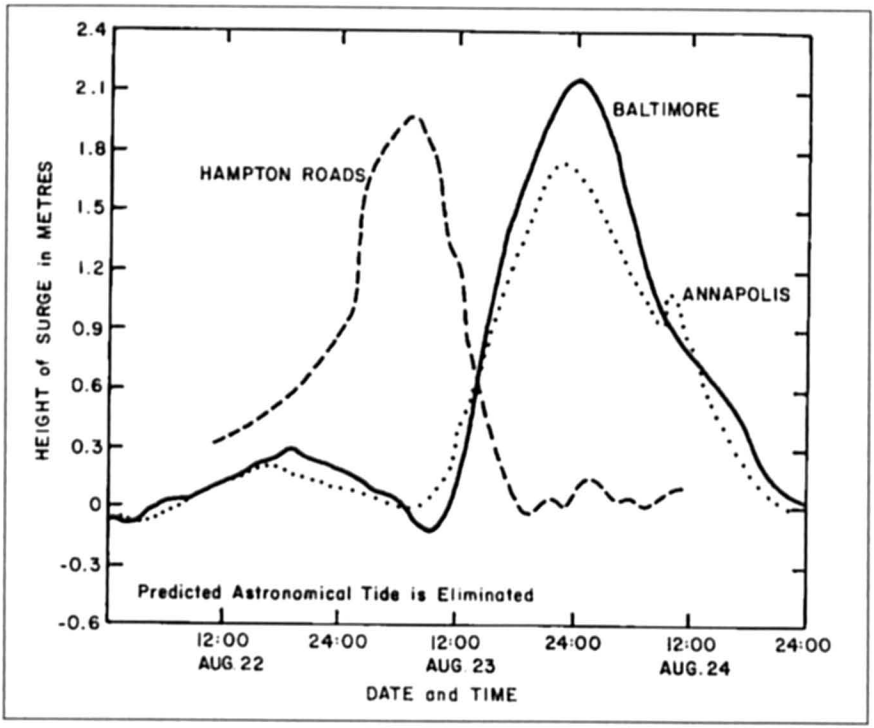


Fig. 6.17: Storm surges at three locations in Chesapeake Bay due to the hurricane of August 22–24, 1933 (BRETSCHNEIDER, 1959)

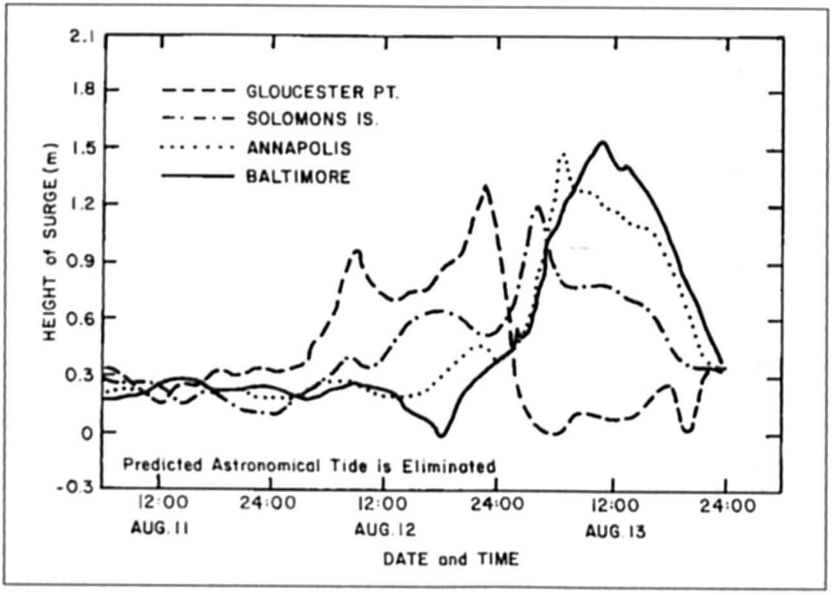


Fig. 6.18: Storm surges at four locations in Chesapeake Bay due to Hurricane Connie of August 11–13, 1955 (BRETSCHNEIDER, 1959)

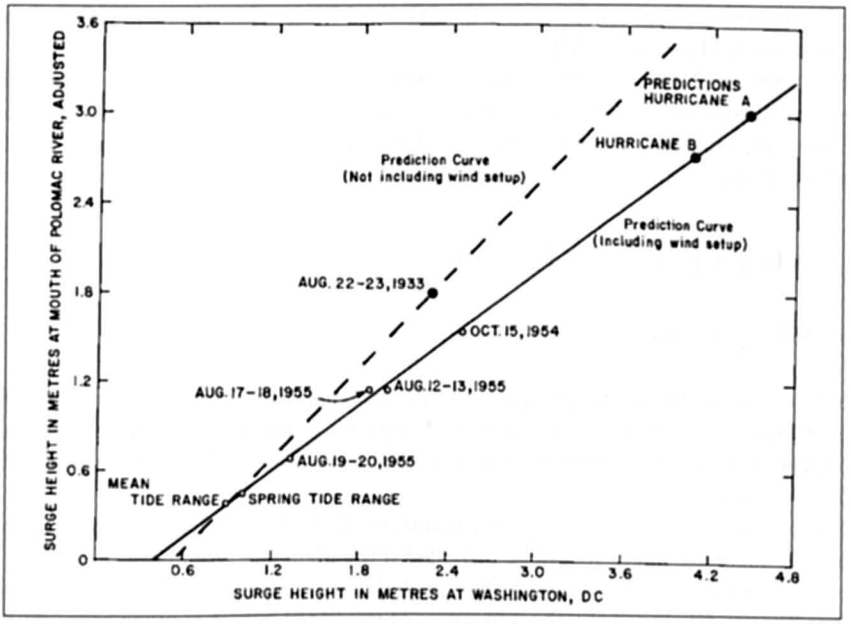


Fig. 6.19: Storm surges prediction curves for hurricane generated storm surges at Washington D.C. (BRETSCHNEIDER, 1959)

BODINE (1971) used the bathystrophic theory to compute storm surges on an open coast and applied this to the Chesapeake Bay area. In this connection, he pointed to the important effect of interaction between tide and surge, especially when it is recognized that the tidal range can vary from 18.2 ft (5.5 m) at East Port, Maine, to 1.3 ft (0.4 m) at Key West, Florida, and that, generally, the tides along the Atlantic coast of the United States are semidiurnal whereas along the Gulf of Mexico coast they are mainly diurnal.

Table 6.13: Computed storm surges in Chesapeake Bay due to hurricanes A and B. These values have an uncertainty of 0.12 m (BRETSCHNEIDER, 1959)

| Location | Maximum surge (m) due to | |
|---|---|---|
| | Hurricane A | Hurricane B |
| Hampton Roads, VA | 3.29 | 3.57 |
| Mouth of York River | 3.14 | 3.44 |
| Mouth of Rappahanock River | 2.99 | 3.26 |
| Mouth of Potomac River | 2.77 | 3.05 |
| Mouth of Severn River | 2.53 | 2.77 |
| Mouth of Patapaco River | 2.87 | 3.11 |

To give the most probable degree of protection required for any given area, the standard practice is to select a hurricane with a given set of characteristics for the particular geographical location. This will be called a "hypothetical" or "hypohurricane". Also, for such a hurricane the characteristics are taken as invariant and the track is assumed to follow a prescribed path. The U.S. Weather Bureau and the U.S. Army Corps of Engineers jointly established two design storms (which depend on the geographical location) for practical use for

coastal engineering purposes. These are the Standard Project Hurricane (SPH) and the Probable Maximum Hurricane (PMH).

GRAHAM and NUNN (1959) defined the SPH as a hypohurricane that is intended to represent the most severe combination of hurricane parameters that is reasonably characteristic of a region, excluding extremely rare combinations. The maximum gradient wind speed in the belt of maximum winds (miles per hour) was determined by the following formulae:

$$V_{gx} = K(p_n - p_0)^{1/2} - R(0.575f) \tag{6.68}$$

$$V_x = 0.865V_{gx} + 0.5V_F \tag{6.69}$$

where K = 73, $p_n$ and $p_0$ are the peripheral and central pressures in inches of mercury, R is the radius of maximum winds in nautical miles, f is the Coriolis parameter in units per hour, $V_F$ is the speed of movement of the hurricane in miles per hour, and $V_x$ is the maximum wind speed 30 ft (9.1 m) above the water.

For protection of the nuclear power plants, the U. S. Atomic Energy Commission concluded that adequate safety would be provided if the plant site would not be flooded by the surge and surface waves associated with a probable maximum hurricane (PMH). The U. S. Weather Bureau developed the characteristics of the PMH, which is much more severe than the SPH. The PMH was defined as a hypothetical hurricane having that combination of characteristics that will make it the most severe storm that can probably occur in the particular region involved. The hurricane should approach the point under study along a critical path and at an optimum rate of movement. Development of the isovel fields is basically the same for the PMH as for the SPH. The difference essentially is that whereas $p_n$ is taken as the standard sea level pressure of 29.92 in. Hg. (1013.2 mb) for the SPH, it is treated as a function of the latitude for the PMH. Also, $K$ is treated as a function of latitude for the PMH whereas it is a constant for SPH. At times it may be desirable to select a design storm other than the SPH or PMH based on the risk or economy factors for a particular location or coastal structure. Using bathystrophic theory, BRETSCHNEIDER (1959) estimated the peak surge (for a selected storm) at the mouth of Chesapeake Bay to be 13.4-ft (4.1 m).

PORE (1965) studied hurricane-generated storm surges in Chesapeake Bay. He made a distinction between western-type (i.e. hurricanes passing west of the bay) and eastern-type (hurricane travelling east of the bay) storms. His study showed that the western-type storms create greater surges in the northern part of the bay whereas the eastern-type storms generate greater surges in the southern portion of the bay. The storm surges resulting from these two types of hurricanes are listed in Tables 6.14 and 6.15.

Table 6.14: Storm surges data for western type storms in the Chesapeake Bay region (PORE, 1965)

| Date | Surge amplitudes (m) at | | | | | | Time lag (h) from Norfolk to Baltimore | Storm movement (km) northward in 12 h |
|---|---|---|---|---|---|---|---|---|
| | Baltimore | Annapolis | Cambridge | Solomon's point | Gloucester point | Hampton Roads | | |
| Oct. 2, 1929 | 1.19 | 1.10 | – | – | – | 0.73 | 18 | 352 |
| Aug. 23, 1933 | 2.13 | 1.68 | – | – | – | 1.86 | 18 | 315 |
| June 19, 1934 | – | – | – | – | – | 0.24 | – | 148 |
| Sept. 18, 1945 | 0.82 | 0.73 | 0.70 | 0.64 | – | 0.73 | 17 | 389 |
| Aug. 29, 1949 | 0.52 | 0.43 | 0.46 | 0.24 | – | –0.06 | – | 519 |
| Sept. 1, 1952 | 1.04 | 0.88 | – | 0.49 | 0.15 | 0.12 | 13 | 241 |
| Oct. 15, 1954 | 1.40 | 1.19 | – | 0.85 | 0.34 | 0.46 | 14 | 945 |
| Aug. 18, 1955 | 1.88 | 0.73 | – | 0.52 | 0.52 | 0.30 | 21 | 241 |

Table 6.15: Storm surge amplitudes (m) for eastern type storms in the Chesapeake Bay region. For certain cases, maximum positive and negative surges are listed (PORE, 1965)

| Date | Baltimore | Annapolis | Cambridge | Solomon's point | Gloucester point | Hampton Roads | Portsmouth |
|---|---|---|---|---|---|---|---|
| Sept. 16, 1933 | 0.27 | 0.30 | – | – | – | 1.55 | – |
| Sept. 8, 1934 | – | – | – | – | – | 0.24 | – |
| Sept. 18, 1936 | –1.74, 0.40 | –1.28, 0.37 | – | – | – | 1.49 | – |
| Sept. 21, 1938 | –0.98, 0.06 | –0.67, 0.03 | – | –0.43 | – | – | 0.55 |
| Oct. 24, 1938 | 0.21 | 0.21 | – | 1.8 | – | – | 0.21 |
| Sept. 1, 1940 | 0.06 | 0.06 | – | 0.06 | – | – | 0.09 |
| Sept. 14, 1944 | –0.64, 0.27 | –0.49, 0.21 | –0.27, 0.24 | –0.18, 0.18 | – | 1.13 | – |
| June 26, 1945 | –0.34, 0.18 | –0.24, 0.24 | –0.18, 0.27 | 0.15 | – | 0.79 | – |
| Aug. 20, 1950 | 0.21 | 0.21 | 0.15 | 0.18 | – | 0.24 | – |
| Aug. 14, 1953 | –0.79, 0.40 | –0.73, 0.34 | – | –0.46, 0.34 | 0.94 | 1.13 | – |
| Aug. 31, 1954 | –0.18, 0.21 | 0.24 | – | 0.24 | 0.49 | 0.79 | – |
| Sept. 11, 1954 | –0.43, 0.15 | –0.30, 0.12 | – | –0.12, 0.15 | 0.67 | 0.88 | – |
| Sept. 27, 1956 | 0.34 | 0.58 | – | 0.64 | – | 1.13 | – |
| Aug. 28, 1958 | –0.37, 0.18 | – | – | 0.18 | – | 0.34 | – |

### 6.1.8 Coast of New Jersey

The greatest loss of life and property, damage on the coast of New England occurred during September 21–22, 1938, as a result of storm surge generated by a West Indian hurricane coupled with river flooding (due to excessive rainfall). The storm surge amplitude was maximum in Rhode Island with values exceeding 17-ft. (5.2) m, and the amplitudes reached record levels all along the coast between New York City and Cape Cod. More than 500 people died (PAULSEN et al., 1940) and the property damage exceeded $ 0.3 billion (at 1938 prices).

The storm surge amplitudes at Sandy Hook on the coast of New Jersey and at three other locations are listed as a function of time in Table 6.16. The surge profiles at Forest Hills and Rockway Park, both in New York State, are shown in Fig. 1.2 and 1.3.

Table 6.16: Storm surge amplitudes (m) as a function of time on the Massachusetts-New York-New Jersey coast during Sept. 21–22, 1938. Time is local time. (PAULSEN et al., 1940)

| Hour | Sandy Hook, NJ | | The Battery, NY | | Boston, MA | | Mill Neck, NY |
|---|---|---|---|---|---|---|---|
| | Sept. 21 | Sept. 22 | Sept. 21 | Sept. 22 | Sept. 21 | Sept. 22 | Sept. 21 |
| 01 | 0.40 | –0.49 | 0.27 | –0.21 | 0.30 | 0.85 | – |
| 02 | 0.85 | –0.37 | 0.73 | –0.18 | –0.18 | –0.03 | – |
| 03 | 1.19 | –0.03 | 1.13 | –0.12 | –0.03 | –0.49 | – |
| 04 | 1.55 | 0.58 | 1.46 | 0.64 | 0.49 | –0.12 | – |
| 05 | 1.71 | 1.52 | 1.59 | 1.34 | 1.16 | 0.24 | – |
| 06 | 1.62 | 1.74 | 1.62 | 1.71 | 1.92 | 0.91 | – |
| 07 | 1.34 | 1.59 | 1.46 | 1.71 | 2.65 | 1.89 | – |
| 08 | 1.04 | 1.16 | 1.22 | 1.43 | 3.14 | 2.80 | – |
| 09 | 0.76 | 0.76 | 0.88 | 1.10 | 3.20 | 3.23 | – |
| 10 | 0.49 | 0.34 | 0.61 | 0.61 | 2.80 | 2.23 | – |
| 11 | 0.30 | 0.09 | 0.37 | 0.34 | 2.19 | 2.80 | – |
| 12 | 0.30 | 0 | 0.15 | 0.09 | 1.55 | 2.16 | – |
| 13 | 0.55 | –0.03 | 0.18 | 0 | 0.79 | 1.34 | – |
| 14 | 1.07 | 0.12 | 0.55 | 0 | 0.21 | 0.43 | – |
| 15 | 1.80 | 0.55 | 1.34 | 0.30 | 0.18 | –0.24 | – |
| 16 | 2.38 | 1.01 | 2.47 | 0.91 | 0.91 | –0.37 | – |
| 17 | 1.55 | 1.46 | 2.04 | 1.37 | 1.62 | 0.15 | – |
| 18 | 0.91 | 1.74 | 1.16 | 1.65 | 2.13 | 0.82 | – |
| 19 | 0.24 | 1.77 | 1.01 | 1.74 | 2.68 | 1.71 | 3.54 |
| 20 | 0.09 | 1.43 | 0.73 | 1.65 | 3.23 | 2.53 | 4.60 |
| 21 | 0.76 | 0.98 | 0.70 | 1.34 | 3.35 | 3.17 | 4.02 |
| 22 | 0.79 | 0.58 | 1.22 | 0.91 | 3.05 | 3.35 | 3.78 |
| 23 | 0.24 | 0.24 | 0.49 | 0.52 | 2.50 | 3.05 | 3.69 |
| 24 | –0.37 | 0 | –0.03 | 0.21 | 1.86 | 2.44 | 3.66 |

PAGENKOPF and PEARCE (1975) developed several storm models and applied these to the New Jersey coast. In particular, these authors compared two-dimensional finite-difference and finite-element methods and concluded that, at least for storm surge calculations, there is no particular advantage to preferring one to the other. They also compared their results with bathystrophic storm surge calculations. All these calculations were made for the hurricane of

September 14, 1974. The results from bathystrophic calculations are not satisfactory in certain circumstances. The horizontal distributions of storm surge heights computed by the finite-difference and finite-element models are compared in Fig. 6.20.

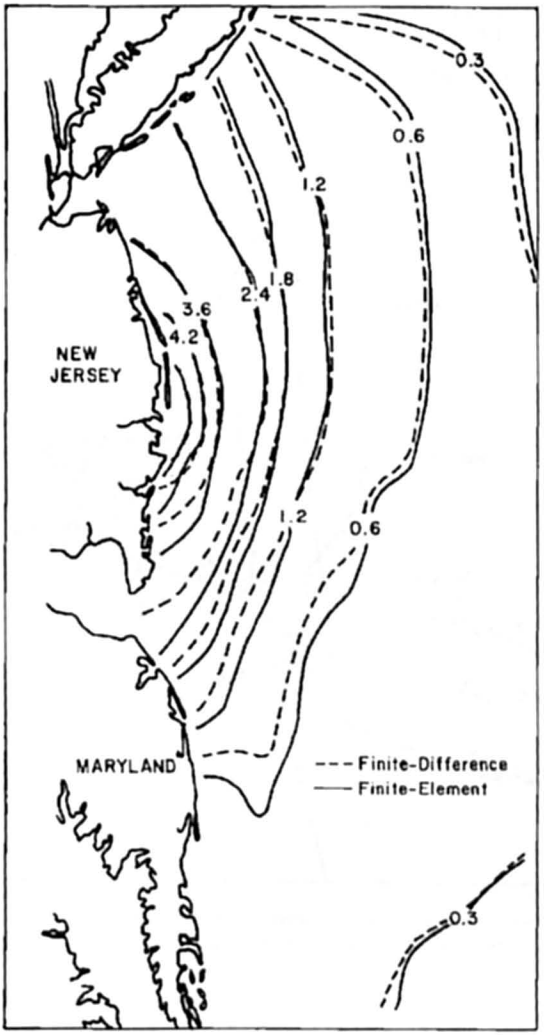


Fig. 6.20: Calculated storm surge heights (meters) along the coast of New Jersey (PAGENKOPF and PEARCE, 1975)

### 6.1.9 Storm Surges in the New York Bight

PORE and BARRIENTOS (1976) studied storm surges in the New York Bight due to hurricanes and extra-tropical cyclones. This subsection will be confined to only hurricane-generated storm surges (extratropical cyclone generated surges will be discussed later). PORE and BARRIENTOS (1976) selected five major hurricanes that affected the New York Bight area: September 21–22, 1938, September 13–15, 1955, August 30–31, 1954 (Carol), September 10–12, 1954 (Edna), and September 12, 1960 (Donna). The storm surge height distributions for the third and fifth hurricanes are given in Fig 6.21 and 6.22, respectively.

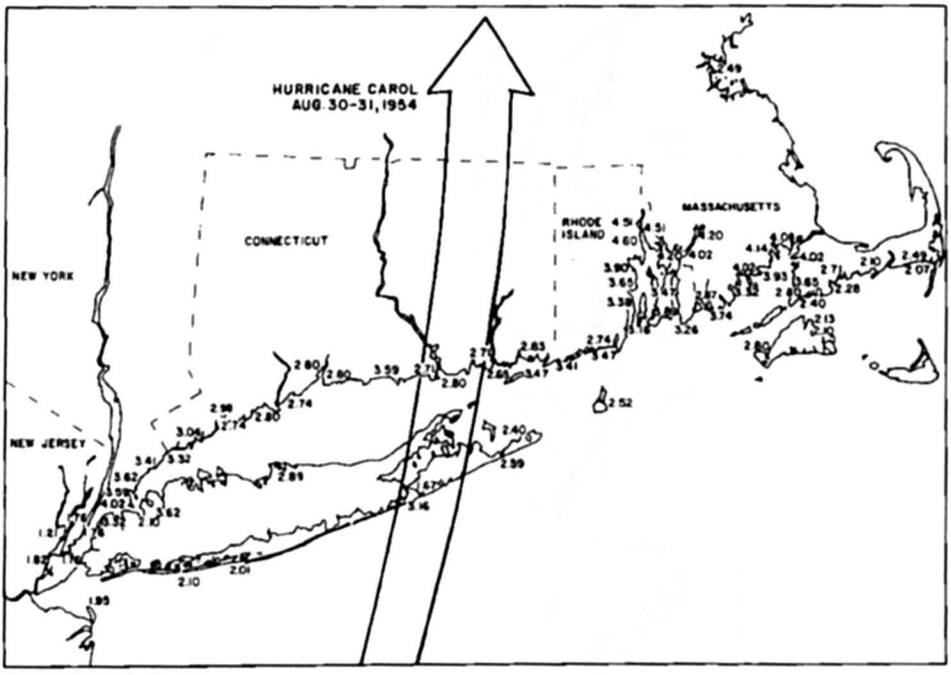


Fig. 6.21: Distribution of storm surge heights (meters) in the New York Bight due to Hurricane Carol of August 30–31, 1954. The arrow shows the hurricane track (PORE and BARRIENTOS, 1976)

SETHURAMAN (1979) studied the storm surge due to Hurricane Belle of august 8–10, 1976. The surge at Shinnecock Inlet (Long Island) is shown in Fig. 6.23. This surge occurred near the time of low tide; hence damage was minimal.

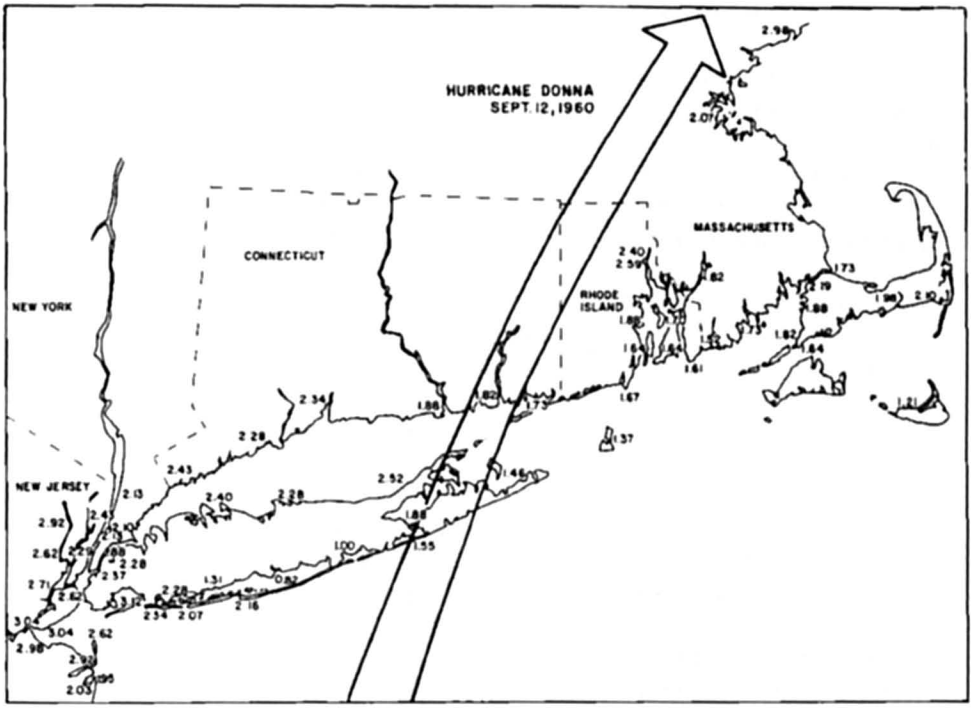


Fig. 6.22: Distribution of storm surge heights (meters) due to Hurricane Donna of September 12, 1960. The arrow shows the hurricane track (PORE and BARRIENTOS, 1976)

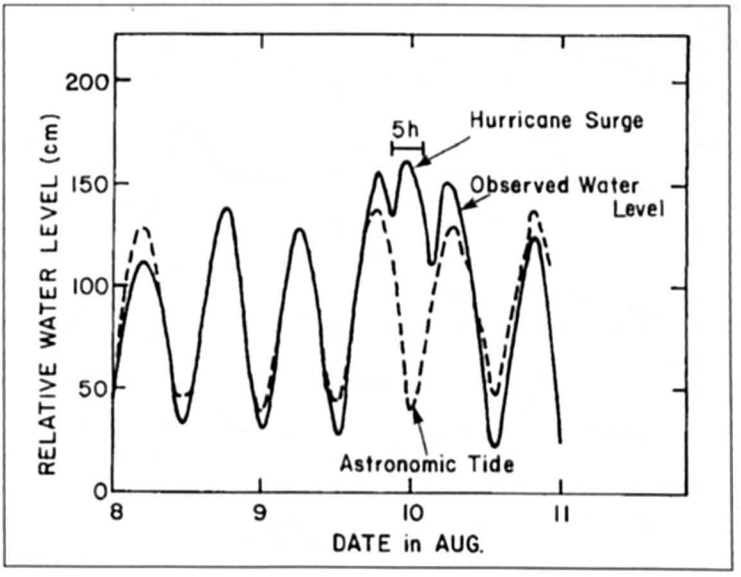


Fig. 6.23: Storm surge and predicted tide at Shinnecock Inlet on Long Island, New York (SETHURAMAN, 1979)

### 6.1.10 Storm Surges in New York Bay

KUSSMAN (1957) examined the storm surge problem for New York City and surrounding area. The storm amplitudes at several locations due to nine hurricanes are listed in Table 6.17.

The arrow shows the hurricane track. (PORE and BARRIENTOS, 1976)

WILSON (1959, 1961) did a comprehensive study of the hurricane generated storm surge problem in New York Bay. The technique of this study was as follows (WILSON, 1961, p. 548):

> A recursion formula is evolved, using the method of finite differences for time increments of $^1/_3$ hour, which relates tide elevation at the bay-mouth with two values of the elevation at $^1/_3$ and $^2/_3$ hour earlier and with values of wind-stress and pressure-gradient driving force components (directed towards New York Bay from several remote two dimensionally spaced off-shore-stations on the continental shelf) at times earlier by the periods taken for free long gravity waves to travel from the stations to the bay-mouth. The formula includes a cumulative forcing function term, which allows for the geostrophic influence of the earth's rotation and also for an "edge wave" effect northward along the eastern seaboard. Moreover it takes into account the observed tendencies of hurricane storm tides in New York Bay to develop resurgences at periods of 7 hours with decay rates of 50 % amplitude decrease per cycle. The coefficients of the "forcing functions", determined by correlation, tend to represent the storm size and speed and also the dynamic augmentation of the forced wave.

The predicted surge curves at selected locations for a design storm moving with a speed of 35 knots (65 km · h$^{-1}$) are shown in Fig. 6.24. The maximum storm surge amplitude and resurgence amplitude at several locations, due to a designed hurricane, are given in Table 6.18.

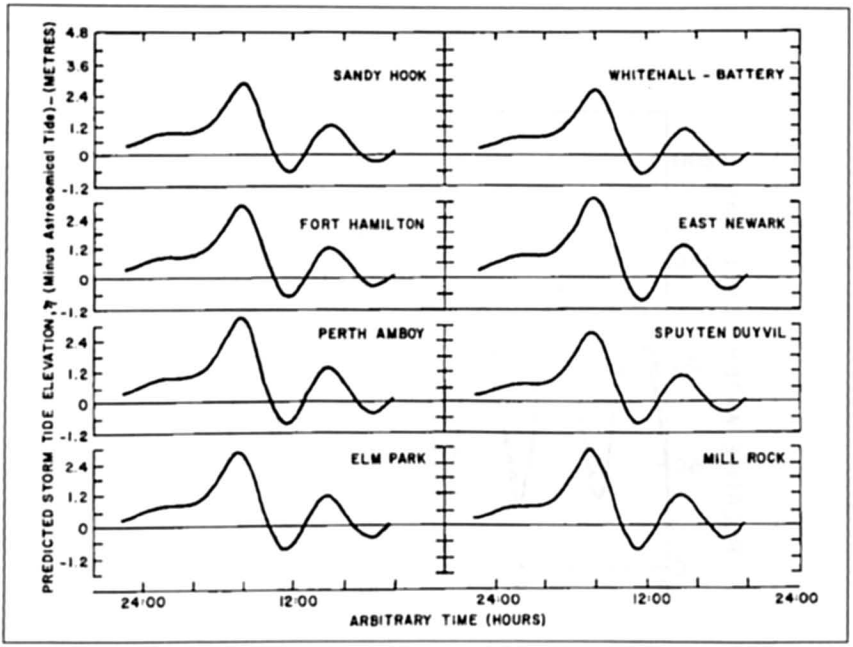


Fig. 6.24: Predicted storm surge heights at various locations in New York Bay for a design hurricane moving with a speed of 65 km · h$^{-1}$. (WILSON, 1959)

Table 6.17: Maximum storm surge amplitudes (m) in the New York City area and vicinity due to hurricanes during the period 1938–55 (KUSSMAN, 1957)

| Location | Sept. 21, 1938 | Sept. 15, 1944 | Nov. 25, 1950 | Nov. 7, 1953 | Aug. 31, 1954 | Sept. 11, 1954 | Oct. 15, 1954 | Aug 12–13 1955 | Oct. 14–16 1955 |
|---|---|---|---|---|---|---|---|---|---|
| Fort Hamilton, NY | 1.95 | 2.04 | 2.29 | 2.35 | 1.80 | 1.31 | – | 1.37 | 1.95 |
| Perth Amboy, NJ | 2.01 | 2.26 | 2.90 | 2.68 | 1.77 | 1.46 | 1.68 | 1.62 | 2.35 |
| Spuyten Duyvil, NY | 1.62 | 1.83 | 2.13 | 2.04 | 1.59 | 1.22 | 1.28 | 1.34 | 1.80 |
| Lawrence Point, NY | – | – | 3.05 | 3.17 | 3.32 | 1.89 | 1.80 | 1.59 | 2.26 |
| The Battery, NY | 1.95 | 1.95 | 2.26 | 2.32 | 1.71 | 1.16 | 1.37 | 1.28 | 1.80 |
| Sandy Hook, NJ | 1.80 | 2.56 | – | 2.41 | 1.86 | 1.34 | 1.40 | 1.25 | 1.89 |
| Willets Point, NY | 3.66 | – | – | 2.65 | 3.47 | 1.95 | 1.86 | 1.62 | 2.38 |
| Montauk (Fort Pond Bay), NY | 4.82 | 2.41 | – | 1.65 | 2.41 | 1.10 | 0.94 | 0.64 | 1.19 |
| New London, CT | 2.99 | 1.86 | 2.19 | 1.80 | 2.65 | 0.91 | 1.22 | 0.76 | 1.28 |

Table 6.18: Predicted maximum storm surge heights due to hurricanes in New York Bay (WILSON, 1959)

| Station | Maximum storm surge height (m) | | | Maximum first resurgence height (m) | |
|---|---|---|---|---|---|
| | Surge | Probable error (90 %) confidence limits | Resurgence | Probable error (90 %) confidence limits | |
| Sandy Hook | 2.71 | ± 0.21 | 1.04 | ± 0.21 | |
| Fort Hamilton | 2.68 | ± 0.21 | 1.04 | ± 0.21 | |
| Perth Amboy | 3.20 | ± 0.30 | 1.25 | ± 0.30 | |
| Elm Park | 2.87 | ± 0.46 | 1.16 | ± 0.46 | |
| Whitehall (Battery) | 2.53 | ± 0.18<br>– 0.24 | 1.01 | ± 0.18<br>– 0.24 | |
| East Newark | 3.11 | ± 0.49 | 1.25 | ± 0.49 | |
| Spuyten Duyvil | 2.65 | ± 0.30 | 1.04 | ± 0.30 | |
| Mill Rock | 2.99 | ± 1.37[a]<br>–0.91[a] | 1.19 | ± 1.37[a]<br>–0.91[a] | |

[a] The 90 % confidence limits are probably better than these for the main surge.

### 6.1.11 Narragansett Bay

MCALEER (1964) studied hurricane-generated storm surges in Narragansett Bay and particularly examined the role of barriers in reducing storm surge levels. The results were arrived at through hydraulic model investigations. Storm surges of up to 10–14 ft (3.0–4.3 m) in amplitude have been observed in Narragansett Bay. A hurricane storm surge in September of 1938 caused $ 100 million damage and killed 110 people. Ten people were killed in another storm surge during 1954. For some of the major hurricane tracks, Narragansett Bay lies in the dangerous northeast quadrant of the storm.

While some of the major hurricanes move relatively slowly along the southern part of the east coast of the United States, they may move faster when they approach the northern part of the coast. Hence, some storms that were reported as having stalled (or as moving

slowly) along the southern east coast suddenly accelerated and caused surges in Narragansett Bay some 8–10 h later.

Numerical and hydraulic models have been used to study the effects of barriers on storm surge amplitudes. The barriers are envisaged as rock fill barriers with large ungated navigation openings across the three entrances to Narragansett Bay. The results indicated tat the barriers would reduce the surge amplitudes by 6–7 ft (1.83–2.13 m) over the 120-mi$^2$ (311km$^2$) bay. These barriers will also decrease the mean tidal range somewhat.

PARARAS-CARAYANNIS (1975) used the bathystrophic model to compute the surges at Narragansett Pier, Rhode Island, generated by Hurricane Carol of 1954. This hurricane had a radius of maximum winds of 25 nautical miles (46.3 km) and moved with an average speed of over 33 knots (61 km.h$^{-1}$). Hurricane Carol arrived over Rhode Island at about 10:30 EST on August 31, 1954,with sustained wind speeds up to 90 mi · h$^{-1}$ (145 km · h$^{-1}$) and gusts up to 105 mi · h$^{-1}$ (169 km$^{-1}$). At Block Island, gusts up to 130 mi · h$^{-1}$ (209 km · h$^{-1}$) were measured.

Because of its intensity, speed of movement, and arrival at the time of high tide, exceptionally large surges and great destruction occurred. About a third of the city of Providence was under 8–10 ft (2.4–3.0 m) of water for several hours. PARARAS-CARAYANNIS (1975) mentioned waves up to 40-ft (12.2 m) in height. Maximum surge at Narragansett Pier was about 12.8-ft (3.9 m). Observed and computed surge profiles at Narragansett Pier are compared in Fig. 6.25.

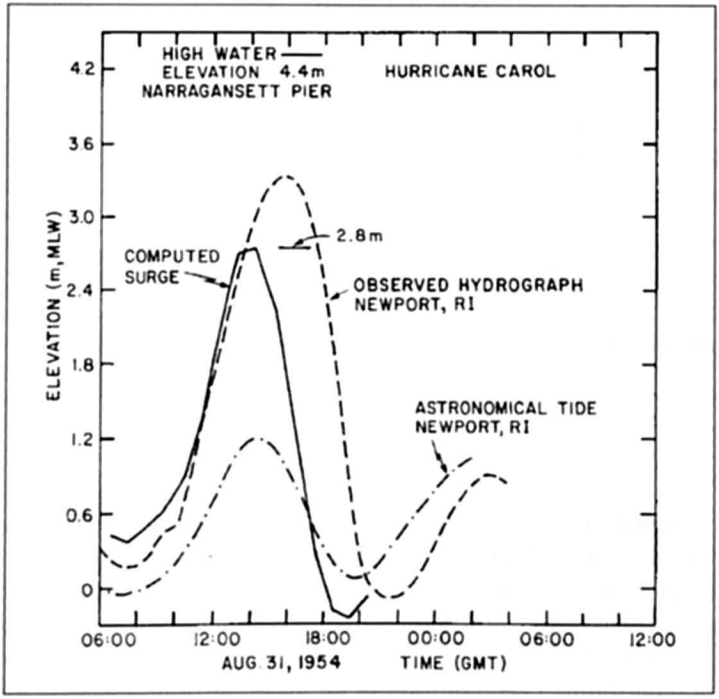


Fig. 6.25: Computed and observed surges at Narragansett Pier due to Hurricane Carol of 1954 (PARARAS-CARAYONNIS, 1975)

## 6.1.12 Hawaii

The Hawaiian Islands are not frequently subjected to storm surges. However, in November 1982 the storm surge caused by Hurricane Eva resulted in extensive damage to the islands of Kaui and Oahu and a few people died. Another major surge occurred in February 1983. Prior to these two surges, major surges occurred in the mid-1950s and some minor ones occurred in the 1970's.

Even though hurricanes are common over the eastern pacific and annually are seen in parts of central pacific, they are not found over Hawaii only. Four hurricanes impacted Hawaii during 1950 to 1992. Hurricane Iniki of September 6–13, 1992 with winds up to 160 mpH (258 kpH) was by far the strongest and most destructive. Fig. 6.26 shows the track of Hurricane Iniki and Fig. 6.27 shows that the passage of the eye over Kauai. Fig. 6.28 shows the wind field.

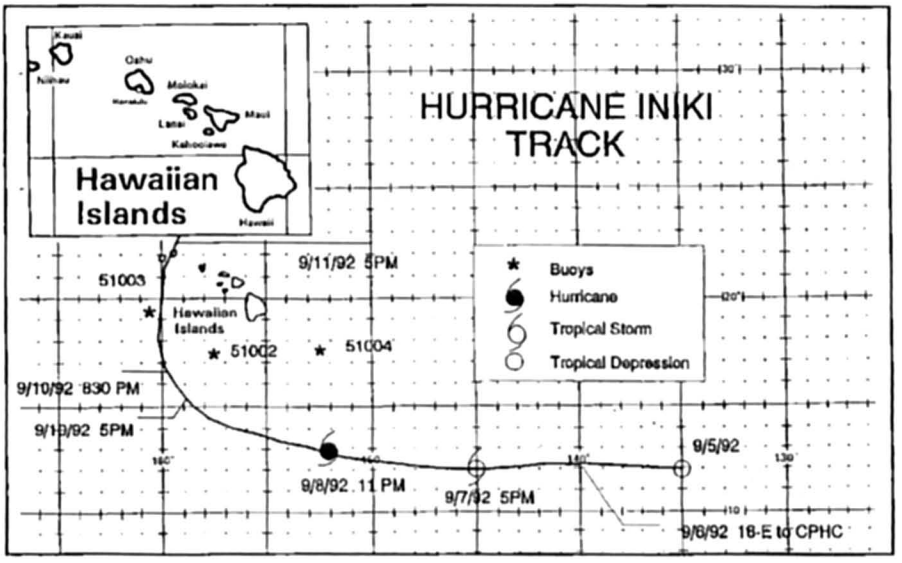


Fig. 6.26: Track of hurricane Iniki (ANON, 1993)

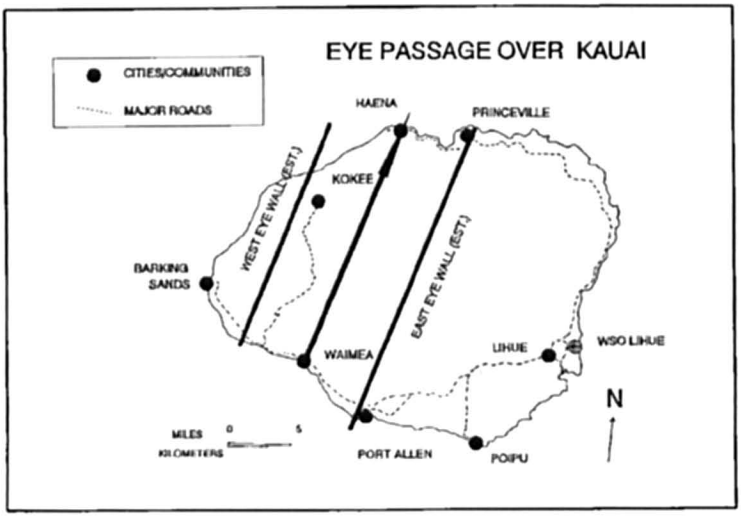


Fig. 6.27: Estimated Iniki Eye Passage over Kauai (ANON, 1993)

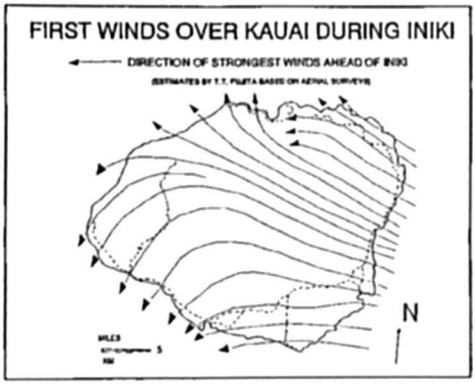


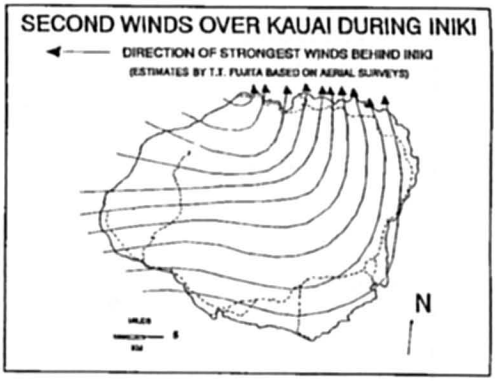


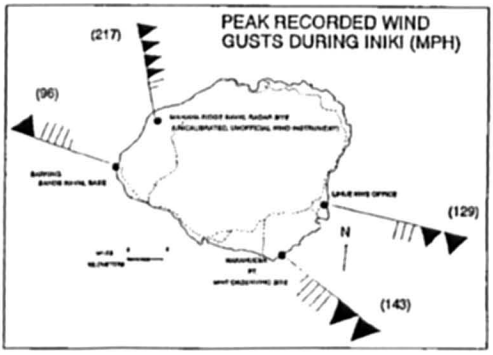


Fig. 6.28: Winds on Kauai from Iniki (ANON, 1993)

### 6.1.13 Mexico

Mexico is affected by storm surges on its Gulf of Mexico coast. Usually, the hurricane tracks over the Gulf of Mexico are such that they strike the United States rather than Mexico. However, on rare occasions, storm surges do occur on the Mexican coast also. On the Pacific coast of Mexico, also, storm surges occur rather infrequently. The storm surge due to Hurricane Paul of September 30, 1982 killed 24 people and caused considerable damage on the Baja California coast. In this hurricane, winds up to 240 $km \cdot h^{-1}$ were reported.

## 6.2 Central and South America Including the Caribbean

### 6.2.1 Caribbean Sea Region

Hurricanes and storm surges cause significant death and damage in the nations of the Caribbean Sea region. Of the four nations Haiti, Cuba, The Dominican Republic, and Honduras, maximum effects occurred in Haiti (FUNK, 1980) where about 8400 people were killed in the twentieth century. In 1963 alone, Hurricane Flora caused 5000 deaths. Hurricane David of August 29, 1979, killed 56 people in Dominica.

Hurricanes originating in the Caribbean Sea south of 15° N, especially in the month of August, are a potential threat to Jamaica (BLAKE, 1981). Winds of up to 45 $m \cdot s^{-1}$ generated storm surges with amplitudes up to 12 m at Manchioneal and Galina. Most of the northern coast of Jamaica was struck by surges of amplitudes between 4 and 8 m. There is evidence that the surge penetrated several kilometres inland. The damage was estimated to be about $ 126 million. About 75 % of the banana crop, 95 % of the fishing industry equipment on the north coast, and more than 800 houses were destroyed.

The storm surge of June 12, 1979, made people aware of what to expect and this helped in the safe evacuation of people during the 1980 surge.

### 6.2.2 Barbados

Barbados and other island of the Lesser Antilles are not usually subjected to storm surges, but they do have severe problems from swell and wind waves. There is a broad reef shelf surrounding Barbados and this makes the problem worse. The swell action is not associated with local storms from the Caribbean Sea but is due to intense extratropical cyclones in the North Atlantic Ocean (DONN and MCGUINNESS, 1959).

Swell with amplitudes up to 20 ft (6.1 m) can occur quite frequently. Between December 1957 and October 1958, at least four occasions of major swell activity occurred.

READING (1990) analysed the annual and decadal frequency of cyclones throughout the Caribbean region. For the "Historical Period" (i.e. period before weather charts were made) the Caribbean has been divided into ten sub-regions as shown in Fig. 6.29 for the modern period (i.e. chated period) a 5° latitude-longitude grid were used as shown in Fig. 6.30. Fig. 6.31 show the mean decadal frequency. Here cyclones are defined as warm cored systems of storm force or above while hurricanes are similar systems of hurricane intensity as defined by the U.S. Weather Bureau.

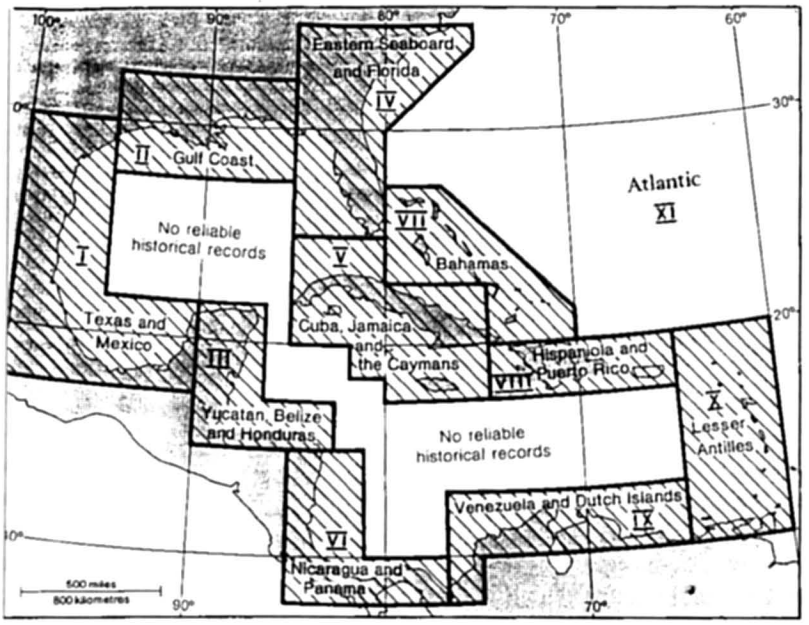


Fig. 6.29: Subregions of the Caribbean: historical data analysis (READING, 1990)

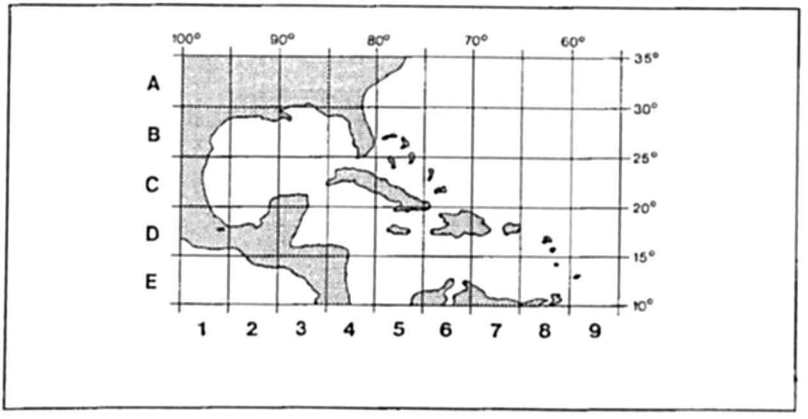


Fig. 6.30: Grid map of Caribbean area: modern data analysis (READING, 1990)

Fig. 6.31 shows that cyclone frequencies are greatest around the Western Bahamas, Eastern Seaboard of U.S and adjacent Atlantic. This can be explained by the fact that this area is within the favoured path of the two types of cyclones that affect this region; the Capeverde (CV) type systems, which recurve around the periphery of the sub-tropical high pressure cell to the north and the western Caribbean (WC) type which, after developing in the warm waters of the western Caribbean, almost immediately become affected by the westerly mid-latitude circulation and move steeply towards higher latitudes. Cyclone frequencies decrease from this northeastern core-region in roughly concentric circles. Areas of anomalously high frequencies between 15° N and 20° N east of 70° W reflect the strong preference of CV

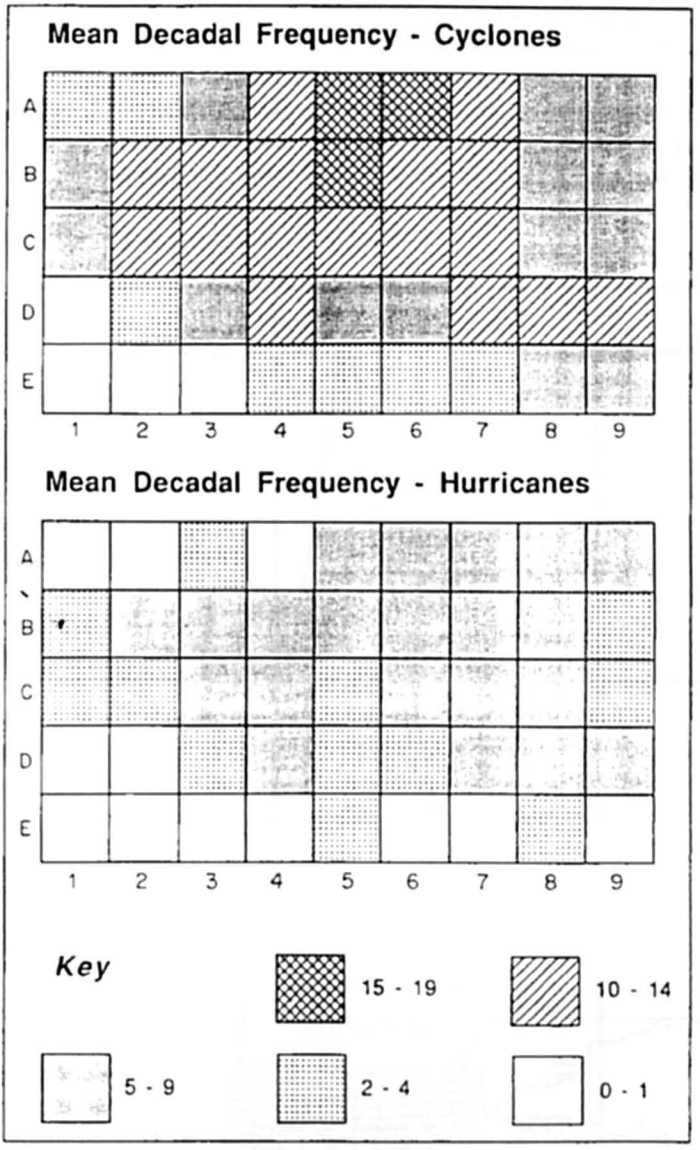


Fig. 6.31: Mean decadal frequency of cyclones and hurricanes: per 5° grid square (READING, 1990)

systems to enter the Caribbean at this latitude. Square D4 represents the major area of intensification for WC type systems.

Areas of relatively high hurricane frequencies (5–9 per decade) occur as two distinct bands. The western band represents the favoured track of WC type systems and the eastern band that of recurving CV type systems. These bands join over the north-central Caribbean, representing an area where both types of system frequently pass.

There is a strong latitudinal and longitudinal preference by the cyclones that develop, possibly a reflection of changes in the relative positions and intensity of the subtropical high pressure cell and the inter-tropical convergence zone. Another important result is that the

proportion of cyclones intensifying to hurricane status within the Caribbean has risen from 45 % in the 1970's to about 63 % in the 1990's.

MERCADO (1994) modelled storm surges in Puerto Rico using the SLOSH model. Fig. 6.32 shows the grid for the SLOSH basin. The grid on which the surge computations and inundation are made has a resolution of approximately 2 x 2 miles (3.2 x 3.2 km). The model was tested against hurricane Hugo storm surge with amplitudes up to 3.5 m.

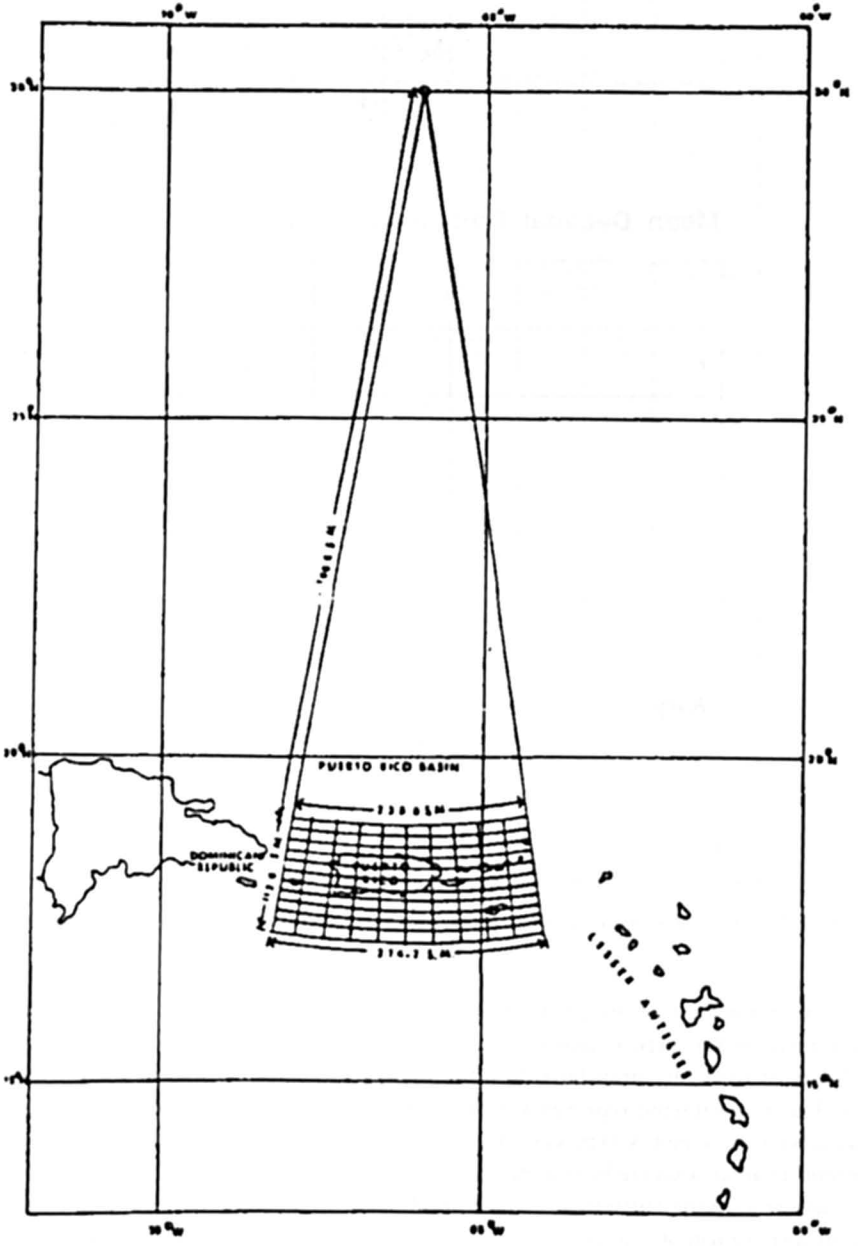


Fig. 6.32: Puerto Rico SLOSH Basin and grid system used (MERCADO, 1994)

Die Küste, 63 Global Storm Surges (2001), 1-623



## 6.3 North Indian Ocean

Discussion in this section will mainly concentrate on the storm surges in the Bay of Bengal and Arabian Sea. Although the frequency of the tropical cyclones in the North Indian Ocean is not quite high, the coastal regions of India, Bangladesh and Myanmar suffer most in terms of loss of life and property caused by the surges. The reason besides the inadequate accurate prediction, are the low lands all along the coasts and considerably low-lying huge deltas, such as, Gangetic delta and Ayeyarwady delta.

### 6.3.1 Bay of Bengal

Storm surges are extremely serious hazards along the east coast of India, Bangladesh, Myanmar and Sri Lanka. Although Sri Lanka is affected only occasionally by the storm surge, however tropical cyclones of November 1964, November 1978 and the recent cyclone of November 1992 have caused extensive loss of life and property in the region. Storm surges affecting Myanmar are also to much less extent in comparison with Bangladesh and India. Notable storm surges, which have affected Myanmar, have been during May 1967, May 1968, May 1970 and May 1975, of which May 1975 was the worst cyclone. The storm surge due to the May 1975 event penetrated at least 100 km into the Ayeyarwady river system and caused serious inland flooding (LWIN, 1980)

A detailed review of the problem of storm surges in the Bay of Bengal is given by RAO (1982), ROY (1984), MURTY (1984), MURTY et al. (1986), DAS (1994 a, b), DUBE (1998a), DUBE et al. (1997, 1999b, 2000c) and CHITTIBABU (1999). In this section, a brief account of the problem of storm surges in Bangladesh, east coast of India, Myanmar and Sri Lanka would be given. Of all the countries surrounding the Bay of Bengal, Bangladesh suffers most from storm surges.

#### *(a) Bangladesh*

It is probably not incorrect to say that Bangladesh suffered more from storm surges than any other country. ALI (1979) summarized the main factors contributing to the disastrous storm surges on the coast of Bangladesh: (1) shallow water, (2) convergence of the bay, (3) high astronomical tide, (4) thickly populated low-lying islands, (5) favorable cyclone track, and (6) innumerable number of inlets and few large estuaries and rivers. Except in the eastern and southeastern parts of the country (where there are hills) most of the land is flat. Many places, although 160 km from the sea are not more than 9.1 m above sea level. A rise of a few meters in sea level can bring large areas of land under water (GILL, 1975).

Another peculiar problem is the topographical changes that appear to occur in decadal periods in the courses of the rivers and tributaries. The storm surge problem became worse after the Assam earthquake of August 1950 because millions of tons of material from the mountains was dislodged by the earthquake, which ultimately found its way into the river system and caused raising of the bottom by as much as 4.3 m in certain locations.

The approximate number of people killed in Bangladesh because of storm surges is listed in Table 6.19. For comparison, a storm surge in 1881 in China supposedly killed 300,000 people. A surge in Japan in 1923 killed 250 000 people. Another surge in Japan in 1960 killed

Table 6.19: Number of people killed in Bangladesh due to storm surges. Only those cases in which the number is more than 5000 are included

| Year | Estimated approximate No. of deaths |
|---|---|
| 1822 | 40, 000 |
| 1876 | 1,00, 000 |
| 1897 | 1,75, 000 |
| 1912 | 40, 000 |
| 1919 | 40, 000 |
| 1960 | 15, 000 |
| 1963 | 11, 520 |
| 1965 | 19, 279 |
| 1970 | 3,00, 000 |
| 1985 | 11,069 |
| 1991 | 1,40,000 |

Table 6.20: Damage in Bangladesh (in addition to human death toll) due to the November 1970 cyclone and storm surge (FRANK and HUSSAIN, 1971)

| Damage | Toll |
|---|---|
| Population affected | 4.7 million |
| Crop loss | U.S.$ 63 million |
| Loss of cattle | 280 000 |
| Loss of Poultry | 500 000 |
| Houses damaged | 400 000 |
| School damaged | 3 500 |
| Fishing boats (marine) destroyed | 9 000 |
| Fishing boats (inland waters) destroyed | 90 000 |

5000 people. A surge in 1780 in the Antilles killed 22 000 people and one in the Cuba-Haiti area in 1963 killed 7196 people (FRANK and HUSSAIN, 1971).

The November 13, 1970, storm surge was supposed to be the worst on record in Bangladesh. The death toll was initially estimated to be over a million people. Later estimates brought it down to 500,000, then 300,000, and finally 200,000. Whatever the correct toll my be, this storm surge event created a new awareness of tropical cyclones in general and of storm surges in particular, not only in Bangladesh but all over the world. In a storm surge event of this magnitude, there is not only the human death toll but there are other damages as well. The damage in Bangladesh due to this storm surge is listed in Table 6.20. The salt water from the sea flooded the land during the surge event, leaving much salt on the land, which for 4–5 years after the event affected crops until rains finally washed away the salt.

There are more than 40 known cases of storm surges in Bangladesh during the period 1800–1999. A partial list is given in Table 6.21 for the period 1876–1999. It is quite probable that some of the entries in the table are wrong. Also, sometimes the total water level (i.e. tide + surge) is reported as surge. The observed water levels during storm surge events at six different locations in Bangladesh during the period 1965–76 are listed in Table 6.22. The storm surge and the pertinent meteorological and tidal information at Chittagong for the period 1960–70 are given in Table 6.23. ALI (1980b) summarized the numerical models that have

Table 6.21: List of storm surges in Bangladesh (1582–1999)

| No. | Date | Location | Damage |
|---|---|---|---|
| 1 | 1582 | Near Backergunge, Bangladesh | 200,000 deaths, Destruction reported due to surge |
| 2 | 1699 | Sundarban coast, Bangladesh | 50,000 deaths |
| 3 | 1760 | Sundarban coast, Bangladesh | Extensive damage |
| 4 | 1765 | Chittagong coast, Bangladesh | Extensive damage |
| 5 | 1767 | Barisal,Bangladesh | 13.03 m surge,30,000 deaths |
| 6 | May–June, 1797 | Chittagong, Bangladesh | 2 ships sank. No estimate of deaths |
| 7 | 6 June, 1822 | Barisal/Backergunge, Bangladesh | 50,000 deaths, storm wave swept the region |
| 8 | 16 May, 1869 | Khulna | Surge entered through the Pussur and Haringhata Rivers and inundated a vast area causing damage of life and property. 250 people died in Morelganj |
| 9 | 31 October, 1876 | Backergunge, Bangladesh | This was the infamous Backergunge cyclone. Peak water levels in Bangladesh varied from 3 to 13.6 m, including tide and wind waves. 100,000 deaths in Bangladesh (then part of India). This India Meteorological Department was expanded following this surge. GILL (1975), but this could be an over-estimate lot of destruction. Inundation subsided in 2 hours |
| 10 | 27 October, 1893 | Noakhali | |
| 11 | October, 1895 | Sunderban/Bagerhat, Subdivision, Bangladesh | Damage estimates not available |
| 12 | 24 October, 1897 | Chittagong, Kutubdia Island, Bangladesh | 175,000 deaths. Thousands died in the epidemic which followed the calamity |
| 13 | May, 1898 | Taknaf, Bangladesh | Surge caused huge damage |
| 14 | November, 1901 | Western Sunderbans, Bangladesh | Damage estimate not available |
| 15 | 15–18 October, 1909 | Backerganj, Bangladesh | 172 deaths, extensive damage |
| 16 | 2–6, December, 1909 | Cox's Bazar, Bangladesh | Storm surge caused heavy damage |
| 17 | April, 1911 | Teknaf, Bangladesh | Damage estimate not available |
| 18 | May, 1917 | Sunderbans, Bangladesh | Damage estimate not available |
| 19 | 20–25 September, 1919 | Barisal, Bangladesh | 3,500 deaths in Bangladesh |
| 20 | 19–24 April, 1922 | Cox Bazar, Bangladesh | Damage to ships, No deaths |
| 21 | 3–7 May, 1923 | Teknaf, Bangladesh | 25000 houses damaged |
| 22 | 19–23 May, 1926 | Cox's Bazar, Bangladesh | 2700 deaths |
| 23 | 22–26 May, 1941 | Between Barisal and Noakhali, Bangladesh | 3.03–3.64 m surge. 5000 deaths due to storm surge |
| 24 | 21–24 October, 1947 | Between Chittagong and Barisal, Bangladesh | 500 deaths |
| 25 | 17–19 May, 1948 | Between Chittagong and Noakhali, Bangladesh | Damage estimate not available |
| 26 | 15–20 November, 1950 | Patuakhali, Bangladesh | Damage estimate not available |
| 27 | 16–19 May, 1958 | East Meghna Estuary, Bangladesh | Cargo and country boats capsized, Sandwip island badly affected |
| 28 | 21–24 October, 1958 | Noakhali and West Meghna Estuary, Bangladesh | Up to 2 m suges in Bangladesh and West Bengal State of India, 500 deaths |
| 29 | 29 May, 1960 | Sunderbans, Bangladesh | 3.2 m surge, extensive damage |

Table 6.21 (continued)

| No. | Date | Location | Damage |
|---|---|---|---|
| 30 | 8–10 October, 1960 | Noakhali, Meghna Estuary, Bangladesh | 6 m surge. 6,000 deaths in offshore island of Noakhali, Barisal, Chittagong. |
| 31 | 30–31 October, 1960 | Nathalie, Chittagong, Bangladesh | 6.6 m surge. 5,149 deaths |
| 32 | 9 May, 1961 | Noakhali West Mehgna Estuary, Bangladesh | 3 m surges. 11,468 deaths |
| 33 | 29–30 May, 1961 | Chittagong, Cox's Bazaar, Noakhali, offshore islands, Bangladesh | 2.6–4.5 m surge. Peak water levels up to 9 m. |
| 34 | 26–30 October, 1962 | Feni, Bangladesh | Damage estimate not available |
| 35 | 28–29 May, 1963 | Noakhali, Chittagong, Bangladesh | Peak water levels up to 8.1 m. 11,520 deaths |
| 36 | 5–8 June, 1963 | Jessore, Bangladesh | Peak surge 3.1 m |
| 37 | 25–27 October, 1963 | Teknaf, Bangladesh | Damage estimate not available |
| 38 | 11 April, 1964 | Bangladesh | 196 deaths |
| 39 | 9–12 May, 1965 | Barisal and Noakhlai, Bangladesh | 3–6 m surge. 19,279 deaths |
| 40 | 26 April – 1 May, 1965 | Hatia, Bangladesh | Up to 7.6 surges. 12,000 deaths |
| 41 | 5 November, 1965 | Bangladesh | Up to 3.7 m surges |
| 42 | 11–15 December, 1965 | Cox's Bazaar, Bangladesh | 2.4 –3.6 m surge. 873 deaths |
| 43 | 23 September– 1 October, 1966 | Noakhali, Bangladesh | 6.0 – 6.7 m surge. 850 deaths |
| 44 | 1 November, 1966 | Bangladesh | Peak water levels up to 10 m |
| 45 | 7–12 December, 1966 | Cox's Bazaar, Bangladesh | Damage estimate not available |
| 46 | 8–11 October, 1967 | Khulna, Bangladesh | Peak water levels up to 9.3 m |
| 47 | 20–24 October, 1967 | Cox's Bazaar, Bangladesh | Up to 7.6 m surge, 51 deaths |
| 48 | 17 April, 1969 | Bangladesh | 75 deaths |
| 49 | 10 October, 1969 | Khulna, Bangladesh | Peak water levels up to 8 m. |
| 50 | 2–7 May, 1970 | Cox's Bazaar, Bangladesh | Up to 5 m surge |
| 51 | 18–23 October, 1970 | Chandpur, Bangladesh | 4.7 m surge. 300 deaths |
| 52 | 8–13 November, 1970 | Between Noakhali and Chittagong, Bangladesh | 3–10 m surge, 300,000 deaths, 2,80,000 cattle killed, 44,00,000 houses destroyed, 18,000 boats destroyed, unofficial estimation of deaths more than 500,000 |
| 53 | 8 May, 1971 | Khulna to Chittagong and offshore islands, Bangladesh | 2.4–4.2 m surge. Other information not available |
| 54 | 28–30 September, 1971 | Chandpur, Bangladesh | Surge plus tide of 5 m |
| 55 | 5–6 November, 1971 | Chittagong, Bangladesh | Water levels up to 5.5 m |
| 56 | 28–30 November, 1971 | Sunderban coast, Khulna, Bangladesh | 1 m surge |
| 57 | 14–18 November, 1973 | Barisal, Bangladesh | 1.0 m surge. Peak water level including wind waves 3.8 m |
| 58 | 5–9 December, 1973 | Patuakhali coast and offshore islands, Bangladesh | Peak water level 6.2 m. Peak surge 4.5 m. 183 deaths |

| | | | |
|---|---|---|---|
| 59 | 13–15 August, 1974 | Khulna, Bangladesh | 6.7 m surge |
| 60 | 24–28 November, 1974 | Chittagong, Bangladesh | 3.0–5.1 m surge. 20 deaths, 50 injured, 280 persons missing, 1,000 cattle killed, 2,300 house destroyed |
| 61 | 9–12 May, 1975 | Bhola, Cox's Bazaar, Khulna, Bangladesh | 5 deaths. 4 injured. 36 fishermen missing |
| 62 | 4–8 June, 1975 | Chittagong, Bangladesh | Peak surge 4.0 m, 50 deaths |
| 63 | 24–28 June, 1975 | Bangladesh | Tide and surge 4.8 m |
| 64 | 7–11 Nov, 1975 | Barisal, Noakhali, Bangladesh | Maximum surge 3.1 m |
| 65 | 15–21 October, 1976 | Meghna Estuary, Bangladesh | Tide plus surge 5.0 m at Comapaniganj |
| 66 | 20 November, 1976 | Chittagong, Bangladesh | 1.0 m surge. 2.1 m tide |
| 67 | 9–13 May, 1977 | Noakhali, Bangladesh | 0.6 m surge. 0.7 m tide |
| 68 | 1–3 October, 1978 | Khulna and Sunderban coast, Bangladesh | Damage estimate not available |
| 69 | 6–10 December, 1981 | Khulna, Bangladesh | 2–4.5 m surge 72 deaths and 200 deaths in India. |
| 70 | 14–15 October, 1983 | Chittagong coast near the Feni River, Bangladesh | 43 deaths. Substantial damage |
| 71 | 5–9 November, 1983 | Chittagong, Cox's Bazaar, Bangladesh | 1.5 m surge, 300 deaths. Substantial damage |
| 72 | 20–25 May, 1985 | Cox's Bazaar, Chittagong, Sandwip, Bangladesh | 4.55 m surge. 11,069 deaths. 94,000 houses destroyed |
| 73 | 7–9 November, 1986 | Chittagong, Bangladesh | 0.61 m surge, 50 deaths. Substantial damage |
| 74 | January 30–<br>Februar–4, 1987 | Chittagong, Bangladesh | Damage estimate not available |
| 75 | 24–30 November, 1988 | Khulna coast near Raimangal river, Bangladesh | 4.4 m surge. 11,683 deaths in Bangladesh, 532 deaths in India 6,000 missing. 65,000 cattle killed. 15,000 deer killed. 9 royal Bengal tigers killed. Substantial crop damage. |
| 76 | 7–8 October, 1990 | Barisal, Bangladesh | 150 fishermen missing. Substantial damage |
| 77 | 16–18 December, 1990 | Khulna coast, Bangladesh | 4.4 m surge, 5683 deaths, 15,000 and 9 tigers killed, 65,000 cattle killed |
| 78 | 25–30 April, 1991 | Chittagong, Cox's Bazaar, Bangladesh | 6–7.6 m surge. 140,000 deaths. 70,000 cattle killed. Great damage |
| 79 | 31 May–2 June, 1991 | Noakhali-Patakhali, Bangladesh | 2.5 m surge, 300 deaths |
| 80 | 16–21, Nov 1992 | Teknoff, Bangladesh Coast | Damage estimation not available |
| 81 | 21–25 Nov 1995 | Coxbazar, Bangladesh | Damage estimation not available |
| 82 | 26–29 October, 1996 | Sundarban coast, Bangladesh | 1.52–2.12 m surge, 9 deaths, 2000 fishermen missing, 15,000 cattle killed, 10,000 houses damaged |
| 83 | 15–20 May, 1997 | Chittogong, Bangladesh | 4.55 m surge, 155 deaths |
| 84 | 24–27 September, 1997 | Noakhali-Chittogong coast, Bangladesh | 3.03–4.55 m surge at Bhoala, 1.52–2.12 m surge at Barguna, 2.42–3.03 m surge at Galachipa, 67 deaths. At Khagrachhari, 16 villages and a part of the district town went under 1.82–2.42 m surge. |
| 85 | 4–9 Nov 1997 | Bangladesh coast | 3.0 m surge, substantial damage |
| 86 | 17–21 May 1998 | Bangladesh coast | 16 deaths |

Table 6.22: Observed water levels (tide + surge) in meters at six locations in Bangladesh (ALI, 1980b)

| Date | Khulna | Barisal | Sandwip | Chittagong | Chandpur | Companigonj |
|---|---|---|---|---|---|---|
| May 12. 1965 | – | 2.84 | 2.90 | – | 2.53 | 2.21 |
| May 31. 1965 | 2.25 | 2.44 | 3.73 | – | 3.80 | 7.13 |
| Oct 11. 1967 | 2.59 | – | – | 2.92 | – | 8.75 |
| Oct 24. 1967 | 2.44 | – | – | 1.89 | – | 7.61 |
| May10. 1968 | – | – | 2.78 | 3.38 | – | 4.74 |
| Oct 10. 1969 | 2.61 | – | 7.21 | 3.20 | 4.27 | 4.63 |
| Oct 23. 1970 | 3.02 | 3.47 | – | – | 4.74 | 4.21 |
| Nov.12. 1970 | – | 2.67 | 3.86 | 5.58 | 4.09 | 5.58 |
| Sep. 30. 1967 | 3.08 | 3.04 | – | – | 5.03 | 4.21 |
| Oct. 20. 1976 | – | 4.64 | 3.00 | 3.17 | 3.54 | 5.02 |

Table 6.23. Some pertinent details for storm surges at Chittagong, Bangladesh (FLIERL and ROBINSON, 1972)

| Date | Storm speed ($km \cdot h^{-1}$) | Maximum observed wind speed ($km \cdot h^{-1}$) | Astronomical tide (m) | Observe sea level (m) | Maximum surge (m) |
|---|---|---|---|---|---|
| Oct 11, 1960 | 20 | 161 | 1.5 | 6.0 | 4.5 |
| Oct 31, 1960 | 38 | 193 | 0.0 | 6.6 | 6.6 |
| May 9, 1960 | 38 | 161 | 1.2 | 4.8 | 3.6 |
| May 30, 1960 | 22 | 161 | 0.6 | – | – |
| May 29, 1960 | 40 | 209 | 0.3 | – | – |
| Nov. 9, 1965 | 42 | 161 | 1.2 | – | – |
| Dec. 15, 1965 | 32 | 161 | 0.3 | – | |
| Nov. 13, 1970 | 20 | 161 | 1 | 6.0–9.0 | 4.2–7.2 |

been developed for storm surges on the coast of Bangladesh. Probably the first model is by DAS (1972) for the coasts of India and Bangladesh, and he simulated the surge dues to the November 1970 cyclone. This was extended by DAS et al. (1974). They investigated the effect of the central pressure drop and the speed of movement of the cyclone. Nomograms were given for the peak surge for three different tracks. This work will be considered under the subsection Storm Surges in India. FLIERL and ROBINSON (1972) also developed a liner linear model specifically for the coast of Bangladesh. A nomogram for practical purpose was also prepared.

ISLAM (1971) discussed the storm surge protection problem in Bangladesh. He mentioned the construction of various types of raised platforms (Machan, Killa., etc.) for people and animals. KIBRIA (1980) discussed the planned delta works to protect the Bangladesh coast from storm surges.

DUBE et al. (1984b, 1985b, 1985c, 1986a, 1986b) and SINHA et al. (1983, 1985, 1986) developed several models to simulate the surges associated with serve severe cyclonic storms hitting the coast of Bangladesh. Their models are confined to the northern shelf of the head Bay region with southern open Sea boundary at 19° N. Curvilinear coastal boundary treatment analogous to that used by Johns et al. (1981) was utilized by them. Experiments were carried out to determine the optimum grid resolution, which turned out to be 30 km in the E-W and

8–20.5 km in the N–S directions (varying because of the coordinate transformation). Authors attempted several problems including the computation of inland inundation using continuously deforming shoreline model and the impact of Meghna river discharge on storm surges. In the absence of the observed reliable data on storm surges it was difficult to compare the results, however limited comparisons with observed peak surge were given.

Fig. 6.33 and 6.34 show respectively the computed peak surge along the Bangladesh associated with November 1970 Chittagong cyclone and the temporal variation of predicted sea surface elevation at Maijdi. The impact of inclusion of the river and its discharge on the peak surge and on the temporal evolution of surge is clearly seen from these experiments.

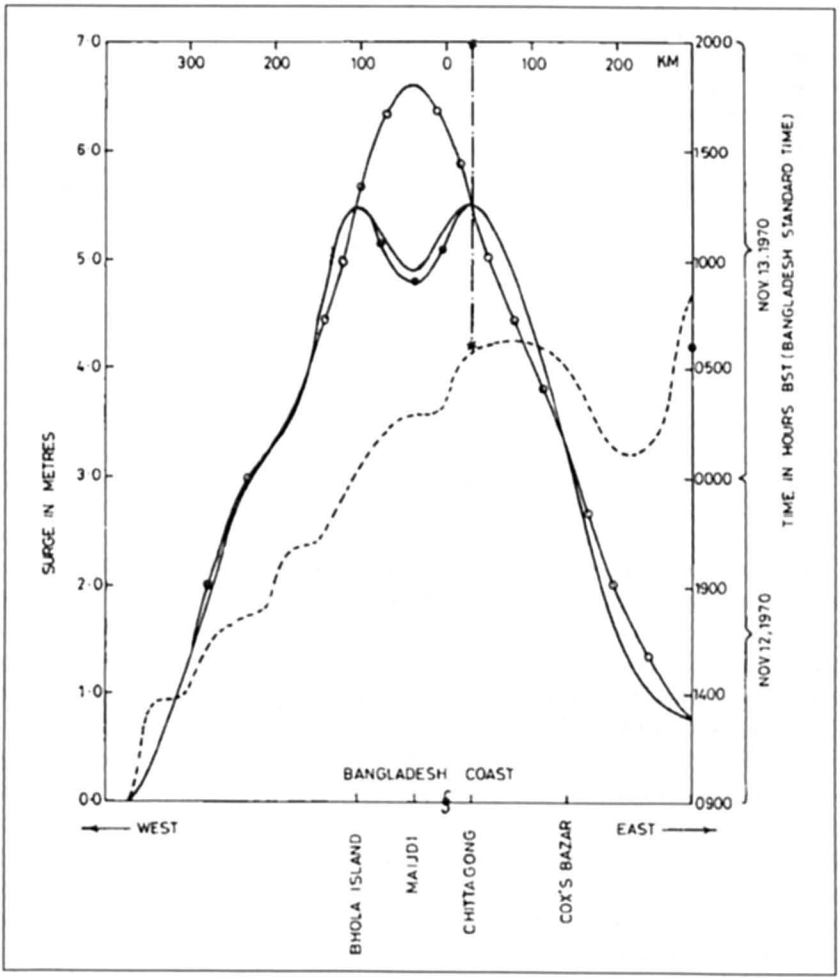


Fig. 6.33: Maximum predicted sea - surface elevation and its time of occurrence along the Bangladesh coast. § = place of landfall; • = time of landfall (on the time axis); - = peak surge envelope (BRM1) with discharge; - - - = time of occurrence (BRM1); -•-•- = peak surge envelop (BRM2) without discharge; -o-o- = peak surge envelope (MWR) without river; *-.-.-* = observed range of sea - surface elevation in excess of predicted tide (DUBE et al., 1986b)

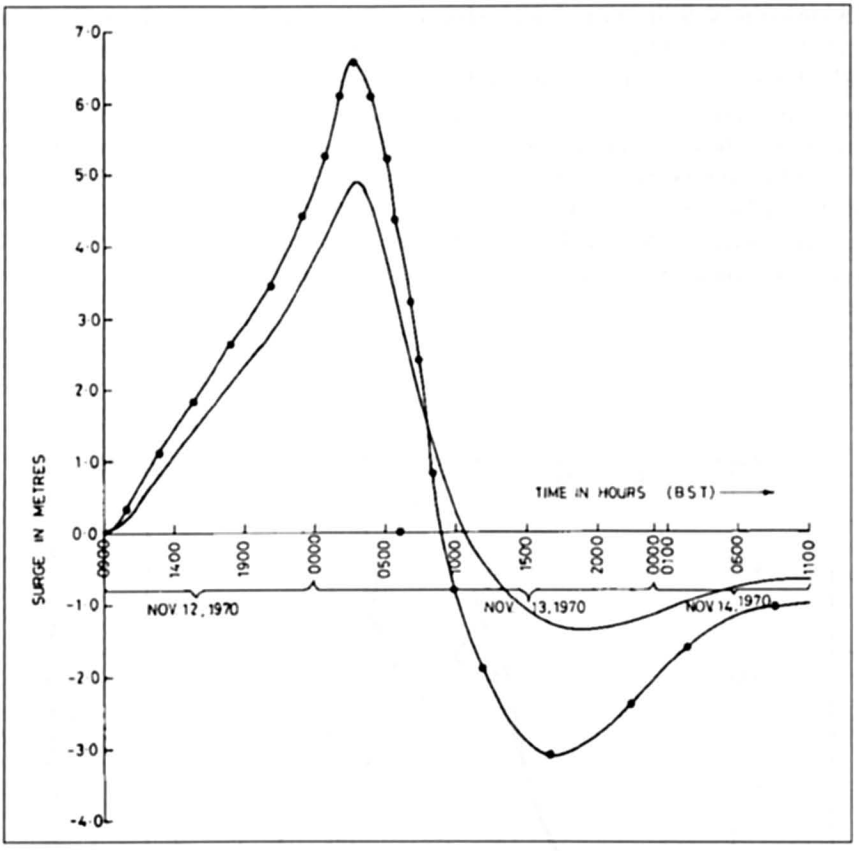


Fig. 6.34: Time variation of the predicted sea – surface elevation at Maijdi. • = time of landfall (on time axis); ___ = BRM1 (with discharge); –•–•– = MWR (without river). (DUBE et al., 1986b)

Considering the complexities of the Bangladesh coastline with numerous inlets, offshore islands and chars, the smooth curves of the model coast resulting from the curvilinear coordinate transformation appear to be a quite limitation of these models. Recognizing this shortcoming, JOHNS et al. (1985) developed a model for the Head Bay region using rectangular Cartesian coordinates. The southern open boundary of the model was at 19° 33' N, the grid size 17.6 km E–W by 19.8 km N–S, and five idealized river models, each of uniform depth and width and length 200 km were included to represent the main channels in the Ganges Delta. The model was nested with in a large curvilinear model of the whole Bay (JOHNS et al., 1981), which provided boundary input of tide and surge. The model was used to study the tide-surge interaction in the Bay of Bengal for details refer to section 4.5.2.

A detailed numerical storm surge prediction model for the Bangladesh region was developed by FLATHER (1994). The formulation used by the author allows the delta to be included in a much more complete and realistic manner. This was achieved by a modification in the standard depth-averaged equations with a numerical scheme in which the solution of one-dimensional equations for narrow channels and two-dimensional equations for the open sea are combined within a unified computational framework. In this manner author was able to realistically model the complex coastal area and the Gangetic Delta. Using the scheme earlier designed by FLATHER and HEAPS (1975), the model also allows the inland inundation.

The model was used to investigate the storm surges generated by November 1970 and April 1991 cyclones. Hindcast and "forecast" simulations of April 1991 event was described using forcing derived from a semi analytical cyclone model with data supplied by the Joint model with data supplied by the Joint. Typhoon Warning Center (JTWC). The results show that the timing of cyclone landfall and its coincidence with high tide determine the areas worst affected by flooding.

ALI et al. (1997b) studied the backwater effect of tides and storm surges on fresh water discharge through the Meghna estuary. In another study ALI et al. (1997a) used a two-dimensional model to study in detail the interactions between river discharge, storm surges and tidal interactions in the Meghna river mouth in the Bangladesh. The study considers the interactions mostly in terms of flow across the river mouth under the three forcing, individually and in different combinations of them. The model has been able to produce some interesting features of the interaction between three forcing in the mouth of Meghna estuary. It is shown by the authors that river discharge and tidal flow across the river mouth act both positively and negatively depending on the tidal phase, positively during the high tide and negatively during low tide. The result is also found true for the combination of all three forces. In most of the cases, river discharge is found to act in opposition to the storm surges. The interaction between river discharge and storm surges is shown to be dependent on their relative magnitudes. However, in respect of the total elevation in the estuarial region, river discharge tends to increase the surge height.

Recently HENRY et al. (1997) used a finite element model to study the tides and storm surges in offshore waters of the Meghna estuary. The model reproduced tidal elevations well at the four coastal sites used for model verification and simulated surge elevations at the coast with acceptable accuracy.

### *(b) East Coast of India*

India is prone to storm surges on both its east and west coast although the frequency and severity of surges is greater on the east coast. Some important storm surges (form the point of view of loss of life) on the Bay of Bengal coast of India are listed in Table 6.24. List, which is based on various sources, might not be totally correct. Also, in this list, several minor surges in which less than 100 people were killed are excluded.

Some pertinent information on six storm surges at Saugor Island (in the northwestern part of the Bay of Bengal) during the period 1948–55 is given in Table 6.25. This table also compares the observed surges with those computed using simple empirical formulae (JANARDHAN, 1967).

RAO and MAZUMDAR (1966) and RAO (1968) used empirical relations to calculate storm surges on the east coast of India, south of 17° N. Topography near the shore and wind waves were also included in the calculations. Based on these calculations, RAO (1968) classified the east coast of India (and the coasts of Bangladesh and Burma for comparison into three types. These results are summarized in Table 6.26. In this table, the values listed under "storm surge amplitude" pertain to a storm with winds up to 40m · s –1. The values listed under "total water level" include the peak surge plus the wind waves.

Classification of types A, B, and C is as follows. For a type A coastline, the maximum total water level is less than or equal to 2 m during storm surge events, for type B the amplitude is between 2 and 5 m, and for type C the amplitude is greater than 5 m. This classification is shown in Fig 6.35, for the east and west coasts of India (the west coast of India will be

Table 6.24: List of storm surges along east coast of India (1681–1999)

| No. | Date | Location | Damage |
|---|---|---|---|
| 1 | 10 November, 1681 | Nagapattinam, Tamilnadu, India | 14,000 deaths |
| 2 | 18 April, 1700 | Visakhapatnam, Andhra Pradesh, India | Several ships lost at sea. No estimate of number of deaths available |
| 3 | December, 1706 | Coringa, Andhra Pradesh, India | No exact estimate of the number of deaths, except a statement that people in great number were lost |
| 4 | 18 December, 1709 | Coastal Ramnad, Tamilnadu, India | Extensive inundation of coastal Ramnad. Major surge. Deaths in thousands |
| 5 | 7–12 October, 1737 | Mouth of Hoogly River, West Bengal, India | 12 m surge (probably includes tide and wind waves). Surge penetrated 100 km inland through the Hoogly River. 300,000 deaths in India and Bangladesh (could be a slight exaggeration) |
| 6 | 2 October, 1747 | Madras, Tamilnadu, India | Extensive damage, no estimate of deaths |
| 7 | 31 October, 1752 | Madras, Tamilnadu, India | Extensive damage, no estimate of deaths |
| 8 | 30 December, 1760 | Pondicherry, Tamilnadu, India | Several ships destroyed. 11,000 deaths |
| 9 | 31 October, 1763 | Madras, Tamilnadu, India | Extensive damage, no estimate of deaths |
| 10 | 13 October, 1779 | Masulipatnam, Andhra Pradesh, India | 3.63 surge, 20,000 deaths |
| 11 | 20 May, 1787 | Coringa, Andhra Pradesh, India | 20,000 deaths. Coastal inundation due to storm surges |
| 12 | December, 1789 | Near Coringa, Andhra Pradesh, India | 3 major waves in the surge. Several ships lost. 20,000 deaths. Inundation of the whole city of Coringa of 1 to 2 m. |
| 13 | 10 December, 1807 | Madras, Tamilnadu, India | Extensive destruction in Madras, no estimate of deaths |
| 14 | 11 May, 1811 | Madras, Tamilnadu, India | Extensive destruction in Madras, no estimate of deaths |
| 15 | 2 May, 1820 | Near Madras, Tamilnadu, India | No estimate of deaths |
| 16 | 8 May, 1820 | Nellore District, Andhra Pradesh, India | Inundation. No estimate of deaths |
| 17 | 27 May, 1823 | Balasore, Orissa, India | Inundation up to 10 km inland. Several ships and whole villages disappeared |
| 18 | 31 October, 1831 | Balasore, Orissa, India | 2.112–4.5 m surges. Extensive inundation. 22,000 deaths. 50,000 cattle lost. This might have been the same storm that also generated at surge at Barisal, Bangladesh. |
| 19 | 10 May, 1832 | Coringa, Andhra Pradesh, India | Extensive damage at Coringa |
| 20 | October, 1832 | Balasore, Orissa, India | More violent storm than in 1823 (No. 16) but the surge was less destructive |
| 21 | 21 May, 1833 | Sagar Island/24 Paraganas, West Bengal, India | 3 m surge. 50,000 deaths. 100,000 cattle lost |
| 22 | 16 November, 1839 | Between Visakhapatnam and Narsapur/Coringa, Injaram, Andhra Pradesh, India | Over 6 m surge. 20,000 deaths |
| 23 | 22 May, 1843 | Masulipatnam, Andhra Pradesh, India | Extensive damage |
| 24 | October, 1854 | Mouth of Hoogly River, West Bengal, India | Up to 12 m water level increase near Calcutta and environs. 50,000 deaths |
| 25 | 21–27 April, 1859 | Near Nagapatnam, Tamilanadu, India | No estimation of deaths. |

Table 6.24 (continued)

| No. | Date | Location | Damage |
|---|---|---|---|
| 26 | 2–5 October, 1864 | Near Contai, West Bengal, India | Up to 12 m surge. Flooded up to 13 km on either side of the Hoogly River. 80,000 deaths. |
| 27 | 1–2 November, 1864 | Masalipatnam, Andhra Pradesh, India | About 130 km long stretch was subjected to surges up to 3.93 m. Surge penetrated up to 27 km inland. 30,000 deaths |
| 28 | 1 November, 1867 | East of Calcutta, West Bengal, India | 1.8 m surge. Damage at Port Canning. 13 m surge at Hatia, Bhola Islands |
| 29 | 4 November, 1870 | Viskhapatnam, Andhra Pradesh, India | Lower parts of the town flooded. Also whole of Anakapalle town flooded. 7 deaths |
| 30 | 1 July 1872 | Near Cuttack, Orissa, India | Extensive damage, no estimate of deaths |
| 31 | 13–16 October, 1874 | Mouth of Hoogly, West Bengal, India | 3049 deaths |
| 32 | 7–8 October, 1876 | Near Bhimilipatnam, Andhra Pradesh, India | Extensive damage, 30 deaths |
| 33 | 6–8 December, 1878 | Kakinada, Andhra Pradesh, India | Local storm surge and inundation |
| 34 | 19–23 September, 1885 | Cuttack (False Point) Orissa, India | 7 m surge. 5,000 deaths by drowning. 300 deaths by falling trees. 50,000 houses destroyed. 10,000 cattle lost |
| 35 | 6–15 September, 1882 | South Orissa coast, India | Extensive damage |
| 36 | 2–16 November, 1886 | Madras coast, India | No estimation of deaths. |
| 37 | 21–28 May, 1887 | False Point, Orissa, India | Major surges |
| 38 | 21–26 September, 1887 | Calcutta, West Bengal, India | No estimation of deaths. |
| 39 | 13–20 September, 1988 | False Point, Orissa | No estimation of deaths. |
| 40 | 21 November, 1988 | Madras, Tamilanadu, India | No estimation of deaths. |
| 41 | 24–27 October, 1909 | Near GopalPur, Orissa, India | Extensive damage, no estimation of deaths. |
| 42 | 20–24 September, 1911 | Kaningapatnam, Andhra Pradesh, India | Extensive damage, no estimation of deaths |
| 43 | 18–29 September, 1916 | West Bengal coast, India | Extensive damage, no estimation of deaths |
| 44 | 21–23 November, 1916 | Near Cuddalore, Tamilanadu, India | Extensive damage, 300 deaths |
| 45 | 12–20 May, 1925 | Masulipatnam, Andhra Pradesh, India | The surge penetrated up to 6 km inland, 80 deaths. |
| 46 | 29 Oct–1 Nov, 1927 | Nellore, Andhra Pradesh, India | 629 deaths, Considerable damage due to surge |
| 47 | 14–19 Nov, 1933 | Ongole, Andhra Pradesh, India | Moderate surge inundated low-lying areas |
| 48 | 25–28 October, 1936 | Masulipatnam, Andhra Pradesh, India | Surge penetrated up to 6 km inland. Destruction of agriculture due to saline water intrusion |
| 49 | 21–25 Nov, 1938 | Machilipatnam, Andhra Pradesh, India | 2 m surge. Railway bridge washed away. Extensive damage to waterworks due to saline water intrusion |
| 50 | 14–16 October, 1942 | Contai, West Bengal, India | 5 m surge at Midnapore (64 km upstream in Hoogly River) 15,000 deaths |
| 51 | 13–23,May 1943 | South of Madras, Tamilanadu, India | Extensive damage, low-lying areas inundated |

Table 6.24 (continued)

| No. | Date | Location | Damage |
|---|---|---|---|
| 52 | 29–31 October, 1943 | Kalingapatnam, Andhra Pradesh, India | Surge combined with floods in River Vamsadhara caused great damage |
| 53 | 15–21 October, 1945 | Masulipatnam, Andhra Pradesh, India | Up to 3.03–4.54 m surges penetrated 24 km inland |
| 54 | 30 November, 1952 | South of Nagapattinam, Tamilnadu, India | 1.21 m surge penetrated 8 km inland. 400 deaths |
| 55 | 6–14 October, 1955 | Kalingapatnam, Andhra Pradesh, India | Surge up to 1.7 m |
| 56 | 28 Nov–2 Dec, 1955 | Tanjavore District, Tamilnadu, India | Surges up to 5 m penetrated 16 km inland. 500 deaths |
| 57 | 29 May–1 June, 1956 | Near Calcutta, West Bengal, India | Inundation in Midnapore District. Damage to agriculture due to saline water intrusion |
| 58 | 21 October, 1963 | Cuddalore, Tamilnadu, India | Almost 7 m surge |
| 59 | 3–8 November, 1964 | Madras coast, India | Low-lying areas of Madras city flooded |
| 60 | 20–23 Dec, 1964 | Tondi (Rameswaram Island), Tamilnadu, India | 3–6 m Surge. 1,000 deaths |
| 61 | 1–3 November, 1966 | North Madras coast, India | Tidal bore flooded a large area of Madras city, 30 deaths, 3 ships grounded |
| 62 | 8–11 October, 1967 | Puri, Orissa, India | Water levels up to 9 m. 1000 deaths. 25 km inland inundation. |
| 63 | 2–8 December, 1967 | Nagapattinam, Tamilnadu, India | Moderate surges. 7 deaths |
| 64 | 7 November, 1969 | Kakinada, Andhra Pradesh, India | 3.1 m surge. 900 deaths |
| 65 | 26–30 October, 1971 | Paradip, Orissa, India | 4–5 m surge. The surge penetrated 25 km inland. 10,000 deaths |
| 66 | 10 September, 1972 | Barua, Orissa, India | 3.4 m surge. 0.8 m tide |
| 67 | 22 September, 1972 | Gopalpur, Orissa, India | Inundation in Puri District |
| 68 | 15–23 November, 1972 | South of Nellore, Andhra Pradesh, India | Minor Surge |
| 69 | 6–12 October, 1973 | Chandbali, Orissa, India | Mild surge in river estuaries caused saline water intrusion in the coastal areas of north Orissa and West Bengal. 100 deaths |
| 70 | 3–9 November, 1973 | Near Paradip, Orissa, India | 3–4.5 surge, Saline water inundation in Basudevpur and Uttar Sumiti |
| 71 | 12–23 December 1968 | Near Nagapattinam, Tamilanadu, Inia | 7 deaths, Tidal waves caused severe damage in coastal districts of Ramanathapuram |
| 72 | 13–20 August, 1974 | Contai, West Bengal, India | 3 m surge. Inundation of low-lying areas of Digha and Juneput. 7 deaths |
| 73 | 11 September, 1976 | Contai, West Bengal, India | 2.5 m surge. 1.4 m tide. 40 deaths. |
| 74 | 14–20 Nov, 1977 | Chirala, Andhra Pradesh, India | Peak surge 5.0 m, Tide 0.3 m. Divi and surroundings totally inundated. 10,000 deaths |
| 75 | 24 November, 1978 | Between Kilakkarai and Rochemary Island, Tamilnadu, India | 3–5 m surges on the coasts of Tamilnadu and Sri Lanka. Extensive damage on the northeast coast of Sri Lanka. 1000 deaths in Sri Lanka. 10 deaths in India |
| 76 | 12 May, 1979 | Kavali, Andhra Pradesh, India | 3 m surge. 0.6 m tide. 700 deaths |
| 77 | 1–4 June, 1982 | Between Paradip and Chandbali, Orissa, India | 2 m surge along the Orissa and West Bengal coasts. Peak surge of 4.8 m 35 km north of Dhamra harbour. 245 deaths. |

Table 6.24 (continued)

| No. | Date | Location | Damage |
|---|---|---|---|
| 78 | 9–14 November, 1984 | Near Sriharikota, Andhra Pradesh, India | 524 deaths, extensive damage |
| 79 | 20 September, 1985 | Close of Puri, Orissa, India | 2 m surge. Inundation lasted for 3 days. Substantial damage |
| 80 | 16 October, 1985 | Near Balasore, Orissa, India | Up to 4 m surge. Damage due to saline water inundation |
| 81 | 13–19 October, 1987 | North of Ongole, Andhra Pradesh, India | Moderate surge. 17 deaths. Substantial damage |
| 82 | 31 October – 3 November, 1987 | Nellore, Andhra Pradesh, India | 50 deaths. 26,000 cattle killed. Substantial damage |
| 83 | 23–27 May, 1989 | Near Balasore, Orissa, India | 3–6 m surge, 71 deaths, 2625 cattle killed, extensive damage in West Bengal and Orissa |
| 84 | 4–7 November, 1989 | Kavali, Andhra Pradesh, India | 3–4 m surge caused destruction in Nellore and Kavali. 69 deaths |
| 85 | 4–11 May, 1990 | Mouth of Krishna River, Andhra Pradesh, India | 4–5 m surge. 967 deaths. 600,000 houses destroyed. 21,600 cattle killed. 3,500,000 poultry killed. 42,700 goats and sheep killed. Substantial damage to agriculture |
| 86 | 11–17 Nov, 1992 | Sri Lanka, and Tutikorin, India | 1–2 m surge at Tuticorin, 170 killed, 160 missing |
| 87 | 1–4 December, 1993 | Near Karaikal | 1–1.5 m surge, 111 killed |
| 88 | 29–31 Oct, 1994 | Madras, India | 1–2 m surge, 304 killed, 100, 000 huts damaged, 60,000 hectares crops dama- |
| ged | | | |
| 89 | 6–10 Nov, 1995 | Gopalpur, Orissa, India | 1.5 m, 96 killed, 2,84,253 hectares crops damaged |
| 90 | 12–16 Jun, 1996 | Visakhapatnam, India | 179 killed, 13,378 hectares of crops damaged |
| 91 | 5–7 Nov, 1996 | Kakinada, India | 2–3 m surge, 978 killed, 1375 missing , 647554 houses damaged, 1.74 lakh hectares crops damaged |
| 92 | 17–21 Nov, 1998 | Visakhapatnam, India | 16 deaths. Damage estimation not available |

Table 6.25. Storm surge at Saugor Island, India, during 1948–55 (JANARDHAN, 1967)

| Date | Distance of storm center to Saugor Island (km) | Observed peak surge (m) | Computed peak surge (m) | State of tide at time of peak surge |
|---|---|---|---|---|
| Aug. 14, 1948 | 306 | 0.34 | 0.43 | High |
| Aug. 15, 1948 | 402 | 0.43 | 0.40 | Low |
| July 25, 1951 | 306 | 0.85 | 0.98 | Low |
| Aug. 05, 1952 | 418 | 0.34 | 0.34 | High |
| Aug. 03, 1953 | 306 | 0.46 | 0.46 | High |
| Aug. 30, 1955 | 217 | 0.46 | 0.46 | High |

considered in the next subsection). The storm surge considered here is the piling up of the water due to wind stress. The inverse barometer effect is not included here, since according to RAO (1968), it does not exceed 0.5 m anywhere on the east coast of India.

Table 6.26: Maximum possible storm amplitudes and total water levels (surge + wind waves) at selected locations on the east coast of India. The hypothetical storm has a wind speed of 40 $m \cdot s^{-1}$. A, total water level <2 m; B, 2–5 m; C, >5 m. A few locations in Bangladesh and one in Burma are included for comparison (RAO, 1968)

| Location | Favorable Wind direction | Storm surge amplitude (m) | Storm surge + Wind wave (total water level) (m) | Classification |
|---|---|---|---|---|
| Dhanushkodi | NNE | 4.8 | 8.2 | C |
| Rameswaram | SE | 6.8 | 11.3 | C |
| Pamban | NNW | 4.4 | 7.3 | C |
| Devipatnam | E | 4.5 | 7.5 | C |
| Adirampatnam | SSE | 5.1 | 8.5 | C |
| Point Calimere | SSE | 4.2 | 7.0 | C |
| Nagapattinam | E | 1.5 | 2.5 | B |
| Karikal | E | 0.3 | 1.3 | A |
| Madras | ENE | 1.5 | 2.5 | B |
| Nizampatnam | SW | 4.5 | 7.4 | C |
| Mouth of Krishna River | SE | 1.6 | 2.7 | B |
| Narasapur | S | 1.7 | 2.9 | B |
| Sacromento Shoals (outer sand banks) | SSE | 1.4 | 2.3 | B |
| Kakinada (outer sand banks) | E | 0.6 | 1.0 | A |
| Visakhapatnam | SE | 0.7 | 1.2 | A |
| Kalingapatnam | E | 1.1 | 1.8 | A |
| Gopalpur | SE | 0.9 | 1.5 | A |
| Mouth of Devi River | SE | 0.8 | 1.3 | A |
| False point | SE | 1.9 | 3.2 | B |
| Balasore | SE | 3.0 | 5.0 | C |
| Mouth of Hoogly River | S | 6.5 | 10.8 | C |
| Mouth of Matla River | S | 5.0 | 8.4 | C |
| Mouth of Baleswar River (Bangladesh) | S | 6.9 | 11.5 | C |
| Mouth of meghna river (Lakhichar Island, Bangladesh) | SSE | 8.0 | 13.4 | C |
| Cox Bazaar (Bangladesh) | WSW | 3.2 | 6.3 | C |
| Moth of Faaf River (Burma) | SW | 3.2 | 5.3 | C |

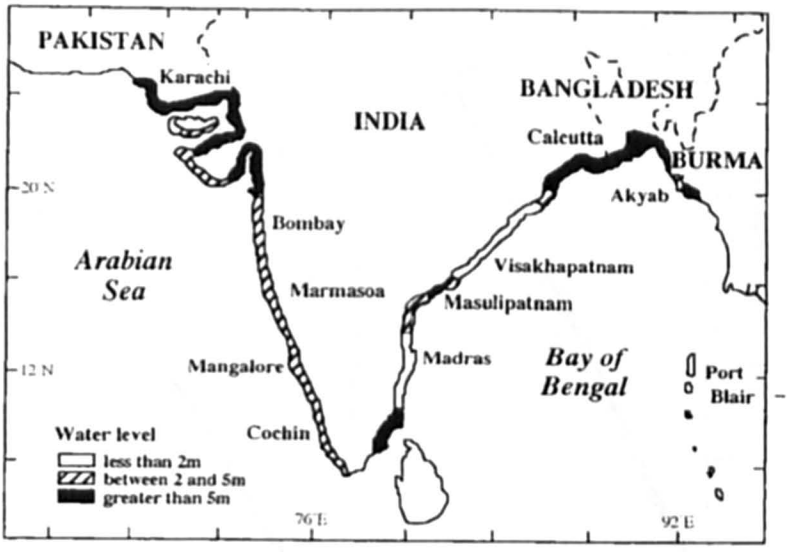


Fig. 6.35: Classification of the Bay of Bengal and the Arabian Sea coasts of India (RAO, 1968)

This classification into types A, B, and C has been verified to certain extent by comparison with actual data (Table 6.27). Thus, type C belts are the most prone to major storm surges. It can be seen from Fig 6.35 that there are four such belts on the coasts of the Indian subcontinent (RAO, 1968). Two are as follows.

1) The coastal belt around the head of the Bay Bengal, approximately to the north of 20° N. The frequency of cyclones is high here and the storm tracks are usually favorable for generating maximum surges, especially in the Sunderbans.
2) South Coromandel coast around the Palk Bay. Although the frequency of storms striking this region is somewhat smaller than for the first belt, the major storms that strike this coast usually produce major surges.

The other two belts are on the west coast of the subcontinent and will be considered in he next subsection.

There is a short, type C belt near Nizampatnam Bay. The Andhra cyclone of November 1977 produced major surges in this general area and killed several thousand people. The east coast of India, between 14 and 16.5° N, is in the type B category. Also, the Coromandel coast between point Calimere and karikal falls into this category.

GHOSH (1977) used the SPLASH model (JELESNIANSKI, 1972) for the east coast of India. He prepared nomograms for calculating peak surges based on pressure drop, radius of maximum winds, vector motion of the storm, and bathymetry offshore. The nomograms were prepared separated for the northern part (where the slope of the shelf is small) and for the remaining part of the coast (where the slope is large). A separate nomogram is presented to include the tidal effects on the northern part of the coast where the tidal range is large. Two typical nomograms prepared in this manner are shown in Fig. 6.36.

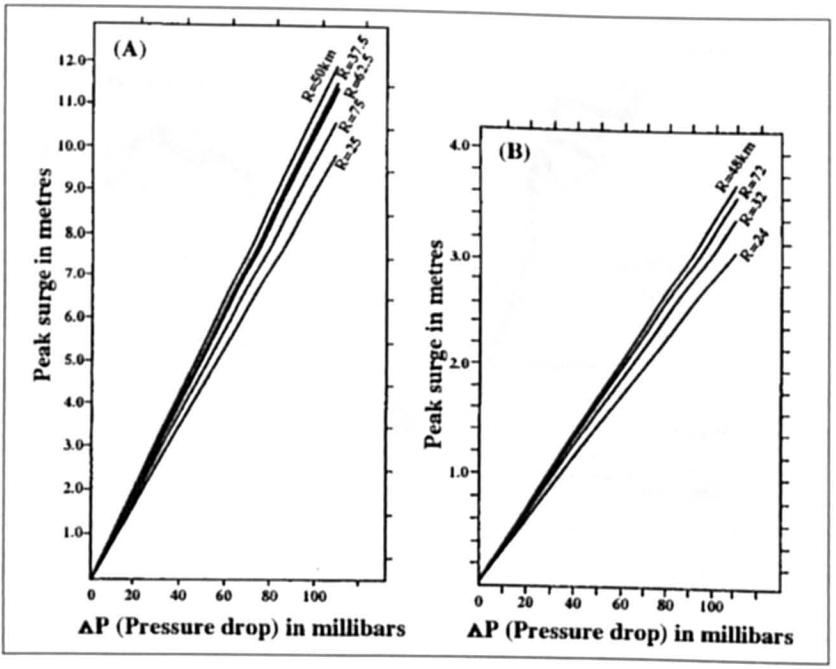


Fig. 6.36: Nomogram of peak storm surge as a function of pressure drop and radius of maximum winds for the (A) northern part and the (B) southern part of the east coast of India (GHOSH, 1977)

Table 6.27: Relationship between type of coastline and occurrence of storm surges on the coast of India. A, surge + wind wave amplitudes <2 m; B, 2–5 m; c, >5 m. Data are mainly for the period 1949–66. (RAO, 1968)

| Type of coast | Intensity of storm | No. of storms that affected the coast | No. of storms that caused major storm surges |
|---|---|---|---|
| A | Moderate | 13 | – |
| | Severe | 12 | – |
| B | Moderate | 19 | – |
| | Severe | 6 | 4 |
| C | Moderate | 1 | – |
| | Severe | 3 | 3 |

DAS (1972) used a numerical model to compute storm surges in the Bay of Bengal, which is probably the first numerical model developed for this area. DAS et al. (1974) extended this model to simulate the storm surge due to the cyclone of November 13, 1970, which caused great loss of life and destruction in Bangladesh. They used a two-dimensional linear model and telescoping grids. The grid scheme used for three different types of tracks is illustrated in Fig. 6.37. Nomograms for the storm surge as a function of the storm intensity and speed of movement of the storm are given (for the three tracks shown in Fig. 6.37, in Fig. 6.38).

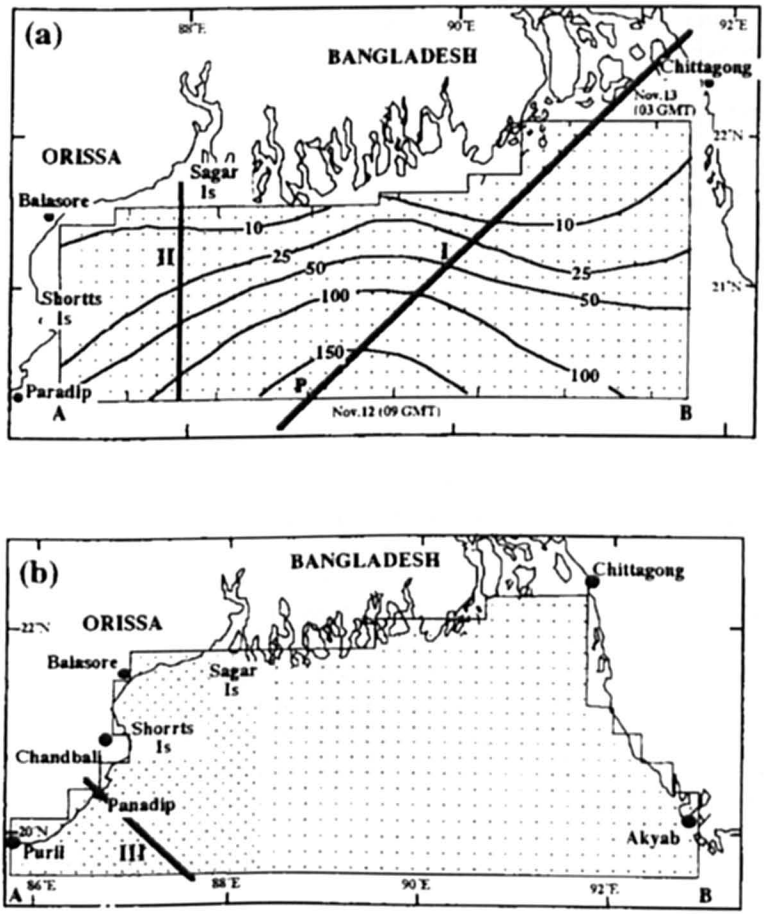


Fig. 6.37: (a) Grids for storms moving northeast (I) and north (II). Contours represent water depth (meters). (b) Grid for storms moving northwest (III) (DAS et al., 1974)

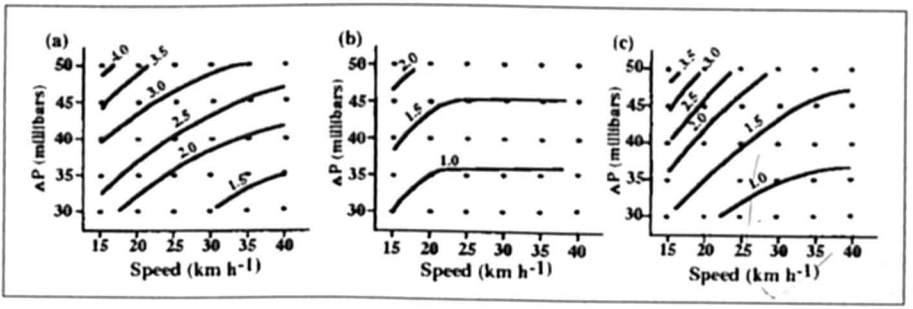


Fig. 6.38: Storm surge amplitude (meters) as a function of storm intensity (millibars) and speed 'c' of storm movement for the (a) northeast track (I), (b) northward track (II) and (c) northwest track (III) of Fig. 6.37 (DAS et al., 1974)

The relationship between the storm surge amplitude $\eta$ and the storm intensity $\Delta p$ and speed of movement of storm c was expressed as

$$\eta = A_0 \Delta p + A_1 (\Delta \Delta p)^2 + A_2 c \qquad (6.69)$$

Table 6.28. Numerical values of the constants $A_0$, $A_1$, and $A_2$ of eq. 6.69 for the three different tracks shown in Fig. 6.37 (DAS et al., 1974)

| Track | $A_0$ ($\times 10^2$) | $A_1$ ($\times 10^4$) | $A_2$ ($\times 10^2$) |
|---|---|---|---|
| Northeast | 9.59 | −0.91 | −4.60 |
| North | 2.88 | 3.08 | −1.20 |
| Northwest | 8.24 | −1.60 | −5.15 |

The numerical values of the constants $A_0$, $A_1$, and $A_2$ are listed for the three different tracks (shown in Fig. 6.37) in Table 6.28. Theseauthors concluded that linear superposition of tide and surge would overestimate the water level by about 1 m.

DAS (1980) included nonlinear advective terms and improved the model of DAS et al. (1974), and the computational area was also enlarged. This model, which includes the tide-surge interaction in a more realistic manner, gave water levels that agreed better with observed levels. NATARAJAN and RAMANATHAN (1980) developed a nonlinear finite-element model and used the same computational area and storm tracks as in DAS et al. (1974)

In a series of papers JOHNS et al. (1981, 1982, 1983a, 1983b, 1985); DUBE et al. (1981, 1982); DAS et al. (1983); DUBE and SINHA (1982) and SINHA et al. (1993) have studied various aspects of storm surge modelling and prediction along the east coast of India. In all these modelling studies the treatment of the coastal boundaries involve a procedure leading to realistic curvilinear representation of the east coast of India, the details of which are described in Chapter 2.

In an attempt to simulate the surge generated by the devastating 1977 Andhra cyclone (Fig. 6.39) JOHNS et al. (1981) used three different numerical models. All the three models considered by the author's are fully nonlinear and based on the vertically integrated equations. The analysis area in the first model (designated $M_1$) includes the entire Bay of Bengal north of 6° N and utilizes a curvilinear boundary treatment to represent both western and eastern sides of the Bay. The second model ($M_2$) is a coastal zone model extending along the east coast of India with curvilinear treatment of the coastline. The third model ($M_3$) that again covers the entire Bay of Bengal uses conventional techniques based on the orthogonal straight-line segments to represent the coastline. Each of these models predict a maximum surge elevation along the Andhra coast in the range of 4–5 m. This compares well with the available observation. However, $M_1$ produced the surge elevation in excess of 6 m at the head of the Bay, which was unrealistic and is not seen in the results of $M_2$. Interesting analysis of the differences in the response obtained from each model has been made. The difference between responses of $M_1$ and $M_2$ in the head Bay is attributed by the author's to the funnelling effect of the converging coastline towards the north. Subsequently DUBE et al. (1981) performed numerical experiments, using $M_1$ with number of alternative cyclone models, to further investigate the phenomenon of large sea surface elevations in the head Bay. Contrary to the earlier explanation given by JOHNS et al. (1981), the authors attribute the anomalous surge produced at Contai in the head Bay to the choice of the cyclone

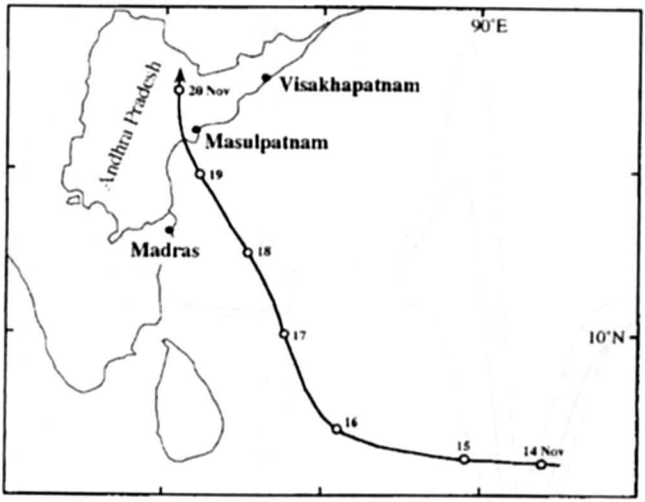


Fig. 6.39: Track of Andhra cyclone: 14–20 November 1977 (JOHNS et al., 1981)

model which gives significantly strong winds at greater distances from the centre of the cyclone.

Frequently, the lateral boundaries in numerical storm surge prediction models are taken to be vertical sidewalls through which no flux of water is allowed. In actuality, however, the water will usually move continuously inland and the use of idealized vertical sidewalls may lead to misrepresentation of the surge development. Recognizing this short coming of earlier models, JOHNS et al. (1982) developed a model which used a continuously deforming lateral fluid boundary instead of using the conventional solid wall boundary at the coast. The model is an extension of the earlier transformed coordinate coastal zone model wherein the coastal topography is included to route the storm surges over the land. As a result of the movement of the coastal boundary with changing water level the horizontal grid deforms with time and the undisturbed water depth at each grid point is recomputed at every time step. Numerical experiments were performed by the authors with different sea-floor slopes and with a fixed boundary version of the model. A comparison of the results slow that the moving boundary model gives a reduced surge response at the initial coastline position than that in fixed boundary model. Further, fixed boundary model yields a significantly greater maximum inland intrusion as compared with deforming coastline model. Calculations based on fixed boundary model also show that the predicted maximum inland inundation occurs some 5 hours earlier than in moving boundary model. The differences decrease as the seabed slope at the coast is increased. Seaward recession of the coastline, following the peak surge is also simulated. Fig. 6.40 gives the variation of the coastline displacement and sea surface elevation at initial position of coastline along two stations of Andhra Coast with seabed slope of $2 \times 10^{-4}$.

JOHNS et al (1983 a) developed a fully three-dimensional coastal zone storm surge model and applied it to the 1977 Andhra cyclone. The model employed a highly sophisticated turbulent energy closure scheme due to JOHNS (1978). The model was developed with the surmise that the shallow water evolution of the surge response may be significantly different in three-dimensional model because of the full representation of the vertical current structure. It was also thought that the sea-surface surge response would be critically dependent on

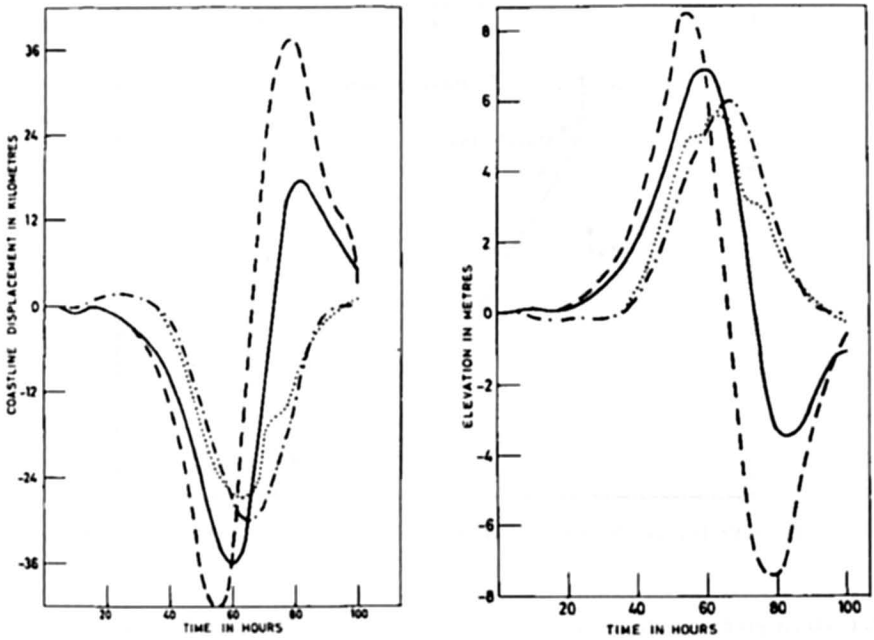


Fig. 6.40:(a) Variation of coastline displacement with $S = 2 \times 10^{-4}$ calculated from MD and MF. Kavali (MD) -; Kavali (MF) - - -; Divi (MD) -.-.-; Divi (MF) ..., (b) Variation of sea surface at initial position of coastline with $S = 2 \times 10^{-4}$ calculated from MD and MF. Kavali (MD) -; Kavali (MF) - - -; Divi (MD) -.-.-; Divi (MF) ..... .

the value chosen for the bottom roughness parameter in the three-dimensional model. Simulations of the Andhra cyclone using two-and three-dimensional models were carried out. The results of their experiment are illuminating.

They found a remarkable qualitative and quantitative similarity between the two simulations, suggesting that details of the dissipative mechanism and vertical current structure were unimportant. They further conclude that if the vertical current structure is not a primary concern, it does not appear worthwhile replacing the depth-averaged procedure by a more complicated three-dimensional model.

Since the coastal surge elevations are effectively dependent upon the near coastal bathymetry, a desirable feature of storm surge simulation schemes is the ability to incorporate increased resolution adjacent to the coastline. This was achieved by JOHNS et al. (1983 b) by introducing an additional transformation of the offshore coordinates in their earlier coastal zone model (JOHNS et al., 1981). This version of the model was used to determine the influence of model resolution and nearshore bathymetry on the computed surge proper resolution of the near shore bathymetry was found to be crucial in determining the storm induced sea surface elevation, one of the interesting results identified by the authors pertain to a northward propagating component of the computed surge response which is found to have the characteristics of a coastally trapped wave. Thus the total response is determined by the contribution from direct wind stress together with the northward propagating component.

For the east coast of India, the phenomenon of alongshore propagation was further identified in a model developed to investigate tide-surge interaction in the Bay of Bengal (JOHNS

et al., 1985). Clear evidence is shown by the authors to the northeasterly propagation in the case of both the 1982 Orissa surge and the 1977 Andhra surge.

Coastal trapping of the energy is implied and the locally shallow water suggests that nonlinear aspects of the propagation process are important. Moreover, the trapped waves cannot have the form of a Kelvin wave, since this is necessarily right bounded, and must, instead, have the form of a topographically trapped edge waves. These findings were further illuminated by JOHNS and LIGHTHILL (1993). They used a simple theoretical model with uniform shelf slope to investigate the formation of anomalous sea-surface elevations remote from the position of landfall of the generating cyclone.

DAS et al. (1983) used the stretched coordinate model of JOHNS et al. (1983b) to simulate the surge generated by the 1982 Orissa cyclone. JARREL et al. (1982) made one of the most comprehensive studies of storm surges in the Bay of Bengal. They developed five models for the Sri Lanka/ India/ Bangladesh coastlines, two models for the Myanmar /Thailand coastline and one for the Andaman Islands region. The analysis areas of the models cover the coastline and the water area up to and slightly beyond the continental shelf. Based on population centers, a total of 16 tropical cyclone impact points were chosen (Table 6.29). The maximum wind speed in the calculations varies from 55 to 130 knots. The directions from which the cyclones could realistically approach the impact points are given in Table 6.29. A total of 258 runs were made for the 16 impact points. Tidal constituents $M_2$, $S_2$, $N_2$, $K_1$, $O_1$ and $S_a$ were included in the models. Model provided surge heights in the case of 1977 Andhra cyclone are shown in Fig. 6.41. These model-simulated surges along the Andhra coast are in good agreement with limited available observations. GHOSH et al. (1983) applied the "SPLASH" model to compute the surge associated with 1977 Andhra and two other cyclones. They obtained a peak surge elevation of 5.7 m about 50 km to the right of the landfall. This is in good agreement with earlier calculation of JARREL et al. (1982).

Table 6.29: Angles of cyclone approach (with respect to the coast line) to be modelled for the individual impact points (JARREL, LEWIS and WHITAKER, 1982)

| Impact Point | Direction from which storm approaches |
|---|---|
| Trinconamalee (Sri Lanka) | SE through NE |
| Jaffna (Sri Lanka) | SE through NE |
| Negapatam (India) | SE through NE |
| Pondicherry (India) | SE through NE |
| Madras (India) | SSE through ENE |
| Masulipatnam (India) | SSE through ENE |
| Coconada (India) | S through ENE |
| Vishakhapatanam (India) | SSW through ESE |
| Berhampur (India) | SSW through ESE |
| Puri (India) | SSW through SE |
| Calcutta (India) | SW through SE |
| Port Blair (Andaman Is.) | S |
| Chittagong (Bangladesh) | SW through S |
| Bassein (Burma) | S through W |
| Rangoon (Burma) | SSE through SSW |
| Phuket (Thailand) | Only ESE |

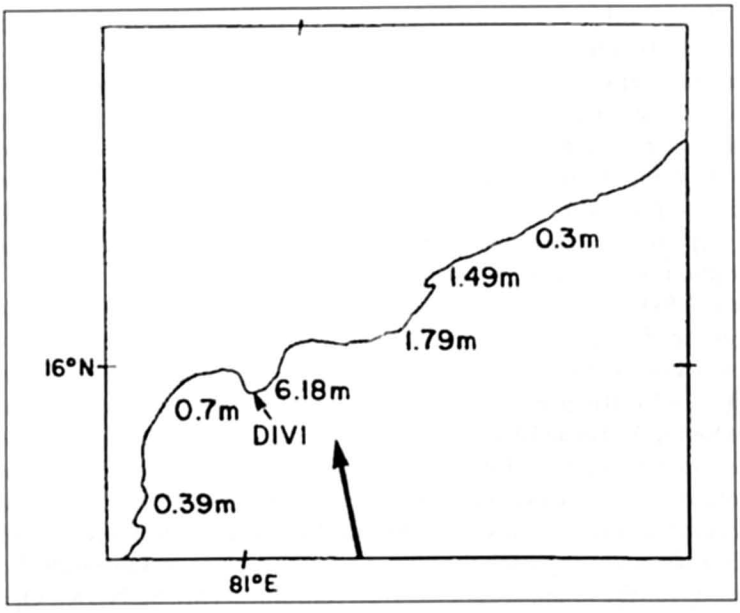


Fig. 6.41: Storm surge height distribution along the east coast of India for the November 1977 Andhra cyclone (JARREL, LEWIS and WHITAKER, 1982)

Advent of powerful personal computers has set up a trend to run storm surge models in real time on PC-based workstations in an operational office. Recognizing this DUBE et al. (1994) describe a real time storm surge prediction system for the east coast of India. The forecasting system proposed by the authors is based on the vertically integrated numerical storm surge models that were developed earlier by the group (JOHNS et al., 1981; 1983 b; DUBE et al., 1985 b). Surface winds associated with a tropical cyclone are derived from a dynamic storm model (JELESNIANSKI and TAYLOR, 1973). The only meteorological inputs required for the model are the positions of the cyclone, pressure drop and radii of maximum winds at any fixed interval of times. The model can be run in a few minutes on a PC in an operational office. The system is operated via a terminal menu and the output consists of the two-dimensional and three-dimensional views of peak sea surface elevations with the facility of zooming the region of interest. One of the significant features of this storm surge predication system is its ability to investigate multiple forecast scenarios to be made in real time. This has an advantage because the meteorological input needed for surge prediction can be periodically updated with the inflow of data on fast telecommunication links. The model has extensively been tested with severe cyclonic storms, which struck the east coast of India during the period 1960–1990. The model results reported for three case studies (June 1982 Orissa cyclone; November 1977 Andhra Cyclone and May 1990 Andhra Cyclone) are in very good agreement with the available observations and estimates of the surge. In Figs. 6.42 and 6.43 we show respectively the track of May 1990 Andhra cyclone and model computed peak surge envelope along the east coast of India. Detailed case studies by using this model may be seen in DUBE and GAUR (1995). This version of the model was tested in near real time during the cyclone periods of 1992–1993 (DUBE and GAUR, 1995). Operational feasibility test of the model is presently undergoing at India Meteorological Department.

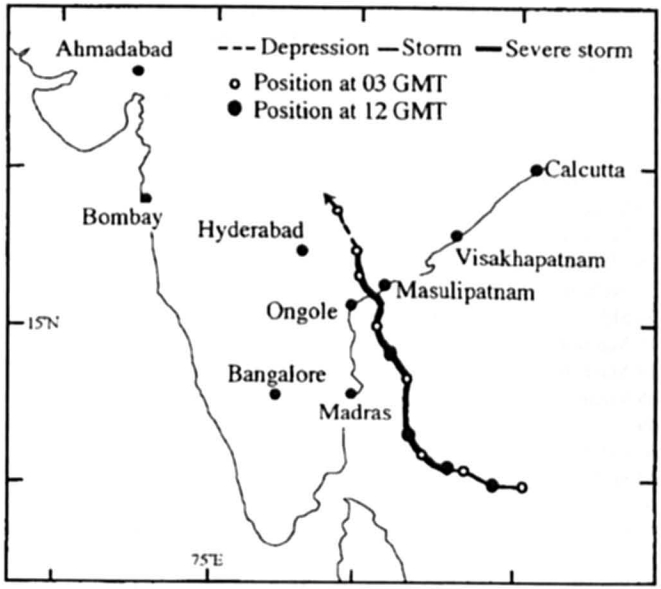


Fig. 6.42: Track of Andhra cyclone; 5–11 May 1990 (DUBE et al., 1994)

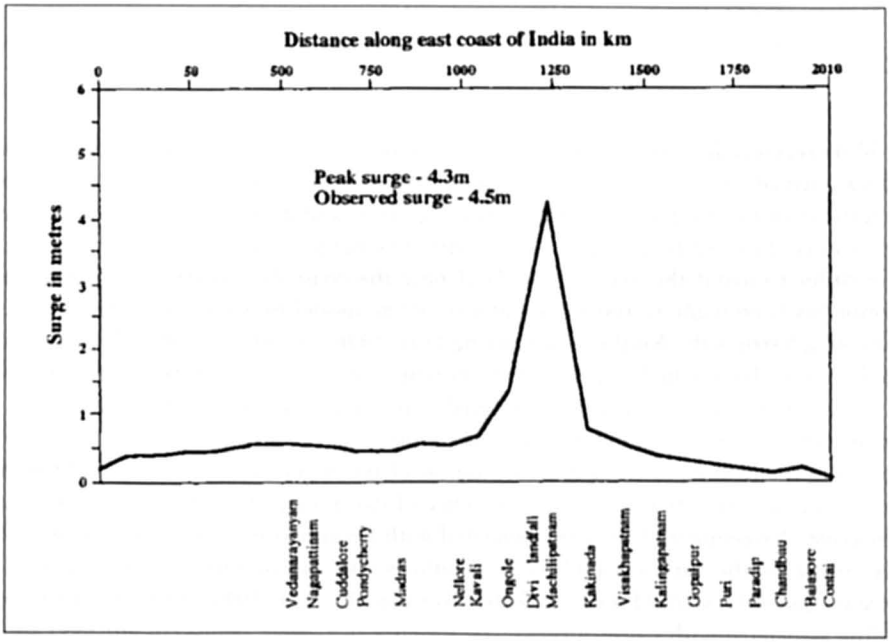


Fig. 6.43: Peak surge envelope associated with 1990 Andhra cyclone (DUBE et al., 1994)

Table 6.30: Severe cyclonic storms having potential of producing significant surges along the Andhra coast during 1895 to 1996

| No. | Cyclone | ΔP (mb) | R (km) | Landfall Lat (N) | Maximum Wind Speed (knots) |
|---|---|---|---|---|---|
| 1 | 1895 Kakinada | 35 | 18 | 17.2 | 70 |
| 2 | 1906 Vizag | 25 | 15 | 17.9 | 60 |
| 3 | 1921 Nellore | 30 | 15 | 14.3 | 60 |
| 4 | 1925 Machili | 60 | 20 | 16.1 | 108 |
| 5 | 1927 Nellore* | 80 | 25 | 14.3 | 100 |
| 6 | 1940 SH | 30 | 22 | 14.0 | 60 |
| 7 | 1945 Machili | 50 | 19 | 16.3 | 90 |
| 8 | 1949 Machili* | 60 | 25 | 16.3 | 110 |
| 9 | 1965 Vizag | 30 | 15 | 17.9 | 62 |
| 10 | 1969 | 45 | 25 | 16.7 | 96 |
| 11 | Kakinada* | 30 | 15 | 13.8 | 80 |
| 12 | 1972 SH* | 30 | 15 | 16.1 | 70 |
| 13 | 1976 Machili | 28 | 15 | 14.8 | 60 |
| 14 | 1976 Kavali | 80 | 40 | 15.8 | 135 |
| 15 | 1977 Divi* | 26 | 15 | 14.8 | 55 |
| 16 | 1977 Kavali | 60 | 35 | 14.8 | 100 |
| 17 | 1979 Kavali* | 60 | 25 | 14.0 | 102 |
| 18 | 1984 SH* | 26 | 15 | 14.4 | 50 |
| 19 | 1987 Nellore | 26 | 15 | 15.9 | 50 |
| 20 | 1987 Machili | 70 | 20 | 14.8 | 110 |
| 21 | 1989 Kavali* | 80 | 40 | 15.7 | 136 |
| 22 | 1990 Divi* | 30 | 25 | 13.0 | 75 |
| 23 | 1994 Madras* | 35 | 20 | 16.7 | 90 |
| | 1996 Kakinada* | | | | |

More recently RAO et al., (1997) developed a location specific high-resolution model for Andhra coast of India, on the lines similar to that of DUBE et al. (1994). One of the important features of the model is that it uses more accurate and detailed bathymetry for the offshore waters of the Andhra Coast. A simple drying scheme has also been included in the model in order to avoid the exposure of land near the coast due to strong negative surges. Attempt has been made to test the reliability of the model by validating it for various cyclones, which struck the Andhra coast during 1891–1996. Table 6.30 list the 23 cyclones identified by the authors, which appear to have potential of producing a peak surge of more than 1m. In Table 6.31, the computed and observed peak surges and their locations of landfall have been listed for eleven cyclones for which post-storm survey surge information could be procured from the records of India Meteorological Department. Authors have used the model results to calculate the frequency of occurrence of storm surge heights at different locations of the coast. Assessment of the risk associated with a major storm surge for a given location is also made by the authors (Table 6.32). Authors also use an empirical formula given by FREEMAN and MEHAUTE (1964) and latter also used by ALI (1996), to estimate the inland flooding associated with storm surges.

Table 6.31: Comparison of observed and computed peak surge amplitude and their locations

| | Surge (m) | | Location of peak surge | |
|---|---|---|---|---|
| Cyclone | Observed/ Reported | Computed | Observed | Computed |
| 1927 Nellore | 3.0 | 3.07 | North of Nellore | Nellore |
| 1949 Machili | 2.5 | 2.093 | Machilipatnam | 10 km N of Machilipatnam |
| 1969 Kakinada | 2.6 | 2.82 | Kakinada | Kakinada |
| 1972 SH | 0.8–1 | 1.23 | Sriharikota | Sriharikota |
| 1977 Divi | 5.0 | 4.93 | Divi | Divi |
| 1979 Kavali | 3.0 | 3.3 | Kavali | 10 km North of Kavali |
| 1984 SH | 2.0 | 2.4 | Sriharikota | Sriharikota |
| 1989 Kaval | 3–4 | 3.8 | 40 km N of Kavali | 48 km N of Kavali |
| 1990 Divi | 4.5 | 4.41 | Divi | Divi |
| 1994 Madras | 1–1.5 | 0.83 | Madras | 20 km North of Madras |
| 1996 Kakinada | 1.5 | 1.6 | Kakinada | Kakinada |

Table 6.32: Risk (%) of exceedence of storm surge heights at Divi (Zone 'G')

| Years | Surge height (m) | | | | |
|---|---|---|---|---|---|
| | ≥ 1 | ≥ 2 | ≥ 3 | ≥ 4 | ≥ 5 |
| 10 | 50 | 22 | 20 | 18 | 8 |
| 20 | 75 | 40 | 36 | 34 | 16 |
| 50 | 97 | 92 | 67 | 65 | 36 |
| 160 | 99.9 | 99.4 | 89 | 87 | 59 |
| 200 | 99.99 | 99.99 | 98.8 | 98.5 | 83.9 |

Before ending this subsection we may like to refer few other storm surge studies, which have been carried out for the east coast of India. Interested readers may refer to the works of KUMAR et al. (1995), MATHEW et al. (1996), HENRY et al. (1997), MURTY and DUBE (2000), and DUBE et al. (1998, 1999a, 2000a, 2000b).

*(c) Myanmar*

Storm surges affecting Myanmar are to much less extent in comparison with Bangladesh and India. However, whenever a severe cyclone struck the coast of Myanmar it leaves severe damage and casualties mostly due to strong winds and storm surge floods. During the period 1884 to 1999 the Myanmar coast was affected by eleven severe cyclonic storms of which seven were associated with significant surges. Table 6.33 lists the impact of these cyclones (THAW, 1998).

During April 22–26, 1936, a severe storm struck the Kyaukpyu area and killed about 2000 people and over 7,000 cattle. Another cyclone that caused heavy loss of life and pro-

Table 6.33: Losses of lives and properties due to severe cyclone during 1884–1998

| Sr. No. | Year | Month | Day | Wind Speed in m.p.h. | Damage to crop | Loss of Lives | Loss of Cattle | No. Of homes damaged | Total loss in Kyats | Point of landfall |
|---|---|---|---|---|---|---|---|---|---|---|
| 1 | 1884 | May | 14–17 | 100 | – | 100 | – | – | 200,000,000 | Sittwe |
| 2 | 1936 | April | 22–26 | 80–100 | – | 2000 | 7000 | – | 200,000,000 | Kyaukpyu |
| 3 | 1948 | October | 5–8 | 80–100 | – | – | – | – | 100,000,000 | Sittwe |
| 4 | 1952 | October | 22–24 | 60–80 | – | 4 | – | – | 10,000,000 | Sittwe |
| 5 | 1967 | May | 7–10 | 80–100 | – | – | – | – | 30,000,000 | Kyaukpyu |
| 6 | 1967 | October | 22–24 | 80 | – | 172 | 656 | – | 100,000,000 | Sittwe |
| 7 | 1968 | May | 4–7 | 130 | – | 1037 | 17 537 | 57 663 | 800,000,000 | Sittwe |
| 8 | 1975 | May | 5–7 | 80–100 | – | 304 | 10 191 | 246 700 | 776,500,000 | Pathein |
| 9 | 1978 | May | 14–17 | 80–100 | – | – | – | – | 20,000,000 | Kyaukpyu |
| 10 | 1982 | May | 2–5 | 80–100 | – | 31 | 63 | – | 38,000,000 | Gwa |
| 11 | 1994 | May | 1–2 | 100–120 | 787 acres | 10 | 150 | 2874 | 78,000,000 | Maungdaw |

perty cross the Myanmar coast near Sittwe on May 7, 1968. The cyclone generated a surge of more than 4 m with loss of more than 1000 human lives. The storm surge due to the May 1975 cyclone killed 304 people and more than 10,000 cattle and destroyed about 28,000 houses (LWIN, 1994a). In recent past a severe cyclonic storm crossed the coast of Myanmar near Maungdaw on 2 May 1994. Storm surge of 3.26 m and loss of 10 lives in addition to some damages were reported (THAW, 1998). The peak surge envelope for May 1994 cyclone is shown in Fig. 6.44.

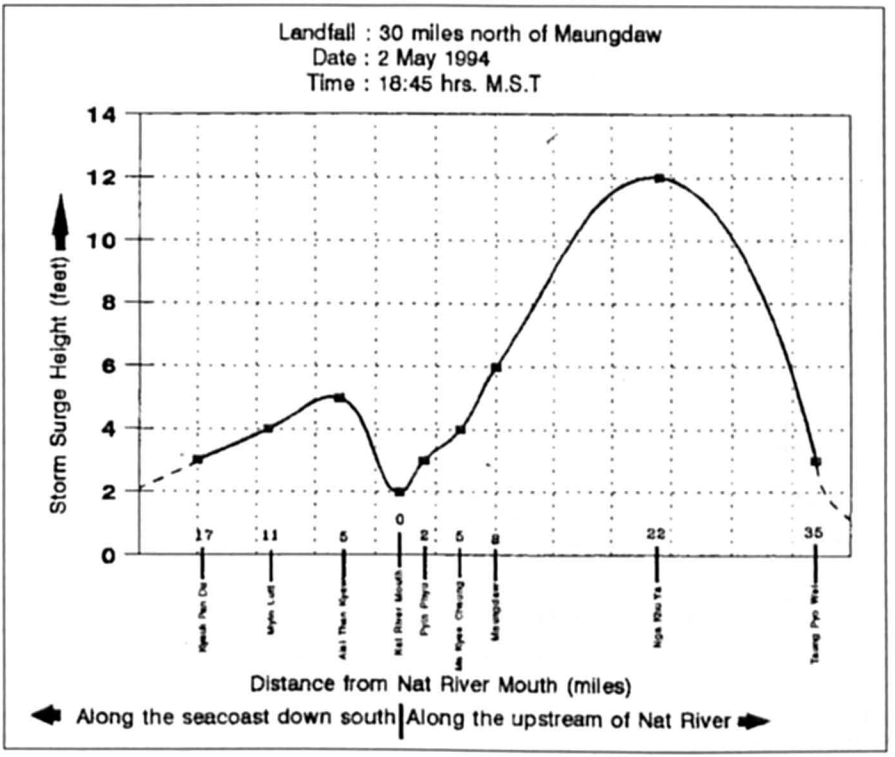


Fig. 6.44: Storm surge envelope of May 1994 severe cyclone storm in Myanmar (LWIN, 1994 a)

In Myanmar, tidal and storm surge data are available at about 10 stations beginning with 1966. The list of the tide gauges available along the coast of Myanmar is shown in Table 6.34. Rakhine coast and Deltaic region are the most favorable places for storm surge inundation. The available surge data during the last 35 years are shown in Table 6.35(a, b). Based on the available data THAW (1998) points out following salient features of storm surges affecting the Myanmar coast

(i) For narrow coastal areas where there is no estuary, storm surge occurred on both sides of the point of landfall. But it was higher and more extensive on the onshore wind region.

(ii) For coastal strip close to Deltaic region, the storm surge entered through estuaries over the delta, which is not directly struck by the high onshore winds of cyclone. The Pathein cyclone of May 1975 and Maungdaw cyclone of May 1994 are the examples. The storm surge due to the May 1975 event penetrated at least 100 km into the river system and

Table 6.34: List of available observed tidal data along the coast of Myanmar

| Name of Station | Latitude | Longitude | Data available since |
|---|---|---|---|
| Kyaukpyu | 19.25 | 93.33 | 1973 |
| Thandwe | 18.28 | 94.21 | 1968 |
| Pathein | 16.46 | 94.56 | 1973 |
| Yangon | 16.46 | 96.10 | 1953 |
| Yangon River Mouth (Elephant Point) | 16.35 | 96.12 | 1968 |
| Mawlamyine | 16.30 | 97.37 | 1965 |
| Amherst | 16.05 | 97.34 | 1967 |
| Dawei | 14.06 | 98.13 | 1972 |
| Myeik | 12.26 | 98.36 | 1966 |
| Kawthoung | 09.58 | 98.35 | 1966 |

caused inland flooding (LWIN, 1980). The distribution of the maximum surge along the Ayeyarwady River for the cyclone of May 1975 is given in Fig. 6.45 (CHO, 1980). The highest surge was recorded 80–90 kilometers inland Duration of storm surge was longest where water logged. It was about 25–30 km inland (Fig. 6.46).

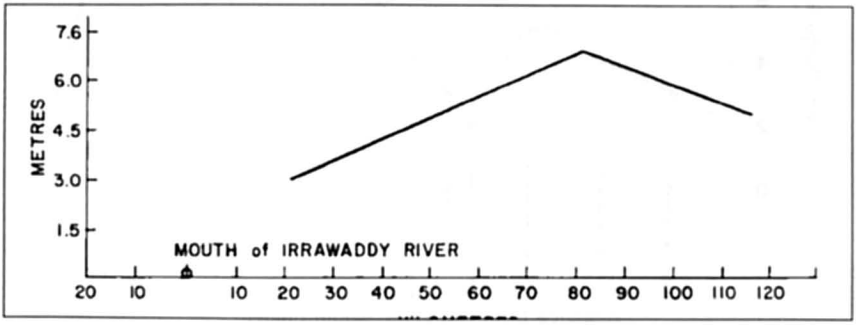


Fig. 6.45: Distribution of the maximum surge along the Ayeyarwady River for the storm of May 5–8, 1975. The ordinate is the surge amplitude and the abscissa is the distance along the river (CHO, 1980)

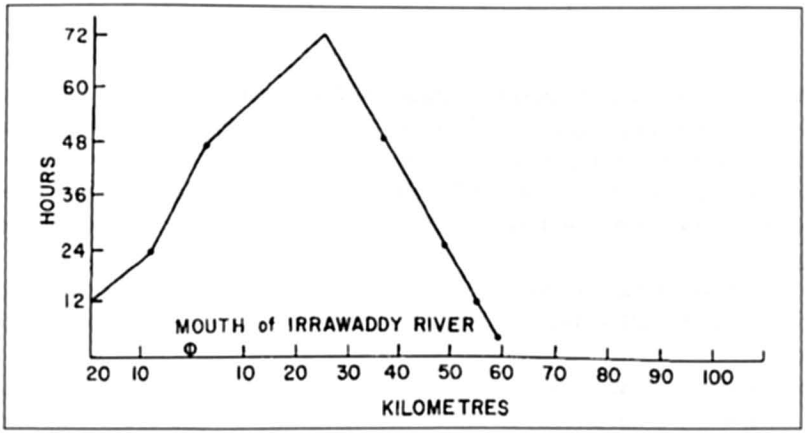


Fig. 6.46: Surge duration versus distance along the Ayeyarwady River for the storm of May 5–8, 1975 (CHO, 1980)

(iii) For deltaic coastal strip covered by many estuaries and islands, storm surge occur with winds, which may be offshore to the general coastline. In the case of 1968 Sittwe cyclone the strong offshore easterly winds have brought in water mass from the underlying surface and inundated the whole of the area.

ODD (1980) studied the storm surges generated by May 1975 cyclone in the Ayeyarwady Delta Area of Myanmar making use of hydraulic and numerical models. He concluded that the surge amplitudes as well as the amplitude of the semidiurnal tide increase rapidly east of China Bakir because of the shallowness and funnel shape of the Gulf of Martaban.

Table 6.35 (a): List of computed and observed surge heights for rakhine coast

| Year | Station | ΔP (mb) | C ($km \cdot hr^{-1}$) | Computed Surge (m) | Observed Surge (m) | E |
|---|---|---|---|---|---|---|
| 1967 | Sittwe | 25 | 10 | 1.85 | 1.80 | +0.08 |
| 1967 | Sittwe | 22 | 10 | 1.66 | NA | NA |
| 1968 | Sittwe (Kyaukpyu) | 50 | 11 | 4.05 | 4.25 | –0.20 |
| 1976 | Thandwe | 20 | 10 | 1.42 | NA | NA |
| 1978 | Kyaukpyu (Myabon) | 34 | 8 | 2.78 | NA | NA |
| 1994 | Maungdaw | 43 | 36 | 3.26 | 3.08 | +0.18 |

NA = Not Available

Table 6.35 (b): List of computed and observed surge heights for deltaic coast

| Year | Station | $V_{max}$ (kt) | $H_c$ (m) | $H_0$ (m) | E |
|---|---|---|---|---|---|
| 1975 | Pathein | 140 | 2.75 | 3.00 | –0.25 |
| 1982 | Latputta | 60 | 0.48 | 0.60 | –0.12 |
| 1982 | Gwa | 120 | 3.75 | 3.70 | +0.05 |

LWIN (1980) developed an analytical and empirical prediction model, which is based on the combination of Miyazak's and Fletcher's equations. The empirical formula developed by LWIN (1980) relates the peak surge h (cm) with the maximum sustained wind Vm ($ms^{-1}$) and the angle between the normal to the coast and the direction of the moment of the storm θ. The relation is

$$h = (A + B \cos \theta) V_m^2$$

where A and B are numerical constants, whose values are determined from the historical records. The values of A and B are:

(i) For Rakhine coast; A = 0.0563, B = 0.0744

(ii) For the Deltaic coast; A = 0.1264, B = 0.0864.

Two precomputed nomograms, one for shallow water corresponding to deltaic coast and the other for deep water corresponding to Rakhine coast were also constructed by the author. These nomograms are given in Fig. 6.47a and 6.47b.

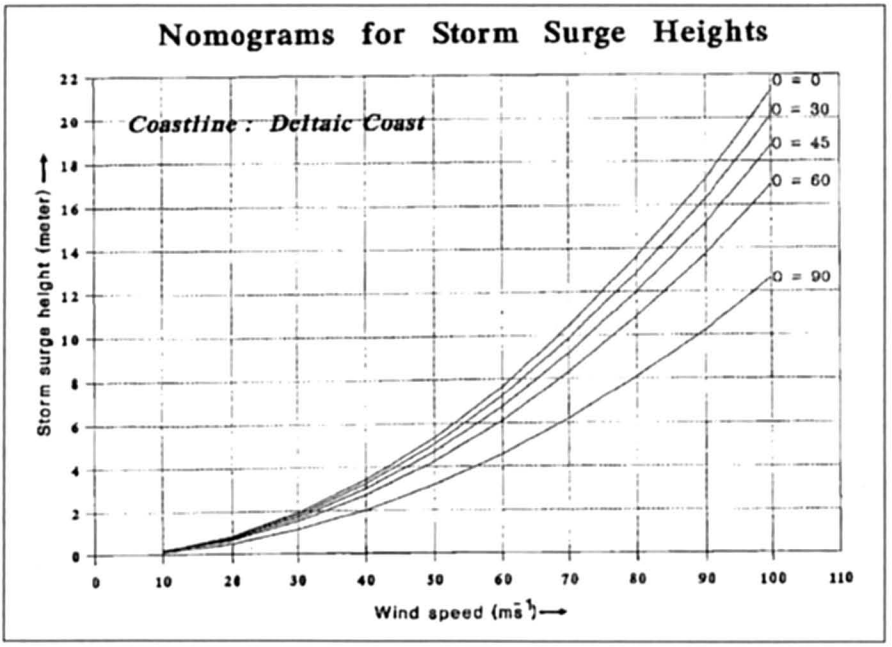


Fig. 6.47a: Nomograms for storm surge heights (deltaic coast) (Lwin, 1994b)

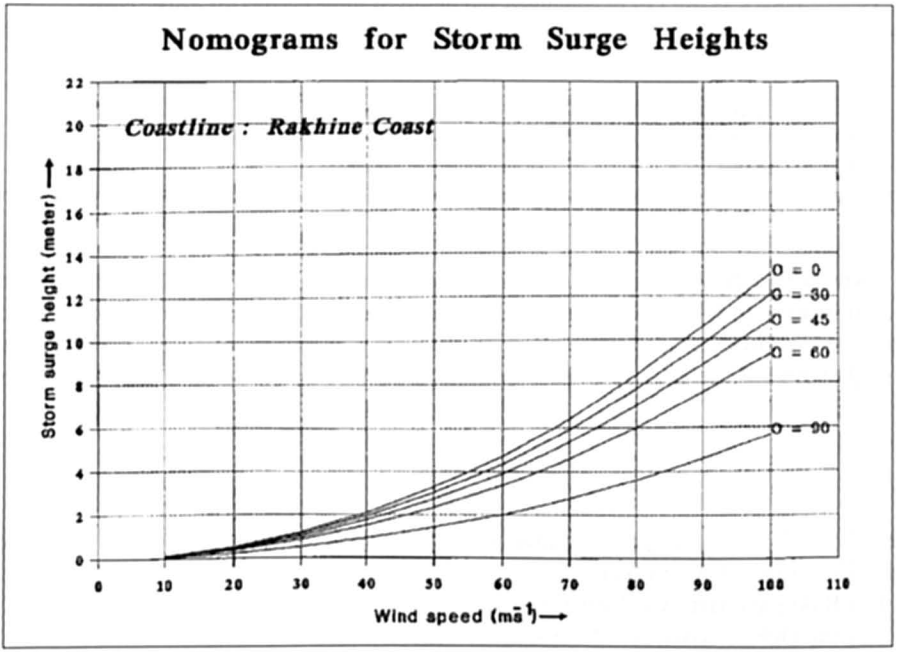


Fig. 6.47b: Nomograms for storm surge heights (Rakhine coast) (Lwin, 1994b)

As already maintained JARREL et al. (1982) developed two models for the Myanmar/ Thailand coastlines. Analysis area of the models included the coastline and offshore region up to and slightly beyond the continental shelf. Three tropical cyclone impact points based on the population were chosen: Two in Myanmar (Pathein and Yangon) and one in Thailand (Phuket). Authors performed several runs for these impact points to assess the storm surge threat in the coastal regions of Myanmar and Thailand.

DUBE et al. (1984a) used a vertically integrated storm surge model to simulate the surge generated by May 1975 Pathain cyclone. Their model is based on fully nonlinear equations and cover the whole Bay of Bengal extending from 6° N to 22.5° N and the western and eastern sides of the analysis area are the east coast of India and Myanmar-Malaya coasts respectively. Their model produced the maximum surge in the range of 3 to 5 m in the deltaic region of Myanmar right from the mouth of Ayeyarwady to the extreme northern regions of the Gulf of Martaban. This is good agreement with the available observations.

Attempts have also been made to predict storm surges in Myanmar using different empirical and statistical techniques. The detailed review of these methods is given by LWIN (1994b). LWIN (1994a) and THAW (1998) give the detailed review of the present status of storm surge fore coasting in Myanmar.

DUBE (1998b) applied a coastal zone vertically integrated numerical storm surge model to Myanmar. He performed several simulation experiments by using the data of severe cyclonic storms hitting the coastal regions of the Myanmar. He compared the simulated sea surface elevation with observations from local tide gauges where ever possible or with post storm survey estimates. The results of the experiments are in general in good agreement with reported values along the deltaic region of Myanmar. The computed peak surge envelope for May 1982 Gwa cyclone is shown in Fig. 6.48.

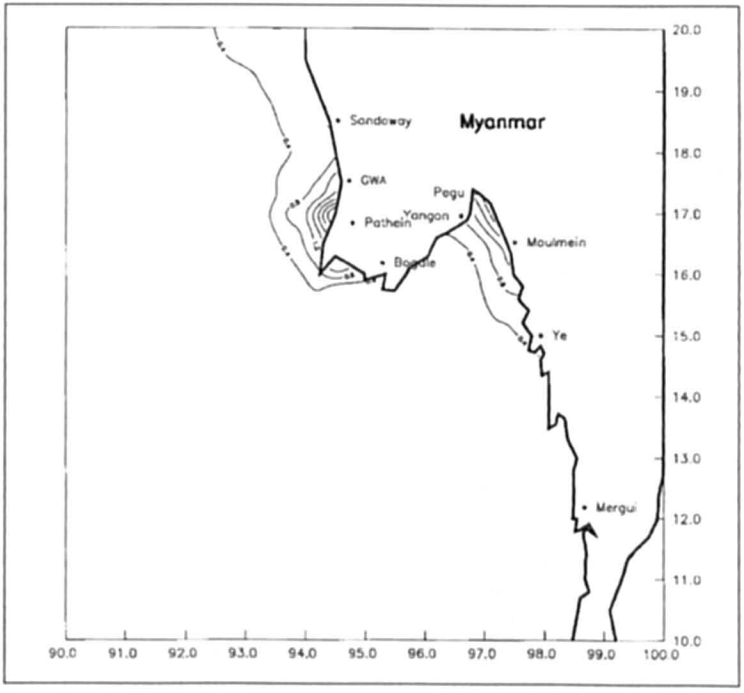


Fig. 6.48: Computed peak surge for May 1982 Gwa cyclone (DUBE, 1998b)

*(d) Sri Lanka*

Storm surges are not frequent in Sri Lanka; however major surges occurred in association with December 1964 and November 1978 cyclone. December 1964 Trincomalee/Rameswaram cyclone was one of the severest storm that affected Sri Lanka and extreme southern India peninsula. Batticoloa cyclone of November 1978 also affected southeast coast of India besides causing extensive loss of life and property in the coastal regions of east coast of Sri Lanka Table 6.36 lists the severe cyclonic storms, which formed in the Bay of Bengal during 184–1999 and crossed Sri Lanka coast. It may be seen from the table that east and north Sri Lanka coast are the most vulnerable coast for the landfall of tropical cyclones.

Table 6.36: Severe cyclonic storms of Sri Lanka

| No. | Date | Location | Damage |
|---|---|---|---|
| 1 | 8–10 March, 1907 | Eastern coast of Sri Lanka | Damage estimation not available |
| 2 | 17–24 December, 1964 | Near Trincomalee | Damage estimation not available |
| 3 | 17–24 November, 1978 | Near Batticaloa | 2 m surge, 915 deaths 100,000 houses damaged, At Kalkudah, the sea had entered land to distance of about 1.5 km. |
| 4 | 11–17 November, 1992 | Eastern coast of Sri Lanka | 4 deaths, 29,116 houses damaged |

Study of the storm surges in Sri Lanka has not attracted many workers. Only studies that came to our notice are by JARREL et al. (1982), RAO et al. (1994), DHARAMRATNA (1996) and CHITTIBABU (1999).

JARREL et al. (1982) developed models for Sri Lanka as a part of their major study to evaluate storm surge threat in the Bay of Bengal. They selected Trincomalee and Jaffna as the tropical cyclone impact points on the northeast coast of Sri Lanka. Several numerical experiments were performed by the authors for the cyclones of varying wind speeds approaching Trincomalle and Jaffna from SE through NE. This study may probably be considered as one of the most comprehensive study to assess the impact of storm surges on the coast of Sri Lanka.

RAO et al. (1994) developed a coastal zone numerical model to simulate storm surges and currents arriving Sri Lanka and Southern Indian Peninsula. The model is based on the conventional depth averaged equations and cover an analysis area extending from 2° N to 20° N and 72° E to 86° E. Experiments are carried out to simulate the surges generated by the December 1964 and November 1992 cyclones. The 1964 Rameswaram cyclone crossed the Sri Lanka coast about 50 km north of Trincomallee on 22 December at about 0600 UTC, Moving north westward it crossed the Sri Lanka and struck the Indian coast about 30 km to the south of Tondi on December 23 at 0600 UTC. Surges therefore occurred both on the northeast coast of Sri Lanka and southeast coast of India in association with this cyclone.

The track of the cyclone is shown in Fig. 6.49 computed maximum sea surface elevations for the landfall of the cyclone in Sri Lanka and later in India are shown in Fig. 6.50. A peak surge of 3.7 m is predicted at about 50 km north of Trincomalee (Sri Lanka) while near Tondi (India) a peak surge of 5.6 m is predicted. This is in agreement with the reported flooding and surge in the region (RAO and MAZUMDAR 1966). Very recently CHITTIBABU (1999) used the model developed by RAO et al. (1994) to simulate the surge generated by November 1978

Batticoloa cyclone. Model computed contours of peak surge elevations for the east coast of Sri Lanka and southeast coast of India are given in Fig. 6.51.The simulated surges are in good agreement with the reported maximum surge values (SRINIVASAN et al., 1978).

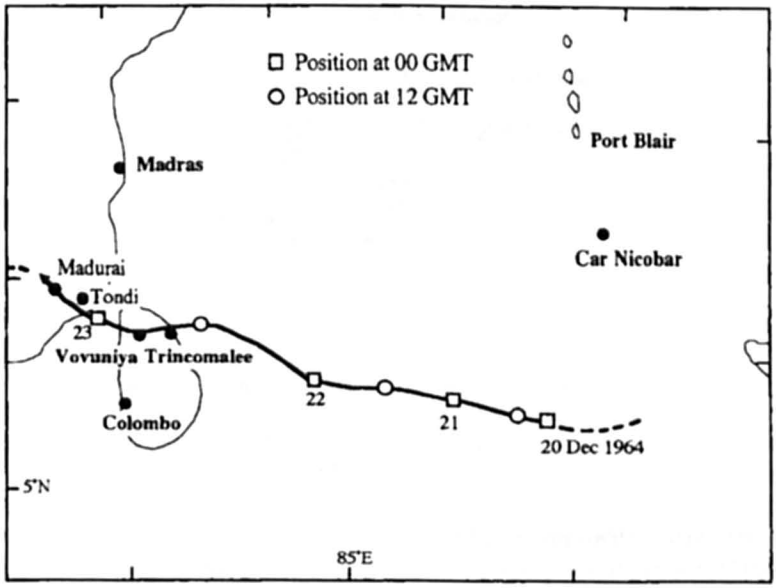


Fig. 6.49: Track of December 1964 Rameshwaram cyclone (RAO et al., 1994)

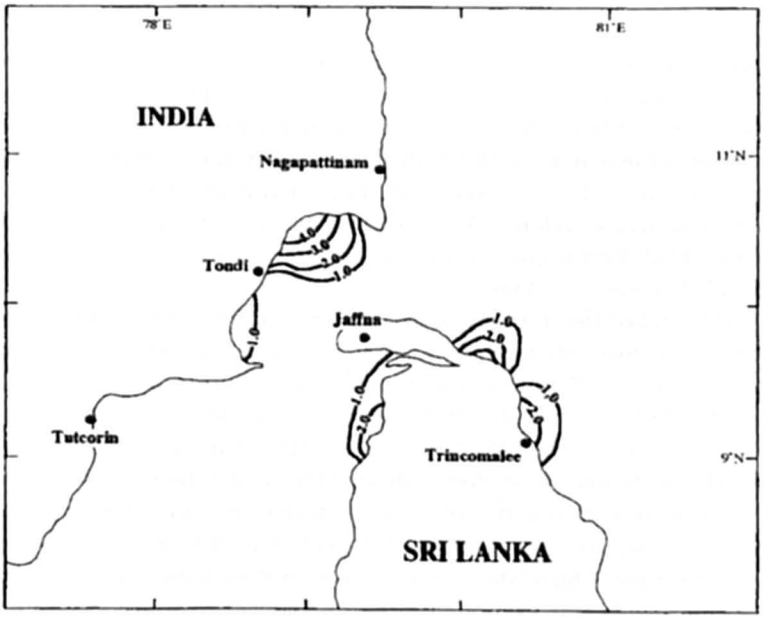


Fig. 6.50: Computed maximum sea surface elevations for the landfall of the cyclone in Sri Lanka and later in India (RAO et al., 1994)

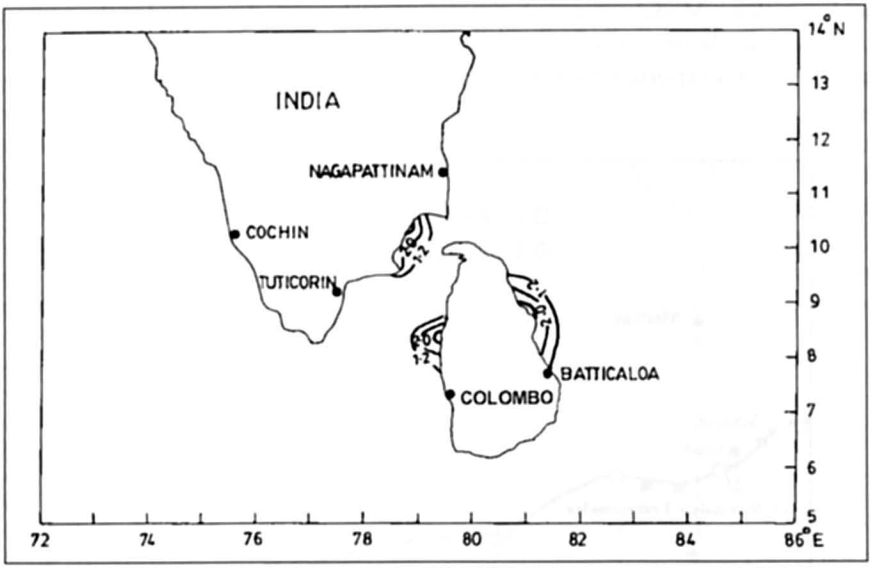


Fig. 6.51: Computed peak surge associated with November 1978 Batticoloa cyclone of Sri Lanka (CHITTIBABU, 1999)

DHARMARATNA (1996) presented the nomograms based on the model output of JELESNIANSKI (1972) for predication of the storm surges on the entire east coast of Sri Lanka. He applied these nomograms to successfully compute the surge associated with 1978 Batticoloa cyclone.

### 6.3.2 Arabian Sea

Although more cyclones occur in the Bay of Bengal than the Arabian Sea, there are several records of severe cyclonic storms hitting the Gujarat and the North Maharashtra regions of the west coast of India. Number of cyclones in the Bay of Bengal over a given period is about four times the number in the Arabian Sea; however, only about one quarter of the Bay of Bengal storms mature into severe storms, whereas about 40 % of the Arabian Sea storms can become severe cyclones. A partial list of major storm surges on the Arabian coast of India during 1782–1999 is given in Table 6.37. Table shows that the Gujarat coast is the most vulnerable to tropical cyclones.

RAO (1968) studied the storm surges on the Arabian Sea coast of India (and Pakistan). Classification of this coast into types A, B, and C is given in Fig 6.35. Previously, it was mentioned that on the Bay of Bengal coast of the subcontinent, there are two dangerous zones (type C). On the Arabian coast, also, there are two dangerous zones. The first one includes the Konkan coast to the north of 18° N and the coastal belt around the Gulf of Cambay.

In this belt, the frequency of storms striking the coast is low. This may be seen from Fig. 6.52, which provide the landfall of cyclonic storms on a district-wise basis. Here, the tidal range is quite large (e. g., 8 m at Mumbai. and 11 m at Cambay). Unless peak surge occurs close to the time of high tide, no major water level oscillations may occur in this belt. It should be emphasized that, even though the Arabian Sea coast experiences major storm surges much less frequently than the Bay of Bengal coast, the reason there are two dangerous belts in the manner of the classification into types A, B, and C. This classification does not

Table 6.37: List of Storm surges along west coast of India (1618–1999)

| No. | Date | Location | Damage |
|---|---|---|---|
| 1 | May 15, 1618 | Mumbai coast Maharastra, India | 2000 deaths, many vessels lost in Bombay port |
| 2 | 20–21 April, 1782 | Near Surat, Gujarat coast, India | Major storm surge in Gulf of Cambay, several Thousands killed, several ships grounded |
| 3 | April 18, 1847 | Laccadive islands, India | 1000 deaths, huge storm wave swept over several of the Laccadive islands |
| 4 | May, 1851 | 32 km west of Karachi | Major storm surge Karachi and environs |
| 5 | 30 October–2 November, 1854 | Bombay coast, India | 1000 deaths |
| 6 | 6–14 June, 1920 | Veeraval, India | Major storm surge in Gulf of Cambay |
| 7 | 9–13 June, 1964 | Naliya, India | 2 m storm surge at Kandla, 1.5 m at Okha, 1 m at Navlakhi, 27 killed, extensive damage |
| 8 | 19–24 October, 1975 | Porbandar, Saurashtra, India | 85 deaths, several thousand houses damaged |
| 9 | 31 May–5 June, 1976 | Mahua, India | 87 deaths, 4500 cattle died, extensive damage |
| 10 | 13–23 November, 1977 | Karwar, India | 72 deaths, major storm surge Karwar and environs |
| 11 | 4–9 November, 1982 | Veeraval, Gulf of Cambay | 542 deaths, 1,50,332 cattle killed, 12624 pucca houses and 54549 kutcha buildings destroyed. Storm surge – 3.5 m at Mangral, 2 m at Diu, 2 m at Veraval, 3 m at Jafarafad |
| 12 | 12–15 Nov., 1993 | North Gujarat and Sindh coast | 50 fishermen missing |
| 13 | 17–20 June, 1996 | Between Kodiar and Diu, India | 5–6 m storm surge near Bharuch. Gulf of Cambay are affected by storm surge of height 3–5 m. 47 killed. 30,000 houses destroyed |
| 14 | 8–11 June, 1998 | Kandla, Gulf of Kutch | 550 killed, 150 kmph winds, great destruction |

include the frequency of occurrence. It only deals with the maximum water level to be expected in the event of major storms, however infrequently they may occur.

The second dangerous belt stretches from Dwarka (India) to Karachi (Pakistan). This region includes the extensive marshy areas (mostly unpopulated) known as the "Rann of Kutch." In this belt, also, the frequency of storm is low and the tracks are not usually favorable for major surge development. However, on rate occasion when they do occur, storm surges several meters in amplitude could result.

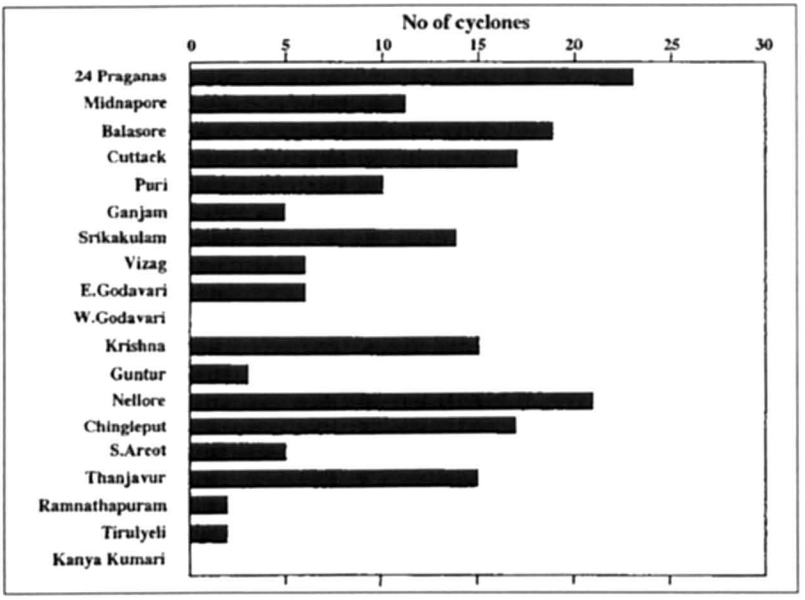


Fig. 6.52: The frequency of storms striking the west coast of India (DUBE et al., 1997)

RAO (1968) mentioned that the extensive marshlands of the Rann of Kutch are subject to large storm surges with the onset of the strong westerlies of the southwest monsoon season. The entire west coast of India south of 18° N falls into the type B category. In this area, also, the frequency of storms is low (Fig. 6.52). Also, the tracks are not generally favorable for major surge development. The coast around the Kathiawar Peninsula between Diu and Dwarak belongs to the type B category. The major surge amplitudes that can occur here are about 1.5 m and are about half the tidal range here. In this area the frequency of storms is high, but usually they are not intense (not of hurricane strength).

The peak storm surge amplitudes, maximum total water level (surge + wind waves), and the classification (into type A, B, or C) at several locations on the west coast of India and the coast of Pakistan are listed in Table 6.38. The track of the Kutch cyclone of June 1964 and the areas where surges occurred are shown in Fig. 6.53 Modeling of storm surges in the North Indian Ocean has attracted more attention to the Bay of Bengal, very few modelling studies have been carried out for the west coast of India.

GHOSH et al. (1983) have run the "SPLASH" model of JELESNIANSKI (1972) to determine storm surge envelope for the November 1982 cyclone. The peak surge computed by them is in good agreement with available estimates from observations. DUBE et al. (1985a) appears to be the among the first to use a two-dimensional fully nonlinear coastal zone numerical model to study the storm surges on the west coast of India. Their model covers an analysis area lying between 10° N and 23.2° N and between 67.8° E and 76° E. Orthogonal straight-line segments represent the coastal boundary of the west coast of India, which has the advantage of representing the Gulf of Cambay. This model has been used to simulate the surge generated by the 1975 Porbandar cyclone (Fig. 6.54a). The predicted maximum surge elevation at Porbandar compares well with the actual observations. The distribution of the predicted maximum sea surface elevations (peak surge envelope), observed surge and the time of occurrence along the Gujarat coast are given in Fig. 6.54b. It is interesting to note from the figure that the predicted peak surge of 2.2 m at Porbandar is in good agreement with the post storm

Table 6.38: Peak surge amplitude and maximum water level; (surge + wind wave) that can occur for storm with maximum winds of 40 $m \cdot s^{-1}$ on the Arabian Sea coast of the Indian subcontinent. Classification: B, total water level 2–5 m; C, > 5 m. (RAO, 1968)

| Location | Favorable wind direction | Peak surge amplitude (m) | Maximum value of total water level (m) | Classification |
|---|---|---|---|---|
| Muthan Point (Nagercoil) | SW | 1.4 | 2.3 | B |
| Cochin | W | 1.6 | 2.7 | B |
| Calicut | WSW | 2.1 | 3.5 | B |
| Mangalore | WSW | 1.8 | 3.0 | B |
| Bhatkal | WSW | 2.7 | 4.5 | B |
| Panjim | WSW | 1.7 | 2.8 | B |
| Devgad | WSW | 1.5 | 2.5 | B |
| Ratnagiri | W | 1.8 | 3.0 | B |
| Harnaf | WSW | 1.7 | 2.8 | B |
| Mouth of Rajpuri River (Murud) | W | 3.1 | 5.2 | C |
| Mouth of Patel Ganga River | W | 4.3 | 7.2 | C |
| Bombay | W | 1.5 | 4.5 | B |
| Agashi Bay | W | 4.2 | 7.0 | C |
| Dahapu | W | 4.0 | 6.7 | C |
| Bulasar Kheri | W | 4.5 | 7.5 | C |
| Suvali Point | WSW | 3.3 | 5.5 | C |
| Mindola | WSW | 5.2 | 8.7 | C |
| Mal Bank | S | 4.3 | 7.2 | C |
| Mahuva Road | SE | 2.0 | 3.4 | B |
| Jafarabad | SSE | 3.1 | 5.2 | C |
| Diu | SSE | 2.2 | 3.7 | B |
| Veeraval | SW | 1.5 | 2.5 | B |
| Porbandar | SSW | 1.6 | 2.7 | B |
| Dwarka | SW | 1.6 | 2.7 | B |
| Balachin | W | 5.1 | 8.5 | C |
| Rann of Kutch | WSW | 3.9 | 6.5 | C |
| Wair Creek | SSW | 4.0 | 6.7 | C |
| Mouth of Indus River | S | 3.0 | 5.0 | C |
| Karachi | S | 3.5 | 5.8 | C |

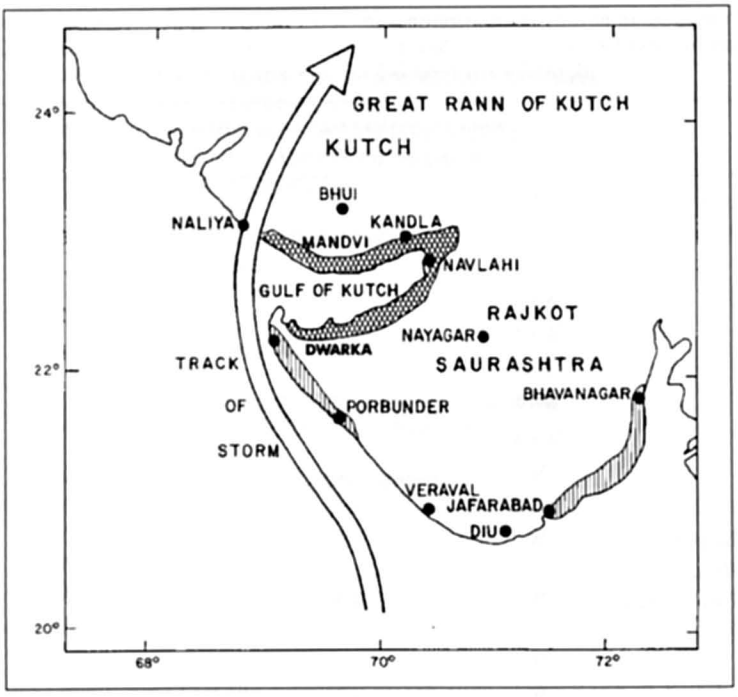


Fig. 6.53: Track of the Kutch cyclone of June 1964 on the west coast of India. Single – hatched area is affected by minor surges; double – hatched areas are affected by major surges (RAO, 1968)

survey estimated sea-surface elevation of 2.7 m (GHOSH 1981). A slightly lower elevation produced by the model has been attributed by the authors to the contribution due to astronomical tides, which was not accounted in the model. At approximately the time of the landfall of the cyclone, the predicted value of astronomical tides was 63 cm. No other observation on the sea surface elevation was, however, available to make a comparison of the observed and predicted surge along this part of the Gujarat coast.

SINHA et al. (1984) used the numerical model developed DUBE et al. (1985 a) to simulate the surge induced by November 1982 Gujarat cyclone. During the period of this event, the estimated heights of water level above normal tide was collected during the post storm survey at certain ports (RAMA SASTRY et al., 1984). Model computed maximum surge height was found to be in good agreement with the estimated values at Veraval, Diu and Jafrabad (Fig. 6.55). However, at Mangral, which is about 80 km to the left of the landfall, the predicted value is much lower than the estimated one, for which the authors could give no satisfactory explanation.

More recently CHITTIBABU et al. (2000) developed a high-resolution location specific model for Gujarat coast. Model has been used to simulate surges associated with recent cyclones hitting the coast of Gujarat.

The coastal area of Pakistan is occasionally affected by severe cyclonic storms, which form in the Arabian Sea. A partial list of severe cyclonic storms during the period 1891–1999 which made landfall on Pakistan coast is given in Table 6.39, Data on storm surges associated with these tropical cyclones are not available. However numerical simulation experiment performed by CHITTIBABU (1999) using the information available for June 1999 cyclone shows that the cyclone could have generated a minor surge on the Sind coast of Pakistan.

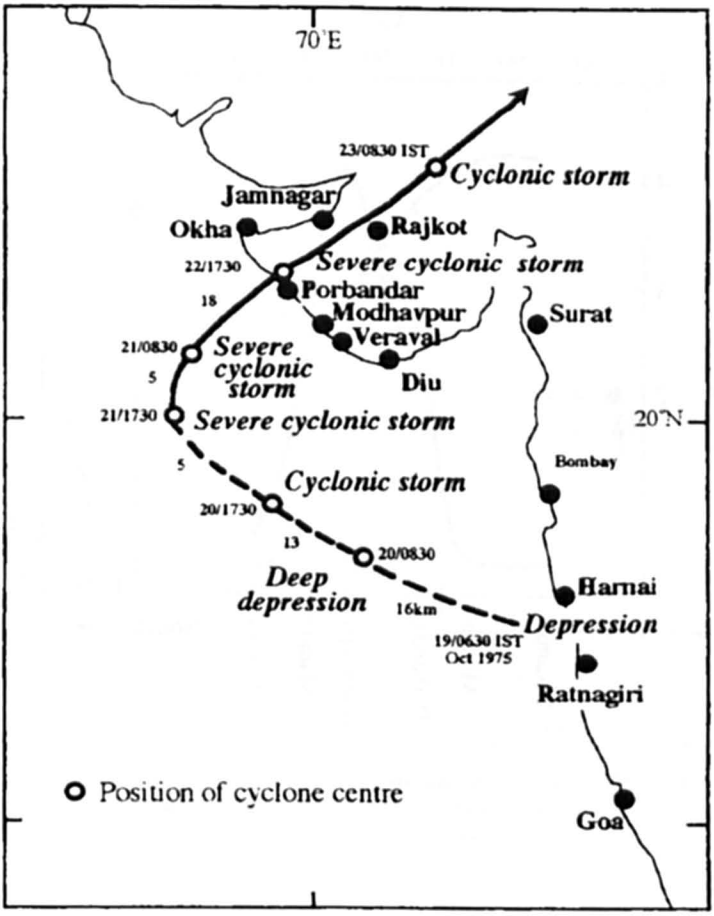


Fig. 6.54a: Path of Porbandar cyclone (DUBE et al., 1985a)

Table 6.39: List of severe cyclonic storms in Pakistan and rest of the Arabian Sea

| No. | Date | Location | Damage |
|---|---|---|---|
| 1 | May 1851 | 32 km west of Karachi | Major storm surge Karachi and environs |
| 2 | 25 April–5 May 1901 | Makran coast | Damage estimation not available |
| 3 | 7–14 May 1902 | Near Karachi | Damage estimation not available |
| 4 | 11–16 June 1902 | Near Karachi | Damage estimation not available |
| 5 | 4–6 June 1907 | Near Karachi | Damage estimation not available |
| 6 | 18–20 June 1920 | South of Karachi | Damage estimation not available |
| 7 | 5–9 June 1994 | Saudi Arabian Coast | Damage estimation not available |
| 8 | 15–20 Nov. 1994 | Somali coast | Damage estimatio not available |

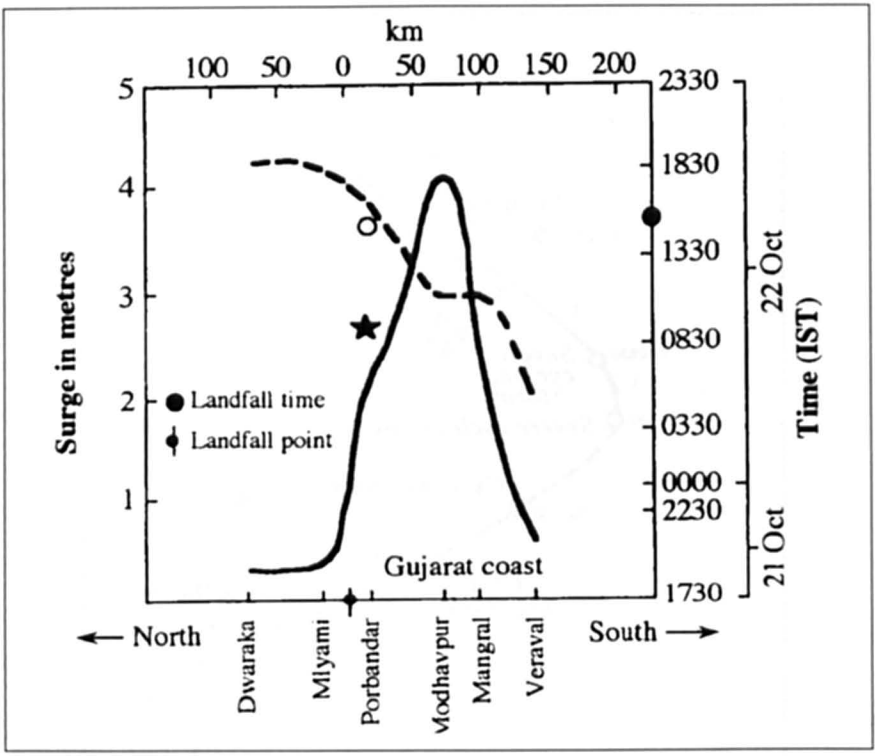


Fig. 6.54b: Maximum sea – surface elevation and time of occurrence along Gujarat coast: –, peak surge envelope; - - -, time of occurrence of peak surge; *, observed storm generated surge; °, observed time of occurrence of peak surge (DUBE et al., 1985)

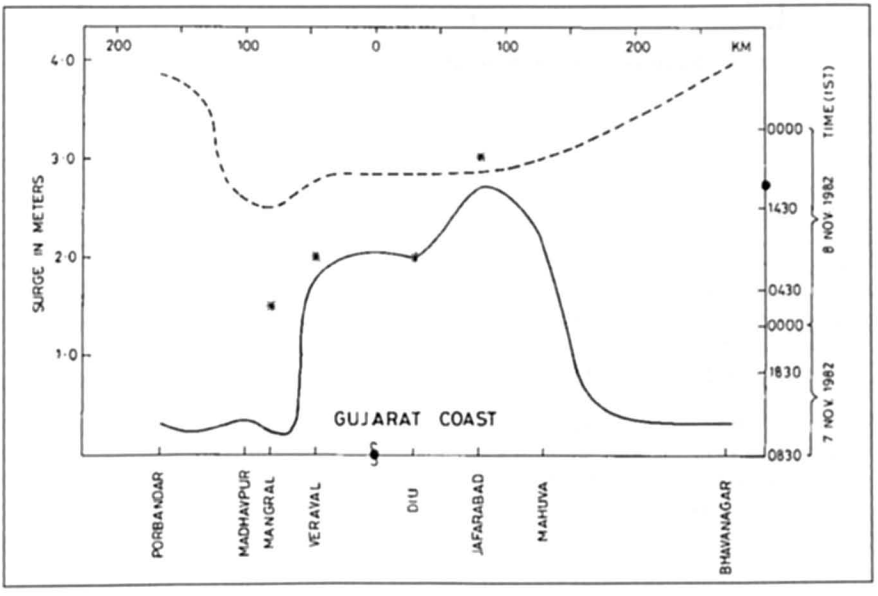


Fig. 6.55: Maximum sea surface elevation and time of occurrence along Saurashtra coast (SINHA et al., 1984)

## 6.4 South West Indian Ocean

### 6.4.1 Storm Surges in Malagasy Republic (Madagascar)

Figure 6.56 shows a geographical map of Madagascar. Figure 6.57 shows the tracks of cyclones that influence Morondava und Fort-Dauphin. Table 6.40 lists some pertinent data about cyclones for the period 1975 to 1992.

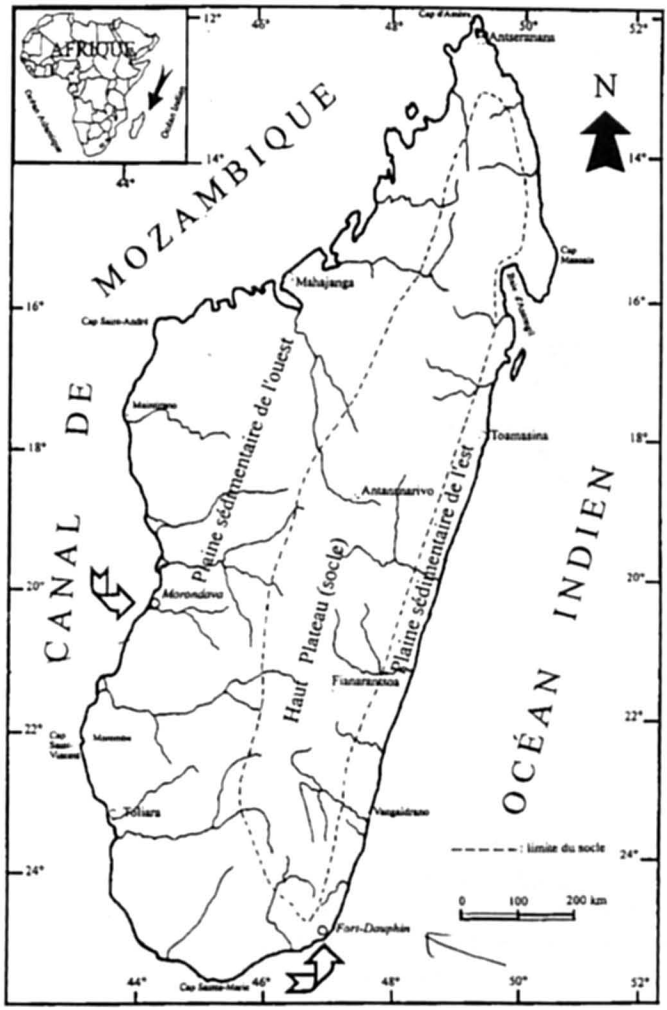


Fig. 6.56: Geographical map of Madagascar.

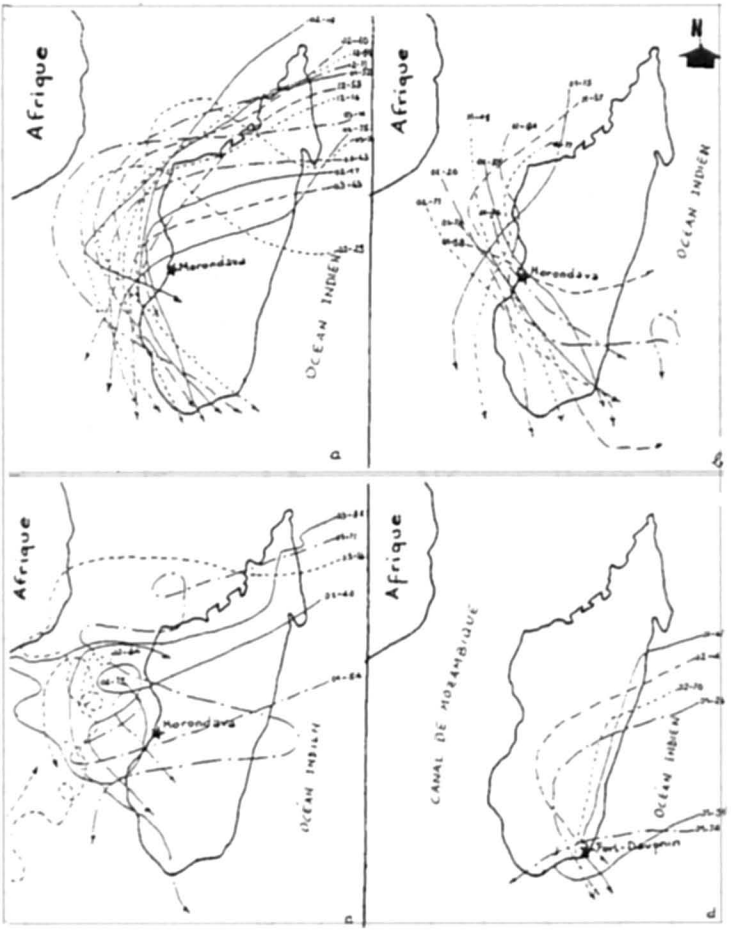


Fig. 6.57: Track of cyclones that influence Morondava and Fort-Dauphin, (a) cyclones from the Indian ocean influencing Morondava, (b) cyclones from the Mozambique channel influencing Morondava, (c) cyclones with complex trajectories influencing Morondava, (d) cyclones influencing Fort-Dauphin (BATTISTINI, 1964).

Earlier, it was mentioned that tropical cyclones travel nearby and sometimes traverse Malagasy Republic. The only study this author could find on the storm surges in this region is by LACOUR (1935). In principle, storm surges could occur along the long east and west coasts of this island (about 1500 km in length). However, favourable cyclone tracks usually generate surges on the east coast of this island, where the tidal range is small (less than 80 cm).

Storm surges appear to be more frequent on the east coast than on the west coast. Also, surges on the east coast are more important south of Tamtave than north of it. Although surges are more frequent on the east coast the amplitudes usually are rather small (20 cm or less). However, the March 1927 event near Tamtave was a major surge and caused some destruction. Major surges could occur at Tuléar on the sourthern part of the west coast (e.g., the event of January 1933). DAS et al. (1978) stated that cyclonic storms in the Island of La Réunion in the South Indian Ocean often produced exceptionally heavy rain accompanied by surges of 4.6 m have been reported from this island.

Table 6.40: Cyclones affecting Madagascar (RASOANILANA, 1997)

| Date | Name | Wind Speed (KPH) | Central Pressure (hPa) |
|---|---|---|---|
| 23–24 Dec 1974 | Adele | | |
| 2–21 Jan 1975 | Camille | 200 | – |
| 1 Feb | Fernande | 200 | – |
| 12–29 Jan 1976 | Danae | 240 | 965 |
| 27 Mar–10 April 1976 | Gladys | 100 | – |
| 23 Jan 1977 | Domitile | 120 | 992 |
| 28 Jan–5 Feb 1977 | Emilie | 130 | 980 |
| 17 Feb–3 Mar 1977 | Herves | 108 | 986 |
| 23–25 Jan 1978 | Georgia | 96 | 992 |
| 10–13 Feb 1978 | Irena | 200 | 985 |
| 16–31 Dec 1978 | Angele | 194 | 958 |
| 4–12 Feb 1979 | Dora | – | – |
| 10–13 Jan 1980 | Gudule | 68 | 1002 |
| 28 Dec 1980 | Edwige | – | 998 |
| Ist Jan 1981 | | | |
| 17–25 Feb 1981 | Iadine | 180 | 991 |
| 31 Jan–5 Feb 1982 | Electre | 95 | 997 |
| 16–27 Mar 1982 | Justine | 135 | 957 |
| 9–16 Jan 1984 | Elinah | – | – |
| 5–10 Jan 1984 | Caboto | 43 | – |
| 18 Jan–2 Feb 1984 | Domoins | 100 | – |
| 1985–1986 | Alifredy | 58 | – |
| | Berobia | 58 | – |
| | Gista | 120 | – |
| | Honorine | 120 | – |
| 1987–1988 | Calidera | – | – |
| | Doaza | – | – |
| 9–17 Jan 1989 | Calasanjy | 133 | 980 |
| 1989 | Iana | 150 | – |
| 16–19 Feb 1991 | Cynthia | 113 | 979 |
| 25 Dec 1991 | Bryna | 65 | 1002 |
| 10 Jan 1992 | | | |

## 6.5 South East Indian Ocean

By South East Indian Ocean, we mean the northern part of the West Coast of Australia, which is subjected to storm surges generated by tropical cyclones, HUBBERT et al. (1991) numerically modelled. Tropical cyclone generated storm surges on the northern part of the Australian coastline. Fig. 6.58 shows the tracks of four hurricanes that made a landfall in the study area. Out of these hurricanes Jason Winifred and Aivu struck the Pacific coast of Australia (these will be considered in section 6.6) and Hazel made landfall on the Indian Ocean coast of Australia. In this section, we will consider only the Indian Ocean coast.

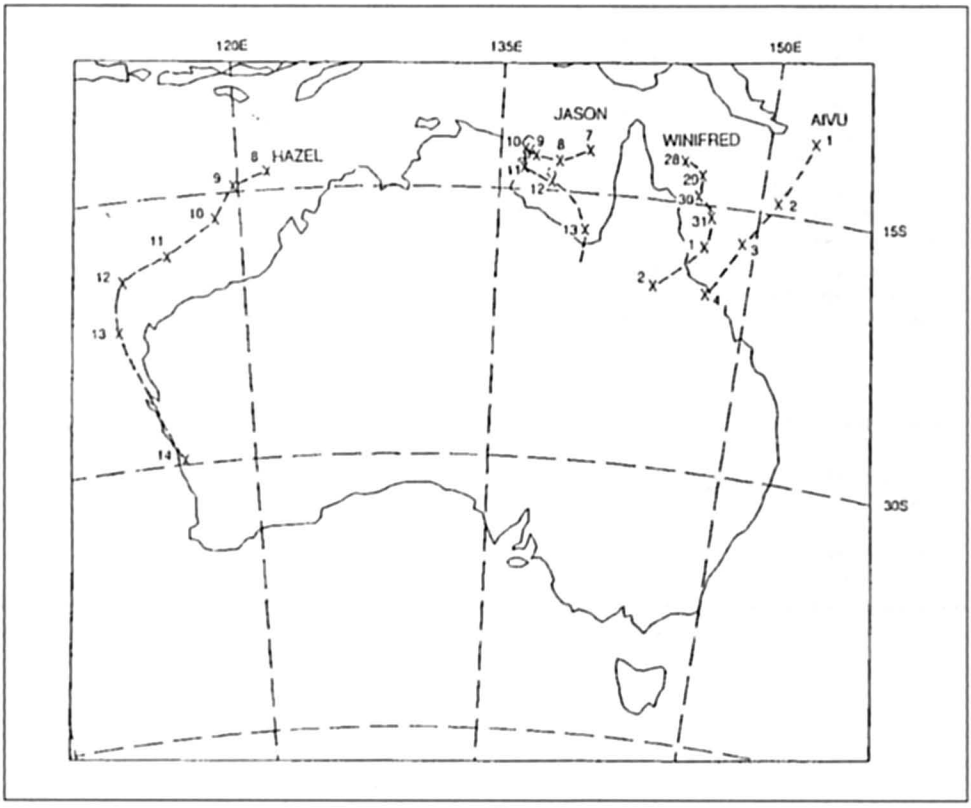


Fig. 6.58: Tracks of the four tropical cyclones (Winifred, Aivu, Jason and Hazel) used in this study. 00 UTC times and dates are shown (HUBBERT et al., 1991)

### 6.5.1 Numerical Model and Results

The two-dimensional depth-averaged model of HUBBERT et al. (1990) was used in conjunction with HOLLAND'S (1980) analytical-empirical model to derive the atmospheric pressure and wind fields at sea level. This model requires only the positions of the hurricane centre, the cyclone intensity and the radius of maximum winds (RMW).

The error in the numerical model for the prediction of surge elevations is 0.1 m to 0.2 m and the arrival times of the surge waves on the coast have atmost an error of one hour. The model includes such second order effects as coastally trapped edge waves.

When a tropical cyclone moves with the coast on the left (Southern Hemisphere) near to the propagation speed of a coastally trapped wave, resonant amplification of the sea surface elevation can occur, which is referred to by JELESNIANSKI (1967) as "Resurgence". This is a particular problem for the West Coast of Australia, where conditions for such resonant amplification are met. FANDRY et al. (1984) showed that the resulting surface elevation could propagate for thousands of kilometres and can cause inundation even at vast distances.

Hurricane Hazel attained a lowest central pressure of 936 hPa as it approached Carnarvon with an RMW of 30 km. As Hazel moved obliquely towards the coast, a region of positive surge developed first. A region of negative surge then formed and moved ahead of the amplifying positive surge wave, with the zero line staying slightly ahead of the cyclone position.

Fig 6.59 shows the contours of the water level at time of maximum surge at the Carnarvon. Significant amplification of the surge wave occurred in Shark Bay with amplitudes greater than 3 m. A second branch continued to propagate down the coast, resonating with the

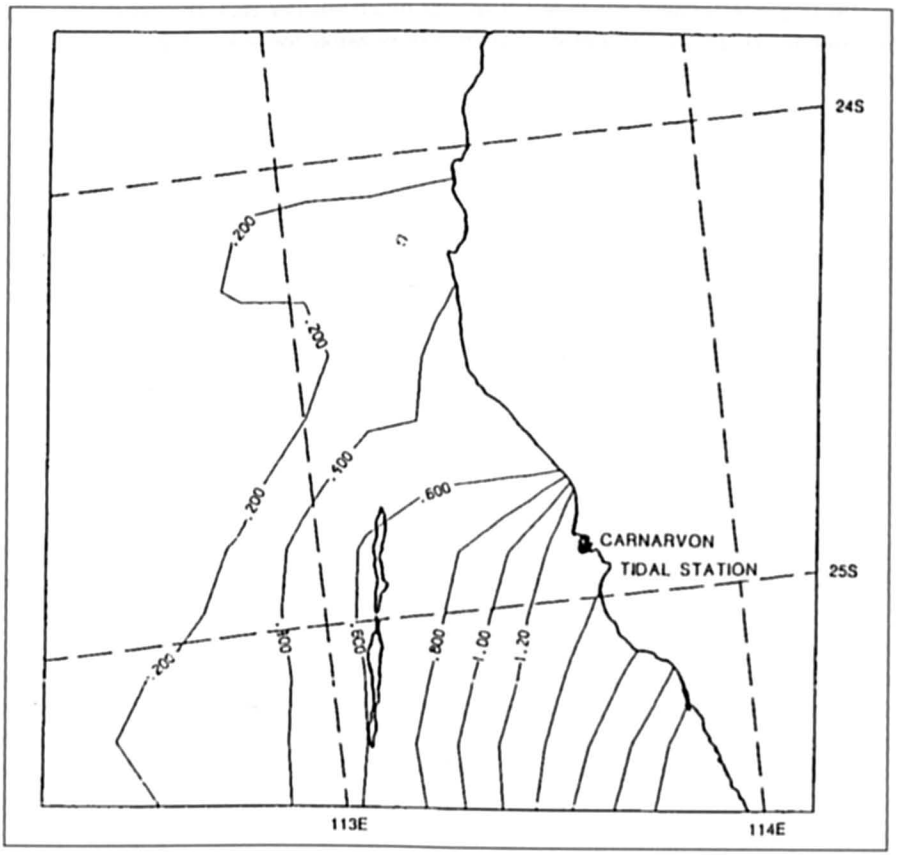


Fig. 6.59: Model results at the time of peak Carnarvon surge for tropical cyclone Hazel (14 UTC, 13 March 1979): (a) Sea surface elevations (m), and (b) depth – integrated currents ($cms^{-1}$) (HUBBERT et. al., 1991)

developing Hazel. After the cyclone rapidly weakened after landfall, the second branch evolved into a freely propagating coastally trapped wave, with amplitude of about 10 cm. Table 6.41 summarises the errors.

Table 6.41: Errors in the results of the numerical model for hurricane Hazel

| | Surge amplitude (m) | | | Time of Max. Surge | | |
|---|---|---|---|---|---|---|
| | Observed | Computed | Error | Observed | Computed | Error |
| Carnarvon | 1.3 | 1.3 | 0.0 | 1400 | 1400 | 0.0 |
| Geraldton | 0.7 | 0.6 | –0.1 | 2100 | 2100 | 0.0 |

Table 6.41 shows that model results are quite accurate. However, the amplitude of the negative surge computed for Carnarvon was much greater than the observed value. Next, the authors made another simulation with a cyclone similar to Hazel but approaching the coast in a perpendicular direction near Carnarvon. Consistent with the analytical study of FANDRY et al. (1984), the maximum surge of 0.8 m was much smaller than the observed surge of 1.3 m, implying that resonant amplification was responsible for some of the surge at Carnarvon.

## 6.6 South West Pacific Ocean

By southwest Pacific, we mean the east coast of Australia and the coastlines of New Zealand.

### 6.6.1 New Zealand

Severe storm surges generally do not occur on the coasts of New Zealand. GILMOUR (1963) reported a surge of 0.78 m at Bluff Harbour; AGNEW (1966) found surges of up to 0.8 m on the west coast of the North Island during July 1965. Two cyclones in April 1972 produced surges up to 0.3 m on the east coast of New Zealand (PICKRILL, 1972). HEATH (1979) mentioned that due to the windy climate of New Zealand, departures from isostatic equilibrium are quite common.

Although storm surge amplitudes are small on the New Zealand coast, they cause considerable erosion (GIBB, 1976, 1977), e.g. in the Bay of Plenty on the west coast of the North Island and all along the east coast of the North Island (north of Auckland).

HEATH (1979) studied three storm surges: April 9–10, 1968, on the east coast of the North Island, July 30–August 1, 1975, on the east coast of the South Island, and September 11–13, 1976, on the west coast of the North Island. These three are the major storm surge events in New Zealand during the period 1968–78. The maximum surge in these events was about 0.6 m.

### 6.6.2 Australia

HOPLEY and HARVEY (1979) studied storm surges in Australia. They questioned the accuracy of the 12.2 m surge in Bathurst Bay in 1899 (WHITTINGHAM, 1958) and the 7.01 m surge at Groote Eylandt in 1923 (WHITTINGHAM, 1958). However, they mentioned that several surges with amplitudes greater than 3 m occur in eastern Queensland. Gulf of Carpentaria, and western Australia. These authors used the JELESNIANSKI (1972) scheme to compute the amplitudes of the surges. The maximum surge height $h_c$ was calculated from

$$h_C = h_S \frac{V_P}{87} F_D \tag{6.70}$$

where, $h_s$ is the precomputed surge height based on cyclone parameters (see the SPLASH model of JELESNIANSKI 1972), $V_p$ is a correction factor based on maximum wind field and pressure drop, and $F_D$ is a depth correction factor for local bathymetry.

Surge amplitudes are generally small on the Australian coastline, with the highest levels usually occurring on the Queensland coast, particularly south of Fraser Island. Storms moving parallel to the west and east coasts of Australia produce edge waves. It is observed that these edge waves tend to amplify the crest of the surge waves on the west coast of Australia, whereas on the coast of Queensland, they tend to amplify the trough. Negative surges also predominantly occur on the Queensland coast.

Storm surge profiles at several locations along the Australian coast are shown in Fig. 6.60. The maximum surge (3 m) in this diagram was at Townsville due to Cyclone Althea during December 22–25, 1976. HOPLEY and HARVEY (1979) analysed the contributions form the forerunner, effects of wind stress and pressure gradients, and semi-diurnal tides to the total

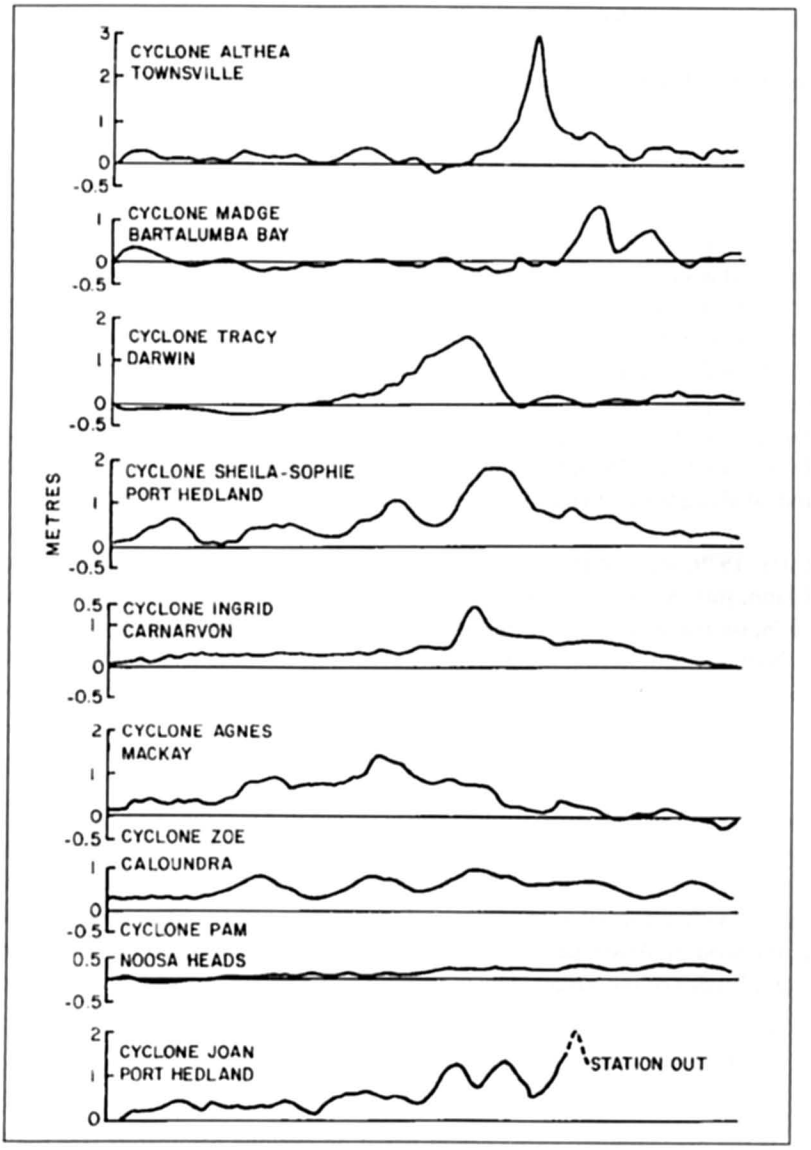


Fig. 6.60: Storm surge profiles at some locations due to selected hurricanes on the coast of Australia. Total length of the abscissa is 72 h, with the exception of cyclone Tracey, for which it is only 18 h. (HOPLEY and HARVEY, 1979)

water level during storm surge events for six regions of Australia. These results are summarised in Table 6.42.

These authors also calculated the peak surge occurrence probability curves for 19 locations around the northern coast of Australia. Brisbane and Noosa have the lowest surge risk. Two locations with the greatest surge risk are Townsville and Karumba. These results, however, change somewhat when one superimposes the tide on the surge. The greatest risk will then be at Miller Bay, followed by Carnarvon, Townsville, and Centre Island. These surge risk results are summarized in Table 6.43.

Table 6.42: Percentage contribution of various factors to the total water during storm surge events in Australia (HOPLEY and HARVEY 1979)

| Region | No. of surges analyzed | Forerunner | Wind and pressure | Semidiurnal | 24-h diurnal tide | Other sources |
|---|---|---|---|---|---|---|
| South Queensland | 22 | 40.4 | 31.5 | 14.1 | 10.0 | 4.0 |
| North Queensland | 28 | 27.1 | 29.1 | 23.8 | 10.9 | 9.1 |
| Gulf of Carpentaria | 15 | 29.1 | 44.1 | 3.9 | 23.8 | – |
| Northwest (Broome-Darwin) | 4 | 15.7 | 31.4 | 37.2 | 4.7 | 9.0 |
| Central Western Australia (Port Hedland Carnarvon | 8 | 50.3 | 25.5 | 9.7 | 5.8 | 8.7 |
| Southwest Australia | 7 | 74.5 | 14.7 | 1.3 | 3.2 | 6.3 |

* Without Melville Bay.

Table 6.43: Maximum surge heights (m) that can occur in 10,100, and 1000 yr at any point along a 100-km coastline centered at specific locations on the coast of Australia (HOPLEY and HARVEY, 1979).

| Station | 10 yr | 100 yr | 1000 yr |
|---|---|---|---|
| Brisbane | 0.15 | 0.43 | 0.73 |
| Noosa | 0.20 | 0.50 | 0.83 |
| Bundaberg | 1.40 | 2.80 | 4.15 |
| Gladstone | 1.30 | 2.50 | 3.78 |
| Mackay | 1.40 | 2.40 | 3.40 |
| Townsville | 1.45 | 3.25 | 4.90 |
| Cairns | 1.03 | 1.78 | 2.55 |
| Thursday Island | 1.25 | 2.50 | 3.70 |
| Weipa | 0.60 | 1.30 | 2.00 |
| Karumba | 2.25 | 3.20 | 4.15 |
| Center island | 1.41 | 2.22 | 3.00 |
| Milner Bay | 1.40 | 2.25 | 3.15 |
| Melville Bay | 1.50 | 2.40 | 3.30 |
| Darwin | 1.65 | 2.30 | 2.90 |
| Wyndham | 1.50 | 2.73 | 3.60 |
| Broome | 1.10 | 1.75 | 2.38 |
| Port Hedland | 1.50 | 2.78 | 3.70 |
| Carnarvon | 0.80 | 1.46 | 2.10 |
| Geraldton | 0.60 | 1.15 | 1.64 |

NELSON (1975) listed 30 major tropical cyclones that caused surges of amplitudes of at least 0.5 m on the north coast of Australia during the period 1880–1970. Hurricane Tracey of December 25, 1974, did great damage near Darwin. DAS et al. (1978) pointed out that although the central pressure was as low as 955 mb and wind gusts attained 200 $km \cdot h^{-1}$, the peak surge was only 1.6 m. RUSSEL (1898) reported that storm surges passing over the Bass Strait. These surges contained waves with periods of about 26 min. Similar phenomena occurred in Lake George. TRONSON and NOYE (1973) developed the statistical models for the Adelaide area were considered.

MACKEY and WHITTINGHAM (1956) studied the storm surges at Port Hedland on the northwest coast of Australia for the events of November 14–20, 1955, and February 24–March 2, 1956. The observed and predicted tides and the observed surge for the latter case are shown in Fig. 6.61.

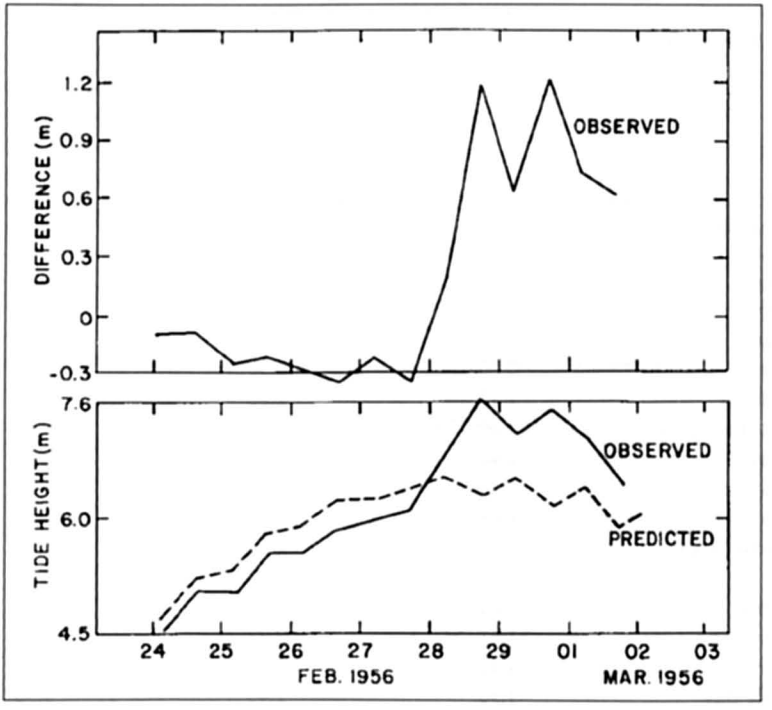


Fig. 6.61: Observed surge (top) and observed and predicted tides (bottom) at Port Hedland on the northwest coast of Australia during February 24–March 2, 1956 (MACKEY and WHITTINGHAM, 1956)

HUBBERT et al. (1991) numerically modelled the storm surges from three tropical cyclones on the East Coast of Australia. The tracks of Jason, Winifred and Aivu have been shown in Fig. 6.58.

Fig. 6.62 shows the surface pressure field for Winifred derived from the HOLLAND's (1980) model and Fig. 6.63 shows the surface wind field computed from the same model. Fig. 6.64 shows the surge amplitude for hurricane Winifred. Fig. 6.65 shows the surge amplitude for hurricane Aivu, whereas Fig. 6.66 similar results for hurricane Jason. Table 6.44 lists the errors in the results of the numerical model.

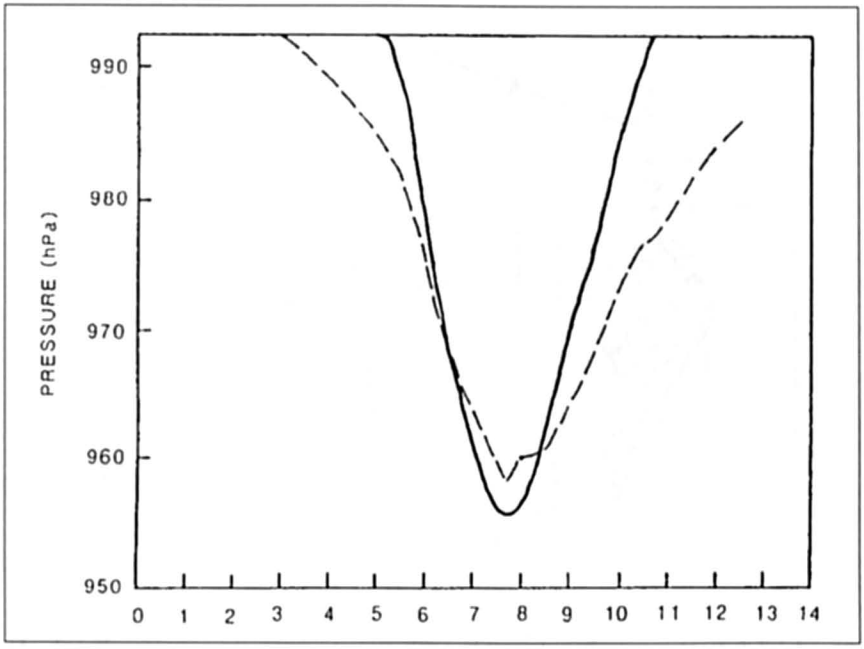


Fig. 6.62: Surface pressures and wind speeds for tropical cyclone Winifred (solid lines) compared with observations (broken lines) at Cowley Beach (just north of the cyclone landfall point) (HUBBERT et al., 1991)

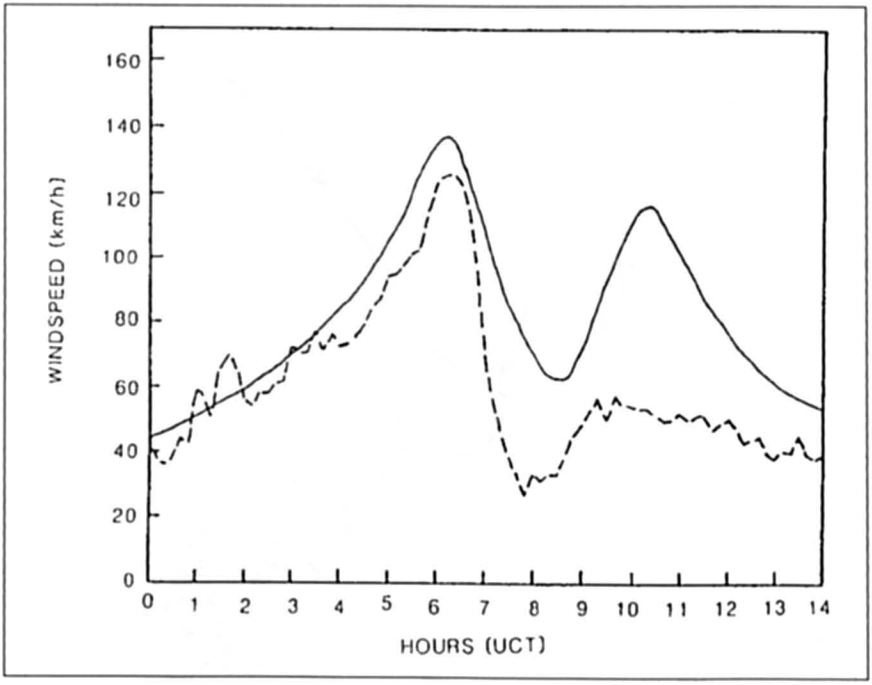


Fig. 6.63: Surface pressures derived from the Holland model for tropical cyclone Winifred (solid lines) compared with observations (broken line) at Cowley Beach (just north of the cyclone landfall point) (HUBBERT et al., 1991)

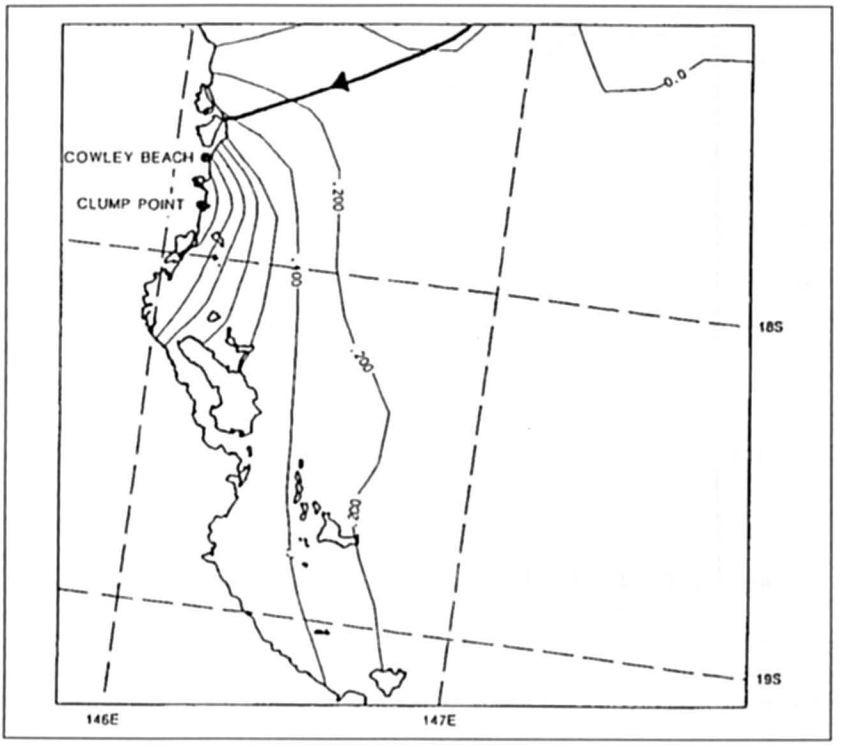


Fig. 6.64: Surge amplitude for hurricane Winifred (HUBBERT et al., 1991)

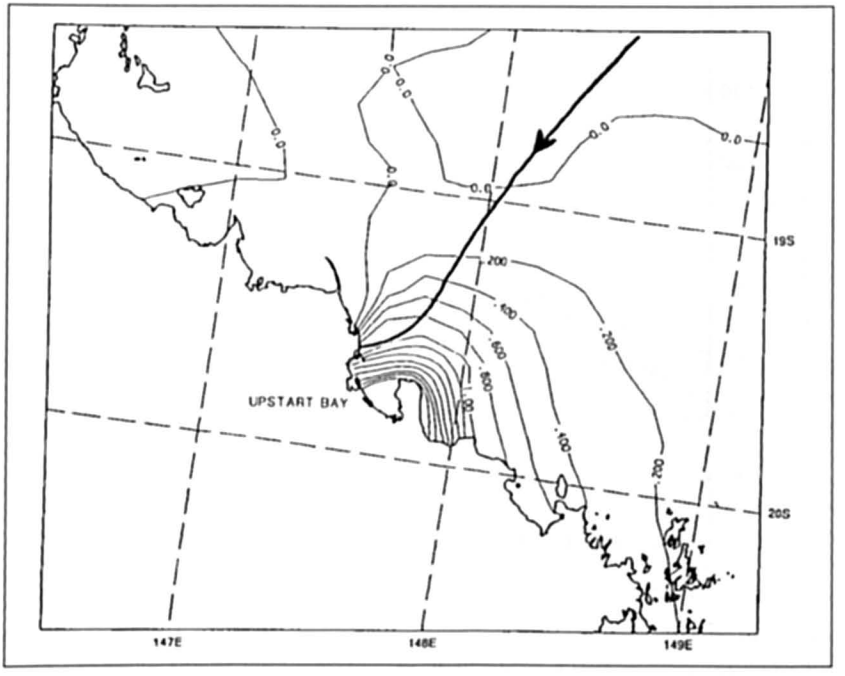


Fig. 6.65: Model results at landfall of tropical cyclone Aivu (00 UTC, April 3, 1989): Sea surface elevation (m) together with Aivu's track (HUBBERT et al., 1991)

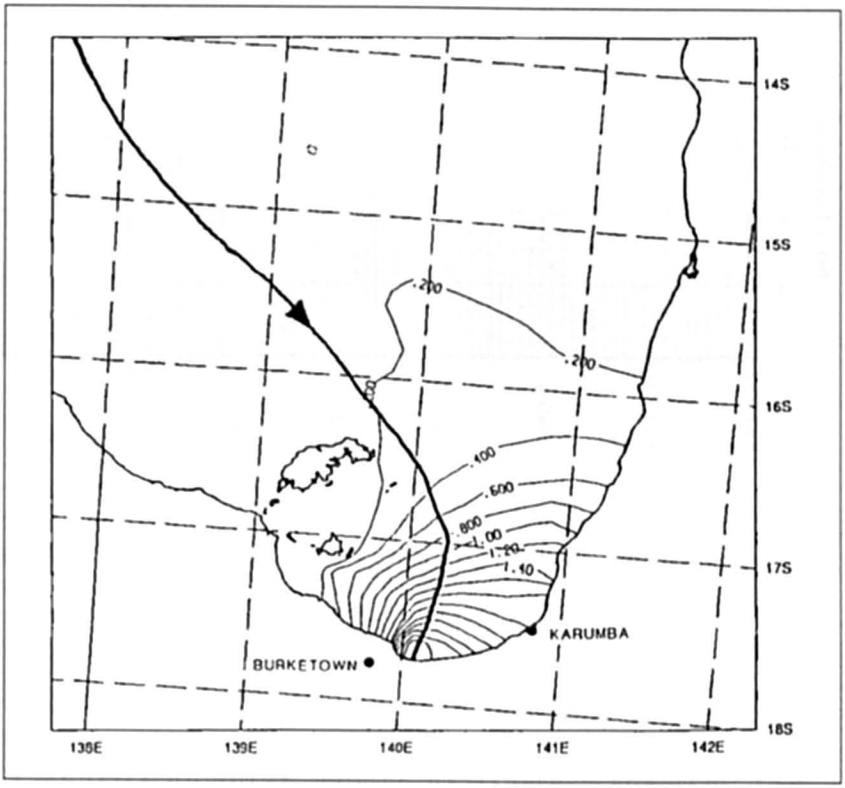


Fig. 6.66: Surge amplitude for hurricane Jason (HUBBERT et al., 1991)

Table 6.44: Errors in the results of the numerical model

| | | <-------- Surge Amplitude (m) --------> | | | Arrival Time of Peak Surge | | |
|---|---|---|---|---|---|---|---|
| Cyclone | Location | *Observed* | *Computed* | *Error (m)* | *Observed* | *Computed* | *Error (H)* |
| Winifred | Clumppoint | 1.6 | 1.5 | –0.1 | 0900 | 0900 | 0 |
| Aivu | Upstart Bay | 2.8 | 2.5 | –0.3 | 0000 | 0100 | 1 |
| Jason | Karumba | 2.0 | 1.9 | –0.1 | 0500 | 0400 | –1 |
| Jason | Burketown | 3.5 | 3.3 | –0.2 | 0500 | 0500 | 0 |

Fig. 6.67 shows the histogram of the number of cyclones in the southwest Pacific for the period 1920 to 1994 (BLONG, 1997) while it appears that there might have been a slight increase during 1970–1980, since then the numbers have decreased.

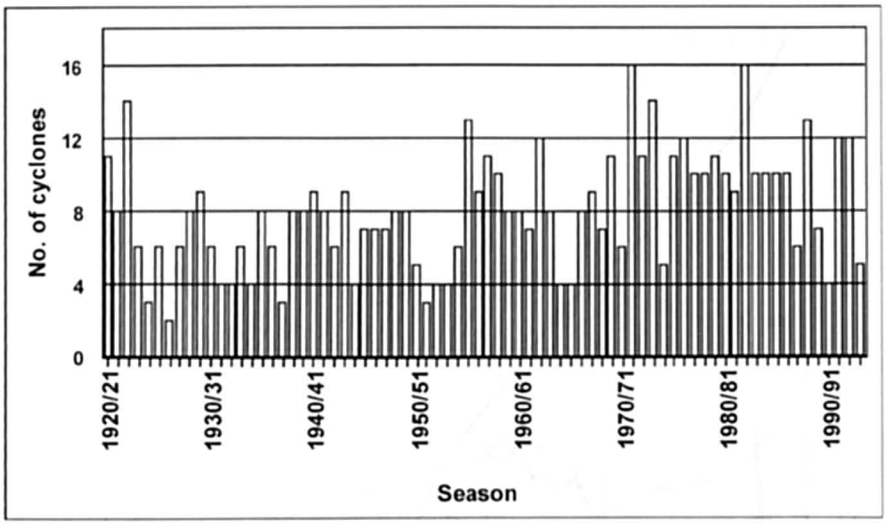


Fig. 6.67: Tropical cyclones in the South West Pacific seasonal occurrence – 1920/21 to 1993/94 (BLONG, 1997)

## 6.7 Western Tropical Pacific

### 6.7.1 Marianas, American Samoa, Solomon Islands, and Tonga

REDFIELD and MILLER (1957) mentioned that near the island of Mille in the Marianas, a storm surge of 12–15 m occurred in 1905 due to a build up of the surge in a lagoon 25 nautical miles (46 km) long.

GALLAGHER (1973) studied the nonlinear distortion produced to the tidal regime due to openings of restricted depth. He showed that the tides in the Pala Lagoon in American Samoa and the Main Lagoon on Christmas Island (in the latter case, very severely) are distorted. Similar behaviour is expected for other long waves such as storm surges and tsunamis.

GROVER (1967) studied storm surges in the Solomon Islands, which is a rare phenomenon there. Cyclones forming in the Coral Sea region and intensifying in the area south and east of the Solomons could cause surges occasionally. The storm surge of January 1952 caused some destruction on the west coast of Guadalcanal and at Malaita. The amplitude of the surge (at the time of low tide) at Honiara was about 3.5 ft (1.07 m). Winds greater than 85 $mi \cdot h^{-1}$ (137 $km \cdot h^{-1}$) were recorded there during this event.

The surge caused serious erosion in a swath 60 m wide. Interesting topographic changes took place in the coastal waters. GROVER (1967) mentioned that some villages that withstood severe tsunamis during a half-century period were obliterated by this surge.

A major storm surge occurred during March 3–4, 1982, in Tonga Island in the South Pacific (which is located about 4025 km northeast of Sydney, Australia), and the surge amplitude was at least 1.3 m (The Citizen, March 4, 1982, Ottawa, Ont.). Winds up to 276 $km \cdot h^{-1}$ coupled with the surge caused great devastation and killed several people.

LUICK et al. (1997) studied storm surges in the so-called Pacific forum region. Fig. 6.68 shows a geographical and climatological map of the area (MCLEAN, 1995). The South Pacific region consists of the following island, nations: Cook Islands, Federated States of Micronesia, Fiji, Kingdom of Tonga, Marshall Islands, Nine, Papua New Guinea, Republic of Kiribati, Republic of Nauru, Solomon Islands, Tuvalu, Vanuatu, Western Samoa.

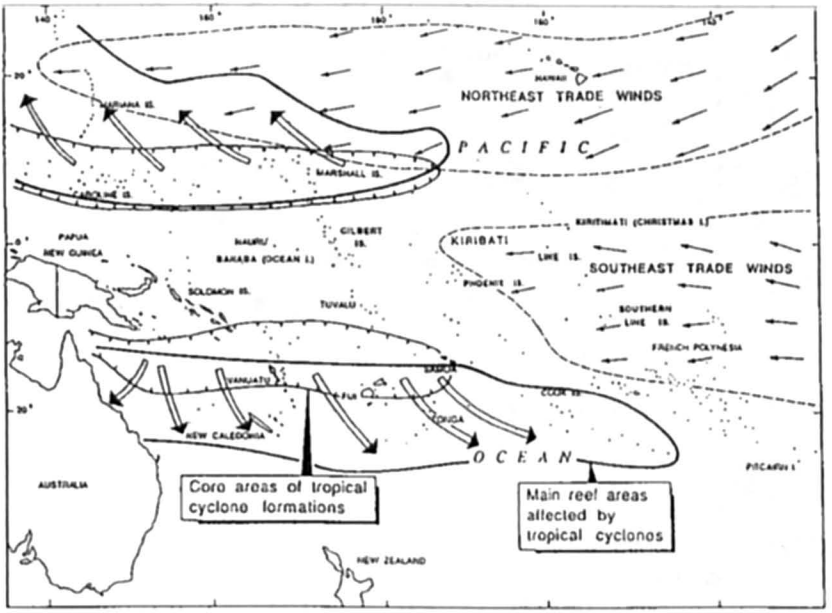


Fig. 6.68: Geographical and climatological map of the Western tropical Pacific area (MCLEAN, 1995)

The nations mainly in the western part e.g. Federated States of Micronesia (FSM) and Fiji, are subject at periodic intervals to tropical cyclones and the storm surges that are produced by them. Even though the lack of extensive continental shelves precludes the development of large amplitude surges such as those that occur in the Bay of Bengal and the Gulf of Mexico, nevertheless, moderate surges are generated. The inundation from such surges could cause problems in small islands with increased coastal erosion and salt-water intrusion into coastal aquifers.

Because of the complex topography (several small islands interspersed over a large area), traditional finite-difference models are not very applicable. Instead more sophisticated irregular triangular grid models are being developed to include not only realistic bathymetry but also the state of the tide. These finite element models were discussed earlier in chapter 3.

A map of the South Pacific Forum region (Fig. 6.69) gives the locations of the eleven SEAFRAME gauges in the region operated by National Tidal Facility (NTF) of Australia. These gauges use acoustic signals and have a precision of about 1 mm as compared to an accuracy of about 1 cm for the more traditional gauges. These gauges were placed to monitor the relative sea level changes that may be caused by the Green house warming.

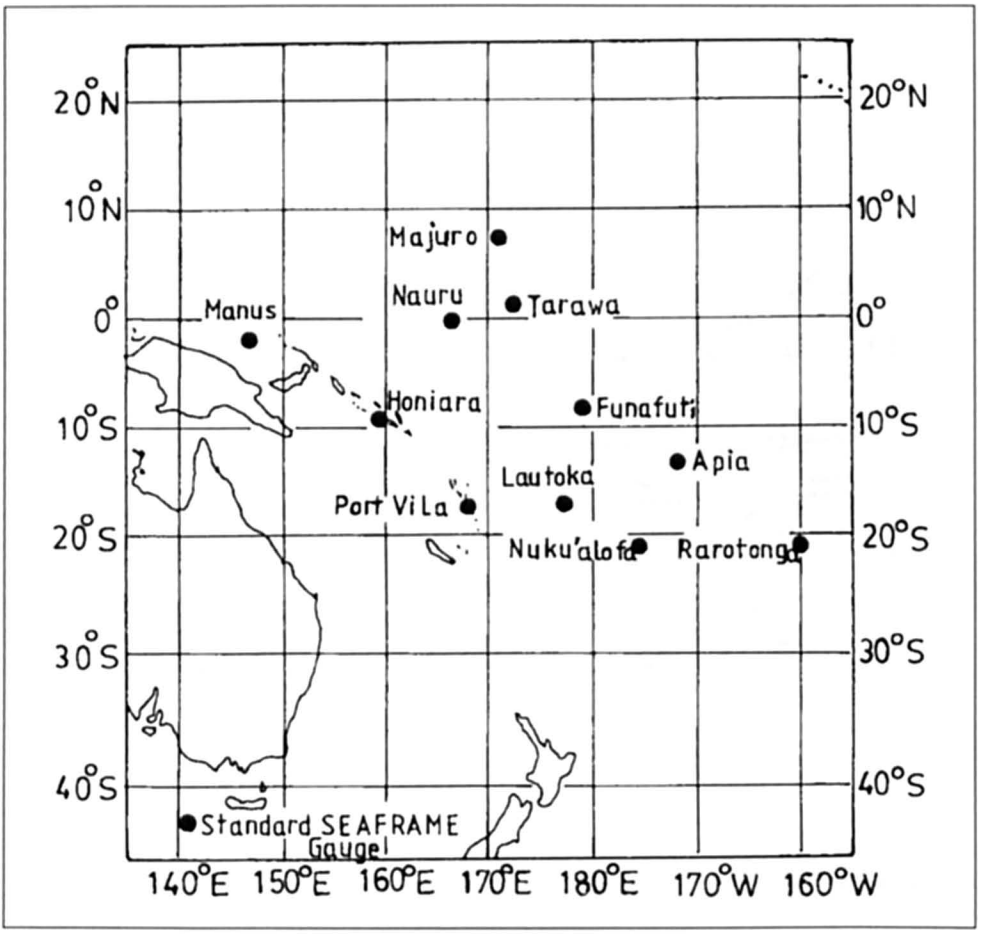


Fig. 6.69: Location of the SEAFRAME gauges in the Pacific operated by the National Tidal Facility of Australia (source: National Tidal Facility)

However, these gauges record all forms of long gravity waves, such as tides, storm surges and tsunamis. Storm surges up to one metre have been noticed occasionally in the residuals of these tide gauge records.

Fig. 6.70 shows the areas north and south of the equator where the tropical cyclones form. There is a clear break at the equator where there are none due to the absence of the Coriolis force.

Tropical cyclones in the South Pacific tend to form in the "monsoon trough" between 10°–15° S in the western South Pacific. During El Nino years the monsoon trough shifts to the east onto the Central Pacific. Very few cyclones intensify south of 20° S (due primarily to increasing westerlies in the upper troposphere).

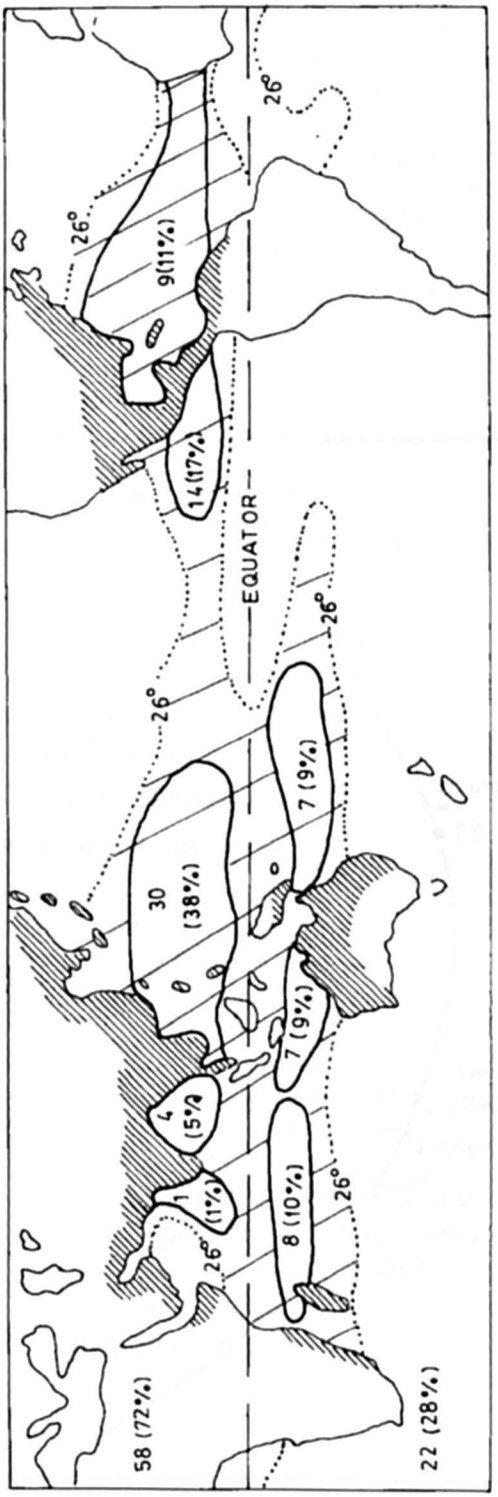


Fig. 6.70: Areas of tropical cyclone occurrence (GRAY, 1975). Land areas affected by cyclone are shown hatched (LUICK et al., 1997)

In the Southwest Pacific, tropical cyclones typically continue to intensify as they move southwards from their points of origin, decaying over cooler subtropical water. More than half however decay prior to reaching 30° S, while a third of tropical cyclones in the southwest Pacific eventually become extra-tropical depressions.

It is known (MURTY, 1984) that looking down the track of movement of a tropical cyclone, peak surges occur to the right of the track in the northern hemisphere and to the left in the southern hemisphere.

Fig. 6.71 shows the track of Hurricane Bebe of 1972. Even though the track is over Viti Levu, there is no coast against which the tangential wind stress can push water to the left of the track and pile it up. On the other hand, depending upon the strength of the wind field a surge could occur on the island, Vanua Levu.

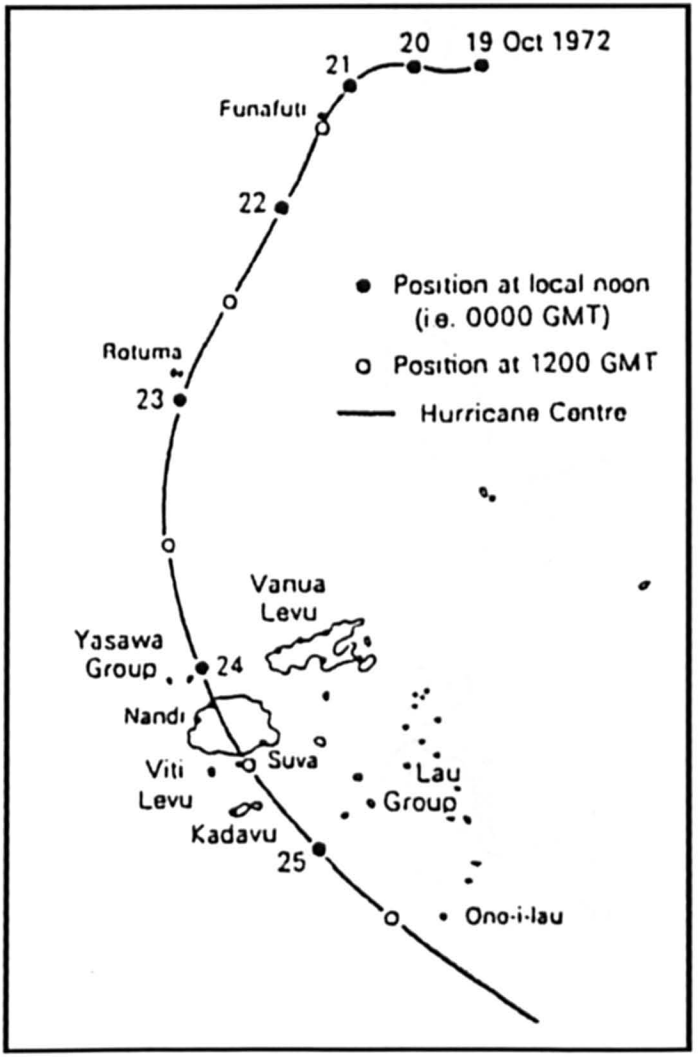


Fig. 6.71: Track of Hurricane Bebe October 1972 (from New Zealand Meteorological Service)

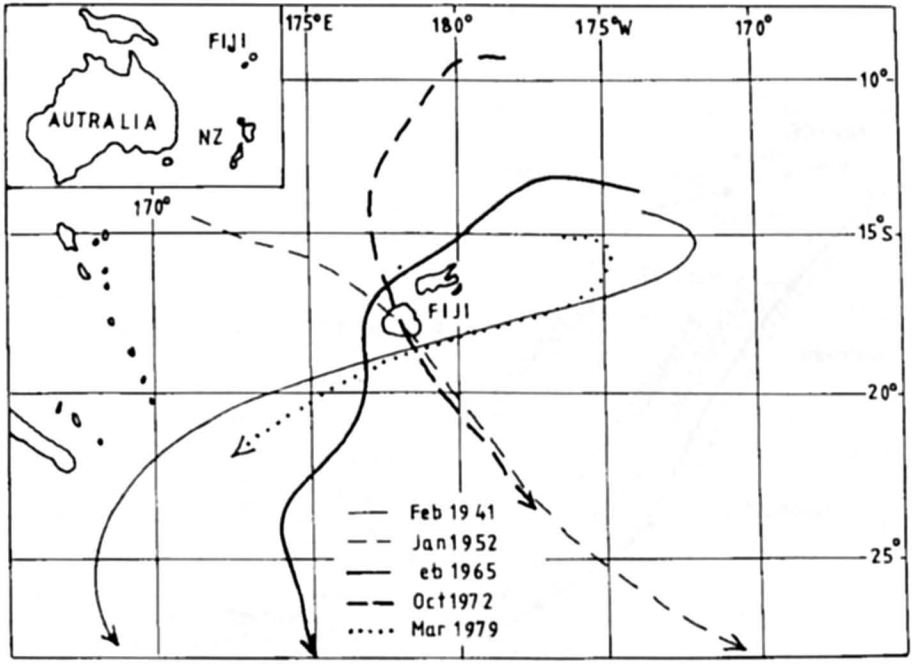


Fig. 6.72: Tracks of severe hurricanes in the Fiji area between 1940 and 1979 (from Fiji Meteorological Service)

The tracks of five hurricanes near Viti Levu are shown in Fig. 6.72. Again using the above rule of thumb, only the track for February 1965 should generate a peak surge on Viti Levu, depending upon the strength of the wind field.

Figs. 6.73 and 6.74 respectively show the tracks of hurricanes, Oscar (24th February to 2nd March 1983) and Meli (24$^{th}$ to 28$^{th}$ March 1979) impinging on the coastlines of Fiji.

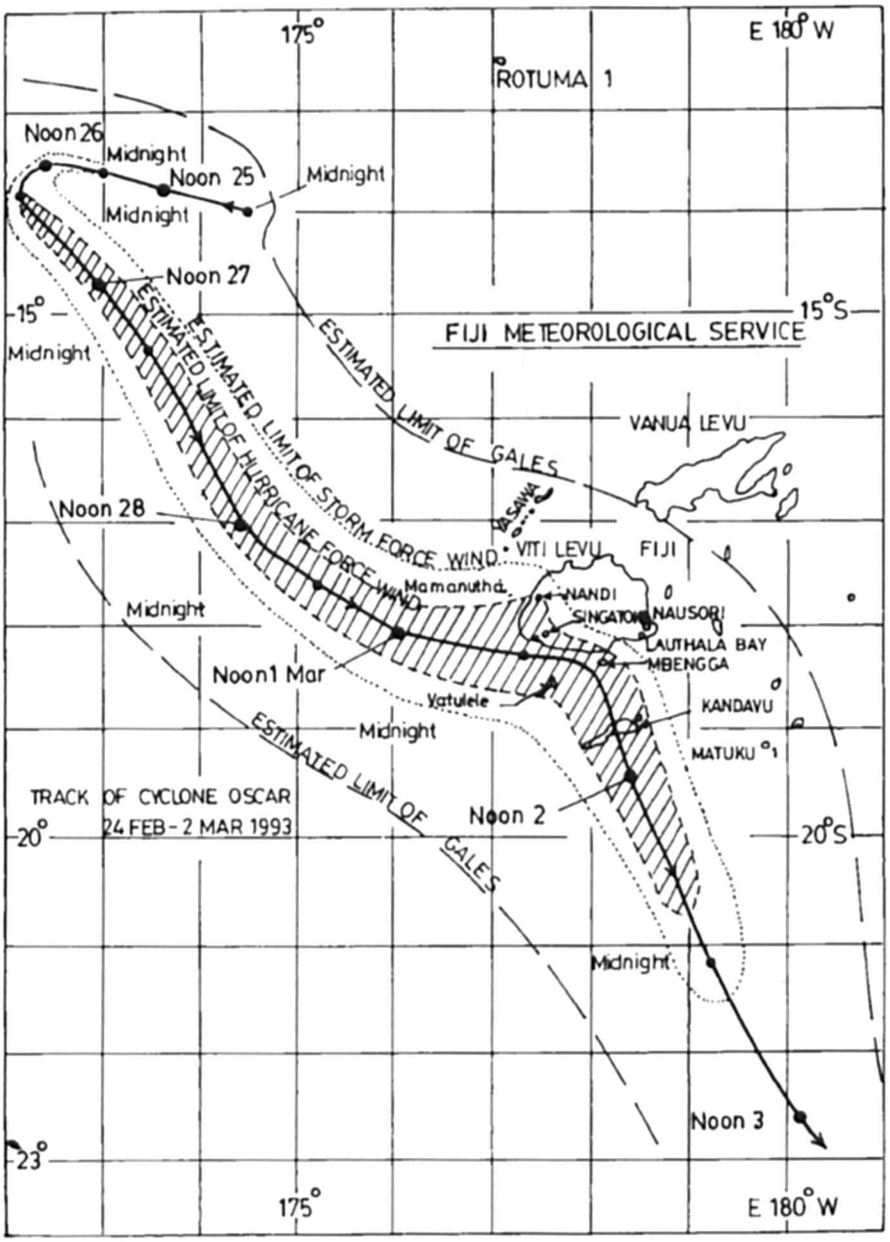


Fig. 6.73: Track of tropical cyclone Oscar, 24 February–2 March 1983 (Fiji Meteorological Service)

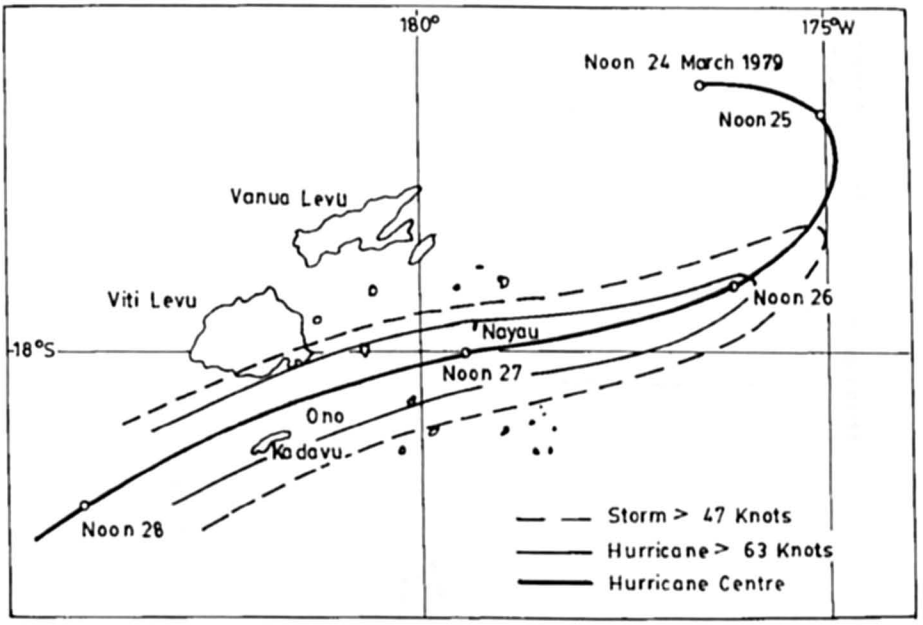


Fig. 6.74: Track of hurricane Meli and associated winds, March 1979 (Fiji Meteorological Service)

During 15–16 January 1996, a minor storm surge occurred in Tonga and was recorded on the SEAFRAME as shown in Fig. 6.75. The following information can be deduced from an examination of this figure.

Total residual or storm surge ~0.33 m.

Wind set-up (residual adjusted for the atmosphere pressure effect) ~0.18 m.

Inverse barometer effect = 0.33–0.18 m = 0.15 m. Pressure drop ~15hPa (hecto Pascals).

The wind set-up can be estimated roughly from the following simple calculation.

$$\frac{\partial \eta}{\partial x} = \frac{\varrho_\alpha}{\varrho} \frac{C_D W^2}{gD} \qquad (6.71)$$

$\eta$ = amplitude of the surge (m)
$x$ = coordinate perpendicular to the shoreline
$\varrho_a$ = density of air = 1.25 kg/m$^3$
$\varrho$ = density of sea water = 1.026 x 10$^3$ kg/m$^3$
$C_D$ = drag coefficient = 2.8 x 10$^{-3}$ (dimensionless)
$g$ = gravity = 9.8 m/s$^2$
$D$ = average depth of the water = 10 m
$W$ = wind speed = 35 m/s

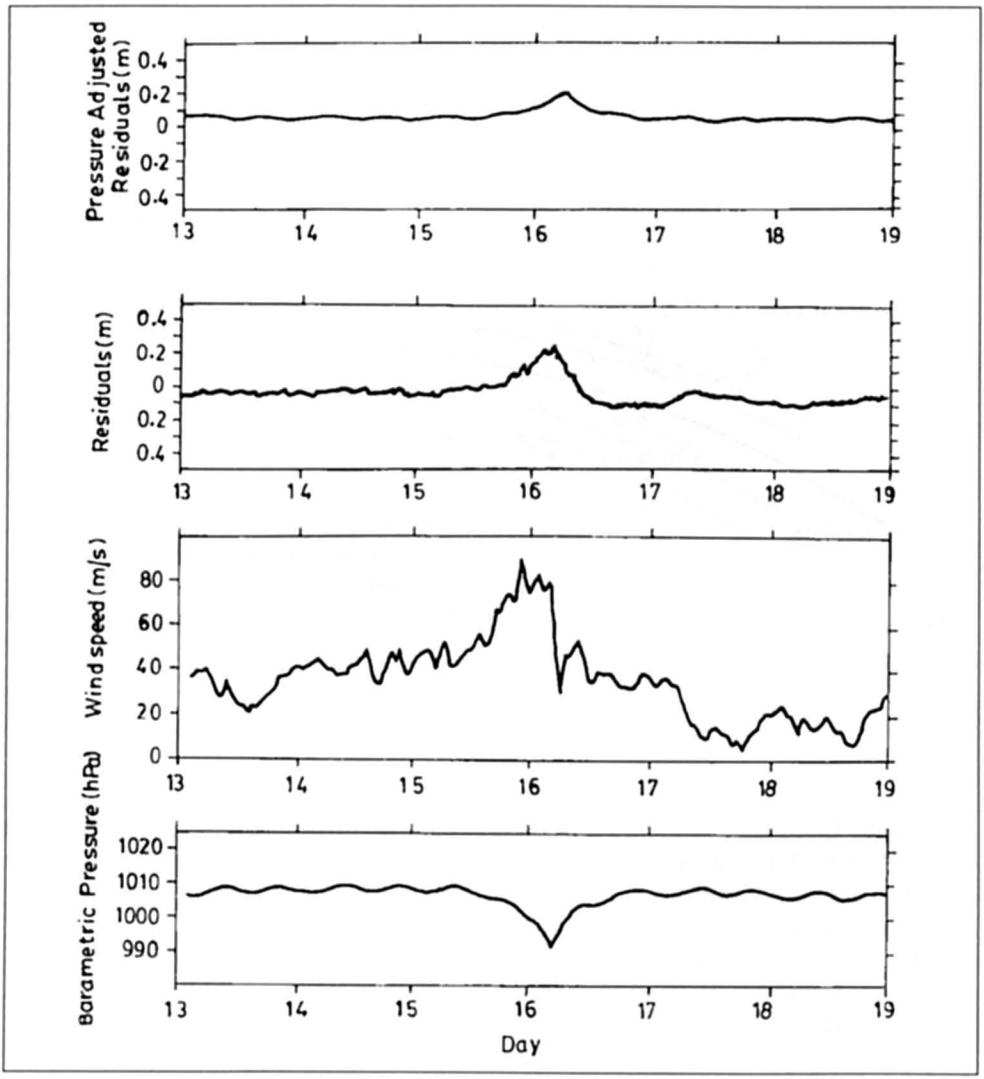


Fig. 6.75: Wind gust, barometric pressure, adjusted residual and residual at Tonga SEAFRAME gauge for January 1996

Using these values, we get

$$\frac{\partial \eta}{\partial x} = 0.42 \times 10^{-4} \tag{6.72}$$

Assuming a fetch of 5 km, one can write.

$$\eta = \frac{\partial \eta}{\partial x} = 0.42 \times 10^{-4} \times 5 \times 10^{3}\,\mathrm{m} = 0.21\mathrm{m} \tag{6.73}$$

The amplitude of the wind set-up computed from the simple formula is 0.21 m, which compares reasonably well with the observed wind set-up of 0.18 m. A numerical model will yield a better agreement. Fig. 6.76 shows the incidence of tropical cyclones for the study area and surroundings (CARTER et al., 1991). Table 6.45 lists the general level of threat from various hazards in the study area whereas Table 6.46 gives the incidence of tropical cyclones in the South Pacific.

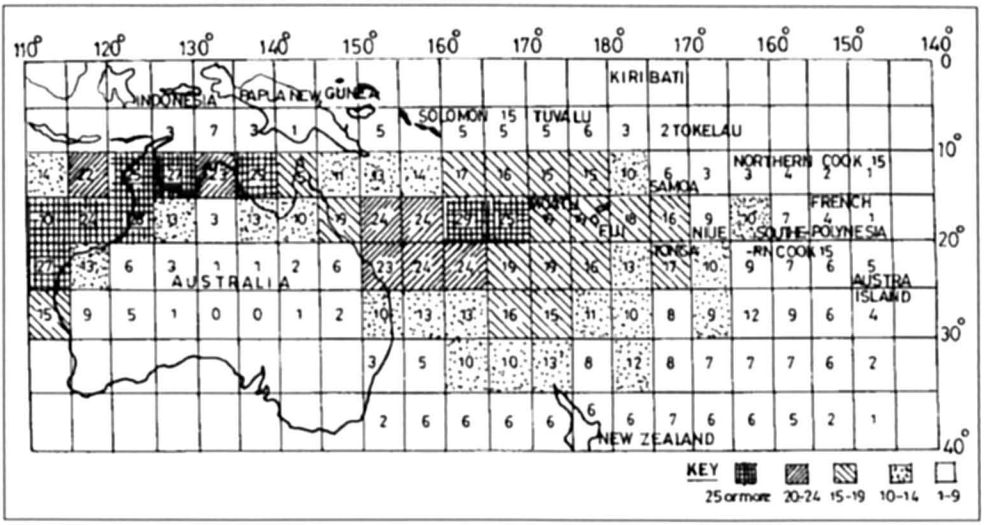


Fig. 6.76: Average decadal incidence of Tropical cyclones in 5-degree latitude – longitude squares. West of 150 east based on data for 1959–1975, East of the Longitude on data for 1969–1979 (CARTER et al., 1991)

Table 6.45: General level of threat (CARTER et al., 1991)

| | Cooks | Fiji | Solomons | Tonga | Vanuatu | W. Samoa | Kiribati | PNG |
|---|---|---|---|---|---|---|---|---|
| Cyclone | M | H | H | H | H | M | L | L |
| Drought | H | M | L | M | L | L | H | M |
| Earthquake | L | M | H | H | H | M | L | H |
| Flood | L | H | H | M | H | H | L | H |
| Landslide | L | H | H | L | H | H | L | H |
| Tsunami | M | H | H | H | H | H | L | H |
| Volcanic Eruption | – | – | H | H | H | L | – | H |

L = Low M = Medium H = High

Table 6.46: Incidence of Tropical Cyclones in the South Pacific (CARTER et al., 1991)

| Year | Cooks | Fiji | Solomons | Tonga | Vanuatu | W. Samoa | PNG |
|---|---|---|---|---|---|---|---|
| 1960 | 1 | – | – | 2 | 1 | – | – |
| 1961 | – | – | – | 1 | 1 | 1 | – |
| 1962 | 1 | – | – | – | – | – | – |
| 1963 | 2 | – | – | 1 | 2 | – | – |
| 1964 | – | 3 | – | 1 | 1 | 1 | – |
| 1965 | – | 1 | – | – | – | – | – |
| 1966 | – | 1 | 2 | – | – | 1 | – |
| 1967 | 1 | 1 | 1 | – | – | – | – |
| 1968 | – | – | 1 | – | 2 | 1 | – |
| 1969 | – | – | 1 | 1 | – | – | – |
| 1970 | – | 3 | – | 1 | – | – | – |
| 1971 | – | – | 1 | 1 | 1 | – | – |
| 1972 | 1 | 1 | 1 | 1 | 4 | – | – |
| 1973 | – | 3 | 2 | 1 | – | – | – |
| 1974 | – | 1 | – | 1 | 1 | 1 | – |
| 1975 | – | 2 | – | – | 1 | 1 | – |
| 1976 | 1 | – | – | – | 1 | 2 | – |
| 1977 | – | 1 | – | 1 | 3 | – | 1 |
| 1978 | – | 3 | 1 | 1 | 1 | – | – |
| 1979 | – | 1 | 1 | 1 | 1 | – | – |
| 1980 | – | 3 | – | – | – | – | – |
| 1981 | 1 | 1 | – | – | 2 | – | – |
| 1982 | – | 1 | 1 | 1 | 1 | – | – |
| 1983 | 2 | 2 | – | – | – | – | – |
| 1984 | – | – | – | – | – | 1 | – |
| 1985 | – | 3 | – | – | 3 | – | 1 |
| 1986 | 2 | 2 | 1 | – | 1 | – | – |
| 1987 | 1 | 1 | – | – | 1 | – | – |
| 1988 | 1 | – | 1 | – | 3 | – | – |
| 1989 | 1 | – | – | – | 1 | 1 | – |
| Total | 15 | 34 | 14 | 15 | 32 | 10 | 2 |

## 6.8 Western Pacific Ocean

Under this heading we will include: China, Japan, South Korea, Philippines, Vietnam and Thailand.

### 6.8.1 China

Storm surges up to 6 m can occur occasionally on the coast of China, with surges up to 2–3 m occurring quite frequently. TSENG-HAO and SHIH-ZAO (1975) used a numerical model to compute storm surges in the Po Hai Sea. JIN-CHUAN and GUANG (1979) developed empirical techniques for hourly predictions of surges due to typhoons on the southeastern coast of China. Their study involved predictions for the following tidal stations: Shacheng, Sansha, Xiamen, Dongshan, Shantou, and Shanwei. The total number of surges considered by them was more than 1000. They used the empirical formulae thus developed operationally since 1977. The hourly predicted and observed surges at three locations due to typhoon 7908 of August 2, 1979 are compared in Table 6.47. JIN-CHUAN and GUANG (1979) gave surge profiles for the 24 most important storm surges on the southeastern coast of China during the 1970's. Five of these profiles are given in Fig. 6.77–6.81. C. Tseng-Hao and F. Shih-Zao (unpublished data) developed numerical models for storm surge prediction on the east coast of China.

Table 6.47: Predicted and observed storm surges at three locations in China due to Typhoon 7908 of August 2, 1979 (JIN-CHUAN and GUANG, 1979)

| | Storm surges (cm) at | | | | | |
|---|---|---|---|---|---|---|
| | Shantou | | Xiamen | | Chongwu | |
| Time (h) GMT | Observed | Predicted | Observed | Predicted | Observed | Predicted |
| 05 | 95 | 106 | 84 | 105 | 78 | 99 |
| 08 | 158 | 163 | 88 | 107 | 61 | 75 |
| 10 | 201 | 223 | 91 | 95 | 47 | 65 |
| 11 | 187 | 199 | 92 | 87 | 35 | 60 |
| 14 | 66 | 100 | 27 | 43 | 21 | 40 |

KENTANG (2000) studied the damage from storm surges in China since 1990. He mentions that storm surges are the number one marine hazard in China. Since 1990, 62 typhoons made a landfall on the coast of China. Three events, one in 1992, the second one in 1994 and the third one in 1997 were particularly disastrous. The direct economic losses from these events were about 1.7, 2.6 and 3.8 billion US Dollars. In average year between 1989–1991 the economic loss is much less and is about 0.7 billion US Dollars.

Fig. 6.82 shows the tracks of these three typhoons and Table 6.48 lists the damage. The author suggests the following counter measures:

1. Raise the society's awareness and public education about storm surge hazard
2. Work out a plan for building new sea walls
3. Improve and perfect the available warning and disaster relief command system and
4. Develop an insurance service in order to promptly mitigate the loss caused by severe storm surge disaster events.

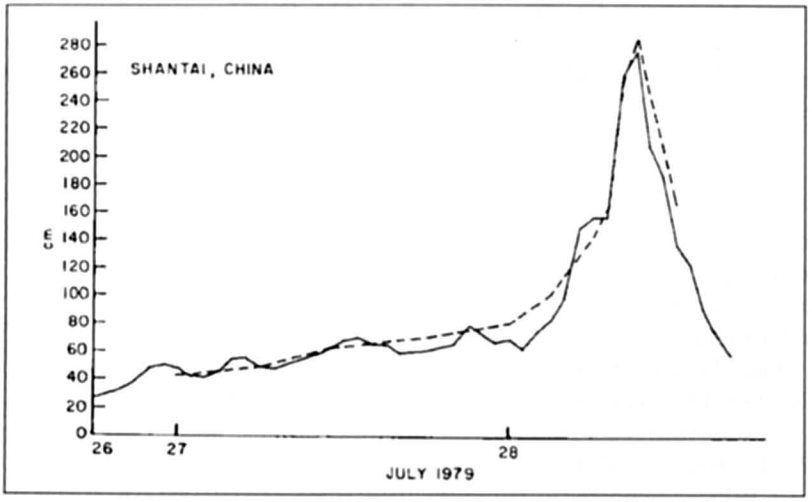


Fig. 6.77: Observed (solid line) and computed (broken line) surges at Shantow, China during July 26–29, 1979 (JIN-CHUAN and GUANG, 1979)

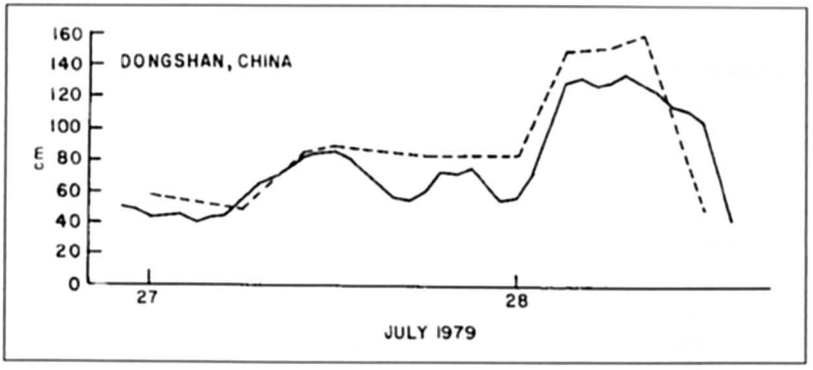


Fig. 6.78: Observed (solid line) and computed (broken line) surges at Dongshan, China during July 27–28, 1979 (JIN-CHUAN and GUANG, 1979)

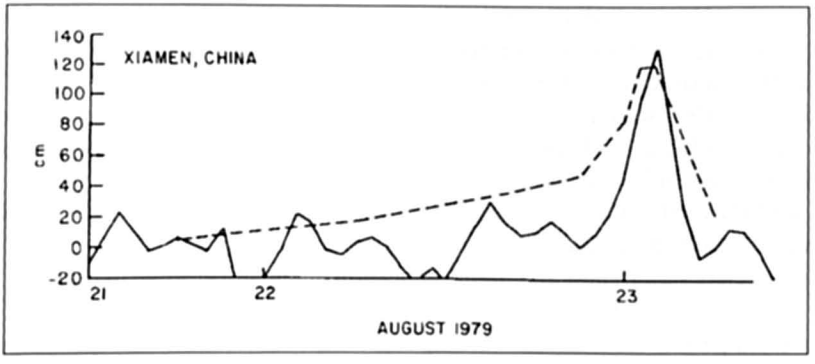


Fig. 6.79: Observed (solid line) and computed (broken line) surges at Xiamen, China during August 21–23, 1979 (JIN-CHUAN and GUANG, 1979)

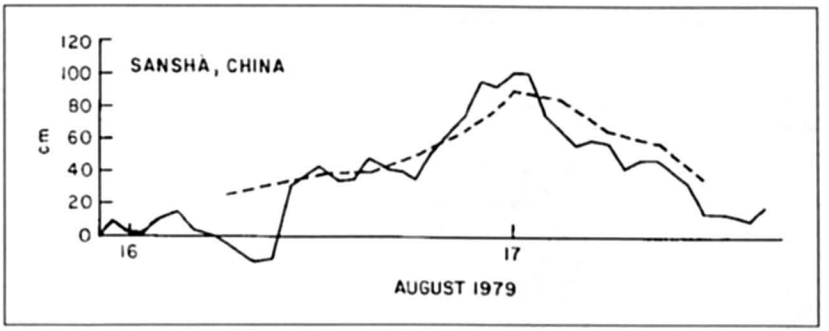


Fig. 6.80: Observed (solid line) and computed (broken line) surges at Sansha, China during August 16–17, 1979 (JIN-CHUAN and GUANG, 1979)

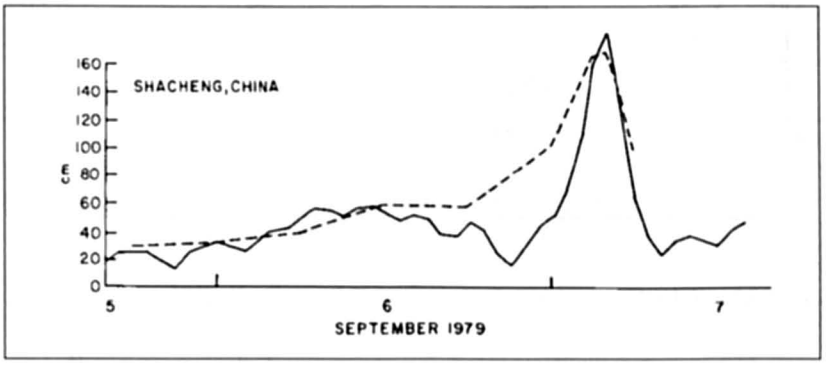


Fig. 6.81: Observed (solid line) and computed (broken line) surges at Shacheng, China during September 5–7, 1979 (JIN-CHUAN and GUANG, 1979)

Table 6.48: Damages of three severe storm surge disaster events (KENTANG, 2000)

| | | destroyed wall and bank (km) | | | killed and missing people (number) | | | direct economic loss (billion yuan, RMB) | | |
|---|---|---|---|---|---|---|---|---|---|---|
| Name of typhoon | | Polly | Fred | Winnie | Polly | Fred | Winnie | Polly | Fred | Winnie |
| Name of disaster | | 9216SSD | 9417SSD | 9711SSD | 9216SSD | 9417SSD | 9711SSD | 9216SSD | 9417SSD | 9711SSD |
| Province or city | Fujian | 203.3 | | * | 12 | | 0 | 0.92 | | * |
| | Zhejiang | 546.3 | 520.7 | 922 | 114 | 1216 | 46 | 3.15 | 17.76 | 18.6 |
| | Shanghai | * | | ~15 | 0 | | 7 | * | | 0.6 |
| | Jiangzu | 77.7 | | 260 | 10 | | 17 | 0.32 | | 3.0 |
| | Shandong | 299 | | 85 | 57 | | 159 | 4.15 | | 11.5 |
| | Hebei | | | | | | | 0.32 | | |
| | Tijanjin | 44.4 | | | 0 | | | 0.40 | | |
| Total | | 1170.0 | 520.7 | 1282 | 193 | 1216 | 229 | 9.26 | 17.76 | 33.7 |

(Note: * stands for the much less damage of the item and is not counted in the total)

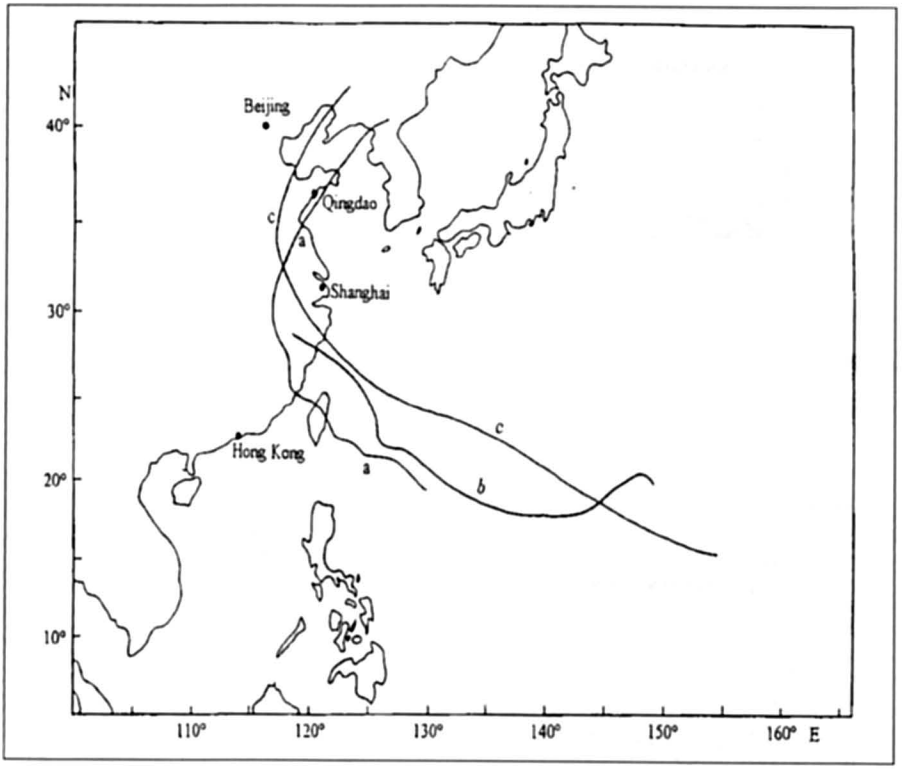


Fig. 6.82: Tracks of the three typhoons in the text (a) Polly, (b) Fred, (c) Winnie (KENTANG, 2000)

*Surges in Shanghai Harbour*

QIN et al. (1994) numerically simulated tides and storm surges in Shanghai harbour and vicinity by including non-linear tide-surge interaction, as opposed to the traditional method in which tides and surges are linearly super-imposed. They simulated the surges from 16 tropical cyclones hitting Shanghai during the period 1949 to 1990. For the tidal simulations, 63 tidal constituents were included.

Fig 6.83 shows the computational domain. Figs 6.84 to 6.86 respectively show the typhoon tracks for 1949–1959, 1960–1979 and 1980–1990. Fig 6.87 compares the computed water levels for Gloria (1949) and Marge (1951). For results for all the other typhoons, we refer the reader to the original paper. Table 6.49 lists the relative errors for all the simulations. Even though the method used here is not necessarily better in every single simulation; in an overall sense the method used here yielded better results than the traditional method.

Table 6.49: Root-mean-square-errors in the neighbouring high water level using the traditional method and the proposed method incorporating nonlinear surge-tide coupling (QIN et al., 1994)

| TC No. | TC Name | Traditional method (cm) | Proposed method (cm) |
|---|---|---|---|
| 4906 | Gloria | 9.0 | 46.5 |
| 5116 | Marge | 24.7 | 21.0 |
| 5410 | Grace | 42.5 | 34.6 |
| 5612 | Wanda | 44.5 | 20.5 |
| 5907 | Sarah | 29.5 | 29.5 |
| 6014 | Carmen | 48.5 | 38.8 |
| 6207 | Nora | 37.6 | 22.4 |
| 7008 | Billie | 45.0 | 37.6 |
| 7308 | Iris | 40.0 | 14.5 |
| 7413 | Mary | 33.0 | 21.1 |
| 7910 | Judy | 40.2 | 28.7 |
| 8114 | Anges | 39.2 | 28.1 |
| 8310 | Forrest | 29.9 | 23.5 |
| 8615 | Vera | 26.7 | 22.2 |
| 8913 | Lola | 33.9 | 25.9 |
| 9015 | Abe | 8.7 | 17.8 |

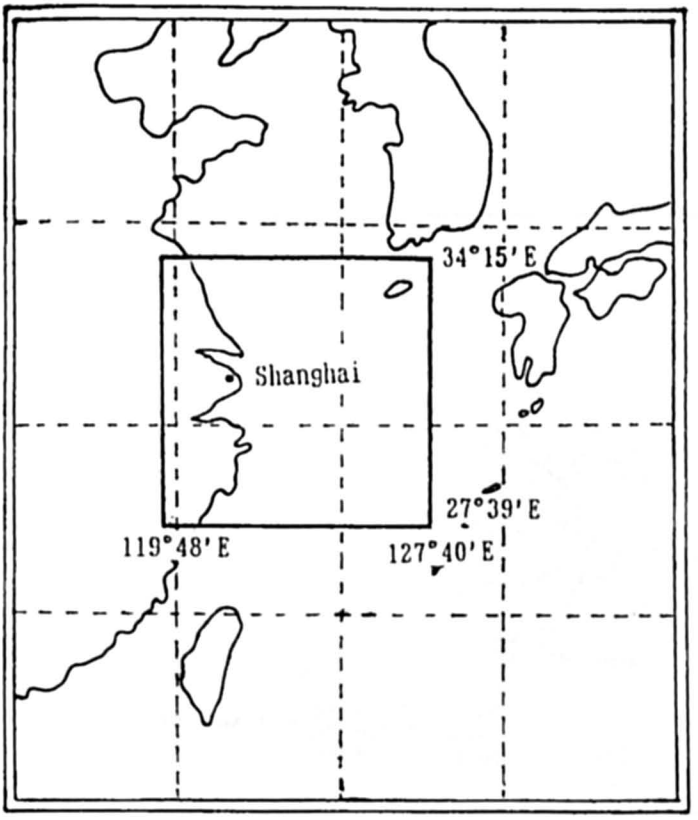


Fig. 6.83: Computational domain (QIN et al., 1994)

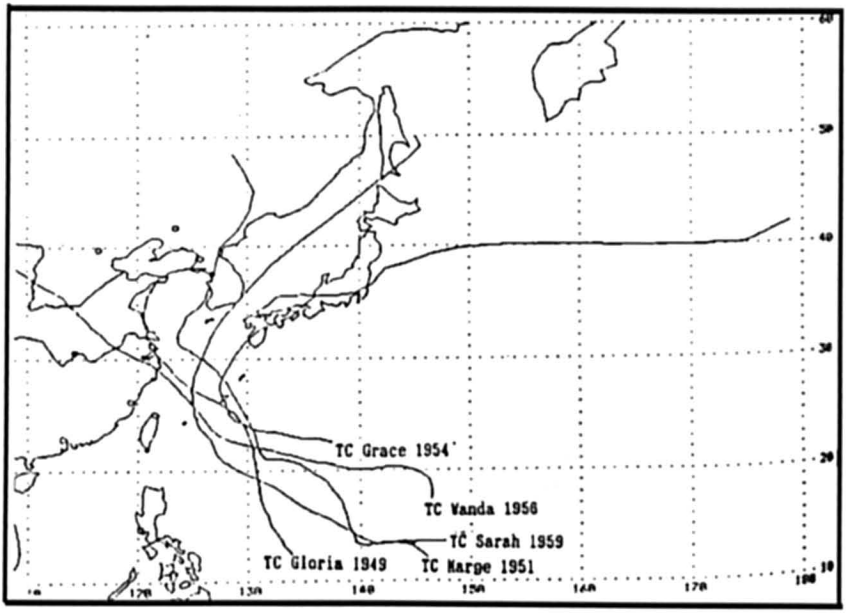


Fig. 6.84: Tracks of tropical cyclones for 1949–1959 (QIN et al., 1994)

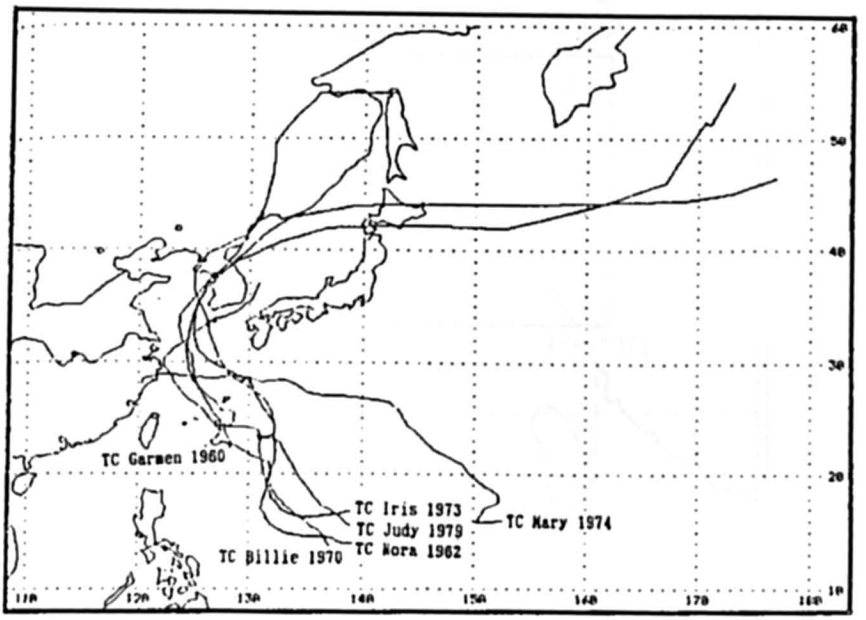


Fig. 6.85: Tracks of tropical cyclones for 1960–1979 (QIN et al., 1994)

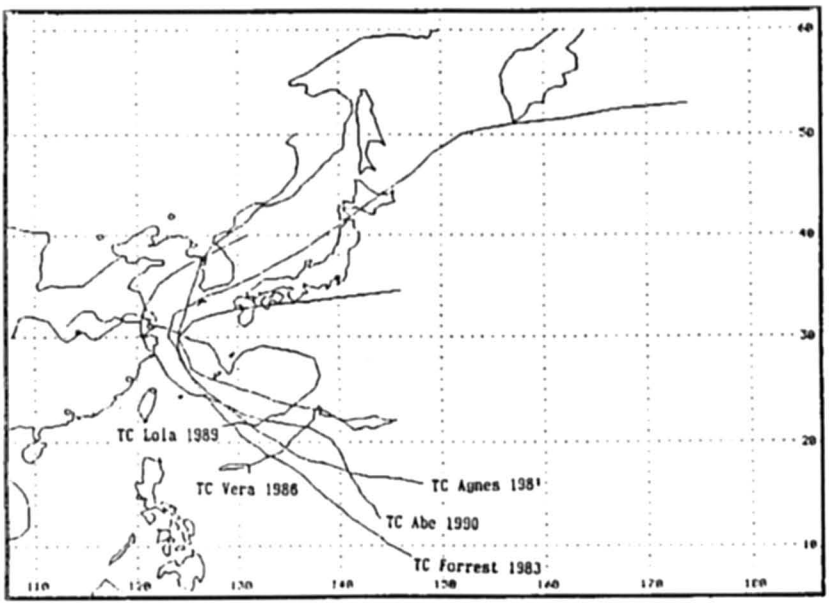


Fig. 6.86: Tracks of tropical cyclones for 1980–1990 (QIN et al., 1994)

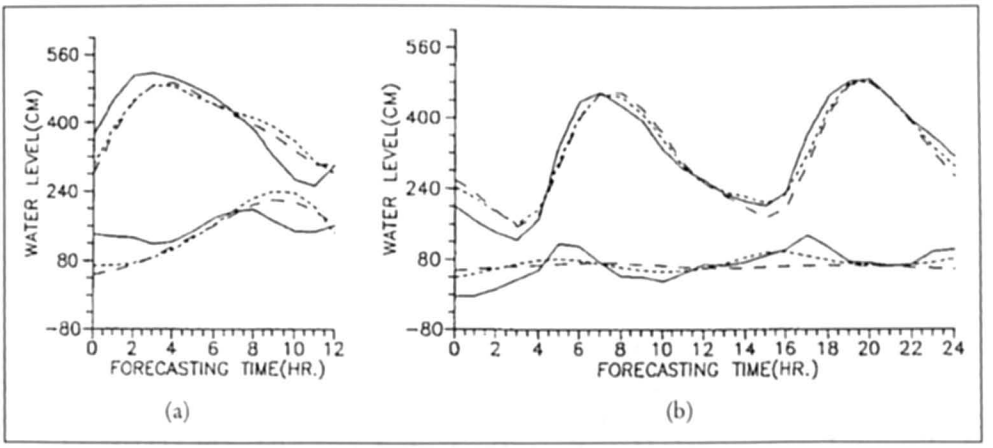


Fig. 6.87: (a) Surge and water level process curves caused by TC Gloria 1949 for Wuson. Legend: solid lines – observed, dashed lines – simulated (longer for the traditional method, shorter for the proposed method); top case for total water-level, bottom case for storm surges (b) same as above except those caused by TC Morge 1951 (QIN et al., 1994)

*Surges in Hong Kong*

Storm surges are reasonably severe in Hong Kong (CHAN and WALKER, 1979) have described three different types of surges and the empirical formulae for predicting them. The return periods for surges of different amplitudes (BELL, 1961), computed using Gumbel's methods and using data from maximum hourly winds, are listed in Table 6.50. SILVESTER (1971) studied storm surges in Hong Kong and developed empirical relations. The pressure deficits and observed storm surges at North Point, Hong Kong Harbour, for seven different typhoons are listed in Table 6.51.

Table 6.50: Return periods for extreme storm surges in Hong Kong (BELL, 1961)

| Surge amplitude ( m) | Return period (Yr) | Surge amplitude (m) | Return period (Yr) |
|---|---|---|---|
| 1.6 | 10 | 2.4 | 200 |
| 1.8 | 20 | 2.7 | 500 |
| 2.0 | 50 | 2.9 | 1000 |
| 2.2 | 100 | | |

Table 6.51: Observed storm surge amplitudes and pressure deficits in typhoons that affected Hong Kong (North Point) (SILVESTER, 1971)

| Typhoon | Date | Pressure deficit (mb) | Observed surge amplitude (m) |
|---|---|---|---|
| Wanda | Sept. 1962 | 61 | 0.62 |
| Faye | Sept. 1963 | 17 | 0.17 |
| Viola | May 1964 | 21 | 0.21 |
| Ida | Aug. 1964 | 38 | 0.39 |
| Ruby | Sept. 1964 | 45 | 0.46 |
| Sally | Sept. 1964 | 24 | 0.24 |
| Shirley | Aug. 1968 | 44 | 0.45 |

LAU (1980b) used the SPLASH model to compute storm surges at North Point and in Tolo Harbour for events of tropical cyclone passages across the northern part of the South China Sea. This study used 93 historical storms during the period September 1906–June 1976 that generated storm surges in Hong Kong. The standard storm of the SPLASH model gives an open-coast peak surge of 1.92 m at North Point. Nomograms for the surge height at North Point are given in Fig. 6.88–6.92, respectively, as a function of the central pressure of the storm, storm direction, storm speed, radius of maximum winds, and distance of nearest approach of storm.

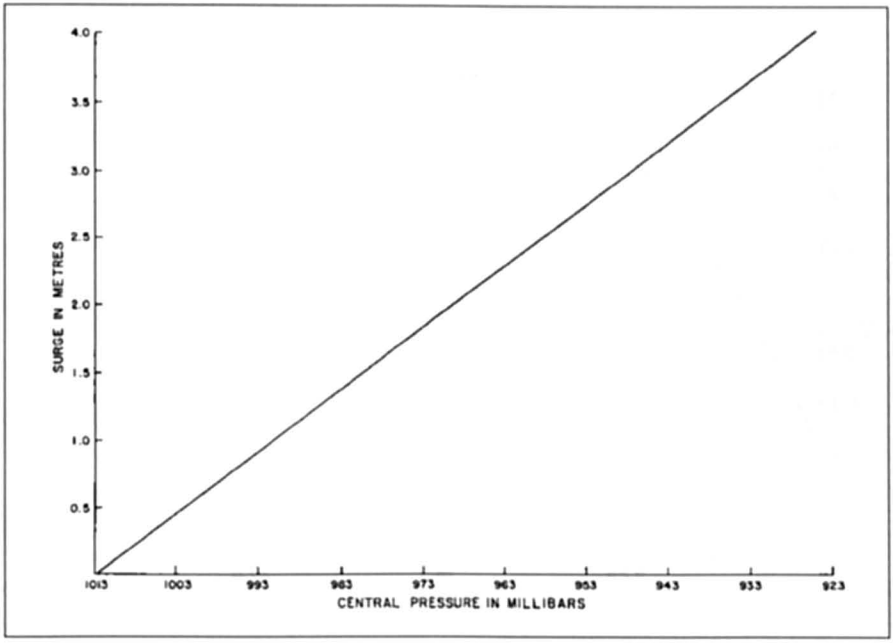


Fig. 6.88: Surge amplitude versus central pressure of storm for North point in Hong Kong harbour (LAU, 1980b)

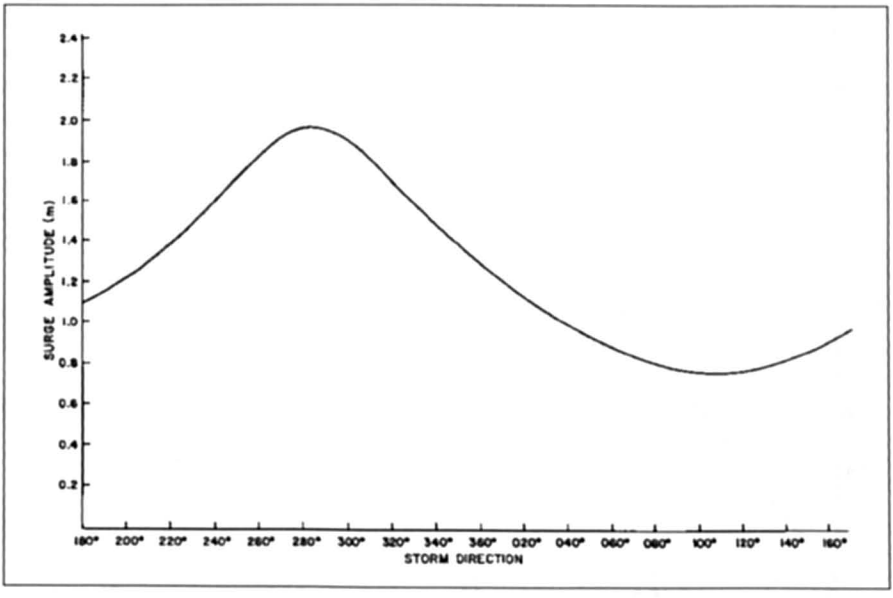


Fig. 6.89: Surge amplitude versus storm direction in 360° compass bearing for North point in Hong Kong harbour (LAU, 1980b)

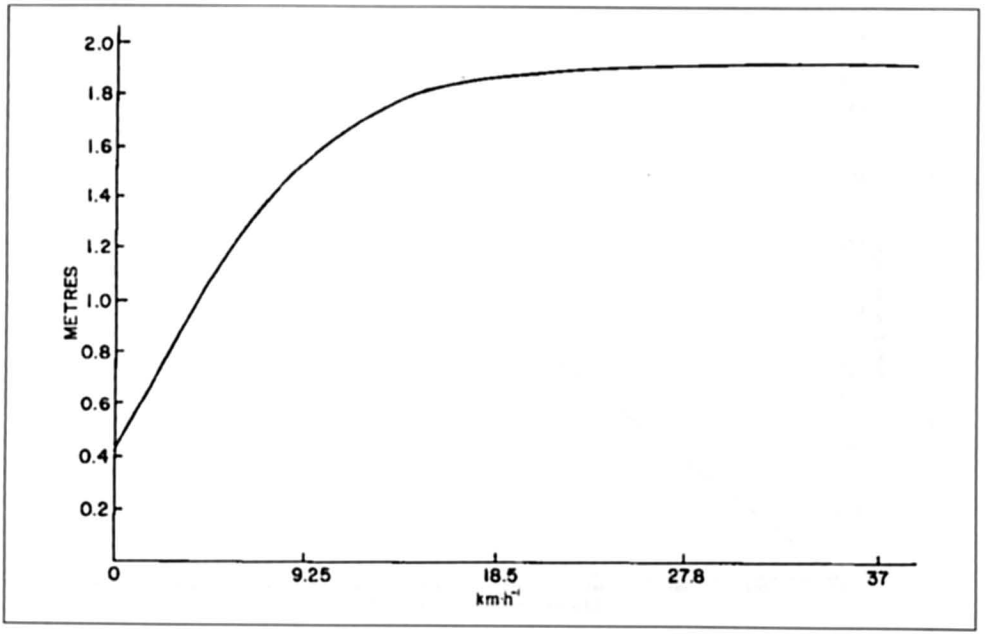


Fig. 6.90: Storm surge amplitude versus storm speed for North point in Hong Kong harbour (LAU, 1980b)

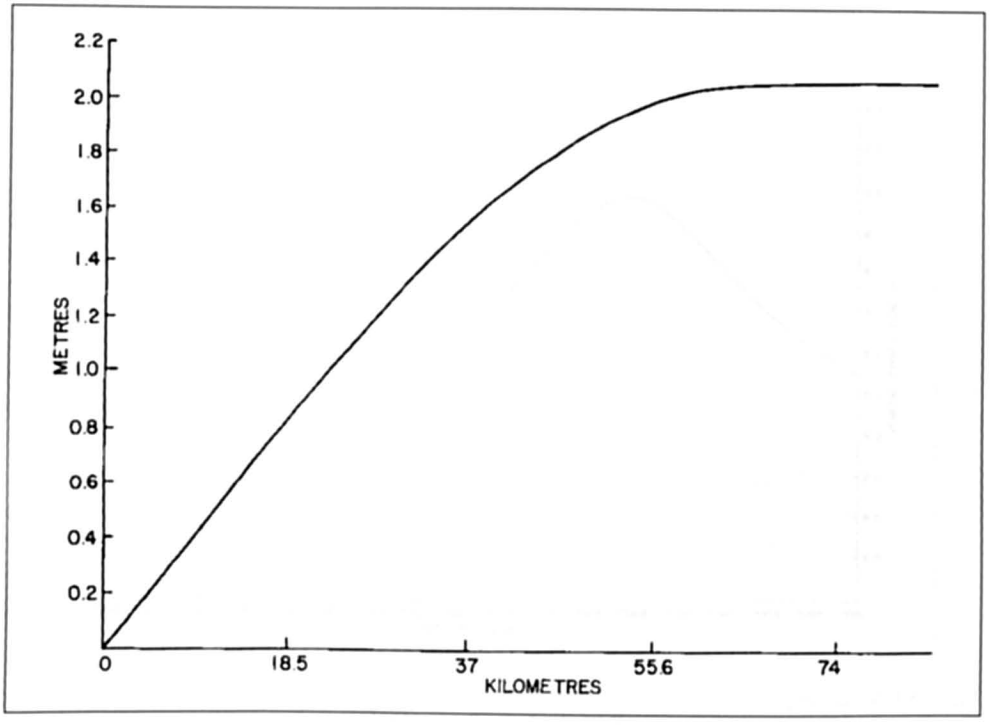


Fig. 6.91: Storm surge amplitude (ordinate) versus radius of maximum winds (abscissa) for North point in Hong Kong harbour (LAU, 1980b)

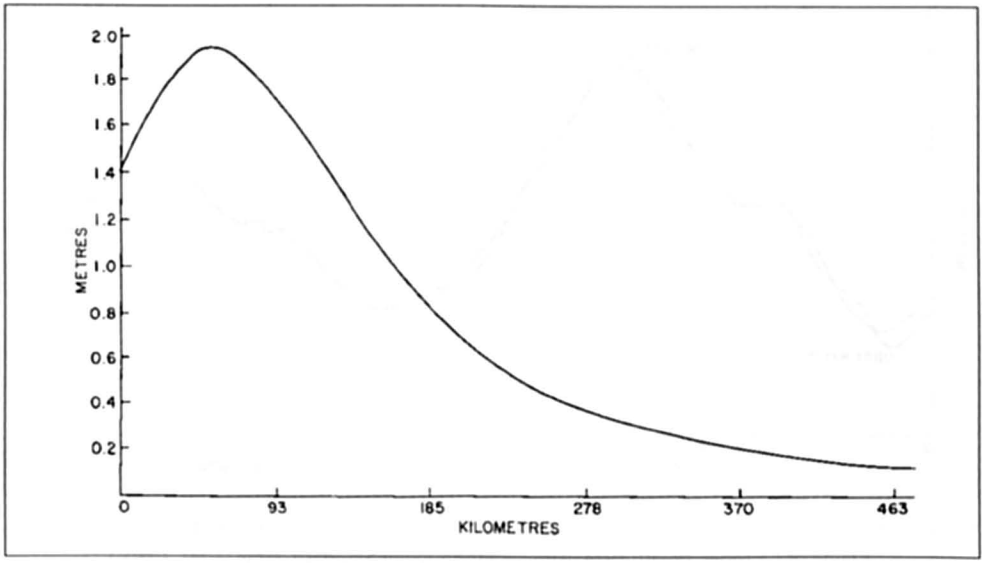


Fig. 6.92: Storm surge amplitude (ordinate) versus distance from the nearest approach of storm for North point in Hong Kong harbour (LAU, 1980b)

LAU (1980a) mentioned that the storm surge problem is getting worse in Hong Kong with more and more people crammed into reclaimed low-lying areas. A typhoon surge on September 2, 1937, killed 11000 people, and several villages around Tolo Harbour were destroyed. Typhoon Wanda of September 1, 1962, killed 127 people. LAU (1980a, 1980b) summarised the empirical relations developed by CHENG (1967) and CHAN (1976). He also included a table from PETERSON (1975) in which joint probabilities for certain combinations of tides and surges at Tolo Harbour and North Point were listed. Finally, LAU (1980a) developed a series of numerical models for computing surges in different areas of Hong Kong and environs. Observed and computed water levels at Tai Po Kau due to Typhoon Elaine of October 29–30, 1974, are compared in Fig. 6.93. Computed and observed water levels at Tai Po Kau due to Typhoon Elsie of October 14–15, 1975, are compared in Fig. 6.94.

DAS et al. (1978) mentioned that storm surges occur at the rate of three to four per year in Hong Kong Harbour. Thirty-five surges with amplitudes from 0.2 to 1.8 m occurred there during 1954–64 (CHENG, 1967). Typhoon Wanda of September 1962 produced a surge of about 3.2 m at Tai Po Kau (farther inland from Hong Kong Harbour), whereas the peak surge in Hong Kong Harbour was 1.8 m.

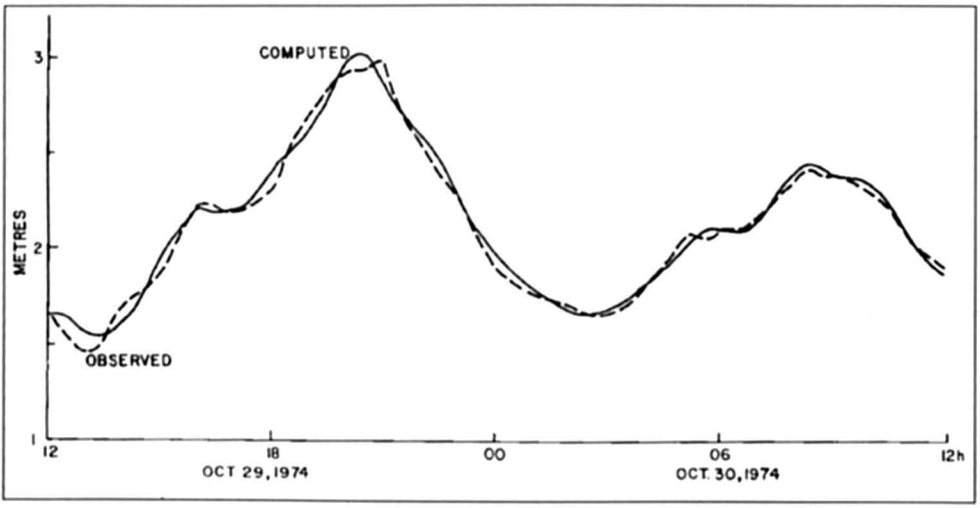


Fig. 6.93: Computed (solid line) and observed (broken line) water levels at Tai Po Kau due to Typhoon Elaine of October 29–30. 1974. Time is Hong Kong Standard Time (LAU, 1980a)

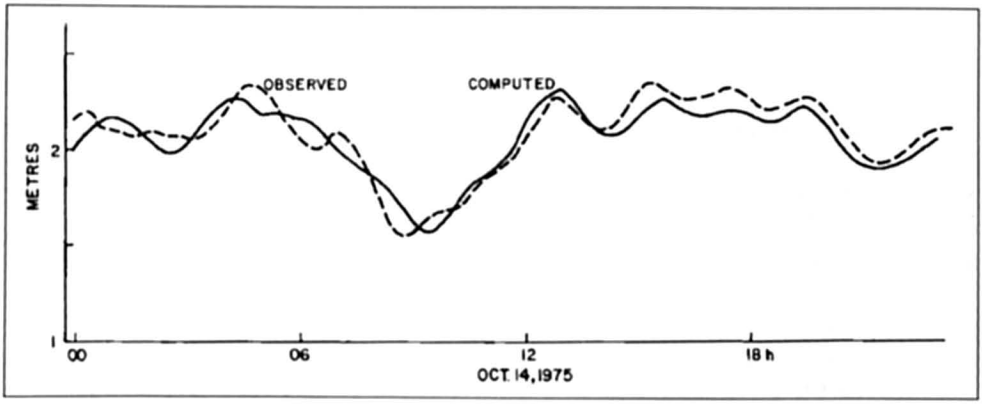


Fig. 6.94: Compared (solid line) and observed (broken line) water levels at Tai Po Kau due to Typhoon Elsie of October 14–15, 1975. Time is Hong Kong Standard Time (LAU, 1980a)

### 6.8.2 Japan

Storm surges in the bays on the coast of Japan are slightly less severe than, for example, in the Bay of Bengal and the Gulf of Mexico but they cause great damage and loss of life when they strike the densely populated coasts of Tokyo Bay, Osaka Bay, Ise Bay, etc. Table 6.52 and 6.53 list the important storm surges in Japan. MIYAZAKI (1975) mentioned that storm surge records in Japan generally exhibit three features: the forerunner, the main surge, and the resurgence. The surge profiles at Nagoya and Toba along the coast of Ise Bay due to the typhoon of September 26–27, 1959, are given in Fig. 6.95. Forerunners with amplitudes of 20–30 cm can be seen. Resurgences with periods of about 7 h can also be seen. MIYAZAKI (1975) also estimated the return periods of surges with different maximum amplitudes at six locations in Japan. These results are summarised in Table 6.54.

Table 6.52: Storm surges in Japan during the period 1900–73 with maximum amplitudes in excess of 2 m. Highest level includes surge and tide (MIYAZAKI, 1975)

| Date | Affected Area | Peak surge (m) | Highest level (m) | Meteorological extreme values Central pressure (mb) | Wind ($m \cdot s^{-1}$) | Location |
|---|---|---|---|---|---|---|
| Oct. 1, 1917 | Tokyo Bay | 2.3 | 3.1 | 950.4 | SSE 40.0 | Tokyo |
| July 18, 1930 | Ariake Sea | 2.5 | – | 954.6 | ENE 30.6 | Tomie |
| Sept. 21, 1934 | Osaka Bay | 3.1 | 3.2 | 954.3 | S 48.4 | Osaka |
| Sept. 1, 1938 | Tokyo Bay | 2.2 | – | 978.6 | S 31.0 | Tokyo |
| Sept. 3, 1950 | Osaka Bay | 2.1 | 2.5 | 964.3 | NE 33.4 | Kobe |
| Aug. 17, 1956 | Ariake Sea | 2.4 | 4.2 | 968.4 | SE 27.0 | Saga |
| Sept. 26, 1959 | Ise Bay | 3.4 | 3.9 | 958.5 | SSE 37.0 | Nagoya |
| Sept. 16, 1961 | Osaka Bay | 2.5 | 2.9 | 937.3 | SSE 33.3 | Osaka |
| Sept. 25, 1964 | Osaka Bay | 2.1 | 2.6 | 983.5 | S 27.1 | Sumoto |
| Sept. 10, 1965 | Osaka Bay | 2.2 | – | 966.0 | SSE 38.8 | Sumoto |
| Aug. 21, 1970 | Tosa Bay | 2.4 | 3.1 | 962.3 | SW 35.8 | Ashizuri |

Table 6.53: Severe damage caused by storm surges in Japan during the period 1900–73 (MIYAZAKI, 1975)

| Date | Affected Area | Highest sea level (m) | Peak surge (m) | Lives Lost | Houses destroyed or swept away |
|---|---|---|---|---|---|
| Oct. 1, 1917 | Tokyo Bay | 3.0 | 2.1 | 1324 | 60 175 |
| Sept. 13, 1927 | Ariake Sea | 3.8 | 0.9 | 439 | 2211 |
| Sept. 21, 1934 | Osaka Bay | 3.1 | 2.9 | 3036 | 92 323 |
| Aug. 27, 1942 | Inland Sea | 3.3 | 1.7 | 1158 | 102 374 |
| Sept. 17, 1945 | South Kyushu | 2.6 | 1.6 | 3121 | 115 984 |
| Sept. 3, 1950 | Osaka Bay | 2.7 | 2.4 | 534 | 120 923 |
| Oct. 14, 1951 | South Kyushu | 2.8 | 1.0 | 943 | 72 648 |
| Sept. 27, 1959 | Ise Bay | 3.9 | 3.4 | 5098 | 156 676 |
| Sept. 16, 1961 | Osaka Bay | 3.0 | 2.5 | 200 | 54 782 |

Table 6.54: Return periods of storm surges in Japan (MIYAZAKI, 1975).

| Location | Maximum Surge observed (m) | Return period (yr) for surges with peak amplitude of at least 0.5 m | 1.0 m | 2.0 m |
|---|---|---|---|---|
| Tokyo | 2.1 | 1.0 | 8 | 35 |
| Yokohama | 1.1 | 1.4 | 19 | – |
| Nagoya | 3.4 | 0.6 | 3 | 15 |
| Osaka | 3.1 | 0.7 | 3 | 10 |
| Kobe | 2.2 | 1.0 | 6 | 30 |
| Beniya (on the Ariake Sea) | 2.5 | – | 7 | 17 |

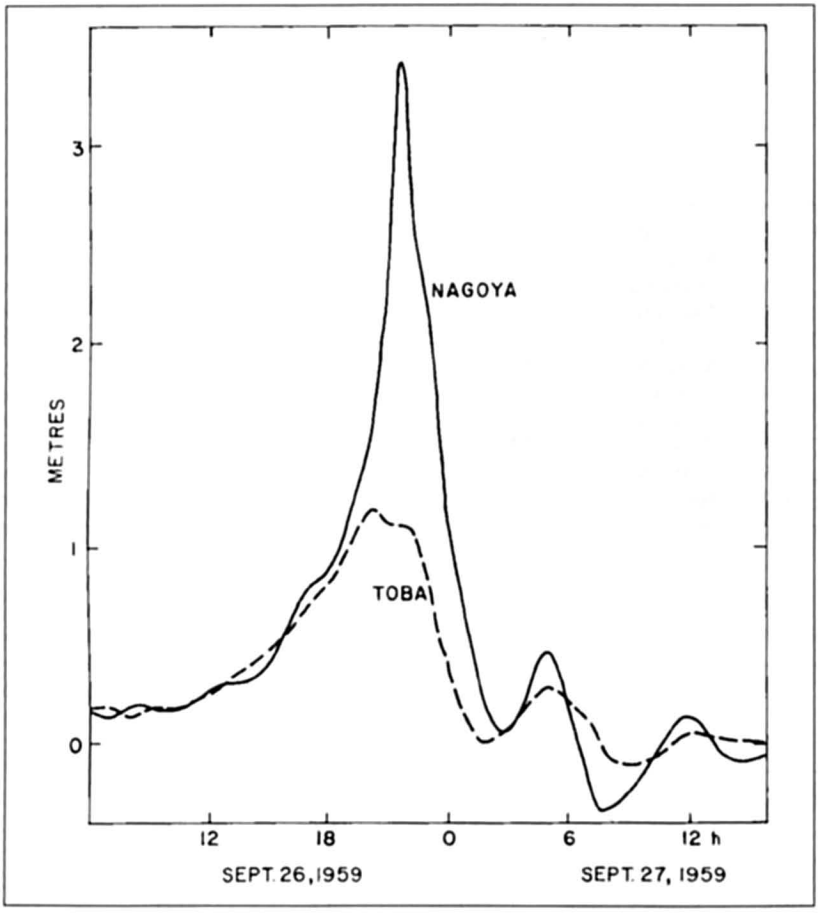


Fig. 6.95: Storm surges at Nagoya and Toba on Ise Bay, Japan, due to the typhoon of September 26–27, 1959. Note the forerunners and the resurgences in addition to the main surge (MIYAZAKI, 1975)

Unusual storm tracks can occur in the Japan area. The track of typhoon Orchid of September 1980 is illustrated in Fig. 6.96. This track is remarkable because it shows three loops. NAKAYAMA (1972) described the telemeter system for the tsunami and storm surge warning service provided by the Japan Meteorological Agency. As of 1972 there were a total of 60 coastal tide gauge stations in this system. Next, storm surge events will be considered in several different bays along the coast of Japan, beginning with Tokyo Bay and proceeding southwest. Note that the storm surge problem on the west coast of Japan (facing the Sea of Japan) is less severe than along the Pacific coast of Japan.

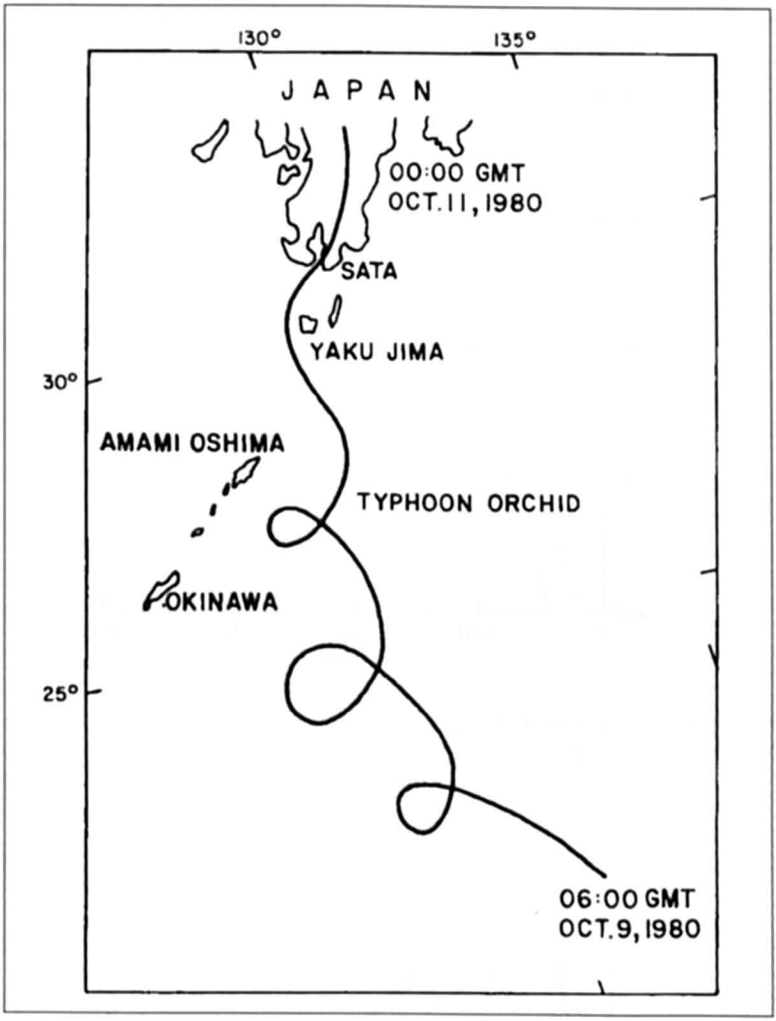


Fig. 6.96: Track of typhoon Orchid during October 9–10, 1980 (JOINT TYPHOON WARNING CENTER, 1981)

MIYAZAKI et al. (1961) used numerical models to compute the storm surges in Tokyo Bay, Ise Bay, and Osaka Bay. They reconstructed the meteorological forcing terms for the Ise Bay typhoon of September 1959. The pressure-distance and wind-distance relations are shown in Fig. 6.97 and 6.98, respectively.

Simulations were made for the following cases: (1) surge in Ise Bay due to the Ise Bay typhoon of September 1959, (2) surges in Tokyo Bay due to the typhoon of October 1, 1917, and Typhoon Kitty of September 1949, and (3) surges in Osaka Bay due to the Muroto typhoon of September 1934 and Typhoon Jane of September 1950.

The horizontal distribution of the storm surge amplitudes in Tokyo Bay due to the typhoon of October 1917 is given in Fig. 6.99. Computed and observed surges at Kishiwada and Osaka due to Typhoon Jane are compared in Fig. 6.100. The spectrum of the storm surge at Kobe due to Typhoon Jane is shown in Fig. 6.101.

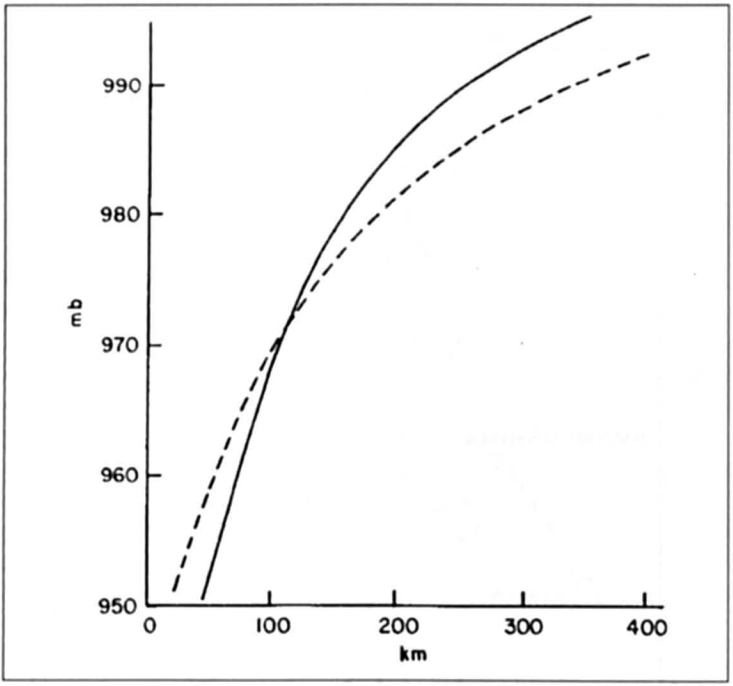


Fig. 6.97: Atmospheric pressure versus distance from the typhoon center for the Ise Bay typhoon of September 1959. Solid curve is obtained using Fujita's formula and the broken curve is from Takahasi's formula (MIYAZAKI et al., 1961)

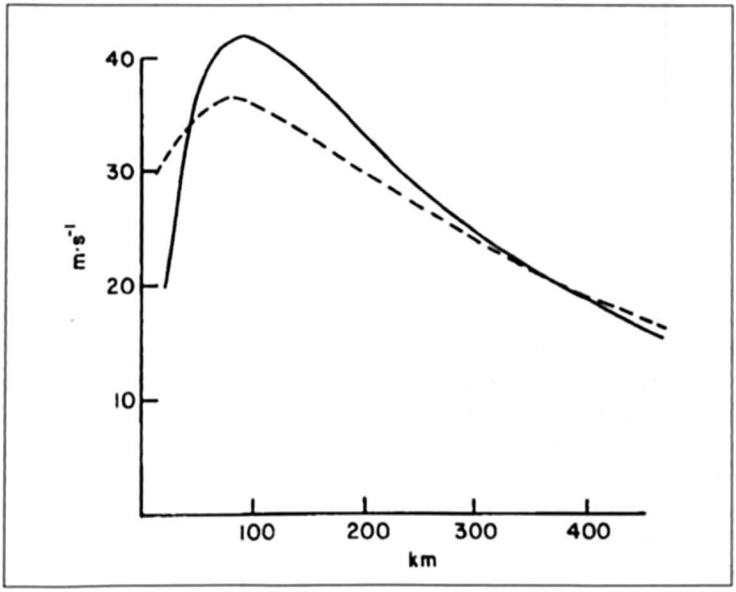


Fig. 6.98: Wind speed versus distance from the typhoon center for the Ise Bay typhoon of September 1959. Solid curve is from Fujita's formula and the broken curve is from Takahasi's formula (MIYAZAKI et al., 1961)

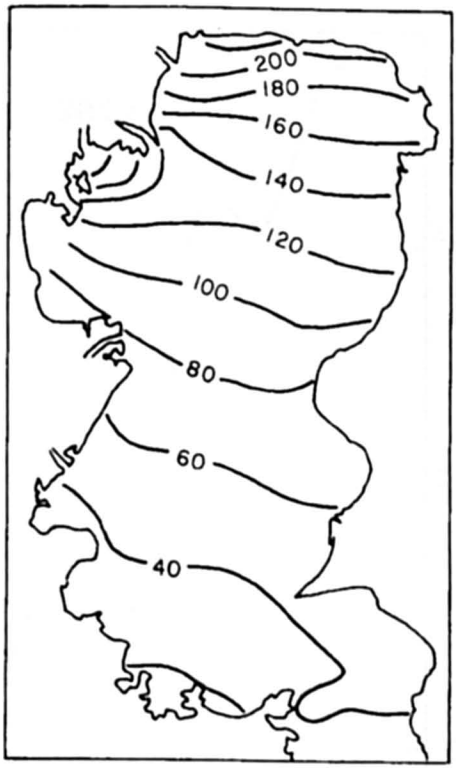


Fig. 6.99: Distribution of storm surge heights (centimeters) in Tokyo Bay at 04:00 on October 1, 1917 (MIYAZAKI et al., 1961)

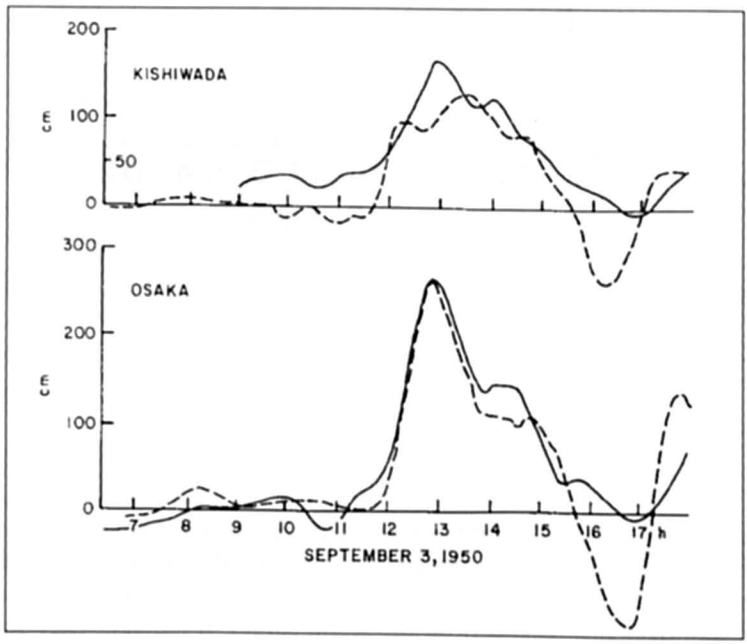


Fig. 6.100: Observed (solid line) and computed (broken line) storm surges at Kishiwada and Osaka due to typhoon Jane of September 1950 (MIYAZAKI et al., 1962)

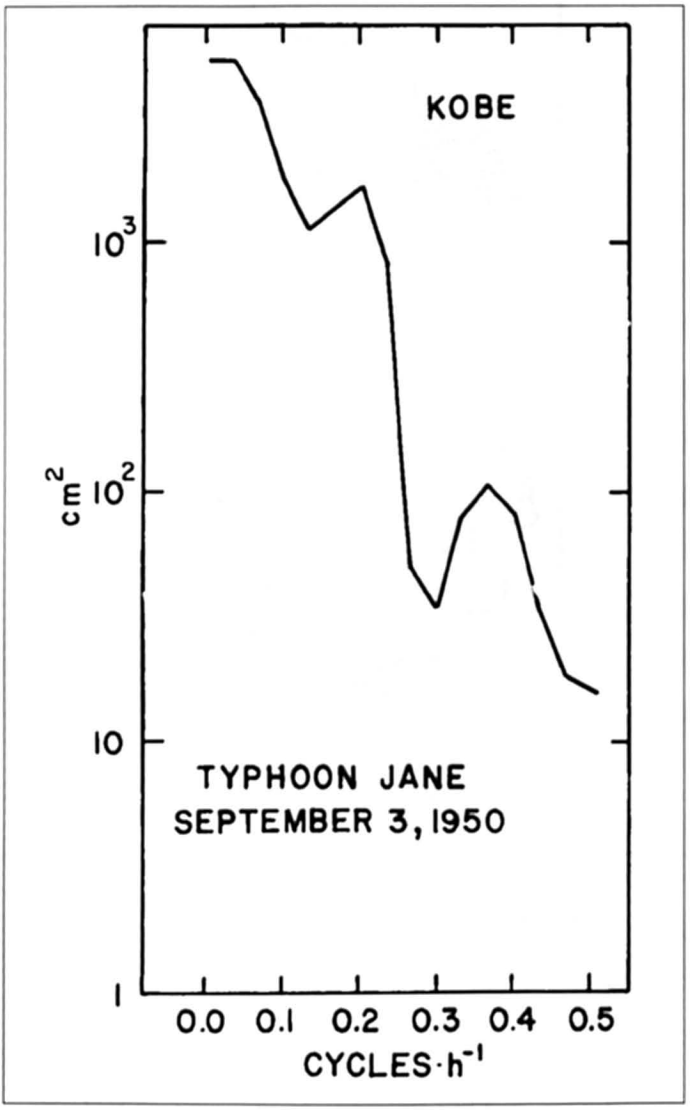


Fig. 6.101: Power spectrum of the storm surge at Kobe due to Typhoon Jane of September 3, 1950 (DAS et al., 1978)

ITO et al. (1965) developed a two-dimensional numerical model for storm surges in Tokyo Bay and the outer shelf using multiple grids. They also studied the problem of tide-surge interaction and the influence of a dyke (with an opening) in Tokyo Bay (north of a line connecting Kawasaki and Kisarazu) on the storm surges in the bay. They simulated the surges due to the October 1, 1917, typhoon and also due to the Ise Bay typhoon of September 1959.

They found the following empirical relation for the maximum water level max in that part of the bay protected by the dyke:

$$\eta_{max} = a + m \log A \qquad (6.74)$$

where, A is the cross-sectional area of the opening, a is a constant that depends on the point of observation, and m is another constant almost independent of location.

Runs were made with the numerical model for openings with widths of 20 m to 2 km and also for a case of two openings, each 0.5 km wide. The results tend to show that the maximum surge amplitudes in the inner bay (i.e. protected by the dyke) decrease when a dyke is present. Also, the maximum surge amplitude decreases for smaller widths of the opening (Fig. 6.102). The problem of tide-surge interaction has already been discussed in section 4.5.8.

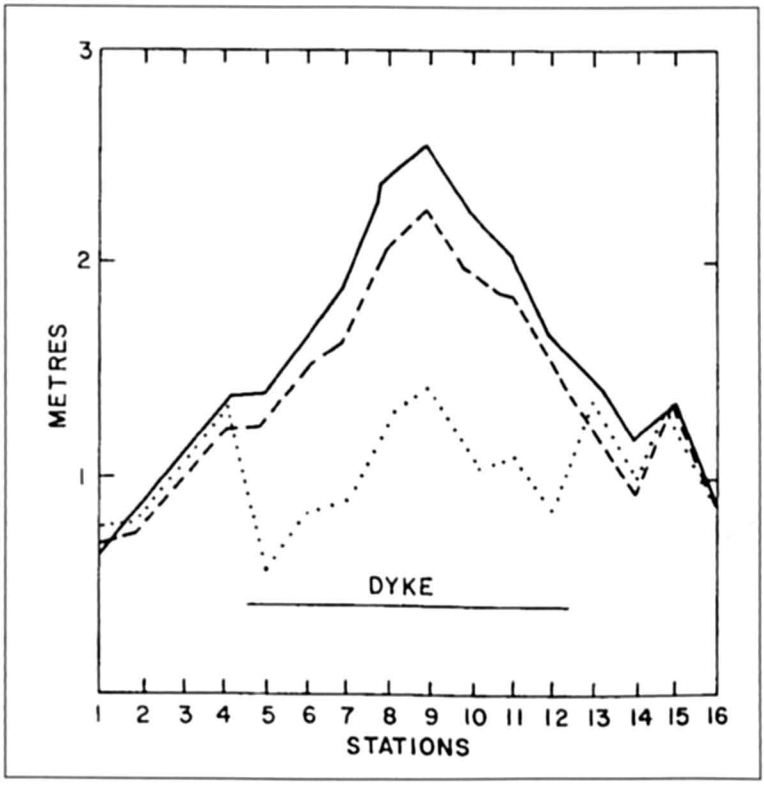


Fig. 6.102: Computed envelope of peak storm surge in Tokyo bay after the construction of a dyke. Solid line: without dyke; broken line: with dyke having an opening of 2 km dotted line with dyke having an opening of 0.5 km width, Stations: 1. Kurihama, 2. Yokosuka; 3. Yokohama; 4. Kawasaki South; 5. Kawasaki North; 6. Tokyo; 7. Urayasu; 8. Funabashi; 9. Chiba,; 10. Goi; 11. Anegasaki; 12. Narawa; 13. Kisarazu; 14. Futtusu; 15. Isone; 16. Kaiho II (ITO et al., 1965)

KAWAHARA et al. (1980) used a finite-element model to compute storm surges in the Surugawan Bay due to the typhoon (No. 6626) of September 24, 1966. The maximum surge produced was about 1 m. After the disastrous storm surge of September 1959 in Ise Bay, a breakwater was constructed in the inner part of the bay to protect the Nagoya district.

(NAKAMURA et al. 1964). These authors also performed hydraulic model tests. The tests showed that the breakwater will not significantly alter the tide but will reduce the surge considerably in the inner part of the bay.

The Muroto typhoon of September 21, 1934, caused major storm surges in Lake Biwa (northeast of Osaka). The southern portion of this lake is very shallow with an average depth of only 3.4 m. Surges up to 2.4 m in amplitude were generated (NOMITSU, 1935).

MIYAZAKI (1955) studied storm surge in the Kobe Harbour. During the period 1925–54, a total of at least 34 storm surges occurred in this harbour. The Muroto typhoon of September 21, 1934, produced a surge of amplitude 2.2 m. Typhoon Jane of September 3, 1950, produced a surge of 1.7 m; the Makurazaki typhoon of September 18, 1945, as well as another typhoon on September 26, 1954, produced surges up to 1.5 m.

MIYAZAKI (1955) gave the following return periods for surges of amplitude 1.0, 1.5, 2.0, and 2.0 m in Kobe harbour: 5, 24, 105, and 455 yr. Of a total of 32 storm surges studied, 22 were caused by tropical cyclones and the remaining 10 were caused by extratropical cyclones. Further, any surges with amplitudes greater than 0.8 m were exclusively produced by tropical cyclones.

Osaka bay is frequently subjected to severe storm surges. The Muroto typhoon of September 21, 1934, killed 2593 people and 110,000 houses were destroyed in Osaka alone. The central pressure of this typhoon was the lowest ever recorded at a land station (912 mb). Wind velocities of up to 60 $m \cdot s^{-1}$ created maximum water level of 4.6 m, and surges with amplitudes of up to 2.3 m inundated large areas (MATSUO, 1934). Osaka Harbour (and several others) was heavily damaged and individual ships of up to 3145 t in weight were carried ashore by the surge. The total weight of the ships carried ashore in Osaka Harbour was about 23,000 t. The envelope of maximum surge amplitude at several locations along Osaka Bay due to Typhoon Nancy of 1961 is shown in Fig. 6.103.

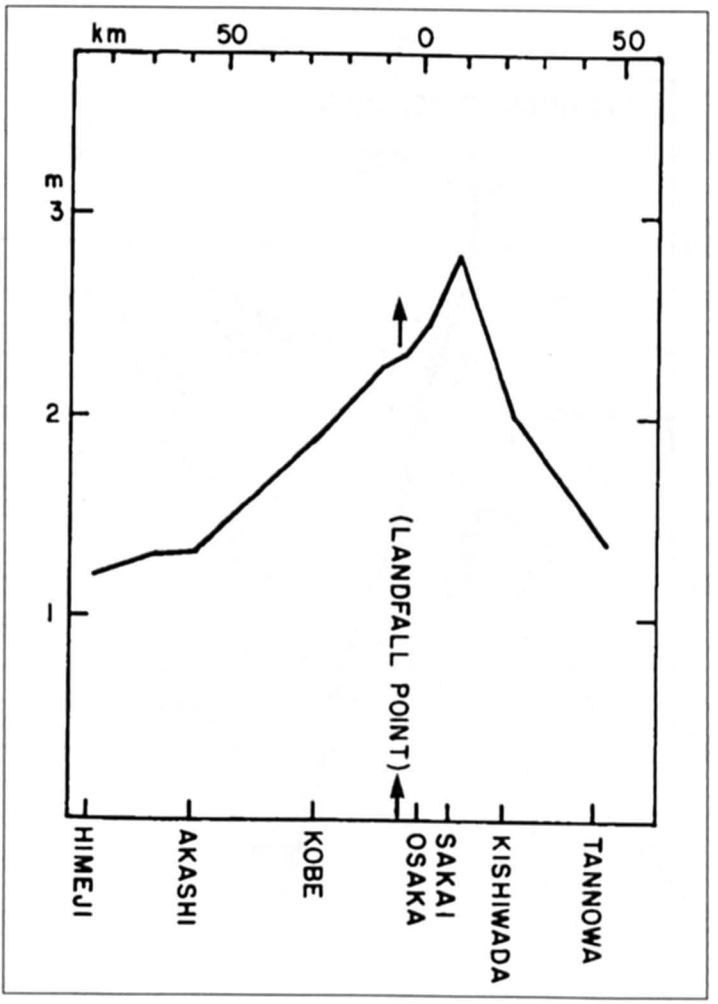


Fig. 6.103: Peak surge envelope at stations along Osaka Bay due to Typhoon Nancy of 1961 (DAS et al., 1978)

HAYAMI et al. (1955) performed hydraulic model experiments to study the propagation of a storm surge as a bore in the rivers and canals near Osaka City and concluded that the embankment under construction (1955) would provide some protection but not total protection from storm surges. MUROTA (1963) also performed hydraulic model studies for Osaka bay and concluded that construction of breakwater would actually increase the amplitudes of storm surges due to increased seiche action. UNEO (1981) used SPLASH and also a numerical model to simulate the storm surge of August 21, 1970, in Tosa Bay, which produced surges up to 2 m in amplitude. He also used a two-layer model to include the effect of stratification.

MINATO (1998) numerically simulated storm surges in Tosa (Fig. 6.104) making use of the three-dimensional terrain following Princeton Ocean Model (POM) with horizontally uniform stratification in the area of Tosa bay. Finer Resolution in the vertical direction and stronger stratification generates slightly greater peak surges.

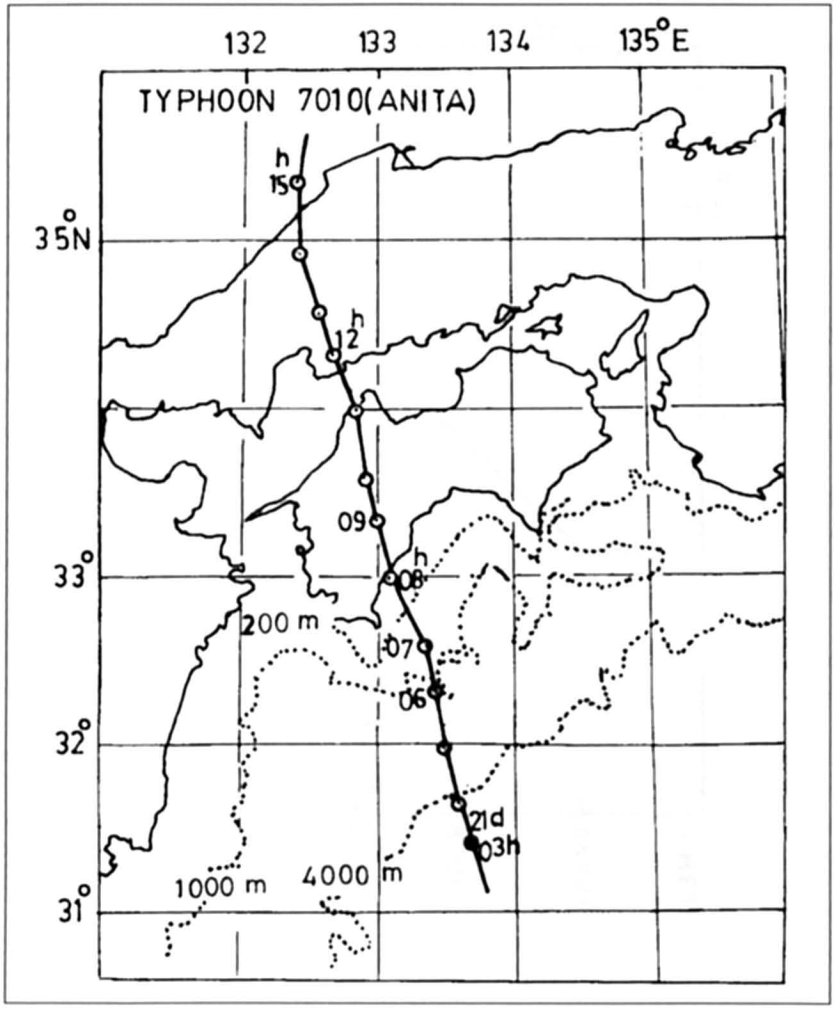


Fig. 6.104: Typhoon 7010 track (MINATO, 1998)

### 6.8.3 South Korea

Storm surges are not a serious problem in the Sea of Japan. Hence, the west coast of Japan and the east coast of Korea are not prone to major storm surges. However, storm surges occur in the Yellow Sea and the Po Hai Sea. Thus, storm surges on the west coast of Korea deserve attention.

On the southern part of the Korean peninsula, the tidal range in the Yellow Sea is about 4 m and it increases to about 10 m in the northern part (AN, 1980). The typhoons that pass over Korea are usually less severe than those that affect Japan.

The observed storm surge at Inchon (tidal range here is about 7 m) during August 30–31, 1979, due to Typhoon Billie is shown in Fig. 6.105. The track of this typhoon is shown in Fig. 6.106. AN (1980) used a two-dimensional numerical model to simulate this storm surge. The range (trough to crest) of the storm surge at Inchon was about 1.4 m. At Mokpo and Kunsan;

the range was only about 0.4 m. On July 29, 1965, a storm that struck the west coast of Korea generated an unusually large surge of 5.2 m (DAS et al., 1978).

CHOI (1987) developed numerical models for tides and surges in the Yellow Sea with application to South Korea. OH et al. (1988) studied storm surges due to typhoons passing through the south sea of Korea. Making use of data from eight tidal stations, they showed that surges have greater amplitudes generally for the western stations as compared to eastern stations also negative surges are more predominant for the western area.

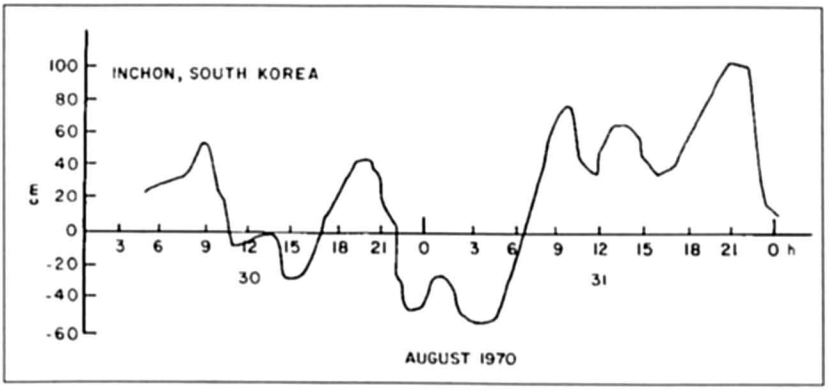


Fig. 6.105: Storm surge at Inchon, South Korea during August 30–31, 1970, due to Typhoon Billie. Time is Korean Standard Time (AN, 1980)

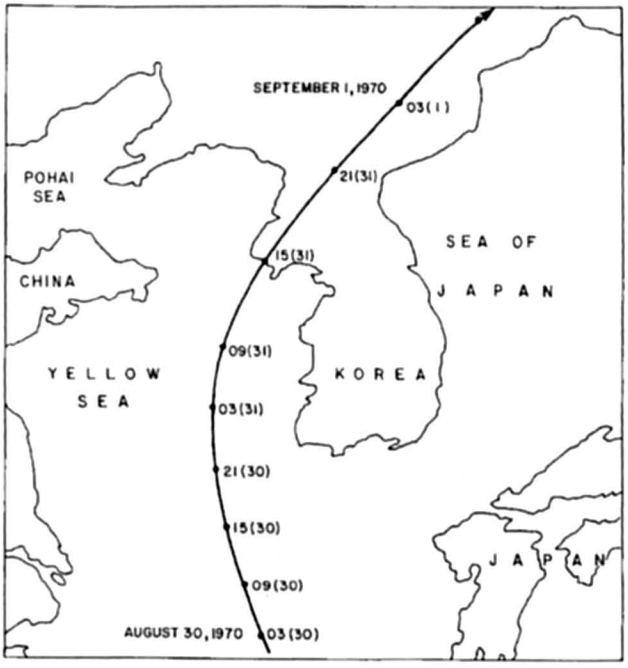


Fig. 6.106: Track of Typhoon Billie during August 30– September 1, 1970. Time is Korean Standard Time. Numbers in the parentheses are the dates (AN, 1980)

SHIN (1994) studied storm surges on the coast of South Korea. Table 6.55 lists the typhoons for the period 1904 to 1983. Fig. 6.107 shows the tracks of the typhoons coming from various directions. Table 6.56 lists the frequency and percentage of typhoon approach from different directions. Table 6.57 lists the peak surge amplitudes at various locations.

Table 6.55: The temporal distribution of the major storms around the Korean Peninsular during the years 1904–1983

| Year | May | Jun. | Jul. | Aug. | Sep. | Oct. | Total | Year | May | Jun. | Jul. | Aug. | Sep. | Oct. | Total |
|---|---|---|---|---|---|---|---|---|---|---|---|---|---|---|---|
| 1904 | | | | 2 | | | 2 | 1945 | | | 1 | 2 | 1 | | 4 |
| 1905 | | | 1 | 1 | 1 | | 3 | 1946 | | | 1 | 2 | | | 3 |
| 1906 | | | | 1 | 1 | 1 | 3 | 1947 | | | | | | | 0 |
| 1907 | | | 2 | | 1 | | 3 | 1948 | | | 1 | 1 | 2 | | 4 |
| 1908 | | | | 1 | | | 1 | 1949 | | 1 | 2 | 1 | | | 4 |
| 1909 | | | | 2 | | | 2 | 1950 | | 2 | 1 | 3 | 2 | | 8 |
| 1910 | | | 1 | | | | 1 | 1951 | | | | 1 | 1 | 1 | 3 |
| 1911 | | | 2 | 1 | 1 | 1 | 5 | 1952 | | 1 | 1 | 1 | 1 | | 4 |
| 1912 | | | 1 | | | | 1 | 1953 | | 1 | 1 | 1 | | | 3 |
| 1913 | | | 1 | | | | 1 | 1954 | | | | 1 | 2 | | 3 |
| 1914 | | 1 | 2 | 1 | 2 | | 6 | 1955 | | | 2 | | 1 | | 3 |
| 1915 | | | 1 | 1 | 1 | | 3 | 1956 | | | | 1 | 3 | | 4 |
| 1916 | | | | 1 | 1 | | 2 | 1957 | | 1 | | 1 | | | 2 |
| 1917 | | | | 1 | 2 | | 3 | 1958 | | | | | 1 | | 1 |
| 1918 | | | 1 | 2 | | | 3 | 1959 | | | 2 | 1 | 4 | | 7 |
| 1919 | | | | 3 | 1 | | 4 | 1960 | | | 1 | 2 | | | 3 |
| 1920 | | | | | | | 0 | 1961 | 1 | | 1 | 1 | 1 | 1 | 5 |
| 1921 | | | | | 2 | | 2 | 1962 | | | 1 | 2 | 1 | | 4 |
| 1922 | | | 2 | | 2 | 1 | 5 | 1963 | | 1 | 1 | 1 | | | 3 |
| 1923 | | 1 | 1 | 2 | | | 4 | 1964 | | | 3 | 1 | | | 4 |
| 1924 | | | 1 | 3 | | | 4 | 1965 | | | 1 | 2 | | | 3 |
| 1925 | | | 3 | 1 | 1 | | 5 | 1966 | | | | 2 | 1 | | 3 |
| 1926 | | | 1 | 2 | | | 3 | 1967 | | | 1 | | | | 1 |
| 1927 | | | | 1 | 1 | | 2 | 1968 | | | 1 | 1 | 1 | | 3 |
| 1928 | | | | | 2 | | 2 | 1969 | | | | | 1 | | 1 |
| 1929 | | | | 1 | | | 1 | 1970 | | | 2 | 2 | | | 4 |
| 1930 | | | 2 | 1 | | | 3 | 1971 | | | | 2 | 1 | | 3 |
| 1931 | | | 2 | 1 | | | 3 | 1972 | | | 2 | 1 | 1 | | 4 |
| 1932 | | | | 2 | | | 2 | 1973 | | | 2 | 1 | | | 3 |
| 1933 | | | 3 | 1 | 2 | | 6 | 1974 | | | 2 | 1 | 1 | | 4 |
| 1934 | | | 1 | 1 | 1 | | 3 | 1975 | | | 1 | 1 | | | 2 |
| 1935 | | | | 1 | 1 | | 2 | 1976 | | | 3 | 2 | 1 | | 6 |
| 1936 | | | 1 | 2 | 1 | | 4 | 1977 | | | | 1 | 1 | | 2 |
| 1937 | | | 1 | | 1 | | 2 | 1978 | | 1 | | 2 | 1 | | 4 |
| 1938 | | | | 1 | 1 | | 2 | 1979 | | | | 2 | | | 2 |
| 1939 | | | 1 | 1 | | | 2 | 1980 | | | 1 | 1 | 1 | | 3 |
| 1940 | | | 2 | 1 | 2 | | 5 | 1981 | | 2 | 1 | | 2 | | 5 |
| 1941 | | | 1 | 2 | | | 3 | 1982 | | | | 3 | 1 | | 4 |
| 1942 | | | 1 | 3 | | | 4 | 1983 | | | | | 1 | | 1 |
| 1943 | | | 3 | 1 | | | 4 | Total | 1 | 12 | 72 | 94 | 63 | 5 | 247 |
| 1944 | | | | 1 | | | 1 | | | | | | | | |

Table 6.56: The frequency and percentage of storms, which were grouped by their routes

| Group | Frequency | Percentage (%) |
|---|---|---|
| S | 58 | 23 |
| W | 48 | 17 |
| E | 34 | 14 |
| WE | 27 | 11 |
| CWEN | 27 | 11 |
| CWES | 21 | 9 |
| CWN | 17 | 7 |
| Others | 20 | 8 |
| Total | 247 | 100 |

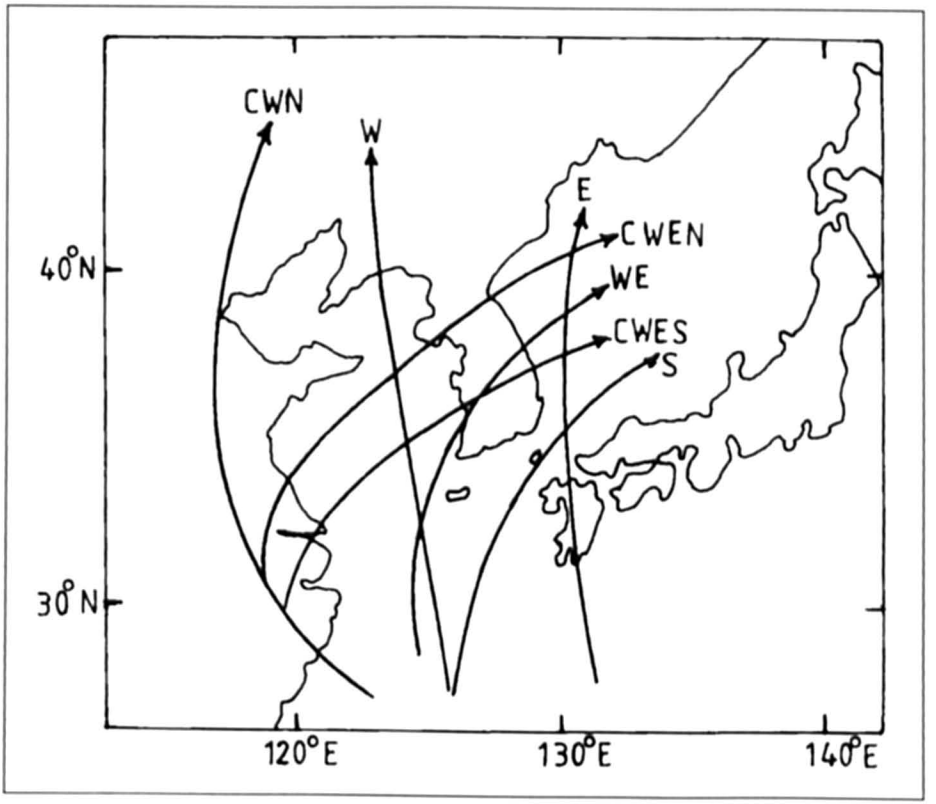


Fig. 6.107: Schematic representation of typhoon tracks (SHIN, 1994)

Table 6.57: Maximum tidal deviation at each station during the years 1957–1970 (SHIN, 1994)

| Year | Cheju | | Taehuksan do | | Mokp'o | | Kunsan | | Inch' on | | Yosu | | Chinhae | | Pusan | | Ulsan | |
|---|---|---|---|---|---|---|---|---|---|---|---|---|---|---|---|---|---|---|
| | Date | Ht. | Date | Ht. | Date | Ht. | Date | Ht. | Date | Ht. | Date | Ht. | Date | Ht. | Date | Ht. | Date | Ht. |
| 1959 | | | | | 7-Feb | 120 | 5-Dec | 90 | 19-Dec | 70 | | | 18-Sep | *110 | | | | |
| 1960 | | | | | 19-Jan | 60 | | | | | | | 21-Mar | 80 | | | | |
| 1961 | | | | | 6-Feb | 70 | 17-Dec | 140 | 29-Aug | 80 | | | 4-Apr | 80 | | | | |
| | | | | | | | | | | | | | 17-Dec | | | | | |
| 1962 | | | | | 16-Nov | 80 | 7-Mar | 110 | 10-Apr | 80 | | | | | | | | |
| 1963 | | | | | 25-May | 57 | 5-Dec | 95 | 7-Jul | 62 | | | 3-Jan | 40 | | | | |
| | | | | | | | | | | | | | 20-Jun | | | | | |
| 1964 | 21-Aug | 60 | | | 2-Apr | 58 | 12-Jan | 62 | 21-Aug | 73 | | | 7-Apr | 40 | | | 21-Dec | 60 |
| | | | | | | | | | | | | | 12-Aug | | | | | |
| 1965 | 6-Jun | 60 | | | 10-Jan | 48 | 18-Mar | 58 | 10-Jan | 88 | 6-Jun | 82 | 2-Jan | 40 | 2-Jan | 27 | | |
| 1966 | 22-Aug | *102 | 14-Oct | 53 | 18-Mar | 54 | 6-May | 95 | 27-Jul | 79 | *24 Aug | 110 | 17-Apr | 40 | Sep | 26 | 11-Sep | 40 |
| | | | | | | | | | | | | | | | | | 3-Jul | |
| 1967 | 27-Jan | 34 | 8-Oct | 98 | 15-Apr | 54 | 8-Apr | 32 | 14-Dec | 87 | 30-Apr | 70 | 11-Dec | 40 | 29-Nov | 29 | 3-Sep | 30 |
| | | | | | | | | | | | | | 21-Aug | 40 | | | | |
| 1968 | 6-Dec | 43 | 3-Sep | 78 | 12-Mar | 59 | 28-Jul | 66 | 2-Jan | 71 | 16-Mar | 70 | 28-Nov | | 12-Dec | 28 | | |
| | | | | | | | | | | | | | 27-May | 50 | | | | |
| 1969 | 16-Apr | 39 | 19-Oct | 73 | 28-Mar | 62 | 28-Apr | 65 | 12-Jun | 53 | 25-Apr | 40 | 31-Oct | | 24-May | 28 | | |
| | | | | | | | | | | | | | | | 6-Jun | | | |
| 1970 | 30-Aug | *69 | 30-Aug | *112 | 30-Aug | *92 | 12-Jan | 98 | 31-Aug | *79 | 30-Aug | 88 | 31-Aug | *40 | 30-Jan | 30 | 6 Jul | 30 |
| | | | | | | | | | | | | | | | | | 16-Aug | |

* Tidal deviation caused by typhoon. ____ Same month

### 6.8.4 Philippines

Philippines is an archipelago of about 7,100 islands located between the South China Sea and the Pacific Ocean and the Southeast Asian continental shelf (BROWN et al., 1991). Its coastline of 17,460 km makes it particularly vulnerable to storm surges as it lies in the path of destructive typhoons.

During the period 1907–31, there were 43 significant storm surges in the Philippines (DAS et al., 1978). A storm of October 15–16, 1912, struck the towns of Leyte and Cebu and apparently caused 9-m surges at Sogod Norte in the Lisayan Islands. Typhoon Irma of October 24–26, 1981, caused major surges and destroyed one village.

Storm surges occur in the Sulu Sea, which is a water body on the southeastern corner of the South China Sea. Surges up to 1.22 m in amplitude and with periods of up to 75 min occur in this water body (HAIGHT, 1928).

Fig. 6.108 shows the various regions of Philippines considered in the study by BROWN et al. (1991). Fig. 6.109 shows the intensity map of strongest typhoons in Philippines. The intensity shown is the maximum wind speed in meters per second (mps) from any typhoon during this thirty year period. The historical distribution of storm surges around Philippines is shown in Fig. 6.110.

Table 6.58 lists the annual average landfall of typhoons in the regions shown in Fig. 6.108 whereas Tables 6.59 and 6.60 respectively show the probability of landfall of typhoons per year (in percent) and probability of at least one typhoon-crossing region. The average monthly frequency of typhoons for the period 1980 to 1989 is shown in Table 6.61. Tables 6.62 and 6.63 respectively list the vulnerability levels by region of typhoon hazards and annual typhoon damage and casualties.

Table 6.58: Annual average landfall of typhoons per region (BROWN et al., 1991)

| Region | Latitude | Annual Average |
|---|---|---|
| Batanes (Region II) | 19–22N | 1.7 |
| Northern Luzon (Regions I & II) | 16–19N | 2.7 |
| Bicol and Quezon (Regions IV & V) | 13–16N | 1.9 |
| Visayas (Regions VI & VII) | 10–13N | 1.9 |
| Mindanao (Regions X, XI & XII) | 7–10N | 1.0 |
| Total | | 9.2 |

Source: Philippine Atmospheric, Geophysical and Astronomical Services Administration (PAGASA)

Table 6.59: Probability of landfall of typhoons per year (in percent) (BROWN et al., 1991)

| | |
|---|---|
| At least one | 100 |
| 2 or more | 100 |
| 3 or more | 100 |
| 4 or more | 100 |
| 5 or more | 94 |
| 6 or more | 77 |
| 7 or more | 71 |
| 8 or more | 64 |
| 9 or more | 48 |
| 10 or more | 39 |

Source: PAGASA

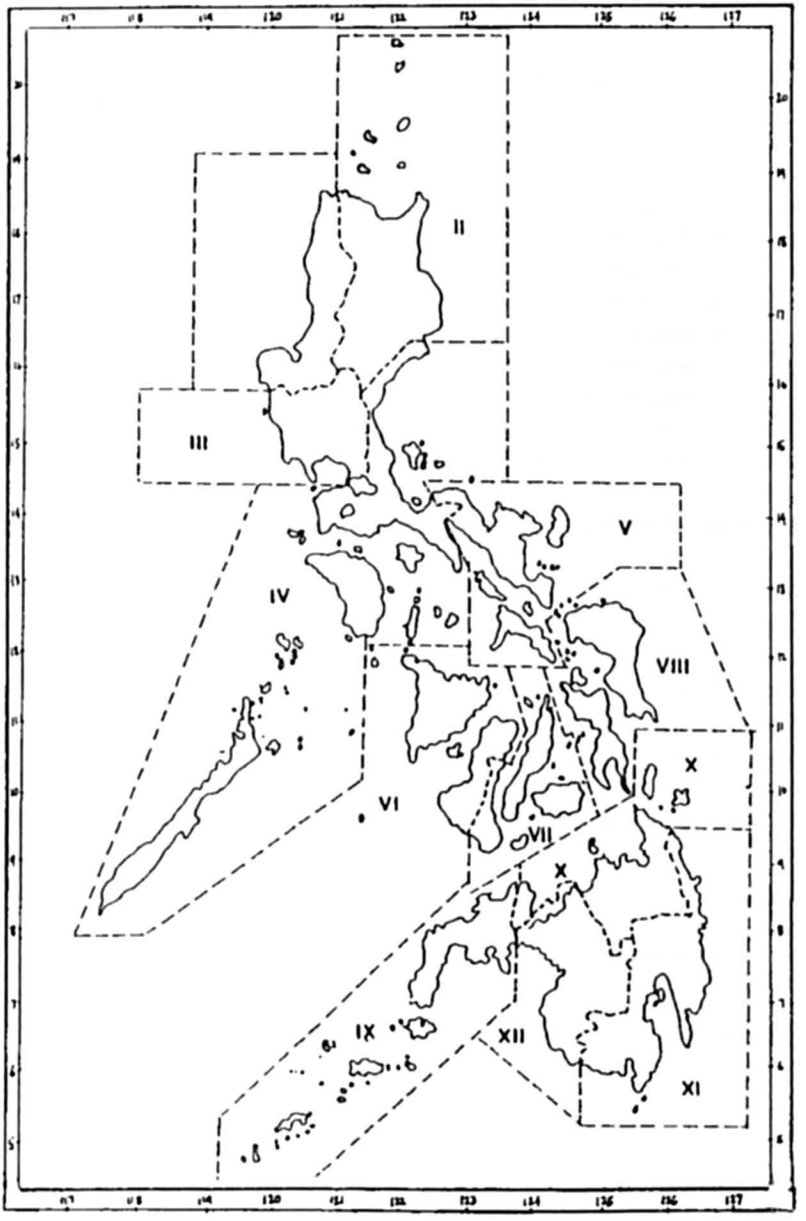


Fig: 6.108: Various regions of Philippines from the point of view of typhoons (BROWN et al., 1991)

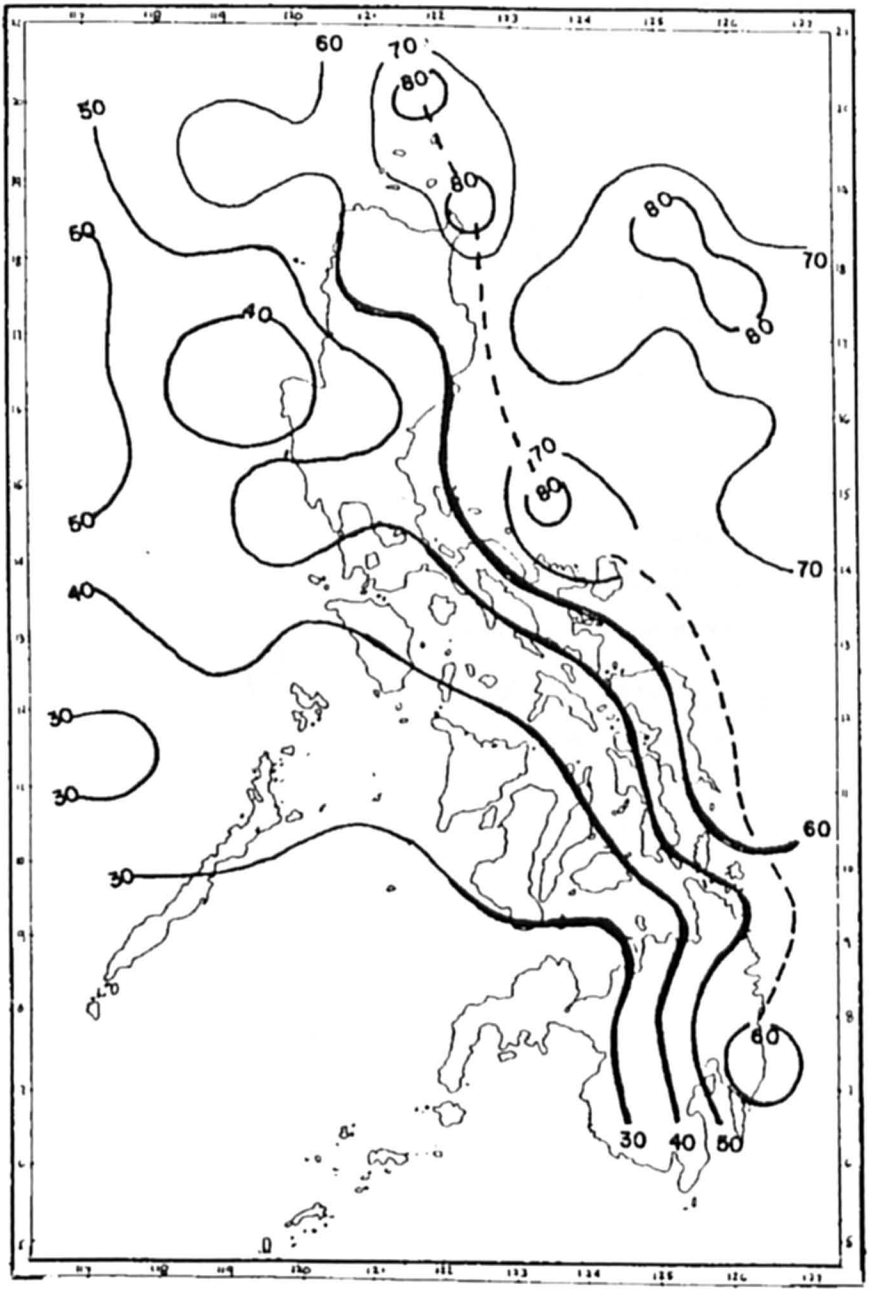


Fig. 6.109: Intensity (mps) of strongest typhoon, which passed every degree latitude – longitude square from 1960–1989 (BROWN et al, 1991)

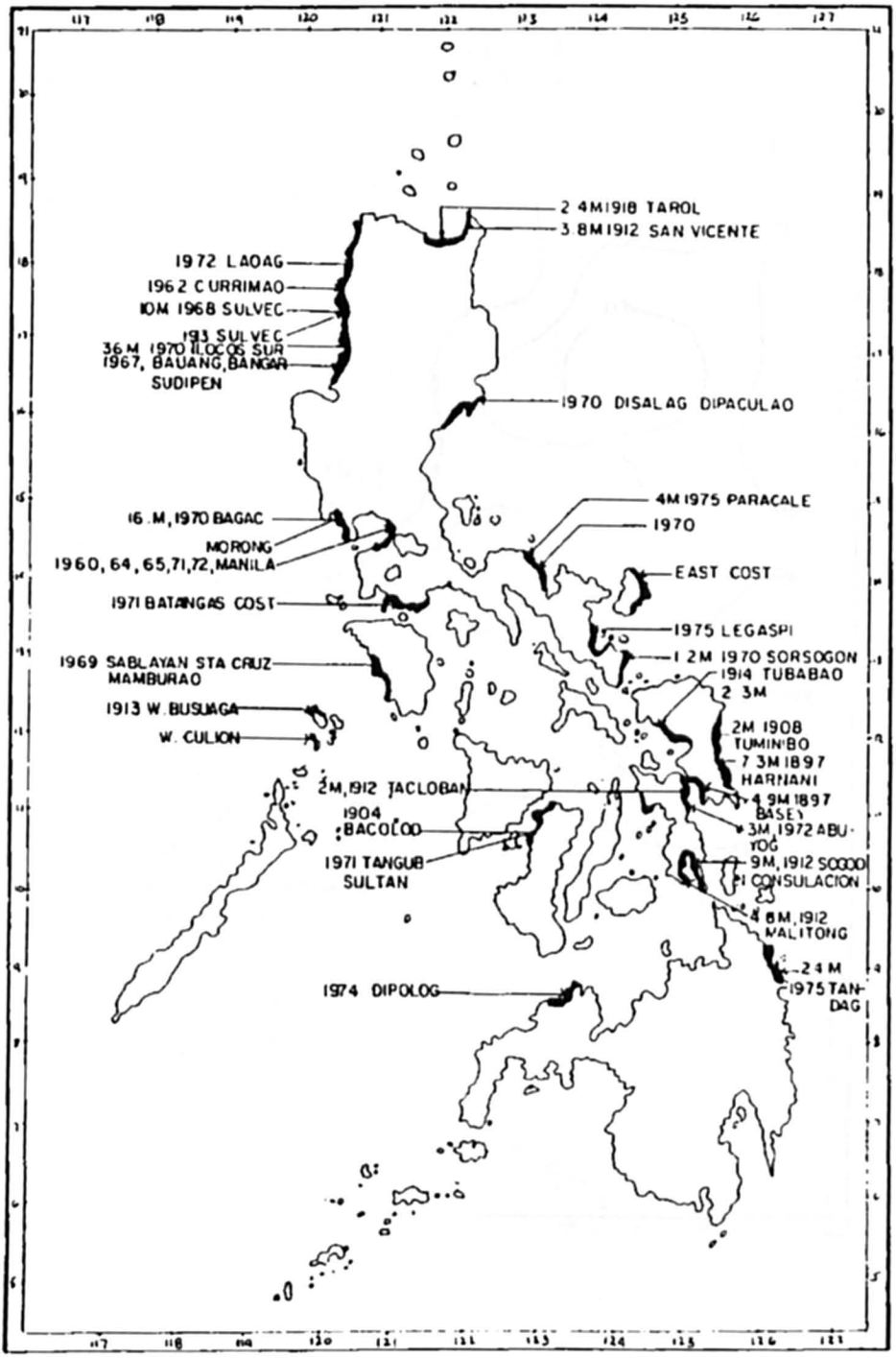


Fig. 6.110: Historical storm surges in the Philippines (BROWN et al., 1991)

Table 6.60: Probability of at least one typhoon crossing a region (BROWN et al., 1991)

| Region | Probability (%) |
|---|---|
| Batanes (Region II) | 90 |
| Northern Luzon (Regions I & II) | 87 |
| Bicol and Quezon (Regions IV & V) | 74 |
| Visayas (Regions VI & VII) | 87 |
| Mindanao (Regions X, XI & XII) | 58 |

Source: PAGASA

Table 6.61: Average monthly frequency of typhoons (1980–1989) (BROWN et al., 1991)

| Months | Average frequency of typhoons | Probability of at least one typhoon making landfall (in percent) | Average frequency of making landfall |
|---|---|---|---|
| January | 0.4 | 23 | 0.4 |
| February | 0.3 | 3 | 0.1 |
| March | 0.3 | 10 | 0.3 |
| April | 0.2 | 5 | 0.2 |
| May | 0.8 | 20 | 0.3 |
| June | 1.7 | 48 | 0.6 |
| July | 3.6 | 58 | 1.1 |
| August | 3.1 | 74 | 1.2 |
| September | 2.6 | 74 | 1.4 |
| October | 3.4 | 55 | 1.3 |
| November | 2.2 | 84 | 1.7 |
| December | 1.6 | 48 | 0.6 |
| Total | 20.2 | 100 | 9.2 |

Source: PAGASA

Table 6.62: Vulnerability levels by region for typhoons hazards (BROWN et al., 1991)

| Region | High Winds | Floods | Storm Surge |
|---|---|---|---|
| National Capital | H | H | L |
| I | H | M | M |
| II | M | H | M |
| III | H | H | M |
| IV | H | M | H |
| V | H | H | H |
| VI | M | M | M |
| VII | M | L | M |
| VIII | H | M | H |
| IX | L | L | L |
| X | H | H | H |
| XI | M | M | L |
| XII | n.a | H | n.a |
| Cordillera[A/] | H | n.a | n.a |

n.a. Not Applicable
A/ Prior to 1989, CAR was part of Region I
Source: Table composed by consultants

Table 6.63: Annual typhoon damage and casualties (BROWN et al., 1991)

| | Billions of Pesos | (in Lives Lost current Prices) |
|---|---|---|
| 1980 | 1.4 | 143 |
| 1981 | 1.3 | 484 |
| 1982 | 1.6 | 337 |
| 1983 | 0.5 | 126 |
| 1984 | 5.8 | 1979 |
| 1985 | 2.7 | 211 |
| 1986 | 1.7 | 171 |
| 1987 | 4.0 | 1020 |
| 1988 | 8.7 | 429 |
| 1989 | 4.5 | 382 |
| Total | 32.2 | 5282 |
| Average | 3.2 | 528 |

Source: Office of Civil Defense (OCD)

### 6.8.5 Vietnam

Storm surges occur on the east coast of North Vietnam and on the east and south coasts of South Vietnam. NICKERSON (1971) used SPLASH models to study these surges. One of the worst storm surges in human history occurred in 1881 in which about 300,000 people were killed in the area surrounding Haiphong (LACOUR, 1917c).

IMAMURA and TO (1997) studied storm surges and other natural disasters in Vietnam for the period subsequent to 1997. Fig. 6.111 shows the cost of natural and human made disasters in Vietnam for this period whereas Fig. 6.112 shows the damage due to typhoons. Fig. 6.113 shows the areas affected by floods and storm surges. Fig. 6.114 shows the tracks of typhoons Andy and Cecil in 1995, which devastated Central Vietnam. Fig. 6.115 shows the dyke system of Vietnam for protection against storm surge inundation and floods.

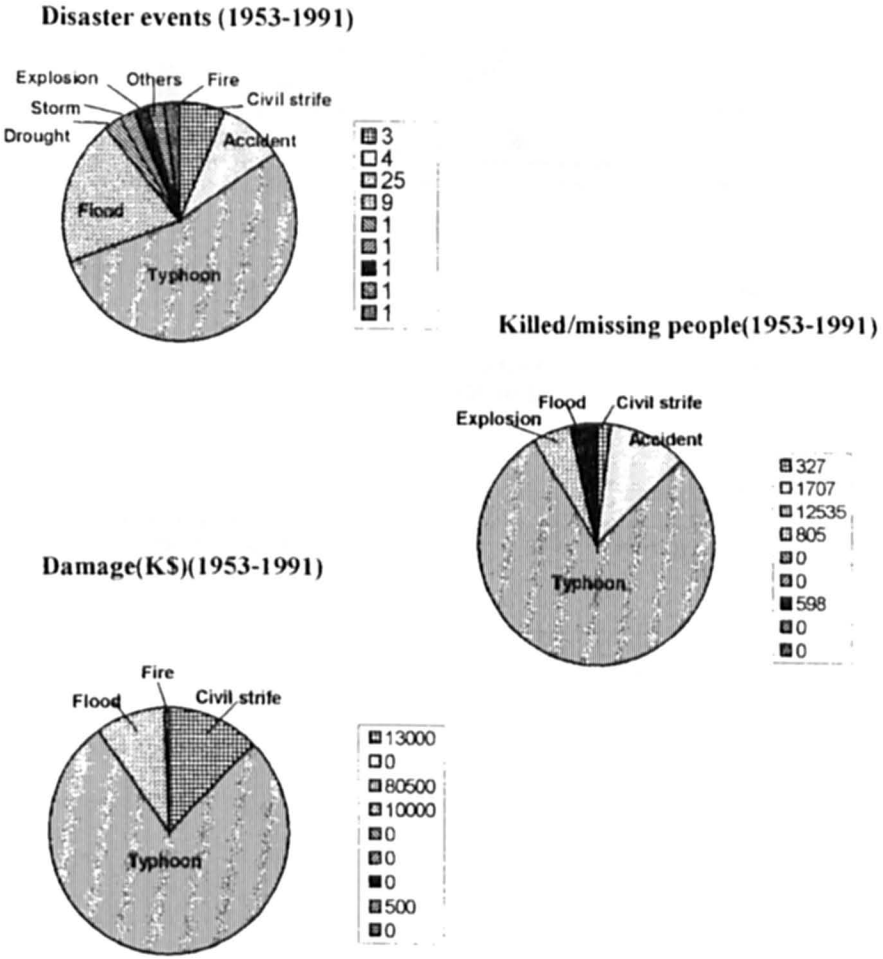


Fig. 6.111: Estimated damage caused by man-induced and natural disasters in Vietnam (1953–1991) (IMAMURA and TO, 1997)

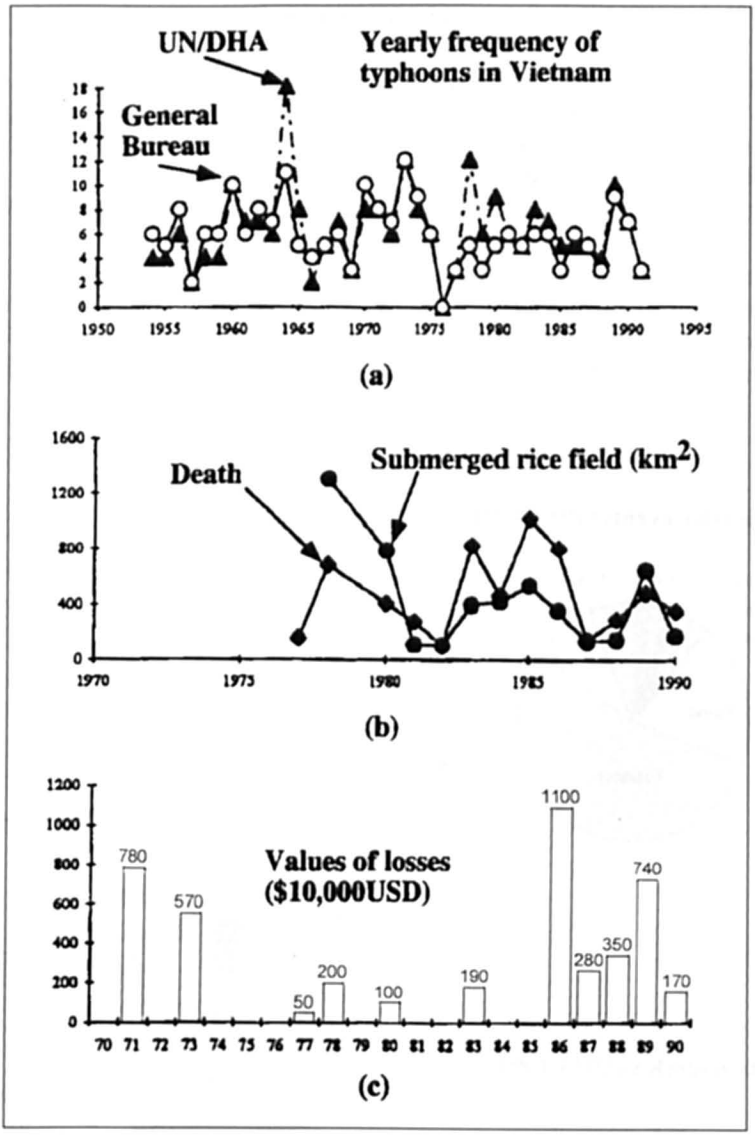


Fig. 6.112: (a) Frequency of typhoons and (b) flood damage death, submerged rice field, and (c) value of losses (IMAMURA and TO, 1997)

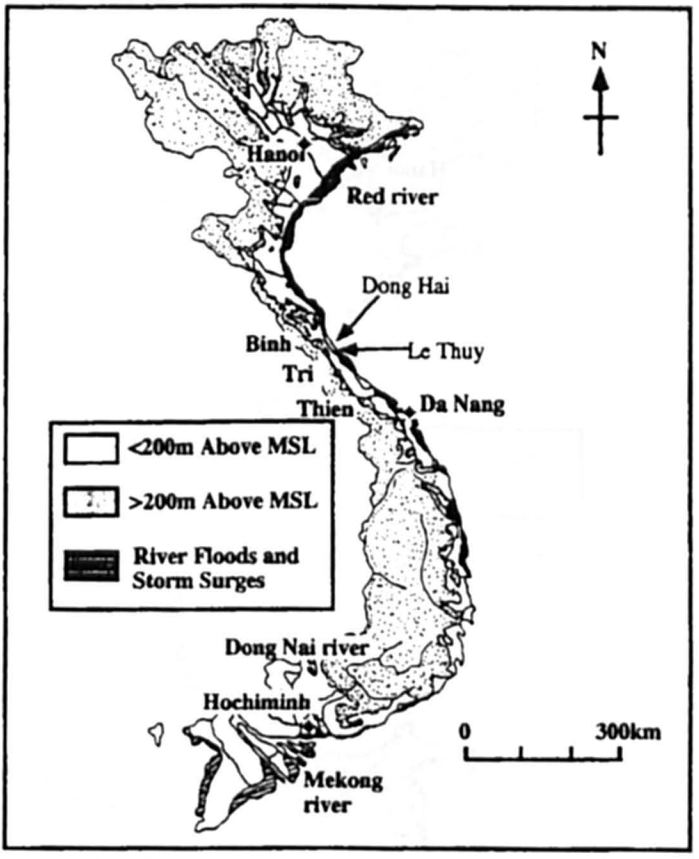


Fig. 6.113: Topography of Vietnam with elevation above sea level and areas damaged by river floods and storm surges shown by the horizontal shades (IMAMURA and TO, 1997)

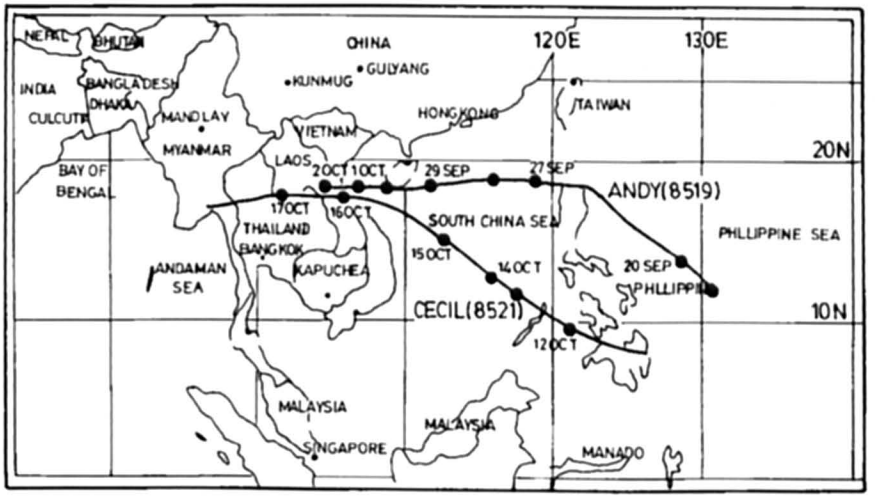


Fig. 6.114: Map of Vietnam, located in eastern Indo-China and the route of typhoons, Andy and Cecil in 1985, which devastated central Vietnam (IMAMURA and TO, 1997)

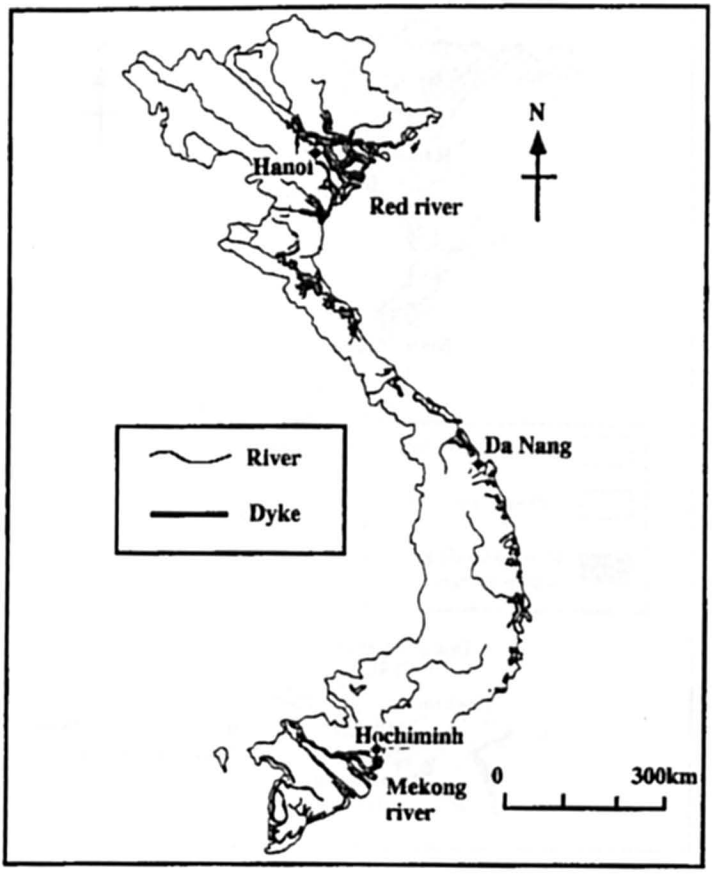


Fig. 6.115: Dike system in Vietnam along river and coasts. The system started more than 2000 years ago (IMAMURA and TO , 1997)

Table 6.64 compares the frequency of typhoons in various Southeast Asian countries. Table 6.65 and 6.66 respectively show the monthly frequency of typhoons during the period 1954 to 1991 and those that struck various districts.

Table: 6.64: Frequency of typhoons in the Southeast Asian countries in 1985–1989 (IMAURA and TO, 1997)

| Country | 1985 | 1986 | 1987 | 1988 | 1989 | Total |
|---|---|---|---|---|---|---|
| China | 8 | 6 | 4 | 4 | 11 | 33 |
| Philippines | 4 | 6 | 5 | 5 | 7 | 27 |
| Japan | 10 | 2 | 3 | 4 | 4 | 23 |
| Rep. Of Korea | 8 | 3 | 2 | 0 | 1 | 14 |
| Vietnam | 2 | 1 | 3 | 2 | 4 | 12 |
| Hong Kong | 2 | 3 | 1 | 3 | 2 | 11 |
| Thailand | 1 | 1 | 2 | 0 | 1 | 5 |
| Malaysia | 0 | 1 | 0 | 2 | 0 | 3 |
| Total | 17 | 11 | 12 | 12 | 19 | 71 |

Table 6.65: Monthly frequency of typhoons in Vietnam in 1954–1991 (IMAURA and TO, 1997)

| Period | Jan | Feb | Mar | Apr | May | Jun | Jul | Aug | Sep | Oct | Nov | Dec | Total | Average |
|---|---|---|---|---|---|---|---|---|---|---|---|---|---|---|
| 1954–59 | 0 | 0 | 0 | 1 | 1 | 4 | 3 | 9 | 7 | 5 | 2 | 1 | 33 | 5.5/yr. |
| 1960–69 | 0 | 0 | 0 | 0 | 1 | 6 | 8 | 15 | 17 | 9 | 8 | 1 | 65 | 6.5/yr. |
| 1970–79 | 0 | 0 | 0 | 0 | – | 6 | 7 | 11 | 15 | 10 | 10 | 4 | 63 | 6.3/yr. |
| 1980–89 | 0 | 0 | 2 | 1 | 1 | 6 | 5 | 5 | 9 | 21 | 5 | 0 | 54 | 5.4/yr. |
| 1990–91 | 0 | 0 | 1 | 0 | 0 | 0 | 1 | 2 | 1 | 3 | 2 | 0 | 10 | 5.0/yr. |
| Total | 0 | 0 | 3 | 2 | 3 | 22 | 24 | 42 | 48 | 48 | 27 | 6 | 225 | 5.9/yr. |

Table 6.66: Monthly frequency of typhoons, which struck the district regions of Vietnam (1954–1991) (IMAMURA and TO, 1997)

| Region | Jan | Feb | Mar | Apr | May | Jun | Jul | Aug | Sep | Oct | Nov | Dec | Total |
|---|---|---|---|---|---|---|---|---|---|---|---|---|---|
| Northern | 0 | 0 | 0 | 0 | 0 | 15 | 24 | 28 | 22 | 7 | 1 | 0 | 97 |
| Central | 0 | 0 | 0 | 1 | 2 | 0 | 0 | 14 | 23 | 35 | 6 | 0 | 81 |
| Southern | 0 | 0 | 3 | 1 | 1 | 7 | 0 | 0 | 3 | 6 | 20 | 6 | 47 |
| Total | 0 | 0 | 3 | 2 | 3 | 22 | 24 | 42 | 48 | 48 | 27 | 6 | 225 |

### 6.8.6 Thailand

VONGVISESSOMJAI (1994) studied storm surges in the upper Gulf of Thailand. Table 6.67 lists the characteristics of historic cyclones for this region. Fig. 6.116 shows the position of the inter tropical convergence zone (ITCZ) at three different times in the year and typhoon approach directions. Fig. 6.117 shows the typhoon tracks for the month of October for the period 1961 to 1970 whereas Fig. 6.118 shows the tracks of tropical cyclones for the period 1952 to 1974. The recurrence interval of maximum wind velocity and central pressure index for cyclones affecting the Gulf of Thailand is shown in Fig. 6.119.

Table 6.67: Historical cyclone characteristics (VONGVISESSOMJAI, 1994)

| No. | Year, Month, Date | | Name | CPI or $P_0$ (millibars) | Max. Velocity $U_{max}$ (mph) | Forward Speed, $V_F$ (miles/hr) | Radius, R (nautical miles) |
|---|---|---|---|---|---|---|---|
| 1 | 1952 | Oct 21–22 | VAE | 990 | 53 | 14.97 | 6.7 |
| 2 | | Oct 24–25 | TRIX | 998 | 44 | 17.27 | 60 |
| 3 | 1960 | Oct 3–4 | – | 992 | 52 | 3.45 | 8.4 |
| 4 | 1962 | Jul 12–13 | – | 990 | 53 | 18.45 | 10.6 |
| 5 | 1966 | Jun 17–18 | – | – | – | 12.67 | – |
| 6 | | Oct 25–26 | – | 990 | 48 | 9.21 | 49 |
| 7 | 1967 | Jun 16–27 | – | 978 | 62 | 12.67 | 140 |
| 8 | | Oct 5–6 | – | 996 | 49 | 11.52 | 16 |
| 9 | | Oct 9–10 | – | 998 | 44 | 17.27 | 90 |
| 10 | | Nov 10–11 | – | – | – | 12.67 | – |
| 11 | 1968 | Sep 5–6 | BESS | 992 | 44 | 2.3 | 115 |
| 12 | | Oct 21–22 | HESTER | 998 | 46 | 11.52 | 10 |
| 13 | | Jun 24–25 | – | 998 | 46 | 6.91 | 7.5 |
| 14 | | Sep 20–21 | – | 992 | 51 | 12.67 | 57 |
| 15 | | Nov 2–3 | – | 1000 | 45 | 16.12 | 10 |
| 16 | 1970 | Sep 20–21 | – | 994 | 52 | 13.82 | 20 |
| 17 | | Oct 25–26 | KATE | 1000 | 27 | 13.82 | 314 |
| 18 | | Nov 29–30 | RUTH | 1000 | 42 | 11.52 | 32 |
| 19 | 1972 | Jun 3–4 | NAMIE | 990 | 48 | 6.91 | 123 |
| 20 | | Sep 6–7 | – | 990 | 49 | 4.61 | 16 |
| 21 | | Sep 18–19 | – | – | – | – | – |
| 22 | | Dec 4–5 | SALLY | 994 | 50 | 5.76 | 5 |
| 23 | 1973 | Nov 12–13 | – | 1002 | 38 | 5.76 | 4 |
| 24 | | Nov 17–18 | THELMA | 998 | 45 | 5.76 | 39 |
| 25 | 1974 | Oct 9–10 | – | 1002 | 34 | 6.91 | 15 |
| 26 | | Nov 5–6 | – | 998 | 45 | 13.82 | 60 |

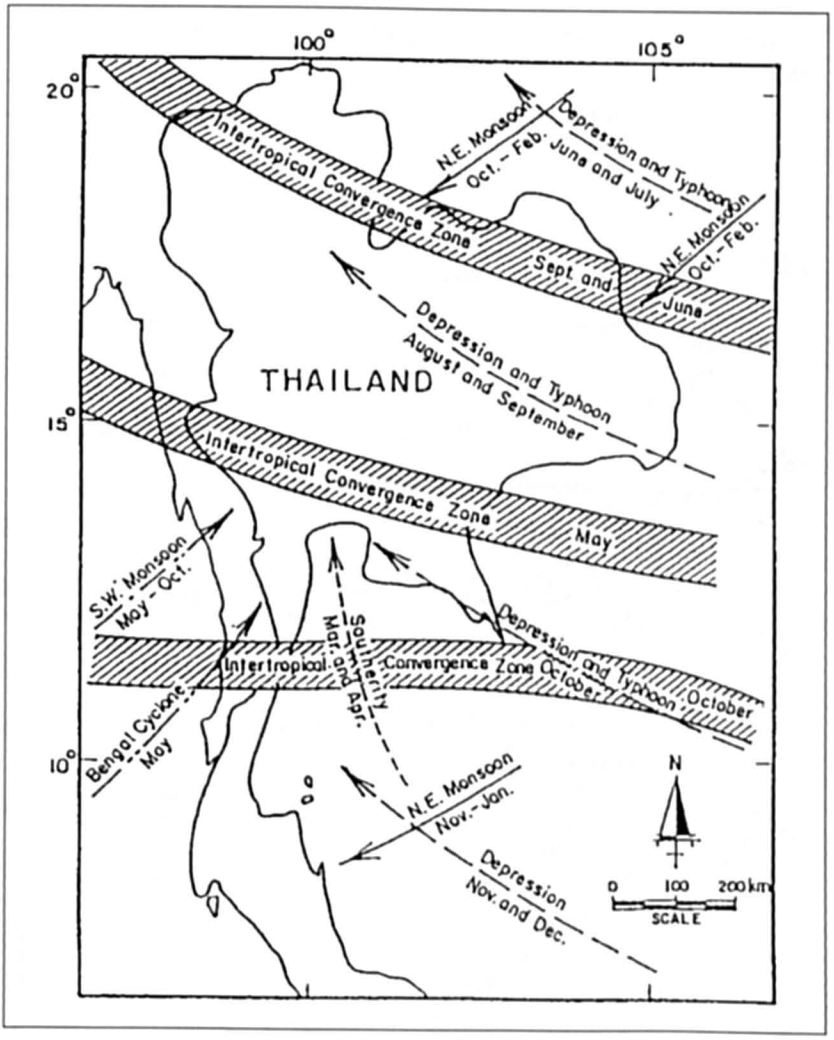


Fig. 6.116: Monsoon and storm tracks in Thailand (VONGVISESSOMJAI, 1994)

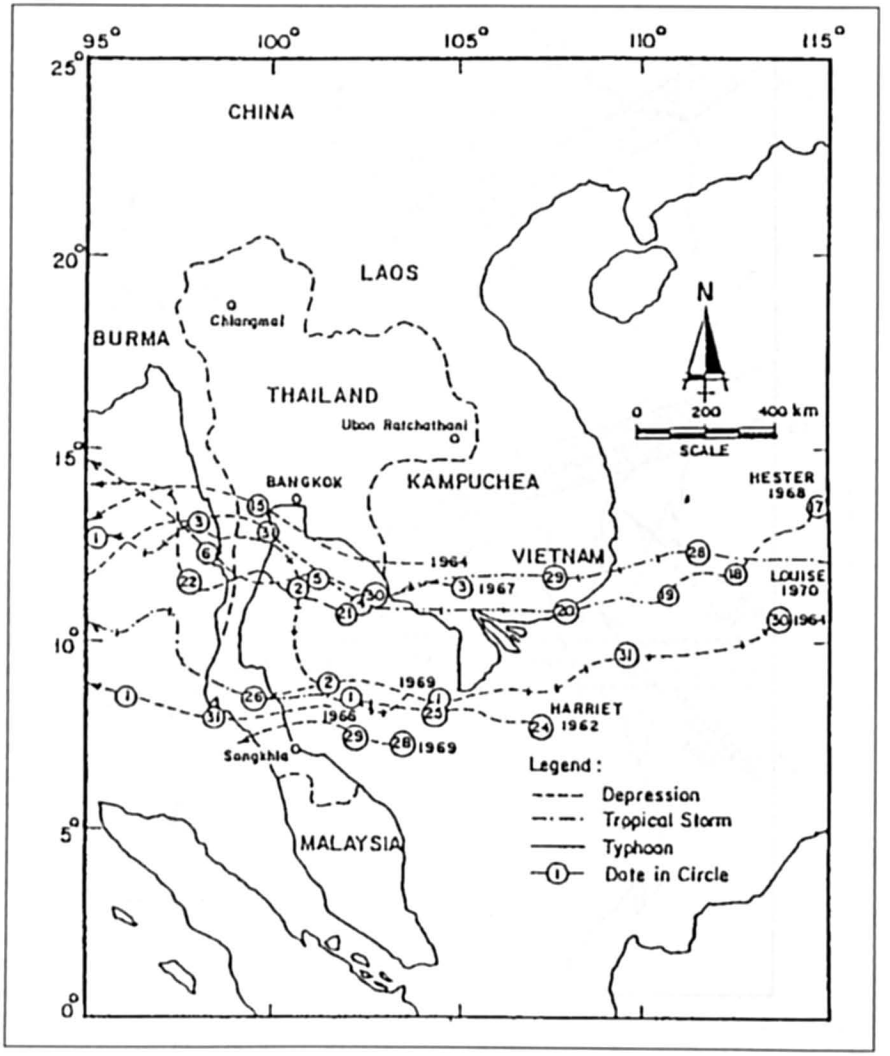


Fig. 6.117: Tracks of cyclones over the Gulf of Thailand in October 1961 to 1970 (VONGVISESSOMJAI, 1994)

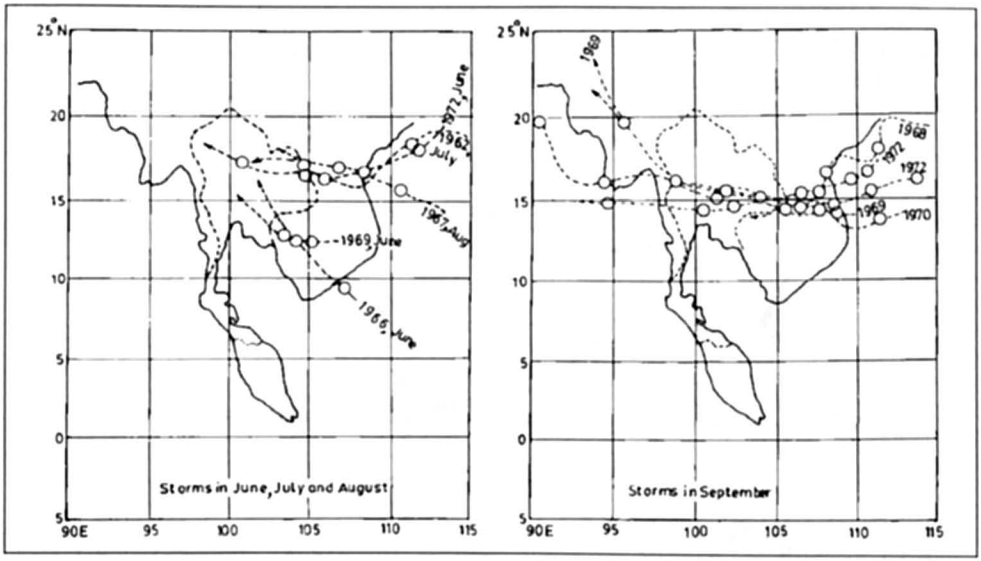


Fig. 6.118: Tracks of tropical cyclones over the Gulf of Thailand and its vicinity between 1952–1974 A. D. Encircled numbers are the positions of storm centers at 7 am on the days shown (VONGVISESSOMJAI, 1994)

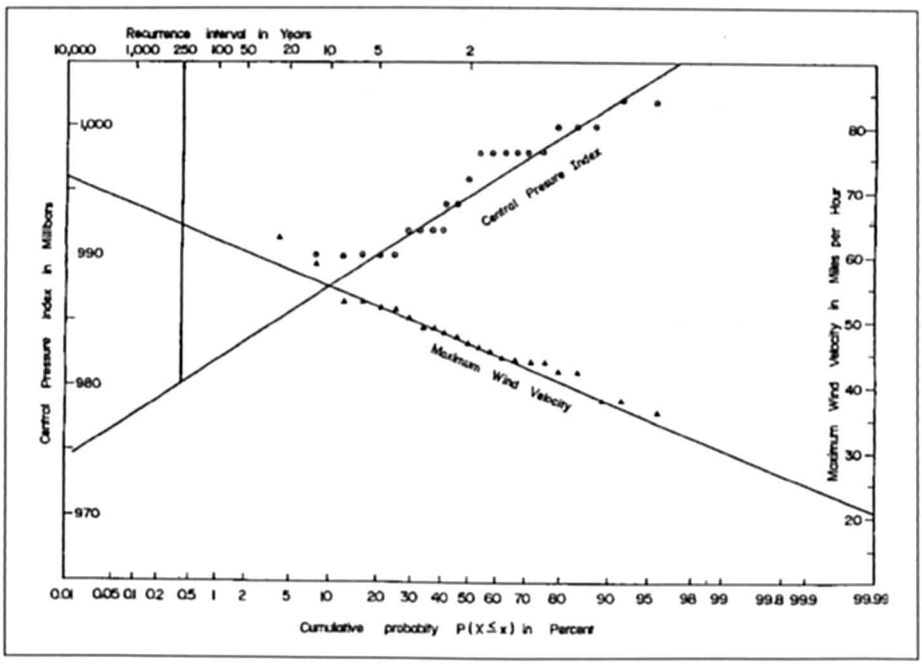


Fig. 6.119: Recurrence interval of cyclone characteristics for the Gulf of Thailand (VONGVISESSOMJAI, 1994)

Fig. 6.120 shows the wind field for the probable maximum cyclone (PMC) for the Gulf of Thailand. Figs. 6.121 and 6.122 respectively show the peak surge and maximum wind wave at Aophai for the PMC and a 250 year typhoon.

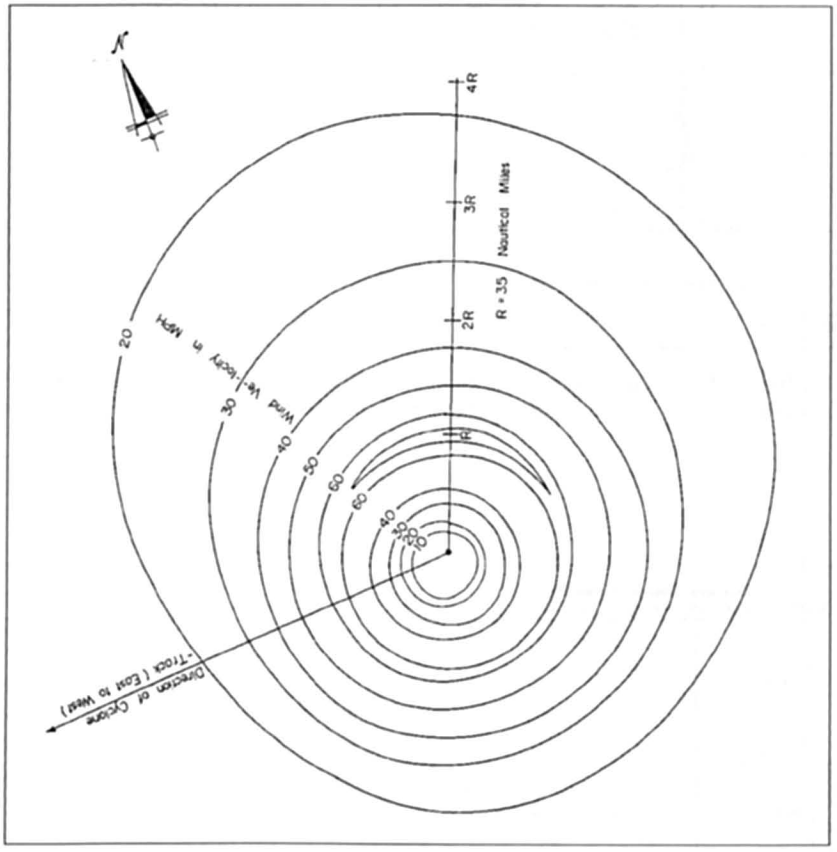


Fig. 6.120: Wind field of the probable maximum cyclone for the Gulf of Thailand (VONGVISESSOMJAI, 1994)

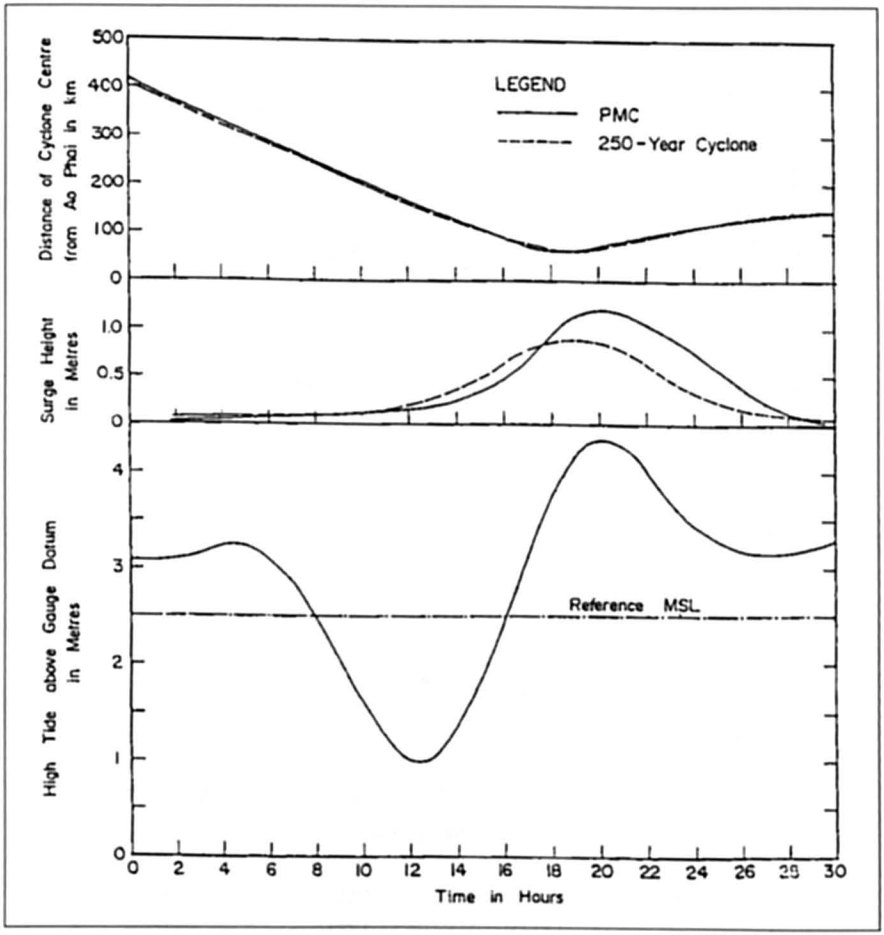


Fig. 6.121: Probable maximum cyclonic surge (PMC & 250 year) and high tide at Ao Phai (VONGVISESSOMJAI, 1994)

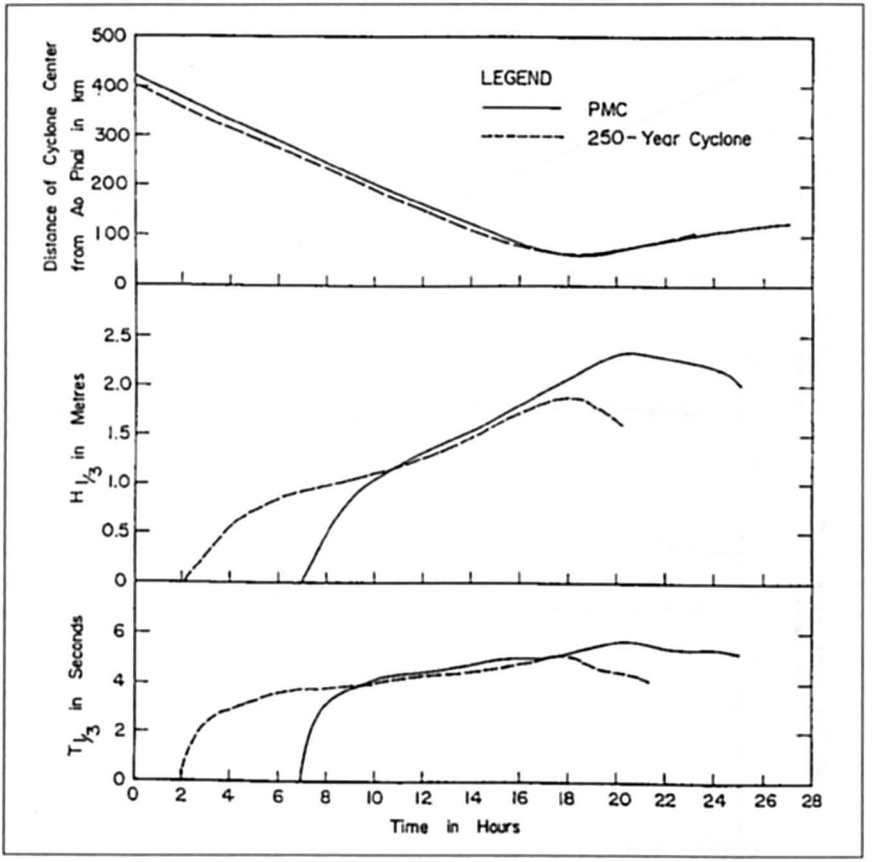


Fig. 6.122: Probable maximum wind wave (PMC & 250 year) at Ao Phai (VONGVISESSOMJAI, 1994)

Die Küste, 63 Global Storm Surges (2001), 1-623



# 7. Storm Surges Generated by Extra-Tropical Cyclones – Case Studies

## 7.1 North America

Earlier we mentioned that there appears to have been a decrease in the frequency of tropical cyclones (TC's) during the second half of the 20th century. For the frequency of extra-tropical cyclones (ETC's) the opposite might be true as can be seen from Fig. 7.1.

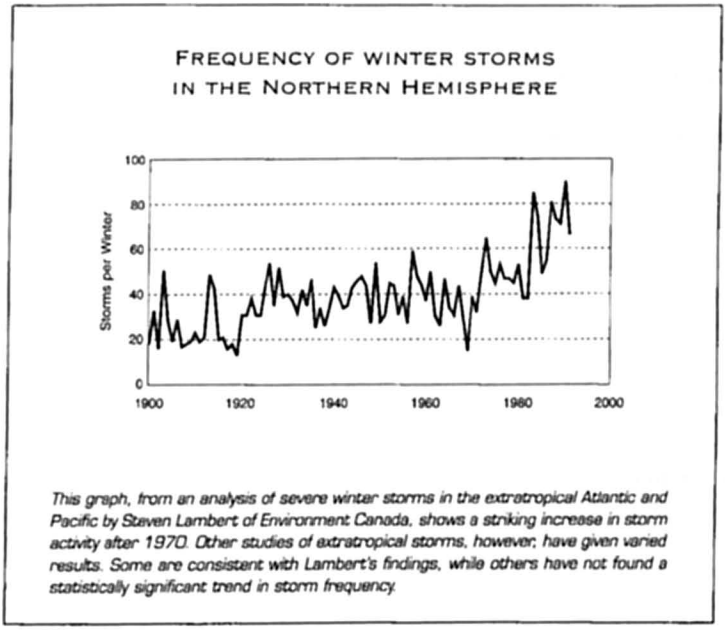


Fig. 7.1: Frequency of winter storms in the Northern Hemisphere (LAMBERT, 1995)

BODE and HARDY (1997) made some interesting observations on the development of research in storm surge modelling (SSM). We quote a few sentences below from their work.

"The storm surge phenomenon has long been characterised by a geographic divide. Surges tend to be associated either with mid-latitude storms or, often more disastrously with tropical cyclones. This divide has also extended, somewhat artificially into the modelling area. The efforts of various modelling groups are usually concentrated in one geographic region or the other. This separation of effort is reflected in recent research, in which many of the noteworthy developments have occurred in Europe, leading to the development of operational mid-latitude operational storm surge warning systems.

However, little corresponding development appears to have been supported in recent times for hurricane surge prediction. Presumably, this is a reflection of the magnitude and difficulty of the problem, but also of relative funding levels allocated for such purposes. A logical starting point is the review of HEAPS (1983), which concentrated on midlatitude storm surges. At that stage, European models have advanced to the point where NWP (Numerical

Weather Prediction) models of National Meteorological Services were being coupled to storm surges models to provide routine operational storm surge forecasts.

The foremost requirement for SSM is an accurate wind field model and the divide between the midlatitude and tropical cases is most pronounced here. Midlatitude models take their wind (and pressure) fields from operational NWP models, which generally perform well. (Although exceptions arise, such as the great storm of 1987 in U. K. for which forecasts largely failed.

### 7.1.1 Errors in the Specification of Wind Fields

CARDONE et al. (1980) discussed errors in the techniques, which are generally in use for the specification of wind fields for ETC's. They make the important point that the accuracy of specifications of extrapolated marine surface winds is limited basically by the sparcity of observations of surface wind and sea-level pressure from ships rather than by intrinsic shortcomings in the technique of analysis. However, it should be noted that during these past two decades subsequent to 1980 when CARDONE et al. (1980), published their paper, there is progressively less reliance on ships for marine winds and more reliance on ocean buoys and remote sensing through satellites.

According to these authors, three basic methods are available for elaborating surface marine wind fields in historical storms: (a) Use of parametric wind models (b) Objective analysis and (c) Direct Kinematic analysis. Parametric wind models have been successfully applied for tropical cyclones, but are not appropriate for the complex patterns of surface winds associated with ETC's.

Objective analysis methods were developed in the 1960's to satisfy the need for fast production, in real time, of fields of meteorological variables on grids for use in numerical forecast models. Objective analysis schemes for surface marine wind fields usually include (1) an initial guess at the surface wind on a regular grid, (2) a method for automatically screening a collection of wind reports from ships to eliminate highly discrepant and presumably erroneous winds, and (3) a method for blending the ship reports into the initial guess. Such schemes usually exploit the relation between the surface marine wind and the local pressure gradient by calculating the initial-guess winds from a marine sea-level pressure field, which in turn derives from an objective analysis of surface pressure measurements on land and sea.

CARDONE (1969) described an objective analysis scheme that included the application of a model of the wind profile in the planetary boundary layer (PBL) that related the surface marine wind velocity to the local pressure gradient, the air/sea temperature difference, and the atmospheric thermal advection. Winds derived from the PBL model, and reduced to a standard height of 19.5 m, are blended with winds from ship reports after the latter are ranked in order of presumed accuracy.

Kinematic analysis is a tedious, time-consuming, entirely manual procedure that only experienced analysts can execute successfully. The basic steps involved are (1) plot all synoptic ship reports on suitable meteorological base maps for the entire storm event, (2) standardize wind measurements to 19.5 m, using a marine-wind-profile model for measured winds where the ship's anemometer height is on file, and using the Beaufort conversion procedure described earlier for estimated winds, (3) identify and reject erroneous and unrepresentative reports so far as possible, (4) construct a continuity chart containing the "solution" for the storm event in terms of the movement of major discontinuities, singularities and other features of the surface wind field, and (5) construct streamlines and isotachs.

### 7.1.2 Great Lakes

Several finite element models are now available which have been referred to in chapter three. Here we will give a few more general references for the application of the impulse response method for storm surge computation, see SIMONS and SCHERTZER (1989). This method will be successful for those situations where there is linear dynamics for storm surge generation.

SCHWAB (1982) showed that this method could be inverted to provide an estimate of Overlake wind fields from observations of water level fluctuations around the shore of the lake. HAMBLIN (1987) provided a review of lake Erie storm surge computation techniques.

SCHWAB and LYNN (1987) developed a simple computer program for estimating the maximum and minimum storm surge amplitudes for the Great Lakes. The user has to provide a mean lakewater level, a wind speed and a wind direction. The program then lists maximum and minimum expected water level at several points on the shoreline of the selected area. The program covers the U. S. Shoreline only, (not Canadian) separately for the following water bodies: Lake Ontario, Central and Eastern Lake Erie, Western Lake Erie, Lake St. Clair, Lake Huron, Saginaw Bay, the Eastern Shore of Lake Michigan, the western shore of Lake Michigan, Green Bay and Lake Superior.

### 7.1.3 East Coast of Canada

PARKES et al. (1997) discussed storm surge events in the Maritime (eastern) provinces of Canada. MURTY et al. (1994) reviewed storm surges in Canadian waters. GRAY et al. (1984) used numerical models to simulate storm surges on the Nova Scotia Coast (Table 7.1). Fig. 7.2 shows the area of study. Here CMC refers to the Canadian Meteorological Center Fig. 7.3 shows the grid used in the numerical model.

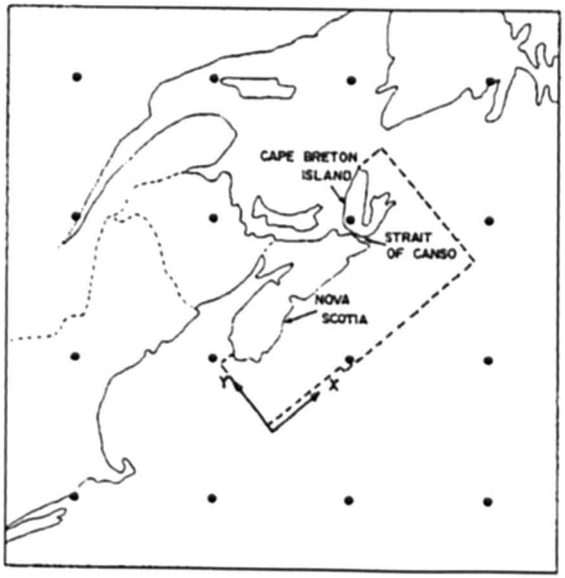


Fig. 7.2: Orientation of CMC and storm surge model grids showing the array of 4 x 4 CMC grid points (dots), and the computational domain of the storm surge model (dashed line) (GRAY et al., 1984)

Table 7.1: Comparison between computed and observed amplitudes (cm) and phases (deg.) of the $M_2$ tide (observed values taken from the Admiralty Tide Tables, except where indicated) ( GRAY et al., 1984)

| Grid Numbers* | Port | Observed | | Computed | |
|---|---|---|---|---|---|
| | | Amp. | Phase | Amp. | Phase |
| 1 | Yarmouth | 163 | 63 | 163 | 63 |
| 2 | Lower E. Pubnico | 127 | 39 | 134 | 38 |
| 3 | Sea Island | 120 | 52 | 127 | 43 |
| 4 | Clark Harbour | 106 | 27 | 110 | 22 |
| 5 | Lockeport | 70 | 359 | 71 | 357 |
| 6 | Liverpool | 65 | 353 | 64 | 355 |
| 7 | Lunenburg | 60 | 353 | 64 | 354 |
| 8 | Boutilier Point | 64 | 352 | 66 | 353 |
| 9 | Halifax | 62 | 352 | 64 | 353 |
| 10 | Jeddore Harbour | 65 | 352 | 64 | 352 |
| 11 | Sheet Harbour | 62 | 347 | 64 | 351 |
| 12 | Sonora | 62 | 351 | 64 | 349 |
| 13 | Isaac's Harbour | 56 | 352 | 65 | 348 |
| 14 | White Head | 54 | 347 | 63 | 347 |
| 15 | Canso Harbour | 59 | 347 | 62 | 346 |
| 16 | Point Tupper | 59 | 344 | 66 | 345 |
| 17 | Cannes | 56 | 351 | 62 | 344 |
| 18 | Louidbourg | 50 | 344 | 52 | 344 |
| 19 | North Sydney | 38 | 355 | 43 | 350 |
| 20 | Dingwall | 27 | 11 | 32 | 354 |
| 21 | St. Paul Island | 31 | 6 | 31 | 6 |
| 22 | Sable Island | 52 | 352 | 57 | 350 |
| 23 | T1** | 48 | 351 | 48 | 353 |
| 24 | 1.2.23 | 49 | 350 | 50 | 354 |
| 25 | T21** | 49 | 357 | 48 | 355 |

* See Fig. 7.21

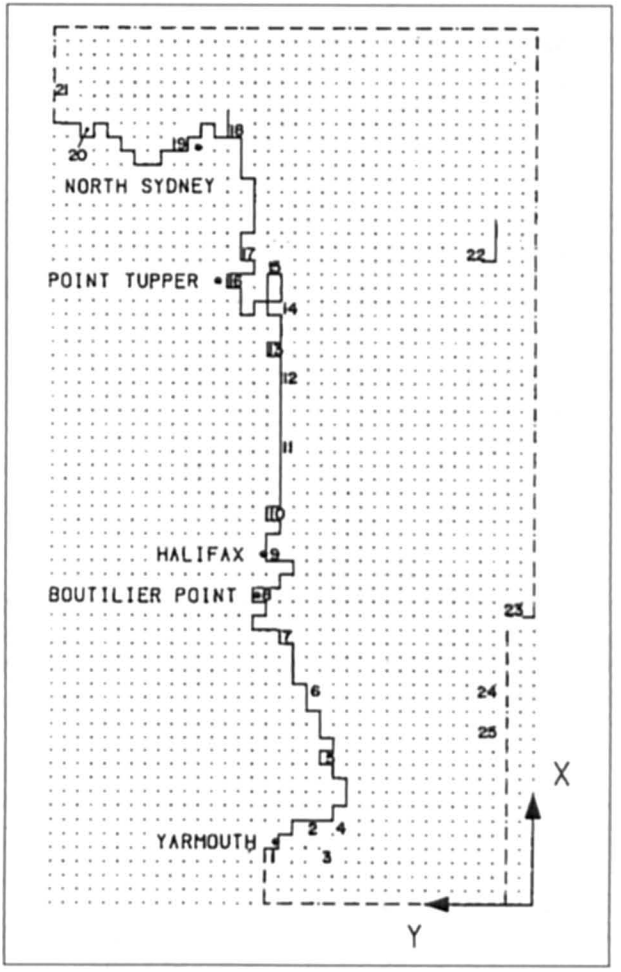


Fig. 7.3: Nova Scotia storm surge grid showing the coastline (solid line) and open – sea radiating boundary (dashed line). Numbers indicate the tidal stations listed in Table 7.1 (GRAY et al., 1984)

Fig. 7.4 shows the track of the Ground Hog Day storm of February 1976. The sea-level pressure map for 2nd February 1976 is shown in Fig. 7.5. Figs. 7.6 and 7.7 respectively show the wind stress computed on two grid spacings.

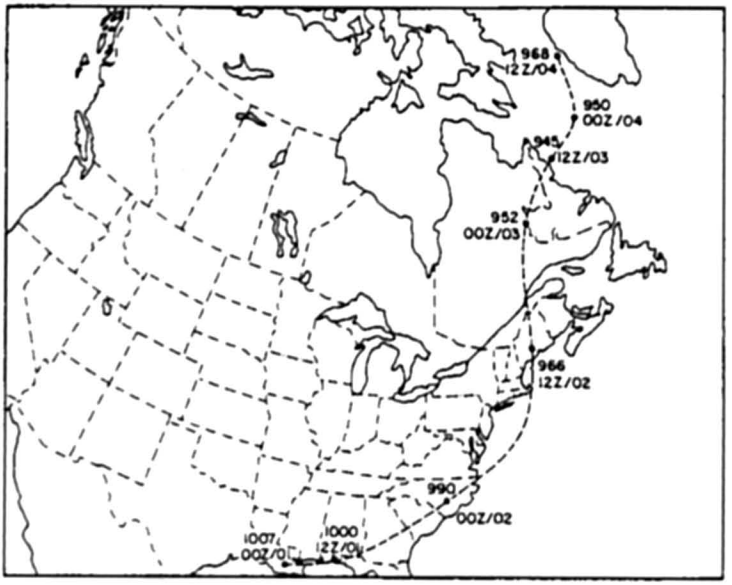


Fig. 7.4: Observed track and central sea-level pressures (mb) of the low center from 0000 GMT 1 February (00Z/01) to 1200 GMT 4 February (12 Z/04) 1976 (GRAY et al., 1984)

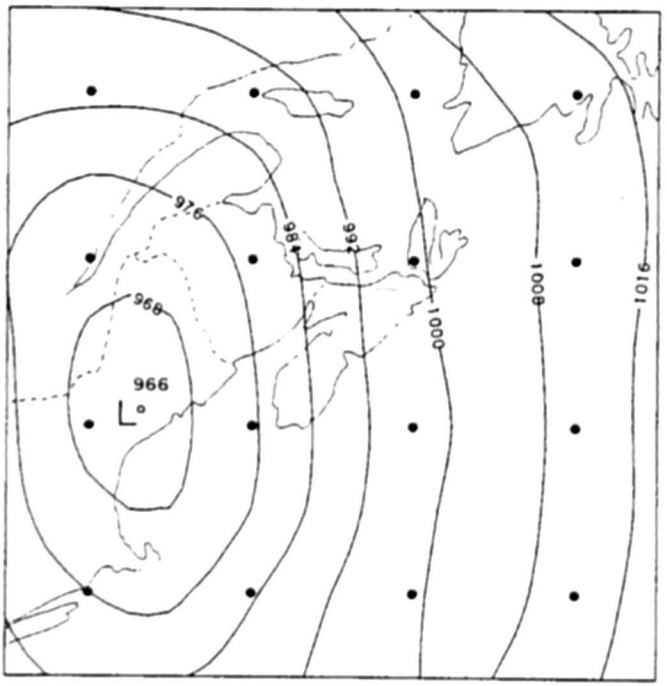


Fig. 7.5: Sea-level pressures (mb) at 1200 GMT 2 February 1976 (GRAY et al., 1984)

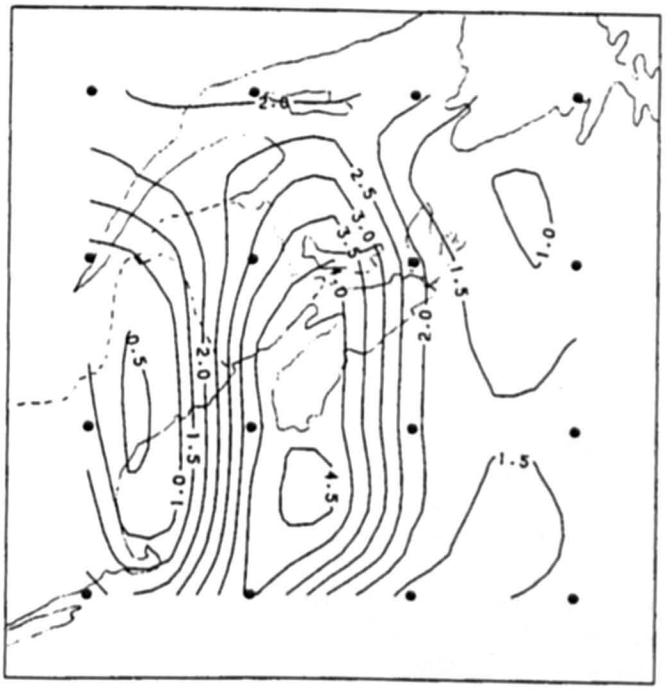


Fig. 7.6: Wind stress (Pa) at 1200 GMT 2 February 1976 computed from subjectively analysed sea-level pressures (190-km grid spacing) (GRAY et al., 1984)


Fig. 7.7: Wind stress (Pa) at 1200 GMT 2 February 1976 computed from CMC analyzed 1000-mb heights (38-km grid spacing) (GRAY et al., 1984)

The model is designed to be run, using CMC (Canadian Meteorological Center) prognostic data. The model incorporates a quadratic bottom friction term and is capable of including advective, topographic and tidal effects. It can simulate a moving land-sea boundary approximately.

The model is applied to the East Coast of Nova Scotia for the "Ground Hog Day" storm of February 1976. Meteorological forcing is calculated using subjectively analysed sea-level pressures. Away from open boundaries, the agreement with observed surge residuals is generally good. However, the results are less satisfactory near the boundaries. CMC meteorological data are found to underestimate the surface wind stress during this period.

## 7.2 South America

The Rio de la Plata estuary is located on the Atlantic Coast of South America, with the cities of Buenos Aires (Argentina) and Montevideo (Uruguay) along its shores (O'CONNOR, 1991). The length of the estuary is about 270 km and its width varies from about 230 km at its mouth to 25 km at its head where the Parana and Uruguay rivers meet. The depth of the estuary at its mouth is 20 m.

GAGLIARDINI et al. (1984) divided the estuary into three regions: (a) Upper region (Playahonda) leads from the river delta and is less than 5 m deep (b) Intermediate region stretches from Buenos Aires to Montevideo and has several shallow banks (c) the outer region is wide and extends to the ocean. Here the continental shelf has a width of about 200 km.

The tidal range in the estuary is about 2 m. Storm surges due to south easterly winds from a stationary cyclone over the estuary can generate storm surges with amplitudes greater than 3 m. Historically, surges up to 4 m in amplitude have occurred over periods of several hours to several days.

The largest surges are along the coast of Argentina near Buenos Aires. This is due to the shallowing and narrowing of the estuary, the long fetch over which the wind acts on the water surface and the effect of the Coriolis Force (O'CONNOR, 1991). According to BALAY (1959) surges with amplitudes greater than 3 m have occurred in the years – 1914, 1922, 1923, 1940, 1958 and 1959. During the 27–28 July 1958 event, the flood depths were 3 to 4 m along the Buenos Aires shore for 100 km, but there was little flooding along the coast of Uruguay.

On the other hand during the storm of 10–12 July 1923, southerly winds lasted two days and surges up to 6 m in amplitude occurred on the coast of Uruguay, east of Montevideo. O'CONNOR (1991) numerically simulated the tides and storm surges in Rio de la Plata estuary and his results agreed reasonably well with those shown in Fig. 7.8.

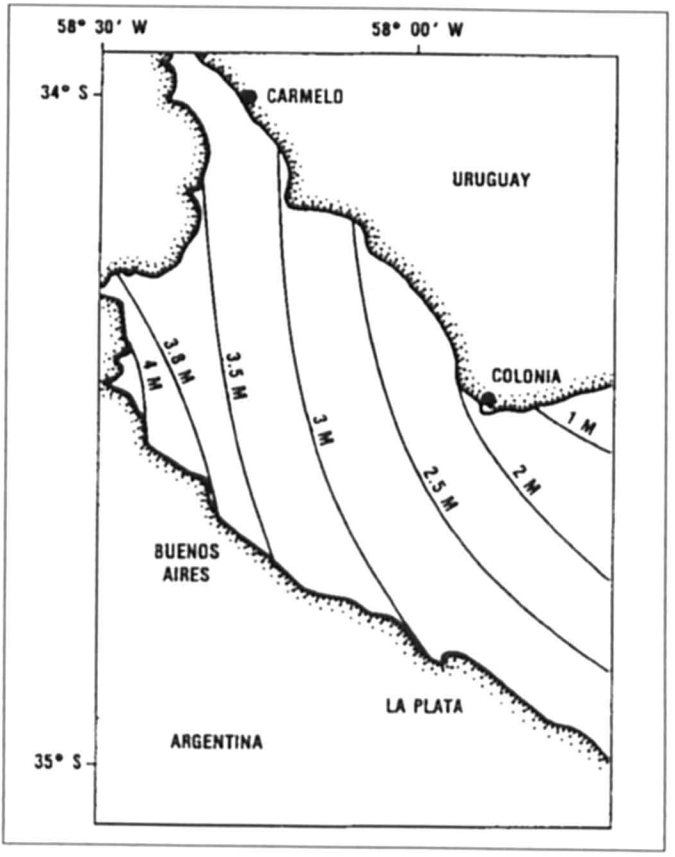


Fig. 7.8: The sea level in meters at the time of maximum surge, 27 July 1958 (BALAY, 1959)

## 7.3 Storm Surges in Europe

In section 5.1.2 the meteorological problems associated with storm surges in European waters were introduced. Here, case studies of storm surges in several water bodies in Europe and environs will be considered.

### 7.3.1 North Sea

The North Sea is a border sea of the Atlantic. The oscillation of the Atlantic effects the North Sea from the north through the channel. The shape of the basin, the depth and coriolis force influence the tide. The tide runs along the Scottish and English coastline with a mean tidal range of 4.20 m at Aberdeen and 7.20 m at Immingham and reaches the Dutch coast after crossing the Strait of Dover. There the tidal range increases from 1.50 m at Den Helder (135 cm at Texel) to 2.28 m at Borkum and 3.00 m at Cuxhaven, is the same till Pellworm and decreases from there to the Danish coast with 1.83 m at Sylt and 1.70 m at Rømø. The tidal range increases again from the islands to the continental coast.

The counterclockwise rotation of the tide can be seen in the progression of a storm surge from Aberdeen over Southend, Dover, Newhaven Hoek van Holland, Cuxhaven to Bergen. Fig. 7.9A shows the surge profiles along the western side of the North Sea during January 6–10, 1949, beginning at Aberdeen and ending at Newhaven. The surge profiles along the eastern boundary of the North Sea during the same period are given in Fig 7.9B. One can see first a counterclockwise progression of the disturbance with about the same propagation velocity as that of the diurnal tide (Fig. 7.10). The interaction between the tide and surge appears to be small (note that in the Thames Estuary the tide-surge interaction is significant). Second, one can see the progression of the surge height, which rises from Aberdeen to Southend and falls in the Strait of Dover from Dover to Newhaven. The increase of water level height at Grimsby, Kings Lynn and London Bridge is influenced by the topography of the locations of these gauges in an estuary or small basin like the Wash. But in general it can be stated that there is a level increase, because at Felixstone and Dover it is higher than at Hartlepool. In this storm event at the eastern boundary of the North Sea the water level increases a little from the Dutch coast to the German coast till Cuxhaven and decreases from there to Norway (Bergen). As the storm surge of April 2–6, 1973, DAVIES and FLATHER (1977) compared the calculated and observed surges at five locations along the south and west coasts of the North Sea, which confirm this. A change of the wind direction can modify this development at the eastern boundary of the North Sea.

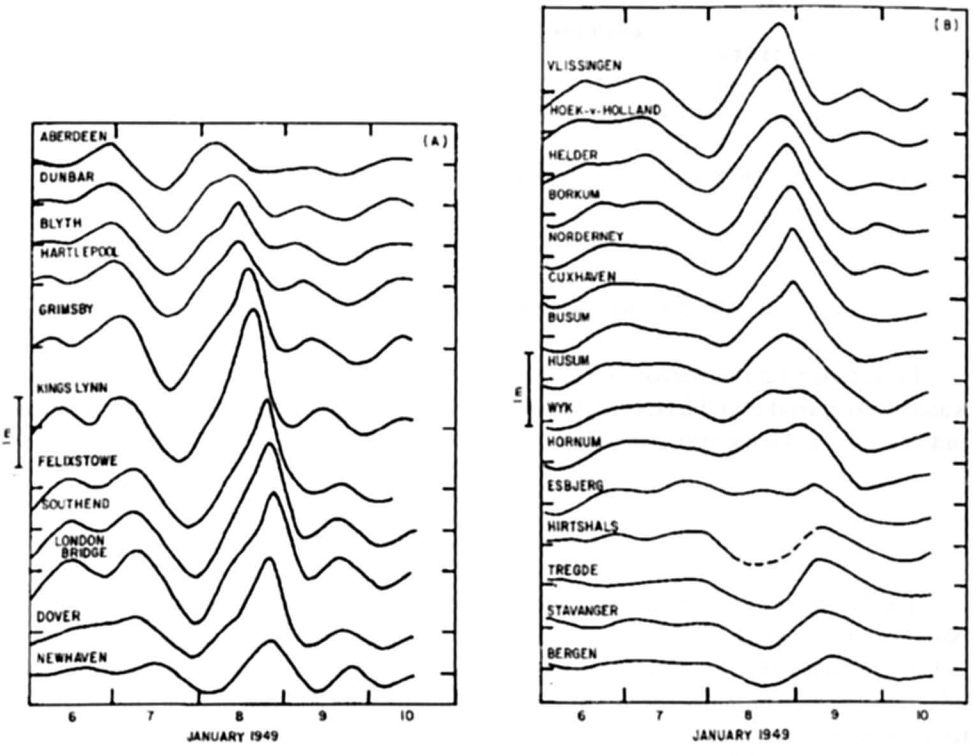


Fig. 7.9: Storm surge profiles at stations along the (A) western boundary of the North Sea and the (B) eastern boundary of the North Sea during January 6–10, 1949 (CHARNOCK and CREASE, 1957)

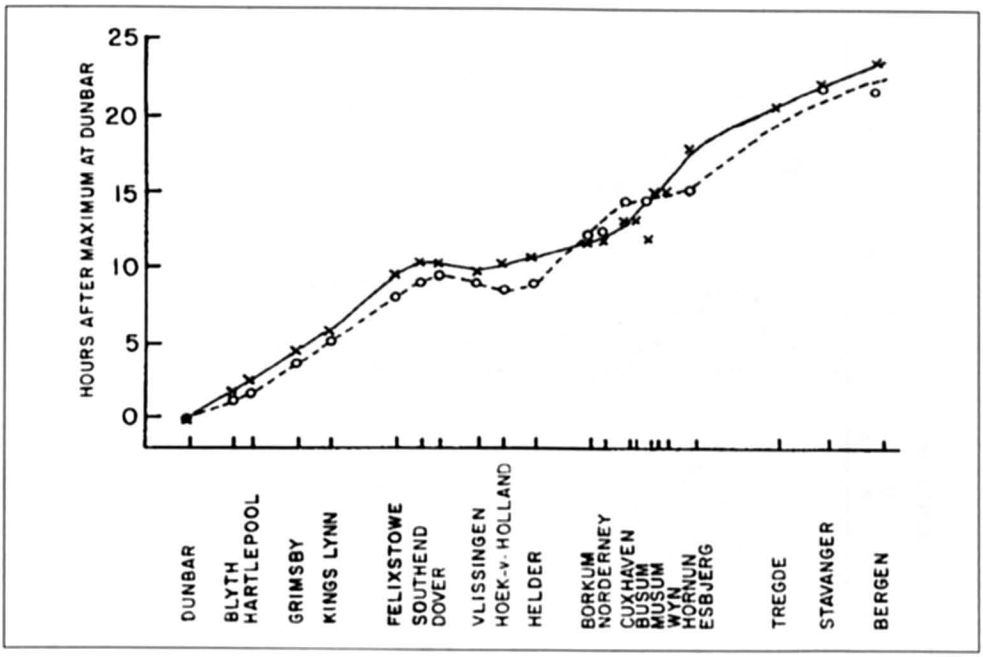


Fig. 7.10: Progression of storm surge and diurnal tide around the North Sea (CHARNOCK and CREASE, 1957)

During the storm surge on January 31–February 1, 1953 the situation at the southeastern and eastern boundary of the North sea was different to the situation on January 6–10, 1949. The track of the storm that produced this major surge is shown in chapter 5, Fig. 5.28. This depression caused a wind situation over the North Sea that produced very high storm surge levels at the British coast with rising level from Tyne over Immingham and Southend to London Bridge and falling levels to Dover and Newhaven (Fig. 7.12a & b.). Afterwards however, the surge reaches Ostende not with a lower level than in Dover; the level increased and reached a level there which was higher than at the British coast. At the German coast the high water level has become lower. A clear decrease of the water level can be seen from Esbjerg to Hornstholm (Denmark).

The horizontal distribution of the storm surge amplitudes during three different periods is summarized in Fig. 7.13. Maximum amplitudes up to 3 m occurred at the Belgian and Netherlands coasts. Amplitudes up to 2.5 m occurred at the coast of France, whereas amplitudes up to 2 m were found in the German Bight. At the Danish coast the maximum amplitudes were about 1 m. So the general principle has been lost since the wind direction and the surge do not increase anymore from the Dutch to the German coast. It must be stated that each location has its special wind direction in which the maximum surge can occur.

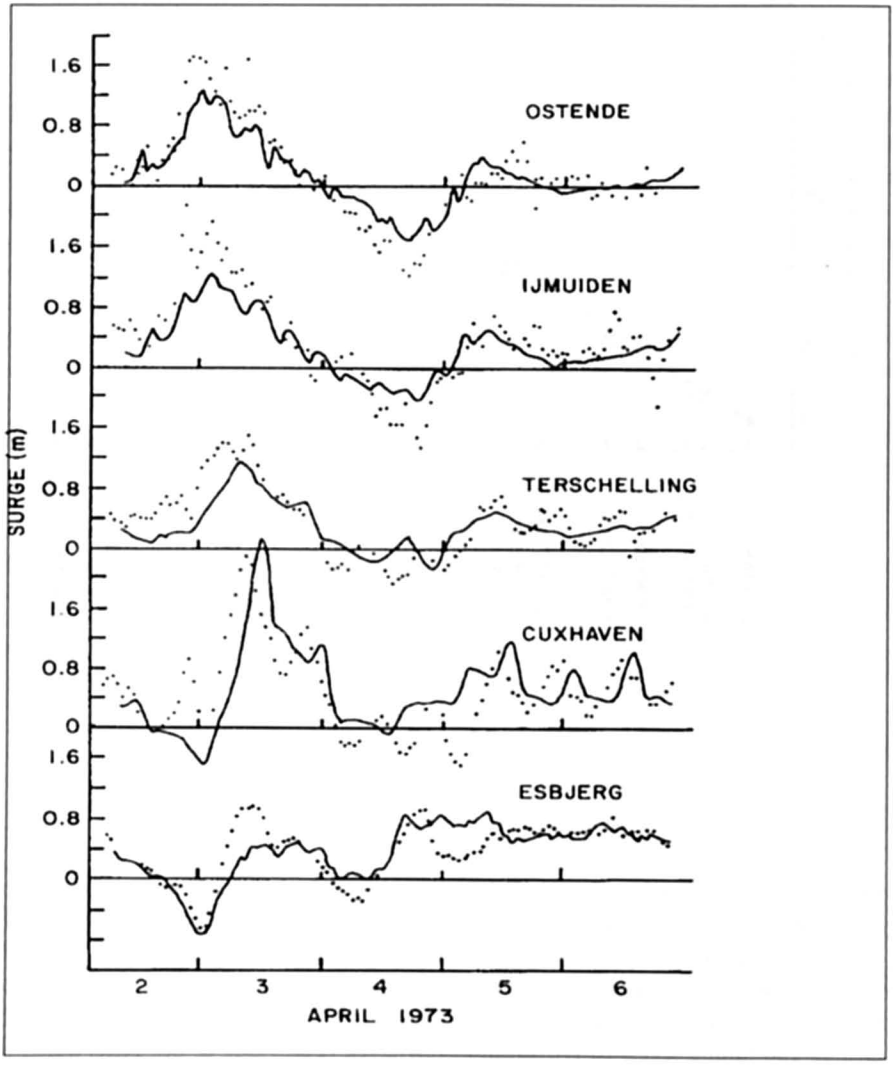


Fig. 7.11: Computed (solid line) and observed (dotted line) storm surges at five locations on the south and west coasts of the North Sea during April 2–6, 1973 (DAVIES and FLATHER, 1977)

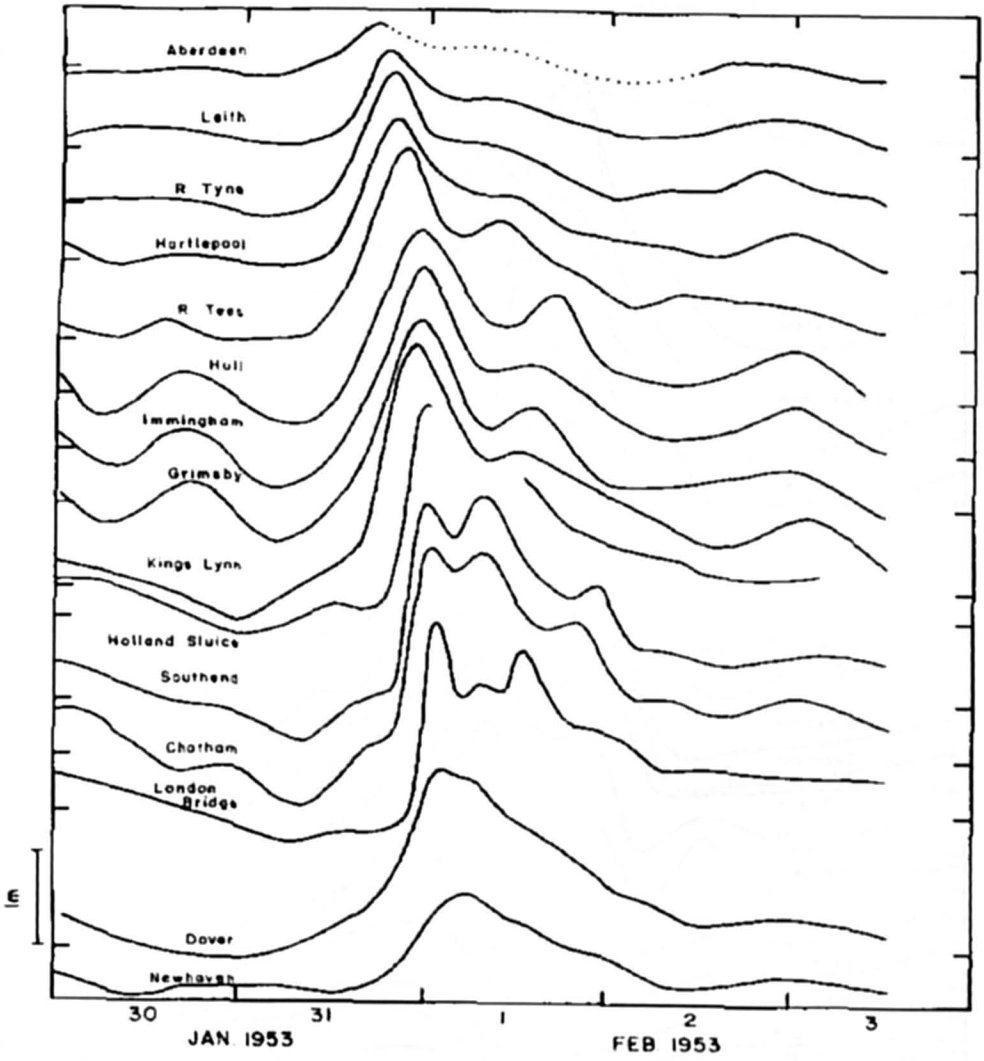


Fig. 7.12a: Storm surges at various locations around the North Sea during January 30–February 3, 1953 (ROSSITER, 1954)

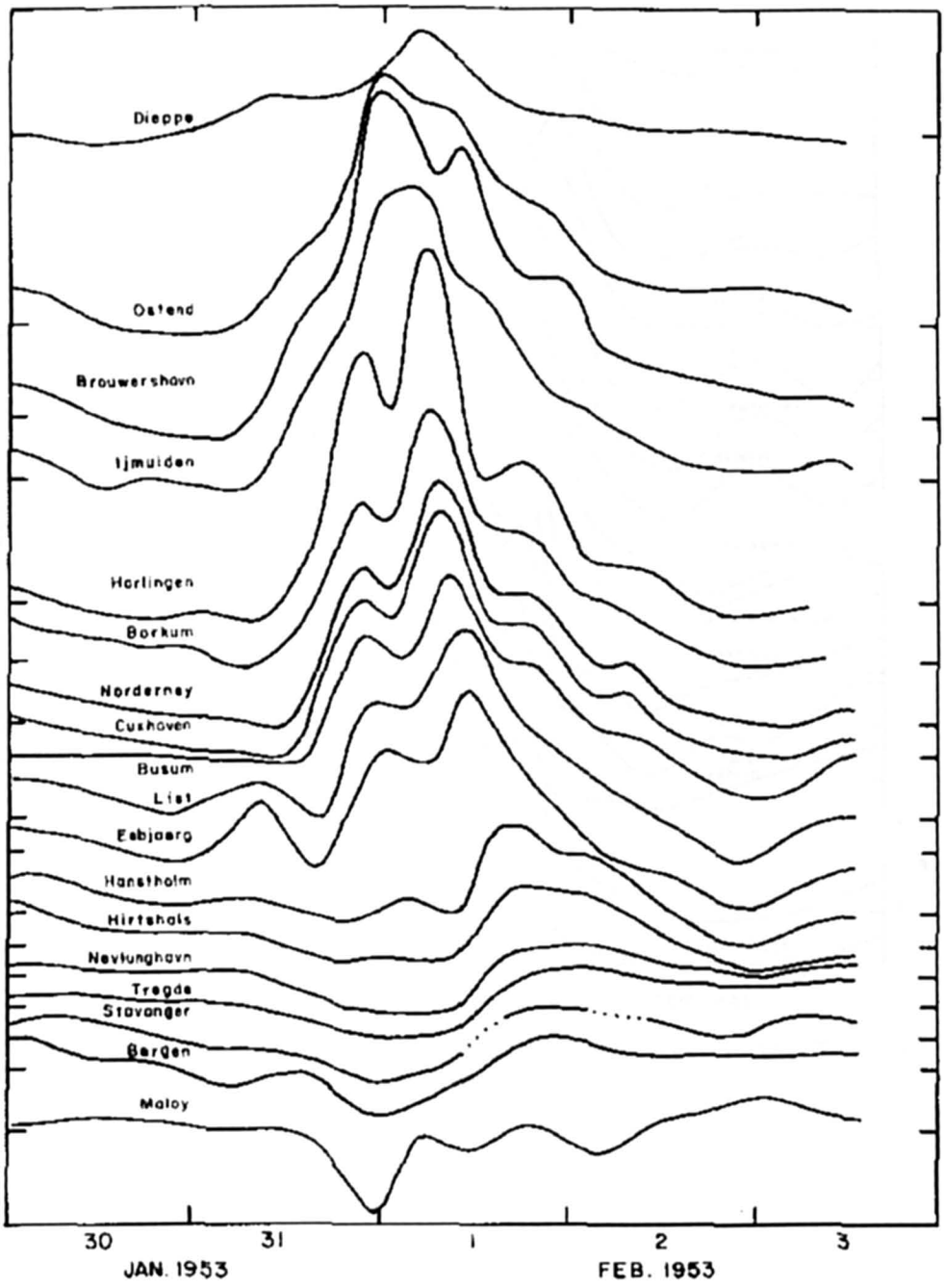


Fig. 7.12b: Storm surges at various locations around the North Sea during January 30–February 3, 1953 (ROSSITER, 1954)

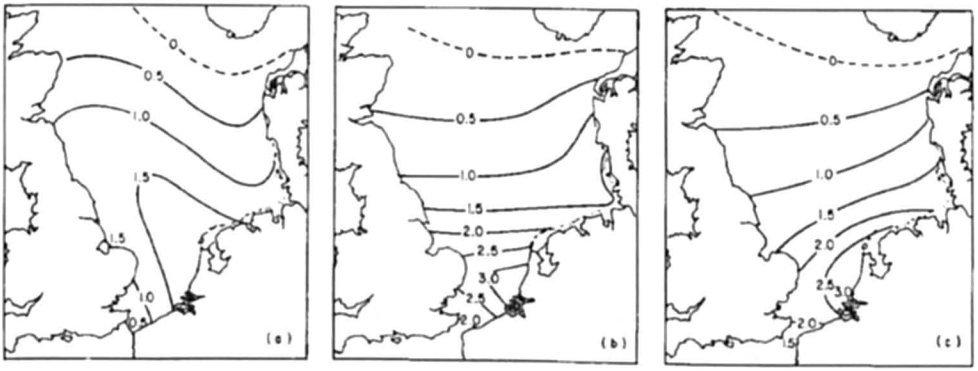


Fig. 7.13: Distribution of storm surge amplitudes (meters) in the North Sea during January 31–February 1, 1953, at (a) 18:00 (GMT) on January 31, (b) 00:00 (GMT) on February 1, and (c) 06:00 (GMT) on February 1

As described before in the English Channel the storm surge heights become smaller. The propagation of the surge through the English Channel from the North Sea is shown in Fig. 7.14.

BOWDEN (1957) mentioned that, in the southern part of the North Sea, the greatest elevation tends to occur along a line from Harwich to Flushing. The surface then slopes downward towards the Strait of Dover due to the flow of water into the English Channel.

LUNDBAK (1956) studied the storm surge of January 31–February 2, 1953, on the west coast of Denmark. He mentioned that one of the worst storm surges on the Danish coast occurred November 12–14, 1872, in which there was great damage and loss of life on the island of Lolland. The storm surge of October 10–11, 1634, was supposed to have killed more than 6000 people. This surge cut the German island, Nordstrand, into two separate islands, which were later named Pellworm and Nordstrand.

The question if the storm surge is the highest at any given instant or not depends first on the location and second on the time scale that one considers. For the coast of the United Kingdom, PETERS (1954) mentioned that a series of surges occurred during the period between 1086–99. A surge in the year 1099 killed 100 000 people. During the twelfth century, there were more surges. Another period of great surges was 1218–23. Other periods when the death toll exceeded 100,000 were in the years 1421 and 1446. Great surges also occurred (though the death toll was much smaller) on November 15, 1875, January 2, 1877, January 18, 1881, and November 29, 1897. After this period, the next comparable surge occurred in 1928 and then in 1953.

For the Netherlands VAN MALDE (1995) used the highest water level as the storm surge level. According to the official storm surge table of the Rijkswaterstaat; starting in 1825, the highest tidal-water levels recorded were those of the storm surge of February 4, 1825. But the question is, whether higher storm surge levels occurred in the past. VAN MALDE (1995) named the surges of 1421, 1446, 1468 and those from 1539 and 1552 as large, but shows that the conversion of such deceptive levels to centimeters is not a simple matter. He shows that the oldest reliable storm surge event was the All Saints Flood of 1570, one of the most disastrous floods that ever ravaged the Netherlands and summarizes that "the storm surges caused along the Dutch coast between Scheveningen and Den Helder were among the highest storm surge levels ever known". Off the northern provinces and the adjacent German coast the storm surge levels were very close to the highest ones having occurred ever

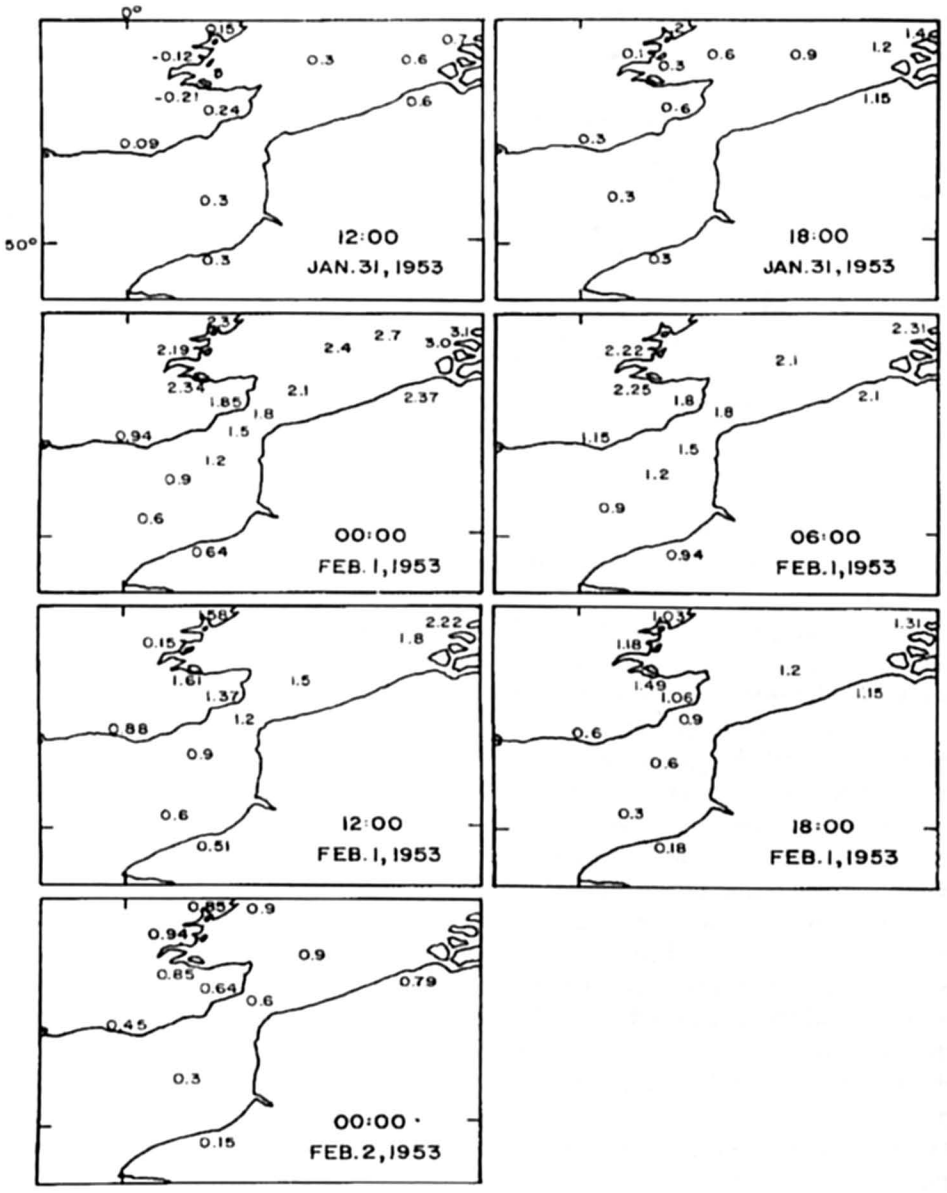


Fig. 7.14: Storm surge heights (meters) in the English Channel during January 31–Feb 2, 1953 (ROSSITER 1954)

since..." (meaning the storm surges of 1570, 1717, 1775, 1776, 1825 and 1953). The conclusion about the German coast is based on the research of ROHDE (1977), who did derive four historical storm surge levels at Emden with the following result:

| | | |
|---|---|---|
| November 1, 1570: ≥ | NN + 470 cm | NN = Normal Null ≈ mean sea level |
| December 14, 1717: | NN + 475 cm | |
| November 15, 1775: | NN + 388 cm | |
| November 21, 1776: | NN + 451 cm | |
| February 3–4, 1825: | NN + 465 cm | |

To these results the following storm surge levels in the German Bight can be added. The highest storm surge level in the German Bight was reached in 1976 with a level of 370 cm over mean high tide level and 1010 cm NN. The storm surge of February 16–17, 1962, when a lot of people died was 355 cm over mean high tide level at Cuxhaven. This level has been reached during the flood of February 3–4, 1825, with 355 cm at Cuxhaven (GÖNNERT, 1999a). Therefore it can be stated that in recent years cause the storm surge level in the German Bight only a little increased and is compared to mean high tide level increase.

While the flood of 1825 caused high water levels along the Dutch and German Coast, the storm surge of 1962 was very high only in the German Bight and especially along the rivers Ems, Weser and Elbe within the cities of Emden, Bremen and Hamburg. The reason is the character of the storm and the location of the island in the deep water area of the North Sea. After the storm surge of 1962 coastal protection has been developed so that the higher storm surge of 1976 did not cause much damage.

A major storm surge occurred in the southern part of the North Sea and in the Thames Estuary during January 31–February 1, 1983, exactly 30 years after the surge of 1953. The meteorological conditions were somewhat different in these two cases. The surge of 1983 was potentially as destructive as the one of 1953. However, because of considerable improvement in storm surge warning services and the development of coastal protection works and the Thames Estuary barrier, loss of life and damage to property were considerably less than in 1953.

### *Negative Surges in the North Sea*

ROSSITER (1971) drew attention to the navigational hazard posed to large ships in the southern North Sea due to negative storm surges. DOODSON (1947) mentioned that negative surges occurred at Dunbar and Southend during the storms of November 10–13, 1929, January 1–3, 1928, and October 17–21, 1935.

Table 7.2: Frequency of negative storm surges in the southern part of the North Sea (GEELHOED, 1973)

| | Amplitude (cm) of negative surge that can occur (at the time of low water) with the frequency per year of | | | Amplitude (cm) of negative surge that can occur (at the time of high water) with the frequency per year of | | |
|---|---|---|---|---|---|---|
| Location | 10 | 1 | $10^{-1}$ | 10 | 1 | $10^{-1}$ |
| Hook of Holland | 50 | 83 | 117 | 50 | 80 | 111 |
| Flushing | 46 | 75 | 103 | 47 | 80 | 113 |
| Dunkerque | 44 | 68 | 92 | 46 | 75 | 105 |
| Dover | 43 | 69 | 96 | 47 | 79 | 111 |

GEELHOED (1973) studied negative storm surges in the southern part of the North Sea, with particular attention to the Sandettie Bank and the Brand Ridge areas because of the shallow water depths there. The data source consisted of 50 years of data for the stations of Hook of Holland and Flushing, 4.7 years of data for Dunkerque, and 20.1 years of data for Dover. The results of a frequency analysis are summarized in Table 7.2. This table must be interpreted as follows. For example, at Hook of Holland, negative surges of amplitudes up to

50 cm occur on the average about 10 times per year; negative surges with amplitudes up to 83 cm occur once a year and negative surges of amplitudes up to 117 cm occur only once in 10 years. The differences between the negative surges at low and at high waters are not significant.

Negative surges predominantly occur in winter. Southerly to westerly winds produce negative surges at Dover whereas at Hook of Holland, southerly to easterly winds cause negative surges. Largest negative surges occur at Southend (up to 2.3 m) and at Tilbury (up to 2.8 m). At other stations, negative surges with amplitudes of 1.0–1.5 m occur. GEELHOED (1973) attributed the differences in the amplitudes of the negative surges at various locations to topographic differences.

Table 7.3: Calculated amplitudes (m) of storm surges at three locations in the southern part of the North Sea for three different wind fields. (GEELHOED, 1973)

| Type of wind field (83 km·h$^{-1}$) | Amplitude (m) of surge at | | |
|---|---|---|---|
| | Sandettie | Brown Ridge | Hook of Holland |
| Easterly | −0.8 | −0.7 | −1.3 |
| Westerly | +0.8 | +0.7 | – |
| Southerly | −1.9 | −1.8 | −2.1 |

Westerly winds appear to cause negative surges exclusively on the east coast of the United Kingdom whereas easterly winds could cause negative surges exclusively on the coast of the Netherlands. On the other hand, southerly winds can cause negative surges on both coasts simultaneously (and indeed in the whole southern part of the North Sea). The calculated negative surges at three locations for three different wind fields are summarized in Table 7.3.

Negative surges in rivers are a special problem for navigation for the example of the Elbe river (German Bight) this has been investigated by RUDOLPH (1999). The following is based on RUDOLPH (1999) and also on personal communication.

The estuaries along the German Bight are well exposed to storms coming over the North Sea from westerly direction. In the Elbe estuary which is orientated from West to East, high water levels at the mouth in combination with strong westerly winds can result in high water levels along the whole estuary, which reaches inland more than 100 km. Even the harbor of Hamburg, which is situated about 120 km upstream of the mouth of the Elbe estuary is endangered by storm surges coming from the North Sea.

There are indeed situations too, where strong winds cause a decrease in water level. This might be called a negative storm surge. In the Elbe estuary for example strong easterly winds blowing for several days can lower high as well as low water levels significantly.

An example of a negative storm surge is found in the first week of October 1992. This period was preceded by a low fresh water discharge of only appr. 200 m$^3$/s while the mean fresh water discharge of the last 50 years was 712 m$^3$/s. During the end of September 1992 the wind over the Elbe estuary had easterly direction with wind speeds between 5 m/s and 10 m/s (Bft 4 to 5). In the first week of October 1992 the wind speed increased and reached up to 15 m/s (Bft 7) from April 10, 1992 until June 10, 1992.

For the period January 10, 1992 until July 10, 1992 the astronomical tide for Cuxhaven at the mouth of the Elbe estuary was calculated from harmonic tidal constants. Fig. 7.15a

shows the comparison between observed and predicted water levels at Cuxhaven. In addition the measured wind speed and wind direction in this area is given.

The difference between these water levels can be interpreted as surge. Fig. 7.15b shows the observed water level, the predicted astronomical tide and the surge during the period of strong easterly wind. In fact, a negative storm surge of up to one meter can be found.

Inside the estuary e.g. close to the harbour of Hamburg the difference between predicted and observed water levels is even higher. In this part of the estuary the effects of the low fresh water discharge and the strong easterly winds add up to differences in the high water level of 110 cm and in the low water level of 80 cm (Table 7.4).

Table 7.4: Measured and predicted water levels in [mNN] as well as the differences at Cuxhaven and Hamburg St. Pauli in the Elbe estuary during negative storm surges

| Date | | Cuxhaven | | | Hamburg St. Pauli | | |
|---|---|---|---|---|---|---|---|
| | | measured | predicted | difference | measured | predicted | difference |
| 10/03/1992 | HW | + 1.13 m | + 1.15 m | − 2 m | + 1.49 m | − 2.00 m | − 51 cm |
| | LW | − 1.79 m | − 1.40 m | − 39 cm | − 2.01 m | − 1.40 m | − 61 cm |
| | HW | + 0.70 m | + 1.30 m | − 60 cm | + 1.07 m | + 1.80 m | − 73 cm |
| | LW | − 1.64 m | − 1.20 m | − 44 cm | − 1.97 m | − 1.30 m | − 67 cm |
| 10/04/1992 | HW | + 1.71 m | + 1.40 m | − 31 cm | + 1.05 m | + 1.90 m | − 85 cm |
| | LW | − 1.80 m | − 1.30 m | − 50 cm | − 2.13 m | − 1.40 m | − 73 cm |
| | HW | + 0.09 m | + 1.10 m | + 101 cm | + 0.43 m | + 1.60 m | − 117 cm |
| 10/05/1992 | LW | − 1.67 m | − 1.10 m | − 57 cm | − 2.11 m | − 1.30 m | − 81 cm |
| | HW | + 0.40 m | + 1.20 m | − 80 cm | + 0.77 m | + 1.80 m | − 103 cm |
| | LW | − 1.61 m | − 1.20 m | − 41 cm | − 2.08 m | − 1.40 m | − 68 cm |
| | HW | − 0.02 m | + 0.90 m | − 92 cm | + 0.44 m | + 1.50 m | − 106 cm |
| 10/06/1992 | LW | − 1.26 m | − 1.00 m | − 26 cm | − 1.72 m | − 1.30 m | − 42 cm |
| | HW | + 0.37 m | + 1.20 m | − 83 cm | + 0.83 m | + 1.80 m | − 97 cm |
| | LW | − 1.40 m | − 1.20 m | − 20 cm | − 1.84 m | − 1.40 m | − 44 cm |
| | HW | + 0.26 m | + 0.90 m | − 64 cm | + 0.77 m | + 1.50 m | − 73 cm |

Investigations with a numerical model of the Elbe estuary showed, that not only the low water levels at the mouth of the Elbe caused the low water levels inside the estuary, but also the strong local wind over the Elbe estuary helped to lower the water level along the Elbe estuary during ebb tide (increasing ebb current) and to keep the water levels low during flood (decreasing flood current).

The processes described here, low fresh water discharge and continuous high easterly winds, resulted in a decrease in low and high water levels along the whole Elbe estuary. This negative storm surge lasted for more than four days. On July 10, 1992, the wind direction changed to North, the wind speed decreased and so the water levels finally reached their normal height again.

In contrast to storm surges these negative storm surges do not endanger the life of the inhabitants of the coastal areas. Nevertheless they are a problem for the traffic on e.g. the navigation channel Elbe, as the navigable depth is reduced significantly in comparison to the usually occurring tide.

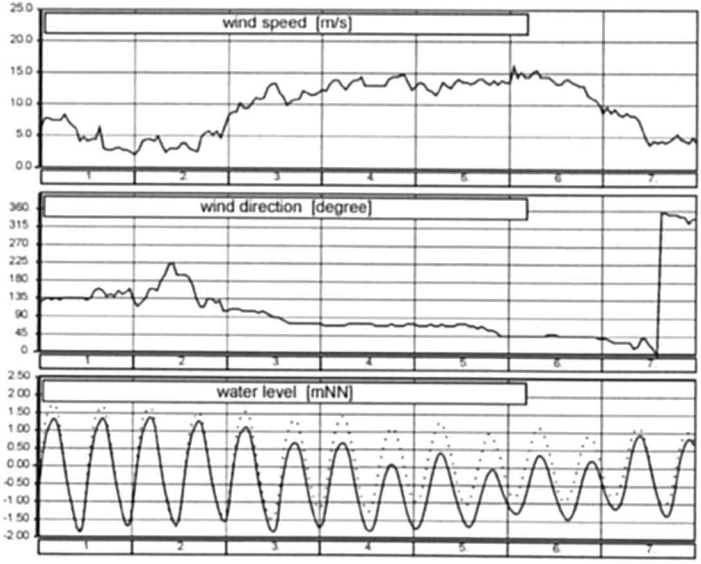


Fig. 7.15a: Negative Surge Elbe: Wind speed and wind direction at the island of Scharhörn in the mouth of the Elbe estuary and measured (dotted) and predicted (solid) water levels at Cuxhaven for the period 10/01/1992 until 10/07/1992. With increasing wind speed the difference between observed and predicted water level also increases

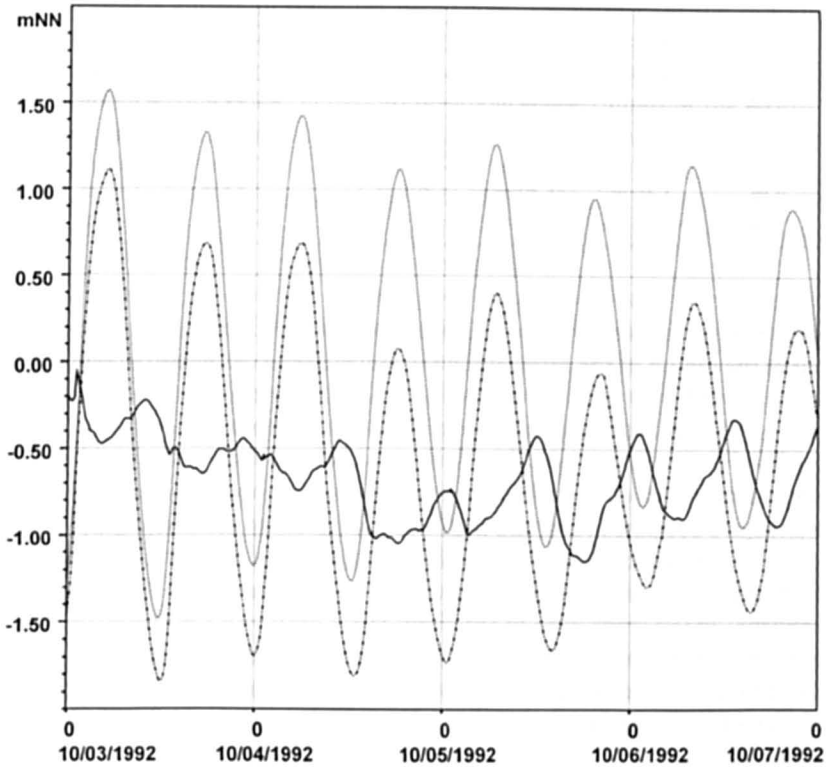


Fig. 7.15b: Negative Surge Elbe: Measured water level (dashed), astronomical tide (dotted) and surge (solid) at Cuxhaven during October 1992

*The Netherlands*

Earlier, the works of GALLÉ (1915) and SCHALKWIFT (1947) were discussed. The storm surge amplitudes along the coast of the Netherlands during the major storm surge of January 31–February 1, 1953, were greater than those at the east coast of the United Kingdom (UFFORD, 1953). Surge amplitudes up to 9 ft (2.74 m) occurred along the coasts of the provinces of Zeeland and Zuid-Holland, with a peak surge of 9.6 ft (2.93 m) occurring at Hellevoetsluis. In the Scheldt Estuary the amplitudes were even greater. At Berger op Zoom the amplitude was about 11 ft (3.35 m).

The water level rose above the dykes, and about 50 dykes collapsed and at least 1800 people died. The damage exceeded £ 100 million (at 1953 prices). UFFORD (1953) mentioned that this was the biggest surge since the one on November 18, 1421, when at least 10000 people died. Since the time tide gauges were set up in 1890, the surge of 1953 was 2 ft higher on the average than any other surge during the period 1890–1953. The extent of the flooding on the coast of the Netherlands is shown in Fig. 7.16.

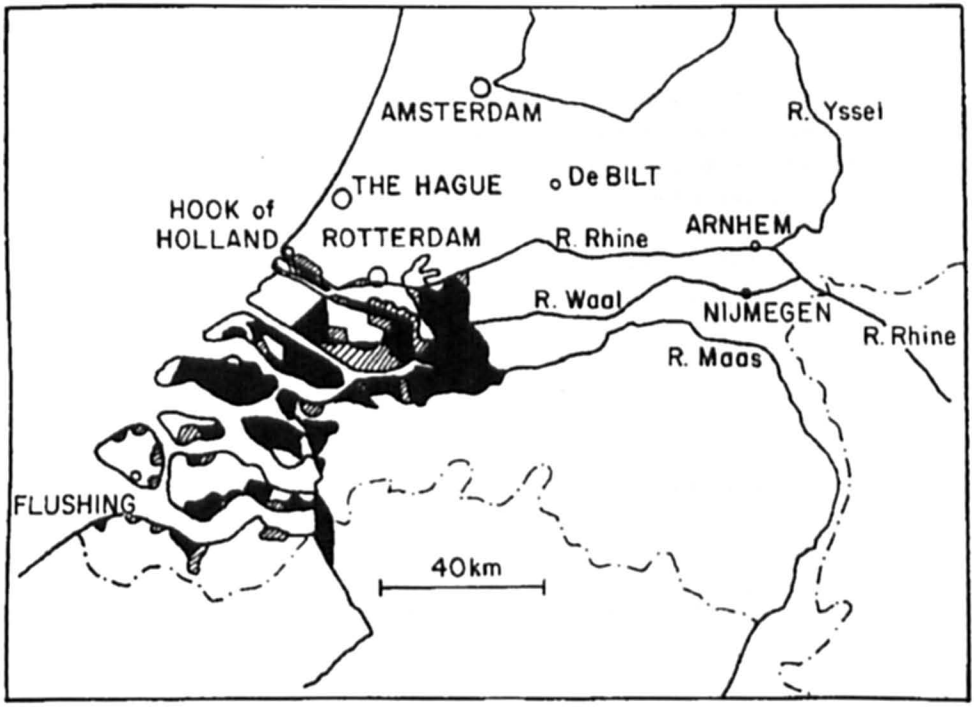


Fig. 7.16: Extent of flooding on the coast of the Netherlands due to the storm surge of January 31–February 1, 1953. Dark areas show regions that were flooded until March 1953. Hatched areas are those that were reclaimed after the flooding (UFFORD, 1953)

WEENINK (1956) studied the so-called twin storm surges that occurred on December 21 and 24, 1954. The observed surge and that computed through an equilibrium wind assumption are shown in Fig. 7.17.

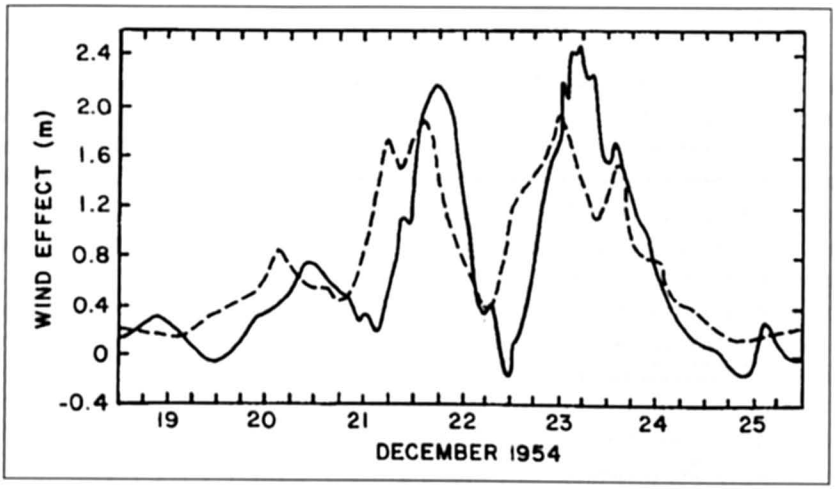


Fig. 7.17: Twin surges of the North Sea in December 1954 as recorded at the Hook of Holland (solid line). Broken line shows the computed surge using the equilibrium wind effect (WEENINK, 1956)

TIMMERMAN (1971) showed that moving cold fronts over the southern part of the North Sea could produce a sudden increase of water levels at the Netherlands coast (he uses the rather inappropriate term "gust bump" to refer to these water level increases). These increases in the water level occur only when the speed of propagation of the cold front lies between 29 and 36 knots (54–67 km/h). This suggests resonance between the traveling atmospheric disturbance and the long surface gravity waves in the water body. He numerically simulated the event of December 13, 1956. One can obtain some idea of the time scale and amplitudes of the gust bumps from Fig. 7.18. One can clearly see the bump at Katwuk at 11 a.m. on March 27, 1966. The locations of these stations can be seen in Fig. 7.19. Similar sudden water level increases for the event of December 13, 1956, are shown in Fig. 7.20.

After the storm surge of 1953 in the Netherlands it was decided to set new safety standards and perform extreme value statistics. It was agreed that the central, and most important, part of Netherlands was given a safety standard with a return period of 10,000 years (...) (RONDE et al., 1995). The wadden islands have a return period of 2000 years and the remaining coastal areas have a return period of 4000 years. With respect to the central coastal part, this gives a reduction of about 40 cm for most coastal areas.

RONDE et al. (1995) describe the extreme value water level as follows. At first the storm surge data were selected by use of depression storm tracks to obtain a homogeneous data set. Only one value per storm was taken to get un-correlated data. This is comparable with the method to calculate a storm surge curve and take only the highest water level. A so called "Peak over Threshold Method" was fitted to choose the extreme value distribution. "Finally a design level of about 5 m + NAP was designated for the Hook of Holland as the event with a return period of 10,000 years." RONDE et al. (1995) described the method to calculate the design level of other stations with help of the design level of Hook van Holland.

Using statistical methods, RONDE et al. (1995) took into account a sea level rise of about 15 to 20 cm and the return period was re-calculated.

For real time forecasting of storm surges the CSM model with a grid size of 8 km is used at the KNMI (Royal Netherlands Meteorological Institute).

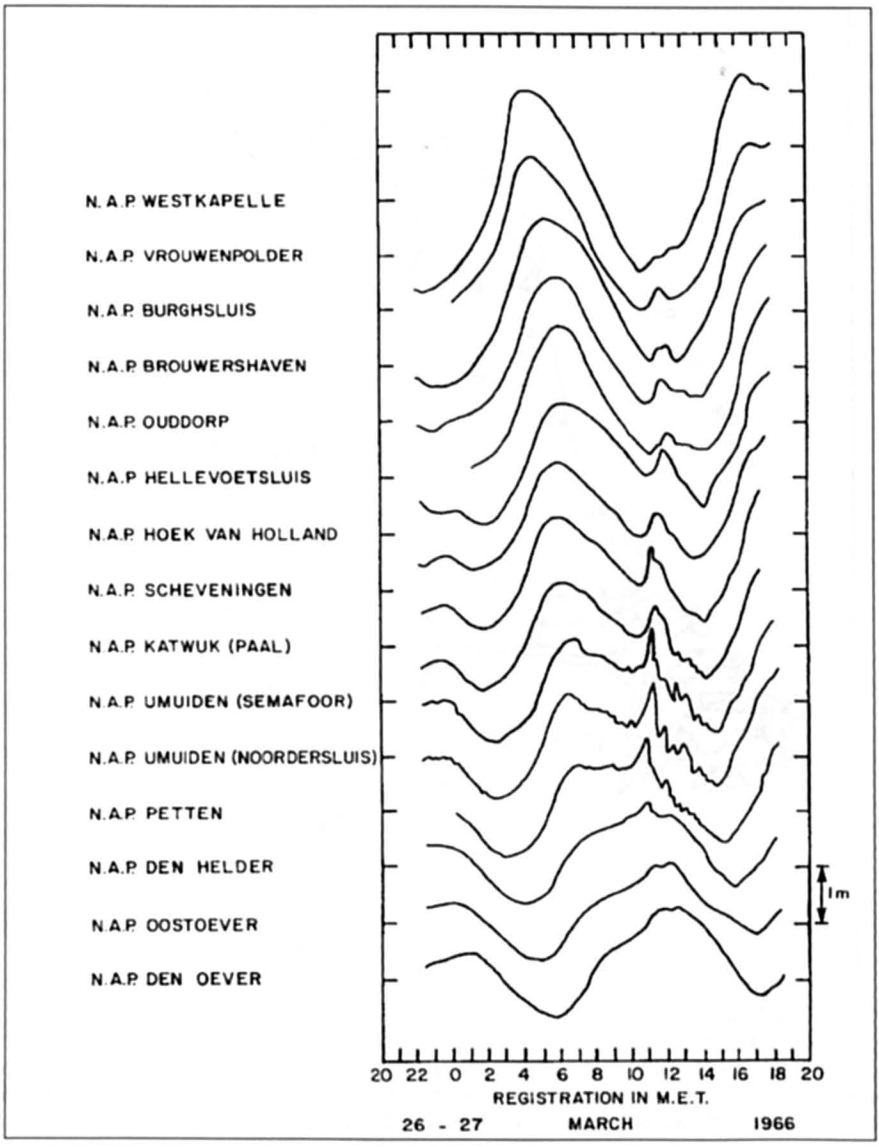


Fig. 7.18: Sudden water level changes (gust bumps) during March 27, 1966, at several locations on the Netherlands coast (TIMMERMAN, 1971)

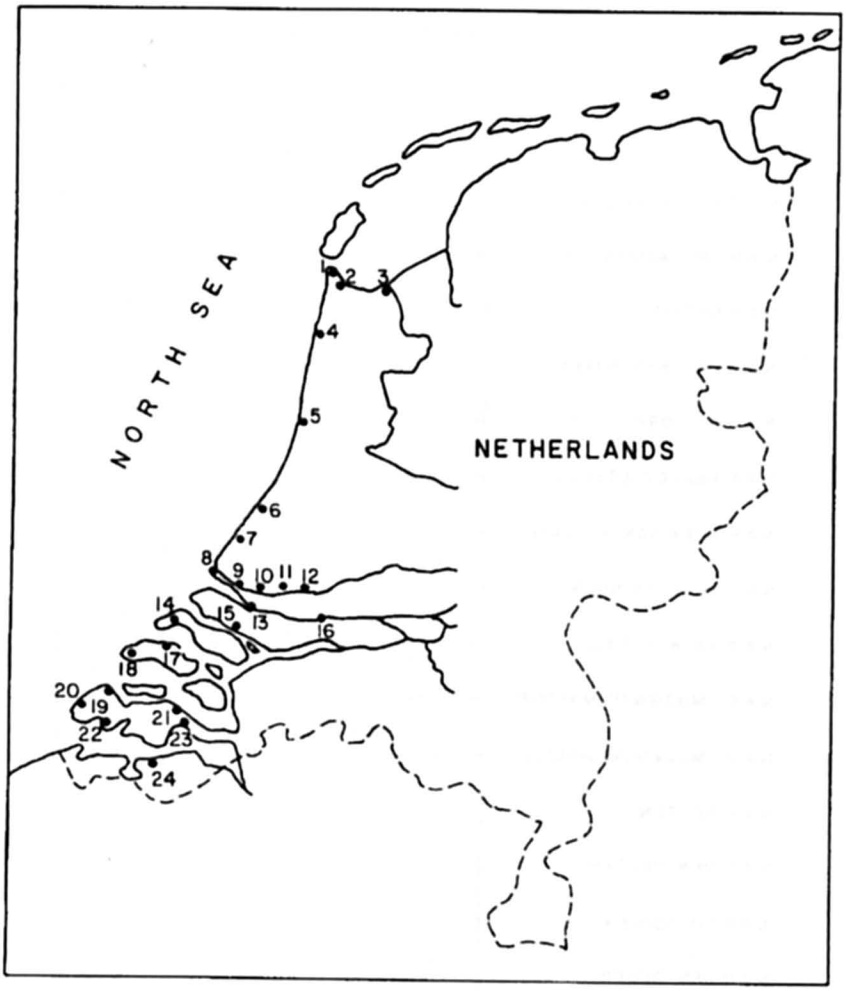


Fig. 7.19: Netherlands coast showing the locations of the tide gauge stations used in the storm surge study, 1, Den Helder; 2, Oostoever.; 3, Den Oever; 4, Petten; 5, Urnuiden; 6, Katwuk aan Zee; 7, Scheveningen; 8, Hoek van Holland; 9, Maassluis; 10, Vlaardingen; 11, Rotterdam; 12, Krimpen aan den Lek; 13, Spukenisse; 14, Ouddorp; 15, Hellevoctssluis; 16, Dordrecht; 17, Brouwershaven; 18, Burghsluis; 19, Vrouwenpolder; 20, Westkapelle; 21, Wemeldinge; 22, Vlissingen; 23, Hansweert; 24, Temeuzen (TIMMERMAN, 1971)

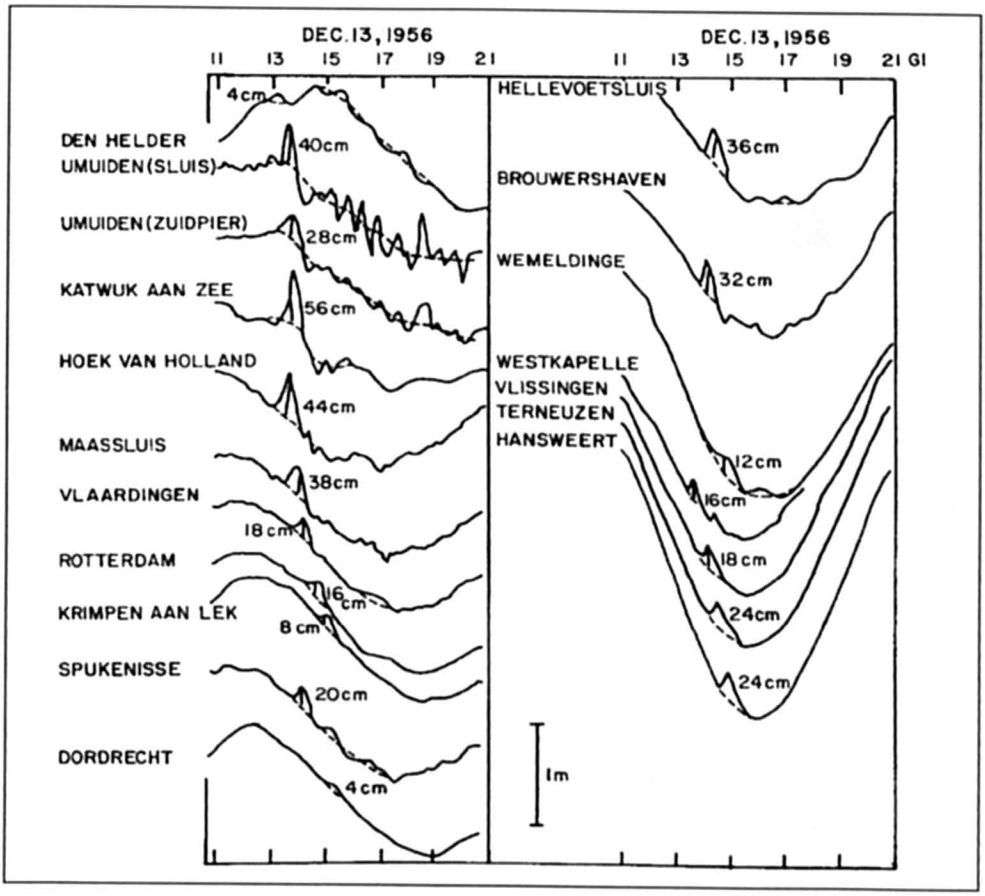


Fig. 7.20: Sudden water level changes (gust bumps) at several locations on the Netherlands coast on December 13, 1956 (TIMMERMAN, 1971)

*German Bight*

Storm surges occur in the German Bight when wind blows over the North Sea from N to NW. To reach a very high water level the duration of a high wind speed must be a minimum of 3 h. The so called critical wind direction for each location is different. For example the critical wind direction for Cuxhaven for very high storm surges lies between 280°–310°, for Helgoland between 265°–280° and for Norderney between 255°–290° (GÖNNERT, 1999b).

In the North Sea near the Amphidromic point the water levels rise only slightly and increase towards the coast.

TOMCZAK (1950) discussed the storm surge of February 9–10, 1949, in the North Sea. The greatest effect of the surge was on the coast of Northern Friesland. One interesting feature was that the storm center remained almost stationary off the island of Sylt on February 9th and blocked the outflow of water from the German Bight northwards. The maximum amplitudes of the water level at several locations are listed in Table 7.5.

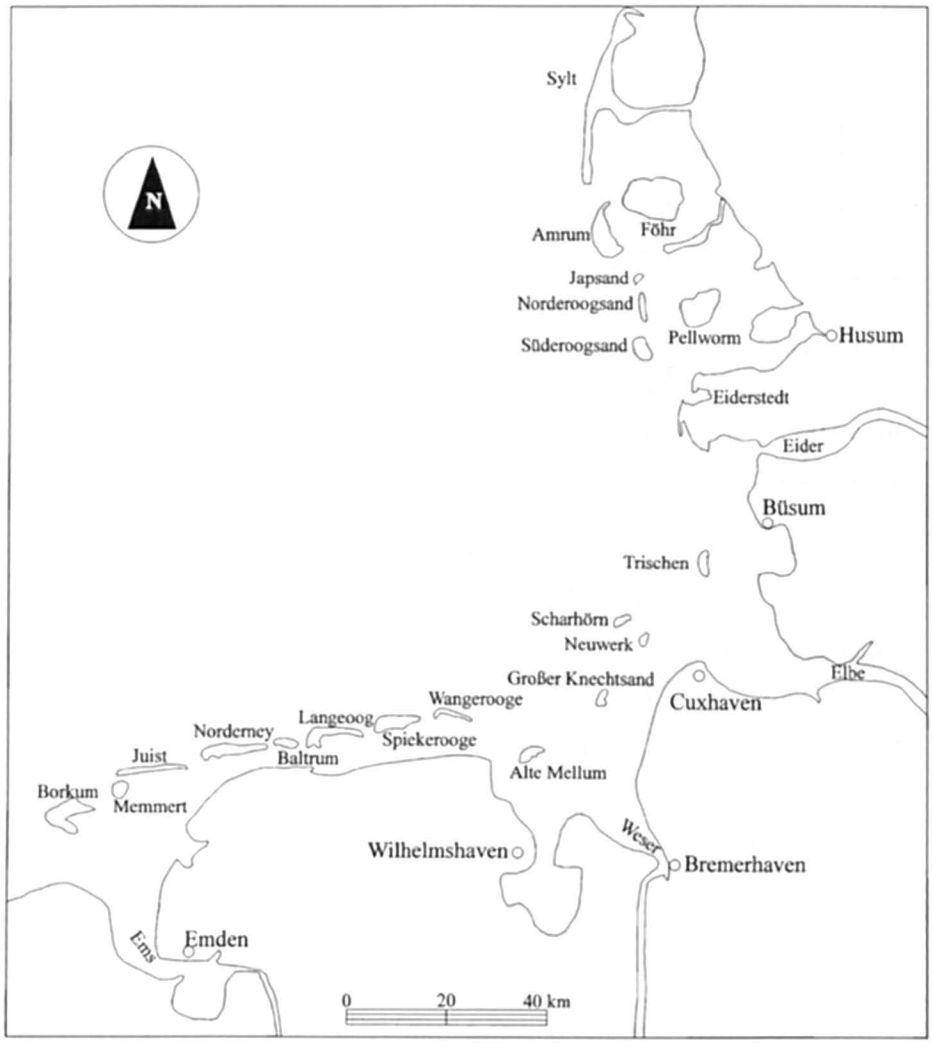


Fig. 7.21: The German Bight

Table 7.5: Maximum water levels during the storm surge of Feb. 9–10, 1949, at the German North Sea Coast (TOMCZAK, 1950)

| Station | Amplitude (m) | Station | Amplitude (m) |
|---|---|---|---|
| Borkum | 2.4 | Bremerhaven | 3.9 |
| Norderney | 3.0 | Cuxhaven | 4.2 |
| Emden | 3.3 | Büsum | 4.8 |
| Wilhelmshaven | 3.4 | Husum | 5.6 |

Other examples are shown in Table 7.6, indicating that the level depends on wind direction and location with each special topography.

Table 7.6: Storm surge level over NN (Normal Zero) in the German Bight

| Storm surge | Feb. 16, 1962 | Jan. 3, 1976 | Feb. 26–28, 1990 | Jan. 10, 1995 |
|---|---|---|---|---|
| Cuxhaven | 495 cm NN | 5010 cm NN | 434 cm NN | 448 cm NN |
| Norderney | 410 cm NN | 386 cm NN | 366 cm NN | 346 cm NN |
| Wittdün | 360 cm NN | 327 cm NN | 324 cm NN | 266 cm NN |
| Helgoland | 414 cm NN | 405 cm NN | 384 cm NN | 301 cm NN |

SIEFERT (1968, 1978, 1982, 1988a, 1988b, 1990), SIEFERT and LASSEN (1985) and GÖNNERT and SIEFERT (1997) studied storm surges in Cuxhaven and the Elbe River. The studies involved a total of 153 storm surges, which included 192 high tide water levels for the period of 1901–1995 (GÖNNERT and SIEFERT, 1998). Only events that generated a surge of 2 m or more between low water time and four hours after high water time are considered for the analysis (SIEFERT and LASSEN, 1985). During low tide the surge reaches a higher level than during high tide. Therefore the data record is restricted to storm tides with a surge level lower than 1.50 m at high tide. To analyze the change of storm tides in the last century utilization of the surge curve (Fig. 7.23) – which is the difference between the storm tide and the astronomical or mean tide curve – is the best approach, because it includes the meteorological factors. With this approach GÖNNERT (1999a & b) studied the 20th century storm tides (level, number, duration and character) in the German Bight (Fig. 7.21). The results showed an increase in the number of storm surges, but no significant increase in the level. The increase in frequency is mainly true for the small events, but the average storm surge curve is longer and there are more events with long duration (GÖNNERT, 1999a & b). For example, during the storm surge of February 26–28, 1990 one storm surge curve includes five height water peaks for Cuxhaven (Fig. 7.22).

In the German Bight the character of very high storm surges is different. At the coast very high crests are associated with a fast increase of wind speed. Since wind fields cannot be reliably predicted too far ahead, storm surges also cannot be predicted reliably for more than 12 hours ahead. But at the islands very high crests are associated with the slow increase of wind speed.

Investigations into the change of storm surge level and frequency by focusing on the tidal crest have been done for example by LÜDERS (1974), PETTERSON and ROHDE (1991), NASNER and PARTENSCKY (1977), FÜHRBÖTER et al. (1988), FÜHRBÖTER (1989), FÜHRBÖTER and TÖPPE (1991), JENSEN (1987), NIEMEYER et al. (1995) and STORCH et al. (1998).

GÖHREN (1976) studied currents on the tidal flats in the German Bight. Note that these tidal flats could be as wide as 20 km. He showed that the currents can increase from an average 30 cm/s to as much as 120 cm/s during storm surges. The destructive storm surges at the North Sea coast of Germany during February 16–17, 1962, December 6–7, 1973, and January 3, 1976, prompted ZSCHAU et al. (1978) to develop a storm surge forecasting technique by measuring the inland crustal tilt and the deflection of the local vertical due to the buildup of the surge. These authors, using a vertical pendulum, measured such tilts with precision. According to them there is advance information about the storm surge in these tilt measurements. The rationale for this is explained below.

There is an indirect effect of tides on tidal gravity, tilt, and strain measurements. Since this effect depends on the elasticity of the crust and the upper mantle, this effect has been used to determine their elastic properties. However, in the regions where the elastic properties are known better than the tides, the inverse problem of determining the tides from measurements

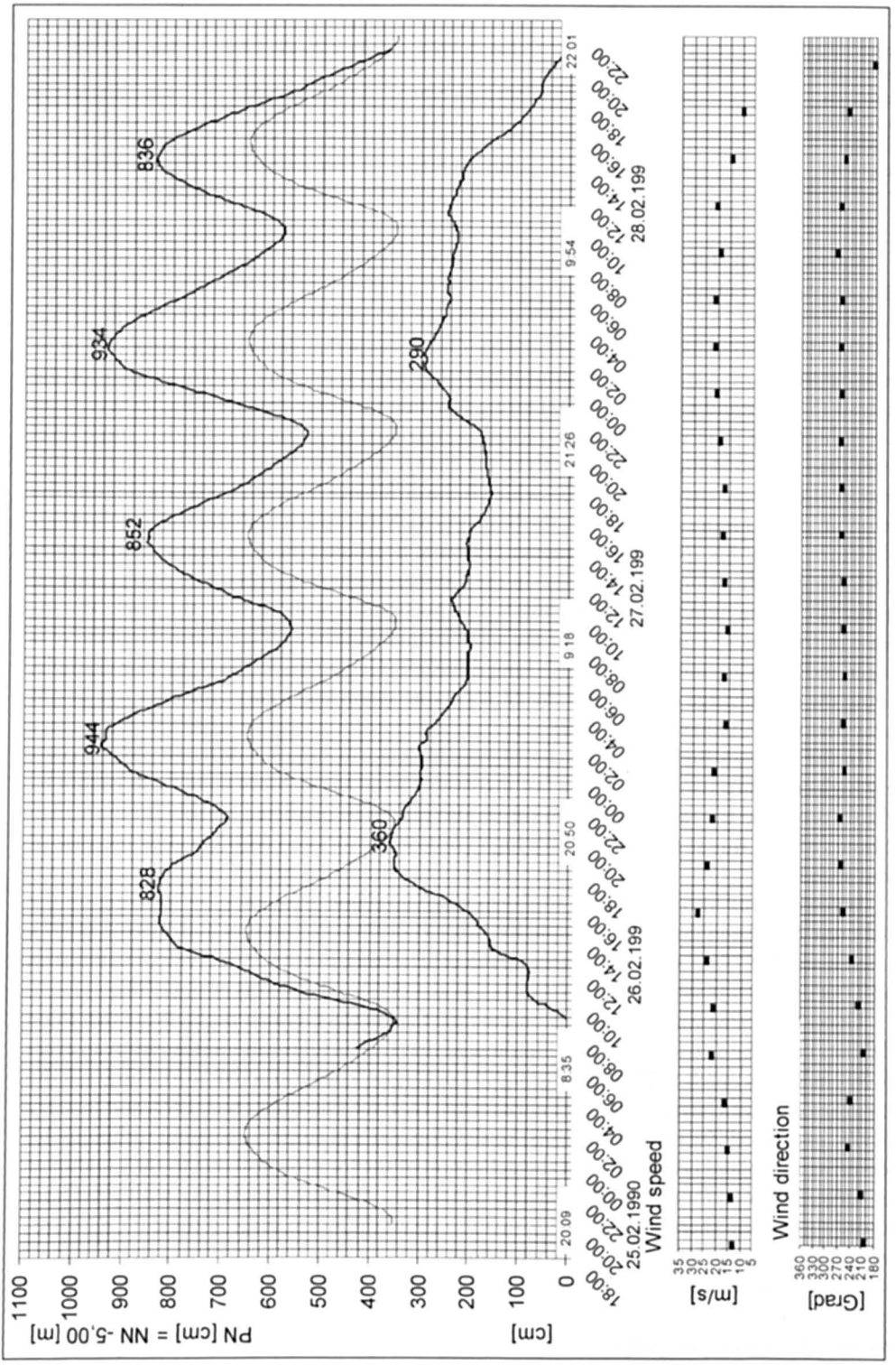


Fig. 7.22: Storm Surge at Cuxhaven February 26–28, 1990 (GÖNNERT and SIEFERT, 1998)

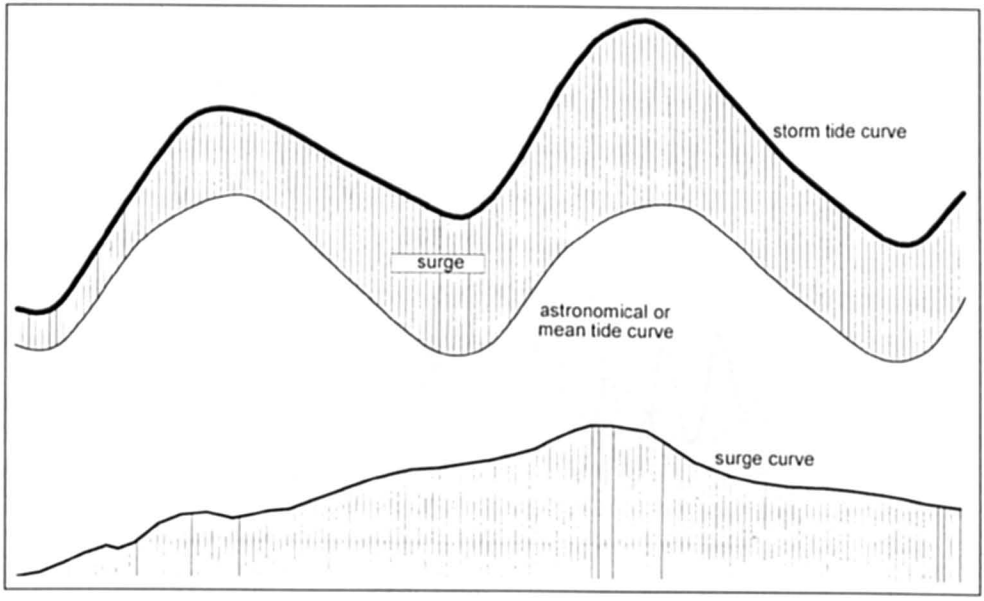


Fig. 7.23: The storm surge curve

of tidal gravity on the land has been used. ZSCHAU et al. (1978) used this inverse approach of determining the storm surge from tilt measurements made inland. According to them, the additional water mass of the surge has three different effects on these measurements: (1) the deflection of the vertical due to the gravitational attraction of the water mass, called the Newtonian tilt; (2) the tilt of the surface due to the loading and unloading of the sea floor, called the primary loading tilt; (3) the secondary deflection of the vertical due to the redistributions of mass caused by the loading and unloading, called the secondary loading tilt.

The secondary loading tilt, generally, is small compared with the primary tilt and it can be combined with the loading tilt. Note that the Newtonian tilt and the primary tilt cause a deflection of a vertical pendulum tilt meter and also tilt it's casing.

The storm surge at Büsum on the west coast of Schleswig Holstein of December 6–7, 1973, is shown in Fig. 7.24. A maximum amplitude of about 3 m was attained. The measured tilt at Kiel-Rehmsberg and also the astronomical tide are shown. It can be seen that the tilt curve matches the storm surge curve except for a 12-h phase advance. This phase advance is explained as due to the amphidromic component of the North Sea surge, which takes roughly a day to propagate in a counterclockwise direction from Scotland along the coasts of the United Kingdom, Belgium, the Netherlands, Germany, and Denmark to Norway.

This same technique was used to simulate four major, two moderate, and three minor surges during November–December 1973. The predictions (Fig. 7.25) 9, 6, and 3 h ahead had average errors of 29, 18, and 11 cm, respectively, in the maximum storm surge amplitudes.

FÜHRBÖTER (1979), JENSEN (1985), FÜHRBÖTER and TÖPPE (1991) studied the frequencies of extreme storm surges on the North Sea coast of Germany. They suggested that the classical extrapolation techniques for return periods might not be applicable in this situation because the time series (representing the storm surge data) are not stationary but changing with time continuing. JENSEN (1999) summarized their work:

The current approaches for estimating a storm surge defence level can be classified into empirical and statistical methods. Statistical methods are mostly based on the consideration

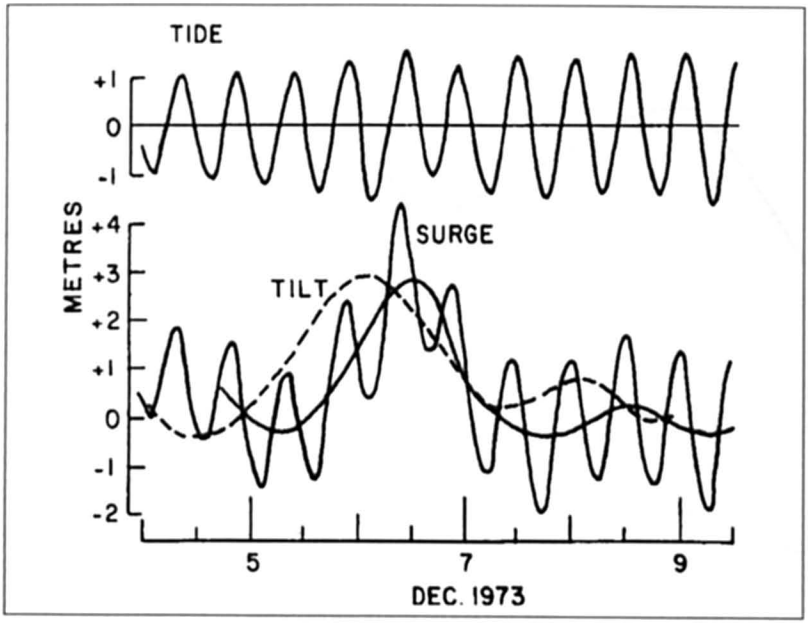


Fig. 7.24: Tide and surge at the coast of Germany during December 6–7, 1973. Top: tide at Büsum; bottom: solid curve shows the surge at Büsum and the broken curve shows the tilt at Kiel-Rehmsberg (ZSCHAU, 1977)

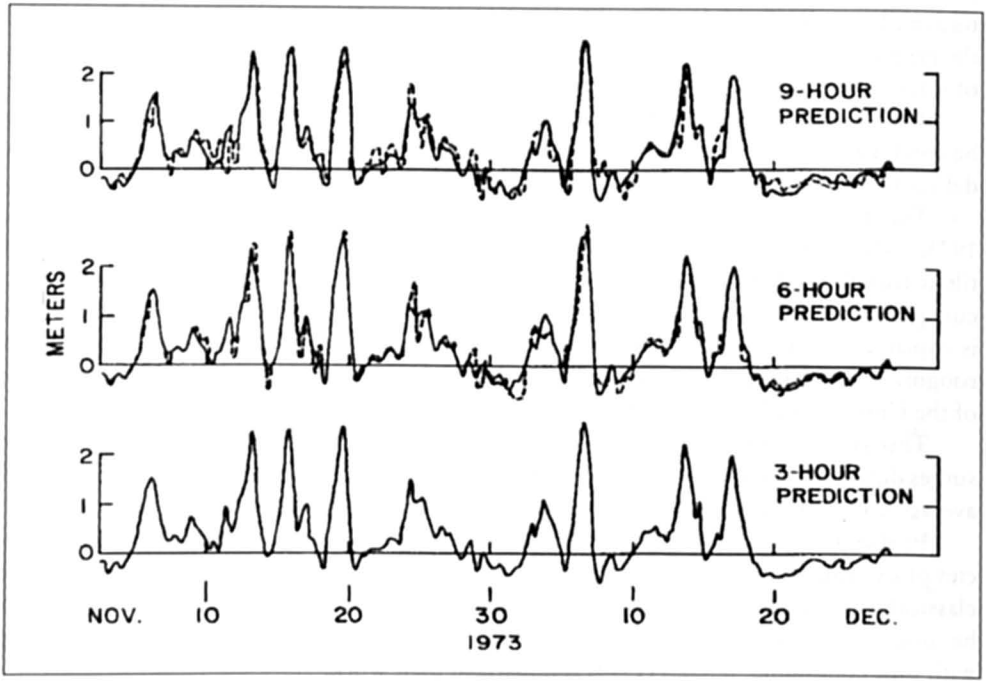


Fig. 7.25: Hindcast of storm surges for Büsum from tilt measurements at Kiel-Rehmsberg 9, 6, and 3 h in advance. Solid line: observed surge; broken line: hindcasted surge (ZSCHAU and KUMPEL, 1979)

of high water levels (HW) of an equidistant period (e.g. yearly maximum). The basic requirements of any data set are consistency, homogeneity and stationarity of the data.

Before further processing, time series should be checked and analysed very carefully for observation errors and inherent defectiveness. If mean values (mean tidal high water) are available, extreme values $HW$ of the gauge should be homogenized using the linear trend $s_T$ of the respective mean values as follows (if the year 2000 is the reference year):

$$BHW_i = HW + (2000 - i) \cdot s_T.$$

For the German Bight, a rise $s_T$ of 25 cm to 50 cm for the mean tidal high water (MHW) has to be used for homogenisation of the extreme water levels. In order to estimate water levels that occur with a given probability or return period, usually some distribution functions are fitted to the observed values and a best-fitting function is selected. The most commonly used distribution functions for extreme water levels in the German Bight are: (LOG) Pearson III, Jenkinson (several procedures) and a linear regression procedure based on empirical return periods. In such an approach, the physical conditions that lead to an extreme water level are ignored.

A more reliable method of estimating extreme water levels is based on the separation of as many as possible single components from the total water level.

Examples of such components are wind set up, external surges, other astronomical influences, local wind set up, oscillations and others. Such a concept requires a continuous record of water levels as well a continuous computation of astronomical tides.

In general, as many components as possible should be regarded separately, but since such data is not yet available for the gauges in the German Bight, the only way of considering single components of the total water level is to analyse storm surge curves has done in SIEFERT (1999) and GÖNNERT (1999).

In doing so, the probabilities of a storm surge of a given level and the probability of that wind set up to occur during a high water period can be combined. Hence, the estimation of storm surge levels with a very low probability of exceedance is more reliable than of those obtained with a "classical statistical method", in particular for extreme water levels.

BARTHEL (1979) showed that significant wind wave activity could occur in the German Bight. One must include this in predicting the total water level.

*Norway*

GJEVIK and ROED (1974) mentioned that catastrophic surges occurred at the island of Grip (a small island on the west coast of Norway) and were discussed by HELLAND (1911). Major surges occur also at the Island of Ona. JOHANSEN (1959) studied the surge along the southeast coast of Norway. GJEVIK and ROED (1974) studied the following three surges on the Norwegian west coast: November 2, 1971, December 30, 1972, and December 31, 1972. The surge curves at three locations for the three cases together are shown in Fig. 7.26 and 7.27, respectively. The peak surge amplitudes at six locations for the first case are given in Table 7.65.

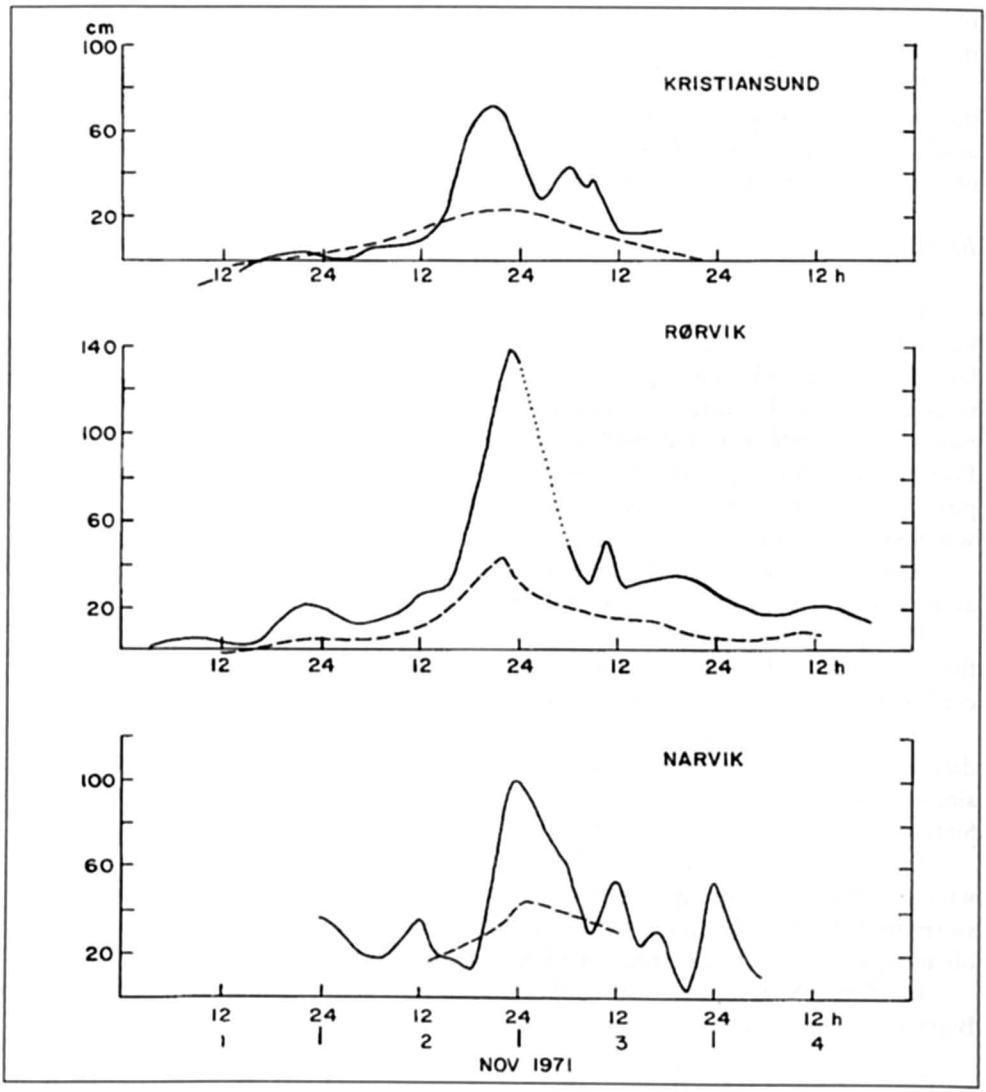


Fig. 7.26: Observed storm surges on the west coast of Norway during November 1–4, 1971. Dots denote missing observations. Broken curve represents the theoretical surge due to the atmospheric pressure gradient only (GJEVIK and ROED, 1974)

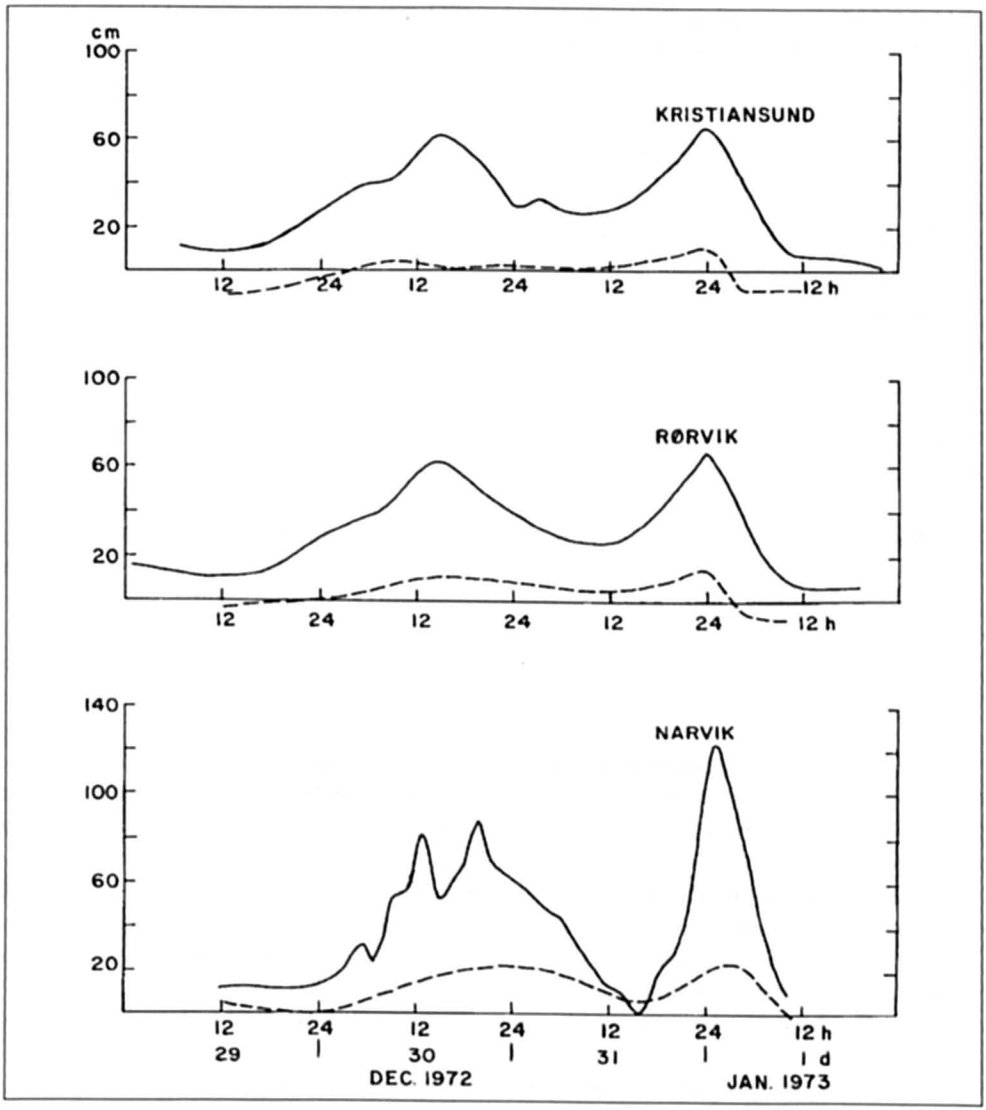


Fig. 7.27: Observed storm surges on the west coast of Norway during December 29, 1972–January 1, 1973 (solid line). Broken line shows the theoretical surge due to the atmospheric pressure gradient only (GJEVIK and ROED, 1974)

Table 7.7: Peak storm surge amplitudes at certain locations on the West coast of Norway for the surge of Nov. 2, 1971 (GJEVIK and ROED, 1974)

| Location | Observed peak surge (m) |
|---|---|
| Alesund | 0.40 |
| Heimsjo | 0.75* |
| Trondheim | 1.00 |
| Sandnessjoen | 1.20 |
| Hammerfest | 0.40 |
| Tromso | 0.50 |

* This value does not agree with that given by MARTINSEN et al. (1979). See Table 7.8.

Table 7.8: Comparison of observed and calculated peak surge amplitudes on the west coast of Norway for the surge of Nov. 2, 1971 (MARTINSEN et al., 1979)

| Location | Observed | Computed |
|---|---|---|
| Kristiansund | 0.7 | 0.98 |
| Heimsjo | 1.0 | 1.08 |
| Rorvik | 1.4 | 1.40 |
| Sandnessjoen | 1.2 | 1.47 |
| Tromso | 0.5 | 0.65 |

MARTINSEN et al. ( 1979) developed a numerical model to simulate storm surges along the west coast of Norway. The observed surges at five locations and those calculated from the numerical model including bottom stress are compared in Table 7.8.

### 7.3.2 Baltic Sea

Storm surge investigations in the Balitc Sea are numerous. They extend from the early part of the 20th century by KRÜGER (1910) to BAERENS and HUPFER (1994). Therefore not all available references can be summarized here. The following discussions follows closely STIGGE (1999).

**Special hydrodynamic conditions:** The Baltic Sea extends between latitudes 54 and 66 in the central area of the circumpolar low pressure zone of the northern hemisphere. Relative to the surface area of this marginal sea, the entrances to the North Sea have very small cross sections, so that only long-period oscillations of North Sea water levels propagate undamped into the Baltic. In its southwestern parts, the semi-diurnal tides are reduced to amplitudes of just 10 cm, and towards the central Baltic they disappear almost completely. Because of its enclosed geographical situation and elongated basin shape, the Baltic Sea tends to produce surface seiches with periods ranging from 26 to 39 hours, depending on the type of forcing of all contributing sea areas. Storm surges are triggered by changes in the wind fields above these areas. Strong southwesterly winds cause high water levels on its northern, and low levels on its southern coasts, with water flowing in through the Straits of Denmark increasing the water volume. A change in the wind direction to north/north-east causes high water levels in the southern Baltic, in which case the potential energy of water masses, which had been pushed north, may produce an additional impact. Both at the northeastern and southwestern end points of the Baltic Sea's longitudinal axis, peak high water values exceeding 3 m above MSL may occur. Storm surges may cause considerable damage along the coastlines, so that adequate coastal protection has to be provided. On the other hand, both storm surges and preventive protection measures may impair the functionality of technical structures. Under environmental protection and landscape preservation aspects, regular flooding of land areas is even indispensable to create a habitat for the highly specific, vulnerable flora and fauna of the salt marshes, which deserve special protection.

**Sustainable coastal development:** Sustainable coastal development in this context means to create a balance between coastal defence and environmental protection. Since 1974, the 9 countries bordering the Baltic have been co-operating within the framework of the Convention on the Protection of the Marine Environment of the Baltic Sea (or Helsinki Convention, according to its venue). Owing to the Baltic Sea's economic and ecological relevance to Northern Europe, it is one of the most intensively investigated marginal seas of the world. In Germany alone, 251 coastal research projects were officially recorded between 1990 and 1996, and the trend is upward. Internet search leads to a large number of national marine research institutes, shipping and environmental authorities, storm surge forecasting services, and to almost all universities in the area. Water level and storm surge forecasting for the Baltic Sea today is based mostly on operational hydrodynamic models using output data of the meteorological Europe model, but also statistical methods are used. HELCOM recommendations may be interpreted and implemented differently depending on local conditions. Both climate and sea level fluctuations as well as people's traditional ways of coping with nature's forces play a role in this respect. Near the oscillation nodes, i.e. near the center of the Baltic's longitudinal axis, storm surges of course do not reach the same high levels as at the end points. Since local coastal defence measures are based on past experience, the dykes built in such areas are generally lower. The problem that has to be dealt with in the different areas thus is identical: local and temporary aspects must be considered in the investigation of storm surge scenarios. The secular coastal dynamics of the Baltic (land gain in the north, land losses in the south) and the different local impacts of land/sea interactions (abrasion and accumulation coasts) require primarily the acceptance of natural processes, and human intervention should only come second.

**Climate and sea level fluctuations:** Since the last ice age, after the melting of glacial ice on Fennoscandia, the North Skandinavian landmasses have risen 80–90 cm per century. At the same time, a tilting motion of the Earth's crust has caused a 10–20 cm subsidence of the German Baltic coast per century. However, this fact only partly explains the increasing number of storm surges observed in the 20th century. Detailed investigations of storm surge occurrences have revealed correlation with characteristic atmospheric circulation patterns and certain parameters of the circumpolar low pressure zone (North Atlantic oscillation). Storm surges in the Baltic Sea thus also serve as an interesting indicator of climate developments in Central and Northern Europe. Numerous astronomical tides, primarily those having very long periods, have been identified in the mean sea levels of the Baltic. A significant cycle of 10–11 years has been found which is related to solar activity. However, as the changes observed in the parameters of the circumpolar low-pressure zone are extremely small, this causal relationship is still considered to be an unsatisfactorily proven despite the informative studies of CURRIE (1981) and LABITZKE and VAN LOON (1988). A different interpretation is rather unlikely, though, considering the fact that the phases of the 10–11 a signal measured at all Baltic gauges differ by about 130° between the northern and southern Baltic areas. The climate signal even exhibits a phase difference of about 170° in this respect. A counter-running trend like this, which could also be interpreted as a variable longitudinal tilt in the water surface, can only mean that the cause is an internal phenomenon of the Baltic region, which is not based primarily on hydrodynamic characteristics of the North Atlantic. Periods attributable to the latter (e.g. the Saros period, or half-period of moon apse-line cycle) only exhibit minor phase differences between the northern and southern Baltic Sea levels. The high correlation between wind fields in the Baltic and water levels in the time window of high and low water occurrences confirms this interpretation.

**Scenarios and statistics:** The physical processes and causes of storm surges in the Baltic will continue unchanged also in the future. The travel time of gravity waves is bound to a mean Baltic Sea depth of some 55 meters, so that even a hypothetical rise or fall of the mean sea level by one meter would not cause major changes in the natural periods of the Baltic. Forcing of storm surges depends, among other factors, on changes in wind direction and speed per space or time unit. For example, higher increase rates in a scenario of rapidly tracking low-pressure zones would be compensated partly by the shorter period available for integration of the water levels until high water stand. A preferred method for predicting regional trends during storm surges does not exist presently. Flood protection measures are based generally on the highest water levels on record and take into account regional sea level trends. In this context, the climate scenarios developed by the IPCC are undoubtedly relevant. However, with regard to the functionality of port facilities or initiatives of environmental protection organisations to protect salt marshes in the area, i.e. wherever a certain acceptance of storm surge events may be assumed, statistical methods are prefered in assessing the probability of flooding. Although they clearly indicate an increase in the number of small and medium-size flood events in the 20th century, they do not show significant increases in the high water crest values. Also statistically significant data beyond the scatter of measurements, which might confirm an acceleration of sea level rise in the 20th century, have not been found. Because of the Baltic's own dynamics, an analysis of its storm surge climate should be based rather on weather scenarios than on water level data.

*Sweden*

BERGSTEN (1955) studied the relationship between winds and the water levels on the coasts of Sweden. He stated (p. 32–133):

Generally, the water level in the South Baltic rises when the winds are northerly, and falls when they are southerly ... The consequence is that on the south coasts of Skane and Blekinge offshore winds will raise the water level, and winds from the sea will reduce it ... Another consequence is that the water level in the Sound and the Belts will be greatly changed in height; e.g., SW gales are blowing, as these will lower the water level in the South Baltic, and raise it on the west coast. The difference between the levels in the South Baltic and the west coast may in extreme cases be as much as a couple of meters. As far as the Sound is concerned, the difference is concentrated on the very short distance from Limhamn to Klagshamn, where a submarine bank runs from the Swedish to the Danish side, constituting the boundary between the Baltic and the western seas. North-easterly gales reverse these conditions.

The surges at five locations on the Baltic coast of Sweden for the storm surge of January 2–5, 1954, are shown in 7.28. This surge was generated by a northerly gale. The surge at Björn on January 3 is particularly interesting because it shows that the Aland archipelago acts as a strong barrier to the southward flow of water.

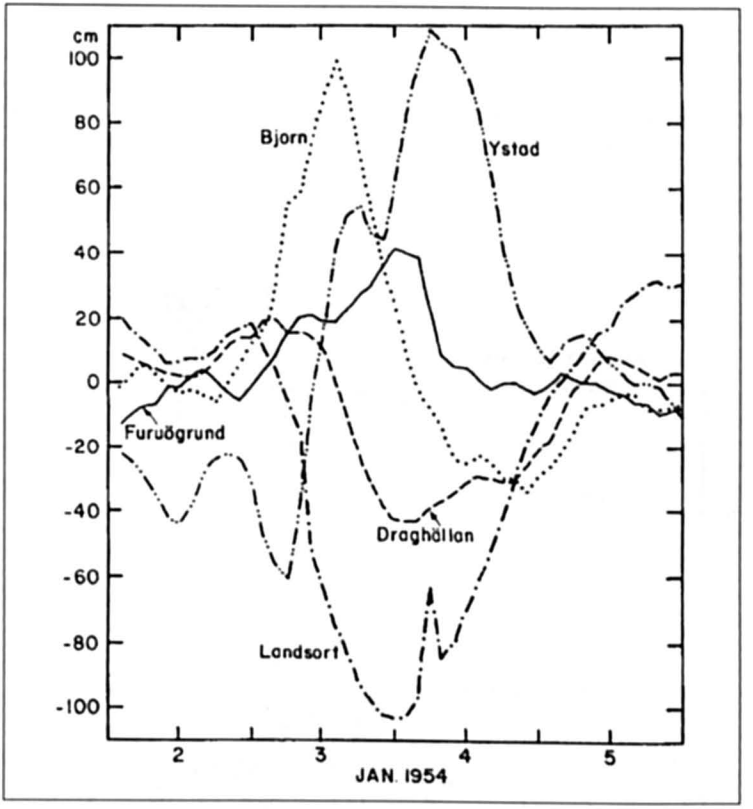


Fig. 7.28: Observed storm surges on the Baltic Sea coast of Sweden during January 2–5, 1954 (BERGSTEN, 1955)

*Denmark*

Denmark is attacked by storm surges at both the east and west coasts, i.e. from the Baltic Sea and the North Sea.

EGEDAL (1957) examined the storm surges at Randers on the east coast of Jutland. Depressions traveling over Jutland from the west cause north-northeasterly winds, which generate surges on the east coast of Jutland. Another area where surges are generated by such a weather system is the Island of Funen (Fyn). EGEDAL remarked that as far as storm surges are concerned, there are similarities between the east coast of Jutland and the east coast of the United Kingdom.

RINGE-JORGENSEN (1958) studied the storm surges along the North Sea coast of Denmark. The tidal amplitude varies from about 1.5 m near the Danish-German boundary to about 0.4 m at Thyboron. This study suggested that a meteorological situation similar to that of January 31–February 2, 1953, event could cause surges with amplitudes up to 3.4 m at Harlingen (Holland) and only about 1 m at Hanstholm (50 km north of Thyboron). The influence of the Norwegian Ditch appears to prevent the occurrence of very large amplitude surges at Thyborbn but permits the occurrence of a large number of moderate surges.

LACOUR (1917a) studied the storm surge of January 15–16, 1916. He presented tables of the surge amplitudes at 46 locations at every hour from 12:00 on the 15th to 00:00 on the 17th. He also showed several diagrams of winds, currents and the water level at various times. Peak surges up to 1.9 m occurred. The distribution of the storm surge heights at 06:00 January 16, 1916, is given in Fig. 7.29.

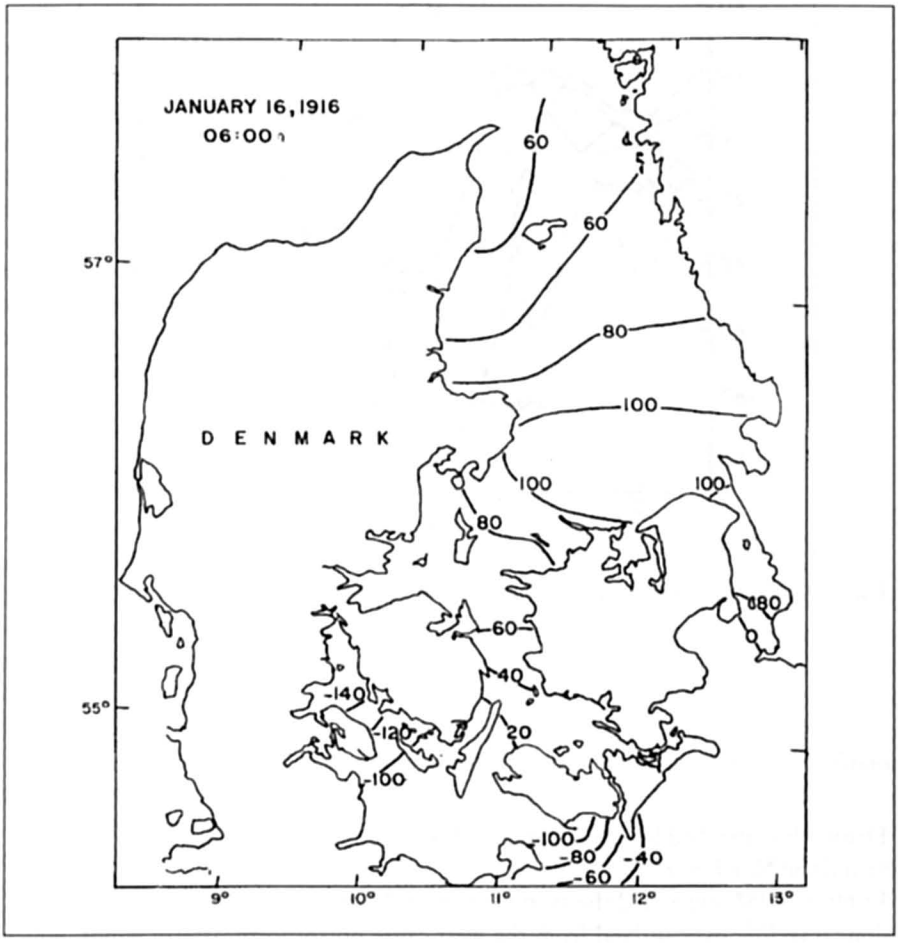


Fig. 7.29: Storm surge amplitudes along the east coast of Denmark at 06:00 on January 16, 1916 (LACOUR, 1932)

### 7.3.3 Irish Sea

In section 5.1.2 the meteorological situations leading to storm surges in the Irish Sea were discussed. The storm surge at Liverpool during December 29, 1921, to January 2, 1922, and the pressure data are shown in Fig. 7.30. CRESWELL (1929) presented storm surge amplitudes at Holyhead, Belfast, Fleetwood and Preston for the surge of October 20–24, 1928. These range from 1 ft 7 in. (48 cm) to 4 ft 7 in. (140 cm). However, a surge on October 29, 1927, had amplitudes of 7 ft 8 in. (2.34 m) at Fleetwood and 10 ft 2 in. (3.1 m) at Preston. For this event, the amplitudes at Holyhead and Belfast were 3 ft 4 in. (1.04 m) and 3 ft 2 in. (0.97 m), respectively.

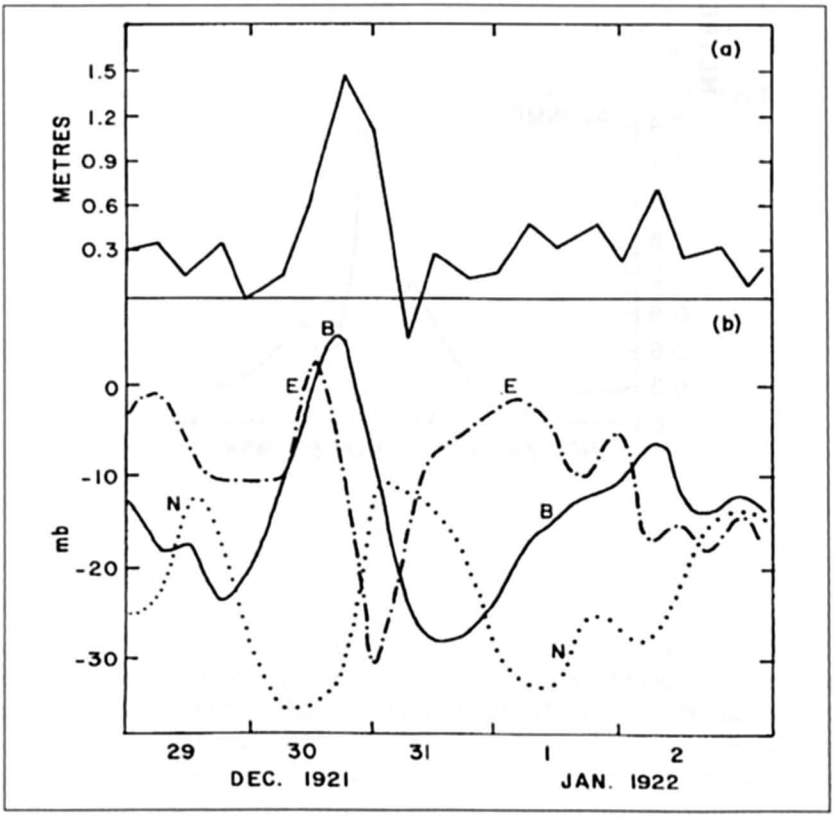


Fig. 7.30: (a) Storm surge at Liverpool, U.K., during December 29, 1921–January 2, 1922. (b) Curve B shows the fall of the atmospheric pressure at Liverpool; curves E and N, respectively, denote the east and north pressure gradients (millibars per 800 km) (DOODSON and DINES, 1929)

During the storm surge event of January 31, 1957, the surge amplitude at Liverpool reached a peak value of 3 ft whereas another event on February 4, 1957, produced a surge with amplitude of 5.8 ft (1.76 m). Another surge event of January 11–12, 1962, produced surges up to 5.5 ft (1.68 m) at Liverpool and up to 6.5 ft (1.98 m) at Avonmouth. The surges at Milfordhaven and Avonmouth during November 29–30, 1954, are shown in Fig. 7.31.

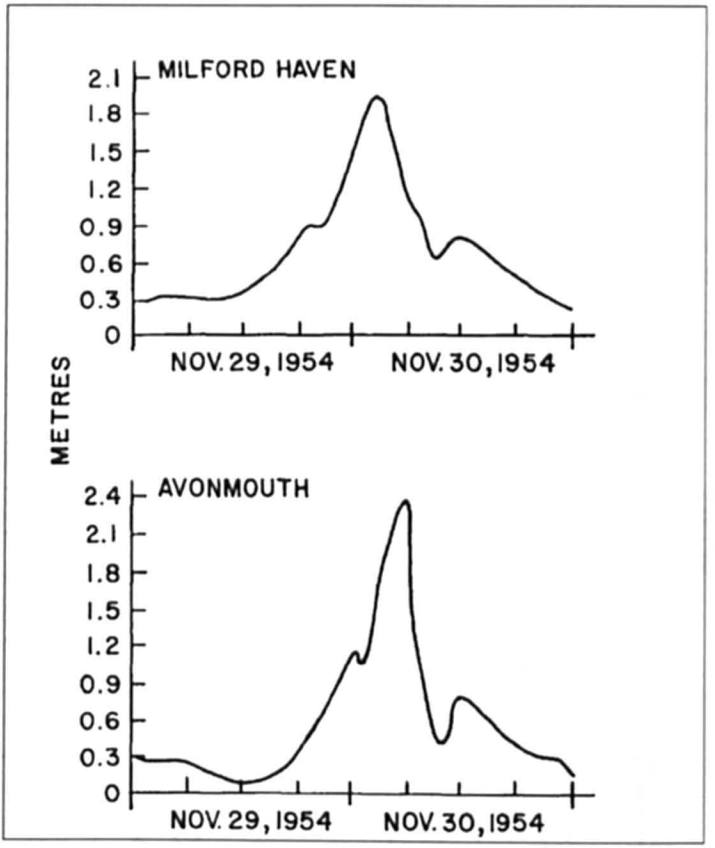


Fig. 7.31: Storm surges at Milford Haven and Avonmouth, U.K., during November 29–30, 1954 (HEAPS, 1967)

CORKAN (1952) mentioned that localized northerly winds over the Irish Sea would lower the water level everywhere in this water body, with the minimum decrease occurring at Liverpool. Strong southerly winds near the southern entrance to the Georges Channel will produce only small surges at locations such as Cork and Newlyn. After several hours, the general level rises in the Irish Sea. On the other hand, when a depression exists south of Ireland (with strong southerly winds blowing steadily) over the Bay of Biscay, surges up to 1–2 ft (03–0.6 m) could occur inside the region bordered by a hypothetical line joining Cork to Newlyn.

HEAPS and JONES (1975) simulated the storm surge in the Irish Sea for the event of January 10–18, 1965, using a two-and-a-half-dimensional model. The surge profiles at several locations in the Irish Sea (observed and computed) are shown in Fig. 7.32. The horizontal distribution of the storm surge heights at two different times is given in Fig. 7.33.

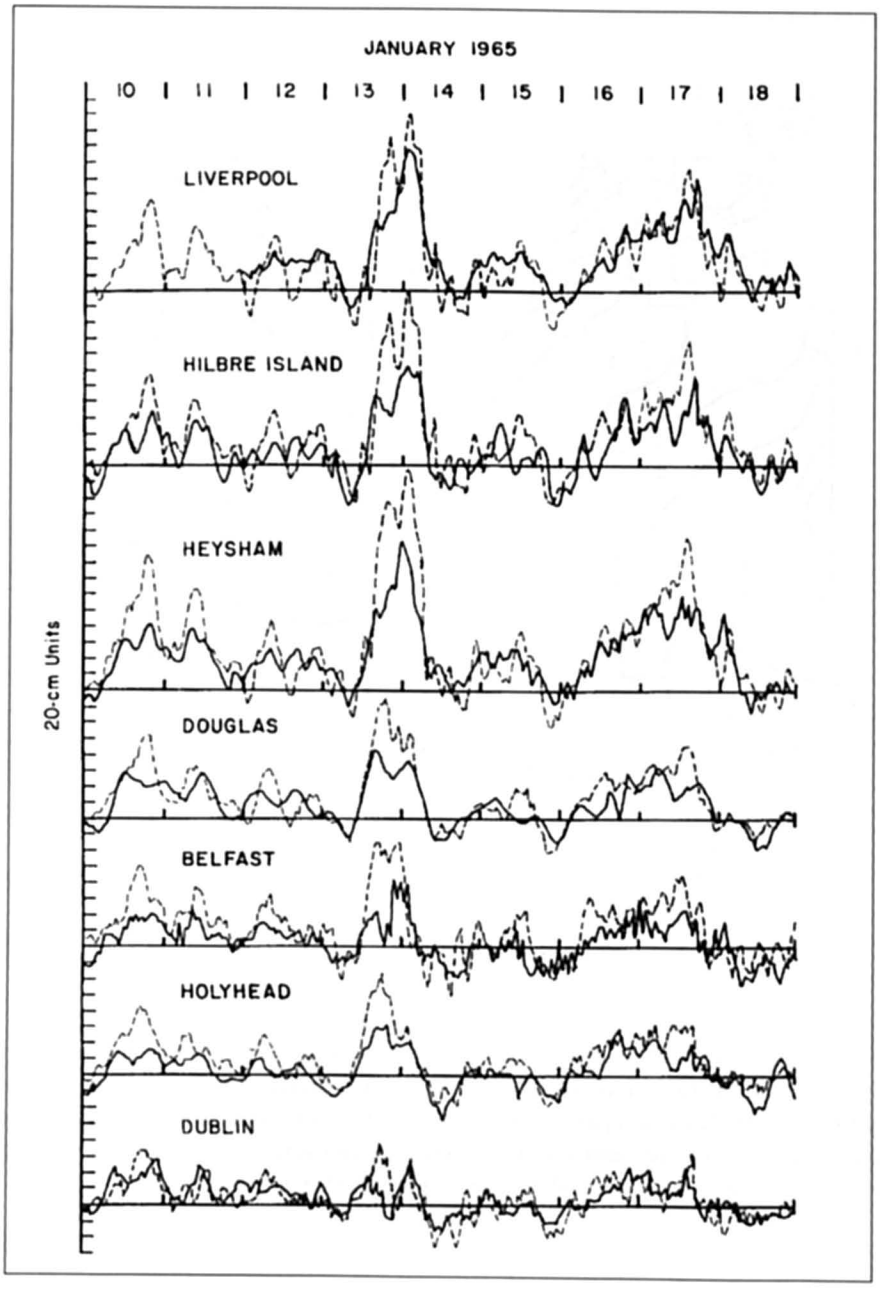


Fig. 7.32: Storm surges at various locations around the Irish Sea during January 10–19, 1965 (One unit = 20 cm along the ordinate) (HEAPS and JONES, 1975)

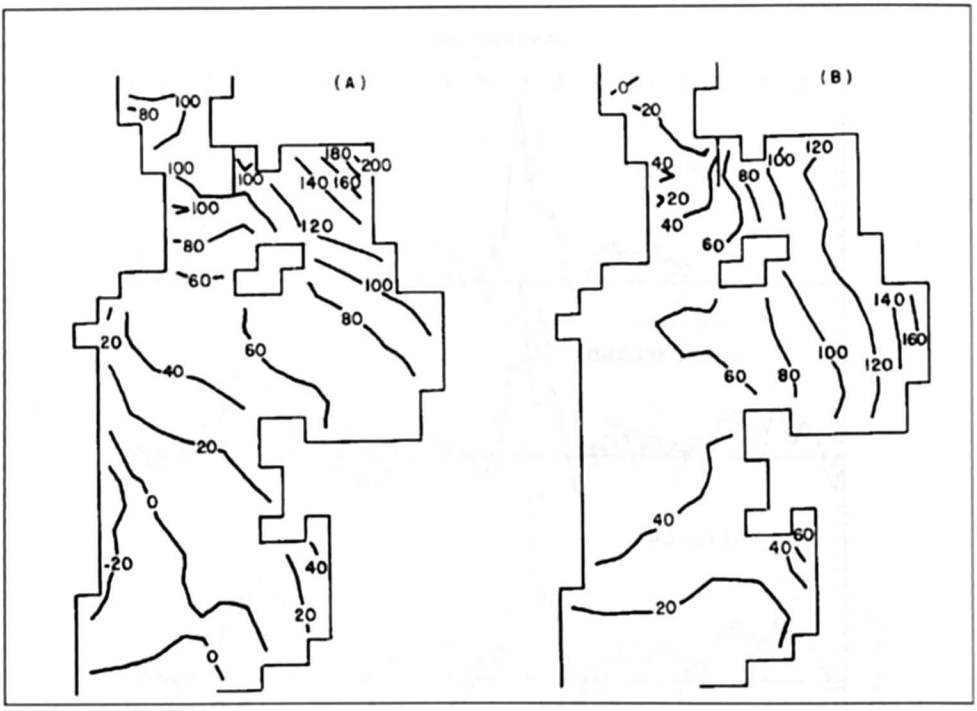


Fig. 7.33: Distribution of storm surge heights (centimeters) in the Irish Sea on January 14, 1965, at (A) 00:00 and (B) 04:00 (HEAPS and JONES, 1975)

HEAPS and JONES (1979) also simulated the storm surges in the Irish Sea for the events of November 11–15, 1977, and January 2–3, 1976, and compared these with the event of January 13–17, 1965. They paid particular attention to the time of occurrence of the peak surge relative to the times of high and low water. The tide and surge (computed and observed) at Liverpool and at Workington are shown in 7.34 and 7.35, respectively.

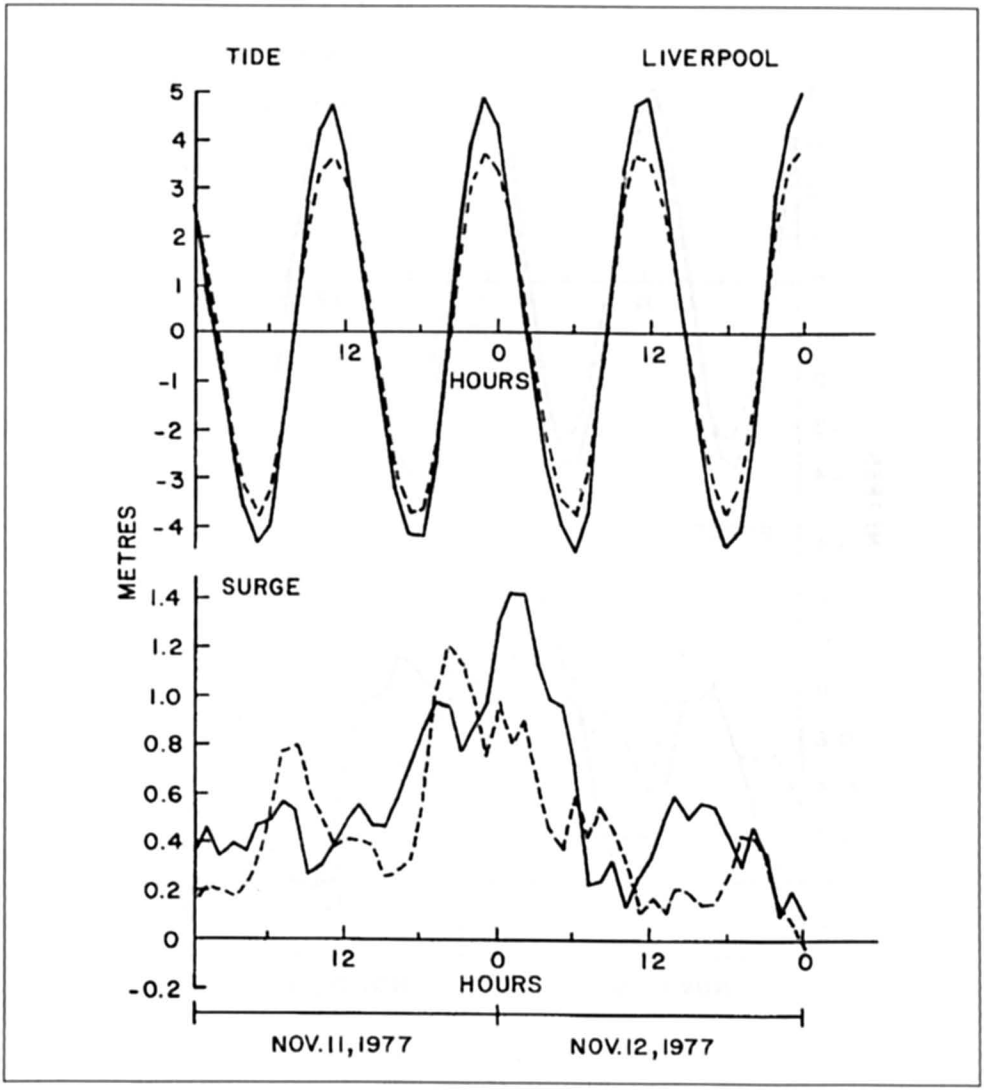


Fig. 7.34: Top: observed (solid line) and computed (broken line) tide at Liverpool during November 11–12, 1977. Bottom: observed (solid line) and computed (broken line) surge at Liverpool for the same period (HEAPS and JONES, 1979)

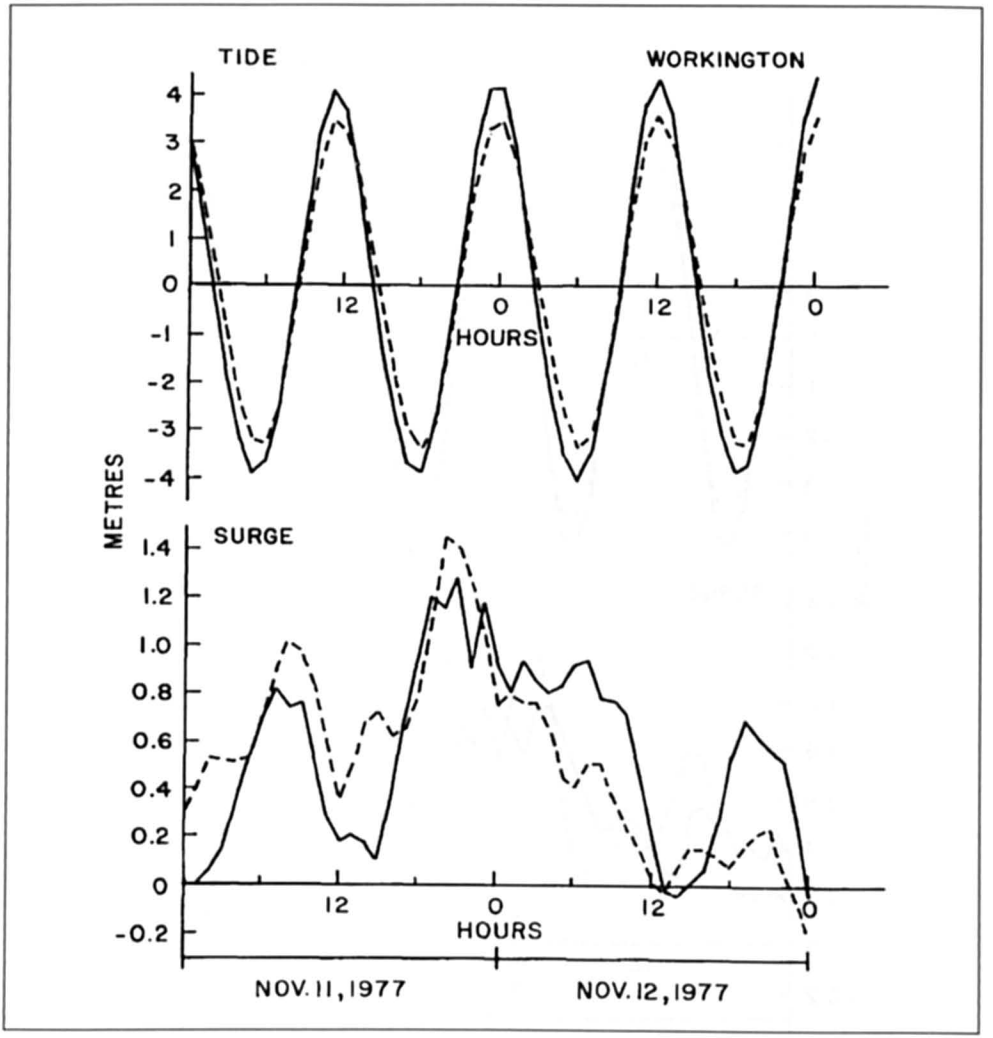


Fig. 7.35: Tide and storm surge at Workington, U.K. See Fig. 7.34 for explanation (HEAPS and JONES, 1979)

## 7.3.4 Mediterranean Sea

*France*

The North Sea coast of France was discussed earlier. Here, the Atlantic and Mediterranean Sea coasts of France will be considered.

FABRY (1909) studied the surge near Marseille (on the Mediterranean Sea coast of France) of June 15, 1909. The surge amplitude was between 0.4 and 0.8 m and an earthquake might have caused this, making this water level oscillation a tsunami rather than a storm surge. Some water level oscillations can occur in this region due to landslides.

CREPON (1974) studied water level oscillations on the Mediterranean coast of France. Note that in this area the tidal range is rather small (less than 1 m). Crepon applied his analytical theory to study the water levels at Sète located at the Mediterranean coast of France. Here, the continental shelf is about 100 km wide with a water depth of 90 m and there are no significant orographic influences on the wind field. The observed and computed water levels at this location for the period January–March 1969 are compared in 7.36. Some storm surge effects can be seen around the following dates: January 3–4, February 17–22, February 27, and March 21–23. It is interesting to note that the calculated water levels are systematically lower than the observed values. Also, the observed maximum values were about 0.5 m.

LACOUR (1917b) studied the storm surges at Brest (on the Atlantic coast of France) for the period 1861–1905. It appears that no significant surges occurred. One may conclude that storm surges are probably not significant in France except on the North Sea coast.

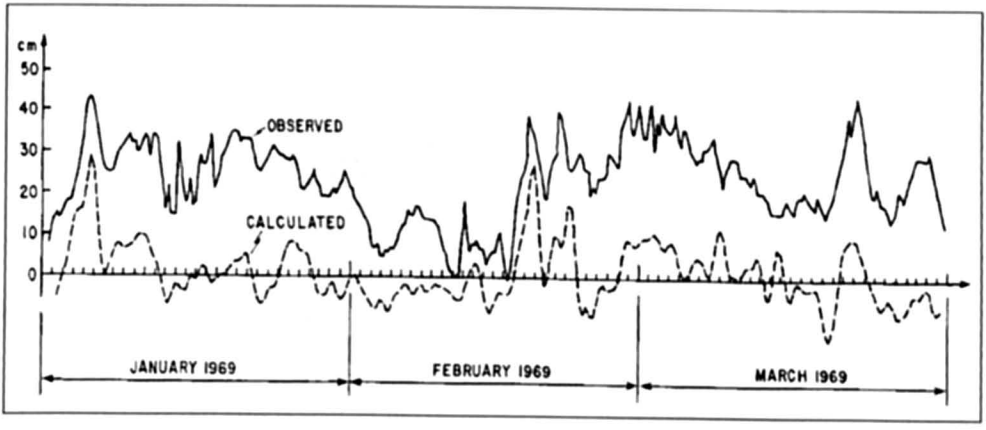


Fig. 7.36: Observed and calculated water levels at Sète (on the Mediterranean coast of France) for the period January–March 1969 (CREPON, 1974)

*Israel*

STRIEM (1974) studied the storm surges at Ashdod at the Mediterranean coast of Israel using the data for a 6yr period (1965–70). The tide here is mainly semidiurnal with a range of less than 1 m. The data for this study were selected whenever the daily mean sea level exceeded the average level by at least 20 cm and when there was a storm present.

STRIEM (1974) used the term "storm surge" to denote the changes in sea level at Ashdod during a period of several days due to storms in the eastern part of the Mediterranean Sea and

the term "storm set-up" to denote the rapid changes in the water level during a few hours. Three examples of these storm set-ups are shown in 7.37.

The six largest positive storm surges at Ashdod during the period of this study are summarized in Table 7.9a. The six largest negative storm surges at Ashdod are listed in Table 7.9b. The factors that cause the sea level to rise and fall at Ashdod are summarized in Tables 7.10 and 7.11, respectively. It was found that the storm surges at Ashdod basically are gradual changes in the daily mean sea level and that these changes could be linearly correlated with daily mean values of wind wave heights and wind velocities at the shore.

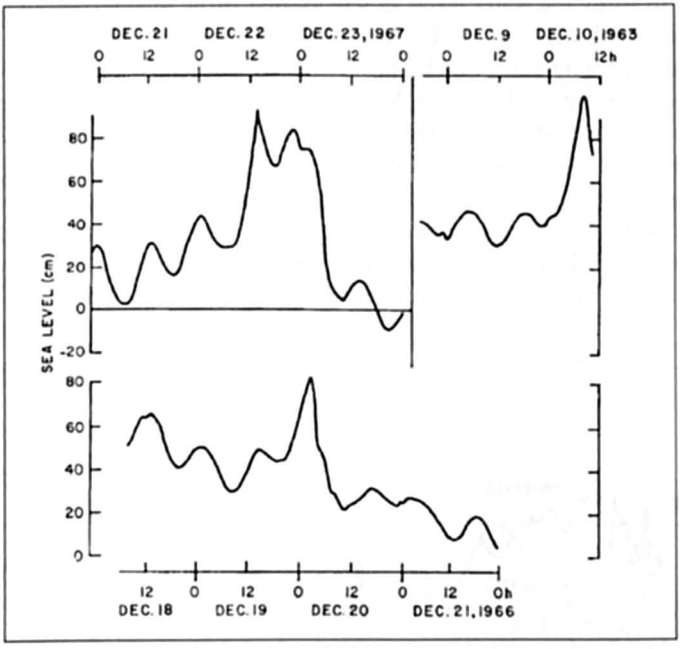


Fig. 7.37: Storm surges at Ashdod, Israel. Examples are shown of rapid changes. Top left: December 21–23, 1967; top right: December 9–10, 1963; bottom: December 19–21, 1966 (STRIEM, 1974)

Table 7.9a: Six largest positive storms surges at Ashdod, Israel, during 1965–70 (STRIEM, 1974)

| Date | Amplitude of surge (cm) |
|---|---|
| Dec. 10, 1963 | 100 |
| Dec. 22, 1967 | 93 |
| Dec. 20, 1966 | 83 |
| Feb. 5, 1965 | 63 |
| Mar. 26, 1967 | 63 |
| Jan. 14, 1968 | 63 |

Table 7.9b: Six largest negative storm surges at Ashdod, Israel, during 1965–70 (STRIEM, 1974)

| Date | Amplitude of surge (cm) |
|---|---|
| Jan. 29, 1964 | 51 |
| Mar. 24, 1966 | 46 |
| Mar. 26, 1968 | 45 |
| Feb. 12, 1968 | 42 |
| Oct. 16, 1970 | 41 |
| Apr. 12, 1968 | 40 |

Table 7.10: Factors contributing to the rise of sea level at Ashdod, Israel (STRIEM, 1974)

| Factor | Time of occurrence | Approx. maximum rise of sea level (cm) |
|---|---|---|
| (a) High of spring tides | Vernal equinox | + 26 |
| (b) High of the seasonal fluctuation | Midsummer | + 10 |
| (c) High annual mean sea level | | + 7 |
| (d) Rise due to daily inequality of the tides | | + 5 |
| Total of effects not due to wind | | + 48 |
| (e) Storm surges | Winter | + 40 |
| (f) Storm set-up | Winter | + 40 |

Table 7.11: Factors contributing to the lowering of sea level at Ashdod, Israel (STRIEM, 1974)

| Factor | Time of occurrence | Approx. maximum fall in sea level (cm) |
|---|---|---|
| (a) Extreme low of spring tides | Vernal equinox | – 26 |
| (b) Low of the seasonal fluctuation | End of spring | – 10 |
| (c) Low of annual levels | | – 6 |
| (d) Lowering due to daily inequality of the tides | | – 5 |
| Total of effects not due to wind | | – 47 |
| (e) Lowering due to eastern (offshore) winds (or down-surge after onshore storms) | | – 15 (or – 30) |
| Possible lowering due to occurrence of all factors | | – 62 (or –77) |

*Egypt*

Storm surges occur in the Suez Canal and also at the Mediterranean coast of Egypt. MURTY and ELSABH (1981) studied the storm surges at Port Said at the northern end of the Suez Canal and at Port Suez at the southern end of the canal using the data for 1966.

Table 7.12: Number of occasions (treating each hourly value as one case) when positive and negative storm surges at Port Said, Egypt, exceeded prescribed amplitudes in 1966

| | Surge height (cm) | | | | | | | | | |
|---|---|---|---|---|---|---|---|---|---|---|
| State of tide | 10 | 20 | 30 | 40 | 50 | 60 | 70 | 80 | 90 | 100 |
| Positive surges | | | | | | | | | | |
| Low tide | 253 | 189 | 90 | 28 | 9 | 5 | 1 | 1 | 1 | 1 |
| Rising tide | 236 | 137 | 51 | 10 | 1 | 0 | 0 | 0 | 0 | 0 |
| High tide | 237 | 131 | 44 | 2 | 0 | 0 | 0 | 0 | 0 | 0 |
| Falling tide | 246 | 175 | 82 | 26 | 6 | 2 | 1 | 0 | 0 | 0 |
| Negative surges | | | | | | | | | | |
| Low tide | 19 | 7 | 3 | 2 | 0 | 0 | 0 | 0 | 0 | 0 |
| Rising tide | 16 | 9 | 3 | 2 | 1 | 1 | 0 | 0 | 0 | 0 |
| High tide | 12 | 5 | 1 | 1 | 1 | 1 | 1 | 1 | 1 | 1 |
| Falling tide | 13 | 5 | 0 | 0 | 0 | 0 | 0 | 0 | 0 | 0 |

The length of the Suez Canal is about 175 km and the average depth is 15 m. At Port Said the tide is co-oscillating with the eastern part of the Mediterranean Sea and has an amplitude of 25 cm. At Port Suez the Red Sea tidal influence is felt and has an amplitude of 75 cm. Based on these features the Suez Canal can be classified into a long estuary, in the Proudman sense (discussed earlier under Tide-Surge Interaction in the North Sea and in the St. Lawrence Estuary).

Treating each hourly surge value as one case, the number of occasions when positive and negative surges exceeded prescribed values at Port Said and Port Suez is given in Tables 7.12 and 7.13, respectively. Earlier, it was seen that PROUDMAN'S theory (1957) suggested that for a long estuary, for a tide of progressive wave type, maximum surges are associated predominantly with low tide (or rising tide), and for a tide of standing wave type, maximum surges are associated predominantly with high tide (or falling tide). Observations for 1966 showed that the theoretical results of PROUDMAN, when interpreted for the Suez Canal, agreed with the observations at Port Said but not with those at Port Suez.

Table 7.13: Number of occasions (treating each hourly value as one case) when positive and negative storm surges at Port Suez, Egypt, exceeded prescribed amplitudes for positive surges and 10–90 cm for negative surges in 1966

| | Surge height (cm) | | | | | | | | | | | | | |
|---|---|---|---|---|---|---|---|---|---|---|---|---|---|---|
| State of tide | 10 | 20 | 30 | 40 | 50 | 60 | 70 | 80 | 90 | 100 | 110 | 120 | 130 | 140 |
| Positive surges | | | | | | | | | | | | | | |
| Low tide | 172 | 111 | 75 | 44 | 32 | 16 | 8 | 3 | 3 | 3 | 3 | 3 | 2 | 1 |
| Rising tide | 191 | 110 | 76 | 38 | 13 | 7 | 6 | 6 | 3 | 1 | 0 | 0 | 0 | 0 |
| High tide | 121 | 57 | 18 | 5 | 2 | 1 | 1 | 1 | 1 | 0 | 0 | 0 | 0 | 0 |
| Falling tide | 174 | 107 | 50 | 34 | 27 | 23 | 10 | 3 | 0 | 0 | 0 | 0 | 0 | 0 |
| Negative surges | | | | | | | | | | | | | | |
| Low tide | 84 | 66 | 46 | 32 | 16 | 11 | 3 | 0 | 0 | | | | | |
| Rising tide | 104 | 69 | 45 | 45 | 14 | 21 | 1 | 0 | 0 | | | | | |
| High tide | 117 | 69 | 59 | 49 | 40 | 24 | 6 | 0 | 0 | | | | | |
| Falling tide | 113 | 84 | 55 | 27 | 38 | 9 | 9 | 2 | 1 | | | | | |

### 7.3.5 European Part of the Atlantic Ocean

Storm surges at the Atlantic coast of France have been described before. Storm surges can also occur at the northern part of the Atlantic coast of Portugal (MORAIS and ABECASIS, 1975). The tidal range in this area is about 3–8 m and wind waves up to 13 m can occur here. A surge during January 16–17, 1973, did considerable damage in the Leixoes Harbour. The damage was severe because the surge occurred at the time of spring tide. The center of a low pressure system passed over Leixoes and its exceptionally long duration of 24 h generated very large wind waves.

In the surge record, waves with periods between 4 and 40 min attained significant amplitudes. Leixoes Harbour exhibits a seiche with a 4-min period, which was amplified by resonance. There is evidence of the occurrence of a Helmholtz mode type motion also.

Storm surges occurred again in January and February 1974 but the damage was minimal.

### 7.3.6 Adriatic Sea

In Italy, storm surges occur along the Ligurian Sea coast, the Tyrrhenian Sea coast, and the Adriatic Sea coast. On February 18, 1955, a cyclone caused great damage to the breakwater in Genoa Harbour (GRIMALDI, 1955; D'ARRIGO, 1955). Strong winds from the southwest-generated wind waves with greater than 7-m amplitudes and possibly also a storm surge. Some of the water level problems in the Ligurian Sea associated with weather systems were discussed in section 5.1.2. Northeastern Italy is a region where storm surges occur. BONDESAN et al. (1995) investigated the effect of global change on sea surges and stated that the frequency would increase.

The city of Venice is located at a lagoon off the Adriatic Sea and less than 1 m above the mean sea level. Hence, storm surges with amplitudes less than even 1 m cause serious flooding problems in Venice. To add to the problem, the openings between the sea and the lagoon are more extensive now (due to dredging) than before, which allows the storm surge from the sea to travel unimpeded. In addition, in the twentieth century the city subsided by 20 cm.

Storm surges occur quite frequently in this area (TOMASIN and FRASETTO, 1979), for example, in the years 1966, 1967 and 1972. The storm surge season lasts from November to February and occasionally to April. The first two normal modes of the Adriatic Sea have periods quite close to the diurnal and semidiurnal tides. The tidal range is 25–80 cm, the tide being forced by the Mediterranean Sea. There appears to be no interaction between the tide and the surge.

TOMASIN and FRASETTO (1979) studied the surge of April 21–22, 1967 (Fig. 7.38). What makes the problem more complicated is a seiche with a period of about 1 d that can be excited by weather systems. Such a seiche during February 16–20, 1967, is shown in Fig. 7.39. Observed and computed surges at Venice for February 12, 1972, are shown in Fig. 7.40. In the fall of 1982, major storm surges occurred at Venice and Trieste causing considerable damage.

In 1975 the Italian government devised a plan to reduce the effects of tides and storm surges at Venice by constructing barriers to narrow the entrances to the Venice lagoon (VITTORI and TAMPIERI, 1979).

The commune of Venice operates a statistical forecast model. ADAMI and NOLI (1992) describe this model and present an alternative modelling tool, which has been tested by the Danish Hydraulic Institute. "It was found that the existence of reliable air pressure predictions could increase the forecast horizon of reliable storm surge prediction from 3 to 24 hours."

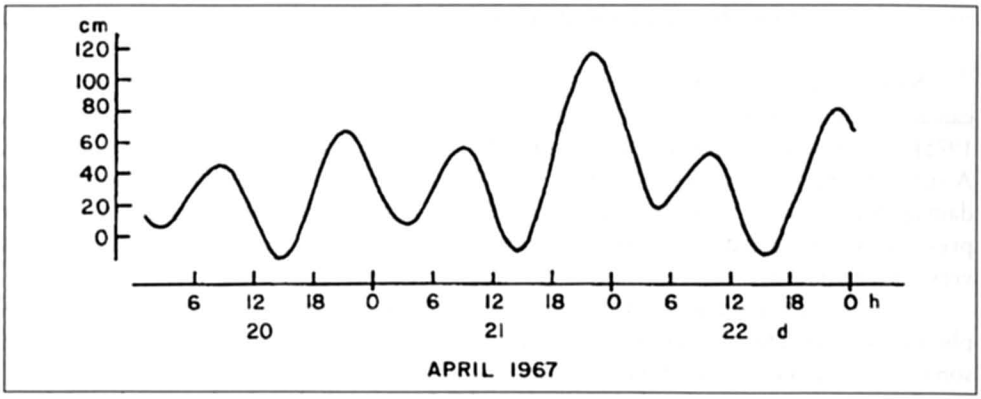


Fig. 7.38: Recorded water level (tide plus surge) at Venice, Italy, during April 20–22, 1967. Time is GMT – 1 (TOMASIN and FRASETTO, 1980)

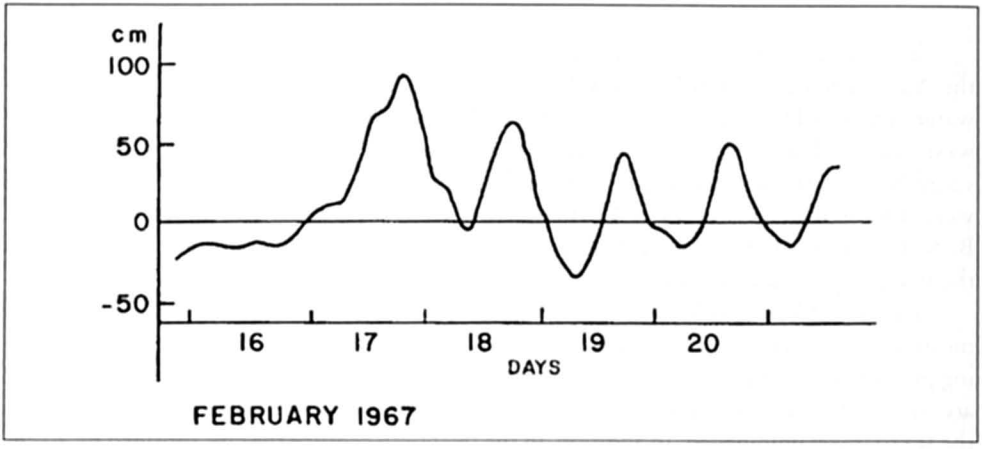


Fig. 7.39: Seiche at Venice, Italy, with a period of approximately 24 h (TOMASIN and FRASETTO, 1979)

STRAVISI (1972) used a one-dimensional numerical model to simulate hypothetical storm surges in the Adriatic Sea. Storm surge amplitudes at two different times are shown in Fig. 41. ADAMI and NOLI (1992) also carried out research on a forecasting system with a hydrodynamic model for the Adriatic. The Danish Hydraulic Institute calibrated a 2D model to reproduce tidal phenomena and seiching. To calibrate the storm surges at least seven historical surge events were simulated with storm winds and air pressures. With good meteorological data storm surge prognosis was very good for forecast up to 5 days.

For the Northern Adriatic Sea MAZARELLA and PALUMBO (1991) took into consideration the seasonal, 11-yr. and secular signals, which are more significant and several times larger than those in the mean sea level for the computation of the storm surge development and mean sea level rise. They stated that analyses of sea level maxima adjusted for such time variations, gives a more adequate and realistic basis for making predictions on the occurrence of damaging storm surges. Data from the gauges at Venice (1924–1970) and Trieste (1944–1988) have been investigated. After using the extension of the annual maxima approach from earlier work for calculation of the occurrence of extreme events calculated non-cycle

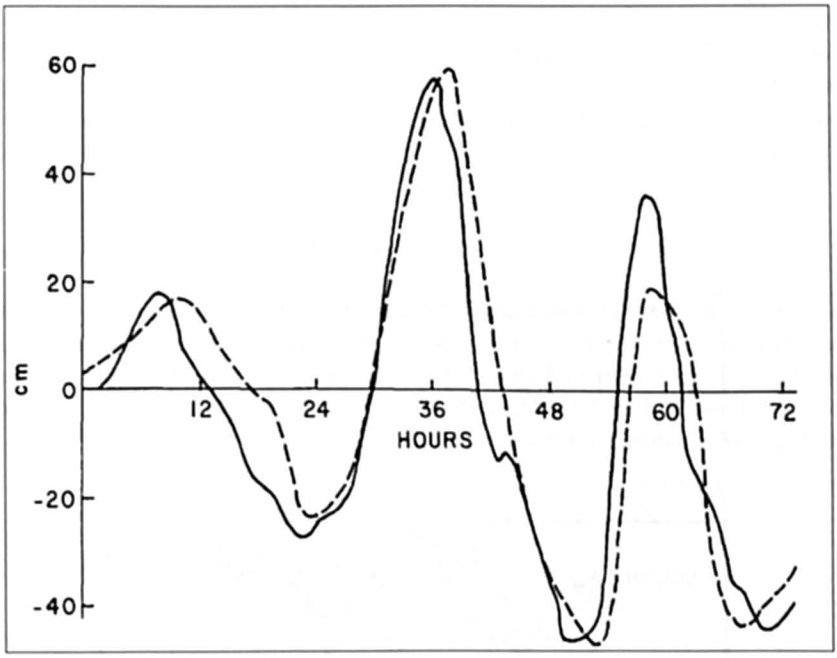


Fig. 7.40: Computed (broken line) and observed (solid line) surges at Venice during February 12–15, 1972. Time is hours from the starting time of 03:00 (GMT) on February 12, 1972 (TOMASIN and FRASETTO, 1979)

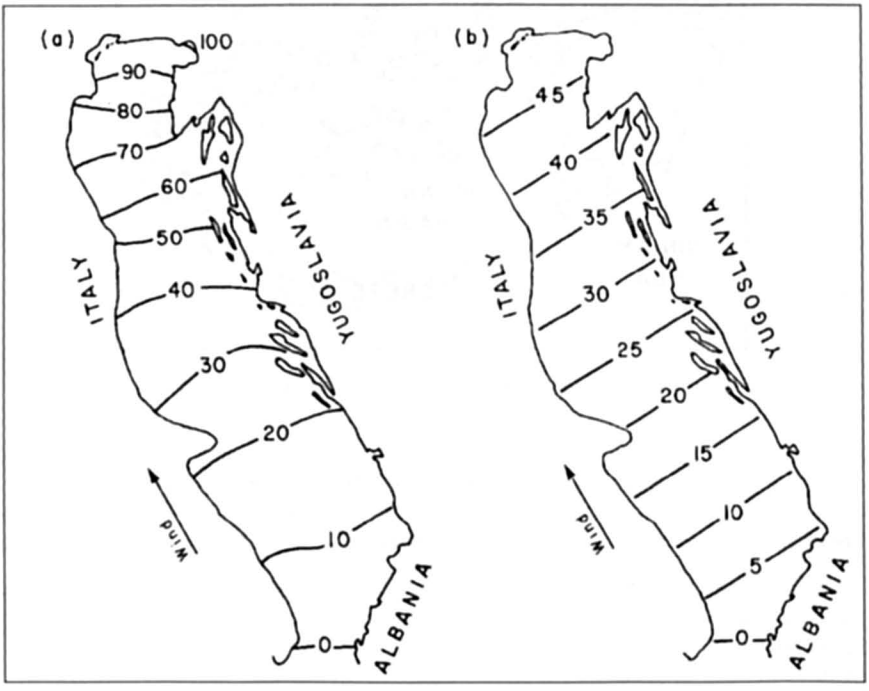


Fig. 7.41: Distribution of the amplitudes (centimeters) of a hypothetical storm surge in the Adriatic Sea at (a) 10 h and (b) 11 h after the start of wind stress application (STRAVISI, 1972)

variations of yearly SL mean and SL max, cycle variations seasonal and 11 yr. Waves have been carried out. MAZARELLA and PALUMBO (1991) summarised their results by stating that "the estimate of the return period obtained by means of the monthly maxima (filtered from seasonal, biennial and longer term non-stationary) is more robust against historical outliers than the analysis of annual maxima."

### 7.3.7 Aegean Sea

WILDING et al. (1980) studied tides and storm surges in the northwestern part of the Aegean Sea. The geography of this area is shown in Fig. 7.42. The tides are rather small in this water body, as can be seen from Table 7.13. The surges during August 20–23, 1975, at three locations are shown in Fig. 7.43. The power spectrum of half-hourly water level records is given in Fig. 7.44. Predominant periods of 2.68 and 2.40 h can be seen.


Fig. 7.42: Geography of the Aegean Sea (WILDING et al., 1980)

Table 7.14: Tides in the Aegean Sea (WILDING et al., 1980)

| Location | Mean spring range (cm) | Mean neap range (cm) |
|---|---|---|
| Port Salonica | 32.4 | 9.6 |
| Saint Trias | 29.0 | 6.6 |
| Krini | 29.6 | 4.4 |
| Whaniona | 29.4 | 5.0 |
| Kayoura | 29.0 | 4.6 |

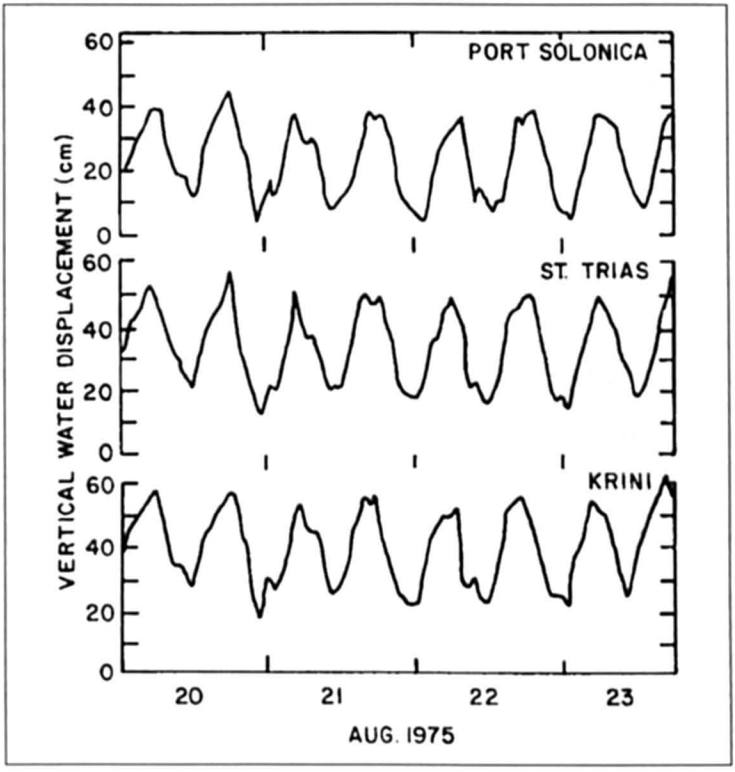


Fig. 7.43: Water level oscillations during August 20–23, 1975, at three locations in the Aegean Sea (WILDING et al., 1980)

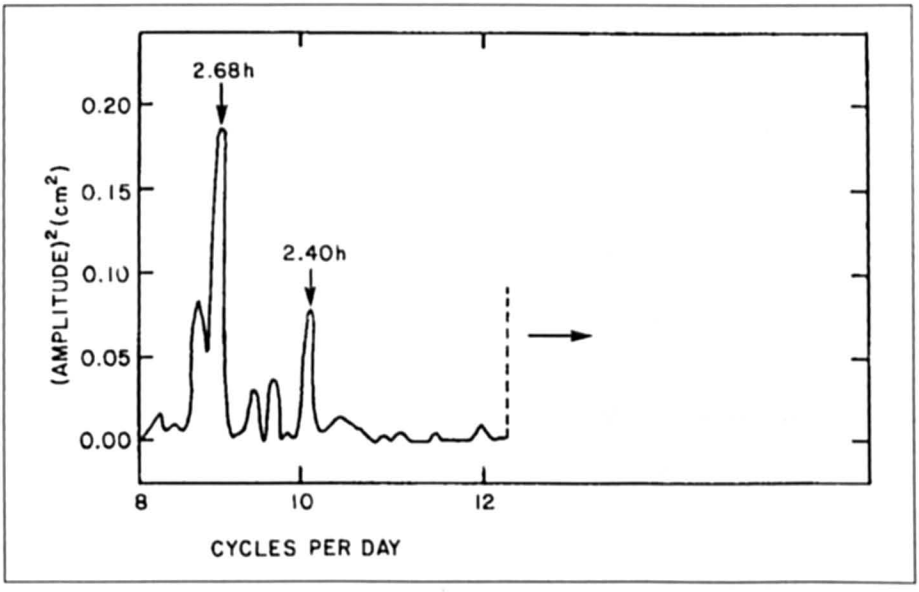


Fig. 7.44: Power spectrum of half-hourly water level data at Port Solonica (Aegean Sea) (WILDING et al., 1980)

### 7.3.8 Black Sea, the Okhotsk Sea and the Pacific

Moderate storm surges occur in the Black Sea, the Okhotsk Sea, the Pacific coast of Russia, the East Siberian Sea, and the Chukehi Sea. Large surges (up to 6 m in amplitude) can occur in Lake Baikal. Winds from north of this lake can produce surges that sometimes take only a few minutes to develop.

Earlier, the work of LAPPO and ROZHDESTVENSKIY (1977, 1979) was discussed in which they considered the lag of storm surges with reference to the atmospheric systems. Their work covered the northwest part of the Pacific Ocean in general and the Pacific coast of Russia near the Kurile Islands in particular. They considered the contribution of the static surge to the total water level deviation and developed the important concept of the hysteresis loop (Fig. 6.123). The lag between the atmospheric forcing and the storm surge could be anywhere between 5 and 18 h on this part of the Russia coast.

KOWALIK and POLYAKOV (1998) studied the tides in the Sea of Okhotsk. This is a region of large tidal sea level oscillations and strong tidal currents. The oscillation reaches 13 m in Penzhinkaya Guba. GORDAY et al. (1991) investigated extreme parameters of tsunamis in the region of Kuril-Kamchatka Trench and the Sea of Okhotsk using numerical simulation results.

MUSTAFIN (1969) studied the storm surges in the East Siberian and Chuckchi seas with the particular aim of predicting the surges at Cape Schmidt. Based on 192 cases during the summer period (July–October) for 1951–55, in which the surges at Cape Schmidt and in Ambarchik Inlet exceeded 30 cm (both positive and negative surges), he prepared the following regression relationships:

$$\Delta h_{Schm} = a_1 \Delta p_1 \cos \alpha_1 + a_2 \Delta p_2 \cos \alpha_2 + a_3 \Delta h_{Amp} \qquad (7.1)$$

$$R = 0.94 \pm 0.001, \qquad \Sigma = 21$$

$$\Delta h_{Schm} = a_4 \Delta h_{Amp} \qquad (7.2)$$

$$R = 0.90 \pm 0.01, \qquad \Sigma = 26$$

$$\Delta h_{Schm} = a_5 \Delta p_1 \cos \alpha_1 + a_6 \Delta h_{Amp} b_1 \qquad (7.3)$$

$$R = 0.93 \pm 0.004, \qquad \Sigma = 23$$

$$\Delta h_{Schm} = a_7 \Delta p_2 \cos \alpha_2 + a_8 \Delta h_{Amp} b_3 \qquad (7.4)$$

$$R = 0.92 \pm 0.007, \qquad \Sigma = 24$$

$$\Delta h_{Schm} = a_9 \Delta p_1 \cos \alpha_1 + a_{10} \Delta p_2 \cos \alpha_2 + b_4 \qquad (7.5)$$

$$R = 0.88 \pm 0.01, \qquad \Sigma = 29 \qquad (7.6)$$

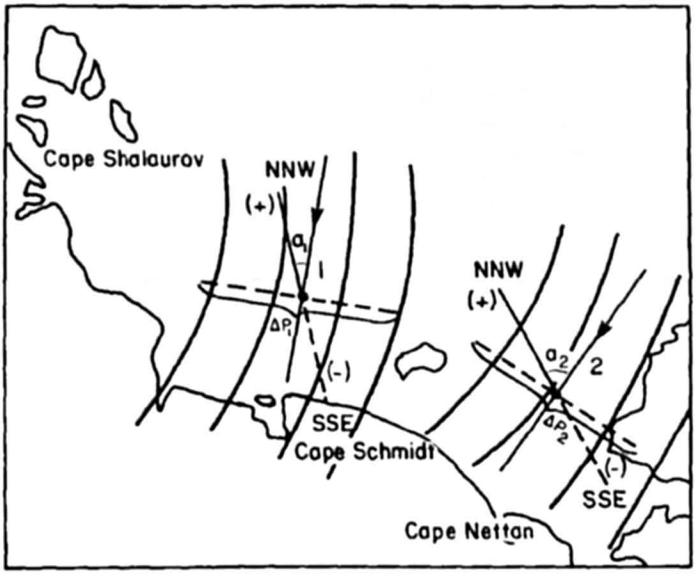


Fig. 7.45. Determination of the quantities $\Delta p_1$, and $\Delta p_2$ and the wind current direction from the isobars at points 1 and 2 (see eq. 7.1–7.6). $a_1$ and $a_2$ are the angles between the wind current direction (arrows) and the effective refluxing-fluxing direction north-northwest to south-southeast. The angles are acute and determine positive components (+) of $\Delta p_1$, and $\Delta p_2$ at the time of sea level fluxing motions and negative components (–) at the time of sea level refluxing wind directions (MUSTAFIN, 1969)

where, $\Delta h_{Schm}$ is the deviation (centimeters) of the no periodic factor in the sea level at Cape Schmidt from the mean annual navigational level, precalculated with an average forewarning period of 12–13 h upward (+) and downward (–); $\Delta h_{Abm}$ is the deviation (centimeters) of the actual sea level in Ambarchik Bay from the mean annual navigational level upward (+) and downward (–); $\Delta p_1$, and $\Delta p_2$ are the respective pressure differences (millibars) at points 1 and 2 at a distance of 600 km (6 cm on a 1 : 10,000,000 scale map) along lines perpendicular to the isobaric trend (Fig. 7.45 of this chapter and Fig. 7 of MUSTAFIN, 1969); $a_1$ and $a_2$ are the angles between the wind direction along the isobars and the line running north-northwest and south-southeast (Fig. 7.45 of this chapter and Fig. 7 of MUSTAFIN (1969); $a_1, \ldots, a_{10}$ are constants; $b_1, \ldots, b_4$ are free terms; R and r are multiple and partial correlation coefficients and their probable errors; and $\Sigma$ is the mean square root error (centimeters) of the regression equation.

Parameters $\Delta p_1$, $\Delta p_2$, $a_1$, $a_2$, etc., needed here are determined as shown in Fig. 7.45. One of the interesting features of this study is that, in contrast with the universally used technique of determining the atmospheric pressure gradients along constant directions, here, these gradients are calculated along variable directions but at pre-selected locations in the water body.

MUSTAFIN's (1969) study was done for nine locations on the Siberian coast. Since knowing the water level at one location in advance might help the prediction at other locations, MUSTAFIN (1969) tabulated the correlation coefficients for the water levels between these stations. These are shown in Table 7.15. On this coast, the surges appear to lag the meteorological forcing by about 12 or 13 h.

Table 7.15: Correlation coefficients between the storm surges at various locations on the East Siberian Sea and Chuckchi Sea coasts (MUSTAFIN, 1969)

| | Cape Shalau-Rov | Ambar-chik Inlet | Rau-Chua | Pevek | Cape Billings | Cape Schmidt | Cape Vanka-rem | Koly-uchin Island | Cape Nettan |
|---|---|---|---|---|---|---|---|---|---|
| Cape Shalaurov | 1 | 0.86 | 0.83 | 0.85 | 0.82 | 0.75 | 0.70 | 0.84 | 0.77 |
| Ambarchik Inlet | | 1 | 0.95 | 0.97 | 0.79 | 0.80 | 0.74 | 0.83 | 0.70 |
| Rau-Chua | | | 1 | 0.97 | 0.88 | 0.87 | 0.86 | 0.80 | 0.74 |
| Pevek | | | | 1 | 0.85 | 0.90 | 0.67 | 0.81 | 0.85 |
| Cape Billings | | | | | 1 | 0.86 | 0.83 | 0.71 | 0.77 |
| Cape Schmidt | | | | | | 1 | 0.84 | 0.84 | 0.91 |
| Cape Vankarem | | | | | | | 1 | 0.78 | 0.81 |
| Kolyuchin Island | | | | | | | | 1 | 0.85 |
| Cape Nettan | | | | | | | | | 1 |

### 7.3.9 Storm Surge Forecasting

Storm surge forecasting and quick dissemination of warnings are of high importance for people living at coastlines and tidal rivers behind the dykes. This addresses the demand, that a storm tide forecasting method must satisfy the highest level of scientific standards that can be reached. Methods that are developed by hindcasting 5 to 10 special storm tides are not serious enough. Investigations show that we have to consider many more different surge types. The description follows closely IHP-OHP (IHP-OHP, SIEFERT and MURTY, 1991), and also based on CHRISTIANSEN and SIEFERT (1979), SIEFERT (1980).

The following examples are designed to give a survey of the state of present-day practice-orientated storm surge research and its application. Regional and supraregional systems will be mentioned in this connection.

#### *The English East Coast*

Following the storm surge of Jan. 31/Feb. 1, 1953, leaving behind on the English east coast 300 victims and 24.000 destroyed homes, a research group came to the decision that a warning system for high storm surges between Northhumerland and Kent should be established and investigations be made simultaneously as to whether such system should also cover the Channel, the Bristol Channel and the Irish Sea. Assuming that surges during the neap tide might be neglected, the warning service decided that storm surge prediction will be made only during spring tide. But since at certain locations on the east coast the height differences between spring and neap tides are insignificant so that a surge during neap tide can cause damage, the warning service must operate independent of the type of surge prevailing.

Storm surges on the English east coast develop from the North to the South. First indications as to potential storm surges can be obtained at the first arrival of tidal waves in the North Sea in the region of the Shetland Islands, partly even near the Hebrides. The forecasting system has been set up accordingly. One tries to recognize the storm surges, if possible, already far away in the north and to determine the height at the reference gauges using wind forecasts. Reference gauges are Stornoway/Hebrides, Wick, and Aberdeen.

From the northern tip of Scotland (John o'Groats) the tidal wave needs about 4 h to reach the English border and then another 9 h to reach the Thames. It is, of course, an advantage that such storm surges at the early stage of inaccurate forecasts first reach almost unpopulated coasts in less need of protection. Actual forecasts are being made only for the English east coast, which is subdivided into 5 divisions with one reference gauge, each Fig. 7.46.

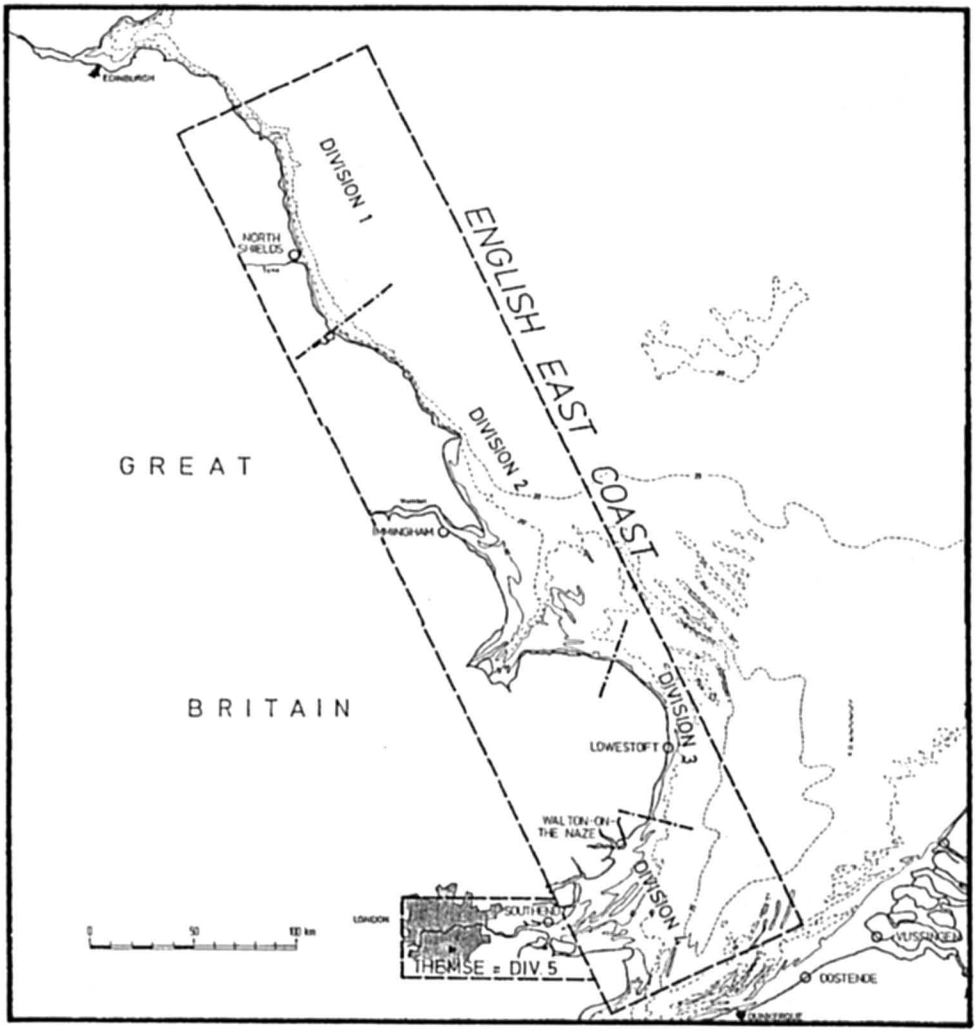


Fig. 7.46: Forecast area English east coast

Whether in the future more attention must also be given to the adjacent Scottish east coast in the north, will be decided in the course of further development in the field of oil exploration. For each reference gauge a "critical level", was fixed. If it is exceeded, certain areas will be flooded. If there is danger that this level will be reached, a warning is issued.

A first early warning (alert) can be given 12 h before HW. The second bulletin i. e. confirmation or withdrawal of the warning, is given 4 h prior to HW. Then, if required, the expected HHW level is pronounced. In the case of warnings for Div. 5 (Thames), a "London Flood Room" is taken over by the Greater London Council. There, the HHW for London is determined using the HHW forecast for Southend and the $Q_0$ discharge. To set off in time such a procedure in London, the 2nd warning is given as early as 6 h prior to HHW Southend.

The "storm surge season" on the English east coast extends from the end of August to 30 April. On average, that means 100 "alerts", 20 real warnings and 5 critical level reports.

There is a number of empirical correlations based on statistically secured regressions between the water levels at the reference gauges (see above), the wind and the water levels at the Stornoway, Wick and Aberdeen gauges, among which the best suited are selected in each case. The mean error is ± 0.2 m, individual deviations reaching 0.6 m. For Division 1 e. (Fig. 7.46), the equation reads as follows:

| | | |
|---|---|---|
| 0.75. | (11 HW - MHW Wick) | 4 h earlier |
| + 0.003. | (320° comp. of the surface wind Fair Isle) | 11 h earlier |
| + 0.002. | (30° comp. of the geostrophic wind between Scotland and Southern Norway) | 6 h earlier |
| + 0.14 m | | |
| = HHW - MHW North Shields | | |

The main problems are at present:
- empiric approaches are based on only a few major storm surges (as these occur only seldom),
- dynamic wind effects are not taken into consideration,
- the interactions of tidal waves and waves due to wind stress are not taken into account, astronomical tide forecasts are inaccurate.

*The Western Schelde*

Storm surge forecasts for the Western Schelde are of great importance in particular for the port of Antwerp (about 80 km upstream of the mouth) with its numerous exposed installations. Therefore, extensive analyses were also made for this region after the storm surge of Feb. 1, 1953. It was thus found, interalia, that northwest winds are the most dangerous winds. As a result of investigations made over many years a forecasting method was presented which, in principle, is based on a correlation of the HHW at Oostende and that at Antwerp (Fig. 7.47).

HWs occur at Oostende little less than 3 h earlier than at Antwerp. As this time period is too short for a reasonable forecast the Oostende HHWs are calculated about 2 h in advance.

These calculations are based, just as those for the Oostende-Antwerp correlations, on empirical estimates. The method is as follows:

extrapolation wind stress Oostende by 2 h ---> $HHW_{Oos}$
+ difference $MHW_{Ant}$ - $MHW_{Oos}$
+ wind according to direction and force off the coast
= HHW Antwerp

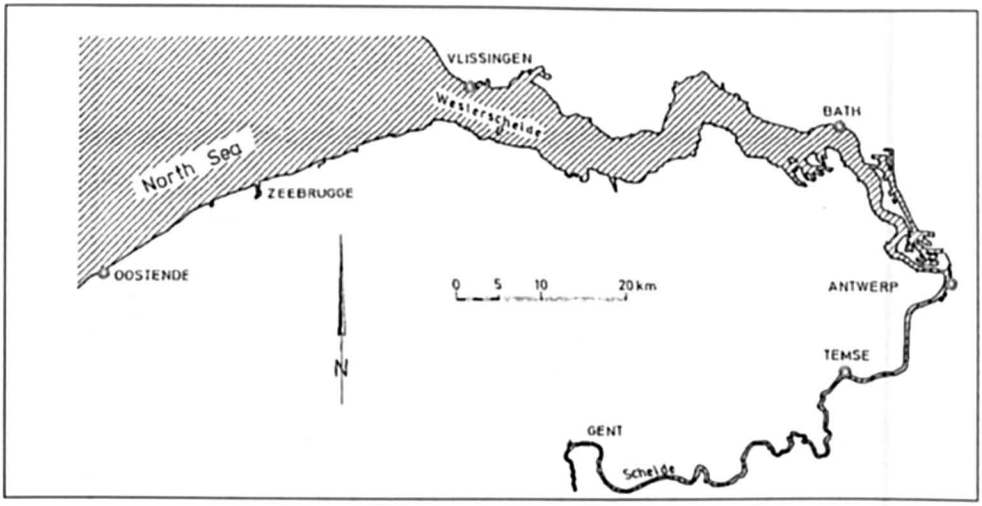


Fig. 7.47: Forecast area Western Schelde

*The Dutch Coast*

The theoretical principles for the methods applied in the Netherlands originated in the 1950s WEENINK and GROEN (1958). Their results have been tested in many practical applications.

For the stations of Vlissingen, Hoek van Holland, Den Helder, Harlingen, and Delfzijl (Fig. 7.48), the Koninklijk Nederlands Meteorologisch Instituut, (KNMI), publishes prognoses for the high water level due to meteorological causes. During a storm surge the "Stormvloedwaarschuwingsdienst" in The Hague determines the exact heights at the above stations and decides based on $Q_0$ and the predicted values whether warnings should be issued.

For the forecasting of water levels, correlations between HHWs of various places are needed. For this purpose, reference curves have been put together. Where the prevailing volumes of discharge have an influence on the rise, they have been covered by the statistical correlations.

As a supplement to this forecasting service, regional water level forecasts are also carried. Such forecasts are made on the basis of surge curves. For this purpose, data from a network of gauges, which have been in operation for several years for other purposes, are also relied upon. They are recorded via remote transmission in a central recording room. Every 5 minutes the water levels are recorded on punched tapes, analog recorders and a printer.

On the Dutch coast, too, one tries to use the possibilities offered by mathematical models for storm surge forecasts.

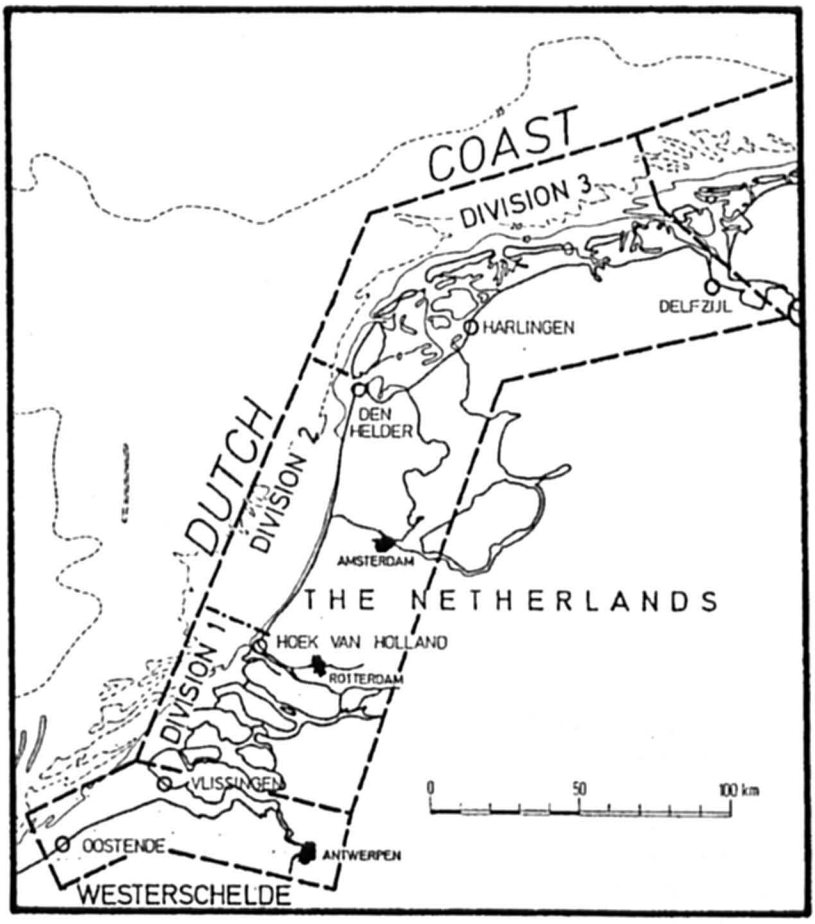


Fig. 7.48: Forecast area Dutch coast

*Inner German Bight*

Many forecasting methods often yield unsatisfactory results as they are based on weather forecasts and these weather forecasts – mainly wind speed and wind direction evolution – are not accurate enough.

The other reason for unsatisfactory predictions are the methods themselves. Usually only the peaks of storm tides are taken into consideration, representing only single points on a curve. Characteristics of tide and surge curves are not developed, and tide/surge interactions are not evaluated.

To exclude such difficulties a storm tide forecasting method should be developed

1. by analysing storm surge curves of storm tides over the last 50 years at several tide gauges on the coastline. A storm surge is defined as the difference between storm and mean tidal water level.
2. by taking into consideration as many wind data as are available;
3. by using only exact (not predicted) tide and wind data.

Fig. 7.49 shows the situation at the German North Sea coast.

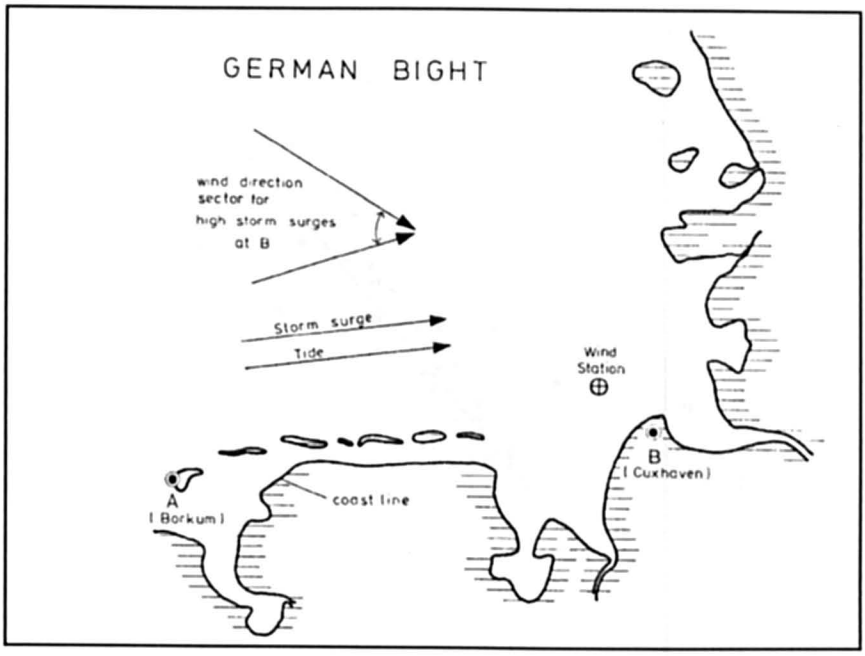


Fig. 7.49: Tide gauge locations A and B in the German Bight

In the German Bight the astronomical tide progresses in an anticlockwise direction. The winds during storms surge events come from west, as does the storm surge. Therefore, a forecast for a point B on this coastline needs information from a location westward of it (gauge A at the island of Borkum). This gauge A is the so-called input gauge for the forecast gauge B. However water level information merely from an input gauge is not sufficient.

Further investigations showed that an explanation for the outliers 7.50 can be given if wind speed and wind direction development within the last 3 hours before high tide at A (Borkum) are taken into account. The wind development in this 3-hour interval (about 3 hours before the expected high water level at B) is the best indicator for what will happen with water level changes in the following 3 hours after high tide at A. So about 3 hours before high tide at B no further wind information is needed to forecast the highest level at B. These conditions are in agreement with results at the Dutch and British coasts.

The high water level at B ($H_B$) can be roughly calculated by a simple linear formula:

$$H_B = 1.2\ H_A + \Delta V + \Delta R - 80\ \text{cm} \qquad (7.7)$$

where, $1.2 \cdot H_A - 80$ cm gives the trend of HW level comparison at A and Fig. 7.49 and $\Delta V$ (Fig. 7.51) and $\Delta R$ (Fig. 7.52) are the partial contributions to wind speed and wind direction developments respectively within 3 hours before forecasting time.

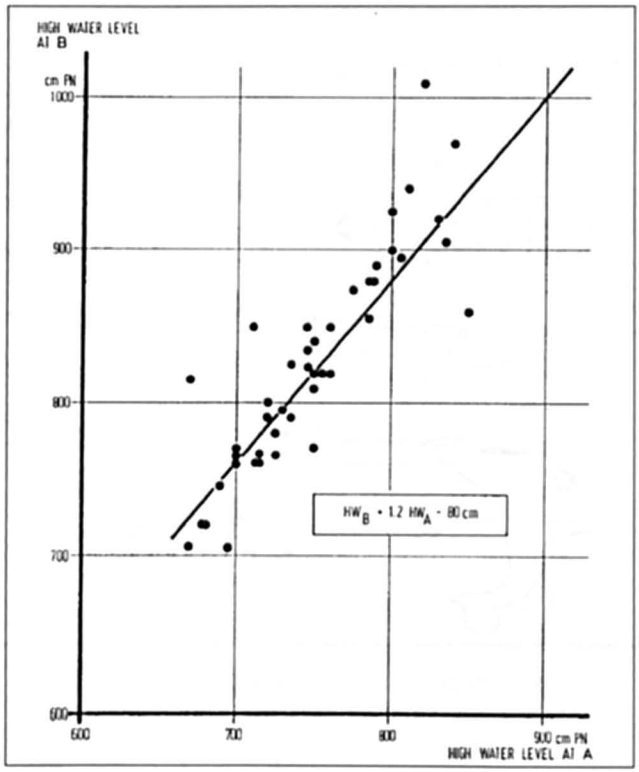


Fig. 7.50: Comparison of high water levels at A and B

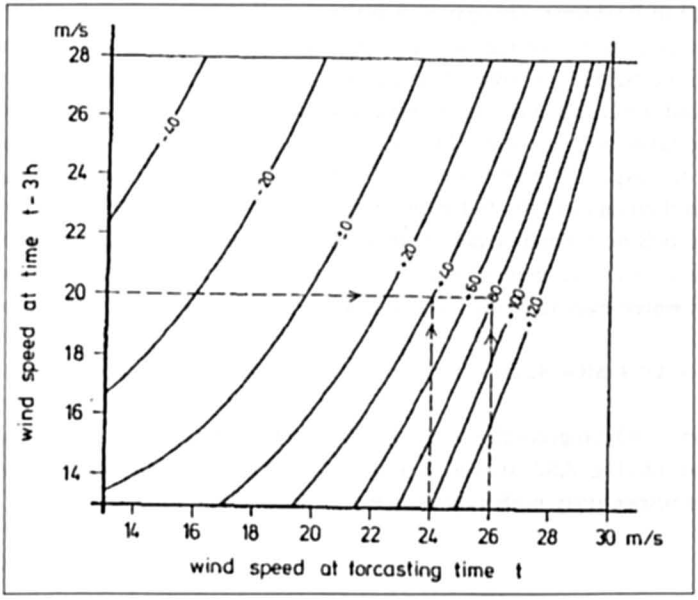


Fig. 7.51: Wind speed development value ΔV in cm

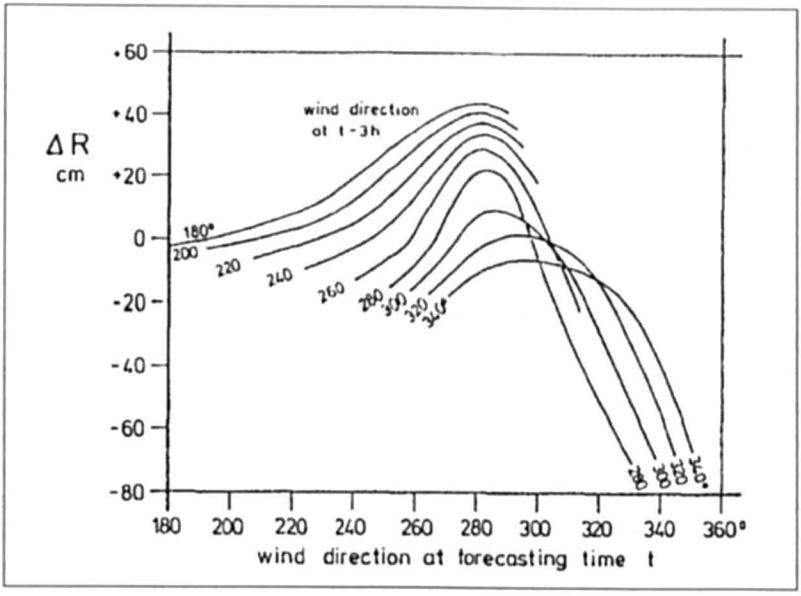


Fig. 7.52: Wind direction development value ΔR

The wind data is needed with a resolution of 1 m/s in speed and 10° in direction. The example in Fig. 7.52 demonstrates the necessity of exact wind speed data. A change in wind speed from 20 to 24 m/s over the 3 hours interval gives a positive value of ΔV = + 40 cm. A change of only 2 m/s (to 26 m/s) doubles this to ΔV = + 80 cm.

Fig. 7.52 shows that highest values for wind direction developments are given by changes from other directions to 280° which is the most effective wind direction for high storm surges at Cuxhaven. Direction changes further northward result in high negative values, up to ΔR 80 cm.

In a second step the forecasted high water levels at B can be modified. This possibility is given by analysing the surge curves at A and B (Fig. 7.53).

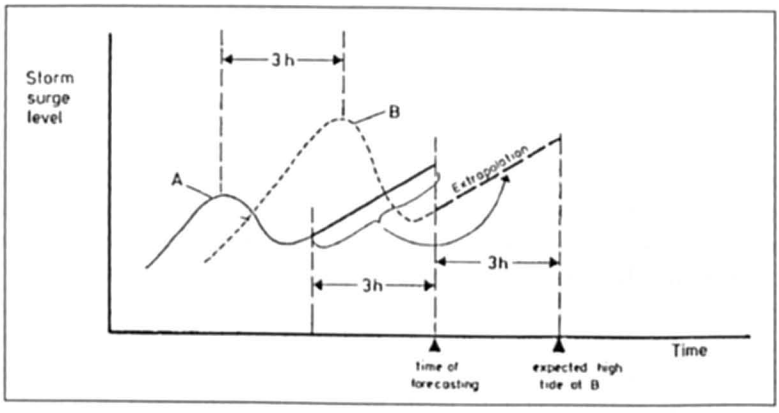


Fig. 7.53: Extrapolation of storm surge curve B by the shape of curve A

This prediction method has been used for the calculation of the high water level in Hamburg using the predicted water level at Cuxhaven + a constant 110 cm. Long-term monitoring shows that this amount must be differentiated more accurately, because fareway and embankments improvement measures at the Elbe River have changed storm surge issue in the Elbe estuary. Since 1996 high water level differences • HTHW between Cuxhaven and Hamburg have been attributed to a class of high surges with • H 0130 cm (FERK, 1999).

The German Hydrographic Service (formerly DHO now BSH) in Hamburg has been charged by a law mandated with the task to inform traffic in the German Bight on anticipated water levels. The empirical-statistical method used is applied in a more simple form for about 50 years.

For the computed surge a distinction is made between local effects (i.e. German Bight) and distant effects. The value of greatest influence is unquestionably the wind (surge approximately proportional to the square of the wind velocity; the greatest surge value is reached after a 3 h influence). Then follow the static atmospheric pressure (the effect is practically spontaneous), the change of atmospheric pressure with time (in case of rapid changes in the pressure free waves up to 1 m height are generated), water temperature and temperature difference air-water (the colder it is and the greater the difference, the stronger the wind effect). In the BSH a mathematical model is being developed covering the influences in their entirety in an overall approach.

Water level forecasts are broadcast twice a day and cover the entire German North Sea coast (Fig. 7.50). Neither the tidal curves nor the times of the onset of peak levels are determined by only rises in such levels (as a measure between anticipated HHW and precalculated astronomical HW). Meteorological details obtained from the German Weather Service.

Because of the uncertainty of the forecasts, water levels are indicated at 25 cm intervals up to a surge height of 1.2 m and thereafter at 50 cm intervals. In the case of a storm surge, the warnings are of use not only for navigation but also for agencies and administrative offices along the coast and tidal rivers.

In the case of anticipated high wind velocities, the BSH needs forecasts on the direction, speed and time of onset of the wind over the North Sea. On the basis of the method applied by the BSH forecasts of sufficient accuracy are possible only if, in addition, the forecast and occurrence of meteorological input data are accurate and external surges are recognized early enough off the English east coast. Only then the first 12 hour forecasts are usable, otherwise only later data are more accurate. But even then there is room for improvements since wind forecasts are made only roughly in units on the Beaufort scale.

### *Danish Southwest Coast*

Although the land behind the Danish tidal flats south of Esbjerg (Fig. 7.54), as the northernmost part of the Dutch-German tidal flat, is only relatively sparsely populated, attempts have been made during the last few years to increase the safety of the population in addition to reinforcing the old dykes by applying storm tide forecasting procedures.

The procedure was developed following the statistical evaluation of water levels measured over six years and allows computation at any time of the tidal cycle of the water levels for the forthcoming 1, 2, and 3 h. Forecasts for a maximum period of 3 h are sufficient to find out in time when an endangered dyke might break at the earliest and then perhaps to evacuate the population concerned which takes atmost 2 h.

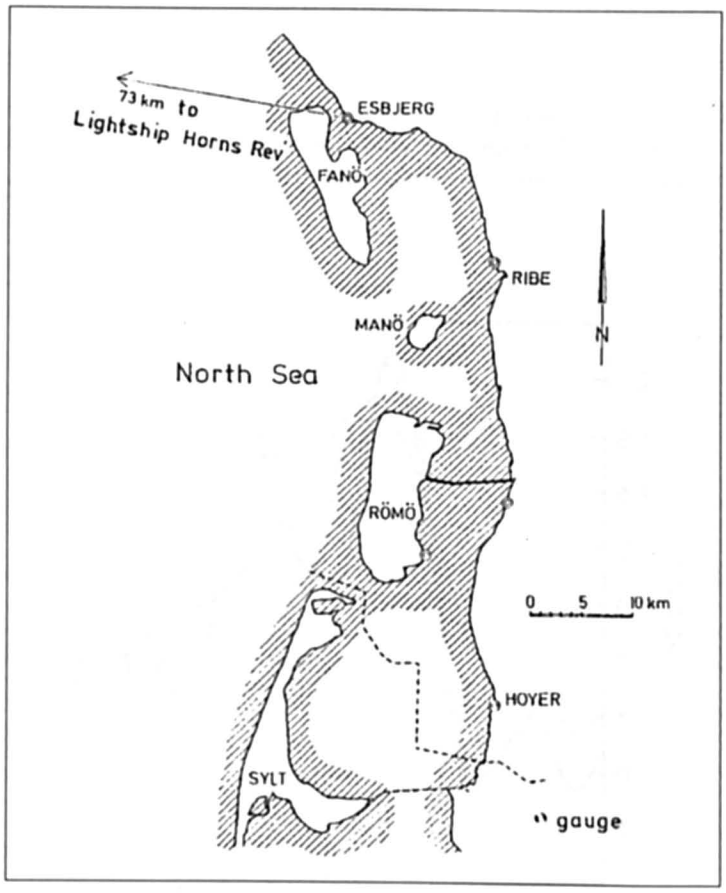


Fig. 7.54: Forecast area Danish Southwest coast

The programmed procedure has been in practice since 1970. It is based on hourly water level data from the Esbjerg and Hojer gauges for which it was developed (Fig. 7.54) and on 3-hourly data of wind velocity, wind direction, and atmospheric pressure from a lightship off the coast. The 95 % confidence intervals are

± 20 cm for a forecast period of 1 h.
± 35 cm for a forecast period of 2 h.
± 45 cm for a forecast period of 3 h.

As during the storm surge of Jan. 03, 1976, the data flow was interrupted because the public telephone system was blocked, independent systems were rented in the meantime. Although the accuracy mentioned meets the requirements, it is planned to supplement the 3 h model in the next few years by a hydrodynamic 12 h model for the North Sea.

### 7.3.10 Modeling

*North Sea*

Following the 1953 disastrous storm surge, several numerical models for the North Sea and Thames Estuary were developed. Results from a linear model and a nonlinear model are compared with the observed surge at Southend of February 16–17, 1962, in Fig. 7.55.

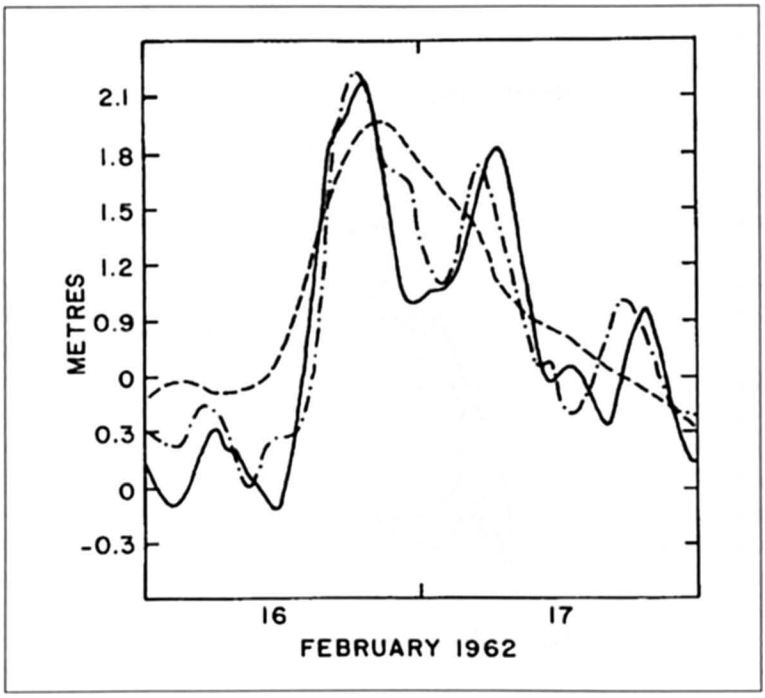


Fig. 7.55: Comparison of observed and computed surges at Southend, U.K., during February 16–17, 1962. Solid line, observed surge; broken line, computed surge using a linear model; dashed-dotted line, computed surge using a nonlinear model (ROSSITER, 1971)

Certain models have already been considered for the North Sea in different sections. ISHIGURO (1976a) showed through electronic analog models that atmospheric pressure gradient generated surges are important in the North Sea (Table 7.16). ISHIGURO (1976b) gave diagrams of estimated peak surges for different wind speeds. Contours of surge height for a wind speed of 36 m/s are illustrated in Fig. 7.56.

DAVIES and FLATHER (1977) computed the storm surge in the North Sea for the case of April 1–6, 1973, using several different numerical models. The features of these models are summarized in Table 7.17 and terms errors at various locations for these models are listed in Table 7.18.

Table 7.16: Comparison of the amplitudes of pressure gradient generated and wind stress generated surges in the North Sea. (ISHIGURO, 1976a)

| Wind direction (degrees) | Wind duration (h) | Wind speed ($m\ s^{-1}$) | Pressure-gradient (mb 100 $km^{-1}$) | Pressure generated surge $Y_p$ (cm) | Wind generated surge $Y_w$ (cm) | $Y_p / Y_w$ (%) |
|---|---|---|---|---|---|---|
| 22 | 30 | 10 | 2.3 | 8 | 33 | 24 |
| | | 20 | 4.5 | 16 | 130 | 12 |
| | | 30 | 6.7 | 23 | 293 | 8 |
| | | 40 | 9.0 | 32 | 520 | 6 |
| 112 | 10 | 10 | 2.3 | 10 | 15 | 67 |
| | | 20 | 4.5 | 20 | 60 | 33 |
| | | 30 | 6.4 | 30 | 135 | 22 |
| | | 40 | 9.0 | 40 | 240 | 17 |

Table 7.17: Features of the different models for the North Sea used in the simulation of the storm surge of Apr. 1–6, 1973. (DAVIES and FLATHER, 1977)

| Calculation | Model | Open boundary condition Surge input | Tidal input |
|---|---|---|---|
| a | Shelf | Radiation Hydrostatic | None |
| b | North Sea | Elevation specified Hydrostatic | None |
| c | Shelf | Radiation Hydrostatic | $M_2 + S_2$ |
| d | North Sea | Elevation specified Hydrostatic | $M_2 + S_2$ |
| e | North Sea | Elevation specified from calculation c + observations from Wick | $M_2 + S_2$ |

Table 7.18: Root-mean-square errors (cm) for calculations using models a to e (see Table 7.17) for the storm surge of Apr. 2–6, 1973. (DAVIES and FLATHER, 1977)

| Port | a | b | c | d | e |
|---|---|---|---|---|---|
| Wick | 18.1 | 12.6 | 13.5 | 12.6 | 0.0 |
| Aberdeen | 20.3 | 13.7 | 15.9 | 13.3 | 10.9 |
| North Shields | 22.5 | 17.7 | 17.0 | 16.6 | 16.3 |
| Inner Dowsing | 26.9 | 27.5 | 21.2 | 27.1 | 25.2 |
| Immingham | 26.6 | 25.6 | 19.5 | 20.8 | 18.2 |
| Lowestoft | 29.8 | 28.5 | 25.0 | 27.5 | 25.3 |
| Walton-on-Naze | 34.3 | 31.2 | 27.2 | 29.0 | 26.8 |
| Southend | 42.9 | 38.6 | 33.9 | 35.1 | 33.0 |
| Ostende | 36.1 | 34.0 | 25.1 | 30.3 | 26.7 |
| Ijrnuiden | 42.3 | 40.6 | 34.6 | 35.4 | 33.3 |
| Terschelling | 32.3 | 31.8 | 27.2 | 27.3 | 26.4 |
| Cuxhaven | 48.0 | 45.0 | 37.4 | 40.2 | 38.4 |
| Esbjerg | 32.6 | 29.0 | 23.3 | 24.11 | 21.2 |

PRANDLE and WOLF (1978a, 1978b) used parallel numerical models to study the modification of the tide due to surge and vice versa in the southern part of the North Sea. The tide and the surge before and after interaction for the case of October 19, 1970, are shown in Fig. 7.57. The interactions at Lowestoft and Southend for the event of January 31–February 1, 1953, are presented in Fig. 7.58 and 7.59, respectively. The contours of the interaction in the southern part of the North Sea are displayed in Fig. 7.60.

FLATHER (1980) summarized the status of a real-time storm surge prediction scheme for the North Sea. In this scheme, the meteorological forcing terms are obtained in real time as output of a 10-level primitive equation atmospheric model. In the storm surge model, a coarse model covers the whole of the Northwest European continental shelf. Models with finer resolution for the southern bight, eastern part of the English Channel, and the Thames Estuary are being developed. The contours of the surge at 03:00 GMT on January 12, 1978, are shown in Fig. 7.61.

VRIES et. al. (1995) compares 2D storm surge models applied to North Sea, Aegean and the Adriatic. They stated that the differences between the North Sea models are less than 10 cm, storm surges are underestimated by up to 50 cm, which indicates that improvement has to be found in the surface drag relations and not in the difference between the models. For the Mediterranean Sea the comparison shows differences of 35 cm with the observed level, which is due to the meteorological input inaccuracies.

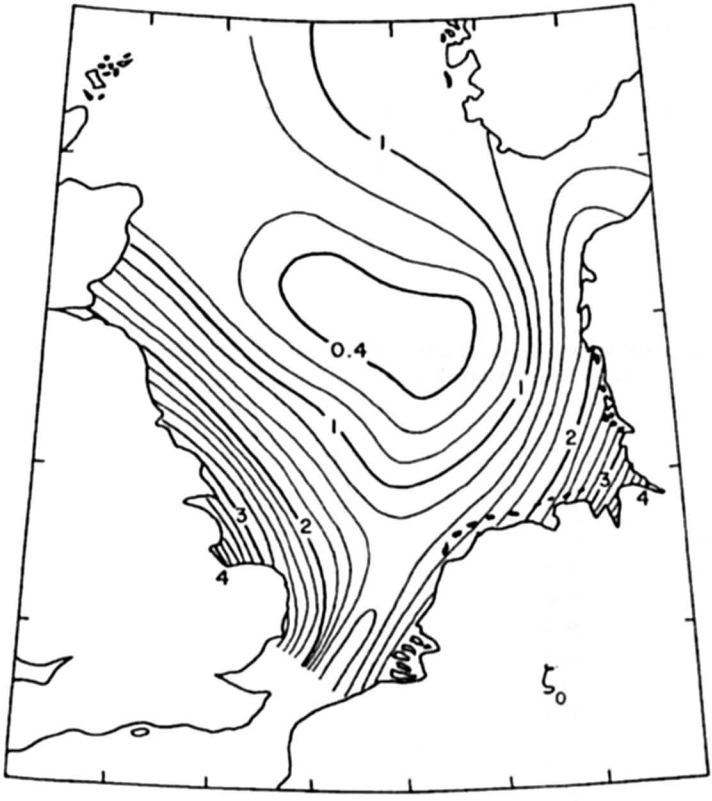


Fig. 7.56: Storm surge heights in the North Sea for a wind speed of 36 m-s-' blowing for 10 h. (ISHIGURO, 1976b)

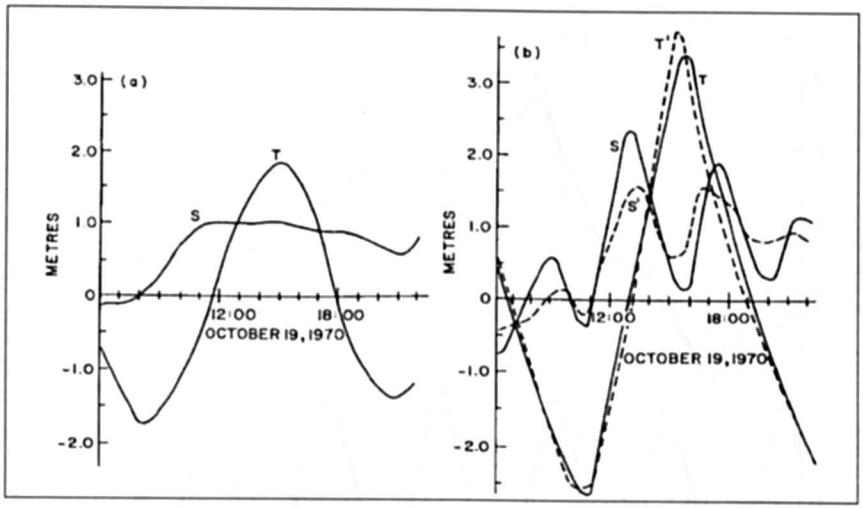


Fig. 7.57: Tide-surge interaction at (a) Walton-Margate (mouth of the model) and (b) Tower Pier. T, tide; S, surge; T', tide modified due to interaction with surge. S', surge modified due to interaction with tide. (PRANDLE and WOLF, 1978b)

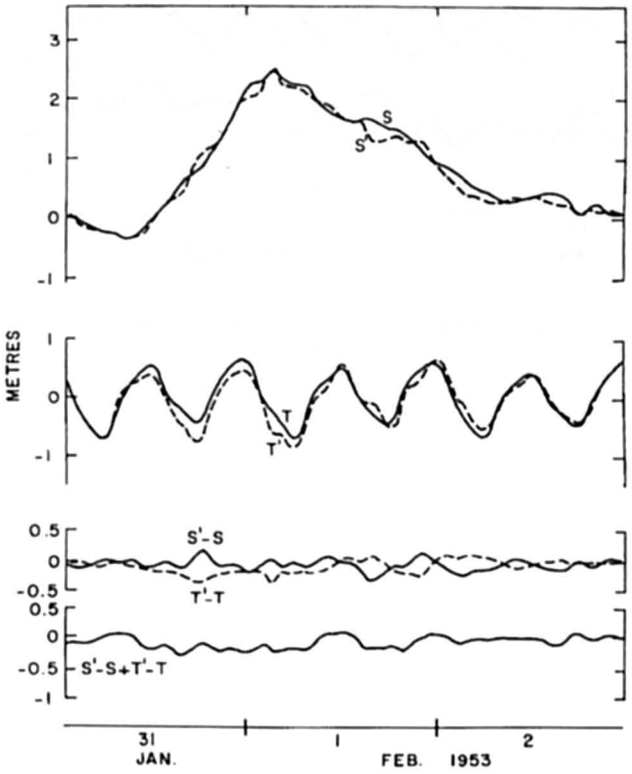


Fig. 7.58: Tide-surge interaction at Lowestoft, U.K. See Fig. 7.47 for explanation. (PRANDLE and WOLF, 1978b)

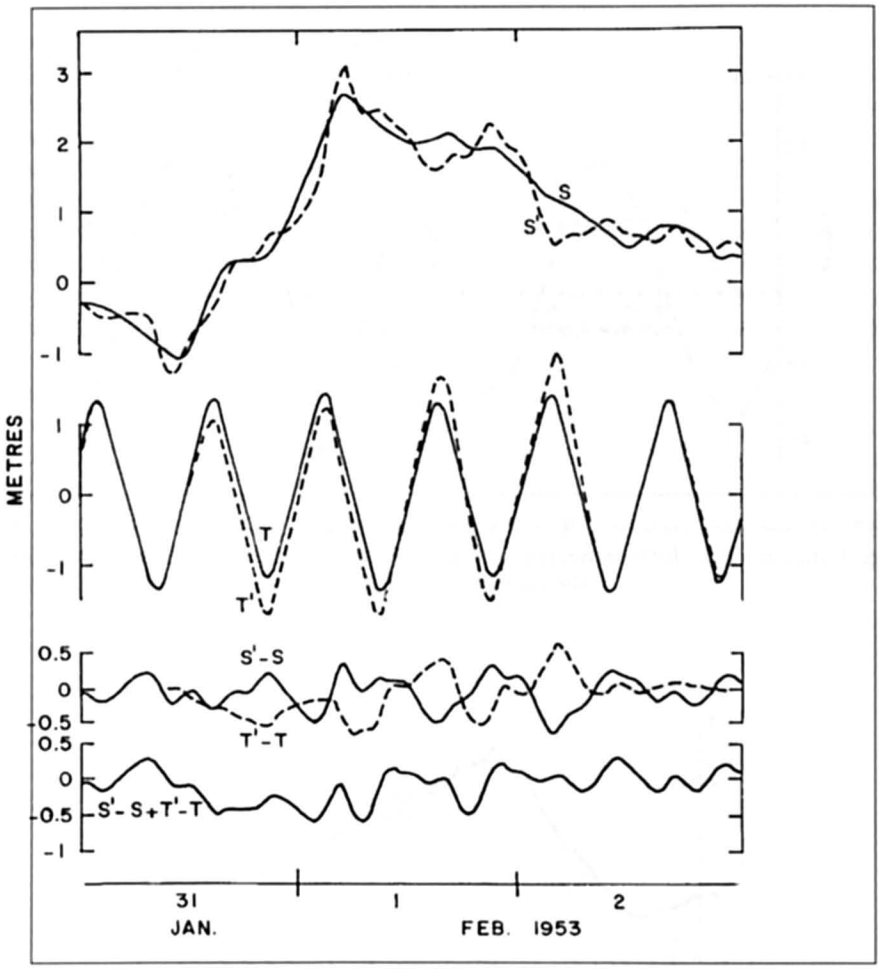


Fig. 7.59: Tide-surge interaction at Southend, U.K. See Fig. 7.57 for explanation. (PRANDLE and WOLF, 1978b)

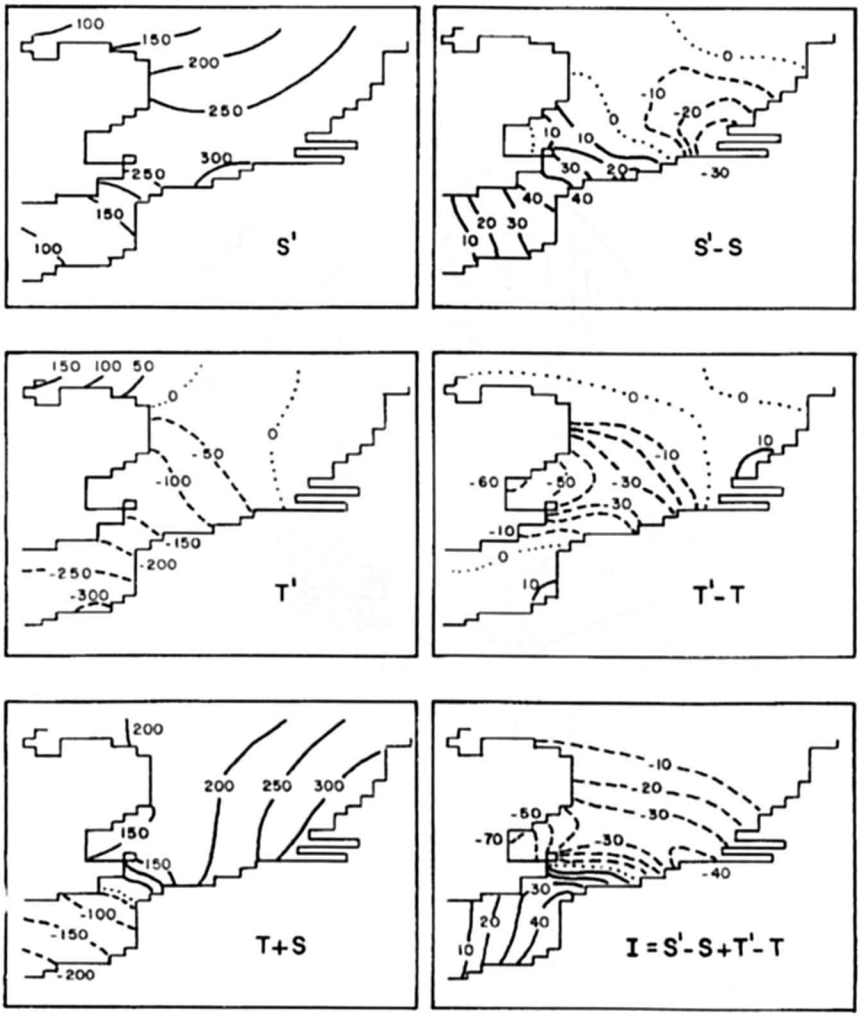


Fig. 7.60: Tide-surge interaction distribution (centimetres) in the southern part of the North Sea. (PRANDLE and WOLF, 1978b)

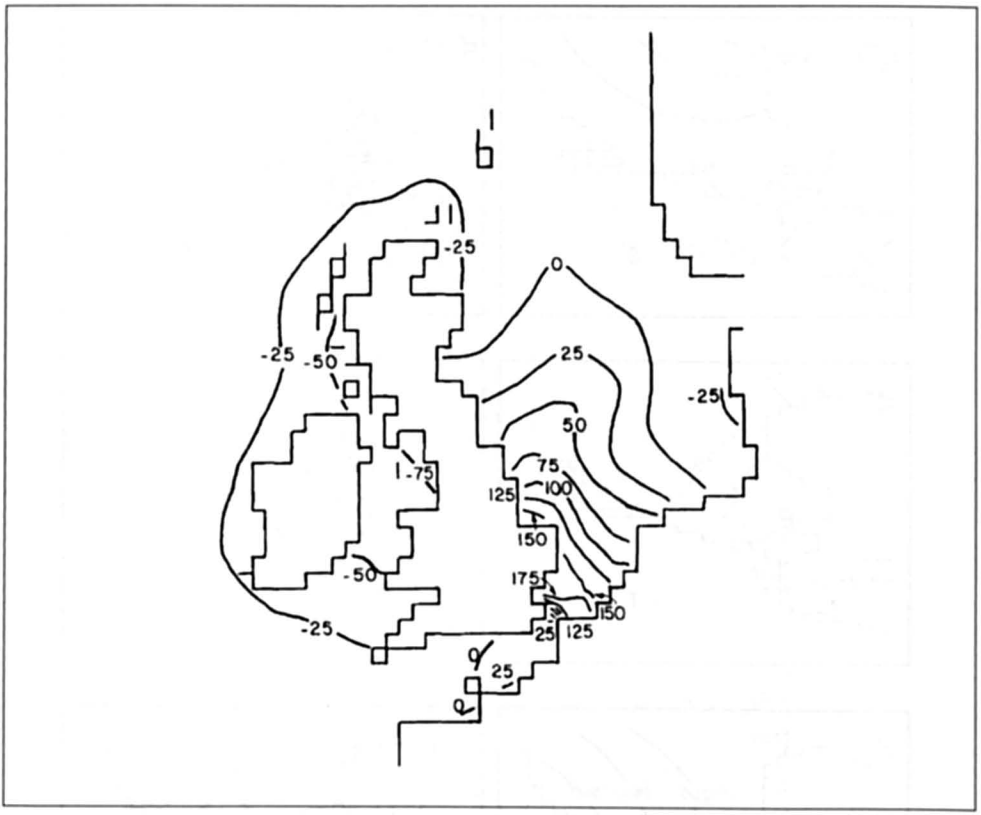


Fig. 7.61: Spatial distribution of surge elevation (centimetres) at 03:00 (GMT) on January 12, 1978, in the northwest continental shelf of Europe. (FLATHER, 1980)

*A North Sea model*

This chapter follows closely IHP-OHP 1987 and based on RODENHUIS et al. (1978), HAVNOE et al. (1983) and SIEFERT et al. (1987).

The emphasis in hydrographic conditions is often on waves. However, for several important problems, knowledge of currents is also essential. During the past, the technique of simulating currents and surface elevations in sea areas by computer has developed into an accepted engineering method. However, to obtain details of currents, the computations must be made on a high resolution grid. The model presented here permits the use of detailed resolution in selected areas, with the main circulation in the North Sea described on a much coarser grid. With the main grid established for the entire North Sea, the model can be focused on different local areas. Its generality makes refocusing simply a matter of providing the programme with the coordinates for the new local area and its bathymetry.

The model uses the full non-linear equations of nearly horizontal flow, which are solved by implicit, time-centred, finite difference scheme. The effects of wind stresses, Coriolis forces, and bed friction are included. Moreover, such nonlinear equations of shallow water and interaction between tide and storm surges. The System 21 has a high degree of accuracy. This has been demonstrated in practical applications e.g. RODENHUIS et al. (1978).

To provide details for resolving complicated areas, the change of resolution for the North Sea model is shown in Fig.s 7.62 and 7.63. The grid 1 with low resolution is named $SD_0$; the grid 2 of high resolution is named $SD_1$; and the higher resolution of nested grid 3 is named $SD_2$ – i. e., subdomains 0, 1, and 2, respectively. In low resolution 1 ($SD_0$), several grids of finer mesh size can be selected at higher resolution 2 ($SD_1$). The mesh size is one-third the original resolution 1. In a nested grid of high resolution 2 ($SD_1$), again several grids of finer mesh size can be selected at higher resolution 3 ($SD_2$). The reduction in mesh size relative to nested grid $SD_1$ is again onethird; relative to nested grid $SD_0$ it is one-ninth. For the North Sea model, this means a refinement from 10 nautical miles in resolution 1 to 1.1 nautical miles in resolution 3. There is no principal restriction for further reduction to higher resolution 4 or 5.

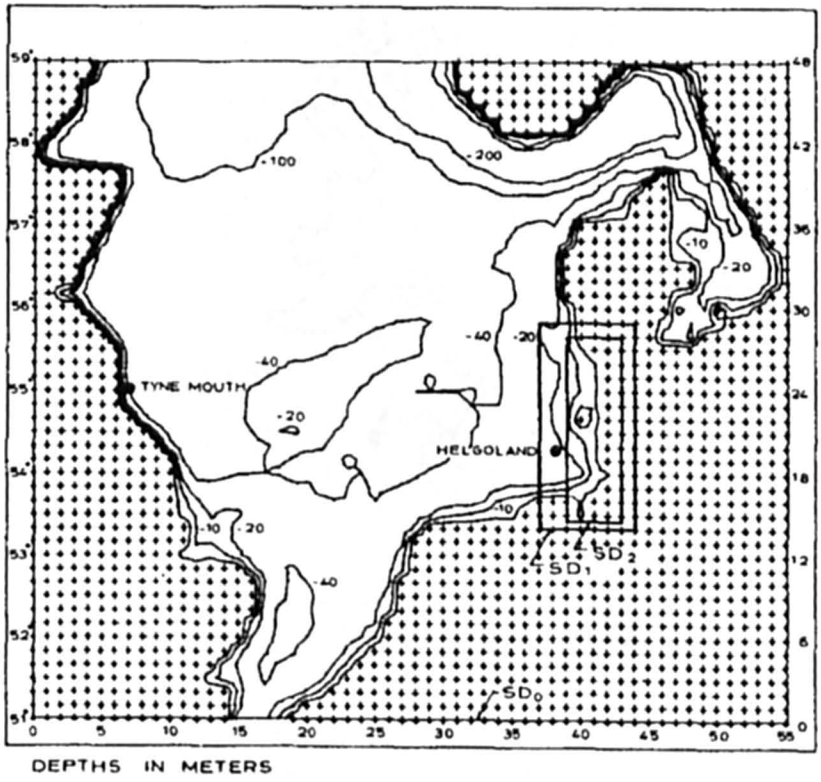


Fig. 7.62: North Sea model with main domain in Scale 1
$SD_0$: Mesh size = 18 km, gridpoints: 2.640
$SD_1$: Mesh size = 6 km, gridpoints: 945
$SD_2$: Mesh size = 2 km, gridpoints: 4.428

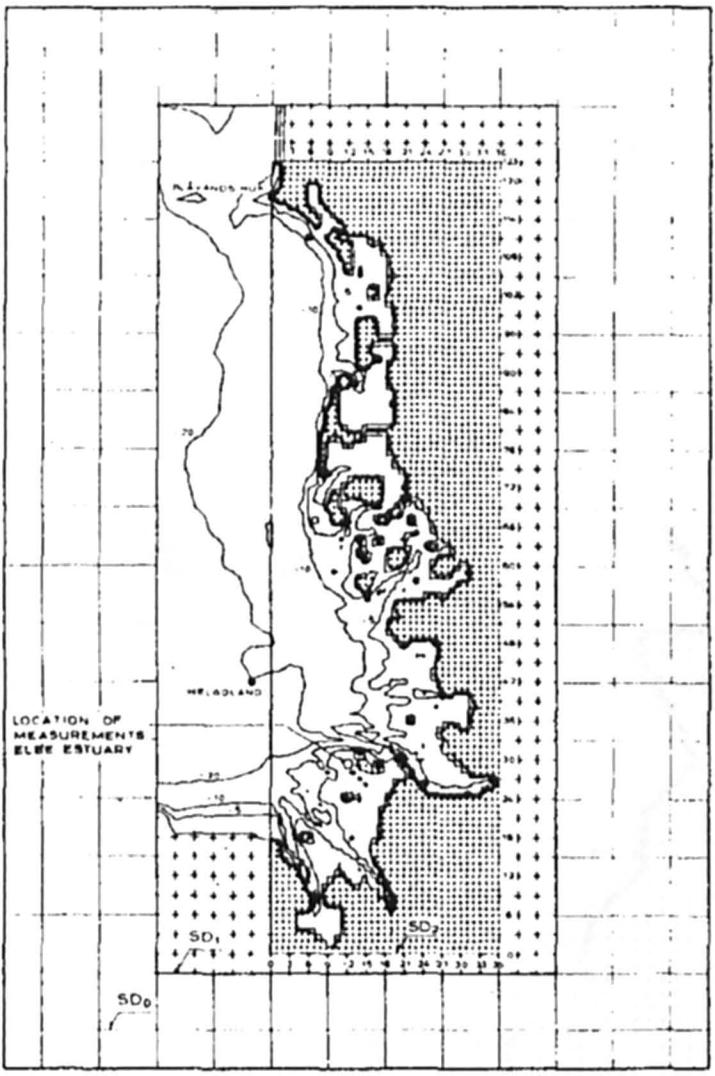


Fig. 7.63: North Sea model with subdomains in Scales 1 and 2

Computations are made simultaneously on all grids. When computing simultaneously, information also can travel from the fine grid to the coarse grid – the conditions in the fine grid can influence the results in the coarse grid.

The model was considered for a storm surge warning system for the Danish west coast and for intended computations of currents in connection with the hydraulic investigations and preliminary design of a gas pipeline that will be brought ashore on the west coast.

The model is set up as follows: The bathymetry of the entire North Sea from Stavanger to the Orkney Islands in the north and Dover–Calais in the south is described on an rectangular finite difference grid with a mesh size of 10 nautical miles. The Skagerak and the Kattegat also are included. The bathymetry off the Danish west coast is described on the finest grid with a mesh size of 2 km. This grid permits detailed representation of this area (Fig. 7.63).

The main grid has to be set up only once, while the fine grid can be refocused on different areas of interest. The only dynamic entry data required are water-level variations along the open boundaries between Stavanger and the Orkney Islands, and between Dover and Calais and the time variation of the atmospheric pressure distribution for the area. The boundary data is computed from tidal constants, in fact, as a tidal prediction for each grid point along the open boundary.

The changing meteorological conditions are represented in the hydrodynamic equations by barometric pressure gradients and wind-stress terms. Meteorological observations are available with 3-hour intervals. The isobar map is based, however, mostly on observations on land, and only a few ship observations are available.

In the model, the atmospheric pressure at sea level is specified every 3 hours in each grid point with a mesh size of 60 nautical miles, with the same boundaries as the main hydrodynamical grid. The actual wind speed is calculated from the geostrophic wind speed.

The square root formula is based on measurements in the German Bight. Coefficients depend on the vertical stability (expressed by the air-sea temperature difference), here corresponding to a neutrally stable atmosphere. The wind direction is found by assuming a cross-isobar angle of 15°. Using interpolation of the wind components in space and time, a wind vector is calculated in each grid point in the main grid and subgrids at each time step.

Calibration of the finest grid off the Danish coast is incomplete, but the accuracy of the model's representation in the finest grid (Scale 3) may be illustrated with results from a similar run for the Elbe Estuary. In Fig. 7.64, the computed and recorded tidal variations at a point 15 nautical miles northwest of Cuxhaven are compared. The location is indicated in Fig. 7.63.

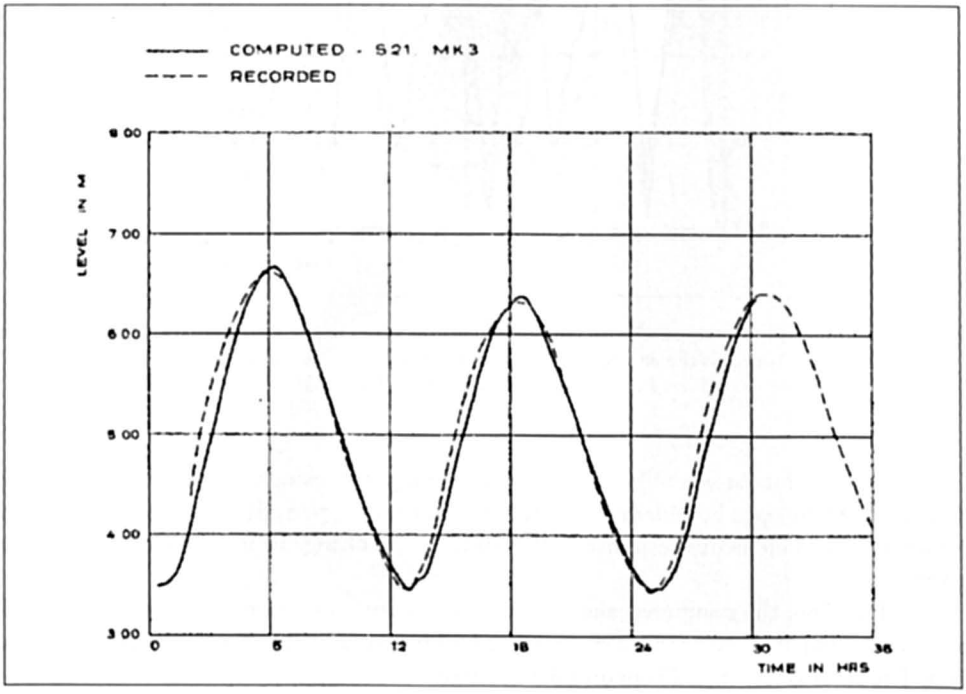


Fig. 7.64: Comparison between recorded and computed tide in Elbe Estuary with subdomain in Scale 3; data source is the Research Group for the Harbour Extension Neuwerk, Hamburg
Note: Location indicated in Fig. 7.63

Again, the computed values agree with the recorded values accurately. Current recordings were made at this location. The computed and recorded currents are compared in Fig. 7.65. The computed current is a depth-averaged current, whereas the recording is at 0.7 m above the seabed in 8 m water. When the velocity profile, $U_z$ over the vertical is expressed as

$$U_z = K \times Z^{1/n}$$

with n = 5 or 6, and K some constant, (7.6) a formulation tested in several areas in the North Sea, the relation between mean current, U, and U 0.7 is

$$U\,0.7 = 0.8\,U \quad (8.3)$$

As shown in Fig. 7.65 this fits accurately for the computed U and recorded U 0.7.

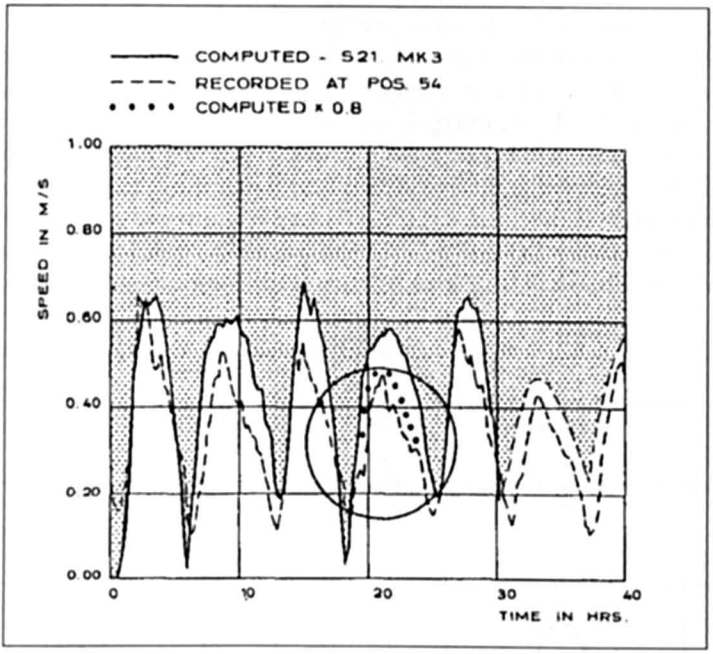


Fig. 7.65: Comparison of recorded with computed current speed in the Elbe Estuary with sub domain in Scale 3; data source is the Research Group for the Harbour Extension 'Neuwerk', Hamburg
Note: Location indicated in Fig. 7.63

The effect of the storm of Jan. 2–3, 1976, was computed, using the storm field previously described. At the open boundaries, the predicted tide for the period and a pressure surge that results as an instantaneous response of the sea level to a change in atmospheric pressure are given.

In Fig. 7.66, the computed and recorded water-level variations at Helgoland for this period are compared. Note that a storm surge builds up gradually over the initial tidal variation. The error is less than 20 cm on a 3.5 m surge.

Fig. 7.67 illustrates the model's ability to resolve the storm surge inside the bays along the Danish west coast: An instantaneous picture of the sea surface in the form of isolines is compared with recordings at two stations at that moment.

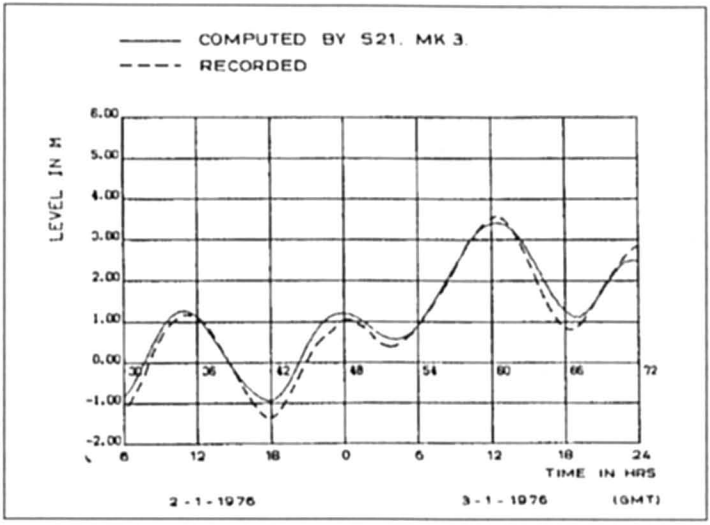


Fig. 7.66: Comparison of recorded with computed storm surge of Jan. 2–3, 1976, at Helgoland with sub domain in Scale 2

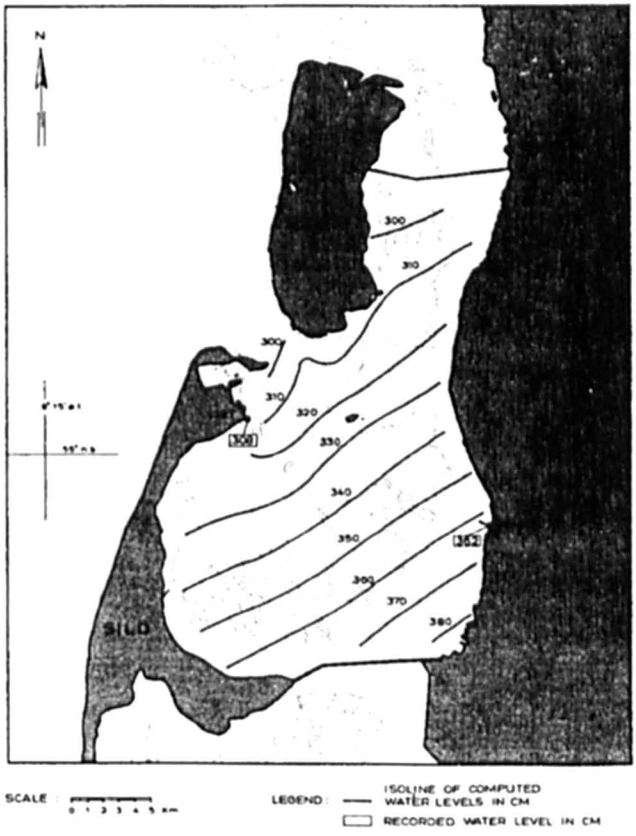


Fig. 7.67: Computed water levels inside a bay on the Danish west coast compared with recordings at two stations on March 1, 1976, 15:00 hours GMT

*North Sea and Baltic Sea Model*

The Federal Maritime and Hydrographic Agency (BSH) developed an operational model system to calculate currents, water level and dispersion processes. Operational model means that the model produces results daily. The description follows closely a paper of the BSH (1992). The model is a predictive one and is based on forecasts of wind and air pressure supplied by the German Weather Service in Offenbach. Tide prediction, current and water levels are computed nightly for periods up to 36 hours.

The water levels are calculated daily using three nested and interactively coupled grid nets. Towards the German Bight the grid resolution increases. Therefore the interaction between the variable coastline (wadden areas, sand banks and island chains) and offshore areas can be represented. Grid spacing near coastal areas in the German Bight and the western Baltic Sea is 1.8 km; in areas further offshore, it is 10 km while elsewhere in the North Sea and Baltic Sea it is 20 km.

In a three dimensional model the following forcing functions were included: wind, air pressure over North and Baltic Seas, tides, external surge and water discharge from large rivers. The model is a valuable tool for the water level and storm surge warning service at the BSH. It is mainly validated by regular comparison between modelled and measured water levels. In addition the model is occasionally checked using measured currents and drift experiments at sea (BSH, 1992).

*Baltic Sea*

Earlier the one-dimensional model of SVANSSON and SZARON (1975) for the Baltic Sea was discussed. Observed and computed surges at several locations for the storm surge event of August 15, 1964, are compared in Fig. 7.68.

HENNING (1962) numerically simulated the surge of January 3–4, 1954, in the Baltic Sea. This surge caused maximum elevations of 1.7 m in the western part of the Baltic Sea. The surface weather chart at 06:00 GMT on January 5, 1954, is given in Fig. 7.69. The distributions of the surge heights at two different times are shown in Fig. 7.70 and 7.71. Observed and computed surges at five locations are compared in Fig. 7.72. Some relevant data on this surge are given in Table 7.19.

WROBLEWSKI (1978) used stochastic techniques to simulate the following surges at Nowyport (at the Polish coast of the Baltic Sea): January 17, 1955, February 15, 1962, February 18, 1962, and February 21, 1962. DEMEL (1934) studied the surges of 1930 and 1931 at the Baltic coast of Poland.

KLEVANNY (1994) modeled long wave oscillation in the Baltic Sea. He used wind data from a set of meteorological stations along the Baltic Sea and big Islands. The storm surges of December 30–31, 1975 and February 17–23, 1990 are the basis to compare observed data with surface level oscillations obtained from modelling.

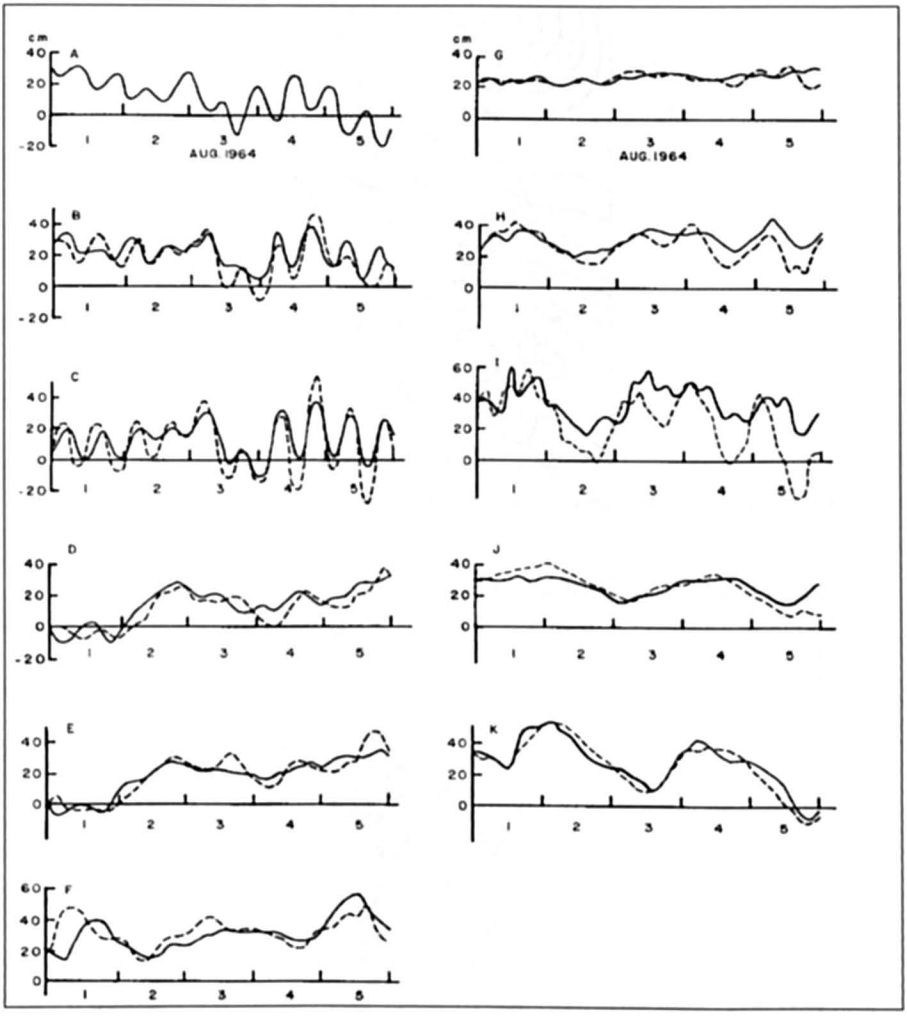


Fig. 7.68: Observed (solid line) and computed (broken line) storm surges at various locations along the Baltic Sea (SVANSSON and SZARON, 1975)

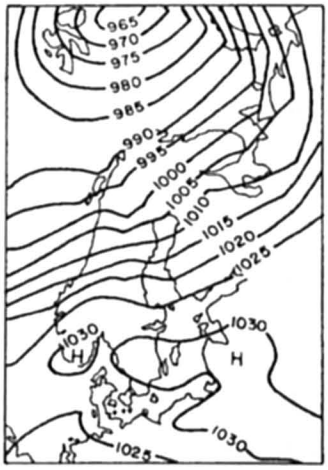


Fig. 7.69: Simplified surface weather chart at 06:00 (GMT) on January 5, 1954, for the Baltic Sea area (HENNING, 1962)

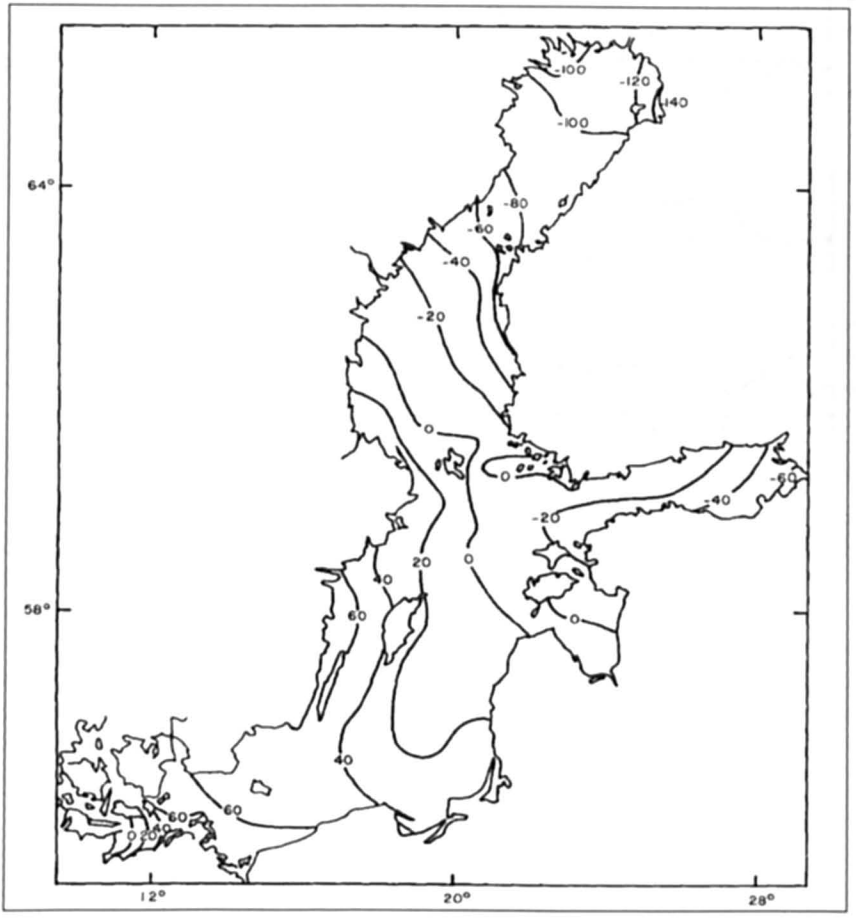


Fig. 7.70: Distribution of storm surge amplitudes (centimeters) in the Baltic Sea at 20:00 (GMT) on January 3, 1954 (HENNING, 1962)

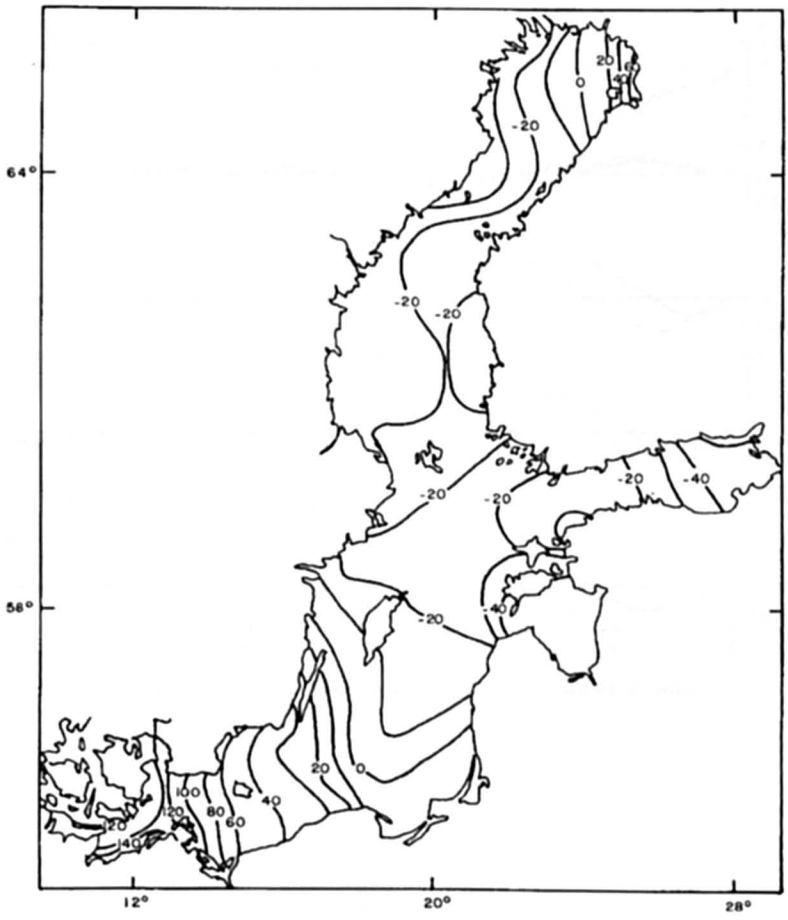


Fig. 7.71: Distribution of storm surge amplitudes (centimeters) in the Baltic Sea at 14:00 (GMT) on January 4, 1954 (HENNING, 1962)

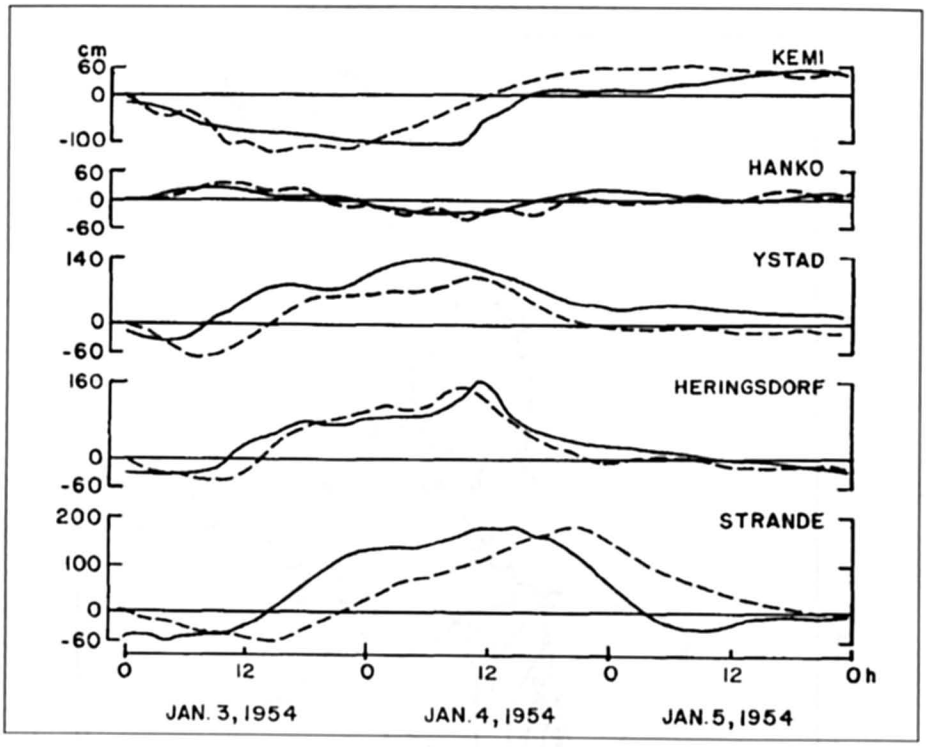


Fig. 7.72: Observed (solid line) and computed (broken line) storm surges in the Baltic Sea during January 3–5, 1954 (HENNING, 1962)

Table 7.19. Comparison between observed and computed storm surges in the Baltic Sea for the event of Jan. 3–4, 1954 (HENNING, 1962)

| Water level Gauge | Time of maximum elevation (observed) | | Surge (cm) | |
|---|---|---|---|---|
| | Day | Time (GMT) | Observed | Computed |
| Degerby | 3 | 8:00 | 47 | 52 |
| Landsort | 4 | 0:00 | 51 | 77 |
| Kungholmsfort | 4 | 8:00 | 100 | 105 |
| Ystad | 4 | 5:00 | 171 | 164 |
| Heringsdorf | 4 | 11:00 | 195 | 197 |
| Sallnitz | 4 | 11:00 | 183 | 171 |
| Kap Arkona | 4 | 10:00 | 187 | 193 |
| Daffier Ort | 4 | 12:00 | 190 | 195 |
| Warnetminde | 4 | 13:00 | 224 | 192 |
| Wismar | 4 | 14:00 | 291 | 192 |
| Travernfinde | 4 | 15:00 | 283 | 192 |
| Gedser | 4 | 12:00 | 231 | 186 |
| Langballigau | 4 | 12:00 | 236 | 262 |
| Strande | 4 | 15:00 | 239 | 236 |

## 7.4 Asia

RABINOVICH and SOKOLOVA (1992) produced a catalogue of storm surges for the Russian coast of the Sea of Japan.

Fig. 7.73 shows the locations of the eleven tide gauges whose data have been used to produce this catalogue. Actually out of the eleven stations, Krilyon is located in the Okhotsk Sea, but close to the Boundary with the Sea of Japan and is influenced by surges from the Sea of Japan.

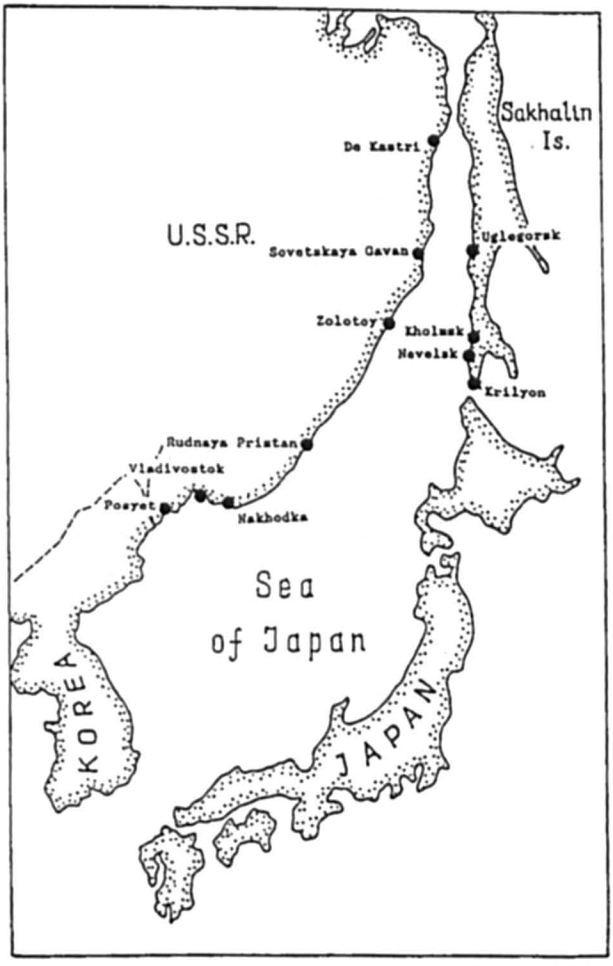


Fig. 7.73: Tide gauge positions (RABINOVICH and SOKOLAVA, 1992)

The residual series (after subtracting predicted tides) $\zeta(t)$, where t is the time, were used to analyse surges. Some simple parameters were chosen to describe each one (Fig. 7.3.2): the maximal height of storm surge $h_s$, estimated from mean monthly level $Z_m$, and of storm surge plus tide, $h_{st}$; the corresponding moments $t_s$, $t_{st}$; duration of surge $T_s$ and of its half-height $T_{s/2}$; surge steepness $\delta = h_s / T_{s/2}$; the variance

$$D = \sigma^2 = \frac{1}{T_s} \sum_{t=t_b}^{t=t_e} [\zeta(t) - Z_m]^2 \qquad (7.8)$$

where, $t_b$ is the time of the beginning and $t_e$ is the end time of the surge; it is supposed that in both moments $\zeta(t_b) = \zeta(t_e) = Z_m$.

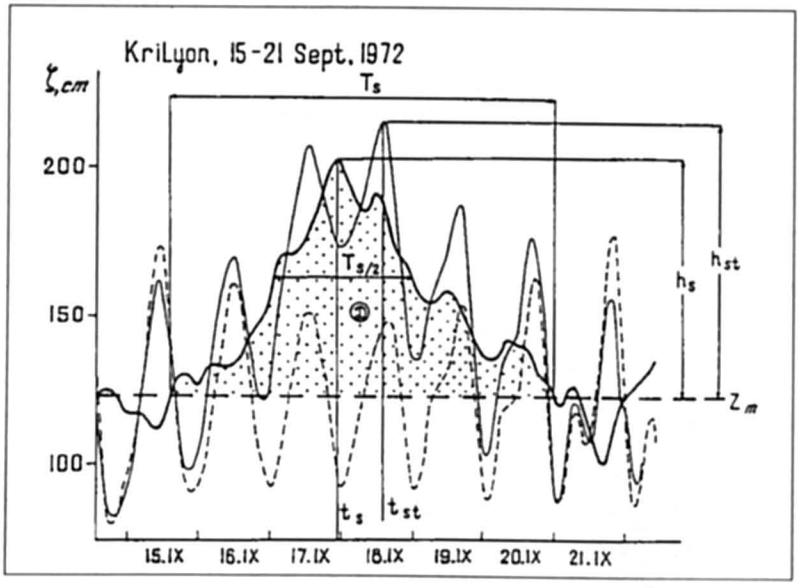


Fig. 7.74: The main parameters of storm surge (RABINOVICH and SOKOLAVA, 1992)

The algorithm of automatic detection of storm surges and calculation of corresponding parameters was used to analyse several years of data. Only the sea-level displacements with $h_s > Z_{cr} = 25$ cm were examined. A number was given to every surge, which had a height $h_s \geq 45$ cm at least at one of the 11 stations mentioned above. This numbering system is similar to that used for typhoons: the first two numbers represent year, the other two are sequential numbers (e.g., 7803, 7911, 8001, etc.) As an example, these parameters for the strongest surges at Nevelsk for 1979–91 are presented in Table 7.20.

Table 7.20: An example of catalogue parameters of several storm surges at Nevelsk (RABINOVICH and SOKOLOVA, 1992)

| Station | Year | Number | $t_s$ (day, month, hour) | $h_s$ (cm) | $h_{st}$ (cm) (+t,hr) | $T_s$ (hr) | $T_{s/2}$ (hr) | δ (cm/hr) | D ($cm^2$) |
|---|---|---|---|---|---|---|---|---|---|
| Nevelsk | 1979 | 7901 | 11.02.17 | 48.4 | 84(+2) | 49 | 15 | 3.22 | – |
| Nevelsk | 1979 | 7902 | 9.04.18 | 43.3 | 85(0) | 78 | 32 | 1.35 | 689 |
| Nevelsk | 1979 | 7904 | 19.08.08 | 43.7 | 104(0) | 76 | 43 | 1.02 | 408 |
| Nevelsk | 1979 | 7905 | 20.12.23 | 48.3 | 103(–3) | 53 | 28 | 1.73 | 858 |
| Nevelsk | 1980 | 8007 | 13.12.14 | 36.2 | 95(0) | 75 | 67 | 0.69 | 447 |
| Nevelsk | 1981 | 8101 | 24.08.06 | 49.2 | 115(0) | 71 | 24 | 2.05 | 465 |
| Nevelsk | 1981 | 8102 | 24.10.04 | 62.6 | 123(0) | 70 | 43 | 1.46 | 1177 |

It is interesting to compare the parameters of the same surge for different stations to better understand the peculiarities of surge formation. For example, the surge occurring during 20–22 October 1976 was not noticed at the southern mainland stations Posyet, Vladivostok, and Nakhodka ($h_s < 25$ cm), but was relatively strong on the southwestern coast of Sakhalin Island (Table 7.21).

Table 7.21: The storm surges of October 1976 at different coastal stations. t = time relative to $t_s$ of surge's maximum (RABINOVICH and SOKOLOVA, 1992)

| Stations | $t_s$ (day, month, hour) | $h_s$ (cm) | $h_{st}$ (cm) (+t,hr) | $T_s$ (hr) | $T_{s/2}$ (hr) | δ (cm/hr) | D ($cm^2$) |
|---|---|---|---|---|---|---|---|
| Krilyon | 21.10.00 | 38.9 | 57(+3) | 23 | 10 | 3.9 | 619 |
| Nevelsk | 21.10.17 | 61.5 | 63(0) | 51 | 24 | 2.6 | 1190 |
| Kholmsk | 21.10.16 | 47.2 | 50(+2) | 46 | 25 | 1.9 | 924 |
| Uglegorsk | 21.10.12 | 49.5 | 73(–3) | 51 | 27 | 1.8 | 880 |
| De-Kastri | 21.10.01 | 34.7 | 89(–3) | 51 | 7 | 4.9 | 267 |

The processing of tide gauge data makes it possible to obtain statistics of the surges, to estimate their seasonal distribution, and to find the most interesting (dangerous) cases. For these cases at least, but preferably for all, it is useful to define the parameters of the atmospheric processes which *forced* these surges. The following parameters were fixed at the moment of surge maxima (Fig. 7.75) the atmospheric pressure in the centre of the cyclone $P_{os}$; its velocity $V_s$ and direction $\alpha_s$; the position of the center relative to the station $r_s$, $\theta_s$; the pressure $P_s$ and in wind $W_s$, $\phi_s$ at the station. The parameters for the surge of 20–22 October 1976 are presented in Table 7.22. The cross correlation analysis of the parameters from the first (sea level) and second (meteorological) groups for the number of storm surges may be an effective instrument to look for empirical relations which may be used for a surge forecast.

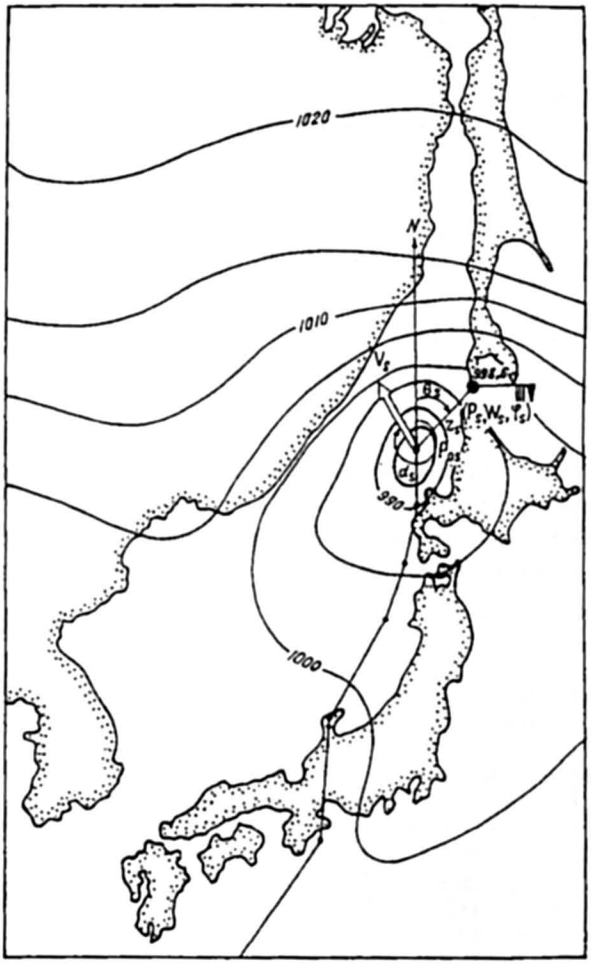


Fig. 7.75: Meteorological parameters of the atmospheric disturbance caused by a storm surge at the Krilyon station (RABINOVICH and SOKOLAVA, 1992)

It is possible also to describe storm surges using regression formulae:

$$\zeta(t) = a_0 + a_1 \cdot P(t) + a_2 \cdot \tau_z(t) + a_3 \cdot \tau_n(t) \qquad (7.9a)$$

where, $a_i$ are regression coefficients; $P(t) = P_a(t) - 1000$; $P_a(t)$ is the atmospheric pressure at the station in millibars; $\tau_z(t) = -0.025 \cdot W^2(t) \cdot \sin(\phi(t))$ and $\tau_n(t) = -0.025 \cdot W^2(t) \cdot \cos(\phi(t))$ are zonal and meridional components of wind stress; $W(t)$ and $\phi(t)$ are wind speed and direction at the station. In this case, four coefficients characterize every storm surge. The regression formulae in the form of eq. (7.9a) for the surge of 20–22 October 1976 are given in Table 7.22.

Table 7.22: The main cyclone and meteorological parameters at the maximum of the surge of October 1976 (RABINOVICH and SOKOLOVA, 1992)

| Stations | $P_{os}$ (mb) | $V_s$ (km /h) | $\alpha_s$ (deg) | $\theta_s$ (km) | $r_s$ (mb) | $P_s$ (mb) | $W_s$ (m/s) | $\phi_s$ (deg) | Regression Formulae |
|---|---|---|---|---|---|---|---|---|---|
| Krilyon | 980 | 67 | 30 | 60 | 12 | 980.7 | 14 | 135 | $\zeta(t) = 12.16 - 0.87P(0) - 14.34\tau_z(0) + 2.30\tau_n(0)$ |
| Nevelsk | 965 | 41 | 340 | 210 | 726 | 991.7 | 19 | 273 | $\zeta(t) = 5.70 - 1.64P(0) + 18.50\tau_z(0) + 5.22\tau_n(0)$ |
| Kholmsk | 965 | 41 | 340 | 210 | 670 | 991.0 | 21 | 263 | $\zeta(t) = -8.34 - 2.14P(0) + 14.55\tau_z(0) + 1.30\tau_n(0)$ |
| Uglegorsk | 965 | 52 | 340 | 225 | 326 | 983.8 | 21 | 269 | $\zeta(t) = -0.76 - 1.66P(0) + 17.50\tau_z(0) + 10.0\tau_n(0)$ |
| De-Kastri | 965 | 79 | 340 | 0 | 780 | 985.6 | 7 | 199 | $\zeta(t) = 13.50 - 0.41P(0) - 13.48\tau_z(0) - 6.10\tau_n(0)$ |

For a better description of individual storm surges, more precise regression formulae may be used:

$$\zeta(t) = a_0 + a_1 \cdot P(t - \Delta t_1) + a_2 \cdot \tau_z(t - \Delta t_2) + a_3 \cdot \tau_n(t - \Delta t_3) \qquad (7.9b)$$

where, $\Delta t_i$ are the corresponding time lags. Three additional parameters are necessary to determine the surge.

## 7.5 Australia

Storm surges on the south coast of Australia occur due to extra tropical cyclones (ETC's). According to VECCHIO (1980) storm surges at Adelaide comprise of a locally generated surge due to the interaction of wind stress with local topography and an external effect arising from the passage of winter depressions across the Great Australian Bight. He cautions that the effects may not be totally independent.

For the positive surge, the local effect contributes about 0.75 m and the external effect adds about another 0.5 m. The 0.75 m of the locally generated surge is made up of about 0.25 m due to the decrease of atmospheric pressure and 0.5 m due to the wind stress.

Between 1948 and 1977, there were 12 surge events in Adelaide. Strong northwest winds prevailing for periods of 24 hours or longer, and associated with deep lows over ocean waters, south of the bight, can generate positive surges up to one meter in amplitude. Along the Adelaide foreshore, the most destructive storm surge of this type occurs when the wind direction rapidly shifts from the northwest to a squally southwesterly, the change in wind direction occurring near the time of maximum tide height. Fig.s 7.76 and 7.77 respectively show typical synoptic situations for NW and SE winds at Adelaide.

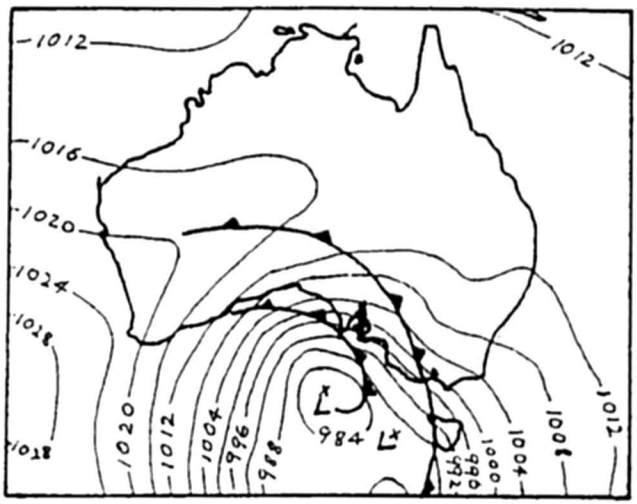


Fig. 7.76: Synoptic chart NW winds at Adelaide (VECCHIO, 1980)

VECCHIO referred to the external component of the surge. MURTY (1995) studied this and showed that surges generated at the southwest coast of Australia propagate eastward along the south coast as far as the Bass Strait. Fig. 7.78 shows the tide gauge locations. One can see from Fig. 7.79 that the surge is quite coherent as it propagates from Hillary's to Port Stanvac (Adelaide) but is not detectable east of Adelaide at Portland. The Bass Strait sets up its own seiches, which can be clearly seen at Lorne, Stony Point and Burnie. Fig. 7.80 shows an event for Nov '94 that is similar to the event of May '94 shown in Fig. 7.79.

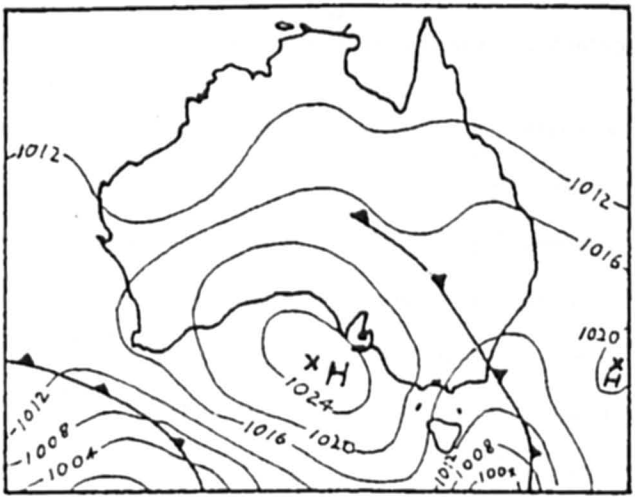


Fig. 7.77: Synoptic chart SE winds at Adelaide (VECCHIO, 1980)

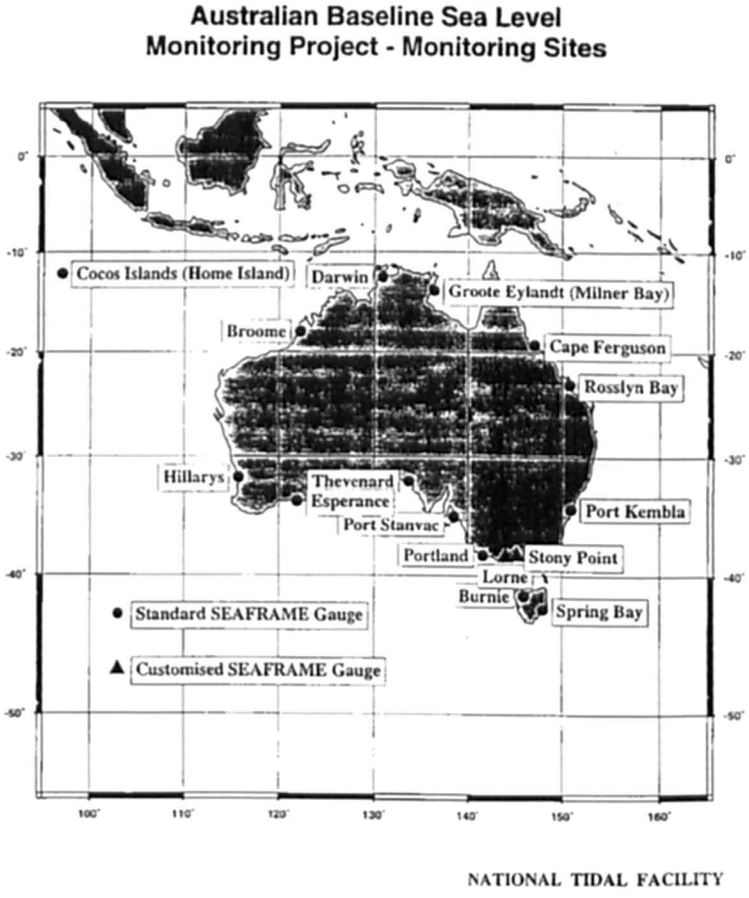


Fig. 7.78: Tide gauge positions (MURTY, 1995)

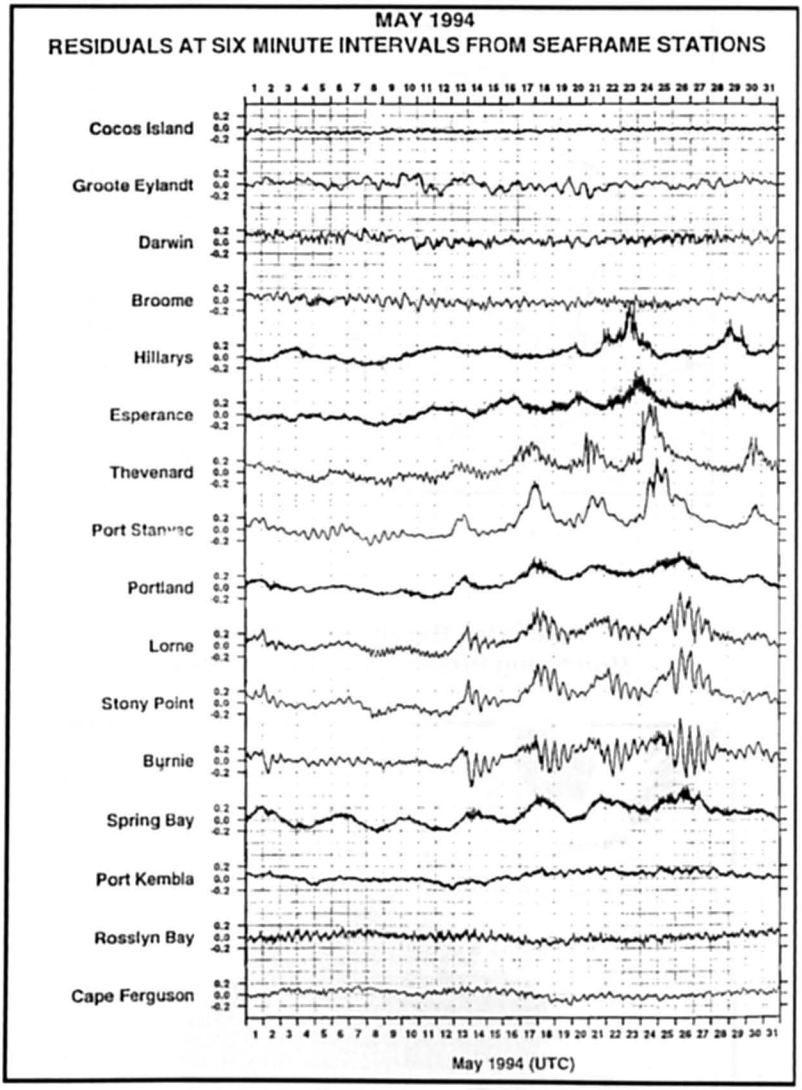


Fig. 7.79: Residuals at six minute intervals from SEAFRAME stations (m) May 1994 (MURTY, 1995)

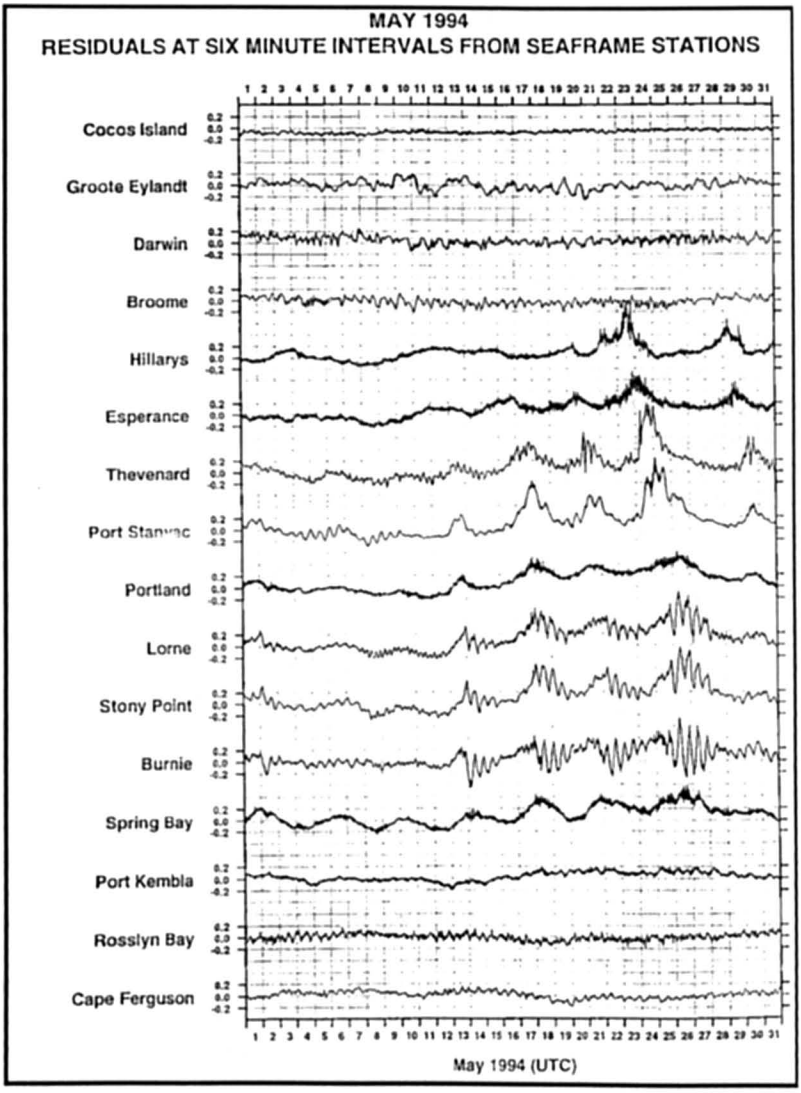


Fig. 7.80: Residuals at six minute intervals from SEAFRAME stations (m) November 1994 (MURTY, 1995)

## 7.6 Oceanic Regions

Some oceanic islands are influenced by a type of weather system known as sub-tropical cyclones, which are similar to tropical cyclones in terms of having a warm core, but otherwise resemble extra-tropical cyclones (HASTENRATH, 1996). SIMPSON (1952) coined the word "sub-tropical cyclone" which was further elaborated by RAMAGE (1971). The subtropical cyclones of the eastern north Pacific during the winter to spring of the Northern Hemisphere are referred to as Kona storms in the Hawaiian Islands. These originate from cut-off lows in the upper level subtropical westerlies.

According to HASTENRATH (1996) the centre of the system is between 400 to 600 HPa (mid-troposphere) and the pressure gradients, winds and convergence increase from the periphery inward. Strong mid-tropospheric convergence is compensated by divergence in the upper troposphere and to a lesser extent in the lower layers. RAMAGE (1971) proposed a conceptual model, which includes an upward and a downward branch within about 500 km from the centre, strong upward, motion gives rise to condensation and deep precipitating clouds. Beyond about 500 km from the centre, there is downward motion with dry adiabatic warming extending to the subsidence inversion (HASTENRATH, 1996).

The relatively warm-cored upper branch is energy producing, while kinetic energy dissipation within a weak surface circulation is small, thus favouring the longevity of the system. Development of an eye similar to tropical systems is common. These subtropical cyclones also occur to the southwest of Azores in the Atlantic Ocean.

Over the northern Indian Ocean, a somewhat different type of a subtropical cyclone can occur. These occur during the southwest monsoon (one to two per month) over the northwestern part of the Arabian Sea and occasionally over the northern part of Bay of Bengal and over southern Indochina. According to RAMAGE (1971) the energy exported from the heat low over the South Asian continent is responsible for the origin of these subtropical cyclones. In contrast to the winter subtropical cyclones of the Northern Pacific, those in the monsoon area do dissipate due to the injection of drier air.

It is well known that tropical cyclones get transformed into extratropical cyclones. This extratropical transition (ET) is complex and highly variable process that is currently poorly understood (MALMQUIST, 1999). According to him, the occurrence of ET's also portends the possibility that a single storm system can impact the tropics, midlatitudes and high latitudes. For example, an Atlantic system might track across the Caribbean and the southern part of the U.S.A. as a tropical cyclone and can change to an extratropical cyclone that can strike the New England, States of U.S.A., Canada and Europe. Some new concepts are (1) Maximum Potential Intensity (MPI) of an ET (2) Maximum Potential Extratropical Transition (MPET). These new concepts could be used to produce real time Damage Potential (DP) maps.

# 8. Impact of Climate Change and Sea Level Rise on Storm Surges

The ideas of Global Change and the Greenhouse Effect are usually interpreted narrowly, in the sense of anthropogenic causes of warming of the earth and climatic change. In reality, the predicted warming of the earth is due to the Greenhouse Effect. However, this is not exclusively a phenomenon of the present, in particular the time since the Industrial Revolution, but, rather, a natural response of the earth and its atmosphere to solar radiation.

The natural Greenhouse gases ensure that the climate remains pretty much constant and that an average temperature between +15° C and –15° C predominates on earth, since they permit the warming sunlight to permeate to the earth and, on the other hand, prevent the thermal radiation from the earth from completely escaping into space. The earth's equilibrium radiation balance is composed of a combination of the following components (GRASSL and KLINGHOLZ, 1990).

An output of 343 Watts reaches each square metre of the earth's surface. Of this, clouds, the brightness of the earth's surface and air molecules reflect 30 %. Opposing this, 49 % of the sun's radiation is absorbed by the earth's surface and 30 % by the atmosphere. This energy also warms the earth and, among other things, causes water to evaporate from the oceans. The earth, in turn, radiates the afore mentioned thermal energy outwards. However, a part is held back because of the clouds and the Greenhouse gases. Whilst the visible sun's energy reaches the earth as short-wave radiation, and thereby penetrates through the earth's atmosphere, the earth in turn emits long-wave radiation.

Carbon dioxide is used here as an example of the Greenhouse gas molecules to explain the "functioning" of the Greenhouse gases. When the thermal radiation hits a carbon dioxide molecule, the oxygen atoms on the side of the carbon begin to rotate and induce the carbon atom to vibrate. In this manner, the carbon atom absorbs the thermal radiation and heats up the atmosphere. A part of the energy that is given off in all directions by the carbon dioxide molecules will be returned to the earth.

The other Greenhouse gases, mainly water vapour, ozone, laughing gas, methane and the anthropogenically-produced chlorofluorocarbons, have a similar effect, so that only 16 % of them will be transmitted to the space directly; the rest will be transmitted through the atmosphere. In this manner a balance arises, which means that out of the 237 W/m$^2$ of solar energy, which reaches earth, 390 W/m$^2$ of the thermal radiation will be returned to the atmosphere. However, only the "equivalent" 237 W/m$^2$ disappears into space the remaining 153 W/m$^2$ will be emitted again and again, ultimately leaving the earth in equilibrium, as a result of the Greenhouse gases. In this manner the Greenhouse gases operate like a pane of the greenhouse. The climate system, like all complex systems, will be variable, as would also be the case without anthropogenic intervention, "depending on the most dominant timescale of the interacting parts of the climatic fluctuations involved. It is then only a question of the average time intervals chosen as to whether the variability of the climatic fluctuations will be significant" (GRASSL, 1993).

## 8.1 The Greenhouse Gases

Water vapour, carbon dioxide, methane, ozone and nitrogen dioxide are Greenhouse gases. In combination they make up an extremely small portion of the air. Dry air – dry due to the very variable portions of water vapour in the air – consists of up to 78.08 % nitrogen, up

to 20.95 % of oxygen and up to 0.93 % of the inert gas argon (GRASSL and KLINGHOLZ, 1990), none of which have any relevant role with regard to the terrestrial thermal equilibrium. These components lack the necessary characteristics to absorb solar radiation and thermal radiation.

As already mentioned, the most important Greenhouse gas affecting the heat balance is water vapour. It varies, depending on temperature and air humidity, in its volumetric proportion from one million parts in the stratosphere (the layer of the atmosphere about 50 km above the earth) to over one thousand parts over the polar regions and up to 300 parts in the tropics near the earth's surface (GRASSL and KLINGHOLZ, 1990).

Carbon dioxide, although one of the most important gases in the air only makes up 0.035 % of the air, but next to water vapour, is one of the most important Greenhouse gases. All Greenhouse gases combined make up, in total, only 3 % by volume of the air.

Table 8.1: A sample of Greenhouse gases affected by human activities (IPCC, 1995)

| | $CO_2$ | $CH_4$ | $N_2O$ | CFC-11 | HCFC-22 (CFC-substitute) | $CFC_4$ (perfluoro-carbon) |
|---|---|---|---|---|---|---|
| pre-industrial concentration | 280 ppmv | ~ 700 ppbv | ~ 275 ppbv | 0 | 0 | 0 |
| Concentration 1994 | 358 ppmv | 1720 ppbv | 312* ppbv | 268* pptv | 110 pptv | 72* pptv |
| Rate of change of concentration* | 1.5 ppmv/yr<br>0.4 %/yr | 10 ppbv/yr<br>0.6 %/yr | 0.8 ppbv/yr<br>0.25 %/yr | 0 pptv/yr<br>0 %/yr | 5 pptv/yr<br>5 %/yr | 1.2 pptv/yr<br>2 %/yr |
| Atmospheric life time | 50–200§§ | 12§§§ | 120 | 50 | 12 | 50.000 |

The growth rates of $CO_2$, $CH_4$ and $N_2O$ are averaged over the decade commencing 1984; halocarbon growth rates are based on recent years (1990s).

* = Estimated from 1992–93 data.

§ = 1 pptv = 1 part per trillion (million million) by volume.

§§ = No single lifetime for $CO_2$ can be defined because of the different rates of uptake by different sink processes.

§§§ = This has been defined as an adjustment time which takes into account the indirect effect of methane on its own lifetime.

CFC = Chlorofluorcarbon.

Tab. 8.1 shows the increase of Greenhouse gases due to anthropogenic activity. The figures are taken from the 1995 IPCC report (IPCC, 1995). Clearly, a rise in the concentration of $CO_2$ has been recorded from 280 ppmv in pre-industrial times to 358 ppmv in 1994. Equally, there is no doubt that this rise is connected with anthropogenic activity, especially the burning of fossil fuels, but also with alterations to the use of land and, to a lesser degree, concrete production. Before the rise in the concentration of $CO_2$, $CO_2$ concentration fluctuated about 280 ppmv ±10 ppmv for around 1000 years.

In addition, methane rose, doubtless due to anthropogenic activity, such as rice cultivation, animal husbandry, burning of biomass and gas leakage, as well as the use of fossil fuels. The global average methane concentration has risen by about 6 % in the decade since 1984 and by about 145 % between the Industrial Revolution and 1994.

$N_2O$ (nitrogen dioxide, laughing gas) has a relatively low rate of increase, but, for all that, a long residence time in the atmosphere. The cause of laughing gas is, above all, nitrogenous manure in the landscape and a succession of industrial processes. Since the Industrial Revolution, the proportion of $N_2O$ in the atmosphere has risen from 275 ppv to 312 ppv, in association with a clear decrease in the growth rate in recent years (in the 80s and early 90s close to 0.8 ppbv/year, reducing to 0.5 ppbv/year in 1993).

In the early 90s, the growth rate of $CO_2$, $CH_4$ and $N_2O$ was insignificant. This natural variation is still not clear, but the data from recent years show that the trend of the 80s is continuing.

Halocarbons include chlorine and bromine and result in ozone depletion. The Montreal Protocol sets limits on emissions, as a result of which the growth rate has been reduced. The growth rate of $CFC_s$ has, as a result, been reduced to zero. The Montreal Protocol also ordered reductions in the concentration of $CFC_s$, $HCFC_s$ and their consumption of ozone.

Greenhouse gases with longer duration times, such as, mainly, $HCFC_s$, $PFC_s$ and $SF_6$, are currently an insignificant influence on radiation intensity. However, their projected growth may greatly increase the intensity of radiation amplification in the twenty-first century.

Ozone, $O_3$, is an important Greenhouse gas, present in both the stratosphere and the troposphere. Alterations to ozone result in increased radiative forcing by influencing both the solar incoming radiation and the outgoing terrestrial radiation. The intensity of the solar radiation is strongly related to the vertical distribution of ozone and reacts with particular sensitivity to alterations at the level of the troposphere. The pattern of tropospheric and stratospheric ozone alterations is spatially variable. The estimation of the radiative forcing due to changes in ozone is essentially more complicated than that for the Greenhouse gases.

Tropospheric ozone levels have clearly risen since 1900, with strong evidence that this has occurred in many places since the 60s. In the 1990s, however, the upward trend has slowed and almost come to a halt. Altogether the northern hemisphere has seen a doubling in tropospheric ozone since the Industrial Revolution, an increase of 25 ppbv; whereas, in the southern hemisphere a diminution has been recognised since the mid-80s.

Decreases in stratospheric ozone have been observed since the 70s, mainly in the lower stratosphere, the most obvious feature of which is the phenomenon of the ozone hole over the Antarctic in September and October. A statistically significant decrease in total ozone levels has been noted in the mid latitudes of both hemispheres. In the tropics there is a slight trend towards ozone reduction, rather than an increase.

The calculation of the global average radiative forcing is a good way to get an overall impression of the potential climatic relevance of the individual components. Looking at this from a global angle has limitations:

1. the spatial pattern of the mixture of Greenhouse gases
2. the regional variation of tropospheric ozone and
3. the regional variation of tropospheric aerosols.

Such a global view of the radiative forcing does not reflect the complete pattern of potential climatic variations. It is not permitted to take negative numbers into account as a balancing factor. Table 8.2 presents the average radiative forcing:

Table 8.2: Annually Average Radiative Forcing

| Factors | Capacity in $Wm^{-2}$ |
|---|---|
| Greenhouse gases ($CO_2$, $CH_4$, $N_2O$ and Halocarbons) | + 2.45 $Wm^{-2}$ (from + 2.1 to + 2.8 $Wm^{-2}$) |
| Tropospheric ozone | + 0.4 $Wm^{-2}$ (from + 0.2 to + 0.6 $Wm^{-2}$) |
| Stratospheric ozone | – 0.1 $Wm^{-2}$ (from – 0.05 to – 0.2 $Wm^{-2}$) |
| Anthropogenic Aerosols (Sulphates, soot from fossil fuel, mainly coal, and organic aerosols resulting from biomass burning) | – 0.5 $Wm^{-2}$ (from – 0.25 to – 1.0 $Wm^{-2}$) |
| Sulphate aerosols (fossil fuel emission) | – 0.4 $Wm^{-2}$ (from – 0.2 to – 0.8 $Wm^{-2}$) |
| Soot in aerosols from fossil fuel sources | + 0.1 $Wm^{-2}$ (from 0.03 to 0.3 $Wm^{-2}$) |
| Direct radiative forcing of particles associated with biomass burning | – 0.2 $Wm^{-2}$ (from – 0.07 to –0.6 $Wm^{-2}$) |
| Tropospheric dust particles influenced by man's activities | not quantifiable |
| Changes in cloud properties caused by aerosols due to man's activities (indirect effect) | 0 to – 1.5 $Wm^{-2}$ (cannot be quantified exactly, which is why, for scenario as a rule, –0.8 $Wm^{-2}$ is used) |
| Alterations to radiative forcing due to changes in solar radioactive output* | + 0.3 $Wm^{-2}$ (from 0.1 to 0.5 $Wm^{-2}$) since 1850 |
| Aerosols resulting from volcanic eruptions* | large for short periods of time (few years), e.g. Mt. Pinatubo –3 to –4 $Wm^{-2}$ |

* The past variation can explain climatic changes of periods of time on a decadal basis.

## 8.2. Global Change

As is seen clearly from the above, changes in global climate are closely correlated with the amount of Greenhouse gases in the atmosphere. In the case of an increase of Greenhouse gases in the atmosphere, the air temperature on earth will also rise, and this, in turn, will stimulate the earth's hydrological cycle: "per degree of temperature change, the amount of water vapour in the air increases by about 10 %" (GRASSL, 1993: 29). It has to be pointed out that the Greenhouse gases are always efficacious at a global scale and cannot be compensated on a regional basis, unlike the anthropogenic alterations of the surface (GRASSL, 1993).

A further feedback arises through alterations of temperature in the hydrological cycle. These temperature variations occur due to the fact that the brightest and darkest natural surfaces of the Earth are constituted of water. The darkest surface is the ocean and powdery snow is the brightest. In the case of warming, the brightness of the surface decreases and it will absorb more solar energy; this means that a further warming will result from the melting of the glaciers.

The clouds, as an additional factor, have two effects: whilst the low clouds mainly have a cooling effect, the high clouds have a warming effect. These thin high clouds are, however, also created by anthropogenic effects through aircraft exhaust emissions. However, the ultimate effect of the clouds on global warming is, currently, not clear.

The mean global surface temperature has risen by about 0.3° to 0.6° C since the late 19th century, and by about 0.2° to 0.3° C over the last 40 years. The warming occurred largely during two periods, between 1910 and 1940 and since the mid-1970s (IPCC, 1995).

The warming has not been globally uniform. The recent warmth has been greatest over the continents between 40° N and 70° N. A few areas, such as the North Atlantic Ocean north of 30° N, and some surrounding land areas, have cooled in recent decades (IPCC, 1995).

It can, however, be pointed out that since 1400 AD the global average temperature has been higher than in all previous centuries during the historic period (IPCC, 1995).

However, this cannot be clearly differentiated from the natural variations of the climate due to the alterations of trace gas concentration since the beginning of the Inertia Revolution, as the uncertainty in the key factors is still too great and the thermal of the ocean to balance the retardation of the effects of the previous influence of each decade have to be considered.

Information on **climatic change in the future** is much more difficult to ascertain, as the main problem lies in the estimation of future anthropogenic trace gas emissions. Therefore different scenarios have been undertaken, which take into account the differing increases in trace gas emissions. Data from the Intergovernmental Panel on Climate Change (IPCC) have been used as a basis for the production of these scenarios. This Panel was founded as an intergovernmental committee and is supposed to be used as the basis for political decisions. However, it must be noted that other institutions sometimes predict a different set of results.

The IPCC differentiates between four scenarios, which are calculated from coupled ocean-atmosphere models. These scenarios, whose assumptions are listed below, take into account the emissions from Greenhouse gases as well as aerosol processes:

A) Economic development remains as at present, so that the world energy consumption quadruples to the year 2100. At the same time the rate of cutting of the tropical rainforests continues as before (Scenario "Business As Usual").
B) Moderate intervention in the global trace gas exchange will occur.
C) Considerable intervention in the global trace gas exchange will occur.
D) An immediate and considerable reduction in the ejection of all climatically significant trace material will occur. In spite of this, all Greenhouse gases initially increase in this scenario until the year 2030.

Equally in the case of – as GRASSL and KLINGHOLZ (1990) (in translation) put it so well – "an immediate and complete cessation" there would be a definite rise in the global average temperature over the next 100 years. The clearest conclusion comes, naturally, from Scenario A "Business As Usual", as a result of which the most favourable outcome for man would be a temperature increase of 2.0° C by 2100, followed by a continued rise with hardly any reduction in rate. "Such a high average temperature has not occurred since at least 200 000 years ago" (GRASSL, 1998). There is, essentially, a slight reduction in the increase for Scenarios B and C. The likely equilibrium response of global surface temperature to a doubling of equivalent carbon dioxide concentration (the "climate sensitivity") was estimated in 1990 to be in the range 1.5 to 4.5° C, with a "best estimate" of 2.5° C (IPCC, 1995).

Although $CO_2$ is the most important Greenhouse gas, the other Greenhouse gases contribute a significant portion (30 %) the projected global warming.

### 8.2.1 Effects

The results of such an increase in temperature would be quite varied and broad. In general, an increase of temperature of just one tenth of a degree would alter the boundary of the deserts by 50–100 km; half a degree would displace the northern forest boundaries by the same distance and cause the glaciers of the mid latitudes to retreat by a vertical distance of at least 200 meters. "The Earth has not experienced a 2 degrees higher average temperature since the existence of modern man, Homo sapiens. A four degrees warmer Earth has not occurred since man first appeared four million years ago" (GRASSL and KLINGHOLZ, 1990).

The following effects for temperature and precipitation may be ascertained from the models (IPCC, 1995):

"All model simulations, whether they are forced with increased concentrations of greenhouse gases and aerosols, or with increased greenhouse gas concentration alone, show the following features:

- generally greater surface warming of the land than of the oceans in winter, as in equilibrium simulations;
- a minimum warming around Antarctica and in the northern North Atlantic which is associated with deep oceanic mixing in those areas;
- maximum warming in high northern latitudes in later autumn and winter associated with reduced sea ice and snow cover;
- little warming over the Arctic in summer;
- little seasonal variation of the warming in low latitudes or over the southern circumpolar ocean;
- a reduction in diurnal temperature range over land in most seasons and most regions;
- an enhanced global mean hydrological cycle;
- increased precipitation in high latitudes in winter.

"Including the effects of aerosols in simulations of future climates leads to a somewhat reduced surface warming, mainly in the mid latitudes of the Northern Hemisphere. The maximum winter warming in high northern latitudes is less extensive.

"However, adding the cooling effect of aerosols is not a simple offset to the warming effect of greenhouse gases, but significantly affects some of the continental-scale patterns of climate change. This is most noticeable in summer where the cooling due to aerosols tends to weaken monsoon circulations. For example, when the effects of both greenhouse gases and aerosols are included, Asian summer monsoon rainfall decreases, whereas in earlier simulations with only the effect of greenhouse gases represented, Asian summer monsoon rainfall increased.

"Conversely, the addition of aerosol effects leads to an increase in precipitation over southern Europe, whereas decreases are found in simulations which employ only the greenhouse gases." (IPCC, 1995).

"All model simulations, whether they are forced with increased concentrations of greenhouse gases and aerosols, or with increased greenhouse gas concentration alone, produce predominantly increased soil moisture in high northern latitudes in winter. Over the northern continents in summer, the changes in soil moisture are sensitive to the inclusion of aerosol effects." (IPCC, 1995:43).

### 8.2.2 Ocean circulation

"In response to increasing greenhouse gases, most models show a decrease in the strength of the northern North Atlantic oceanic circulation further reducing the strength of the warming around the North Atlantic. The increase in precipitation in high latitudes decreases the surface salinity, inhibiting the sinking of water at high latitude, which drives this circulation." (IPCC, 1995).

The alterations of the regional gradients are, as a rule, greater than the global gradients, because the amount of aerosols, the land use and the combined ecological effects of the individual factors can amplify or, depending on circumstances, can also reduce the variation.

The variability of the climatic change has a greater effect than the equivalent changes in average climate variations. They can lead to alterations in the frequency of extremes (IPCC, 1995):

### 8.2.3 Temperature

A general warming tends to lead to an increase in the occurrence of extremely high temperatures and a decrease in extremely low temperatures (e.g., frost days).

### 8.2.4 Hydrology

New results reinforce the view that variability associated with an enhanced hydrological cycle translates into prospects of more severe droughts and/or floods in some places and less severe droughts and/or floods in other places.

### 8.2.5 Mid-latitude storms

Conclusions regarding extreme storm events are, obviously, even more uncertain.

### 8.2.6 Hurricanes/Tropical cyclones

Although some models now represent tropical storms with some realism for present day climate, the state of the science does not allow assessment of future changes.

### 8.2.7 El Nino-Southern Oscillation

An average warming of the sea surface in the tropics will result from increased Greenhouse gas emissions, so the variability of the precipitation could be increased, as occurs in connection with ENSO events.

## 8.3 Sea-Level Rise

One of the major consequences of climate change could be the rise of sea level.

There are hundreds of publications about this phenomenon, these can be distinguished between those, which focus their research on the postglacial sea-level rise, and those, which look at the changes over the last 100 years and calculate future trends.

This chapter concentrates on the second approach. The results and conclusions refer to IPCC 1995, except where indicated to the contrary.

### 8.3.1 Reasons for Sea-Level Rise (GRASSL, 1993)

In the case of global warming, the sea level will rise. There are mainly two reasons for this reaction to the rise of temperature. Firstly the thermal expansion of the oceans, secondly melting of mountain glaciers. The two other big potential resources of water for sea-level rise are the Antarctic and the Greenland ice sheets.

Thermal expansion of water depends on the depth of the warming of the water body and the ocean currents. Therefore the thermal expansion results in a regional pattern of sea-level rise and global estimation is very difficult. It is certain that areas of the ocean, which are mixed in depth, will have a greater thermal expansion in relation to the warming of the surface.

By contrast, melting of the ice sheets cause a sea-level rise, which results in the same alterations in level globally. Whereas the mountain glaciers can cause a global sea-level rise the reaction of the ice sheet from Greenland cannot be calculated very well, because the answer to the question as to whether it is melting or expanding is not certain.

The IPCC (1995) summarises the function of the Greenland and Antarctic ice sheets as being relatively minor over the next century. However, the possibility of large changes in volumes of these ice sheets (and consequently, in sea-level) cannot be ruled out, although the likelihood is considered low. (IPCC, 1995)

### 8.3.2 Has Sea-Level Risen? (IPCC, 1995)

The analyses of tide gauge records show a sea-level rise by about 10–25 cm over the last 100 years. The main uncertainty of results from tide gauges is the vertical land movement, but methods for filtering out the effects of long-term vertical land movements as well as greater reliance on the longest tide-gauge records for estimating trends have given greater confidence in the results.

Over the period of the last 100 years much of the sea-level rise has been related to the concurrent rise in the global temperature. The observed sea-level rise may account initially for about 2 to 7 cm from the warming and consequent expansion of the oceans and secondly for about 2 to 5 cm from the retreat of glaciers and ice caps. "Only a small change in sea-level has been caused by surface and groundwater storage."

"The rate of observed sea-level rise suggest that there has been a net positive contribution from the huge ice sheet of Greenland and Antarctica, but observations of the ice sheets do not yet allow meaningful quantitative estimates of their separate contributions. The ice sheets remain a major source of uncertainty in accounting for past changes in sea-level, because there are insufficient data about these ice sheets over the last 100 years." (IPCC, 1995) Furthermore is not really clear if they cause a sea-level rise or decrease (GRASSL, 1993).

### 8.3.3 Global mean Sea-Level Projections

Projections of the global sea-level rise are taken from the results of IPCC 1995: Summary and 40 ff.; for the calculation for the 21st century IS92 scenarios are used. "For the IS92a scenario assuming the "best estimate" values of climate sensitivity and of ice melt sensitivity to warming, and including the effects of future changes in aerosol, models project an increase of sea-level of about 50 cm from the present to 2100." (IPCC, 1995). The range between the lowest emission scenario (IS92c) and the highest emission scenario (IS92e) is 15 cm to 95 cm from present to 2100 (Fig. 8.1).

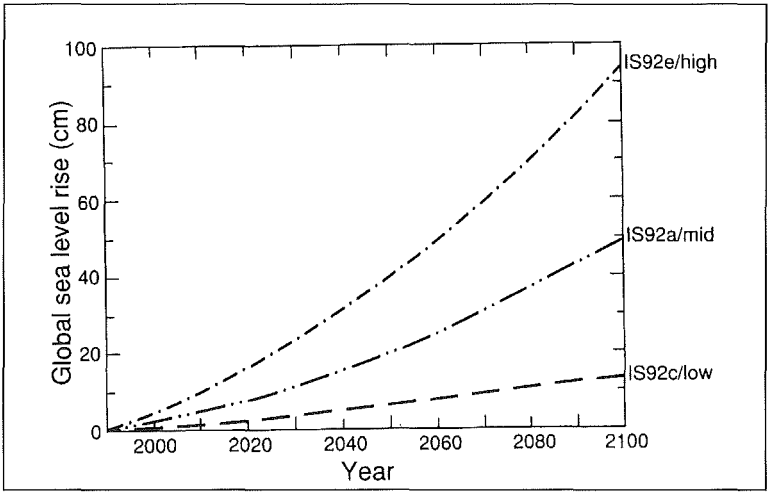


Fig. 8.1: Projected global mean sea-level rise extremes from 1990 to 2100. The highest sea-level rise curve assumes a climate sensitivity of 4.5° C, high ice melt parameters and the IS92e emission scenario; the lowest a climate sensitivity of 1.5° C, low ice melt parameters and the IS92c emission scenario and the middle curve a climate sensitivity of 2.5° C, mid-value ice melt parameters and the IS92a scenario (IPCC, 1995)

Due to the large thermal inertia of the ocean-ice-atmosphere climate system the choice of emission scenario has relatively little effect on the projected sea level rise. In the second part of the 21st century the effects increase.

Moreover the sea-level "would continue to rise at a similar rate in future beyond 2100, even if concentrations of greenhouse gases were stabilised by that time, and would continue to do so even beyond the time of stabilisation of global mean temperature." (IPCC, 1995)

The future sea-level rise will differ regionally owing to regional differences in heating and circulation changes.

## 8.4 Possible Impact on the Intensity and Frequency of Cyclones

One of the widely recognized consequences of global warming would be increased sea surface temperature (SST). It is known that the tropical cyclones derive their energy mainly from the latent heat of evaporation from the ocean. Warm water of at least 26–27° C is needed to supply energy for cyclogenesis. The behaviour of tropical cyclones in warmer world, where we may have larger area of sea having temperature over this critical value, has been the subject of considerable speculation and concern.

Although the casual relationship between SST and the formation of tropical cyclones suggest that the theoretical maximum intensity may increase with temperature, the evidence inferred from several observational and modelling studies is still conflicting (RAPER, 1993; RYAN et al., 1992; STEIN and HENSEN, 1994). This may be attributed to the fact that the formation of tropical cyclones depends not only on SST but a number of other factors which include, the vertical lapse rate of the atmosphere, vertical wind shear, mid-tropospheric relative humidity and the prior existence of a center of low-level cyclone vorticity (GRAY, 1979). The factors change in complex ways with changing climate. An estimate of such changes is therefore not straightforward and may only be derived from state-of-the-art climate models. Present day climate models are able to simulate some of the aspects of tropical cyclone occurrence (MANABE and BROCCOLI, 1990; HAARSMA et al., 1993), they are not adequate enough to predict changes in warming climate. Most of the impact assessment studies carried so far use indirect techniques, rather than direct simulation of the tropical cyclones.

EMANUEL (1987) combined the $CO_2$ induced SST changes simulated by the Goddard Institute of Space Studies (GISS) climate model (HANSEN et al., 1984) with a theoretical tropical cyclone model (EMANUEL, 1986) to estimate the potential change in the intensity of tropical cyclones. His estimate showed that the intensity of tropical cyclones would increase as a result of increased tropical SSTs. However, in the absence of any empirical evidence in this regard. Emanuel's modelling results may not be considered very realistic.

NICHOLLS (1989) examined the activities of tropical cyclones and their intensities with SST from observations. He found little evidence of any relationship between monthly average SST and the number of tropical cyclones.

RAPER (1993) studied in detail the relationship between climate change and the frequency and intensity of severe tropical cyclones for the six tropical cyclogenesis regions, viz., North Atlantic, Western North Pacific, Eastern North Pacific, North Indian and extended Australian region (Southwest Pacific/Australian region). He used the US National Oceanic and Atmospheric Administration tropical cyclone data set (NOAA, 1988) for his study. He did not find any convincing empirical evidence in support of the relationship between SSTs and cyclone intensities. However, an increase in SSTs indicated a threshold effect that could lead to increase in the intensity of most severe storms. With regard to the relationship between tropical cyclone activity and SSTs, RAPER (1993) found different relationships in different areas. While predominantly negative correlation is found in two (North Indian Ocean and West North Pacific) of the six cyclone regions, four other regions showed a predominantly positive correlation. In the regions with highest positive correlation, simple regression suggests an increase of 37–63 % in severe tropical storm frequency per degree increase in SST. However, this relationship may not be constructed as having predictive skill for long term climate change as evidence suggest that the relationship is not necessarily directly casual because the areas of correlation are not always coincident with the areas of cyclone origin and tracks. Thus, the effect of SSTs may be indirect, through the connection with the regional-

scale atmospheric circulation. The main conclusion emerged from the analysis of RAPER (1993) was that changes in tropical cyclone activity in warmer world will depend crucially on the changes that may occur in the regional-scale atmospheric circulation.

A study undertaken by GRAY (1990) suggests that Atlantic hurricane activity over the period 1970 to 1987 was less than half that in the period 1947 to 1969, Western North Pacific also showed a decrease in the number of very intense tropical cyclones. In the Northeast and Southwest Pacific the number of cyclones appears to have increased (THOMPSON et al., 1992; LANDSEA et al., 1996).

EVANS (1993) looked into the relationship between SST and intensity of TCs for different regions where they form. Except for intense storms in the North Atlantic, his results indicate that there is little evidence to support the direct relationship between SSTs and cyclone intensities in most of the regions. CHANGNON (1993) studied historical variations in 146 major storms during 1950–1990 to describe their temporal characteristics and possible relationship to climate change. His results suggest that a warmer regime over North America would be associated with a greater incidence of major storms in the US.

In the North Indian Ocean the frequency of tropical disturbances has noticeably decreased (GADGIL, 1995) since 1970 (Fig. 8.2) while SSTs have risen here since 1970, probably more than in any other region (RAPER, 1993).

PITTOCK (1992) reports that sensitivity studies using limited area models in response to modelled increase in SST, suggests that cyclones may be more intense under warmer conditions. He notes, however, that historical data do not demonstrate any strong link between tropical cyclone numbers or intensity and SST, other than the lower limit for occurrence of around 27° C.

LIGHTHILL et al. (1994) observed that although substantial regional changes are expected but there are no compelling reasons to believe a major change in global tropical cyclone frequency.

As mentioned earlier, present day climate models are not able to simulate tropical cyclones well, nevertheless there have been large numbers of modelling studies carried out using low resolution GCMs. RYAN et al. (1992) used a GCM to assess tropical cyclone frequencies from yearly Genesis Parameter defined by GRAY (1975). He showed that the Gray's parameter forced by the output of a GCM gives a good representation of the observed tropical cyclone climatology. He, however, notes that changes in the Gray's Genesis Parameter due to enhanced greenhouse conditions were dominated by the SST changes.

In another numerical experiment carried out with the GFDL coupled ocean-atmosphere model, STEPHENSON (1993) showed that the Atlantic storm track weakens with increasing $CO_2$, while the Pacific storm track changes little. HAARSMA et al. (1993) analyzed the results of a GCM to show that the number of simulated tropical disturbance increases by about 50 % with the doubling of the $CO_2$ concentration. His GCM analysis also indicated a change in cyclone tracks as a result of $CO_2$ induced global warming. On the other hand, BENGTSSON et al. (1994) indicated that with a doubling of $CO_2$ over the next 50 years, the global and seasonal distribution of storms should be similar to the present observations. They also found a significantly reduced number of tropical cyclones for enhanced greenhouse scenario. This decrease in the number of tropical cyclones was substantial in the Southern Hemisphere, which seems unusual.

Recently DRUYAN and LONERGAN (1997) adapted hurricane frequency index (GRAY, 1979) so that it can be computed from simulations by the NASA/GISS climate model. Based on simulation experiments, they found that an atmosphere with double the present concentrations of $CO_2$ could lead to an increase of about 50 % in the number of tropical storms

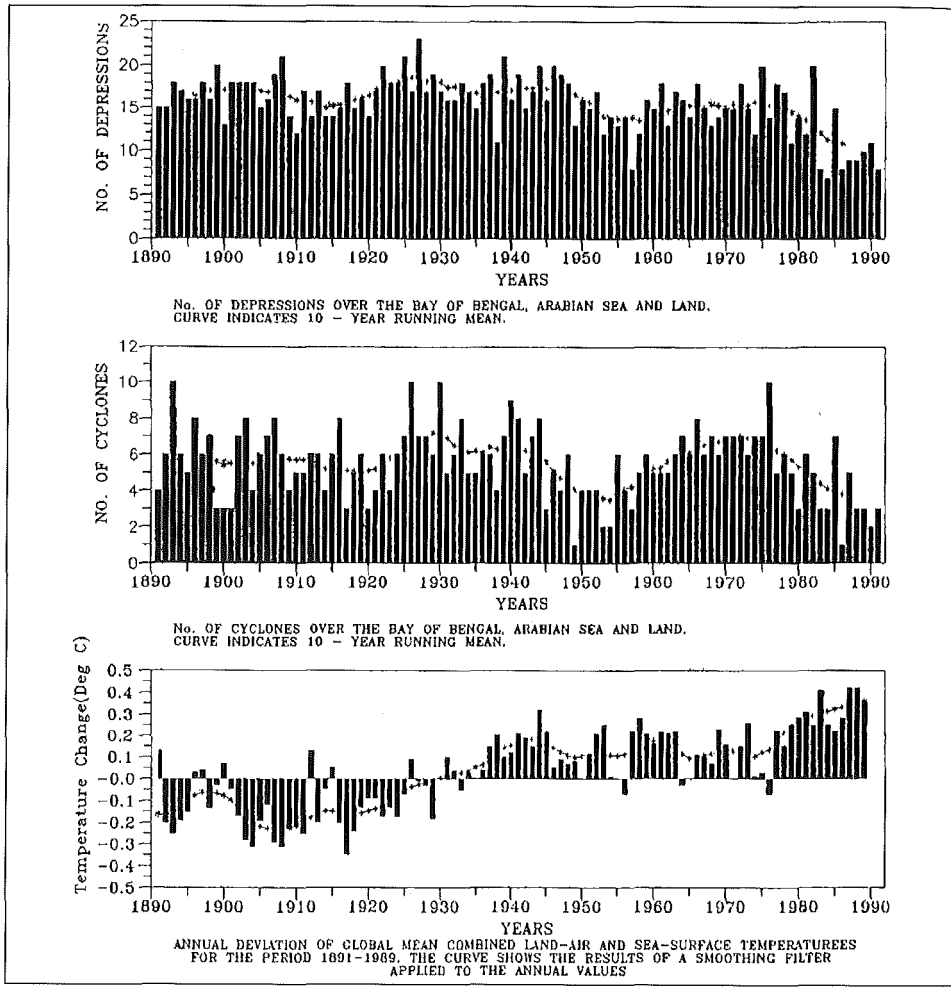


Fig. 8.2: Variation of the frequency of depressions and cyclones over the Indian seas (GADGIL, 1995)

(winds exceeding 64 km/h) and hurricanes that form over the Gulf of Mexico, and an increase of more than 100 % over the tropical North Pacific Ocean.

More recently WALSH and PITTOCK (1998) indicate that because of the insufficient resolution of climate models and their generally crude representation of sub-grid scale and convective processes, little confidence can be placed in any definite predictions of potential changes in tropical storms as a result of climate change. However, a tendency for more heavy rainfall events seems likely, and a modest increase in tropical cyclone intensities is possible. In the views of the author, it would be unwise to exclude substantial local changes in the climatologies of these phenomena, especially at regional (sub-continental) scale.

In the end we can say that the formulation and intensification of tropical cyclones depend not only on SST but also on a number of atmospheric factors. The tropical cyclone activity in a warmer world will, therefore, depend on regional changes that may occur. In the absence of the models that may adequately predict these regional changes, it is not possible to make future projections for changes in global tropical cyclone frequency and intensity.

## 8.5 ENSO and Tropical Cyclone Activity

### 8.5.1 Impact on Tropical Cyclone Frequency

The role of environmental or external forcing processes on tropical cyclone formation, structure, structural change and motion has been known and accepted in varying degrees by meteorologists for many years. El-Nino/Southern Oscillation (ENSO) is the most important short-term climatic fluctuation of tropical circulation. In recent years its possible role in modulating tropical cyclone activities in different parts of the world has been emphasized (GRAY, 1984a).

The pioneering work in this field was by NICHOLLS (1979, 1984, 1985) for cyclones in the two Australian basins. He demonstrated an association between the Southern Oscillation Index (SOI) during the Southern Hemisphere winter and the number of tropical cyclones close to Australia (from 105–165 E) during the subsequent cyclone season (i.e., from October to April). The number of cyclone days over a season is correlated with mean sea-level pressure for the preceding July–September. The linear correlation coefficient for the two series over this 25-year sample is –0.68. NICHOLLS (1985) demonstrated the robustness of the relationship by calculating separate lag correlations for each ten-year data set from 1909 to 1982. For all seven 10-year subsets, the correlation coefficient between July–September pressure and subsequent October–April cyclone numbers ranged from –0.41 to –0.72.

However, NICHOLLS (1992) detected a sudden decrease in cyclone numbers within the region following the end of the 1985/86 season that has not been accompanied by a corresponding decrease in the Southern Oscillation Index (SOI). Thus, his method would have consistently over-predicted cyclone activity during the 1986/87–1990–91 seasons. This sudden change in the SOI-cyclone numbers relationship may have been a real physical change, or is perhaps a result of changes in satellite imagery interpretation, or inadvertent changes in the Southern Oscillation Index. NICHOLLS (1992) suggests that a possible remedy may be to correlate the trend in the SOI versus the change in cyclone numbers from one season to the next.

The second major work on seasonal prediction of tropical cyclone activity has been for the North Atlantic basin. Relationships between numbers of cyclones and the large-scale pressure patterns were originally found by NAMIAS (1955) and BALENZWEIG (1959). Major developments in documenting the predictability of this basin have been recently achieved (GRAY, 1984a, 1984b, 1990; GRAY et al., 1992, 1993; SHAPIRO, 1982a, 1982b, 1987, 1989). The number of tropical cyclones in a season has been related to various aspects of the large-scale flow, including the sea-level pressure, the patterns of sea-surface temperature, the upper-tropospheric zonal winds, and seasonal rainfall in the Sahel of West Africa. The strongest relationships have been with the Southern Oscillation and with the Stratospheric Quasi-Biennial Oscillation (QBO), which is a quasi-periodic reversal of zonal winds over the Equator. The tropical cyclone activity in seasons during the west phase of the QBO is a factor of 1.4 greater than during the east phase. Ascribing a simple index of +1 for a season in the west phase, 0 for transition seasons and –1 for east phase of the QBO, the correlation of this index with the cyclone numbers accounts for 33 % of the variance. Similarly, large correlations are found between cyclone numbers and an index of Southern Oscillation/El-Nino activity based on SST anomalies over the equator eastern Pacific.

Each of the above three forecast relationships for annual tropical cyclone activity included some aspect of El Nino/Southern Oscillation (ENSO) phenomenon as a key component.

NICHOLLS' forecasts for the Australian region are based completely on various indices of the Southern Oscillation. The correlation of cyclone numbers in the Australian region and the SOI in the months preceding the season is approximately 0.7 (i.e., accounting for 50 % of the variance). Perhaps the physical reason for the association is that the number of tropical cyclones during the season has a simultaneous high negative correlation with the large-scale surface pressure in the region; i.e., a low surface pressure is consistent with a large number of tropical cyclones. Since northern Australia is close to one of the centers of action of the Southern Oscillation, variations in this large-scale pressure are effectively equivalent to variations in the SOI. The predictability (or lag relationship) comes through the slow variation (or large serial correlation) of the SOI at the time of year preceding the Southern Hemisphere cyclone season.

During an ENSO warm event in the eastern Pacific, the pressure over Australia is high, which leads to a reduced number of cyclones in that region. REVELL and GOULTER (1986), HASTINGS (1990) and EVANS and ALLEN (1992) have pointed out that the frequency of cyclone formation at the eastern end of the Australian/South Pacific basin (i.e., east of 170E) actually increases during an ENSO warm event. Although the relationship between the formation longitudes in the region and the SOI is weak, it is statistically significant. However, the relationship appears to be dominated by the extreme events (i.e., warm events). If the relationship is real, the eastward movement of formation locations may be explained in terms of the favorable factors for cyclone formation discussed in Chapter 3.2. During an ENSO warm event, the region with SSTs exceeding 26° C extends much farther eastward across the South Pacific.

A number of authors has studied the association between the SOI and cyclone activity in the western North Pacific basin (ATKINSON, 1977; CHAN, 1985; DONG, 1988; ZHANG et al., 1990; LANDER, 1994). In each study, the simultaneous SOI relationship with the total number of cyclones over the basin has been quite weak. DONG (1988) suggested that the typhoon activity is suppressed by the El-Nino events in the basin west of 160° E but enhanced east of this longitude. Another study for northwest Pacific by AOKI (1985) shows the minimum frequency in typhoon formation during El-Nino events and maximum frequency two years later. CHAN (1985) reports that the number of cyclones east of 150 E increases when the large-scale pressure is high, i.e., during an ENSO warm event. The reason (given by CHAN) is the same as given above for the South Pacific. During an ENSO warm event, the monsoon shearline extends farther eastward than normal, which is a condition conducive for cyclone formation. This was extended by LANDER (1994) who showed that a large number of monsoon-shearline type cyclone formations occur late in the season of a warm event in a region east of 160E and south of 20E. Conversely during a cold event, no formations occur in that southern and eastward part of the basin.

The relationship between ENSO and cyclone activity in the North Atlantic basin apparently is quite different. It has been observed that El-Nino events reduce hurricane activities significantly in north Atlantic during the season following the onset of El-Nino and hurricane activity usually resumes to normal in the second summer following the events (GRAY, 1984a, 1988). Numbers of hurricane days are less by 60 % in moderate and severe El-Nino events in comparison to the non El-Nino years. The seasonal reductions in hurricane activity in the Atlantic in El-Nino years are reported to be due to the development of strong anomalous westerly zonal winds in the upper troposphere over the Lower Caribbean Sea and eastern Tropical Atlantic, which almost always occurred during the El-Nino years in comparison to the other years. SHAPIRO (1987) reports a correlation of –0.34 (only 12 % of the variance) between cyclone numbers and the warm water anomaly in the equatorial eastern

Pacific. Both SHAPIRO (1987) and GRAY (1984a) give evidence that the physical link is that higher equatorial SST values increase the activity of tropical convection, which increases the upper-level westerly zonal winds and the vertical wind shear downstream over the primary formation region of the Atlantic cyclones. As discussed above, large vertical shear represents an unfavorable condition for tropical cyclone formation (on this seasonal timescale).

The relationship between El-Nino events and tropical cyclone activities over northeast Pacific region are reverse to that of the Atlantic and northwest Pacific. It has been observed that in 5 El-Nino events since 1966 there is a strong indication that tropical cyclone activities have increased, especially, in the case of intense tropical storms. During El-Nino events, on the other hand, tropical cyclone activity is found to be suppressed over northeast Pacific.

Results for southwest Pacific (RAMAKRISHNA, 1989) appear to be interesting, as an enhancement in tropical cyclone activity has been observed in both the high and low phases of southern oscillation index.

The relationship between tropical cyclone behaviour and ENSO for North Indian Ocean has been examined by MANDAL (1989), but unlike the Atlantic and the Pacific, the relationship is found to be very weak. There is practically no change in frequency of the tropical cyclones during the ENSO episode in North Indian Ocean in comparison to the non El-Nino years or mean values.

### 8.5.2 Impact on Tropical Cyclone Tracks

GRAY (1984a, 1988) has shown that to some extent, El-Nino events also affect the intensity and track of the tropical storms in Atlantic. In El-Nino years the storms are less intense and more recurving over the Caribbean Sea. JOSEPH (1981) studied the motion of post-monsoon cyclonic storms over the Bay of Bengal with respect to years of highly deficient rainfall of India. JOSEPH (1976) pointed out that during the epochs of frequent drought years in all India monsoon rainfall, severe cyclonic storms of the Bay of Bengal of the post-monsoon season have preferred northward movement affecting Bangladesh and adjoining Indian coastal areas. A study by SINGH et al. (1987) for North Indian Ocean also shows some influence of southern oscillation on the latitude of the tracks of cyclones during post-monsoon season (October–December) crossing east coast of India. The above study also shows the increase in frequency of cyclones in low latitude (Andhra Pradesh coast) and the decrease in the higher latitude (Orissa and West Bengal coasts) during low phases of southern oscillation (El-Nino years). The study made by MANDAL (1989) for North Indian Ocean (NIO) has, however, shown that numbers of recurving and non-recurving tropical cyclones were found to be in almost equal proportion in El-Nino years. The study takes account of all the storms, which formed over the Bay of Bengal and Arabian Sea during a year (including monsoon season).

A notable study made by GUPTA and MUTHUCHAMI (1991) for the storms of Bay of Bengal region during post monsoon season (October–December) has shown significant relationship between El-Nino and the tropical storm tracks over the Bay of Bengal. The authors studied tracks of the storms during El-Nino and other years such as El-Nino (–1) years, El-Nino (+1) years and so on. After a careful analysis of the storm tracks in these years, it has been seen that the behaviour of storms tracks has some definite patterns during El-Nino and El-Nino (–1) years. While the storms tracks are mostly straight and less recurving during El-Nino years, they are more recurving during El-Nino (–1) years [Fig. 8.3 (a) & (b) and 8.4 (a) & (b)].

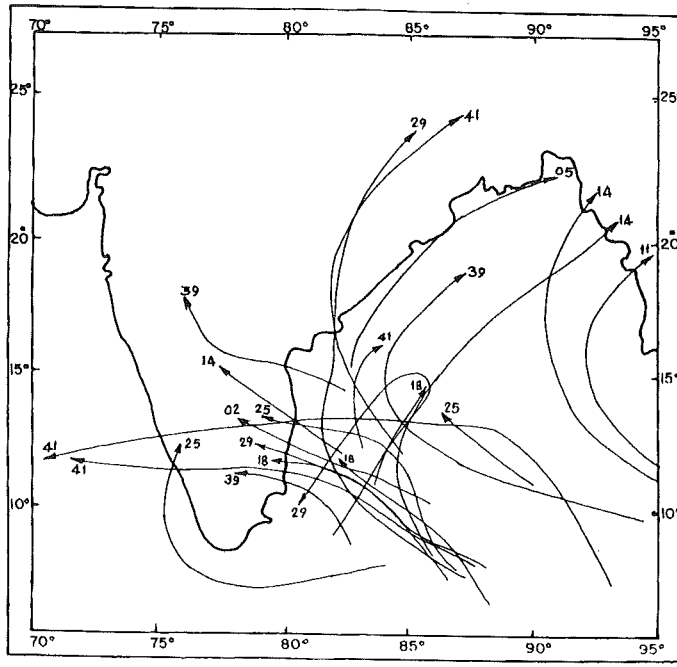


Fig. 8.3(a): Tracks of depression and cyclones over Bay of Bengal during post-monsoon season in El-Nino years (1901–1950). (Number written ahead of tracks indicates years of storm formation)

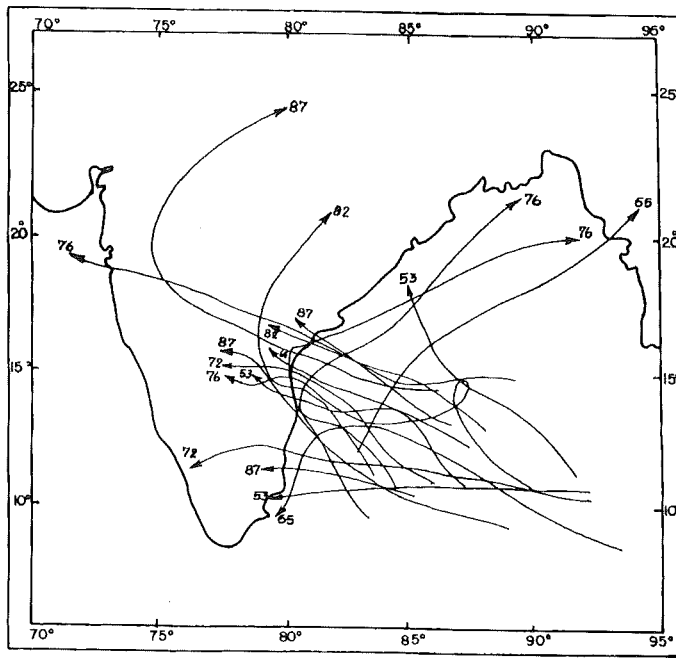


Fig. 8.3(b): Tracks of depression and cyclones over Bay of Bengal during post-monsoon season in El-Nino years (1951–1987). (Number written ahead of tracks indicates years of storm formation)

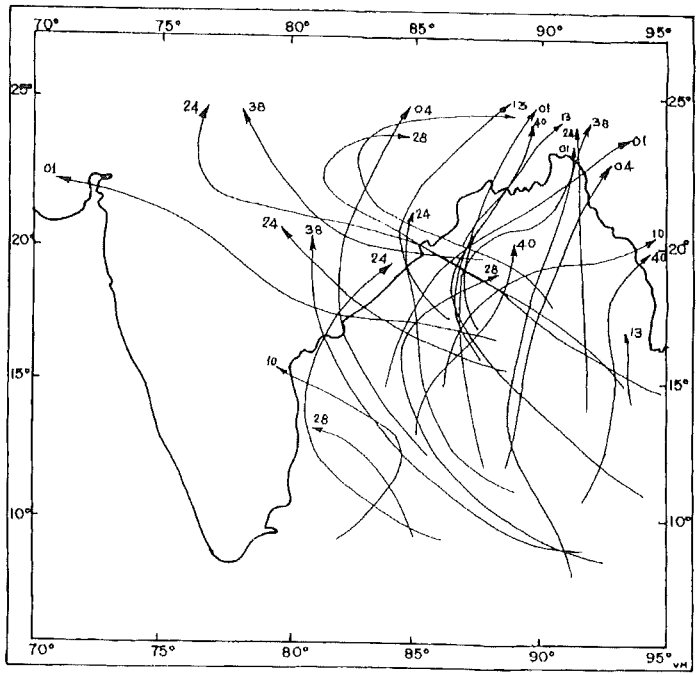


Fig. 8.4(a): Tracks of depression and cyclones over Bay of Bengal during post-monsoon season in El-Nino (–1) years (1901–1950). (Number written ahead of tracks indicates years of storm formation)

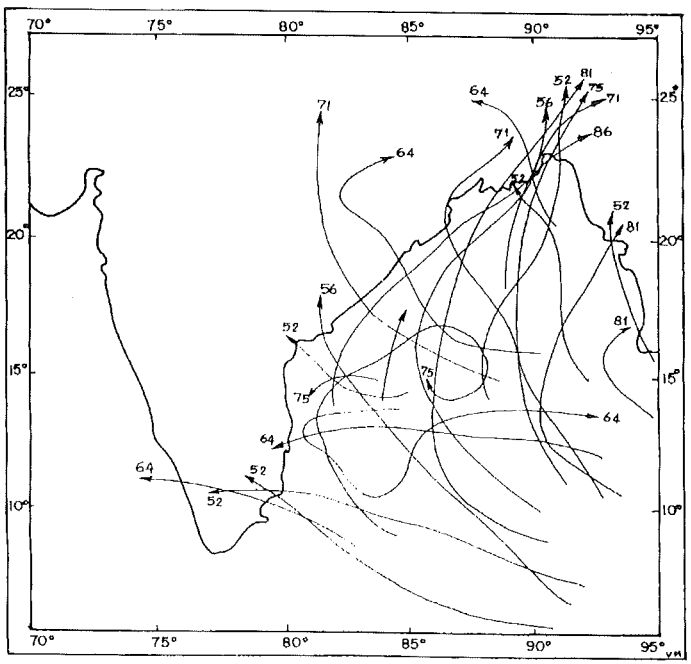


Fig. 8.4(b): Tracks of depression and cyclones over Bay of Bengal during post-monsoon season in El-Nino (–1) years (1951–1987). (Number written ahead of tracks indicates years of storm formation)

These results are opposite to those of GRAY (1984a, 1988) for Atlantic where the storms are found to be more recurving during El-Nino years. It is evident from these figures that El-Nino years have more numbers of storms crossing at lower latitudes on the Indian east coast compared to El-Nino (–1) years. To establish a quantitative approach to this behaviour, the storms were classified into two categories, viz., (1) recurving or those crossing north of 17° N and (2) non-recurving or those of which crossing south of 17° N on the east coast of India. There were mainly two considerations for choosing the latitude 17° N as the boundary between recurving and non-recurving systems. From the analysis of cyclone formation and their movement over the Bay of Bengal, it is observed that no cyclone forms north of 17° N during post-monsoon season and that maximum numbers of recurvature of the cyclones take place between the latitudes 15° and 17° N. Another observation was that almost all the storms crossing north of 17° N move north to northeastward during this season. Table 1 gives the details of the number of storms crossing Indian east coast under these two categories during El-Nino and El-Nino (–1) years. It may be seen from this table that 33 out of 38 tropical cyclones (about 87 %) during El-Nino years are non-recurving or crossing south of 17° N whereas 38 out of 48 tropical cyclones (about 79 %) during El-Nino (–1) years are either recurving or crossing north of 17° N. It may also be inferred from this table that during severe El-Nino years 15 out of 16 storms (about 94 %) have crossed south of 17° N whereas during years previous to these severe El-Nino years, 17 out of 19 storms (about 89 %) were either recurving or crossed north of 17° N.

To establish a correlation between the number of storms crossing south of 17° N during El-Nino years and the number of storm recurving/crossing north of 17° N during El-Nino (–1) years, fractional values of these numbers (n = 16) were statistically correlated and test of significance (t-test) was applied. The correlation coefficient of +0.84 was found between these two parameters, which are significant at 1 % level.

Although, considering past 87 years period (1901–1987) the total number of storms during 16 El-Nino years (38), as shown in Table 8.3, is less compared to the number in 16 El-Nino (–1) years (48), no preferred behaviour in terms of reduction or increase in the frequency of the storms is noticed in any kind of year [El-Nino, El-Nino (–1), etc]. Also, though characteristics of the storm tracks are distinctly different during El-Nino years compared to El-Nino (–1) years, but the prediction of onset of El-Nino based on the characteristics of the storm tracks in a particular year may not be possible as the storm frequency over North Indian Ocean is very low. On an average, 2 to 3 storms form over Bay of Bengal during post-monsoon season.

Table 8.3: Number of cyclonic storms recurving/crossing north of 17° N and those crossing south of 17° N during El-Nino and El-Nino (–1) years

| El-Nino Years | No. of C.S. | No. of CS recurving/ crossing north of 17° N | No. of CS crossing south of 17° N | El Nino (–1) Years | No. of CS | No. of CS recurving/ crossing north of 17° N | No. of CS crossing south of 17° N |
|---|---|---|---|---|---|---|---|
| 1902 (M) | 1 | 0 | 1 | 1901 | 2 | 2 | 0 |
| 1905(M) | 1 | 1 | 0 | 1904 | 1 | 1 | 0 |
| 1911(S) | 1 | 1 | 0 | 1910 | 2 | 1 | 1 |
| 1914(M) | 1 | 1 | 0 | 1913 | 4 | 3 | 1 |
| 1918(S) | 3 | 0 | 3 | 1917 | 2 | 2 | 0 |
| 1925(S) | 3 | 0 | 3 | 1924 | 5 | 4 | 1 |
| 1929(M) | 3 | 0 | 3 | 1928 | 4 | 3 | 1 |
| 1939(M) | 3 | 1 | 2 | 1938 | 3 | 2 | 1 |
| 1941(S) | 4 | 0 | 4 | 1940 | 2 | 2 | 0 |
| 1953(M) | 3 | 1 | 2 | 1952 | 7 | 4 | 3 |
| 1957(S) | 0 | 0 | 0 | 1956 | 2 | 2 | 0 |
| 1965(M) | 3 | 0 | 3 | 1964 | 4 | 2 | 2 |
| 1972(S) | 3 | 0 | 3 | 1971 | 3 | 3 | 0 |
| 1976(M) | 3 | 0 | 3 | 1975 | 3 | 3 | 0 |
| 1982(S) | 2 | 0 | 2 | 1981 | 3 | 3 | 0 |
| 1987(M) | 4 | 0 | 4 | 1986 | 1 | 1 | 0 |
| Total | 38 | 5 | 33 | | 48 | 36 | 10 |
| Mean | 2.38 | 0.31 | 2.07 | | 3.0 | 2.38 | 0.62 |
| In % | | 13.1 | 86.9 | | | 79.2 | 20.8 |

C.S. = Cyclonic Storms; S = Severe El-Nino years; M = Moderate El-Nino years

The fractional values of storms crossing south of 17° N and southern oscillation indices (Tahiti-Darwin pressures) for the period 1901–1987 (n = 87) were statistically correlated and test of significance (t-test) was applied. The correlation coefficient of the –0.63 is found between SOI and storms crossing south of 17° N, which is significant at 1 % level. These results are in agreement with those of SINGH et al. (1987).

Similar studies for other basins are yet to be made available.

## 8.6 Possible Implications of Sea-Level Rise on Storm Surges

Projected sea-level rise due to global warming would inundate low lying areas, erode shore lines and destroy mangrove and Nepa palm forests. This would be particularly hard-felt in the deltaic regions where substantial area is barely above sea-level. Many coastal areas are at present submerging. Fig. 8.5 shows the sectors of the worlds' coast line that have been subsiding in recent decades, as indicated by the evidences of tectonic movements, logical and ecological indications, geodetic surveys, and groups of tide gauges recording a rise o mean sea level greater than 2 mm per year over the past three decades (BIRD, 1993).

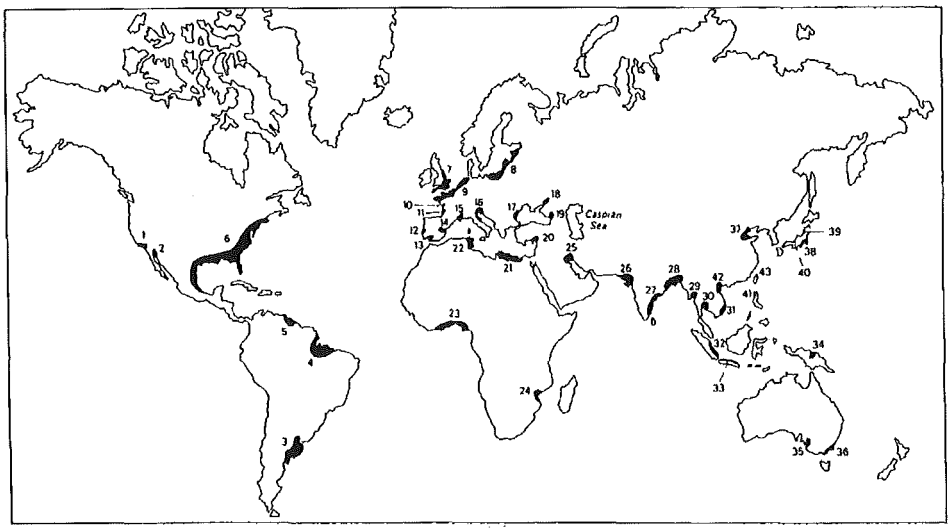


Fig. 8.5: Sectors of the world's coastline that have been subsiding in recent decades, as indicated by evidence of tectonic movements, increasing marine flooding, geomorphological and ecological indications, geodetic surveys, and groups of tide gauges recording a rise of mean sea level greater than 2 mm/yr over the past three decades (BIRD, 1993). 1, Long Beach area; 2, Colorado River delta; 3, Gulf of Laplata; 4, Amazon delta; 5, Orinoco delta; 6, Gulf and Atlantic coasts; 7, southern and eastern England; 8, southern Baltic coasts; 9, southern coasts of the North Sea and Channel coasts; 10, Loire estuary; 11, Vendée coasts; 12, Lisbon region; 13, Gaudalquivir delta; 14, Ebro delta; 15, Rhône delta; 16, northern Adriatic low coasts of Italy; 17, Danube delta; 18, eastern Sea of Azov; 19, Poti swamp; 20, southern Turkey; 21, Nile delta to Libya; 22, northeast Tunisia; 23, Niger delta and north coasts of the Gulf of Guinea; 24, Zambezi delta; 25, Tigris-Euphrates delta; 26, Rann of Kutch; 27, southern India; 28, Ganges-Brahmaputra delta; 29, Irrawaddy delta; 30, Bangkok coastal region; 31, Mekong delta; 32, eastern Sumatra; 33, northern Java deltaic coast; 34, Sepik delta; 35, Port Adelaide; 36, Corner Inlet region; 37, Hwang-He (Yellow River) delta; 38, head of Tokyo Bay; 39, Niigata; 40, Maizuru; 41, Manila; 42, Red River delta; 43, northern Taiwan

According to NICHOLLS and LEATHERMAN (1995), a 1 m sea level rise would affect six million people in Egypt, with 12 % to 15 % of the agricultural land lost 13 million in Bangladesh, with 16 % of national rice production lost, 72 million in China and tons of thousands of hectare of agricultural land. This could greatly increase existing storm surge threat because of the increase in the coastal area exposed to the surges originating in the sea, and loss of

coastal forests, which act as a buffer against the force of storm surges. The situation would be worse if the intensity and frequency of tropical cyclones increases due to warmer SSTs as projected by many workers.

Some conclusions drawn on the global vulnerability of storm surges due to sea level rise are (HOOZEMANS et al., 1993; BAARSE, 1995; IPCC, 1996):

(i) Some 200 hundred million people are estimated to live currently below the highest storm surge level (the once-per-1000-years storm surge level). Based on this population estimate, as well as on first order estimate on storm surge probability and existing level of protection, 46 million of people are estimated to experience flooding due to storm surge in an average year under present condition. Most of these people live in the developing countries.

(ii) The figure will double if the sea level rises 50 cm (92 million people per year) and almost triple if it rises 1 m (118 million people per year).

(iii) Because of regional differences in storm surge regimes, the increase of flood risk due to sea level rise is greater than average for the Asian region (especially in the Indian Ocean Coast), the south Mediterranean coast, the African Atlantic and Indian Ocean Coasts, Caribbean Coasts and many of the small islands.

The surges are superimposed on raised mean sea level (MSL). In view of the dynamical effects in a shallow coastal area, the components of total water level due to storm surge, astronomical tide and MSL are mutual dependent and interact dynamically with each other. Therefore, for estimating the total water level one cannot assume that MSL, tide and surge are linearly additive and there is no non-linear interaction.

There are two important issues associated with implication of sea-level rise on storm surges. Firstly, raised mean sea level implies greater potential inland inundation due to storm surges and in second place higher mean sea level may itself affect the surge and tidal components of the rise. Another issue, which has attracted attention, is related to the sensitivity of storm surges to change in projected cyclone intensity as a result of changes in SST. In the following section we will briefly discuss these issues and describe attempts made by various workers to address the problems of different vulnerable regions.

### 8.6.1 Bay of Bengal

Storm surges in the Bay of Bengal are the major cause of coastal flooding along the east coast of India and Bangladesh. In the context of the projected rise in the sea level due to green house warming, it may be interesting to examine how changes in mean sea level (MSL) may affect the storm surges and consequently the coastal flooding in the Bay of Bengal.

As mentioned earlier, low lying coastal regions of Bangladesh are worst affected due to storm surges. Exposure of population to sea level rise and storm surges is particularly an extremely grave consideration in Ganga-Brahmaputra-Meghna delta of Bangladesh. Local subsidence in this region is very significant which may increase the relative rate of sea-level rise. Ganga-Brahmaputra-Meghna river systems together deliver approximately 1.6 billion tonnes of sediments annually (MILLMAN and MEADE, 1983). The damming of Meghna River could prevent sediment influx from compensating for local subsidence, increasing coastal erosion. Thus making the problem of coastal flooding due to storm surges and MSL more serious.

BROADUS et al. (1986) and BROADUS (1993) have made a detailed study of the possible effect of sea level rise and damming of rivers in the coastal areas of Bangladesh and Egypt.

The potential economic implications of two relative sea levels rise scenarios for the year 2050 and 2100 has been examined.

Table 8.4 gives these scenarios of relative sea level rise for Bangladesh together with the economic activities/assets in affected areas (BROADUS, 1993).

Table 8.4: Relative Sea Level Scenarios and Economic Activities/Assets in Affected Areas of Bangladesh

| Activities/ Assets | 1 m (2050) | 3 m (2100) |
|---|---|---|
| Total sea level rise | 0.83 m | 3.4 m |
| (Global) | (0.13 m) | (2.2 m) |
| (Local subsidence) | (0.70 m) | (1.2 m) |
| Loss habitable land | 7 % | 26 % |
| Population | 5 % | 27% |
| Gross Domestic Product (GDP) | 5 % | 20 % |

Fig. 8.6 gives the landward transgression scenarios from a 1 m, 2 m, 3 m, and 5 m rise in relative sea level. The 1 m and 3 m scenarios correspond to the projected 13 cm and 2 m of global sea level rise by 2050 and 2100 respectively. It may be seen from these scenarios that even with 1 m relative sea level rise large population and economic activities will be exposed to serious threats from storm surge flooding. Percentage of population lying between 1 m and 3 m transgression lines is very high which includes the city of Khulna having population density more than 29000 per $km^2$ (BROADUS, 1993).

Another significant consequence of the relative sea level rise pointed out by BROADUS (1993) is the loss of Sunderban Forest Reserve in Khulna district which at present provides vital protection for this area by acting as a buffer against storm surges. Loss of this buffer could increase the threat of storm surge floods, which could reach up to greater inland distances.

DUBE and RAO (1989, 1991) used a continuously moving coastal boundary numerical model to examine how changes in MSL may affect the storm surges and the low lying coastal flooding along the east coast of India. The authors have presented different scenarios indicating the implication of a rise in the sea level on the surge generated by the 1977 Andhra cyclone. Authors found that higher MSL of the Bay of Bengal allows the storm surges to build on a higher base with increased inland inundation along the low lying regions of Andhra coast of India.

Using a numerical storm surge model FLATHER and KHANDKER (1993) examined the effect of rise in mean sea level on tides, storm surges and their interaction for the Bay of Bengal. They simulated the surge generated by the Bangladesh cyclone of May 24–25, 1985 with and without 2 m rise in sea level. For the M2 tides, authors found an increase in amplitude by 10 cm in NE and decrease by similar amount NW of the Bay when the sea level is raised by 2 m. For the storm surge a reduction in the maximum computed surge elevation of 20–30 cm was predicted by a 2 m rise in MSL (Fig. 8.7). Authors attribute this to a decrease in the ratio, wind stress/water depth that occurred in the case of an elevated MSL, which is also consistent with theory and other model studies. Tide-surge interaction response with raised MSL resulted in a reduction of maximum computed water level in the NE and NW corners of the Bay, with an increase in level in an area between (Fig. 8.8 a, b). Authors attribute this more

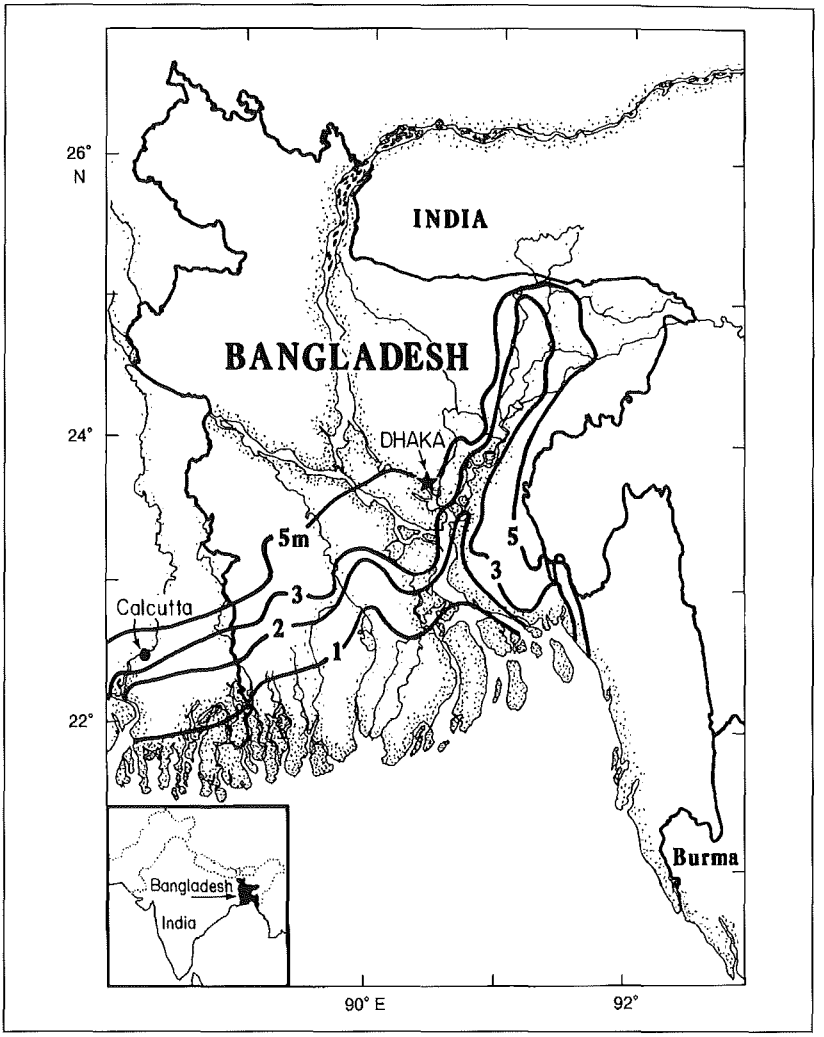


Fig. 8.6: Sea level transgression scenarios for Bangladesh (BROADUS, 1993)

complex behaviour to the variations in the relative timing of tidal high water and peak surge. FLATHER and KHANDKER (1993) further noted that a reduction of 20 cm in maximum computed water level suggests that the effect of the 2 m increase in MSL would be to raise the highest flood level by about 1.8 m above those expected with the present MSL.

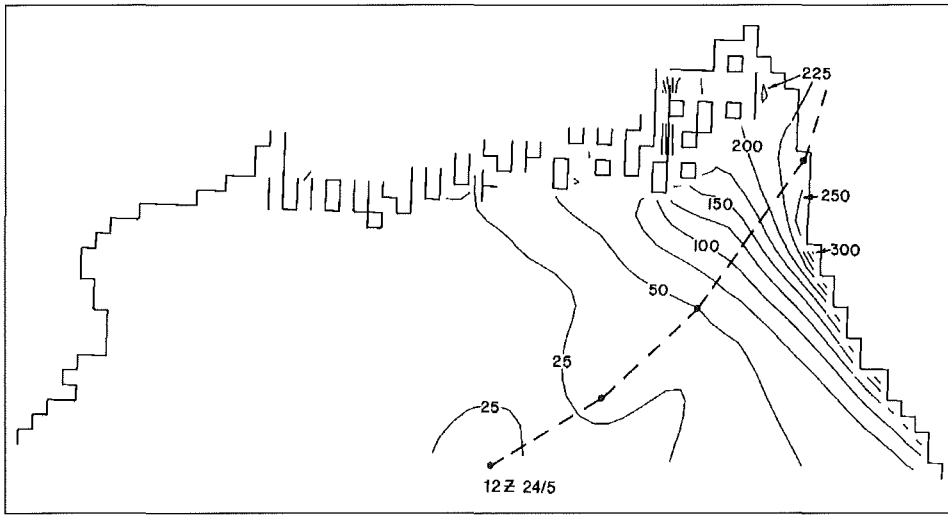


Fig. 8.7(a): Contours of maximum computed surge elevation (cm) in the period 1200 GMT 24 May to 1200 GMT 25 May 1985. The broken line indicates the track of the cyclone
(FLATHER and KHANDKER, 1993)

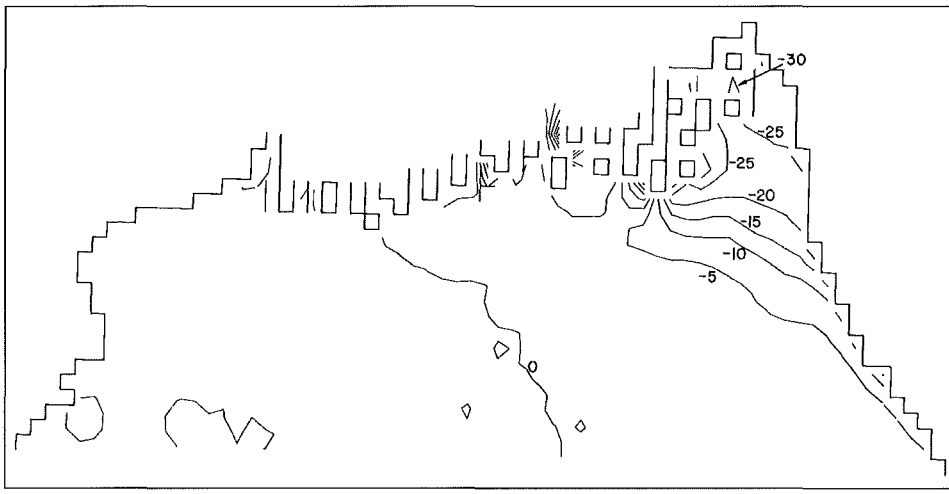


Fig. 8.7(b): Change (cm) in maximum computed elevation (cm) produced by a 2 m rise in MSL
(FLATHER and KHANDKER, 1993)

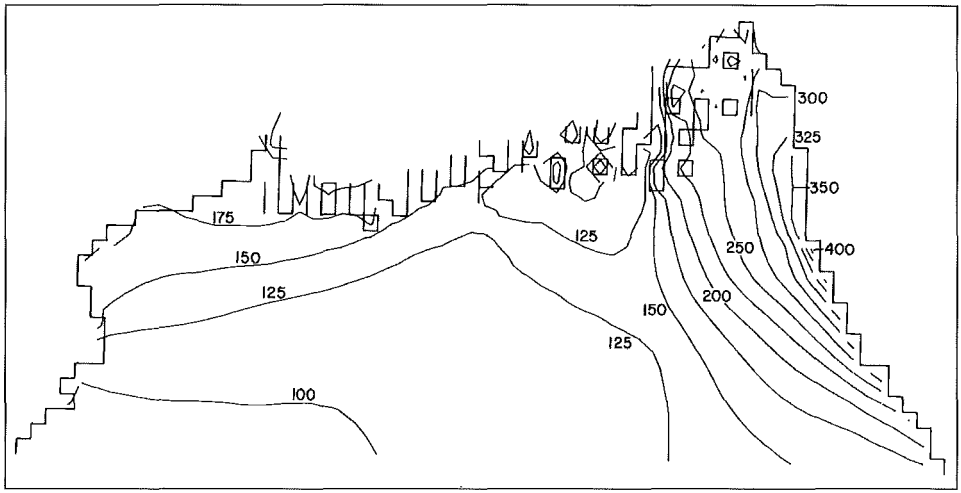


Fig. 8.8(a): Contours of maximum computed elevation (cm) due to tide and surge in the period 1200 GMT 24 May to 1200 GMT 25 May 1985 (FLATHER and KHANDKER, 1993)

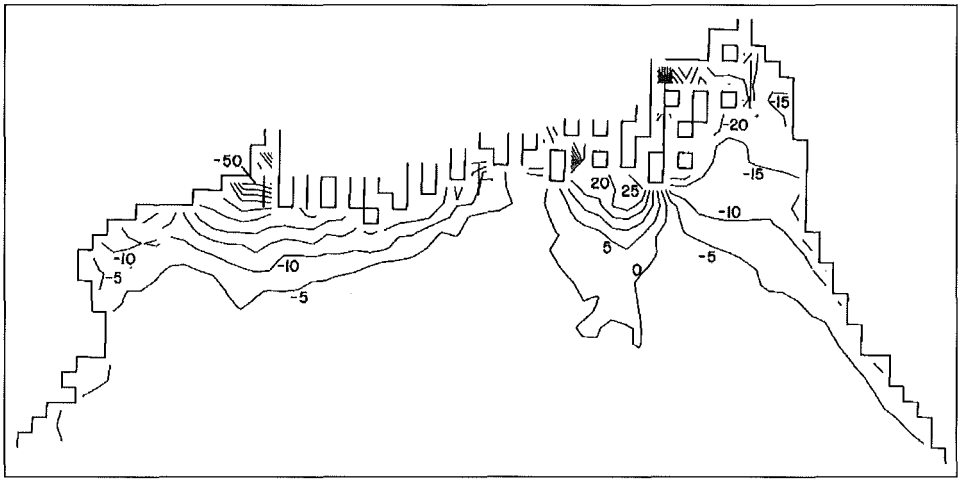


Fig. 8.8(b): Change (cm) in maximum computed tide + surge elevation produced by a 2 m rise in MSL (FLATHER and KHANDKER, 1993)

ALI (1996) used a numerical model to generate storm surge scenarios for Bangladesh under increased cyclone intensity and sea level rise. Using the temperature and wind relation given by EMANUEL (1987), the likely wind speeds of the April 1991 cyclone that hit Bangladesh under two sea surface temperature scenarios of 2° C and 4° C have been estimated by the author. These wind speeds were then used to compute storm surges for a sea surface temperature rise of 2 and 4° C, and sea level rise of 0.3 and 1.0 m. Surge heights computed by ALI (1996) under these conditions are given in Table 8.5. Numbers in parentheses indicate percentage increase or decrease in storm surge heights from the present surge height. It may be seen from the table that a rise in the sea level tends to reduce storm surge heights which is on expected lines as the increase in sea level results in increased water depth over the continental shelf. On the other hand a maximum increase of about 49 % in the surge height is predicted for the increased intensity of cyclone corresponding to a 4° C rise in SST.

Table 8.5: Storm surge heights (m) under different sea surface temperatures and sea level rise scenarios (wind speed of 225 km $h^{-1}$ corresponds to that of the April 1991 cyclone) (ALI, 1996)

| | Current Temp. (27° C) | 2° C Increase | 4° C Increase |
|---|---|---|---|
| Wind (km $h^{-1}$) | 225 | 248 | 275 |
| No Sea Level Rise<br>Surge Height (% change) | 7.6 (0 %) | 9.2 (21 %) | 11.3 (49 %) |
| Sea Level Rise = 0.3 m<br>Surge Height (% change) | 7.4 (–3 %) | 9.1 (20 %) | 11.1 (46 %) |
| Sea Level Rise = 0.1m<br>Surge Height (% change) | 7.1 (–7 %) | 8.6 (13 %) | 10.6 (40 %) |

ALI (1996) also used an empirical formula to compute inland inundation along flat land around Meghna estuary associated with April 1991 cyclone under the present and warmer SST conditions. He found increased inland penetration of the surge by 13 % and 31 % for a SST rise of 2° C and 4° C respectively. In conclusion author considers these results as indicative only because of several simplifying assumptions, which are used, and uncertainties concerning the relationship of SST's and cyclone intensities.

In a recent study SINHA et al. (1997) applied a tidal circulation model to examine how a sea level rise might affect the water level and currents in the Hooghly estuary situated in the head Bay of Bengal. For this study the authors did not consider the changes in the shoreline as a result of rise in sea level. Model results show a substantial increase in the amplitude and velocities of the tidal wave due to the sea level rise by 50 cm and 1 m in Hooghly estuary. Results also indicate that variations in the tidal wave due to raised mean sea level become more prominent in the upstream regions of Hooghly estuary. Magnitude of tidal currents is also found to increase significantly with rise in sea level. The results are important as they suggest that these changes in the flow field of Hooghly estuary may increase the salinity intrusion. Besides the increase in currents due to sea level rise may cause more erosion of banks of estuary, shifting the net deposition further northward.

### 8.6.2 Arabian Sea and Maldives

The threat from sea level rise and storm surges is not a serious consideration in most parts of the west coast of India, coast of Pakistan, Arabian/Persian Gulf, Saudi Arabia, Red Sea and east coast of Africa. The only region that is vulnerable to severe storm surge is the Gujarat coast of India. While projected sea level rise of 50 cm to 1 m by 2100 is expected to affect hundreds of thousands square kilometers of coastal wetlands and low lands in these countries, many small island countries face a bigger threat as they could loose a significant part of their land area.

The problem is particularly acute in the Maldives, which is in southern part of the Arabian Sea. The Maldives archipelago consists of 1,190 islands stretched in a chain 820 km in length extending from Ihavandiffula (6° 57'N) to Addu Atoll (0° 34'S). The average elevation of these islands is 1 to 1.5 m above existing sea level (PERNETTA, 1992). Much of the island, and almost all the village, is 0.8–1.1 m above mean sea level.

Tropical storms are rare in Maldives, but increase in occurrence and intensity towards the north. Storms are experienced on Minicoy, and Lakshdweep Islands of India, which are to the north of Maldives. The tidal range is up to 1.2 m in the north and 1.4 m in the south of Maldives. Occasional storms accompanied by high astronomical tides cause destructive flooding in islands. In fact, flooding is the major concern as 80 % of the nation's land area is less than 1 m above sea level. Particularly affected has been the capital Male' which is heavily crowded with over 70,000 people inhabiting the 1.8 sq. km area. Due to large population pressure the island has been extended in all directions, and the combinations of all reclaimed shoreline and mined reef, have increased the vulnerability of Male. This was especially the case on 10–12 April 1987 when Male' experienced high waves which inundated much of the island.

Rising sea levels would almost certainly cause most of the islands to become uninhabitable, displacing more than 225,000 Maldivians. In fact, a rise of one meter sea level would sink about 80 % of the Maldives beneath the sea.

In conclusion we may say that although storm surge is not a threat to Maldives, the nation stands to loose heavily from the adverse effects of global warming and sea level rise.

Lakshadweep Islands of India are also vulnerable to sea level rise. Anticipated rise of sea level by 1m may cause heavy land loss in Kiltan, Kaviratti, Kadmat, Kalpani, Cheriyan and Agati-Bingaram Islands (NIGAM, 1989).

### 8.6.3 Persian Gulf, Red Sea and the Mediterranean Sea

The Persian Gulf region is mainly influenced by extra-tropical weather systems, whereas the region south of the Strait of Hormuz is affected by tropical cyclones. The Gulf is subjected to major negative and positive storm surges. Particularly vulnerable to sea level rise in the Persian Gulf is the region Tigris-Euphrates delta (Fig. 8.5), which is characterised by negative surges (EL-SABH and MURTY, 1989). Impact of sea level rise on storm surges, therefore, does not appear to be a threat in the Persian Gulf. On the other hand, there is no present indication of rising sea level in Red Sea.

Regions, which are vulnerable to sea level rise in Mediterranean, are Ebro delta, Rhone delta, northern Adriatic low coasts of Italy, Danube delta, eastern sea of Azov, Poti Swamp, Southeast Turkey, Nile delta of Libya and northeast Tunisia. Regionally, Southern Mediterranean appears to be most vulnerable to sea level rise (Fig. 8.5).

BROADUS (1993) made a detailed study of the impact of projected sea level rise in the deltaic regions of Nile River in Egypt. Scenarios of exposure of population and economic activities relative to sea level rise of 1 m by 2050 and 3 m by 2100 is presented by the author. The analysis suggests that a 1 m rise in sea level (including local subsidence) would cover areas currently accounting for about 12 % of habitable land, 14 % of population and 14 % of Gross Domestic Product (GDP) in Egypt. The figures corresponding to 3 m rise are much higher. Storm surge is not a problem in Egypt; however, with rising sea level the region is likely to be frequently flooded due to waves and tides in the Mediterranean.

### 8.6.4 European Seas

The regions which are vulnerable to sea level rise in Europe are: Southern and Eastern England, Southern Baltic Coast, Southern Coast of the North Sea and Channel coasts, Loire estuary, Vendée coasts, Lisbon region and Gaudalquivir delta (Fig. 8.5). From the storm surge point of view the North Sea region is of importance and concern and therefore, has been investigated by many workers.

A two-dimensional hydronamic model of the North Sea and part of the continental shelf was used by DE RONDE (1993) to calculate the tidal system changes as a result of arbitrary sea level increase of 2.5 and 5.0 m. He considered the Netherlands' complex coast in detail for his study. The author also examined impact of sea level rise on storm surge. Some of the conclusions reached by DE RONDE (1993) for the case of a 1 m sea level rise are:

(i) 0.95–1.1 m rise in mean high water level with insignificant changes in the tidal motion in the North Sea and along Dutch coast.
(ii) Less than 5 cm change in storm surge amplitudes.

JELGERSMA et al. (1995) examined in detail the Holocene storm surge signatures in the coastal dunes along the central Netherlands' coast. They describe and discuss the occurrence and possible significance of Holocene shell deposits, which have been found intercalated in the dune sands. These deposits are believed to be the result of storm surge activity on the foreshore, either through swash or over wash action, and of subsequent preservation due to aeolian coverage of basically sedimentry coastal system. Taking into account of the contemporary mean sea level, the authors gave an interpretation of the surge level elevations associated with the depositions. Authors found an increasing level of storm surge elevations with increasing time. They suggest that climatic variations on the one hand and foreshore bathymetry on the other hand may be factors of relevance to explain these results.

Several observational and modelling studies have been carried out to examine changes in mean sea level on the German Baltic coast and German Bight of North Sea. Mention may be made of some of the recent observation and studies in this regard (SIEFERT, 1990; HOFSTEDE, 1991; SIEFERT and JENSEN, 1993; TOPPE, 1993; PUNNING, 1993; KUNZ, 1993, STIGGE, 1993). Almost all of these studies confirm a rise in mean sea level on both the Baltic and North Sea coast of Germany. Fig. 8.9 shows that observed MSL and its trend at Cuxhaven, (Germany).

STIGGE (1993) investigated sea level changes and high water levels probability on the German Baltic coast with the purpose of defining the defence level (maximum high water crest) for the next fifty years. An accelerated rise of storm surge frequency during last 50 years was observed (Fig. 8.10). He notes that a rise in MSL could produce an increase in the storm

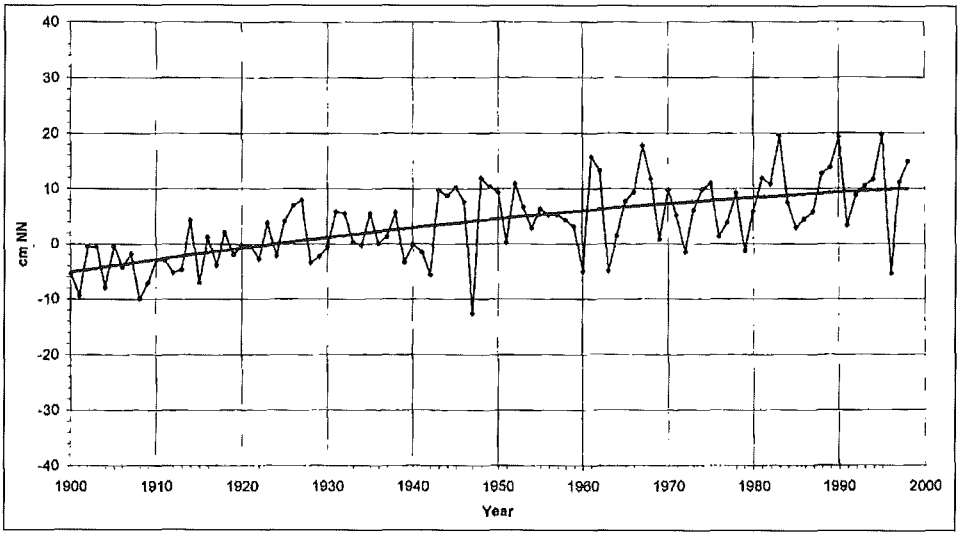


Fig. 8.9: Mean Sea Level at Cuxhaven (FERK, 1999)

surge frequency both in the North Sea and in the Baltic Sea. At first glance a differentiation between these two cases seems of little importance, but it may be noted that storm surges can be influenced by stronger winds associated with intense cyclones, in addition to the effect of a slow rise in MSL. STIGGE (1993), therefore, did not accept the widely held opinion that an increase of storm surge frequency in the western Baltic necessarily has to be connected with a significant increase of the high water crests.

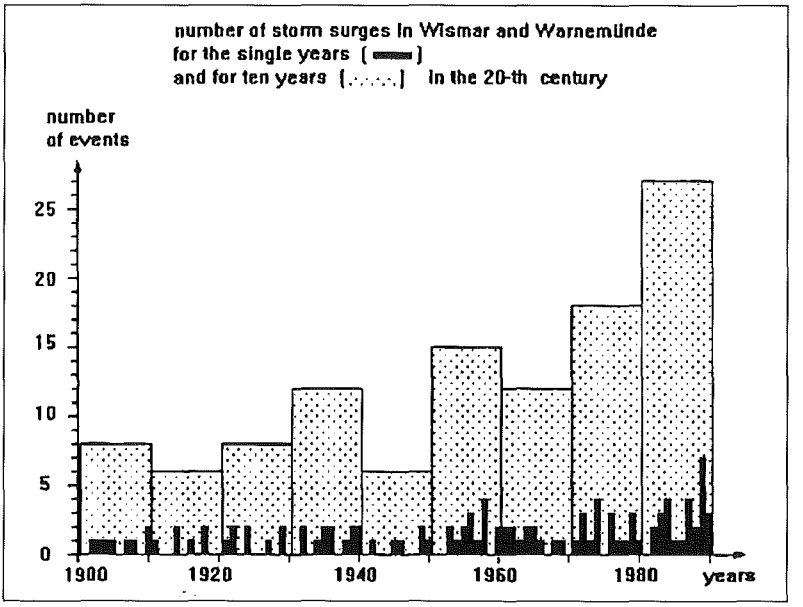


Fig. 8.10: Frequency of storm surges on the German Baltic coast (STIGGE, 1993)

### 8.6.5 The Americas

Sectors of the American coastline which are particularly vulnerable to relative rise in mean sea level are Long Beach area and Colorado River delta on the Pacific coast and Gulf of La Plata, Amazon delta, Orinoco delta, Gulf of Mexico on the Atlantic coast (Fig. 8.5).

Impact of sea level rise on coastal systems of Mississippi River deltaic plain in the Gulf of Mexico was examined by DAY et al. (1993). Mississippi delta consists of lakes, bays, near sea level wetlands and low-lying uplands. Water levels in this region have increased substantially, primarily from regional land subsidence rather than eustatic sea level rise. Because of continuing subsidence and apparent sea level rise, many low-lying areas are experiencing increased flooding from the river and from the sea (during storm surges).

New England is not frequently visited by hurricanes; however, severe hurricanes about once a decade strike Southern New England. If sea level continues to rise as a result of global warming, the destruction wrought by future storms could wipe out many seaside oases. In the event of a severe hurricane striking the coast, the rise in the sea level would be compounded by a storm surge that would make high 10 to 15 feet water level some to higher than usual (ALLEN, 1998). ALLEN (1998) further indicates that severe hurricanes like the one that struck New England three times between 1938 to 1954 may generate very large amplitudes the storm surge.

Impact of sea level rise on the east coast of south America has been examined in detail by LEATHERMAN (1986) and SCHNACK (1993). This coast is not vulnerable to severe tropical cyclones and storm surges.

### 8.6.6 Australia

LOVE (1988) derived a number of tropical cyclones storm surge climatologies for three Australian parts, Darwin, Mackay and Port Hedland. For his analysis he considered the present climatological scenario and the scenarios after specifying possible responses of the tropical cyclones climatology to a SST warming of the order of 1.0 °C in the oceans surrounding northern Australia accompanied by a sea level rise of 1 m. He demonstrated that sea level rise will have a significant impact on estimates of the return periods for extreme surge events, shortening them at all the three locations (i.e., the frequency of surge events is increased). Table 8.6 gives the return period of tropical cyclone storm surges of 5 m, 2.5 m and 4 m above high astronomical tide (HAT) at Port Hedland, Darwin and Mackay respectively.

Table 8.6: Return period (in years) for tropical cyclone storm surges above specified level for the three selected ports under a variety of warm climate scenarios (LOVE, 1988)

| | Port Hedland | Darwin | Mackay |
|---|---|---|---|
| Surge level above HAT | 5 m | 2.5 m | 4 m |
| "Present" | 13 000 | 36 000 | 16 000 |
| "Present" plus 1 m sea level rise | 1000 | 4100 | 600 |
| Increase "Frequency" of cyclones plus 1 m sea level rise | 900 | 1800 | 650 |
| Increased "Intensity" of cyclone plus 1 m sea level rise | 430 | 650 | 200 |
| Increased "Frequency" and "Intensity" cyclone plus 1 m sea level rise | 350 | 450 | 180 |

MCINNES and HUBBERT (1995) used a sophisticated storm surge model capable of simulating the inundation associated with May 1994 and November 1994 mid-latitudes severe storms of Port Phillip Bay in the southeast pait of Australia. They performed three experiments: (i) Exp 1: Controlled experiment, (ii) Exp 2: Sensitivity experiment with increased sea level rise of 80 cm, and (iii) Sensitivity experiment with 10 % increase in the wind forcing in addition to a sea level rise of 80 cm. Results were presented for the entire Port Phillip Bay as well as the three small domains Werribee, Hobson's Bay and Mordialloc. They found different order of inundation in these three areas, leading to the conclusion that the estimation of the climate impact in the coastal region is highly site-specific problem. The areas of inundation in each of the three regions increased with the increase of sea level and with a further inundation with 10 % increase in wind strength (Table 8.7).

Table 8.7: Summary of the ratio area inundated to the area of inundation in Exp. 1 for the same event and model domains. The three domains are Werribee (W), Hobson's Bay (HB) and Mordialloc (M). The value in brackets denotes the total area inundated in km$^2$ (PITTOCK et al., 1996)

| | May 1994 | | | Nov. 1994 | | |
|---|---|---|---|---|---|---|
| | W | HB | M | W | HB | M |
| Exp. 1 | 1.0 (11.2) | 1.0 (0.9) | 1.0 (0.7) | 1.0 (15.8) | 1.0 (0.9) | 1.0 (0.7) |
| Exp. 2 | 2.7 (30.4) | 1.9 (1.7) | 9.3 (6.5) | 2.2 (34.4) | 2.0 (1.8) | 8.9 (6.2) |
| Exp. 3 | 3.1 (34.3) | 2.6 (2.3) | 11.0 (7.7) | 2.6 (41.0) | 3.2 (2.9) | 12.6 (8.8) |

PITTOCK et al. (1996) made a detailed review of the effect of enhanced green house on the climatology of tropical cyclones. They also reviewed the changes in storm surges due to tropical and extra-tropical cyclones as a result of mean sea level rise. They highlighted the requirement of site-specific inundation modelling studies as the magnitude of increase in coastal inundation due to rise in mean sea level heavily depends upon the specific characteristics of the site, including both meteorology and coastal geomorphology. More recently HUBBERT and MCINNES (1999) developed a high resolution storm surge inundation model

for coastal planning and impact studies. Model simulations were successfully carried out for the town of Port Hedland on the northwest coast of Australia and for the Port Phillip Bay, upon which the city of Melbourne is located. Scenarios of sea level rise and increased storm wind strength were imposed on the model simulations to explore the possible impact of climate change on two potentially vulnerable regions in south eastern Australia as well as demonstrate the application of the model to impact studies of this kind.

### 8.6.7 China

China has extensive coastal low lands with three great deltas of Yellow River, Yangtze River and Pearl River. Although all these deltaic regions are vulnerable to sea level rise, the Yangtze River deltaic plain is most vulnerable to accelerating sea level rise.

REN (1993, 1994) made a detailed study of sea level rise and its impact on coastal regions of China. The most significant impact of future sea level rise will be the increased vulnerability to sea inundation of coastal low land due to storm surges. Heaviest casualties ad loss of property from storm surges in China occur in the Yangtze River delta. Shanghai area especially experiences enormous losses as a result of combination of flood, astronomical high tidal level and typhoons.

Rising trends in storm surge levels of Shanghai area is currently indicated by observations (YANG, 1996). ZHU and XIE (1995) used a numerical model to compute tidal current and storm surges in the Yangtze River estuary for a projected sea level rise of 50 cm. According to the results of numerical calculations, slight decrease in surge amplitude is seen with a rise in sea level (average decrease in 9 cm in the northern coast and 6 cm in the southern coast of the Yangtze River). Although, the effect of sea level rise is small, the probabilities of occurrence of the storm surge level at a given height will have significant increase due to raised initial mean sea level. Table 8.8 gives the storm surge level with different probabilities of occurrence in the Yangtze River deltaic plain (YANG, 1996).

More recently QIN (1997) used a numerical storm surge and tide model to estimate the impact of sea level rise in the coming decades on the storm surges and tides in Shanghai regions. He estimated a mean annual relative sea level rise of 15–20 cm by 2010, 25–35 cm by 2030 and 40–50 cm by 2050 in Shanghai region as compared to unaltered sea level in 1990. To examine the impact of relative sea level rise on storm surges and tides, QIN (1997) used six severe tropical cyclones hitting Shanghai region. The effect of sea level rise on the storm surges at Wusong is shown is Fig. 8.11. It may be seen from the figure that the amplitude of storm surge decreases with increasing sea level. The maximum effect of the sea level rise on the storm surges in 2010, 2030, and 2050 relative to 1990 could be –0.5, –2.5, and –5.0 cm respectively.

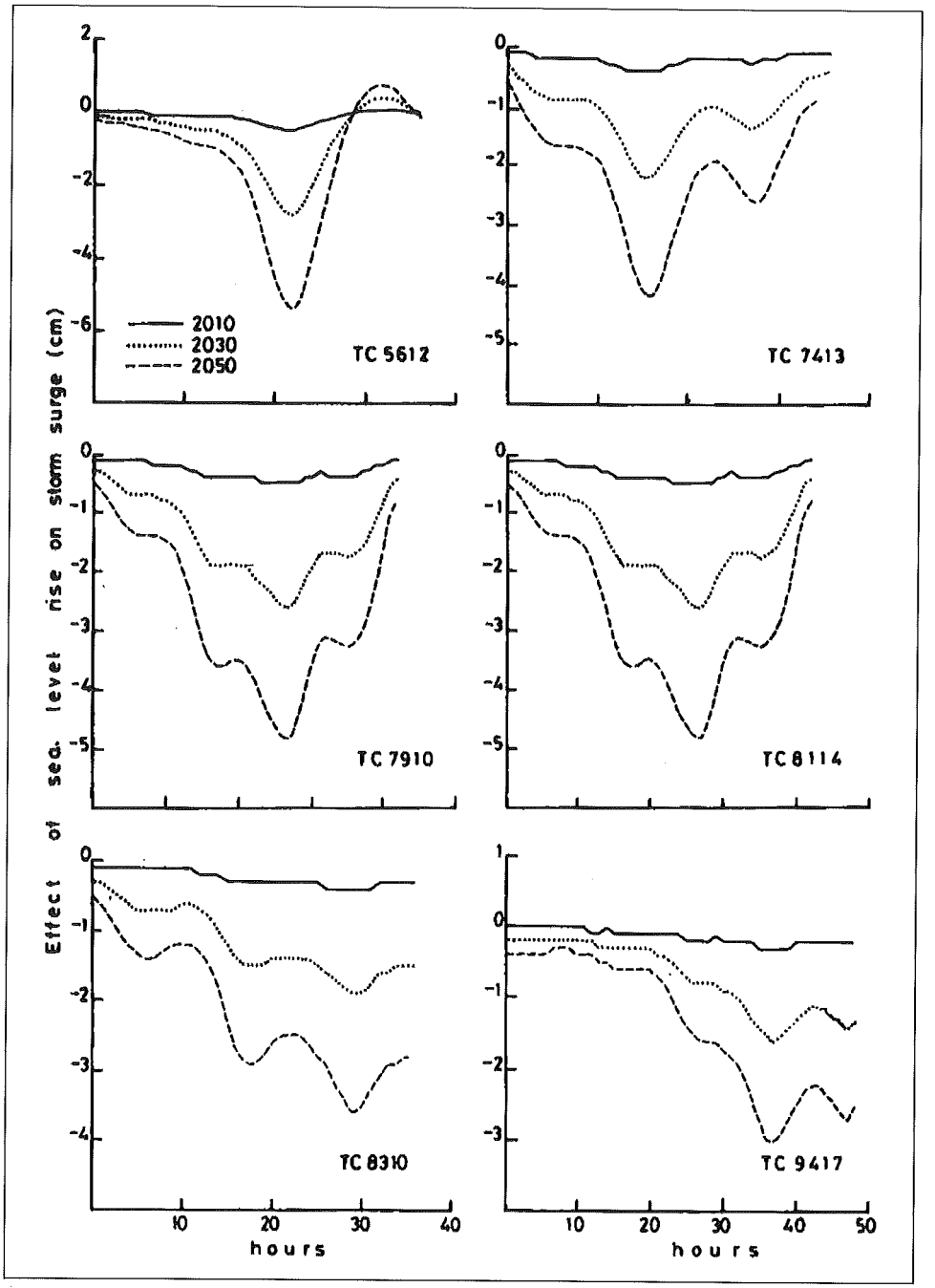


Fig. 8.11: The effect of sea level rise on the storm surge at Wusong (QIN, 1997)

Table 8.8: The impact of sea level rise on storm surge in the Yangtze River deltaic plain (Wusong Datum Plane, m) (YANG, 1996)

| Coast section | SLR (cm) | Storm surge level with different probabilities of occurrence | | | | | |
|---|---|---|---|---|---|---|---|
| | | 1/5 | 1/10 | 1/20 | 1/50 | 1/100 | 1/1000 |
| The southern coast | 0 | 5.02 | 5.17 | 5.32 | 5.54 | 5.69 | 6.24 |
| The northern | 50 | 5.46 | 5.61 | 5.76 | 5.98 | 6.13 | 6.68 |
| coast | 0 | 4.22 | 4.45 | 4.68 | 4.96 | 5.17 | 5.88 |
| | 50 | 4.63 | 4.86 | 5.09 | 5.37 | 5.58 | 6.29 |

This negative effect was expected as the rise in sea level results in the decrease of local wind set up and deeper local water than the initial one which leads to decrease of storm surge amplitude. Regarding impact of future relative sea level rise on tides, he found that tides exhibit periodic variations with the same periods as that of tide. The effect increases with increasing rise in relative sea level and retains its period unaltered.

WANG and WANG (1997) calculated maximum storm surge elevations with certain return periods for Guangdong Province of China. They used joint probability method to compute maximum elevations.

Hong Kong is threatened by the possibility of inundation from the sea whenever a tropical cyclone approaches. A number of studies has been carried out in the past (WATTS, 1959; CHENG, 1967; PETERSEN, 1975; LAU, 1980b; CHAN, 1983; CHAN and CHANG, 1997) on maximum sea level during storm surges. Sea level has been rising at an average rate of about 0.3 mm/yr in Hong Kong (YIM, 1993). It is estimated that as a result of global warming sea level may rise 31–110 cm by the year 2100. This will have major environmental effects on coastal lowlands, especially low-lying land reclaimed from the sea in Hong Kong. Although presently there is no evidence for an increase in the frequency of storm surges which may be the result of a rising sea level, Hong Kong is facing a continuing, and perhaps increasing risk of marine inundation from tropical cyclone surges.

## 9. References


ABBOTT, M. B., J. A. BERTELSEN, and I. R. WARREN, (1976). Modelling of storm surges in stratified flow. Proc. 15th Coastal Eng. Conf., July 11–17, 1976, Honolulu, HI.ASCE, New York, NY. 4 p.

ABBOTT, M. B., A. DANESGAARD, and G. S. RODENHUIS, (1973). System 21, Jupiter: a design system for two dimensional nearly-horizontal flow. J. Hydraul. Res. 11, 1–28.

ABRAMOVITZ, M., and I. E. STEGUN, (1965). Handbook of Mathematical Functions, 7th ed. Dover, New York, 1046 pp.

ADAMI, A., and A NOLI, (1992). Storm Surge Forecast Modelling. In: Danish Hydraulics, 12, pp. 6–7.

AGNEW, R., (1966). Storm tides in the Tasman Sea, New Zealand. J. Geol. Geophys. 9, 239–242.

ALAKA, M. A., (1976). Climatology of Atlantic tropical storms and hurricanes. In W. Schwerdtfeger [ed.] Climates of Central and South America. Elsevier Scientific Publishing Company, Amsterdam, Netherlands, p. 479–508.

ALI, A., (1979). Storm surges in the Bay of Bengal and some related problems. Ph.D., Thesis, University of Reading, England, pp. 227.

ALI, A., (1980a). The dynamic effects of barometric forcing on storm surges in the Bay of Bengal. Mausam 31, 517–522.

ALI, A., (1980b). A numerical model for the prediction of storm surges in the Bay of Bengal. Presented at the Indo-French School on recent advances in computer techniques in meteorology, biomechanics, and applied systems, New Delhi, Feb. 4–13, 1980.

ALI, A., (1980c). Some experiments with a numerical model developed for the prediction of storm surges in the Bay of Bengal, Symp. Typhoons, Oct. 6–11, 1980, p. 162–169, Sanghai. (Preprint volume).

ALI, A., (1996). Vulnerability of Bangladesh to Climate Change and Sea Level Rise through tropical cyclones and storm surges. Water, Air and Soil Pollution, 92, 171–179.

ALI, A., H. RAHMAN, S. SAZZAD, and H. CHOUDHARY, (1997a). River discharge, storm surges and tidal interaction in the Meghna River mouth in Bangladesh. Mausam. 48, 531–540.

ALI, A., H. RAHMAN, S. S. H. CHOUDHARY and Q. N. BEGUM, (1997b). Back water effect of tides and storm surges on fresh water discharge through the Meghna estuary. J. Remote Sensing & Environment, 1, 85–95.

ALLEN, SCOTT, (1998). Storm scenarios for 2100: havoc on Mass coast, Private Communication.

AMADORE, L. A., (1972). An evaluation of the accuracy of some objective techniques for predicting tropical cyclone movement in the western North Pacific. Tech. Ser. No. 14, W.M.O./U.N.D.P. Project. 74 p.

AMIN, A., (1982). On analysis and forecasting of surges on the west coast of Great Britain. Geophys. J. R. Astron. Soc. 68, 79–94.

AMIN, M., (1985). Temporal variations of Tides on the West coast of Great Britain. In: Geophys. J. Roy. Astr. Soc., 82, 79–94.

AN, M.B., (1980). A survey of storm surges along the West Coast of the Korean Peninsula. Report to the W. M. O. Workshop on storm surges, Nov. 10–15, 1980, Rangoon. 12 p.

ANDERSON, R. J., (1993). A study of wind stress and heat flux over the open ocean by the inertial dissipation method. J. Phys. Oceanogr. 23, 2153–2161.

ANDREWS, J. C., and L. BODE, (1988). The tides of the Central Great Barrier Reef. Continental Shelf Res., 8, 1057–1085.

ANGELL, J. K., J. KORSHOVER and G. F. COTTON, (1969). Quasi-biennial variations in the centers of action. Mon. Weather Rev. 97, 867–872.

ANON, (1978). A trigger for great stores? Mysteries of the mesoscale. NOAA 8, 42–45.

ANON, (1992). Path of Destruction, Hurricane Andrew, August 1992: B. D. Publishing Inc., Charleston, S. C., U.S.A, 98 pp.

ANON, (1993). Natural Disaster Survey Report, Hurricane Iniki: September 6–13, 1992, National Weather Service, NOAA, U.S.A., April 1993, 54, pp.

ANTHES, R. A., (1972). Development of asymmetries in a three-dimensional numerical model of the tropical cyclone. Mon. Weather Rev. 100, 461–476.

ANTHES, R. A., (1977). Hurricane model experiments with a new cumulus parameterization scheme. Mon. Weather Rev. 105, 287300.

ANTHES, R. A., S. L. ROSENTHAL, and J. W. TROUT, (1971a). Preliminary results from an asymmetric model of the tropical cyclone. Mon. Weather Rev. 99, 744–758.

ANTHES, R. A., S. L. ROSENTHAL, and J. W. TROUT, (1971b). Comparisons of tropical cyclone simulations with and without the assumption of circular symmetry. Mon. Weather Rev. 99, 759–766.

AOKI, T., (1979). A statistical prediction of the tropical cyclone position based on persistence and climatological factor in the western North Pacific (the PC method). Geophys. Mag. 38, 17–27.

AOKI, T., (1985). A climatological study of typhoon formation and typhoon visit to Japan, Paper Meteorology and Geophysics, 36, 61–118.

ARAKAWA, A., (1966). Computational design for long term numerical integration of the equations of fluid motion: two-dimensional incompressible flow. Part 1. Comput. Phys. 1, 119–143.

ARAKAWA, A., (1972). Design of the U.C.L.A. general circulation model, numerical simulation of weather and climate. Department of Meteorology, University of California, Los Angeles, CA.

ARAKAWA, H., (1995). Climates of northern and eastern Asia, World survey of climatology. Elsevier Scientific Publishing Company, Amsterdam, Netherlands, Vol. 8., p. 12–173.

ARCHIBALD, D. C., (1945). Intense storm tracks over Hudson Bay, the eastern Nova Scotia coast and the Grand Banks. Report of the Meteorological Branch, Department of Transport, Toronto, Ont. 9 pp.

ATKINSON, G. D., (1977). Proposed system of near real time monitoring of global tropical circulation and weather pattern, Preprints 11th Tech. Conf. on Hurricanes and tropical meteorology, Amer. Met. Soc., 645–652.

BAARSE, G., (1995). Development of an operational tool for global vulnerability assessment to sea level rise and coastal zone management (McLean, R. and N. Mimura, Editors), Proc. IPCC/WCC '93 Eastern Hemisphere Workshop, Tsukuba, 3–6 August 1993, Department of Environment, Sports and Territories, Canberra, Australia, pp. 333–340.

BACKHAUS, J., (1976). Zur Hydrodynamik im Flachwassergebiet, ein numerisches Modell. Dtsch. Hydrogr. Z. 29, 222–238.

BAERENS, C., and P. HUPFER, (1994). On the frequency of Storm Surges at the German Baltic Coast. In: Proceeding of the 19th Conference Baltic Oceanography, 1, S. 311–317.

BALAY, M. A., (1959). Causes and periodicity of large floods in Rio de la Plata (Flood of 27 and 28 July 1958), International Hydrographic Review, 36, No. 1, 123–151.

BALLENZWEIG, E. M., (1959). A practical equal-area grid. J. Geophys. Res. 64, 647–651.

BANKS, J. E., (1974). A mathematical model of a river-shallow sea used to investigate tide, Surge and their interaction in the Thames-Southern North sea region, Phil. Trans. Roy. Soc. London, A 275, 567–609.

BARRIENTOS, C. S., (1970). An objective method for forecasting winds over Lake Erie and Lake Ontario. E.S.S.A. Tech. Memo. WBTM TDL-34, Aug. 1970, Silver Spring, MD.

BARRIENTOS, C. S., and C. P. JELESNINSKI, (1976). Honolulu, HI. ASCE, New York, NY. (Abstr.).

BARRIENTOS, C. S., and C. P. JELESNINSKI, (1978). SPLASH – A model for forecasting tropical storm surges, p. 941–958. Proc. 15th Coastal Eng. Conf., June 24–28, 1976, Copenhagen, Denmark. ASCE, New York, NY.

BARRY, R. G., and R. J. CHORLEY, (1970). Atmosphere, weather and climate. Holt, Rinehart and Winston, Inc., New York, NY. 70 p.

BARRY, R.G., and R.C. CHORLEY, (1992). Atmosphere, weather and climate. 392 S. London and New York.

BARTHEL, V., (1979). Analysis of storm tide waves, 10161029. Proc. 16th Coastal Eng. Conf., Aug. 27–Sept. 3, 1978, Hamburg, W. Germany. ASCE, New York, NY.

BASANO, L., and L. PAPA, (1978). Correlation of the free oscillation of the Ligurian Sea with meteorological perturbations: a preliminary investigation. Boll. Geofis. Teor. Appl. 20, 223–234.

BATES, J., (1977). Vertical shear of the horizontal wind speed in tropical cyclones. Tech. Memo, ERL-WMPO-39, NOAA, National Weather Service, Silver Spring, MD.

BATTISTINI, R., (1964). L'extrême Sud de Madagascar, ètude gèomorphologique. Tome 1. le relief de l'intèrieur; These de doctorat; Editions Cujas; 636 p.

BEDARD, A. J., W. H. HOOKE, and D. W. BERAN, (1977). The Dulles Airport pressure-jump detector array for gust front detection. Bull. Am. Meteorol. Soc. 58, 920–926.

BEDARD, A. J., and H. B. MEADE, (1977). The design and use of sensitive pressure-jump sensors to detect thunderstorm gust fronts. Part 1: Pressure-jump detector design. J. Appl. Meteorol. 16, 1049–1055.

BELL, G. J., (1961). Surface winds in Hong Kong typhoons. Proc. U.S. – Asian Symp. Typhoons, Baguio, Philippines.

BELL, G. J., (1962). Predicting the movement of tropical cyclones in the region of the China Sea, p. 195–198. Proc. Interreg, Sernin. Trop. Cyclones, Tokyo. Japan.

BELL, G. J., (1979). Severe tropical storm Agnes, July 1978. Mar. Weather Log 23; 227–230.

BENGTSSON, L., M. BOTZET, and M. ESCH, (1994). Will green house gas-induced warming over the next 50 years lead to a higher frequency and greater intensity of hurricanes. Max-plane Institute fur Meteorologie, Report No. 139, MI, Hamburg, Germany, 23, pp.

BENWELL, G. R., A. J. GADD, J. F. KEERS, M. S. TIMPSON, and P. W. WHITE, (1971). The BushbyTimpson 10-level model on a fine mesh. Sci. Pap. No. 32, Meteorol. Off., London, England. 23 p.

BERGERON, T., (1954). The problem of tropical hurricanes. Q. J. Roy. Meteorol. Soc. 80, 131–164.

BERGSTEN, F., (1955). Winds and water levels on the coasts of Sweden. Geogr. Ann. Band. 37, 119–140.

BERSON, F. A., (1949). Summary of a theoretical investigation into the factors controlling the instability of long waves in zonal currents. Tellus 1, 44–52.

BETTS, A. K., R. W. GROVER, and M. W. MONCRIEFF, (1976). Structure and motion of tropical squall lines over Venezuela. Q. J. R. Meteorol. Soc. 2, 395–404.

BIRD, E. C. F., (1993). Submerging coasts: The effect of a rising sea level on coastal environments. John Wiley, Chichester, U.K.

BJERKNES, J., (1919). On the structure of moving cyclones. Geofys. Publ. 1, 1–8.

BJERKNES, J., and H. SOLBERG, (1921). Meteorological conditions for the formation of rain. Geofys. Publ. 2, 1–61.

BJERKNES, J., and H. SOLBERG, (1922). Life cycle of cyclones and the polar front theory of atmospheric circulation. Geofys. Publ. 3, 1–18.

BLAIN CHERYL ANN, (1997). Modeling Methodologies for the Prediction of Hurricane storm surge in recent advances in Marine Science and Technology, 96 Edited by N. K. Saxena, PACON International, Honolulu, 177–189.

BLAKE, J. T., (1981). Jamaica's encounter with Hurricane Allen. W.M.O. Bull. 30, 101–104.

BLANFORD, H. F., (1883). Indian Meteorologist's VadeMecum, Government of India, Calcutta, India.

BLASIUS, W., (1875). Storms, their nature, classification and laws. Porter and Coates Publishers, Philadelphia, PA. 342 p.

BLECKER, W., and J. M. ANDRE, (1950). Convective phenomena in the atmosphere, J. Meteorol. 7, 195–209.

BLONG, R., (1997). Natural Hazards News Letter (Personal Communication).

BLÜTHGEN, J., and WEISCHET, W. (1980). Allgemeine Klimageographie. Berlin, New York, 887 pages.

BODE L., and T. A. HARDY, (1997). Progress and recent developments in storm surge modeling. Journal of Hydraulic Engineering, 123 (4), 315–331.

BODINE, B. R., (1971). Storm surge on the open coast: fundamentals and simplified prediction. U.S. Army Coastal Eng. Res. Cent. Tech. Memo. 35, 55 p.

BONDESAN, M., G. B. CASTIGLIONI, C. ELMI, G. GABBIANELLI, R. MAROCCO, P. A. PIRAZOLLI, A. TOMASSIN, (1995). Coastal Areas Risk from Storm Surges and Sea-level Rise in Northeastern Italy. In: Journal of Coastal Research (11), 4, pp. 1354–1379.

BOOK, D. L., J. P. BORIS, and K. HAIN, (1975). Flux corrected transport. II. Generalization of the method. J. Comput. Phys. 18, 248–283.

BOWDEN, K. F., (1957). The effect of flow through the Strait of Dover on storm surges in the North Sea. Assoc. Oceanogr. Phys. Publ. Sci. No. 18, 61.

BRADBURY, D., (1954). Frequencies of cyclones and anticyclones and high and low zonal indexes. Department of Meteorology, University of Chicago, Chicago, IL. (Manuscript.)

BRAND, S., (1971). The effects on a tropical cyclone of colder surface waters due to upwelling and mixing produced by a tropical cyclone. J. Appl. Meteorol. 10, 865–874.

BRAND, S., R. J. GRAFF, and R. M. DE ANGELIS, (1978b). Tokyo Bay as a typhoon haven. Mar. Weather Log 22, 387–395.

BRAND, S., and C. P. GUARD, (1979). An observational study of extratropical storms evolved from tropical cyclones in the western North Pacific. J. Meteorol. Soc. Jpn. 57, 479–483.

BREBBIA, C. A., and P. W. PARTRIDGE, (1976). Finite element simulation of water circulation in the North Sea. Appl. Math. Model. 1, 101–107.

BRETSCHNEIDER, C. L., (1959). Hurricane surge predictions for Chesapeake Bay, Corps of Engineers, Washington, DC, Sept. 1959, Tech. Rep. AD 699408, 51 p.

BRETSCHNEIDER, C. L., (1967). Storm surges, Advances in Hydroscience. Vol. 4, p. 341–418, Academic Press, New York, NY.

BROADUS, J. M., (1993). Possible impacts of and adjustments to, sea level rise: the case of Bangladesh and Egypt. In Climate and sea level changes; observations, projections and implications. (Editors: R. A. Warrick, E. M. Barrew, and T. M. L. Wigley), Cambridge University Press, pp. 263–275.

BROADUS, J. M., J. D. MILLIMAN, S. F. EDWARDS, D. G. AUBREY, and F. GABLE, (1986). Rising sea level and damming of rivers: Possible effects in Egypt and Bangladesh. In "Effects of changes in Stratospheric Ozone and Global climate", Vol. 4, Sea Level Rise (Editor: J. G. Titus) UNEP/EPA, pp. 165–189.

BROWN. N., L. A. AMADORE, and E. C. TORRENTE, (1991). Philippine country study in „Disaster Mitigation in Asia anf the Pacific", Asian Development Bank, Manila, 193–253.

BROWN, P. S., and J. P. PANDOLFO, (1978). Merging finite difference schemes having dissimilar time-differencing operators. Mon. Weather Rev. 106, 268–270.

BRUNT, A. T., and J. HOGAN, (1956). The occurrence of tropical cyclones in the Australian region, p. 5–18. Proc. Trop. Cyclone Symp., Brisbane, December 1956. Bureau of Meteorology, Melbourne, Australia.

BRUUN, P., T. Y. CHIU, F. GERRITSEN, and W. H. MORGAN, (1962). Storm tides in Florida as related to coastal topography. Florida Eng. Ind. Exp. Stat. Res. Issue. 16 p.

BRYSON, R. A., and F. K. HARE [ed.] (1974). Climates of North America, p. 31–360. World survey of climatology. Vol. 11. Elsevier Scientific Publishing Company, Amsterdam, Netherlands.

BSH (Bundesamt für Seeschiffahrt und Hydrographie), (1992). The operational model of the North Sea and Baltic Sea. Hamburg.

BUCHWALD, V. T., (1971). The diffraction of tides by a narrow channel, J. Fluid Mech. 46, 501–511.

BUCHWALD, V. T., and R. A. DE SZOEKE, (1973). The response of a continental shelf to a travelling pressure disturbance, Aust. J. Mar. Freshwater Res. 24, 143–158.

BURNS, B. M., (1973). The climates of the MacKenzie Valley. Beaufort Sea. Vol. 1. Atmospheric Environment Service, Toronto, Ont. 227 p.

BURROUGHS, L. D., and S. BRAND, (1973). Speed of tropical storms and typhoons after recurvature in the western North Pacific Ocean. J. Appl. Metcorol. 12, 452–458.

BUTLER, H. L., (1979). Coastal flood simulation in stretched coordinates, p. 1030–1048 Proc. 16th Coastal Eng. Conf., Aug. 27–Sept. 3, 1978, Hamburg. W. Germany. ASCE. New York, NY.

CARDONE V. J., (1969). Specification of the wind distribution in the Marine Boundary Layer for wave forecasting, Report TR 69–1, New York University, New York.

CARDONE V. J., A. J. BROCCOLI, C. V. GREENWOOD, and J. A. GREENWOOD, (1980). Error characteristics of extratropical storm wind fields specified from historical data, J. Of Petroleum Technology, May 1980, 872–880.

CARRIER, G. F., (1971). The intensification of hurricanes. J. Fluid Mech. 49, 145–158.

CARTER, N. W., J. M. CHUNG, and S. P. GUPTA, (1991). South Pacific country study in "Disaster mitigation in Asia and the Pacific", Asian Development Bank, Manila, 255–307.

CERC, (1984). Shore protection Manual. US Army Corps of. Eng., Washington D.C.

CESELSKI, B. F., (1974). Cumulus convection in weak and strong tropical disturbances. J. Atmos. Sci. 31, 1241–1255.

CHAI FEI, and WANG JINGYONG, (1990). The nonlinear interaction of the surge and tide in the East China Sea. J. Ocean university of the Qissgdao, 20 (3), 56–62.

CHAKRAVORTHY, K. C., (1956). Calm centers of storms originating in the Bay of Bengal, p. 171–175. Proc. Trop. Cyclone Symp., Brisbane, Dec. 1956. Bureau of Meteorology, Melbourne, Australia.

CHAKRAVORTHY, K. C., and S. C. BASU, (1956). How to predict recurvature of storms in the Bay of Bengal, p. 359–365. Proc. Trop. Cyclone Symp., Brisbane, Dec. 1956. Bureau of Meteorology. Melbourne, Australia.

CHAN, H. F., (1976). A study of the characteristics of storm surges at Hong Kong. M. Phil. thesis, University of Hong Kong, Hong Kong.

CHAN H. F., and G.O. WALKER, (1979). Empirical studies of the peak surge due to tropical storms at Hong Kong. J Oceanogr. Soc. Jpn. 35, 110–117.

CHAN, J. C. L., (1985). Tropical cyclone activity in the northwest Pacific in relation to the El Nino/Southern Oscillation phenomenon. Mon. Wea. Rev., 113, 599–606.

CHAN, J. C. L., W. C. GRAY, and S. Q. KIDDER, (1980). Forecasting tropical cyclone turning motion from surrounding wind and temperature fields. Mon. Weather Rev. 108, 778–792.

CHAN, M. Y., (1978). Satellite photographs as an aid to forecast tropical cyclone recurvature. Tech. note 44, Royal Observatory, Hong Kong.

CHAN, Y. K., (1983). Statistics of extreme sea levels in Hong Kong, Royal Observatory, Hong Kong, tech. Note 35.

CHAN, Y. W., and W. L. CHANG, (1997). Statistics of storm surge in Hong Kong, Mausam, 48, 515–518.

CHANG, S. W. J., (1981). The impact of satellite-sensed winds on intensity forecasts of tropical cyclones. Mon. Weather Rev. 109, 539–553.

CHANG, S. W. J., and R. V. MADALA, (1980). Numerical simulation of the influence of sea surface temperature on translating tropical cyclones. J. Atmos. Sci. 37, 2617–2630.

CHANGNON, S. A., (1993). Historical variations in weather disasters. Implications of climate change. World Resour. Rev. 5 (3), Sept. 1993.

CHARBA, J., (1974). Application of gravity current model to analysis of squall line gust front. Mon. Weather Rev. 102, 140–156.

CHARNEY, J. G., (1947). The dynamics of long waves in a baroclinic westerly current. J. Meteorol. 4, 135–162.

CHARNEY, J. G., and A. ELIASSEN, (1964). On the growth of the hurricane depression. J. Atmos. Sci. 21, 68–75.

CHARNOK, H., (1955). Wind stress on a water surface. Qtly. J. R. Met. Soc., 81, 639–640.

CHARNOCK, H., and J. CREASE, (1957). Recent advances in science. North Sea surges. Sci. Prog. 45, 494–511.

CHENG, R. T., (1972). Numerical investigation of lake circulation around islands by the finite-element method. Int. J. Num. Methods Eng. 5, 103–112.

CHENG, R. T., (1974). On the study of convective-dispersion equation, p. 29–48. In J. T. Oden et al. [ed.] Finite element methods in flow problems. University of Alabama Press, Huntsville, AL.

CHENG, R. T., (1978). Modelling of hydraulic systems by finite element methods, p. 207–284. In V. T. Chow [ed.] Advances in hydroscience. Vol. 11. Academic Press, New York, NY.

CHENG, R. T., T. M. POWELL, and T. M. DILLON, (1976). Numerical models of wind-driven circulation in lakes. Appl. Math. Model. 1, 141–159.

CHENG, R. T., and C. TUNG, (1970). Wind driven lake circulation by the finite element method, p. 891–903. Proc. 13th Conf. Great Lakes Res. Int. Assoc. Great Lakes Res.

CHENG, T. T., (1967). Storm surges in Hong Kong. p. 1–16. Tech. Note 26, Royal Observatory, Hong Kong.

CHIN, P. C., (1970). The control point method for prediction of tropical cyclone movement. Tech. Note 30, Royal Observatory, Hong Kong. 25 p.

CHITTIBABU, P., (1999). Developement of storm surge prediction models for the Bay of Bengal and the Arabian Sea. Ph. D. Thesis, IIT Delhi, India, 262 pp.

CHITTIBABU, P., S. K. DUBE, A. D. RAO, P. C. SINHA, and T. S. MURTY, (2000). Numerical simulation of extreme sea levels using location specific high resolution model for Gujarat coast of India. Marine Geodesy, 23, 133–142.

CHO, H.A., (1980). Methods of observation of storm surges and astronomical tides. Report to the WMO Workshop on Storm Surges, November 10–15, 1980, Rangoon, Burma, 7 p.

CHOI, B. H., (1986). Surge hindcast in the East China Sea. Prog. Oceanog. 7, 177–192.

CHOI, B. H., (1987). Development of tide surge models of the Yellow Sea for coastal engineering application, Proc. 2nd Conf. on Coastal and Port Engineering in Developing Countries, Beijing, China, Sept 7–11, 1987, 1880–1894.

CHRISTIANSEN, H., and W. SIEFERT, (1979). Storm surge prediction by combined wind and tide data, p. 965–974. Proc. 16th Coastal Eng. Conf., Aug. 27–Sept. 3, 1978, Hamburg, W. Germany. ASCE New York, NY.

CHU, K. K., S. T. WANG, and H. P. PAD, (1978). Surface wind fields and moving tracks of typhoons when encountering the Island of Taiwan, p. 84–87. Proc. 11th Tech. Conf. Hurricanes Trop. Meteorol., Dec. 13–16, 1977, Miami Beach, FL. Am. Meteorol. Soc., Boston, MA.

CHUNYAN, LI, (1990). On the Nonlinear interaction between free tide waves and forced storm surge waves, Acta Oceanologica Sinica, 8, 95–104.

CIALONE, M. A., (1991). Coastal Modeling System (CMS) user's manual, Instruction Report CERC-91-1, Coastal Engineering Research Center, U. S. Army Engineer Waterways Experiment Station, Vicksburg, MS.

CLARK, J. D., (1978a). Rapid developing cast Pacific tropical cyclones, p. 642–644. Proc. 11th Tech. Conf. Hurricanes Trop. Meteorol. Dec. 13–16, 1977, Miami Beach, FL. Am. Meteorol. Soc., Boston, MA.

CLARK, J. D., (1978b). Rapidly developing eastern North Pacific tropical cyclones. Mar. Weather Log 22, 325–327.

CLINE, I. M., (1920). Relation of changes in storm tides on the coast of the Gulf of Mexico to the centre and movement of hurricanes. Mon. Weather Rev. 48, 127–146.

CLINE, I. M., (1926). Tropical cyclones. Macmillan and Co., Ltd., New York, NY.

CLINE, I. M., (1933). Tides and coastal currents developed by tropical cyclones Mon. Weather Rev. 61, 36–38.

COLDING, A., (1880). Det. Kong. Dan. Selsk. Skrifter. Natur. Math. (Afh.) 5, Raekke Xl, 3, 247.

COLDING, A., (1881). Det. Kong. Dan. Selsk. Skrifter. (Afli.) 6, Raekke 1, 243.

COLEMAN, F., (1972). Frequencies, tracks and intensities of tropical cyclones in the Australian region 1909–1969. Commonwealth Bureau of Meteorology, Melbourne, Australia. (Meteorological summary).

CONNOR, J. J., and C. A. BREBBIA, (1976). Finite elements for fluid flow. Butterworths Press, London, England.

CONNOR, J. L., and J. D. WANG, (1973). Mathematical models of the Massachusetts Bay. Part 1. Finite element modelling of two-dimensional hydrodynamical circulation. Rep. No. 172, Department of Civil Engineering, M.I.T., Cambridge, MA. 57 p.

CONNOR, W. C., R. H. KRAFT, and D. L. HARRIS, (1957). Empirical methods for forecasting the maximum storm tide due to hurricanes and other tropical storms. Mon. Weather Rev. 85, 113–116.

CORKAN, R. H., (1948). Storm surges: their importance in modern tidal science and some results of a recent investigation, p. 266–271. U.K. Dock and Harbour Authority, Feb. 1948.

CORKAN, R. H., (1950). The levels in the North Sea associated with the storm disturbance of January 8, 1949. Philos. Trans. Roy. Soc. London Ser. A 242, 493–525.

CORKAN, R. H., (1952). Storm effects in the Irish Sea, p. 170. Proc. I.U.G.G. Gen. Assem., Aug. 1951, Bergen, ProcesVerbaux, No. 5. (Abstr.).

CREAN, P. B., (1978). A numerical model of barotropic mixed tides between Vancouver Island and the mainland and its relation to studies of the estuarine circulation, p. 283–313. In J. C. J. Nihoul [ed.] Hydrodynamics of estuaries and fjords. Proc. 9th Int. Liège Colloq. Ocean Hydrodyn. Scientific Publishing Company, Amsterdam, Netherlands.

CREPON, M., (1974). The influence of wind on sea level. Manuscr. Rep. Mus. Nad. Hist. Nat. Paris. 8 p.

CRESSMAN, G. P., (1960). Improved terrain in Barotropic forecasts, Mon. Wea. Rev., 88, 327–342.

CRESWELL, M., (1929). Wind and tidal height in the Irish Sea. Mar. Obs. 6, 226–227.

CROWLEY, W. P., (1970). A numerical model for viscous, free surface, barotropic wind driven ocean circulations. J. Comput. Phys. 5, 139–168.

CRUTCHER, H. L., (1971a). Atlantic tropical cyclone statistics. NASA Contract Rep., NASA-CR-61335. George P. Marshall Space Flight Center, Huntsville, AL. 16 p. plus appendices.

CRUTCHER, H. L, (1971b). Atlantic tropical cyclone strike probabilities. NASA Contract Rep., NASA-CR-61361. George P. Marshall Space Flight Centre. 13 p. plus 2 appendices.

CRUTCHER, H. L., M. L. NICODEMUS, and M. J. CHANGERY, (1978). Tropical storm accelerations, p. 466–471. Proc. 11th Tech. Conf. Hurricanes Trop. Meteorol., Dec. 13–16, 1977, Miami Beach, FL. Am. Meteorol. Soc., Boston, MA.

CRUTCHER, H. L., and G. QUAYLE, (1974). Mariners worldwide climatic guide to tropical storms at sea. Published by the direction of the Commander, U.S. Naval Weather Service Command, NAVAIR, 50-IC-61, Superintendent of Documents, U.S. Government Printing Office, Washington, DC. 114 p. plus 311 charts.

CRUTCHER, H. L., and F. T. QUINLAN, (1971). Atlantic tropical cyclone vector mean charts. Published by the direction of the Commander, U.S. Naval Weather Service Command, National Climatic Center, Asheville, NC. 7 p. plus charts.

CURRIE, R. G., (1981). Amplitude and phase of 11-yr term in sea level of Europe. In: Geophysical Journal of the Royal Astronomical Society, 67.

DALLAS, W. L., (1891a). Cyclone memoirs – Part IV. Govemment of India, Calcutta, India.

DALLAS, W. L., (1891b). An inquiry into the nature and course of storms in the Arabian Sea and a catalogue and brief history of all recorded cyclones in that sea from 1648 to 1889. India Meteorol. Dep. Cyclone Mem. 4, 301–424.

DAMSGARRD, A., and A. F. DINSMORE, (1975). Numerical simulation of storm surges in bays, p. 1533–1551. Proc. Symp. Model. Techn. Vol. 2, Sept. 3–5, 1975, San Francisco, CA. ASCE, New York, NY.

DANARD, M. B., (1981). A note on estimating the height of the constant flux layer, Bound-Layer Meteorology 20, 397–398.

DANARD, M. B., and G. E. ELLENTON, (1980). Physical influences on east coast cyclongenesis. Atmosphere-Ocean 18, 65–82.

DANARD M. B., and T. S. MURTY, (1994). Storm Surge Migration through Vegetation Canopies, Natural Hazards, Vol. 9, 155–166.

D'ARRIGO, A., (1955). The recent damage to the Genoa Breakwater: the effect of sea conditions on vertical walls, p. 53–57. U.K. Dock and Harbour Authority, June 1955.

DAS, P. K., (1972). A prediction model for storm surges in the Bay of Bengal. Nature 239, 211–213.

DAS, P. K., (1980). Storm surges in the Bay of Bengal, p. 171–183. Proc. Symp. Typhoons, Oct. 6–11, 1980, Shanghai, China.

DAS, P. K., (1994a). Prediction of storm surges in the Bay of Bengal. Proc. Inidan natn. Sci. Acad., 60, 513–533.

DAS, P. K., (1994b). On the Prediction of storm surges. Sadhana, 19,583–595.

DAS, P. K., S. K. DUBE, U. C. MOHANTY, P. C. SINHA, and A. D. RAO, (1983). Numerical simulation of the surge generated by the June 1982 Orissa cyclone. Mausam, 34, 359–366.

DAS, P. K., M. MIYAZAKI, and C. P. JELESNIANSKI, (1978). Present techniques of tropical storm surge prediction. W. M. O. No. 500, Geneva, Switzerland. 87 p.

DAS P. K., M. C. SINHA, and V. BALASUBRAMANYAM, (1974). Storm Surges in the Bay of Bengal, Quart. J. Roy. Met. Soc., 100, 437–449.

DAVIES, A. M., (1976). A numerical model of the North Sea and its use in choosing locations for the deployment of offshore tide gauges in the JONSDAP 76 oceanographic experiment. Sonderd. Dtsch. Hydrogr. 29, 11–24.

DAVIES, A. M., (1980). Numerical sea model with two-dimensional and three dimensional regions dynamically connected. Dtsch. Hydrogr. Z. 33, 1937.

DAVIES, A. M., and R. A. FLATHER, (1977). Computation of the storm surge of 1 to 6 April 1973, using numerical models of the northwest European continental shelf and the North Sea. Dtsch. Hydrogr. Z. 30, 139–162.

DAVIES, A. M., and R. A. FLATHER, (1978). Application of numerical models of the Northwest European continental shelf and the North Sea to the computation of storm surges of November to December 1973. Dtsch. Hydrogr. Z. Ergänzungsheft Reihe A, Nr 14, 7–72.

DAVIES, A. M., and G. K. FURNES, (1980). Observed and computed $M_2$ tidal currents in the North Sea. J. Phys. Oceanogr. 10, 237–257.

DAVIES , A. M., and J. E. JONES, (1992). A three dimensional wind driven circulation model of the Celtic and Irish seas. 12, 159–188.

DAVIES, A, M., and J. K. JONES, (1996). The influence of the wind and wave turbulence upon tidal currents. Taylors problem in three-dimensions with wind forcing. Continental Shelf Research 16, 25–99.

DAY, J. W., W. H. CONNER, R. COSTANZA, G. P. KEMP, and I. A. MENDELSSOHN, (1993). Impact of sea level rise on coastal systems with special emphasis on the Mississippi River deltaic plain, In 'Climate and sea level change: Observations, projections and implications' (Edited by R. A. Warrick, E. M. Barraw, and T. M. Wigley), Cambridge University Press, 276–296.

DE, A. C., (1963). Movement of pre-monsoon squall lines over Gangetic West Bengal as observed by radar at Dum Dum Airport. Indian J. Meteorol. Geophys. 14, 37–45.
DE ANGELIS, R. M., (1977). Hurricane alley. Mar. Weather Log 21, 16–18.
DE ANGELIS, R. M., (1978a). Hurricane alley. Mar. Weather Log 22, 21–23.
DE ANGELIS, R. M., (1978b). Hurricane alley. Mar. Weather Log 22, 182–183.
DE ANGELIS, R. M., (1978c). Hurricane alley. Mar. Weather Log 22, 265–266.
DE ANGELIS, R. M., (1978d). Hurricane alley. Mar. Weather Log 22, 337–339.
DE ANGELIS, R. M., (1979a). Hurricane alley. Mar. Weather Log 23, 21–22.
DE ANGELIS, R. M., (1979b). Hurricane alley. Mar. Weather Log 23, 91–94.
DE ANGELIS, R. M., (1979c). Hurricane alley. Mar. Weather Log 23, 247–249.
DE RONDE, J. G., (1993). What will happen to The Netherlands is sea level rise accelerates?, In 'Climate and sea level change: Observations, projections and implications' (Edited by R. A. Warrick, E. M. Barraw, and T. M. Wigley), Cambridge University Press, 322–335.
DE RONDE, J. G., D. DILLINGH, and M. E. PHILIPPART, (1995). Design criteria along the Dutch coast. In: Hydrocoast, 95, S. 138–151.
DEAN, R. G., (1966). Tides and Harmonic Analysis. Estuary and Coastline Hydrodynamics (Ippen Ed.). McGraw-Hill Book Co. Inc., New York.
DEARDROFF, J. W., (1972). Parameterization of the planetary boundary layer for use in general circulation models Mon. Wea. Rev. 100, 93–106.
DEFANT, A., (1961). Physical oceanography. Vol. 2. Pergarnon Press, Inc., New York, NY. 598 p.
DEMEL, K., (1934). Les oscillations du Niveau de la Mer A Hel (c6te polonaise de la battique) en fonction des vents. Kosmos LIX (3), 135–146.
DHARMARATNA, G. H. P., (1996). An application of Jelesnianski technique to the east coast of Sri Lanka. Report to the International Workshop on storm surges, December 2–6, 1996, Tirupati, India.
DIETRICH, G., K., KALLE, W., KRAUSS, G. SIEDLER, (1975). Allgemeine Meereskunde. 3. Aufl. Berlin.
DINES, J. S., (1929). Meteorological conditions associated with high tides in the Thames, p. 27–39. Geophys. Mem. No. 47. Meteorological Office, Air Ministry, London, U.K.
DOBSON, G. M. B., (1963). Exploring the atmosphere. Clarendon Press, Oxford, U.K. 209 p.
DOHLER, G. C., (1967). Tides in Canadian waters. Department of Energy, Mines, and Resources, Ottawa, Ont. 14 p.
DONELAN, M. A., (1975). On the coupling between wind and waves. Tech. Rep. Canada Center for Inland Waters, Burlington, Ont. 42 p.
DONELAN, M. A., (1982). The dependence of the aerodynamic drag coefficient on wave parameters. Proc. First Int. Conf. Meteorology and Air-sea Interaction of the Coastal Zone, The Hague, 381–387.
DONELAN, M. A., (1990). Air-sea interaction. The sea, Ocean Engineering Science, 9, 239–292.
DONG, K. Q., (1988). El Nino and tropical cyclone frequency in the Australian region and the Northwest Pacific. Aust. Meteor. Mag., 36, 219–225.
DONN, W. L., (1959). The Great Lakes storm surge of May 5, 1952. J. Geophys. Res. 64, 191–198.
DONN, W. L., and N. K. BALACHANDRAN, (1969). Coupling between moving air pressure disturbance and the sea surface. Tellus 21, 701–706.
DONN, W. L., and M. EWING, (1956). Stokes' edge waves in Lake Michigan. Science (Washington, DC) 124, 1238–1242.
DONN, W., and W. T. MCGUINNESS, (1959). Barbados storm swell. J. Geophys Res. 64, 2341–2349.
DOODSON, A. T., (1924). Meteorological perturbations of sea level and tides. Geophys. Suppl. R. Astron. Soc. London 1, 124–127.
DOODSON, A. T., (1929). Report on Thames floods, p. 1–26. Geophys. Mem. No. 47. Meteorological Office, Air Ministry, London, U.K.
DOODSON, A. T., (1947). Storm surges. Int. Hydrogr. Rev. 24, 108–120.
DOODSON, A. T., and J. S. DINES, (1929). Meteorological conditions associated with high tides in the Thames. Geophys. Mem. No. 47. U.K. Meteorological Office, London. 26 p.
DOUGLAS, S. K. M., (1929). The line squall and channel wave of July 20, 1929. Meteorol. Mag. 64, 187–189.
DRUYAN, L., and P. LONERGAN, (1997). The impact of climate change on tropical cyclones. Risk Prediction Initiative Workshop, May 5–6, 1997, Hamilton, Bermuda.

DUBE, S. K., (1998a). Mathematical Modelling of Storm Surges Associated with Tropical Cyclones. Proceedings of the National Seminar on Application of Mathematics in Industries and Environment, Agra, December 17–18. Chapter 4, 13–25.

DUBE S. K., (1998b). Storm surges modelling and prediction in the Bay of Bengal: An application to Myanmar. Presented at MYANMAR – INDIA Workshop on Oceanography of Bay of Bengal and the Andaman Sea, 25–28 November 1998, Yangon, Maynmar, 16 p.

DUBE, S. K., P. CHITTIBABU, P. C. SINHA, A. D. RAO, and T. S. MURTY, (1999a). Storm Surges and inundation on the Andhra Coast, India. In: Recent advances in Marine Science and Technology – 98, pp. 57–66.

DUBE, S. K., P. CHITTIBABU, A. D. RAO, P. C. SINHA, and T. S. MURTY, (2000a). Extreme sea levels associated with severe tropical cyclones hitting Orissa coast of India, Marine Geodesy, 23, 65–73.

DUBE, S. K., P. CHITTIBABU, A. D. RAO, P. C. SINHA, and T. S. MURTY, (2000b). Sea levels and coastal inundation due to tropical cyclones in Indian coastal regions of Andhra and Orissa. Marine Geodesy, 23, 65–73.

DUBE, S. K., and V. K. GAUR, (1995). Real time storm surge prediction system for the Bay of Bengal. Current Science 68, 103–113.

DUBE, S. K., and A. D. RAO, (1989). Coastal flooding due to storm surges in the Bay of Bengal. In: Coastal Zone Management in India (Editors: S. N. Dwiwedi, V. S. Bhatt and Pradeep Chaturvedi), Indian Association for the Advancement of Science, pp. 136–144.

DUBE, S. K., and A. D. RAO, (1991). Sea level rise and coastal flooding by storm surges in the Bay of Bengal. Proc. Indian Natn. Sci. Acad., 57A, 565–572.

DUBE, S. K., A. D. RAO, P. C. SINHA, and P. CHITTIBABU, (1994). A real time storm surge prediction system: An Application to east coast of India. Proc. Indian Natn. Sci. Acad., 60, 157–170.

DUBE, S. K., A. D. RAO, P. C. SINHA, and P. CHITTIBABU, (2000c). Storm surge modeling and prediction, In Mathematical Analysis and Applications (Edited by: A. P. Dwivedi), Narosa Publishing House, New Delhi, India. Pp. 109–124.

DUBE, S. K., A. D. RAO, P. C.SINHA, and T. S. MURTY, (1998). Storm Surges in the Bay of Bengal, In "Maritime Natural Hazards in the Indian Ocean Region" (Edited by: Colin D. Woodreffe), Wollongong University Press, 1998, 43–82.

DUBE, S. K., A. D. RAO, P. C. SINHA, T. S. MURTY, and N. BAHULAYAN, (1997). Storm surge in the Bay of Bengal and Arabian Sea: The problem and its Prediction. Mausam 48, 283–304.

DUBE, S. K., and P. C. SINHA, (1982). Storm surge prediction in India – A Review. Bull. SOSEUTI 4. 5–12.

DUBE, S. K., P. C. SINHA, M. LAL, and A. D. RAO, (1984a). Numerical simulation of storm surges in Burma, Proceedings of the 13th National Conference on Fluid Mechanics and Fluid Power –84, Tiruchirapalli, India, 469–473.

DUBE, S.K., P.C. SINHA, and A. D. RAO, (1981). The response of different wind stress forcing on the surges along the east coast of India. Mausam 32, 315–320.

DUBE S. K., P. C. SINHA, and A. D. RAO, (1982). The effect of coastal geometry on the location of peak surge. Mausam, 33, 445–450.

DUBE, S. K., P. C. SINHA, A. D. RAO, and P. CHITTIBABU, (1999b). Recent developments in storm surge modeling and future trends, In Meteorology Beyond 2000 (Ed. A. K. Bhatnagar, S. Raghavan, R. N. Keshavamurthy, G. S. Ganesan, J. Shanmugasundram, S. Rajarathnam, N. Jayanthi, S. K. Subramanian, R. Suresh and Y. E. A. Raj), Indian Meteorological Society, Chennai, India. pp. 521–531.

DUBE, S. K., P. C. SINHA, A. D. RAO, and G. S. RAO, (1985a). Numerical modelling of storm surges in the Arabian Sea, Applied Mathematical Modelling, 9, 289–294.

DUBE, S. K., P. C. SINHA, and G. D. ROY, (1984b). Storm surges in Bangladesh: The problem and the numerical simulation. Vayu Mandal 14, 34–39.

DUBE, S. K., P. C. SINHA, and G. D. ROY, (1985b). The numerical simulation of storm surges along the Bangladesh coast. Dyn. Atmos. Oceans. 9, 121–133.

DUBE, S. K., P. C. SINHA, and G. D. ROY, (1985c). Numerical Simulation of Storm Surges induced by tropical storms impinging on the Bangladesh Coast. In "Coastal Engineering" (Editor: Billi L. Edge), American Society of Civil Engineers, Chapter XIII, pp. 190–198.

DUBE S. K., P. C. SINHA, and G. D. ROY, (1986a). The effect of continuously deforming coastline on the numerical simulation of storm surges in Bangladesh. Math. Comput. Simul. 28, 41–56.

DUBE, S. K., P. C. SINHA, and G. D. ROY, (1986b). Numerical simulation of storm surges in Bangladesh using a River-Bay coupled model. Coastal Engineering, 10, 85–101.

DUNN-CHRISTERISEN, J. T., (1971). Investigation on the practical use of a hydro-dynamic model for calculation of the Sea level variations in the North Sea, the Skaggerak and the Kattegat, Deutsche Hydrographische Zeitschrift, 24, 210–240.

DUNN, G. E., (1958). Hurricanes and hurricane tides. p. 19–29. In J. W. Johnson [ed.] Proc. 6th Coastal Eng. Conf., Dec. 1957. Florida. Council on Wave Resources. The Engineering Foundation, New York. NY.

DUNN, G. E., and B. I. MILLER, (1960). Atlantic hurricanes. Louisiana State University Press, Baton Rouge, LA.

DUNNAVAN, G. M., and J. W. DIERCKS, (1980). An analysis of supertyphoon Tip, October 1979. Mon. Wea. Rev. 108, 1915–1923.

DVORAK, V. F., (1975a). Tropical cyclone intensity analysis and forecasting from satellite imagery. Mon. Weather Rev. 102, 420–430.

DVORAK, V. F., (1975b). Tropical cyclone intensity analysis and forecasting. Mar. Weather Log 19, 199–206.

EADY, E. T., (1949). Long waves and cyclone waves. Tellus 1, 33–52.

EASTON, A. K., (1970). The tides of the continent of Australia. PILD. thesis, Horace Lamb Center, Flinders University of South Australia, Bedford Park, South Australia. 326 p.

EGEDAL, J., (1957). Some remarks on storm surges in interior Danish waters. Proces Verbaux Assoc. Oceanogr. Phys. Publ. Sci. No. 18, 200–201.

ELIASSEN, A., (1956). A procedure for numerical integration of the primitive equations of the two-parameter model of the atmosphere. Sci. Rep. No. 4, Department of Meteorology, U.C. L. A., Los Angeles, CA. 53 p.

ELIOT, J., (1890). Handbook of cyclonic storms in the Bay of Bengal. Publ. Indian Meteorol. Dep., Calcutta, India.

ELIOT, J., (1900). Cyclonic storms in the Bay of Bengal. Rep. Indian Meteorol. Dep., Calcutta, India.

EL-SABH, M. I., and T. S. MURTY, (1989). Storm surges in the Arabian Gulf. Natural Hazards, 1, 371–385.

ELSBERRY, R. L., (1979). Applications of tropical cyclone models. Bull. Am. Meteorol. Soc. 60 (7), 750–762.

EMANUEL, K. A., (1986). An air-sea interaction theory for tropical cyclones. Part I: Steady state maintenance J. Atmos. Sci., 43, 585–604.

EMANUEL, K. A., (1987). The dependence of hurricane intensity on climate. Nature, 326, pp. 483–485.

ERASLAN, A. H., (1974). A transient, two-dimensional discrete-element model for far field analysis of thermal discharges in coastal regions. Proc. Conf. Therm. Pollut. Anal. Virginia Polytechnique Institute and State University, Blacksburg, VA.

ESTOQUE, M. A., and J. M. GROSS, (1979). Diurnal wind and temperature variations over Lake Ontario. Mon. Weather Rev. 106, 1742–1746.

EVANS, J. L., (1993). Sensitivity of tropical cyclone intensity to sea surface temperature, J. Climate 6, pp. 1133–1140.

EVANS, J. L., and R. J. ALLEN, (1992). El Nino/Southern Oscillation modification to the structure of the monsoon and tropical activity in the Australian region. Intl. J. Climatology, 12, 611–623.

FABRY, L., (1909). Sur unc oscillation de la mer Constatde le 15 juin 1909 dans le port de Marseille. C.R. 149, 324–325.

FALCONER, R. A., (1980). Numerical modelling of tidal circulation in harbors, p. 31–48. J. Of the Waterway, Port, Coastal and Ocean Division. Proc. ASCE, Feb. 1980, WWi.

FANDRY, C. B., L. M. LESLIE, and R. K. STEEDMAN, (1984). Kelvin-type coastal surges generated by tropical cyclones. J. Phys. Oceanogr. 14, 582–593.

FARRER, L. A., (1958). Wind tides in Lake Okeechobee, p. 134–136. In J. W. Johnson [ed.] Proc. 6th Coastal Eng. Conf., Dec. 1957, FL. Chap. 7. Council on Wave Resources, The Engineering Foundation, New York, NY.

FEIT, D. M., and C. S. BARRIENTOS, (1974). Great Lakes wind forecasts based on model output statistics, p. 725–732. Proc. 17th Conf. Great Lakes Res., Hamilton, Ont.

FEIT, D. M., and N. A. PORE, (1978). Objective wind forecasting and verification on the Great Lakes. J. Great Lakes Res. 4, 10–18.

FENGSHU, LIU, and DING WENLAN, (1990). A preliminary study of the in interaction between astronomical tides and storm surges. In: storm Surges Observation and Modelling (edited by Chao Jiping, T. S. Murty, Bao Cheanglan, M. I. El-Sabh, and Liu Fengshu, China Ocean Press, 17–33).

FERK, U. (1999): New development in the storm surge forecasting method for Hamburg. Written correspondence, unpublished.

FETT, R. W., and S. BRAND, (1975). Tropical cyclone movement forecasts based on observations from satellites. J. Appl. Meteorol. 14, 452–465.

FINLAYSON, G. A., and L. E. SCRIVEN, (1965). The method of weighted residuals and its relation to certain variational principles for the analysis of transport processes. Chem. Eng. Sci. 20.

FISHER, G., (1959). Ein numerisches Verfahren zur Errechnung von Windstau und Gezciten in Randmeeren. Tellus 11, 60–76.

FISHER, G., (1965). Comments on some problems involved in numerical solutions of tidal hydraulics equations. Mon. Weather Rev. 93, 110–111.

FISHER, G., (1979). Results of a 36-hour storm surge prediction of the North Sea for January 3, 1976, on the basis of numerical models. Dtsch. Hydrogr. Z. 32, 89–99.

FITZ-ROY, R., (1863). Weather book: a manual of practical meteorology. London, U.K.

FIX, G. J., (1975). Finite element models for ocean circulation problems, S.I.A.M. J. Appl. Math. 29, 371–387.

FJORTOFT, R., (1950). Application of integral theorems in deriving criteria of stability of laminar blows and of baroclinic circular vortex. Geofys. Publ. 17, 1–52.

FLATHER, R. A., (1976). Practical aspects of the use of numerical models for surge prediction. Report No. 30, Inst. of Ocean. Sci., Bidston, U.K.

FLATHER, R. A., (1979). Recent results from a storm surge prediction for the North Sea, in J. C. J. Nihoul (ed.) Marine Forecasting, proc. 10th Int. Liege Colloquium on ocean Hydrodynamics, Elsevier Scientific Pub. Co. Amsterdam, 385–409.

FLATHER, R. A., (1980). Recent results from a storm surge prediction scheme for the North Sea, p. 385–409. In J. C. J. Nihoul [ed.] Proc. 10th Int. Liêge Colloq. Ocean Hydrodyn. Elsevier Scientific Publishing Company, Amsterdam, Netherlands.

FLATHER, R. A. (1981). Practical surge prediction using numerical models, p. 21–43. In D. H. Peregrine [ed.] Floods due to high winds and tides. Academic Press, London. 109 p.

FLATHER, R. A., (1984). A numerical model investigation of the storm surge of 31 January and 1 February1953 in the North Sea. Quart. J. R. Met. Soc., 110, 591–612.

FLATHER, R. A., (1987). Estimates of extreme conditions of tide and surge using a numerical model of the northwest European Continental Shelf. In: Estuarian Coast Shelf Science, 24, p. 69–93.

FLATHER, R. A., (1988). A numerical model investigation of tides and diurnal-period continental shelf waves along Vancouver Island, Journal of Physical Oceanography 18, 115–139.

FLATHER, R. A., (1994). A storm surge prediction model for the northern Bay of Bengal with application to the cyclone disaster in April 1991. Jr. Phys. Oceanogr. 24. 172–190.

FLATHER, R. A., and A. M. DAVIES, (1975). The application of numerical models to storm surge prediction. Inst. Oceanogr. Sci. Rep. No. 16.

FLATHER, R. A., and A. M. DAVIES, (1976). Note on a preliminary scheme for storm surge prediction using numerical models. Q. J. Roy. Meteorol. Soc., 102, 123–132.

FLATHER, R. A., and A. M. DAVIES, (1978). On the specification of meteorological forcing in numerical models for North Sea storm surge prediction with application to the surge of January 2–4, 1976. Dtsch. Hydrogr. Z. Reihe A, Nr. 15, 7–51.

FLATHER, R. A., and N. S. HEAPS, (1975). Tidal computations for Morecambe Bay, Geophys. J. Roy. Astronom. Soc. 42. 489–517.

FLATHER, R. A., and H. KHANDEKAR, (1993). The storm surge problem and possible effects of sea level changes on coastal flooding in the Bay of Bengal. In: Climate and sea level change: Observations, projections and implications. (Edited by: R. A. Warrick, E. M. Barrow, and T. M. Wigley), Cambridge University Press, 229–245.

FLATHER R. A., and R. PROCTOR, (1983). Prediction of North-Sea storm surges using numerical models: Recent developments in UK. In "North Sea Dynamics" (Ed. Sünderman/Lenz) Springer-Verlag, Berlin Heidelberg, 299–317.

FLIERL, G., and A. R. ROBINSON, (1972). Deadly surges in the Bay of Bengal, dynamics and storm tide tables. Nature (London) 239, 213–215.

FLOHN, H., (1971). Zur Didaktik der allgemeinen Zirkulation der Atmosphäre. In: Arbeiten zur Allgemeinen Klimatologie, [Geographische Rundschau, 1960], S. 127–156.

FOREMAN, M. G. G., (1983). An analysis of the 'Wave Equation' model for finite element tidal computations. J. Comput. Phys. 52 (2), 290–312.

FOREMAN, M. G. G., (1988). A comparison of tidal models for the southwest coast of Vancouver Island. Proc. 7th Int. Conf. On Comput. Methods in Water Resour. Elsevier.

FORRISTALL, G. Z., (1974). Three-dimensional structure of storm-generated currents. Geophys. Res. 79, 2721–2729.

FRANK, N. L., (1978). Tropical systems – a ten year summary, p. 455–458 Proc. 11th Tech. Conf. Hurricanes Trop. Meteorol. Dec. 13–16, 1977, Miami Beach, FL. Am. Meteorol. Soc., Boston, MA.

FRANK, N. L., and S. A. HUSSAIN, (1971). The deadliest tropical cyclone in history. Bull. Am. Meteorol. Soc. 52, 438–444.

FRANK, W. M., (1977). The structure and energetics of the tropical cyclone. Part II: Dynamics and energetics. Mon. Weather Rev. 105, 1136–1150.

FREEMAN, J. C., L. BAER, and G. H. JUNG, (1957). The bathystrophic storm tide. J. Mar. Res. 16, 12–22.

FREEMAN, J. C., and B. HE. MEHAUTE, (1964). ASCE J. Of the Hydraulic Division 90, 187.

FÜHRBÖTER, A., (1979). Frequencies and probabilities of extreme surges: On the time-dependent changes of the probability of extreme storm floods at the German North Sea coast. Proc. of the 16th Coastal Eng. Conf., August 27–Sept. 3, 1978, Hamburg, vol. 1, ASCE, New York, 949–964.

FÜHRBÖTER, A., J. JENSEN, M. SCHULZE, and A. TÖPPE, (1988). Sturmflutwahrscheinlichkeit an der deutschen Nordseeküste nach verschiedenen Anpassungsfunktionen und Zeitreihen. In: Die Küste, 47, 164–186.

FÜHRBÖTER, A., and A. TÖPPE, (1991). Duration of Storm Tides at High Water Levels. In: Storm Surges, River Flow and Combined Effects. A contribution to the UNESCO-IHP Project H-2-2. Hamburg, 45–54.

FUJITA, T., (1955). Results of detailed synoptic studies of squall lines. Tellus 4, 405–436.

FUJITA, T., (1959). Precipitation and cold air production in mesoscale thunderstorm systems. J. Meteorol. 16, 454–466.

FUJITA, T., H. NEWTON, and M. TEPPER, (1956). Mesoanalysis: an important scale in the analysis of weather data. U.S. Weather Bur. Res. Pap. No. 39, 83 p.

FUJIWHARA, S., (1921). The natural tendency towards symmetry of motion and its application as a principle of meteorology. Q. J. Roy. Meteorol. Soc. 47, 287–293.

FUNK, B., (1980). Hurricane! Natl. Geogr. Sept. 1980, 346–379.

GADGIL, S., (1995). Climate change and agriculture – An Indian perspective. Current Science, 69, 649–659.

GAGLIARDINI D. A., H. KARSZENBAUM, R. LEGECKIS, and V. KLEMAS, (1984). Application of LANDSAT MSS, NOAA/TIROS AVHRR, and NIMBUS CZCS to study the La Plata river and its interaction with the ocean, Remote sensing of Environment, Vol. 15, 21–36.

GALLAGHER, B., (1973). Model for nonlinear tides in small basins with openings of restricted depth. J. Hydraul. Res. 78 (27), 6395–6400.

GALLAGHER, R. H., and S. T. K. CHAN, (1973). Higher order finite element analysis of lake circulation. Comp. Fluids 1, 119–132.

GALLAGHER, R. H., J. A. LIGGET, and S. T. K. CHAN, (1973). Finite element shallow lake circulation analysis. J. Hydraul. Res. Div. ASCE 99 (HY7), 1083–1098.

GALLÉ, P. H., (1915). On the relation between the departures from the normal in the strength of the trade winds of the Atlantic Ocean and those in the water level and temperature in the northern European seas. Proc. K. Ned. Akad. Wet. Ser. B Phys. Sci. 17, 1147–1158.

GARABEDIAN, P. R., (1964). Partial differential equations. John Wiley & Sons, New York, NY, 672 p.

GARRETT, C. J. R., (1975). Tides in Gulfs. Deep Sea Res. 22, 23–35.

GEELHOED, P. T., (1973). Negative surges in the southern North Sea. Int. Hydrogr. Rev. L(I), 61–73.

GEERNAERNT, G. L., K. B. KATSAROS, and K. RITCHER, (1986). Variation of the drag coefficient and its dependence on sea state. J. Geophys. Res., 91, 7667–7679.

GENTILLI, J., (1971). Climates of Australia and New Zealand, p. 86–222. World survey of climatology. Vol. 13. Elsevier Scientific Publishing Company, Amsterdam, Netherlands.

GEORGE, K. J., (1980). Anatomy of an amphidrome. Hydrogr, J. 18, 5–12.

GHOSH, S. K., (1977). Prediction of storm surges on the coast of India. Ind. J. Meteo. Geophys., 28, 157–168.

GHOSH, S. K., (1980). The intensity of the Andhra Cyclone of 1977. Indian Meteorological Department, New Delhi, India. 6 p.

GHOSH, S. K., (1981). Objective prediction of storm surges on Indian coasts, Proc. Symp. on Meteorological and Oceanic Fluid dynamics, 7–8 February 1981, Jadavpur University, Calcutta, India.

GHOSH, S. K., B. N. DEWAN, and V. B. SINGH, (1983). Numerical simulation of storm surge envelopes associated with the recent severe cyclones impinging on the east and west coast of India, Mausam, 34, 399–404.

GIBB, J. G., (1976). Coastal erosion along Wellington's west coast. Soil Water 13, 6–7.

GIBB, J. G., (1977). Late quaternary sedimentary processes at Ohiwa harbour, eastern Bay of Plenty, with special reference to property loss. Tech. Publ. No. 5. Water and soil division, Ministry of Works and Development, Wellington. 16 p.

GILL, S. M., (1975). The discovery of Bangladesh. The Offington Press, Melksham, U.K. 138 p.

GILMOUR, A. E., (1963). Note on the relation between high sea level and atmospheric pressure at Bluff Harbour, N. Z. J. Geol. Geophys. 6, 582–586.

GJEVIK, B., and L. P. ROED, (1974). Storm surges along the western coast of Norway. Rep. No. 7, Oct. 1974, Institute of Geophysics, University of Oslo, Oslo, Norway.

GODIN, G., (1972). The analysis of tides. University of Toronto Press, Downsview, Ont. 264 p.

GODIN, G., (1980a). Cotidal charts for Canada. Manuser. Rep. No. 55. Marine Sciences and Information Directorate, Department of Fisheries and Oceans, Ottawa, Ont. 93 p.

GODIN, G., (1980b). Modification of the tide in the Canadian Arctic by an ice cover. Manuscr. Rep. No. 56. Marine Sciences and Information Directorate, Department of Fisheries and Oceans, Ottawa, Ont. 29 p.

GODIN, G., (1988). Tides. Ottawa. pp. 348.

GODIN, G., (1991). The Analyses of Tides and Currents. In: Tidal Hydrodynamics, S. 675–709.

GODIN, G., (1996). Reprints in Oceanography 1965–1995. Ottawa.

GOFF, R. C., (1975). Thunderstorm outflow kinematics and dynamics. NOAA Tech. Mem. ERL-NSSL-75, 63 p.

GÖHREN, H., (1976). Currents in tidal flats during storm surges, p. 959–970. Proc. 15th Coastal Eng. Conf., July 11–17, 1976, Honolulu, HI. ASCE, New York, NY.

GOMIS, D., S. MONSERRAT, and J. TINTORE, (1993). Pressure forced seiches of large amplitude in inlets of the Balearic Islands, J. Geophys. Res. 98, 14437–14445.

GÖNNERT, G., (1998). Sturmfluten im Elbeästuars. In: Schriftenreihe der Niedersächsischen Akademie für Geowissenschaften, Heft 14, S. 24–35.

GÖNNERT, G., (1999a). The analysis of storm surge climate chang along the German coast during the 20th century. In: Journal of Quarternary International, S. 115–121.

GÖNNERT, G., (1999b). Veränderung des Charakters von Sturmfluten in der Nordsee aufgrund von Klimaänderung in den letzten 100 Jahren. In: Marburger Geographische Schriften, 134, S. 24–39.

GÖNNERT, G. (1999c). Sturmfluthöhen in der Nordsee. Auswirkungen der Klimaänderung in den letzten 100 Jahren. In: Jahrbuch der Hafenbautechnischen Gesellschaft, 52, S. 192–201.

GÖNNERT, G., and W. SIEFERT, (1997). Storm surge development in the Sothern North Sea and the Elbe river in Europe during the last century and its practical application, Mausam, 48, 499–514.

GÖNNERT, G., and W. SIEFERT, (1998). Sturmflutatlas Cuxhaven. Hamburg, Strom- und Hafenbau. Studie Nr. 92. 1998.

GÖNNERT, G. Storm Surges in the North Sea. Conclusion paper of an investigation project (unpublished.).

GOUDEAU, D. A., and W. C. CONNOR, (1968). Storm surge over the Mississippi River Delta accompanying Hurricane Betsy 1965. Mon. Weather Rev. 96, 118–124.

GORDAY, S. P., I. E. KOCHERGIN, and M. N. KULINCHENKO, (1991). Estimation of extreme parameters of Tsunami on the northeastern Sakhalin coast from numerical results. In. Soviet Meteorology and Hydrology, 8, p. 67–72.

GRAF, W. H., and J. P. PROST, (1979). The aerodynamic drag: experiments on Lake Geneva, p. 303–312. In H. Graf, and C. H. Mortimer [ed.] Hydrodynamics of lakes. Proc. Symp. Oct. 12–13, 1978, Lausanne, Switzerland. Elsevier Scientific Publishing Company, Amsterdam, Netherlands.

GRAHAM, H. E., and D. E. NUNN, (1959). Meteorological considerations pertinent to standard project hurricane, Atlantic and Gulf coasts of the United States. National Hurricane Res. Proj. Rep. No. 33, U.S. Weather Bureau and Army Corps. of Engineers, Washington, DC.

GRASSL, H. (1993). Globaler Wandel. In: Schellhuber, H. J., und Sterr, H. (Hg.): Klimaänderung und Küste. Einblick ins Treibhaus. S. 28–37. Berlin.

GRASSL, H., (1998). Nur aus Forschung zum globalen Wandel folgt Nachhaltigkeit. In. Geographische Rundschau, 5, 268–272.

GRASSL, H., and R. KLINGHOLZ, (1990). Wir Klimamacher – Auswege aus dem globalen Treibhaus. 296 S. Frankfurt/Main.

GRAY M., M. B. DANARD, R. A. FLATHER, R. F. HENRY, T. S. MURTY, S. VENKATESH, and C. JARVIS, (1984). A preliminary investigation using a Nova Scotia Storm surge prediction model, Atmosphere Ocean, 22, No. 2, 207–225.

GRAY, W. M., (1975). Tropical Cyclone Genesis. Atmos. Sci. Paper 234, Colorado State University, Fort Collins, and Colorado.

GRAY, W. M., (1978a). Hurricanes: their formation, structure and likely role in the tropical circulation, p. 155–218. In D. B. Shaw [ed.] Meteorology over the tropical oceans. Royal Meteorol. Soc., Bracknell, U.K.

GRAY, W. M., (1978b). Tropical disturbance to cyclone transformation, p. 27–34. Proc. 11th Tech. Conf. Hurricanes Trop. Meteorol., Dec. 13–16, 1977, Miami Beach, FL. Am. Meteorol. Soc., Boston, MA.

GRAY, W. M., (1978c). Tropical cyclone motion and steering flow relationships in the western Atlantic and in the western Pacific, p. 472–477. Proc. 11th Tech. Conf. Hurricanes Trop. Meteorol., Dec. 13–16, 1977, Miami Beach, FL. Am. Meteorol. Soc., Boston, MA.

GRAY, W. M., (1978d). Cyclone intensity determination through upper troposphere reconnaissance, p. 288–293. Proc. I 11th Tech. Conf. Hurricanes Trop. Meteorol., Dec. 13–16, 1977, Miami Beach, FL. Am. Meteorol. Soc., Boston, MA.

GRAY, W. M., (1979). Hurricanes: their formation, structure and likely role in the tropical circulation. In: Meteorology over the Tropical Oceans, Shaw O. B. (ed), Royal Meteorological Society, London, pp. 155–218.

GRAY, W. M., (1984a). Atlantic seasonal hurricane frequency. Part I: El Nino and 30 mb QBO influences. Mon. Wea. Rev. 112, 1649–1668.

GRAY, W. M., (1984b). Atlantic seasonal hurricane frequency. Part II: Forecasting its variability. Mon. Wea. Rev., 112, 1669–1683.

GRAY, W. M., (1988). Environmental influences on Tropical cyclone, Aust. Met. Mag., 36, 127–129.

GRAY, W. M., (1989). Tropical cyclone formation, Invited paper presented at the International Workshop on Tropical Cyclones, Manila, Philippines, Proc. of 2nd WMO sponsored Workshop on Tropical cyclones, Issued by WMO, Nov. 25–Dec. 7, 95–121.

GRAY, W. M., C. W. LANDSEA, P. MIELKE, and K. BERRY, (1992). Predicting Atlantic seasonal hurricane activity 6–11 months in advance. Wea. and Forecasting 7, 440–455.

GRAY, W. M., C. W. LANDSEA, P. W. MIELKE, and K. J. BERRY, (1993). Predicting Atlantic basin seasonal tropical cyclone activity by 1 August. Wea. Forecasting, 8, 73–86.

GRAY, W. M., (1990). Strong association between West African rainfall and U. S. landfall of intense hurricanes. Science, 249, 1251–1256.

GRAY, W. G., (1982). Some inadequacies of finite element models as simulators of two-dimensional circulation. Adv. Water Resour., 5, 171–177.

GRAY, W. G., and D. R. LYNCH, (1977). Time-stepping schemes for finite element tidal model computations, Adv. Water Resour. 1, 83–95.

GRAY, W. G., and D. R. LYNCH, (1979). On the control of noise in finite element tidal computations: a semi-implicit approach. Comput. Fluids 7, 47–67.

GRAY, W. G., and G. F. PINDER, (1976). On the relationship between the finite element and finite difference methods. Int. J. Numer. Methods Eng. 10, 893–923.

GREENBERG, D. A., (1975). Mathematical studies of tidal behavior in the Bay of Fundy. Ph. D. thesis, University of Liverpool, Liverpool, U.K. 139 p.

GREENBERG, D. A., (1976). Mathematical description of the Bay of Fundy – Gulf of Maine numerical model. Tech. Note 16, Marine Environmental Data Service, Ottawa, Ont.

GREENBERG, D. A., (1977). Mathematical studies of tidal behavior in the Bay of Fundy. Rep. No. 46, Marine Sciences Directorate, Ottawa, Ont.

GREENBERG, D. A., (1979). A numerical model investigation of tidal phenomena in the Bay of Fundy and Gulf of Maine. Mar. Geod. 2, 161–187.

GREENSPAN, H. P., (1956). The generation of edge waves by moving pressure distributions. J. Fluid Mech. 1, 574–592.

GREENSPAN, H. P., (1970). A note on edge waves in a stratified fluid. Stud. Appl. Math. 49, 381–388.

GRIFFITHS, J. F., (1972). Climates of Africa, p. 80–481. World survey of climatology. Vol. 10. Elsevier Scientific Publishing Company, Amsterdam, Netherlands.

GRIMALDI, M., (1955). Disastrous cyclone damage at Genoa; causes of the breakwater failure examined, p. 117–121, Dock and Harbour Authority, Italy, Aug. 1955.

GROTKOP, G., (1973). Finite element analysis of long period water waves. Comput. Methods Appl. Mech. Eng. 2, 147–157.

GROVER, J. C., (1967). Storm surge effects in the Solomon Islands, p. 43–46. Proc. Symp. Tsunamis Storm Surges, Aug. 25–26, 1996. Committee for the Pacific Science Congress, Tokyo, Japan.

GUNTHER, E. B., (1977). Eastern North Pacific tropical cyclones, 1976. Mar. Weather Log 21, 143–154.

GUNTHER, E. B., (1978). Eastern North Pacific tropical cyclones, 1977. Mar. Weather Log 22, 157–166.

GUNTHER, E. B., (1979). Eastern North Pacific tropical cyclones, 1978. Mar. Weather Log 23, 152–165.

GUPTA, AKHILESH, and A. MUTHUCHAMI, (1991). El-Nino and tropical storm tracks over Bay of Bengal during post-monsoon season, Mausam, 42, 3, 257–260.

HAARSMA, R. J., J. F. B. MITCHELL, and C. A. SENIOR, (1993). Tropical disturbances in a GCM. Clim. Dyn. 8 (5), 247–257.

HAIGHT, F. J., (1928). Unusual tidal movements in the Sulu Sea. Mil. Eng. 20, 471–475.

HALTINER, G. J., and F. L. MARTIN, (1957). Dynamical and Physical Meteorology, McGraw-Hill, New York, 470 pp.

HAMBLIN, P. F., (1976). Seiches, circulation and storm surges of an ice-free Lake Winnipeg. J. Fish Res. Board Can. 33, 2377–2391.

HAMBLIN, P. F., (1979). Great Lakes storm surge of April 6, 1979. J. Great Lakes Res. 5 (3–4), 312–315.

HAMBLIN, P. F., (1987). Meteorological Forcing and water level fluctuations on lake Erie, J. Of Great Lakes Research, 5, 312–315.

HAMILTON, R. A., and J. W. ARCHBOLD, (1945). Meteorology of Nigeria and adjacent territory. Q. J. Roy. Meteorol. Soc. 71, 231–262.

HANSEN, J., A. LACIS, D. RIND, G. RUSSELL, P. STONE, I. FUNG, R. RUEDY, and J. LERNER, (1984). Climate sensitivity: Analysis of feedback mechanisms. In climate processes and climate sensitivity, Maurice Ewing Series, 5, J. E. Hansen, and T. Takahasi (eds). American Geophysical Union, Washington, DC, pp. 130–163.

HANSEN, W., (1956). Theorie Zeer Errectiriung des Wasserstandes und de stromungen in Tandmeeren nebst Anwendungen. Tellus 8, 287–300.

HARPER, B. A., and R. J. SOBEY, (1983). Open boundary conditions for open coast hurricane storm-surge. Coastal Engg. 7. 41–60.

HARRIS, D. L., (1956). Some problems involved in the study of storm surges. Natl. Hurricane Res. Proj. Rep. No. 4.U.S. Weather Bureau, Washington, DC. 16 p.

HARRIS, D. L., (1958a). The hurricane surge, p. 96–114. In J.W. Johnson. Proc. 6th Coastal Eng. Conf., Dec.1957, Florida. Chap. 5 Council on Wave Research, The Engineering Foundation. Berkeley, CA.

HARRIS, D. L., (1958b). Hurricane Audrey storm tide. Natl. Hurricane Res. Proj. Rep. No. 23. U.S. Weather Bureau, Washington, DC. 15 p.

HARRIS, D. L., and C. P. JELESNIANSKI, (1964). Some problems involved in the numerical solutions of tidal hydraulic equations. Mon. Weather Rev. 92, 409–422.

HARRISON, E. J., (1973). Three-dimensional numerical simulations of tropical storms utilising nested fine grids. J. Atmos. Sci. 30, 1528–1543.

HARRISON, H. T., and W. K. ORENDORFF, (1941). Pre-frontal squall lines. United Airlines Meteorol. Circ. No. 16, 12 p.

HASSE, L., and V. WAGNER, (1971). On the relationship between geostrophic and surface wind at sea. Mon. Weather Rev. 99, 255–260.

HASTENRATH S., (1996). Climate dynamics of the tropics, Kluwer Academic Publishers, 508 pp. HASTINGS, P. A., (1990). Southern Oscillation influences on tropical cyclone activity in the Australian/Southwest Pacific region. Intl. J. Climatology, 10, 291–298.

HAUGUEL, A., (1978). A combined FE-BIE method for water waves. Pap. No. 115. Summ. 16th Int. Conf. Coastal Eng., Aug. 27–Sept. 3, 1978, Hamburg, W. Germany.

HAURWITZ, B., (1935). The height of tropical cyclones and the eye of the storm. Mon. Weather Rev. 63, 45–49.

HAURWITZ, B., and J. M. AUSTIN, (1944). Climatology. McGraw-Hill Publications, New York, NY. 410 p.

HAVNOE, K., A. KEJ, and W. SIEFERT, (1983). Mathematical Modelling of Water Levels and Flows in the Port of Hamburg. In: The Dock and Harbour Auth.

HAY, F. M., and J. LAING, (1954). The storm of January 31–February 1, 1953. Mar. Obs. 24(164), 87–91.

HAYDEN, B. P., (1981a). Secular variation in Atlantic coast extratropical cyclones. Mon. Weather Rev. 109, 159–167.

HAYDEN, B. P., (1981b). Cyclone occurrence mapping: equal area or raw frequencies? Mon. Weather Rev. 109, 168–172.

HAYAMI, S., K. YANO, S. ADACHI, and H. KUNISHI, (1955). Experimental studies on meteorological tsunamis travelling up the rivers and canals in Osaka City, p. 1–47. Bull. No. 9, Disaster Prevention Research Institute. Kyoto University, Kyoto, Japan.

HEAPS, N. S., (1965). Storm surges on a continental shelf. Philos. Trans. Roy. Soc. London Ser. A 257, 351–383.

HEAPS, N. S., (1967). Storm surges, Oceanography and Marine Biology. Annu. Rev. 5, 11–47.

HEAPS, N. S., (1969). A two dimensional numerical Sea model. Philos. Trans. Roy. Soc. London Ser. A. 275, 93–137.

HEAPS, N. S., (1972). On the numerical solution of the three dimensional hydrodynamical equations for the tides and storm surges. Mem. Soc. R. Sci. Lige Collect. Huit 2, 143–180.

HEAPS, N. S., (1973). Three-dimensional numerical model for the Irish Sea. Geophys. J. Roy. Astron. Soc., 35, 99–120.

HEAPS, N. S., (1974). Development of a three-dimensional numerical model of the Irish Sea. Rapp. P. V. Reun. Cons. Int. Explor. Mer. 167, 147–162.

HEAPS, N. S., (1975). Resonant tidal co oscillations in a narrow gulf. Arch. Meteorol. Geophys. Bioklimatol. Ser. A 24, 361–384.

HEAPS, N. S., (1976). On formulating a non – linear numerical model in three dimensions for tides and storm surges. , Computing methods in the applied sciences, Springer-Verlag 593, 368–387.

HEAPS, N. S., (1981). Three-dimensional model for tides and surges with vertical eddy viscosity prescribed in two layers – I. Mathematical formulation. Geophys. J. Roy. Astr. Soc. 64, 291–302.

HEAPS, N. S., (1983). Storm surges, 1967–1982, Geophys. J. Roy. Astr, Soc., 74, 331–376.

HEAPS, N. S., and J. E. JONES, (1975). Storm surge computations for the Irish Sea using a three-dimensional numerical model. Mem. Soc. R. Sci. Liège Collect. Huit 6, 289–333.

HEAPS, N. S., and J. E. JONES, (1979). Recent storm surges in the Irish Sea, p. 285–319. In J. C. J. Nihoul [ed.] Marine Forecasting. Proc. 10th Liège Colloq. Ocean Hydrodyn. Elsevier Oceanographic Series No. 25, Amsterdam, Netherlands.

HEAPS, N. S., and J. E. JONES, (1981). Three-dimensional model for tides and surges with vertical eddy viscosity prescribed in two layers. II. Irish Sea with bed friction layer. Geophys. J. R. Astron. Soc. 64, 303–320.

HEATH, R. A., (1979). Significance of storm surges on the New Zealand coast. N. Z. J. Geol. Geophys. 22, 259–266.

HEBERT, P. J., (1979). Empirical techniques, p. 11.3.111.3.20. Operational techniques for forecasting tropical cyclone intensity and movement. Chap. 3. WMO No. 528, Geneva, Switzerland.

HEFFERMAN, R. F., (1972). Hurricane heat potential of the North Atlantic and North Pacific oceans. M.Sc. thesis, Naval Post Graduate School, Monterey, CA.

HELLand, A., (1911). Norges land og folk, Romsdals Amt., Kristiania, Norway.

HELMHOLTZ, H., (1888). Über atmosphärische Bewegungen, I. Akad. Ber., Berlin.

HELMHOLTZ, H., (1889). Über atmosphärische Bewegungen, II. Akad. Ber., Berlin.

HENDERSHOTT, M. C., (1981). Long waves and ocean tides. Evolution of physical oceanography, B. A. Warren, and C. Wunsch, eds., MIT Press, Cambridge, Mass., 292–346.

HENNING, D., (1962). Computation of a storm surge in the Baltic Sea, p. 257–263. Proc. Symp. Math. Hydrodyn. Methods. Physical Oceanography, University of Hamburg, Hamburg, W. Germany.

HENRY, R. F., (1975). Storm surges. Tech. Rep. No. 19, Beaufort Sea Project. Department of the Environment. Victoria, B. C. 41 p.

HENRY, R. F., (1982). Automated programming of explicit shallow-water models. Part I. Linearized models with linear or quadratic friction. Pac. Mar. Sci. Rep. 3, Dec. 1981. Institute of Ocean Sciences, Department of Fisheries and Oceans, Victoria, B. C. 70 p.

HENRY R. F., D. S. DUNCALF, R. A. WALTERS, M. J. OSBORNE, and T. S. MURTY, (1997). A study of tides and storm surges in offshore waters of the Meghna estuary using a finite element model, Mausam 48 (4), 519–530.

HENRY, R. F., and N. S. HEAPS, (1976). Storm surges in the southern Beaufort Sea. J. Fish. Res. Board Can. 33, 2362–2376.

HENRY, R. F., and T. S. MURTY, (1982). Tides in the Bay of Bengal. Proc. Int. Conf. Comput. Methods Exp. Meas, (Editors: G. A. Keramidas, and C. A. Brebbia), June 30–July 2, 1982, Washington, DC., Springer Verlag, New York, p. 541–550.

HINSMAN, D. E., (1977). Preliminary results from the Fleet Numerical Weather Central tropical cyclone model. Proc. 3rd Conf. Numer. Weather Predict., Omaha, NB.

HOBBS, P. V., (1981). The Seattle Workshop on extratropical cyclones: a call for a national cyclone project. Bull. Am. Meteorol. Soc. 62, 244–254.

HOFSTEDE, J. L. A., (1991). Sea level rise in the inner German Bight (Germany) since AD600 and its implications upon tidal flats geomorphology, In the „Von der Nordsee bis zum Indischen Ozean", S. 11–27.

HOLLAND, G. J., (1980). An analytical model of the wind and pressure profiles in hurricanes. Mon. Wea. Rev. 108, 1212–1218.

HOLLAND, G. J., (1981). Comments on – The numerical modelling of storm surges in the Bay of Bengal, by B. Johns, and M. A. Ali. 1980. Q. J. Roy. Meteorol. Soc. 106, 1–18. Q. J. Roy. Meteorol. Soc. 107, 268–270.

HOLLIDAY, C. R., and A. H. THOMPSON, (1979). Climatological characteristics of rapidly intensifying typhoons. Mon. Weather Rev. 107, 1022–1034.

HONSYU, K., (1932). Statistical investigation on the effect of winds and air pressure on the height of sea level at some tidal stations in Japan. Geophys. Mag. 6, 123–145.

HOOVER, R. A., (1957). Empirical relationships of the central pressures in hurricanes to the maximum surge and storm tide. Mon. Weather Rev. 85, 167–174.

HOOZEMANS, F. M. J., M. MARCHAND, and H. A. PENNEKAMP, (1993). A global vulnerability analysis: Vulnerability assessment for population, coastal wetlands and rice production on a global scale, 2nd ed. Delft Hydraulics and Ministry of Transport, Public Works and Water Management, Delft and The Hague, The Netherlands.

HOPLEY, D., and N. HARVEY, (1979). Regional variation in the storm surge characterizations around the Australian coast: a preliminary investigation. Proc. Conf. Nat. disasters Australia . Australian Academy of Science, p. 164–185, Canberra Australia.

HOSKINS, J., and P. J. VALDES, (1990). On the existence of storm tracks. In: Journal of Atmospheric Sciences 47, 1854–1864.

HOUSTON, J. R., (1978). Interaction of tsunamis with the Hawaii Islands calculated by a finite element numerical model. J. Phys. Oceanogr. 8, 93–102.

HOUZE, R. A., (1977). Structure and dynamics of a tropical squall line system. Mon. Weather Rev. 105, 1540–1567.

HOVERMALE, J. B., and R. E. LIVIZEY, (1978). Three-year performance characteristics of the NNIC hurricane model, p. 122–125. Proc. 11th Tech. Conf. Hurricanes Trop. Meteorol., Dec. 13–16, 1977, Miami Beach, FL. American Meteorological Society, Boston, MA.

HUBBERT, G. D., G. J. HOLLAND, L. M. LESLIE, and M. J. MANTON, (1991). A real-time system for forecasting tropical cyclone storm surges. Wea. Forecasting, 6, 86–97.

HUBBERT, G. D., L. M. LESLIE, and M. J. MANTON, (1990). A storm surge model for the Australian region. Quart. J. Roy. Met. Soc. 116, 1005–1020.

HUBBERT, G. D., and K. L. MCINNES, (1999). A storm surge inundation model for coastal planning and impact studies. Journal of Coastal Research, 15, 168–185.

HUBBERT, L. F., and G. B. CLARK, (1955). The hurricane surge. Interim Rep., June 1955. U. S. Weather Bureau. Washington, DC. 34 p.

HUBERTZ, J. M., (1985). Modeling of near shore wave driven currents. Proc, 19th Int. Conf. Coast. Engg. Houston, 2208–2219.

HUGHES, L. A., (1965). The prediction of surges in the southern basin of Lake Michigan. Part III. The operational basis for prediction. Mon. Weather Rev. 93, 292–296.

HUEBNER, K. H., (1974). Finite element method – stress analysis and much, much more. Mach. Des. 46, 92–103.

HUNT, I. A., (1959). Winds, wind set-ups and seiches on Lake Erie. Res. Rep. Nos. 1 and 2, January 1959. U. S. Lake Survey, Detroit, MI. 59 p.

HUNT, R. D., (1972). North Sea storm surges. Mar. Obs. 42, 115–124.

IHP-OHP, W. SIEFERT, (1987). On Tides and Storm Surges – Theory, Practice, Instruments. Koblenz. (IHP/OHP-Berichte, Sonderheft 3, 312 S.).

IHP-OHP, W. SIEFERT, and T. S. MURTY, (1991). Storm Surges, River Flow and Combined Effects. Koblenz. (IHP/OHP-Berichte, Sonderheft 4, 151 S.).

IMAMURA F., and D. V. TO, (1997). Flood and typhoon disasters in Vietnam in the half-century since 1950, Natural Hazards, 15, No. 1, 71–87.

IPCC, (1995). Climate Change. J. T. Houghton, G. J. Jenkins, and J. J. Ephruams, (HG.) S. 2–64. Cambridge, University Press.

IPCC, (1996). Climate Change 1995; Impacts, adaptations and imaginations of climate change: Scientific-Technical Analysis (Editors: R. T. Watson, M. C. Zinyowera, and R. H. Moss), Cambridge University Press, 876 pp.

IRISH, S. M., (1965). The prediction of surges in the southern basin of Lake Michigan. Part II. A case study of the surge of August 3, 1960. Mon. Weather Rev. 93, 282–291.

IRISH, S. M., and G. W. PLATZMAN, (1961). An investigation of the meteorological conditions associated with extreme wind tides on Lake Erie. U.S. Weather Bur. Tech. Rep. No. 4. Department of Meteorology, University of Chicago, May 1961. 35 p.

ISHIGURO, S., (1976a). Pressure-generated surges in the North Sea. Rep. No. 35. Institute of Oceanographic Sciences, Wormley, U.K. 26 p.

ISHIGURO, S., (1976b). Highest surge in the North Sea. Rep. No. 36. Institute of Oceanographic Services, Wormley, U.K. 31 p.

ISLAM, M. A., (1971). Human adjustment to cyclone hazards: a case study of Char Jabbar. Working paper No. 18. Department of Geography, University of Dacca, Dacca, Bangladesh. 34 p.

ISOZAKI, I., (1970a). An investigation on the variations of sea level due to meteorological disturbances on the coast of the Japanese Islands. 5. Storm surges on the coast of the Kanto and Tokai districts. Pap. Meteorol. Geophys. 21, 1–32.

ISOZAKI, I., (1970b). An investigation on the variations of sea level due to meteorological disturbances on the coast of the Japanese Islands. 6. Storm surges on the coasts of the Inland Sea and Osaka Bay. Pap. Meteorol. Geophys. 21, 291–322.

ISOZAKI, I., (1970c). An investigation of the variations of sea level due to meteorological disturbances on the coast of the Japanese Islands. 7. Storm surges on the coast of West Japan facing the Pacific and the East China Sea. Pap. Meteorol. Geophys. 21, 421–448.

ITO, T., M. HIRONO, J. WATANABE, and K. HINO, (1965). Numerical Prediction on typhoon tide in Tokyo Bay, p. 686–712. Chap. 43. Proc. 9th Conf. Coastal Eng., June 1964, Lisbon. ASCE, New York, NY.

JAMART, B. M., and D. F. WINTER, (1978). A new approach to the computation of tidal motions in estuaries, p. 261–282. In J. C. J. Nihoul [ed.] Hydrodynamics of estuaries and fjords. Elsevier Oceanography Series No. 23, Amsterdam, The Netherlands.

JAMART, B. M., and D. F. WINTER, (1979). Finite element computation of the barotropic tides in Night Inlet, B.C., p. 283–290. In H. J. Freeland, D. M. Farmer, and C. D. Levings [ed.] Fjord oceanography. Plenum Press, New York, NY. 715 p.

JAMISON, M. V., (1956). Typhoon research and forecasting methods in the 1st weather wing, United States Air Force, p. 97–102. Proc. Trop. Cyclone Symp., December 1956, Brisbane. Bureau of Meteorology, Melbourne, Australia.

JANARDAN, S., (1967). Storm-induced sea level changes at Saugar Island situated in the North Bay of Bengal. Indian J. Meteorol. Geophys. 18, 205–212.

JANJIC, Z. I., (1974). A stable centered difference scheme free of two-grid interval noise. Mon. Weather Rev. 102, 319–323.

JANSA, A., (1986). Marine response to mesoscale-meteorological disturbances: The June 21, 1984, event in Ciutadella (Menorca) (in Spanish), Rev. Meteorol, 7, 5–29.

JANSSEN, P. A. E. M., (1991). Quasi-linear theory of wind wave generation applied to wave forecasting. J. Phys. Oceanogr. 21, 1631–1642.

JARREL, J. D., J. K. LEWIS, and R. E. WHITACKER, (1982). Bay of Bengal – A system to evaluate storm surge threat, Final Report Contract. A. I. D, S. O. D. and P. D. C-C-0294, Science Application Inc., Monterey, California, 66 pp.

JELESNIANSKI C. P., (1965). A numerical calculation of storm tides induced by a tropical storm impinging on a continental shelf. Month. Wea. Rev., 93, 343–358.

JELESNIANSKI, C. P., (1966). Numerical computations of storm surges without bottom stress. Mon. Weather Rev. 94, 379–394.

JELESNIANSKI, C. P., (1967). Numerical computations of storm surges with bottom stress. Mon. Weather Rev. 95, 740–756.

JELESNIANSKI, C. P., (1970). Bottom stress time history in linearized equations of motion for storm surges. Mon. Weather Rev. 98, 462–478.

JELESNIANSKI, C. P., (1972). SPLASH I: Landfall storms, NOAA tech. Memo., NWS TDL – 46, Washington D. C., 52 pp.

JELESNIANSKI, C. P., (1974). SPLASH (Special Program to List Amplitudes of Surges from Hurricanes) II. General track and variant storm conditions. NOAA Tech. Mem.NWS-TDL-52. NOAA, Washington, DC. 50 p.

JELESNIANSKI, C. P., (1976). A sheared coordinate system for the storm surge equations of motion with a mildly curved coast. NOAA Tech. Mem. NWS-TDL-61. NOAA, Washington. DC. 52 p.

JELESNIANSKI, C. P., (1989). Storm-surge and sea-state. Topic 5.2, Second International Workshop on Tropical Cyclones, Manila December 1989. WMO/TD-No. 319, WMO, Geneva, Switzerland, 277–293.

JELESNIANSKI, C. P., and C. S. BARRIENTOS, (1975). A preliminary view of storm surges before and after storm modifications for alongshore moving storms. Techniques Development Lab., NWS-TDL-58. National Weather Service. Silver Spring. MD. 16 p.

JELESNIANSKI, C. P., and J. CHEN, (1979). SLOSH (Sea, Lake and Overland Surges from Hurricanes). Report of Techniques Development Laboratory, National Weather Service, Silver Spring, MD., 16 p.

JELESNIANSKI C. P., J. CHEN, and W. A. SHAFFER, (1992). SLOSH: Sea, Lake and Overland Surges from Hurricanes, NOAA Technical Report NWS 48, April 1992, 71 p.

JELESNIANSKI C. P., and A. D. TAYLOR, (1973). A preliminary view of storm surges before and after storm modification. NOAA Technical Memorandum ERL WMPO-3, pp. 33.

JELGERSMA, S., M. J. F. STIVE, and L. VAN DER VALK, (1995). Holocene storm surge signatures in the coastal dunes of the western Netherlands, Marine Geology, 125, 95–110.

JENSEN, J. (1985). Über instationäre Entwicklungen von Wasserständen an der deutschen Nordseeküste. In: Mitteilungen des Leichtweiss-Institutes für Wasserbau der Technischen Universität Braunschweig, 88, S. 141–320.

JENSEN, J., (1987). Überlegungen zur künftigen Entwicklung der Sturmflutwasserstände an der Nordseeküste. In: Mitteilungsblatt der Bundesanstalt für Wasserbau, 60, S. 235–255.

JENSEN, J. (1999). Criteria to calculate storm surge level for North Sea gauges. Personal Communication, (unpublished).

JIN-CHUAN, C., and C. GUANG, (1979). A dynamic model for hourly predictions of typhoon surges along the southeastern coast of China. Contribution (October 1979) of the Department of Oceanography, Amoy University, Fujian, China. 24 p.

JINQUAN, CHEN, SHAOPING SHANG, KE LIN, and HONGJIN ZHANG, (1990). A two dimensional numerical model for predicting total water elevation in tidal rivers or bays, In: storm Surges Observation and Modelling (edited by Chao Jiping, T. S. Murty, Bao Cheanglan, M. I. El- Sabh, and Liu Fengshu, China Ocean Press, 163–172.

JIPING, C., T. S. MURTHY, B. CHENGLAN, M. I. EL-SABH, and L. FENGSHU, (1990). Storm Surges: Observations and Modelling. China Ocean Press, 326 pp.

JOHANSEN, S., (1959). On the effect of meteorological conditions upon the height of the sea level at the coast of southern Norway. Meteorol. Arm., 4 (14). Det Norske Meteorologiske Institut, Norway.

JOHNS, B., (1978). The modelling of tidal flow in a channel using a turbulence energy closure scheme. J. Phys. Oceanogr. 8, 1042–1049.

JOHNS, B., (1981). Numerical simulation of storm surges in the Bay of Bengal. In "Monsoon Dynamics" (Ed. M. J. Lighthill, and R. P. Pearce), Cambridge University Press, pp. 690–705.

JOHNS, B., and A. ALI, (1980). The numerical modelling of storm surges in the Bay of Bengal. Q. J. R. Meteorol. Soc. 106, 1–18.

JOHNS, B., and A. ALI, (1981). Reply to J. Holland comment on paper by B. Johns, and M. A. Ali "The numerical modelling of storm surges in the Bay of Bengal." Q. J. Roy. Meteorol. Soc. 107, 271–272.

JOHNS, B., S. K. DUBE, U. C. MOHANTY, and P. C. SINHA, (1981). Numerical simulation of the surge generated by the 1977 Andhra cyclone. Q. J. Roy. Meteorol. Soc. 107, 919–934.

JOHNS, B., S. K. DUBE, P. C. SINHA, U. C. MOHANTY, and A. D. RAO, (1982). The simulation of continuously deforming lateral boundary in problems involving the shallow water equations. Comp. Fluids, 10, 105–116.

JOHNS, B., and J. LIGHTHILL, (1993). Modelling of storm surges in the Bay of Bengal. In: Tropical cyclone Disasters (edited by James Lighthill, Greg Holland, Zheng Zhemin, and Kerry Emanuel), Peking University Press, China, 410–422.

JOHNS, B., A. D. RAO, S. K. DUBE, and P. C. SINHA, (1985). Numerical Modelling of the tide surge interaction in the Bay of Bengal. Phil. Trans. Roy. Soc. London, A 313, 507–535.

JOHNS, B., P. C. SINHA, S. K. DUBE, U. C. MOHANTY, and A. D. RAO, (1983a). Simulation of storm surges using a three-dimensional numerical model: an application to the 1977 Andhra Cyclone. Quart. J. Roy. Met. Soc., 109, 211–224.

JOHNS, B., P. C. SINHA, S. K. DUBE, U. C. MOHANTY, and A. D. RAO, (1983b). On the effect of bathymetry in numerical storm surge simulation experiments. Computers and Fluids 11, 161–174.

JOHNSON, H. K., and H. J. VESTED, (1992). Effects of water waves on wind shear stress for current modelling. J. Atmospheric Oceanic Technol., 9, 850–861.

JONES, J. E., and A. M. DAVIES, (1998). Storm surge computations for the Irish Sea using a three dimensional numerical model including wave – current interaction. Cont. shelf. Res. 18., 201–251.

JOINT TYPHOON WARNING CENTER, (1978). Western North Pacific typhoons 1977. Mar. Weather Log 22, 237–254.

JOINT TYPHOON WARNING CENTER, (1979). Western North Pacific typhoons 1978. Mar. Weather Log 23, 306–319.

JOINT TYPHOON WARNING CENTER, (1981). Western North Pacific typhoons 1981. Mar. Weather Log 25, 237–252.

JOSEPH, P. V., (1976). Symposium "Tropical monsoons" Indian Institute of Tropical Meteorology, Pune, India, 257–260.

JOSEPH, P. V., (1981). Ocean atmosphere interaction on seasonal scale over north Indian ocean and Indian monsoon rainfall and cyclone tracks. Mausam, 32, 237–246.

KAHLFELD, A., (1999). Numerische Seegangsmodellierung als Bestandteil einer funktionellen Hafenplanung. Dissertation. Institut für Strömungsmechanik und Elektronisches Rechnen im Bauwesen der Universität Hannover, Berichte, 58.

KAJIURA, K., (1959). A theoretical and empirical study of storm induced water level anomalies. Tech. Rep.59–23F. Department of Oceanography and Meteorology, Texas A&M University, College Station, TX. 97 p.

KAWABATA, Y.,and M. FUJITO, (1951). Elevation of the sea surface caused by typhoons. J. Meteorol. Soc. Jpn. W.N.D. Ser. 29, 37–43.

KAWAHARA, M., K. HASEGAWA, and Y. KAWANAGO, (1977). Periodic tidal flow analysis by finite element perturbation method. Comput. Fluids 5, 175–189.

KAWAHARA. M, M. KOBAYASHI, and K. NAKATA, (1982). A three-dimensional multiple level finite element method considering variable water density, Chapter 7 in "Finite Elements in Fluids", 4, (edited by R. H. Gallagher, D. H. Norrie, J. T. Oden, and O. C. Zienkiewicz), John Wiley and Sons. Inc., New York.

KAWAHARA, M., M. KOBAYASHI, and M. NAKATA, (1983). Multiple level finite element analysis and its applications to tidal current flow in Tokyo Bay, Applied Mathematical Modeling, Vol. 7, 215–233.

KAWAHARA, M., S. NAKAZAWA, S. OHMORI, and T. TAGAKI, (1980). Two-step explicit finite element method for storm surge propagation analysis. Int. J. Numer. Methods Eng. 15, 1129–1148.

KENTANG LE, (2000). An analysis of recent severe storm surge disaster events in China, Natural Hazards, vol. 20, in press.

KEULEGAN, G. H., (1951). Wind tides in small enclosed channels. J. Res. U.S. Nat. Bur. Stand. 46, 358–381.

KEULEGAN, G. H., (1953). Hydrodynamic effects of gales on Lake Erie. J. Res. U.S. Nat. Bur. Stand. 50, 99–109.

KIBRIA, A. M. M., (1980). Protection of Bangladesh against cyclone generated surges, p. 759–769. In P. Karasudhi, A. S. Balsubramanyam, and W. Karokm Ikalchou [ed.] Engineering for protection from natural disasters. John Wiley & Sons Ltd., Chichester, U.K.

KINNMARK, I. P. E., (1984). The shallow water wave equations: formulations, analysis and application, Ph. D. dissertation, Princeton University, Princeton, N. J.

KITAIGORODSKII, S. A., (1973). The physics of air-sea interaction. Israel Program for scientific Translations.

KITAIGORODSKII, S. A., and Y. A. VOLKOV, (1965). On the roughness parameter of the sea surface and the calculation of momentum flux in the lower layer of the atmosphere. Izv. Atmospheric Oc. Phys. 1, 973–978.

KIVISILD, H. R., (1954). Wind effects on shallow bodies of water with special reference to Lake Okeechobee. UDC 551. 481. 115. 551.556, Goteborg, Elanders Boktryckeri Aktiebolag.

KLEIN, W. H., (1957). Principal tracks and mean frequencies of cyclones and anticyclones in the Northern Hemisphere. Res. Pap. No. 40. U.S. Weather Bureau, Washington, DC. 22 p. + 72 charts.

KLEINSTREUER, C., and J. T. HOLDEMAN, (1980). A triangular finite element mesh generator for fluid dynamic systems of arbitrary geometry. Int. J. Num. Methods Eng. 15, 1325–1334.

KLEVANNY, K. A., (1994). Simulation on storm surges in the Baltic Sea using an integrated modelling system Cardinal. In: Proceedings of teh 19th Conference Baltic Oceanography (1), pp. 328–336.

KOLAR, R. L., W. J. GRAY, J. J. WESTERINK, and R. A. LUETTICH, (1994). Shallow water modeling in spherical coordinates: Equation formulation, numerical implementation, and application, J. Hydraulic. Res. 32, 3–24.

KOLAR, R. L., J. J. WESTERINK, M. E. CATEKIN, and C. A. BLAIN, (1994). Aspects of non-linear simulation using shallow-water models based on the wave continuity equation, Comput. Fluids, 23, 523–538.

KONDO, H., K. SAITO, Y. MAMIYA, and M. HARA, (1982). On the conservation of the energy of low-frequency waves in iterative time integration schemes. J. Meteorol. Soc. Jpn. 60, 824–829.

KOOPMANN, G., (1962). Wasserstandserhöhungen in der Deutschen Bucht infolge von Schwingungen und Schwallerscheinungen und deren Bedeutung bei der Sturmflut vom 16.–17. February 1962. In: Deutsche Hydrographische Zeitschrift 15-5, S. 181–198.

KOOPMAN, G., (1963). Schwallerscheinungenam October 16–17, 1963, in der Deutschen Bucht. Dtsch. Hydrogr. Z. 16, 231.

KOTESWARAM, P., and S. GASPER, (1956). The surface structure of tropical cyclones in the Indian Area. Indian J. Meteorol. Geophys. 7, 339–352.

KOWALIK, Z., and I. POLYAKOV, (1998). Tides in the Sea of Okhotsk. In: Journal of Physical Ozeanography, (20)7, p.1389–1409.

KRAUSS, E. B., (1978). The response of a stratified viscous sea to moving meteorological fronts and squall lines. Dtsch. Hydrogr. Z. 31, 16–29.

KREUGER, D. W., (1959). A relation between the mass circulation through hurricanes and their intensity. Bull. Am. Meteorol. Soc. 40, 182–189.

KRÜGER, G., (1910). Über Sturmfluten an den Deutschen Küsten der westlichen Ostsee. XII. Jahresbericht der Geogrges. Greifswald.

KUMAR, A., K. MURALI, and R. MAHADEVAN, (1995). Finite element simulation of storm surges along the east coast of India. Proc. Of the Third Seminars on Port and Inland Waterways, Goa, India, November 13–18, 1995, 55–65.

KUNZ, H., (1993). Impact of sea level changes on shoreline protection strategies of the German North Sea Coast, of the International Workshop on Sea level changes and their consequences for Hydrology and Water Management, 19–23 April 1993, Noordwijkerhout, Netherlands, pp. 39–48.

KUO, H. L., (1949). Dynamic instability of twodimensional nondivergent flow in a barotropic atmosphere. J. Meteorol. 6, 105–122.

KUO, H. L., (1965). On the formation and intensification of tropical cyclones through latent heat release by cumulus convection. J. Atmos. Sci. 22, 40–63.

KURATORIUM FÜR FORSCHUNG IM KÜSTENINGENIEURWESEN (Ed.) (1993). EAK. Empfehlungen für die Ausführung von Küstenschutzwerken durch den Ausschuß für Küstenschutzwerke der deutschen Gesellschaft für Erd- und Grundbau e.V. und der Hafenbautechnischen Gesellschaft e.V. (= Die Küste, H. 55).

KURIHARA, Y., (1965). On the use of implicit and iterative methods for the time integration of the wave equation. Mon. Weather Rev. 93, 33–46.

KURIHARA, Y., and R. E. TULEYA, (1974). Structure of a tropical cyclone developed in a three dimensional numerical simulation model. J. Atmos. Sci. 31, 893–919.

KUSSMAN, A. S., (1957). The storm surge problem in New York City, p. 751–763. Proceedings of the New York Academy of Science, Section of Oceanography and Meteorology, New York, NY.

LABITZKE, K., and H. VAN LOON, (1988/1989). Associations between the 11-year solar cycle, the QBO and the Atmosphere. In: Journal of Climate, Part I–III.

LACOUR, D., (1917a). Conditions anormales du niveau de la mer dans les eaux danoises les 15 et 16 janvier 1916, p. 30–117. Annales de la Commission des Raz-de-Maree. Publikationer fra det danske meteorologiske Institut Middelelser, Nr 4. Copenhagen, Denmark.

LACOUR, D., (1917b). Sur la variation du niveau rnoyen de la mer A Brest (France) en function de la pression atmospherique, p. 22–34. Annales de la Commission des Raz-de-Maree. Publikationer fra det danske meteorologiske Institut Middelelser, Nr 4. Copenhagen, Denmark.

LACOUR, D., (1917c). Raz de Maree aux Pays-Bas et leurs previsions, p. 116–129. Annales de la Commission des Raz-de-Maree. Publikationer fra det danske meteorologiske Institut Meddelelser. Nr 4. Copenhagen, Denmark.

LACOUR, D., (1932). Conditions anormales du niveau de la mer dans les lava danoises les 15 et 16 janvier 1916. Ann. Comm. Raz-de-Marde 2, 30–117.

LACOUR, D., (1935). Madagascar: note sur les mares et courants cotiers produits apr les cyclones tropicaux. Ann. Comm. Raz-de-Maree 5, 67–89.

LAJOIE, F. A., and N. NICHOLLS, (1974). A relationship between the direction of movement of tropical cyclones and the structure of their cloud systems. Tech. Rep. No. I. Bureau of Meteorology, Australia, 1, 22 p.

LAM, D. C. L., (1977). Comparison of finite element and finite difference methods for near shore advection-diffusion transport models, p. 115–129. In W. G. Gray, G. F. Pinder, and C. A. Brebbia [ed.] Finite elements in water resources. Pentech Press, London, U.K.

LAMB, H., (1945). Hydrodynamics. Dover, New York. 738 p.

LAMB, H., (1991). Historic Storms of the North Sea, British Isles and Nortwest Europe. Cambridge.

LAMBERT, S. J., (1995). The effect of enhanced green house warming on winter cyclone frequencies and strength, J. of Climate, vol. 8, 1447–1452.

LANDER, M. A., (1994). An exploratory analysis of the relationship between tropical storm formation in the Western North Pacific and ENSO. Mon. Wea. Rev. 122, 636–651.

LANDSEA, C. W., N. NICHOLLS, W. M. GRAY, and L. A. AVILA, (1996). Downward Trend in the Frequency of Intense Atlantic Hurricanes during past five decades, Geophysical Research Letters, 213, 1697–1700.

LANG, G., (1999). The Mathematical Models of the Federal Waterways Engineering and Research Institute. Internet http://www/hnm/hnm-en.htm.

LANGHAAR, H. L., (1951). Wind tide in inland waters p. 278–296. Proc. 1st Mid-winter Conf. Fluid Dyn. J. W. Edwards and Co., Ann Arbor, MI.

LAPPO, S. S., and A. Y. ROZHDESTVENSKIY, (1977). An estimate of the energy transferred to the ocean by a moving atmospheric pressure disturbance. Atmos. Oceanic Phys. 13, 120–124.

LAPPO, S. S., and A. Y. ROZHDESTVENSKIY, (1979). Calculation of the energy transferred by the atmosphere to a meteorological ocean tide. Atmos. Oceanic Phys. 15, 907–911.

LAU, R., (1980a). Storm surge investigations and the use of vertical by integrated hydrodynamical models. Tech. Note No. 53, Jan. 1980. Royal Observatory, Hong Kong. 42 p.

LAU, R., (1980b). Evaluating peak storm surge heights and high sea levels from SPLASH outputs. Tech. Note No. 54, Feb. 1980. Royal Observatory, Hong Kong. 30 p.

LAUWERIER, H. A., (1962). Some recent work of the Amsterdam Mathematical Center on the hydrodynamics of the North Sea, p. 13–24. Proc. Symp. Math. Hydrodyn. Math Phys. Ocean. University of Hamburg, Hamburg, W. Germany.

LAX, P., and R. RICHTMEYER, (1956). Survey of the stability of linear finite difference equations. Commun. Pure Appl. Math. 9, 267–293.

LAX, P. D., and B. WENDROFF, (1960). Systems of conservation laws. Commun. Pure Appl. Math. 13, 217–237.

LEATHERMAN, S. P., (1986). Coastal geomorphic impacts of sea level rise on coasts of South America, In the Effects of changes in stratospheric ozone and Global climate (Edited by James G. Titus), Sea Level Rise, UNEP, EPA, vol. 4, 73–82.

LEBLOND, P. H., and L. A. MYSAK, (1978). Waves in the ocean. Elsevier Oceanography Series 20, Amsterdam, The Netherlands. 602 p.

LEENDERTSE, J. J., (1967). Aspects of a computational model for long-period water wave propagation. RM – 5294 – PR, May 1967. The Rand Corporation, Santa Monica, CA.

LEENDERTSE, J. J., (1970). A water quality simulation model for well mixed estuaries and coastal seas. Vol. 1. Principles of computation. RM 6230-RC, Feb. 1970. The Rand Corporation, Santa Monica, CA.

LEENDERTSE, J. J., and E. C. GRITTON, (1971). A water quality simulation model for well mixed estuaries and coastal seas. Vol. II. Principles of computation. RM-6230-RC. The Rand Corporation. New York. R-708-NJC.

LEIMKUHLER, W., J. J. CONNOR, J. WANG, G. CHRISTODOWLOW, and S. SUNDGREN, (1975). Two dimensional finite element dispersion model, p. 1467–1486. Proc. Symp. Model. Tech. Volume 11. Sept. 3–5, 1975, San Francisco, CA. ASCE, New York, NY.

LEIPPER, D. F., and J. JENSEN, (1971). Changes in energy input from the sea into hurricanes. Bull. Am. Meteorol. Soc. 52, 9–28.

LEIPPER, D. F., and D. VOLGENAU, (1972). Hurricane heat potential of the Gulf of Mexico. J. Phys. Oceanogr. 2, 218–224.

LEITH, C. E., (1965). Numerical simulation of the earth's atmosphere. Math. Comp. Phys. 4, 1–28.

LEMON, D. D., (1975). Seiche excitation in coastal bay travelling on the continental shelf, B. C. M. Sc. Thesis, Univ. of Br. C. Vancouver, Canada.

LENNON, G. W., (1963). The identification of weather conditions associated with the generation of major storm surges along the west coast of the British Isles. Q. J. Roy. Meteorol. Soc. 89, 381–394.

LE PROVOST, C., (1978). A new approach for tidal computations, p. 1104–1121, Summ. 16th Int. Conf.. Coastal Eng., Aug. 27–Sept. 3, 1978, Hamburg, W. Germany. Pap. No. 112.

LIGHTHILL, J., G. J. HOLLAND, W. M. GRAY, C. LANDSEA, K. EMANUEL, G. CRAIG, J. EVANS, Y. KUNIHARA, and C. P. GUARD, (1994). Global climate change and tropical cyclones. Bull. Am. Met. Soc., 75, 2147–2157.

LILLY, D. K., (1961). A proposed staggered grid system for numerical integration of dynamic equations. Commun. Pure Appl. Math. 9, 267–293.

LILLY, D. K., (1965). On the computational stability of numerical solutions of time-dependent nonlinear geophysical fluid dynamics problems. Mon. Weather Rev. 93, 11–26.

LILLY, D. K., (1979). The dynamical structure and evolution of thunderstorms and squall lines. Annu. Rev. Earth Planet. Sci. 7, 117–161.

LINDZEN, R. S., and K. K. TUNG, (1976). Banded convective activity and ducted gravity waves, Mon. Weather Rev., 104, 1602–1617.

LIU, S. K., and J. J. LEENDERTSE, (1979). A three-dimensional model for estuaries and coastal seas. Vol. VI. Bristol Bay simulations. R-2405-NOAA, Sept. 1979. The Rand Corporation, Santa Monica, CA. 121 p.

LONGUET-HIGGINS, M. S., and R. W. STEWART, (1964). Radiation stresses in water waves; a physical discussion, with applications. Deep-Sea Res., 11, 529–562.

LOVE, G., (1988). Cyclone storm surges: post greenhouse, In: Greenhouse Planning for Climate Change, Pearman G. I., (ed), E. J. Brill, Leiden Netherlands, pp. 202–215.

LÜDERS, K., (1974). Sturmtidenketten. In: Forschungsstelle für Insel und Küstenschutz der niedersächsischen Wasserwirtschaftsverwaltung, Jahresbericht 1973, XXV, 79–107.

LUDLAM, D. M., (1963). Early American hurricanes 1492–1870. American Meteorological Society, Boston, MA. 198 p.

LUETTICH, R. A., WESTERINK, J. J., and N. W. SCHEFFNER, (1991). ADCIRC: An advanced three-dimensional circulation model for shelves, coasts and estuaries: Report 1: Theory and methodology of ADCIRC-2DDI and ADCIRC-3DL. Coast. Engg. Res. Ctr., U. S. Army Engineer Waterways Experiment Station, Vicksburg, MS.

LUETTICH, R. A, J. J. WESTERINK, and N. W. SCHEFFNER, (1992). ADCIRC: An advanced three-dimensional circulation model for shelves, coasts and estuaries; Report 1: Theory and methodology of ADCIRC-2DDI and ADCIRC-3DL, Technical Report DRP Coastal Engineering Research Center, U. S. Army Engineer Waterways Experiment Station, Vicksburg, MS.

LUICK, J. L., R. F. HENRY, and T. S. MURTY, (1997). Storm surges in the Pacific Forum Region, In Recent advances in Marine Science and Technology-96, edited by N. K. Saxena, PACON International, Honolulu, 167–176.

LUNDBAK, A., (1956). The North Sea storm surge of February 1, 1953: its origin and development. Int. Hydrogr. Rev. 33, 185–196.

LUTGENS, F. K., TARBUCK, E. J. (1986). The Atmosphere. An Intorduction to Meteorology. Prentice-Hak, Englewood-Cliff, 492 p.

LWIN, T., (1980). Review of methods of storm surge prediction currently used in Burma, Report to the WMO Workshop on Storm Surges, November 10–15, 1980., Rangoon, Burma, 8 p.

LWIN, T., (1994a). Review of storm surge hindcasting techniques in Myanmar. Proceeding of the WMO Workshop on Storm Surges for the Bay of Bengal, November 14–19, 1994. Bangkok, Thailand. WMO/TD – No. 653, Report No. TCP-35, 1995.

LWIN, T., (1994 b). Empirical and statistical storm surge Forecasting Methods in Myanmar. Proceeding of the WMO Workshop on Storm Surges for the Bay of Bengal, November 14–19, 1994. Bangkok, Thailand. WMO/TD – No. 653, Report No. TCP-35, 1995.

LYDOLPH, P. E., (1977). Climates of the Soviet Union, p. 17–196. In World Survey of Climatology. Vol. 7. Elsevier Press, Amsterdam, The Netherlands.

LYNCH, D. R., (1980). Moving boundary numerical surge model. J. Waterway Port Coastal Ocean Div. Proc. 106 (WW3), 425–428.

LYNCH, D. R., and W. G. GRAY, (1978). Finite element simulation of shallow water problems with moving boundaries. Resource Policy Center, Thayer School of Engineering, Dartmouth College, Hanover, N.H., DSD No. 22 1. Reprinted from C. Brebbia, W. G. Gray, and G. F. Pinder [ed.] Finite elements in water resources II. Pentech Press Limited, Plymouth, U.K. 20 p.

LYNCH, D. R., and W. G. GRAY, (1979). A wave equation model for finite element tidal computation, Comput. Fluids, 7, 207–228 (1979).

LYNCH, D. R., and W. G. GRAY, (1980a). An explicit model for two-dimensional tidal circulation in triangular finite element elements. WAVETL User's Manual, U.S. Geological Survey, Water Resources Investigations 80–42, 63 p.

LYNCH, D. R., and W. G. GRAY, (1980b). Finite element simulation of flow in deforming regions. J. Comput. Phys. 36 (2), 135–153.

MAAT, N., C. KRAAN, and W. A. OOST, (1991). The roughness of wind waves. Boundary Layer Met., 54, 89–103.

MACKEY, G. W., and H. E. WHITTINGHAM, (1956). Sea and Swell in tropical cyclone, p. 413–431. Proc – Trop. Cyclone Symp. Dec. 1956, Brisbane. Bureau of Meteorology Melbourne, Australia.

MAI, S., K. F. DAEMRICH, and C. ZIMMERMANN, (1997). Wellentransformation an Sommerdeichen. In: Wasser und Boden, 9.

MALDE, J. VAN, (1996). Historical extraordinary water movements in the North Sea area. In: Mededelingen Rijks Geologischer Dienst, Nr. 57, pp. 27–40.

MALKUS, J. S., and H. RIEHL, (1960). On the dynamics and energy transformation in steady state hurricanes. Tellus 12, 1–20.

MALMQUIST, D. M., (1999). Meteorologists and Insurers explore extratropical transition of tropical cyclones, E. O. S. Feb. 16, 1999, 79–80.

MANABE, S., and A. J. BROCCOLIL, (1990). Can existing climate models be used to study anthropogenic changes in tropical cyclone climate? Geophys. Res. Let., 17, 1917–1920.

MANABE, S., and R. V. STOUFFER, (1980). Sensitivity of a global climate model to an increase of $CO_2$ concentration in the atmosphere. J. Geophys. Res. 85, 5529–5554.

MANDAL, G. S., (1989). Low frequency Oscillations and seasonal variability of Tropical cyclones-North Indian Ocean, Chairman report, International Workshop on Tropical Cyclone (IWTC), Manila, Philippines, November1989.

MARGULES, M., (1905). Über die Energie der Stürme. Jahrb. K. K. Zentralbl. Meteorol. W. Geodyn. (Wien). Bd. XL.

MARINOS, G., and J. W. WOODWARD, (1968). Estimation of hurricane surge hydrographs. J. Waterways Harbors Div. Proc. ASCE WW2, 189–216.

MARK, D. J., and N. W. SCHEFFNER, (1993). Validation of a continental-scale storm surge model for the coast of Delaware. 3rd International Conference on Estuarine and Coastal Modeling. Chicago, IL, 8–10 September 1993.

MARTINSEN, E. A., B. GIEVIK, and L. P. ROED, (1979). A numerical model for long barotropic waves and storm surges along the western coast of Norway. J. Phys. Oceanogr. 9, 1126–1138.

MASTENBROEK, C., (1992). The effect of waves on surges in the North Sea, Proc. 23rd Int. Conf. Coastal Engg., ASCE, 874–882.

MASTENBROEK, C., G. BURGERS, and P. A. E. M. JANSSEN, (1993). The dynamical coupling of a wave model and a storm surge model through the atmospheric boundray layer. J. Phys. Oceanography, 23, 1856–1866.

MATANO, H., and M. SEKIOKA, (1971a). On the synoptic structure of Typhoon Cora, 1969, as the compound system of tropical and extra-tropical cyclones. J. Meteorol. Soc. Jpn. 49, 282–295.

MATANO, H., and M. SEKIOKA, (1971b). Some aspects of the extra-tropical transformation of a tropical cyclone. J. Meteorol. Soc. Jpn. 49, 736–743.

MATHEW, J. P., R. MAHADEVAN, B. H. BHARATKUMAR, and V. SUBRAMANIAN, (1996). Numerical simulation of open coast surges. Part I. Experiments on offshore Boundary conditions. Jr. of Coastal Res. 12, 112–122.

MATHUR, M. B., (1972). Simulation of an asymmetric hurricane with a fine mesh multiple grid primitive equation mode. Ph.D. thesis, Florida State University, Tallahassee, FL.

MATSUO, H., (1934). Typhoon damage in Japan caused by record high tide. Engineering News-Rec. 13, 656–657.

MAYERLE, R., A. SCHROETER, and W. ZIELKE, (1994). Simulation of Nearshore Wave Current Interaction by Coupling a Boussinesqu Wave Model with 3d Hydrodynamic Model. In: Proceedings of the International Conference on Coastal Engineering (ICCE), Kobe.

MAZARELLA, A., and A. PALUMBO, (1991). Effect of Sea Level Time Variations on the Occurrence of Extreme Storm-Surges: An Application to the Northern Adriatic Sea. In: Bolletino di Oceanologia Teorica ed Applicata, (9)1, S. 33–38.

MAZURÉ, J. P., (1937). The computation of tides and storm surges in Maritime rivers. Ph.D. thesis, Technical University of Delft, Delft, The Netherlands.

MCALEER, J. B., (1964). Hurricane studies for Narragansett Bay, p.660–685. Proc. 9th Conf. Coastal Eng., June 1964. Lisbon. ASCE, New York, NY.

MCINNES, K. L., and G. D. HUBBERT, (1995). Extreme events and the impact of climate change on Victoria's coastline. Victoria Environment Protection Authority, 69 pp.

McINTYRE, R. J., (1979). Analytic models for west coast storm surges, with application to events of January 1976. Appl. Math. Model. 3, 89–98.

McLEAN, R. F., (1991) Weather and climate interactions with coastal environment systems in the South Pacific. Proc. Conference on South Pacific Environments (Edit: J. E. Hay), Environmental Science, University of Auckland, New Zealand, 49–56.

McLEAN, R. F., (1995). Personal Communication.

MEI, C. C., and H. S. CHEN, (1975). Hybrid-element method for water waves, p. 63–8 1. Symp. Model. Tech. 2nd Annu. Symp. ASCE, Sept. 3–5, 1975, San Francisco, CA.

MERCADO, A., (1994). On the use of NOAA's storm surge model, SLOSH, in managing coastal hazards, The Experience in Puerto Rico, Natural Hazards, 10, 235–246.

MESINGER, F., (1973). A method for construction of second order accuracy difference schemes permitting no false two grid interval wave in the height field. Tellus 25, 444–458.

MESINGER, F., and A. ARAKAWA, (1976). Numerical methods used in atmospheric models. WMO, GARP Publ. No. 17, 64 p.

MIDDLETON, J. H., V. T. BUCHWALD, and J. M. HUTHNANCE, (1984). The anomalous tides near Broad Sound. Contin. Shelf. Res., 4, 359–381.

MILES, J. W., (1971). Resonant response of harbours: An equivalent-circuit analysis, J. Fluid Mech., 46, 241–265.

MILES, J., and W. MUNK, (1961). Harbour paradox, J. Waterways Harbour Division 87, 111–130.

MILLER, A. R., (1957). The effect of steady winds on sea level at Atlantic City. Meteorol. Monogr. Am. Meteorol. Soc. 2, 24–31.

MILLER, B. I., (1963). On the filling of tropical cyclones overland. Nail. Hurricane Res. Proj. Rep. No. 66. U.S. Weather Bureau. Washington, DC. 82 p.

MILLER, B. I., (1969). Experiment in forecasting hurricane development with real data. ESSA. Tech. Mem. ERLTMNHRL-85, Miami, FL.

MILLER, F. R., and R. N. KESHAVAMURTHY, (1968). Structure of an Arabian Sea summer monsoon system. East-West Center Press, Honolulu, HI. 94 p.

MILLER, M. J., and A. K. BETTS, (1977). Travelling convective storms over Venezuela. Mon. Weather Rev. 105, 833–848.

MILLIMAN, J. D., J. M. BROADUS, and F. GABLE, (1989). Environmental and Economic Impacts of rising sea level and subsiding deltas: The Nile and Bengal examples. Ambio, 18, 340–345.

MILLIMAN, J. D., and R. H. MEADE, (1983). World-wide delivery of river sediment to the oceans. Journal of Geology, 91, 1–21.

MINATO, S., (1998). Storm surge simulation using POM and a revisitation of dynamics of sea-surface elevation short-term variation. Meteorology and Geophysics, 48, 79–88.

MISHRA, D. K., and G. R. GUPTA, (1976). Estimation of maximum wind speeds in tropical cyclones occurring in Indian Seas. Indian J. Meteorol. Hydrol. Geophys. 27, 285–290.

MITCHELL, K. E., and J. B. HOVERMALE, (1977). A numerical investigation of the severe thunderstorm gust front, Mon. Weather Rev. 105, 657–675.

MITRA, A. K., (1990). Numerical simulation of tidally induced flow along Indian Coastal regions. Ph.D. Thesis of Indian Institute of Technology, Delhi, India, pp. 118.

MIYAKODA, K., (1962). Contribution to the numerical weather prediction computation with finite difference. Jpn. J. Geophys. 3, 75–190.

MIYAZAKI, M., (1955). Storm surges at the Kobe Harbour (Part I). Oceanogr. Mag. 7 (1), 11–19.

MIYAZAKI, M., (1962). Theoretical investigation of typhoon surges along the Japanese coast (II). Oceanogr. Mag. 13, 103117.

MIYAZAKI, M., (1965). A numerical computation of the storm surge of Hurricane Carla 1961 in the Gulf of Mexico. Oceanogr. Mag. 17, 109–140.

MIYAZAKI, M., (1975). Characteristics of storm surges induced by typhoons along the Japanese coast. In Typhoon modification. Proc. WMO Tech. Conf., Oct. 15–18. 1974, Manila. WMO 408, 37–44.

MIYAZAKI, M., T. VENO, and S. UNOKI, (1961). Theoretical investigations of typhoon surges along the Japanese coast. Oceanogr. Mag. 13, 51–75.

MONCRIFFF, M. W., and M. J. MILLER, (1976). The dynamics and simulation of tropical cumulonimbus and squall lines. Q. J. Roy. Metcorol. Soc. 102, 373–394.

MONSERRAT, S., A. IBBETSON, and A. J. THORPE, (1991b). Atmospheric gravity waves and "Rissaga" phenomenon. Q. J. Roy. Meteorol. Soc., 117, 553–570.

MONSERRAT, S., and A. J. THORPE, (1992). Gravity wave observations using an array of Microbarographs in the Balearic Islands, Q. J. Roy, Met. Soc., 118, 259–282.

MOOLEY, D. A., (1980a). Severe cyclonic storms in the Bay of Bengal, 1877–1977. Mon. Weather Rev. 108, 1647–1655.

MOOLEY, D. A., (1980b). Suitable probability model for severe cyclonic storms striking the coast around the Bay of Bengal, p. 349–357. In S. Ikeda et al. [ed.] Statistical climatology: developments in atmospheric science. Rep. No. 13. Elsevier Scientific Publishing Company, Amsterdam, The Netherlands.

MORAIS, C. C., and F. ABECASIS, (1975). Storm surge effects at Leixoes, p. 98–111. Proc. 14th Coastal Eng. Conf., June 24–28, 1974, Copenhagen, Denmark. Chap. 3. ASCE, New York, NY.

MORCOS, S. A., (1970). Physical and Chemical oceanography of the Red Sea. Oceanogr, Mar, Biology Annu. Rev., 8, 73–202.

MORRISON, S. F., (1952). Of Plymouth plantation. W. Bradford [ed.] Knopf Press. New. NY. 448 p.

MOWLA, K. G., (1968). Cyclogenesis in the Bay of Bengal and Arabian Sea. Tellus 20, 151–162.

MUNK, W. H., F. SNODGRASS, and G. F. CARRIER, (1956). Edge waves on the continental shelf. Science. (Washington, DC) 123, 127–132.

MUROTA, A., (1963). The model study on the validity of the large breakwaters in the Osaka Bay against storm surges. Technol. Rep. Osaka Univ. 13, 173–189.

MURTY, T. S., (1971). The response of a lake with a depth discontinuity to a time-dependent wind stress. Arch. Meteorol. Geophys. Bioklimatol. Ser. A 20, 55–66.

MURTY, T. S., (1972). Circulation in James Bay, p. 143–193. Manuscr. Rep. No. 24. Marine Sciences Branch, Department of the Environment, Ottawa, Ont.

MURTY, T. S., (1977). Seismic sea waves – tsunamis. Bull. Fish. Res. Board Can. 198, 337 p.

MURTY, T. S., (1984). Storm surges-Meteorological Ocean Tides. Ottawa: Department of Fisheries and Oceans.

MURTY, T. S., (1995). Mathematical simulation of hydrological events in and around Australia, Hydrocoast-95, 13–17 Nov '95, Bangkok.

MURTY, T. S., and S. K. DUBE, (2000). Mitigation of Marine hazards in India, Proc. of the Indian Ocean Studies, 92–1114.

MURTY, T. S, and M. I. EL-SABH, (1981). Interaction between storm surges and tides in shallow waters, Marine Geodesy, 5,19–33.

MURTY, T. S., and M. I. EL-SABH, (1984). Weather systems and sea state in the Red Sea and the Gulf of Aden. Proc. Symp. Coral Reef Environ, Red Sea, 8–38, Jeddah, Saudi Arabia.

MURTY, T. S., R. A. FLATHER, and R. F. HENRY, (1986). The storm surge problem in the Bay of Bengal. Prog. Oceanog.16, 195–233.

MURTY, T. S., and N. G. FREEMAN, (1973). Applications of the concepts of edge waves and numerical modelling to storm surge studies on Lake Huron. Proc. 16th Conf. Great Lakes Res. Int. Assoc. Great Lakes. Res. 16, 533–548.

MURTY, T. S., and R. F. HENRY, (1983). Tides in the Bay of Bengal. J. Geophys. Res. 88, 6069–6076.

MURTY T. S., S. VENKATESH, M. B. DANARD, and M. I. EL-SABH, (1994). Storm surges in Canadian waters, Atmosphere Ocean, 33, No. 1, 359–387.

MUSTAFIN, N. V., (1969). Methods of computative forecasting of nonperiodic oscillations in the sea level. Occanol. 8, 414–421.

MYERS, V. A., (1954). Characteristics of United States hurricanes pertinent to levee design for Lake Okeechobee. Florida. Hydrometeorol. Rep. No. 32, March 1954. U.S. Weather Bureau, Washington. DC. 106 p.

MYERS, V. A., (1957). Maximum hurricane winds. Bull. Am. Meteorol. Soc. 38, 227–228.

MYERS, V. A., (1975). Storm tide frequencies on the South Carolina coast. U.S. National Weather Service. NOAA Tech. Rep. NWS – 16, 90 p.

MYERS, V. A., and W. MALKIN, (1961). Some properties of hurricane wind fields as deduced from trajectories, p. 145. Nat. Hurricane Res. Rep. No. 49. U.S. Weather Bureau, Washington, DC.

NAKAMURA, M., H. SHIRASHI, and Y. SASAKI, (1964). A model study on tide and storm surge due to a typhoon in Ise Bay., Coastal Eng. Jpn. 8, 45–63.

NAKANO, M., (1949). On the secondary undulations of tides caused by cyclonic storms. Oceanogr. Mag. 1 (1), 1332.

NAKAYAMA, M., (1972). On the PCM-FS-FM tide telemetering system for warning of tsunamis and storm surges. Oceanogr. Mag. 23 (2) 59–67.

NAMIAS, J., (1955). Secular fluctuations in vulnerability to tropical cyclones in and off New England. Mon. Weather. Rev. 83, 155–162.

NASNER, H., und H. W. PARTENSCKY, (1977). Sturmfluten in der Elbe und an der deutschen Nordseeküste von 1901 bis zum Januar 1976. In: Mitteilungen des Franzius Instituts für Wasserbau und Küsteningenieurswesen der TU Hannover, 45, 179–221.

NATARAJAN, R., and N. RAMANATHAN, (1980). Estimation of storm surges in a bay. Presented at the Indo-French school on Recent Advances in Computer Techniques in Meteorology, Bio-Mechanics and Applied Systems, Feb 4–13, 1980, New Delhi, India.

NELSON, R. C., (1975). Tropical cyclone storm surges in Australia 1880 to 1970 p. 193 – 197. Proc. 2nd Aust. Conf. Coastal Ocean Engg., Queensland, Australia.

NEUMANN, C. J., (1979). Statistical techniques. In Operation techniques for forecasting tropical cyclone intensity and movement. Chap. 4. No. 528, World Meteorological Organization, Geneva, Switzerland.

NEUMANN, C. J., (1993). "Global Overview" – Chapter 1 „Global Guide to Tropical Cyclone Forecasting", WMO/TC-No. 560, Report No. TCP-31, World Meteorological Organization; Geneva, Switzerland.

NEUMANN, C. J., and G. W. CRY, (1978). A revised Atlantic tropical cyclone climatology. Mar. Weather Log 22, 231–236.

NEUMANN, C. J., G. W. CRY, E. L. CASO, and B. R. JARVINEN, (1978). Tropical cyclones of the North Atlantic Ocean, 1871–1977. National Climatic Center, Asheville, NC. 170 p.

NEUMANN, C. J., and D. A. HILL, (1976). Computerized tropical cyclone climatology. Mar. Weather Log 20, 257–262.

NEUMANN, C. J., and G. S. MANDAL, (1978). Statistical prediction of storm motion: motion over the Bay of Bengal and Arabian Sea. Indian J. Meteorol. Hydrol. Geophys. 29, 487–500.

NEUMANN, C. J., and J. M. PELISSIER, (1981). Models for the prediction of tropical cyclone motion over the North Atlantic: an operational evaluation. Mon. Weather Rev. 109, 522–538.

NEWTON, C. W., (1967). Severe convective storms. Adv. Geophys. 12, 257–308.

NEWTON, C. W., and H. R. NEWTON, (1959). Dynamical interactions between large convective clouds and environment with vertical shear. J. Meteorol. 16, 483–496.

NICHOLLS, N., (1979). A possible method for predicting seasonal tropical cyclone activity in the Australian region. Mon. Wea. Rev., 107, 1221–1224.

NICHOLLS, N., (1984). The Southern Oscillation, sea-surface temperature, and interannual fluctuations in Australian tropical cyclone activity. J. Climatol., 4, 661–670.

NICHOLLS, N., (1985). Predictability of inter-annual variations of Australian seasonal tropical cyclone activity. Mon. Wea. Rev., 113, 1144–1149.

NICHOLLS, N., (1989). Global warming, tropical cyclones and ENSO, In: Proceedings of workshop on responding to the threat of global warming. Options for the Pacific and Asia, Argonne, Illinois, pp. 2.19–2.36.

NICHOLLS, N., (1992). Recent performance of a method for forecasting Australian seasonal tropical cyclone activity. Aust. Meteor. Mag., 21, 105–110.

NICHOLLS, R. J., and S. P. LEATHERMAN, (1995). Global Sea Level Rise. In: Strzepek and Smith, 92–123.

NICKERSON, J. W., (1971). Storm-surge forecasting. Tech. Rep. AD-751 578, Apr. 1971. Navy Weather Research Facility, Norfolk, VA. 91 p.

NIEMEYER, H. D., (1979a). Long wave model independent of stability criteria. J. Waterway Port Coastal Ocean Div. WW1, 51–65.

NIEMEYER, H. D., (1979b). Wave climate study in the region of the east Frisian Islands and coast, p. 134–151. Proc. 16th Coastal Eng. Conf., Hamburg, W. Germany, ASCE, New York, NY.

NIEMEYER, H. D., and R. KAISER, (1997). Variationen im lokalen Seeklima infolge morphologischer Änderungen im Riffbogen. In: Berichte der Forschungsstelle Küste, 41, pp. 107–117.

NIEMEYER, H., and R. KAISER & D. GLÄSER, (1995). Sturmfluthäufigkeiten zwischen Ems und Weser von 1946–1994 – Pegel Emden, Borkum, Norderney, Bremerhaven (unveröffentlicht).

NIGAM, R., (1989). Sea level rise and impact on coastal zone. In 'Coastal Zone Management in India' (Editors: S. N. Dwivedi, V. S. Bhatt, Pradeep Chaturvedi), Indian Association for the advancement of Science, pp. 144–147.

NIHOUL, J. C. J., (1973). Mathematical Models, in North Sea Science, E. P. Goldbeng (Ed), MIT university press, Cambridge Mass. U. S. A., 43–57.

NIHOUL, J. C. J., (1977). Three-dimensional model of tides and storm surges in a shallow well mixed continental sea. Dyn. Atmos. Oceans. 2, 29–47.

NIHOUL, J. C. J., and F. C. RONDAY, (1976). Hydrodynamic models of the North Sea, Mem. Soc. Roy. Sc. Lg., 10, 61–96.

NOMITSU, T., (1935). Surface fluctuations of Lake Biwa caused by the Muroto typhoon. Mem. Coll. Sci. Kyoto Imp. Univ. Ser. A 18, 221–238.

NORTON, W. R., I. P. KING, and G. T. ORLOB, (1973). A finite element model for lower granite reservoir. Prepared for Walla Walla district, U.S. Army Corps of Engineers. Rep. No. 10560. Water Resources Engineers Inc., March 1973.

NUNEZ, E., and W. M. GRAY, (1978). A comparison between West ladies hurricanes and Pacific typhoons, p. 528–534. Proc. 11th Tech. Conf. Hurricanes Trop. Meteorol., Dec. 13–16, 1977, Miami Beach, FL. American Meteorological Society. Boston MA.

OBUKHOV, A. M., (1957). O tochnosti predvychislenia advektionyklu izmenenii polei pri chislenom prognoze pogody. Izv. Akad. Nauk SSSR Ser. Geofiz. 9, 1133–1141.

O'CONNOR, J. F., (1964). Hemispheric distribution of 5-day mean 700 nib circulation centers. Mon. Weather Rev. 92, 303–315.

O'CONNOR, W. P., (1991). A numerical model of tides and storm surges in the Rio de la Plata Estuary, Continental Shelf Research, 11 & 12, 1491–1508.

ODD, N., (1980). Mathematical model studies of the Irrawaddy Delta. Hydraulic Research Station, Wallingford , UK. 7 p.

OGURA, S., (1925). Effect of atmospheric pressure on sea level in western part of the North Pacific Ocean. Jpn. J. Astron. Geophys. If, 209–231.

OGURA, Y., (1964). Frictional 1 y-control led, thermal 1 y-driven circulations in a circular vortex with application to tropical cyclones. J. Atmos. Sci. 21, 610–621.

OGURA, Y., and M. T. LIOU, (1980). The structure of a mid-latitude squall line: a case study. J. Atmos. Sci. 37, 553–567.

OH, I. S., S. I. KIM, and J. H. BONG, (1988). Storm surges by the typhoons passing through the south sea of Korea, J. of the Korean Met. Soc. , 24, No. 3, 72–84 (in Korean).

OOYAMA, K., (1964). A dynamical model for the study of tropical cyclone development. Geoffis. Int. 4, 197–198.

ORFORD, D., (1989). A review of tides, currents and waves in the Irish Sea. In: Sweeney, J. C. (ed.) The Irish Sea. A resource at risk. Geographical Society of Ireland special publications, 3, p. 18–46.

ORLOB, G. T., (1972). Mathematical modelling of estuarial systems, p. 1–127. In A. K. Biswas [ed.] Proc. Int. Symp. Model. Tech. Water Resour. Syst., May 9–12, 1972. Vol. 1. Environment Canada, Ottawa, Ont.

ORTT, F. L., (1897). De invloed vap zinel en luchtdruk op de getijden. K. Inst. Ingen. Verb. 1896–1897, 117–130 (Nature (London) 56, 80–84).

OUMARACI, H., N. W. H. ALLSOP, M. B. DE GROOT, R. S. CROUCH, J. K. VRIJLING, S. A. KORTENHAU, and H. G. VOORTMANN, (1999). Probabilistic Design Tools for Vertical Breakwaters. Rotterdam. Published soon.

OWEN, T. B., (1980). Hurricane preparedness: a team effort. NOAA Magazine, May–June 1980. p. 5.

PAGENKOPF J. R., and B. R. PEARCE, (1975). Evaluation of techniques for numerical calculation of storm surges. Rep. No. 199. Feb. 1975. Department of Civil Engineering, MIT, Cambridge, MA. 120 p.

PALMÉN, E., (1932). Versuch zur bestimmung des Tan gentialdruckes des Windes ant die Meeresoberfläche miltels Wasserstandsbeobachtungen. Arm. Hydrogr. Mar. Meteorol. Heft Xl, Berlin.

PALMÉN, E., (1949). On the formation and structure of tropical hurricanes. Geophysics 3.

PALMÉN, E., (1955). Improved terrain effects in barotropic forecasts. Mon Weather Rev. 83, 327–342.

PALMÉN, E., and C. W. NEWTON, (1969). Atmospheric circulation systems: their structure and physical interpretation, p. 515–522. Academic Press, New York, NY.

PANT, P. S., A. R. RAMAKRISHRAN, and R. JAMBUNATHAN, (1980). Cyclones and depressions over the Indian Seas in 1977. Mausam (formerly Indian J. Meteor. Hydrol. Geophys.) 31, 337–356.

PARARAS-CARAYANNIS, G., (1975). Verification study of a bathystrophic storm surge model. Tech. Memo. No. 50, May 1975. U. S. Army Corps of Engineers, Coastal Engineering Research Center, Fort Belvar, VA. 248 p.

PARKES G. S., L. A. KETCH, and C. T. O'REILLY, (1997). Storm surge events in the Maritimes, Proceedings of the 1997 Canadian coastal conference-Abstracts.

PAULSEN, C. G., B. L. BIGWOOD, A. W. HARRINGTON, C. W. HARTWELL, and H. B. KINNISON, (1940). Hurricane floods of September 1938. U. S. Geological Survey. Water Supply Pap. 867. U.S. Government Printing Office, Washington, DC. 555 p.

PEARCE, B. R., (1972). Numerical calculation of the response of coastal waters to storm systems – with application to Hurricane Camille of August 17–22, 1969. Tech. Rep. No. 12 Aug. 1952. Coastal and Oceanographic Engineering Lab. University of Florida, Gainesville, FL. 152 p.

PEARSON, F., (1990). Map Projections: Theory and applications. CRC Press, Boca Raton, FL.

PEDGELEY, D. E., (1969). Cyclones along the Arabian Coast. Weather 24, 456–468.

PELISSIER, J. M., (1979). Dynamical techniques. In Operational techniques for forecasting tropical cyclone intensity and movement. Chap. 5. WMO No. 528, 1 I.r. 1–11.5. 11.

PERLROTH, I., (1967). Hurricane behavior as related to oceanographical environmental conditions. Tellus 19, 258–268.

PERLROTH, I., (1969). Effects of oceanographic media on equatorial Atlantic hurricanes. Tellus 21, 230–244.

PERNETTA, J. C., (1992). Impacts of climate change and sea level rise on small island states: national and international responses, Global Environmental Change, 2, 19–31.

PETERS, S. P., (1954). Some meteorological aspects of North Sea floods, with special reference to February 1953. Proc. Conf. North Sea Floods. Weather 9, 28–36.

PETERSEN, M., and H. ROHDE, (1991). Sturmflut. Die großen Fluten an den Kuesten Schleswig-Holsteins und in der Elbe. Neumünster.

PETERSON, P., (1975). Storm Surges Statistics, Royal Observatory, Hong Kong, Tech. Note 20.

PETTERSSEN, S. (1956). Weather analysis and forecasting. Vol. I and II. 2nd ed. McGraw-Hill Publications, New York, NY. 428 p.

PETTERSSEN, S. (1969). Introduction to meteorology. McGraw-Hill Publications, New York, NY. 333 p.

PHILLIPS, E. F., (1959). The association of spherics with tropical cyclones. Aust. Meteorol. Mag. 26, 76–85.

PHILLIPS, N. A., (1960). Numerical weather prediction, p. 43–90. In F. L. Alt [ed.] Advances in computers. Vol. 1. Academic Press, New York, NY.

PICKRILL, R. A., (1972). Storm surge on the east coast of New Zealand. M. A. thesis, Geography Department, University of Canterbury, Canterbury, New Zealand.

PIKE, A. C., (1972). Improved barotropical hurricane track prediction by adjustment of the initial wind field. NOAA Tech. Memo. NWS-SR-66.

PITTOCK, A. B., (1992). Regional climate change scenarios for the South Pacific. Proc. second SPREP Meeting on climate change and sea level rise in the South Pacific region, Noumea, New Caledonia, 6–10 April 1992, SEREP Report, pp. 50–57.

PITTOCK, A. B., K. WALSH, and K. MCINNES, (1996). Tropical cyclones and coastal inundation under enhanced greenhouse conditions. Water, Air & Soil Pollution, 92, 159–169.

PLATZMAN, G. W., (1958a). A numerical computation of the surge of June 26, 1954, on Lake Michigan. Geophysica 6, 407–438.

PLATZMAN, G. W., (1958b). The lattice structure of the finite-difference primitive and vorticity equations. Mon. Weather Rev. 86, 285–292.

PLATZMAN, G. W., (1963). The dynamic prediction of wind tides on Lake Erie. Meteorol. Mongr. 4, 44 p.

PLATZMAN, G. W., (1965). The prediction of surges in the southern basin of Lake Michigan. Part 1. The dynamical basis for prediction. Mon. Weather Rev. 93, 275–28 1.

NIGAM, R., (1989). Sea level rise and impact on coastal zone. In 'Coastal Zone Management in India' (Editors: S. N. Dwivedi, V. S. Bhatt, Pradeep Chaturvedi), Indian Association for the advancement of Science, pp. 144–147.

NIHOUL, J. C. J., (1973). Mathematical Models, in North Sea Science, E. P. Goldbeng (Ed), MIT university press, Cambridge Mass. U. S. A., 43–57.

NIHOUL, J. C. J., (1977). Three-dimensional model of tides and storm surges in a shallow well mixed continental sea. Dyn. Atmos. Oceans. 2, 29–47.

NIHOUL, J. C. J., and F. C. RONDAY, (1976). Hydrodynamic models of the North Sea, Mem. Soc. Roy. Sc. Lg., 10, 61–96.

NOMITSU, T., (1935). Surface fluctuations of Lake Biwa caused by the Muroto typhoon. Mem. Coll. Sci. Kyoto Imp. Univ. Ser. A 18, 221–238.

NORTON, W. R., I. P. KING, and G. T. ORLOB, (1973). A finite element model for lower granite reservoir. Prepared for Walla Walla district, U.S. Army Corps of Engineers. Rep. No. 10560. Water Resources Engineers Inc., March 1973.

NUNEZ, E., and W. M. GRAY, (1978). A comparison between West ladies hurricanes and Pacific typhoons, p. 528–534. Proc. 11th Tech. Conf. Hurricanes Trop. Meteorol., Dec. 13–16, 1977, Miami Beach, FL. American Meteorological Society. Boston MA.

OBUKHOV, A. M., (1957). O tochnosti predvychislenia advektionyklu izmenenii polei pri chislenom prognoze pogody. Izv. Akad. Nauk SSSR Ser. Geofiz. 9, 1133–1141.

O'CONNOR, J. F., (1964). Hemispheric distribution of 5-day mean 700 nib circulation centers. Mon. Weather Rev. 92, 303–315.

O'CONNOR, W. P., (1991). A numerical model of tides and storm surges in the Rio de la Plata Estuary, Continental Shelf Research, 11 & 12, 1491–1508.

ODD, N., (1980). Mathematical model studies of the Irrawaddy Delta. Hydraulic Research Station, Wallingford , UK. 7 p.

OGURA, S., (1925). Effect of atmospheric pressure on sea level in western part of the North Pacific Ocean. Jpn. J. Astron. Geophys. If, 209–231.

OGURA, Y., (1964). Frictional 1 y-control led, thermal 1 y-driven circulations in a circular vortex with application to tropical cyclones. J. Atmos. Sci. 21, 610–621.

OGURA, Y., and M. T. LIOU, (1980). The structure of a mid-latitude squall line: a case study. J. Atmos. Sci. 37, 553–567.

OH, I. S., S. I. KIM, and J. H. BONG, (1988). Storm surges by the typhoons passing through the south sea of Korea, J. of the Korean Met. Soc. , 24, No. 3, 72–84 (in Korean).

OOYAMA, K., (1964). A dynamical model for the study of tropical cyclone development. Geoffis. Int. 4, 197–198.

ORFORD, D., (1989). A review of tides, currents and waves in the Irish Sea. In: Sweeney, J. C. (ed.) The Irish Sea. A resource at risk. Geographical Society of Ireland special publications, 3, p. 18–46.

ORLOB, G. T., (1972). Mathematical modelling of estuarial systems, p. 1–127. In A. K. Biswas [ed.] Proc. Int. Symp. Model. Tech. Water Resour. Syst., May 9–12, 1972. Vol. 1. Environment Canada, Ottawa, Ont.

ORTT, F. L., (1897). De invloed vap zinel en luchtdruk op de getijden. K. Inst. Ingen. Verb. 1896–1897, 117–130 (Nature (London) 56, 80–84).

OUMARACI, H., N. W. H. ALLSOP, M. B. DE GROOT, R. S. CROUCH, J. K. VRIJLING, S. A. KORTENHAU, and H. G. VOORTMANN, (1999). Probabilistic Design Tools for Vertical Breakwaters. Rotterdam. Published soon.

OWEN, T. B., (1980). Hurricane preparedness: a team effort. NOAA Magazine, May–June 1980. p. 5.

PAGENKOPF J. R., and B. R. PEARCE, (1975). Evaluation of techniques for numerical calculation of storm surges. Rep. No. 199. Feb. 1975. Department of Civil Engineering, MIT, Cambridge, MA. 120 p.

PALMÉN, E., (1932). Versuch zur bestimmung des Tan gentialdruckes des Windes ant die Meeresoberfläche miltels Wasserstandsbeobachtungen. Arm. Hydrogr. Mar. Meteorol. Heft Xl, Berlin.

PALMÉN, E., (1949). On the formation and structure of tropical hurricanes. Geophysics 3.

PALMÉN, E., (1955). Improved terrain effects in barotropic forecasts. Mon Weather Rev. 83, 327–342.

PALMÉN, E., and C. W. NEWTON, (1969). Atmospheric circulation systems: their structure and physical interpretation, p. 515–522. Academic Press, New York, NY.

PANT, P. S., A. R. RAMAKRISHRAN, and R. JAMBUNATHAN, (1980). Cyclones and depressions over the Indian Seas in 1977. Mausam (formerly Indian J. Meteor. Hydrol. Geophys.) 31, 337–356.

PARARAS-CARAYANNIS, G., (1975). Verification study of a bathystrophic storm surge model. Tech. Memo. No. 50, May 1975. U. S. Army Corps of Engineers, Coastal Engineering Research Center, Fort Belvar, VA. 248 p.

PARKES G. S., L. A. KETCH, and C. T. O'REILLY, (1997). Storm surge events in the Maritimes, Proceedings of the 1997 Canadian coastal conference-Abstracts.

PAULSEN, C. G., B. L. BIGWOOD, A. W. HARRINGTON, C. W. HARTWELL, and H. B. KINNISON, (1940). Hurricane floods of September 1938. U. S. Geological Survey. Water Supply Pap. 867. U.S. Government Printing Office, Washington, DC. 555 p.

PEARCE, B. R., (1972). Numerical calculation of the response of coastal waters to storm systems – with application to Hurricane Camille of August 17–22, 1969. Tech. Rep. No. 12 Aug. 1952. Coastal and Oceanographic Engineering Lab. University of Florida, Gainesville, FL. 152 p.

PEARSON, F., (1990). Map Projections: Theory and applications. CRC Press, Boca Raton, FL.

PEDGELEY, D. E., (1969). Cyclones along the Arabian Coast. Weather 24, 456–468.

PELISSIER, J. M., (1979). Dynamical techniques. In Operational techniques for forecasting tropical cyclone intensity and movement. Chap. 5. WMO No. 528, 1 I.r. 1–11.5. 11.

PERLROTH, I., (1967). Hurricane behavior as related to oceanographical environmental conditions. Tellus 19, 258–268.

PERLROTH, I., (1969). Effects of oceanographic media on equatorial Atlantic hurricanes. Tellus 21, 230–244.

PERNETTA, J. C., (1992). Impacts of climate change and sea level rise on small island states: national and international responses, Global Environmental Change, 2, 19–31.

PETERS, S. P., (1954). Some meteorological aspects of North Sea floods, with special reference to February 1953. Proc. Conf. North Sea Floods. Weather 9, 28–36.

PETERSEN, M., and H. ROHDE, (1991). Sturmflut. Die großen Fluten an den Kuesten Schleswig-Holsteins und in der Elbe. Neumünster.

PETERSON, P., (1975). Storm Surges Statistics, Royal Observatory, Hong Kong, Tech. Note 20.

PETTERSSEN, S. (1956). Weather analysis and forecasting. Vol. I and II. 2nd ed. McGraw-Hill Publications, New York, NY. 428 p.

PETTERSSEN, S. (1969). Introduction to meteorology. McGraw-Hill Publications, New York, NY. 333 p.

PHILLIPS, E. F., (1959). The association of spherics with tropical cyclones. Aust. Meteorol. Mag. 26, 76–85.

PHILLIPS, N. A., (1960). Numerical weather prediction, p. 43–90. In F. L. Alt [ed.] Advances in computers. Vol. 1. Academic Press, New York, NY.

PICKRILL, R. A., (1972). Storm surge on the east coast of New Zealand. M. A. thesis, Geography Department, University of Canterbury, Canterbury, New Zealand.

PIKE, A. C., (1972). Improved barotropical hurricane track prediction by adjustment of the initial wind field. NOAA Tech. Memo. NWS-SR-66.

PITTOCK, A. B., (1992). Regional climate change scenarios for the South Pacific. Proc. second SPREP Meeting on climate change and sea level rise in the South Pacific region, Noumea, New Caledonia, 6–10 April 1992, SEREP Report, pp. 50–57.

PITTOCK, A. B., K. WALSH, and K. MCINNES, (1996). Tropical cyclones and coastal inundation under enhanced greenhouse conditions. Water, Air & Soil Pollution, 92, 159–169.

PLATZMAN, G. W., (1958a). A numerical computation of the surge of June 26, 1954, on Lake Michigan. Geophysica 6, 407–438.

PLATZMAN, G. W., (1958b). The lattice structure of the finite-difference primitive and vorticity equations. Mon. Weather Rev. 86, 285–292.

PLATZMAN, G. W., (1963). The dynamic prediction of wind tides on Lake Erie. Meteorol. Mongr. 4, 44 p.

PLATZMAN, G. W., (1965). The prediction of surges in the southern basin of Lake Michigan. Part 1. The dynamical basis for prediction. Mon. Weather Rev. 93, 275–28 1.

PLATZMAN, G. W., (1971). Ocean tides and related waves. Lectures for the American Mathematical Society, 1970. Summer seminars on mathematical problems in the geophysical sciences, held at Rensselaer Polytechnic Institute, Troy, NY. 94 p. (Also *In* W. H. Reid [ed.] Mathematical problems in the geophysical sciences. Vol. 14. Part 2. p. 239–291.)

PLATZMAN, G. W., (1979). Effects of multiple connectivity on a finite element barotropic model. J. Phys. Oceanogr. 9, 12761283.

PLATZMAN, G. W., (1981). 'Some response characteristics of finite element tidal models', J. Comput. Phys., 40, 36–63 (1981).

PORE, N. A., (1964). The relation of wind and pressure to extra-tropical storm surges at Atlantic City. J. Appl. Meteorol. 3, 155–163.

PORE, N. A., (1965). Chesapeake Bay extratropical storm surges. Chesapeake Sci. 6, 172–182.

PORE, N. A., and C. S. BARRIENTOS, (1976). Storm surge. In Marine ecosystem analysis (MESA). New York Bight Atlas Monogr. No. 6, Feb. 1976. New York Sea Grant Institute, Albany, NY. 44 p.

PRANDLE, D., (1974). A numerical model of the southern North Sea and River Thames. Rep. No. 4, Institute of Oceanographic Sciences, Bidston, U.K. 25 p.

PRANDLE, D., (1975). Storm surge in the Southern North Sea and Riva Thames, Proc. Roy. Soc. London., A 344, 509–539.

PRANDLE, D., (1978). Residual flows and elevations in the southern North Sea. Proc. Roy. Soc. London Ser. A 359, 189–228.

PRANDLE, D., and J. WOLF, (1978a). The interaction of the surge and tide in the North Sea and river Thames. Geophys. J. Roy. Astron. Soc., 55, 203–216.

PRANDLE, D., and J. WOLF, (1978b). Surge tide interaction in the Southern North-Sea – Hydrodyn., Estuaries and fjords. 23 161–185.

PRICE, W. A., (1956). Hurricanes affecting the coast of Texas from Galveston to Rio Grande. Tech. Memo. No. 78, Mar. 1956. Beach Erosion Board, Corps of Engineers. 17 p.

PROUDMAN, J., (1929). The effects on the sea of changes in atmospheric pressure. Mon. Not. R. Astron. Soc. Geophys. Suppl. 2, 197–209.

PROUDMAN, J., (1954). Note on the dynamics of storm surges. Mon. Not. R. Astron. Soc. Geophys. Suppl. 7, 44–48.

PROUDMAN, J., (1955a). The propagation of tide and surge in an estuary. Proc. Roy. Soc. London Ser. A 231, 8–24.

PROUDMAN, J., (1955b). The effect of friction on a progressive wave of tide and surge in an estuary. Proc. Roy. Soc. London Ser. A 233, 407–418.

PROUDMAN, J., (1957). Oscillations of tide and surge in an estuary of finite length. J. Fluid Mech. 2, 347– 382.

PROUDMAN, J., (1958). On the series that represent tide and surge in the Thames. J. Fluid Mech. 3, 411– 417.

PUGH, D. T., (1987). Tides, Surges and Mean-Sea-Level. A Handbook for Engineers and Scientist. John Wiley and Sons, pp. 472.

PUGH, D. T., and J. M. VASSIE, (1979). Extreme sea levels from tide and surge probability, p. 911–930. Proc. 16th Coastal Eng. Conf., Aug. 27–Sept. 3, 1978, Hamburg, W. Germany. Vol. 1. ASCE, New York, NY.

PUNNING, J. M., (1993). Sea level changes and Paleogeographical History of the Baltic Sea, Proceedings of the International Workshop on Sea level changes and their consequences for Hydrology and Water Management, 19–23 April 1993, Noordwijkerhout, Netherlands, pp. 61–71.

QIN, Z., (1997). Sea level rise and its impact on storm surge and tide in Shanghai, Mausam, 48, 541–554.

QIN, Z., and DUAN, YIHONG, (1996). Numerical study of nonlinear tide – surge interaction in the coastal waters of Shanghai. In: Land – based and Marine Hazards (edited by M. I. El-Sabh, S. Venkatesh, H. Devis, and T. S. Murthy), Kluwa Academic Publishers, pp. 139–156.

QIN, Z., Y. DUAN, Y. WANG, Z. SHEN, and K. XU, (1994). Numerical simulation and prediction of storm surge and water level in Shanghai harbour and its vicinity, Natural Hazards, 9, 167–188.

RABE, K., and S. BRANDO, (1980). A numerical simulation of an occurrence of extreme sea states within a typhoon. J. Meteorol. Soc. Jpn. 58, 394–402.

RABINOVICH, A. B., (1993). Long Ocean Gravity Waves: Trapping Resonance, Leaking, St. Petersberg, Gidrometeoizdat (in Russian).

RABINOVICH, A. B., and S. MONSERRAT, (1996). Meteorological Tsunamis near the Balearic and Kuril Islands: Descriptive and Statistical analysis, Natural Hazards, 13, 55–90.

RABINOVICH, A. B., and S. MONSERRAT, (1998). Generation of Meteorological Tsunamis (Large amplitude seiches) near the Balearic Islands, Natural Hazards, 18, No. 1, July 98, 27–55.

RABINOVICH, A. B., and S. E. SOKOLOVA, (1992). On organizing a catalogue of storm surges for the sea of Japan, Natural Hazards, 5, 319–325.

RADY, M. A., M. I., EL-SABH, T. S. MURTY, and J. O. BACKHAUS. (1994a). Numerical modelling of tides in the Gulf of Suez , Egypt. Marine Geodesy, 17,11–36.

RADY, M. A., M. I. EL-SABH, T. S. MURTY, and J. A. BACKHAUS, (1994b). Tide-Surge interaction in the Gulf of Suez, Egypt., 17. 45–62.

RAGHAVENDRA, V. K., (1973). A statistical analysis of the number of tropical storms and depressions in the Bay of Bengal during 1890 to 1969. Indian J. Meteorol. Geophys. 24, 125– 130.

RAMAGE, C. S., (1962). The subtropical cyclone. J. Geophys. Res. 67, 1401–1411.

RAMAGE, C. S., (1971). Monsoon Meteorology. Academic Press. New York, NY. 296 p.

RAMAGE, C. S., (1973). The typhoon of October 1970 in the South China Sea: intensification, decay and ocean interaction. Environmental Prediction Research Facility, Monterey, CA.

RAMAKRISHNA, (1989). Low frequency and seasonal variability within ocean basins: Southwest Pacific Ocean, Rapporteur report, International Workshop on Tropical Cyclone (IWTC), Manila, Philippines, November, 1989.

RAMAN, K., R. VENKATARAMAN, and A. A. RAMASASTRY, (1967). Unusually large number of cyclonic storms in the Bay of Bengal during the postmonsoon season of 1966. Indian J. Meteorol. Hydrol. Geophys. 18, 1015–1037.

RAMANADHAM, R., and R. VARADARAJULU, (1965). Storm tides at Visakhapatnam. Indian J. Pure Appl. Phys. 3, 173–176.

RAMA SASTRY, A. A., A. K. CHAUDHURY, and N. C. BISWAS, (1984). Cyclones and depressions over Indian Seas in 1982, Mausam, 35, 1–10.

RAMIS, C., and A. JANSA, (1983). Meteorological conditions during the large amplitude sea level oscillations in the western Mediterranean Sea (in Spanish), Rev. Geofis., 39, 35–42.

RAMMING, H. G., (1972). Reproduction of physical processes in coastal areas, p. 2197–2216. Proc. 13th Conf. Coastal Eng., Vancouver, B. C. ASCE, New York, NY.

RAMMING, H. G., (1976). A nested North Sea model with fine resolution in shallow coastal areas. Mem. Soc. R. Sci. Liège 10, 9–26.

RAO, A. D., (1982). Numerical storm surge prediction in India. P. D. Thesis, Indian Institute of Technology, Delhi, pp. 211.

RAO, A. D., S. K. DUBE, and P. CHITTIBABU, (1994). Finite difference techniques applied to the simulation of surges and currents around Sri Lanka and Southern Indian Peninsula. Comp. Fluid Dyn., 3, 71–77.

RAO, D. B., (1967). Response of a lake to a time dependent wind stress. J. Geophys. Res. 72, 1697–1708.

RAO, D. B., (1969). Effect of travelling disturbances on a rectangular bay of uniform depth. Arch. Meteorol. Geophys. Bioklimatol. Ser. A 18, 171–190.

RAO, D. B., and T. S. MURTY, (1970). Calculation of the steady state wind-driven circulations in Lake Ontario. Arch. Meteorol. Geophys. Bioklimatol. Ser. A 19, 195–210.

RAO, N. S. B., (1968). On some aspect of local and tropical storms in India Ph. D. Thesis University of Jadavpur, Calcutta, India.

RAO, N. S. B., and S. MAJUMDAR, (1966). A technique for forecasting storm waves. Indian J. Meteorol. Geophys., 17, 333–346.

RAO, Y. R., P. CHITTIBABU, S.K. DUBE, A. D. RAO, and P. C. SINHA, (1997). Storm surge prediction and frequency analysis for Andhra coast of India. Mausam 48, 555–566.

RAPER, S. C. B., (1993). Observational data on the relationships between climate change and the frequency and magnitude of severe tropical storms. In: Climate and Sea level change observations, prediction and implications (edited by R. A. Warrick, E. M. Barrow and T. M. L. Wigley), Cambridge University Press, pp. 192–212.

RASOANILANA, R. P. R., (1997). Modelisation a grande echelle de l erosion et de la sedimentation du littoral, Personal Communication.

RAYLEIGH LORD (J. W. STRUTT), (1945). Theory of sound, Dover, New York.
READING, A. J., (1990). Caribbean tropical storm activity over the past four centuries, International Journal of Climatology, 10, 365–376.
REDFIELD, A. C., and A. R. Miller, (1957). Water levels accompanying Atlantic coast hurricanes, In Interaction of sea and atmosphere. Met. Monogr. 2, 1–23.
REED, R. J., (1979). Cyclogenesis in polar air streams. Mon. Weather Rev. 107, 38–52.
REID, R. O., (1975). Comment on Three-dimensional structure of storm-generated currents, by G. Z. Forristall. J. Geophys. Res. 80, 1184–1187.
REID R. O., (1990). Water level changes, handbook of coastal and ocean engineering, J. Herbich edited, Gulf Publishing, Houston, U.S.A.
REID, R. O., and B. R. BODINE, (1968). Numerical model for storm surges in Galveston Bay. Proc. American Soc. Civil Eng. J. Waterways Harbors Div. 94(WW1), 33–57.
REID, R. O., A. C. VASTANO, and T. J. REID, (1977a). Development of Surge II Program with application to the Sabine-Calcasieu area for Hurricane Carla and design hurricanes. Tech. Pap. No. 77–13, Nov. 1977. U. S. Army Corps of Engineers, Coastal Eng. Research Center, Fort Belvoir, VA. 218 p.
REID, R. O., A. C. VASTANO, R. E. WHITAKER, and J. J. WANSTROTH, (1977b). Experiments in storm surge simulation, p. 145–168. In E. D. Goldberg, I. N. McCave, J. J. O'Brien, and J. H. Steele [ed.] The Sea, vol. 6 Chap. 5. Wiley Interscience Publication, New York, NY. 1048 p.
REID, R. O., and R. E. WHITAKER, (1976). Wind-driven flow of water influenced by a canopy, J. Waterways Harbors and Coastal Eng. Div. WW1, Feb. 1976, 61–77.
REITAN, C. H., (1974). Frequencies of cyclones and cyclogenesis for North America, 1951–1970. Mon. Weather Rev. 102, 861–868.
REITAN, C. H., (1979). Trends in the frequencies of cyclone activity over North America. Mon. Weather Rev. 107, 1684–1688.
REN, MEI-E, (1993). Relative sea level changes in China over the last 80 years, Journal of Coastal Research, 9, 229–241.
REN, MEI-E, (1994). Relative sea level rise in China and its socioeconomic implications. Marine Geodesy, 17, 37–44.
RESIO, D. T., and C. L. VINCENT, (1977). Estimation of winds over the Great Lakes. J. Waterway Port Coastal and Ocean Div. Proc. American Soc. Civil Eng. WW2, 265–283.
REVELL, C.G., and S.W. GOULTER, (1986). South Pacific tropical cyclones and the Southern Oscillation. Mon. Wea. Rev., 114, 1138–1145.
RICHARDSON, L. F., (1922). Weather prediction by numerical process. Cambridge University Press, London and New York.
RICHTMEYER, R. D., (1957). Difference methods for initial value problems. No. 4. Inter-science, New York, NY.
RICHTMEYER, R. D., (1963). A survey of difference methods for non-steady fluid dynamics. NCAR Tech. Notes 63–2, 25 p.
RIEHL, H., (1954). Tropical meteorology. McGraw-Hill Publications, New York, NY. 392 p.
RIEHL, H., (1956). Sea surface temperature anomalies and hurricanes. Bull. Am. Meteorol. Soc. 37, 413–417.
RIEHL, H., (1979). Climate and weather in the tropics. Academic Press, New York, NY. 611 p.
RINGE-JORGENSEN, C., (1958). High-water problems on the Danish North Sea coast, p. 115–133. In J. W. Johnson [ed.] Proc. 6th Conf. Coastal Eng., Dec. 1957, Florida. Council on Wave Research, The Engineering Foundation.
ROBERT, A. J., (1966). The integration of a low order spectral form of the primitive meteorological equations. J. Meteorol. Soc. Jpn. Ser. 2, 44, 237–245.
ROBERTS, K. V., and N. O. WEISS, (1966). Convective difference schemes. Math. Comp. 20, 272–299.
RODENHUIS, G. S., O. BRINK-KJAER, and J. A. BERTELSEN, (1978). A North Sea Model for Detailed Current and Water-Level Predictions. In: Jour. of Petrol. Techn.
ROELOFS, E. W., and D. R. BUMPUS, (1953). The hydrography of Pamlico Sound. Woods Hole Oceanogr. Inst. Collect. Repr. No. 547, 181–205.
ROHDE, H., (1977). Sturmfluthöhen und säkularer Meeresspiegelanstieg an der deutschen Nordsseküste. In: Die Küste, 30, S. 52–143.

ROLL, H. U., and R. E. WHITAKER, (1965). Physics of the Marine Atmosphere, Academic Press, New York, 426 pp.

RONDAY, F. C., (1973). Modele mathematique pour 1', etude de la ciraulation dua a la Mareee en mer du Nord, Marine Sciences Directorate , Canada, 29, 42 pp.

ROSENTHAL, S. L., (1970). A circularly symmetric primitive equation model of tropical cyclone development containing an explicit water vapour cyclone. Mon. Weather Rev. 98, 643–663.

ROSENTHAL, S. L., (1978). Numerical simulation of tropical cyclone development with latent heat release by the resolvable scales. 1. Model description and preliminary results, J. Atmos. Sci. 35, 258–271.

ROSS, B. E., and P. JERKINS, (1977). A comparison of the application of two computer models of Tampa Bay, Florida, p. 91–101 . In C. A. Brebbia [ed.] Applied numerical modelling. Proc. 1st Int. Conf. Appl. Numer. Model, July 11–15, 1977, University of Southampton, Southampton, U.K. John Wiley & Sons Ltd., New York, NY.

ROSSITER, J. R., (1954). The North Sea storm surge of January 31 and February 1943. Philos. Trans. Roy. Soc. London Ser. A 251, 139.

ROSSITER, J. R., (1971). Long period waves: seiches, surges and tides in coastal waters, p. 155–168. In D. A. Howells, 1. P. Haigh, and C. Taylor [ed.] Dynamic waves in civil engineering. Wiley Interscience, New York, NY. 575 p.

ROY, G. D., (1984). Numerical storm surge prediction in Bangladesh. Ph. D. Thesis, Indian Institute of Technology, Delhi, pp. 188.

ROY, G. D., (1995). Estimation of expected maximum possible water level along the Meghna estuary using a tide and surge interaction model. Environment International, 21, 671–677.

ROY, G. D., (1999a). Inclusion of off-shore islands in a transformed coordinates shallow water model along the coast of Bangladesh, Environment International, 25, 67–74.

ROY, G. D., (1999b). Sensitivity of water level associated with tropical storms along the Meghna estuary in Bangladesh, Environment International, 25, 109–116.

RUDOLPH, E., (1999). Negative Storm Surges in the Elbe. Personell communication.

RUNCHAL, A. K., (1975). Numerical model for storm surge and tidal run-up studies. Vol. II. ASCE, New York, NY.

RUSSELL, H. C., (1898). The source of periodic waves. Nature (London) 62, 493–494.

RYAN, B. F., I. G. WATTERSON, and J. L. EVANS, (1992). Tropical cyclone frequencies inferred from Gray's yearly genesis parameter: Validation of GCM tropical climates. Geophys. Res. Let., 19, pp. 1831–1834.

SADLER, J. E., and R. E. GIDLEY, (1973). Tropical cyclones of the North Indian Ocean. UHMET-73–02, Mar. 1973. Department of Meteorology, University of Hawaii at Manoa, Honolulu, HI.

SANDERS, F., A. L. ADAMS, N. J. R. GORDON, and W. D. JENSEN, (1978). A study of forecast errors in a barotropic operational model for predicting paths of tropical storms, p. 389–396. Proc. 11th Tech. Conf. Trop. Meteorol., Dec. 13–16, 1977, Miami Beach, FL.

SANDERS, F., and R. W. BURPEE, (1968). Experiments in barotropic hurricane track forecasting. J. Appl. Meteorol. 7(3), 313–323.

SAUNDERS, P. M., (1977). Wind stress on the ocean over the eastern continental shelf of North America. J. Phys. Oceanogr. 7, 555–566.

SCHAFER, P. J., (1966). Computation of a storm surge at Barrow, Alaska. Arch. Meteorol. Geophys. Biolkimatol. Ser. A 15, 372–393.

SCHALKWIJK, W. F., (1947). A contribution to the study of storm surges on the Dutch coast. K. Ned. Meteorol. Inst. De Bilt, No. 125, Medeelingen Envertandelingen Ser. B, 111 p.

SCHEFFNER, N. W., D. J. MARK, C. A. BLAIN, J. J. WESTERINK, and R. A. LUETTICH, (1994). ADCIRC: – An Advanced Three-dimensional Circulation Model for Shelves, Coasts and Estuaries, Report 5. A tropical storm data base for the East and Gulf of Mexico coasts of the United States, Dredging Research program, Tech. Rept. DRP-92-6, August 1994, U. S. Army Corps of Engineers, Washington, D.C., U.S.A, 48 pages plus appendices.

SCHLOEMER, R. W., (1954). Analysis and synthesis of hurricane wind patterns over Lake Okeechobee, Florida. Hydrometeorol. Rep. No. 31, Mar. 1954. U.S. Weather Bureau, Washington, DC. 49 p.

SCHMITZ, H. P., D. HABICHT, and H. VOLKERT, (1988). Barotropic numerical experiments on external surge generation at the edge of the north western European shelf. – Gerlands Beitr. Geophysik (97) 5, 422–437.

SCHNACK, E. J., (1993). The vulnerability of the east coast of South America to sea level rise and possible adjustment strategies, In the "Climate and sea level change: Observations, projections and implications' (Edited by R. A. Warrick, E. M. Barraw, and T. M. Wigley), Cambridge University Press, 336–348.

SCHWAB, D. J. (1978). Simulation and forecasting of Lake Erie storm surges. Mon. Weather Rev. 106, 1476–1487.

SCHWAB, D. J., (1982). An inverse method for determining wind stress from water level fluctuations, Dynamics of atmospheres and oceans, 6, 251–278.

SCHWAB, D. J., and E. W. LYNN, (1987). Great Lakes storm surge planning program (SSPP), NOAA. Tech Memo, ERL. GLERL-65, 9 pages.

SCHWERDT, R. W., (1976). Revised values of parameters for the probable maximum hurricane and standard project hurricanes, p. 126–127. Proc. Conf. Coastal Meteorol., Sept. 21–23, 1976, Virginian Beach, VA. American Meteorological Society, Boston, MA.

SCHWERDT, R. W., (1978). Reduction of overwater wind speed when intense hurricanes move overland, p. 490–495. Proc. 11th Tech. Conf. Hurricanes Trop. Meteorol. Dec. 13–16, 1977, Miami Beach, FL. American Meteorological Society, Boston, MA.

SCHWIDERSKI, E. W., (1980). On chanting global ocean tides. Rev. Geophys. Space Phys., 18, 243–268.

SEKIOKA, M., (1970). On the behavior of cloud patterns as seen on satellite photographs in the transformation of a typhoon in to an extra-tropical cyclone. J. Meteorol. Soc. Jpn. 48, 224–233.

SEKIOKA, M., (1972a). A kinematical consideration on behavior of a front within a typhoon area. Arch. Meteorol. Geophys. Bioklimatol. Ser. A 21, 1–12.

SEKIOKA, M., (1972b). A note on the extratropical transformation on a typhoon in relation with cold outbreaks. Arch. Meteorol. Geophys. Bioklimatol. Ser. A 21, 413–418.

SETHURAMAN, S., (1979). Atmospheric turbulence and storm surge due to Hurricane Belle (1976). Mon. Weather Rev. 107, 314–321.

SHAPIRO, L. J., (1982a). Hurricane climatic fluctuations: Part I: Patterns and cycles. Mon. Wea. Rev., 110, 1007–1013.

SHAPIRO, L. J., (1982b). Hurricane climatic fluctuations. Part II: Relation to the large-scale circulation. Mon. Wea. Rev., 11, 1014–1040.

SHAPIRO, L. J., (1987). Month-to-month variability of the Atlantic tropical circulation and its relationship to tropical cyclone formation. Mon. Wea. Rev., 115, 2598–2614.

SHAPIRO, L. J., (1989). The relationship of the Quasi-Biennial Oscillation to Atlantic tropical storm activity. Mon. Wea. Rev. 117, 1545–1552.

SHAW, SIR NAPIER, (1921). Forecasting weather. 2nd ed. British Meteorological Office, London, U.K.

SHAW, S. L., (1979). Central North Pacific tropical cyclones, 1978. Mar. Weather Log 23, 166–172.

SHEETS, R. C., (1969). Some mean hurricane sounding. J. Appl. Meteorol. 8, 134–146.

SHEETS, R. C., and N. E. LASEUR, (1978). Project Stormfury: present status – future plans, p. 280–287. Proc. 11th Tech. Conf. Hurricanes Trop. Meteorol., Dec. 13–16, Miami Beach FL.

SHILLINGTON, F. A. (1984). Long period edge waves off southern Africa Cont. Shelf Res. 3, 343–357.

SHILLINGTON, F. A., and D. VAN FOREEST, (1986). Numerical model studies of long period edge-waves, J. Phys. Oceanogr.16, 1487–1492.

SHIN D. H., (1994). Storm surge problem and technique in Korea, Notes of Korea Meteorological Administration, Seol, 24 p.

SHUMAN, F. G., (1957). Numerical methods in weather prediction. II. Smoothing and filtering. Mon. Weather Rev. 85, 357–361.

SIEFERT, W., (1968). Sturmflutvorhersage für den Tidebereich der Elbe aus dem Verlauf der Windstaukurven in Cuxhaven. In: Mitteilungen des Franzius-Institutes für Grund- und Wasserbau der TU Hannover, 30, 1–142.

SIEFERT, W., (1974). Über den Seegang in Flachwassergebieten. In: Leichtweiß-Institut für Wasserbau der Technischen Universität Braunschweig, 40.

SIEFERT, W., (1978a). Storm surge prediction in tidal rivers: a new conception. Proc. 16th Coastal Eng. Conf., Aug. 27–Sep. 3, 1978, Hamburg, Germany, Published by ASCE, New York, 986–997.

SIEFERT, W., (1978b). Über das Sturmflutgeschehen in Tideflüssen. In: Mitteilungen des Leichtweiß-Institutes für Wasserbau der TU Braunschweig, 63.

SIEFERT, W., (1979). Sturmflutanalyse und -vorhersage über die Windstaukurven. In: Die Küste, (34), S. 87–101.

SIEFERT, W., (1980). Sturmflutvorhersage-Verfahren für Küsten und Flüsse im Tidegebiet. In: Jahrbuch der Hafenbautechnischen Gesellschaft, 37, S. 221–234.

SIEFERT, W., (1982). Bemerkenswerte Veränderungen der Wasserstände in den deutschen Tideflüssen. In: Die Küste, 37, S. 1–36.

SIEFERT, W., (1988a). Einige Anmerkungen zur Sturmflutentwicklung im Nordsee Küstengebiet. In: HANSA-Schiffahrt-Schiffbau-Hafen, Cuxhaven. (125) 20, S. 1301–1306 (S. 217–224).

SIEFERT, W., (1988b). Einige Anmerkungen zur Sturmflutentwicklung im Nordsee-Küstengebiet. In: Jahrbuch der Hafenbautechnischen Gesellschaft, (43), S. 217–225.

SIEFERT, W., (1990). Sea level changes and tidal flat characteristics, In the 'Expected effects of climate change on Marine coastal ecosystems' (Edited by J. J. Beukema, W. J. Wolft, and J. J. W. M. Brouus), Kluwer Academic Publishers, The Netherlands, pp. 105–112.

SIEFERT, W., (1991). Hydrologische Grundlagen des Hochwasserschutzes in Hamburg und entlang der Elbe. In: Hamburger Küstenforschung, 47.

SIEFERT, W., (1998). Auswertung der Ergebnisse des Projektes für den HTG-Ausschuß Küstenschutzwerke, Empfehlungen G. (unpublished.).

SIEFERT, W., (1998). Bemessungswasserstände 2085A entlang der Elbe . Ergebnisse einer Überprüfung durch die Länderarbeitsgruppe nach 10 Jahren 1995/1996. In: Die Küste, Heft 60, p. 227–255.

SIEFERT, W., and K. HAVNOE, (1989). Sturmfluuntersuchungen für die Elbe mit mathematisch-hydraulischen Modellen des Dänisch Hydraulischen Institutes. In Hamburger Küstenforschung, 46.

SIEFERT, W., K. HAVNOE, and A. KEJ, (1987). Storm Surge Forecasting Facilities for an Estuary. In: 2nd. Intern. Conf. on Port and Coastal Eng. in Developing Countries, Beijing.

SIEFERT, W., and H. LASSEN, (1985). Gesamtdarstellung der Wasserstandsverhältnisse im Küstenvorfeld der Deutschen Bucht. In: Die Küste, 42, S. 1–77.

SIEFERT, W., and J. JENSEN, (1993). Mean sea level at the German coast, Marine Geodesy, 16, 43–56.

SIELECKI, A., (1968). An energy-conserving difference scheme for the storm surge equations. Mon. Weather Rev. 96, 150–156.

SIELECKI, A., and M. G. WURTELE, (1970). The numerical integration of the non-linear shallow water equations with sloping boundaries. J. Computat. Phys. 6, 219–236.

SILVESTER, R., (1971). Computation of storm surge, p. 1995–2010. Proc. 12th Conf. Coastal Eng. Vol. 3. ASCE, New York. NY.

SIMONS, T. J., (1973). Development of three-dimensional numerical models of the Great Lakes Sci. Ser. No. 12. Inland Waters Directorate, Canada Center for Inland Waters, Burlington, Ont. 26 p.

SIMONS, T. J., (1975). Effective wind stress over the Great Lakes derived from long term numerical model simulations. Atmosphere 13, 169–179.

SIMONS, T. J., (1978). Wind driven circulations in the southwest Baltic, Tellus 30, 272–283.

SIMONS, T. J., (1980). Circulation models of lakes. Bull. Fish Res. Board Can. 203, 146 p.

SIMONS T. J., and W. M. SCHERTZER, (1989). Modeling wind-induced set up in lake St. Clair, J. Of Great Lakes Research, 15, 452–464.

SIMON-TOV, M., (1974). A time-dependent, two-dimensional mathematical model for simulating the hydraulic, thermal and water quality characteristics in shallow water bodies. ORNL-TIvi-4626. Oak Ridge National Lab, Tennessee.

SIMPSON, R. H., (1952). Exploring the eye of Typhoon Marge 1951. Bull. Am. Meteorol. Soc. 33, 286–298.

SIMPSON, R. H., and H. RIEHL, (1981). The hurricane and its impact. Louisiana State University Press, Baton Rouge, LA. 398 p.

SINGH, S. V., C. M. MOHILE, and S. R. INAMDAR, (1987). Relationships of southern oscillation and other large scale features with Bay of Bengal cyclones during the post monsoon season, Advance in Atmospheric Science, 4, 169–174.

SINHA, P. C., S. K. DUBE, A. K. MITRA, and T. S. MURTY, (2000). A tidal flow model for the Gulf of Kachchh, West coast of India, Marine Geodesy, 23, 117–132.

SINHA, P. C., S. K. DUBE, A. D. RAO, and P. CHITTIBABU, (1993). Mathematical Modelling of Storm Surges in the Bay of Bengal – Proceedings of the First Annual Conference of "Indian Society of Industrial and Applied Mathematics", Roorkee University, Roorkee, February 4–7, pp. 92–97.

SINHA, P. C., S. K. DUBE, A. D. RAO, and G. S. RAO, (1984). Numerical simulation of the surge generated by the 1982 Gujarat cyclone, Vayu Mandal, 14, 31–33.

SINHA, P. C., S. K. DUBE, and G. D. ROY, (1983). Numerical storm surge prediction in Bangladesh – Proc. of the 12th Nat. Conference on Fluid Mech. and Fluid Power, New Delhi, December 8–10, pp. 215–218.

SINHA, P. C., S. K. DUBE, and G. D. ROY, (1985). Influence of a river on the storm surges in the Bay of Bengal – Proceedings of the International Workshop on Operational Applications of Mathematical Models in Developing Countries, New Delhi, Feb. 26–March 1, Vol. I, pp. 365–373.

SINHA, P. C., S. K. DUBE, G. D. ROY, and SUNIL JAGGI, (1986). Numerical simulation of storm surges in Bangladesh using a multilevel model. Int. J. of Numerical Methods in Fluids 6, 305–311.

SINHA, P. C., Y. R. RAO, S. K. DUBE, and T. S. MURTY, (1997). Effect of sea level rise on tidal circulation in Hoogly Estuary, Bay of Bengal. Marine Geodesy. 20, 341–366.

SINHA, P. C., Y. R. RAO, S. K. DUBE, and A. D. RAO, (1996). Numerical investigation of tide-surge interaction in Hooghly estuary, India, Marine Geodesy. 19, 235–255.

SMITH, S. D., (1980). Wind stress and heat flux over the ocean in gale force winds. J. Phys. Oceanography, 10, 709–726.

SMITH, S. D., (1988). Coefficients for sea surface wind stress, heat flux, and wind profiles as a function of wind speed and temperature. J. Geophys. Res., 93, 15,467–15,472.

SMITH, S. D., R. J. ANDERSON, W. A. OOST, C. KRAAN, N. MAAT, J. DECOSMO, K. B. KATSAROS, K. L. DAVIDSON, K. BUMKE, L. HASSE, and H. M. CHADWICH, (1992). Sea Surface Wind Stress and Drag Coefficient: The HEXOS results. Boundary Layer Meteorology, 60, 109–142.

SMITH, S. D., and E. G. BANKE, (1975). Variation of the sea surface drag coefficient with wind speed. Quarterly J. Roy. Met. Soc., 101, 665–673.

SNEYERS, R., (1953). La tempete et le débordement de la mer du 1er février 1953. Ciel Terre 69, 97–108.

SNODGRASS, F. E., W. H. MUNK, and G. R. MILLER, (1962). Long period waves over California's continental borderland, 1, background spectra, J. Mar. Res. 20, 3–30.

SOLBERG, H, (1936). Le mouvement d'inertie de Atmosphäre stable et son r61e dans la thdorie des cyclones. P-V. Meteorol., I. U. G. G., Intern II, 66–82. Edinburgh, U.K.

SOM, N. C., and D. SOM, (1995). A review of the preventive measure for reduction of impact of cyclone and flood in coastal areas of Bay of Bengal. A case study. Bangkok. (Hydrocoast – A contribution to the UNESCO-IHP-Project H-2-2).

SOMMERFELD, A., (1949). Partial differential equations. Academic Press, New York, NY. 333 p.

SRINIVASAN, V., A. R. RAMAKRISHNAN, and R. JAMBUNATHAN, (1978). Cyclones and depressions in the Indian seas in 1978, Mausam, 31, 495–506.

STEERS, J. A., (1954). The east coast floods: January 31–February 1, 1953. Proc. Conf. North Sea Floods. Weather 9, 280–298.

STEIN, O., and A. HENSEN, (1994). A reconstructed time series of the number of extreme low pressure events since 1880. Meteorol. Zeitschrift, N. F. 3. Jg. H. 43–46.

STEPHENSON, D. B., (1993). GCM response of northern winter stationary waves and storm tracks to increasing amounts of storm tracks to increasing amounts of carbon dioxide. J. Clim. 6, 1859–1870.

STIGGE, H. J., (1993). Sea level changes and high-water probability on the German Baltic Coast, of the International Workshop on Sea level changes and their consequences for Hydrology and Water Management, 19–23 April 1993, Noordwijkerhout, Netherlands, pp. 19–27.

STIGGE, H. J., (1999). Storm Surges in the Baltic Sea. Written correspondence, unpublished.

SÜNDERMANN, J., and W. LENZ, (1983). North Sea Dynamics, Springer-Verlag, Berlin. Heidelberg, 693 pp.

SUNDQVIST, H., (1970a). Numerical simulation of the development of tropical cyclones with a ten layer model. Part 1. Tellus 22, 359–390.

SUNDQVIST, H., (1970b). Numerical simulation of the development of tropical cyclones with a ten level model. Part 11. Tellus 22, 504–510.

STOKES, G. G., (1847). On the theory of oscillatory waves. Trans. Cambridge Philos. Soc. 8, 441.

STORCH, H. VON, H. LANGENBERG, and T. POHLMANN, (1998). Stürme, Seegang und Sturmfluten im Nordostatlantik. In: lozan, J. L., and H. Grassl, and P. Hupfer (1998): Das Klima des 21. Jahrhunderts. Hamburg, 182–189.

STRAVISI, F., (1972). A numerical experiment on wind effects in the Adriatic Sea, p. 187–196. Accad. Naz. Lincei, Estratto dal fase 2. Ser. VIII. February 1972, Rome.

STRIEM, H. L., (1974). Storm surges and unusual sea levels on Israel's Mediterranean Coast. Int. Hydrogr. Rev. 51, 59–70.

STRYBNY, J., (1999). Hochauflösende Seegangsmodellierung mit BOWAM2 im Hafen und Küstennahfeld. HTG-Kongressband 1999, Hafenbautechnische Gesellschaft Hamburg.

SVANSSON, A., and J. SZARON, (1975). Sea level computations of the Baltic with a 20 canal model. Tellus 27, 596–605.

SWAMINATHAN, D. R., (1966). The extra-ordinary path of the Bay of Bengal storm of December 7–15, 1965, in relation to the Tiros 10 satellite observations and the upper tropospheric wind field. Indian J. Meteorol. Geophys. 20, 357–360.

SWANSON, R. H., (1976). Tides in Marine ecosystem analysis (MESA), New York.

TA IJAARD, J. J., (1967). Development, distribution and movement of cyclones and anticyclones in the Southern Hemisphere during the I.G.Y. J. Appl. Meteorol. 6, 973–987.

TAKAHASHI, K., (1939). Distribution of pressure and wind in a typhoon. J. Meteorol. Soc. Jpn. 17, 417–421.

TANCRETO, A. E., (1958). A method for forecasting the maximum surge at Boston due to extratropical storms. Mon. Weather Rev. 86, 197–200.

TANG, Y. M., ROGER GRIMSHAW, BRIAN SANDERSON, and GREG HOLLand, (1996). A Numerical study of Storm Surges and tides, with Application to the North Queensland Coast. Jr. of Phys. Oceangr. 26. 2700–2711.

TAYLOR, C., and J. DAVIS, (1972). Tidal and long wave propagation – a finite element approach. C/R/ 189/72. Department of Civil Engineering, University College of Swansea, U.K.

TAYLOR, C., and P. HOOD, (1973). A numerical solution of the Navier-Stokes equations using the finite element technique. Comput. Fluids 1, 73–100.

TENNEKES, H., and J. L. LUMLEY, (1972). A first course in turbulence. MIT Press, Cambridge, Mass.

TEPPER, M., (1950a). A proposed mechanism of squall lines: the pressure jump-line. J. Meteorol. 7(l), 21–29.

TEPPER, M., (1950b). On the generation of pressure jump lines by the impulsive addition of momentum to simple current systems. J. Meteorol. 12, 287–297.

TERADA, K., (1939). On „tsunami" or destructive sea waves excited by a travelling typhoon. Mem. Imp. Mar. Obs. Kobe, Japan 7, 209–230.

TERADA, K., (1912). Secondary undulations of tides caused by cyclonic storms. Proc. Tokyo Math-Phys. Soc. 2nd Ser. 6, 196–201.

TERADA, T., and S. YAMAGUTI, (1928). On the effect of cyclones upon sea level. Proc. Imp. Acad. Jpn. 28, 478–480.

TETRA, Tech. Inc., (1978). Coastal flooding storm surge model. Part I: Methodology. Prepared by Tetra Tech. Inc. for the U. S. Department of Insurance Administration, Washington, DC. May 1978.

THACKER, W. C., (1977). Irregular grid finite difference techniques: simulations of oscillations in shallow circular basins. J. Phys. Oceanogr. 7, 284–292.

THAW, S. H., (1998). Storm surges and status of prediction in Myanmar. Report to the Myanmar-India Workshop on Oceanography of the Bay of Bengal and the Andman Sea. November 25–28, 1998 Yangon, Myanmar, 19 p.

THOMPSON, C., S. READY, and X. ZHENG, (1992). Tropical cyclones in the South West Pacific: November 1979 to May 1989. National Institute of water and Atmospheric Research Report, pp. 35.

THOMPSON, R. D., (1981). Weather, Bracknell, U.K., 138–140.

TIMMERMAN, H., (1971). On the connection between cold fronts and gust bumps. Ditsch. Hydrogr. Z. 24, 159–172.

TIMMERMAN, H., (1975). On the importance of atmospheric pressure gradients for the generation of external surges in the North Sea. Dtsch. Hydrogr. Z. 28, 62–71.

TINTORE, J., D. GOMIS, S. ALONSO, and D. P. WANG, (1988). A Theoretical study of large sea-level oscillations in the western Mediterranean, J. Geophys. Res. C9, 2804–2830.

TOMASIN, A., and R. FRASETTO, (1979). Cyclogenesis and forecast of dramatic water elevations in Venice. In J. C. J. Nihoul [ed.] Marine Forecasting. Proc. 10th Int. Liège Colloq. Ocean Hydrodyn. Elsevier Oceanogr. Ser. 25, 427–438.

TOMCZAK, V. G., (1950). Die Sturmfluten vom 9. und 10. Februar 1949 an der Deutschen NordseekOste. Dtsch. Hydrogr. Z. 3, 227–240.

TÖPPE, A., (1993). Longtime cycles in mean tidal levels, Proceedings of the International Workshop on Sea level changes and their consequences for Hydrology and Water Management, 19–23 April 1993, Noordwijkerhout, Netherlands, pp. 133–143.

TOWNSEND, J., (1979). The storm surge of January 11–12, 1978. Meteorol. Mag. 108, 147–153.

TREWARTHA, G. T., (1968). An introduction to climate. McGraw-Hill Publications, New York, NY. 408 p.

TRONSON, K. C., and B. J. NOYE, (1973). Numerical Simulation of tides in the South Australian gulfs. In proceedings of the second Australian Regional Conference on physical Oceanography, pp. 217. The University of Adelaide.

TSCHIRHART, G., (1958). Les conditions aérologiques à l'avant des lignes de grains en Afrique Equatoriale. Meteorol. Natl. Monogr. Roll. 28 p.

TSENG-HAO, C., and F. SHIS-ZAO, (1975). A preliminary study on the mechanism of shallow water storm surges Sci. Sin. 18, 242–261.

UENO, T., (1964). Nonlinear numerical studies on tides and surges in the central part of Seto Inland Sea. Oceanogr. Mag. 16, 53–124.

UENO, T., (1981). Numerical computations of the storm surges in Tosa Bay. J. Oceanogr. Soc. Jpn. 37, 61–73.

UFFORD, H. A. Q., (1953). The disastrous storm surge of February 1. Weather 8, 116–120.

UNOKI, S., (1959). An investigation on meteorological tides in the neighboring seas of Japan. IV. General features of regional distribution and seasonal variation. Occanogr. Mag. 11, 51–63.

URSELL, F., (1952). Edge waves on a sloping beach. Proc. Roy. Soc. London Ser. A 214, 79–97.

VAN HAMME, J. L., (1979). Observations and studies of the cyclogenesis in the Ligurian Sea, p. 493–509. I.O.C. Workshop Rep. No. 17. Supplement papers submitted to the Joint I.O.C./W.M.O. Seminar on oceanographic products and the I.G.O.S.S. data processing and services system, Apr. 2–6, 1979, Moscow.

VASTANO, A. C., and R. O. REID, (1967). Tsunami response for islands: verification of a numerical procedure. J. Mar. Res. 25, 129–139.

VECCHIO, G., (1980). A study of storm surges along the Adelaide foreshore, Meteorological Note 107, Bureau of Meteorology, Dept. of Science and the Environment, May 1980, Regional Office, Adelaide, 13 pages.

VENKATESH, S., and M. B. DANARD, (1976). A model for computing small scale wind variations over a water surface. Report of the Atmospheric Dynamics Corn, Dec. 1976, Elmira, Ont. 45 p.

VERBOOM, G. K., J. G. DE RONDE, and R. P. VAN DUK, (1992). A fine grid tidal flow and storm surge model of the North Sea. In: Continental Shelf Research, 2–3, pp. 213–233.

VERMA, A. P., and R. G. DEAN, (1969). Numerical modelling of hydromechanics of bay systems, p. 1069–1087. In. Civil Engineering in the oceans. Part II. ASCE Conf., Dec. 10–12, 1969, Miami Beach, FL.

VITTORI, O., and F. TAMPIERI, (1979). Venice: sea-lagoon exchange in a modified tide regime. Science (Washington, DC) 204, 261–264.

VLADIMIR, E. R., O. I. ZILBERSTERIN, and W. SIEFERT, (1996). Storm Surges WMO / TD – No. 779 pp. 121.

VONGVISESSOMJAI S., (1994). Personal communication, Storm Surges in Southeast Asia, unpublished report, Asian Institute of Technology, Bangkok, 109 pages.

VRIES, H. DE, M. BRETON, T. DE MULDER, Y. K RESTENITIS, J. OZER, R. PROCTOR, K. RUDDICK, J. C. SALOMON, and A. VOORRIPS, (1995). A comparison of 2D storm surge models applied to three shallow European seas. In: Elsvier (10) 1, pp. 23–42.

WADATI, K., and T. HIRONO, (1954). Storm tides caused by typhoons. Proc. UNESCO Symp. Typhoons: 31–48.

WALLEN, C. C., (1970). Climates of northern and western Europe, p. 9–205. World survey of climatology. Vol. 5. Elsevier Press, Amsterdam, The Netherlands.

WALSH, K., and A. B. PITTOCK, (1998). Potential changes in tropical storms, hurricanes, and extreme rainfall events as a result of climate change, Climate Change, 39, 199–213.

WALTERS, R. A., (1983). Numerically induced oscillations in finite element approximations to the shallow water and equations, Int. J. Numer. Method. Fluids, 3, 591–604.

WALTERS, R. A., (1988). A finite element model for tides and currents with field applications, Comm. Applied Numerical Methods 4, 401–11.

WALTERS, R. A., (1992). A three-dimensional, finite element model for coastal and estuarine circulation, Continental Shelf Res., 12, 83–102.

WALTERS, R. A., and E. J. BARRAGY, (1996). Comparison of *h* and *p* finite element approximations of the shallow water equations', Int. J. Numer. Water Fluids, 16.

WALTERS, R. A., and V. CASULLI, (1998). A Robust, finite element model for hydrostatic surface water flows, Communications in Numerical Methods in Engineering, 14, 931–940.

WALTERS, R. A., and R. T. CHENG, (1980a). Calculations of estuarine residual currents using the finite element method. In D. H. Norric [ed.] Proc. 3rd Int. Conf. Finite Elem. Flow Probl. University of Calgary, Calgary, Alta.

WALTERS, R. A., and R. T. CHENG, (1980b). Accuracy of an estuarine hydrodynamic model using smooth elements, Water Resour. Res., 16, 187–195.

WALTERS, R. A., and F. E. WERNER, (1989). A comparison of two finite element models of tidal hydrodynamics using a North Sea data set, Advances in Water Resources 12(4), 184–93.

WANG, D. P., (1979). Extratropical storm surges in the Chesapeake Bay, p. 323–332. In J. C. J. Nihoul [ed.] Marine Forecasting. Proc. 10th Int. Liège Colloq. Ocean Hydrodyn. Elsevier Oceanogr. Ser. Elsevier Press, Amsterdam, The Netherlands.

WANG, J. D., (1977). Comments on "Irregular grid finite difference techniques: simulations of oscillations in shallow circular basins." J. Phys. Oceanogr. 7, 932–933. Reply by W. C. Thacker. J. Phys. Oceanogr. 7, 933–934.

WANG, J. D., and J. J. CONNER, (1975a). Mathematical modelling of near coastal circulation. Rep. No. MIT SG75-13, Apr. 20, 1975. Sea Grant Program, MIT. 272 p.

WANG, J. D., and J. J. CONNER, (1975b). Finite element model of two payer coastal circulation, p. 2401–2420. Proc. Coastal Eng. Conf., 1975, Copenhagen, Denmark. Chap. 141. Vol. 3.

WANG, X., and J. WANG, (1997). The calculation of maximum elevation due to storm surge by using joint probability method, Mausam, 48, 587–594.

WANG, X., K. LI, Z. YU, and J. WU, (1987). Statistical characteristics of sieches in Longkou Harbour, J. Phys. Oceanogr. 17, 1063–1065.

WANSTRATH, J. J., (1977a). An open coast storm surge model with inland flooding, p. 676–679. Proc. 11th Tech. Conf. Hurricanes Trop. Meteorol., Dec. 13–16, 1977, Miami Beach, FL. American Meteorological Society, Boston, MA.

WANSTRATH, J. J., (1977b). Near shore numerical storm surge and tidal simulation. Tech. Rep. H-77-17. U. S. Army Engineer Waterways Experiment Station, CE, Vicksburg, MS.

WARNECKE, G., (1997). Meteorologie und Umwelt. 354 S. Berlin und Heidelberg.

WATTS, I. E. M., (1959). The effect of meteorological conditions on tide height at Hong Kong. Tech Memo. No. 8. Royal Observatory, Hong Kong. 30 p.

WATTS, I. E. M., (1969). Climates of China and Korea. p. 1–117. Chap. *1.* In H. Arakawa [ed.] Climates of northern and eastern Asia. Survey of climatology. Vol. 8. Elsevier, New York and Amsterdam.

WEARE, T. J., (1976). Finite element or finite difference methods for the two dimensional shallow water equations. Comput. Methods Appl. Mech. Eng. 7, 351–357.

WEBB, D. J., (1976). A model of continental shelf resonances. Deep-Sea Res. 23, 1–15.

WEENINK, M. P. H., (1956). The twin storm surges during December 21–24, 1954: a case of resonance. Dtsch. Hydrogr. Z. 9, 240–249.

WELANDER, P., (1957). Wind action on a shallow sea: some generalizations of Ekman's theory. Tellus 9, 45–52.

WELANDER, P., (1961). Numerical prediction of storm surges, p. 315–317. In H. E. Landsberg, and J. van Miegham [ed.] Advances in geophysics. Vol. 8. Academic Press, New York, NY.

WEMELSFELDER, P. J., (1954). The disaster in the Netherlands caused by the storm flood of February 1, 1953, p. 258271. Proc. 4th Conf. Coastal Eng.

WESTERINK, J. J., and W. G. GRAY, (1991). Progress in surface water modelling. Rev. Geophys. 29, Apr., 210–217.

WESTERINK, J. J., R. A. LUETTICH, A. M. BAPTISTA, N. W. SCHEFFNER, and P. FARRAR, (1992). Tide and storm surge predictions using a finite element model, Journal of Hydraulic Engineering 118, 1373–90.

WESTERINK, J. J., R. A. LUETTICH, C. A. BLAIN, and N. W. SCHEFFNER, (1993a). "ADCIRC: An advanced three-dimensional circulation model for shelves, coasts and estuaries; Report 2: Users manual for ADCIRC-2DDI," Technical Report DRP-92-6, Coastal Engineering Research Center, U. S. Army Engineer Waterways Experiment Station, Vicksburg, MS.

WESTERINK, J. J., R. A., LUETTICH, and N. W. SCHEFFNER, (1993b). "ADCIRC: An advanced three-dimensional circulation model for shelves, coasts and estuaries; Report 3, Development of a tidal constituent database for the western North Atlantic and Gulf of Mexico," Technical Report DRP-92-6, Coastal Engineering Research Center, U. S. Army Engineer Waterways Experiment Station, Vicksburg, MS.

WHITTINGHAM, H., (1958). The Bathurst Bay hurricane and associated storm surge. Aust. Meteorol . Mag. 23. 14–36.

WIEGEL, R. L., (1964). Oceanographical engineering Prentice-Hall Inc., Englewood Cliffs, NJ. 532 p.

WILDING, A., M. COLLINS, and G. FERENTINOS, (1980). Analyses of sea level fluctuations in Thermaicos Gulf and Salonica Bay, Northwestern Aegean Sea. Estuarine Coastal Mar. Sci. 10, 325–334.

WILLIAMS, D. T., (1948). A surface micro-study of squall line thunderstorms. Mon. Weather Rev. 76, 239–246.

WILLIAMSON, D., (1999). Finite element model for water levels computation in lake Winnipeg. (Personal Communication), Baird and Associates Coastal Engineers, Ottawa, Canada.

WILSON, B. W., (1959). The prediction of hurricane storm tides in New York Bay. Rep. No. 165–3, Oct. 1959. Department of Oceanography and Meteorology. Texas A&M University, College Station, TX.

WILSON, B. W., (1961). The prediction of hurricane storm tides in New York Bay (discussion). Tech. Memo. No. 120-A. Beach Erosion Board, U. S. Army Corps of Engineers, Washington, DC.

WILSON, J. W., (1978). Meteorological considerations for use in storm surge models. Presented at the 58th annual meeting of the American Meteorological Society, Feb. 1, 1978, Savannah, GA.

WINCHESTER, P., (1979). Disaster relief operations in Andhra Pradesh, southern India, following the cyclone in November 1977. Disasters 3, 173–177.

WOLF, J., (1978). Interaction of tide and storm surge in a Semi- infinite uniform channel, with application to surge propagation down the east coast of Britain. Appl. Math. Model. 2, 245–253.

WORLD METEOROLOGICAL ORGANIZATION (WMO), (1975). Typhoon modification. WMO No. 408. Geneva, Switzerland. 141 p.

WMO, (1978). Present techniques of tropical storm surge prediction. Rep. No. 13. Marine Science Affairs, WMO No. 500. Geneva, Switzerland. 87 p.

WMO, (1988). Hydrological Aspects of Combined effects of Storm Surges and Heavy Rainfall on River Flow. In. Oper. Hydrology Report, 30, 704.

WMO, (1990). Proc. WMO Second International Workshop on Tropical Cyclones (IWTC-II), WMO/TD No. 83, WMO Geneva Switzerland, (in Press).

WROBLEWSKI, A., (1978). Stochastic computations of Baltic storm surges in Nowy Port. Pap. No. 135. Summ. 16th Int. Conf. Coastal Eng., Aug. 27-Sept. 3. 1978, Hamburg, W. Germany.

WU, J., (1980). Wind-stress coefficients over sea surface near neutral conditions: a revisit. J. Phys. Oceanography, 10, 727–740.

WU, J., (1982). Wind stress coefficients over sea surface from sea breeze to hurricane. J. Geophys. Res., 87, 9704–9706.

WU, X., and R. A. FLATHER, (1992). Hindcasting waves using a coupled wave-tide-surge model. Third Int. Workshop on Wave Hindcasting and Forecasting, Environment Canada, 159–170.

WU, X., R. A. FLTHER, and J. WOLF, (1994). A third generation wave model of European continental shelf seas with depth and current refraction due to tides and surges and its validation using GEOSAT and buoy measurements. Rep. No. 33, Proudman Oceanographic Lab., U.K.

WURTELE, M. G., J. PAEGLE, and A. SIELECKI, (1971). The use of open boundary conditions with the storm surge equations. Mon. Weather Rev. 99, 537–544.

YAMAGUCHI, M. et al., (1979). Numerical prediction method for fetch-limited ocean waves. (in Japanese). Proc. 26th. Coastal Engg. Conf. (Japan), 96–100.

YAMAGUTI, S., (1929). On the effect of cyclones upon sea level. Bull. Earthquake Res. Inst. 7, 115–132.

YAMASAKI, M., (1968). Numerical simulation of tropical cyclone development with the use of primitive equations. J. Meteorol. Soc. Jpn. 46, 178–201.

YAMASHITA T., and G. WATSON, (1997). Wind-Wave-Surge Interaction Prediction, In: Recent advances in marine science and Technology, Ed. N. K. Saxena, PACON International, Honolulu, 153–165.

YANG, G., (1996). Hazards from sea level rise and their impacts on resources utilization in the Yangtze River Deltaic plain, China, In Land-based and Marine Hazards (Ed. M. I. El-Sabh, S. Venkatesh, H. Denis, and T. S. Murty), pp. 179–189.

YANTING, ZHANG, and YIJIAO WANG, (1986). A preliminary interaction into the nonlinear interaction between storm surges and astronomical tide during Typhoon No. 8114. Acta Oceanologica Sinica , 8, 283–290.

YANTING, ZHANG, and YIJIAO WANG, (1990). Numerical simulations of the coupling effects between storm surge and astronomical tide, Sea level and current Fields in the Bohai Sea In: storm Surges Observation and Modelling (edited by Chao Jiping, T. S. Murty, Bao Cheanglan, M. I. El- Sabh and Liu Fengshu, China Ocean Press, 71– 81.

YANTING, ZHANG, YONGLIANG ZHAO, and YIJIAO WANG, (1992). Analysis of disaster caused by Typhoon Surge and study of the Numerical prediction methods for the disastrous Sea level. In: Tropical Cyclone Disasters (editors James Ligthill, Greg Holland, Zheng Zhemin, Kerry Emanuel) Peking University Press, Beijing China, 452–459.

YEH, G. T., and F. K. CHOU, (1979). Moving boundary numerical surge model. J. Waterway Port Coastal Ocean Div. Proc. American Soc. Civil Eng. WW3, 247–263.

YEH, G. T., and F. F. YEH, (1976). A generalized model for storm surges, p. 921–933. Proc. 15th Int. Conf. Coastal Eng. July 7–11, 1976, Honolulu, HI. Vol. 1, Chap. 54.

YELLand, M. J. et al., (1994). The use of the inertial dissipation technique for shipboard wind stress determination. J. Atmos. Oceanic Technology. 11, 1093–1108.

YELLand, M. J., and P. K. TAYLOR, (1996). Wind stress measurements from the Open Ocean. J. Phys. Oceanogr. 26, 541–558.

YIM, W. W. S., (1993). Future sea level rise in Hong Kong and possible environmental effects, In: Climate and sera level changes: Observations, Projections and Implications. (Editors: R. A. Warrick, E. M. Barraw, and T. M. L. Wigley), Cambridge University Press, pp. 349–376.

YOUNG, J. A., (1968). Comparative properties of some time differencing schemes for linear and nonlinear oscillations. Mon. Weather Rev. 96, 357–364.

ZHANG, G. Z., W. DROSDOWSKY, and N. NICHOLLS, (1990). Environmental influences on Northwest Pacific tropical cyclone numbers. Acta Meteorologica Sinica, 4, 180–188.

ZHANG, M.Y., and Y. S. LI, (1996). The synchronous coupling of a third-generation wave model and a two-dimensional storm surge model. Ocean Engineering. 23, 533–543.

ZHANG, Y., and Y. WANG, (1989). Numerical modeling of the Sea level under the action of the tide and strong wind in the Bohai Sea. Acta Oceanologia Sinica, 8, 511–520.

ZHU, J. W., and Z. R. XIE, (1995). The trends of sea level change and evaluation on its impacts in the Yangtze River Delta. In ' Sea level changes in China: past, present and future (Ed. Y. F. Shi), Shandong Science and Technology Press, Jinan, pp. 249–348.

ZIENKEWICZ, O. C., (1971). The finite element method in engineering sciences. McGraw-Hill Publications, New York, NY.

ZIPSER, E. J., (1969). The role of organized unsaturated convective downdrafts in the structure and rapid decay of an equatorial disturbance. J. Appl. Meteorol. 8, 799–814.

ZIPSER, E. J., (1977). Mesoscale and convective scale downdrafts as distinct components of squall line structure. Mon. Weather Rev. 105, 1568–1589.

ZISHIKA, K. M., and P. J. SMITH, (1980). The climatology of cyclones and anticyclones over North America and surrounding ocean environs for January and July, 1950–77. Mon. Weather Rev. 108, 387–401.

ZSCHAU, J., (1977). Prediction of storm surges from marine loading tilt measured inland from the sea, p. 787–801. In M. Bonatz, and P. Melchior [ed.] Proc. 8th Int. Symp. Earth Tides, Sept. 19–24, 1977, Bonn, Germany. Institut für Theoretische GeodSsie der Universität Bonn.

ZSCHAU, J., U. CAROW, and R. MEIBNER, (1978). A new geophysical method in forecasting storm surges. Pap. No. 137. Summ. 16th Int. Conf. Coastal Eng., Aug. 27–Sept. 3, 1978, Hamburg, W. Germany. ASCE, New York, NY.

ZSCHAU, J., and H. J. KÜMPEL, (1979). Prediction of storm surges using vertical pendulums. Geophys. Astrophys. Fluid Dyn. 13, 245–252.